

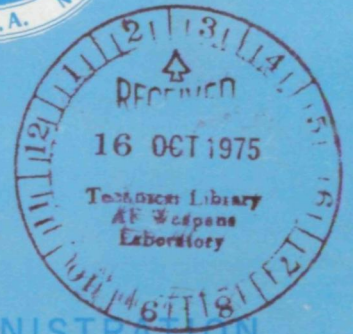
LOAN COPY: RETURN TO
AFWL TECHNICAL LIBRARY
KIRTLAND AFB, NM



AERODYNAMIC ANALYSES REQUIRING ADVANCED COMPUTERS

Part II

A conference held at
LANGLEY RESEARCH CENTER
Hampton, Virginia
March 4 -6, 1975





AERODYNAMIC ANALYSES REQUIRING ADVANCED COMPUTERS

Part II

*A conference held at
Langley Research Center in Hampton, Virginia
on March 4-6, 1975*

Prepared by Langley Research Center



Scientific and Technical Information Office
NATIONAL AERONAUTICS AND SPACE ADMINISTRATION
Washington, D.C.

1975

nc

I

a

ec

av

oc

br

For sale by the National Technical Information Service
Springfield, Virginia 22161
Price - \$17.25

PREFACE

This compilation consists of papers presented at a conference on Aerodynamic Analyses Requiring Advanced Computers held at the NASA Langley Research Center on March 4-6, 1975.

The purpose of the conference was to present results of recent theoretical research on aerodynamic flow problems requiring the use of advanced computers. The conference was divided into the following sessions: (1) Viscous Flows, (2) Internal Flows, (3) Two-Dimensional Configurations, and (4) Three-Dimensional Configurations. Papers were presented by members of NASA Centers, Universities, and Industry.

Page intentionally left blank

CONTENTS

Part I*

PREFACE	iii
-------------------	-----

Cochairmen: Percy J. Bobbitt
Victor L. Peterson
Alfred Gessow

1. INTRODUCTORY REMARKS	1
2. REMOTE ACCESS OF THE ILLIAC IV	9
K. G. Stephens, Jr.	

VISCOUS FLOWS

Studies Involving Boundary-Layer Equations

Chairman: Dennis M. Bushnell

3. CALCULATION OF THREE-DIMENSIONAL COMPRESSIBLE LAMINAR AND TURBULENT BOUNDARY LAYERS	17
PREFACE	17
Julius E. Harris	
AN IMPLICIT FINITE-DIFFERENCE PROCEDURE FOR SOLVING THE THREE-DIMENSIONAL COMPRESSIBLE LAMINAR, TRANSITIONAL, AND TURBULENT BOUNDARY-LAYER EQUATIONS	19
Julius E. Harris	
CALCULATION OF THREE-DIMENSIONAL COMPRESSIBLE BOUNDARY LAYERS ON ARBITRARY WINGS	41
Tuncer Cebeci, Kalle Kaups, Judy Ramsey, and Alfred Moser	
THREE-DIMENSIONAL COMPRESSIBLE BOUNDARY LAYERS OF REACTING GASES OVER REALISTIC CONFIGURATIONS	77
Robert M. Kendall, William S. Bonnett, Charles T. Nardo, and Michael J. Abbett	
4. A NUMERICAL METHOD FOR THE PREDICTION OF HIGH-SPEED BOUNDARY-LAYER TRANSITION USING LINEAR THEORY	101
Leslie M. Mack	

*Papers 1 to 22 are presented under separate cover.

5. SOLUTIONS FOR INCOMPRESSIBLE SEPARATED BOUNDARY LAYERS INCLUDING VISCOUS-INVISCID INTERACTION	125
James E. Carter and Stephen F. Wornom	
6. ON THE CALCULATION OF SUPERSONIC SEPARATING AND REATTACHING FLOWS	151
John D. Murphy, Leroy L. Presley, and W. C. Rose	
7. ASYMPTOTIC THEORY OF TWO-DIMENSIONAL TRAILING-EDGE FLOWS . . .	177
R. E. Melnik and R. Chow	
8. ANALYTICAL STUDY OF MIXING AND REACTING THREE-DIMENSIONAL SUPERSONIC COMBUSTOR FLOW FIELDS	251
A. J. Baker, R. Clayton Rogers, and S. W. Zelazny	

Turbulence Modeling and Navier-Stokes Equations

Chairman: Joseph G. Marvin

9. SUBGRID- OR REYNOLDS STRESS-MODELING FOR THREE-DIMENSIONAL TURBULENCE COMPUTATIONS	317
Morris W. Rubesin	
10. INFLUENCE OF EXTERNAL DISTURBANCES AND COMPRESSIBILITY ON FREE TURBULENT MIXING	341
Youn H. Oh and Dennis M. Bushnell	
11. AN EXPERIMENTAL AND NUMERICAL INVESTIGATION OF SHOCK-WAVE INDUCED TURBULENT BOUNDARY-LAYER SEPARATION AT HYPERSONIC SPEEDS	377
J. G. Marvin, C. C. Horstman, M. W. Rubesin, T. J. Coakley, and M. I. Kussoy	
12. CALCULATION OF SHOCK-SEPARATED TURBULENT BOUNDARY LAYERS	401
B. S. Baldwin and W. C. Rose	
13. SIMULATION OF TURBULENT TRANSONIC SEPARATED FLOW OVER AN AIRFOIL	419
George S. Deiwert, John B. McDevitt, and Lionel L. Levy, Jr.	
14. AN INVESTIGATION OF SEVERAL NUMERICAL PROCEDURES FOR TIME- ASYMPTOTIC COMPRESSIBLE NAVIER-STOKES SOLUTIONS	437
David H. Rudy, Dana J. Morris, Doris K. Blanchard, Charlie H. Cooke, and Stanley G. Rubin	

15. NUMERICAL SOLUTION OF THE NAVIER-STOKES EQUATIONS FOR ARBITRARY TWO-DIMENSIONAL AIRFOILS	469
Frank C. Thames, Joe F. Thompson, and C. Wayne Mastin	
16. NUMERICAL COMPUTATION OF VISCOUS FLOWS ON THE LEE SIDE OF BLUNT SHAPES FLYING AT SUPERSONIC SPEEDS	531
John V. Rakich and Stephen C. Lubard	
17. CALCULATION OF SUPERSONIC THREE-DIMENSIONAL FREE-MIXING FLOWS USING THE PARABOLIC-ELLIPTIC NAVIER-STOKES EQUATIONS	543
Richard S. Hirsh	

INTERNAL FLOWS

Chairman: Bernhard H. Anderson

18. COMPUTATIONAL ASPECTS OF THE PREDICTION OF MULTIDIMENSIONAL TRANSONIC FLOWS IN TURBOMACHINERY	567
David A. Oliver and Panagiotis Sparis	
19. TIME-DEPENDENT TRANSONIC FLOW SOLUTIONS FOR AXIAL TURBOMACHINERY	587
John Erdos, Edgar Alzner, Paul Kalben, William McNally, and Simon Slutsky	
20. A COMPARISON OF A SHOCK-CAPTURING TECHNIQUE WITH EXPERIMENTAL DATA FOR THREE-DIMENSIONAL INTERNAL FLOWS	623
Leroy L. Presley	
21. INTERNAL AND EXTERNAL AXIAL CORNER FLOWS	643
Paul Kutler, Vijaya Shankar, Dale A. Anderson, and Reese L. Sorenson	
22. NUMERICAL METHODS FOR THE CALCULATION OF THREE- DIMENSIONAL NOZZLE EXHAUST FLOW FIELDS	659
Sanford M. Dash and Paul D. Del Guidice	

Part II

TWO-DIMENSIONAL CONFIGURATIONS

Chairman: Alfred Gessow

23. COMPUTERIZED PROCEDURES FOR AIRFOIL DESIGN	703
Raymond L. Barger and Cuyler W. Brooks, Jr.	
24. A COMPUTER PROGRAM FOR THE ANALYSIS OF MULTIELEMENT AIRFOILS IN TWO-DIMENSIONAL SUBSONIC, VISCOUS FLOW	713
Harry L. Morgan, Jr.	
25. APPLICATION OF NUMERICAL OPTIMIZATION TECHNIQUES TO AIRFOIL DESIGN	749
Garret N. Vanderplaats, Raymond N. Hicks, and Earll M. Murman	
26. TSFOIL - A COMPUTER CODE FOR TWO-DIMENSIONAL TRANSONIC CALCULATIONS, INCLUDING WIND-TUNNEL WALL EFFECTS AND WAVE-DRAG EVALUATION	769
Earll M. Murman, Frank R. Bailey, and Margaret L. Johnson	
27. NUMERICAL INTEGRATION OF THE SMALL-DISTURBANCE POTENTIAL AND EULER EQUATIONS FOR UNSTEADY TRANSONIC FLOW	789
Richard M. Beam and William F. Ballhaus	
28. CALCULATION OF INVISCID SHEAR FLOW USING A RELAXATION METHOD FOR THE EULER EQUATIONS	811
Joseph L. Steger and Harvard Lomax	
29. PROGRESS IN APPLICATION OF DIRECT ELLIPTIC SOLVERS TO TRANSONIC FLOW COMPUTATIONS	839
E. Dale Martin	

THREE-DIMENSIONAL CONFIGURATIONS

Subsonic and Supersonic Aircraft

Chairman: Roy V. Harris, Jr.

30. RECENT DEVELOPMENTS IN PROPULSIVE-LIFT AERODYNAMIC THEORY	871
Richard J. Margason, Long P. Yip, and Thomas G. Gainer	

31. SURVEY OF COMPUTATIONAL METHODS FOR LIFT-GENERATED WAKES	897
Vernon J. Rossow	
32. SIMULATION OF UNSTEADY THREE-DIMENSIONAL SEPARATED FLOWS WITH INTERACTING VORTEX FILAMENTS	925
A. Leonard	
33. ADVANCED PANEL-TYPE INFLUENCE COEFFICIENT METHODS APPLIED TO SUBSONIC AND SUPERSONIC FLOWS	939
F. Edward Ehlers, Forrester T. Johnson, and Paul E. Rubbert	
34. SOME RECENT APPLICATIONS OF THE SUCTION ANALOGY TO VORTEX-LIFT ESTIMATES	985
John E. Lamar	
35. A THREE-DIMENSIONAL SOLUTION OF FLOWS OVER WINGS WITH LEADING EDGE VORTEX SEPARATION	1013
James A. Weber, Guenter W. Brune, Forrester T. Johnson, Paul Lu, and Paul E. Rubbert	
36. ADVANCES IN SONIC BOOM THEORY	1033
J. L. Lung, B. Tiegerman, N. J. Yu, and A. R. Seebass	
37. AN INTEGRATED SYSTEM FOR THE AERODYNAMIC DESIGN AND ANALYSIS OF SUPERSONIC AIRCRAFT	1049
David S. Miller and Wilbur D. Middleton	
38. INDICIAL COMPRESSIBLE POTENTIAL AERODYNAMICS AROUND COMPLEX AIRCRAFT CONFIGURATIONS	1067
Luigi Morino and Lee-Tzong Chen	
39. THREE-DIMENSIONAL, SHOCK-ON-SHOCK INTERACTION PROBLEM	1111
Paul Kutler and Leonidas Sakell	

Transonic Aircraft

Chairman: Jerry C. South, Jr.

40. COMPARISONS OF THEORETICAL AND EXPERIMENTAL PRESSURE DISTRIBUTIONS ON AN ARROW-WING CONFIGURATION AT TRANSONIC SPEEDS	1141
Marjorie E. Manro, Edward N. Tinoco, Percy J. Bobbitt, and John T. Rogers	

41. NUMERICAL MODELING OF TUNNEL-WALL AND BODY-SHAPE EFFECTS ON TRANSONIC FLOWS OVER FINTE LIFTING WINGS	1189
Perry A. Newman and E. B. Klunker	
42. COMPARISONS OF COMPUTED AND EXPERIMENTAL PRESSURES FOR TRANSONIC FLOWS ABOUT ISOLATED WINGS AND WING-FUSELAGE CONFIGURATIONS	1213
F. R. Bailey and W. F. Ballhaus	
43. AXISYMMETRIC TRANSONIC FLOW INCLUDING WIND-TUNNEL WALL EFFECTS	1233
Jerry C. South, Jr., and James D. Keller	
44. COMPUTATIONAL TRANSONICS	1269
Paul R. Garabedian	
45. APPROXIMATE METHOD FOR CALCULATING TRANSONIC FLOW ABOUT LIFTING WING-BODY COMBINATIONS	1281
Richard W. Barnwell	
46. RECENT ADVANCES AND CONCEPTS IN UNSTEADY AERODYNAMICS THEORY	1305
Samuel R. Bland	

Space Shuttle

Chairman: Victor L. Peterson

47. REACTING NONEQUILIBRIUM FLOW AROUND THE SPACE SHUTTLE USING A TIME-SPLIT METHOD	1327
Arthur W. Rizzi and Harry E. Bailey	
48. COMPUTATION OF SHUTTLE NONEQUILIBRIUM FLOW FIELDS ON A PARALLEL PROCESSOR	1351
W. C. Davy and W. A. Reinhardt	
49. FLOW FIELD AND HEATING ON THE WINDWARD SIDE OF THE SPACE SHUTTLE ORBITER	1377
John V. Rakich and Eva B. Pegot	
50. SCALING OF ORBITER AEROTHERMODYNAMIC DATA THROUGH NUMERICAL FLOW FIELD SIMULATIONS	1395
W. D. Goodrich, C. P. Li, C. K. Houston, R. M. Meyers, and L. Olmedo	

51. COMPUTATION OF HIGH-SPEED INVISCID FLOWS ABOUT REAL CONFIGURATIONS	1411
Frank Marconi, Larry Yaeger, and H. Harris Hamilton	
52. NUMERICAL COMPUTATION OF VISCOUS BLUNT BODY FLOWS WITH A PLANAR IMPINGING SHOCK	1457
Terry L. Holst, John C. Tannehill, and John V. Rakich	

19

20

21

22

23

24

25

26

27

28

29

30

31

32

33

34

35

36

37

38

39

40

41

42

43

44

45

46

47

COMPUTERIZED PROCEDURES FOR AIRFOIL DESIGN

By Raymond L. Barger and Cuyler W. Brooks, Jr.
NASA Langley Research Center

SUMMARY

Several airfoil design procedures are described. The first is a procedure for designing an airfoil shape to have a prescribed surface pressure distribution. It is applicable to the design of supercritical as well as subcritical airfoils. The second is a computerized procedure based on the Theodorsen ϵ -function design technique and is essentially incompressible. It also permits prescription of the pressure distribution, but with the additional feature that it provides simple means of controlling important airfoil parameters. The remainder of the discussion is concerned with the application of various techniques based on the ϵ -function theory to specialized design problems.

INTRODUCTION

The in-house airfoil design investigation with which this paper is concerned was initiated as part of the general airfoil research program at Langley. An interesting aspect of this program is the variety of directions that the design problem has taken; for example, supercritical wing sections, general aviation wing sections, helicopter rotor blades, and "span-loader" sections. There are also numerous airfoil characteristics, such as design lift coefficient, ideal angle of attack, pitching moment, shape of the pressure distribution, maximum thickness, and distribution of thickness, that must be controlled in the design process, to a greater or lesser degree, depending on the application.

For example, in the design of helicopter rotor blades, a low pitching moment is an important factor. On the other hand, for general aviation wing sections, the pitching moment is not a primary consideration, but such characteristics as the ideal angle of attack and the design lift coefficient assume a more important role. For supercritical wing sections, the essential consideration is the shape of the compressible flow pressure distribution. For a "span-loader" section, the pitching moment again becomes important together with such factors as the distribution of thickness and the design lift coefficient. Of course, the maximum thickness has to be controlled in all these applications.

To handle such a variety of design problems, a number of design procedures have been developed. Several of them are described briefly in this paper, and some examples are discussed.

SYMBOLS

A_1, A_2	Fourier coefficients
c	airfoil chord
c_l	airfoil lift coefficient
$c_{l,0}$	airfoil lift coefficient at zero angle of attack
c_m	airfoil pitching-moment coefficient
c_p	airfoil pressure coefficient
M	Mach number
t	airfoil thickness
x	axial distance with origin at airfoil leading edge
α	angle of attack
α_{ideal}	ideal angle of attack
β	$= \epsilon(\pi)$
δ_1, δ_2	phase angles
ϵ	function relating angular coordinates of near-circle and exact-circle airfoil transformations
φ	angular coordinate of exact-circle transformation of airfoil
ψ	function relating radial coordinates of near-circle and exact-circle airfoil transformations
ψ_0	average value of ψ

DESIGN OF SUPERCRITICAL AIRFOILS FOR A PRESCRIBED PRESSURE DISTRIBUTION

Figure 1 is a schematic outline of a computerized procedure that is intended to provide the designer with one of his most important tools: a means of obtaining the kind of pressure distribution that he wants (ref. 1). This computer program requires an initial airfoil whose pressure distribution, indicated by a solid line, is known. It then tailors the airfoil to obtain the desired pressure distribution, indicated by a dashed line, as nearly as possible within the constraints of the program. A formula based on the streamline curvature momentum equation relates the prescribed changes in local velocity to corresponding changes in local curvature. The new curvature distribution is used to reconstitute, by a purely geometric construction, a revised contour. This contour is then adjusted linearly so that it will have the prescribed trailing-edge thickness. This linear adjustment does not alter the curvature distribution except very slightly at the leading edge of the airfoil, where the pressure has a high positive value anyway. The pressure distribution of the revised airfoil is then computed by means of the Korn-Garabedian analysis program (ref. 2), which is utilized as a subprogram in this procedure. This pressure distribution is compared with the desired distribution, and the process is iterated to obtain a closer approximation to the desired result. This entire procedure is automated without any man-machine interaction.

Inasmuch as neither the Korn-Garabedian program used in the analysis phase of this procedure nor the streamline curvature relation used in the design phase is restricted to subsonic flow, the entire procedure is applicable not only to the compressible flow case but even to the design of supercritical airfoils. The procedure is not limited to a particular class of airfoils, and there are no small perturbation or linearization limitations. Furthermore, it can be used to design for a pressure distribution prescribed at a positive or a negative angle of attack.

The example shown in figure 2 was calculated to demonstrate the applicability of the procedure in the presence of shock waves. On the original airfoil the initial supersonic expansion is terminated by a shock, with subsequent reexpansion followed by a second shock. The prescribed distribution replaces these two shocks with a single weaker shock at an intermediate location. As can be seen in the figure, this distribution is fairly closely obtained.

DESIGN APPLICATION OF THE ϵ -FUNCTION THEORY

The streamline curvature design method is also applicable at low speeds, but for such applications another method, which is in some respects more versatile, is more often used. This method is based on the Theodorsen transformation (ref. 3), as indicated

in figure 3. The ψ -function and ϵ -function shown in this scheme are theoretically obtained by comparing successive conformal mappings of the airfoil, first into an approximate circle and then into an exact circle. The abscissa φ for these functions is the angular coordinate on the circle. The point at zero corresponds to the leading edge of the airfoil; the interval $(0, \pi)$ corresponds to the upper surface; and the interval $(\pi, 2\pi)$ corresponds to the lower surface, from the trailing edge back to the leading edge.

In actual practice ψ can be calculated directly from the airfoil coordinates. Then its average value ψ_0 is obtained, and ϵ is calculated as the conjugate function of $\psi - \psi_0$. The pressure distribution can then be computed from the ψ - and ϵ -functions.

This theory is admittedly complicated, but it is invaluable in airfoil design work because the ψ - and ϵ -functions have an almost "magical" quality in the way that they control in a simple manner the important airfoil characteristics. For example, ψ_0 controls the thickness of the airfoil and the level of the pressure-distribution curves (but not their shape). The value of ψ at the leading edge determines the leading-edge radius, and the value of ψ in the trailing-edge region determines the trailing-edge angle and the pressure recovery. The ordinate β of ϵ at π is the negative of the angle of zero lift. Consequently, β is very closely proportional to the lift at zero angle of attack. The value of ϵ at zero and the value of β determine the ideal angle of attack and the design lift coefficient. If the ϵ -function is resolved into its Fourier components, the pitching moment is determined by the coefficients of only the two lowest modes.

Furthermore, small variations in the pressure distribution are approximately proportional to local changes in the slope of the ϵ -function. Consequently, the ϵ -function theory can also be used to obtain a prescribed pressure distribution, according to the following procedure (refs. 4 and 5):

- (1) Calculate the pressure distribution of the initial airfoil and assign the desired changes.
- (2) From these prescribed changes in the pressure distribution, compute the corresponding variations in the slope of the ϵ -function.
- (3) By integration, obtain the new ϵ -function. Adjustments to the ϵ -function to insure that it satisfies the appropriate mathematical constraints are included in the computer program.
- (4) Obtain the function $\psi - \psi_0$ as the conjugate of ϵ .
- (5) Assign a value to ψ_0 to obtain the desired thickness.
- (6) From ψ and ψ_0 , compute the revised airfoil coordinates.

(7) Iterate, if necessary, to obtain a closer approximation.

Once the various calculations indicated in figure 3 have been computerized, a number of design short cuts or "tricks" become available. The discussion of two specialized design problems which follows may give an indication of the versatility of the ϵ -function theory.

DESIGN OF AIRFOIL FAMILIES

Figure 4 represents a design problem in which it is desired to maintain the basic form of the pressure distribution of the original airfoil and to increase the lift by 20 percent without changing the thickness. To accomplish this result, one increases the slope of the ϵ -function over the interval $(0, \pi)$ by a constant so as to increase β by 20 percent. Over the interval $(\pi, 2\pi)$, the slope is decreased by the same amount. The result is a nearly constant increase in suction on the upper surface with a corresponding decrease on the lower surface, and the lift is consequently increased.

To generate a family of airfoils in which the various members have different lift values, the slope of the ϵ -function is simply altered by the various appropriate constants. Then, in order to vary the thickness ratios of the members of the family, one varies the parameter ψ_0 .

An alternate procedure that can be used to generate airfoil families is to multiply the ϵ -function by an appropriate factor. For example, the factor required to increase the lift by 20 percent would be 1.2. The corresponding ψ -function is then automatically changed by the same factor, but the thickness can be varied at will since the parameter ψ_0 is entirely arbitrary (ref. 6).

Another approach to the problem of designing families is to use the thin airfoil theory (ref. 7); that is, multiply the basic camber line ordinates by an appropriate constant to obtain the desired lift and superpose various multiples of the thickness distribution. The problem with this method is that, although the desired lift is obtained, the superposition of velocities approximation is not uniformly valid. Consequently, airfoil shapes generated by this method often have unsatisfactory pressure distributions and, therefore, require considerable tailoring.

LOW-PITCHING-MOMENT AIRFOIL DESIGN

A second specialized problem of current interest is that of designing airfoils which are characterized by a low value of the pitching-moment coefficient. Again, it is possible to apply the thin airfoil superposition theory to this problem, inasmuch as it is relatively easy to specify camber line parameters that will yield desired values for lift and

pitching moment. However, as has already been stated, such designs usually require extensive tailoring.

An approach that is not limited by thin airfoil approximations is indicated in figure 5. This procedure does not modify an initial airfoil but starts at the ϵ -function phase in the design process (see fig. 3). A two-Fourier-component formula is assumed for the ϵ -function (ref. 3), and this form also determines the conjugate $\psi - \psi_0$. Five arbitrary parameters are involved: the two amplitudes A_1 and A_2 , the phase angles δ_1 and δ_2 , and the parameter ψ_0 , the average value of ψ . The pitching moment about the aerodynamic center can be expressed in terms of these five parameters by a complicated highly nonlinear relation. Four of the parameters (ψ_0 , A_1 , A_2 , δ_1) are selected to provide desired values of lift, thickness ratio, etc., and then the relation is solved by means of an interval-halving algorithm for the value of δ_1 that yields the specified value for the pitching moment.

The calculations shown in figure 5 for the sample case include the boundary layer at a chord Reynolds number of 6×10^6 . It is seen that very low pitching-moment values are obtained with a reasonable positive lift at zero angle of attack.

CONCLUDING REMARKS

Several airfoil design techniques have been developed and computerized. These include a procedure applicable to the design of a supercritical section for a prescribed surface pressure distribution. Other methods, based on the ϵ -function theory, although essentially incompressible, are appropriate for certain specialized design problems as well as for designing for a prescribed pressure distribution. These techniques do not exhaust the available means for designing airfoils, but they are representative of the methods that have been studied in the course of this investigation.

REFERENCES

1. Barger, Raymond L.; and Brooks, Cuyler W., Jr.: A Streamline Curvature Method for Design of Supercritical and Subcritical Airfoils. NASA TN D-7770, 1974.
2. Garabedian, P. R.; and Korn, D. G.: Analysis of Transonic Airfoils. Commun. Pure & Appl. Math., vol. 24, no. 6, Nov. 1971, pp. 841-851.
3. Theodorsen, T.; and Garrick, I. E.: General Potential Theory of Arbitrary Wing Sections. NACA Rep. 452, 1933.
4. Theodorsen, Theodore: Airfoil-Contour Modifications Based on ϵ -Curve Method of Calculating Pressure Distribution. NACA WR L-135, 1944. (Formerly NACA ARR L4G05.)
5. Barger, Raymond L.: A Modified Theodorsen ϵ -Function Airfoil Design Procedure. NASA TN D-7741, 1974.
6. Barger, Raymond L.: On the Use of Thick-Airfoil Theory to Design Airfoil Families in Which Thickness and Lift Are Varied Independently. NASA TN D-7579, 1974.
7. Allen, H. Julian: General Theory of Airfoil Sections Having Arbitrary Shape or Pressure Distribution. NACA Rep. 833, 1945.

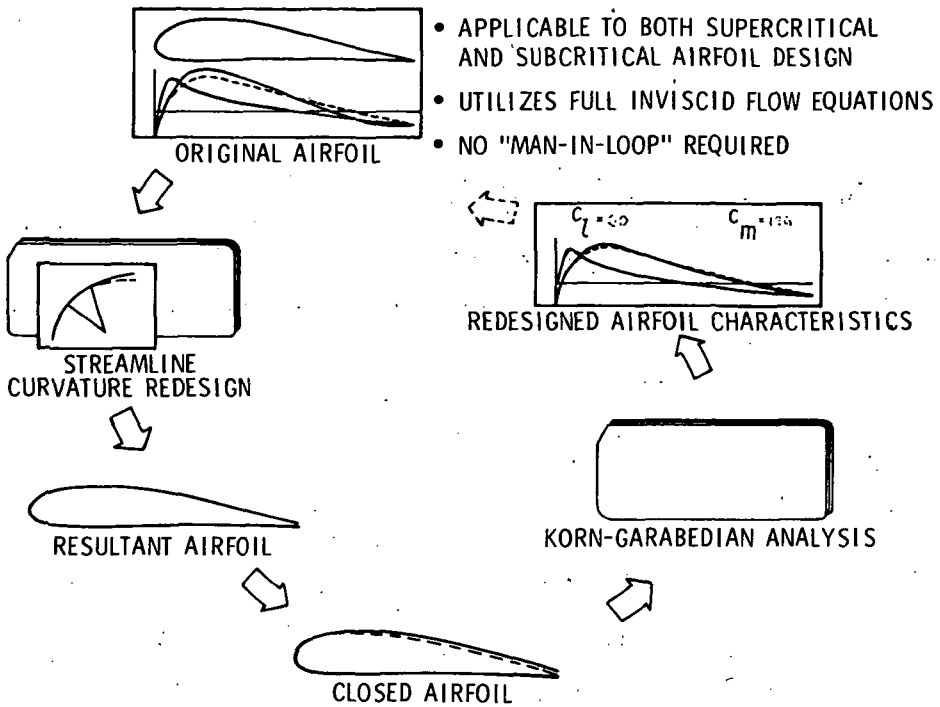


Figure 1.- Streamline curvature approach to airfoil design.

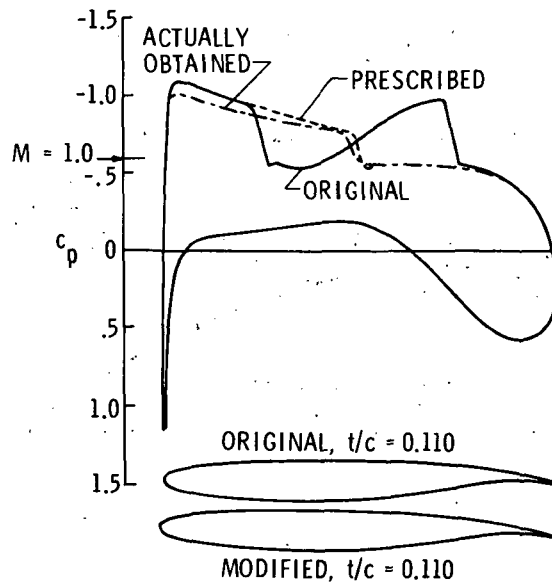


Figure 2.- Example of streamline curvature design method.

$\alpha = 0$; $M = 0.75$.

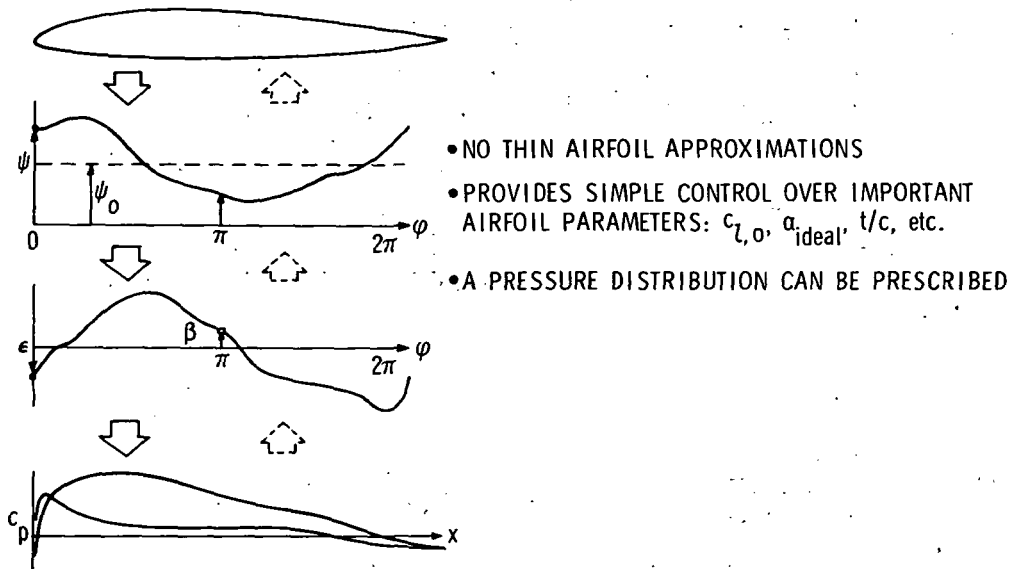


Figure 3.- Airfoil design using Theodorsen ϵ -function.

DESIGN GOALS FOR THIS EXAMPLE:

- INCREASE LIFT BY 20%
- RETAIN SAME t/c VALUE
- MAINTAIN SIMILAR PRESSURE DISTRIBUTION

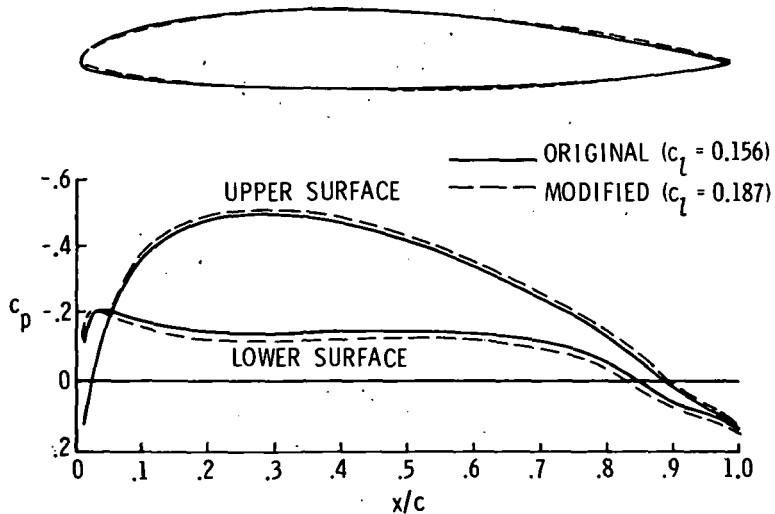
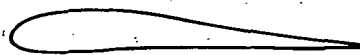
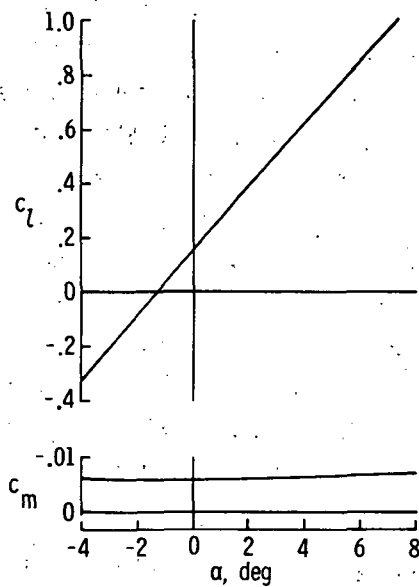


Figure 4.- Example of technique for generating airfoil families.



$$\epsilon(\varphi) = A_1 \sin(\varphi - \delta_1) + A_2 \sin(2\varphi - \delta_2)$$

$$\psi - \psi_0 = A_1 \cos(\varphi - \delta_1) + A_2 \cos(2\varphi - \delta_2)$$

$$c_m = f(\psi_0, A_1, A_2, \delta_1, \delta_2)$$

Figure 5. - Low-pitching-moment airfoil design from special ϵ -function formula.

A COMPUTER PROGRAM FOR THE ANALYSIS OF MULTIELEMENT AIRFOILS IN TWO-DIMENSIONAL SUBSONIC, VISCOUS FLOW

By Harry L. Morgan, Jr.
NASA Langley Research Center

SUMMARY

A computerized analytical model which computes the performance characteristics of multielement airfoils in subsonic, viscous flow has been developed under NASA contract to the Lockheed-Georgia Company. The model computes the viscous pressure distributions, lift, moments, and local boundary-layer properties on each element of an arbitrarily arranged slotted airfoil in attached flow. The final viscous solution is obtained by an iterative technique for successively combining an inviscid solution with boundary-layer displacement thicknesses. The surface of each airfoil element is approximated as a closed polygon with segments represented by distributed vortex singularities. The ordinary boundary-layer solution is comprised of mathematical models representing state-of-the-art technology for laminar, transition, and turbulent boundary layers. An additional boundary-layer model has been incorporated to compute the characteristics of a confluent boundary layer which reflects the merging of the upper-surface boundary layer with the slot efflux.

This computer program has been used extensively at Langley and throughout the industrial and academic communities for both the design and the analysis of airfoils. Presented in this paper are summary descriptions of the general operation and capabilities of this program and a detailed description of the major improvements that have been made to the program since its initial formulation. Sample comparisons between theoretical predictions and experimental data are presented for several types of multielement airfoils. Areas of agreement and disagreement are discussed with recommendations for areas of needed program improvement.

INTRODUCTION

During the initial design phase of an airfoil the effects of various modifications can be easily evaluated by describing the potential (inviscid) flow around the airfoil. Many methods are available to compute the potential flow and most generally require rather small computer storage and execution times, which make them very desirable during the initial trial-and-error design phase. However, during the final design phase a more

accurate assessment of the selected modification can be evaluated by describing the viscous (viscid) flow around the airfoil, which means simply that the boundary-layer properties have been included in the analysis.

No general, mathematically closed form solution presently exists which describes the viscous flow around an airfoil. Until very recently, airfoil design has relied mainly on potential-flow theory to obtain the theoretical pressure distribution from which the boundary-layer properties were approximated, with the interrelationship between the two being largely ignored. However, the use of iterative techniques has provided a practical solution for defining the interrelationship between the potential and viscous flows around an airfoil. State-of-the-art technology in the areas of potential flow and boundary layers, plus the availability of high-speed large-capacity computers, has provided the background capability essential to the formulation of computer codes to compute accurately the performance of an airfoil in viscous flow.

One such computer code used extensively at the Langley Research Center and throughout the industrial and academic communities was developed by the Lockheed-Georgia Company under NASA Contract NAS 1-9143 in 1969. This computer program, entitled "2-D Subsonic Multi-Element Airfoil Program," was formulated to handle single-element and multielement airfoils (a maximum of four elements) in subsonic, viscous flow. A complete description of this original program is given in detail in reference 1. Since the initial formulation of this program, there has been a continuing effort to improve and modify the program to handle an ever increasing range of airfoil geometries. The initial debugging and general program maintenance and improvements have been performed through in-house efforts at Langley. The only other major contribution to the program improvement has been the work done by Delbert C. Summey and Neill S. Smith under NASA Grant NGR 34-022-179 to North Carolina State University. Their work was concerned primarily with the single-element version of the program and consisted of program modifications to improve the lift and drag predictions, to reduce the computer storage requirement, and to reduce the computer execution time. A detailed description of their work is presented in reference 2.

A summary description of the general operation and capabilities of the airfoil program and detailed descriptions of the major changes to it are presented in this paper. Sample comparisons between theoretical predictions and experimental data are also presented for several airfoil geometries. Areas of agreement and disagreement are discussed with recommendations for areas of needed program improvement.

SYMBOLS

a_1, a_2, a_3 coefficients of quadratic equation of the form $f(x) = a_1x^2 + a_2x + a_3$

A_{ij}	aerodynamic influence coefficient
c	chord of airfoil, cm (in.)
c_d	section profile-drag coefficient
c_f	skin-friction coefficient
c_l	section lift coefficient
c_m	section quarter-chord, pitching-moment coefficient
c_n	section normal-force coefficient
c_p	local static-pressure coefficient, $\frac{P_{\text{static}} - P_{\infty}}{q_{\infty}}$
H	boundary-layer form factor, δ^*/θ
K	local curvature, cm^{-1} (in ⁻¹)
M	Mach number
N	number of corner points for polygon approximation of airfoil
p	static pressure, N/m^2 (lb/ft ²)
q_{∞}	free-stream dynamic pressure, N/m^2 (lb/ft ²)
R_{θ}	Reynolds number based on momentum thickness, $\frac{v\theta}{\nu}$
s	surface distance along airfoil contour, cm (in.)
U_e	velocity at edge of boundary layer, m/sec (ft/sec)

U_{∞}	free-stream velocity, m/sec (ft/sec)
v	local velocity on airfoil surface, m/sec (ft/sec)
x	airfoil abscissa, cm (in.)
z	airfoil ordinate, cm (in.)
α	angle of attack of airfoil, deg
γ	strength of vortex singularity, m^2/sec (ft^2/sec)
δ	boundary-layer thickness, cm (in.)
$\delta_{f,s}$, or ν	angular deflection of flap, slat, or vane, deg
δ^*	boundary-layer displacement thickness, cm (in.)
θ	boundary-layer momentum thickness, cm (in.)
ν	kinematic viscosity, m^2/sec (ft^2/sec)
ϕ	cosine distribution angle, $\phi_i = \frac{i\pi}{N}$, deg
ψ	stream function, m^2/sec (ft^2/sec)

Subscripts:

c	control point
i	matrix row
j	matrix column
l	lower
te	trailing edge

u upper
 ∞ free stream

Abbreviations:

B.L. boundary layer
NC number of components
TE trailing edge

PROGRAM OPERATION AND CAPABILITIES

The original airfoil program developed by the Lockheed-Georgia Company was designed to handle single-element and multielement airfoils. As many as four elements can be handled which typically consist of an airfoil with a leading-edge slat device and a double-slotted trailing-edge flap system. The airfoil program is composed of three main parts: (1) geometry specification, (2) potential flow, and (3) boundary layer. The non-overlay version of the program requires a computer storage of approximately 200 000 octal locations (CDC 6600) and an execution time of approximately 200 CPU seconds for a typical four-element airfoil. An overlay version has reduced the required storage to approximately 65 000 octal locations with only a slight increase in execution time. The single-element version developed by North Carolina State University requires a computer storage of approximately 110 000 nonoverlay octal locations and 53 000 overlay octal locations with execution times of the order of 30 CPU seconds for a single case.

A flow chart of the single-element version of the airfoil program is presented in figure 1. After data input and geometry specification (subroutine READIT and GEOM), the program enters an iterative cycle which involves the determination of interrelationship between the potential flow and the boundary layer (subroutines MAIN2 and MAIN3). After each iteration a convergence check is made which consists of a simple comparison of the computed normal-force coefficients. Experience has shown that only five iterations are necessary to obtain a converged solution. This rapid convergence is possible because of the unique method used to combine the physical airfoil geometry and the computed displacement thicknesses from the boundary-layer computations in order to obtain the next iteration geometry. This convergence method will be discussed further in a following portion of this paper.

The flow chart for the multielement version is very similar to that for the single-element version, the exceptions being an expanded geometry routine to handle the posi-

tioning of the elements relative to one another and an additional boundary-layer routine to handle the merging of boundary layers between fore and aft elements (confluent boundary layers). A program routine was available in the original multielement version to correct the pressures in the slot regions between elements to account for the high frictional and surface curvature effects. This routine employed a marching-type calculation procedure which required an accurate definition of the slot inlet conditions. An empirical formula was derived to estimate the inlet conditions from the potential-flow solution. Experience has shown that this slot-analysis routine produces erroneous results and it has, therefore, been omitted from the more recent program version.

Since the inception of the airfoil program, the program input has been kept as simple as possible to make it more user oriented. The coordinates of each element of a multielement airfoil can be input with respect to a separate coordinate system and easily positioned relative to other elements by specifying the pivot point location and deflection of the element. The boundary-layer transition location (transition from laminar to turbulent) on each surface of an element can be input as either fixed or free. The total number of calculation points at which the pressures are desired can also be input and will be automatically allocated using the formula

$$N_i = 2 \left[\left(\frac{N_{sp} - 21N_c}{4} \right) \frac{c_i}{c_T} + 5 \right] \quad (1)$$

where N_i is the number of points allocated to the i th element, N_{sp} is the total number of calculation points, N_c is number of components, c_i is the chord of a given element, and c_T is the summation of the values of c_i . During a single machine pass, the angle of attack and Mach number can be varied for a constant Reynolds number, Prandtl number, and stagnation temperature. To represent the effects of compressibility, the well-known Kármán-Tsien pressure correction law is employed which, therefore, limits the input Mach number to that producing critical flow. The laminar and turbulent boundary-layer routines contain methods to predict boundary-layer separation, but do not contain methods to model the flow after separation. Therefore, the angle of attack should be limited to that producing only minor separation (less than one percent of the surface).

PROGRAM THEORY AND MODIFICATIONS

Airfoil Geometry Specification

The user inputs to the airfoil program are the upper- and lower-surface coordinates of the airfoil shape. The airfoil is modeled within the program as a polygon approximation which is illustrated in figure 2. This polygon consists of N number of corner points with $N - 1$ number of straight line segments. Previous experience has shown that an N equal to 65 is sufficient to obtain an accurate viscous flow solution for a

single-element airfoil. Of the 65 total points, 32 points are distributed on the upper surface, 32 on the lower surface, and 1 at the leading-edge nose location. In most instances, the user desires to input more than 65 coordinates and does not want to be concerned about whether or not the input spacing will affect the computed results. For this reason, an automatic collocation method has been included in the airfoil program.

The original version of the airfoil program distributed corner points with the cosine formula

$$x_i = \frac{c}{2}(1 + \cos \phi_i) \quad (2)$$

where $\phi_i = \frac{i\pi}{N}$, $i = 1, 2, \dots, N$. This procedure is illustrated in figure 3 and a sample distribution shown in figure 4(a). This method, in effect, closely spaces points near the leading and trailing edges of the airfoil. A close spacing near the leading edge is very desirable because of the high curvature and high velocities occurring in that region. Experience has shown, however, that closely spacing points near the relatively thin trailing-edge region can result in extreme oscillations in the computed velocities. The reason for these oscillations is discussed further in the potential-flow portion of this paper. To overcome this problem, a new collocation method has been formulated and incorporated into the airfoil program.

The basis of the new method is that points are spaced relative to the local curvature. This method will closely space points only in regions of high curvature. To utilize this method the curvature at each user input coordinate is computed with the formula

$$K = \frac{a_1 z^2 - \left(a_1 x + \frac{a_2}{2}\right)^2}{\left[z^2 + \left(a_1 x + \frac{a_2}{2}\right)^2\right]^{3/2}} \quad (3)$$

where a_1 , a_2 , and a_3 are taken from a curve fit of the airfoil points of the form

$$z^2 = a_1 x^2 + a_2 x + a_3 \quad (0 \leq x \leq 0.8c) \quad (4)$$

and

$$z = a_1 x^2 + a_2 x + a_3 \quad (0.8c \leq x \leq c) \quad (5)$$

A curvature summation is then computed from the following equation and stored for backward interpolation:

$$\bar{K}_i = \int_0^{s_i} |K|^{1/4} ds \quad (6)$$

where

$$s_i = s_{i-1} + \sqrt{(x_i - x_{i-1})^2 + (z_i - z_{i-1})^2}$$

The maximum value of \bar{K} is divided into N equal portions and the s value corresponding to each portion is then determined by backward interpolation between the s_i and \bar{K}_i arrays. Additional backward interpolations are then made between the s_i , x_i , and z_i arrays to determine the new distributed airfoil coordinates. A sample of the results of this collocation method is presented in figure 4(b). Note the improvement in the distribution of points as compared with the cosine method.

Caution by the user should be exercised regarding the number and relative positions of the input coordinates. If more input points are given, the computation of the curvature summation array will be more accurate and, therefore, the distribution of points more accurate. The curve fit formula of equation (4), which is used in the nose region, is designed to approximate an infinite slope and a better estimation of the high curvature in that region can be obtained if more points are input.

Potential-Flow Solution

The potential-flow methods used to determine the velocity at specified locations on the surface of an airfoil generally fall into two categories. One category consists of conformal transformation methods and the second, singularity distribution methods. Conformal transformation methods have not been greatly utilized because of the difficulties encountered when trying to obtain transformation equations for airfoils of arbitrary shape and because of the inability of this method to handle blunt-base airfoils. Singularity distribution methods have been widely utilized since the advent of the high-speed, high-capacity digital computers which are needed to solve the large systems of simultaneous equations characteristic of these methods. These methods can handle arbitrarily shaped airfoils at any orientation relative to the free stream.

For singularity distribution methods, either source, sink, or vortex singularities are distributed on the surface of the airfoil and integral equations formulated to determine the velocity induced at a point by the singularity. By dividing the airfoil surface into N segments and specifying either zero-normal or a tangential flow boundary condition for each segment, the integral equations can be approximated by a corresponding system of $N - 1$ simultaneous equations. By satisfying the Kutta condition at the trailing edge of the airfoil, the N th equation can be formulated and then the singularity strengths determined with any one of a number of matrix-inversion techniques. The Kutta condition usually employed is that the velocities at the upper- and lower-surface trailing edge be tangent to the surface and equal in magnitude.

The singularity distribution method used in the original version of the airfoil program consisted of a distribution of vortices at the corners of the polygon approximation of the airfoil, with an additional constraint that the vortex strength vary linearly along the surface segments. A control point was selected at the midpoint of each segment and a boundary condition of no flow normal to the surface was applied. This resulted in N unknown vortex strengths and $N - 1$ boundary conditions and equations. An additional equation was obtained by satisfying the Kutta condition at the trailing edge as

$$\gamma_1 = -\gamma_N \quad (7)$$

because, for a vortex singularity, the magnitude of the tangential surface velocity is equal to the vortex strength at the corner point.

Several problems were encountered with the original singularity distribution method. For airfoils with a trailing-edge cusp, the upper- and lower-surface vortices near the trailing edge tend to become identical and, thereby, generate an almost singular matrix. For other types of airfoils, a too close spacing of vortices near the trailing edge results in extreme oscillations of the vortex strengths. This method could not handle airfoils with an open or blunt-base characteristic of the recently developed Langley supercritical or "shockless" airfoils. To overcome these handicaps an improved singularity distribution method has been incorporated into the airfoil program.

The new singularity distribution method was first formulated by H. J. Oellers to compute the pressure distribution on the surface of airfoils in cascade, and is described in reference 3. Instead of working with induced velocities, characteristic of the previous method, Oellers' method employs stream functions. The stream function for a uniform free stream plus that of the vortex sheet is set to be a constant on the airfoil surface. This is represented mathematically by the Fredholm integral equation

$$\psi + \frac{1}{2\pi} \int_0^{ste} \gamma(\xi) \ln [r(s, \xi)] d\xi = U_\infty x(s) \cos(\alpha) - U_\infty z(s) \sin(\alpha) \quad (8)$$

where ψ is the unknown stream function constant, $r(s, \xi)$ is the distance between two points on the airfoil surface, $x(s)$ and $z(s)$ are coordinates of a point on the surface, and $\gamma(\xi)$ is vortex strength at a point. By dividing the surface into N segments and assuming constant vortex strength for each segment the above equation becomes

$$\psi - \sum_{j=1}^N A_{ij} \gamma_j = U_\infty [x_i \cos(\alpha) - z_i \sin(\alpha)] \quad (9)$$

where the influence coefficient A_{ij} is

$$A_{ij} = \int_{s_j}^{s_{j+1}} \ln [r(s_i, \xi)] d\xi \quad (10)$$

By specifying a control point at the midpoint of each segment (denoted by a "c" subscript), the influence coefficient becomes

$$A_{ij} = \frac{1}{4\pi} \left[t_2 \ln(r_2) - t_1 \ln(r_1) \right] - \frac{\Delta s}{2\pi} + \frac{t_3}{2\pi} \left[\tan^{-1} \left(\frac{t_2}{t_3} \right) - \tan^{-1} \left(\frac{t_1}{t_3} \right) \right] \quad (i \neq j) \quad (11)$$

and

$$A_{ij} = \frac{\Delta s}{2\pi} \left[\ln \left(\frac{\Delta s}{2} \right) - 1 \right] \quad (i = j) \quad (12)$$

where

$$\left. \begin{aligned} \Delta s &= s_{j+1} - s_j \\ r_1 &= (x_j - x_{c,i})^2 + (z_j - z_{c,i})^2 \\ r_2 &= (x_{j+1} - x_{c,i})^2 + (z_{j+1} - z_{c,i})^2 \\ t_1 &= \frac{(x_j - x_{c,i})(x_{j+1} - x_j) + (z_j - z_{c,i})(z_{j+1} - z_j)}{\Delta s} \\ t_2 &= \frac{(x_{j+1} - x_{c,i})(x_{j+1} - x_j) + (z_{j+1} - z_{c,i})(z_{j+1} - z_j)}{\Delta s} \\ t_3 &= \frac{(x_j - x_{c,i})(z_{j+1} - z_j) - (z_j - z_{c,i})(x_{j+1} - x_j)}{\Delta s} \end{aligned} \right\} \quad (13)$$

To determine the vortex strength ($\bar{\gamma}$) at the intersection of two segments, the following interpolation formula is used:

$$\bar{\gamma}_j = \frac{\gamma_{j-1}(s_j - s_{j-1}) + \gamma_j(s_{j+1} - s_j)}{s_{j+1} - s_{j-1}} \quad (j \neq 1 \text{ or } N) \quad (14)$$

For this method, an additional equation is needed to obtain an N by N system of equations. (The unknowns are N - 1 number of γ 's and ψ .) A new method of applying the Kutta condition has been formulated to reduce the oscillations of the vortex strengths caused by a too close spacing of points near the trailing edge. This new Kutta condition simply requires that the vortex strengths ($\bar{\gamma}$) vary quadratically for the last four segment corners near the upper and lower surface of the trailing edge and that at the trailing edge

$$(\bar{\gamma}_1)_l = -(\bar{\gamma}_N)_u \quad (15)$$

This quadratic variation is expressed as

$$\bar{\gamma}(s) = a_1 s^2 + a_2 s + a_3 \quad (16)$$

By combining equations (14) and (16), the equation for the vortex strength at the lower-surface trailing edge becomes

$$(\bar{\gamma}_1)_1 = \gamma_1 J_1 + \gamma_2 J_2 + \gamma_3 J_3 + \gamma_4 J_4 \quad (17)$$

where

$$J_1 = \frac{s_4 s_2 (s_3 - s_4)}{D}$$

$$J_2 = \frac{s_4 (s_3 - s_2) (s_3 + s_2 - s_4)}{D}$$

$$J_3 = \frac{s_2 (s_4 - s_3) \left[s_4 + \frac{s_3 (s_2 - s_3)}{s_5 - s_3} \right]}{D}$$

$$J_4 = \frac{s_3 s_2 (s_2 - s_3) (s_5 - s_4)}{D (s_5 - s_3)}$$

and

$$D = s_2^2 (s_3 - s_4) + s_3^2 (s_4 - s_2) + s_4^2 (s_2 - s_3)$$

A similar expression can be obtained for the upper-surface trailing-edge vortex by replacing the subscripts in equation (17) as follows:

$$s_i = s_N - s_{N+1-i} \quad (i = 1, 2, \dots, 5)$$

$$\left. \begin{aligned} J_i &= J_{N-i} \\ \gamma_i &= \gamma_{N-i} \end{aligned} \right\} \quad (i = 1, 2, 3, 4)$$

Combining equations (16) and (17) with equation (15) yields the needed Nth equation in the form

$$\sum J_i \gamma_i = 0 \quad (i = 1, 2, 3, 4, N-4, N-3, N-2, N-1) \quad (18)$$

The Oellers' method with the modified Kutta condition has been incorporated into the current version of the airfoil program. This new potential-flow method combined

with the new geometry specification method has successfully overcome the problems encountered with the original methods.

Boundary-Layer Solution

The pressure coefficients computed in the potential-flow portion of the airfoil program are corrected to account for compressibility with the well-known Kármán-Tsien correction law. Using the isentropic flow relations, the local Mach number is computed and input to the boundary-layer portion of the program. The boundary-layer development on a typical multielement airfoil is illustrated in figure 5. The boundary layer consists of an ordinary boundary layer (nonmerging boundary layer) and a confluent boundary layer (merging boundary layer). The ordinary boundary layer is composed of laminar, transition, and turbulent regions. The confluent boundary layer is composed of core, main I, main II, and turbulent regions as shown in figure 6. The confluent boundary-layer model was developed by Suresh H. Goradia from the Lockheed-Georgia Company and is one of the unique features of this program. The meaningful parameters output from the boundary-layer portion of the program are (1) the displacement thickness δ^* , (2) the momentum thickness θ , (3) the form factor H , and (4) the skin-friction coefficient c_f . The theoretical development of the boundary-layer methods used in this program are quite lengthy and, therefore, only a brief description will be presented in this paper.

A flat-plate boundary-layer analysis is performed on each surface of an airfoil element, and the leading-edge stagnation point is the plate leading edge. A flow chart of the boundary-layer computations is presented in figure 7. An initial laminar boundary-layer region exists from the stagnation point to the point of transition from laminar to turbulent. The laminar boundary-layer model used is the method of Cohen and Reshotko as presented in reference 4. After computing the laminar boundary-layer characteristics at a discrete point, routine BLTRAN is called to check for transition and, if transition has occurred, to check for the formation of a long or short transition bubble and for laminar stall. The sequence of calculations within BLTRAN is presented in figure 8. An initial check is made to determine if the laminar boundary layer is stable or unstable based on the instability criterion established by Schlichting and Ulrich as presented in reference 5. If the boundary layer is unstable, a transition check is then made based on an empirically derived transition prediction curve. If transition has occurred, the initial quantities needed to start the turbulent calculations are computed. If transition has not occurred, the formation of either a long bubble with corresponding laminar stall or a short bubble with corresponding reattachment is determined. The user can input a fixed transition location and a check will be made at the beginning of BLTRAN to determine whether or not the fixed location has been reached.

After computing the transition location and corresponding initial boundary-layer properties, the turbulent boundary-layer calculations are made. The original version of

the program used a modified Truckenbrodt method derived by Goradia to compute the turbulent boundary-layer properties. The Goradia method was less sensitive to local pressure oscillations and was capable of traversing localized separated/reattaching flow regions. These local pressure oscillations were caused primarily by the numerical inaccuracies associated with the potential-flow method. The Goradia method underestimated the boundary-layer displacement thicknesses which, therefore, resulted in an underestimation of the lift and pitching-moment coefficients. After incorporating Oellers' potential-flow method, the pressure oscillations were reduced which meant that the original Truckenbrodt method described in reference 6 could be used to improve the turbulent boundary-layer computations. The original Truckenbrodt method was coded and incorporated into the recent program version and has resulted in an improvement in the estimation of the lift and pitching-moment coefficients.

If a slot exiting plane is reached during the turbulent boundary-layer computations, the confluent boundary-layer computation is initiated. The confluent boundary layer is a result of the mixing between the slot efflux and the wake from the forward element, and can exist from the slot exit to the trailing edge of the element depending upon the pressure distribution. The confluent boundary-layer model was formulated by Goradia and consists of various regions and layers as illustrated in figure 6. The model is based on the assumption that the merging of fore-and-aft element boundary layers will have "similar" velocity profiles if nondimensionalized in a way analogous to that for a free-jet flow. By utilizing this assumption, the governing partial differential equations were reduced to a set of ordinary differential equations which could be easily solved with available numerical techniques. Several empirical constants were needed to establish the similar velocity profiles and were obtained from experimental tests performed by Goradia as reported in reference 7. The only improvement made to the original confluent boundary-layer routines has been minor adjustments in the values of these empirical constants. The model formulated by Goradia assumed that the core velocity exiting the slot is greater than the velocity at the upper edge of the wake layer at the slot exit. Experience has shown that this velocity relationship is not always true and, therefore, erroneous performance predictions can occur. It is generally believed that this velocity relationship should be true for an efficient design and, therefore, no additional work has been done in this area.

None of the boundary-layer methods used in the airfoil program include curvature effects. All the methods used are basically integral methods which are generally less accurate than finite-difference methods but require considerably less computer time. More accurate infinite-difference methods are available, as described in references 8, 9, and 10, and can be easily incorporated into the existing program.

Equivalent Airfoil Geometry

The airfoil program uses an iterative procedure to obtain the viscous solution and the basic steps are as follows:

- (1) Compute a potential-flow solution for the basic airfoil.
- (2) Compute boundary-layer properties based on the potential-flow solution.
- (3) Construct a modified airfoil by adding the boundary-layer displacement thickness to the original airfoil.
- (4) Compute the aerodynamic performance coefficients.
- (5) Repeat steps (1) through (4) until convergence of the performance coefficients is obtained.

The most important step in the iterative procedure is step (3) which involves selecting a geometry modification method that will insure convergence for almost any input airfoil shape in a reasonable number of iterations. The method developed by Lockheed has been highly successful and has provided converged solutions after only four or five iterations.

The method developed by Lockheed to modify the airfoil shape is based on the assumption that the effect of the boundary layer on the basic thickness and basic camber can be considered separately and then superimposed to determine the net effect. The addition of the boundary layer has an uncambering effect near the trailing edge which causes a reduction in the effective angle of attack and lift coefficient, and it has a thickening effect along the airfoil which causes an increase in the local surface velocities and lift coefficient. Experience has shown that the thickness effects are of secondary importance for multielement airfoils and are, therefore, omitted in the multielement program version. Thickness effects are, however, included in the single-element program version to improve the overall accuracy of the performance predictions. The camber change is given as the difference in the magnitude of the upper- and lower-surface displacement thicknesses as illustrated in figure 9(a). The thickness change is given as the difference in two thickness solutions as shown in figure 9(b). The first thickness solution is for a symmetric airfoil at a 0° angle of attack with the same thickness distribution as the original input airfoil. The second thickness solution is also for a symmetric airfoil at a 0° angle of attack with the thickness distribution of the original input airfoil plus the sum of the upper- and lower-surface displacement thicknesses.

Applying superposition and a proportioning technique to prevent over-correction during the initial iterations, the velocity distribution becomes

$$(v_{\text{total}})_i = (v_{\text{camber}})_i + \frac{2}{3}(v_{\text{BT}+\delta^*})_i + \frac{1}{3}(v_{\text{BT}+\delta^*})_{i-1} - k_i(v_{\text{BT}})_1 \quad (19)$$

where BT stands for the basic thickness distribution and

$$k_i = 1 \quad (i \neq 2)$$

$$k_i = \frac{2}{3} \quad (i = 2)$$

The addition of the displacement thickness to obtain the thickness solution often produces a symmetric airfoil with a very thick trailing edge. In actual flow the wake acts as an afterbody with a rapidly decreasing thickness distribution. Based on the work of Powell as reported in reference 11 and from observations of available experimental data, Summey and Smith from the North Carolina State University formulated the following analytical expression to represent the afterbody shape:

$$(z)_{+u} = \pm \frac{1}{2} \left[(z_{te} - z_{\infty}) e^{-6.9xx} + z_{\infty} \right] (1 - xx) \quad (20)$$

where $xx = \frac{x}{c} - 1$ for $c \leq x \leq 2c$ and $z_{\infty} = \frac{1}{2} c_{d_{\infty}} c$. The Squire and Young drag formula from reference 5 is used to compute the drag coefficient at infinity and is given as

$$c_{d_{\infty}} = 2 \left[\frac{\theta_u}{c} \left(\frac{v_{te}}{U_{\infty}} \right)^{\frac{H_u+5}{2}} + \frac{\theta_l}{c} \left(\frac{v_{te}}{U_{\infty}} \right)^{\frac{H_l+5}{2}} \right] \quad (21)$$

After each boundary-layer solution, the displacement thickness distribution is smoothed three times by using a standard least-squares smoothing technique. To prevent over-correction during the initial iterations, a proportioning technique similar to that used for the velocities is used to compute the effective displacement thickness distribution and is given as

$$(\delta_{total}^*)_i = \frac{2}{3} (\delta_{BL}^*)_i + \frac{1}{3} (\delta_{total}^*)_{i-1} \quad (22)$$

where BL stands for the present boundary-layer solution.

COMPARISONS BETWEEN EXPERIMENT AND THEORY

Both the single-element and multielement versions of the airfoil program have been widely distributed and utilized by the industrial and academic communities. The program is widely used within Langley for the design and analysis of new subsonic and transonic airfoils for application to helicopters, general aviation aircraft, and transport aircraft. Shown in figure 10 is a comparison between the theoretical and experimental performance characteristics for the recently developed NASA GA(W)-1 airfoil that was designed by Richard T. Whitcomb especially for application to general aviation aircraft. (See ref. 12.)

Excellent agreement is demonstrated until an angle of attack is reached at which the boundary layer begins to separate near the upper-surface trailing edge. Currently, a flow separation model does not exist in the program; however, a research study is being proposed by Langley in this area of boundary-layer research. Excellent agreement is also demonstrated for the drag prediction of the GA(W)-1 airfoil, but this is not generally true for all airfoils. The method used in the program to compute drag consists of a simple integration of the pressure and shear (skin friction) forces. An improved drag computation method is currently under development by Lockheed-Georgia, under NASA Contract NAS 1-12170, which computes the drag from computed downstream wake characteristics. This improved drag method will be incorporated into the single-element airfoil program after verification at Langley.

A Fowler-type, single-slotted flap was also designed for the GA(W)-1 airfoil and later tested at Wichita State University under a NASA grant. The results of the flapped airfoil tests are presented in reference 13, and a summary of the agreement between experiment and theory is presented in figure 11. Excellent agreement is demonstrated until a 40° flap deflection is reached where separation occurs on the upper surface of the flap. Similar agreement was obtained from tests of a blunt-base airfoil with a single-slotted flap reported in reference 14. Typical agreement between the experimental and theoretical confluent boundary-layer velocity profiles for this airfoil is shown in figure 12. The multielement airfoil program can also be used to perform a gap optimization study of a given flap system. Presented in figure 13 are the results of a gap optimization study for a 10° drooped-nose airfoil with a single-slotted flap as reported in reference 15. The viscous and inviscid theory predictions are also presented in this figure, and although the agreement between viscous theory and experiment is fair, the viscous theory does predict the correct optimum gap of 2 percent.

The agreement between theory and experiment for multielement airfoils with three or more elements has not been generally as good as that for single- or two-element airfoils. This can usually be attributed to the fact that an airfoil with three or more elements generally will have some separated flow on at least one element. Shown in figures 14(a) and 14(b) is the agreement between viscous and inviscid theory and experiment for a typical three-element airfoil with a leading-edge slat and a single-slotted, trailing-edge flap. (See ref. 16.) Excellent agreement is demonstrated over an angle-of-attack range from -4° to 12° for the force and moment coefficients. A typical pressure-distribution agreement is shown in figure 14(b) for an angle of attack of 8° . Shown in figure 15 is the agreement between theory and experiment for a typical four-element airfoil with a leading-edge slat and a double-slotted, trailing-edge flap. (This is model C in ref. 14.) The low $-5^\circ/15^\circ$ vane/flap deflection case showed poor agreement because at those deflections there were large overlap areas between the vane and flap and the airfoil program does not correct the pressure distribution for slot effects. (Previous

discussion pointed out that the original slot flow correction method proposed by Lockheed was erroneous and, therefore, has been dropped from the program.) The high $30^\circ/65^\circ$ deflection case showed very poor agreement because of the large amount of flow separation on the upper surface of the flap element. The intermediate $14^\circ/33^\circ$ case, however, showed good agreement because there were no large overlap or separated flow areas present. Shown also in figure 15 is the extremely poor drag agreement which is typical for multielement airfoil cases.

The sample cases presented in this paper were selected to demonstrate some of the good as well as bad features of the airfoil program. The first major area of needed program improvement is the computation of profile drag. Many researchers use the well-known Squire and Young drag formula (eq. (21)) to compute the profile drag; however, this formula was derived based on a proven erroneous assumption about the variation of the downstream boundary-layer form factor, H . The second major area of improvement is the computation of the characteristics of the flow region after boundary-layer separation. The lack of experimental data for separated flow regions has greatly hampered the development of a theoretical model. Experimental tests have recently been completed at Wichita State University to map the velocities and pressures in the separated regions of the GA(W)-1 airfoil. The third major area of improvement is the computation of the pressure corrections in the slot areas between overlapping elements of multielement airfoils. This area has been of lesser importance because the designer generally desires to have as much Fowler motion (increase in effective chord) as possible which results in relatively small overlap regions.

CONCLUDING REMARKS

This paper has discussed in detail the theoretical and operational features and capabilities of the Langley "2-D Subsonic Multi-Element Airfoil Program." Several major modifications have been made to improve the applicability and prediction accuracy of this program and involve the use of:

- (1) Curvature instead of cosine method to distribute segment corner points for polygon representation of the airfoil
- (2) Oellers' stream function method to obtain the potential-flow solution
- (3) Modified Kutta condition to reduce pressure oscillations at the trailing edge
- (4) Truckenbrodt method to obtain the turbulent boundary-layer characteristics

Comparisons between experimental data and theoretical predictions indicate excellent agreement for single-element airfoils in attached flow and good agreement for multi-

element airfoils in attached flow with small overlap regions between elements. Three major areas of program improvement are needed and involve the computation of:

- (1) Profile drag from downstream wake characteristics
- (2) Flow characteristics after boundary-layer separation
- (3) Pressure corrections in the slot areas between overlapping elements of multi-element airfoils

The airfoil program has been demonstrated as an effective tool for the design and analysis of single-element and multielement airfoils in viscous flow, and has been widely distributed to and utilized by both the academic and industrial communities.

REFERENCES

1. Stevens, W. A.; Goradia, S. H.; and Braden, J. A.: *Mathematical Model for Two-Dimensional Multi-Component Airfoils in Viscous Flow*. NASA CR-1843, 1971.
2. Smetana, Frederick O.; Summey, Delbert C.; Smith, Neill S.; and Carden, Ronald K.: *Light Aircraft Lift, Drag, and Moment Prediction - A Review and Analysis*. NASA CR-2523, 1975.
3. Oellers, Heinz J.: *Incompressible Potential Flow in a Plane Cascade Stage*. NASA TT F-13,982, 1971.
4. Cohen, Clarence B.; and Reshotko Eli: *The Compressible Laminar Boundary Layer With Heat Transfer and Arbitrary Pressure Gradient*. NACA Rep. 1294, 1956. (Supersedes NACA TN 3326.)
5. Schlichting, Hermann (J. Kestin, transl.): *Boundary-Layer Theory*. Sixth ed., McGraw-Hill Book Co., Inc., 1968.
6. Truckenbrodt, E.: *A Method of Quadrature for Calculation of the Laminar and Turbulent Boundary Layer in Case of Plane and Rotationally Symmetrical Flow*. NACA TM 1379, 1955.
7. Goradia, S. H.: *Confluent Boundary Layer Flow Development With Arbitrary Pressure Distribution*. Ph. D. Thesis, Georgia Inst. Technol., 1971.
8. Dvorak, F. A.; and Woodward, F. A.: *A Viscous/Potential Flow Interaction Analysis Method for Multi-Element Infinite Swept Wings*. Volume I. NASA CR-2476, 1974.
9. Callaghan, J. G.; and Beatty, T. D.: *A Theoretical Method for the Analysis and Design of Multi-Element Airfoils*. AIAA Paper No. 72-3, Jan. 1972.
10. Bhateley, I. C.; and Bradley, R. G.: *A Simplified Mathematical Model for the Analysis of Multi-Element Airfoils Near Stall*. *Fluid Dynamics of Aircraft Stalling*. AGARD Conf. Pre-Print No. 102, Apr. 1972, pp. 12-1 - 12-12.
11. Powell, B. J.: *The Calculation of the Pressure Distribution on a Thick Cambered Aerofoil at Subsonic Speeds Including the Effects of the Boundary Layer*. C.P. No.1005, British A.R.C., June 1967.
12. McGhee, Robert J.; and Beasley, William D.: *Low-Speed Aerodynamic Characteristics of a 17-Percent-Thick Airfoil Section Designed for General Aviation Applications*. NASA TN D-7428, 1973.
13. Wentz, W. H., Jr.; and Seetharam, H. C.: *Development of a Fowler Flap System for a High Performance General Aviation Airfoil*. NASA CR-2443, 1974.

14. Omar, E.; Zierten, T.; and Mahal, A.: Two-Dimensional Wind-Tunnel Tests of a NASA Supercritical Airfoil With Various High-Lift Systems. Volume I - Data Analysis. NASA CR-2214, 1973.
15. Foster, D. N.; Irwin, H. P. A. H.; and Williams, B. R.: The Two-Dimensional Flow Around a Slotted Flap. R. & M. No. 3681, British A.R.C., 1971.
16. Harris, Thomas A.; and Lowry, John G.: Pressure Distribution Over an NACA 23012 Airfoil With a Fixed Slot and a Slotted Flap. NACA Rep. 732, 1942.

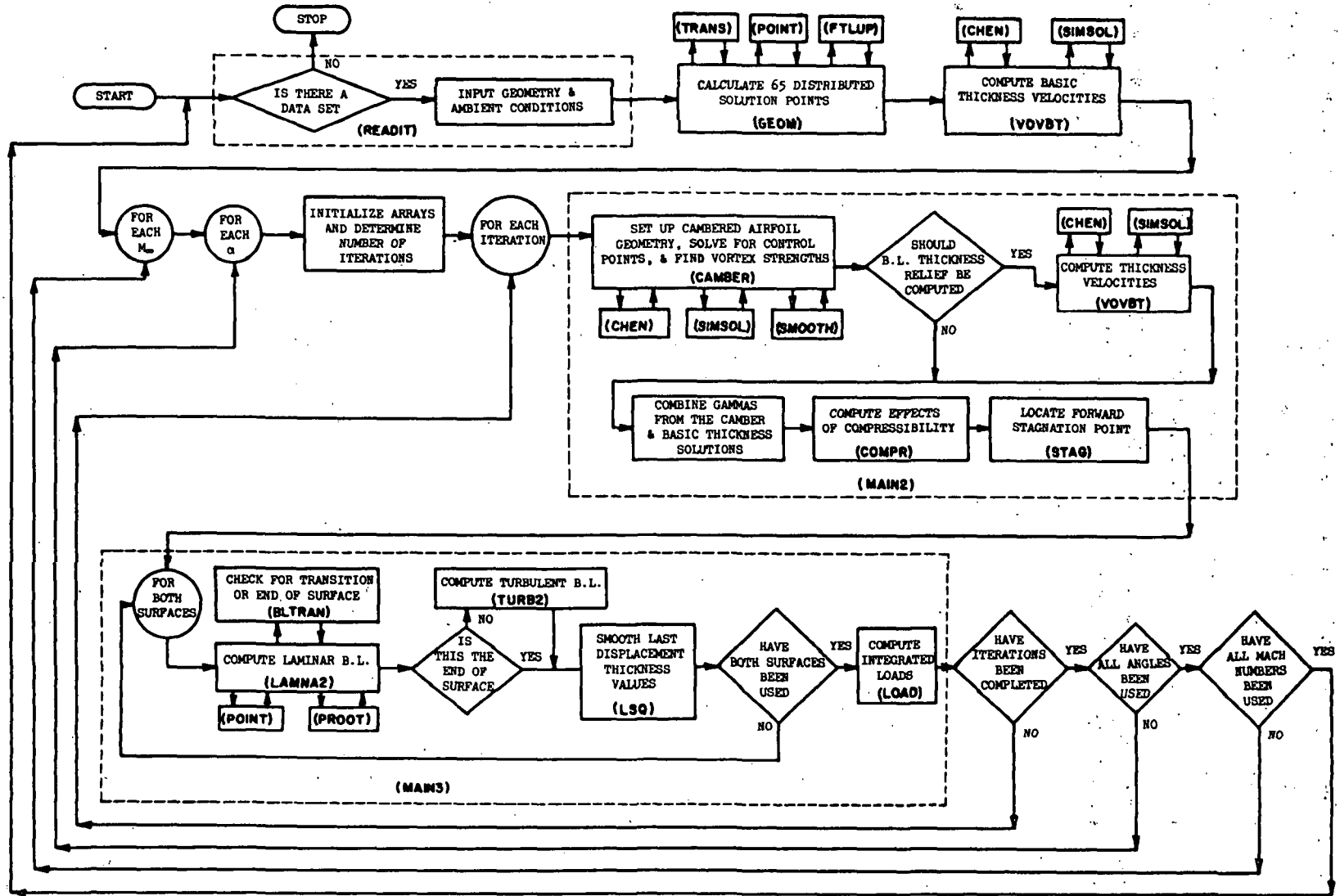


Figure 1.- Flow chart for single-element version of airfoil program.

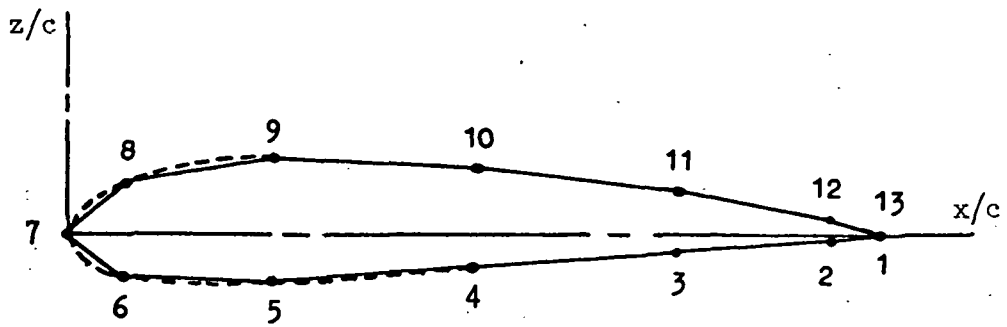


Figure 2.- Polygon approximation of airfoil.

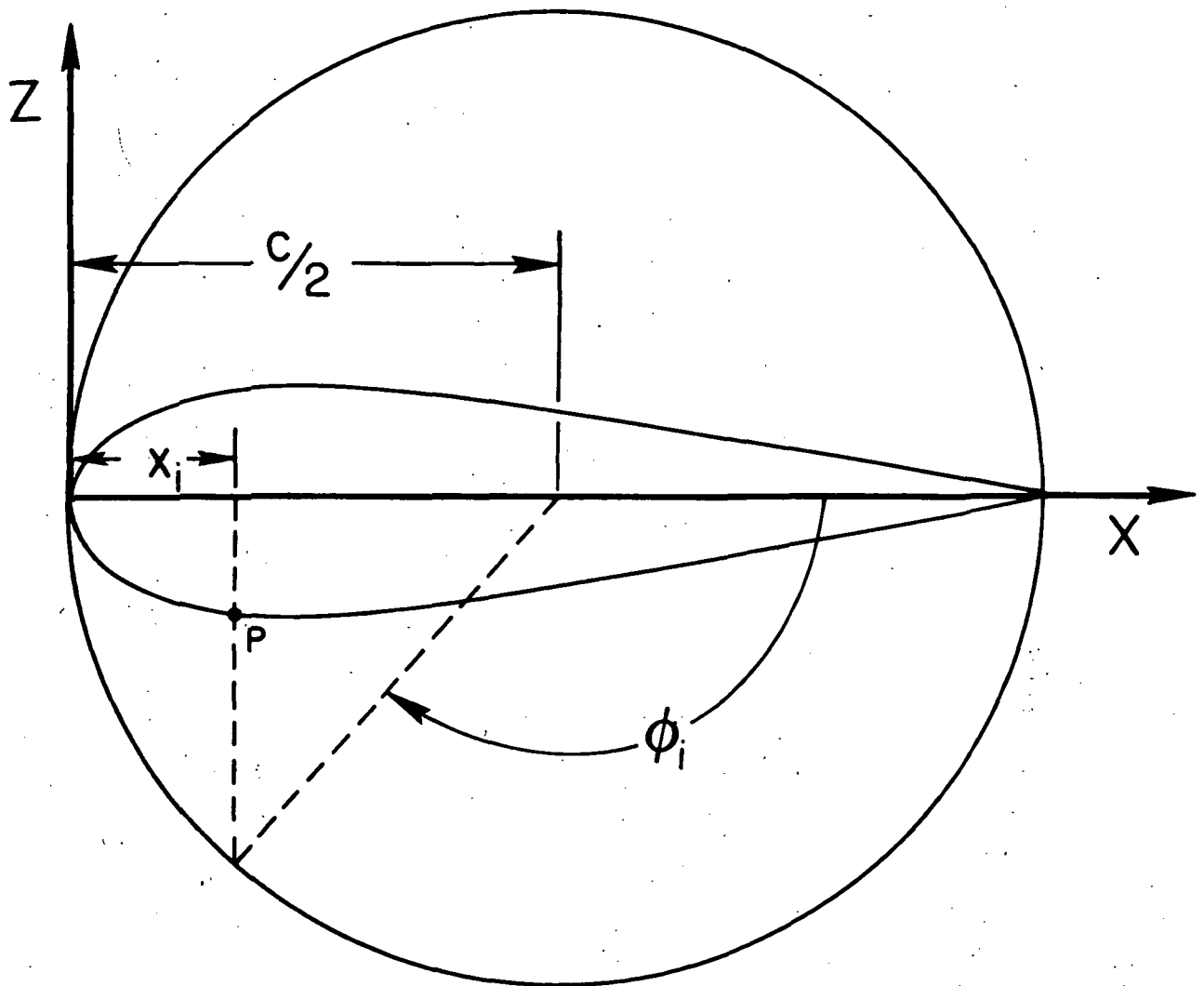
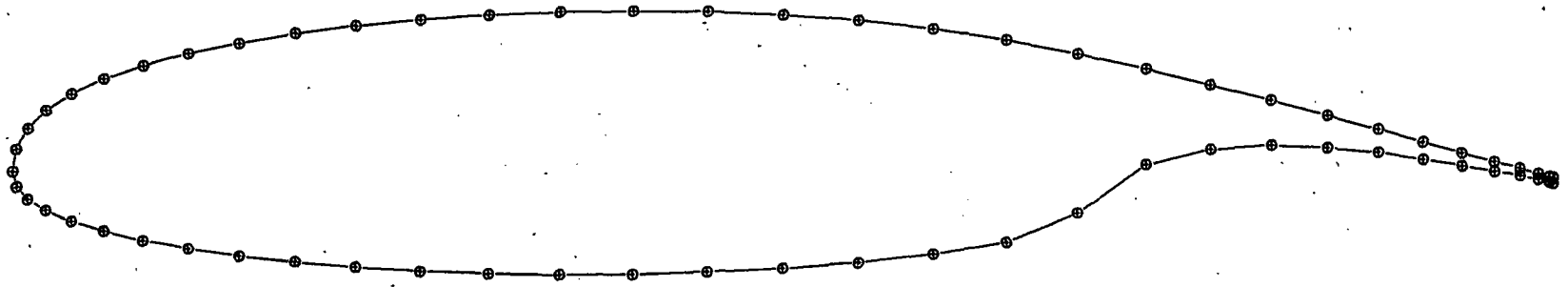
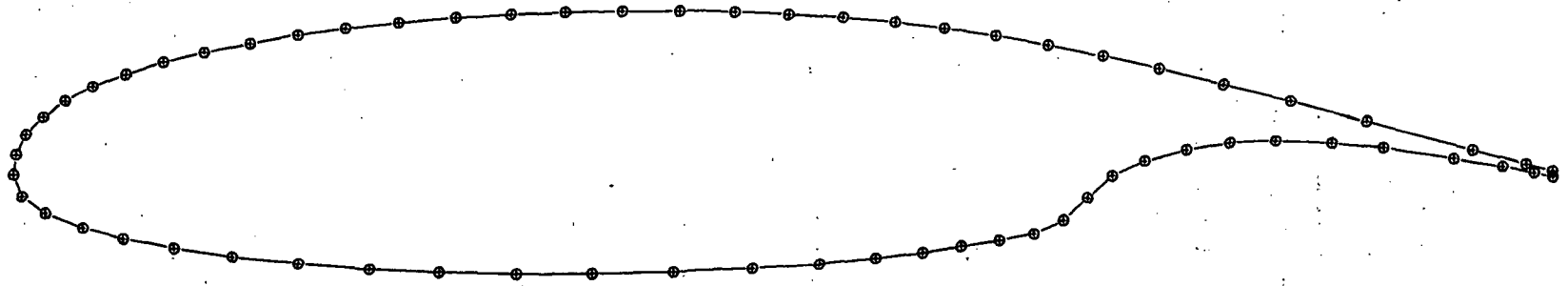


Figure 3.- Cosine method for distribution of airfoil corner points.

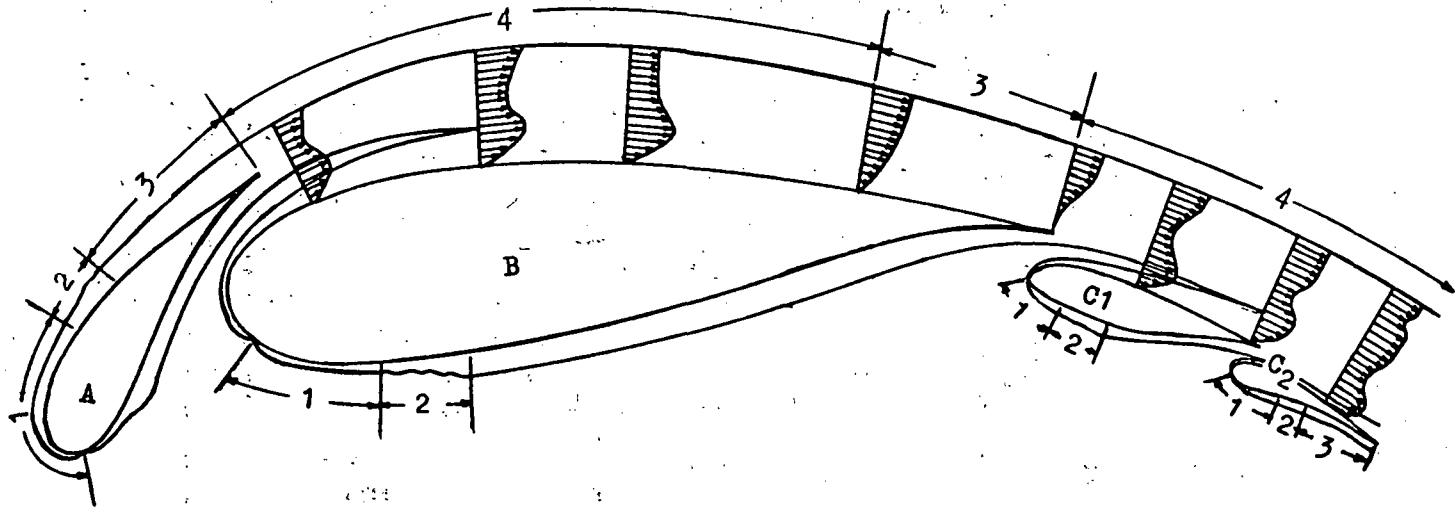


(a) Cosine method.



(b) Curvature method.

Figure 4.- Comparison of cosine and curvature methods for distribution of segment corner points.



A LEADING-EDGE SLAT

B MAIN COMPONENT

C1 } DOUBLE-SLOTTED FLAP
C2 }

1 = LAMINAR BOUNDARY LAYER

2 = TRANSITION REGION

3 = TURBULENT BOUNDARY LAYER

4 = CONFLUENT BOUNDARY LAYER

Figure 5.- Boundary-layer development on multi-element airfoil.

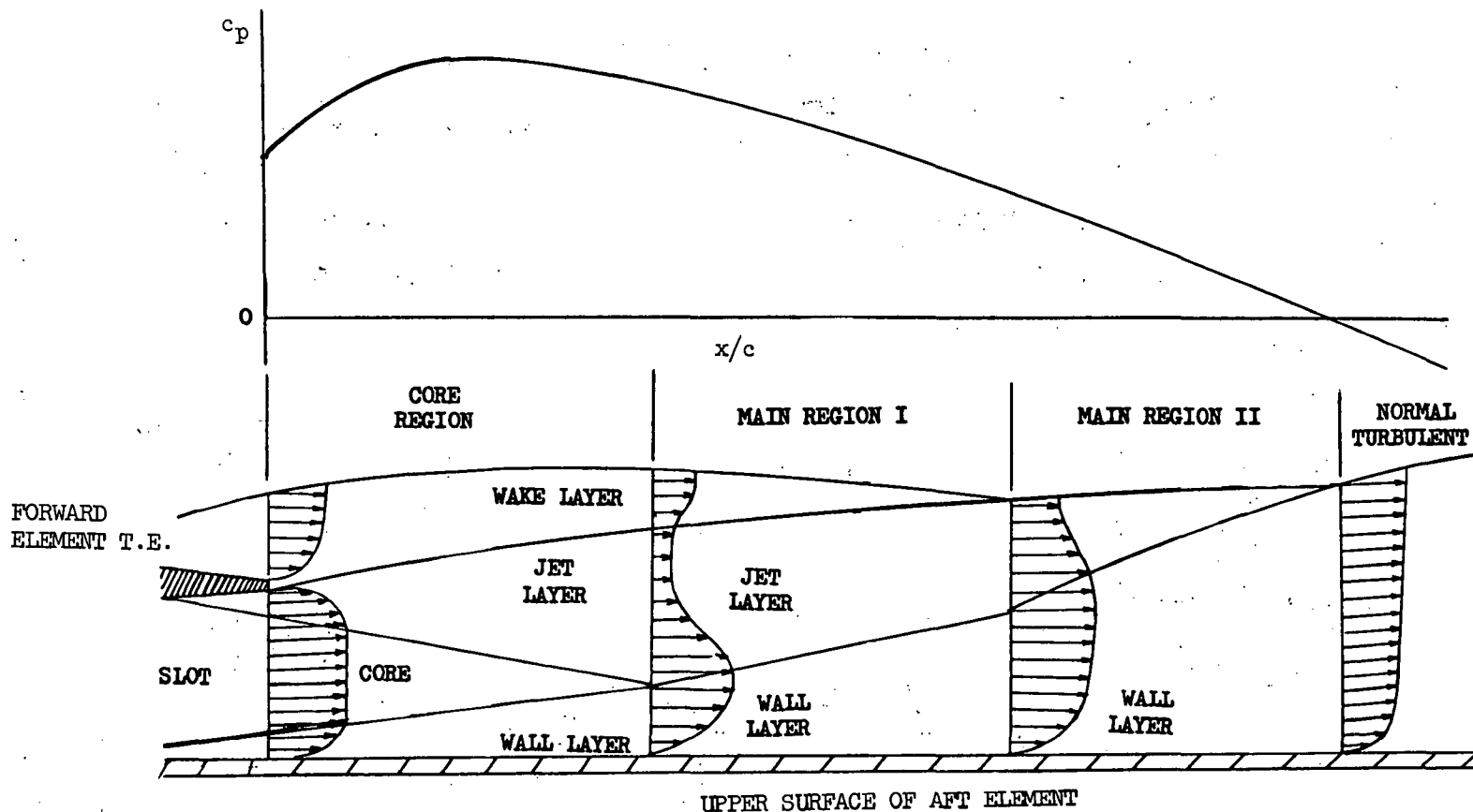


Figure 6.- Confluent boundary-layer model.

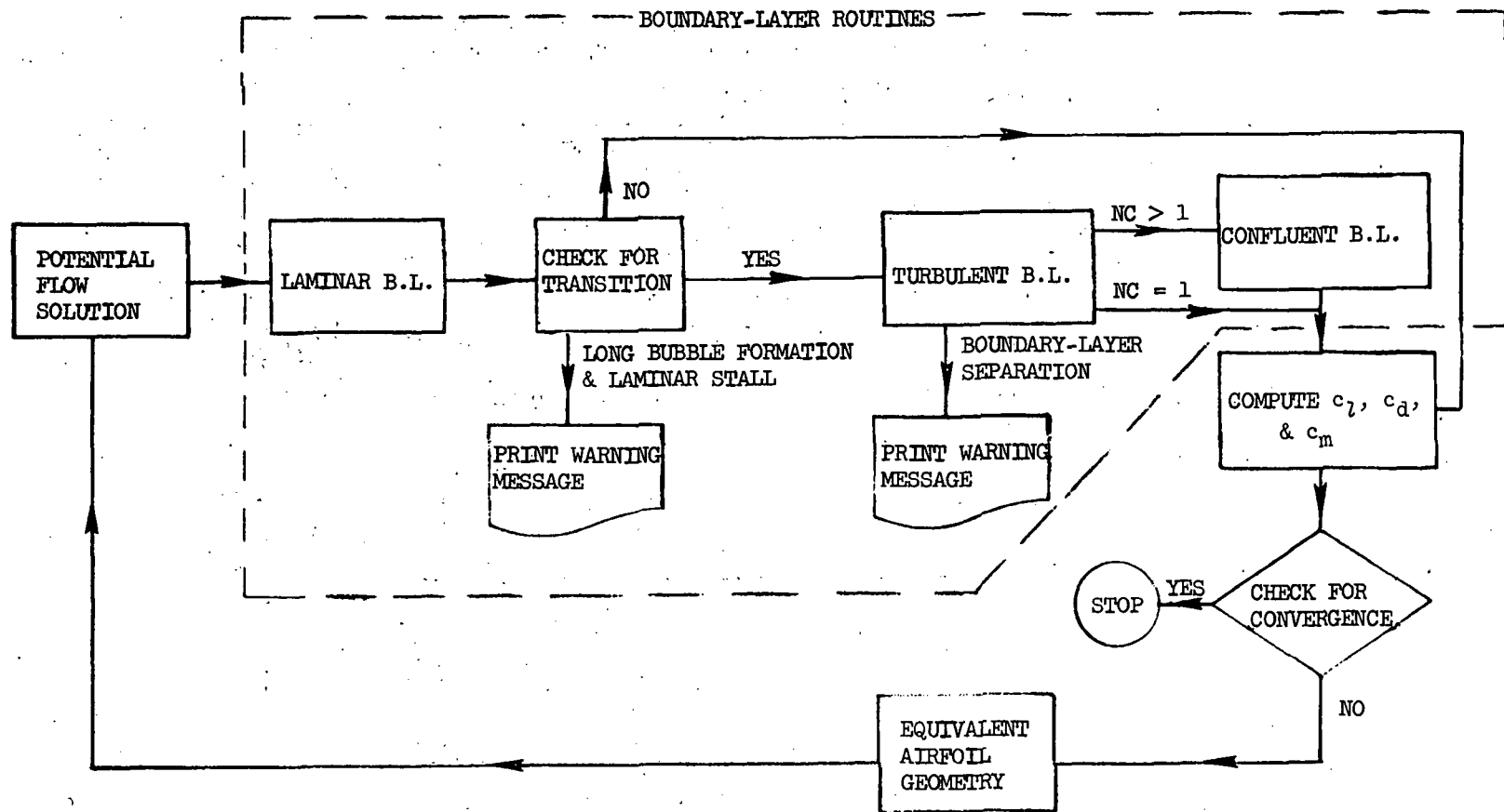


Figure 7.- Flow chart for boundary-layer computations.

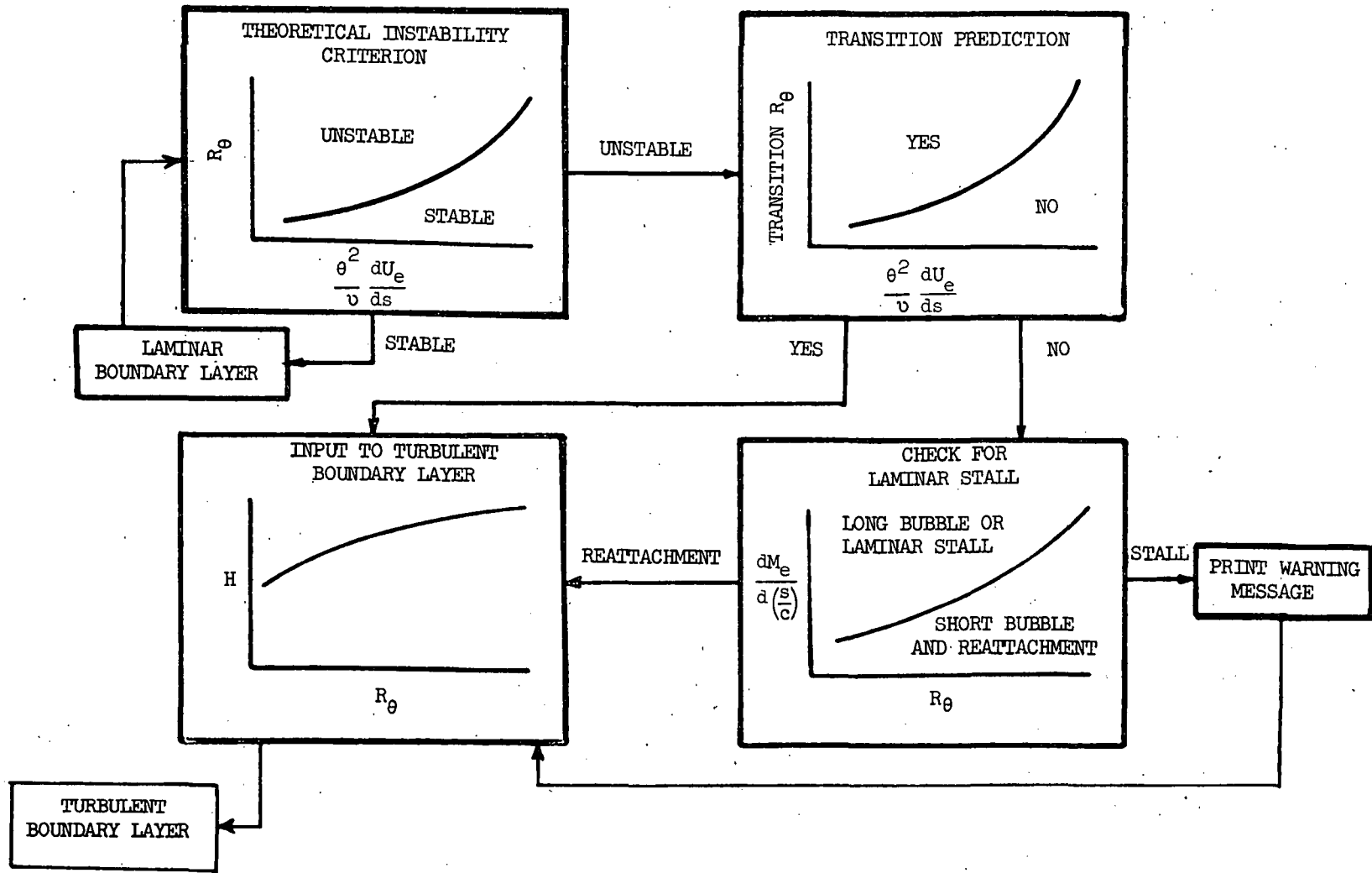


Figure 8.- Flow chart for boundary-layer transition criteria.

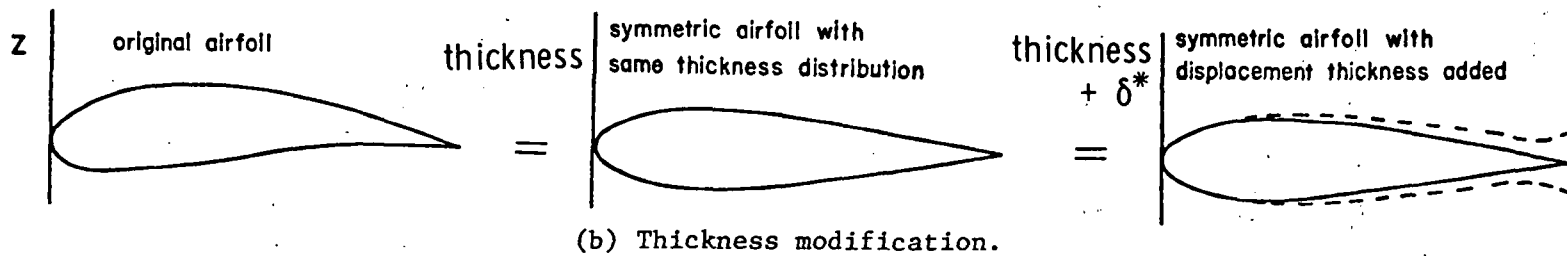
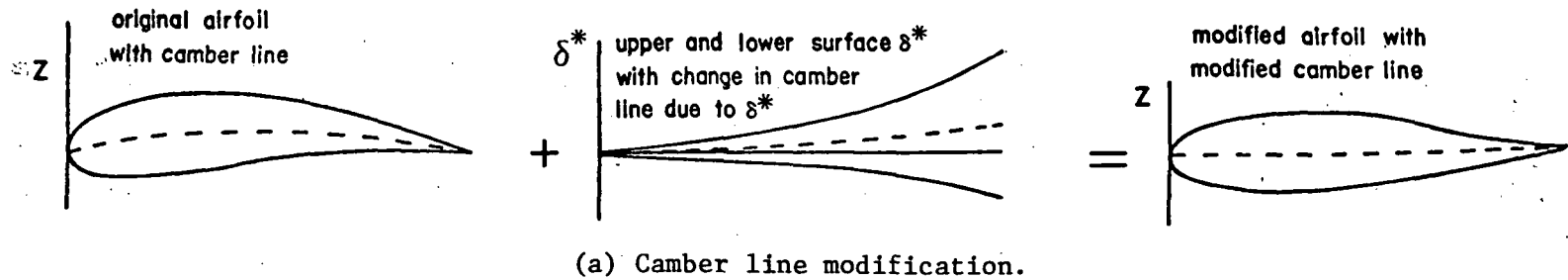


Figure 9.- Modification of airfoil due to boundary-layer displacement thickness.

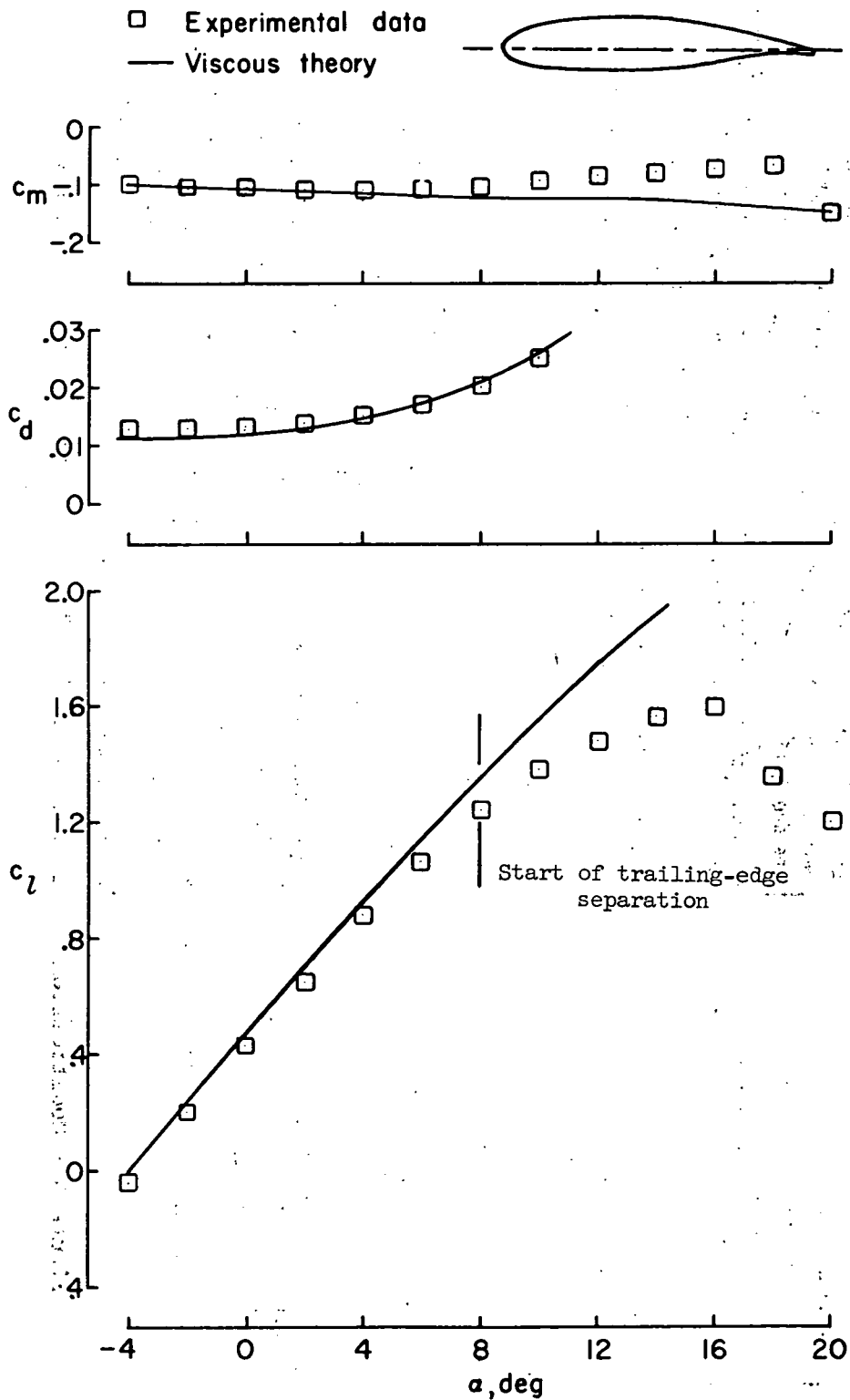


Figure 10.- Comparison between experiment and theory for NASA GA(W)-1 airfoil.

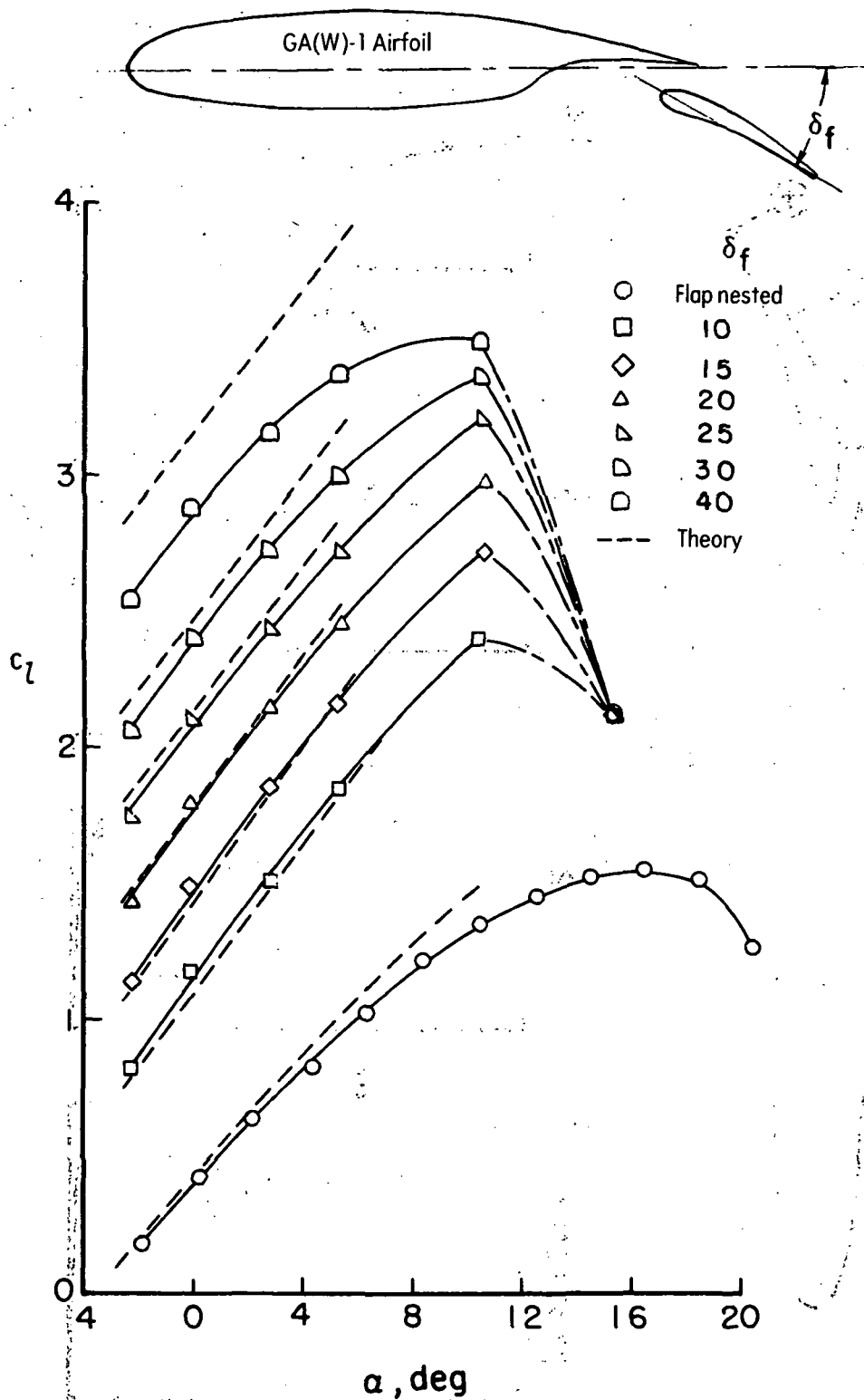
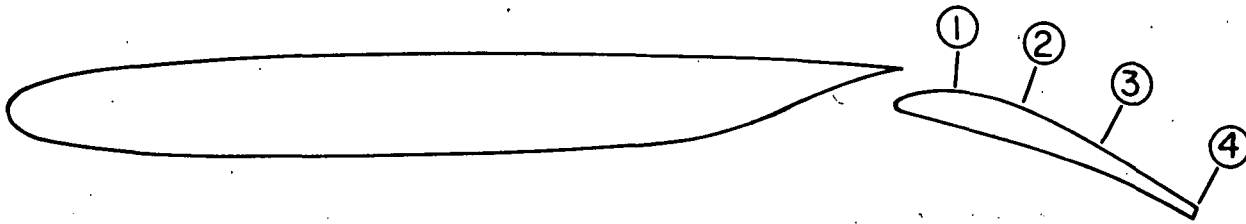


Figure 11.- Comparison between experiment and theory for GA(W)-1 airfoil with a 29% chord Fowler flap.



○ EXPERIMENT
 — THEORY

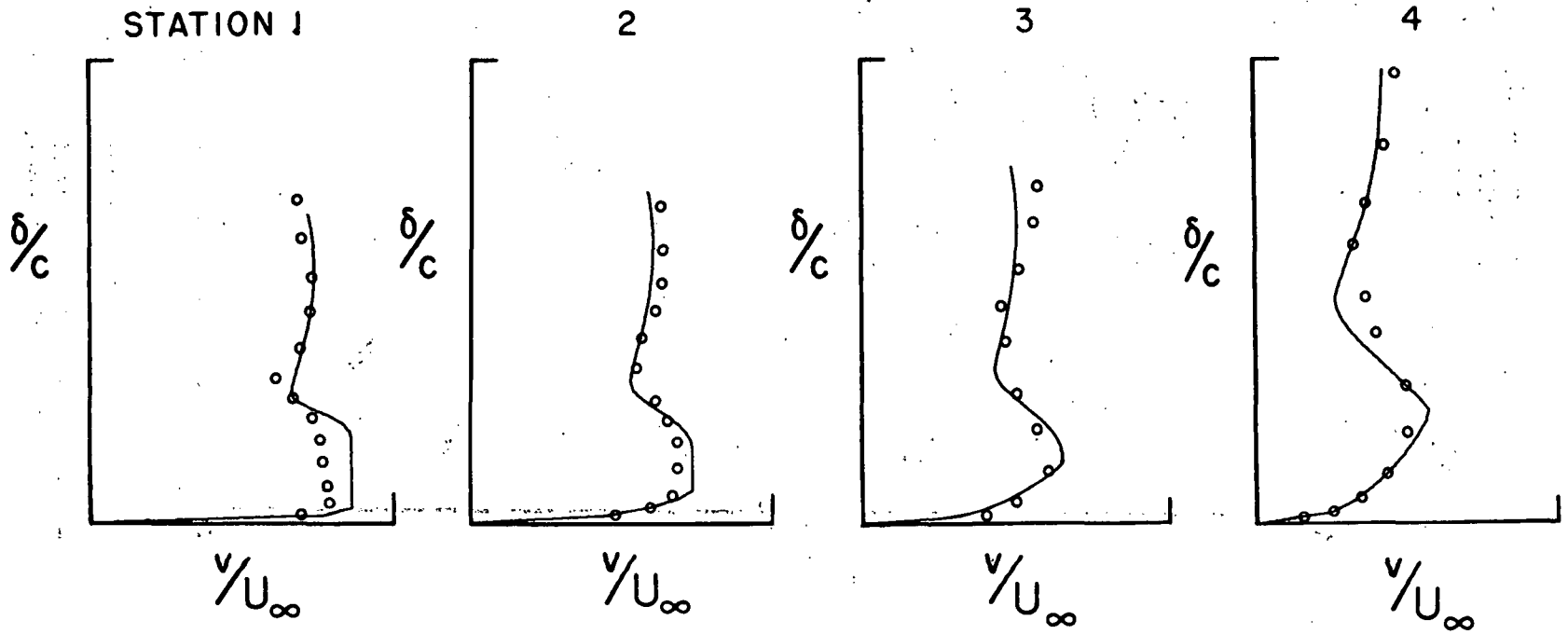


Figure 12.- Confluent boundary-layer profiles for typical airfoil with single-slotted, trailing-edge flap.

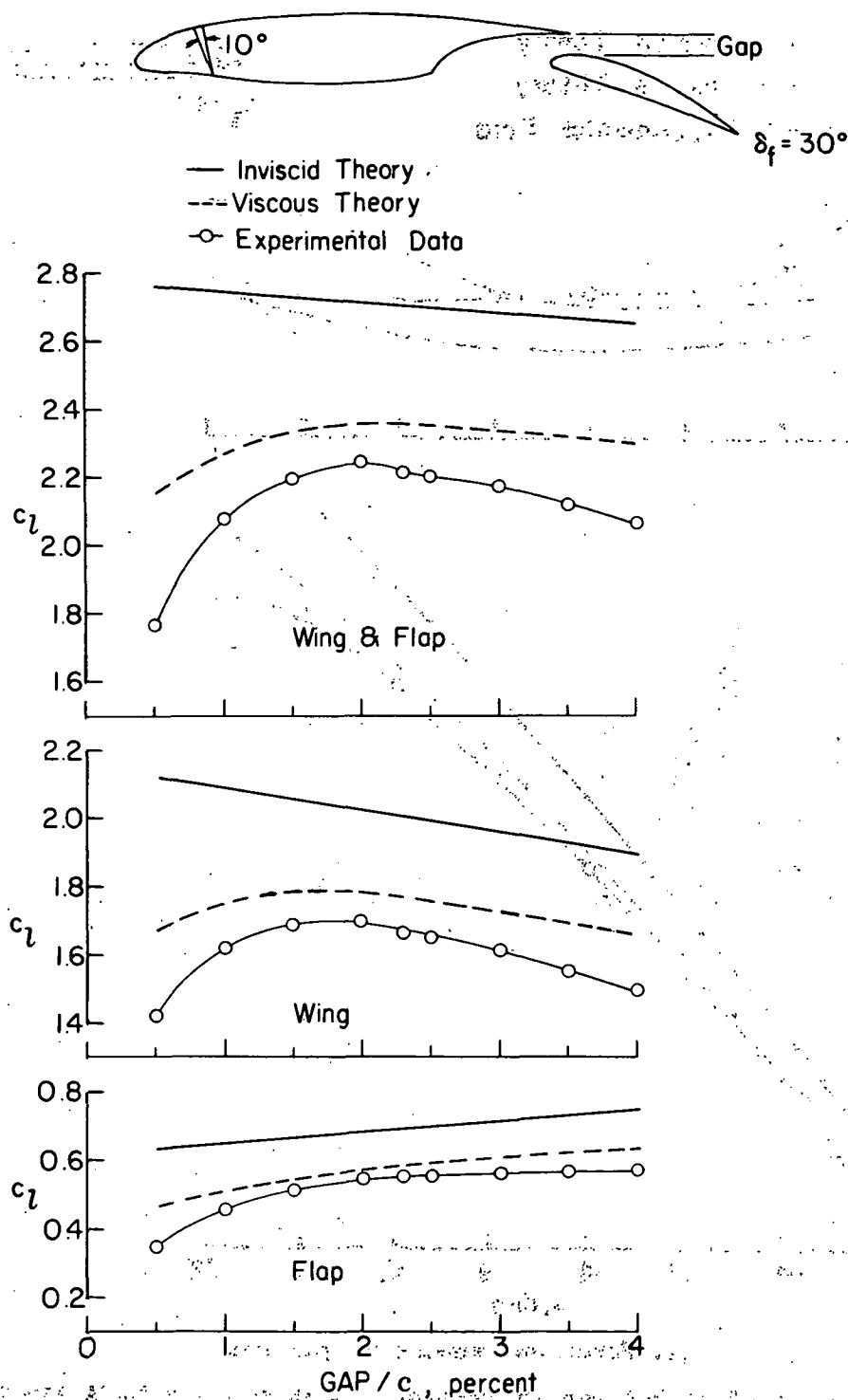
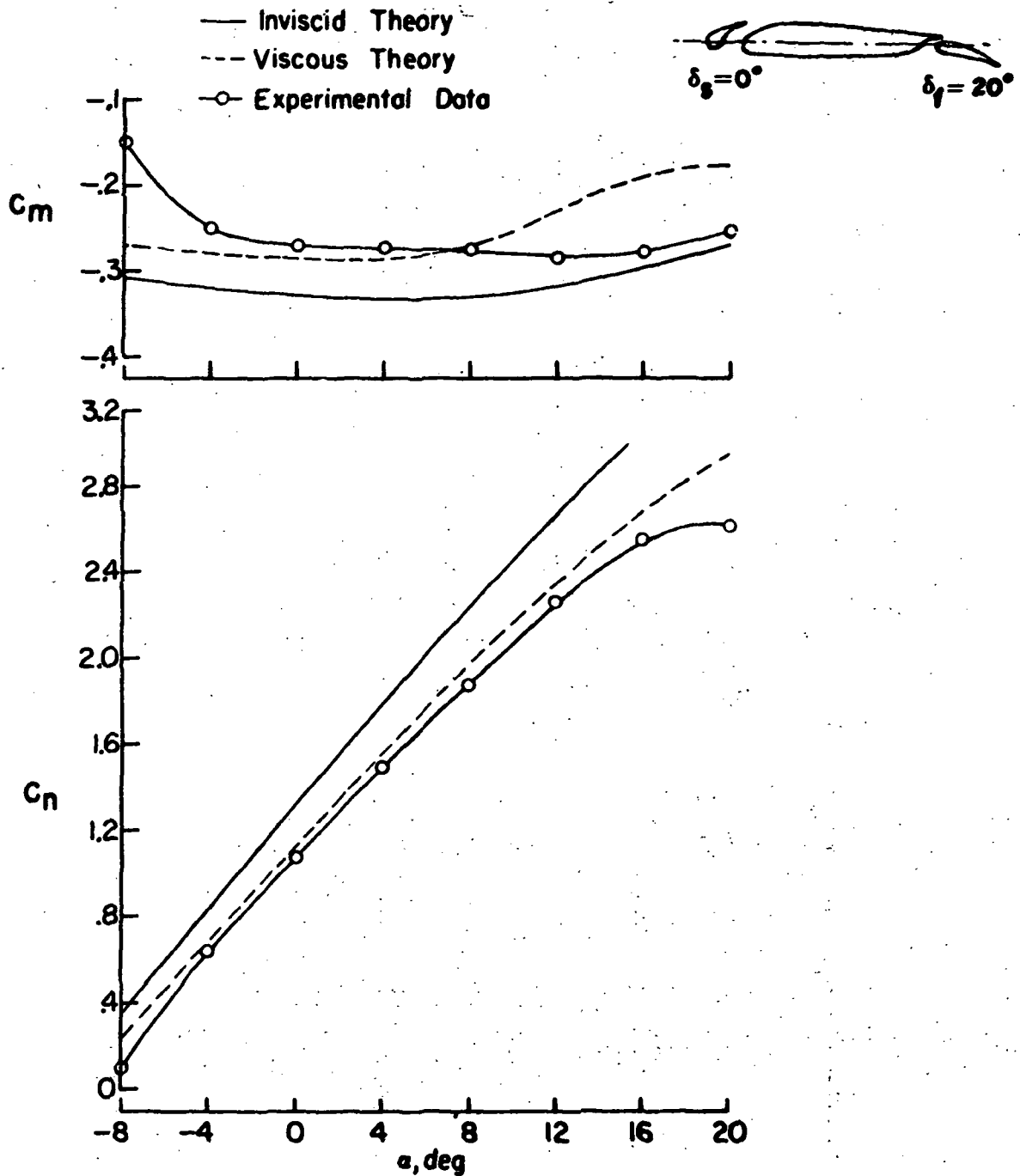
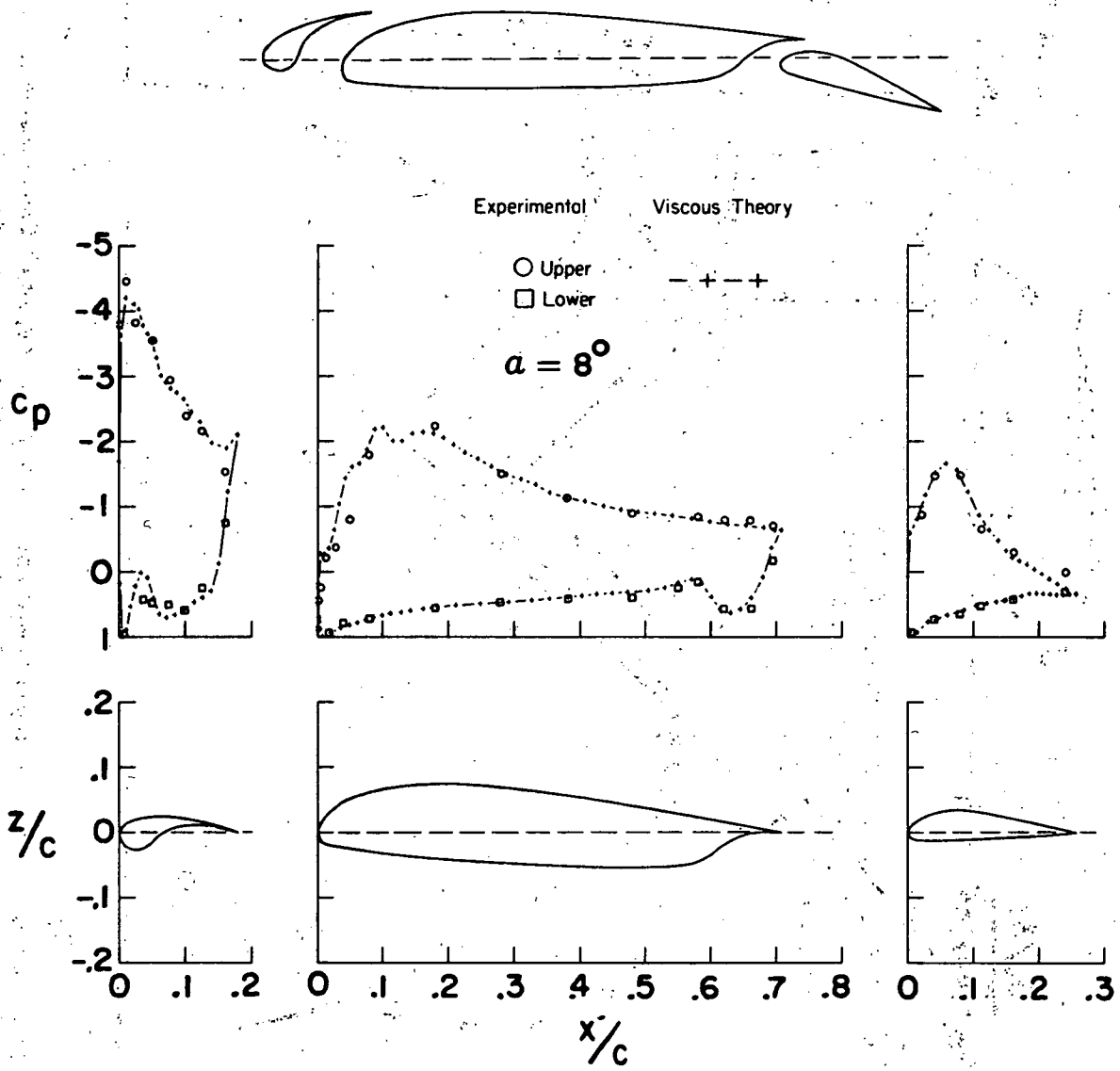


Figure 13.- Gap optimization of 10° drooped-nose airfoil with a single-slotted, trailing-edge flap.



(a) Force and moment comparison.

Figure 14.- Comparison between experiment and theory for NACA 23012 airfoil with leading-edge slat and trailing-edge flap.



(b) Pressure distribution comparison.

Figure 14.- Concluded.

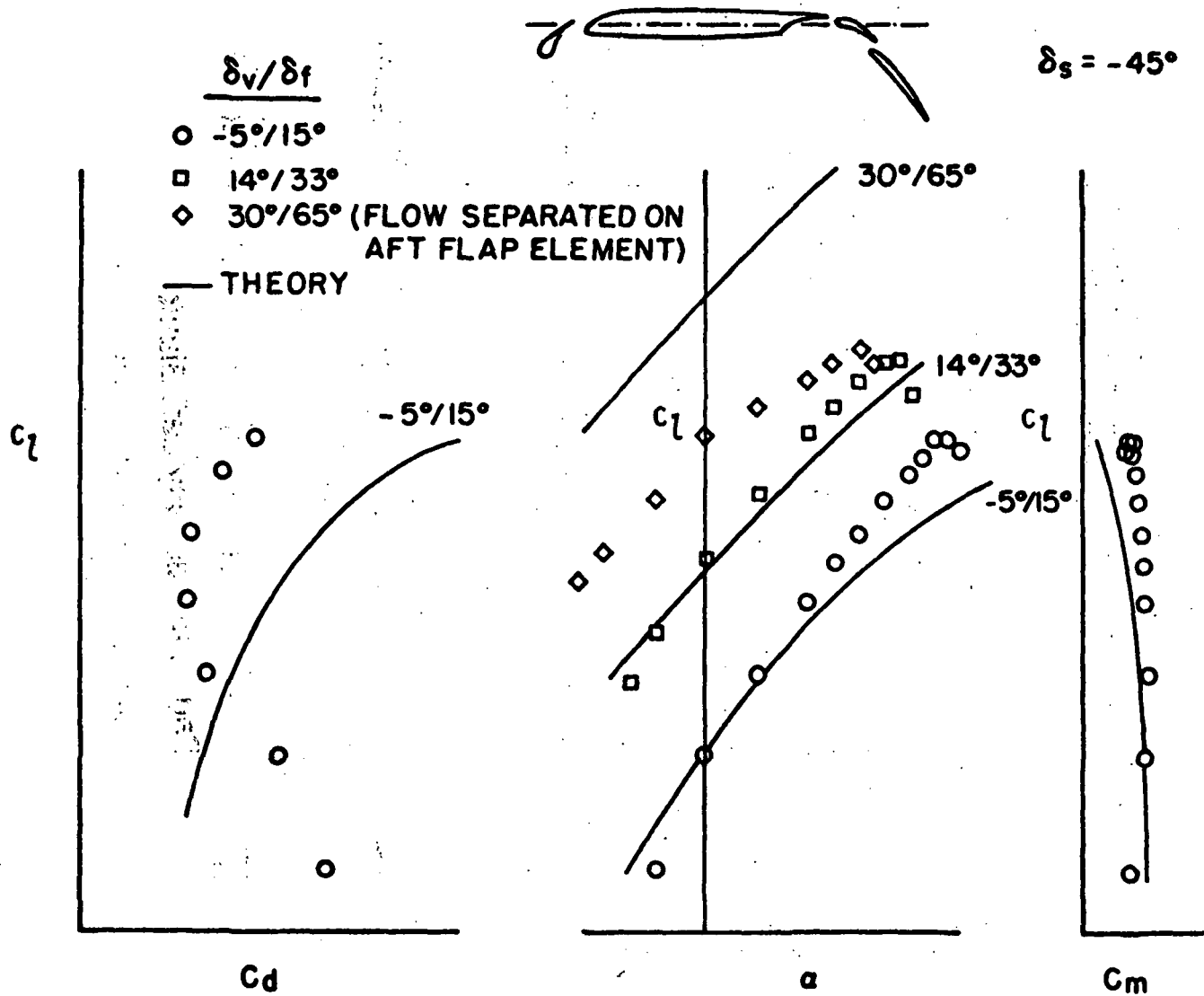


Figure 15.- Comparison between experiment and theory for typical four-element airfoil with leading-edge slat and double-slotted, trailing-edge flap.

Page intentionally left blank

APPLICATION OF NUMERICAL OPTIMIZATION TECHNIQUES TO AIRFOIL DESIGN

By Garret N. Vanderplaats, Raymond N. Hicks,

NASA Ames Research Center

and Earll M. Murman

Flow Research, Inc.

SUMMARY

A practical procedure is presented for automated airfoil design using numerical optimization techniques. The procedure uses an optimization program based on conjugate directions for locally unconstrained problems and feasible directions for locally constrained problems. This program is coupled with an aerodynamic analysis program which uses a relaxation method to solve the partial differential equation that governs the inviscid small-disturbance fluid flow.

Basic optimization concepts and the techniques used in the optimization program are described. The procedure for automating airfoil design is outlined. Design objectives which are considered include lift maximization, drag minimization, and pitching-moment minimization. Various aerodynamic and geometric constraints on the design are accounted for. Design results are presented to demonstrate the simplicity and generality of the method.

INTRODUCTION

Computational techniques for aerodynamic analysis have been considerably improved in recent years, both in efficiency and reliability. Concurrently, numerical methods of optimization have been developed which provide an efficient means for automating the design process. In the study reported here, two existing programs, one for aerodynamic analysis and the other for optimization, have been coupled to provide a general and efficient design tool. The aerodynamic analysis program uses a relaxation method to solve the partial differential equation that governs the inviscid, small-disturbance fluid flow. Complete details of the theory and solution procedure are given in reference 1. The optimization program is based on the method of feasible directions. A conjugate direction algorithm is included in the optimization program for locally unconstrained problems. Details of the optimization theory and computer program can be found in references 2 to 5. This combined design program is described here with particular emphasis on the optimization techniques and on the formulation of the numerical design problem.

Basic optimization concepts are discussed first, and the techniques used in the optimization program are described. Next, the procedure for automating

airfoil design is outlined. Finally, several examples are presented to demonstrate the simplicity and generality of the method.

SYMBOLS

a_i, b_i	polynomial coefficients
a_{ij}, b_j	coefficients of j th polynomial
c	chord
C_D	section drag coefficient
C_L	section lift coefficient
C_m	section pitching-moment coefficient
C_p	pressure coefficient
$F(\bar{X})$	function of design variables
$G_i(\bar{X})$	function defining design constraint
M	Mach number
OBJ	design objective
q	design iteration number
\bar{S}	search direction in design space
x_i	i th design variable
x	chordwise distance
\bar{X}	vector of design variables
y	airfoil coordinate
y'	airfoil surface slope
Y	airfoil shape function
α	angle of attack
α^*	one-dimensional search parameter
β	objective of direction-finding problem
∇	gradient operator
θ	pushoff factor

Subscripts:

ℓ_s lower surface

us upper surface

min minimum

Superscripts:

ℓ lower surface

u upper surface

q design iteration

OPTIMIZATION CONCEPTS

Consider the airfoil shown in figure 1 in which the upper surface is defined by the functional relationship $Y_{us}(x/c)$, and the lower surface is defined by the functional relationship $Y_{\ell s}(x/c)$. If we choose to use a polynomial representation for the upper surface, the equation for the upper surface of the airfoil would be given by

$$Y_{us} = b\sqrt{x/c} + a_0 + a_1x/c + a_2(x/c)^2 + \dots + a_n(x/c)^n \quad (1)$$

where the square root term allows for a blunt leading edge. Another polynomial of the same form could be used to describe the lower surface of the airfoil.

Now assume we wish to design an airfoil for minimum drag at some Mach number and angle of attack. Furthermore, the airfoil must have a lift coefficient C_L of at least C_{Lmin} . Additionally, the thickness of the airfoil must be positive for all x/c . We can now state the optimization problem as

$$\text{minimize } C_D \quad (2)$$

$$\text{subject to } C_{Lmin} - C_L \leq 0 \quad (3)$$

$$\text{and } Y_{us} - Y_{\ell s} \geq 0 \text{ for all } 0 \leq x/c \leq 1 \quad (4)$$

In this example the drag coefficient C_D is defined as the objective function. The minimum lift requirement of equation (3) and positive thickness requirements of equation (4) are referred to as constraints on the design problem. If we use the polynomial representations for the airfoil shape, the problem becomes one of determining the coefficients of the polynomials so that drag is minimum, subject to the constraints on the design. The

polynomial coefficients, then, are called the design variables. Note that the objective function and the constraint on lift are both implicit functions of the design variables and are computed using the aerodynamic analysis program. The requirement of positive airfoil thickness is an explicit function of the design variables and is determined directly from the geometry of the airfoil. This statement of the problem is not unique and we could just as well maximize the lift coefficient with an upper bound on drag, in which case the objective would be C_L with C_D being constrained. This ability to arbitrarily choose the objective and constraint functions forms the basis for the generality of the method.

It is of course possible to impose constraints on the design problem which cannot be met. For example, an unrealistically high lift requirement may be imposed on the drag minimization problem. In this case the optimization program will obtain the design which is as nearly acceptable as possible (i.e., greatest lift) while some man-machine interaction will be necessary to obtain the final optimized airfoil which most nearly meets designer's requirements.

In general, the numerical optimization problem is stated mathematically as

$$\text{minimize } OBJ = F(\bar{X}) \quad (5)$$

subject to:

$$G_i(\bar{X}) \leq 0 \quad (i = 1, m) \quad (6)$$

$$x_i^l \leq x_i \leq x_i^u \quad (i = 1, n) \quad (7)$$

where OBJ is the objective function, for example, drag coefficient. The vector \bar{X} contains the n design variables. In the case of a polynomial representation for the airfoil shape, the vector \bar{X} would simply contain the coefficients of the polynomial which would be changed during the design process in such a way as to minimize the objective function OBJ while satisfying the constraints. $G_i(\bar{X})$ defines the constraints which the designer wishes to impose on the optimization problem. $F(\bar{X})$ and $G_i(\bar{X})$ may be either implicit or explicit functions of the design variables \bar{X} but must be continuous. Variables x_i^l and x_i^u define the lower and upper bounds, respectively, on the design variable and are the limits over which $F(\bar{X})$ and $G_i(\bar{X})$ are defined. If the inequality condition of equation (6) is violated ($G_i(\bar{X}) > 0$) for any constraint, the constraint is said to be violated. If the equality condition is met ($G_i(\bar{X}) = 0$), the constraint is called active, and if the strict inequality is met ($G_i(\bar{X}) < 0$), the constraint is inactive. Because a precise zero is seldom meaningful on the digital computer, a constraint is called active if its value is within a specified tolerance of zero.

The n -dimensional space spanned by the design variables \bar{X} is referred to as the design space. Any design which satisfies the inequalities of equations (6) and (7) is referred to as a feasible design. If a design violates one or more of these inequalities, it is said to be infeasible. The

minimum feasible design is said to be optimal. Note that if one wishes to maximize some function such as lift, it can be done simply by minimizing the negative of lift. Thus, any design problem can be cast in the above form.

The optimization program begins with an initial \bar{X} vector which is input to the program and may or may not define a feasible design. The optimization process then proceeds iteratively by the following recursive relationship:

$$\bar{X}^{q+1} = \bar{X}^q + \alpha^* \bar{S}^q \quad (8)$$

where q is the iteration number, vector \bar{S} is the direction of search in the n -dimensional design space, and α^* is a scalar which defines distance of travel and direction \bar{S} . The notation α^* for the move parameter is used here for consistency with mathematical programming nomenclature and should not be confused with the airfoil angle of attack α .

The optimization process then proceeds in two steps. The first is the determination of a direction \bar{S} which will reduce the objective function without violating constraints. The second is the determination of the scalar α^* so that the objective function is minimized in this direction, a new constraint is encountered, or a currently active constraint is encountered again.

Consider, for example, a hypothetical drag minimization problem in two variables x_1 and x_2 which may correspond to two coefficients in the polynomial shape function. Assume that the lift coefficient must be greater than or equal to some specified value $C_{L_{min}}$, and that the cross-sectional area contained in the airfoil must be greater than or equal to some specified value A_{min} . Figure 2 is a graphical representation of such a problem showing contours of constant objective function value as well as the constraint boundaries. Assume that a design at point A is given so that initially no constraints are active or violated. The program then begins by perturbing each of the \bar{X} variables to determine its effect on the objective (drag). That is, the gradient of C_D is calculated by finite difference using a single forward step, and the gradient vector is constructed as

$$\bar{\nabla} \text{ OBJ} \equiv \bar{\nabla} C_D = \begin{pmatrix} \frac{\partial C_D}{\partial x_1} \\ \frac{\partial C_D}{\partial x_2} \\ \vdots \\ \frac{\partial C_D}{\partial x_n} \end{pmatrix} = \begin{pmatrix} \frac{\Delta C_D}{\Delta x_1} \\ \frac{\Delta C_D}{\Delta x_2} \\ \vdots \\ \frac{\Delta C_D}{\Delta x_n} \end{pmatrix} \quad (9)$$

Because no constraints are active or violated, it is obvious that the greatest improvement in the objective function is obtained by moving in the negative gradient or steepest descent direction so that $\bar{S} = -\bar{\nabla}C_D$. Having determined \bar{S} , the scalar α^* in equation (8) must now be determined so that either the objective function is minimized in this direction or some constraint boundary is encountered. That is, a one-dimensional search is done in direction \bar{S} to determine the appropriate value for α^* so that an improved design is obtained at point B. No further improvement can be achieved in this direction; it is now necessary to determine a new \bar{S} vector which will improve the design. Point B defines the end of the first design iteration. The second design iteration begins by again perturbing the two design variables (x_1 and x_2) to obtain the gradient of the objective function C_D . Now, instead of moving in a steepest descent direction, the \bar{S} vector is calculated from the following relationship

$$\bar{S}^q = -\bar{\nabla} OBJ^q + \frac{|\bar{\nabla} OBJ^q|^2}{|\bar{\nabla} OBJ^{q-1}|^2} \bar{S}^{q-1} \quad (10)$$

where OBJ is drag C_D in this example. Equation (10) defines the conjugate direction as developed by Fletcher and Reeves in reference 4. The advantage that this definition of the \bar{S} vector has over the steepest descent direction is that if the objective is a quadratic function of the design variables, convergence to the optimum can be guaranteed to occur in n iterations or less. Although most problems of practical interest are not quadratic functions of the design variables, they may still be approximated as quadratic in the region of the solution. In other words, if the first three terms of a Taylor series expansion of the objective function form a reasonable approximation to that function, then equation (10) can be expected to provide more rapid convergence in a steepest descent search, since steepest descent uses only the first two terms in the Taylor series expansion. Having determined the new direction \bar{S} , one searches in that direction until the lift constraint is encountered at point C in figure 2, which ends the second design iteration. The design variables are again perturbed to obtain the gradient of the objective function C_D . At the same time we obtain the gradient of the active lift constraint C_L . Now a search direction must be found which will reduce the objective function without violating the lift constraint. Such a direction can be found by solving the following sub-problem, which is a linear programming problem with a single quadratic constraint.

Find \bar{S} to maximize β (11)

Subject to:

$$\bar{\nabla} OBJ(\bar{X}) \cdot \bar{S} + \beta \leq 0 \quad (12)$$

$$\bar{\nabla} G_j(\bar{X}) \cdot \bar{S} + \theta_j \beta \leq 0 \quad (j = 1 \text{ NAC}) \quad (13)$$

$$\bar{S} \cdot \bar{S} \leq 1 \quad (14)$$

where $\bar{\nabla} \text{OBJ}(\bar{X}) \equiv \bar{\nabla} C_D$, $\bar{\nabla} G_j(\bar{X}) \equiv -\bar{\nabla} C_L$, and $G_j(X) = C_{L_{\min}} - C_L$. NAC is the number of active constraints. In this example $\text{NAC} = 1$. The details for solving this problem are given in references 2 and 3. Note that if equation (12) is satisfied and β is positive, the resulting direction will reduce the objective function and is defined as a "usable" direction. Similarly, if equation (13) is satisfied and β is positive, \bar{S} is called a "feasible" direction because, for a small move in this direction, no constraints will be violated. The prespecified parameter θ_j is referred to as a pushoff factor for the j th constraint and has the effect of pushing the design away from the active constraint. The value of θ_j must be zero or positive to maintain a feasible design. If θ_j were zero, the resulting direction would be precisely tangent to the active constraint. On the other hand, a very large θ_j would push the design away from the active constraint and nearly tangent to a line of constant objective function. A value of $\theta_j = 1$ will yield a direction which approximately bisects the angle between constant objective function and the constraint as shown in figure 2. If the maximum value of β obtainable from equations (11) to (14) is zero, then no direction exists which will both reduce the objective function and satisfy the constraint, and the current design is optimal or is at least a local minimum. In this example, a direction can be found, and a one-dimensional search leads to point D in figure 2, ending the third iteration in the optimization process. The design variables are again perturbed to obtain the gradient of the objective and the active constraint. This time the constraint is on area. The subproblem of equations (11) to (14) is again solved to obtain a new \bar{S} vector. Note here that the area constraint is a linear function of the design variables x_1 and x_2 ; therefore in equations (12) and (13) the pushoff factor θ_j is set to zero allowing the \bar{S} vector to precisely follow the linear constraint. A one-dimensional search now yields a solution at point E in figure 2 which is the vertex of two constraints and ends this design iteration. Once again the design variables are perturbed to obtain the gradient of the objective and both active constraints, and the subproblem of equations (11) to (14) is again solved. This time the solution of the subproblem will be zero, indicating that the optimal design has been achieved. Point E is clearly optimal since no direction exists at this point which will reduce the objective function any further without violating one or both of the constraints.

In the airfoil design problem, it is often difficult to insure that the initial design will satisfy all the constraints. It is quite possible that the initial design will lie in the infeasible region, say at point F in figure 2. Logic is included in the optimization program so that if this situation occurs, a direction vector \bar{S} is obtained which will point toward the feasible region with minimal increase in the objective function.

Consider the case where an initial design is described at point G in figure 2, and assume that we wish to obtain the optimal solution simply by perturbing each variable in sequence to obtain the minimum drag coefficient which satisfies the constraint. Note that if either x_1 or x_2 is increased, the value of the objective function will increase. On the other hand, if

x_1 or x_2 is decreased, the constraint on minimum area will be violated. Therefore, it is not possible to improve the objective function by minimizing with respect to one variable at a time. It is only by changing the variables in the proper combination that the optimal solution is obtained. This again underscores the value of using optimization techniques to solve the design problem.

The methods used in this simple example are, in principle, directly extendable to n-dimensional problems. Also, additional constraints can be imposed on the problem without increasing the complexity of the design process.

There are, however, two important limitations on the use of optimization techniques for airfoil design. First, the computation times increase dramatically as the number of design variables is increased. This is because the number of required aerodynamic analyses increases in order to obtain gradient information. Also, large problems tend to converge more slowly due to the interaction between design variables and because of numerical inaccuracy during the optimization process. It is desirable to use as few design variables as possible. Experience suggests that between 10 and 15 design variables are adequate to define the airfoil shape, and this is well within the capabilities of the optimization program.

Aerodynamic analysis programs, which are based on an iterative solution of the fluid-flow equations, are particularly well suited for use in optimization. These programs begin with an initial estimate for the solution of the fluid-flow equations, and iteratively update the solution until convergence is obtained. The program efficiency is then largely dependent on this initial estimate, and if a good estimate for the solution is available, the program will converge quite rapidly. During optimization, the majority of the aerodynamic analyses are required to obtain finite difference gradient information. However, the gradient computations require only very small perturbations from the previously analyzed airfoil, and the previous solution of the fluid-flow equations usually provides a good starting point for the new analysis. The result is that the optimization process is computationally more efficient than would be anticipated based on the computer run time for a single aerodynamic analysis.

The second concern when using optimization techniques for airfoil design is that there is no guarantee that the absolute optimum solution will be obtained. It is quite conceivable that the optimization process will drive the design to a relative rather than a global minimum. The probability of obtaining a true optimum is improved by beginning the optimization from several different initial designs. In this study, each design resulted in improvement over the initial airfoil shape, so that even if the true optimum was not obtained, some improvement was realized.

A block diagram of the airfoil shape optimization program is shown in figure 3. The optimization program modifies the vector of design variables X to minimize the objective, while the aerodynamics program evaluates the objective and constraint functions for each proposed X vector. The

aerodynamic program requires a table of y-coordinates of the lower and upper surfaces at numerous stations along the airfoil. The optimization program deals only with the vector of design variables \bar{X} which may be coefficients of a polynomial, as described earlier. A principal consideration in the airfoil design problem is that of choosing the relationship between the design variables and the y-coordinates of the airfoil so that the design process is both general and efficient. This interface between design and analysis variables is discussed in the following section.

AIRFOIL DEFINITION

In choosing the mathematical description for airfoil shape optimization, it is important to have the capability of modeling a wide range of airfoil shapes while maintaining computational efficiency. The aerodynamic analysis routine to describe the airfoil typically requires the y-coordinates at 50 stations along the upper and lower surface of the airfoil for a total of 100 points. A direct approach to optimization might be to treat each of these coordinates as design variables so that the optimization would maintain the same degree of generality in describing the airfoil as dealt with by the analysis program. However, this would lead to an optimization problem of 100 variables, which would clearly be quite costly from a computational standpoint. A logical compromise is to choose a functional relationship to describe the airfoil with as few variables as is practicable. A wide variety of functions may be developed which will adequately describe most airfoils with fewer than 15 design variables. The problem then becomes one of choosing a functional relationship which is numerically well conditioned; that is, the design variables should be chosen so that the optimization process will converge in as few iterations as possible while retaining a high degree of geometric flexibility.

The solution to this problem is far more subtle than that of reducing the number of design variables. Even though a function may be chosen which is mathematically precise and which adequately defines the airfoil, the numerical optimization process may converge very slowly or not at all as a result of the numerical interdependence between design variables; that is, the n-dimensional design space defined by these variables may be highly non-linear and may even contain relative minima as a result of the functional relationship used. Numerical experimentation is usually required to determine if a proposed mathematical model is adequate.

Several alternative geometric descriptions for the airfoil are considered. The polynomial

$$y = b\sqrt{x/c} + a_0 + a_1x/c + a_2(x/c)^2 + \dots + a_n(x/c)^n \quad (15)$$

was chosen as the basic functional relationship used to describe the geometry of the airfoil. Using this relationship, the geometry may be described in various ways.

The classical approach is to use one polynomial for the camber line of the airfoil, and another polynomial for the thickness distribution. Although this description of the airfoil shape is physically meaningful, it has the disadvantage that the upper and lower surfaces of the airfoil cannot be changed independently. If the optimization process requires a reshaping of the upper surface only, it is necessary to change both polynomials in the proper ratio in order to maintain a constant lower surface geometry. Numerically this may be difficult.

A second approach is to define the upper surface with one polynomial and the lower surface with another. This effectively uncouples the design variables associated with upper and lower surfaces.

However, another problem exists with both of these descriptions. Assume the optimization problem requires reshaping of the leading edge of the airfoil without changing the aft contour, so that the important design variable is the coefficient on the square-root term in equation (15). If this term is changed, it is also necessary to change the other coefficients so that the airfoil shape aft of the leading edge remains essentially unchanged. This situation arises if we require that the trailing edge of the airfoil have very small thickness. In other words, the design variables may not be coupled only with respect to the objective and constraint functions, but they may be geometrically coupled in order to maintain a meaningful airfoil.

Another factor which affects the numerical stability of the optimization process is that the result of changing one design variable on the objective and constraint functions may be much different from that of changing another design variable. For example, the effect of changing the coefficient on $(x/c)^5$ is different from the effect of changing the coefficient on x/c . This problem may be alleviated somewhat by using an orthogonal set of polynomials, such as Legendre polynomials, an approach which has been used with some success. However, the problem is not completely alleviated, and an alternative approach based on the original simple polynomials is proposed.

The ideal mathematical model would be one in which the effect of changing one design variable on the objective and constraint functions would be independent of the value of the other design variables, so that the design variables are completely uncoupled. If this were the case, the optimization problem could be solved independently with respect to each variable, and the true optimum would be obtained. Then the optimization techniques described here would be totally unnecessary. While this is seldom achievable in design problems of practical interest, some degree of design variable uncoupling can be achieved. The geometric airfoil description shown in figure 4 is considered to be relatively well conditioned from a numerical optimization standpoint, and yet to maintain most of the desired simplicity and generality. The airfoil is made up of several polynomial sections, each being defined by the general relationship given in equation (15).

Figure 5 shows a typical segment of the airfoil. Except for special design situations, it is desirable that both the y-coordinate and slope be continuous between segments in order to insure geometric continuity. One

method of doing this would be to eliminate two of the coefficients of each polynomial in favor of the boundary conditions, so that geometric requirement is always satisfied. For a segment defining the leading edge of the airfoil, only one coefficient would be eliminated since the infinite slope at the leading edge is satisfied as a natural condition of equation (15). This would essentially result in a spline function modeling of the airfoil surface. The remaining polynomial coefficients would then be treated as design variables in the optimization process. This has the disadvantage that if one of the coefficients of a polynomial defining the leading edge of the airfoil were changed, the geometry would be changed over the entire airfoil surface, just as if a single polynomial had been used to define the surface. In other words, the desired uncoupling of the design variables cannot be achieved with this approach.

A second approach, and the one which was used in this study, is to treat the y-coordinate and slope at the match point between segments as design variables. For each such geometric boundary condition to a segment, one polynomial coefficient can be eliminated. Then the design variables in the optimization process will be the coordinates and slopes at the match point between polynomial segments plus the polynomial coefficients which have not been eliminated in favor of these boundary conditions. The slope at the leading edge of the airfoil will not be treated as a design variable since it is a natural boundary condition of equation (15). By using geometric variables and polynomial coefficients in this way to define the airfoil shape, the segments are now coupled only by the coordinate and slope at the match point. For example, if the y-coordinate is changed in figure 4 at the match point between segments 1 and 2 on the upper surface, only the geometry of these two segments is changed. The geometry of segment 3 on the upper surface and segments 4 and 5 on the lower surface will not be affected.

The method used here for defining the airfoil shape may be summarized by considering a simple example. Figure 6 is an airfoil in which the upper and lower surfaces are each defined by 2 segments, the match point being at the 50-percent chord. This is the basic airfoil definition which will be used in the design examples. The segments are defined by the following set of polynomials:

$$y_1 = b_1\sqrt{x/c} + a_{01} + a_{11}x/c + a_{21}(x/c)^2 + a_{31}(x/c)^3 + a_{41}(x/c)^4 \quad (16)$$

$$y_2 = a_{02} + a_{12}x/c + a_{22}(x/c)^2 + a_{32}(x/c)^3 \quad (17)$$

$$y_3 = b_3\sqrt{x/c} + a_{03} + a_{13}x/c + a_{23}(x/c)^2 + a_{33}(x/c)^3 \quad (18)$$

$$y_4 = a_{04} + a_{14}x/c + a_{24}(x/c)^2 + a_{34}(x/c)^3 \quad (19)$$

where the subscript on y and the second subscript on the coefficients denote the segment number. The geometric boundary conditions imposed on the airfoil are

$$y_1[x/c = 0] = 0 \quad (20)$$

$$y_2[x/c = 1] = 0 \quad (21)$$

$$y_3[x/c = 0] = 0 \quad (22)$$

$$y_4[x/c = 1] = 0 \quad (23)$$

The upper surface leading edge is defined by a fourth-order polynomial while the remaining segments are defined by third-order polynomials. The square-root term is omitted from segments 2 and 4 since it is unnecessary for these segments to satisfy the infinite slope requirement. This definition of the airfoil is arbitrary and other segmentation or polynomial order could be used just as easily.

The coordinates and slopes of the match points at the 50-percent chord for the upper and lower surface will be treated as design variables as will the slope at the trailing edge for the upper and lower surface. A total of 19 coefficients of the polynomials define the entire airfoil. Four of these coefficients are automatically eliminated in order to satisfy the geometric boundary conditions at the leading and trailing edge. An additional four coefficients are eliminated to satisfy geometric continuity at the match points so that 11 independent variables can now be used as design variables in the optimization process. The set of design variables chosen here is

$$\bar{X}^T = \left\{ y_{12} \ y'_{12} \ b_1 \ a_{11} \ a_{41} \ y'_{22} \ y_{32} \ y'_{32} \ b_3 \ a_{13} \ y'_{42} \right\} \quad (24)$$

where the second subscript on y denotes the end point of the segment (fig. 5). The remaining coefficients of the polynomials in equations (16) to (19) will be used to satisfy the geometric continuity and boundary conditions.

Having specified the airfoil definition for design it is now only necessary to provide an interface between the optimization and analyses programs to calculate the table of y -coordinates required by the aerodynamics program. This interface has been coded to provide the general airfoil design capability. The following section contains several examples to demonstrate the efficient application of the program.

DESIGN EXAMPLES

The following examples serve to identify the applicability of optimization techniques to airfoil design problems of general interest. The computer code is written in FORTRAN IV and was executed on a CDC 7600 computer.

Case 1: Lift Maximization, $M = 0.1$, $\alpha = 6^\circ$

The airfoil shown as a solid line in figure 7 was optimized to obtain maximum lift. Constraints were imposed on the area enclosed by the airfoil,

upper surface pressure coefficient near the leading edge, and maximum pitching-moment coefficient. The airfoil definition was the same as that described by equations (16) to (24) and by figure 6. The final airfoil is shown as dashed lines on figure 7, together with the initial and final pressure distributions and the airfoil characteristics. The section lift coefficient was improved by approximately 10 percent, and the constraint on pitching moment was active at the optimum. The design required 103 aerodynamic analyses and used 2 CPU minutes of computer time.

Case 2: Pitching-Moment Minimization, $M = 0.1$, $\alpha = 6^\circ$

The airfoil designed in case 1 was redesigned, except this time the absolute value of pitching-moment coefficient was minimized subject to a minimum section lift coefficient of 0.1. The results are shown in figure 8. In this case the initial design did not satisfy the lift requirement. The program overcame this constraint violation, while reducing the pitching-moment coefficient by approximately 10 percent. This design required 140 airfoil analyses and 3 minutes of CPU time.

Case 3: Lift Maximization, $M = 0.75$, $\alpha = 0^\circ$

Figure 9 presents the results of lift maximization for a high-speed airfoil with a wave drag constraint. The initial airfoil is the same as that used for low-speed optimization in the previous two examples and represents an extreme violation of the drag limit. This constraint violation was overcome, resulting also in a lower lift coefficient at optimum. The final airfoil represents the maximum lift that could be achieved while satisfying this drag constraint. The design required 143 aerodynamic analyses and 9 CPU minutes of computer time. While the design time could be reduced by beginning with a more reasonable initial airfoil, this example demonstrates that major improvements can be achieved even beginning with an arbitrary initial design which violates one or more constraints.

Case 4: Design of Wind-Tunnel Strut for Minimum Wave Drag

The final example of this study was the design of the strut for the Ames 12-ft wind tunnel which will have a higher drag divergence Mach number than the commonly used double wedge strut. The results of the design are shown in figure 10. Only the leading and trailing edges of the strut were redesigned, and the strut was required to be symmetric about the midplane. The wave drag was minimized at $M = 0.82$, and the design required 47 airfoil analyses and 1.5 CPU minutes of computer time. As shown in figure 10, the drag divergence Mach number is increased by approximately 0.1 for the optimized strut. It is also interesting to note that the rate of increase in drag after divergence is less for the optimized strut than for the double wedge.

Such reshaping of the strut is important from energy considerations. Lower wave drag means less power to run the tunnel at a fixed Mach number

and total pressure. Or the excess power could be used to attain a higher test Mach number than could be achieved with a double wedge strut.

CONCLUDING REMARKS

A practical procedure has been presented for automated airfoil design using numerical optimization techniques. The approach is to couple an existing aerodynamic analysis program with a general application optimization program. This is possible as a result of simultaneous development in recent years of efficient optimization techniques and reliable aerodynamic analysis methods. Because the optimization process usually requires only small perturbations of a previously analyzed airfoil, iterative methods for aerodynamic analysis are well suited to this process. The choice of functional relationships used to describe the airfoil is a critical factor in achieving efficiency and reliability of the method.

The procedure is efficient and easy to use; the engineer is free to specify the objective and constraints in order to satisfy his particular set of design requirements. Extension of the technique to viscous drag minimization or lift/drag maximization appears to be straightforward. Additionally, application to other aerodynamic design problems, such as rotor blade design or engine inlet design, appears feasible. Each of these extensions is primarily dependent on the availability of the appropriate aerodynamic programs.

Extension of the method to include constraints on off-design aerodynamic characteristics is desirable. The feasibility of this extension was demonstrated in reference 6 where an airfoil was designed for a minimum wave drag at $M = 0.8$ with a drag rise constraint at $M = 0.81$. The addition of constraints on off-design conditions is straightforward but does increase computer run times because of the required aerodynamic analyses. However, for finite difference gradient computations only those off-design conditions for which constraints are active or violated need to be analyzed, thereby reducing the required computational effort.

Optimization techniques, together with efficient aerodynamic analysis, offer a general and efficient automated design capability. It is desirable that the aerodynamic programs be written so that they are easily incorporated into the design program. This is readily achieved by separating the program into input, execution, and output segments so that the execution portion of the program can be called repeatedly during the design process. Because many aerodynamic analyses are required for design, it is important that this program be as efficient as possible. Major effort is warranted to develop programs which perform efficient re-analysis for a variety of flight conditions. Development of such "design-oriented" aerodynamic analysis programs will greatly enhance the automated airfoil design process.

REFERENCES

1. Jameson, Antony: Transonic Flow Calculations for Airfoils and Bodies of Revolution. Grumman Aerodynamics Report 390-71-1, Dec. 1971.
2. Zoutendijk, G. G.: Methods of Feasible Directions. Elsevier, Amsterdam, 1960.
3. Vanderplaats, Garret N., and Moses, Fred: Structural Optimization by Methods of Feasible Directions. Journal of Computers and Structures, vol. 3, 1973, pp. 739-755.
4. Fletcher, R., and Reeves, C. M.: Function Minimization by Conjugate Directions. Brit. Computer Jour., vol. 7, no. 2, 1964, pp. 149-154.
5. Vanderplaats, Garret N.: CONMIN - A Fortran Program for Constrained Function Minimization. NASA TM X-62,282, 1973.
6. Hicks, Raymond M., Murman, Earll M., and Vanderplaats, Garret N.: An Assessment of Airfoil Design by Numerical Optimization. NASA TM-X 3092, 1974.

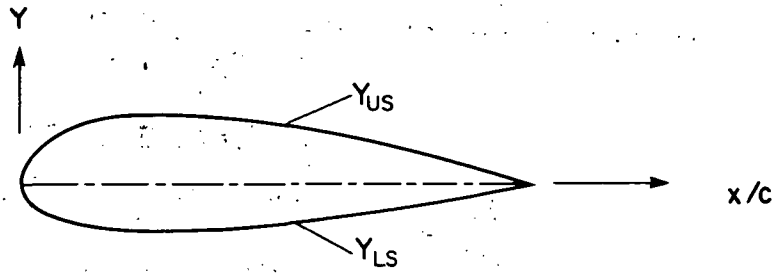


Figure 1.— Airfoil geometry.

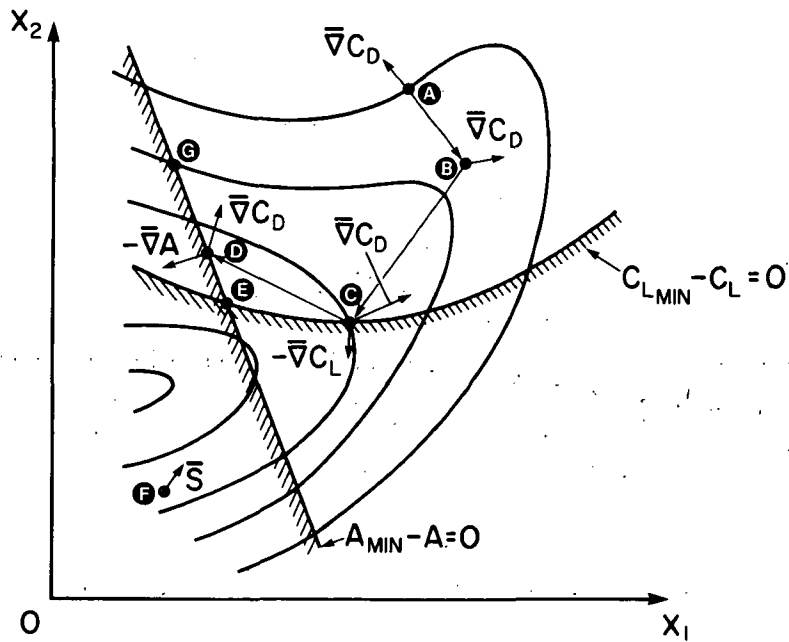


Figure 2.— Two-variable design space.

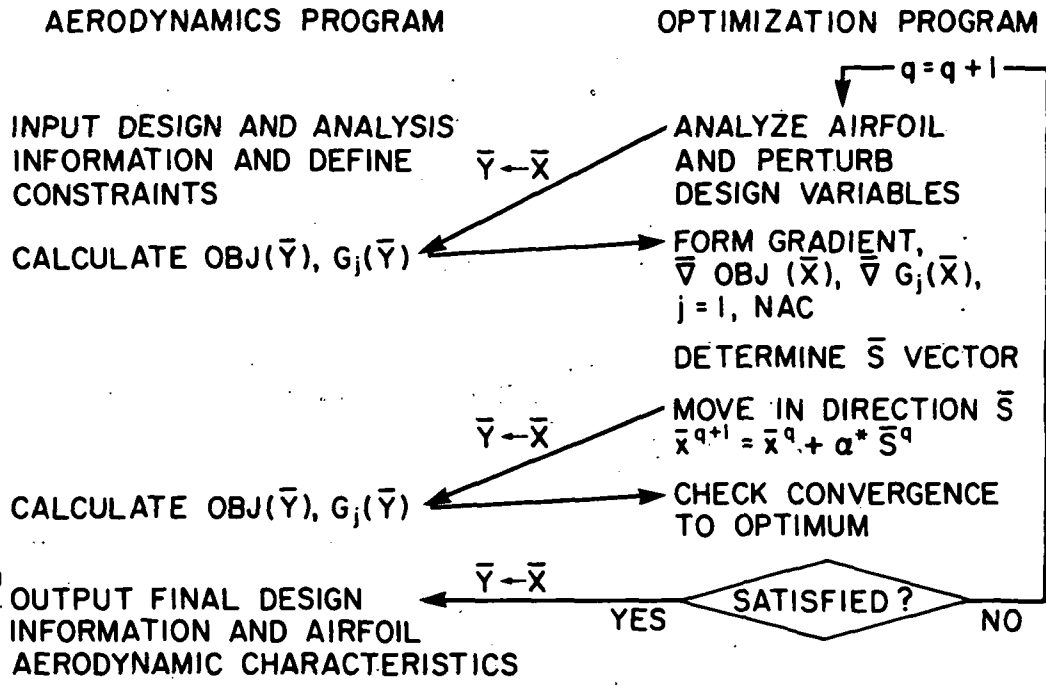


Figure 3.— Program organization.

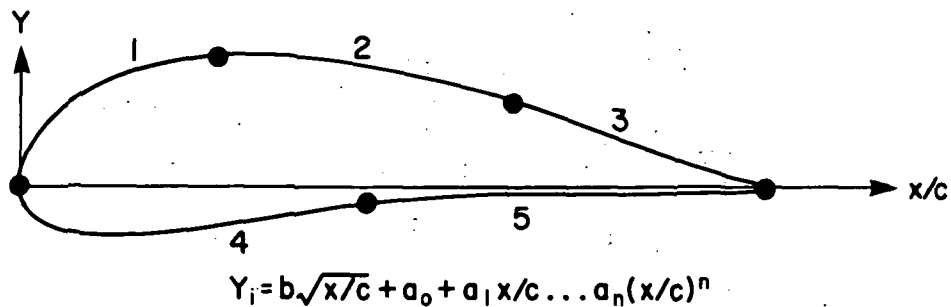


Figure 4.— Typical airfoil description.

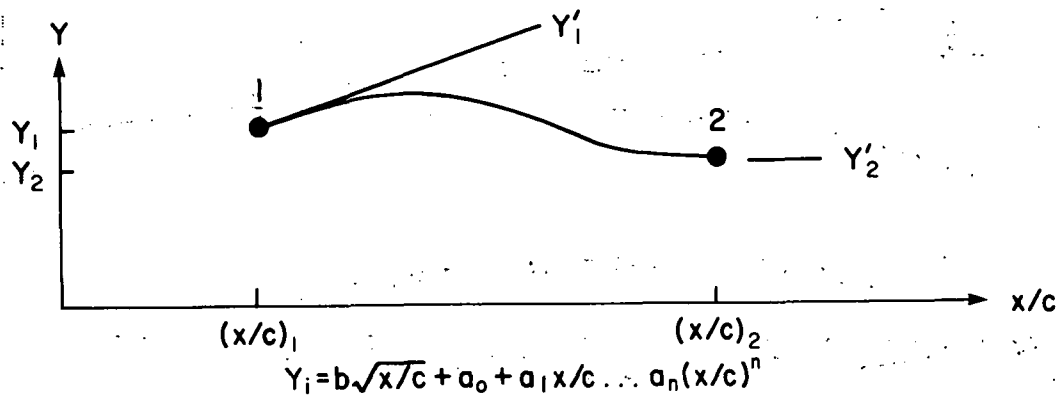


Figure 5.— Typical airfoil segment.

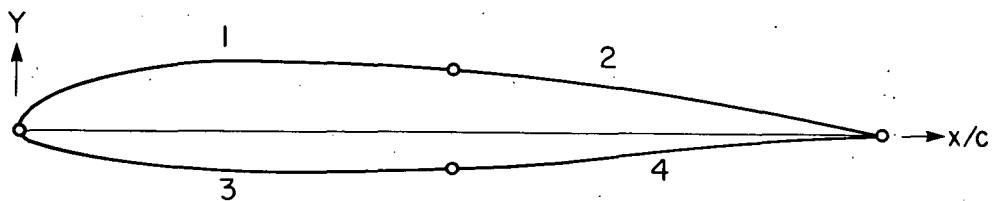
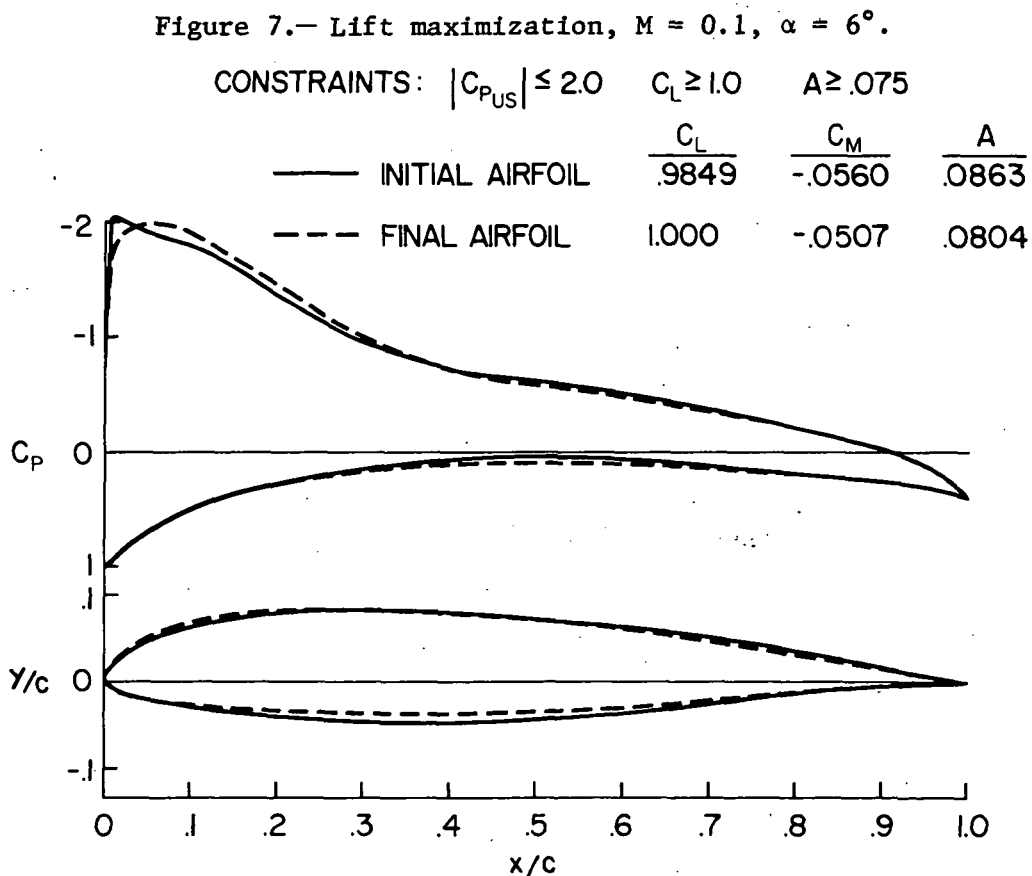
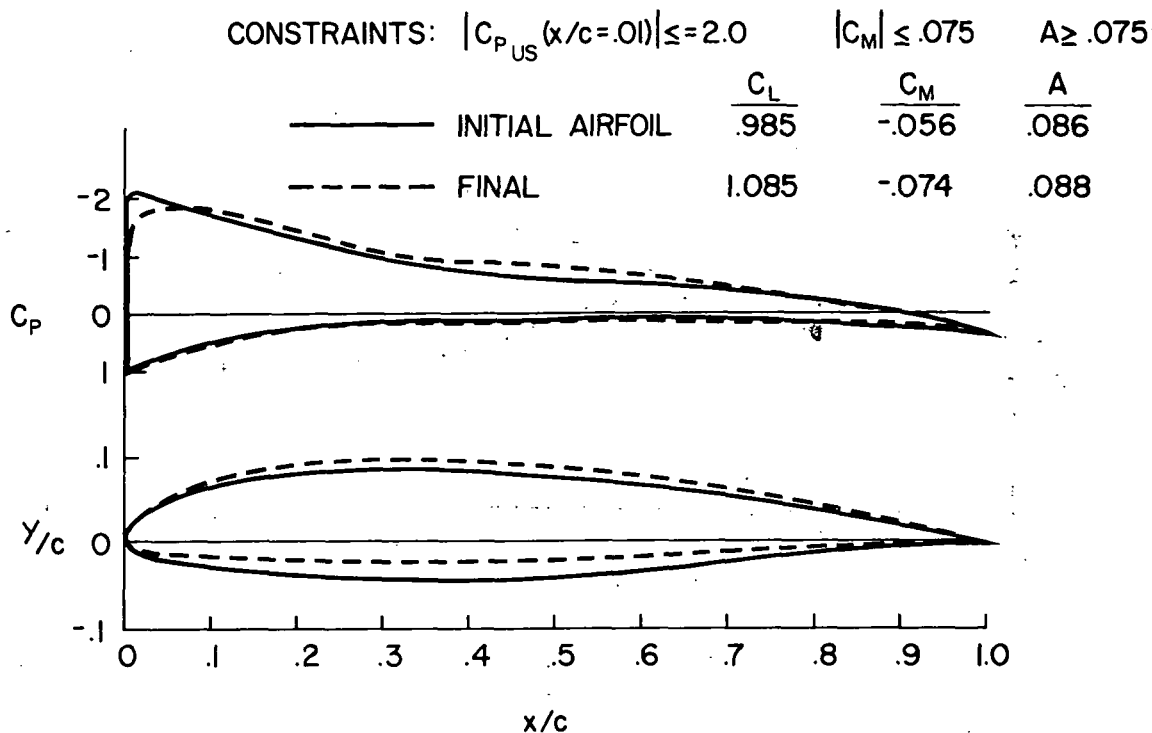


Figure 6.— Airfoil design example.



CONSTRAINTS $C_D \leq 0.004$ $A \geq 0.075$

	C_L	C_D	C_M	A
INITIAL AIRFOIL	.4873	.0149	-.0848	.0863
FINAL AIRFOIL	.3884	.0040	-.0741	.0896

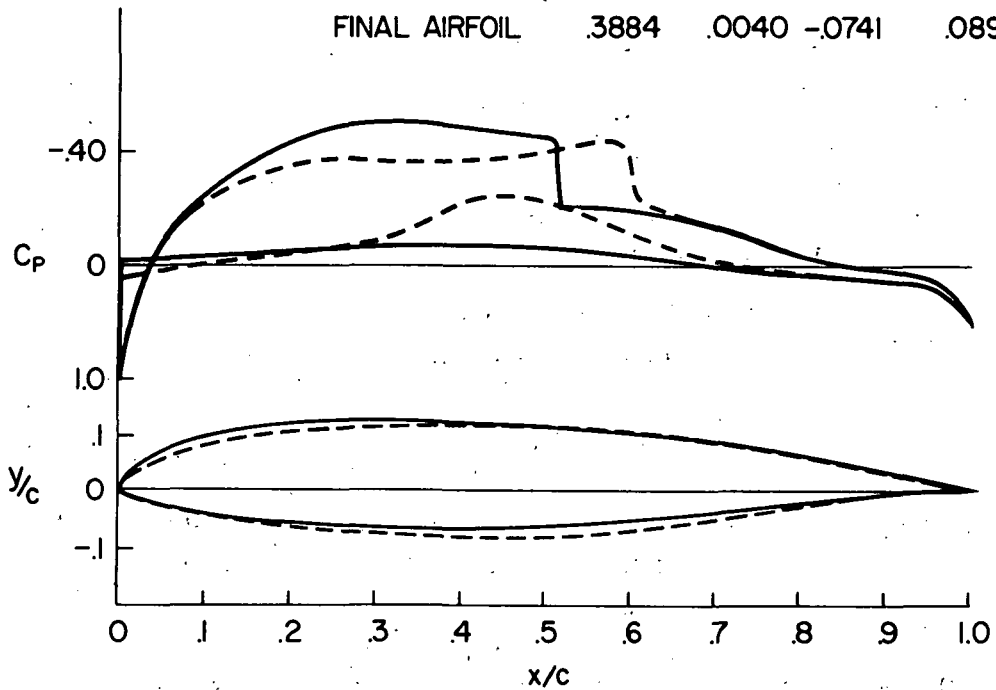


Figure 9.— Lift maximization, $M = 0.75$, $\alpha = 0^\circ$.

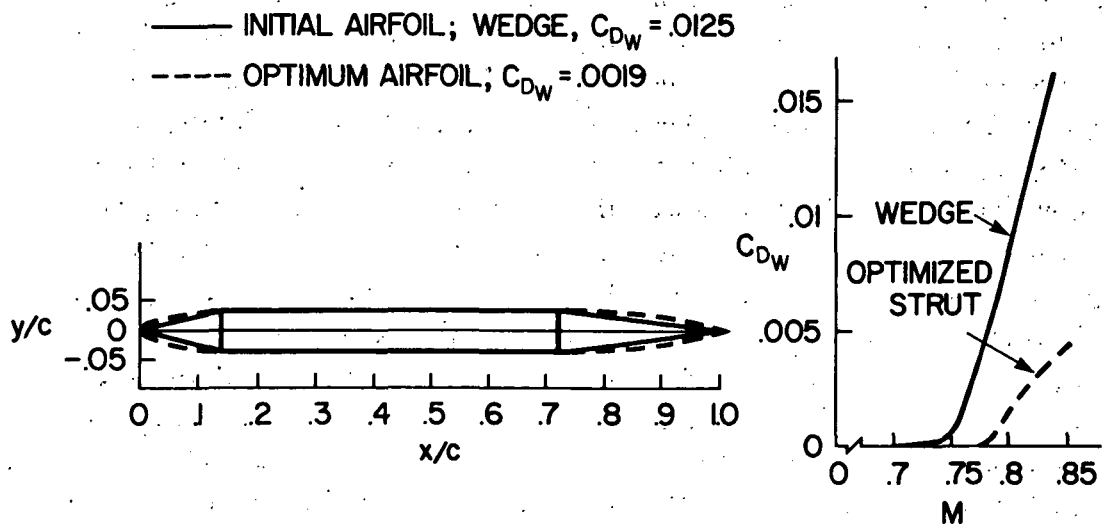


Figure 10.— Wave drag minimization of strut, $M = 0.82$.

TSFOIL - A COMPUTER CODE FOR TWO-DIMENSIONAL TRANSONIC
CALCULATIONS, INCLUDING WIND-TUNNEL WALL EFFECTS
AND WAVE-DRAG EVALUATION

By Earll M. Murman,
Flow Research, Inc.

Frank R. Bailey,
NASA Ames Research Center
and Margaret L. Johnson
Computer Sciences Corporation

SUMMARY

An up-to-date computer program to solve the transonic small-disturbance equation for two-dimensional flow past lifting airfoils has been written. The theoretical and numerical formulation of the code is outlined and several computed examples are included. The user-oriented code is capable of computing both free-air flows and various wind-tunnel wall conditions. Applications and limitations of the program are discussed.

INTRODUCTION

During the past 5 years, many transonic flow design and analysis problems have been solved using computational methods. Rapid advancement has been made in the speed and accuracy of the numerical techniques, in the level of approximations used in the governing equations, and in the complexity of the configurations analyzed. In this period of growth, it has been difficult for the development of the user-oriented or production computer programs to keep pace with the basic research computer programs. A notable exception has been the two-dimensional codes employing the full-potential equations developed at the Courant Institute (ref. 1). The present work was undertaken to provide a user-oriented program for solving the two-dimensional transonic small-perturbation equations for lifting airfoils. The objectives have been to assemble a well-organized computer program which could solve a variety of problems, and to provide sufficient documentation to allow users to modify and extend the basic code to new cases. It is anticipated that the solution of the small-disturbance problem embodied in TSFOIL

will provide a complementary analysis tool to the programs incorporating the full-potential equations.

This paper describes the features and capabilities of the program and presents some sample calculations. Full documentation of the governing equations, numerical analysis, and computer program will follow in future NASA publications. The basic solution of the problem follows the work of Krupp and Murman (refs. 2 and 3). Various improvements in the numerical techniques (refs. 4 and 5) have been incorporated as well as the extensions of transonic small-disturbance theory to evaluate inviscid drag (ref. 6) and to treat wind-tunnel-wall boundary conditions (ref. 7) and supersonic free-stream flows (ref. 8). The basic program has been assembled and mostly debugged during this past year. Although the final version is not yet available, some preliminary copies have been distributed on request.

SYMBOLS

$$A = \frac{\alpha}{\delta}$$

C	contour of integration
C_D	inviscid drag coefficient
C_L	lift coefficient
C_M	pitching-moment coefficient
C_p	pressure coefficient
C_p^*	critical pressure coefficient
F	slot parameter
F(x)	airfoil shape function
H	ratio of tunnel half-height to airfoil chord
\tilde{H}	transonic-scaled tunnel height
K	transonic similarity parameter

M	Mach number
p_0	total pressure
P	porosity
\tilde{P}	transonic-scaled porosity
S	shock
U	velocity
x, y	Cartesian coordinates normalized by the airfoil chord
x_m	location of pitching-moment axis
\tilde{y}	transonic similarity coordinate
Δx	mesh spacing in x -direction
$\Delta \tilde{y}$	mesh spacing in \tilde{y} -direction
α	angle of attack
γ	ratio of specific heats
Γ	circulation
δ	airfoil thickness ratio
θ	flow angle
Φ, ϕ	perturbation potentials
Φ_t	total potential

Subscripts:

- i** denotes the x mesh point
- J** denotes the \tilde{y} mesh point on tunnel wall boundary
- s** evaluated on shock
- l** lower surface
- u** upper surface
- max** maximum
- min** minimum
- ∞ free-stream conditions

Superscripts:

- k,m,n** exponents for transonic similarity parameters (see table I)

THEORETICAL FORMULATION

The partial differential equation solved by TSFOIL is the transonic small-disturbance equation which may be written either in physical variables

$$\left[(1 - M_\infty^2) \Phi_x - \frac{\gamma + 1}{2} M_\infty^k \Phi_x^2 \right]_x + \Phi_{yy} = 0 \quad (1)$$

or in similarity variables

$$\left(K \phi_x - \frac{\gamma + 1}{2} \phi_x^2 \right)_x + \phi_{\tilde{y}\tilde{y}} = 0 \quad (2)$$

where Φ, ϕ are the perturbation potentials defined as

$$\Phi_t = U_\infty (x + \Phi + \dots) = U_\infty (x + \delta^{2/3} M_\infty^{-n} \phi + \dots) \quad (3)$$

and where δ is the airfoil thickness ratio, M_∞ is the free-stream Mach number, γ is the ratio of specific heats, x and y are the Cartesian coordinates normalized by the airfoil chord, and

$$\tilde{y} = \delta^{1/3} M_\infty^m y \quad (4)$$

$$K = \frac{1 - M_\infty^2}{M_\infty^{2m} \delta^{2/3}} \quad (5)$$

In the actual program, the similarity notation (eq. (2)) has been adopted to properly scale the variables and to provide consistency with the theory developed in the references. As one of the input options, the user may choose to specify all information in either the physically scaled variables (M_∞ , δ , α , etc.) or the similarity variables (K , $A = \alpha/\delta$, etc.). By selecting the values for k , m , and n in equations (1), (3), (4), and (5), the scaling rules given by Cole, Spreiter, or Krupp (table I) may be selected. The choice of these exponents of M_∞ basically modify or "tune-up" the small-disturbance theory to provide a more accurate approximation of solutions to the full-potential equation over a wider range of M_∞ and δ .

The airfoil is assumed to be at an angle of attack α with a shape described by

$$y_{u,\ell} = \delta F(x)_{u,\ell} \quad 0 \leq x \leq 1 \quad (6)$$

for the upper (u) and lower (ℓ) surfaces. Again, the user may choose to input the physical variables $y_{u,\ell}$ and α or the similarity variables $F_{u,\ell}$ and $A = \alpha/\delta$ by either a formula or a table of ordinates. Incorporated in the program are descriptions of the parabolic arc airfoil,

$$F(x)_{u,\ell} = \pm 2x(1 - x) \quad (7)$$

NACA four-digit series airfoil,

$$F(x)_{u,\ell} = \pm (1.4845\sqrt{x} - 0.63x - 1.758x^2 + 1.4215x^3 - 0.5075x^4) \quad (8)$$

and Korn (ref. 9) airfoil as default cases. In the small-disturbance theory the airfoil boundary condition is applied as a Neumann condition

$$(\phi_{\tilde{y}})_{u,\ell} = \left[\frac{dF(x)}{dx} \right]_{u,\ell} - A \quad (9)$$

on the mean surface slit ($y = \pm 0$, $0 \leq x \leq 1$). Small-disturbance theory is singular at the leading- and trailing-edge stagnation points. However, if in the region of the leading edge, the airfoil shape is described as

$$F(x) = ax^p + \dots \quad (10)$$

the singularity is integrable if $p > 0.4$, and local solutions show that no leading-edge singular drag force is present for nonlifting shapes (ref. 10).

To complete the specification of the potential flow problem past a lifting body, a condition must be added to give a unique value of lift or circulation. Two choices have been incorporated. The first option is the usual Kutta condition wherein it is required that the pressures or velocity perturbations at the trailing edge be equal, i.e.,

$$\phi_x(1, 0+) = \phi_x(1, 0-) \quad (11)$$

The method proposed by Ballhaus and Bailey (ref. 5) has been used to enforce the Kutta condition. When the Kutta condition is specified, the value of lift constitutes part of the solution to the problem. The second option is to specify the value of lift as an input and to eliminate the Kutta condition requirement (eq. (11)). In this case, the pressure is double-valued at the trailing edge. A third option of specifying both the lift and Kutta condition and computing the angle of attack as part of the solution has not been incorporated. In any of these cases, the pressure and flow angle downstream of the airfoil slit must be continuous but the potential must jump by the value of the circulation (fig. 1).

For the conditions far away from the body, boundary conditions have been incorporated to represent free-air flows and various wind-tunnel wall conditions at both subsonic and supersonic free-stream conditions. For free-air flow with $M_\infty < 1$, the appropriate conditions at infinity require that all velocity perturbations vanish

$$\phi_x, \phi_{\tilde{y}} \rightarrow 0 \text{ as } x^2 + \tilde{y}^2 \rightarrow \infty \quad (12)$$

In the program a far-field solution for a compressible vortex and a doublet (ref. 7) are used to specify ϕ on outer boundaries (fig. 1). For free-air flows with $M_\infty > 1$, the appropriate boundary (or initial) conditions are

$$\phi_x, \phi_{\tilde{y}} \rightarrow 0 \text{ as } x \rightarrow -\infty \quad (13)$$

On the top and bottom boundaries a far-field condition is specified

$$\phi_{\tilde{y}} = \mp \sqrt{K} \phi_x \quad (14)$$

to prohibit reflected waves (fig. 2). At the downstream boundary, the flow is required to be supersonic so that no condition is needed.

To simulate flow in a wind tunnel, the classical homogeneous tunnel-wall boundary condition

$$\phi_x \pm FH\phi_{xy} \pm \frac{1}{P} \phi_y = 0 \quad (15)$$

is applied at the tunnel walls ($y = \pm H$), where H is the tunnel half-height to chord ratio, F is the slot parameter (ref. 7), and P is the porosity. Equation (15) is transformed to the similarity variables

$$\phi_x \pm F\tilde{H}\phi_{x\tilde{y}} \pm \frac{1}{\tilde{P}} \phi_{\tilde{y}} = 0 \quad \text{on } \tilde{y} = \pm\tilde{H} \quad (16)$$

The following special cases extracted from equation (16) have been computed:

solid wall	$\tilde{P} \rightarrow 0$	$\phi_{\tilde{y}} = 0$	(17)
------------	---------------------------	------------------------	------

free jet	$F \rightarrow 0, \tilde{P} \rightarrow \infty$	$\phi_x = 0$	(18)
----------	---	--------------	------

perforated wall	$F \rightarrow 0$	$\tilde{P}\phi_x \pm \phi_{\tilde{y}} = 0$	(19)
-----------------	-------------------	--	------

ideal slotted wall	$\tilde{P} \rightarrow \infty$	$\phi_x \pm F\tilde{H}\phi_{x\tilde{y}} = 0$	(20)
--------------------	--------------------------------	--	------

The general case given by equation (16) has been included in the theoretical formulation but has not yet been included in the numerical analysis. For tunnel flows with subsonic free streams, upstream and downstream far-field boundary conditions are derived for ϕ which satisfy $\phi_x \rightarrow 0$ at $x \rightarrow \pm\infty$ together with equation (16) and the linearized version of equation (2). The case of choked tunnels has not been considered. For supersonic free-stream Mach numbers, the upstream conditions $\phi_x, \phi_{\tilde{y}} \rightarrow 0$ at $x \rightarrow -\infty$ are incorporated directly, and at the downstream boundary, the flow is required to be supersonic. Figure 3 summarizes the boundary conditions used for the wind-tunnel simulation problems.

It is hoped that the theoretical formulation has been kept sufficiently general that other flow conditions besides the above can be incorporated into the program by future

users: The simplifications of transonic small-disturbance theory, particularly in regards to the mean surface approximation for applying boundary conditions, should permit this with minimum modifications to the basic code.

When the solution for ϕ is known, virtually all quantities of interest may easily be obtained throughout the entire flow field. These include the pressure coefficient, flow angle, Mach number, and total pressure loss across embedded shock waves given by the respective formulas:

$$C_p = \delta^{2/3} M_\infty^{-n} (-2\phi_x) \quad (21)$$

$$\theta = \delta\phi_{\tilde{y}} \quad (22)$$

$$M = \left\{ 1 - [K - (\gamma + 1)\phi_x] \delta^{2/3} M_\infty^{2m} \right\}^{1/2} \quad (23)$$

$$\frac{[p_0]}{p_{0\infty}} = 1 + \delta^2 \frac{(\gamma + 1)}{12} [\phi_x]_s^3 \quad (24)$$

where $[]$ denotes the jump in a quantity across a shock wave. The lift and pitching moment are computed by integrating equation (21) around the airfoil in the usual way

$$C_L = - \int_0^1 (C_{p,u} - C_{p,l}) dx \quad (25)$$

$$C_M = \int_0^1 (x - x_m)(C_{p,u} - C_{p,l}) dx \quad (26)$$

The inviscid drag coefficient is obtained by integrating the appropriate momentum flux relationship around a contour C enclosing the airfoil and including an integral along all shocks S contained within C as illustrated in figure 4 and discussed in reference 6. The formula is

$$C_D = \delta^{5/3} M_\infty^{-n} \left\{ \oint_C \left[K\phi_x^2 - \phi_{\tilde{y}}^2 - \frac{2}{3}(\gamma + 1)\phi_x^3 \right] d\tilde{y} - (\phi_x\phi_{\tilde{y}}) dx - \frac{\gamma + 1}{6} \int_{S \subset C} [\phi_x]^3 d\tilde{y} \right\} \quad (27)$$

NUMERICAL FORMULATION

Equation (2) is replaced by a system of mixed finite-difference equations which are solved by an iterative successive line overrelaxation (SLOR) algorithm. The difference equations are in the fully conservative form (ref. 4) to guarantee that the correct shock jumps are calculated. A Cartesian mesh with variable spacing used by the authors in

previous work has been retained in lieu of the coordinate mapping procedures adopted by some workers. Although either approach would be acceptable for the present problems, it was felt that the variable Cartesian mesh would ease the extension of the program to new problems, while it also retains the ability to locally refine the mesh where desired. The initial guess for ϕ needed to start the relaxation solution may be selected either as undisturbed flow ($\phi = 0$), or from a previously calculated case stored in core or on a peripheral unit.

Convergence of the relaxation iterations to a desired residual error is accelerated by using overrelaxation and mesh refinement. The latter is incorporated in the following way. An input x and y mesh is specified which has an odd number of mesh points (including the end points) equal to $4N + 1$ in each of the four intervals: (1) x_{\min} to $x = 1$ (trailing edge), (2) $x = 1$ to x_{\max} , (3) y_{\min} to $y = 0$, and (4) $y = 0$ to y_{\max} .

With this arrangement, every other mesh point may be deleted, leaving $2N + 1$ mesh points with the same end-point location. Once again, every other mesh point may be deleted, leaving $N + 1$ mesh points with the same end points to each interval. The process can be repeated again if all N are odd or if there are $8N + 1$ initial mesh points, etc. The iterative solution may then be started on the coarsest mesh and, after suitable convergence is achieved, continued on the next fine mesh by reinserting every other mesh point. The advantage of this is twofold. First, the user may input the mesh on which the final solution is desired, and all the intermediate mesh deletions and refinements proceed automatically. Second, the points on which boundary conditions are applied remain unchanged. In practice, we have found that three meshes (coarse, medium, and final) are adequate. On each mesh, overrelaxation factors are used for elliptic points, and slight underrelaxation factors are used for the other points. The rate of convergence is greatly enhanced by increasing the overrelaxation factor as much as possible while maintaining stability. We try to achieve 1.8 on the finest mesh. Other convergence acceleration techniques, such as the extrapolation methods explored by Hafez and Cheng (ref. 11) and the circulation updating techniques employed by Ives and Melnik (ref. 12), have not been incorporated as yet into the code.

The numerical procedures employed here are of the shock-capturing variety; i.e., the shock is spread over several mesh intervals rather than being an exact discontinuity. Use of the fully conservative difference equations ensures that the correct shock jump will be computed as the mesh is refined (ref. 4). Earlier versions of the difference equations were not in fully conservative form, and incorrect shock jumps were often computed. Fortunately, the incorrect shock jumps are in better agreement with the data. As an input option, the user may specify the not fully conservative form of the difference equations. The authors do not recommend such calculations as they are generally incorrect.

The difference equations for $\phi_{\tilde{y}\tilde{y}}$ must be modified at the top and bottom boundaries ($\tilde{y} = \pm\tilde{H}$) to incorporate the wind-tunnel-wall boundary conditions (eqs. (17) to (20)). These modifications are given below for $\tilde{y} = \tilde{H}$ and for an even mesh ($\Delta\tilde{y} = \text{Constant}$, $\Delta x = \text{Constant}$). Extensions to the uneven mesh case and for $\tilde{y} = -\tilde{H}$ follow directly. For the free jet and perforated wall with $\tilde{P} > 1.5$, equations (18) and (19) are integrated once in x to yield, respectively,

$$\phi_{\tilde{y}\tilde{y}}^{n+1}(x, \tilde{H}) = \phi(-\infty, \tilde{H}) \quad (28)$$

$$\phi_{\tilde{y}\tilde{y}}^{n+1}(x, \tilde{H}) = \phi(-\infty, \tilde{H}) - \frac{1}{\tilde{P}} \int_{-\infty}^x \phi_{\tilde{y}}^n dx \quad (29)$$

at the $(n+1)$ th iteration. Let i denote the x mesh point and J the \tilde{y} mesh point at the wall ($\tilde{y} = \tilde{H}$). These Dirichlet boundary conditions for $\phi(x, \tilde{H})$ are then incorporated into the difference formula for $\phi_{\tilde{y}\tilde{y}}$ at the mesh point $i, J-1$ as

$$\phi_{\tilde{y}\tilde{y}}^{n+1} = \frac{\phi_{i,J}^{n+1} - 2\phi_{i,J-1}^{n+1} + \phi_{i,J-2}^{n+1}}{(\Delta\tilde{y})^2} \quad (30)$$

For the solid wall, perforated wall with $\tilde{P} \leq 1.5$, and ideal slotted wall, equations (17), (19), and (20) are applied as Neumann boundary conditions for $\phi_{\tilde{y}}$. The difference equations used for $\phi_{\tilde{y}\tilde{y}}$ at the mesh point i, J is

$$\phi_{\tilde{y}\tilde{y}}^{n+1} = \frac{2}{\Delta\tilde{y}} \phi_{\tilde{y},J}^{n+1} - \frac{\phi_{i,J}^{n+1} - \phi_{i,J-1}^{n+1}}{\Delta\tilde{y}} \quad (31)$$

For the solid wall, $\phi_{\tilde{y},J}^{n+1} = 0$. For the perforated wall, $\phi_{\tilde{y},J}^{n+1}$ is computed from the upwind formula

$$\phi_{\tilde{y},J}^{n+1} = -\tilde{P} \left(\frac{\phi_{i,J}^{n+1} - \phi_{i-1,J}^{n+1}}{\Delta x} \right) \quad (32)$$

The ideal slotted-wall condition is applied by integrating equation (20) once in x to give

$$\phi_{\tilde{y},J}^{n+1} = \phi_{\tilde{y}}(-\infty, \tilde{H}) - \frac{1}{F\tilde{H}} \phi_{i,J}^{n+1} - \phi(-\infty, \tilde{H}) \quad (33)$$

Applying the perforated-wall condition differently, depending on the value of \tilde{P} , increases numerical stability and permits a smooth transition to the limiting cases of a free jet

($\tilde{P} \rightarrow \infty$) and a solid wall ($\tilde{P} \rightarrow 0$). Equation (33) has proven to be quite stable for the range of $F\tilde{H}$ computed to date.

COMPUTER PROGRAM

TSFOIL is written in FORTRAN IV and has been run and debugged on a CDC 7600. Clarity in the program structure and function has been stressed whenever it does not unduly compromise computational efficiency. As a result, TSFOIL consists of approximately 50 subroutines, 30 common blocks, and is liberally laced with comment cards. All input, except for an identifying header card, is read in NAMELIST form into one subroutine, READIN. Each input quantity contains a default value so that the entire program could be executed by only reading a header card and the required minimum of one value into NAMELIST INP. Multiple cases may be run sequentially. A number of "fail-safe" checks are included to identify bad input data and divergent calculations. Output includes (1) all input data, (2) convergence history, C_L , C_M , and computed pressure distribution with printer plots for each mesh (coarse, medium, final), (3) additional flow-field information and drag coefficient for the final mesh, and (4) pressures on the tunnel wall.

A number of cases have been computed using TSFOIL during the last 6 months and the program has been essentially debugged. There are, however, some ongoing problems which are discussed subsequently.

COMPUTED EXAMPLES

Several computed examples are included here to illustrate the capabilities and accuracy of program TSFOIL. Figure 5 shows the calculation for a shock-free lifting transonic airfoil designed by Korn (ref. 9). The result is essentially identical to the original calculation by Krupp (ref. 3) except that the original result did not include evaluation of the drag coefficient by equation (27). The three integrated force coefficients are in good agreement with the exact solution, although the pressure distributions are somewhat different. This calculation represents the default calculation in TSFOIL and requires approximately 10 CPU seconds of CDC 7600 time with the use of the FTN, OPT-2 compiler. On the coarse x,y-mesh (15×20) the calculation took 300 iterations and the residual in ϕ did not converge. On the medium mesh (29×39), the calculation converged in 130 iterations to a residual of 5×10^{-5} . On the fine mesh (57×77), the calculation converged in 180 iterations to a residual of 5×10^{-5} .

Free-air and ideal slotted wind-tunnel calculations are compared in figure 6 with the data of Stivers (unpublished data from Ames Research Center) for a NACA 64A010 airfoil at a measured $M_\infty = 0.802$ and geometric $\alpha = 2.0^\circ$. The data were obtained in the

Ames 2- by 2-foot transonic wind tunnel, using a 15.2-cm (6 in.) chord model ($H = 2$) at a Reynolds number of 4×10^6 . The formula of Baldwin, et al. (in ref. 7) was used for the slot parameter F giving a value of 0.066. Three calculations are shown. The free-air result is seen to greatly overpredict the value of lift and, consequently, the pressure distribution is in poor agreement with the data. When the slotted-wall boundary condition representative of the Ames 2- by 2-foot transonic wind tunnel is included, the lift is substantially decreased and the shock wave is displaced upstream approximately 10 percent of chord. A considerable discrepancy between data and calculations still remains, however, due to the displacement thickness of the turbulent boundary layer. Finally, when the lift is set at the measured value and the tunnel wall is included, the theory and data are in good agreement everywhere except downstream of the shock. It appears for this case that approximately 40 percent of the difference between free-air theory and measured results for lift and shock position are attributable to tunnel-wall effects, and the remaining 60 percent is a result of viscous effects. Clearly, a complete theory for airfoils must treat both of these effects, since they can be of the same order of magnitude.

Figures 7(a) to 7(d) illustrate the effect of different tunnel-wall boundary conditions for an NACA 64A010 airfoil at $M_\infty = 0.75$, $\alpha = 2^\circ$, and $H = 2$. For the range of parameters selected, the slotted tunnel produces the least interference drag. The large interference drag of the perforated tunnel is caused by a transonic buoyancy effect (ref. 6).

A final result (fig. 8) shows a comparison between the results of TSFOIL and a supercritical airfoil designed using the optimization method reported at this conference (ref. 13) and the full-potential equation program of Jameson (ref. 14). The differences between the two results are evident but not severe for this rather thick (12.8 percent) airfoil. The two results yield the same shock position with some difference in strength. The small-disturbance solution using fully conservative difference equations predicts a considerably lower wave drag as was earlier discovered for nonlifting airfoils (ref. 6).

DISCUSSION

Several computational problems have been encountered in using TSFOIL. One of these, illustrated in figure 8, is the appearance of oscillations or irregularities near the leading edge. The oscillations appear greater than in the earlier results of Krupp (ref. 3) and may be due to some differences in the numerical procedures or to an undiscovered error in the program. However, it would be desirable to eventually incorporate a local solution for a lifting blunt-nosed airfoil to avoid numerically integrating through this region. A number of calculations which were anticipated to be successful were divergent and this might be attributable to a nose problem. A second difficulty has been encountered when the shock wave on the upper surface reaches the trailing edge, although we cannot see any fundamental reason why this case cannot be computed. The current

treatment of the Kutta condition and/or jump relations across the slit ($y = 0, x > 1$) appears inadequate. A third source of difficulty has been the computation of supersonic free-stream cases for lifting airfoils. Nonlifting symmetric airfoil cases have successfully been reproduced. Again, we feel there is no fundamental reason to prohibit successful solution of this category of problems.

CONCLUDING REMARKS

The program TSFOIL has been written for calculating a variety of two-dimensional transonic flows using small-disturbance theory. The program incorporates many of the advances in numerical methods and theoretical extensions of small-disturbance theory made during the past few years. Although the program is not in its final form, the major part of the development is complete, and a number of interesting examples have been computed. The input/output and program structure have been kept as simple as possible. It is hoped that the program will provide a basic tool which can be used to analyze free-air and wind-tunnel flows, which can be extended to other problems of interest, and in which can be incorporated the ever increasing number of improvements in numerical methods.

REFERENCES

1. Bauer, F.; Garabedian, P.; and Korn, D.: A Theory of Supercritical Wing Sections, With Computer Programs and Examples. Lecture Notes in Economics and Mathematical Systems, Volume 66, M. Beckmann and H. P. Kunzi, eds., Springer-Verlag, c.1972.
2. Krupp, J. A.; and Murman, E. M.: Computation of Transonic Flows Past Lifting Airfoils and Slender Bodies. AIAA J., vol. 10, no. 7, July 1972, pp. 880-886.
3. Krupp, J. A.: The Numerical Calculation of Plane Steady Transonic Flows Past Thin Lifting Airfoils. Ph. D. Diss., Univ. of Washington, 1971.
4. Murman, E. M.: Analysis of Embedded Shock Waves Calculated by Relaxation Methods. AIAA J., vol. 12, no. 5, May 1974, pp. 626-632.
5. Ballhaus, W. F.; and Bailey, F. R.: Numerical Calculation of Transonic Flow About Swept Wings. AIAA Paper No. 72-677, June 1972.
6. Murman, E. M.; and Cole, J. D.: Inviscid Drag at Transonic Speeds. AIAA Paper No. 74-540, July 1974.
7. Murman, E. M.: Computation of Wall Effects in Ventilated Transonic Wind Tunnels. AIAA Paper No. 72-1007, Sept. 1972.
8. Murman, E. M.: A Relaxation Method for Calculating Transonic Flows With Detached Bow Shock Waves. Proceedings of the Third International Conference on Numerical Methods in Fluid Mechanics. Lecture Notes in Physics, vol. 19, pp. 201-206, July 1972.
9. Kacprzyński, J. J.; Ohman, L. H.; Garabedian, P. R.; and Korn, D. G.: Analysis of the Flow Past a Shockless Lifting Airfoil in Design and Off-Design Conditions. LR-554 (NRC No. 12315), Nat. Res. Council. Can. (Ottawa), Nov. 1971.
10. Nonweiler, T. R. F.: The Sonic Flow About Some Symmetric Half Bodies. J. Fluid Mech., vol. 4, pt. 2, June 1958, pp. 140-148.
11. Hafez, M. M.; and Cheng, H. K.: Convergence Acceleration and Shock Fitting for Transonic Aerodynamics Computations. AIAA Paper 75-51, Jan. 1975.
12. Ives, D. C.; and Melnik, R. E.: Numerical Calculation of the Compressible Flow Over an Airfoil With a Jet Flap. AIAA Paper 74-542, June 1974.
13. Vanderplaats, Garret N.; Hicks, Raymond N.; and Murman, Earl M.: Application of Numerical Optimization Techniques to Airfoil Design. Aerodynamic Analyses Requiring Advanced Computers, Part II, NASA SP-347, 1975, pp. 749-768.
14. Jameson, A.: Transonic Flow Calculations for Airfoils and Bodies of Revolution. Rep. 390-71-1, Grumman Aerospace Corp., 1971.

**TABLE I.- EXPONENTS FOR TRANSONIC
SIMILARITY PARAMETERS**

	k	n	m
Cole	0	0	0
Spreiter	2	2/3	2/3
Krupp	7/4	3/4	1/2

$$\begin{array}{c}
 \phi_{ff} \\
 \hline
 \phi_{\tilde{y}} = \frac{dF_u}{dx} - A [\phi_x] = [\phi_{\tilde{y}}] = 0 \\
 \hline
 \phi_{\tilde{y}} = \frac{dF_l}{dx} - A [\phi] = \Gamma \\
 \hline
 \phi_{ff} = \phi \text{ for field}
 \end{array}$$

Figure 1.- Boundary value problem for lifting airfoil in subsonic free stream.

$$\begin{array}{c}
 \phi_{\tilde{y}} = -\sqrt{K} \phi_x \\
 \hline
 \phi_x = 0 \\
 \phi_{\tilde{y}} = 0 \\
 \hline
 \phi_{\tilde{y}} = \frac{dF_u}{dx} - A [\phi_x] = [\phi_{\tilde{y}}] = 0 \\
 \hline
 \phi_{\tilde{y}} = \frac{dF_l}{dx} - A [\phi] = \Gamma \\
 \hline
 \phi_{\tilde{y}} = -\sqrt{K} \phi_x
 \end{array}$$

Figure 2.- Boundary value problem for lifting airfoil in supersonic free stream.

$$\phi_x + F\tilde{H}\phi_{xy} + \frac{1}{P}\phi_{yy} = 0$$

$$\tilde{y} = \tilde{H}$$

$$\phi_{\tilde{y}} = \frac{dF_U}{dx} - A [\phi_x] = [\phi_{\tilde{y}}] = 0$$

$$\phi_{\tilde{y}} = \frac{dF_L}{dx} - A [\phi] = \Gamma$$

$$\tilde{y} = -\tilde{H}$$

$$\phi_x - F\tilde{H}\phi_{xy} - \frac{1}{P}\phi_{yy} = 0$$

$\phi = \phi_{ff}$
($M_\infty < 1$)

$\phi_x = 0$
 $\phi_{\tilde{y}} = 0$
($M_\infty > 1$)

$\phi_{ff} = \phi_{far \text{ field}}$
($M_\infty < 1$)

Figure 3.- Boundary value problem for lifting airfoil in ventilated wind tunnel.

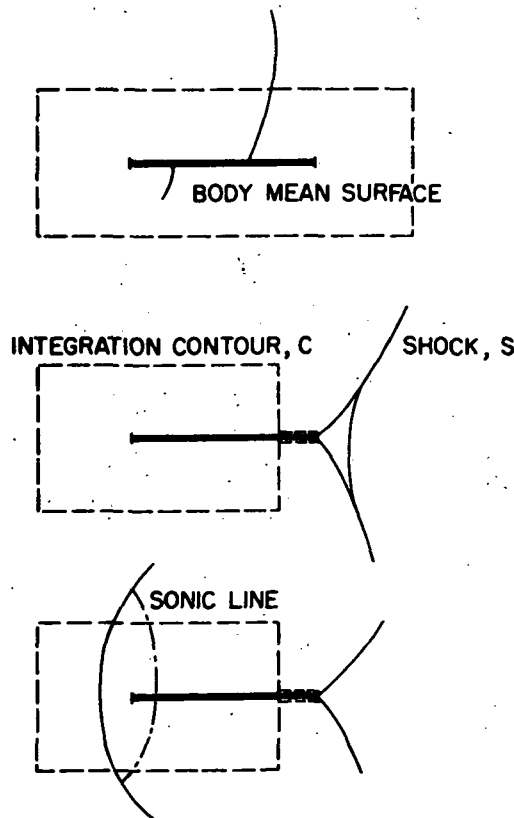


Figure 4.- Contours for evaluating drag integral.

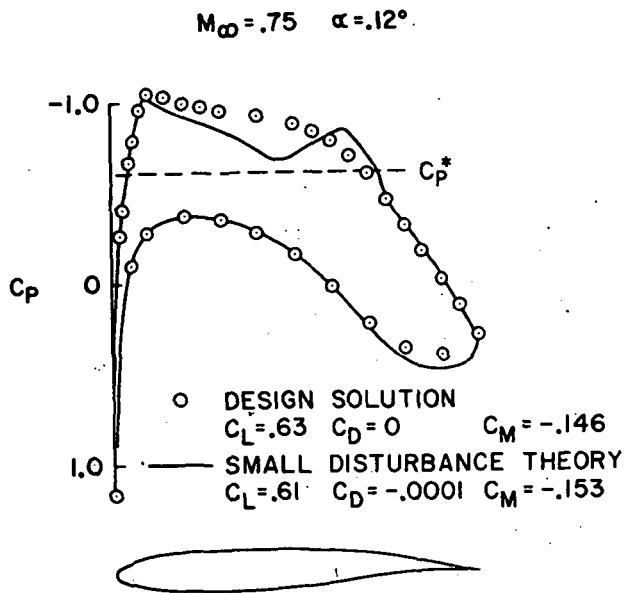


Figure 5.- Comparison with exact solution for Korn shock-free airfoil.

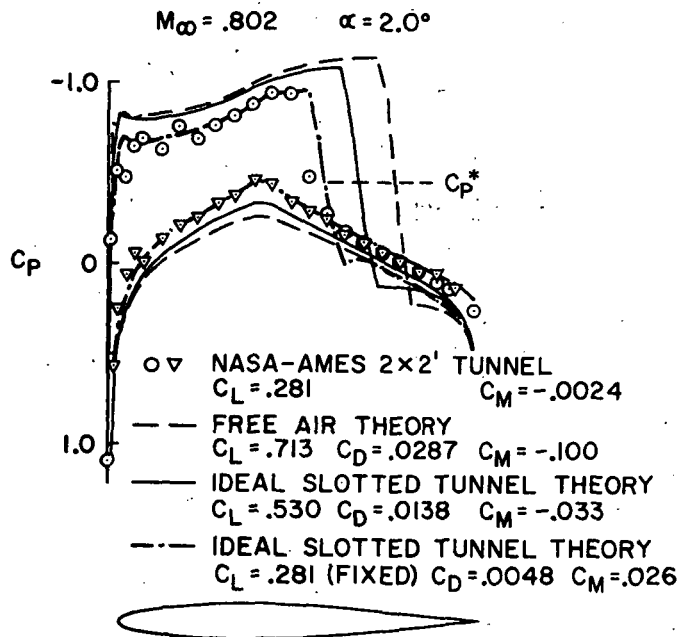
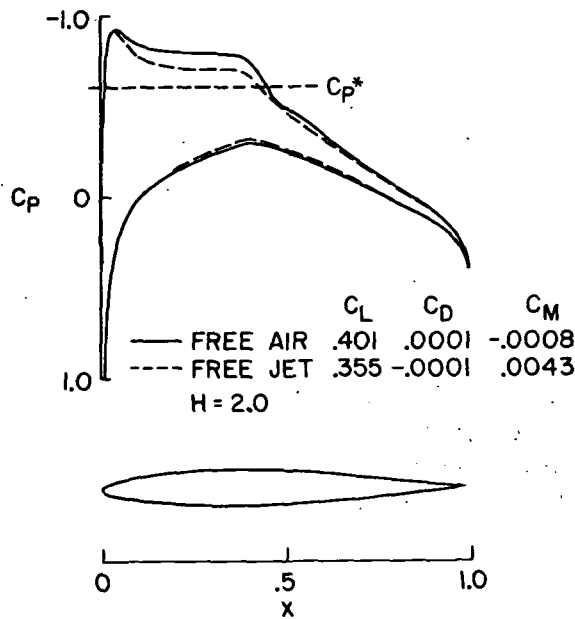
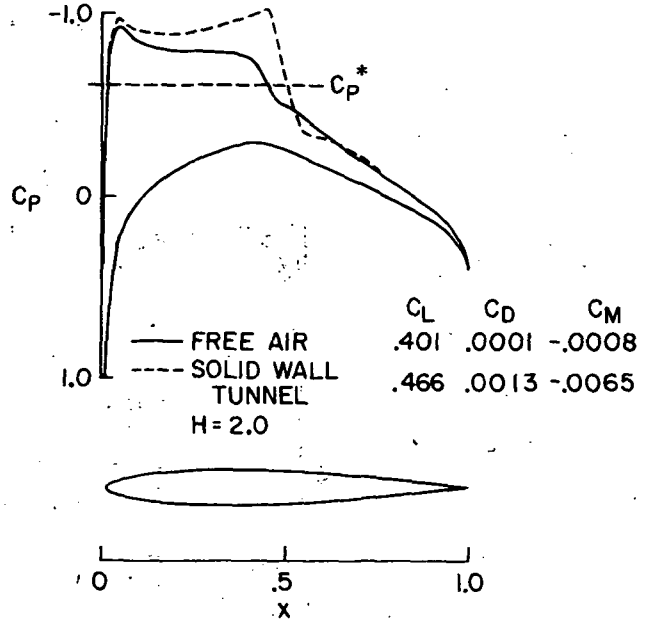


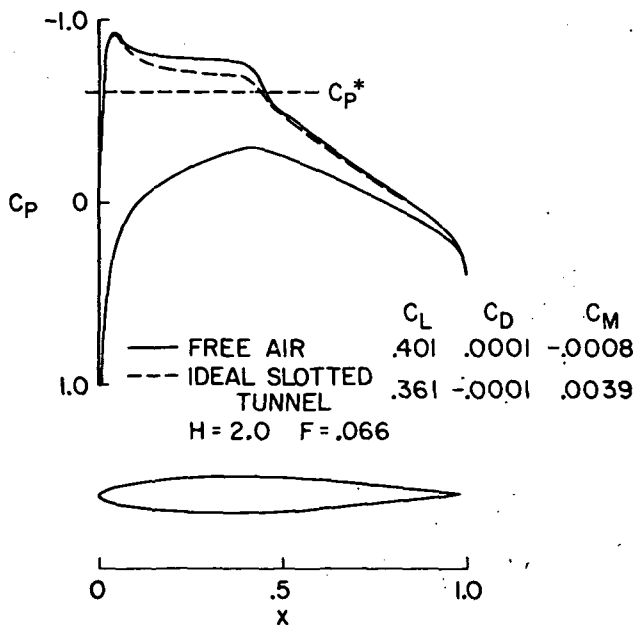
Figure 6.- Comparison of free-air and wind-tunnel solutions with data of Stivers for NACA 64A010 airfoil.



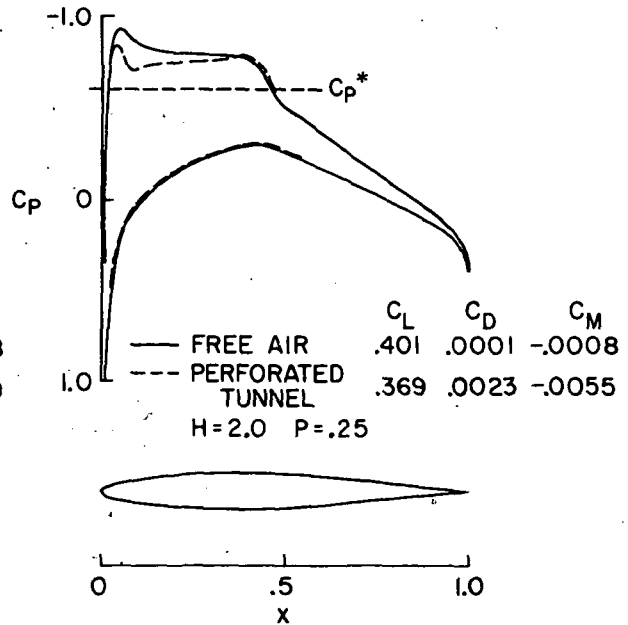
(a) Comparison of free-air and free-jet results.



(b) Comparison of free-air and solid-wall tunnel results.



(c) Comparison of free-air and slotted-wall tunnel results.



(d) Comparison of free-air and perforated-wall tunnel results.

Figure 7.- Comparisons of results using free-air and various wind-tunnel-wall boundary conditions for NACA 64A010 airfoil.

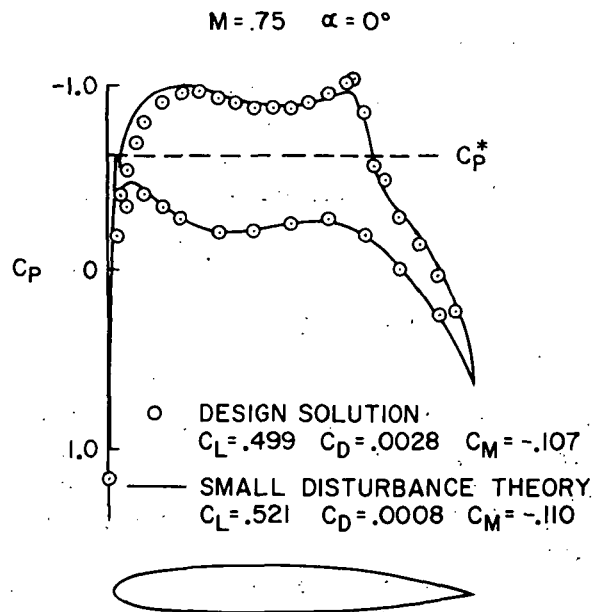


Figure 8.- Comparison with airfoil designed by optimization method.

NUMERICAL INTEGRATION OF THE SMALL-DISTURBANCE POTENTIAL

AND EULER EQUATIONS FOR UNSTEADY TRANSONIC FLOW

By Richard M. Beam

NASA Ames Research Center

and

William F. Ballhaus

U.S. Army Air Mobility R & D Laboratory

INTRODUCTION

Subsonic and supersonic unsteady aerodynamic coefficients generally have been satisfactorily determined from linear theory. Classically, two different but compatible approaches have been taken. In one approach, it is assumed that the solution depends harmonically on time (refs. 1 to 3). For application in flutter analysis, the solutions, in the form of lift and moment coefficients, are tabulated as functions of reduced frequency and Mach number. The flutter (stability) boundary is obtained by using the unsteady coefficients in the airfoil equations of motion with the assumption that the motion is harmonic in time (ref. 4).

The second approach (refs. 5 and 6) is the indicial method. For example, if an airfoil is given an instantaneous sinking velocity (i.e., a discontinuous change in vertical velocity), the resulting flow field is the indicial response. For a given step change in motion (sinking, pitching, etc.) the solutions, generally in terms of lift and moment coefficients, can be tabulated as functions of time. With the aid of Duhamel's integral, the indicial solutions can be used to obtain the solution for a general time history of the airfoil motion. The oscillatory aerodynamic coefficients can be computed by Fourier transforms of the indicial functions and, conversely, although rarely done in practice, the indicial functions can be obtained by the inverse transform of the oscillatory aerodynamic coefficients computed by the first approach (ref. 7).

Both approaches can be used to obtain unsteady aerodynamic coefficients for certain cases of transonic flows by assuming that the unsteadiness of the flow can be treated as a small (linear) perturbation about a nonlinear steady state solution (ref. 8). The solutions are only valid for the particular airfoil used to generate the initial steady state solution as opposed to the classical solutions (refs. 1 to 3), which are valid for all airfoil shapes (i.e., the initial steady state flow was assumed uniform).

Although the linear perturbation assumption removes the nonlinearities from the unsteady flow equations, variable coefficient partial differential

equations must be solved, and numerical methods are generally required. The oscillatory approach has been used in reference 9 to solve the small-disturbance potential equation and in reference 10 to solve the low-frequency, small-disturbance potential equation. The steady state solution and the unsteady perturbation solution were computed using relaxation algorithms. The numerical indicial approach was investigated in reference 11. A third-order-accurate, explicit finite-difference scheme applied to the Euler equations was used to develop the indicial functions for small perturbations about a nonlinear steady state. Although the method of reference 11 is not restricted to the linear perturbation assumption, no investigation was made of large amplitude nonlinear motions.

For some flow situations the unsteady linear perturbation assumption is not valid, and the niceties of the superposition principle must be abandoned. The solutions must then be computed by time accurate integration of the unsteady flow equations for the particular airfoil motion of interest. An example of such a flow situation is the blade element on a high speed helicopter rotor tip. During a cycle the blade element accelerates from a relatively low subsonic Mach number up into the transonic regime, where it can experience increased drag and moment. The onset of these adverse transonic effects can severely limit high speed helicopter performance. On the other hand, since transonic flows depend so strongly on airfoil shape, improved design should significantly increase helicopter performance. The expense and difficulty involved in rotary wing testing make the computational approach particularly attractive in this regard.

The limitation of the linear unsteady perturbation assumption to airfoils traveling with a constant forward velocity (i.e., flutter and stability analyses) is not well defined. The capability of solving the nonlinear flow equations is necessary, therefore, to establish the limitations of the linear analysis as well as to solve the truly nonlinear problems.

Explicit numerical methods were used in references 11 and 12 to solve for the flow fields about oscillating airfoils. Both methods solve the Euler equations and, although neither is limited to linear perturbations, only reference 12 considers large amplitude rotating motions of the airfoil. The motivation for considering additional numerical methods and/or forms of the equations of motion comes from the computational time required for the explicit methods applied to the Euler equations. Most nonlinear unsteady transonic phenomena of practical interest are anticipated in the low reduced frequency spectrum (ref. 8). The low frequency (long period) coupled with the numerical stability time step limitation of the explicit schemes leads to orders of magnitude more time steps per cycle of oscillation than are required for numerical accuracy.

In this paper we investigate and compare two methods that solve unsteady, nonlinear, transonic flow problems. Each method is an attempt to remove the numerical stability limitation discussed above; thus the computational time is reduced while the numerical accuracy is preserved. One method is to solve the Euler equations by using an implicit numerical scheme to increase the integration time step. The second method is an extension of the approach

described in reference 13 to the lifting case. This method uses a semi-implicit scheme to solve the low-frequency, transonic, small-disturbance potential equation.

Although the second method is more limited (small disturbance, low frequency) than the first, it offers considerable savings in computer time and storage requirements over the first method. The details of the two methods are presented in section I. In section II we compare results from the two methods and the results of linear theory. The two sample motions, a sinking airfoil with steady forward velocity and an airfoil with increasing thickness, were chosen to provide a simple representation of the flutter-maneuver and rotor tip motions, respectively. Finally, results are presented for an NACA 0010 airfoil undergoing simultaneous angle of attack and free stream Mach number oscillations. This computation is a strip theory simulation of the flowfield about an advancing helicopter rotor.

I. NUMERICAL METHODS

Implicit Scheme for Euler Equations

The gasdynamic equations for two-dimensional, unsteady, inviscid flow are expressed in conservative (or divergence law) form as

$$\frac{\partial U}{\partial t} + \frac{\partial F}{\partial x} + \frac{\partial G}{\partial y} = 0 \quad (1)$$

where t , x , and y represent the time and Cartesian space coordinates, and U , F , and G are the vectors:

$$U = \begin{bmatrix} \rho \\ \rho u \\ \rho v \\ e \end{bmatrix}, \quad F = \begin{bmatrix} \rho u \\ \rho u^2 + p \\ \rho uv \\ (e+p)u \end{bmatrix}, \quad G = \begin{bmatrix} \rho v \\ \rho uv \\ \rho v^2 + p \\ (e+p)v \end{bmatrix} \quad (2)$$

The variables in equations (2) are the density ρ , the velocity components u and v , pressure p , and total energy per unit volume e . The additional required equation is the equation of state (for a perfect gas):

$$\rho = (\gamma - 1) \left[e - \frac{\rho}{2} (u^2 + v^2) \right] \quad (3)$$

where γ , a constant, is equal to the ratio of specific heats (taken as 1.4 in this study). The conservative form of the differential equations is chosen to insure accurate resolution of the weak solution (shock wave) to the differential equations.

The numerical method for solving equations (1) is an implicit, time-split, finite-difference scheme.¹ The development of the scheme starts with a Taylor's series in t (as does the Lax-Wendroff explicit scheme, ref. 14, p. 302),

$$U^{n+1} = U^n + \Delta t \left(\frac{\partial U}{\partial t} \right)^n + \frac{\Delta t^2}{2} \left(\frac{\partial^2 U}{\partial t^2} \right)^n + \dots \quad (4)$$

For simplicity, consider the one-dimensional form of equation (1)

$$\frac{\partial U}{\partial t} + \frac{\partial F}{\partial x} = 0 \quad (5)$$

The highest order term retained in equation (4) may be rewritten with the aid of equation (5) as

$$\frac{\partial^2 U}{\partial t^2} = - \frac{\partial}{\partial t} \left(\frac{\partial F}{\partial x} \right) = - \frac{\partial}{\partial x} \left(\frac{\partial F}{\partial t} \right) = - \frac{\partial}{\partial x} \left(A \frac{\partial U}{\partial t} \right) \quad (6)$$

where the matrix $A = A(U)$ is the Jacobian of $F(U)$; that is, $a_{ij} = \partial F_i / \partial U_j$. The Lax-Wendroff scheme replaces the final time derivative in equation (6) by substitution from equation (5) to obtain the explicit scheme

$$U^{n+1} = U^n - \Delta t \left(\frac{\partial F}{\partial x} \right)^n + \frac{\Delta t^2}{2} \left(\frac{\partial}{\partial x} A \frac{\partial F}{\partial x} \right)^n \quad (7)$$

The implicit scheme used in this paper was obtained by using a forward time difference to replace $\partial U / \partial t$ in the final step of equation (6)

$$U^{n+1} = U^n - \Delta t \left(\frac{\partial F}{\partial x} \right)^n - \frac{\Delta t^2}{2} \frac{\partial}{\partial x} \left[\frac{A^n (U^{n+1} - U^n)}{\Delta t} \right] \quad (8)$$

For the two-dimensional equations (1), the implicit scheme has the form:

$$U^{n+1} = U^n - \Delta t \left(\frac{\partial F}{\partial x} + \frac{\partial G}{\partial y} \right)^n - \frac{\Delta t}{2} \left[\frac{\partial}{\partial x} \left(A^n (U^{n+1} - U^n) \right) + \frac{\partial}{\partial y} \left(B^n (U^{n+1} - U^n) \right) \right] \quad (9)$$

Where the matrix $B = B(U)$ is the Jacobian of $G(U)$. The spatial differences are approximated by central differences, and a fourth-order dissipative term is added to the otherwise nondissipative scheme. The resulting difference

¹The algorithm was developed by R. F. Warming and Richard M. Beam of Ames Research Center.

equations are solved by a time split algorithm which employs a block tri-diagonal matrix inversion routine.

Semi-Implicit Scheme for the Low-Frequency, Small-Disturbance, Transonic Potential Equation

Because of the success obtained using the small-disturbance approach to predict two- and three-dimensional steady transonic flows, an effort was initiated to develop a similar approach for unsteady transonic flows. In reference 13, semi-implicit difference operators were developed for the unsteady, transonic, small-disturbance equation and its low-frequency approximation. The former,

$$S_1 \phi_{tt} + 2S_2 \phi_{xt} = V_c \phi_{xx} + \phi_{yy} \quad (10)$$

is the lowest order approximation to the Euler equations for unsteady, transonic flow about a thin airfoil. Here $V_c = S_3 - (\gamma+1)M_\infty^2 \phi_x$, $S_3 = (1-M_\infty^2)/\delta^{2/3}$, $S_1 = M_\infty^2(2k)^2/\delta^{2/3}$, $S_2 = M_\infty^2 2k/\delta^{2/3}$, ϕ = disturbance velocity potential, M_∞ = free-stream Mach number, and δ = airfoil thickness/chord ratio. The reduced frequency k is a measure of the degree of unsteadiness of the motion. For an airfoil of chord length c , traveling at a mean velocity of U_∞ , and undergoing some periodic motion of frequency ω , $k = \omega c/2U_\infty$. Equation (10) is derived under the assumption $\delta^{2/3} \sim 1 - M_\infty^2 \ll 1$. ϕ , t , y , and x have been scaled by $c\delta^{2/3}U_\infty$, $1/\omega$, $c/\delta^{1/3}$, and c , respectively. Contained in equation (10) is a relationship for the jumps in the derivatives of the velocity potential across shock waves. This relationship is the lowest order approximation to the Rankine-Hugoniot shock relations.

The equation for low-frequency, transonic flows is obtained by taking the limit $k \sim \delta^{2/3} \sim 1 - M_\infty^2 \rightarrow 0$. The first term in equation (10) drops out leaving

$$2S_2 \phi_{xt} = V_c \phi_{xx} + \phi_{yy} \quad (11)$$

Retarded differences in both x and t are used to approximate ϕ_{xt} . The term $V_c \phi_{xx}$ is evaluated at the old time level using Murman-Cole type mixed difference operators (including the shock point operator) (ref. 15). For meshes with variable grid spacing, special care must be taken to ensure that the difference operators are conservative. The term ϕ_{yy} is obtained using central differences in y . Half of ϕ_{yy} is evaluated at the new time level and half at the old. At each time level, the scheme is marched in the x direction solving (directly) a tridiagonal matrix for each $x = \text{constant}$ grid line.

In the low-frequency approximation, the lift can be handled in a manner similar to that commonly used in two-dimensional, steady, relaxation methods.

The circulation is given by the jump in potential at the airfoil trailing edge. This jump in potential is enforced from the trailing edge to the downstream boundary. (The assumption here, which is a consequence of the low-frequency limit, is that the time scale associated with the change in lift (i.e., the time scale of the oscillatory motion) is much greater than the time scale of the forward flight; i.e., $1/\omega \gg c/U_\infty \rightarrow 2k \equiv \omega c/U_\infty \ll 1$. So the jump in potential across the vortex sheet appears nearly uniform to an observer on the airfoil). Ideally, the far field boundaries should be removed sufficiently far that the interaction of disturbances with the boundary does not affect the solution near the airfoil during the computed time period. In practice a variable grid is used in both x and y so that the far field boundary conditions are applied at distances of from ten to thirty chord lengths from the airfoil. At the downstream boundary, a constant pressure condition is applied; at the other boundaries, the mean lift vortex solution is applied.

Considerable experience in the computation of two- and three-dimensional steady transonic flows has shown that the small disturbance approach provides solutions that agree very well with solutions to the full potential and Euler equations for thin airfoils at free-stream Mach numbers close to one. Good agreement can also be obtained for thicker airfoils at lower Mach numbers provided the small disturbance formulation is properly "tuned." For example, Krupp (ref. 16) modified the nonlinear coefficient of ϕ_{xx} by replacing

$$V_c = S_3 - (\gamma+1)M_\infty^2 \phi_x \quad (12a)$$

by

$$V_c = S_3 - (\gamma+1)M_\infty^{1.75} \phi_x \quad (12b)$$

to force the small-disturbance equation to change type for a value of $C_p = C_p^*$ (critical pressure coefficient) that is a good approximation to the critical pressure coefficient obtained from the full potential equations for a wide range of free-stream Mach numbers. Krupp also, in effect, divided the airfoil slopes by $M_\infty^{1/4}$ so that the airfoil boundary condition applied corresponds to an airfoil of thickness ratio $\delta/M_\infty^{1/4}$. Notice that as M_∞ approaches unity, the effects of Krupp's "tuning" diminish.

In the present unsteady, small-disturbance approach, the coefficient of ϕ_{xx} is expressed as

$$V_c = S_3 - (\gamma+1)M_\infty^n \phi_x \quad (13)$$

where n is selected so that the steady form of equation (11) changes type for a value of $C_p = C_p^*$ that is the same as the critical pressure

coefficient obtained from the full potential equations. For example, $n = 1.64$ for $M_\infty = 0.85$, $n = 1.65$ for $M_\infty = 0.825$, and $n = 1.69$ for $M_\infty = 0.72$. Here we also increase the airfoil slopes by a factor of $M_\infty^{-1/4}$. In this report, we refer to equation (12a) as "Von Karman-Spreiter scaling" and to equation (13) (and the slope factor of $M_\infty^{-1/4}$) as " C_p^* scaling." This approach agrees remarkably well (ref. 17) with solutions to the steady Euler equations computed by Magnus and Yoshihara (ref. 12) for transonic flow about an NACA 64A410 airfoil, provided the Mach number immediately upstream of the shock does not exceed about 1.3. For shock Mach numbers greater than 1.3, the small-disturbance shock jumps become considerably stronger than the Rankine-Hugoniot jumps; it is at this point that the small-disturbance approach breaks down. However, this is also the point at which the inviscid assumption breaks down, since for shock Mach numbers greater than 1.3 the shock usually separates the boundary layer.

Just as tuning the small-disturbance equations for steady flows has extended the ranges of thickness ratios and free-stream Mach numbers over which the small-disturbance approach can be successfully applied, tuning the unsteady term in equation (11) should increase the range of reduced frequencies over which the low-frequency approximation can be successfully applied. For example, the upstream propagation rates (characteristic traces in the $x-t$ plane) for the linearized forms of equations (10) and (11) differ by a ratio $2M_\infty/(M_\infty+1)$. Changing S_2 in equation (11) from $S_2 = 2kM_\infty^2$ to $S_2 = (M_\infty+1)kM_\infty$ forces the (linear) upstream propagation rate of the low-frequency approximation to match that of equation (10), which is valid for all frequencies. Here we refer to equation (11) with this modification as the "modified low-frequency approximation." Some solutions using this form of the equation are presented in the section on results.

II. NUMERICAL RESULTS

Types of Unsteady Motion

Two types of unsteady airfoil motion are of primary importance in transonic flows. One is the acceleration of the airfoil in the streamwise direction, for example, the rotor blade on a helicopter in forward flight or an aircraft experiencing gross maneuvers. The second motion consists of perturbations (not necessarily small) about a mean forward velocity. These perturbations may be pitching, plunging, or complex elastic deformations of the airfoil. This second class of motion includes most flutter (usually small perturbation) and aerodynamic stability phenomena.

Two simple motions have been chosen for the comparison of the numerical methods. They were chosen because (1) we believe they present the basic

physical phenomena and numerical problems associated with the more general motions, (2) linear theory solutions are readily available for comparison, and (3) they provide a simple basis of comparison for various numerical methods.

Nonlifting airfoil with increasing thickness (growing airfoil). First we consider a parabolic arc airfoil, in a uniform free stream, whose thickness increases from zero as a function of time (fig. 1(a)). (The slowly growing motion can be related to that of an accelerating airfoil.) The thickness increases from zero to δ_0 in time τ_0 . The transition is taken as the polynomial in τ :

$$\delta = \delta_0 \begin{cases} 10 - 15 \left(\frac{\tau}{\tau_0} \right) + 6 \left(\frac{\tau}{\tau_0} \right)^2 \left[\left(\frac{\tau}{\tau_0} \right)^3 \right] & 0 \leq \tau \leq \tau_0 \\ = \delta_0 & \tau > \tau_0 \end{cases} \quad (14)$$

Linear theory solutions for this problem are available (ref. 13).

Oscillatory plunging airfoil. Next we consider a parabolic arc airfoil with a mean forward velocity and a sinusoidal velocity normal to the free stream (fig. 1(b)). This is usually referred to as a sinking or plunging airfoil and has the characteristic of a sinusoidal variation in angle of attack. The linear theory solutions are available for many Mach numbers and frequencies.

Results for Growing Airfoil

In figure 2(a) we consider the pressure coefficient near midchord for an airfoil growing to its maximum thickness (eq. (14)) while traveling two chord lengths ($\tau_0 = 2$). The final thickness to chord ratio, $\delta_0 = 0.10$, and the free-stream Mach number, $M_\infty = 0.785$, lead to a transonic (embedded supersonic) steady state flow field, $C_{p_{\min}} < C_p^*$, where C_p^* denotes the sonic condition. The linear theory is, of course, proportional to thickness and does not have a supercritical steady state. In figure 2(a) results from the linear form of equation (10) (linear theory) are compared with results from the modified low-frequency approximation and the Euler equations. In figure 2(b) the low-frequency approximation with Von Karman - Spreiter and C_p^* scaling are compared with the Euler solution for the same motion. Notice that the Von Karman-Spreiter scaled results have a subcritical steady state pressure.

As the airfoil begins to grow, the disturbances are very small and the nonlinear effects negligible. Thus the Euler equation numerical solution agrees with linear theory. The numerical low-frequency approximation pressure leads the other solutions. This initial discrepancy and the later amplitude difference between the low-frequency and Euler numerical solutions are due to the high frequency content of the airfoil growth rate ($k = 0$ ($\pi/\tau_0 \approx 1.6$)). To have primarily low-frequency content in the growth rate

($k = 0(0.1)$), the rise time, τ_0 , must be greater than about 30 chords. Both the lead in the initial C_p and the subsequent underexpansion in C_p for the low-frequency approximation are also apparent in a comparison of the analytical solutions for the small-disturbance equation and the low-frequency, small-disturbance equation (fig. 3). As τ_0 is increased to 10 (fig. 4), the difference between the two solutions diminishes.

The differences between the Euler and low-frequency numerical solutions for $\tau_0 = 2$ (fig. 2) can also be attributed to the low-frequency approximation. As τ_0 is increased to 20 (fig. 5), the difference between the two solutions diminishes. For this case $k = 0(\pi/\tau_0 \approx 0.16)$.

From an aerodynamic viewpoint the significant features of figure 2 are the nonlinear effects: (1) the near doubling of the maximum midchord pressure and (2) the significant increase in time to reach steady state, when compared with linear theory predictions.

Results for Oscillatory Plunging Airfoil

First we consider small amplitude motions for very thin airfoils, i.e., cases where linear theory is valid. This provides a test of the numerical schemes against known analytical solutions. In figure 6 we compare the lift and leading-edge moment coefficients obtained from analytical solutions of the linear potential equation to numerical solutions of the linear ($\gamma = -1$) low-frequency potential equation and the Euler equations. The low-frequency approximation begins to deviate (especially the phase angle) from the other solutions as the reduced frequency exceeds $0(0.1)$. This result is, of course, anticipated from the development of the approximation. The numerical solutions of the Euler equations provide reasonable agreement with the analytical solutions throughout the entire frequency range investigated.

In order to investigate the nonlinear effects, we consider a 7.5% thick parabolic-arc airfoil for various Mach numbers between 0.8 and 0.875 (fig. 7). The reduced frequency is 0.05 and the amplitude of oscillation is $\pm 1^\circ$. Shown for comparison are the analytical results from linear theory and the numerical results for thin airfoils. Solutions are given in terms of the real and imaginary components of the midchord moment and are compared as functions of Mach number. Note that linear theory predicts minor dependence on Mach number. However, the thicker airfoil shows a drastic change in both real and imaginary parts of the midchord moment as the center of pressure passes through midchord with the development of a shock wave on the airfoil. The change in sign of the midchord moment near Mach number 0.86 agrees with experimental results (ref. 18) which show that this airfoil, oscillating about midchord, exhibits an oscillatory instability (one degree of freedom flutter) from Mach numbers of approximately 0.87 to 0.89.

The difference in the imaginary part of the pitching-moment coefficient due to angle of attack α , $\text{Im}[C_{m\alpha}]$, determined from the low-frequency and Euler numerical solutions (fig. 7) has not been completely resolved, but it is probably due to the breakdown of small-disturbance theory for strong shocks, which was anticipated in section I. That is, for large shock Mach

numbers, the small-disturbance shock jumps become considerably stronger than the Rankine-Hugoniot jumps. This moves the shock and center of pressure aft, and thereby increases $|C_l|$ and $|C_m|$ for the small-disturbance results relative to the Euler results. Small changes in shock strength (and, hence, shock location) can have a large effect on lift and pitching-moment coefficients C_l and C_m . This is especially true for a parabolic-arc airfoil, for which the flow expands rapidly streamwise up to the shock point. The unsteady effects in the small-disturbance solutions are also more amplitude dependent, hence, more nonlinear than those in the Euler solutions. At $M_\infty = 0.85$, results were computed (fig. 7) for oscillation amplitudes of $|\alpha| = 0.1^\circ, 0.5^\circ, 1.0^\circ$. Considerable amplitude dependence is apparent for $\text{Im}[\bar{C}_{m\alpha}]$ in the low-frequency calculations. On the other hand, Euler solutions were nearly independent of amplitude. (Therefore only one value is shown.) Nonlinear unsteady effects would be expected to occur at smaller amplitudes for lower reduced frequencies (ref. 8).

For the small-disturbance potential calculations, a uniform chordwise mesh spacing of five percent chord was maintained on the airfoil surface. For the calculations using the Euler equations, the grid spacing near mid-chord was five percent chord, but additional points were grouped near leading and trailing edges for a total of 25 grid spaces on the airfoil surface (as opposed to 20 for the potential calculations). In all the calculations airfoil slopes were applied on the mean surface.

Results for a Helicopter Blade Element

A small-disturbance equation governing the subsonic and transonic flow field resulting from the motion of a helicopter rotor blade in forward flight was derived in reference 19. The (two-dimensional) equivalent of that equation for a blade element has the same form as equation (11) with

$$\left. \begin{aligned} S_2 &= M_\infty^2 (1 + \mu \cos t) \epsilon / \delta^{2/3} \\ S_3 &= \left[1 - M_\infty^2 (1 + \mu \cos t)^2 \right] / \delta^{2/3} \\ V_c &= S_3 - (\gamma + 1) M_\infty^n (1 + \mu \cos t)^{n-1} \phi_x \end{aligned} \right\} \quad (15)$$

Here $\phi \equiv$ disturbance velocity potential and is scaled by $c\delta^{2/3}U_\infty$; x and y are the chord and vertical coordinates fixed with respect to the rotor and are scaled by c and $c/\delta^{1/3}$, respectively; t is scaled by $1/\omega$, where ω is the rotor rotational velocity in radians/sec; the free-stream velocity and Mach number are $U_\infty(1 + \mu \cos t)$ and $M_\infty(1 + \mu \cos t)$, respectively, where μ , the advance ratio, is the ratio of the rotor forward flight to rotational velocity. The exponent n varies with M_∞ as previously discussed. In equation (15) ϵ is equal to the inverse of the blade aspect ratio and is, essentially, a reduced frequency (see ref. 19, pp. 20-21). For an airfoil section given in unscaled coordinates by $y = \delta f(x)$, the airfoil boundary

condition applied on the mean surface is $\phi_y = (1 + \mu \cos t)f'(x)/(M_\infty^{1/4}(1 + \mu \cos t)^{1/4})$ (C_p^* scaling used). The pressure coefficient is given by $C_p = -2\delta^{2/3}\phi_x/(1 + \mu \cos t)$.

For an example we solve equation (15) for the flow field about an NACA 0010 airfoil with a free-stream Mach number and angle of attack given by $0.61(1 + 0.4 \cos t)$ and $2^\circ(1 - \cos t)$, i.e., $M_\infty = 0.61$ and $\mu = 0.4$. Here t is the azimuth angle on the rotor disc. The reduced frequency, ϵ , is 0.1. Surface pressure coefficients at selected times during the motion are compared with quasi-steady results in figure 8. At $t = -180^\circ$ the angle of attack has a maximum (4.0°) and the free-stream Mach number a minimum (0.366). Over the region $-180^\circ < t < -65^\circ$, the C_p , C_ℓ , and C_m phase lags are all small as expected. The flow first becomes supercritical at about $t = -65^\circ$. Here the C_p phase lags begin to increase considerably, as shown by the increasingly large differences between the unsteady and quasi-steady pressure coefficients. This is also apparent, more so for center of pressure, x_p , than for C_ℓ , in figure 9. At $t = 0$ the angle of attack has a minimum (0°) and the free-stream Mach number a maximum (0.854). As the Mach number decreases and the angle of attack increases, the flow continues to expand in the upper surface supersonic region, as shown in figures 8(c), 8(d), and 8(e). However, the shock wave moves forward and decreases the lift and center of pressure. The center of pressure actually decreases past the quarter chord point to reach a minimum of $x_p = 0.2$ at $t = 56^\circ$ (see fig. 9). The surface pressures for $t = 56^\circ$ are shown in figure 8(e). As t increases further, the shock continues to move forward into the supersonic region. The center of pressure moves aft and reaches the vicinity of the quarter chord at $t = 68^\circ$, which corresponds to the disappearance of the supersonic flow region. A similar shift in x_p was reported in reference 20 for a nonlifting, three-dimensional rotor with a parabolic-arc section.

Computational Efficiency

Although our applications of the two numerical schemes are at present quite limited, we may draw some preliminary conclusions concerning their applicability and limitation.

First we consider the numerical effort per time step or the machine time required to advance the numerical solution one time step. With an explicit scheme applied to the Euler equations as reference, table 1 presents a comparison of the two methods considered herein. The extra work for the implicit method comes from the block tridiagonal matrix inversion. The reduced effort of the low-frequency potential equation is derived basically from the fact that one (small-disturbance) equation is solved instead of four. The machine storage requirement for the potential equation will also be one-fourth that of the Euler equations.

The time step limitation of the implicit method is basically accuracy dependent, while that of the explicit method is generally numerical-stability dependent. The semi-implicit scheme for the potential equation has a numerical-stability time step limit of 2 to 20 times (depending on the stagnation region in the flow field, see ref. 13) that of an explicit method. The time

step limitations, combined with the numerical effort per time step (Table I), imply that the explicit method for the Euler equations will achieve best overall numerical efficiency for high reduced frequencies, while an implicit method will achieve best overall efficiency for low reduced frequencies. The "cross-over" frequency based on a uniform grid spacing and Mach number near unity is estimated to be $k = \omega c / 2U_\infty \approx 0.2$. For the low-frequency calculations, the semi-implicit method for the potential equation will have superior numerical efficiency except for very low reduced frequencies $k = 0(0.001)$, where the implicit method for the Euler equation will once again become most efficient. This implies that an implicit method (in place of the semi-implicit method) should be used to solve the low-frequency equation for very low reduced frequencies.

TABLE I

Equations (Numerical Scheme)	Numerical Effort Per Time Step
Euler (explicit)	1
Euler (implicit)	4
Low-frequency, small-disturbance, potential (semi-implicit)	0.25

CONCLUDING REMARKS

Two numerical algorithms have been used to compute unsteady transonic flows about airfoils. Each scheme was developed for its anticipated high numerical efficiency when applied to low-frequency motions. For such motions previously developed (explicit) numerical schemes have a severe time-step limitation that is based on numerical stability rather than numerical accuracy. The implicit method applied to the Euler equations provides satisfactory results over a wide frequency range and achieves considerably better (relative to an explicit scheme) numerical efficiency for low reduced frequencies. The semi-implicit method applied to the small-disturbance, low-frequency potential equation results in an order of magnitude further increase in efficiency and is recommended for application when the assumptions used in developing the equation are fulfilled, i.e., (1) small disturbances and (2) low reduced frequencies. Based on our present calculations, these restrictions imply reduced frequencies less than one-tenth ($k = \omega c / 2U_\infty < 0.1$) and shock Mach numbers less than 1.3.

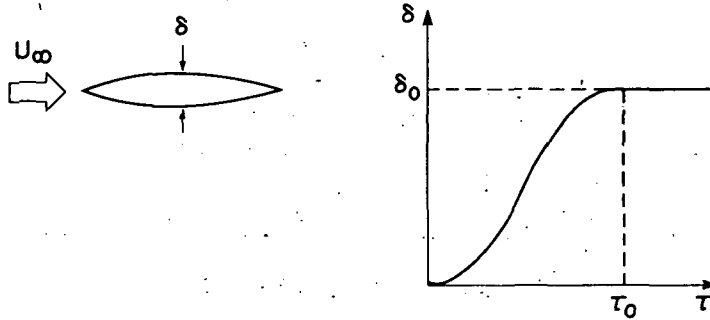
The semi-implicit, small-disturbance approach was applied to the case of an NACA 0010 airfoil simulating the motion of a helicopter rotor in forward flight. The most interesting result here was the forward overshoot in the center of pressure, which occurred as the airfoil decelerated. This was caused by the forward motion of the shock wave just before the flow became subcritical.

REFERENCES

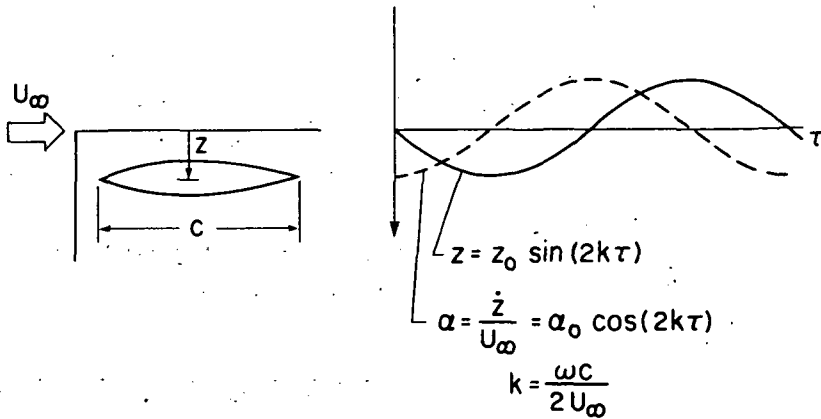
1. Jordan, P. F.: Aerodynamic Flutter Coefficients for Subsonic, Sonic, and Supersonic Flow (Linear Two-Dimensional Theory). ARC RM 2932, April 1953.
2. Garrick, I. E.; and Rubinow, S. I.: Flutter and Oscillating Air Force Calculations for an Airfoil in a Two-Dimensional Supersonic Flow. NACA Rept. 846, 1946.
3. Luke, Y. L.: Tables of Coefficients for Compressible Flutter Calculations. AF Tech. Rept. No. 6200, August 1950.
4. Fung, Y. C.: An Introduction to the Theory of Aeroelasticity. John Wiley, 1955.
5. Lomax, H.; Heaslet, M. A.; Fuller, F. B.; and Sluder, L.: Two- and Three-Dimensional Unsteady Lift Problems in High-Speed Flight. NACA Rept. 1007, 1952.
6. Tobak, M.: On the Use of the Indicial Function Concept in the Analysis of Unsteady Motions of Wings and Wing-Tail Combinations. NACA Rept. 1188, 1954.
7. Mazelsky, B.: Numerical Determination of Indicial Lift of a Two-Dimensional Sinking Airfoil at Subsonic Mach Numbers from Oscillatory Lift Coefficients with Calculations for Mach Number 0.7. NACA TN 2562, 1951.
8. Landahl, M. T.: Unsteady Transonic Flow. Pergamon Press, New York, 1961.
9. Ehlers, F. E.: A Finite Difference Method for the Solution of Transonic Flow Around Harmonically Oscillating Wings. NASA CR 2257, 1974.
10. Traci, R. M.; Albano, E. D.; Favi, J. L., Jr.; Cheng, H. K.: Small Disturbance Transonic Flows About Oscillating Airfoils. AFFDL Technical Report TR-74-37, June 1974.
11. Beam, R. M.; and Warming, R. F.: Numerical Calculations of Two-Dimensional Unsteady Transonic Flows With Circulation. NASA TN D-7605, 1974.
12. Magnus, R.; and Yoshihara, H.: Finite Difference Calculations of the NACA 64A-410 Airfoil Oscillating Sinusoidally in Pitch at $M = 0.72$. General Dynamics TR CASD-NSC-74-004, Aug. 1974.

13. Ballhaus, W. F.; and Lomax, H.: The Numerical Simulation of Low Frequency Unsteady Transonic Flow Fields. Presented at the Fourth International Conference on Numerical Methods in Fluid Dynamics, Boulder, Colorado, June 24-29, 1974.
14. Richtmyer, R. D.; and Morton, K. W.: Difference Methods for Initial-Volume Problems. Interscience Publishers, New York, 1967.
15. Murman, E. M.: An Analysis of Embedded Shock Waves Calculated by Relaxation Methods. AIAA Paper 27-40, July 1973.
16. Krupp, J. A.: The Numerical Calculation of Plane Steady Transonic Flows Past Thin Lifting Airfoils. Boeing Scientific Research Lab. Rept. D180-12958-1, June 1971.
17. Ballhaus, W. F.; Magnus, R.; and Yoshihara, H.: Unsteady Transonic Flows Over Airfoils. Paper presented at Symposium on Unsteady Aerodynamics, University of Arizona, Mar. 1975.
18. Bratt, J. B.; and Chinneck, A.: Measurement of Mid-Chord Pitching Moment Derivatives at High Speeds. ARC RM 2680, June 1947.
19. Isom, M. P.: Unsteady Subsonic and Transonic Potential Flow Over Helicopter Rotor Blades. NASA CR-2463, 1974.
20. Caradonna, F. X.; and Isom, M. P.: Numerical Calculation of Unsteady Transonic Potential Flow Over Helicopter Rotor Blades. AIAA Paper No. 75-168, January 1975.

$$\delta = \begin{cases} \delta_0 \left[10 - 15 \left(\frac{\tau}{\tau_0} \right) + 6 \left(\frac{\tau}{\tau_0} \right)^2 \right] \left(\frac{\tau}{\tau_0} \right)^3 & 0 \leq \tau \leq \tau_0 \\ \delta_0 & \tau > \tau_0 \end{cases}$$



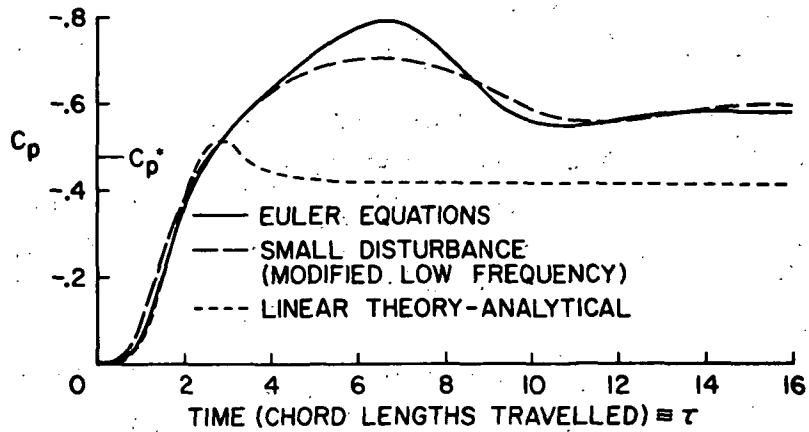
(a) Growing airfoil.



(b) Oscillating plunging airfoil.

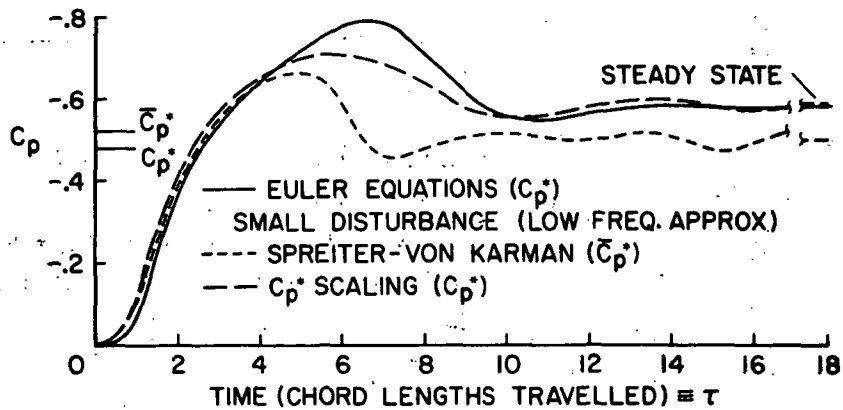
Figure 1.- Unsteady motions for comparison of numerical and analytical results.

$$\delta = \begin{cases} 0.1 \left[10 - 15 \left(\frac{\tau}{2} \right) + 6 \left(\frac{\tau}{2} \right)^2 \right] \left(\frac{\tau}{2} \right)^3, & 0 \leq \tau \leq 2 \\ 0.1, & \tau > 2 \end{cases}$$



(a)

$$\delta = \begin{cases} 0.1 \left[10 - 15 \left(\frac{\tau}{2} \right) + 6 \left(\frac{\tau}{2} \right)^2 \right] \left(\frac{\tau}{2} \right)^3, & 0 \leq \tau \leq 2 \\ 0.1, & \tau > 2 \end{cases}$$



(b)

Figure 2.- Variation of C_p with time at $x/c = 0.525$ for a parabolic-arc airfoil. $M = 0.785$.

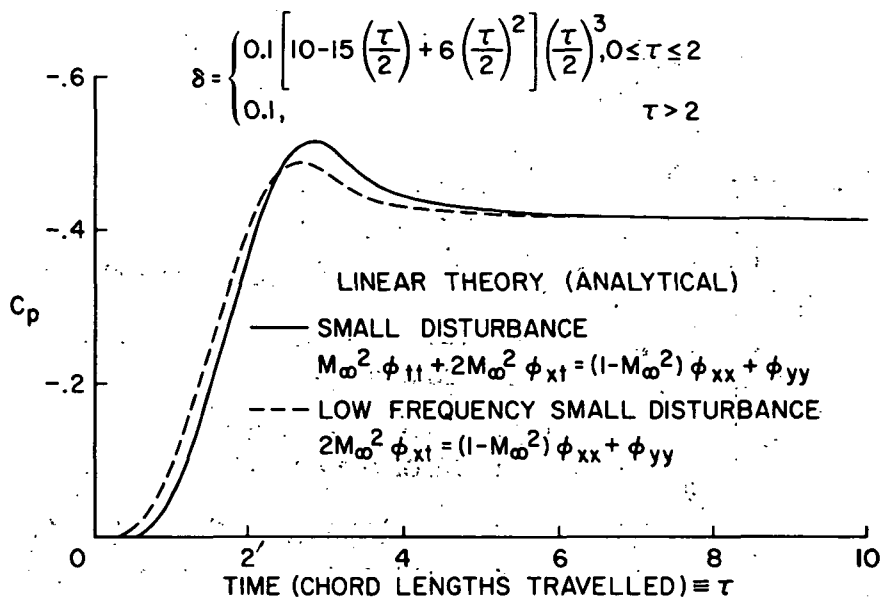


Figure 3.- Variation of C_p with time at $x/c = 0.50$ for a parabolic-arc airfoil. $M_{\infty} = 0.785$; $\tau_0 = 2$.

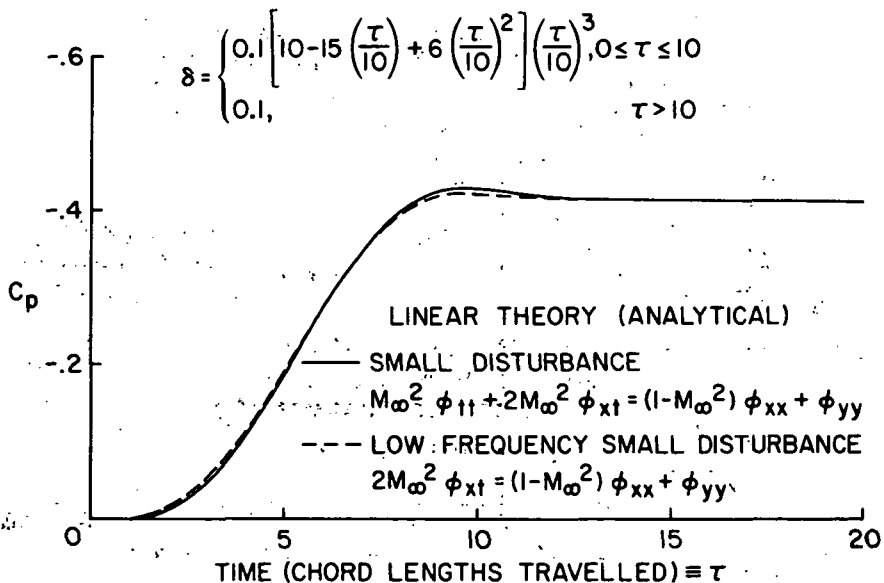


Figure 4.- Variation of C_p with time at $x/c = 0.50$ for a parabolic-arc airfoil. $M_{\infty} = 0.785$; $\tau_0 = 10$.

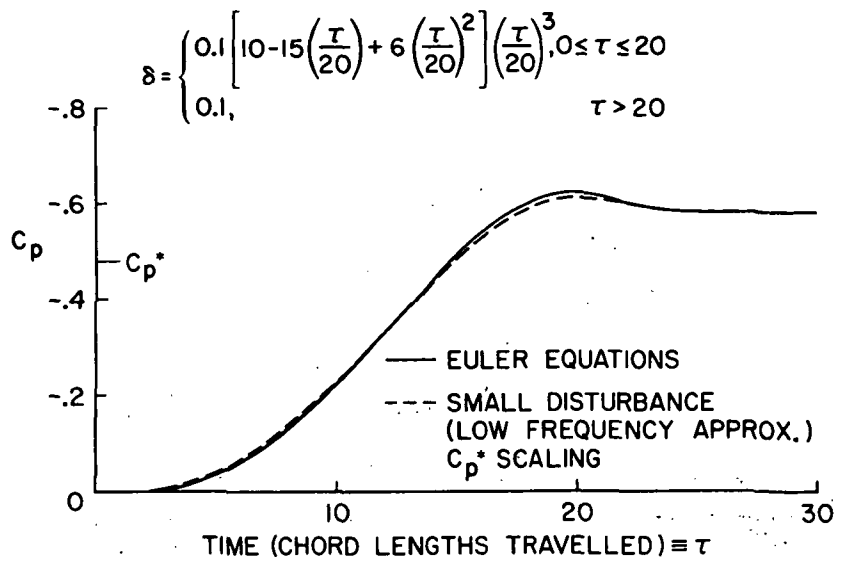


Figure 5.- Variation of C_p with time at $x/c = 0.525$ for a parabolic-arc airfoil. $M_\infty = 0.785$; $\tau_0 = 20$.

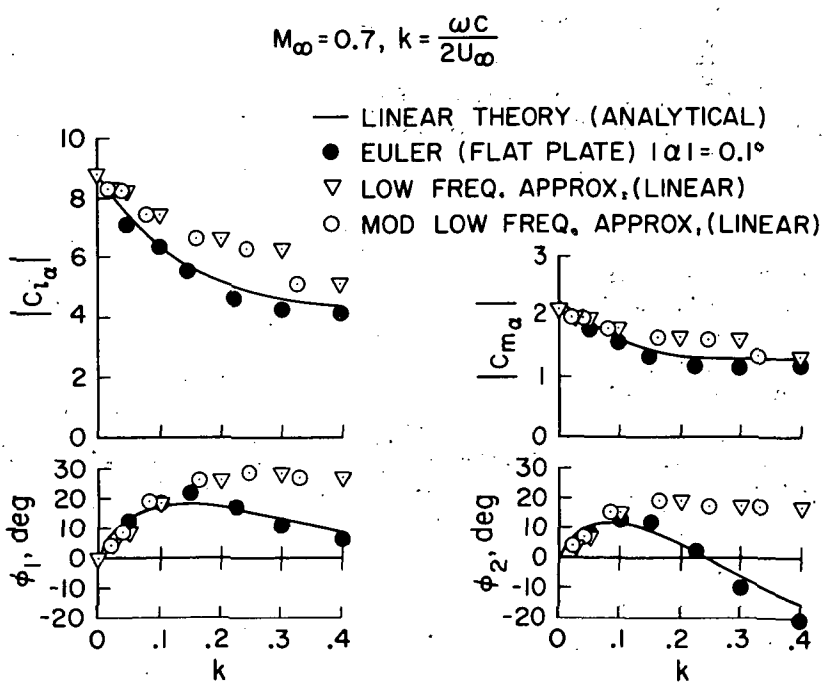


Figure 6.- Lift and moment coefficients (amplitude and phase) as functions of reduced frequency for an oscillatory plunging airfoil.

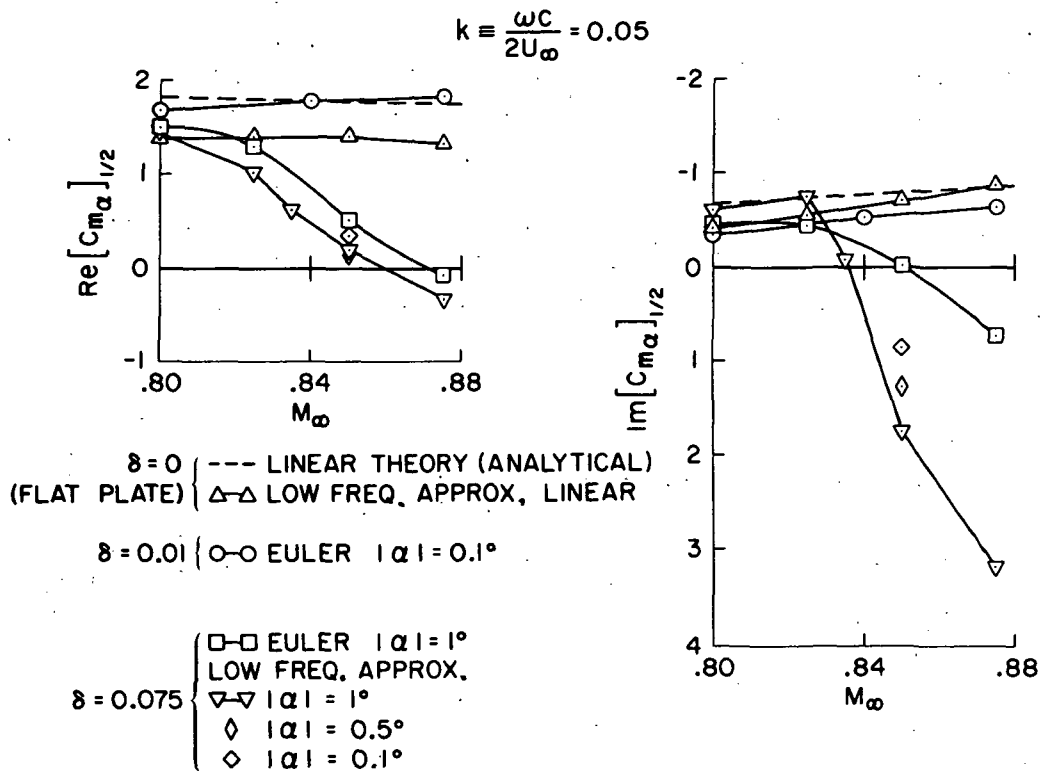
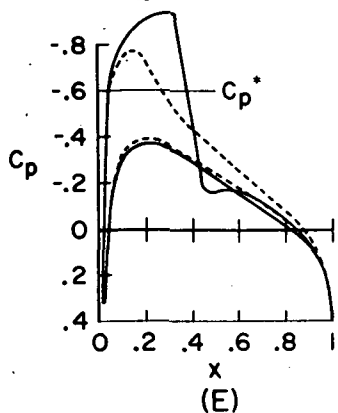


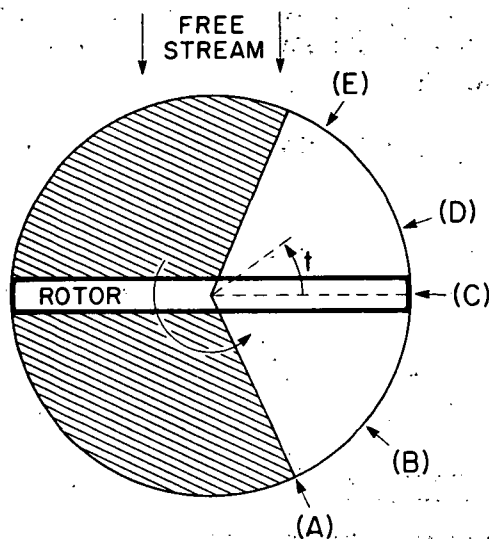
Figure 7.- Mid-chord moment coefficients as functions of Mach number for plunging oscillations of a parabolic-arc airfoil.

$t = 56^\circ, M_\infty = 0.747, \alpha = 0.880^\circ$

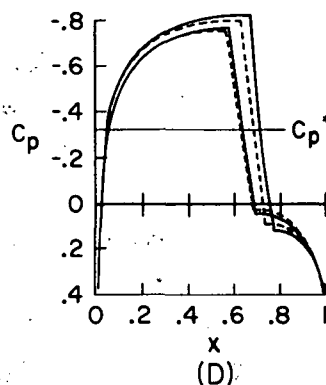


----- QUASI-STEADY

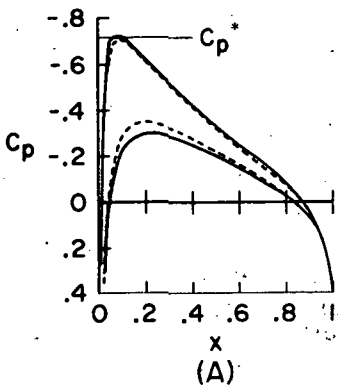
— UNSTEADY



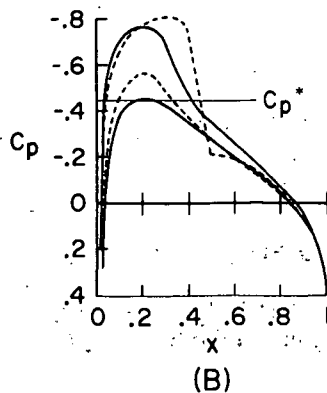
$t = 19^\circ, M_\infty = 0.841, \alpha = 0.1$



$t = -65^\circ, M_\infty = 0.714, \alpha = 1.15^\circ$



$t = -40^\circ, M_\infty = 0.796, \alpha = 0.477^\circ$



$t = 0^\circ, M_\infty = 0.854, \alpha = 0^\circ$

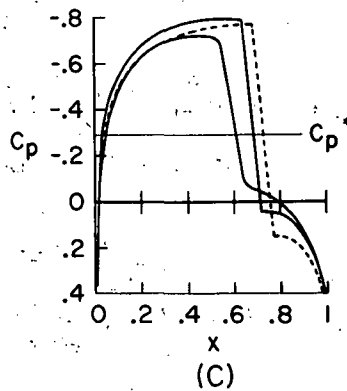


Figure 8.- Simulated helicopter motion. NACA 0010,

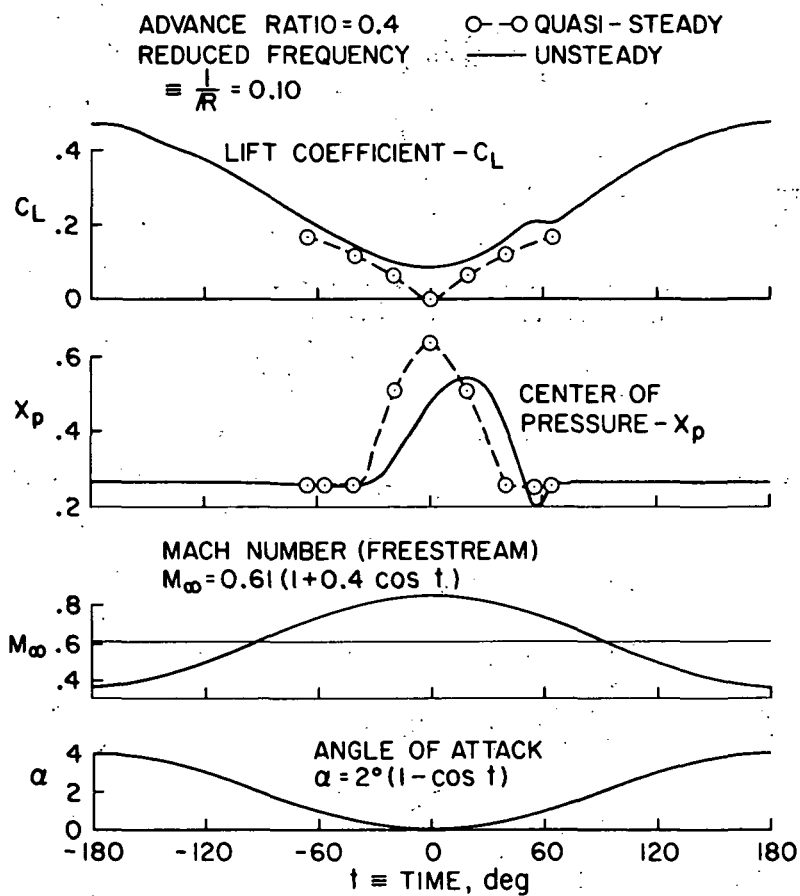


Figure 9.- Lift coefficient and center of pressure for a simulated helicopter blade element (NACA 0010 airfoil).

Page intentionally left blank

CALCULATION OF INVISCID SHEAR FLOW USING A RELAXATION METHOD
FOR THE EULER EQUATIONS

By Joseph L. Steger and Harvard Lomax

NASA Ames Research Center

SUMMARY

A fast block relaxation method is developed for the subsonic two-dimensional Euler equations. The procedure is applied to the problem of computing inviscid flow about a thin airfoil in a moderately nonuniform stream (shear flow). It is demonstrated that the technique of overlapping grid regions can be used to improve the convergence rate of block relaxation methods. Solutions and possible extensions are discussed.

I INTRODUCTION

In aerodynamic applications there are numerous problems in which large portions of the flow field can be characterized as inviscid but rotational. This can be true, for example, for flow behind a propeller or for the vortex flow behind a highly loaded wing. This type of flow is described by the Euler equations, and an accurate and fast numerical procedure for the solution of these equations is needed for subsonic flow regions.

In this paper, a block relaxation method for the subsonic steady Euler equations is developed. The procedure uses the equations in nonconservative form and, for the formulation used here, the sonic line is a singularity. In sections II and III the Euler equations are formulated in a successive approximation scheme where, at each iteration, a Poisson equation (or a set of nonhomogeneous Cauchy-Riemann-like equations) is solved. A block relaxation procedure for the Poisson equation is reported in section IV. Results for a thin lifting airfoil in moderately nonuniform flow are given in section V. Extensions of the present formulation to transonic flows and three dimensions are suggested in section VI.

II FORMULATION

The steady Euler equations in two dimensions can be written in the non-conservative form for Cartesian coordinates as

$$A\partial_x \vec{q} + B\partial_y \vec{q} = \vec{0} \quad (1)$$

with

$$\vec{q} = \begin{bmatrix} u \\ v \\ p \\ \rho \end{bmatrix} \quad A = \begin{bmatrix} u & 0 & \rho^{-1} & 0 \\ 0 & u & 0 & 0 \\ \rho c^2 & 0 & u & 0 \\ \rho & 0 & 0 & u \end{bmatrix} \quad B = \begin{bmatrix} v & 0 & 0 & 0 \\ 0 & v & \rho^{-1} & 0 \\ 0 & \rho c^2 & v & 0 \\ 0 & \rho & 0 & v \end{bmatrix} \quad (2)$$

where u and v are the x and y velocity components, $c^2 = \gamma p / \rho$, and p and ρ are the state variables of fluid pressure and fluid density. The nonlinear coefficient matrix A has eigenvalues u , u , $u+c$, and $u-c$, and B has eigenvalues of v , v , $v+c$, and $v-c$; consequently, A is nonsingular if $u \neq 0$ and $u \neq c$, while B is nonsingular if $v \neq 0$ and $v \neq c$. Therefore, in the absence of "sonic" points (i.e., $u=c$) or "stagnation" points ($u=0$), equation (1) may be rewritten as

$$\partial_x \vec{q} + A^{-1} B \partial_y \vec{q} = \vec{0} \quad (3)$$

An alternate but untried formulation, valid at $u=c$ points, will be suggested in a later section. The matrix $A^{-1}B$ is rewritten as the difference between a constant reference matrix and a perturbation matrix

$$A^{-1}B = (A^{-1}B)_r - \tilde{P} \quad (4)$$

such that \tilde{P} contains the nonlinear terms. Applying equation (4) to equation (3) results in

$$\partial_x \vec{q} + (A^{-1}B)_r \partial_y \vec{q} = \tilde{P} \partial_y \vec{q} \quad (5)$$

and solution of equation (5) can be obtained by successive approximation

$$\left[\partial_x \vec{q} + (A^{-1}B)_r \partial_y \vec{q} \right]^{(n+1)} = (\tilde{P} \partial_y \vec{q})^{(n)}, \quad n = 0, 1, 2, 3, \dots \quad (6)$$

if $\vec{q}^{(n+1)} \rightarrow \vec{q}^{(n)}$ for large n .

Equation (6) is in a conventional form for numerical solution, and indeed, the solution process described by equation (6) may be termed a simple relaxation algorithm once finite difference approximations are introduced. The difficulties in this process are associated with: (1) the iterative convergence of the solution procedure, (2) the convergence of the difference equations solution to the differential equation solution, and (3) the efficiency with which the solution is obtained. There are numerous ways to proceed. In the following method, in order to keep simple boundary conditions and to have \tilde{P} small, it is assumed that the airfoil is thin although the upstream flow is not necessarily uniform.

The matrix $A^{-1}B$ has as its elements

$$\begin{bmatrix} -uv\phi & c^2\phi & v\rho^{-1}\phi & 0 \\ 0 & u^{-1}v & (u\rho)^{-1} & 0 \\ \rho vc^2\phi & -\rho uc^2\phi & -uv\phi & 0 \\ \rho v\phi & -\rho u\phi & -u^{-1}v\phi & u^{-1}v \end{bmatrix} \quad (7)$$

where ϕ is defined by

$$\phi = (c^2 - u^2)^{-1} \quad (8)$$

If the coordinate system is closely aligned with the flow streamlines as is often the case in the study of thin airfoils, v should be small compared to u . In certain other problems the same effect might be achieved by coordinate transformations. The terms of $A^{-1}B$ not containing v could also be referenced to a linear solution or to the upstream flow profiles. Here, to illustrate the method, these terms are perturbed about an upstream constant value denoted by subscript ∞ . That is

$$A^{-1}B = (A^{-1}B)_{\infty} - \tilde{P} \quad (9)$$

with

$$(A^{-1}B)_{\infty} = \begin{bmatrix} 0 & (c^2\phi)_{\infty} & 0 & 0 \\ 0 & 0 & (u\rho)_{\infty}^{-1} & 0 \\ 0 & -(\rho uc^2\phi)_{\infty} & 0 & 0 \\ 0 & -(\rho u\phi)_{\infty} & 0 & 0 \end{bmatrix} \quad (10)$$

and

$$\tilde{P} = - \begin{bmatrix} -uv\phi & c^2\phi - (c^2\phi)_{\infty} & v\rho^{-1}\phi & 0 \\ 0 & u^{-1}v & (u\rho)^{-1} - (u\rho)_{\infty}^{-1} & 0 \\ \rho vc^2\phi & (\rho uc^2\phi)_{\infty} - \rho uc^2\phi & -uv\phi & 0 \\ \rho v\phi & (\rho u\phi)_{\infty} - \rho u\phi & -u^{-1}v\phi & u^{-1}v \end{bmatrix} \quad (11)$$

Henceforth, $P \partial_{\tilde{y}} \vec{q}^{(n)}$ is denoted by $\vec{f}^{(n)}$, and equation (6) is rewritten as

$$[\partial_x \vec{q} + (A^{-1}B)_{\infty} \partial_y \vec{q}]^{(n+1)} = \vec{f}^{(n)} \quad (12)$$

At any iteration level the system, equation (12), can be reduced to a coupled set of two equations for p and v , that is

$$(\partial_x v + (u\rho)_\infty^{-1} \partial_y p)^{(n+1)} = f_2^{(n)} \quad (13a)$$

$$(\partial_x p - (\rho c^2 \phi)_\infty \partial_y v)^{(n+1)} = f_3^{(n)} \quad (13b)$$

After these equations are solved, u and ρ are found by integrating

$$(\partial_x u + (c^2 \phi)_\infty \partial_y v)^{(n+1)} = f_1^{(n)} \quad (14a)$$

$$(\partial_x \rho - (\rho u \phi)_\infty \partial_y v)^{(n+1)} = f_4^{(n)} \quad (14b)$$

At any successive approximation level, equations (13) are essentially the nonhomogeneous Cauchy-Riemann equations (or the wave equations, $\phi < 0$) with Prandtl-Glauert transformation and source terms. If, in fact, the equations are linearized so that $\bar{f} = 0$, then comparing equation (13b) with equation (14a) shows that $\rho_\infty u_\infty = -p$, and as expected, equations (13) are simply equivalent to the classical Prandtl-Glauert equations

$$\partial_x v - \partial_y u = 0 \quad (15)$$

$$\partial_x u + (1 - M_\infty^2)^{-1} \partial_y v = 0$$

Equations (13) can also be cast as a Poisson equation ($\phi > 0$) or a wave equation ($\phi < 0$) in terms of either v or p by appropriate differentiation, scaling, and addition. Elimination of p gives

$$(\partial_{xx} v + c_\infty^2 \phi_\infty \partial_{yy} v)^{(n+1)} = \partial_x f_2^{(n)} - (\rho_\infty u_\infty)^{-1} \partial_y f_3^{(n)} \quad (16)$$

For boundary conditions, v is assumed known at infinity and along the airfoil it is given by

$$v = u \left(\frac{dy}{dx} \right) \quad (17)$$

Depending on the incoming flow, for a thin airfoil u may often be taken as a constant on the body, $u = u(x = -\infty, y = 0)$. For lifting cases, the Kutta condition must also be imposed. The procedure used here consists of adjusting the value of v just prior to the leading edge so that the streamline that stagnates the airfoil is the one that gives an equal trailing edge pressure on the upper and lower surface (see fig. 1). This procedure is equivalent to adjusting the value of the stream function ψ_B , which is constant on the body, until the trailing edge pressures are matched. Adjusting v as described above also permits the proper leading edge singularity to form for a lifting profile. If equation (16) is linearized to the Laplace equation, $\bar{f} = 0$, the maximum and minimum values of v can occur only on the boundaries and the correct leading edge behavior is excluded unless it is specified as part of the boundary conditions.

III. SOLUTION PROCEDURE

A solution procedure for equation (12) could now proceed as follows: begin with $\bar{f}^{(0)} = 0$ and numerically solve equations (13) for $v^{(1)}$ and $p^{(1)}$ followed by numerical integration of $u^{(1)}$ and $\rho^{(1)}$. Use these updated values to evaluate $\bar{f}^{(1)}$ and successively repeat this solution process until convergence is obtained — although in certain cases this procedure can also diverge.

The major computational part of this successive approximation scheme is the solution of the linear elliptic problem — equations (13) or the Poisson equation. A fast direct solver for numerical solution of equations (13) has been developed by Lomax and Martin (ref. 1). This procedure has been extended to transonic flows, see Martin and Lomax (ref. 2), and Martin (ref. 3), but not to lifting airfoils. Even more extensively developed, from the early work of Buzbee, Golub, and Nielson (ref. 4), Hockney (ref. 5), and Buneman (ref. 6), are the fast direct algorithms for the Poisson equation. All of the fast direct solvers rely upon the orderliness of the finite difference operators and are limited in the type of grid spacing permitted. Furthermore, internal boundary conditions (such as needed for a lifting profile) require special procedures (see, for example, refs. 7 and 8). For these reasons it was decided to solve equation (16), not by a direct solver, but by a block relaxation technique where the grid is divided into layers and a direct solver is used to solve the Poisson equation over each layer. This is a flexible procedure, although it is much less efficient than the use of fast direct solvers for problems where direct solvers are applicable.

In differencing equation (16), centered three-point second-order accurate difference operators are used to approximate all x and y derivatives. Since variable grid spacing is employed, three-point approximations to second derivatives are formally first-order accurate; however, the grid variation is kept sufficiently gradual so that the actual accuracy is effectively "second order." Once v is updated from the Poisson equation, p , u , and ρ are integrated from left to right using equations (13b) and (14) and second-order differencing schemes.

With some variations, the solution procedure from (n) to $(n+1)$ is to solve the Poisson equation for v with given values of v on the boundaries. To impose the Kutta condition, a single value of $v (=v_{KC})$ is specified at the mesh point just prior to the nose (a very fine x grid spacing is used there). If the trailing edge pressures fail to match, v_{KC} is adjusted as a function of Δp and previous changes of v_{KC} . As this portion of the solution process is a linear problem, solutions at two difference values of v_{KC} can always be extrapolated to find the v_{KC} that gives a zero Δp at the trailing edge. Once the linear problem is solved, the nonlinear terms, $\bar{f}^{(n+1)}$, are updated and the process is repeated until $\bar{f}^{(n+1)} = \bar{f}^{(n)}$. In relaxation procedures it is often advantageous to update the nonlinear terms and the Kutta condition at the same time the iterative process for the linear terms takes place. For the present block relaxation procedure this has not been an appropriate technique.

IV SOLUTION OF THE POISSON EQUATION

A block relaxation method was used to solve the Poisson equation in an effort to combine some of the good properties of both direct and iterative methods. A description of the direct method is included for completeness. It follows an approach outlined by Buzbee, Golub, and Nielson (ref. 4) and Dorr (ref. 9).

Consider the Poisson equation defined on a rectangle

$$\partial_{xx}v + \beta\partial_{yy}v = g \quad (18)$$

with Dirichlet conditions, and let the derivatives be approximated by three-point centered difference schemes. We require that the space in the y direction be covered by K equispaced rows, but allow the grid in the x direction to consist of J lines not necessarily equispaced. See figure 2 for the case when K = 7. The difference equations corresponding to equation (18) form a linear system of equations

$$\vec{A}\vec{v} = \vec{f} \quad (19a)$$

and with the notation given in figure 2, these can be expressed in block matrix-vector form

$$\begin{bmatrix} T_1 & c_1 I & & & & \\ a_2 I & T_2 & c_2 I & & & \\ & a_3 I & T_3 & c_3 I & & \\ & & \ddots & \ddots & \ddots & \\ & & & \ddots & \ddots & \\ & & & & a_{J-1} I & T_{J-1} & c_{J-1} I \\ & & & & & a_J I & T_J \end{bmatrix} \begin{bmatrix} \vec{v}_1 \\ \vec{v}_2 \\ \vdots \\ \vdots \\ \vec{v}_j \\ \vdots \\ \vdots \\ \vec{v}_J \end{bmatrix} = \begin{bmatrix} \vec{f}_1 \\ \vec{f}_2 \\ \vdots \\ \vdots \\ \vec{f}_j \\ \vdots \\ \vdots \\ \vec{f}_J \end{bmatrix} \quad (19b)$$

where

$$T_j = \text{trid}_K \left[\frac{\beta}{(\Delta y)^2}, \frac{-2\beta}{(\Delta y)^2} - (a_j + c_j), \frac{\beta}{(\Delta y)^2} \right], \quad T_j \text{ is order } K$$

\vec{f}_j contains elements of g_{jk} and boundary values

and

$$a_j = \frac{2}{(x_j - x_{j-1})(x_{j+1} - x_{j-1})}, \quad c_j = \frac{2}{(x_{j+1} - x_j)(x_{j+1} - x_{j-1})}$$

There are as many block matrices T_j as there are columns of mesh points and each T_j is a K by K tridiagonal matrix. The first remark to be made is that all the T_j have identical eigenvectors. In fact if the elements of the matrix X are

$$x_{lk} = \sqrt{(K+1)^{-1}} \sin\left(\frac{lk\pi}{K+1}\right) \quad (20)$$

the columns of X are the eigenvectors of T_j . It follows that $X^{-1}T_jX$ is a diagonal matrix having elements which are eigenvalues of T_j , that is

$$t_{jj} = -a_j - c_j - \frac{4\beta}{\Delta y^2} \sin^2\left(\frac{m\pi}{2(K+1)}\right), \quad m = 1, 2, \dots, K. \quad \text{The second remark is that } X^{-1} = X, \text{ or } XX = I; \text{ that is, the matrix of eigenvectors } X \text{ is its own inverse.}$$

The solution of equation (19) can be computed in the following way. Multiply the equations by the block diagonal matrix

$$Y = \begin{bmatrix} X & & & \\ & X & & \\ & & X & \\ & & & \ddots \\ & & & & X \end{bmatrix} \quad (21)$$

noting that $Y^{-1} = Y$. Equation (19) then becomes $Y\vec{A}\vec{v} = Y\vec{f}$ or $YAY\vec{v} = Y\vec{f}$. The solution for \vec{v} is given by

$$\vec{v} = Y[YAY]^{-1}Y\vec{f} \quad (22)$$

The value of such a solution lies in the fact that each of the three operations implied in equation (22) is computationally simple. The expression $Y\vec{f}$ is computed by a multiplication of each \vec{f}_j vector by X . The results can be stored back in \vec{f}_j . The next operation, $[YAY]^{-1}\vec{f}$, is carried out by K solutions of a scalar tridiagonal system — one for each row in the layer. The results can again be stored back in \vec{f}_j . Finally, J multiplications by X results in the complete solution.

The above process involves extensive matrix multiplications, namely the dual calculation of $X\vec{f}_j$, $j = 1, 2, \dots, J$. Since the eigenvector matrix X is dense, this would ordinarily require K^2 multiplications and $K(K-1)$ additions for each matrix multiplication. It is apparent from an inspection of equation (20), however, that this matrix operation is identical to a sine transform. This means that the symmetry in rows and columns of X can be

used to greatly reduce the arithmetic required. More precisely, the matrix X can be factored and replaced by the product of much sparser matrices. Figure 3 gives an example when $K = 7$. (The simple matrix of 1's is identical to Hockney's (ref. 5) folding matrix.) Notice that in this case the arithmetic operations are cut from 49 multiplies and 42 adds to 11 multiplies and 18 adds. Other efficient cases occur when the order of X is $2^m - 1$, although the factoring concept is not restricted to this order. Cooley, Lewis, and Welch (ref. 10) have shown how to efficiently implement the fast Fourier transform in the factorization of X and this approach is preferred when the order of X is large.

As mentioned in section III, the Poisson equation is solved in blocks or layers each one of which is inverted directly by a fast solver. In computing flows about airfoils, there can be advantages to this layer approach. For example, one has the ability to decrease the grid spacing from one layer to the next if the flow gradients warrant better resolution. Furthermore, the use of special difference operators near the airfoil can be restricted to relatively narrow layers and, if need be, the transforming eigenvectors can be found numerically. For thin layers the dimension of the eigenvector transform matrix is small so it is not even essential that this matrix or its inverse be factorable.

In solving a given layer it is necessary to use points from adjacent layers as boundary data. The updating of the points within a layer is carried out using a weighting parameter to provide the acceleration customarily associated with overrelaxation. However, there is another way to improve the convergence rate—a technique we refer to as overlap. The basic idea is to allow an intersection of layers so that the boundary condition for one layer lies several lines deep within an adjacent layer. In this way a band of points is common to both.

The advantage of overlapping grid regions was found in analysis of the simple equation

$$\partial_{yy}u = f(y) \quad (23)$$

with specified end points and use of the three-point-centered difference operator. Let a finite difference grid of K interior points be partitioned into two grids of R interior points and S interior points such that $K \leq R + S < 2K$. The difference equations are inverted directly, using as boundary conditions the latest updated values of u in the adjacent grid until $u_k^{(n+1)} \rightarrow u_k^{(n)}$. The spectral radius of this two-layer relaxation scheme is given by

$$\lambda_{SR} = \frac{(K - R)(K - S)}{(S + 1)(R + 1)} \quad (24)$$

(see the appendix for the derivation and possible extension of this result). If, for example, $K = 28$ and R and S are each taken as 14—a block Gauss-Seidel scheme—then $\lambda_{SR} = 0.871$. But if R and S are each taken as 15, while K remains equal to 28, there is a slight overlap and $\lambda_{SR} = 0.66$.

Since $(0.871)^3 \doteq 0.66$, the effect of overlap in this simple case results in a 3 to 1 improvement in the number of iterations needed to converge.

The block overrelaxation method in two dimensions is also considerably improved by overlapping the blocks. For example, on a square grid of 47×47 the y direction can be split into three layers each of which has 15 interior points from $1 \leq j \leq 47$: $1 \leq k \leq 17$, $16 \leq k \leq 32$, and $31 \leq k \leq 47$. However, a better procedure is to use four of the 15-point layers in overlap (each for $1 \leq j \leq 47$) as $1 \leq k \leq 17$, $11 \leq k \leq 27$, $21 \leq k \leq 37$, and $31 \leq k \leq 47$. In figure 4 a comparison of these methods is given where each technique begins from a bad guess and is run until the solution is less than 10^{-6} of its exact value. At optimum conditions the overlap method requires about half as many iterations as the three-strip successive block overrelaxation method, and although it requires $4/3$ more work, the overall improvement is substantial. The efficiency of the overlap method is also less sensitive to the choice of an optimum relaxation parameter. (In this respect, both methods are much superior to the successive line overrelaxation (SLOR) scheme which is also shown in figure 4.)

There is generally a clear advantage to overlapping the grids in the block relaxation procedure. This advantage must be weighed against the cost of doing larger block inversions under the constraint that the number of points in the layer should correspond to the most efficient eigenvector transform number. More complicated problems have to be analyzed, but numerical experimentation, in general, shows that the block overlap method maintains its advantage for multiple strips and for overrelaxation factors. A good guess hastens convergence, and doubling of the grid spacing from one region to the next is not detrimental and can be advantageous. Finally, if special algorithms are isolated in a region covering the boundary, overlapping and (sometimes) more frequent calls to adjacent strips can improve overall computer time.

V RESULTS

All results for a lifting airfoil have been obtained on a grid of $J \times K = 59 \times 90$ where the grid spacing in x is variable but changes gradually. The grid spacing in y is uniform over layers of 17 points (15 interior points) and consists of 6 main layers for an accumulation of 90 points. For adjacent layers above and below the body $\Delta y = 0.03$, the intermediate strips have spacing of 0.09, and the final outermost layers have grid spacing of 0.27. The grids are overlapped and the airfoil is contained midway between the innermost grids. Overlapping and connecting the innermost grids above and below the airfoil is another 15-point layer which extends from $x = "-\infty"$ up to the nose of the airfoil and from beyond the tail of the airfoil to $x = "\infty."$ For the entire grid, "infinity" conditions with $v = 0$ occur at $y_{\pm\infty} = \pm 5.54$ and $x_{\mp\infty} = -1.74, 2.74$ where a chord length is unity.

A linear solution for a 6 percent thick biconvex airfoil at 3° angle of attack and $M_\infty = 0.5$ is compared to the exact solution in figure 5 to indicate how well the procedure can handle the leading edge singularity. While

the results are reasonably good there is an inconsistency, not unexpected, that at y locations in the plane of the airfoil the running integrations for u , p , and ρ do not return exactly to free-stream values at x_∞ . At zero angle of attack the leading-edge square-root singularity is not present and downstream values match upstream values to at least 5 significant figures.

For the shear flow calculations, all of the upstream profiles have the form shown in figure 6 where the parameter δ can be positive or negative and represents half of the percentage defect. The spacing of the vectors also indicates the actual inner grid spacing, which is tripled beyond $y = \pm 0.495$. The grid overlap is also indicated by flagging of vectors that are common to the intermediate layer. Two C_p distributions for an 8 percent thick parabolic arc airfoil at 2° angle of attack and $M_\infty = 0.5$ are shown in figure 7 for $\delta = \pm 0.1$. Here C_p uses reference infinity values at $x = -\infty$, $y = +\infty$, that is, the undisturbed flow. Also, a linearized tangency condition is used, $v = u(-\infty, 0) \tan \theta$ where $\tan \theta$ is the slope along the body surface. In these calculations only the u profile is perturbed; v , p , and ρ are all at uniform M_∞ conditions so the upstream stagnation enthalpy is variable. In figure 8, C_L versus α data are presented for the same airfoil and flow conditions. The calculations show that a loss of lift occurs for a defect in u and that gradients in pressure are reduced. The steepened pressure gradients that correspond to the negative defect (i.e., accelerated) flow are likely to intensify separation effects so that the increased lift due to the higher kinetic energy may not be fully realized.

Flows with large defects in the incoming profile will not converge—after perhaps 4 or 5 successive corrections of $f^{(n+1)}$, the corrections begin to grow. This situation is aggravated at an increasing angle of attack and higher Mach number. However, all of the computations use reference values of $[A^{-1}B]_\infty$ at $x = -\infty$, $y = \infty$. Perturbation of $A^{-1}B$ about the incoming profiles, or some midpoint of the profile, should extend the range of convergence.

Computation times for the solutions shown in figure 7 are approximately 17 seconds for the case $\delta = 0.1$ and 19 seconds for the case $\delta = -0.1$. Times were measured on a Control Data Corp. 7600 computer and they include all initialization and output. In both cases the solutions begin from parallel flow conditions and use a 59×90 grid. The same fine grid in x is used throughout, and reduced times would result if the grid spacing in x were doubled in the outer strips away from the body.

The solution procedure allows arbitrary incoming profiles to be specified, and figure 9 shows calculations with incoming profiles in both variables u and ρ for flow over a parabolic arc airfoil at $\alpha = 0^\circ$ and $M_\infty = 0.4$. In these cases u is accelerated and ρ is defective (a higher temperature than free stream) and these conditions lead to the expanded pressure distributions shown.

All of the preceding calculations used the linearized tangency condition that is typically used with thin airfoil theory. This is not necessarily consistent with using the full nonlinear Euler equations in the outer flow, so calculations for the lifting airfoil case were repeated with the tangency condition

$$v(x, \pm 0) = u(x, \pm 0) \tan \theta_{\pm}, \quad 0 \leq x \leq 1 \quad (25)$$

Consequently, tangency is still applied along the $y = 0$ plane, which neglects displacement effects but is otherwise precise. Changing the boundary conditions in this manner leads to the more expanded solutions indicated in figures 10 and 11, although peak leading edge pressure gradients are reduced. At higher angles of attack the amount of change due to altering the tangency condition would seem to justify a more precise boundary condition fit.

VI POSSIBLE EXTENSIONS TO TRANSONIC AND THREE-DIMENSIONAL FLOWS

The previous formulation is excluded from points $u = c$ because the equations were multiplied by A^{-1} . If instead, equation (1) is multiplied through by the nonsingular matrix (unless $u = 0$)

$$H = \begin{bmatrix} 1 & & & & \\ & 1 & & & \\ \rho c^2 & & -u & & \\ & & & & \\ 0 & & 0 & & 1 \end{bmatrix} \quad (26)$$

the following equations are obtained:

$$\left. \begin{aligned} u \partial_x v + \rho^{-1} \partial_y p &= -v \partial_y v \\ (c^2 - u^2) \partial_x p - \rho u c^2 \partial_y v &= v(u \partial_y p - \rho c^2 \partial_y u) \end{aligned} \right\} \quad (27)$$

and

$$\left. \begin{aligned} u \partial_x u &= -v \partial_y u - \rho^{-1} \partial_x p \\ u \partial_x \rho &= -v \partial_y \rho - \rho \partial_x u - \rho \partial_y v \end{aligned} \right\} \quad (28)$$

For small v , equations (27) are similar to the transonic small perturbation equations.

If equations (27) are further perturbed about ∞ (or sonic conditions), there results

$$\left. \begin{aligned} \rho_{\infty} u_{\infty} \partial_x v + \partial_y p &= \tilde{f} \\ (1 - M^2) \partial_x p - \rho_{\infty} u_{\infty} \partial_y v &= \tilde{g} \end{aligned} \right\} \quad (29)$$

or if $v_{yx} = v_{xy}$

$$\partial_x[(1 - M^2)\partial_x p] + \partial_{yy} p = \partial_y \bar{f} + \partial_x \bar{g} \quad (30)$$

where $\partial_{yp} = -(\rho u \partial_{xv} + \rho v \partial_{yv})$ might be used to supply a Neumann condition if v is specified on the body. The above formulation has not been tried, but it is conjectured that a stable iteration scheme could be developed based on schemes developed for the transonic small perturbation equations (for example, Murman and Cole (ref. 11) and Murman (ref. 12), Martin and Lomax (ref. 2)). If shock waves are not fit but captured, an alternate conservative set of equations would have to be substituted in these regions.

The extension of the original formulation of the equations to three dimensions is straightforward. Let $\bar{q}^t = (u, v, w, p, \rho)$ and begin with

$$\partial_x \bar{q} + A^{-1} B \partial_y \bar{q} + A^{-1} C \partial_z \bar{q} = 0 \quad (31)$$

with

$$A^{-1} B = \begin{bmatrix} vu^{-1} & \rho v \phi & -\rho u \phi & 0 & -vu^{-1} \phi \\ 0 & -vu \phi & c^2 \phi & 0 & v \rho^{-1} \phi \\ 0 & 0 & vu^{-1} & 0 & (\rho u)^{-1} \\ 0 & 0 & 0 & vu^{-1} & 0 \\ 0 & \rho v^2 c^2 \phi & -\rho u c^2 \phi & 0 & -uv \phi \end{bmatrix} \quad (32)$$

and

$$A^{-1} C = \begin{bmatrix} wu^{-1} & \rho w \phi & 0 & -\rho u \phi & -wu^{-1} \phi \\ 0 & -uw \phi & 0 & c^2 \phi & w \rho^{-1} \phi \\ 0 & 0 & wu^{-1} & 0 & 0 \\ 0 & 0 & 0 & wu^{-1} & (\rho u)^{-1} \\ 0 & \rho w c^2 \phi & 0 & -\rho c^2 u \phi & -wu \phi \end{bmatrix} \quad (33)$$

Bringing derivatives whose coefficients contain v and w to the right-hand side, and perturbing the remaining terms about infinity values results in the reduced system

$$\partial_x v + (\rho u)_\infty^{-1} \partial_y p = g_3$$

$$\partial_x w + (\rho u)_\infty^{-1} \partial_z p = g_4 \quad (34)$$

$$\partial_x p - (\rho u c^2 \phi)_\infty (\partial_y v + \partial_z w) = g_5$$

Once values of v , w , and p are updated, ρ and u follow from the integrations

$$\begin{aligned}\partial_x \rho &= g_1 + (\rho u \phi)_\infty (\partial_y v + \partial_z w) \\ \partial_x u &= g_2 - (c^2 \phi)_\infty (\partial_y v + \partial_z w)\end{aligned}\tag{35}$$

If $v_{xy} = v_{yx}$ and $w_{zx} = w_{xz}$, equations (34) can be replaced by a Poisson equation in p and the integrations of $\partial_x v$ and $\partial_x w$.

CONCLUDING REMARKS

The block-overlap relaxation procedure that has been described here is efficient for certain problems, but it is limited to subsonic flows. Further developments in efficiency and generality are expected, but for immediate applications the procedure could be coupled with conventional time-dependent procedures. These more general methods could be used, for example, in regions of sonic flow and shock waves and the relaxation procedures could be used elsewhere with, perhaps, an overlapping of the two methods in compatible regions. A most useful extension of the present method will be in the calculation of nonuniform three-dimensional flows which are so prevalent in many V-STOL configurations.

APPENDIX

The improvement in iterative convergence due to overlapping the grids can be analyzed by considering the one-dimensional problem

$$\partial_{yy}v - \sigma v = f, \quad \sigma \geq 0 \quad (\text{A-1})$$

As indicated in section IV, the difference equations corresponding to equation (A-1) are equivalent to those of equation (18) in the transform variable — that is, for purposes of analysis the difference equations are considered to be ordered and transformed by the eigenvectors of the tridiagonal blocks generated by differencing of $\partial_{xx}v$.

For simplicity, only two strips will be considered and the relaxation parameter will be taken as 1. The iteration procedure is given in two steps

$$\begin{array}{c}
 \begin{array}{|c|} \hline \text{(i)} \\ \hline \end{array}
 \begin{array}{|c|} \hline \begin{array}{c} b \ c \\ a \ b \ c \\ \dots \\ a \ b \ c \\ a \ b \end{array} \\ \hline \end{array}
 \begin{array}{|c|} \hline \begin{array}{c} v_1^* \\ \dots \\ v_s^* \\ v_{s+1}^* \\ \dots \\ v_M^* \end{array} \\ \hline \end{array}
 =
 \begin{array}{|c|} \hline \begin{array}{c} 0 \\ \dots \\ 0 \ -c \\ 1 \end{array} \\ \hline \end{array}
 \begin{array}{|c|} \hline \begin{array}{c} v_1^n \\ \dots \\ v_s^n \\ v_{s+1}^n \\ \dots \\ v_M^n \end{array} \\ \hline \end{array}
 +
 \begin{array}{|c|} \hline \begin{array}{c} f_1 \\ \dots \\ f_s \\ 0 \\ \dots \\ 0 \end{array} \\ \hline \end{array}
 \quad (\text{A-2})
 \end{array}$$

and

$$\begin{array}{c}
 \begin{array}{|c|} \hline \text{(ii)} \\ \hline \end{array}
 \begin{array}{|c|} \hline \begin{array}{c} 1 \\ \dots \\ 1 \end{array} \\ \hline \end{array}
 \begin{array}{|c|} \hline \begin{array}{c} v_1^{n+1} \\ \dots \\ v_{M-R}^{n+1} \\ v_{M+1-R}^{n+1} \\ \dots \\ v_M^{n+1} \end{array} \\ \hline \end{array}
 =
 \begin{array}{|c|} \hline \begin{array}{c} 1 \\ \dots \\ -a \ 0 \end{array} \\ \hline \end{array}
 \begin{array}{|c|} \hline \begin{array}{c} v_1^* \\ \dots \\ v_{M-R}^* \\ v_{M+1-R}^* \\ \dots \\ v_M^* \end{array} \\ \hline \end{array}
 +
 \begin{array}{|c|} \hline \begin{array}{c} 0 \\ \dots \\ 0 \\ f_{M+1-R} \\ \dots \\ f_M \end{array} \\ \hline \end{array}
 \quad (\text{A-3})
 \end{array}$$

An intermediate result for the iteration matrix is obtained by performing the inversions in equations (A-2) and (A-3) and eliminating \vec{v}^* .

$$\begin{bmatrix} v_1^{n+1} \\ \vdots \\ v_M^{n+1} \end{bmatrix} = \begin{bmatrix} 1 & & & & & \\ & \ddots & & & & \\ & & 1 & & & \\ \hline & & \eta_1 & & & \\ & & \eta_2 & & & \\ & & \vdots & & 0 & \\ & & \eta_R & & & \end{bmatrix} \begin{bmatrix} \zeta_1 \\ \zeta_2 \\ \vdots \\ \zeta_S \\ \hline 1 \\ \vdots \\ 1 \end{bmatrix} \begin{bmatrix} v_1^n \\ \vdots \\ v_M^n \end{bmatrix} \quad (\text{A-4})$$

where

$$(\eta_1, \eta_2, \dots, \eta_r, \dots, \eta_R)^t = -aT_{(R)}^{-1} \hat{e}_1 \quad (\text{A-5})$$

$$T_{(R)} = \text{trid}(a, b, c) \quad (\text{A-6})$$

and \hat{e}_1 is the first unit vector of order R (i.e., the first column of the order R identity matrix). Likewise

$$(\zeta_1, \zeta_2, \dots, \zeta_S, \dots, \zeta_S)^t = -cT_{(S)}^{-1} \hat{e}_S \quad (\text{A-7})$$

With this notation defined, the multiplications in equation (A-4) yield

$$\vec{v}(n+1) = B\vec{v}(n) \quad (\text{A-8})$$

with B a matrix of zeroes save for column $S+1$,

$$\eta_r = \frac{R - r + 1}{R + 1} \quad r = 1, 2, \dots, R \quad (\text{A-13})$$

$$\zeta_s = \frac{s}{S + 1} \quad s = 1, 2, \dots, S \quad (\text{A-14})$$

Consequently, the term $\eta_Q \zeta_{N-R}$ (which is the spectral radius in this the worst case) is

$$\eta_Q \zeta_{N-R} = \frac{(M - S)(M - R)}{(R + 1)(S + 1)}, \quad R + S \geq M \quad (\text{A-15})$$

and the greater $(R + S)$ is than M (i.e., the more the overlap), the fewer iterations are needed to drive $(\eta_Q \zeta_{N-R})^{m-1} \rightarrow 0$.

If overrelaxation parameters or more than two layers are used, it is necessary to find the eigenvalues of a tridiagonal matrix in order to determine the spectral radius of the iteration matrix. The eigenvalues will have to be found numerically; however, the order of the tridiagonal is only equal to the number of layers.

REFERENCES

1. Lomax, H., and Martin, E. D.: Fast Direct Numerical Solution of the Nonhomogeneous Cauchy-Riemann Equations. *J. of Computational Phys.*, vol. 15, 1974, pp. 55-80.
2. Martin, E. D., and Lomax, H.: Rapid Finite-Difference Computation of Subsonic and Transonic Aerodynamic Flows. AIAA Paper No. 74-11, 1974.
3. Martin, E. Dale: Progress in Application of Direct Elliptic Solvers to Transonic Flow Computations. Aerodynamic Analyses Requiring Advanced Computers, Part II, NASA SP-347, 1975, pp. 839-870.
4. Buzbee, B. L., Golub, G. H., Nielson, C. W.: On Direct Methods for Solving Poisson's Equations. *SIAM. J. Numer. Anal.*, vol. 7, 1970, pp. 627-656.
5. Hockney, R. W.: The Potential Calculation and Some Applications. In *Methods in Computational Physics*, vol. 9, ed. Alder, B., Fernbach, S., and Rotenberg, M. Academic Press, N.Y. 1970, pp. 135-211.
6. Buneman, O.: A Compact Non-iterative Poisson Solver. SUIPR Report 294, 1969. Inst. for Plasma Res., Stanford Univ., Stanford, Calif.
7. Buzbee, B. L., Dorr, F. W., George, J. A., and Golub, G. H.: The Direct Solution of the Discrete Poisson Equation on Irregular Regions. *SIAM J. Numer. Anal.*, vol. 8, 1971, pp. 722-736.
8. Martin, E. D.: A Generalized-Capacity-Matrix Technique for Computing Aerodynamic Flows. *Computers and Fluids*, vol. 2, 1974, pp. 79-97.
9. Dorr, F.: The Direct Solution of the Discrete Poisson Equation on a Rectangle. *SIAM Review*, vol. 12, 1970, pp. 248-263.
10. Cooley, J. W., Lewis, P. A. W., and Welch, P. D.: The Fast Fourier Transform Algorithm: Programming Considerations in the Calculation of Sine, Cosine and Laplace Transforms. *J. Sound Vib.*, vol. 12, 1970, pp. 315-337.
11. Murman, E. M., and Cole, J. D.: Calculation of Plane Steady Transonic Flows. *AIAA Journal*, vol. 9, 1971, pp. 114-121.
12. Murman, E. M.: Analysis of Embedded Shock Waves Calculated by Relaxation Methods. *Proc. AIAA Comp. Fluid Dyn. Conf.*, Palm Springs, CA., 1973.
13. Steger, J. L.; and Warming, R. F.: On the Convergence of Certain Finite-Difference Schemes by an Inverse-Matrix Method. *J. Comput. Phys.*, vol. 17, no. 2, Feb. 1975, pp. 103-121.

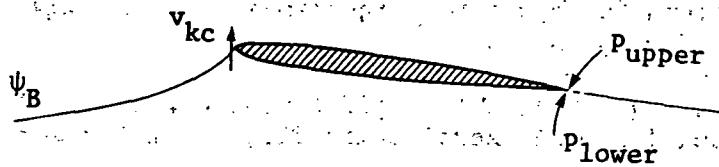


Figure 1.- Imposition of the Kutta condition by adjusting v_{kc} so that trailing edge pressures match.

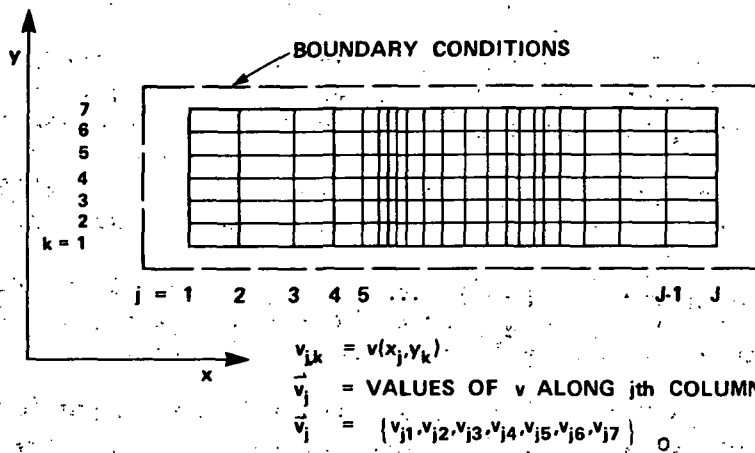


Figure 2.- Seven-row layer, equispaced in y with arbitrary length and spacing in x .

$$\begin{aligned}
 a &= 0.5 \sin\left(\frac{\pi}{8}\right) & c &= 0.5 \sin\left(\frac{3\pi}{8}\right) \\
 b &= 0.5 \sin\left(\frac{5\pi}{8}\right) & d &= 0.5
 \end{aligned}$$

$$\begin{aligned}
 & \begin{bmatrix} 1 & & & & & & 1 \\ & 1 & & & & & \\ & & 1 & & & & \\ & & & 1 & & & \\ & & & & 1 & & \\ & -1 & & & & & \\ & & -1 & & & & \\ & & & -1 & & & \\ -1 & & & & & & 1 \end{bmatrix} & \begin{bmatrix} 1 & & & & & & 1 \\ & 1 & & & & & \\ & & 1 & & & & \\ & & & 1 & & & \\ & & & & 1 & & \\ & -1 & & & & & \\ & & -1 & & & & \\ & & & -1 & & & \\ & & & & -1 & & \\ & & & & & -1 & \\ & & & & & & 1 \end{bmatrix} & \begin{bmatrix} 0 & 0 & 0 & d & 0 & 0 & 0 \\ 0 & 0 & 0 & 0 & 0 & -d & 0 \\ 0 & b & 0 & 0 & 0 & 0 & 0 \\ 0 & 0 & 0 & 0 & d & 0 & -d \\ c & 0 & -a & 0 & 0 & 0 & 0 \\ 0 & 0 & 0 & 0 & -b & 0 & -b \\ a & 0 & c & 0 & 0 & 0 & 0 \end{bmatrix} \\
 \\
 \times & \begin{bmatrix} 1 & & & & & & 1 \\ & 1 & & & & & \\ & & 1 & & & & \\ & & & 1 & & & \\ & & & & 1 & & \\ & & & & & 1 & \\ & -1 & & & & & \\ & & -1 & & & & \\ & & & -1 & & & \\ & & & & -1 & & \\ -1 & & & & & & 1 \end{bmatrix} & \begin{bmatrix} f_1 \\ f_2 \\ f_3 \\ f_4 \\ f_5 \\ f_6 \\ f_7 \end{bmatrix} & = & \begin{bmatrix} a & b & c & d & c & b & a \\ b & d & b & 0 & -b & -d & -b \\ c & b & -a & -d & -a & b & c \\ d & 0 & -d & 0 & d & 0 & -d \\ c & -b & -a & d & -a & -b & c \\ b & -d & b & 0 & -b & d & -b \\ a & -b & c & -d & c & -b & a \end{bmatrix} & \begin{bmatrix} f_1 \\ f_2 \\ f_3 \\ f_4 \\ f_5 \\ f_6 \\ f_7 \end{bmatrix}
 \end{aligned}$$

Figure 3.- Factorization of the 7x7 sine-eigenvector transform matrix by repetitive use of the folding matrix.

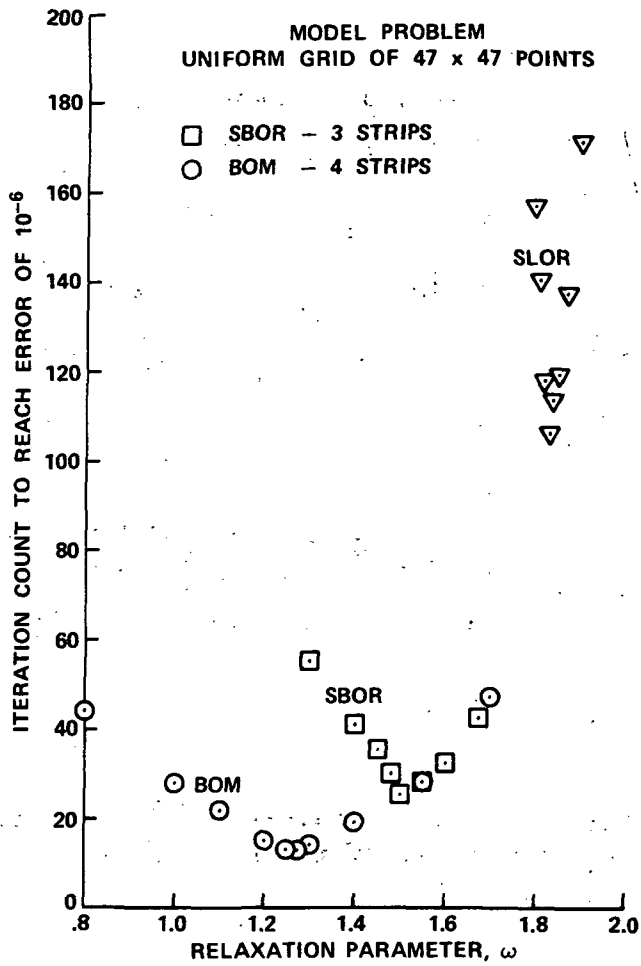


Figure 4.- Comparison of successive block overrelaxation (SBOR) to the block overlap method (BOM) for the model problem.

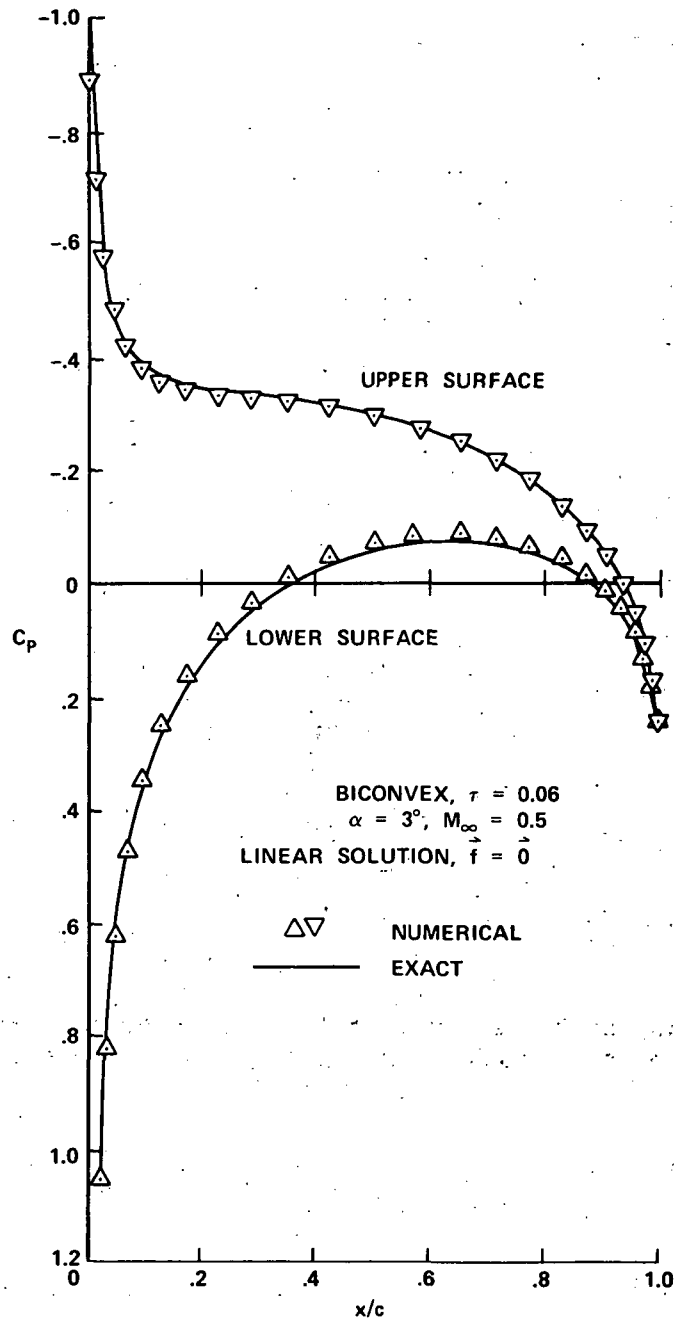


Figure 5.- Linear solution for a 6 percent thick parabolic arc airfoil.

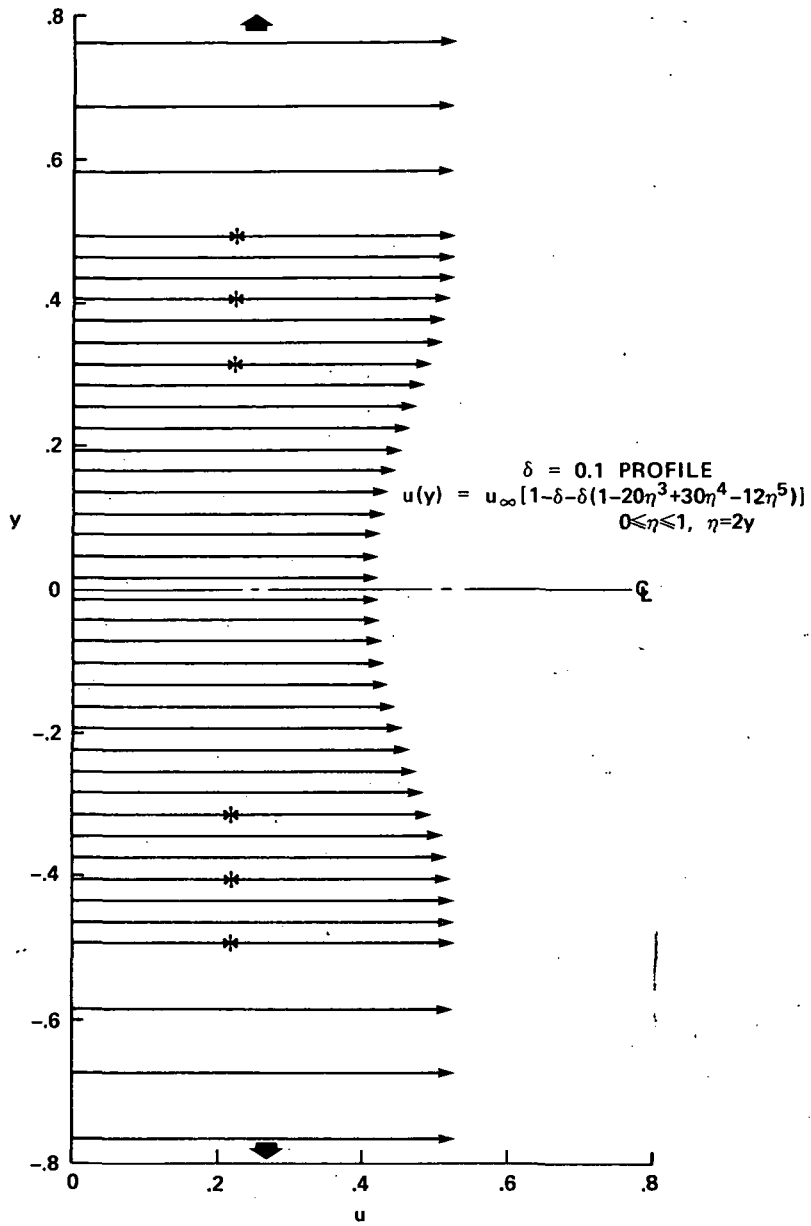


Figure 6.- Typical incoming velocity profile.

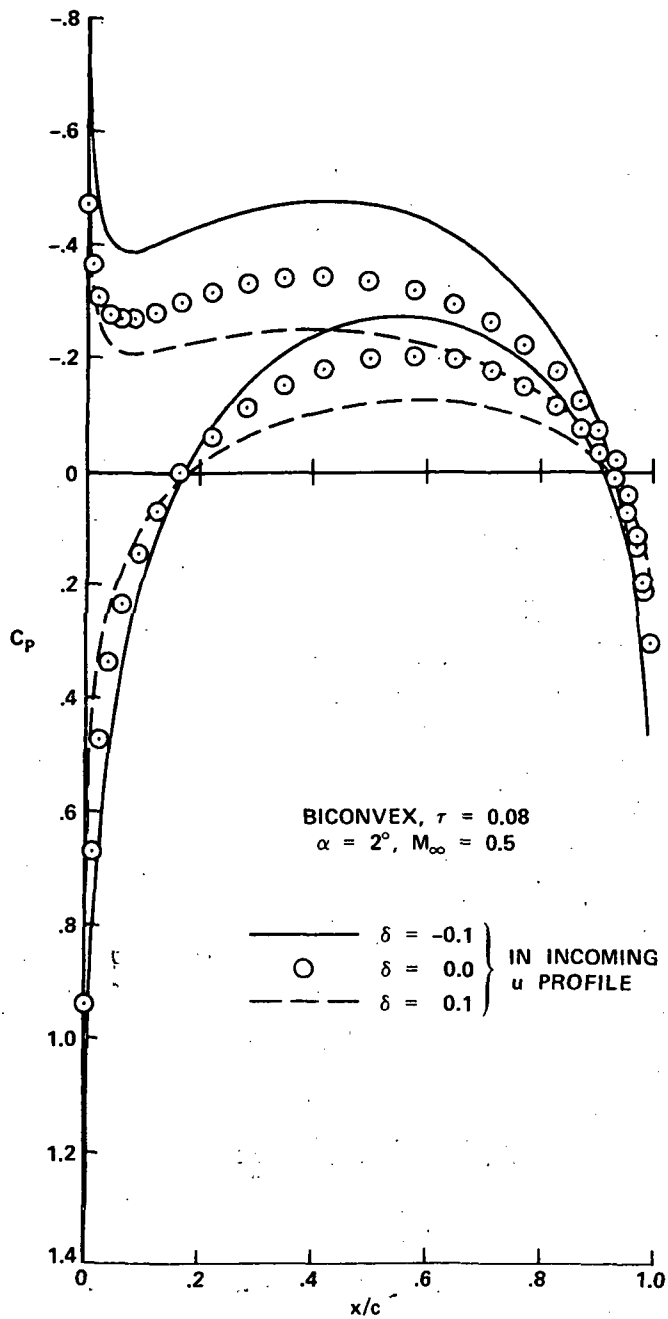


Figure 7.- Parabolic arc airfoil in moderate incoming shear flow using linearized boundary conditions, $v_{\pm} = u(-\infty, \pm 0) \tan \theta_{\pm}$.

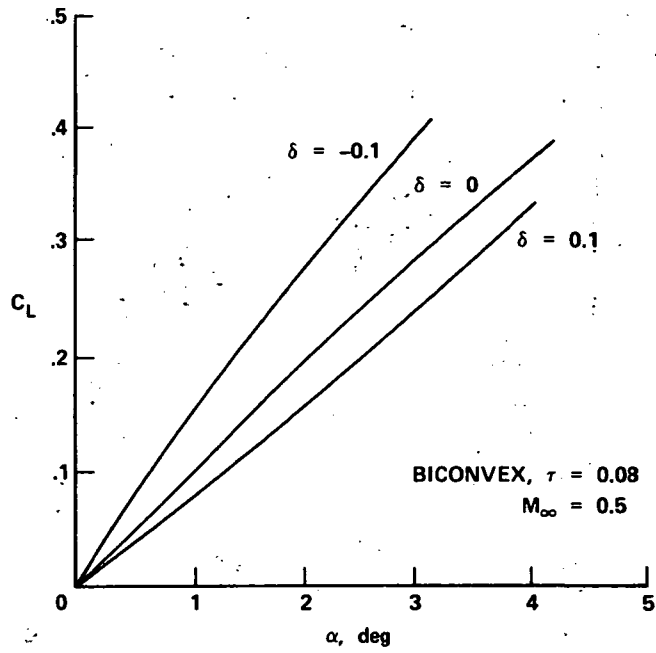


Figure 8.- C_L versus α for moderate incoming shear flow using linearized boundary conditions.

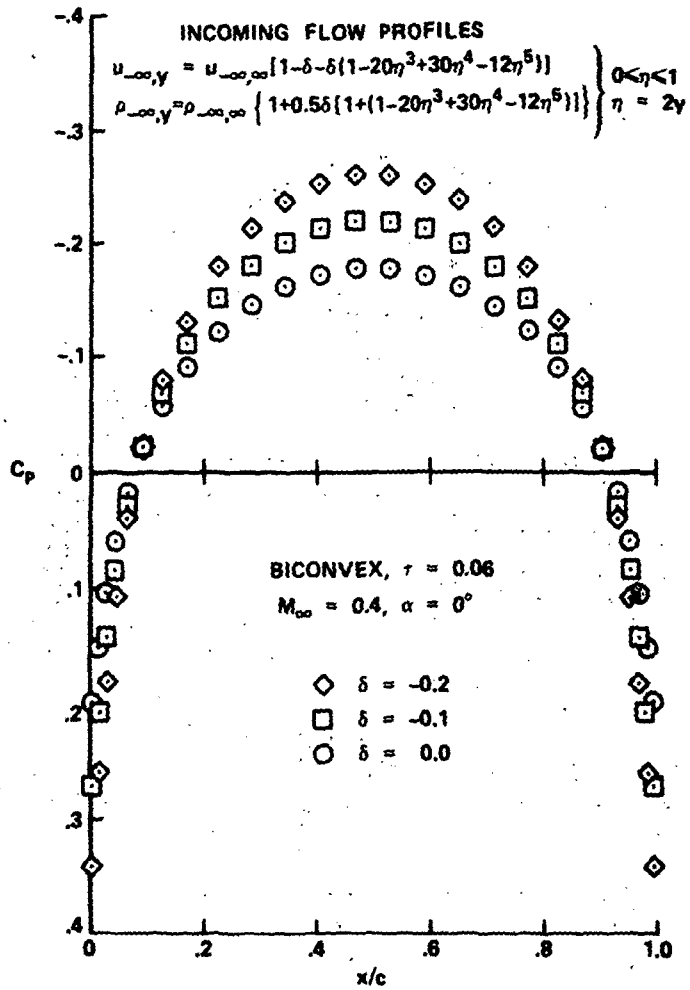


Figure 9.- Flow over a parabolic arc airfoil with accelerated and heated incoming flow profiles.

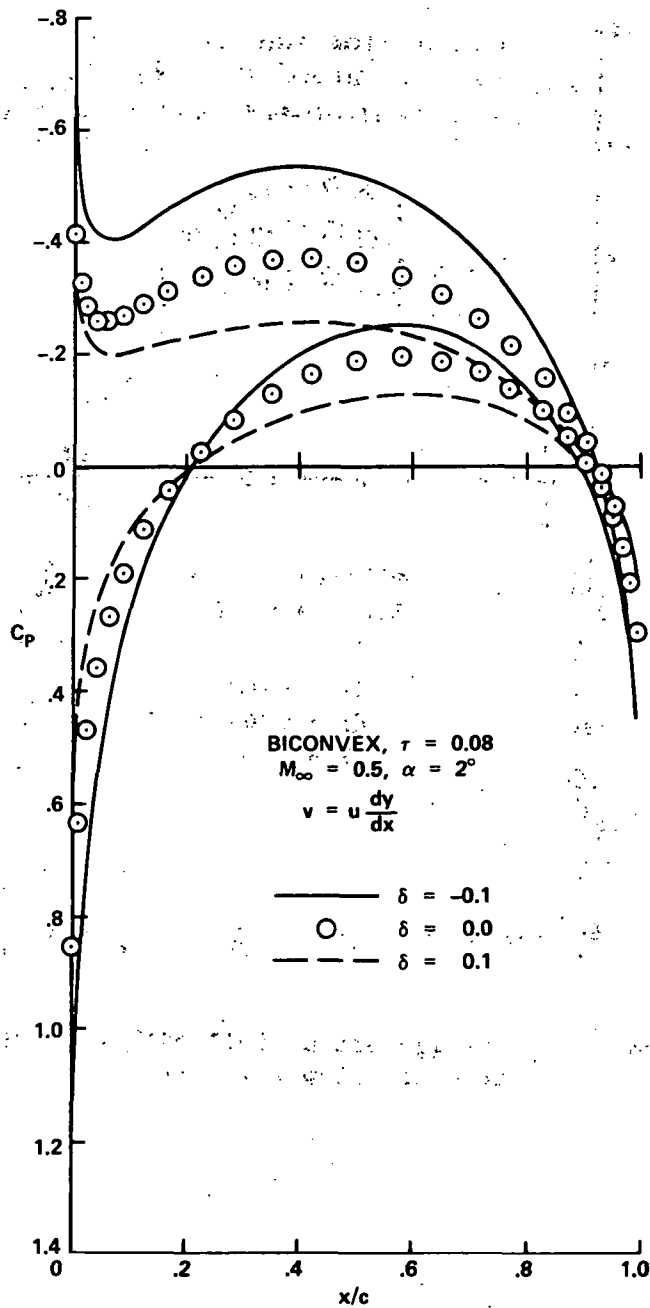


Figure 10.- Parabolic arc airfoil in moderate incoming shear flow.

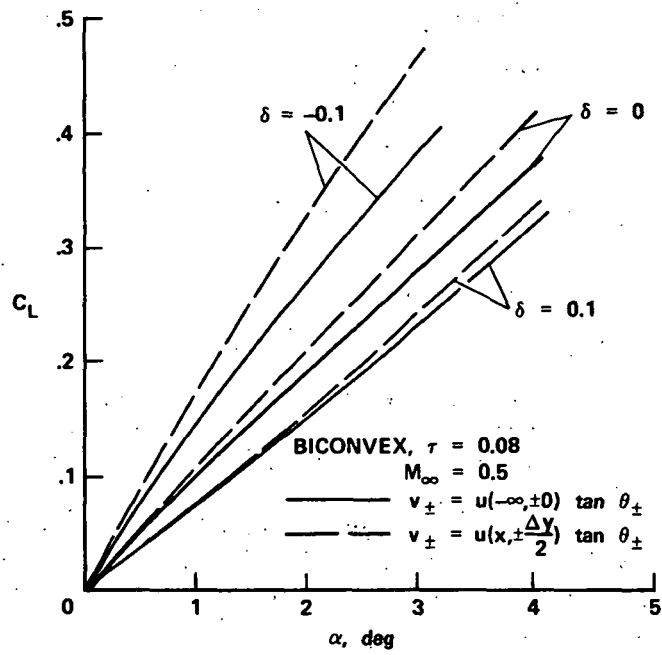


Figure 11.- C_L versus α for moderate incoming shear flow.

PROGRESS IN APPLICATION OF DIRECT ELLIPTIC SOLVERS
TO TRANSONIC FLOW COMPUTATIONS

By E. Dale Martin

NASA Ames Research Center

SUMMARY

Recent progress is described in the continuing development and extension of a semi-direct iterative computational method for the rapid finite-difference solution of transonic flow over airfoils. Additions and modifications to an earlier formulation are shown to produce stability, and therefore iterative convergence, of the iteration procedure based on use of an extended direct elliptic solver for strongly supercritical flows, governed by mixed elliptic-hyperbolic equations. An improved version of an extrapolation technique introduced earlier is also described.

Preliminary results computed by the semi-direct method for pressure distributions on a biconvex airfoil agree with solutions computed using the improved Murman-Cole line relaxation method. The preliminary time per iteration for a 39×32 mesh on a Control Data 7600 computer is 0.040 sec, and a strong transonic case required 23 iterations, or 0.92 sec. These results, which are expected to be improved, indicate a significant potential for highly efficient transonic flow computations.

INTRODUCTION

The continuing development of advanced computers is complemented by the continuing development of advanced efficient computational techniques, which multiply the power of the computers. Regardless of the computing power and efficiency inherent in any computer, its ultimate potential in obtaining solutions to complex problems can be realized only with use of the most efficient computational methods.

The purpose of this paper is to describe recent progress in the continuing development and extension of an iterative computational method for the rapid finite-difference solution of transonic flow over airfoils. In the first phase of this investigation, reference 1 introduced the basic iterative computational method based on the use of a *direct elliptic solver*. That semi-direct iterative method did not converge for flows at more than slightly supercritical conditions, so it was restricted to subsonic and slightly supercritical flow. The present paper (a) shows that some additions and modifications provide more general stability of the iteration to allow convergence at higher Mach numbers, (b) very briefly describes a research computer program that is being used for numerical experiments to determine optimal values of

some free parameters for most rapid convergence, and (c) presents some preliminary results computed for strongly supercritical flows.

The investigation is limited to two-dimensional, steady, inviscid, irrotational flow over simple thin symmetrical airfoil shapes in a uniform subsonic free stream. The transonic small-disturbance equations, which are written in terms of u, v velocity components, are assumed to apply.

The basic idea in the method of reference 1 is to use a fast, direct, linear elliptic solver to determine the solution at all points in the entire computation field simultaneously at each iteration in the treatment of the nonlinear finite-difference equations governing the flow. As a result, changes are felt immediately at all points in each succeeding iteration, so rapid convergence is possible. The direct solver used in reference 1 was a "Cauchy-Riemann solver" (ref. 2), based on Buneman's (ref. 3) recursive cyclic reduction, for the equations in terms of the velocity components. The finite-difference equations that are solved in this approach are equivalent, in the "converged form," to those of Murman and Cole (ref. 4) with inclusion of the "parabolic-point operator" (ref. 5) and the "shock-point operator" (ref. 6). Therefore, even though an elliptic operator is solved at each iteration, the appropriate type-dependent differencing (e.g., upstream differencing for hyperbolic points) is used where needed. At convergence, the elliptic character of the left side of the equations is cancelled out at nonelliptic points by appropriate terms on the right side. An additional feature of the method of reference 1 is an effective new approach to applying the Aitken/Shanks formula (refs. 7 and 8) for accelerating the convergence of the iteration.

The developments in this paper show that the addition of certain terms to the finite-difference equations makes the iterations "time-like." Simplified stability considerations then indicate that certain ranges of free parameters multiplying the extra terms should provide stability, and therefore iterative convergence, for transonic flows including large supersonic regions. To handle the inclusion of the additional terms, the Cauchy-Riemann solver of reference 2 has been extended (ref. 9), and the more general form is used for all present computations. Additional free parameters are introduced by "shifting and scaling" of terms in the equations and by inclusion of a relaxation factor. A more precise method of applying the Aitken/Shanks formula is also introduced.

The main significance of the results that are presented lies in the fact that a direct elliptic solver is used successfully to obtain converged solutions to strongly supercritical flows, governed by equations of mixed type with significantly large embedded regions in which the equations are hyperbolic, and containing relatively strong shock waves. Although semi-direct methods have been used previously (e.g., refs. 10-12), reference 1 contained the first such computation of a slightly supercritical flow, and now the present results extend the semi-direct method to strongly supercritical flows.

The present results are considered to be only preliminary. A systematic parametric study is in progress to determine the optimal values of all free parameters for most rapid convergence, and the method is continually being improved.

EQUATIONS AND BOUNDARY CONDITIONS

For present purposes consider only a symmetrical thin airfoil, with the Cartesian x - and y -axes respectively parallel and normal to the airfoil chord. Both x and y are normalized by the chord length c , and the y -axis bisects the chord. Let U and V be the x - and y -components of velocity normalized by the free-stream velocity q_∞ , and let M_∞ be the free-stream Mach number and γ be the ratio of specific heats. Then with the small perturbation velocities u and v defined by

$$U = 1 + \tau u, \quad V = \tau v \quad (1)$$

where τ is the small thickness ratio of the airfoil, the transonic small-disturbance equations are

$$u_x + v_y = bu_x + a(u^2)_x \quad (2a)$$

$$u_y - v_x = 0 \quad (2b)$$

where

$$a = (1/2)(\gamma + 1)\tau f(M_\infty); \quad b = M_\infty^2 \quad (3)$$

and where

$$f(M_\infty) = O(1) \quad \text{as } M_\infty \rightarrow 1.$$

In what may be considered to be the classical formulation, $f(M_\infty) = f_S \equiv M_\infty^2$. A study by Spreiter (ref. 13) recommended this form. More recently, Murman and Krupp (ref. 5; see also ref. 14) found that $f(M_\infty) = f_{MK1} \equiv M_\infty^{3/2}$ gives equally good results under Spreiter's criteria and also gives results that compare well with numerical solutions to the full inviscid equations. Similarity parameters incorporating these respective choices are

$$K_S = \frac{1 - M_\infty^2}{[(\gamma + 1)M_\infty^2 \tau]^{2/3}}, \quad K_{MK1} = \frac{1 - M_\infty^2}{M_\infty \tau^{2/3}} \quad (4)$$

(In later work, e.g., refs. 15 and 6, Krupp and Murman use $f = f_{MK2} \equiv M_\infty^{7/4}$ and the same similarity parameter K_{MK1} .) Since the purpose here is to describe a method for solving equations (2), these differences are not discussed further. In later discussion of results, an arbitrary choice is made for $f(M_\infty)$ as f_S . Table 1 shows values of K_S for which computations are later performed. The computed scaled solutions will be the same for a corresponding K_{MK1} numerically equal to $(\gamma + 1)^{2/3} K_S$, also shown in table 1, but these correspond to slightly different M_∞ and τ .

For the thin-airfoil problem, the outer boundary conditions are

$$u, v \rightarrow 0 \text{ as } x^2 + y^2 \rightarrow \infty \quad (5)$$

and for a symmetrical thin airfoil specified as

$$y_b(x) = \pm \tau Y(x) \quad (-.5 \leq x \leq .5) \quad (6)$$

the condition at $y = 0$ for an airfoil at zero incidence is

$$\left. \begin{aligned} v(x, \pm 0) &= \pm dY(x)/dx & (-.5 < x < .5) \\ &= 0 & (|x| > .5) \end{aligned} \right\} \quad (7)$$

For a parabolic-arc biconvex airfoil,

$$Y(x) = .5 - 2x^2 \quad (-.5 \leq x \leq .5) \quad (8)$$

The pressure coefficient in the small-disturbance theory is $C_p = -2\tau u$.

A number of free parameters are introduced by more general scaling and shifting transformations than were used in reference 1. It is convenient to also include a relaxation parameter v_1 in the transformations. It will be seen in a later section that both "Method 1" and "Method 2" can then employ the relaxation parameter, whereas in reference 1, Method 2 did not include the relaxation parameter.

The transformations are derived as follows. In a straightforward iteration procedure for equations (2) with a relaxation parameter v_1 , the solution for u at iteration n could be written

$$u_n = (1 - v_1)u_{n-1} + v_1 u_n^* \quad (9)$$

where u_n^* is the solution to

$$(u_n^*)_x + (v_n)_y = b(u_{n-1})_x + a(u_{n-1}^2)_x \quad (10a)$$

$$(u_n^*)_y - (v_n)_x = 0 \quad (10b)$$

If now u_n^* is obtained in terms of u_n and u_{n-1} from equation (9) and put into equations (10) and if the following defined first step of the transformation is used

$$\tilde{u}(x, y) = (1/v_1)u(x, y) \quad (11)$$

one obtains the following equations to solve for \tilde{u}_n when \tilde{u}_{n-1} is known at all x, y :

$$(\tilde{u}_n)_x + (v_n)_y = (1 - v_1 + v_1 b)(\tilde{u}_{n-1})_x + av_1^2(\tilde{u}_{n-1}^2)_x \quad (12a)$$

$$(\tilde{u}_n)_y - (v_n)_x = (1 - v_1)(\tilde{u}_{n-1})_y \quad (12b)$$

One can see from these equations (if eq. (11) were put back into eq. (12)) that use of a relaxation factor $v_1 \neq 1$ is equivalent to a *shifting* from one side to the other of a certain portion of the u_x term in equation (10a) and a certain portion of the u_y term in equation (10b). Noting that at convergence $\tilde{u}_{n-1} = \tilde{u}_n$, one can take as the equations to be solved (by either method to be described in a later section):

$$\tilde{u}_x + v_y = (1 - v_1 + v_1 b)\tilde{u}_x + av_1^2(\tilde{u}^2)_x \quad (13a)$$

$$\tilde{u}_y - v_x = (1 - v_1)\tilde{u}_y \quad (13b)$$

Of course, equations (13) and (11) reduce directly to equations (2), but the forms of equations (12) and (13) will be useful in several ways. First, one may introduce an arbitrary parameter b' to provide an *arbitrary* shifting and corresponding appropriate scaling. Rewrite equations (13) as

$$v_1(1 - b + b')\tilde{u}_x + v_y = v_1 b' \tilde{u}_x + av_1^2(\tilde{u}^2)_x \quad (14a)$$

$$\tilde{u}_y - v_x = (1 - v_1)\tilde{u}_y \quad (14b)$$

Then with the definitions:

$$\left. \begin{aligned} \bar{a} &= \frac{av_1^{1/2}}{(1 - b + b')^{3/2}}, & \bar{b} &= \frac{b'}{1 - b + b'} \\ \beta &= (1 - b)^{1/2} = (1 - M_\infty^2)^{1/2} \\ \beta^* &= (1 - \bar{b})^{1/2} \\ \bar{\beta} &= (1 - b + b')^{1/2} = \beta/\beta^* \end{aligned} \right\} \quad (15)$$

the transformation

$$\bar{u}(x, \bar{y}) = v_1^{1/2} \bar{\beta} \tilde{u}(x, y) = v_1^{-1/2} \bar{\beta} u(x, y) \quad (16a)$$

$$\bar{v}(x, \bar{y}) = v(x, y) \quad (16b)$$

$$\bar{y} = v_1^{1/2} \bar{\beta} y \quad (16c)$$

produces from equations (14a) and (14b)

$$\bar{u}_x + \bar{v}_y = \bar{b}\bar{u}_x + \bar{a}(\bar{u}^2)_x \quad (17a)$$

$$\bar{u}_y - \bar{v}_x = (1 - \nu_1)\bar{u}_y \quad (17b)$$

One may note at this point that equations (14) (put in terms of u with eq. (11)) could have been obtained directly from equations (2) by a simple shifting in both equations (2a) and (2b) without going through equations (9) to (13); but the *motivation* for the $(1 - \nu_1)$ on the right side of equation (14b) is provided by this procedure, and the resulting equations (17) are a combination of arbitrary shifting in equation (17a), use of an arbitrary relaxation factor ν_1 , and appropriate scaling.

Special cases of equations (17) are:

- (a) $\nu_1 = 1$ and $b' = \bar{b} = b = M_\infty^2$: Equations (17) are then the same as equations (2), without transformation, and $\bar{a} = a$;
- (b) $\nu_1 = 1$ and $b' = \bar{b} = 0$: Equations (15) and (16) then give the Prandtl-Glauert transformation, and equations (17) are the P-G scaled equations used in reference 1. In this case

$$\bar{a} = a/\beta^3 = \left(\frac{\gamma + 1}{2}\right) \frac{\tau f(M_\infty)}{(1 - M_\infty^2)^{3/2}} \equiv \bar{a}_1 \quad (18)$$

where

$$\bar{a}_1 = \frac{1}{2} K_S^{-3/2} \quad \text{if } f(M_\infty) = f_S = M_\infty^2 \quad (19a)$$

$$= \frac{1}{2} (\gamma + 1) K_{MK1}^{-3/2} \quad \text{if } f(M_\infty) = f_{MK1} = M_\infty^{3/2} \quad (19b)$$

(See eqs. (4).)

To complete the biconvex-airfoil problem governed by equations (17), the corresponding boundary conditions are given by equations (5) and (7). For the computations, the infinity conditions (eq. (5)) can be replaced by corresponding approximate far-field conditions applied on a boundary at some distance from the airfoil, for example, on a rectangular boundary denoted by B. Either \bar{u} or \bar{v} may be specified on portions of B. On the left and upper sides of B, $\bar{u} = \bar{u}_B(x, \bar{y}) = \nu_1^{-1/2} \bar{b}u_B(x, y)$. On the right side of B, $\bar{v} = \bar{v}_B(x, \bar{y}) = \nu_B(x, y)$. For example, u_B and ν_B may be the analytical Prandtl-Glauert solution (ref. 1). On $y = 0$:

$$\bar{v}(x, 0^+) = -4x \quad (-.5 < x < .5)$$

$$= 0 \quad (|x| > .5)$$

The transformed critical velocity in equations (17) is obtained by writing those equations as

$$(1 - \bar{b} - 2\bar{a}\bar{u})\bar{u}_x + \bar{v}_y = 0 \quad (20a)$$

$$v_1\bar{u}_y - \bar{v}_x = 0 \quad (20b)$$

and by noting that for positive v_1 this system is elliptic if $\bar{u} < \bar{u}_{CR}$, parabolic if $\bar{u} = \bar{u}_{CR}$, and hyperbolic if $\bar{u} > \bar{u}_{CR}$, where

$$\bar{u}_{CR} = (1 - \bar{b})/2\bar{a} = v_1^{-1/2} \bar{b}u_{CR} ; \quad u_{CR} = (1 - b)/2a \quad (21)$$

SEMI-DIRECT METHOD WITH STABILIZING TERMS

This section describes the semi-direct finite-difference method as developed in reference 1, but applied to equations obtained from the transformed equations (17) incorporating the free parameters \bar{b} and v_1 and with added stabilizing terms containing free parameters. In addition: (a) simplified stability considerations are outlined, which indicate the time-like character of the iterations as well as indicating a stable iteration process; (b) the use of multiple relaxation factors is described; and (c) a modified version is described for "Method 2," the new approach developed in reference 1 for applying the Aitken/Shanks acceleration formula.

For all developments that follow, the "bars" on the variables and parameters in equations (17) are omitted, with the understanding that u represents \bar{u} , etc. The terms to be added to both sides of equation (17a) are denoted as a^+u^+ and a^-u^- , where a^+ and a^- are free parameters and

$$u^+ = u(x + \frac{1}{2} \Delta x, y), \quad u^- = u(x - \frac{1}{2} \Delta x, y) \quad (22)$$

with Δx being the uniform mesh interval in the x-direction. The reason for specifying these terms at half intervals from point x, y will be evident when the difference equations to be satisfied at x, y are written. With these terms, equations (17) are

$$u_x + v_y + a^-u^- + a^+u^+ = a^-u^- + a^+u^+ + bu_x + a(u^2)_x \quad (23a)$$

$$u_y - v_x = (1 - v_1)u_y \quad (23b)$$

with conditions

$$v(x, 0^+) = -4x \quad (-.5 < x < .5) \quad (24a)$$

$$= 0 \quad (|x| > .5) \quad (24b)$$

and on B:

$$u = u_B \quad \text{or} \quad v = v_B \quad (24c)$$

The Differencing Mesh, Finite Differences, and Converged Forms of the Difference Equations

The equations in terms of u and v (eqs. (23)) are to be written in finite-difference form and solved by using an extension of the direct Cauchy-Riemann solver that treats the left side of equations (23) (ref. 9) when the right side is known. A staggered u, v mesh is used, a portion of which is shown in figure 1. The indices j and k respectively denote the x - and y -directions. The dots and the point labeled $s_{j,k}$ on figure 1 are the points where the continuity equation (23a) is to be satisfied; the crosses and the point labeled $\omega_{j,k}$ are the points where the vorticity equation (23b) is to be satisfied. Here $u_{j,k}$ and $v_{j,k}$ are to be evaluated at the points indicated. Thus, for x, y at the point labeled $s_{j,k}$ on figure 1, u^+ and u^- (eqs. (22)) are respectively $u_{j,k}$ and $u_{j-1,k}$, and *central differences* for u_x , $(u^2)_x$, and v_y are

$$u_{xc} = (u_{j,k} - u_{j-1,k})/\Delta x \quad (25a)$$

$$(u^2)_{xc} = (u_{j,k}^2 - u_{j-1,k}^2)/\Delta x \quad (25b)$$

$$v_{yc} = (v_{j,k} - v_{j,k-1})/\Delta y \quad (25c)$$

which are second-order accurate at the point $s_{j,k}$. Also needed will be upstream, or *backward differences* for u_x and $(u^2)_x$:

$$u_{xb} = (u_{j-1,k} - u_{j-2,k})/\Delta x \quad (26a)$$

$$(u^2)_{xb} = (u_{j-1,k}^2 - u_{j-2,k}^2)/\Delta x \quad (26b)$$

which are first-order accurate at the point $s_{j,k}$. For the point labeled $\omega_{j,k}$ on figure 1, where equation (23b) is to be satisfied, the second-order accurate *central differences* are

$$u_{yc} = (u_{j,k+1} - u_{j,k})/\Delta y \quad (27a)$$

$$v_{xc} = (v_{j+1,k} - v_{j,k})/\Delta x \quad (27b)$$

Without type-dependent differencing, the iterative solution of equations (23) would be done by putting subscript n on the left side, subscript $n-1$ on the right side, and by representing all the derivatives by finite differences such as equations (25) and (27) and solving the resulting difference equations iteratively. However, in this iterative method for the problem with both elliptic and hyperbolic regions (the latter requiring upstream differences), it is desired to solve, *at convergence*, finite-difference equations that are equivalent to those solved by Murman (ref. 6), with the four type-dependent operators (elliptic, hyperbolic, parabolic, and shock), although Murman's equations are in terms of a perturbation velocity potential and this method is in terms of u and v . Thus we may first write, for each type point, what we call the appropriate *converged forms* of the difference equations as follows:

Nothing about equation (20b) or (23b) changes when the system changes type, so equation (23b) is central differenced at all $\omega_{j,k}$ points (crosses on fig. 1), and the converged form for equation (23b) is

$$u_{yc} - v_{xc} = (1 - v_1)u_{yc} \quad (28)$$

However, equation (20a) or (23a) changes the character of the system according to the sign of $u - u_{CR}$, so the points $s_{j,k}$ (dots on fig. 1), where equation (23a) is to be solved, are distinguished as "elliptic, hyperbolic, parabolic, or shock points" (E,H,P,S) following Murman (ref. 6). For an E point, all central differences are used in equation (23a), and the converged form is

$$E: \quad u_{xc} + v_{yc} = bu_{xc} + a(u^2)_{xc} \quad (29a)$$

If equations (25) to (27) are substituted into equations (28) and (29a), one finds that the difference equations are an appropriate elliptic system if

$$(u_e)_{j,k} \equiv \frac{1}{2} (u_{j,k} + u_{j-1,k}) < u_{CR} \quad (30a)$$

For an H point, all x-derivatives in equation (23a) are backward differenced, and the converged form is

$$H: \quad u_{xb} + v_{yc} = bu_{xb} + a(u^2)_{xb} \quad (29b)$$

If equations (25) to (27) are substituted into equations (28) and (29b) one finds that the difference equations are an appropriate hyperbolic system if

$$(u_h)_{j,k} \equiv \frac{1}{2} (u_{j-1,k} + u_{j-2,k}) > u_{CR} \quad (30b)$$

where we note that

$$(u_h)_{j,k} = (u_e)_{j-1,k} \quad (31)$$

Therefore, an E point has at least the one condition (eq. (30a)), and an H point has at least the one condition (eq. (30b)). However at a point (labeled $s_{j,k}$ on fig. 1) near the sonic point where the flow is accelerating from subsonic to supersonic, neither equation (30a) nor (30b) is satisfied (because of eq. (31)) since $(u_h)_{j,k} < u_{CR} < (u_e)_{j,k}$. This is a P point (refs. 5 and 6), and equation (23a) is represented by the converged form

$$P: \quad v_{yc} = 0 \quad (29c)$$

At a point $s_{j,k}$ near the shock wave, where the flow is decelerating rapidly from supersonic to subsonic, both equations (30a) and (30b) are satisfied. Murman (ref. 6) has found that a shock-point operator is then needed to maintain a fully conservative computation, and equation (23a) is replaced by

$$S: \quad (u_{xc} + u_{xb}) + v_{yc} = b(u_{xc} + u_{xb}) + a[(u^2)_{xc} + (u^2)_{xb}] \quad (29d)$$

The test conditions determining the type of point are therefore:

$$\left. \begin{array}{l} E: \quad (u_h)_{j,k} < u_{CR} \quad \text{and} \quad (u_e)_{j,k} < u_{CR} \\ H: \quad (u_h)_{j,k} > u_{CR} \quad \text{and} \quad (u_e)_{j,k} > u_{CR} \\ P: \quad (u_h)_{j,k} < u_{CR} < (u_e)_{j,k} \\ S: \quad (u_h)_{j,k} > u_{CR} > (u_e)_{j,k} \end{array} \right\} \quad (32)$$

and, since the extension of the Cauchy-Riemann solver from reference 9 that solves the left side of equations (23) always solves the *central differenced* form, the converged forms of the finite-difference equations (eqs. (29a,b,c,d) with eq. (28)) are written equivalently as

$$u_{xc} + v_{yc} + a^- u^- + a^+ u^+ = s_{j,k} \{u\} \quad (33a)$$

$$u_{yc} - v_{xc} = (1 - v_1) u_{yc} \quad (33b)$$

where

$$E: \quad s_{j,k} \{u\} = a^- u^- + a^+ u^+ + b u_{xc} + a(u^2)_{xc} \quad (34a)$$

$$H: \quad s_{j,k} \{u\} = a^- u^- + a^+ u^+ + u_{xc} + (b - 1) u_{xb} + a(u^2)_{xb} \quad (34b)$$

$$P: \quad s_{j,k} \{u\} = a^- u^- + a^+ u^+ + u_{xc} \quad (34c)$$

$$S: \quad s_{j,k}\{u\} = a^-u^- + a^+u^+ + bu_{xc} + (b-1)u_{xb} + a\left[(u^2)_{xc} + (u^2)_{xb}\right] \quad (34d)$$

Preconverged Forms of the Equations in Method 1

Consider now the solution of the difference equations (33) with equations (34) by the straightforward semi-direct iterative Method 1, as described in reference 1. Although a relaxation parameter v_1 is already incorporated into the equations through the transformation equations (16) leading to equations (17), and thus to equations (23) and (33), that built-in parameter is necessarily constant at all points and at each iteration n . It is desirable to have this parameter built in when switching to Method 2, to be described later. However, during the treatment by Method 1, it is also desirable to be able to vary the relaxation parameter depending on the sign of $u - u_{CR}$, on the iteration n , or on considerations such as the extent to which the solution is converged. Therefore, an additional relaxation parameter v_2 is introduced by

$$u_n = (1 - v_2)u_{n-1} + v_2u_n^* \quad (35)$$

where v_2 may vary with j, k and with n . Here u_n^* is the solution to

$$(u_n^*)_{xc} + (v_n)_{yc} + a^-(u_n^*)^- + a^+(u_n^*)^+ = s_{j,k}\{u_{n-1}\} \quad (36a)$$

$$(u_n^*)_{yc} - v_{xc} = (1 - v_1)(u_{n-1})_{yc} \quad (36b)$$

where the $s_{j,k}\{u_{n-1}\}$ are obtained from equations (34) at each point. By this scheme "multiple relaxation parameters" are used. The terminology "multiple" is used because it can be shown that such successive use of relaxation parameters (if done without shifting or scaling) amounts to using the product v_1v_2 as a single relaxation parameter.

For later convenience, the difference equations (36) are written, letting

$$\alpha_1 = -a^+\Delta x, \quad \alpha_2 = -a^-\Delta x, \quad \mu = \Delta y/\Delta x \quad (37)$$

as

$$(1 - \alpha_1)(u_{j,k}^*)_n - (1 + \alpha_2)(u_{j-1,k}^*)_n + (1/\mu)(v_{j,k} - v_{j,k-1})_n = \Delta x s_{j,k}\{u_{n-1}\} \quad (38a)$$

and

$$-(u_{j,k}^*)_n + (u_{j,k+1}^*)_n + \mu(v_{j,k} - v_{j+1,k})_n = (1 - v_1)(u_{j,k+1} - u_{j,k})_{n-1} \quad (38b)$$

where

$$E: \quad \Delta x s_{j,k}\{u\} = (b - \alpha_1)u_{j,k} - (b + \alpha_2)u_{j-1,k} + a(u_{j,k}^2 - u_{j-1,k}^2) \quad (39a)$$

$$H: \quad \Delta x s_{j,k}\{u\} = (1 - \alpha_1)u_{j,k} - (1 + \alpha_2)u_{j-1,k} + (b - 1)(u_{j-1,k} - u_{j-2,k}) \\ + a(u_{j-1,k}^2 - u_{j-2,k}^2) \quad (39b)$$

$$P: \quad \Delta x s_{j,k}\{u\} = (1 - \alpha_1)u_{j,k} - (1 + \alpha_2)u_{j-1,k} \quad (39c)$$

$$S: \quad \Delta x s_{j,k}\{u\} = (b - \alpha_1)u_{j,k} - (b + \alpha_2)u_{j-1,k} + (b - 1)(u_{j-1,k} - u_{j-2,k}) \\ + a(u_{j,k}^2 - u_{j-2,k}^2) \quad (39d)$$

The extended Cauchy-Riemann solver (ref. 9) can be applied at each iteration n to solve equations (38) with equations (39), and then equation (35) is used to find $(u_{j,k})_n$. The boundary conditions applied at each n are:

$$\left. \begin{aligned} \text{on } x = x_l \text{ and } y = y_u : (u_{j,k}^*)_n &= u_B(x,y) \\ \text{on } x = x_r : (v_{j,k})_n &= v_B(x,y) \\ \text{on } y = 0 : (v_{j,k})_n &= -4x \quad (-.5 < x < .5) \\ &= 0 \quad (|x| > .5) \end{aligned} \right\} \quad (40)$$

At $n = 1$, the right side of equations (38) requires specification of u_0 at each j,k , which may be taken to be, for example, either the Prandtl-Glauert solution or a numerical solution obtained previously.

Time-Like Character and Simplified Stability Considerations

In this subsection a simplified heuristic stability analysis is considered in order to estimate the conditions for convergence of the iteration of equations (35), (38), and (39) for each type of point. Assume for this discussion that $v_1 = v_2 = 1$ in those equations so that each u^* is replaced by u in equations (38) and the right side of equation (38b) is zero. This simplified analysis is not considered to be rigorous, so the results are to be used only as a guide in estimating the free parameters. From experience, this type of analysis is known to give generally conservative estimates of stability bounds.

The existence of the extra terms in both sides of equation (36a) in the iteration scheme of Method 1 makes the iterations time-like. If t is an

artificial time, these terms contribute to terms involving u_t , u_{tt} , u_{xt} , etc. (See related discussion by Garabedian, ref. 16, and by Lomax and Steger, ref. 17.) For the following discussion, *define* the artificial time t , its increment Δt , a parameter λ determining the artificial time scale relative to the mesh interval Δx , and a related parameter α by

$$t = n\Delta t, \quad \Delta t = \lambda\Delta x, \quad \alpha = (\alpha_1 + \alpha_2)\lambda \quad (41)$$

A simplification is introduced by also using the transformation

$$\left. \begin{aligned} \tilde{u} &= 2au + b - 1 = 2a(u - u_{CR}) = (1 - b)(u/u_{CR} - 1) \\ \tilde{v} &= 2av \end{aligned} \right\} \quad (42)$$

To discuss the time-like character and the stability, we consider the "modified equation" approach (refs. 18 and 19). In that approach, a system of (modified) partial differential equations is found that represents the actual equation system that is being solved by the particular finite-difference scheme being used and thus includes all truncation errors as terms involving higher derivatives. For a linear equation with one dependent variable, one can always eliminate all higher order time derivatives to obtain what Warming and Hyett (ref. 19) refer to as the modified equation, which then contains terms involving higher derivatives only in the space variables. These terms can be interpreted explicitly in terms of dissipation and dispersion and relate to accuracy, consistency, and stability. If care is taken, one need not eliminate time derivatives in order to determine the latter qualities. One first substitutes a Taylor series for each term in the finite-difference equations, expanded about the point where the equation is being solved (e.g., the point labeled $s_{j,k}$, or the dots, on fig. 1, where eq. (38a) applies). One may refer to the resulting equation, which contains both time and space derivatives, as an "intermediate modified equation." One may eliminate some time derivatives to obtain another intermediate form (e.g., corresponding to the sum of the first few rows in Warming and Hyett's table 1). The first equation obtained after substituting Taylor series for all terms may be called the "first intermediate form" of the modified equation, and the form with all time derivatives eliminated, up to the order desired, (Warming and Hyett's modified equation) as the "final form." If done properly, *all* intermediate forms yield the same or equivalent results for the stability investigation.

For an E point, the result of expanding the terms of equations (38) with equation (39a) in Taylor series in x , y , and t for small Δx , Δy , and Δt and using the transformation equation (42) is

$$\alpha\tilde{u}_t + \tilde{u}\tilde{u}_x - \tilde{v}_y + \frac{\Delta t}{2} \left[-\alpha\tilde{u}_{tt} + (\alpha_1 - \alpha_2 - 2)\tilde{u}_{tx} - 2(\tilde{u}\tilde{u}_x)_t \right] = 0(\Delta x^2, \Delta t^2) \quad (43a)$$

$$\tilde{u}_y - \tilde{v}_x = 0(\Delta x^2) \quad (43b)$$

This is the first intermediate form of the nonlinear modified equations representing equations (38) with equation (39a). As Δt and Δx approach zero, equations (43) are consistent with equations (20) (with the transformation equation (42) and $v_1 = 1$) except for the artificial time-derivative term $\alpha \tilde{u}_t$ resulting from insertion of the extra terms in equations (23). This exhibits the time-like character of the iteration method if $\alpha \neq 0$. When all time derivatives vanish (i.e., as the iterated solution converges), the accuracy is seen to be second order. Before considering the stability of the iteration at an E point, note that one can eliminate the \tilde{u}_{tt} term from equation (43a) by differentiating that equation with respect to t , multiplying the result through by $\Delta t/2$, and adding to equation (43a). The result is

$$\alpha \tilde{u}_t + \tilde{u} \tilde{u}_x - \tilde{v}_y + \frac{\Delta t}{2} \left[(\alpha_1 - \alpha_2 - 2) \tilde{u}_{xt} - (\tilde{u} \tilde{u}_x)_t - \tilde{v}_{yt} \right] = 0(\Delta x^2, \Delta t^2) \quad (44)$$

which is a second intermediate form of the modified equation. For the stability analysis, either equation (43) or (44) could be used. Consider equation (44) with equation (43b). First locally linearize equation (44), with \tilde{u}_ℓ representing a constant local value, to obtain

$$\alpha \tilde{u}_t + \tilde{u}_\ell \tilde{u}_x - \tilde{v}_y + \frac{\Delta t}{2} \left[(\alpha_1 - \alpha_2 - 2 - \tilde{u}_\ell) \tilde{u}_{xt} - \tilde{v}_{yt} \right] = 0(\Delta x^2, \Delta t^2) \quad (45)$$

Equation (43b) is satisfied to second order by the assumed locally periodic solution

$$\tilde{u} = im_1 e^{(c_1 + ic_2)t} e^{im_1 x} e^{im_2 y} \quad (46a)$$

$$\tilde{v} = im_2 e^{(c_1 + ic_2)t} e^{im_1 x} e^{im_2 y} \quad (46b)$$

where m_1 and m_2 are local "wave numbers" and $i = \sqrt{-1}$. A *negative* value for c_1 would indicate a stable iteration. To determine the condition on c_1 , substitute equations (46) into equation (45) and separate the result into real and imaginary parts:

$$\alpha c_1 m_1 = \frac{\Delta t c}{2} \left[m_1^2 (\alpha_1 - \alpha_2 - 2 - \tilde{u}_\ell) - m_2^2 \right] + 0(\Delta t^2, \Delta x^2) \quad (47a)$$

$$-\alpha c_2 m_1 - \tilde{u}_\ell m_1^2 + m_2^2 = \frac{\Delta t c}{2} \left[m_1^2 (\alpha_1 - \alpha_2 - 2 - \tilde{u}_\ell) - m_2^2 \right] + 0(\Delta t^2, \Delta x^2) \quad (47b)$$

From equation (47a), assuming m_1 and m_2 to be $O(1)$ as Δt and $\Delta x \rightarrow 0$, we see that $c_1 = O(\Delta t)$; therefore, to first order; equation (47b) gives

$$c_2 = \frac{m_1}{\alpha} \left[\left(\frac{m_2}{m_1} \right)^2 - \tilde{u}_\ell \right] \quad (48a)$$

and then equation (47a) gives

$$c_1 = \frac{m_1^2 \Delta t}{2\alpha^2} \left[\left(\frac{m_2}{m_1} \right)^2 - \tilde{u}_\ell \right] \left[\alpha_1 - \alpha_2 - 2 - \tilde{u}_\ell - \left(\frac{m_2}{m_1} \right)^2 \right] \quad (48b)$$

(Identical results to first order are obtained from eq. (43a).) The first factor in equation (48b) is always positive. Recalling the transformation equation (42), we note that \tilde{u}_ℓ is always negative in subsonic regions (E points), so the second factor is also positive. Therefore the condition for stability requires, from the third factor in equation (48b) with use of equation (42),

$$\alpha_2 > \alpha_1 - 2 - R + (1 - b)(1 - u_\ell/u_{CR}) \quad (49)$$

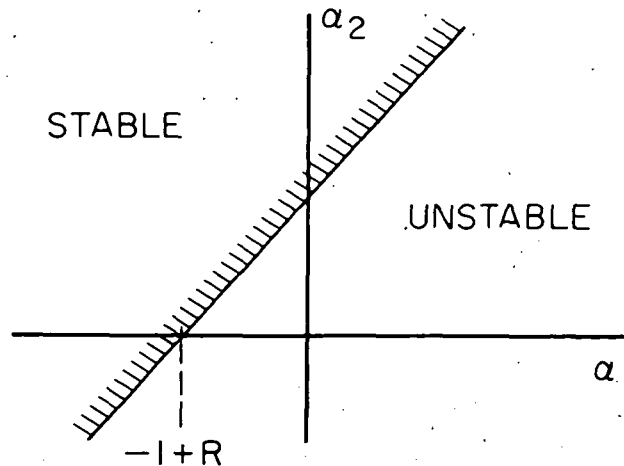
where

$$R \equiv (m_2/m_1)^2 \quad (50)$$

and where it is recalled that "bars" have been omitted from b , u_ℓ , and u_{CR} . Since the arbitrary b must be < 1 and the minimum value of u_ℓ is negative in the elliptic region (at the leading or trailing edge), that minimum value is the crucial value for condition (49). If $(u_\ell)_{\min} \approx -2u_{CR}$ and if b is taken to be zero, then condition (49) becomes

$$\alpha_2 > \alpha_1 + 1 - R \quad (51)$$

Sketch (a) illustrates this roughly determined stability condition for an E



Sketch (a) - Stability diagram for an E point.

point. If R is very large, condition (51) is not crucial, but when R is very small, the condition is the most crucial, i.e.,

$$\alpha_2 > \alpha_1 + 1 \quad (52)$$

A similar procedure can be used for H, P, and S points. For an H point, expansion of the terms of equation (38a) with equation (39b) in Taylor series leads to the first intermediate modified equation,

$$\alpha \tilde{u}_t + \tilde{u} \tilde{u}_x - \tilde{v}_y + \frac{\Delta t}{2} \left[-\alpha \tilde{u}_{tt} + (\alpha_1 - \alpha_2 - 2) \tilde{u}_{tx} - 2(\tilde{u} \tilde{u}_x)_t \right] - \Delta x (\tilde{u} \tilde{u}_x)_x = 0(\Delta t^2, \Delta x^2) \quad (53)$$

along with equation (43b). At convergence, when all time derivatives vanish, equation (53) with equation (43b) is first-order accurate and, with the $0(\Delta x)$ term locally linearized, is equivalent (ref. 14) to the viscous-transonic equation derived by Sichel (ref. 20; see also ref. 21 for the u, v form). The second intermediate form of the modified equation is the same as equation (44) but with the $0(\Delta x)$ term from equation (53) added. Local linearization, as in the case of the E point, and substitution of equations (46) leads, to first order, to

$$c_2 = \frac{m_1}{\alpha} (R - \tilde{u}_\ell) \quad (54a)$$

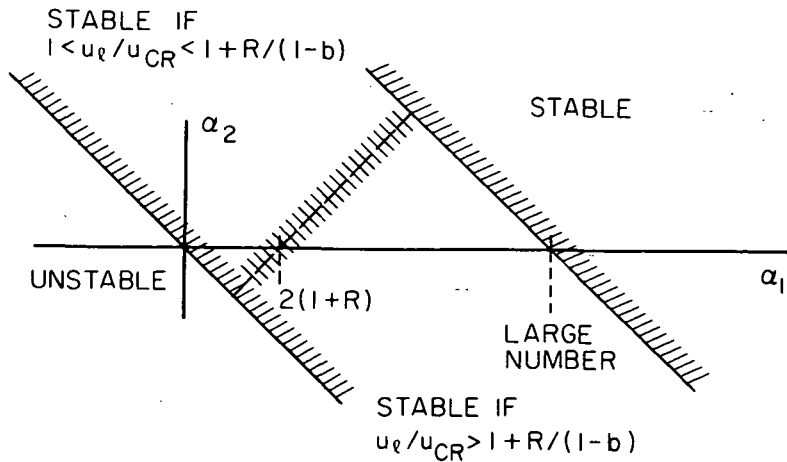
and

$$c_1 = \frac{m_1^2 \Delta t}{2\alpha^2} (R - \tilde{u}_\ell) (\alpha_1 - \alpha_2 - 2 - \tilde{u}_\ell - R) - \frac{m_1^2 \tilde{u}_\ell \Delta x}{\alpha} \quad (54b)$$

where R is defined by equation (50). The only difference from the E point is the last term of equation (54b). In a supersonic region, where H points are located, \tilde{u}_ℓ is positive. Therefore the last term in equation (54b) is always negative if $\alpha > 0$. Noting then that the first term has α^2 in the denominator and the second term has α in the denominator, we can always rely, at worst, on the condition that α , or $\alpha_1 + \alpha_2$, be positive and sufficiently large so that the last term in equation (54b) dominates. (See the right end of sketch (b1).) However, it would also be sufficient for stability to have both terms in equation (54b) negative without requiring α to be large. For the second term, we therefore need $\alpha > 0$, or

$$\alpha_2 > -\alpha_1 \quad (55a)$$

(indicated by the left oblique line on sketch (b1)).



Sketch (b1) - Stability diagram for an H point.

In the first term of equation (54b), the first factor is positive but the second factor may be either negative or positive depending on the magnitude of R relative to $\tilde{u}_\ell + (1 - b)(u_\ell/u_{CR} - 1)$, which is positive in supersonic regions (H points). If $\tilde{u}_\ell < R$, then the condition for stability, from the third factor is

$$\alpha_2 > \alpha_1 - 2(1 + R) \quad (55b)$$

(above the dashed line on sketch (b1)). On the other hand, if $\tilde{u}_\ell > R$, then the condition is

$$\alpha_2 < \alpha_1 - 2(1 + R) \quad (55c)$$

(below the dashed line). Sketch (b1) is more difficult to interpret than sketch (a), but will be useful as a guide. A more precise condition for an H point can also be stated. From equations (41), $\alpha \Delta x / \Delta t = \alpha_1 + \alpha_2$, so equation (54b) yields the condition

$$c_1 = \frac{m_1^2 \Delta t}{2\alpha^2} \left[(R - \tilde{u}_\ell)(\alpha_1 - \alpha_2 - 2 - \tilde{u}_\ell - R) - 2\tilde{u}_\ell(\alpha_1 + \alpha_2) \right] < 0 \quad (56)$$

from which

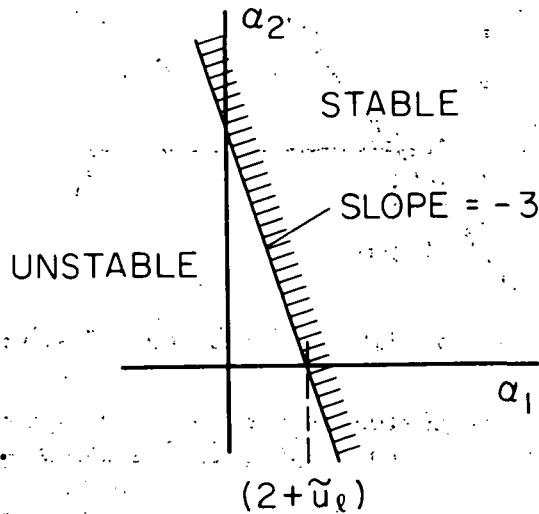
$$\alpha_2 > \left(\frac{R - 3\tilde{u}_\ell}{R + \tilde{u}_\ell} \right) \alpha_1 - (R - \tilde{u}_\ell) \left(1 + \frac{2}{R + \tilde{u}_\ell} \right) \quad (57)$$

For very large R , condition (57) requires only that

$$\alpha_2 > \alpha_1 - R \quad \text{as } R \rightarrow \infty \quad (58a)$$

but for very small R, condition (57) requires

$$\alpha_2 > -3\alpha_1 + (2 + \tilde{u}_\rho) \text{ as } R \rightarrow 0. \quad (58b)$$



Sketch (b2) - Stability diagram for an H point with R very small.

Sketch (b2) illustrates condition (58b), but this is pertinent only at a point where a small value of R is dominating the solution.

For a P point, expansion of the terms of equation (38a) with equation (39c) in Taylor series leads to the first intermediate modified equation,

$$\alpha \tilde{u}_t - \tilde{v}_y + \frac{\Delta t}{2} [-\alpha \tilde{u}_{tt} + (\alpha_1 - \alpha_2 - 2) \tilde{u}_{tx}] = 0 (\Delta t^2, \Delta x^2) \quad (59)$$

to be used along with equation (43b). Noting that within a distance of order Δx of a sonic point, where the quantity $1 - b - 2au$ in equation (20a) vanishes, that quantity is of order Δx , we see that equation (59) is consistent with equation (20a) and is first-order accurate as the solution converges (when time derivatives vanish). Equation (59) is already linear, so direct substitution of the assumed solution (eq. (46)) leads, to first order, to

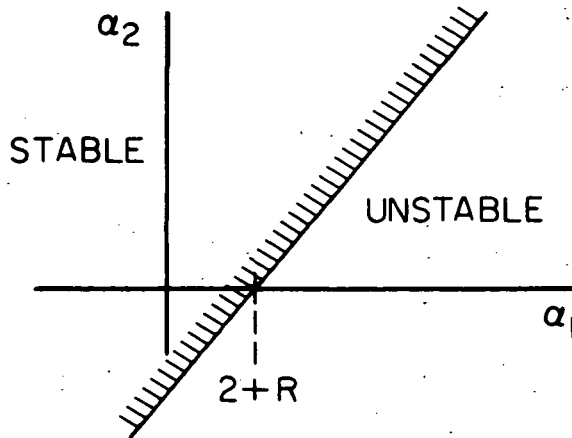
$$c_2 = \left(\frac{m_1}{\alpha}\right) R \quad (60a)$$

$$c_1 = \left(\frac{m_1^2 \Delta t}{2\alpha^2}\right) R (\alpha_1 - \alpha_2 - 2 - R) \quad (60b)$$

where R is defined by equation (50). Stability at a P point therefore requires

$$\alpha_2 > \alpha_1 - (2 + R) \quad (61)$$

which is illustrated in sketch (c).



Sketch (c) - Stability diagram for a P point.

For an S point, formal expansion of the terms of equation (38a) with equation (39d) in Taylor series leads to the first intermediate modified equation,

$$\alpha \tilde{u}_t + 2\tilde{u}_x - \tilde{v}_y + \frac{\Delta t}{2} \left[-\alpha \tilde{u}_{tt} + (\alpha_1 - \alpha_2 - 2)\tilde{u}_{tx} - 4(\tilde{u}\tilde{u}_x)_t \right] - \Delta x (\tilde{u}\tilde{u}_x)_x = 0(\Delta t^2, \Delta x^2) \quad (62a)$$

to be used along with equation (43b). The second intermediate form is

$$\alpha \tilde{u}_t + 2\tilde{u}_x - \tilde{v}_y + \frac{\Delta t}{2} \left[(\alpha_1 - \alpha_2 - 2)\tilde{u}_{tx} - 2(\tilde{u}\tilde{u}_x)_t - \tilde{v}_{yt} \right] - \Delta x (\tilde{u}\tilde{u}_x)_x = 0(\Delta t^2, \Delta x^2) \quad (62b)$$

Equations (62) are not consistent with equations (20) as time derivatives vanish and as Δt and $\Delta x \rightarrow 0$, but Murman (ref. 6) has shown that instead the correct jump conditions are given corresponding to a shock-wave discontinuity and that a fully conservative computation is insured. Nevertheless, equations (62) can be formally investigated for stability of an S point by a procedure similar to the other type points. Local linearization, as before, and substitution of equations (46) into either equation (62a) or (62b) leads, to first order, to

$$c_2 = \frac{m_1}{\alpha} (R - 2\tilde{u}_\ell) \quad (63a)$$

and

$$c_1 = \frac{m_1^2 \Delta t}{2\alpha^2} (R - 2\tilde{u}_\ell) (\alpha_1 - \alpha_2 - 2 - 2\tilde{u}_\ell - R) - \frac{m_1^2 \tilde{u}_\ell \Delta x}{\alpha} \quad (63b)$$

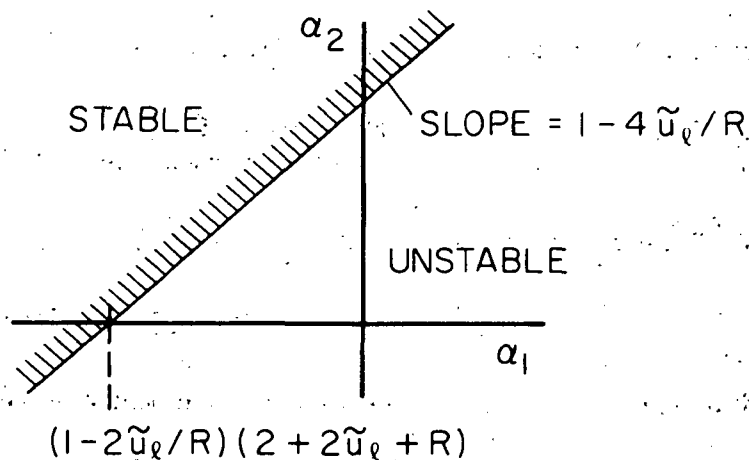
where R is defined by equation (50). As for the H point, equation (63b) can be rewritten using equation (41), to require

$$c_1 = \frac{m_1^2 \Delta t}{2\alpha^2} \left[(R - 2\tilde{u}_\ell)(\alpha_1 - \alpha_2 - 2 - 2\tilde{u}_\ell - R) - 2\tilde{u}_\ell(\alpha_1 + \alpha_2) \right] < 0 \quad (64a)$$

from which

$$\alpha_2 > \left(1 - \frac{4\tilde{u}_\ell}{R}\right)\alpha_1 - \left(1 - \frac{2\tilde{u}_\ell}{R}\right)(2 + 2\tilde{u}_\ell + R) \quad (64b)$$

At an S point, $\tilde{u}_\ell < 0$, since it is the first dot on figure 1 behind an H-point dot at which $(u_e)_{j,k} < u_{CR}$. Therefore the coefficient of α_1 in condition (64b) is positive but the last term may be positive or negative. Sketch (d) illustrates the stability for an S point.



Sketch (d) - Stability diagram for an S point.

Looking at sketches (a), (b2), (c), and (d), we see that there are some values of α_1 and α_2 for which all four operators are stable. For example, taking $\alpha_1 = 0$ and α_2 sufficiently large provides stability. Further study of such diagrams along with numerical experiments will determine the most appropriate values of α_1 and α_2 for most rapid convergence of the iteration.

Preconverged Forms of the Equations in Method 2

Method 2, as introduced in reference 1, constitutes a new approach to applying the Aitken/Shanks formula (refs. 7,8) for accelerating convergence, or extrapolating from successive iterates to an approximation of the correct solution. (A quite different method of applying the Aitken/Shanks formula is used by Hafez and Cheng in reference 22 to accelerate convergence of iterations in line-relaxation of transonic flow computations.) The approach of reference 1 finds the successive iterates in a most appropriate form (i.e., in a nearly geometric sequence) for use in the Aitken/Shanks formula. The method entails expanding the unknown solution in powers of an artificial parameter ϵ , substituting this expansion into an *extended form* of the original

equations, and then collecting coefficients of powers of ϵ to obtain the respective problems for the successive iterates. Three successive iterates at each mesh point are then obtained from these problems for substitution into the Aitken/Shanks formula, which yields the extrapolated solution at each point. The method as formulated and used in reference 1 works well if the solution is not too nearly converged. However, when the successive iterates of the solution are very nearly the same at any one point, that formulation experiences difficulty by introducing errors caused by the loss of significant figures in the subtraction of nearly equal numbers.

To avoid the above difficulty, Method 2 is now formulated in a manner that eliminates the subtraction of nearly equal numbers, and thus gives precise results even when the solution is nearly converged at some points. The new procedure is the following:

The *extended form* (see ref. 1) of equations (33) is

$$u_{xc} + v_{yc} + a^-u^- + a^+u^+ = (1 - \epsilon)s_{j,k}\{u_0\} + \epsilon s_{j,k}\{u\} \quad (65a)$$

$$u_{yc} - v_{xc} = (1 - \epsilon)(1 - v_1)(u_0)_{yc} + \epsilon(1 - v_1)u_{yc} \quad (65b)$$

where $s_{j,k}\{u_0\}$ and $s_{j,k}\{u\}$ are given by equations (34) and where $u_0 = u_0(x,y)$ is a previously determined approximate solution (e.g., after some n in Method 1). The tests in equations (32), to determine which of equations (34) apply to the right side of equation (65a), depend on $(u_e)_{j,k}$ and $(u_h)_{j,k}$ obtained from equations (30a) and (30b) using u_0 at each j,k . The boundary conditions on equations (65) are the same as equations (24) (see eq. (40)). Formally expand the unknown solution to equations (65) in powers of the artificial parameter ϵ (equivalent to a Taylor series about $\epsilon = 0$);

$$u(x,y,\epsilon) = u_1(x,y) + \epsilon u_2(x,y) + \epsilon^2 u_3(x,y) + \dots \quad (66a)$$

$$v(x,y,\epsilon) = v_1(x,y) + \epsilon v_2(x,y) + \epsilon^2 v_3(x,y) + \dots \quad (66b)$$

Although the *successive approximations* to u , which were used in Method 2 as formulated in reference 1, are u_1 , $u_1 + \epsilon u_2$, and $u_1 + \epsilon u_2 + \epsilon^2 u_3$, the new formulation will use the *terms* u_1 , ϵu_2 , $\epsilon^2 u_3$, where ϵu_2 is the *difference* between the first and second approximations and $\epsilon^2 u_3$ is the *difference* between the second and third approximations. As in reference 1, it is convenient to *evaluate* the solutions, as represented by equations (66), at $\epsilon = 1$. The corresponding form of the Aitken/Shanks formula in terms of these differences (ref. 8) is then

$$u^1 = u_1 - \frac{u_2^2}{u_3 - u_2} \quad (67)$$

where $u^1(x,y)$ is the extrapolated solution at each x,y . To obtain u_1, u_2 , and u_3 , substitute equations (66) into equations (65) with equations (34) and the boundary conditions. Collecting coefficients of powers of ϵ then yields the respective problems for $n = 1, 2, 3$:

$$(u_n)_{xc} + (v_n)_{yc} + a^-u_n^- + a^+u_n^+ = s_{n-1} \quad (68a)$$

$$(u_n)_{yc} - (v_n)_{xc} = -\omega_{n-1} \quad (68b)$$

with conditions for $n = 1$:

$$\begin{aligned} v_1(x,0) &= -4x \quad (-.5 < x < .5) \\ &= 0 \quad (|x| > .5) \end{aligned} \quad (69a)$$

$$\text{on } B: u_1 = u_B \quad \text{or} \quad v_1 = v_B \quad (69b)$$

and for $n = 2,3$:

$$v_n(x,0) = 0 \quad (70a)$$

$$\text{on } B: u_n = 0 \quad \text{or} \quad v_n = 0 \quad (70b)$$

and where (with $s_{j,k}\{u\}$ given by eqs. (34)):

$$-\omega_0 = (1 - v_1)(u_0)_{yc} \quad (71a)$$

$$-\omega_1 = (1 - v_1) \left[(u_1)_{yc} - (u_0)_{yc} \right] \quad (71b)$$

$$-\omega_2 = (1 - v_1)(u_2)_{yc} \quad (71c)$$

$$s_0 = s_{j,k}\{u_0\} \quad (72a)$$

$$s_1 = s_{j,k}\{u_1\} - s_{j,k}\{u_0\} \quad (72b)$$

and

$$E: s_2 = a^-u_2^- + a^+u_2^+ + b(u_2)_{xc} + a(2u_1u_2)_{xc} \quad (73a)$$

$$H: s_2 = a^-u_2^- + a^+u_2^+ + (u_2)_{xc} + (b - 1)(u_2)_{xb} + a(2u_1u_2)_{xb} \quad (73b)$$

$$P: \quad s_2 = a^- u_2^- + a^+ u_2^+ + (u_2)_{xc} \quad (73c)$$

$$S: \quad s_2 = a^- u_2^- + a^+ u_2^+ + b(u_2)_{xc} + (b-1)(u_2)_{xb} \\ + a \left[(2u_1 u_2)_{xb} + (2u_1 u_2)_{xc} \right] \quad (73d)$$

Substitution of the finite-difference expressions (eqs. (25) to (27)), along with the definitions in equation (37), into equations (68) to (73) yields the final forms of the difference equations to be solved by the extended Cauchy-Riemann solver for $n = 1, 2, 3$ in Method 2. The resulting values of u_n at j, k are then put into equation (67) to obtain the extrapolated solution.

COMPUTATIONAL CONSIDERATIONS AND SOME PRELIMINARY RESULTS

Research versions of a computer program have been written to solve rapidly the small-disturbance equations for transonic flow over a thin, symmetrical, biconvex airfoil at zero incidence by Methods 1 and 2 as described above. Use of Method 1 with $v_2 = 1$ (so that eq. (35) would not be used) would require only two two-dimensional arrays: u and v , with $s_{j,k}$ being put into the v array to start each iteration using the extended Cauchy-Riemann solver (ref. 9). With $v_2 \neq 1$, Method 1 requires three two-dimensional arrays, and Method 2 requires four arrays.

The program was run both on a Control Data 7600 computer and also on an IBM 360/67 computer. All timing runs were made on the 7600. The 360/67 was used to run the program conversationally, for interacting with the program. This capability is especially important to numerical experiments currently being done and was used to accomplish some results to be presented here.

In the earlier study (ref. 1), which did not include the arbitrary parameters α_1 , α_2 , and b , subcritical cases converged very fast — in a few iterations — and also a slightly supercritical case ($\bar{\alpha}_1 = .3555556$) converged rather rapidly. At slightly stronger supercritical conditions, the computed results evolved in cycles and would not settle down, and at yet stronger conditions the iterations diverged catastrophically. However, because the simplified stability considerations for the revised method outlined above indicate stability of the iterative procedure for some ranges of values of the arbitrary parameters, and also because switching to Method 2 after an arbitrary number of iterations is now made more effective by the slightly modified approach for Method 2 outlined above, the conversational version of the program containing numerous options was developed for investigating the many possibilities. The capabilities of this research computer program include (1) display of the peak velocity and the maximum residual after each iteration, (2) the optional plotting of the iterated velocity distribution versus x after any iteration, (3) the optional plotting of the *type* of all points (labeled $s_{j,k}$ on fig. 1) where the continuity equation is solved, at any iteration, including indication of any change of type from the previous iteration (see fig. 2),

(4) accumulation of the number of iterations since a change of type occurred, (5) ability to arbitrarily specify v_1 , \bar{b} , α_1 , and α_2 at the beginning of each case, (6) ability to change α_1 and α_2 at any iteration depending on conditions such as the magnitude of the maximum residual or the number of iterations since a change of type occurred, (7) ability to arbitrarily specify and change v_2 at each point depending on conditions such as the sign of $u - u_{CR}$ and the extent to which the solution is converged, (8) ability to switch to Method 2 after any n (e.g., if some condition is satisfied) and back to Method 1 if desired, and (9) ability to store $u_{j,k}$ at a given n , then continue the iterations and later stop, recall the stored $u_{j,k}$, change one or more parameters in the problem, then continue the iterations again starting with the stored $u_{j,k}$, and compare the succeeding results with the previous results. After the best values of parameters are determined by numerical experiments, their evaluation can then be built into the final computer program.

Preliminary results for pressure distributions on the biconvex airfoil, obtained by the research computer program, are shown plotted in figure 3, parts (a) to (d), for a range of transonic conditions. For these computations the classical formulation (eq. (19a)) was arbitrarily chosen. (Some values of parameters corresponding to Murman and Krupp's similarity parameter are given in Table 1.) Figure 3(a) shows the only supercritical case that was presented in reference 1. Parts (b), (c), and (d) of figure 3 show cases with strong shock waves. The shock in figure 3(d) is nearly at the trailing edge. These results were computed on a 39×32 mesh with upstream and downstream computation boundaries at about one-half chord length from the leading and trailing edges. The upper boundary was at about 3.5 chord lengths above the airfoil for figures 3(a) and (b) and at 5 chord lengths for figures 3(c) and (d). The conditions on u and v applied on the outer boundaries were the Prandtl-Glauert solutions for u and v evaluated at the Mach number and thickness ratios indicated on the figures.

The pressure distributions on figure 3 are compared with results from the line-relaxation program of Murman, Bailey, and Johnson (ref. 23), based on the method of references 4-6. In that program, the option of using the classical formulation corresponding to equation (19a) was chosen for a proper comparison. The outer condition on the velocity potential in that method is the far-field condition of Klunker (ref. 24), and their outer boundary was at one chord length in front of the leading edge, .875 chord behind the trailing edge, and 5.2 chords above and below the airfoil. The mesh used in their program is variable and finer than the uniform mesh used for the present computations, so the agreement and differences are as expected. Even the case for which the shock is nearly at the trailing edge (fig. 3(d)) shows good agreement despite the coarseness of the mesh.

The results in figures 3(a) to (d) were all computed using Method 1 to convergence. Figure 4 shows an interesting effect of switching to Method 2 before the iteration has converged enough, when the type of all points is not yet the same as the final type. Method 1 was used for nine iterations; then

Method 2 was used to obtain the three successive terms at each point and the extrapolated solution shown in figure 4. A property of the Aitken/Shanks extrapolation as used in Method 2 is that *all* the significant figures of the three successive approximations at any point contain information about the exact solution, even though those successive approximations themselves are not very close to the exact solution (see example problem in ref. 1). It thus appears in figure 4 that this procedure may be picking up the fact that the exact solution to the equations (or the solution on a very fine mesh) has the well-known logarithmic singularity just behind the shock, even though the converged solution on the coarse mesh smears over this singularity. Even the finer mesh used by the program of reference 23 was not fine enough to pick up the singularity, partly because that point apparently occurs between the mesh points for this case. (There is also the possibility that the extrapolation technique may be merely overpredicting changes near the steep shock, but consideration of the process that obtains the extrapolated values in Method 2 tends to exclude that explanation.) This phenomenon illustrated on figure 4 is not an isolated case but is a typical occurrence in Method 2. It may be that the numerical solution in figure 4 is just as good a representation of the exact solution to the equations as is the fully converged solution in figure 3(b).

Corresponding to the cases computed in figure 3, figure 5 shows the sonic-line locations obtained by linear interpolation between the velocities on the two sides of the forward sonic line and of the shock wave.

For these computations on a 39×32 mesh, the Control Data 7600 computer required 40 milliseconds per iteration. (This is a preliminary result; the time can still be significantly reduced by modifying the program.) The slightly supercritical case of figure 3(a) required only 6 iterations (0.24 sec) for the peak velocity to be converged to within 1 percent of its final converged value, 9 iterations (0.36 sec) for 0.1 percent, and 14 iterations (0.56 sec) for .01 percent. For these results, Method 2 was used successively for $n = 1$ to 9 (i.e., three cycles of Method 2), then the program was switched to Method 1. For the strong transonic case of figure 3(b), the results computed in 23 iterations (0.92 sec) are virtually indistinguishable from the fully converged results shown. It may be noted that the test on the residuals used to determine sufficient convergence may be much less stringent than conventionally required by line-relaxation programs because errors are felt simultaneously at all points in succeeding iterations, rather than requiring time to propagate. Results for the strong cases in parts (c) and (d) have relatively low iteration counts, but no reportable numbers or times are available yet because those results were obtained during experimentation with the arbitrary parameters. The optimal values of the parameters and the corresponding computing times will be reported later, after a parametric study is completed.

CONCLUDING REMARKS

The recent progress in the application of semi-direct iterative methods to transonic flow computations has been described here. The extension described,

of the earlier method to strong transonic cases. is part of the second stage of the overall study. The modifications that produce stability of the iterative procedure, as well as a more effective version of an extrapolation technique, have been described and analyzed.

The results of the computations agree with those computed using accepted methods, and the computations are rapid. This demonstrates that the fast semi-direct method is definitely applicable to strongly supercritical transonic flows. This demonstration, with a direct elliptic solver being used successfully to compute iteratively the solution to the mixed elliptic-hyperbolic problem, is regarded as the most significant result of the present study. The short computing times indicate a significant potential for highly efficient transonic flow computations.

The research computer program has been briefly described for use in a parametric study that will in the near future determine the optimal values of free parameters in the method for most rapid convergence.

REFERENCES

1. Martin, E. D., and Lomax, H.: Rapid Finite-Difference Computation of Subsonic and Slightly Supercritical Aerodynamic Flows. AIAA J., vol. 13, no. 5, May 1975. (Presented as a portion of AIAA Paper No. 74-11, 1974.)
2. Lomax, H., and Martin, E. D.: Fast Direct Numerical Solution of the Non-homogeneous Cauchy-Riemann Equations. J. Comp. Phys., vol. 15, 1974, pp. 55-80.
3. Buneman, O.: A Compact Non-iterative Poisson Solver. SUIPR Rept. 294, 1969, Inst. for Plasma Research, Stanford Univ., Stanford, Calif.
4. Murman, E. M., and Cole, J. D.: Calculation of Plane Transonic Flows. AIAA Jour., vol. 9, 1971, pp. 114-121.
5. Murman, E. M., and Krupp, J. A.: Solution of the Transonic Potential Equation Using a Mixed Finite Difference System. In Lecture Notes in Physics, vol. 8, Proceedings of the Second International Conference on Numerical Methods in Fluid Dynamics, Sept. 15-19, 1970 (ed. by M. Holt). Springer-Verlag, Berlin, 1971, pp. 199-206.
6. Murman, E. M.: Analysis of Embedded Shock Waves Calculated by Relaxation Methods. AIAA Jour., vol. 12, 1974, pp. 626-633.
7. Aitken, A. C.: On Bernoulli's Numerical Solution of Algebraic Equations. Proc. of the Royal Soc. Edinburgh, vol. 46, 1926, pp. 289-305.
8. Shanks, D.: Nonlinear Transformations of Divergent and Slowly Convergent Sequences. Jour. of Math. and Phys., vol. 34, 1955, pp. 1-42.

9. Lomax, H., and Martin, E. D.: Variants and Extensions of a Fast Direct Numerical Cauchy-Riemann Solver, with Illustrative Applications. NASA TN D-7934, 1975.
10. Roache, P. J.: Finite-Difference Methods for the Steady-State Navier-Stokes Equations. Rept. SC-RR-72 0419, 1972, Sandia Labs., Albuquerque, New Mexico.
11. Widlund, O. B.: On the Use of Fast Methods for Separable Finite-Difference Equations for the Solution of General Elliptic Problems. In *Sparse Matrices and Their Applications* (D. J. Rose and R. A. Willoughby, eds.), Plenum Press, New York, 1972, pp. 121-134.
12. Concus, P., and Golub, G. H.: Use of Fast Direct Methods for the Efficient Numerical Solution of Nonseparable Elliptic Equations. *SIAM Jour. on Numer. Anal.*, vol. 10, 1973, pp. 1103-1120.
13. Spreiter, J. R.: On the Application of Transonic Similarity Rules to Wings of Finite Span. NACA Rept. 1153, 1953.
14. Murman, E. M.: Computational Methods for Inviscid Transonic Flows with Imbedded Shock Waves. AGARD Lecture Series No. 48, Numerical Methods in Fluid Dynamics (J. J. Smolderen, ed.). AGARD-NATO, 1972.
15. Krupp, J. A., and Murman, E. M.: Computation of Transonic Flows Past Lifting Airfoils and Slender Bodies. *AIAA Jour.*, vol. 10, 1972, pp. 880-886.
16. Garabedian, P. R.: Partial Differential Equations. Wiley, New York, 1964.
17. Lomax, H., and Steger, J. L.: Relaxation Methods in Fluid Mechanics. In *Annual Review of Fluid Mechanics*, vol. 7 (M. Van Dyke, W. G. Vincenti, and J. V. Wehausen, eds.). Annual Reviews, Inc., Palo Alto, Calif., 1975, pp. 63-88.
18. Lomax, H., Kutler, P., and Fuller, F. B.: The Numerical Solution of Partial Differential Equations Governing Convection. AGARDograph No. 146, AGARD-NATO, 1970.
19. Warming, R. F., and Hyett, B. J.: The Modified Equation Approach to the Stability and Accuracy Analysis of Finite-Difference Methods. *J. Comp. Phys.*, vol. 14, 1974, pp. 159-179.
20. Sichel, M.: Theory of Viscous Transonic Flow — A Survey. In *Transonic Aerodynamics*, AGARD Conference Proceedings No. 35, AGARD-NATO, 1968.
21. Nieuwland, G. Y., and Spee, B. M.: Transonic Airfoils: Recent Developments in Theory, Experiment, and Design. In *Annual Review of Fluid Mechanics*, vol. 5 (M. Van Dyke, W. G. Vincenti, and J. V. Wehausen, eds.). Annual Reviews, Inc., Palo Alto, Calif., 1973, pp. 119-150.

22. Hafez, M. M., and Cheng, H. K.: Convergence Acceleration and Shock Fitting for Transonic Aerodynamics Computations. AIAA Paper No. 75-51, 1975.
23. Murman, Earll M., Bailey, Frank R., and Johnson, Margaret L.: TSFOIL - A Computer Code for Two-Dimensional Transonic Calculations, Including Wind-Tunnel Wall Effects and Wave-Drag Evaluation. Aerodynamic Analyses Requiring Advanced Computers, Part II, NASA SP-347, 1975, pp. 769-788.
24. Klunker, E. B.: Contribution to Methods for Calculating the Flow About Thin Lifting Wings at Transonic Speeds - Analytical Expression for the Far Field. NASA TN D-6530, 1971.

TABLE 1.- SIMILARITY PARAMETERS AND CORRESPONDING CONDITIONS.

\bar{a}_1	K_S	M_∞ ($\tau = .10$)	M_∞ ($\tau = .06$)	Corresponding* K_{MK1}	M_∞ ($\tau = .10$)	M_∞ ($\tau = .06$)
.3555556	1.2551867	.800	.850	2.2499998	.7870	.8425
.4525193	1.0687807	.825	.870	1.9158555	.8145	.8635
.5930949	.8924089	.850	.889	1.5996981	.8425	.8855
.8097111	.7251479	.875	.9085	1.2998725	.8695	.906

*The corresponding K_{MK1} is taken to be $(\gamma + 1)^{2/3} K_S$.

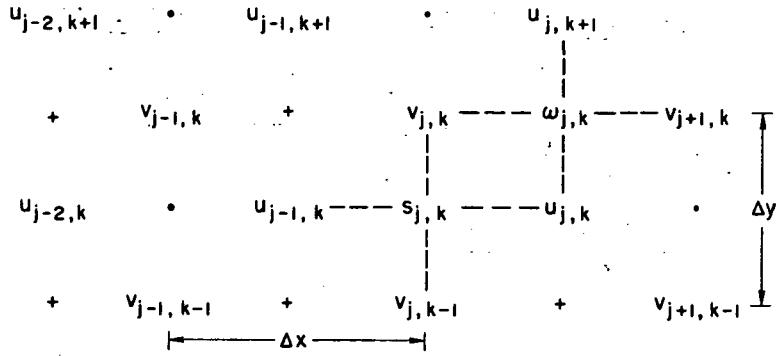


Figure 1.— Staggered meshes for u and v.

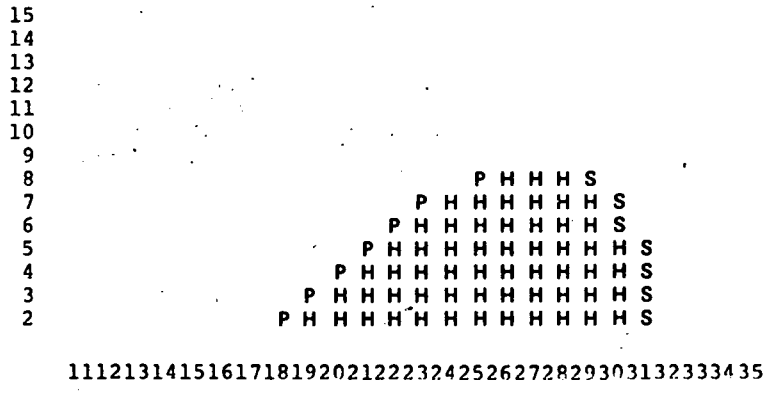
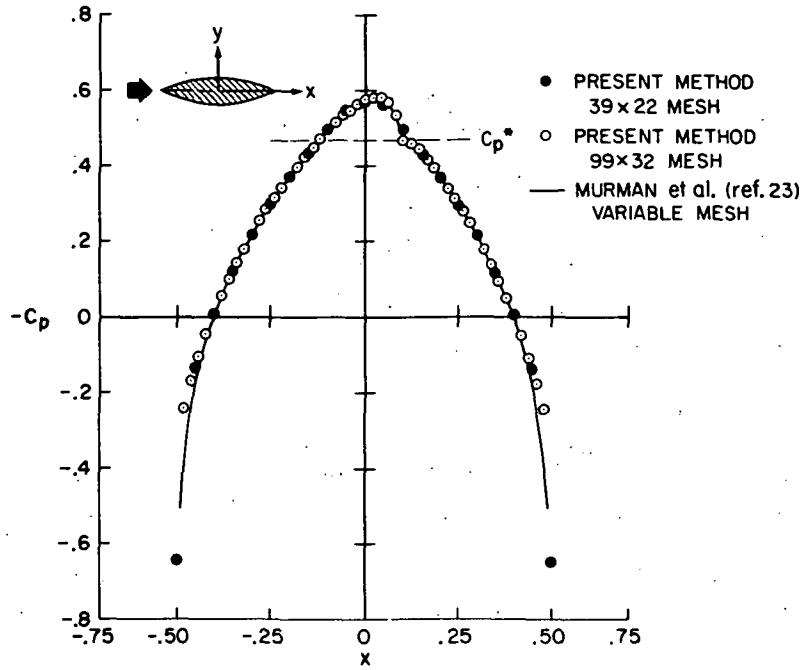
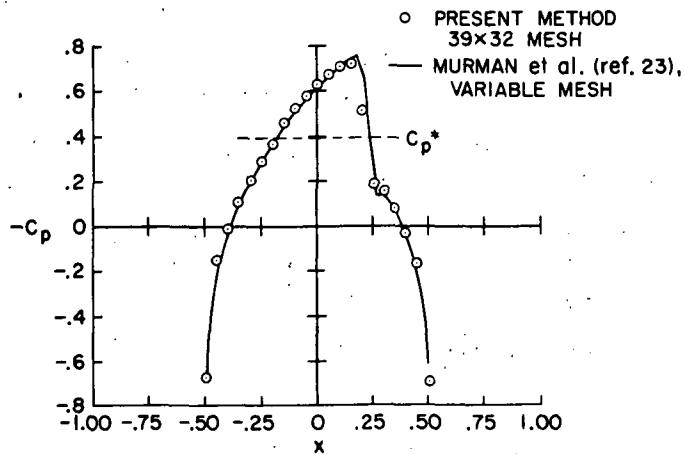


Figure 2.— Conversational computer printout of plot of type of points. Blank is elliptic; H, P, and S are hyperbolic, parabolic, and shock points. Asterisk in front of a symbol indicates change in type of point from previous iteration.

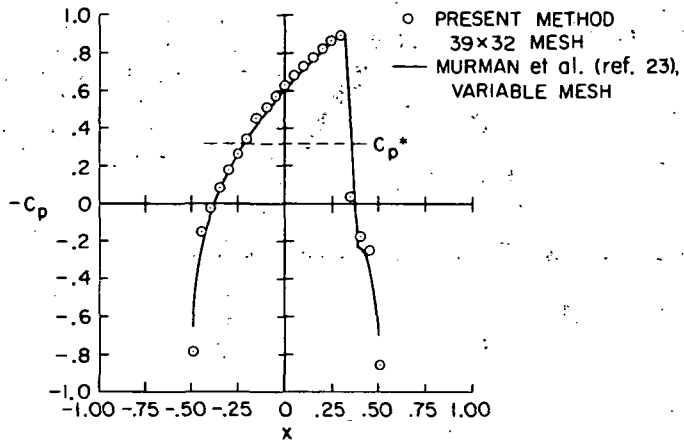


(a) $\bar{a}_1 = .3555556$ ($K_S = 1.2551867$; $M_\infty = .800$, $\tau = .10$)

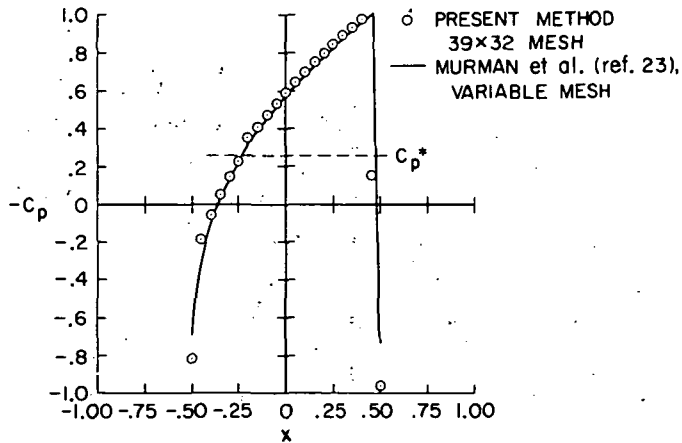


(b) $\bar{a}_1 = .4525193$ ($K_S = 1.0687807$; $M_\infty = .825$, $\tau = .10$)

Figure 3.- Pressure on a thin biconvex airfoil.



(c) $\bar{a}_1 = .5930949$ ($K_S = .8924089$; $M_\infty = .850$, $\tau = .10$)



(d) $\bar{a}_1 = .8097111$ ($K_S = .7251479$; $M_\infty = .875$, $\tau = .10$)

Figure 3.— Concluded.

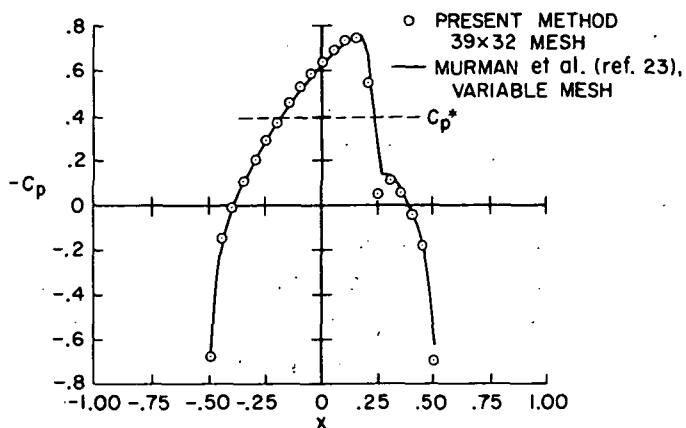


Figure 4.— Pressure distribution resulting from Aitken/Shanks extrapolation (Method 2), before iterative convergence ($\bar{a}_1 = .4525193$, $K_S = 1.0687807$: $M_\infty = .825$, $\tau = .10$).

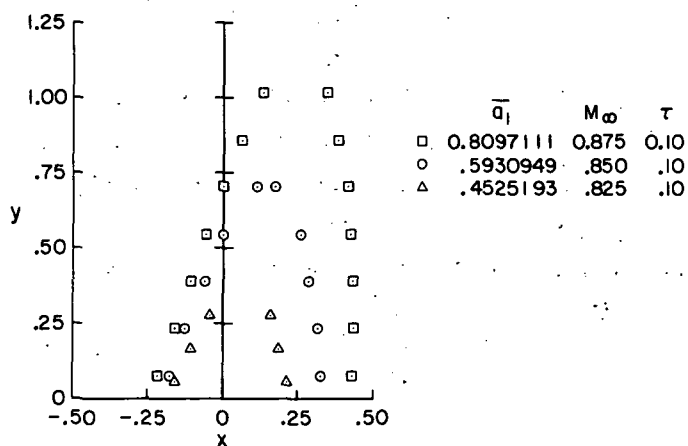


Figure 5.— Sonic line over a thin biconvex airfoil computed on a 39x32 mesh.

RECENT DEVELOPMENTS IN PROPULSIVE-LIFT AERODYNAMIC THEORY

By Richard J. Margason, Long P. Yip, and Thomas G. Gainer
NASA Langley Research Center

SUMMARY

This paper reviews the progress of propulsive-lift theories from their beginning in 1956 with Spence's development of a two-dimensional jet flap to the present general three-dimensional theories that require a large computer. Results of jet-flap theories are compared for high-aspect-ratio wings with full- or partial-span blowing. Applications of the jet-flap theory and the more general wing-jet interaction theories under development to externally blown flap and upper-surface blowing configurations are also discussed. The possible direction of future developments is indicated.

INTRODUCTION

Propulsive lift began in the early days of aviation when the propeller slipstream flowing over the wing was used to attain increased lift. Various propulsive-lift concepts are shown in figure 1. The most advanced example of this type of propulsive lift is illustrated by the Breguet 941, first flown in 1965. The Germans first used jet-powered high lift in the 1930's with the experiments using jet flaps in which a sheet of high-velocity air was ejected from the trailing edge of the wing. Later work in Germany, England, and the United States further developed the concept. The first jet-flap research aircraft, the British Hunting H.126, flew in 1963. During the 1960's, the augmentor flap, which adds an ejector to augment the thrust of the jet flap, was developed in a cooperative program by NASA Ames Research Center and DeHavilland Aircraft Company of Canada and resulted in the Buffalo augmentor wing research airplane, first flown in 1972. Recently, the U.S. Air Force has developed two advanced short take-off and landing (STOL) aircraft: the YC-15 externally blown flap (EBF) configuration scheduled for flight later this year and the YC-14 upper-surface blown flap configuration scheduled for flight in 1976.

Along with the concept development and experimental work done (ref. 1) on configurations with propulsive lift, a number of theoretical and computational methods have been developed to predict the characteristics of these configurations. These methods have increased in complexity from those requiring a simple back-of-the-envelope calcu-

lation to those requiring the largest, modern digital computer. The purpose of this paper is to outline the development of these computational methods for powered lift.

SYMBOLS

A	aspect ratio, b^2/S
b	wing span, m (ft)
C_D	drag coefficient
C_L	lift coefficient
C_m	pitching-moment coefficient
C_μ	momentum coefficient, $\frac{\text{Thrust}}{qS}$
c	chord, m (ft)
c_l	section-lift coefficient, $\frac{\text{Section lift}}{qc}$
c_p	section-pressure coefficient
c'_μ	section-momentum coefficient
d	jet diameter, m (ft)
h	height of jet center line relative to the wing-chord plane (positive above the wing), m (ft)
q	free-stream dynamic pressure, N/m^2 (lb/ft ²)
r	radius of curvature of jet sheet, m (ft)
S	wing area, m ² (ft ²)

V_{∞}	free-stream velocity, m/sec (ft/sec)
x	fraction of chord
α	angle of attack, deg
γ	vorticity, m/sec (ft/sec)
δ_f	flap deflection, deg
δ_j	jet-wake deflection, deg
δ_j^s	section jet-wake deflection, deg
η	nondimensional spanwise location
ϕ	velocity potential, m ² /sec (ft ² /sec)

Abbreviations:

EBF	externally blown flap
EVD	elementary vortex distribution
SDM	section design method
USB	upper-surface blown

JET-FLAP THEORIES

2-D Jet Flap

The first theoretical method for a wing with powered lift was developed by Spence. (See refs. 2 and 3.) This method gave the lift and pressure distribution on a two-dimensional wing with a jet flap. Spence used a vortex sheet whose vorticity depended on the section-momentum coefficient and curvature of the sheet to represent the thin jet wake behind the wing as shown below:

$$\gamma = \frac{cc_{\mu}}{2} \frac{V_{\infty}}{r} \quad (1)$$

Spence approximated the solutions to the integral equations involved by a Fourier series expression and then, by solving for Fourier coefficients on a computer, was able to obtain the general results shown in figure 2. The lift results in Spence's method are in the form of two equations - one for lift-curve slope $\partial c_l / \partial \alpha$ and the other for lift due to jet deflection $\partial c_l / \partial \delta_j$. Both equations contain terms that depend on section-momentum coefficient c'_μ . The lift-curve slope, for example, is 2π modified by two additional terms that account for c'_μ effects. The chordwise pressure distribution on the wing was also obtained and is given by the following equation:

$$\Delta c_p = 2 \left[\frac{c'_\mu}{\pi x(1-x)} \right]^{1/2} \delta_j \quad (2)$$

The pressure difference Δc_p between the upper and lower surface is a function of jet-deflection angle, section-momentum coefficient, and chordwise location. In the pressure-coefficient plot in figure 2, the computed pressure difference has been combined with the pressure distributions over an ellipse to obtain the total pressure distribution for an elliptical airfoil with jet flap. The Spence formulation is valid from the leading edge to a point near the trailing edge at

$$x = 1 - \frac{\pi c'_\mu}{16} \quad (3)$$

and is seen to give a very good approximation of the experimental data (symbolized points) over most of this range.

Limited 3-D Jet-Flap Methods

Based on Spence's vortex sheet approximation for the two-dimensional jet wake, a number of three-dimensional methods for jet flaps were then developed. However, because of the limited capacities of the computers at that time, these were also limited by assumptions that had to be made in evaluating the integral equations. The earliest three-dimensional jet-flap methods, which included those of Maskell and Spence (ref. 4), Hartunian (ref. 5), and Das (ref. 6), assumed a large aspect ratio and an elliptical spanload distribution. Later work by Kerney (ref. 7) and Tokuda (ref. 8) assumed large aspect ratios and low momentum coefficients. In addition, Kida and Miyai (ref. 9) obtained a solution for a jet flap in ground effect, and Adessio (ref. 10) obtained a solution that assumed an elliptical C_μ distribution over part span flaps with high momentum coefficient and included a computation of the flow-field characteristics.

More General 3-D Jet-Flap Methods

It is not until computers of the CDC 6000 class became available that more general jet-flap methods began to be developed. These were completely numerical methods pat-

turned after methods developed for conventional wings (fig. 3) – that is, they assumed potential flow and used numerical integration of influence coefficient matrices to obtain a solution. (See, for example, ref. 11.) They extended the conventional theory by including Spence's relationship for the high-momentum jet wake. This implies the assumptions of thin jet sheet and modest wake deflection angles. The methods that were developed included lifting-line methods by Lissaman (ref. 12) or Lopez and Shen (ref. 13) and lifting-surface methods by Clever (ref. 14) and Goldhammer, Lopez, and Shen (ref. 15). In addition, Hackett and Lyman (ref. 16) and Holmes, Barnett, and Jacobs (ref. 17) developed equivalent mechanical-flap methods.

Transonic 2-D Theories

Additional methods for transonic two-dimensional theories have been developed by Malmuth and Murphy (ref. 18) and Ives and Melnick (ref. 19). These methods include both jet-flap and shock-induced effects. There will be no attempt to discuss these methods in the present paper other than to recognize the need for these efforts and their future extension to three-dimensional methods.

Jet-Flap Theory Experiment Comparisons

In figure 4, the results of some of these jet-flap theories are compared with the experimental data obtained in reference 20 for a wing with a rectangular planform, an aspect ratio of 6.8, and a full-span jet deflected 31.3° . Basically, the agreement between the theories and experiment is good for a high-aspect-ratio wing with a modest jet deflection. The Lissaman and Addessio methods somewhat underpredict the lift, while the Maskell and Spence, Tokuda, and Hackett and Lyman methods either go through the data at the low values of C_μ or slightly overpredict the data at the higher values of C_μ .

A similar comparison for a partial-span jet flap deflected 37° in one case and 67° in the other is presented in figure 5 using experimental data from reference 21. For the lower flap deflection, generally there is good agreement with the experimental data with only the Lissaman method being somewhat low. For the higher flap deflection, there is relatively good agreement from the Lopez methods, while the other methods underpredict the data at low values of C_μ or are somewhat off at the higher values of C_μ .

To evaluate these jet-flap theories for a larger variety of partial-span combinations and deflection angles, data were obtained in the Langley V/STOL tunnel on the model shown in figure 6. This model, known as the jet-flap theory verification model, was jointly funded by NASA and the U.S. Air Force Flight Dynamics Laboratory. It was configured both as a pure jet flap with a 60° trailing-edge deflection and as a jet-augmented simple flap with the jet blowing from the knee of the flap for a large range of deflections.

The wing was equipped with pressure orifices at six spanwise stations to indicate the spanload distribution for various blowing arrangements.

The lift, drag, and pitching-moment coefficient results obtained with this model and the corresponding calculated values using the elementary vortex distribution (EVD) theory are presented in figure 7 for the case of the jet flap blowing over the inboard two-thirds of the span, 45° flap deflection, and values of C_μ from 0.5 to 4.0. The data show generally very good agreement between theory and experiment, especially for the lift and pitching-moment coefficients. It should be noted that the profile drag has not been included in the EVD calculations; adding it would bring the calculated drag into closer agreement with the experimental values.

The calculated and experimental spanload distributions at a C_μ of 4 and an angle of attack of 0° are presented in figure 8. The high loading inboard is seen to be represented fairly well by the theory, and the general shape of the spanload distribution is in good agreement with the experimental distribution. This would indicate that in general the jet-flap theories are valid as long as the jet-flap assumptions are closely met.

Externally Blown Flap

An example of an application of the jet-flap theory to a configuration for which the assumption of a thin jet exhausting near the trailing edge of the wing was violated is presented in figure 9. The experimental data, presented in reference 22, are for an externally blown flap configuration having four engines whose exhausts impinge on a double-slotted flap. Calculations were made for this configuration using experimentally measured distributions of the exhaust deflection angle and momentum coefficient at the flap trailing edge (shown on the right in fig. 9). Such calculations might not be practical in the general situation, of course, since this information would not ordinarily be available. A method, such as that described by Hirsh (ref. 23), would be needed to describe the wake as it leaves the engine exits until it reaches the trailing edge. The purpose here was to determine if the jet-flap methods could give useful results even though the powered-lift system and resulting flow pattern were more complicated than a simple jet flap. The measurements, shown in figure 9, of deflection angle and momentum coefficient were made with a hot-film velocity probe while the model was at an angle of attack of 8° and a momentum coefficient of 4. The data show that the maximum and minimum deflection angles occurred on approximately the center lines of the inboard and outboard engines, respectively; whereas, the peak momentum coefficient occurred between the center lines.

The results on the left in figure 9 show that the two jet-flap theories - Lissaman and EVD - give fairly good approximations of C_L for values of C_μ of 0 and 2, but not at a C_μ of 4. The EVD program underpredicted the lift and the Lissaman program

overpredicted it. At least part of this discrepancy could be attributed to the fact that the flap, rather than having a thin jet emanating from its trailing edge, was operating within a relatively thick jet. As a result, noticeable jet interference effects come into play which are not accounted for by the jet-flap theory.

WING-PLUS-JET THEORIES

It was shown in references 24, 25, and 26 that as a wing or flap gets close to or becomes immersed in jet exhaust, there is an increase in the local lift coefficient which can be significant even for the case of a jet located more than one jet diameter above or below the wing. An example of the lift that can be developed by wing-jet interaction, along with some of the methods being developed to account for the interaction effects, is shown in figure 10. The sketch on the upper left in figure 9, which was taken from reference 24, shows lift coefficient plotted against the height-to-diameter ratio of a jet exhausting in the presence of a wing. The wing is at a 10° angle of attack and its basic lift coefficient without power is 1.1 (the line marked "wing alone"). If the wing was equipped with a jet flap at a C_μ of 0.25, its lift coefficient would be 1.28, but if that same momentum were put into a relatively thick jet (as indicated by the sketch), its lift coefficient would vary with the height of the jet relative to the wing as shown by the "wing and jet" curve. Its maximum lift coefficient would be approximately 1.6 when the jet is immersing the wing in the high-velocity flow.

The three theoretical methods illustrated in figure 10 for solving the general wing-jet interaction problem are the methods developed by Dillenius, et al. (ref. 27), Shollenberger (ref. 28), and Lan (ref. 29). These methods use systems of vortex or source sheets to represent the jet exhaust and a vortex-lattice system to represent the wing. The Dillenius method is semiempirical in that the vortex strengths and the cross-sectional shape of the jet are prescribed. While the curvature of the jet center line is allowed to vary, the jet may penetrate the flap system. The boundary condition that determines the curvature of the jet center line requires that the jet flow at the boundaries must be parallel to the outer flow. In the Shollenberger method, the vortices of the sheets enclosing the jet region, the curvature of the jet, and its cross-sectional shape are all allowed to vary; this is done by satisfying the additional boundary condition that at the edge of the jet the pressure inside the jet is equal to that in the outer flow. Lan's method also satisfies these two boundary conditions - tangent flow and pressure continuity at the jet boundaries - but uses double vortex sheets to represent the upper and lower edges of the jet. These vortex sheets remain straight during the computation. The changes in the vortices in the calculated sheets account for the effects of the wing flow field on the jet and of the jet in the wing flow field. These methods are primarily in

their developmental stage, and none has yet been systematically applied to a wing with upper-surface blowing.

Externally Blown Flap

The Dillenius method, however, has been fairly extensively applied to an EBF configuration, and some of the results are shown in figure 11. The comparison shown indicates good agreement (below the stall) between theory and experiment for the cruise configuration ($\delta_f = 0^\circ$, $C_{\mu} = 0$) and for the $C_{\mu} = 5.5$ case with $\delta_f = 35^\circ$, but only moderately good agreement at lower values of C_{μ} with $\delta_f = 35^\circ$. The pitching moments predicted by the theory are noticeably more negative than the measured values.

Figure 12 compares the Dillenius theory with data obtained by Perry and Greene (ref. 30) with an EBF configuration in the NASA Ames 12.2- by 24.4-m (40- by 80-ft) Full-Scale Wind Tunnel. In this investigation, the wing and flap pressure distributions were measured as well as overall model forces and moments. The distributions of section-lift coefficient obtained from these pressure distributions are shown on the right of figure 12. The pressure integrations were carried out separately for the portion of the wing ahead of the flap and for the flap. These are indicated by the "wing alone" and "flap alone" plots, respectively. The data indicate differences in the chordwise as well as spanwise pressure distributions between theory and experiment. The calculated values of section-lift coefficient show peaks (corresponding approximately to the engine locations) on the wing that were about the same magnitude as those on the flap. The experimental data on the other hand show no peaks on the wing but very high peaks on the flap, indicating a more rearward distribution of pressure for the experiment. The data for the wing-alone and flap-alone distributions have been combined to give a total wing-flap lift coefficient on the left of figure 12. It can be seen that the theoretical (dashed curves) and experimental (circle data points) data obtained from the pressure distributions were not in very good agreement. Although the shape of the calculated lift curve and the experimental data (square data points) for the complete configuration, which included a fuselage, empennage, and nacelles, were similar, the calculated lift was substantially lower. This case, in contrast to figure 11, indicates that the model with the jet exhausting through the wing is not totally realistic when compared with experimental results. Further development of the method is currently under way to improve the representation of this problem and to apply it to the upper-surface blown flap.

Upper-Surface Blown Flap

The upper-surface blown (USB) flap configurations represent another propulsive-lift concept for application of the wing-plus-jet theories. The twin-engine configuration (ref. 31) operating at a momentum coefficient of 2 is shown in figure 13. The wing has

an aspect ratio of 7.8. The experimental data are represented by the symbols for flap deflections of 0° , 20° , and 60° . The jet-flap theory results are based on the Lopez EVD method. Like all jet-flap theories, the jet is assumed to exit at the trailing edge of the wing. Hence, there is no high-velocity flow over the approximate 14 percent of the wing upper surface immersed in the engine efflux. As a result, the jet-flap theories under-predict the lift coefficient at all three flap deflections as illustrated by the results of EVD theory in figure 13. This deficiency of the jet-flap theory shows the need for the wing-plus-jet theory. As an illustration of such a method, results of the Lan theory (ref. 29) are presented by the dashed curves in figure 13. At a flap deflection of 0° , there is excellent agreement between theory and experiment; at 20° flap deflection, the values of the theoretical and experimental lift coefficient are similar, but the theoretical lift-curve slope is low. At the highest flap deflection, 60° , the values of the theoretical lift coefficient are high and the slope is low. While these results represent an improvement over jet-flap theory, there is room for further improvements which may come from additional use of these methods.

CONCLUDING REMARKS

The progress of propulsive-lift theory began in 1956 with Spence's simple two-dimensional jet-flap computation which represented a back-of-the-envelope computation. In the early sixties, limited three-dimensional jet-flap methods which usually assumed an elliptic spanload were developed and required the use of a modest digital computer, such as an IBM 709. In the early seventies, more general three-dimensional jet-flap, wing-plus-jet, and transonic two-dimensional theories which account for shock effect were developed. These require large digital computers, such as the CDC 6600. For future applications, methods for complete wing-body-tail configurations that use either the three-dimensional jet-flap or wing-plus-jet theory will be needed. There is also a need to develop transonic three-dimensional powered-lift theories. Ultimate solutions for propulsive-lift configurations may require the formulation of this problem using the Navier-Stokes equations. To solve these problems properly, the use of very large digital computers which are capable of solving matrices and vectors which contain up to 10 000 elements will be required.

REFERENCES

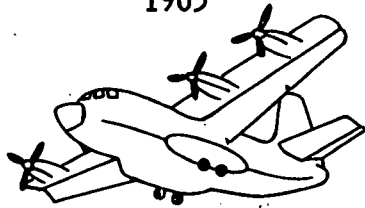
1. Lowry, John G.; Riebe, John M.; and Campbell, John P.: The Jet-Augmented Flap. Preprint No. 715, S.M.F. Fund Paper, Inst. Aeronaut. Sci., Jan. 1957.
2. Spence, D. A.: The Lift Coefficient of a Thin, Jet-Flapped Wing. Proc. Roy. Soc. (London), ser. A, vol. 238, no. 1212, Dec. 4, 1956, pp. 46-68.
3. Spence, D. A.: Some Simple Results for Two-Dimensional Jet-Flap Aerofoils. Aeronaut. Quart., vol. IX, pt. IV, Nov. 1958, pp. 395-406.
4. Maskell, E. C.; and Spence, D. A.: A Theory of the Jet Flap in Three Dimensions. Proc. Roy. Soc. (London), ser. A, vol. 251, no. 1266, June 9, 1959, pp. 407-425.
5. Hartunian, Richard A.: The Finite Aspect Ratio Jet Flap. Rep. No. A1-1190-A-3 (Contract No. DA 44-177-TC-439), Cornell Aeronaut. Lab., Inc., Oct. 1959.
6. Das, A.: Theoretical and Experimental Testing on Jet Flap Wings. Part I: Testing of a Rectangular Wing at Various Aspect Ratios. NASA TT F-13715, 1971.
7. Kerney, Keith Prior: An Asymptotic Theory of the High-Aspect-Ratio Jet Flap. Ph. D. Thesis, Cornell Univ., 1967.
8. Tokuda, Naoyuki: An Asymptotic Theory of the Jet Flap in Three Dimensions. J. Fluid Mech., vol. 46, pt. 4, 1971, pp. 705-726.
9. Kida, Teruhiko; and Miyai, Yoshihiro: Jet-Flapped Wings in Very Close Proximity to the Ground. AIAA J., vol. 10, no. 5, May 1972, pp. 611-616.
10. Adessio, F. L.: Theory of an Airfoil Equipped With a Jet Flap Under Low-Speed Flight Conditions. Ph. D. Diss., Purdue Univ., 1974.
11. Margason, Richard J.; and Lamar, John E.: Vortex-Lattice FORTRAN Program for Estimating Subsonic Aerodynamic Characteristics of Complex Planforms. NASA TN D-6142, 1971.
12. Lissaman, Peter B. S.: Analysis of High-Aspect-Ratio Jet-Flap Wings of Arbitrary Geometry. NASA CR-2179, 1973.
13. Lopez, M. L.; and Shen, C. C.: Recent Developments in Jet Flap Theory and Its Application to STOL Aerodynamic Analysis. AIAA Paper No. 71-578; June 1971.
14. Clever, W. C.: A Vortex Lattice Program for Jet Flapped Airfoils. TFD-73-70, Los Angeles Div., North American Rockwell, Jan. 26, 1973.
15. Goldhammer, M. I.; Lopez, M. L.; and Shen, C. C.: Methods for Predicting the Aerodynamic and Stability and Control Characteristics of STOL Aircraft. Volume I - Basic Theoretical Methods. AFFDL-TR-73-146-Vol. I, U.S. Air Force, Dec. 1973.

16. Hackett, J. E.; and Lyman, V.: The Jet Flap in Three Dimensions: Theory and Experiment. AIAA Paper No. 73-653, July 1973.
17. Holmes, A. E.; Barnett, Lane; and Jacobs, Willi F.: Application of the Equivalent Mechanical Flap Concept to Jet Flapped Wing-Body Combinations. ARL-TR-74-0136, U.S. Air Force, 1974.
18. Malmuth, N. D.; and Murphy, W. D.: A Relaxation Solution for Transonic Flow Over Jet Flapped Airfoils. AIAA Paper 75-82, Jan. 1975.
19. Ives, D. C.; and Melnik, R. E.: Numerical Calculation of the Compressible Flow Over an Airfoil With a Jet Flap. AIAA Paper No. 74-542, June 1974.
20. Williams, J.; and Alexander, A. J.: Three-Dimensional Wind-Tunnel Tests of a 30° Jet Flap Model. C.P. No. 304, British A.R.C., 1957.
21. Williams J.; Butler, S. F. J.; and Wood, M. N.: The Aerodynamics of Jet Flaps. R. & M. No. 3304, Brit. A.R.C., 1963.
22. Johnson, William G., Jr.; and Kardas, Gerald E.: A Wind-Tunnel Investigation of the Wake Near the Trailing Edge of a Deflected Externally Blown Flap. NASA TM X-3079, 1974.
23. Hirsh, Richard S.: Calculation of Supersonic Three-Dimensional Free-Mixing Flows Using the Parabolic-Elliptic Navier-Stokes Equations. Aerodynamic Analyses Requiring Advanced Computers, Part I, NASA SP-347, 1975, pp. 543-565.
24. Shollenberger, C. A.: Analysis of the Interaction of Jets and Airfoils in Two Dimensions. J. Aircraft, vol. 10, no. 5, May 1973, pp. 267-273.
25. Davenport, F. J.; and Hunt, D. N.: Deflection of a Thick Jet by a Convex Surface: A Practical Problem for Powered Lift. AIAA Paper No. 75-167, Jan. 1975.
26. Putnam, Lawrence E.: An Analytical Study of the Effects of Jets Located More Than One Jet Diameter Above a Wing at Subsonic Speeds. NASA TN D-7754, 1974.
27. Dillenius, Marnix F. E.; Mendenhall, Michael R.; and Spangler, S. B.: Calculation of the Longitudinal Aerodynamic Characteristics of STOL Aircraft With Externally-Blown Jet-Augmented Flaps. NASA CR-2358, 1974.
28. Shollenberger, C. A.: A Three-Dimensional Wing/Jet Interaction Analysis Including Jet Distortion Influences. AIAA Paper No. 73-655, July 1973.
29. Lan, C. Edward: An Analytical Investigation of Wing-Jet Interaction. CRINC-FRL 74-001 (NASA Grant NGR 17-002-107), Univ. of Kansas, Apr. 1974. (Available as NASA CR-138140.)

30. Perry, Boyd, III; and Greene, George C.: Wind-Tunnel Investigation of Aerodynamic Loads on a Large-Scale Externally Blown Flap Model and Comparison With Theory. NASA TN D-7863, 1975.
31. Smith, Charles C., Jr.; Phelps, Arthur E., III; and Copeland, W. Latham: Wind-Tunnel Investigation of a Large-Scale Semispan Model With an Unswept Wing and an Upper-Surface Blown Jet Flap. NASA TN D-7526, 1974.

PROPELLER POWERED

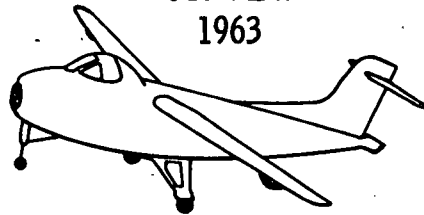
DEFLECTED SLIPSTREAM
1965



JET POWERED

JET-FLAP EXPERIMENTS SINCE EARLY 1930'S
GERMAN, BRITISH, AMERICAN

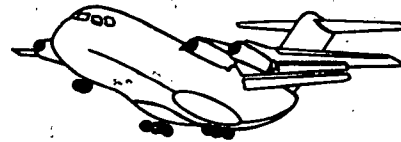
JET FLAP
1963



AUGMENTOR FLAP
1972



EXTERNALLY BLOWN FLAP
1975



UPPER-SURFACE BLOWN FLAP
1976



Figure 1.- Configurations with propulsive lift.

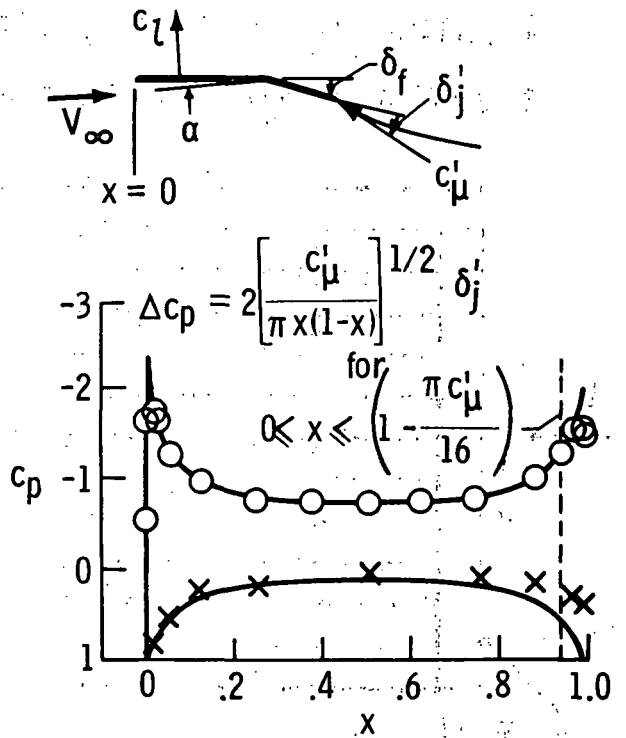
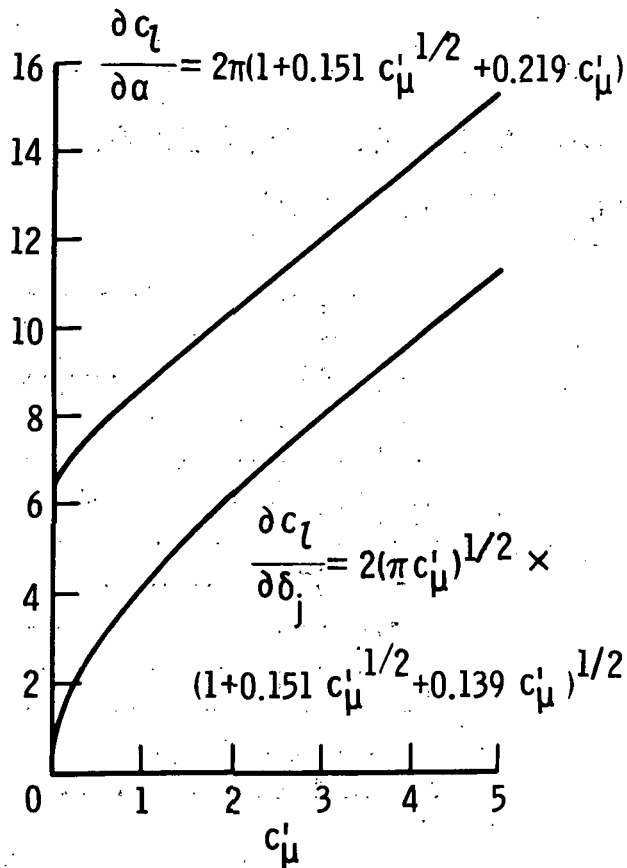


Figure 2. - Variation of lift and pressure coefficients according to Spence's two-dimensional jet-flap theory.

- $\nabla^2 \phi = 0$ INVISCID, INCOMPRESSIBLE FLOW
- LIFTING-LINE OR LIFTING-SURFACE INFLUENCE COEFFICIENT METHODS
- WING AND WAKE COUPLED BY SPENCE JET-FLAP EQUATIONS

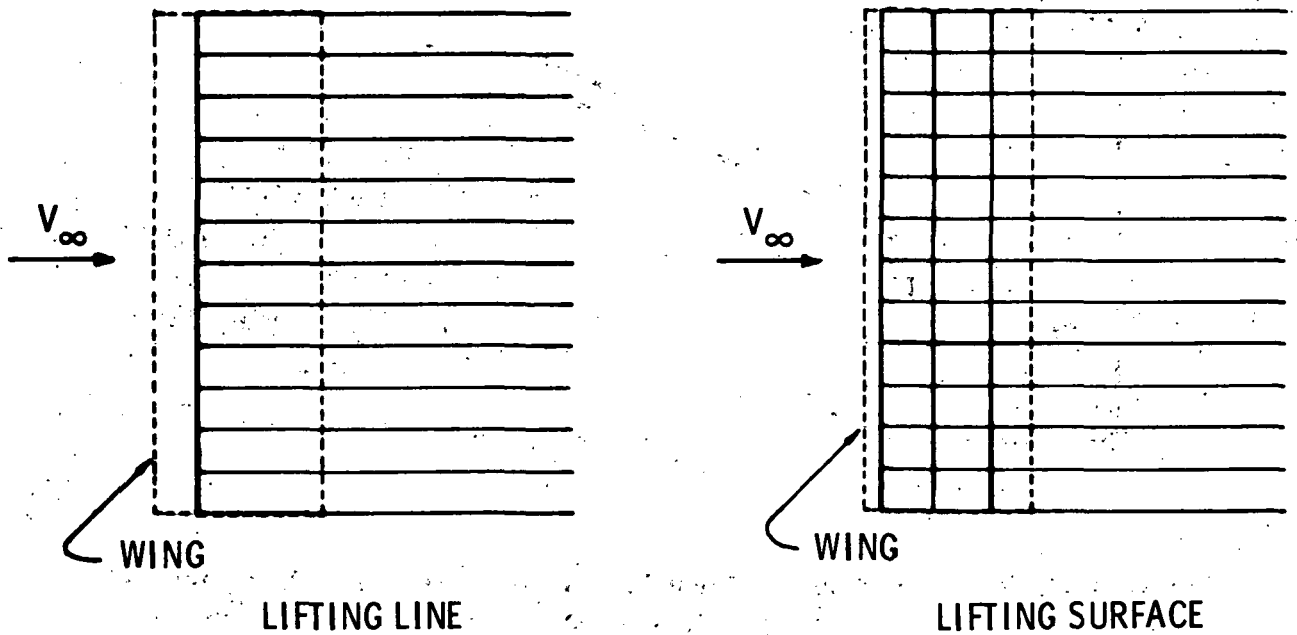


Figure 3.- Schematic of three-dimensional jet-flap wing methods.

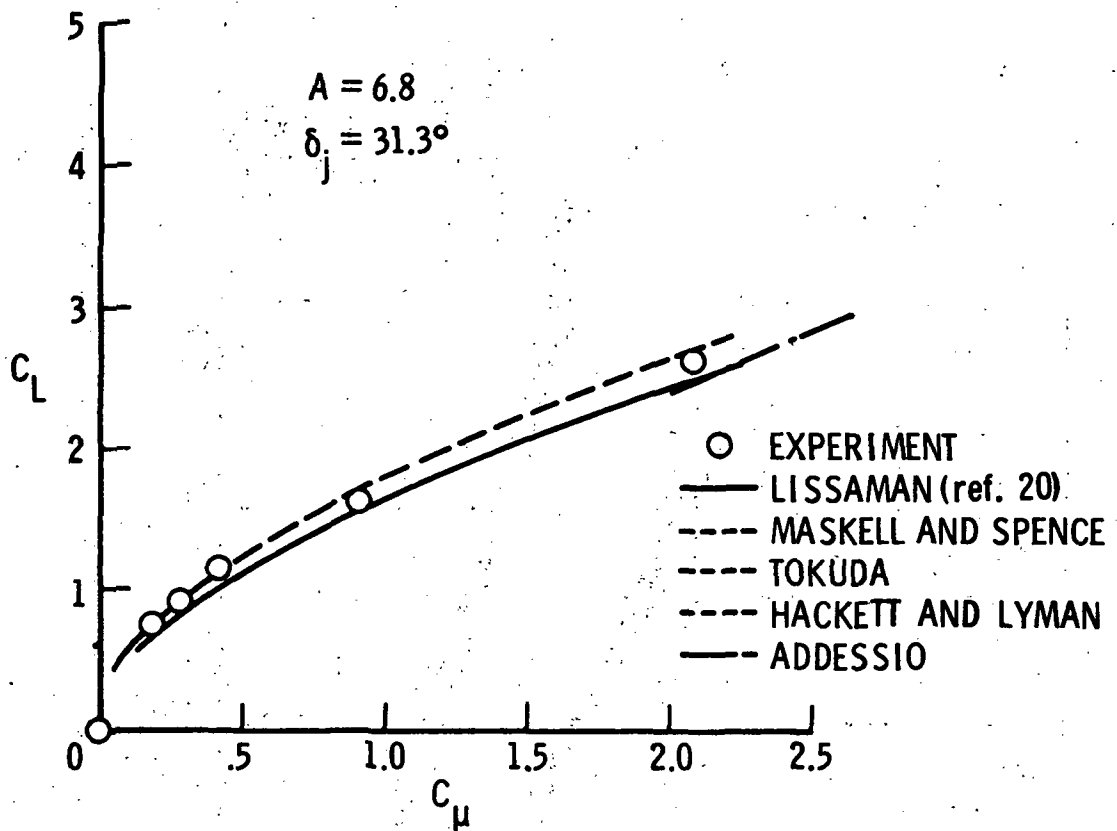


Figure 4.- Comparison of three-dimensional jet-flap theories with experiment (full-span flap).

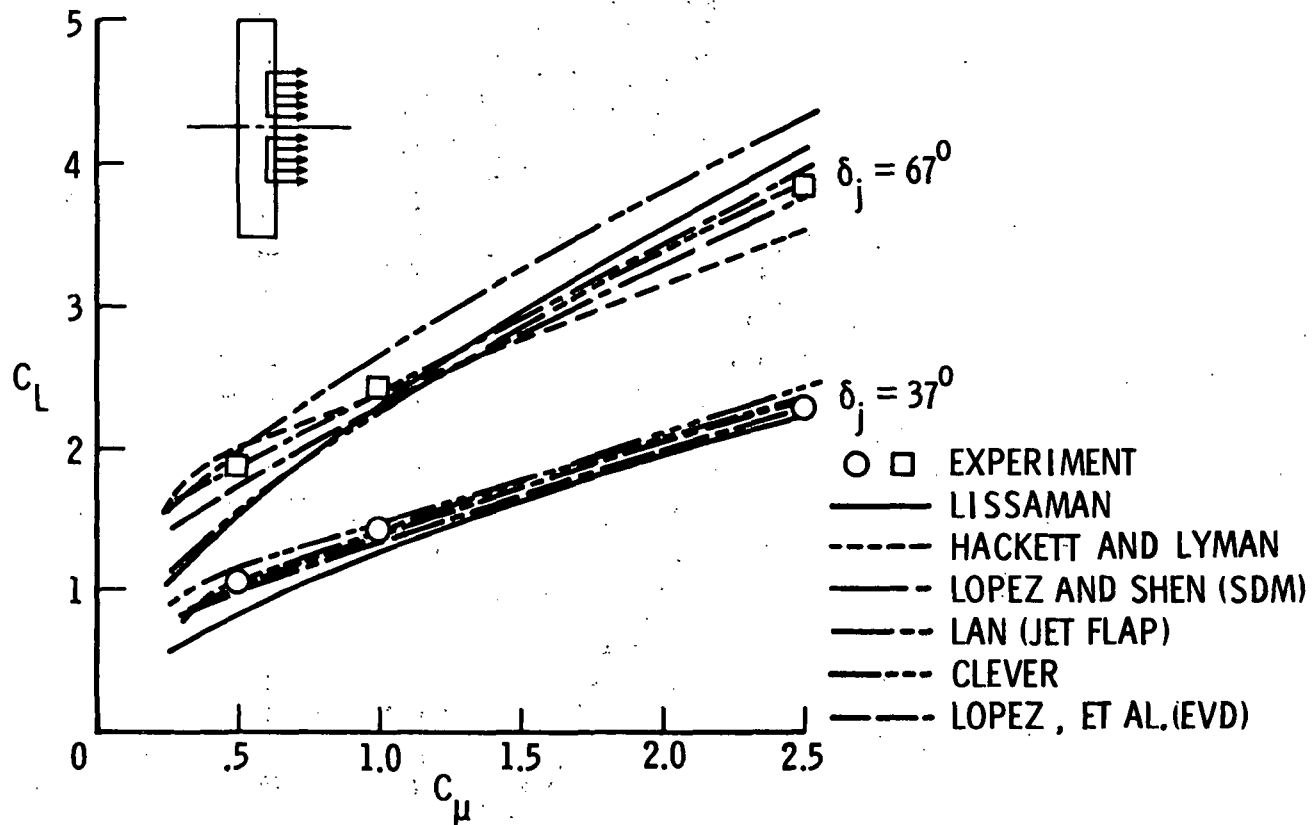


Figure 5.- Comparison of jet-flap theories with experiment for a partial-span flap.

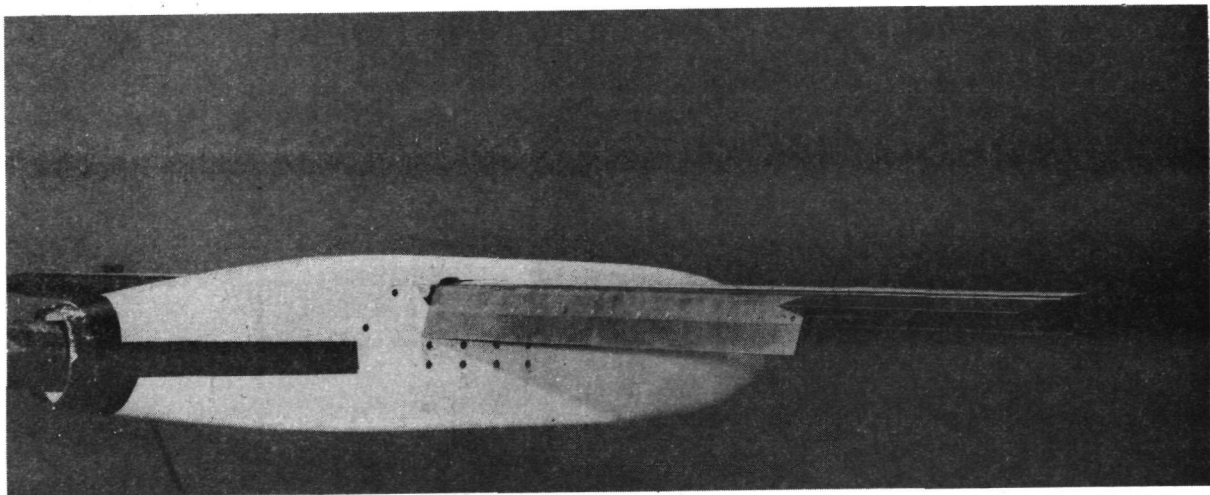


Figure 6.- NASA/USAF jet-flap theory verification model.

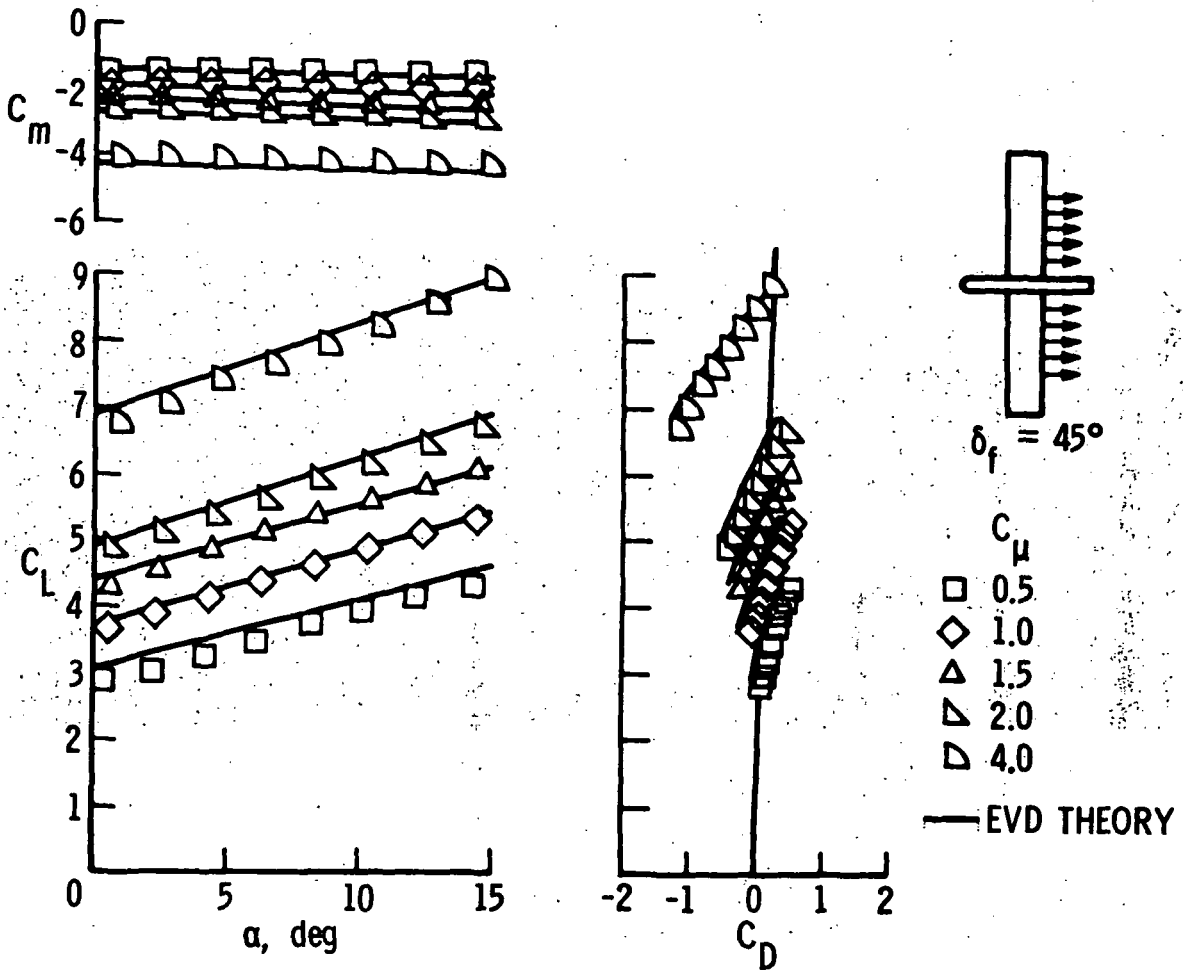


Figure 7.- Comparison of EVD jet-flap theory with experimental data for model of figure 6. Two-thirds span blowing.

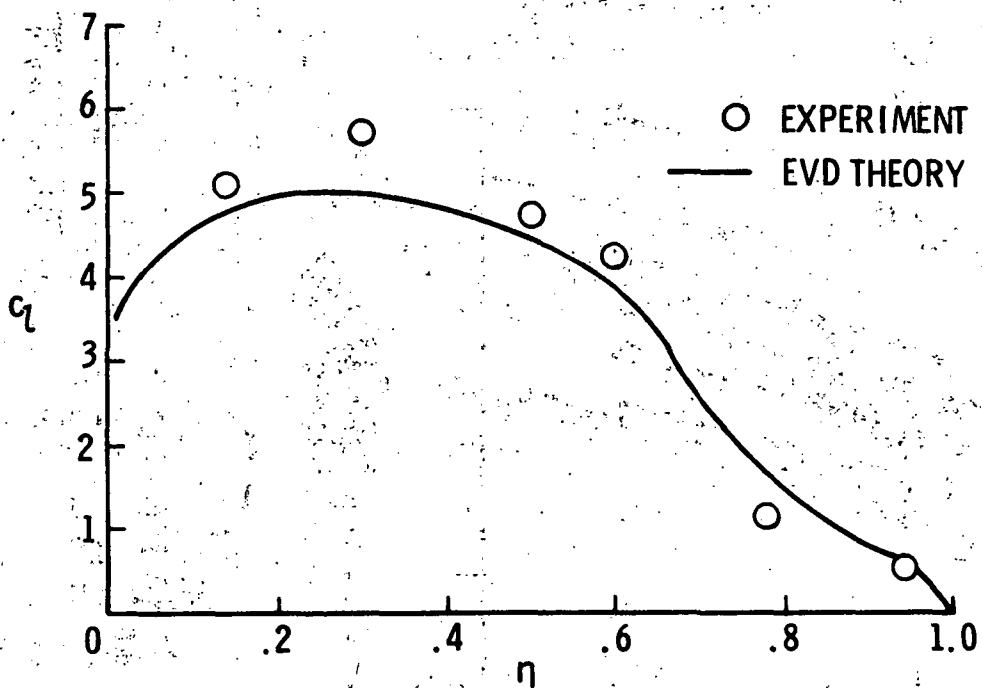


Figure 8. - Comparison of theoretical and experimental spanwise lift distribution for model of figure 6. Two-thirds span blowing; $C_{\mu} = 4$; $\delta_f = 45^\circ$; $\alpha = 0^\circ$.

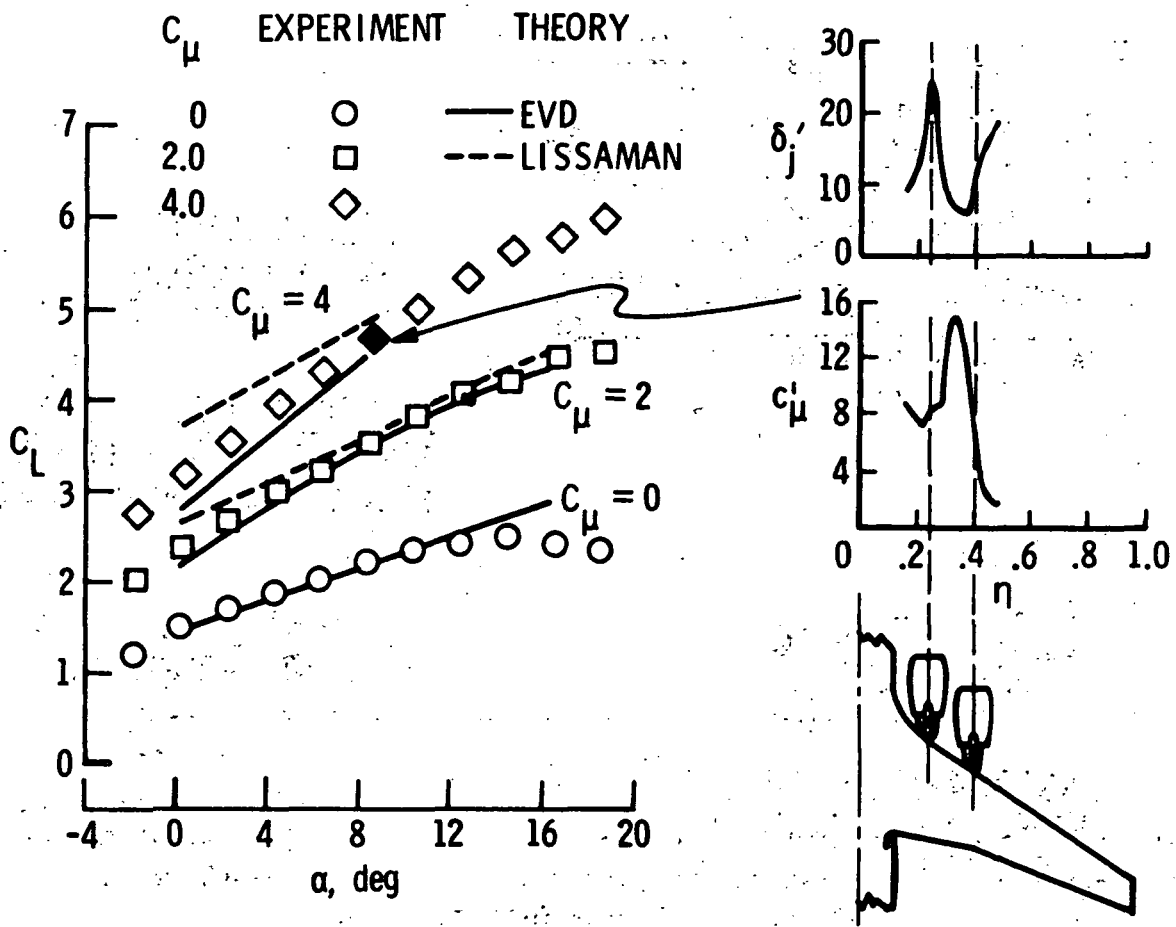
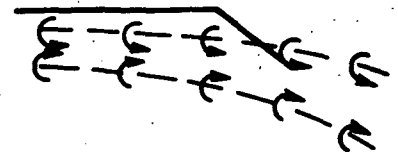
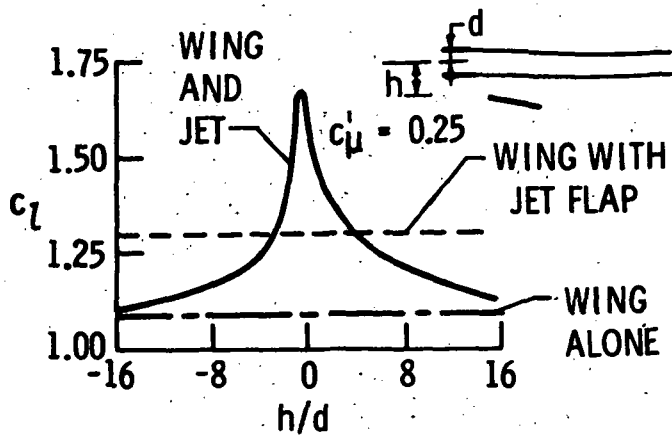
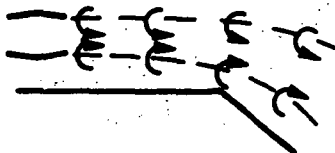


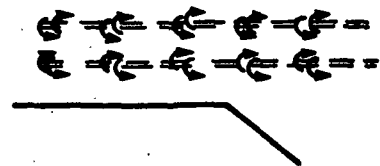
Figure 9.- Comparison of jet-flap theory with experimental data for an externally blown flap configuration.



DILLENIOUS ET AL. - VORTEX STRENGTHS AND JET CROSS-SECTION SHAPE PRESCRIBED



SHOLLENBERGER - VORTEX STRENGTHS AND JET SHAPE CALCULATED



LAN - VORTEX STRENGTHS CALCULATED

Figure 10. - Theories for wing plus jets.

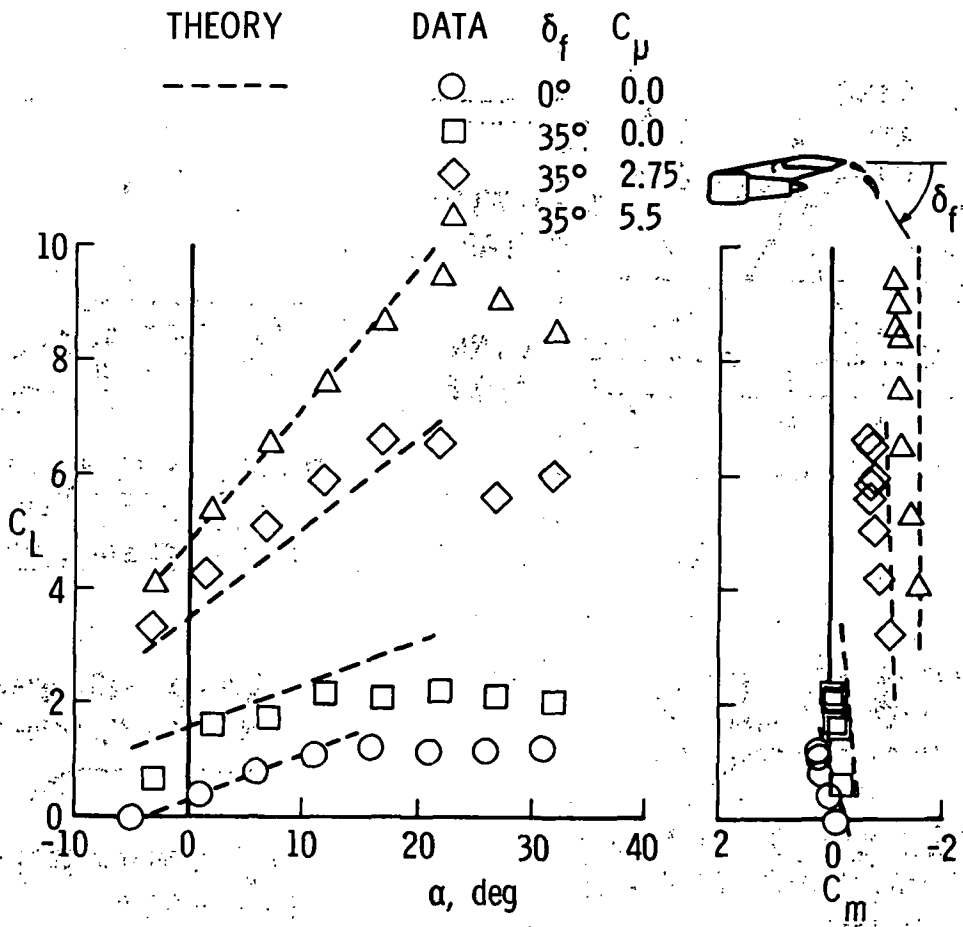


Figure 11.- Use of the wing-jet theory of reference 27 to predict lift and pitching-moment characteristics of an externally blown flap configuration.

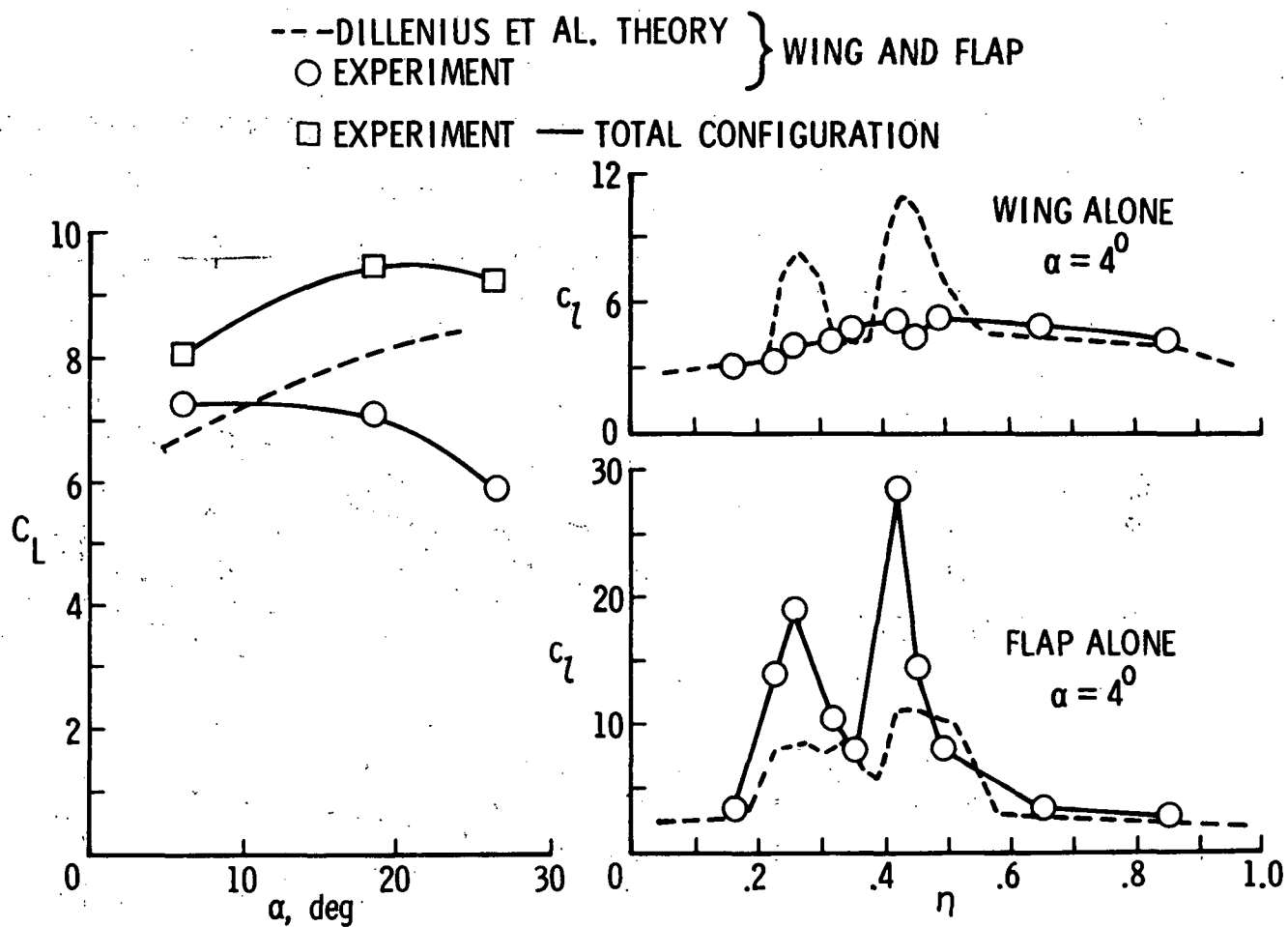


Figure 12.- Use of the theory of reference 27 to predict section and overall lift coefficients for an externally blown flap configuration. $C_{\mu} = 4$.

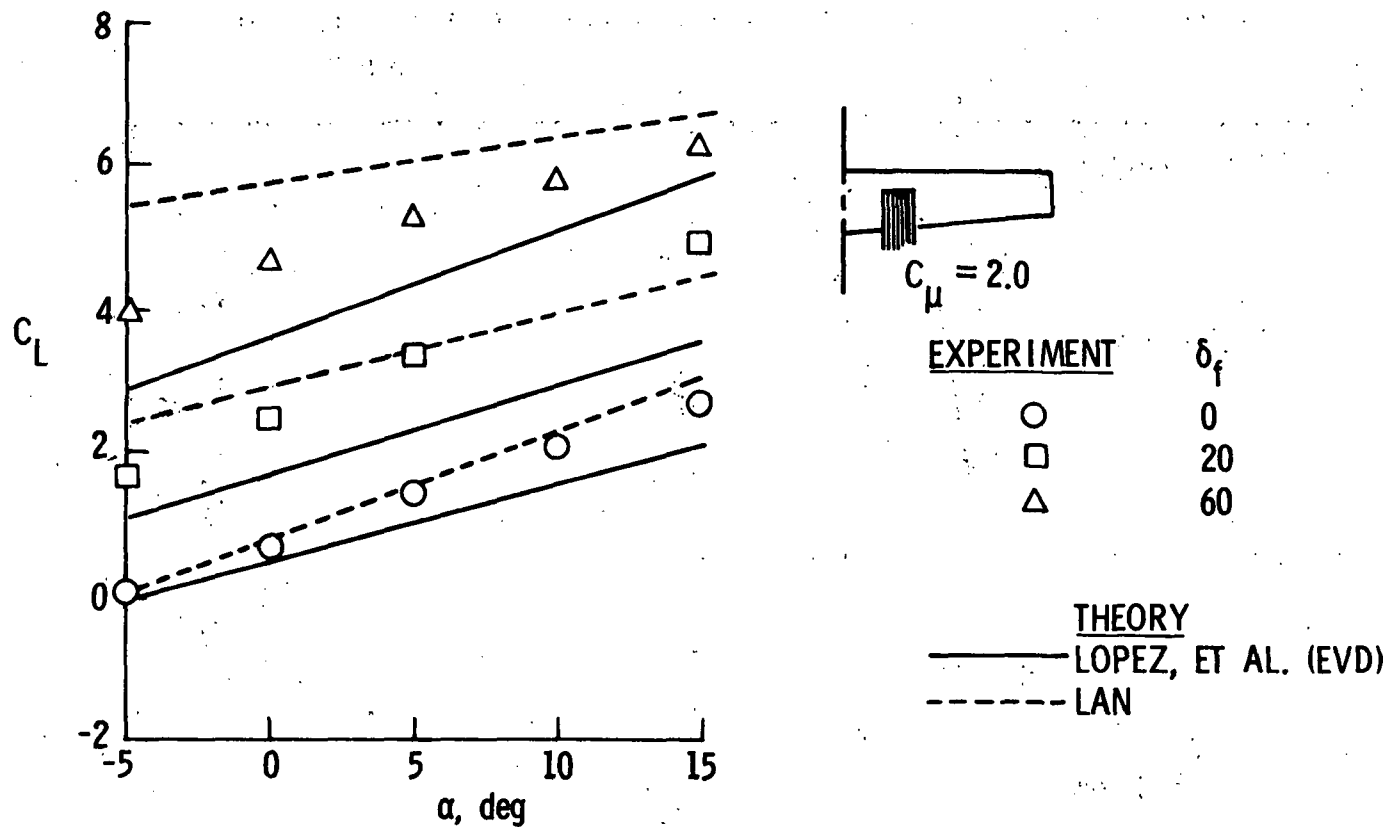


Figure 13. - Comparison of theoretical and experimental lift curves for an upper-surface blowing configuration.

Page intentionally left blank

SURVEY OF COMPUTATIONAL METHODS FOR LIFT-GENERATED WAKES

By Vernon J. Rossow
NASA Ames Research Center

SUMMARY

The persistence and strength of vortices that trail behind heavy aircraft have recently caused attention to be focused on the potential hazard they present to smaller aircraft that might encounter them. A survey is made here of some computational methods that are used to predict the structure and duration of these lift-generated vortices and to explore mechanisms that might significantly reduce their lifetime and hazard potential.

INTRODUCTION

Large aircraft leave behind them substantial disturbances to the air that may pose a hazard to smaller aircraft entering that airspace. The turbulence in the wake caused by engine exhaust dissipates rather quickly, but the circular motions produced by the wing-tip vortices persist for distances of the order of miles behind the generating wing. During cruise, aircraft can usually be separated laterally and vertically to avoid encountering one another's wake, but near airports the aircraft are usually confined to a relatively few entry and exit corridors, so that the probability of encountering the wake of a preceding aircraft is greatly increased.

In the early 1950's concern was expressed when the DC-6B was put into operation because it was a new large aircraft. A rather complete analysis of the hazard in the wake of the DC-6B aircraft by Bleviss (ref. 1) concluded that the hazard is due to the wake vortices and not the "propwash," and that the vortices decay very slowly. The suggested solution was to increase the separation between aircraft. This solution is no longer acceptable because the increase in air traffic volume at airports has brought about the desire for decreased aircraft spacing. A decrease in spacing with the present large variation in aircraft size and without a compromise in safety of flight can be accomplished either by locating the hazardous volumes posed by the vortices and directing the aircraft around them or by changing the lift-generated wake so that the hazardous distance behind the generator is substantially decreased. The FAA and Transportation System Center (DOT) have concentrated their efforts on the development of avoidance systems. NASA is studying means for aerodynamic alleviation of the hazard

posed by lift-generated wakes. This paper discusses some of the theoretical methods used to analyze lift-generated wakes and will not discuss avoidance schemes. Although the theoretical methods used at NASA Ames Research Center rely heavily on electronic computers, the programs are not of a size that requires large advance computers. However, as refinements are made in the methods used to analyze complex wakes with multiple vortex pairs, larger and faster computers will probably expedite the research effort. Since the survey as given here does not cover all the literature on wake vortices, the reader is referred to references 2 to 4 for a more complete bibliography.

It is convenient to divide the flow field into the several regions shown in figure 1. Each of these regions and some methods for analyzing the properties will be discussed briefly in the following sections. It should be noted in figure 1 that the vortices are shown as extending straight behind the generating aircraft. Distortions due to atmospheric motions (ref. 5) and due to various instabilities (e.g., refs. 2 and 6) will not be discussed. It is assumed here that the alleviation achieved by aerodynamic means must also be effective even under calm conditions.

SYMBOLS

AR	aspect ratio
b	span of wing
C_L	lift coefficient, $\frac{\text{Lift}}{\frac{1}{2}\rho U_\infty^2 S}$
C_ℓ	local lift coefficient
C_l	rolling-moment coefficient, $\frac{\text{Rolling moment}}{\frac{1}{2}\rho U_\infty^2 S b}$
c	wing chord
\bar{c}	mean geometric chord
$f(\Gamma_0/\nu)$	Reynolds number function
$\ell(y)$	local lift

N	number of vortices
r	radius of vortex
S	wing area
T	dimensionless time
t	time
U_∞	free-stream velocity, aligned with x-axis
V_1	maximum circumferential velocity in vortex
v_θ	circumferential velocity in vortex
X, Y, Z	dimensionless coordinates, e.g., $X = 2x/b$
x, y, z	coordinates, x is streamwise and z is vertical
α	angle of attack
Γ	circulation
γ	circulation in point vortex
ν	kinematic viscosity
ρ	air density

Subscripts:

f	following model that encounters wake
g	model that generates wake
o	centerline value of circulation
v	vortex

A bar over a coordinate indicates the center of gravity of vortex.

GENERATION OF WAKE

If the vortex wake calculations are to be meaningful, the starting conditions at the generator must be known as accurately as possible because the rest of the calculations depend on those data. That is, the properties of the wake are predicted only as completely as the analysis of the generator aircraft is carried out. This aspect of the wake-vortex problem has received considerable attention during the past several decades, but a general method for finding the complete wake is not yet available. However, very good approximations to the lift-distribution and wake starting conditions may be obtained by use of inviscid vortex-lattice computer programs. The status of these methods can be found in references 7 to 9. Efforts are currently being made to include the effect of the rollup of the wake on the lift distribution (e.g., refs. 10 and 11). The comparisons in figure 2 prepared by Brian Maskew at Ames Research Center show that the rollup of the vortex sheet can affect the span loading substantially at the wing tips when the wing is at high angles of attack. The agreement of that prediction with the experimental span-loading measurements of Chigier and Corsiglia (ref. 12) is much better than the result obtained when the vortex wake is assumed to remain flat. Such a change in span loading has an effect on total lift, but the much larger effect appears in the distribution of vorticity in the wake. Caution should therefore be exercised when a flat wake is assumed in calculating the span loading on the generating wing because the loading gradients at the wing tip may not represent the correct concentration of vorticity. Most of the wind-tunnel studies at Ames Research Center were made at small angles of attack so the accuracy of the flat wake approximation was adequate. For these calculations, a modified version of a program by Hough (ref. 13) was used.

CONVENTIONAL WAKES

The first part of the discussion on the dynamics of vortex wakes will be restricted to wakes produced by approximately elliptical spanwise loadings on the generating wing. They are called conventional because most aircraft have this kind of loading, so that the wake then consists of two vortices of opposite sign. Immediately behind the generating wing these wakes often contain a number of small vortices that originate from flap edges, pylons, and so forth. In the far field, only two vortices are found because the weaker vortices merge with the stronger wing-tip vortices to form a single vortex pair that is quite stable and persists for a large number of span lengths behind the generator. In an

effort to reduce the wake-vortex problem, the second part of this discussion treats unconventional wakes produced by span loadings that differ appreciably from elliptic.

Near-Field Wake Structure

The vorticity distribution in the wake immediately behind the lift-generating surfaces usually changes rapidly from a flat spanwise distribution into two circular regions of vorticity. (See fig. 3.) This reshaping process is usually referred to as the rollup of the wake or vortex sheet shed by the wing. Ideally, it would be desirable to treat the rollup of the distributed vorticity by a numerical scheme that includes the boundary layer on the wing, fuselage, and other surfaces along with the drag of the landing gear and the thrust of the engines. Since this technology is not available and would probably be quite cumbersome to operate if it were, most researchers resort to the very approximate method introduced by Rosenhead (ref. 14) and Westwater (ref. 15) over 40 years ago. As is well known, the continuous vorticity distribution in the wake is approximated by a number of two-dimensional point vortices so that the reshaping of the wake distribution can be solved as a two-dimensional time-dependent problem in the so-called Trefftz plane (fig. 3). An example of an elliptically loaded wing is presented in figure 4 (taken from ref. 16). Estimating the wake restructuring by such a time-dependent method has two principal difficulties. The first is to assess the numerical accuracy of the calculations and the second is to interpret the results.

A variety of papers have been written to elaborate on the shortcomings of the method and to introduce ways to remedy these shortcomings (e.g., refs. 17 to 24). These discussions generally agree that the spiral shape at the edges of vortex sheets is often not well simulated by the vortex array and that the point vortices sometimes undergo excursions believed to be associated with the vortex array and not with the vortex sheet being represented. Several methods have been introduced recently (refs. 21 to 23) to stabilize these vortex motions and to eliminate the excursions believed not to be a part of the vortex-sheet structure. Although these techniques suppress vortex excursions and sheet kinking, they also introduce another error source. The use of finite cores in the vortices suggested by Chorin and Bernard (ref. 21) and Kuwahara and Takami (ref. 22) or the accumulation of vortices at the center of the spiral as suggested by Moore (ref. 23) all contain arbitrary parameters that are not related to the conservation equations for the fluid they are to represent. The computed results may then appear more reasonable than those obtained from point vortices, but the quantitative accuracy is uncertain. Finite vortex cores instead of point vortices were used in some of the cases analyzed, and the vortex motions were smoothed. The qualitative nature of the solutions was found not to change if the core radius chosen for the vortices was less than the initial spacing of the vortices. However, the vortex motions were found to depend on the core size chosen.

Numerical accuracy. - The motion of a number of two-dimensional point vortices in an incompressible fluid is a problem for which numerical calculations are known to be unstable; consequently, any initial error grows with each time step. For this reason, the calculations are usually begun with a large number of significant figures (double precision on most computers) in the hope that the desired result can be achieved before accumulated errors wipe out all the accuracy. It is also essential that the accuracy or error accumulation be monitored during the calculations to detect an inappropriate choice of mesh size or excessive error growth. For example, Westwater (ref. 15) used the first moment of vorticity as an indicator of accuracy. When suitable error monitors are used, it is possible to determine whether seemingly unrealistic results are attributable to numerical error or to properties of the vortex array being analyzed.

Three error monitoring parameters are used in the calculations made at Ames:

- (1) The first moment of vorticity for each side (to reduce the likelihood of compensating errors due to symmetry):

$$\bar{y}\Gamma_0 = \bar{y} \sum_{j=1}^{N/2} \gamma_j = \sum_{j=1}^{N/2} y_j \gamma_j \quad (1)$$

- (2) The second moment of vorticity J about the center of gravity for the vortices on each side:

$$J = \sum_{j=1}^{N/2} \left[(y_j - \bar{y})^2 + (z_j - \bar{z})^2 \right] \gamma_j \quad (2)$$

- (3) The Kirchhoff-Routh path function W_r for the entire array of vortices:

$$W_r = \sum_{i=1}^{N-1} \sum_{j=i+1}^N \left(\frac{\gamma_i \gamma_j}{4\pi} \right) \ln \left[(y_i - y_j)^2 + (z_i - z_j)^2 \right] \quad (3)$$

Note that none of these quantities are used in the time-dependent calculations nor do they depend on the numerical integration scheme used. They are continually evaluated (usually after every 10 or 20 steps) to ascertain how much error has accumulated in the positions of the assembly of vortices. It was found that the Kirchhoff-Routh path function was the first to indicate the presence of errors in the calculations and that the first moment of vorticity was hardly ever affected. That is, the first moment is the least sensitive of the three accuracy monitors. When enough significant figures are retained in the results to cover the plotting accuracy, the gross aspects and trends of the vortex sheet observed in various experiments appear to be modeled correctly.

Interpretation of data. - The interpretation of the point vortex distribution in terms of a continuous distribution is not straightforward. A technique from reference 16 provided a vortex structure when a group of point vortices in the wake were known to be associated with a given rotational motion, e.g., vortices on one side of an elliptically loaded wing. Within each such group, the distribution of point vortices was first reinterpreted as a stepwise radial distribution of circulation about the centroid of vorticity for one side of the wing. This was done by assuming that the vorticity associated with a point vortex in the array is spread uniformly on a ring with a radius equal to the distance of the vortex from the centroid. As indicated in figure 5, the resulting stepwise curve for circulation as a function of radius agrees quite well with the variation predicted by Betz' theory (refs. 25 and 26) for elliptic loading even though rollup is not entirely completed (fig. 4(b)). A faired curve through the stepwise variation could then be used to determine the circumferential velocity distribution in the vortex.

Direct- and Inverse-Rollup Theories

Direct-rollup theory. - A theoretical tool frequently used to study the circumferential velocity distribution in lift-generated vortices is the simple rollup method of Betz (ref. 25). His theory is based on the conservation equations for inviscid, two-dimensional vortices and relates the circulation in the fully developed vortex to the span loading on the generating wing. The simplicity of the method results from the assumptions that the vortex is completely rolled up and that the rollup process is inviscid. In order to achieve a unique result, the vortex sheet is assumed to roll up in an orderly fashion from the wing tip inboard, so that successive layers of the sheet are wrapped around the center and over previous wrappings. (See fig. 3.) Any axial or streamwise variation in the flow velocity is assumed to have a negligible effect on the rollup process. The Betz method does not treat the transition or intermediate stages between the initial vortex sheet behind the wing and the final rolled-up vortex structure. When the derivation is completed (e.g., ref. 26), the vortex structure is related to the span loading on the generating wing by

$$\Gamma_v(r_1) = \Gamma_w(y_1) \quad (4)$$

where the radius in the vortex r_1 is related to a spanwise station on the wing y_1 by

$$r_1 = -\frac{1}{\Gamma_w(y_1)} \int_{b/2}^{y_1} \Gamma_w(y) dy \quad (5)$$

The symbol Γ_w denotes the bound circulation on the wing, and Γ_v , the circulation in the fully developed vortex. Although the Betz theory does not appear to have been used extensively for a number of years after its first derivation, it has recently been demonstrated by Donaldson et al. (refs. 27 and 28) to be useful and often more accurate than

more complex methods. The favorable publicity given to Betz' method by Donaldson led to an elaboration of the theory and more examples by Mason and Marchman (ref. 29) and to use by Brown (ref. 30) of the rollup theory to predict the axial flow velocity in the vortex. Another example of the good representation provided by the inviscid rollup theory is presented in figure 6. The experimental data (ref. 31) were obtained with a three-component hot-wire probe, and the span loading for the Betz calculation was obtained with a vortex-lattice theory (ref. 13). It appears that viscous effects have not altered the vortex structure appreciably.

Inverse rollup theory. - As more experimental velocity data were accumulated with the ground-based facilities (refs. 31 and 32), it became desirable to relate the vortex structure backward to the span loading on the wing that generated the vortex. This led to what might be called an inverse Betz method (ref. 33) which is based on the same basic equations and assumptions as the direct Betz method. The derivation is begun with the expression presented previously that relates the radius r_1 in the vortex to the spanwise station on the wing y_1 which contains a given amount of circulation. After some simple manipulations and because the vortex is axially symmetric, so that the circulation may be written as $\Gamma_v = 2\pi r_1 v_\theta$, the inverse relationship becomes

$$\frac{b}{2} - y_1 = r_1 + \int_0^{r_1} \frac{d(rv_\theta)}{v_\theta} \quad (6)$$

where v_θ is the measured circumferential velocity in the vortex.

Two sample cases presented in figures 7(a) and 7(b) include the measured vortex structure, the span loading inferred from these measurements by the inverse rollup method, and, for comparative purposes, the span loading predicted by vortex-lattice theory. These results show that the inverse rollup theory can recover the span loading on the generating wing fairly accurately. With almost all configurations a difference occurs near the wing tip as a result of the finite core size and solid-body rotation in the vortex near $r = 0$. The magnitude of the distortion in span loading depends on the size of the core, which is influenced by the character of the boundary layer on the wing and on the viscous and turbulent shear forces in the vortex itself. In most cases, these distortions appear to be small and to occur only near the wing tip.

Region of applicability of rollup theories. - The simplicity of both the direct and the inverse rollup methods results from the assumptions that the vortex is completely rolled up and that the rollup process is inviscid. These two assumptions then limit the downstream interval over which the theories apply. The upstream end of the region of applicability begins where the rollup of the vortex sheet is largely completed and can be estimated by use of inviscid, time-dependent rollup calculations. Results such as those in figures 6 and 10 of Rossow (ref. 16) indicate that a major part of the rollup process

behind many wings can be considered as practically complete within three to five span lengths behind the generating wing.

The downstream end of the region of applicability is the distance at which viscous and turbulent decay of the vortex has modified its structure to the extent that the inviscid theory no longer approximates it. An estimate for this limit can be obtained from the recent data of Ciffone and Orloff (ref. 32) wherein a so-called plateau region (to be discussed in the next section) is identified. Within this plateau region, they found that the vortex decays very little, but it is followed by a region where the vortex decays roughly as $t^{-1/2}$. These considerations suggest that the region of applicability of the Betz method lies between about three span lengths and the downstream end of the plateau region, which is estimated from the data of Ciffone and Orloff (ref. 32). Another consequence of the inviscid rollup assumption is that excessively high velocities are often predicted at and near the center of the vortex. Nevertheless, comparisons made by Donaldson et al. (refs. 27 and 28) have shown that outside the core region (radius of maximum circumferential velocity), the Betz rollup theory yields reliable estimates for the vortex structure.

Plateau and Decay Regions for Isolated Vortex

The accuracy with which both the inviscid direct and inverse Betz methods relate the span loading to the vortex structure suggests that either the early history of the vortex is nearly inviscid or that the decay process is very slow. The correct interpretation appeared when the circumferential velocity was measured by Ciffone and Orloff (ref. 32) at a number of stations behind several generating wings. Figure 8, taken directly from their paper, shows that the maximum circumferential velocity is essentially unchanged for approximately 40 span lengths behind those three wings. The expected decay of the vortex, which is inversely proportional to the square root of distance, then begins to occur. The two straight lines for each configuration shown in figure 8 approximate the data in each region, and the sharp corner at their intersection is not intended to approximate the transition between the two regimes. The presence of both a plateau (nearly inviscid) and decay region is also indicated in Donaldson's analysis (ref. 34) of the decay of a vortex using his second-order closure model for turbulence. Since a wide variety of wing planforms all exhibited the same characteristic plateau and decay regions, Iversen (ref. 35) set about finding an explanation for the onset of decay. By using a self-similar turbulent vortex, he was able to correlate the data obtained in ground-based facilities and in flight into the single curve shown in figure 9 (taken from Iversen, ref. 35). The variation of the Reynolds number function $f(\Gamma_0/\nu)$ (fig. 10) shows that it is conveniently 1.0 for Reynolds numbers over 10^6 . From the data of reference 32 and these correlation functions, Ciffone (ref. 36) has developed an empirical relationship that makes it possible to predict easily the peak swirl velocity in vortices. The information gained by Iversen

(ref. 35) and Ciffone (ref. 36) was then extended by Iversen in reference 37 to a numerical analysis of an isolated vortex using a mixing length model for the eddy viscosity. The initial data for the structure of the vortex were obtained using the rollup theory based on span loading. The numerical analysis is then able to predict the structure of the vortex in the plateau region, through the transition process, and into the decay region.

Rossow (ref. 33) and Iversen (ref. 37) assumed that each vortex in the pair acted independently of the other (i.e., as if it were isolated). The fact that such an assumption is valid for large distances into the wake was predicted in the theoretical work of Nielsen and Schwind (ref. 2, p. 413). The very slow decay of an isolated vortex or of a single pair indicates that radical changes must be made in these lift-generated wakes if the hazard to encountering aircraft is to be substantially reduced.

Rolling Moment On Encountering Wing-Axial Penetration

The encounter of a wing or aircraft with a vortex was restricted in the NASA studies to axial penetration. This is not meant to imply that a cross-vortex encounter is less hazardous, but that entry into the vortex along the axis is probably most likely to occur during landing and take-off operations. The experimental setup used in the Ames 40- by 80-foot wind tunnel to simulate this flight condition is shown in figure 11. The swept-wing model used to generate the vortex wake was mounted on the tunnel centerline at the entrance to the test section. The encountering model was mounted at the exit of the test section on a tower that moved horizontally and on a strut that moved vertically. In this way the following model could be moved throughout the wake to find the largest rolling moment. Theoretical results show that this rolling moment occurs when the centerline of the encountering wing is aligned with the center of a vortex. In these experiments, only rectangular wings at zero angle of incidence were used because they were simple to make and to analyze. The schematic diagram in figure 12 indicates the way in which the rolling moment on the following wing is analyzed. The axial velocity is assumed to be nearly constant and equal to that of the oncoming stream. The upwash or downwash on the wing is then equal to the circumferential velocity v_θ in the vortex. The rolling-moment coefficient, defined as $C_{l_f} = \text{Rolling moment} / (1/2\rho U_\infty^2 S_f b_f)$, can then be calculated by a lifting-surface theory or a variety of strip theories. Good agreement with experiment was found in most cases for several followers when vortex-lattice theory was used with the measured vortex velocity profiles to find the rolling moment (ref. 31). Consequently, it is desirable to measure the pressure distribution on a following wing and to compare it with predictions made by various theories. Also the unsteady aspects of the flow field were ignored here. Furthermore, data taken on wings making various types of penetrations need to be compared with the corresponding theoretical methods for predicting the pressure distributions.

UNCONVENTIONAL WAKES

Alleviation of Rolling-Moment Hazard

The single vortex pair shed by wings with conventional span loadings persists for such distances behind the generating aircraft that the traffic density at airports during peak times cannot be accommodated. Efforts made to enhance the decay process of the two-vortex wake by injection of turbulence (refs. 2, 38 to 41) and by stimulation of instabilities in the vortex system (e.g., refs. 42 and 43) provide a degree of alleviation. The various investigations by NASA on minimization of wake turbulence by aerodynamic means is summarized by Gessow (ref. 44). A mechanism is needed, however, in the wake dynamics to bring about mixing on a scale comparable to the span of the wing rather than the usual eddy size so that angular momentum is convected rapidly across the wake. Two hypothetical span loadings, first explored theoretically by Rossow (ref. 16), were derived by specifying that the vortex wake remain flat and not roll up from its edges as illustrated in figures 13(a) and 13(b). The first wake considered was designed to rotate as a unit so that it would appear as if a twisted ribbon were shed from each side of the wing. The objective of this design was to produce as large a vortex core as possible. The span loading would then taper gradually to zero at the wing tips rather than dropping abruptly as with elliptic loading. When compared with an elliptically loaded wing, this tailored loading was found to be only moderately effective for small following wings and worse for larger followers. The higher centerline lift required to maintain a given lift on the generator leads to higher rolling moments when the span of the follower is more than about 0.2 of the span of the generating wing. (See Rossow, refs. 16 and 31.)

The second wake studied consists not of a continuous vortex sheet but of an array of vortices designed to move downward as a unit behind the generating wing. Since the sign of the vortices alternates, the loading is stepped or sawtooth shaped. When the time-dependent method discussed previously is used to predict the shape of the wake, it is found to remain flat because all the individual vortices move downward at the same velocity. If, however, a disturbance is given to one of the vortices, the specified uniform motion breaks down and the vortices form pairs that make large excursions across the wake as shown in figure 14(a). Hence, although the shape of the sawtooth loading fluctuates about elliptic loading, the vortices in the wake do not revolve about the edge or tip vortices in the way that they do for elliptic loading (fig. 14(b)). If a similar disturbance is given to the vortices shed by elliptic loading, the general shape of the wake is not altered although the positions of some of the vortices change slightly.

The numerical result shown in figure 14(a) suggests that wakes with multiple vortex pairs can be designed so that they are unstable to disturbances and convection of vor-

ticity across the wake can be considerably enhanced by the resulting excursions of the vortex pairs. Similarly, wakes with only a single vortex pair are to be avoided because they tend to be stable to disturbances and, as described in the foregoing sections, tend to persist for large distances behind the generating wing.

Wings That Shed Multiple Vortex Pairs

The discussion in the previous section was based on inviscid calculations using two-dimensional point vortices. It remains then to find out whether the sawtooth span loadings can be implemented so that the large vortex excursions in the wake can be achieved. Two experimental wings were modified to approximate to a limited extent the sawtooth loading. The first wing was swept and equipped with seven flap segments per side (refs. 31 and 32). When these segments were deflected alternately up and down across the span, the loading is predicted by vortex-lattice theory to be as shown in figure 15. Tests by Ciffone and Orloff (ref. 32) in a water tow tank showed that the vortices shed by this wing did undergo large excursions in the wake and that various pairs linked in the way described by Crow (ref. 6) and MacCready (ref. 2, p. 289). But when the various excursions and linking were completed, a vortex pair still remained in the wake. These preliminary results indicate that generation of multiple vortex pairs will bring about large vortex excursions that lead to linking but that additional criteria are needed to achieve adequate diffusion of the wake vorticity.

A second wing on which vortex wake alleviation was attempted by span load modification was that of the Boeing 747 subsonic transport (refs. 44 and 45). The wing has inboard and outboard flaps (fig. 16) that can be deflected separately so that the loading can be enhanced inboard or outboard within the limits indicated in figure 17. If the inboard flaps are deflected their full amount (30° setting), the span loading has a large hump inboard resembling a combination of tailored and sawtooth span loading. Although that loading produces three vortex pairs in the near-field rollup region, the two flap vortices combine, so that only two vortices per side persist into the far-field region. Far downstream these two vortices, which are of the same sign, merge into a single diffuse vortex. Tests in a water tow tank and in a wind tunnel indicated that the rolling moment imposed on a following aircraft by the wake of this configuration would be less than half of that posed by the wake of the landing configuration at the same lift coefficient. Furthermore, this reduced value was below the roll-control capability of a Learjet aircraft which could be used to probe the wake.

Flight tests conducted with the Boeing 747, the Learjet, and a T-37 aircraft (ref. 45) confirmed the predictions of the ground-based facilities when the landing gear was retracted. It was found, however, that if any of the landing gears were extended or if the aircraft were yawed, the hazard alleviation achieved with the unconventional flap settings

was greatly reduced. Efforts are now underway first to identify the mechanism by which the drag of the landing gear destroys the favorable vortex interactions, and second to find ways to remedy the configuration so that alleviation is operable and effective under all conditions.

It should be mentioned at this point that tests were also made with the outboard flaps deflected fully and the inboard ones withdrawn. (See fig. 17.) Both the data from ground-based facilities and the flight experiments indicated that this configuration was not an improvement over the conventional landing configuration. Also, a few other flap settings were tried but none were as effective as the $(30^{\circ}/0^{\circ})$ configuration.

Tests on both of these wings indicate that the hazard posed by lift-generated wakes can be significantly reduced by changing the spanwise lift distribution so that several pairs, rather than one pair, of vortices are shed into the wake. Strong interactions between the vortices through linking, merging, or some other process diffuse the wake vorticity to a tolerable level. At this time, however, no adequate theoretical tools are available to aid in explaining the effect of gear or yaw found in the flight tests. NASA has several studies underway which should lead to the development of numerical methods that are capable of treating multiple vortex wakes and the interactions that occur. Since the flow field is three-dimensional and time-dependent, the computer programs will no doubt be complex.

CONCLUDING REMARKS

None of the theoretical methods described here for analyzing lift-generated wakes that consist of a single vortex pair were complex enough to require large or advanced computers. The results of the analyses and experiments indicate, however, that the hazard posed by these simple wakes is unacceptable, and means must be sought to enhance the diffusion of the angular momentum in the wake. Preliminary tests of wakes with multiple vortex pairs indicate that the interactions that occur may provide the mechanism for reducing the wake hazard. However, better design guidelines and better theoretical methods for checking them in various installations must be developed so that failures of the alleviating mechanisms under certain circumstances can be avoided. Any theoretical study of multiple vortex wakes will probably be so complex as to require a numerical analysis. Even though some simplifications can be made based on experience with vortex wakes of a single pair, the three-dimensional time-dependent nature of these wakes will require large computer capacity and long computing times. It can be anticipated therefore that the availability of larger and faster computers will expedite the finding of acceptable ways to alleviate the wake vortex hazard behind aircraft.

REFERENCES

1. Bleviss, Z. O.: Theoretical Analysis of Light Plane Landing and Take-off Accidents Due to Encountering the Wakes of Large Airplanes. Rep. No. SM-18647, Douglas Aircraft Corp., Santa Monica Division, Dec. 1954.
2. Olsen, John H.; Goldberg, Arnold; Rogers, Milton, eds.: Aircraft Wake Turbulence. Plenum Publishing Corp., Sept. 1970.
3. El-Ramly, Z.: Aircraft Trailing Vortices - a Survey of the Problem. Tech. Rep. ME/A 72-1, Carleton Univ., Ottawa, Canada, Nov. 1972.
4. Roberts, L.: On Wake Vortex Alleviation. NASA/University Conf. on Aeronautics - Theme: The Future of Aeronautics, Univ. of Kansas, Oct. 23-24, 1974.
5. Tombach, I.: Observations of Atmospheric Effects on Vortex Wake Behavior. AIAA J. Aircraft, vol. 10, no. 11, Nov. 1973, pp. 641-647.
6. Crow, S. C.: Stability Theory for a Pair of Trailing Vortices. AIAA J., vol. 8, no. 12, Dec. 1970, pp. 2172-2179.
7. Analytic Methods in Aircraft Aerodynamics. A Symposium Held at Ames Research Center, Moffett Field, Calif., NASA SP-228, Oct. 28-30, 1969.
8. Aerodynamic Interference. AGARD Conference Proceedings No. 71, AGARD-CP-71-71, 1971.
9. Ashley, H.; and Rodden, W. P.: Wing-Body Aerodynamic Interaction. Annual Review of Fluid Mechanics, vol. 4, 1972, pp. 431-472.
10. Maskew, B.: Numerical Lifting Surface Methods for Calculating the Potential Flow About Wings and Wing-Bodies of Arbitrary Geometry. Ph. D. Thesis, Loughborough Univ. of Tech., Oct. 1972.
11. Kandil, O. A.; Mook, D. T.; and Nayfeh, A. H.: Nonlinear Prediction of the Aerodynamic Loads on Lifting Surfaces. AIAA Paper 74-503, 1974.
12. Chigier, N. A.; and Corsiglia, V. R.: Tip Vortices - Velocity Distributions. NASA TM X-62,087, 1971.
13. Hough, G.: Remarks on Vortex-Lattice Methods. AIAA J. Aircraft, vol. 10, no. 5, May 1973, pp. 314-317.
14. Rosenhead, L.: The Formation of Vortices from a Surface of Discontinuity. Proc. Roy. Soc. (London), vol. A134, 1931, pp. 170-192.
15. Westwater, F. L.: The Rolling Up of the Surface of Discontinuity Behind an Aerofoil of Finite Span. Reports and Memoranda 1692, British A.R.C., 1935, pp. 116-131.

16. Rossow, V. J.: Theoretical Study of Lift-Generated Vortex Wakes Designed To Avoid Roll Up. AIAA J., vol. 13, no. 4, April 1975, pp. 476-484.
17. Spreiter, J. R.; and Sacks, A. H.: The Rolling-Up of the Trailing Vortex Sheet and Its Effect on the Downwash Behind Wings. J. Aeronaut. Sci., vol. 18, no. 1, Jan. 1951, pp. 21-32.
18. Hama, F. R.; and Burke, E. R.: On the Rolling-Up of a Vortex Sheet. Tech. Note BN-220, AFOSR-TN 60-1069, Univ. of Maryland, 1960.
19. Takami, H.: A Numerical Experiment with Discrete-Vortex Approximation, with Reference to the Rolling Up of a Vortex Sheet. Sudaer 202(AFOSR 64-1536), Sept. 1964.
20. Moore, D. W.: The Discrete Vortex Approximation of a Vortex Sheet. Rep. AFOSR-1084-69, California Inst. of Tech., 1971.
21. Chorin, A. J.; and Bernard, P. S.: Discretization of a Vortex Sheet, with an Example of Roll-Up. College of Engineering Rep. FM-72-5, Univ. of California, Berkeley, Nov. 1972.
22. Kuwahara, K.; and Takami, H.: Numerical Studies of Two-Dimensional Vortex Motion by a System of Point Vortices. J. Phys. Soc. Jap., vol. 34, no. 1, Jan. 1973, pp. 247-253.
23. Moore, D. W.: A Numerical Study of the Roll-Up of a Finite Vortex Sheet. J. Fluid Mech., vol. 63, pt. 2, 1974, pp. 225-235.
24. Lin, C. C.: On the Motion of Vortices in Two Dimensions. No. 5, Applied Mathematics Series, The Univ. of Toronto Press, Toronto, Canada, 1943.
25. Betz, A.: Verhalten von Wirbelsystemen. Z.A.M.M., Bd. XII, Nr. 3, 1932, pp. 164-174. (Available as NACA TM 713.)
26. Rossow, V. J.: On the Inviscid Rolled-Up Structure of Lift Generated Vortices. AIAA J. Aircraft, vol. 10, no. 11, Nov. 1973, pp. 647-650.
27. Donaldson, Coleman du P.: A Brief Review of the Aircraft Trailing Vortex Problem, A.R.A.P. Report No. 155, Presented at the National Aerospace Electronics Conference, Dayton, Ohio, May 17-19, 1971.
28. Donaldson, C. du P.; Snedeker, R. S.; and Sullivan, R. D.: A Method of Calculating Aircraft Wake Velocity Profiles and Comparison with Full-Scale Experimental Measurements. AIAA Paper 74-39, 1974.
29. Mason, H. W.; and Marchman, J. F., III: The Farfield Structure of Aircraft Wake Turbulence. AIAA Paper 72-40, 1972.

30. Brown, C. E.: Aerodynamics of Wake Vortices. AIAA J., vol. 11, no. 4, April 1973, pp. 531-536.
31. Rossow, V. J.; Corsiglia, V. R.; Schwind, R. G.; Frick, J. K. D.; and Lemmer, O. J.: Velocity and Rolling Moment Measurements in the Wake of a Swept Wing Model in the 40- by 80-Foot Wind Tunnel. NASA TM X-62,414, 1975.
32. Ciffone, D. L.; and Orloff, K. L.: Far-Field Wake-Vortex Characteristics of Wings. AIAA Paper 74-505, 1974. (To be published in AIAA J. Aircraft.)
33. Rossow, V. J.: Prediction of Span Loading From Measured Wake-Vortex Structure - An Inverse Betz Method. AIAA J. Aircraft, vol. 12, no. 6, June 1975. (To be published.)
34. Donaldson, C. du P.: Calculation of Turbulent Shear Flows For Atmospheric and Vortex Motions. AIAA J., vol. 10, 1972, pp. 4-12.
35. Iversen, J. D.: Correlation of Turbulent Trailing Vortex Decay Data. AIAA J. Aircraft. (To be published.)
36. Ciffone, D. L.: Correlation for Estimating Vortex Rotational Velocity Downstream Dependence. AIAA J. Aircraft, vol. 11, no. 11, Nov. 1974, pp. 716-717.
37. Iversen, J. D.: Inviscid to Turbulent Transition of Trailing Vortices. Paper ISU-ERI-Ames-74241, Iowa State Univ., Engineering Research Inst., Nov. 1974.
38. Wentz, W. H., Jr.: Evaluation of Several Vortex Dissipators by Wind Tunnel Measurements of Vortex-Induced Upset Loads. Aeronautical Rep. 72-3, Wichita State Univ., Sept. 1972.
39. Banta, A. J.: Effects of Planform and Mass Injection on Rolling Moments Induced by Trailing Vortices. M.S. Thesis, Wichita State Univ., Dec. 1973.
40. Patterson, J. C., Jr.: Lift-Induced Wing-Tip Vortex Attenuation. AIAA Paper No. 74-38, January 30-February 1, 1974.
41. Hastings, E. C., Jr.; Shanks, R. E.; Champine, R. A.; and Copeland, W. L.: Preliminary Results of Flight Tests of Vortex Attenuating Splines. NASA TM X-71928, 1974.
42. Bilanin, A. J.; and Widnall, S. E.: Aircraft Wake Dissipation by Sinusoidal Instability and Vortex Breakdown. AIAA Paper 73-107, 1973.
43. Lessen, M.; and Paillet, F.: The Stability of a Trailing Line Vortex. II Viscous Theory. J. Fluid Mech., vol. 65, Oct. 2, 1974, pp. 769-779.

44. Gessow, A.: Aircraft Wake Turbulence Minimization by Aerodynamic Means. 6th Conference on Aerospace and Aeronautical Meteorology, El Paso, Texas, Nov. 12-14, 1974.
45. Tymczyszyn, J.; and Barber, M. R.: A Review of Recent Wake Vortex Flight Tests. 18th Annual Symposium of Society of Experimental Test Pilots, Los Angeles, California, Sept. 26, 1974.

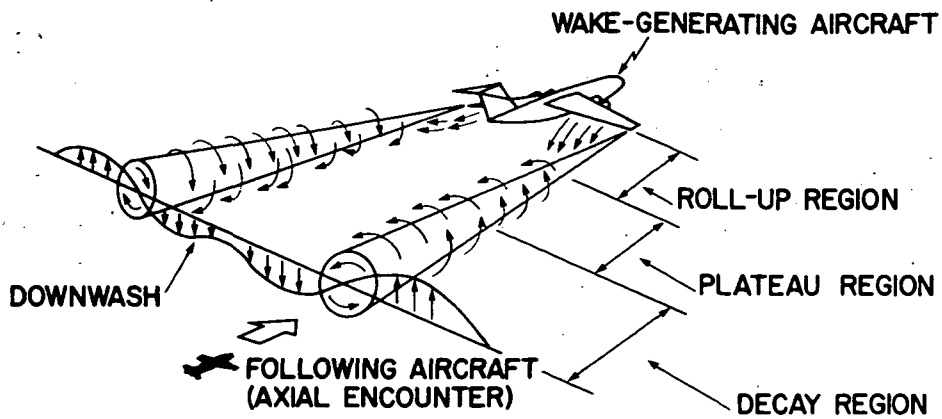


Figure 1.- Flow field produced by lift-generated vortices. Distances are not drawn to scale.

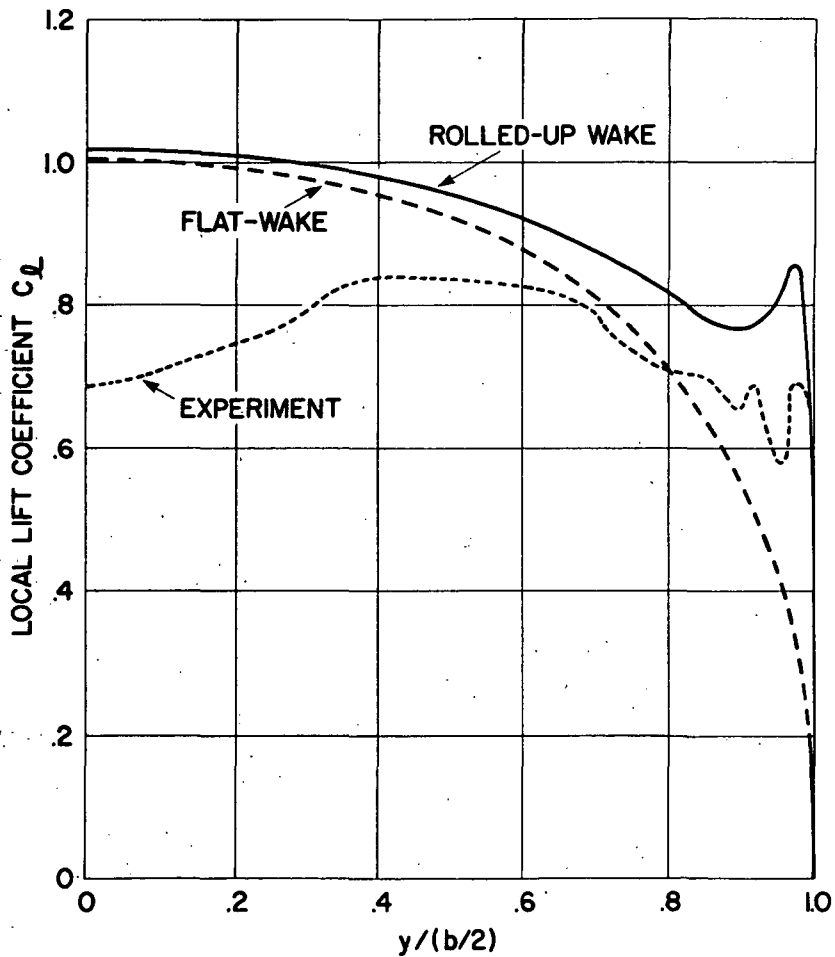


Figure 2.- Measured spanwise lift distribution on rectangular wing compared with loading predicted by vortex-lattice theory assuming a flat wake and that near wake is rolling up.

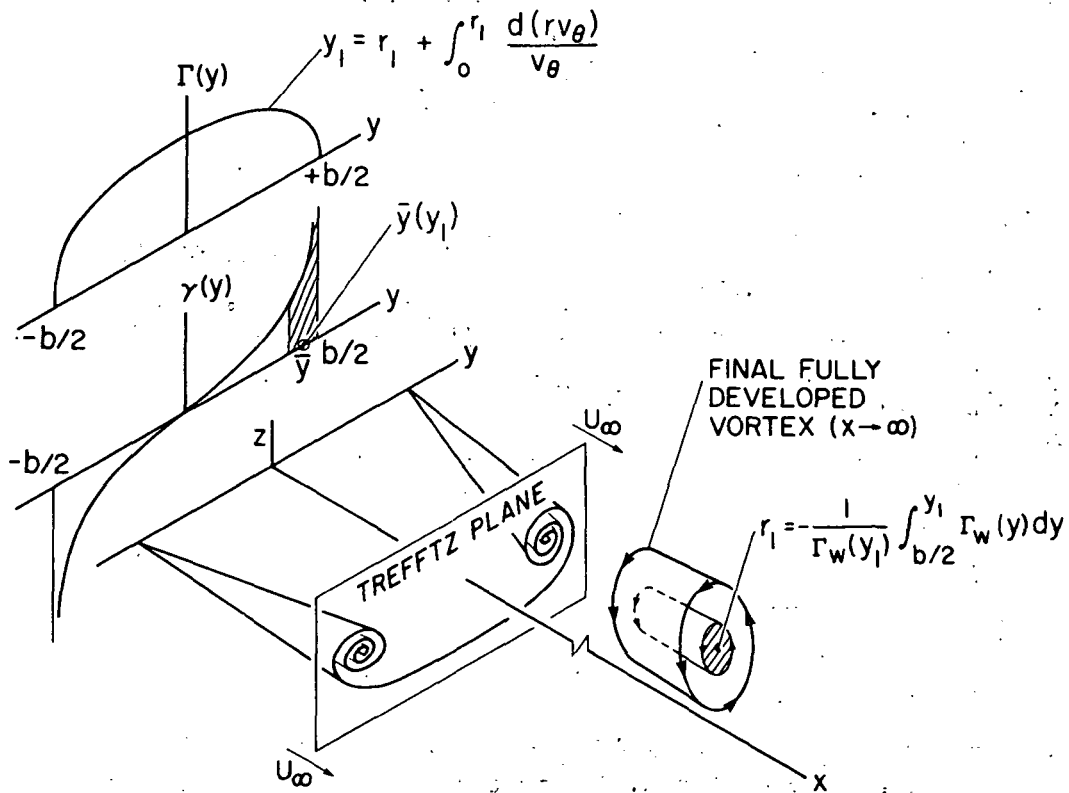


Figure 3.- Schematic diagram of wake rollup and relationships between span loading and vortex structure.

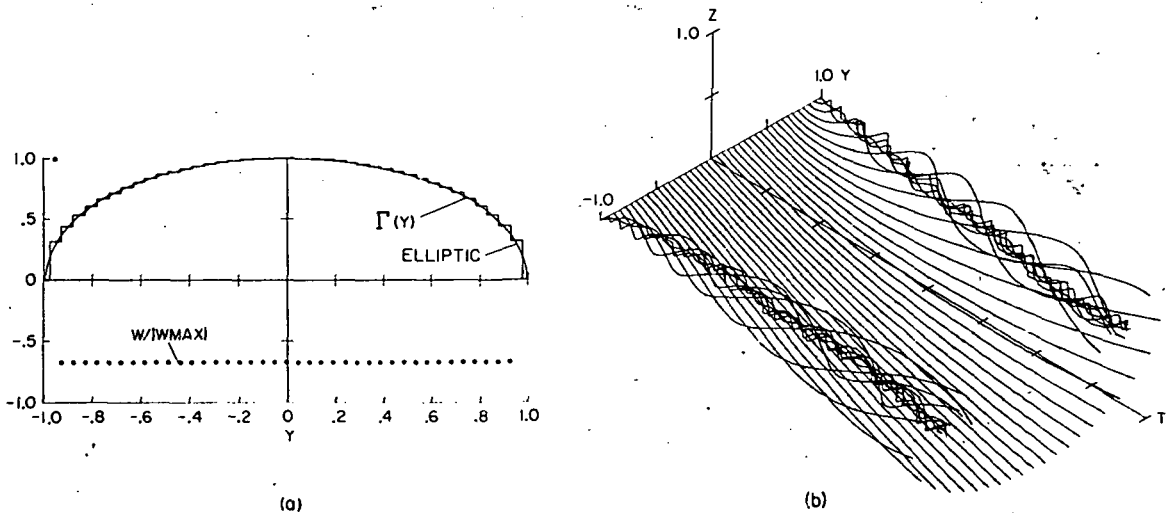


Figure 4.- Rollup of vortex wake shed by elliptic loading calculated by inviscid two-dimensional time-dependent approximation. W is dimensionless vertical velocity.

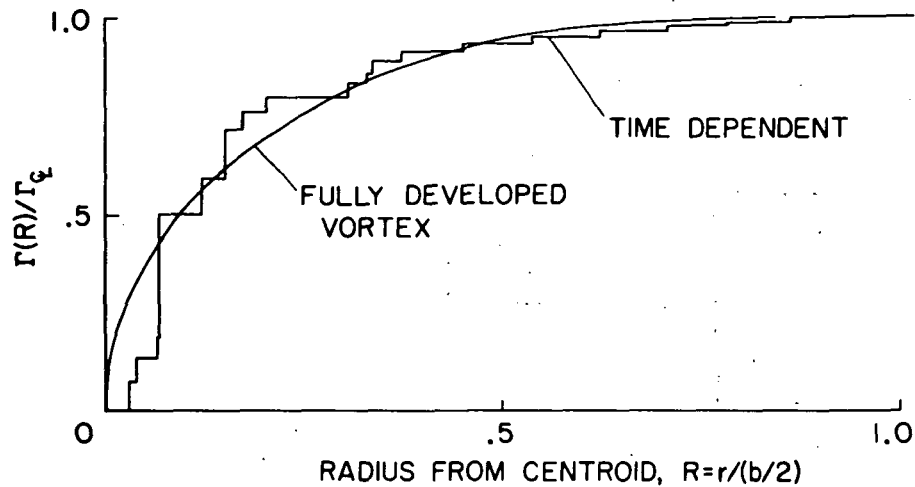


Figure 5.- Comparison of structure of vortex shed by elliptic loading as predicted by time-dependent method with that predicted by Betz direct rollup theory. Γ_c is circulation on centerline.

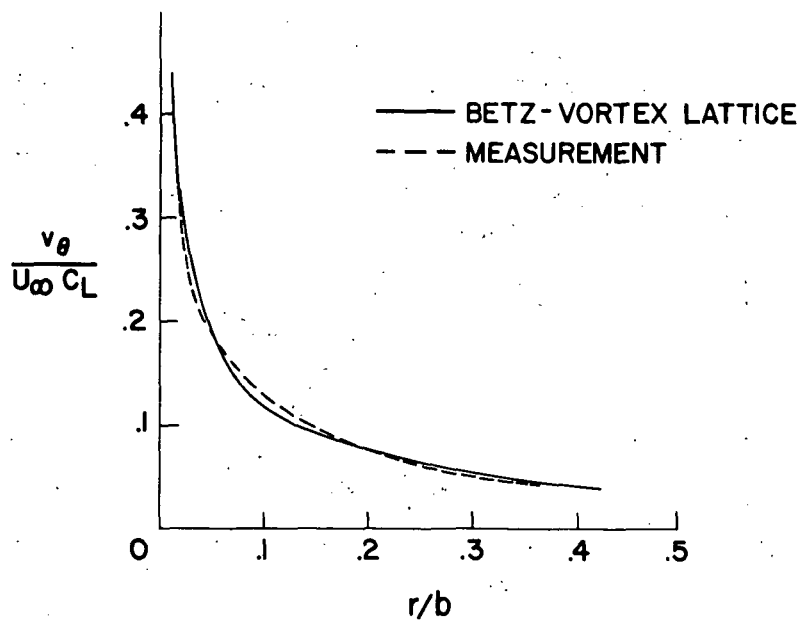
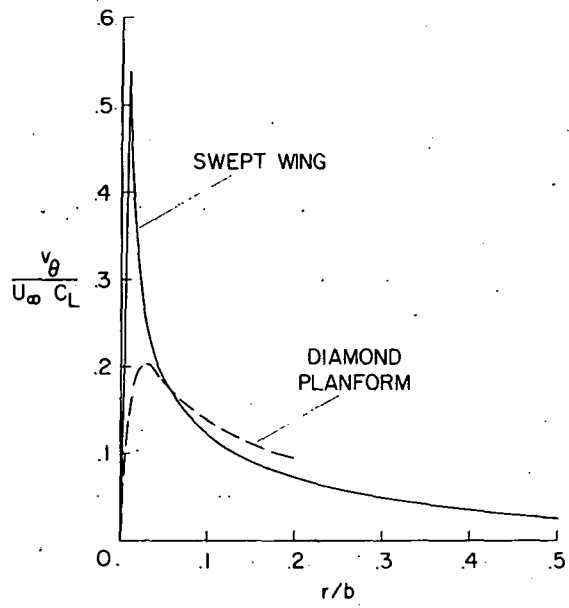
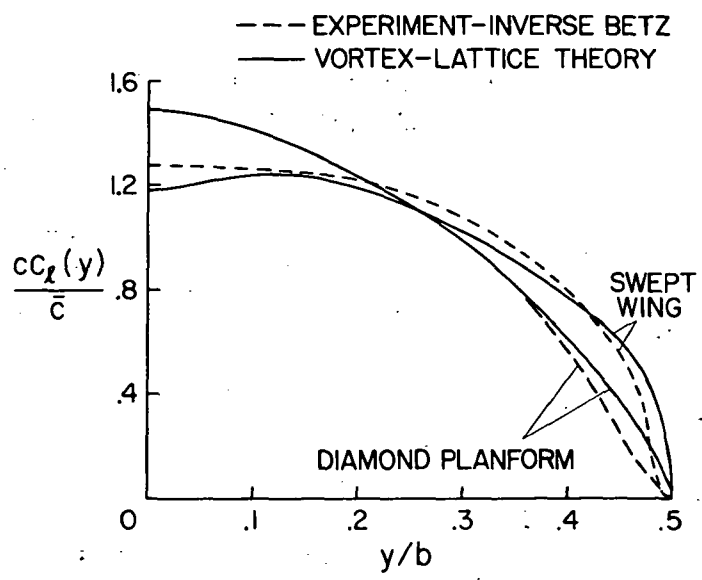


Figure 6.- Comparison of measured vortex structure with prediction made by Betz rollup theory using span loading predicted by vortex-lattice theory for a swept wing.



(a) Measured vortex velocity profiles (ref. 31).



(b) Calculated span loadings.

Figure 7.- Comparison of inverse rollup theory with vortex-lattice theory.

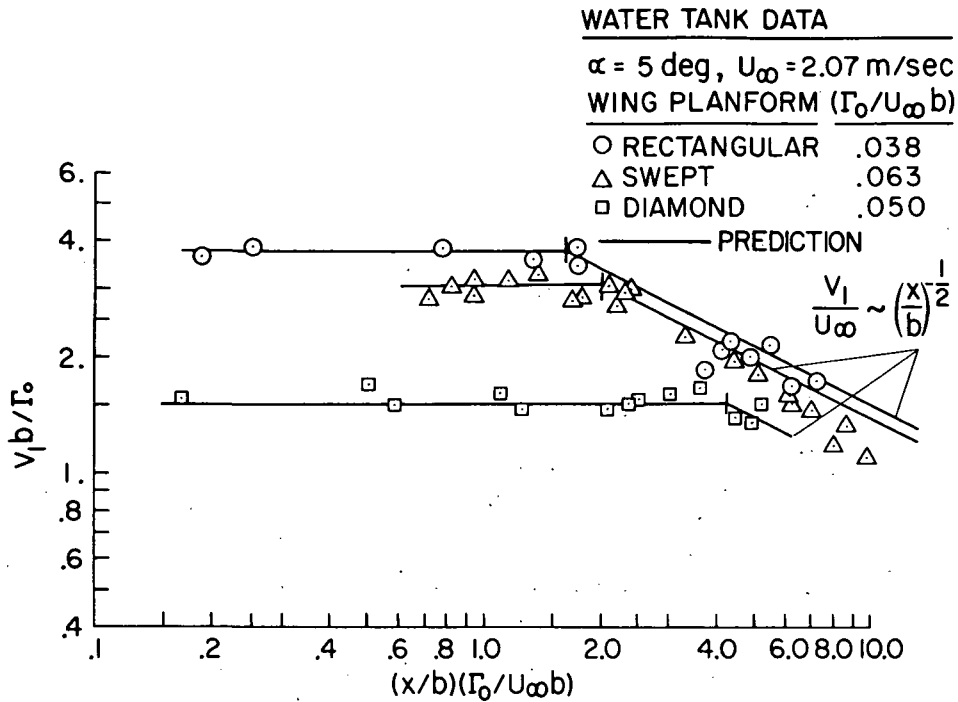


Figure 8.- Maximum circumferential velocity in vortices behind wings as measured in water tow tank (from Ciffone and Orloff, ref. 32).

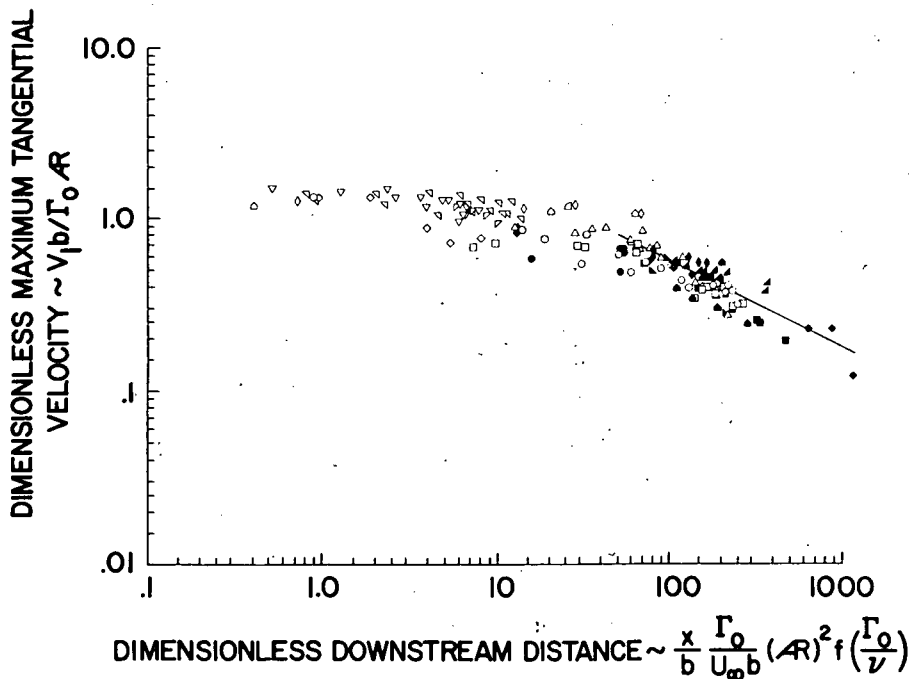


Figure 9.- Correlation of data from ground-based and flight experiments on maximum circumferential velocity in vortices shed by various conventional span loadings (from Iversen, ref. 35).

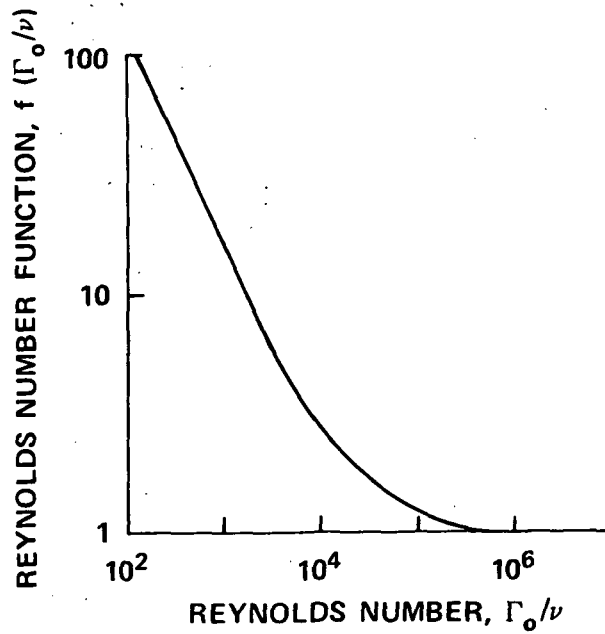


Figure 10.- Reynolds number function used to correlate data in figure 9 (from Iversen, ref. 35).

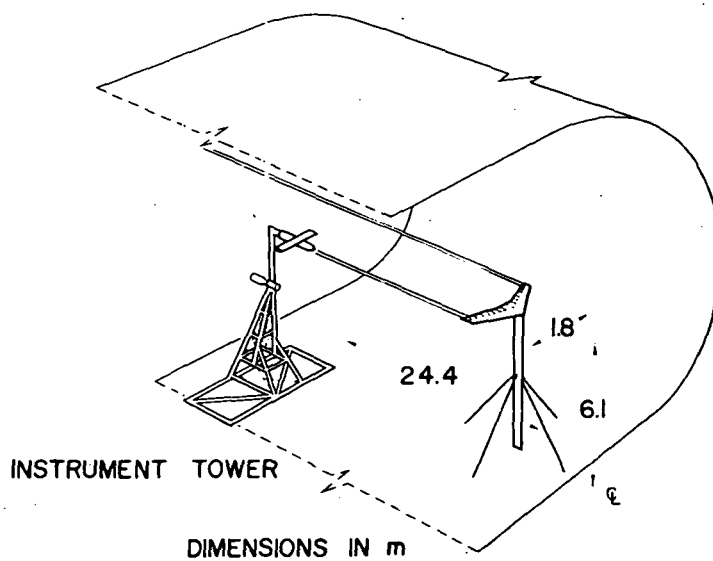


Figure 11.- Experimental setup used in 40- by 80-ft Wind Tunnel to measure rolling moment on an encountering wing.

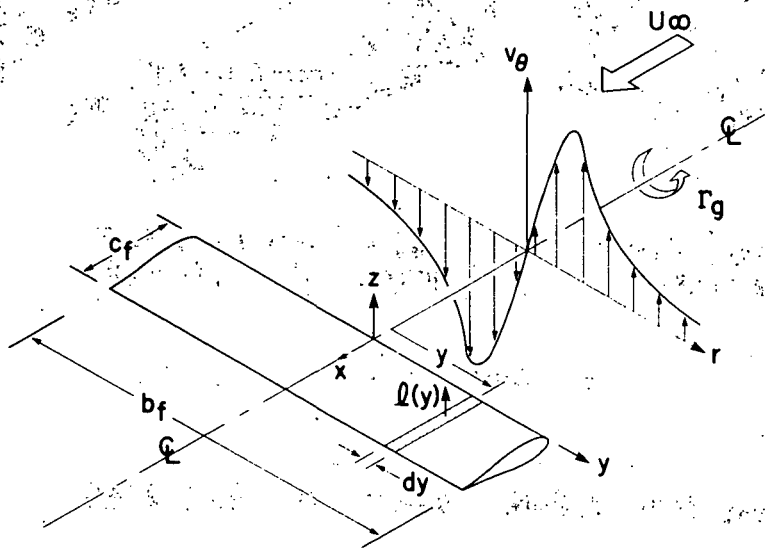
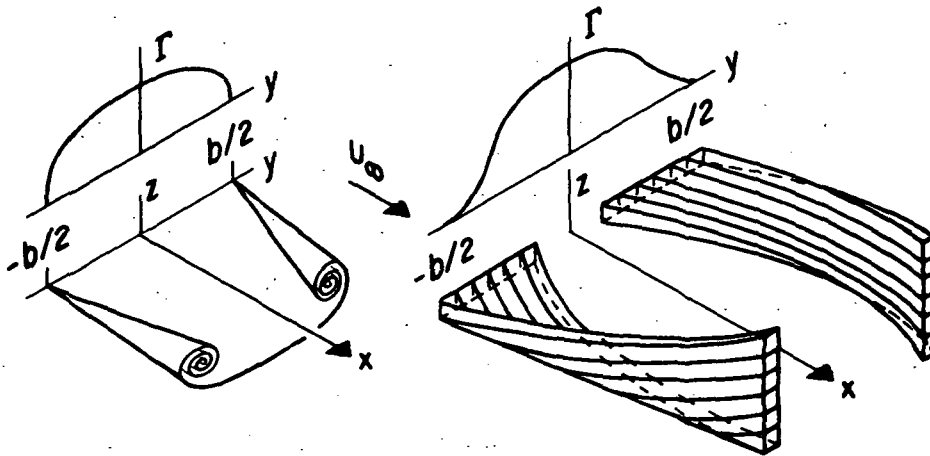


Figure 12.- Wake vortex impinging on following wing.

CONVENTIONAL SPAN LOADING

TAILORED SPAN LOADING



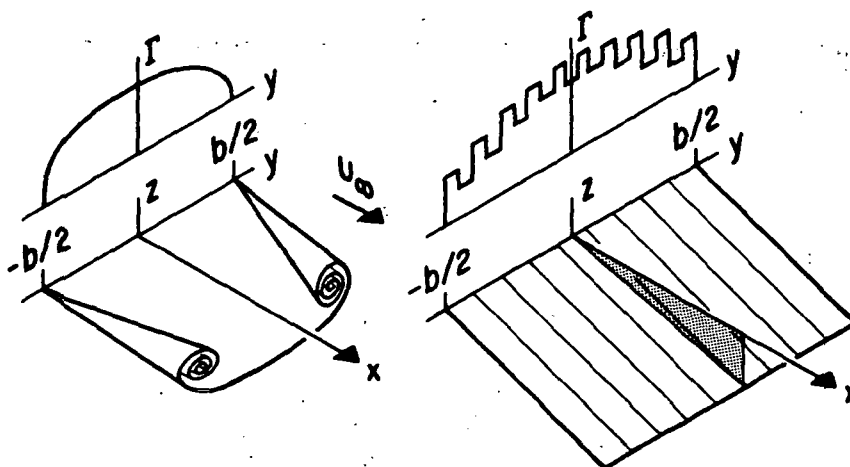
WAKE ROLLS UP
FROM EDGES

WAKE FROM EACH SIDE
ROTATES AS RIGID SHEET

(a) Rotating wakes.

CONVENTIONAL SPAN LOADING

SAWTOOTH SPAN LOADING



WAKE ROLLS UP
FROM EDGES

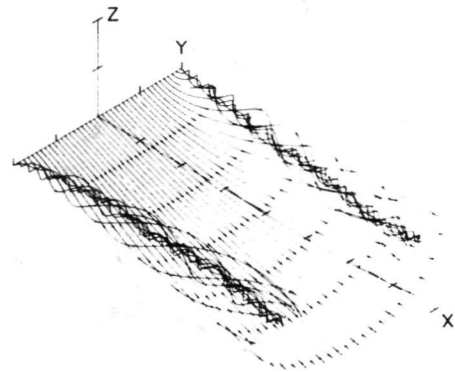
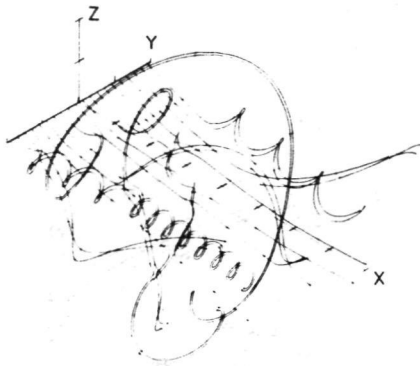
WAKE TRANSLATES DOWNWARD
AS A RIGID SHEET

(b) Translating wake.

Figure 13.- Comparison of conventional wakes with wakes designed to avoid rollup from the edges of the vortex wake.

SAWTOOTH LOADING

CONVENTIONAL LOADING



(a) Large-scale wake mixing.

(b) No wake mixing.

Figure 14.- Wake structure predicted by time-dependent vortex calculations for elliptic and sawtooth span loadings.

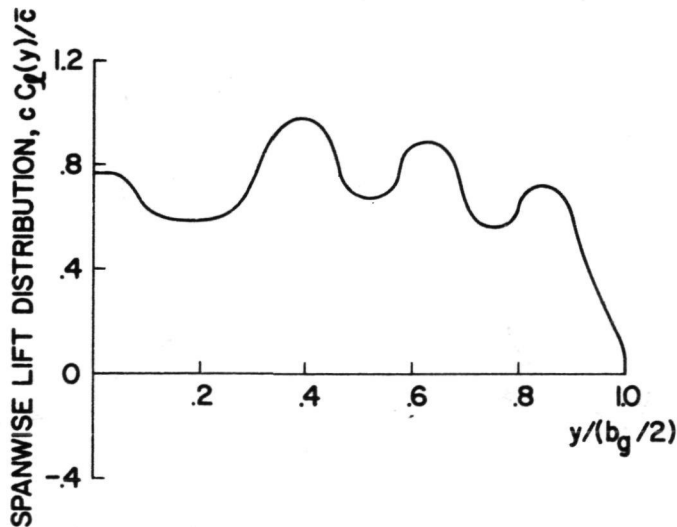


Figure 15.- Span loading predicted by vortex-lattice theory for swept wing with seven flap segments per side deflected alternately up and down 15° . $C_L = 0.7$.

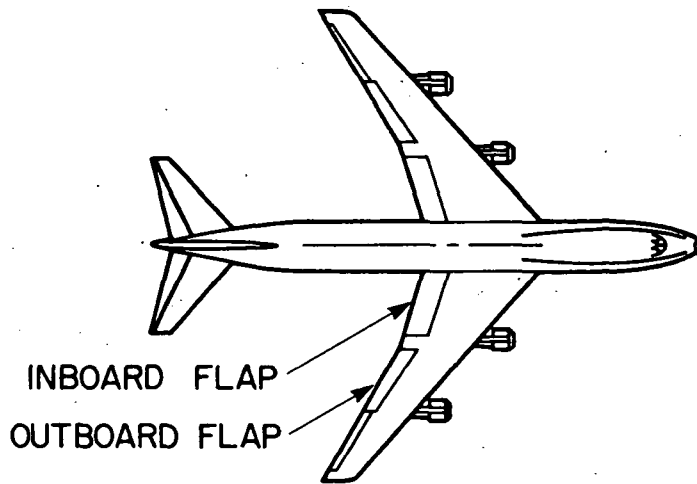


Figure 16.- Plan view of Boeing 747 subsonic transport.

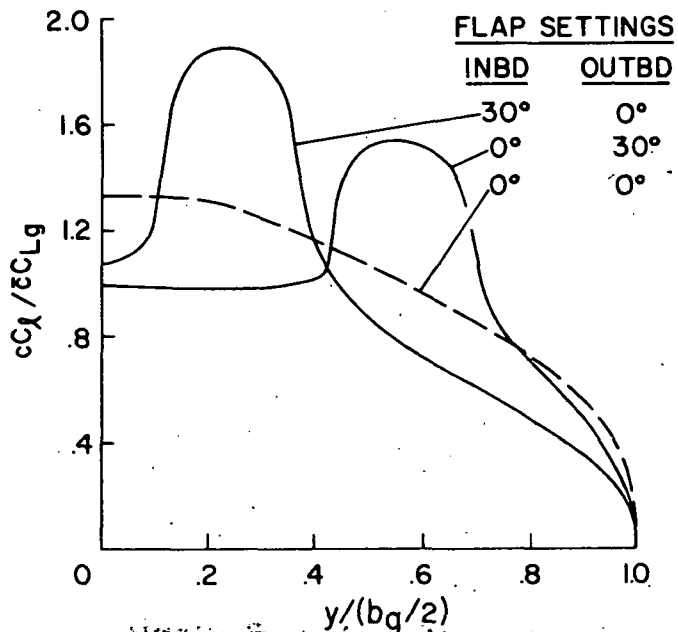


Figure 17.- Span loadings calculated for Boeing 747 wing using vortex-lattice theory.

Page Intentionally Left Blank

SIMULATION OF UNSTEADY THREE-DIMENSIONAL SEPARATED
FLOWS WITH INTERACTING VORTEX FILAMENTS

A. Leonard*

NASA Ames Research Center

SUMMARY

Interacting, three-dimensional vortex filaments are used for the numerical simulation of separated, incompressible flow past solid bodies. Vortices are introduced at the boundary to simulate the boundary-layer vorticity. These filaments then move with the local fluid velocity determined kinematically from a Biot-Savart integral over the vortex filaments plus a time-dependent potential flow. Preliminary results are given for three-dimensional flow past a sphere.

I. INTRODUCTION

Recent success using discrete vortices to simulate unsteady two-dimensional, incompressible flows at high Reynolds numbers (ref. 1) including separated flows over airfoils (data supplied by R. S. Rogallo) has prompted development of a similar technique for three-dimensional problems. The basic idea is to model the vorticity distribution in terms of continuous filaments and to track these filaments in a Lagrangian reference frame. Viscous effects are assumed to be important only in the determination of the fine structure within the filament core. Each filament moves according to the local fluid velocity appropriately averaged over the filament core. The vorticity distribution within a filament is parameterized by a locally defined, effective core radius determined dynamically by the effects of viscous diffusion and vortex stretching.

Initially, the three-dimensional simulations were limited to rotational flows away from solid boundaries such as jets, vortex rings, and aircraft trailing vortices after initial rollup (ref. 2). In this paper, an extension of the method is presented which allows simulation of flows about solid bodies including vortex shedding to the wake. The influence of the boundary is twofold. First, to ensure tangency of the velocity field at the boundary, a harmonic contribution to the velocity field must be computed at each time

*NRC-NASA Resident Research Associate.

step. Second, the mechanics of the boundary layer must be approximated with sufficient accuracy so that the separation lines are located correctly on the surface of the body.

After a brief review in Sec. II of the physics of the unsteady flow field in terms of vorticity dynamics, an efficient procedure for the calculation of the above-mentioned harmonic velocity field is given in Sec. III. In Sec. IV a simple model of the boundary layer is described which provides for ejection of vorticity into the wake. Additional computational aspects of the problem are discussed in Sec. V and in Sec. VI some preliminary results are presented from the application of the method to flow past a sphere.

Another approach to the simulation of unsteady separated flows which requires less modeling is, of course, to use the full Navier-Stokes equations with an Eulerian grid. In two dimensions, for example, such methods have been successful in computing unsteady laminar flow past an elliptic cylinder (ref. 3) and an airfoil (ref. 4) at angle of attack. These computations were costly, however, and such three-dimensional simulations promise to be very time consuming even on advanced computers (ILLIAC IV or CDC STAR).

II. PROBLEM FORMULATION

To motivate our approach to the computation of unsteady, separated flows past solid bodies at high Reynolds number, some of the fundamental aspects of the problem will first be reviewed (ref. 5). Vorticity, initially formed at the surface of the body through the action of pressure gradients along the surface, is ejected into the wake region at separation lines. The locations of these lines are determined by the internal dynamics of the boundary layer which, in turn, are strongly influenced by outer flow boundary data at the top or edge of the boundary layer, namely pressure gradient and edge velocity. The wake or outer flow region is characterized by fluctuating concentrations of vorticity immersed in an unsteady potential flow (see fig. 1).

The vorticity field $\underline{\omega}$ in the outer flow satisfies the incompressible vorticity transport equation

$$\frac{D\underline{\omega}}{Dt} = \underline{\omega} \cdot \nabla \underline{u} + \nu \nabla^2 \underline{\omega} \quad (2.1)$$

where ν is the kinematic viscosity. The velocity field \underline{u} can be determined from the kinematic relation

$$\nabla^2 \underline{u} = -\nabla \times \underline{\omega} \quad (2.2)$$

where again incompressibility ($\nabla \cdot \underline{u} = 0$) has been assumed. Boundary conditions on (2.2) appropriate to this problem are

$$\lim_{|\underline{r}| \rightarrow \infty} \underline{u}(\underline{r}, t) = \underline{u}_{\infty} \quad (2.3a)$$

and

$$\underline{u}(\underline{r}_s) \cdot \underline{n} = 0 \quad (2.3b)$$

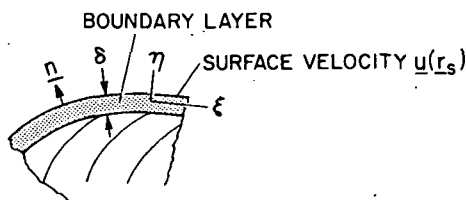
where \underline{n} is the unit outward normal at the surface and, neglecting a term which is $O(\text{Re}^{-2})$, \underline{r}_s is an arbitrary point on the body surface S . Condition (2.3b) excludes that part of the surface where the boundary layer is separating (i.e., at the separation lines). Within the separating region the flow is entering the wake region. Elsewhere, along the outer flow boundary near the solid surface, the flow is either tangent to the boundary or is leaving the outer flow region and is assumed inviscid. Thus the integration of the outer flow vorticity equation (2.1) requires only a knowledge of the fluid velocity distribution within the separated shear layers at the time of separation (ref. 6).

In the boundary layer away from the separation lines, the Navier-Stokes equations reduce to the boundary-layer equations under the usual approximations. These reduced equations require as input the pressure gradient along the surface, ∇_{sp} , and the edge velocity of the boundary layer. Both are available from the outer flow solution. The latter quantity is simply $\underline{u}(\underline{r}_s)$. Near the separation lines the full Navier-Stokes equations may be required to achieve an accurate solution to the boundary-layer flow. In any case, the boundary-layer calculation must supply the locations of the separation lines and the velocity distributions of the separated shear layers at separation as input to the outer flow computation.

However, the boundary-layer model employed in this work does not explicitly rely on the use of the boundary-layer equations, so there is no need to write these equations here. Rather, the following integral properties of the boundary layer will be stated for later use. The total vorticity per unit area of the boundary layer is perpendicular to and equal in magnitude to the external flow velocity,

$$\int_0^{\delta} \underline{\omega}(\eta) d\eta = \underline{n} \times \underline{u}(\underline{r}_s) \quad (2.4)$$

Here δ is the boundary-layer thickness and η is the coordinate normal to the surface.



The circulation within the boundary layer passing a given surface point per unit time in the direction of $\underline{u}(\underline{r}_s)$ is given by

$$\frac{d\Gamma}{dt} = - \int_0^{\delta} (\underline{n} \times \underline{\omega}(\eta))_{\xi} u_{\xi}(\eta) d\eta = \frac{|\underline{u}(\underline{r}_s)|^2}{2} \quad (2.5)$$

where ξ is the coordinate in the direction of $\underline{u}(\underline{r}_s)$. Thus, the average vorticity in the boundary layer has an apparent speed of $|\underline{u}(\underline{r}_s)|/2$. Finally,

it should be noted that the vorticity flux into the boundary layer at the solid surface is

$$\left. \nu \frac{\partial \omega}{\partial \eta} \right|_{\text{surface}} = \frac{1}{\rho} \nabla_s p \times \underline{n} \quad (2.6)$$

where ρ is the fluid density.

III. OUTER FLOW SIMULATION

As in the earlier study (ref. 2), the vorticity distribution in the wake is modeled in terms of a set of closed vortex filaments. These filaments are marked with a sequence of node points and are tracked in a Lagrangian reference frame. The vorticity distribution within each filament is parameterized by a locally defined, effective core radius. Thus, each filament is completely specified in terms of the positions of the node points, the local core radii, and its circulation.

The velocity of each node point is given as an appropriate average of the velocity field over the filament core velocity. The velocity \underline{u} is the solution to (2.2) and may be written as

$$\underline{u}(\underline{r}, t) = -\frac{1}{4\pi} \int \frac{(\underline{r} - \underline{r}') \times \underline{\omega}(\underline{r}', t) d\underline{r}'}{|\underline{r} - \underline{r}'|^3} + \underline{v}(\underline{r}, t) \quad (3.1)$$

where the integral is over all the vorticity containing fluid in the outer flow and \underline{v} is the irrotational contribution constructed so as to ensure that boundary conditions (2.3) are satisfied. The model for the vorticity field described above is used to split the Biot-Savart integral in (3.1) into two contributions, one due to nonadjacent segments and the other due to the two segments adjacent to the given node point. The latter contribution is inversely proportional to the local radius of curvature of the filament and depends logarithmically on the local core radius. The details of this procedure are given in reference 2 along with dynamical equations for the core radii based on vortex stretching and viscous diffusion effects.

The computation of the potential flow \underline{v} proceeds as follows. Write \underline{v} as the sum of three contributions

$$\underline{v} = \underline{v}_\infty + \underline{v}_{IM} + \tilde{\underline{v}} \quad (3.2)$$

where \underline{v}_∞ satisfies

$$\lim_{|\underline{r}| \rightarrow \infty} \underline{v}_\infty = \underline{u}_\infty \quad (3.3)$$

and \underline{v}_{IM} represents the irrotational velocity field induced by vortex filaments within the solid body serving as approximate images to filaments in the outer flow which are close to the surface. Use of images allows a relatively coarse surface mesh for the determination of the remaining contribution $\tilde{\underline{v}}$.

The velocity \tilde{v} is constructed to ensure that $\underline{u}(\underline{r}_S) \cdot \underline{n} = 0$. If q is defined by

$$q(\underline{r}_S) = -\frac{1}{4\pi} \int \frac{\underline{n} \cdot (\underline{r}_S - \underline{r}') \times \underline{\omega}(\underline{r}') d\underline{r}'}{|\underline{r}_S - \underline{r}'|^3} + [\underline{v}_\infty(\underline{r}_S) + \underline{v}_{IM}(\underline{r}_S)] \cdot \underline{n} \quad (3.4)$$

then (2.3a) requires that

$$\tilde{v}(\underline{r}_S) \cdot \underline{n} = -q(\underline{r}_S) \quad (3.5)$$

Let the potential for \tilde{v} be ϕ ,

$$\tilde{v} = -\nabla\phi \quad (3.6)$$

then ϕ is the solution to the Neumann problem,

$$\nabla^2 \phi = 0 \quad (3.7)$$

exterior to the solid body and

$$\frac{\partial \phi}{\partial n} = q(\underline{r}_S) \quad (3.8)$$

on S . The function ϕ is conveniently expressed as a single layer potential in terms of a density γ ,

$$\phi(\underline{r}) = \frac{1}{2\pi} \int_S \frac{\gamma(\underline{r}_S) d\underline{r}_S}{|\underline{r} - \underline{r}_S|} \quad (3.9)$$

Then γ satisfies the integral equation (ref. 7)

$$\gamma(\underline{r}_S) + \frac{1}{2\pi} \int_S \frac{\underline{n} \cdot (\underline{r}_S - \underline{r}_S') \gamma(\underline{r}_S') d\underline{r}_S'}{|\underline{r}_S - \underline{r}_S'|^3} = -\frac{\partial \phi}{\partial n} = q(\underline{r}_S) \quad (3.10)$$

where \underline{n} is the outward normal at \underline{r}_S .

Once (3.10) is solved for γ , (3.6) and (3.9) combine to yield the contribution \tilde{v} at any desired point on S or in the outer flow region.

For numerical purposes, the body surface S is partitioned into a set of surface patches $\{S_1, S_2, \dots, S_M\}$. Within each the density γ is assumed constant. With this assumption, integration of (3.10) over S_i gives

$$\gamma^i + \sum_{j=1}^M K^{ij} \gamma^j = q^i \quad (i = 1, 2, \dots, M) \quad (3.11)$$

where

$$\gamma^i = \int_{S_i} \gamma(\underline{r}_S) d\underline{r}_S \quad (3.12)$$

$$K^{ij} = \frac{1}{2\pi} \int_{S_i} d\mathbf{r}_S \int_{S_j} \frac{d\mathbf{r}'_S \mathbf{n} \cdot (\mathbf{r}_S - \mathbf{r}'_S)}{A_j |\mathbf{r}_S - \mathbf{r}'_S|^3} \quad (3.13)$$

$$q^i = \int_{S_i} q(\mathbf{r}_S) d\mathbf{r}_S \quad (3.14)$$

and A_j is the area of patch S_j . The q^i may be computed from (3.4) using the vortex filament description for the vorticity field. Therefore, q^i reduces to a sum over all the filament segments in the outer flow plus the image segments with a possible additional free-stream contribution.

Physically, if one were solving a radiation heat-transfer problem interior to S , then K^{ij} would be the view factor of patch S_i for radiation emitted at S_j ; that is, K^{ij} is the probability that a photon starting from S_i will pass through S_j (assuming the interior is vacuous). For a strictly convex body the matrix $I + K$ is therefore positive and strictly diagonally dominant. Hence, solving the system (3.11) by, say, the LU algorithm (ref. 8) presents no problem.

At each time step then, the q^i are computed, then γ^i are solved for and used in (3.9) and (3.6) to give $\tilde{\mathbf{v}}$ at each of the filament node point positions. The other contributions, \mathbf{v}_∞ , \mathbf{v}_{IM} , and the Biot-Savart term, are added in to give the net velocity at each node point. The node positions are then stepped forward in time.

IV. BOUNDARY LAYER MODEL

As discussed in Sec. II, vorticity is ejected into the outer flow from the boundary layer at separation lines. Accurate simulation of the boundary layer and therefore the location of separation might require the use of an unsteady boundary-layer calculation with the full Navier-Stokes equations near separation.

On the other hand, the outer flow strongly influences separation through $\mathbf{u}(\mathbf{r}_S)$ and ∇_{Sp} irrespective of the internal dynamics of the boundary layer. A relatively crude approximation of the mechanics of the boundary layer might then suffice to yield accurate characteristics of the wake. Therefore, in the application of the method to flow past a sphere described in Sec. VI below, a simplified, economical model of the boundary layer was used.

In this model the boundary-layer vorticity is divided into two parts — (1) an upstream attached layer of vorticity (composed of a single sheet) and (2) vortex filaments downstream of this sheet. The downstream boundary or front of the sheet moves with local velocity $\mathbf{u}(\mathbf{r}_S)/2$ which is consistent with the discussion following equation (2.5). When the front moves past a specified downstream latitude, a ribbon of the sheet is removed from the downstream edge and formed into a vortex filament (see fig. 2). For a given cir-

ulation, the heights of the new filament nodes above the surface are chosen so that the filament speed is $|\underline{u}_{rs}|/2$ and the new position of the sheet boundary is determined to maintain (2.5). The initial core radius of the filament is allowed to vary parametrically within a specific range. The minimum of this range is determined by matching the volume of vorticity in the ribbon to the volume of the new filament. The former is, of course, proportional to boundary-layer thickness which in turn is proportional to $Re^{-1/2}$. The maximum core radius in the range is simply the initial height of the node points above the surface so that the edge of the core touches the surface.

The newly formed filament and its unseparated predecessors constitute the vorticity in the remaining part of the attached boundary layer. Computationally they are treated as part of the outer flow. Chorin (ref. 1) and Rogallo use discrete vortices in simulations of two-dimensional separated flows with similar boundary-layer models and have achieved reasonable success in predicting unsteady wake characteristics and body forces. In their studies, new vortices are created at the surface to kill the slip velocity there. In the present study, downstream vorticity production at the surface past the edge of the sheet is ignored. Downstream of separation, however, vorticity production at the surface is known from experiments to be small (ref. 9) due to the nearly flat pressure coefficient in this region. The remaining error can be minimized by adjusting the cutoff latitude to be close to separation.

For general three-dimensional flows more elaborate models most likely will be required. For example, the present model assumes that all the vorticity released from the sheet is locally parallel with the sheet boundary. For spinning bodies or even bodies at angle of attack the vorticity will not be monodirectional from the surface to the top of the boundary layer. Rather, external streamline curvature will produce new vorticity at the surface in the streamwise direction.

V. COMPUTATIONAL ASPECTS

If N is the total number of filament node points and M is the number of surface patches, then the total number of arithmetic operations required at each time step n is given by

$$n = K_1 N^2 + K_2 MN + K_3 M^2 + O(N) + O(M)$$

The first term is due to vortex-vortex interactions (i.e., each vortex segment induces an incremental velocity on all others). The constant K_1 is roughly 50-100 or higher if images are used extensively. The second term arises from the computation of the velocities induced by the filaments at each surface patch and the calculation of \tilde{v} at each node point. The factor K_2 is larger than K_1 but of the same order. With respect to the third term, the LU solution for the single layer potential γ and the calculation of \tilde{v} at each surface patch require $O(M^2)$ operations. The constant K_3 is in the range 5-10, an order of magnitude smaller than K_1 .

The simulation runs for a sphere reported below were performed on an IBM 360/67. The number of node points N could range up to 500 with $M \approx 100$ be-

fore computing times become unreasonable (> 2 min/step). For the same calculation scheme, upper limits for the CDC 7600 and the ILLIAC IV are probably around $N \approx 2,500$ and $N \approx 10,000$, respectively. These limits do not compare favorably with Eulerian grid schemes for, say, the problem of turbulence simulation. There, $32^3 (= 32,768)$ grid points are typically used and run about 3-5 sec/step on a CDC 7600 (refs. 10, 11). The reason is that u grows asymptotically as $N \log N$ for grid calculations if efficient Poisson solvers or spectral methods with FFT are employed.

On the other hand, the Lagrangian vorticity method described in this paper should require fewer mesh points for the same accuracy because (1) mesh or node points are needed only where the vorticity is nonzero, (2) the mesh points concentrate themselves only where required to achieve high concentrations and/or gradients of vorticity, and (3) some of the fine scales are pre-calculated as the structure of the filament cores.

If desired, however, large ($N \approx 10^5$) simulations would be possible by a more efficient algorithm for the vortex-vortex interactions. Several modifications are possible. One is to expand the Biot-Savart integral in equation (3.1) if $|\underline{r} - \underline{r}'|$ is large and retain only the leading terms (ref. 3). Another remedy would be to solve the velocity potential equation $\nabla^2 \psi = -\underline{\omega}$ on a relatively coarse grid and then interpolate the velocities at the filament nodes (ref. 12). The flow segmentation method of Wu (ref. 13) is a third possibility related to the first one in which the influence of distant vorticity is essentially treated on a coarse grid.

VI. SIMULATION RESULTS

In this section preliminary results are given from the simulation of flow past a sphere. These results reveal some of the qualitative features of the structure of the wake and the initial drag and side forces after an impulsive start. More quantitative results, such as pressure distributions, Strouhal number and time-dependent drag and side-force coefficients over several Strouhal periods, are being compiled.

For Reynolds numbers below a few hundred the wake of a sphere takes the form of a steady, axisymmetric separation bubble (ref. 14). As Re increases above this value, the separation bubble becomes unstable and periodically forms into vortex loops which break away (refs. 15, 16). In figure 3 a schematic representation of the vortex configuration in the wake of a sphere at $Re = 10^3$ is shown as observed experimentally by Achenbach using flow visualization techniques in a water channel (ref. 16). The flow is observed from two directions perpendicular to one another. Notice the persistent asymmetry in the depicted wake structure. In figure 4 a sequence of CRT displays is shown from a simulation of flow past a sphere with an impulsive start. The boundary-layer vortices were initially perturbed by a small rigid translation upward normal to the flow axis to excite the wake instability. Each point represents a surface patch on the sphere and the loop farthest upstream to the left is not a vortex but the front of the attached sheet of the boundary lay-

er. Notice the tendency for some of the vortex rings to deform into horizontal loops and lie in a plane containing the flow axis; similar in nature to those shown in figure 3. Longer simulations with provision to remove downstream vortices from the calculation will be required to identify persistent periodic structures with certainty.

Finally, in figure 5, time-dependent drag and side-force coefficients are shown for the simulation depicted in figure 4. The points shown represent averages over time spans during which the number of vortices in the outer flow is constant. The drag force is clearly in the correct range, but, again, longer runs will be necessary to obtain an accurate time average to compare with experiment. Notice that significant side forces develop initially at an exponential rate. These side forces are, of course, consistent with the observed instability of the axisymmetric separation bubble and the resulting horizontal vortex loops in the wake.

REFERENCES

1. Chorin, A. J.: Numerical Study of Slightly Viscous Flow. *J. Fluid Mech.* 57, 785, 1973.
2. Leonard, A.: Numerical Simulation of Interacting, Three-Dimensional Vortex Filaments. Proceedings of the Fourth International Conference on Numerical Methods in Fluid Dynamics. Volume 35 of Lecture Notes in Physics, Robert D. Richtmyer, ed., Springer-Verlag, 1975, pp. 245-250.
3. Lugt, H. J. and Haussling, H. J.: Laminar Flow Past an Abruptly Accelerated Elliptic Cylinder at 45° Incidence. *J. Fluid Mech.* 65, 711, 1974.
4. Mehta, U. B. and Lavan, Z.: Starting Vortex, Separation Bubbles, and Stall—A Numerical Study of Laminar Unsteady Flow Around an Airfoil. *J. Fluid Mech.* 67, 227, 1975.
5. Lighthill, M. J.: Introduction. Boundary Layer Theory, in Laminar Boundary Layers, p. 46, ed. by L. Rosenhead, Clarendon Press, Oxford, 1963.
6. Orszag, S. A.: "Numerical Simulation of Boundary Layer Transition on a Flat Plate," Flow Research Report No. 33, Flow Research, Inc., May 1974.
7. Garabedian, P. R.: Partial Differential Equations, p. 334-340, John Wiley & Sons, Inc., New York, 1964.
8. Forsythe, G. and Moler, C. B.: Computer Solution of Linear Algebraic Systems, Prentice-Hall, Englewood Cliffs, 1967.
9. Achenbach, E.: Experiments on the Flow Past Spheres at Very High Reynolds Numbers. *J. Fluid Mech.* 54, 565, 1972.

10. Orszag, S. A. and Patterson, G. S., Jr.: Numerical Simulation of Three-Dimensional Homogeneous Isotropic Turbulence. Phys. Rev. Letters 28, 76, 1972.
11. Orszag, S. A. and Pao, Y. H.: Numerical Computation of Turbulent Shear Flows, in Adv. in Geophysics, Vol. 18A, ed. by F. N. Frenkiel and R. E. Munn, Academic Press, New York, 1974.
12. Christiansen, J. P.: Numerical Simulation of Hydrodynamics by the Method of Point Vortices. J. Comp. Phys. 13, 364, 1973.
13. Wu, J. C.; Spring, A. H.; and Sankar, N. L.: A Flowfield Segmentation Method for the Numerical Solution of Viscous Flow Problems. Proceedings of the Fourth International Conference on Numerical Methods in Fluid Dynamics. Volume 35 of Lecture Notes in Physics, Robert D. Richtmyer, ed., Springer-Verlag, 1975, pp. 452-457.
14. Taneda, S.: Studies on the Wake Vortices (III). Experimental Investigation of the Wake Behind a Sphere at Low Reynolds Numbers. Res. Inst. Appl. Mech., Kyushu University, Fukuoka, Japan, Rep. 4, 99, 1956.
15. Magarvey, R. H. and MacLatchy, C. S.: Vortices in Sphere Wakes. Can. J. Phys. 43, 1649, 1965.
16. Achenbach, E.: Vortex Shedding from Spheres. J. Fluid Mech. 62, 209, 1974.

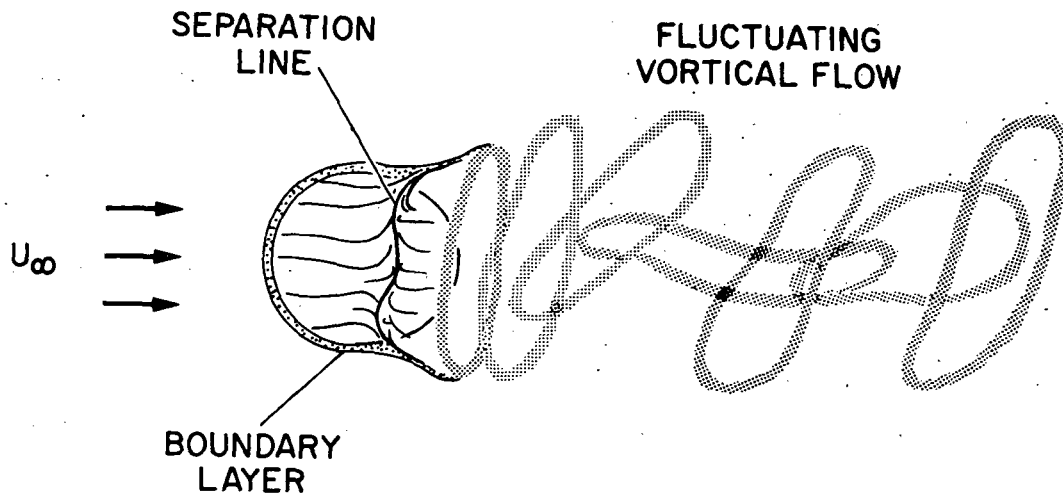


Figure 1.—Schematic drawing of 3-dimensional unsteady, separated flow.

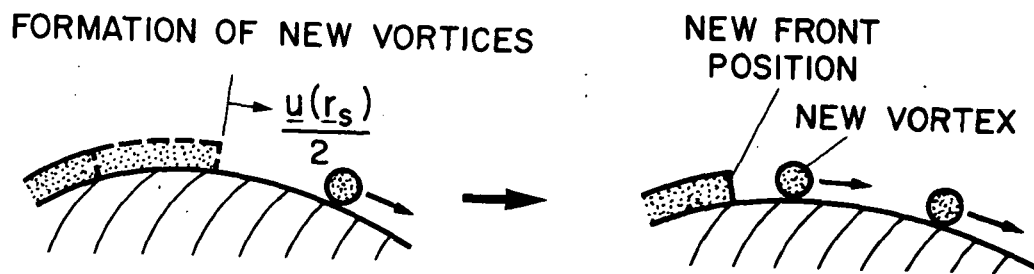


Figure 2.—Formation of new vortices from the attached sheet.

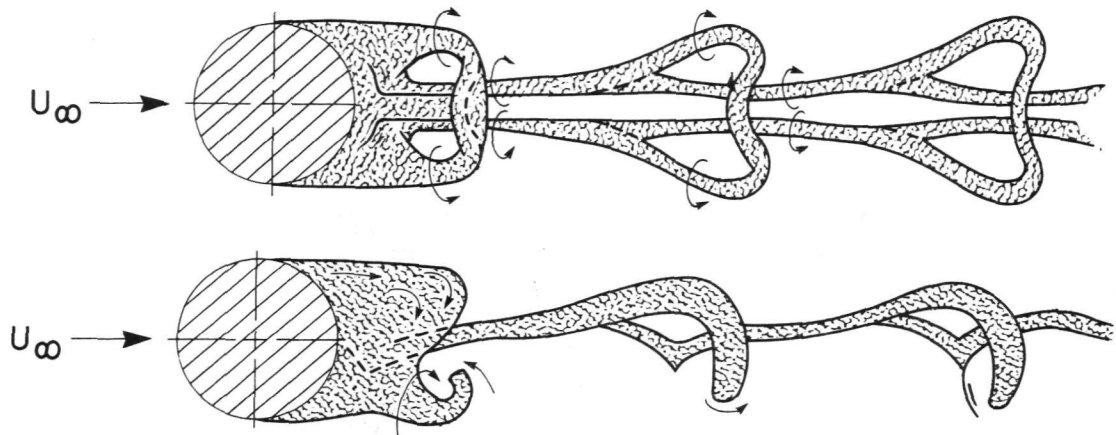


Figure 3.—Vortex structure in the wake of a sphere as observed by Achenbach (ref. 16) $Re = 10^3$.

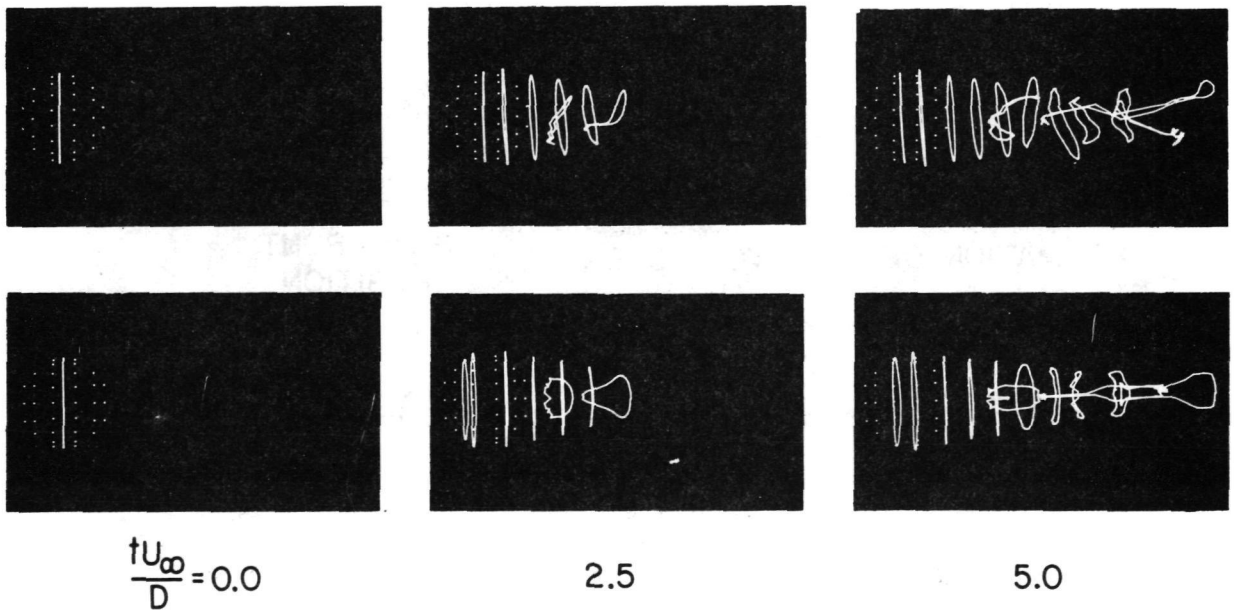


Figure 4.—Simulation of flow past a sphere with an impulsive start as observed from two directions perpendicular to one another.

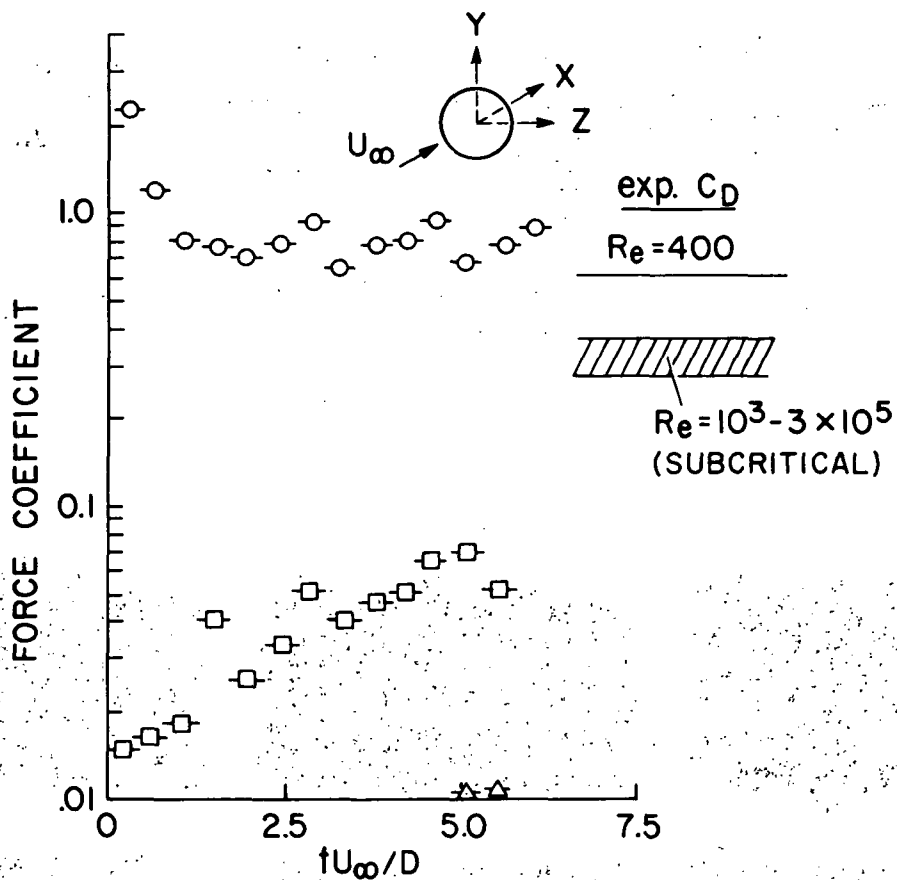


Figure 5.- Force coefficients vs. time for an impulsive start. $C_X = C_D$, \circ ; C_Y , \square , C_Z , \triangle . Sphere radius = 1, $U_\infty = 1$. Filament viscosity = .002, maximum latitude of attached sheet = 90° from front stagnation point, initial filament core radius = initial filament displacement from surface of sphere, filament circulation = 0.5.

Page Intentionally Left Blank

ADVANCED PANEL-TYPE INFLUENCE COEFFICIENT
METHODS APPLIED TO SUBSONIC
AND SUPERSONIC FLOWS*

By F. Edward Ehlers, Forrester T. Johnson,
and Paul E. Rubbert
Boeing Commercial Airplane Company

SUMMARY

Advanced techniques are presented for solving the linear integral equations of subsonic and supersonic potential flow in three dimensions. Both analysis (Neumann) and design (Dirichlet) boundary conditions are treated. Influence coefficient methods are used that encompass both source and doublet panels as boundary surfaces. The methods employ curved panels possessing singularity strengths which vary as polynomials. These and other features were selected to produce a stable, reliable, accurate, and economical scheme, overcoming many problems experienced with earlier methods. Computational results are presented that illustrate these advantages.

INTRODUCTION

Steady, inviscid, and irrotational fluid flow in a domain D is characterized by a perturbation velocity potential ϕ which for incompressible flow satisfies Laplace's equation

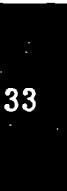
$$\phi_{XX} + \phi_{YY} + \phi_{ZZ} = 0 \quad (P \in D) \quad (1)$$

and for a free-stream supersonic Mach number of $\sqrt{2}$, the wave equation

$$\phi_{XX} - \phi_{YY} - \phi_{ZZ} = 0 \quad (P \in D) \quad (2)$$

The solutions of equations (1) and (2) are readily extended to linearized subsonic compressible flows or supersonic flows at other Mach numbers by a scale transformation of the x variable and by Gothert's rule.

*Work supported by NASA Ames Contract NAS2-7729.



Both analysis and design boundary conditions are considered. Analysis conditions are employed on portions of the boundary where geometry is considered fixed and resultant pressure distributions are desired. The permeability of the fixed geometry is known; hence, analysis conditions are of the Neumann type (specification of normal velocity). Design boundary conditions are used wherever a geometry perturbation is allowed for the purpose of achieving a specific pressure distribution. Here a perturbation to an existing tangential velocity vector field is made; hence, design conditions are fundamentally of the Dirichlet type (specification of potential). The design problem is the more difficult of the two and involves such aspects as stream surface lofting and the relationship between a velocity field and its potential.

Under rather general assumptions, Green's third identity shows that a solution of equation (1) or (2) may be expressed as the potential induced by a combination of source singularities of strength σ and doublet singularities of strength μ distributed on the boundary surface B . For incompressible flow from reference 12,

$$\phi(P) = \iint_B \sigma(Q) \left(\frac{-1}{4\pi r} \right) dB + \iint_B \mu(Q) \frac{\partial}{\partial n_Q} \left(\frac{1}{4\pi r} \right) dB \quad (3)$$

where r is the distance from the field point P to the surface point Q , and $\partial/\partial n_Q$ is the derivative in the direction of the inner surface normal, i.e., directed into the domain D .

For supersonic flow, Green's third identity takes the form

$$\phi(P) = \frac{1}{2\pi} \left[\iint_{C_B} \frac{\sigma(Q)}{-H} dB + \iint_{C_B} \mu(Q) \frac{\partial}{\partial \nu_Q} \left(\frac{1}{H} \right) dB \right] \quad (4)$$

where

$$H = \sqrt{(X_Q - X_P)^2 - (Y_Q - Y_P)^2 - (Z_Q - Z_P)^2}$$

is the so-called hyperbolic distance between the points P and Q , and the lines around the integral denote the taking of the finite part in the sense of Hadamard (ref. 14). The region C_B is the portion of the boundary surface intercepted by the upstream Mach cone ($H^2 > 0$) from the field point P . The quantity $\vec{\nu}$ is the conormal vector and is related to the normal by the relation $\vec{\nu} = (-n_X, n_Y, n_Z)$.

The specification of zero perturbation potential in the region exterior to D leads to a surface distribution on B comprised of $\sigma = \partial\phi/\partial n$ and $\mu = \phi$. The specification of continuity of ϕ across B leads to a source-alone representation. The specification of continuity of $\partial\phi/\partial n$ across B leads to a doublet-alone representation. All three representations have been employed successfully in practice. (See refs. 1, 2, and 3.)

Determination of σ and μ is equivalent to solving equations (1) and (2) in view of equations (3) and (4). Once a priori restrictions on σ and μ have been specified, the entire flow may be rendered unique by imposition of a proper set of boundary conditions. This may be done explicitly, e.g., direct specification of σ and/or μ , as well as implicitly, e.g., sending P to B in equation (3) or (4) and producing an integral equation for σ and μ . In the latter case, it may be necessary to differentiate equation (3) or (4) first. Thus for analysis boundary conditions in subsonic flow,

$$\frac{\partial\phi}{\partial n_P} = \iint_B \sigma(Q) \frac{\partial}{\partial n_P} \left(\frac{-1}{4\pi r} \right) dB + \iint_B \mu(Q) \frac{\partial}{\partial n_P} \frac{\partial}{\partial n_Q} \left(\frac{1}{4\pi r} \right) dB \quad (5)$$

For design boundary conditions, the normal derivative is replaced by the tangential derivative $\partial/\partial t_P$.

For supersonic flow, the conormal and tangential derivatives are used for the analysis and design conditions, respectively. For the analysis boundary conditions, equation (4) yields

$$\frac{\partial\phi}{\partial\nu_P} = \frac{1}{2\pi} \left[- \iint_{C_B} \sigma(Q) \frac{\partial}{\partial\nu_P} \left(\frac{1}{H} \right) dB + \iint_{C_B} \mu(Q) \frac{\partial^2}{\partial\nu_P \partial\nu_Q} \left(\frac{1}{H} \right) dB \right] \quad (6)$$

The numerical solution of equations (3) to (6) is usually accomplished by panel-type influence coefficient methods. The surface B is divided into panels, and singularity distributions dependent on a finite number of unknown parameters are defined for each panel. Then a finite set of control points on B are selected at which the boundary conditions are required to be satisfied. Upon performing the indicated integration, a finite set of linear algebraic equations results, which is denoted symbolically by

$$Ax = b \quad (7)$$

where x is the vector of unknown singularity parameters, b is the vector of known boundary conditions, and A is a matrix of influence coefficients. (A_{ij} represents the influence of x_j on the boundary condition b_i .) The solution of equation (7) may be

accomplished by any number of computer algorithms; whereupon, substitution of the solution into equation (3) yields the potential at any point in D . Sophisticated computer programs based on this procedure have been developed for analyzing the flow about complex configurations involving wings, bodies, nacelles, and propulsion unit effects. (See refs. 4, 5, and 6.)

The earliest methods approximated the boundary surface by flat panels and employed constant-strength source, doublet, or vortex singularities distributed on each panel. These methods display a variety of practical difficulties. First, an excessive number of flat panels are required to represent portions of surfaces with large curvature, e.g., leading edges. Second, quantities of increasing interest, e.g., velocity gradients for boundary-layer analysis, require precise calculation of local velocities, which in turn are affected by local curvature and singularity strength gradient. Third, flat-surface—constant-singularity-strength methods can be quite sensitive to panel configuration. Numerical problems arise when edges of some panels are near control points of others, and fine paneling in regions of rapid flow variation often forces fine paneling elsewhere. Experience and thorough understanding of panel arrangement criteria are often required to obtain reliable solutions; therefore, practical usability is limited. Moreover, paneling configurations desired by other disciplines, e.g., structural analysis and boundary-layer analysis, frequently cannot be accommodated. Finally, the extra degrees of freedom inherent in design boundary conditions require singularity distributions with more than one degree of freedom per panel.

Recently, some improvements to the original flat-surface—constant-strength panels have been studied and in several cases implemented (refs. 6, 7, and 8). The present work arose from extensive operational experience (ref. 4), which provided the motivation to carry out an analysis (not presented) identifying the numerical features required to eliminate the practical difficulties encountered. This led to the present computational scheme employing curved panels, linearly varying source strengths, and quadratically varying doublet strengths and also featuring the capability to handle the mixed analysis/design problems of frequent practical interest.

INCOMPRESSIBLE FLOW

Outline of Method

The approach to the solution of the flow problem via equations (3) and (5) is a building-block approach, wherein the solution is achieved by assembling select networks for incorporation into the matrix equation (7). A network is viewed as a portion of the boundary surface on which a source or doublet distribution is defined, accompanied by a properly posed set of analysis (Neumann) or design (Dirichlet) boundary conditions. A network is defined to be logically consistent in that it contributes as many equations to

the overall problem as it contributes unknowns. Four general network types are used: source/analysis; doublet/analysis; source/design; and doublet/design. The construction of a network involves four tasks: (A) Surface Geometry Definition, (B) Singularity Strength Definition, (C) Control Point and Boundary Condition Specification, and (D) Calculation of Induced Potential or Velocity. Essential features of our computational scheme for accomplishing each task are summarized below and discussed in detail in appendixes A, B, C, and D, respectively.

(A) Geometry input for a network is assumed to be a matrix of corner-point coordinates partitioning the surface into panels. Panel surface shape is obtained by fitting a paraboloid to corner points in an immediate neighborhood by the method of least squares.

(B) Discrete values of singularity strength are assigned to certain standard points on each network. A distribution of surface singularity strength is obtained by fitting a linear (source) or quadratic (doublet) form to these discrete values by the method of least squares.

(C) Certain standard points on each network are assigned as control points. These points include panel center points, as well as edge abutment downwash points in the case of doublet networks. The latter serve to enforce standard aerodynamic edge conditions, e.g., the Kutta condition, zero potential jump at thin edges, and continuity of singularity strength across network junctions. They also serve to render the individual networks logically independent from one another by automatically conveying the proper continuity of singularity strength and gradient across the edges of adjoining networks. In the case of the source design network, certain linear integral conditions are imposed to achieve closure.

(D) Two expansions of the induced potential kernel are employed. The near-field expansion is based upon the assumption of relatively small panel curvature; the far-field expansion is dependent upon a relatively large separation between the field point and panel. All resultant integrals are evaluated in closed form by means of linear recursion relations that have as initial conditions the fundamental logarithm and arc tangent transcendental terms appearing in flat-panel, constant-strength techniques.

Results and Discussion

In this section results from a preliminary investigation of the capabilities of the four network types are discussed. (Further investigation, including comparative analyses with respect to timing, accuracy, etc., is continuing.) The first example consists of an analysis of a thin circular wing at unit angle of attack. The wing surface is represented by a doublet/analysis network with the paneling scheme for the right half of the wing displayed in figure 1(a). Cosine spacing was employed along latitude and longitude lines with panels becoming triangular at the tip. The wake network is not shown but consists of

panels elongated in the stream direction that abut corresponding trailing-edge panels. The entire wing and wake have 108 effective panels (54 per semispan). The resultant spanwise lift distribution is plotted in figure 1(b). The plotted points are obtained from doublet strength along the trailing edge and agree well with the exact solution of reference 9. The present method yields a lift coefficient of 1.776 as compared with the exact coefficient of 1.790. Pressures at three span stations are plotted in figure 1(c); they also agree well with the exact solution.

The circular wing is a reasonably difficult case for any method because of the necessity of using nonuniform paneling. Nevertheless, the panels are convex, similar in size, and possess two streamwise parallel edges. The local least-square definitions of geometry and singularity strength do not in theory require such limiting features. Figures 2 and 3 show the stability of the present formulation under extreme conditions of panel size, shape, and control-point location. In figure 2, an 8 by 6 doublet/analysis network is used to represent the right half of a thin swept wing at 5.7° angle of attack. The panel layout was defined by means of a random number generator resulting in panels that vary considerably in shape and size, that are occasionally nonconvex, overlapping, and inverted. Nevertheless, the calculated spanwise lift distribution, as shown in figure 2(b), is highly accurate. Chordwise pressure distributions displayed in figure 2(c) are likewise stable and deviate appreciably from the reference solution only near the leading edge where pressures become singular. Mismatches in doublet strength and derivative across panels occur in this region indicating that finer leading-edge paneling is required for accuracy. (The method does not enforce strict continuity across edges except for extreme cases where the paneling is too coarse to reproduce the proper singularity strength variation. Thus, the appearance of doublet strength mismatch provides a valuable indicator of locally inadequate paneling.)

In figure 3, a 9 by 9 source/analysis network is employed to represent the right half of a unit sphere immersed in uniform flow. The corner-point generation was again accomplished by means of a random number generator leading to a wide variation in panel size and shape. The use of curved panels produced a geometry remarkably close to spherical. All 81 control points are within a distance of 0.005 from the surface of the unit sphere. Velocity magnitude at each control point is plotted in figure 3(b) as a function of polar angle relative to the free-stream direction. Agreement with the exact solution is good, especially considering the fact that the diameters of some of the panels span an arc of over 60° in violation of our curvature restrictions (appendix A). For comparison, a flat constant-strength source panel analysis was carried out with the same panel arrangement, and the magnitudes of the calculated velocities (V/V_∞) were scattered between 1.2 and 1.7 in the range $85^\circ < \theta < 95^\circ$.

These latter examples demonstrate the extreme "forgiveness" of the method to irregular paneling, a feature which greatly enhances its practical usability for applica-

tions involving complex configurations where regular, evenly spaced paneling cannot always be constructed.

Aerodynamic data for a symmetric wing-body configuration at 10° angle of attack are presented in figure 4. The fuselage is a body of revolution of fineness ratio 0.11. The wing is symmetric, 10 percent thick, and of aspect ratio 5.6 with a leading-edge sweep of 47° . The configuration was first analyzed by the method of reference 4 with 936 flat, constant-strength source panels on the standard wing and body surfaces accompanied with 12 lifting elements. (This represents a typical number of panels used for wing-body applications with the method of ref. 4.)

The paneling scheme for analysis by the present method is depicted in figure 4(a) and comprises 160 surface panels. The body is represented by four source/analysis networks with a total of 96 panels. Two options have been employed for the wing. In the first or source wing option, the wing surface is represented by a 64-panel source/analysis network as shown. The lifting system (not shown) is composed of four networks. The first is a 32-panel (bound) doublet/analysis network on the camber surface of the wing with stream-surface boundary conditions. The second is a 4-panel (shed) doublet/wake network emanating from the wing trailing edge. The third is an 8-panel doublet/wake network inside the body, which extends the bound system to the center plane. The fourth is a 1-panel doublet/wake network, which extends the shed wake network to the center plane. In the second or doublet wing option, the wing surface is represented by a 64-panel doublet/analysis network as shown. No internal doublet/analysis network is required on the wing camber surface; however, a 16-panel doublet/wake network is employed to extend the wing to the center plane. The trailing wake networks are identical to those of the source wing with the following exception. For convenience each wake panel is constructed to bisect the angle formed by the upper and lower surface wing panels at the trailing edge. Three-edge control-point boundary conditions then control the flow off the wing onto the wake at the center of a panel column. One condition forces the sum of the doublet strengths (signed) on the three panel edges to be zero. The remaining two have been artificially modified to reflect the correct wake position, i.e., tangent to the upper surface in this case. This leads to a doublet derivative perpendicular to the trailing edge, which is zero on the lower wing surface and is continuous onto the wake from the upper wing surface.

Spanwise circulation for both wings is displayed in figure 4(b), and a chordwise pressure distribution is displayed in figure 4(c). Note that pitching moment C_M is computed at a predetermined point denoted in figure 4(a) by a cross. The discrepancy between the moments produced by the source wing and the method of reference 4 is equivalent to a shift in the center of pressure of less than 0.5 percent chord. In order to obtain good pressure data for the doublet wing, it was necessary to add a row of narrow panels

to the upper and lower surfaces at the trailing edge. Apparently, the doublet distribution on a wide trailing-edge panel is unable to represent both the flow conditions at the panel center as well as the local trailing-edge flow. Pressure data agreement was uniformly good along the span except for a deterioration on the outboard panels of the doublet wing. Here again the doublet distribution is apparently unable to produce precise pressures at the panel center while simultaneously maintaining zero load at the wing tip. A row of narrow panels at the tip corrects this deficiency as well. Because of such anomalies, the relative advantages of the doublet wing compared with the source wing in terms of efficiency and practical usability are not yet clear. In the future, the intent is to study a variety of wing-body representations from the standpoint of cost and usability. However, it is already evident that a large reduction in the required number of panels as compared with the method of reference 4 is possible. This significantly reduces computation cost and provides opportunity for analysis of exceedingly large and complex configurations.

Figure 5 shows the application of a doublet/design network to the solution of separated flow off the leading edge of a sharp-edge delta wing.¹ The vortex sheet shed from the leading edge was modeled with a doublet/design network, whose strength and position were iteratively established to satisfy the design-type condition of zero pressure jump across the sheet as well as the requirement that the sheet be a stream surface. The thin wing was modeled by means of a 30-panel doublet/analysis network. A simple kinematic model of the vortex core was simulated with a wake network. Other wake networks (not shown) extended downstream from the wing and leading-edge sheets. A typical pressure distribution comparison is shown in figure 5(b) (experimental data from ref. 13). Further details concerning the application of the method to leading-edge vortex flows are presented in reference 10.

Figure 6 shows an application of the source/design network to a two-dimensional airfoil design problem. An NACA 65-010 symmetric airfoil at zero angle of attack was chosen as the nominal configuration. The arbitrary problem selected was a redesign of the airfoil between 20 percent and 90 percent chord producing zero C_p there. Analysis of the NACA 65-010 airfoil was accomplished by means of three source/analysis networks placed between 0 and 20 percent chord, 20 and 90 percent chord, and 90 and 100 percent chord as shown in figure 6(a). The resultant pressure distribution is displayed in figure 6(b) and is virtually identical to that in reference 11. The center network was then replaced by a source/design network with tangential velocities of free-stream magnitude as boundary conditions. Together with the closure (average stream surface) condition, these boundary conditions produced a flow with nonzero normal velocities at the control points. The center network geometry was then updated to eliminate the normal flow and the process repeated. Three iterations produced the reasonably converged geometry

¹The work in this area was performed under NASA Langley contract NAS1-12185.

displayed in figure 6(a). Analysis of this geometry produced the pressure distribution in figure 6(b), which is close to that desired.

Figure 7 shows a three-dimensional test of the source/design network. Paneling of the wing-body model used for the test is displayed in figure 7(a). For economy, the model is somewhat abbreviated; nevertheless, the wing has camber, dihedral, and twist. The purpose of the test was to determine if the source/design network in conjunction with a geometry lofting routine could reproduce the original geometry from a perturbed geometry, using as boundary conditions the pressure distribution of the original wing. Analysis of the original geometry produced the wing pressures at four span stations displayed in figure 7(b). A perturbed or modified wing geometry was achieved by compressing the upper surface approximately 30 percent at four span stations as shown in figure 7(c). Resultant analysis pressure distributions on the modified wing are displayed in figure 7(b). These latter examples illustrate the combined analysis/design capabilities of the method for both thin and thick surface shapes.

SUPERSONIC FLOW

Outline of Method and Preliminary Results

The success of the subsonic method in achieving reliability and accuracy strongly suggests that essentially the same approach be applied to the solution of equation (2) by means of equation (4) for supersonic flow. This is currently being investigated with the effort concentrated in the development of six supersonic network types. Four of these are being developed for application to thin, flat surfaces where linearized boundary conditions suffice. These are source/analysis, doublet/analysis, source/design, and doublet/design. The remaining two are for arbitrary curved surfaces with exact boundary conditions and are of the source/analysis and doublet/analysis type. The developments to date have yielded closed-form integration of the aerodynamic influence coefficients for linear source and quadratic doublet distributions. The inclusion of panel curvature contributes additional terms to the integrals, but these are easily obtained from the integrals for the flat panels of constant strength by simple recursion relations in the same way as for subsonic flow. The integrals all contain the hyperbolic distance which is real for points inside the upstream Mach cone, zero for points on the cone, and imaginary for points outside of it. The domain of influence of points on the panel is properly accounted for by retaining only the real terms as in Woodward's constant vortex strength panel method (ref. 15).

The general supersonic method for arbitrary configurations just described is now in the process of development. However, a related method particularly suited for thin wings was first studied with some success. Although this earlier approach is not planned

to be continued, the basic approach and major findings are summarized in view of its excellent accuracy and extreme computational efficiency for certain classes of problems.

Earlier Approach

Since wings in supersonic flow are usually thin and thus adequately described by linearized boundary conditions, it is natural to represent the wing by doublet and source distributions on a plane. Discontinuities in velocity and velocity gradients occur only along Mach lines emanating from corners of the planform for smooth wings. It is natural in the light of this property to utilize panels formed by a grid of Mach lines on the wing plane. With the introduction of Mach line variables, the hyperbolic distance on the wing plane becomes separable in the variables, and the downwash for a doublet distribution as well as the pressure coefficient for a source distribution takes on forms easily integrable in closed form when the singularity strengths are represented by polynomials in each panel. For panels rectangular in Mach line coordinates, the influence coefficients are simple rational algebraic functions, for triangular panels on supersonic and subsonic leading and trailing edges, inverse sine and logarithmic terms occur, respectively. Additional mathematical details of the method are presented in appendix E.

For the source method representing the thickness distribution of the wing, the value of the source strength is directly related to the downwash on the wing for analysis boundary conditions; while design boundary conditions, in which velocity is specified, lead to an integral equation for the downwash. To test the source method, a 30° swept wing having double parabolic arc profile with a supersonic straight leading edge followed by a subsonic leading edge was chosen. The locations of the control points for both the source and doublet methods are shown in figure 8 for six panels. The calculated pressure coefficient is seen by the points in figure 9 to be indistinguishable from the exact linearized theory solution to equation (4). Prescribing the exact linearized pressure distribution yielded the downwash distribution shown in figure 10. The agreement with the actual wing slopes is seen to be very good.

To test the doublet method, a wing having a parabolic arc of zero thickness with linear spanwise variation of maximum camber was chosen. The pressure coefficient in the portion of the wing behind the supersonic leading edge is shown in figure 11 for three panels and for 10 panels. In this example, as in the source results, increasing panel density improved the accuracy of the panel method and the results were also not sensitive to location of control points in the panel. The solution of the set of algebraic equations for determining the influence coefficients can be speeded up by solving the equations for each panel moving downstream along characteristic strips. This feature of supersonic flow together with the simple formulas for the influence coefficients produces a very efficient numerical method.

Unfortunately, difficulty occurs in the doublet panel method when a subsonic leading-edge region is added. It was found that values of two coefficients in the corner subsonic leading-edge panel are fixed by the requirement of continuity of the doublet distribution across the Mach line emanating from the corner. The downwash contribution from these two terms is large and must be canceled partially by the other two terms in order to represent a smooth wing. To accomplish this, the values of the other two coefficients must be large. The difference between the downwash distribution from the exact linearized solution and the panel method on a cross section of the wing is shown in figure 12. The oscillation increases in amplitude and period as panel density is increased.

Since this appears to be an effect of the corner, the flat-plate corner solution was superimposed on the panel method. This completely solved the difficulties of the method in the first column of panels downstream of the subsonic leading edge as seen in figure 13. However, the triangular leading-edge panels away from the corner still induce instability in the solution.

Although it is likely that some changes may be found to correct the difficulty with the subsonic leading-edge Mach line panel, the flexibility of panel choices in a more general method based on the well-tested subsonic approach will be developed. A single method suitable for both curved panels and planar wings is also a considerable advantage for ease in application. Somewhat greater difficulty in developing a reliable and accurate supersonic method is anticipated, but the added flexibility in the choices of panel shape should aid in achieving satisfactory accuracy and ease in application.

CONCLUDING REMARKS

An advanced numerical technique for calculating subsonic and supersonic potential flows about arbitrary configurations has been presented. The technique is completed for subsonic flow and is accurate, stable, and reliable. Its extreme versatility and adaptability to complex panel patterns fulfill the requirements for acceptance demanded by the user community. The added feature of combined analysis/design provides a capability that is extremely powerful for an extensive variety of applications. Most design applications involve the aerodynamic design of one or more components of a configuration in the presence of others whose geometrical shapes are fixed. The present method provides this capability along with the limiting cases of pure design or analysis. The method is now being extended to supersonic flows.

APPENDIX A

SURFACE GEOMETRY DEFINITION

Geometry input for a network consists of an $M \times N$ array of mesh point coordinates. The network surface is defined locally by a panel passing through four adjacent corner points. It is assumed that discontinuities in surface position, slope, and curvature occur only at network edges; hence for a sufficiently fine mesh, each panel can be approximated by a paraboloid whose shape depends on network mesh points in a surrounding neighborhood. The paraboloid may be defined in a variety of ways; the following way was selected.

Let S be the panel surface corresponding to four adjacent corner points. Construct an orthogonal ξ, η, ζ coordinate system whose origin is the average of the corner points and whose ξ, η plane is the average plane of the corner points. In this coordinate system, S is assumed to be represented in the following form:

$$\zeta = a\xi^2 + b\eta^2 + 2c\xi\eta + d\xi + e\eta + f \quad (\text{A1})$$

The coefficients are obtained by minimizing

$$R = \frac{1}{2} \sum_k W_k \left(\zeta(\xi_k, \eta_k) - \zeta_k \right)^2 \quad (\text{A2})$$

where (ξ_k, η_k, ζ_k) is a corner point of S or a mesh adjacent to a corner point of S . The weights W_k are chosen large when (ξ_k, η_k, ζ_k) is a corner point of S so that S very nearly passes through its corner points. The coefficients d and e may be eliminated by an iterative process of rotation about the ξ, η axes followed by another minimization of R . The coefficients c and f may be eliminated in the usual way by a rotation about the ζ axis and translation of the ξ, η plane, respectively. A canonical local coordinate system is finally achieved with S defined by

$$\zeta = a\xi^2 + b\eta^2 \quad ((\xi, \eta) \in \Sigma) \quad (\text{A3})$$

where Σ is the quadrilateral formed by the projection of the corner points of S on the ξ, η plane. Let

$$\delta = \frac{1}{2} \text{Max}_{(\xi, \eta) \in \Sigma} \left\{ \sqrt{a^2\xi^2 + b^2\eta^2} \right\} \quad (\text{A4})$$

The assumption is now made that

$$\delta \ll 1 \tag{A5}$$

Define the diameter D of S by

$$D = 2 \operatorname{Max}_{(\xi, \eta) \in \Sigma} \left\{ \sqrt{\xi^2 + \eta^2} \right\} \tag{A6}$$

and the height ω of S by

$$\omega = \operatorname{Max}_{(\xi, \eta) \in \Sigma} \left\{ \left| \zeta(\xi, \eta) \right| \right\} \tag{A7}$$

It can be shown that δ is an upper bound for ω/D ; hence, equation (A5) implies that the ratio of the height of S to its diameter is small. Equation (A5) can always be ensured by sufficiently fine paneling. As a practical matter,

$$\delta < 0.066 \tag{A8}$$

has been adopted as a "rule of thumb" governing panel density. For a two-dimensional circular cylinder, equation (A8) would imply a maximum of 30° subtended angle per panel or a minimum of 12 total panels.

The primary purpose of equation (A5) is to allow for expansion and subsequent integration in closed form of the induced velocity kernels. However, there are other reasons as well. The geometry interpolation scheme for S begins degenerating at higher δ . Moreover, it is doubtful that the assumed linear or quadratic distribution of singularity strengths on S would be adequate for more highly curved panels.

APPENDIX B

SINGULARITY STRENGTH DEFINITION

The distribution of singularity strength on a panel S is assumed to be linear in the case of a source network and quadratic in the case of a doublet network. Specifically, the singularity strength λ at a point $(\xi, \eta, \zeta) \in S$ is assumed to be given by

Source:

$$\lambda(\xi, \eta) = \sigma(\xi, \eta) = \sigma_0 + \sigma_\xi \xi + \sigma_\eta \eta \quad (\text{B1})$$

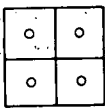
Doublet:

$$\lambda(\xi, \eta) = \mu(\xi, \eta) = \mu_0 + \mu_\xi \xi + \mu_\eta \eta + \frac{1}{2} \mu_{\xi\xi} \xi^2 + \mu_{\xi\eta} \xi\eta + \frac{1}{2} \mu_{\eta\eta} \eta^2 \quad (\text{B2})$$

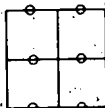
The approximations are valid when paneling is sufficiently fine. The coefficients are not assumed independent; rather they are linear combinations of an independent set of parameters Λ . The parameters Λ are chosen to be the singularity strengths at a set of discrete points Ω on the network surface. The linear relationships between the coefficients and independent parameters are determined by the method of weighted least squares. For each panel S , we minimize

$$R = \frac{1}{2} \sum_k W_k \left(\lambda(\xi_k, \eta_k) - \lambda_k \right)^2 \quad (\lambda_k \in \Lambda) \quad (\text{B3})$$

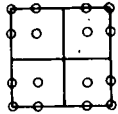
Source/Analysis



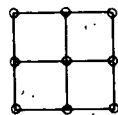
Source/Design



Doublet/Analysis



Doublet/Design



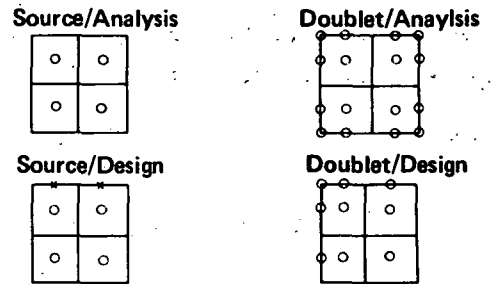
Sketch (B1).

where the summation extends over all points $(\xi_k, \eta_k, \zeta_k) \in \Omega$ which lie on S or one of its immediate neighbors. The weights W_k are chosen large when (ξ_k, η_k, ζ_k) actually lies on S . The choice of Ω for the networks employed is shown in sketch (B1). The circles represent points in Ω . A doublet/wake network was also employed, which is the same as the doublet/analysis network except that the singularity parameters in each column are assumed identical.

APPENDIX C

CONTROL POINT AND BOUNDARY CONDITION SPECIFICATION

On each network a set of control points Γ is chosen at which boundary conditions are to be applied. The set Γ for each network type is shown in sketch (C1). The circles represent points in Γ at which velocity components are specified; the \times 's on the source/design network represent special integral conditions to be explained later. Our doublet/wake network is similar to the doublet/analysis network but with control points only along the upstream edge.



Sketch (C1).

At panel centers, control-point conditions of the following type may be imposed:

$$c_1(\hat{n} \cdot \vec{v}) + c_2\lambda = \beta \quad \left(\text{Specify } c_1, c_2, \beta\right) \quad (C1)$$

or

$$\left(\vec{t}_1 \cdot \vec{v}\right) + \left(\vec{t}_2 \cdot \vec{\nabla}\lambda\right) = \beta \quad \left(\text{Specify } \vec{t}_1, \vec{t}_2, \beta\right) \quad (C2)$$

Here \vec{v} is total inner surface velocity (perturbation plus free stream), λ is local singularity strength (with $\vec{\nabla}\lambda$ its gradient), \hat{n} is the inner surface normal, and \vec{t}_1, \vec{t}_2 are surface tangent vectors. Conditions of type equation (C1) are employed on analysis networks, while those of type equation (C2) are used on design networks. These conditions cover problems involving both interior and exterior flows as well as thin sheets. For example, conditions of type equation (C1) with $c_1 = 1$, $c_2 = 0$, $\beta = 0$ are the usual analysis conditions for flows with impermeable boundaries. For camber design of a thin wing by a doublet/design network, $\vec{t}_1 = 0$, $\vec{t}_2 = \hat{X}$, $\beta = -2 \Delta V_x$ might be used.

The edge control points on the doublet/analysis network serve to control edge downwash and provide for precise network matching. Analysis conditions (eq. (C1)) with $c_1 = 1$, $c_2 = 0$, β finite are applied at all edge points. (These points are slightly withdrawn from the edges for this purpose.)

To give an example of what such edge conditions imply, it is noted that near the common edge of two smoothly adjoining networks, downwash is given by

$$w(\eta) = \Delta\mu/\eta + \Delta(\partial\mu/\partial\eta) \ln(|\eta|) + \text{Regular terms} \quad (\text{C3})$$

where η is the tangential coordinate perpendicular to the edge, $\Delta\mu$ is the jump in doublet strength across the edge, and $\Delta(\partial\mu/\partial\eta)$ is the jump in the derivative of doublet strength perpendicular to the edge. A control point placed near the edge requiring that downwash be finite will tend to make $\Delta\mu$ vanish, i.e., μ continuous across the edge. A similar control point on the opposing panel of an adjoining network will, in addition, force $\Delta(\partial\mu/\partial\eta)$ to vanish, thereby establishing continuity of $\partial\mu/\partial\eta$. As an example of the function of these edge conditions, consider the doublet/analysis network in sketch (C1) to be the right side of a planar symmetric wing with free-stream flow perpendicular to the upper or leading edge. The control points on the leading edge will force μ to zero on that edge since μ is zero ahead of the leading edge. A similar situation exists for the tip edge. The control points along the centerline in conjunction with a reflected doublet surface will ensure that $\partial\mu/\partial\eta$ vanishes along the centerline. Finally, the control points along the trailing edge in conjunction with the control points on an abutting wake network will produce continuity of μ and $\partial\mu/\partial\eta$ onto the wake. Because of the particular construction of the doublet distribution on wake networks, this implies that the derivative of μ in the free-stream direction will vanish along the trailing edge. Recalling now that doublet strength is identical to potential jump, it is seen that all the usual planar wing edge conditions including the Kutta condition are automatically satisfied.

The edge boundary conditions for the particular doublet/design network displayed in sketch (C1) are identical to those of the doublet/analysis network. They control edge downwash and consequently control $\Delta\mu$ and $\Delta(\partial\mu/\partial\eta)$ as well. In the case of the design network these conditions are fundamental to the boundary value problem and remove the degrees of freedom produced by specifying only tangential derivatives of the potential. The design network in sketch (C1) assumes inflow on the left and upper edges (i.e., edges with control points), and, of course, the specified tangential velocity components at panel centers must reflect this fact. Other variants are possible with edge control points wherever inflow occurs.

The source design network is assumed to be paneled with columns aligned along streamlines. In practice this requirement may be relaxed considerably, and only a general streamwise alinement appears necessary. The auxiliary conditions schematically denoted in sketch (C1) by \times at the head of each column are of the form

$$\iint_c (c_1(\hat{n} \cdot \vec{v}) + c_2\lambda) ds = \iint_c \beta ds \quad (\text{C4})$$

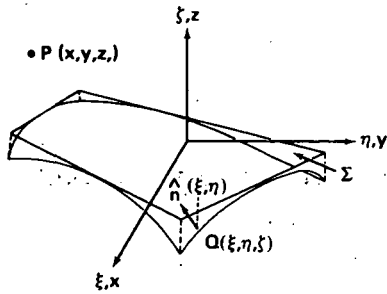
where c denotes a panel column of the network.

Equation (C1) is assumed to be satisfied in the mean for each column of the network. This represents a closure condition, which enables a designed surface to continuously join abutting upstream and downstream surfaces or to form closed airfoils in the case of thin wing design.

Finally, note that the doublet/wake network is fundamentally of doublet/design type. It is used in place of a doublet/design network when a reasonable guess of the geometry and direction of vorticity is deemed sufficient. (A common use is for the representation of vortex wakes where it is deemed unnecessary to establish the precise wake position.)

APPENDIX D

CALCULATION OF INDUCED POTENTIAL OR VELOCITY



Sketch (D1).

In this appendix, the potential induced by a linearly varying source distribution over a curved panel is calculated. The calculation of induced velocity or doublet potential and velocity is not essentially different. As shown in sketch (D1), let S be the curved panel surface; Σ , its tangent plane projection; Q , a point on S ; \hat{n} , the inner normal to S at Q ; and P , a field point. The potential induced at P by a linear source distribution σ on S is given by

$$\phi(P) = \frac{1}{4\pi} \iint_S \frac{\sigma}{R} ds = \frac{1}{4\pi} \iint_{\Sigma} \frac{\sigma}{R} \sec(\hat{\zeta}, \hat{n}) d\xi d\eta \quad (D1)$$

where

$$\sigma = \sigma_0 + \sigma_{\xi} \xi + \sigma_{\eta} \eta \quad \vec{R} = (x - \xi, y - \eta, z - \zeta)$$

and

$$R = |\vec{R}| = [(x - \xi)^2 + (y - \eta)^2 + (z - \zeta)^2]^{1/2}$$

The surface S is defined by

$$\zeta(\xi, \eta) = a\xi^2 + b\eta^2 \quad (D2)$$

hence,

$$\sec(\hat{\zeta}, \hat{n}) = [1 + 4a^2\xi^2 + 4b^2\eta^2]^{-1/2} \quad (D3)$$

The integral of equation (D1) cannot be integrated in closed form as it stands. However, employing the hypothesis that δ^2 is negligible compared to unity (see eq. (A5)),

the integrand can be approximated by terms that are integrable in closed form. A uniform approximation to $\sec(\hat{\xi}, \hat{\eta})$ can be obtained by noting

$$4a^2\xi^2 + 4b^2\eta^2 \leq (4b)^2 \quad (D4)$$

hence,

$$\sec(\hat{\xi}, \hat{\eta}) \approx 1 \quad (D5)$$

A uniform approximation to $1/R$ is somewhat more difficult to obtain since this factor is singular. Let (x_0, y_0) be the point on Σ closest to (x, y) and set

$$z_0 = \zeta(x_0, y_0) \quad h = z - z_0 \quad r = [(x - \xi)^2 + (y - \eta)^2]^{1/2} \quad (D6)$$

Then

$$\frac{1}{R} = \left[(r^2 + h^2) + 2h(z_0 - \zeta) + (z_0 - \zeta)^2 \right]^{-1/2} = [r^2 + h^2]^{-1/2} \left[1 + \frac{2h(z_0 - \zeta) + (z_0 - \zeta)^2}{r^2 + h^2} \right]^{-1/2} \quad (D7)$$

Let

$$\epsilon = \text{Max}_{(\xi, \eta) \in \Sigma} \left\{ \frac{|z_0 - \zeta|}{r} \right\}$$

Then

$$\left| \frac{2h(z_0 - \zeta) + (z_0 - \zeta)^2}{r^2 + h^2} \right| \leq \frac{2her + \epsilon^2 r^2}{r^2 + h^2} \leq \epsilon + \epsilon^2 \quad (D8)$$

Therefore, if ϵ^2 is everywhere negligible, equation (D7) may be uniformly approximated by

$$\frac{1}{R} \approx \frac{1}{\rho} = \frac{h(z_0 - \zeta)}{\rho^3} \quad \left(\rho = (r^2 + h^2)^{1/2} \right) \quad (D9)$$

But

$$\begin{aligned}
 \epsilon &= \text{Max}_{(\xi, \eta) \in \Sigma} \left\{ \frac{\zeta(x_0, y_0) - \zeta(\xi, \eta)}{r} \right\} \\
 &= \text{Max}_{(\xi, \eta) \in \Sigma} \left\{ \frac{a(x_0 + \xi)(x_0 - \xi) + b(y_0 + \eta)(y_0 - \eta)}{r} \right\} \\
 &\cong \text{Max}_{(\xi, \eta) \in \Sigma} \left\{ \left[a^2(x_0 + \xi)^2 + b^2(y_0 + \eta)^2 \right]^{1/2} \frac{[(x_0 - \xi)^2 + (y_0 - \eta)^2]^{1/2}}{r} \right\} \\
 &\cong \text{Max}_{(\xi, \eta) \in \Sigma} 2 \left\{ \left[a^2(x_0 + \xi)^2 + b^2(y_0 + \eta)^2 \right]^{1/2} \right\} \cong 8\delta
 \end{aligned}$$

A much better bound on ϵ is possible when (x, y) is several diameters from Σ and the assumption that δ^2 is negligible becomes unnecessary. However, in this case we resort to the usual far-field expansion of $1/R$ requiring only moment integrals of the form

$$G(M, N) = \iint_{\Sigma} \xi^M \eta^N d\xi d\eta \quad (D10)$$

Upon substituting equations (D5) and (D9) into equation (D1), an expression is obtained which involves only integrals of the form

$$H(M, N, K) = \iint_{\Sigma} \frac{(x - \xi)^M (y - \eta)^N}{\rho^K} d\xi d\eta \quad (D11)$$

where

$$M = 0, 1, 2, \dots \quad N = 0, 1, 2, \dots \quad K = 1, 3, 5, \dots$$

These integrals may be evaluated in closed form. The term $H(0, 0, 1)$ is well known and contains the familiar logarithm and arc tangent terms (ref. 1). No new tran-

scendental terms appear for higher order integrals. In fact, $H(M,N,K)$ may be calculated with the aid of algebraic recursion relations. We have the obvious identity

$$H(M+2, N, K) + H(M, N+2, K) + h^2 H(M, N, K) = H(M, N, K-2) \quad (D12)$$

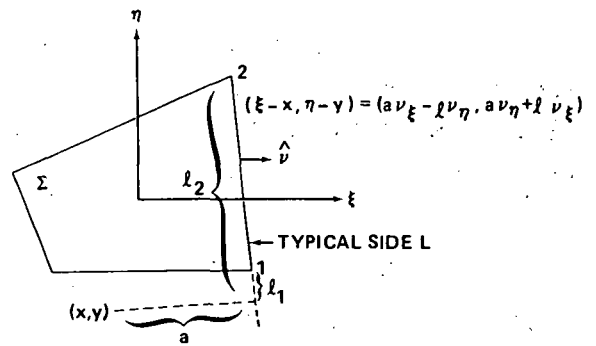
Integration by parts yields

$$(K - 2)H(M,N,K) = (M - 1)H(M-2, N, K-2) + \sum_1^4 \nu_\xi F(M-1, N, K-2) \quad (D13)$$

and

$$(K - 2)H(M,N,K) = (N - 1)H(M, N-2, K-2) + \sum_1^4 \nu_\eta F(M, N-1, K-2) \quad (D14)$$

The summation on the right side of equations (D13) and (D14) is over all four sides of Σ with the contribution of a typical side L displayed in sketch (D2). Here $\nu = \nu(\xi, \eta)$ is the unit outer normal of L , and $F(M,N,K)$ is the line integral defined by



Sketch (D2).

$$F(M,N,K) = \int_L \frac{(x - \xi)^M (y - \eta)^N}{\rho^K} dl \quad (D15)$$

The expression $F(M,N,K)$ satisfies three recursion relations of its own.

We have the identities

$$F(M+2, N, K) + F(M, N+2, K) + h^2 F(M, N, K) = F(M, N, K-2) \quad (D16)$$

and

$$\nu_\xi F(M+1, N, K) + \nu_\eta F(M, N+1, K) = -a F(M, N, K) \quad (D17)$$

Integration by parts yields

$$(K - 2)\nu_{\xi}F(M, N+1, K) - (K - 2)\nu_{\eta}F(M+1, N, K) = N\nu_{\xi}F(M, N-1, K-2) - M\nu_{\eta}F(M-1, N, K-2) + E(M, N, K-2) \quad (D18)$$

where

$$E(M, N, K) = \frac{(x - \xi)^M (y - \eta)^N}{\rho^K} \Big|_1^2 \quad (D19)$$

The quantities $E(M, N, K)$ may be evaluated directly from equation (D19), although recursion relations exist for them as well.

The recursion relations for H and F may be recombined to yield efficient and accurate evaluation procedures. For example, one should employ equation (D12) as an outer recursion relation since the recursion relations for F must be applied separately to each side L of Σ . Some care must be exercised, however, in view of the fact that S is a singular surface for H . In the interior of S

$$H(M, N, K) = \lambda(M+N+2, K) |h|^{M+N+2-K} + \text{Finite terms} \quad (D20)$$

where the $\lambda(M+N+2, K)$ are constants. This singular behavior of H is reflected in the fundamental K recursion relation

$$(K - 2)h^2 H(0, 0, K) = (K - 4)H(0, 0, K-2) - \sum_1^4 \nu_{\xi} F(1, 0, K-2) + \nu_{\eta} F(0, 1, K-2) \quad (D21)$$

that becomes singular as $h \rightarrow 0$. When h is sufficiently small, equation (D21) must be reversed and applied to the finite part of H only. A similar situation exists for F when $\sqrt{a^2 + h^2} \rightarrow 0$.

APPENDIX E

PLANAR MACH LINE PANEL METHOD IN SUPERSONIC LINEARIZED FLOW

With the introduction of Mach line variables,

$$\left. \begin{aligned} x &= \frac{M(x - \beta y)}{2\beta} \\ y &= \frac{M(x + \beta y)}{2\beta} \end{aligned} \right\} \quad (E1)$$

with

$$\beta = \sqrt{M^2 - 1}$$

the hyperbolic distance H on the plane becomes separable in the variables and the downwash $w = \partial\phi/\partial\nu = \partial\phi/\partial z$ for a doublet distribution from equation (6) reduces to

$$w = -\frac{M}{2\pi} \frac{\partial^2}{\partial x \partial y} \int_{S_w} \frac{\Delta\phi(x_1, y_1) dx_1 dy_1}{\sqrt{(x - x_1)(y - y_1)}} \quad (E2)$$

Similarly, the pressure coefficient C_p from a source distribution σ becomes

$$C_p = -\frac{1}{\pi\beta} \left(\frac{\partial}{\partial x} + \frac{\partial}{\partial y} \right) \int_{S_w} \frac{\sigma(x_1, y_1) dx_1 dy_1}{\sqrt{(x - x_1)(y - y_1)}} \quad (E3)$$

where S_w is the region on the wing upstream of the Mach lines $x_1 = x$ and $y_1 = y$. The differentiation may be performed before the integration when new variables of integration ξ, η are introduced and are defined by

$$d\xi = \frac{dx_1}{\sqrt{x - x_1}} \qquad d\eta = \frac{dy_1}{\sqrt{y - y_1}}$$

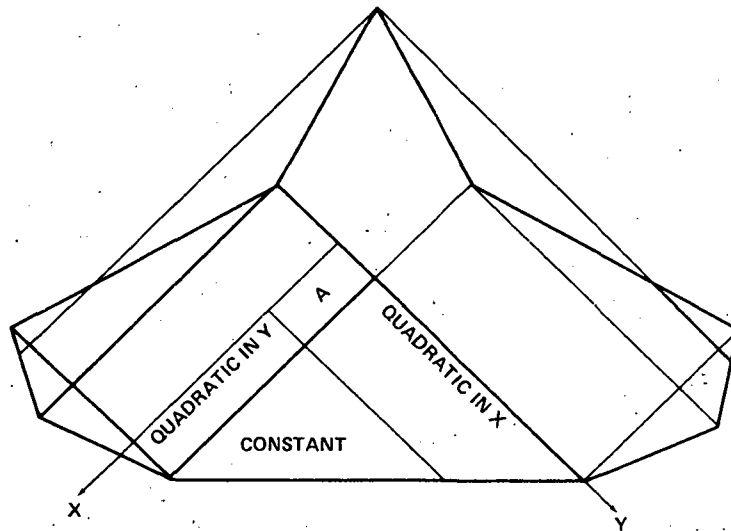
Since the doublet distribution must vanish on the wing leading edge, $\Delta\phi$ on triangular panels was chosen in the form

$$\Delta\phi = (x + \epsilon_1 y)(a_1 + a_2 x + a_3 y + a_4 xy) \quad (\text{E4})$$

where $x + \epsilon_1 y = 0$ is the equation of the panel leading edge. For rectangular panels,

$$\Delta\phi = xy(a_1 + a_2 x + a_3 y + a_4 xy) \quad (\text{E5})$$

where the origin is the upstream panel corner. To ensure continuity of the doublet distribution, the panel edge distribution is continued downstream along characteristic strips as shown in sketch (E1).



Sketch (E1).

For the source distribution,

$$\sigma = a_1 + a_2 x + a_3 y + a_4 xy \quad (\text{E6})$$

on supersonic leading-edge triangular panels, and $\sigma = a_1 xy$ on rectangular panels. For subsonic leading-edge triangular panels, the source distribution is

$$\sigma = a_1 y + a_2 xy$$

A method of analytic continuation along characteristic strips similar to the doublet method is also applied to the source panel method.

Substituting equation (E4) into equation (E2) and performing the integration leads to a relation of the form

$$\frac{2\pi w}{M} = - \sum_{i=1}^4 a_i g_i(x,y) \quad (E7)$$

For supersonic leading-edge panels ($\epsilon_1 > 0$), the g_i functions are

$$g_1(x,y) = f_1(x,y) - f_1(x+\epsilon, s, y-s)$$

$$g_2(x,y) = \epsilon_1 \left\{ y \left[f_1(x+\epsilon_1 s, y-s) - f_1(x,y) \right] + 3 \left[f_2(x,y) - f_2(x+\epsilon_1 s, y-s) \right] \right. \\ \left. + 2\sqrt{y-s} \left[\sqrt{\frac{x}{\epsilon_1}} - \sqrt{\frac{x+\epsilon_1 s}{\epsilon_1}} \right] \right\}$$

$$g_3(x,y) = y \left[f_1(x,y) - f_1(x+\epsilon_1 s, y-s) \right] + f_2(x,y) - f_2(x+\epsilon_1 s, y-s)$$

$$+ 2\sqrt{y-s} \left[\frac{x}{\epsilon_1} - \sqrt{\frac{x+\epsilon_1 s}{\epsilon_1}} \right]$$

$$g_4(x,y) = \epsilon_1 \left\{ y^2 \left[f_1(x+\epsilon_1 s, y-s) - f_1(x,y) \right] - \frac{1}{3}(5x+11y) \left[f_2(x+\epsilon_1 s, y-s) - f_2(x,y) \right] \right.$$

$$\left. - \frac{5}{3} \left[f_3(x+\epsilon_1 s, y-s) - f_3(x,y) \right] + \frac{4}{3} \sqrt{y-s} \left[s \sqrt{\frac{x}{\epsilon_1}} + 2 \left(\frac{x}{\epsilon_1} + y \right) \left(\sqrt{\frac{x}{\epsilon_1}} - \sqrt{\frac{x}{\epsilon_1} + s} \right) \right] \right\}$$

(E8)

where

$$\left. \begin{aligned}
 f_1(x,y) &= \frac{\pi}{2} && \left(x < 0, y \geq -\frac{x}{\epsilon_1} \right) \\
 &= \sin^{-1} \sqrt{\frac{y}{y + (x/\epsilon_1)}} && (x > 0, y > 0) \\
 f_2(x,y) &= \frac{\pi \left[(x/\epsilon_1) + y \right]}{4} && \left(x < 0, y \geq -\frac{x}{\epsilon_1} \right) \\
 &= -\frac{\sqrt{xy/\epsilon_1}}{2} + \frac{\left[(x/\epsilon_1) + y \right] f_1(x,y)}{2} && (x > 0, y > 0) \\
 f_3(x,y) &= \frac{\pi \left[(x/\epsilon_1) + y \right]^2}{16} && \left(x < 0, y \geq -\frac{x}{\epsilon_1} \right) \\
 &= \frac{y\sqrt{xy/\epsilon_1}}{4} + \frac{\left[(x/\epsilon_1) + y \right] f_2(x,y)}{4} && (x > 0, y > 0)
 \end{aligned} \right\} \quad (E9)$$

Here the origin of x, y is defined so that points on the panel are $0 \geq x \geq -\epsilon_1 s$, $-\epsilon_1 s \leq y \leq s$. Equations (E9) hold for points outside the panel $x > 0, y > s$ and may be applied to evaluate the downwash as other points on the wing by setting all terms with negative radicands to zero. (Terms like $\sqrt{(x - \epsilon s)(y - s)}$ must be discarded even though they yield real values.) This rule applies to the influence coefficients in the subsequent analysis as well.

Similarly for a subsonic leading edge, with $\epsilon_1 = -\epsilon_2$,

$$\frac{2\pi w}{M} = - \sum_{i=1}^4 a_i S_i(x,y) \quad (E10)$$

where

$$\left. \begin{aligned}
 S_1(x,y) &= \sqrt{\epsilon_2} [f_4(x-\epsilon_2 s, y-s) - f_4(x,y)] \\
 S_2(x,y) &= x S_1(x,y) + \sqrt{\epsilon_2^3} [f_5(x-\epsilon_2 s, y-s) - f_5(x,y)] + 2\sqrt{x-\epsilon_2 s} [\sqrt{y} - \sqrt{y-s}] \\
 S_3(x,y) &= \frac{x S_1(x,y)}{\epsilon_2} + 3\sqrt{\epsilon_2} [f_5(x,y) - f_5(x-\epsilon_2 s, y-s)] - 2\sqrt{x-\epsilon_2 s} [\sqrt{y} - \sqrt{y-s}] \\
 S_4(x,y) &= \frac{x^2}{\epsilon_2} S_1(x,y) + \sqrt{\frac{\epsilon_2^3}{3}} \left(\frac{11x}{\epsilon_2} - 5y \right) [f_5(x,y) - f_5(x-\epsilon_2 s, y-s)] \\
 &\quad + 5\sqrt{\frac{\epsilon_2^3}{3}} [f_6(x,y) - f_6(x-\epsilon_2 s, y-s)] - \frac{8}{3}(x-\epsilon_2 y)\sqrt{x-\epsilon_2 s} [\sqrt{y} - \sqrt{y-s}] \\
 &\quad - 4s\sqrt{\frac{\epsilon_2^3}{3}} \sqrt{\frac{y(x-\epsilon_2 s)}{\epsilon_2}}
 \end{aligned} \right\} \quad (E11)$$

and

$$\left. \begin{aligned}
 f_4 &= \log \frac{\sqrt{y} + \sqrt{x/\epsilon_2}}{\sqrt{(x/\epsilon_2) - y}} \quad (x,y > 0) \\
 f_5 &= \frac{\sqrt{xy/\epsilon_2}}{2} + \frac{[(x/\epsilon_2) - y]}{2} f_4(x,y) \\
 f_6 &= \frac{x\sqrt{xy/\epsilon_2}}{4\epsilon_2} - \frac{[(x/\epsilon_2) - 1]}{4} f_5(x,y)
 \end{aligned} \right\} \quad (E12)$$

The origin for the coordinates x, y is the upstream leading-edge corner. The panel is defined as $0 \leq x \leq \epsilon_2 s$, $x/\epsilon_2 \leq y \leq s$.

For rectangular panels, substitution of equation (E5) into equation (E2) yields

$$\frac{2\pi w}{M} = - \sum_{i=1}^4 a_i h_i(x,y) \quad (E13)$$

where

$$\left. \begin{aligned} h_1(x,y) &= 2 \left\{ \sqrt{xy} - \sqrt{x(y - \Delta y)} - \sqrt{(x - \Delta x)y} + \sqrt{(x - \Delta x)(y - \Delta y)} \right\} \\ h_2(x,y) &= \frac{4}{3} x h_1(x,y) + \frac{4}{3} \Delta x \sqrt{(x - \Delta x)} \left[\sqrt{y - \Delta y} - \sqrt{y} \right] \\ h_3(x,y) &= \frac{4}{3} y h_1(x,y) + \frac{4}{3} \Delta y \sqrt{y - \Delta y} \left[\sqrt{x - \Delta x} - \sqrt{x} \right] \\ h_4(x,y) &= \frac{16}{9} \left\{ x y h_1(x,y) + \sqrt{y - \Delta y} \left[-x \Delta y \sqrt{x} + \left(x \Delta y + \frac{\Delta x \Delta y}{2} + y \Delta x \right) \sqrt{x - \Delta x} \right] \right. \\ &\quad \left. - \Delta x y \sqrt{y} \left(\sqrt{x - \Delta x} \right) \right\} \end{aligned} \right\} \quad (E14)$$

The panel is defined by $0 \leq x \leq \Delta x$, $0 \leq y \leq \Delta y$, and $h_i = 0$ for x or $y < 0$.

The functions g_i , S_i , and h_i are the influence coefficients in the matrix A of equation (7) from the downwash boundary conditions on the panel. Except for the transcendental functions

$$\sin^{-1} \sqrt{\frac{y}{y + (x/\epsilon_1)}}$$

and

$$\log \left[\frac{\sqrt{y} + \sqrt{x/\epsilon_1}}{\sqrt{(x/\epsilon_1) - y}} \right]$$

the influence coefficients are rational algebraic functions. Note that the inverse sine is finite on the supersonic leading edge ($\pi/2$) while the log term becomes infinite on the leading edge $\frac{x}{\epsilon_2} - y = 0$. Since the jump in pressure on the wing is given by

$$\Delta C_p = -\frac{M}{\beta} (\Delta \phi_x + \Delta \phi_y) \quad (\text{E15})$$

with $\Delta \phi$ defined by equation (E4), the pressure is finite at the subsonic leading edge instead of exhibiting an infinite square root singularity.

For the supersonic source panel method, the singularity distribution is equal to the downwash on the wing surface. Hence, for analysis boundary conditions, the influence coefficients at any point of the wing are simple polynomials of second degree since σ is continued analytically beyond the panel along characteristic strips by its values on the panel downstream edges. Since each rectangular panel adds a parameter, there is only one control point at which downwash is prescribed for analysis boundary conditions or the pressure coefficient is prescribed for design boundary conditions. On leading-edge panels there are two downwash control points and one leading-edge corner continuity condition on the supersonic leading edge. (See fig. 8.) With design-type boundary conditions, the pressure coefficient C_p is given and equation (E3) yields an integral equation for the downwash on the wing which must be integrated to yield the wing shape.

Substituting equation (E6) into equation (E3) and performing the differentiation and integration yields

$$\beta \pi C_p = - \sum_{i=1}^4 a_i C_i(x,y) \quad (\text{E16})$$

where

$$C_1(x,y) = \frac{2(1 + \epsilon_1)}{\sqrt{\epsilon_1}} [f_1(x,y) - f_1(x + \epsilon_1 s, y - s)] \quad (\text{E17a})$$

$$C_2(x,y) = -2\sqrt{\epsilon_1} \left\{ (1 + \epsilon_1)y [f_1(x,y) - f_1(x + \epsilon_1 s, y - s)] - (3 + \epsilon_1) [f_2(x,y) - f_2(x + \epsilon_1 s, y - s)] \right\} \quad (\text{E17b})$$

$$C_3(x,y) = \frac{2}{\sqrt{\epsilon_1}} \left\{ (1 + \epsilon_1)y [f_1(x,y) - f_1(x + \epsilon_1 s, y - s)] + (\epsilon_1 - 1) [f_2(x,y) - f_2(x + \epsilon_1 s, y - s)] \right. \\ \left. + 2\sqrt{xy\epsilon_1} - 2\sqrt{(x + \epsilon_1 s)(y - s)\epsilon_1} \right\} \quad (\text{E17c})$$

$$\begin{aligned}
C_4(x,y) = & -2\epsilon_1 \left\{ \frac{(1 + \epsilon_1)y^2}{3} [f_1(x,y) - f_1(x+\epsilon_1 s, y-s)] + \left[\left(3 - \epsilon_1\right) \frac{x}{\epsilon_1} - (a + \epsilon_1)y \right] \right. \\
& [f_2(x,y) - f_2(x+\epsilon_1 s, y-s)] + \frac{(3 - 5\epsilon_1)}{3} [f_3(x,y) - f_3(x+\epsilon_1 s, y-s)] - 2(1 - \epsilon_1)y \sqrt{\frac{xy}{\epsilon_1}} \\
& \left. - \frac{2}{3} \sqrt{y-s} \left[2(x+y-s) \sqrt{\frac{x}{\epsilon_1}} - (2x+3y - \epsilon_1 y - 3s) \sqrt{\frac{x}{\epsilon_1} + s} \right] \right\} \quad (E17d)
\end{aligned}$$

Here $f_1(x)$, $f_2(x)$, and $f_3(x)$ are defined in equations (E9) and the panel definition is the same as for the supersonic leading-edge doublet panel. For rectangular source panels the singularity distribution is in the form

$$\sigma = axy$$

with origin at the upstream corner of the panel. Substituting $\sigma = axy$ into equation (E3) and performing the differentiation and integration lead to

$$\pi\beta C_p = -ah(x,y) \quad (E18)$$

where

$$\begin{aligned}
h(x,y) = & (x+y)\sqrt{xy} - (x+y-\Delta y)\sqrt{x(y-\Delta y)} - (x-\Delta x+y)\sqrt{y(x-\Delta x)} \\
& + (x-\Delta x+y-\Delta y)\sqrt{(x-\Delta x)(y-\Delta y)} \quad (E19)
\end{aligned}$$

As in the doublet panels, the panel is defined by $0 \leq x \leq \Delta x$, $0 \leq y \leq \Delta y$. For subsonic leading- and trailing-edge panels, the source distribution has two parameters and is of the form

$$\sigma = a_1 y + a_2 xy \quad (E20)$$

with the origin at the upstream corner of the panel. With its non Mach line edge defined by $x - \epsilon_2 y = 0$, the substitution of equation (E20) into equation (E3) yields after integration and differentiation

$$\frac{\pi\beta C_p}{2\sqrt{\epsilon_2}} = a_1 S_1(x,y) + a_2 S_2(x,y) \quad (E21)$$

where

$$S_1(x,y) = (1 - \epsilon_2) \left[\left(\frac{x}{\epsilon_2} \right) f_4(x,y) - \left(\frac{x}{\epsilon_2} - s \right) f_4(x - \epsilon_2 s, y - s) - f_5(x,y) + f_5(x - \epsilon_2 s, y - s) \right]$$

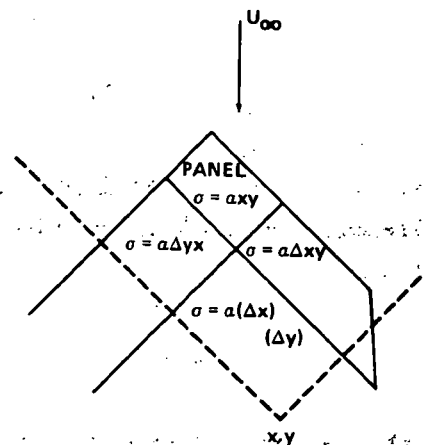
$$S_2(x,y) = (1 - \epsilon_2) x^2 \left[\frac{f_4(x,y) - f_4(x - \epsilon_2 s, y - s)}{\epsilon_2^2} \right] + \left[\frac{(7\epsilon_2 - 3)x}{\epsilon_2} \right.$$

$$+ (5\epsilon_2 + 3)y \left[\frac{f_5(x,y) - f_5(x - \epsilon_2 s, y - s)}{3} \right] - (5\epsilon_2 + 3) \left[\frac{f_6(x,y) - f_6(x - \epsilon_2 s, y - s)}{3} \right]$$

$$+ (1 - \epsilon_2) s^2 f_4(x - \epsilon_2 s, y - s) + \frac{4\sqrt{x/\epsilon_2 - s}}{3} \left[(x - \epsilon_2 s + y - s)\sqrt{y - s} \right.$$

$$\left. - (x - \epsilon_2 + y - s)\sqrt{y} \right] \quad (E22)$$

The influence coefficients in equations (E16) to (E22) were derived under the assumption that σ_1 is continued along characteristic strips by its value on the downstream panel edges. If the y constant Mach line through the point (x,y) intersects a point on the subsonic leading edge or trailing edge (see sketch (E2)), then there is a contribution to the pressure coefficient from the subsonic portion of the leading edge intercepted by the strip and the y characteristic through the point (x,y) . This has the same form for rectangular and supersonic leading-edge panels and is given by



Sketch (E2).

$$\begin{aligned}
E(x,y) = & (1 + \epsilon_2) \left[f_5(x,y) - f_5(x-\epsilon_2 s, y-s) \right] + \frac{(1 - \epsilon_2)^x}{\epsilon_2} \left[f_4(x,y) - f_4(x-\epsilon_2 s, y-s) \right] \\
& + (1 - \epsilon_2) s_3 f_4(x-\epsilon_2 s, y-s) - 2 \sqrt{\frac{xy}{\epsilon_2}} + 2 \sqrt{\left(\frac{x}{\epsilon_2} - s \right) (y - s)}
\end{aligned} \tag{E23}$$

When the parameters associated with the doublet or source distribution are numbered consecutively by moving downstream on characteristic strips of panels and downstream panel to panel on each strip, the matrix of coefficients for equation (7) is almost triangular. If, in those panels having more than one parameter, the associated equations are combined appropriately, the matrix can be easily made triangular. Solving for the parameters is then considerably faster than by the usual process of Gaussian elimination. This property along with the simple influence coefficients makes the Mach line panel method for planar wings very efficient.

APPENDIX F

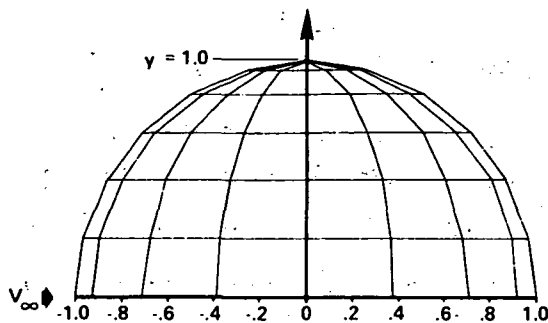
SYMBOLS

The symbols used in the figures are defined in this appendix as follows:

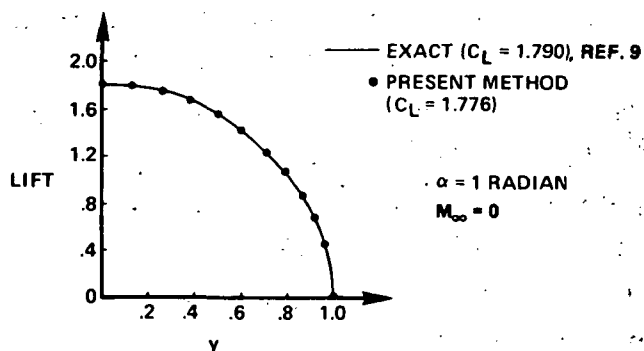
AR	aspect ratio
b	span
C_L	lift coefficient
C_M	pitching-moment coefficient
C_{MAX}	maximum camber
C_p	pressure coefficient
c	chord
L	length
M	Mach number
M_∞	free-stream Mach number
t	thickness ratio
V	velocity
V_∞, U_∞	free-stream velocity
w	downwash
x, y, z	coordinates
α	angle of attack
Λ	sweep angle
θ	polar angle relative to free stream

REFERENCES

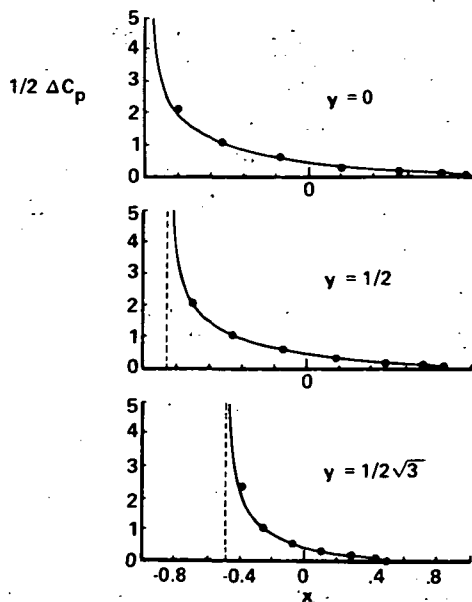
1. Hess, J. L.; and Smith, A. M. O.: Calculation of Nonlifting Potential Flow About Arbitrary Three Three Dimensional Bodies. ES40622, Douglas Aircraft Co., 1962.
2. Rubbert, Paul E.: Theoretical Characteristics of Arbitrary Wings by a Non-Planar Vortex Lattice Method. Doc. No. D6-9244, Boeing Co., Feb. 1964.
3. Morino, Luigi; and Kuo, Ching-Chiang: Subsonic Potential Aerodynamics for Complex Configurations: A General Theory. AIAA J., vol. 12, no. 2, Feb. 1974, pp. 191-197
4. Rubbert, P. E.; and Saaris, G. R.: Review and Evaluation of a Three-Dimensional Lifting Potential Flow Analysis Method for Arbitrary Configurations. AIAA Paper No. 72-188, Jan. 1972.
5. Hess, J. L.: Calculation of Potential Flow About Arbitrary Three-Dimensional Lifting Bodies. Final Tech. Rep., MDC McDonnell Douglas, Oct. 1972.
6. Roberts, A.; and Rundle, K.: The Computation of First Order Compressible Flow About Wing-Body Configurations. AERO MA 20, British Aircraft Corp., Feb. 1973.
7. Mercer, J. E.; and Weber, J. A.: Aerodynamic Influence Coefficient Method Using Singularity Splines. AIAA Paper No. 73-123, Jan. 1973.
8. Hess, J. L.: Higher Order Numerical Solution of the Integral Equation for the Two-Dimensional Neumann Problem. Comput. Methods Appl. Mech. & Eng., vol. 2, 1973, pp. 1-15.
9. Van Spiegel, E.: Boundary Value Problems in Lifting Surface Theory. Verslagen en Verhandelingen, 22, National Luchtvaart-laboratorium, Amsterdam, 1959.
10. Weber, James A.; Brune, Guenter W.; Johnson, Forrester T.; Lu, Paul; and Rubbert, Paul E.: A Three-Dimensional Solution of Flows Over Wings With Leading Edge Vortex Separation. Aerodynamic Analyses Requiring Advanced Computers, Part II, NASA SP-347, 1975, pp. 1013-1032.
11. Abbott, Ira H.; and Von Doenhoff, Albert E.: Theory of Wing Sections. Dover Publ., Inc., c.1959.
12. Kellogg, O. D.: Foundations of Potential Theory. Dover Publ. Co., 1953.
13. Marsden, D. J.; et al.: An Investigation Into the Flow Over Delta Wings at Low Speeds With Leading Edge Separation. Rep. No. 114, College of Aeronautics Cranfield, 1958.
14. Hadamard, Jacques: Lectures on Cauchy's Problem in Linear Partial Differential Equations. Yale Univ. Press, 1928.
15. Woodward, F. A.: An Improved Method for the Aerodynamic Analysis of Wing-Body-Tail Configurations in Subsonic and Supersonic Flow. Part I - Theory and Application. NASA CR-2228, Pt. I, 1973.



(a) Circular wing paneling.

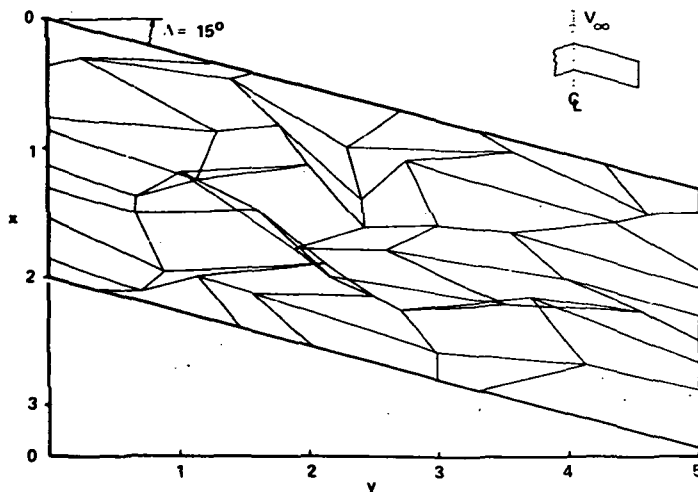


(b) Spanwise lift distribution.

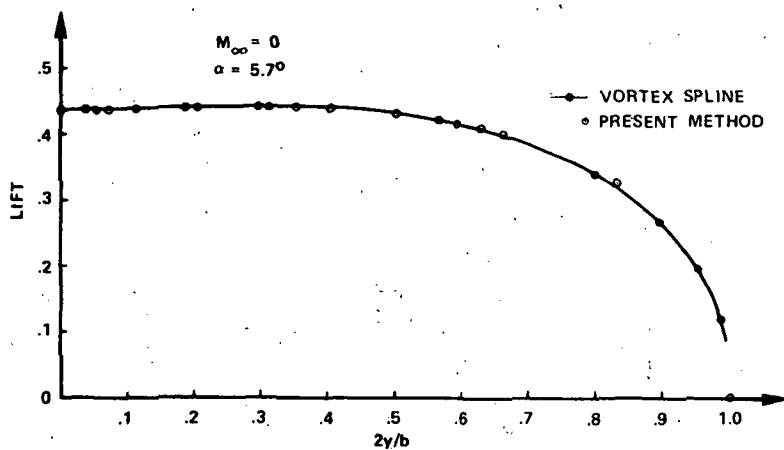


(c) Chordwise pressure distributions.

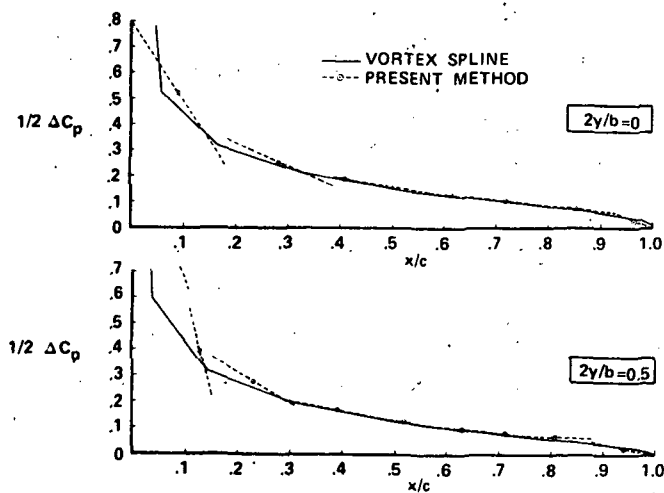
Figure 1.- Circular wing.



(a) Swept-wing random paneling.

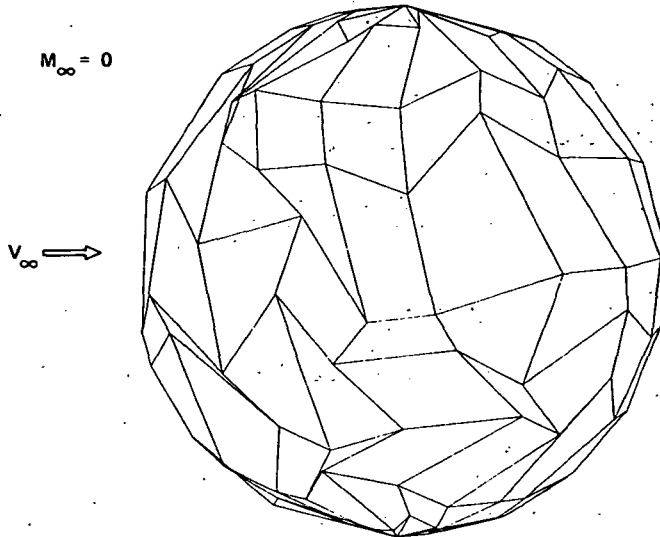


(b) Spanwise lift distribution of swept wing.

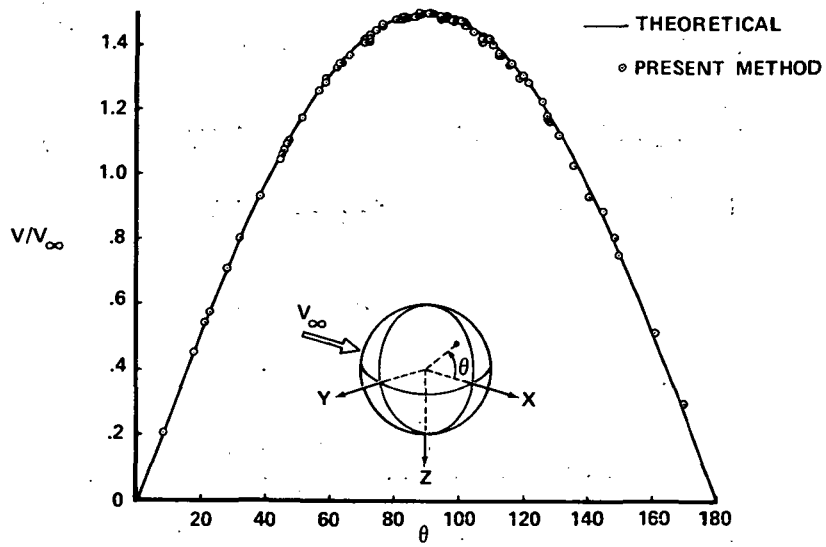


(c) Chordwise pressure distributions for swept wing.

Figure 2.- Swept wing.

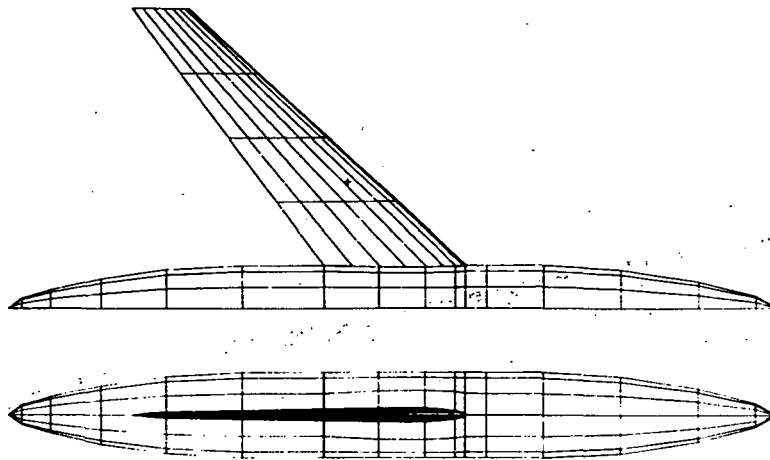


(a) Random paneling of sphere, side view.

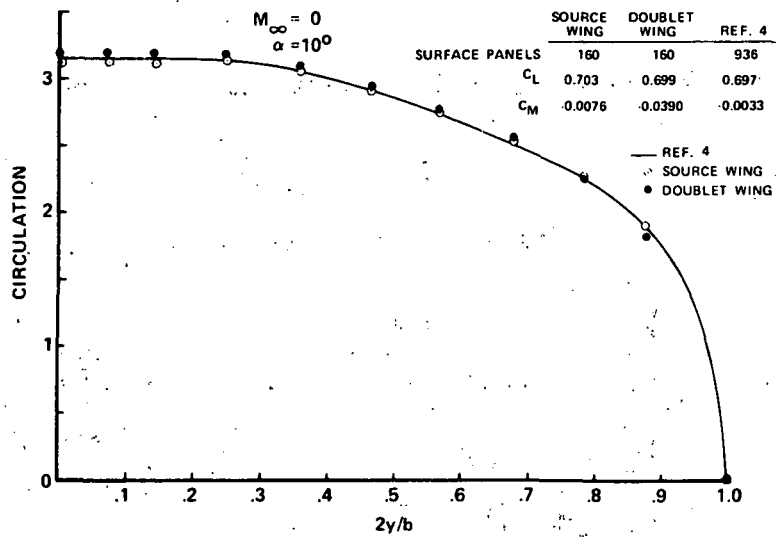


(b) Velocity magnitude at control points.

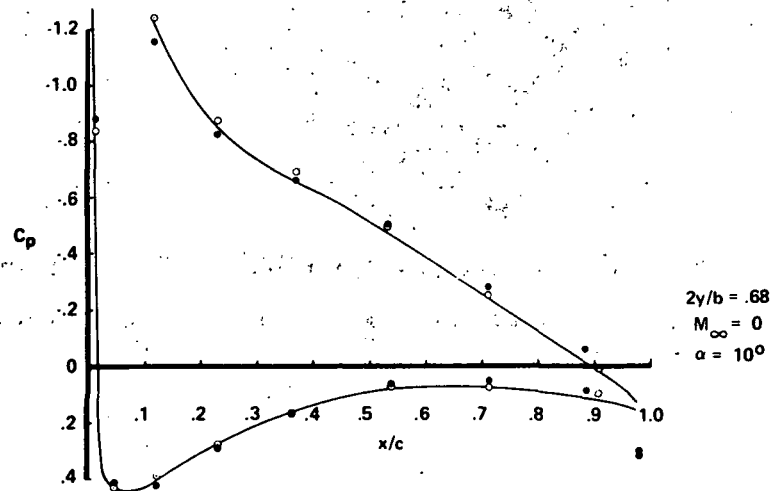
Figure 3.- Sphere.



(a) Paneling scheme for wing-body model.

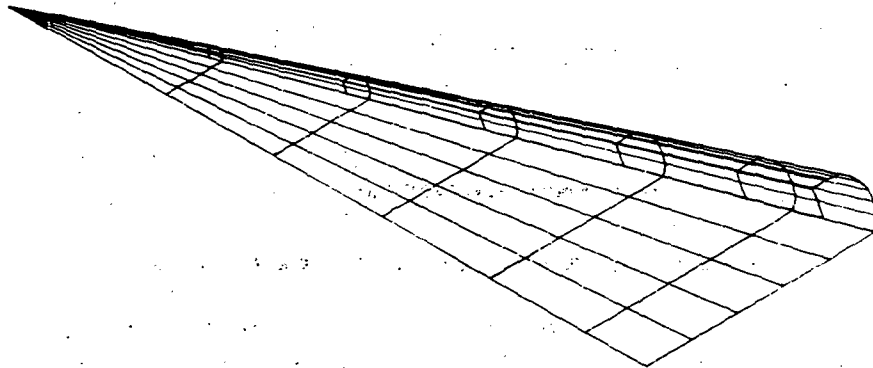


(b) Spanwise circulation.

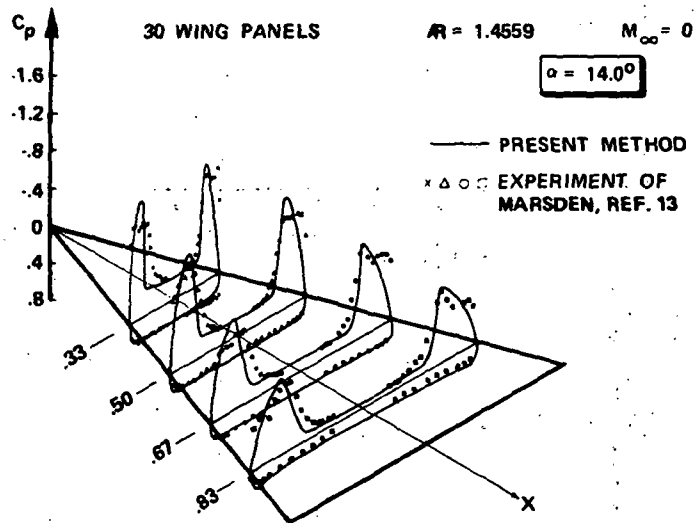


(c) Wing pressures.

Figure 4.- Wing-body analysis.

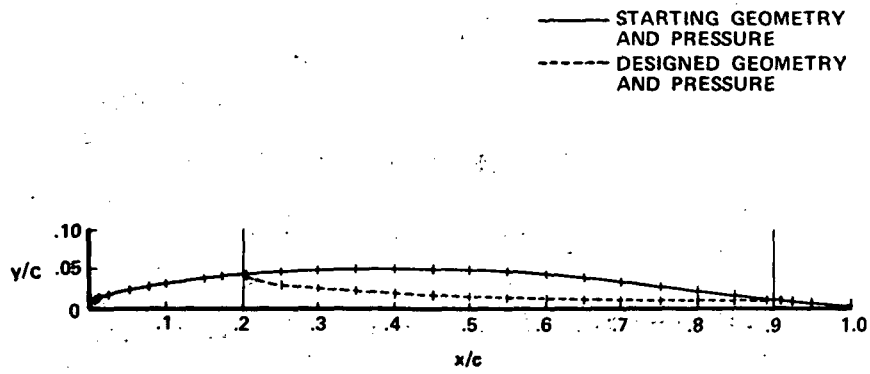


(a) Paneling of delta wing and vortex sheet.

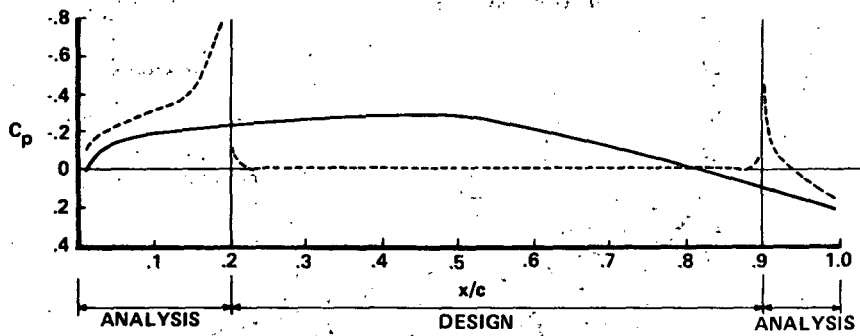


(b) Surface-pressure distribution of delta wing.

Figure 5.- Delta wing with leading-edge separation.

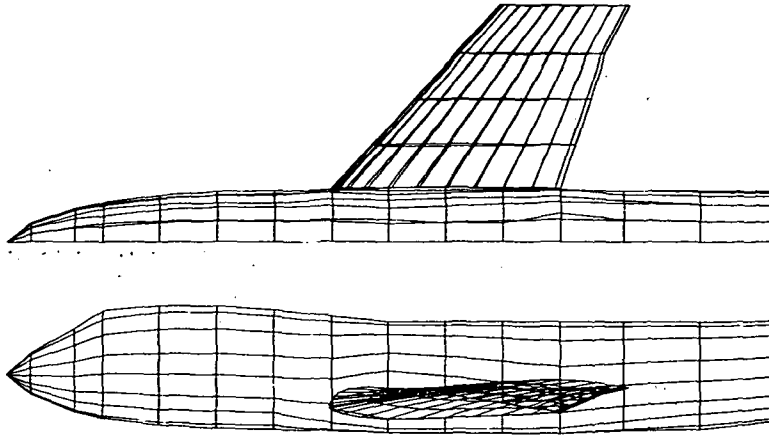


(a) Geometry.

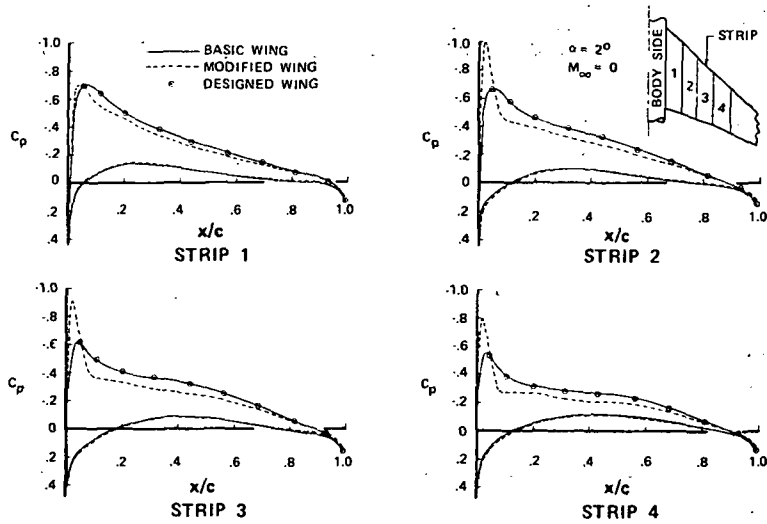


(b) Pressure distribution.

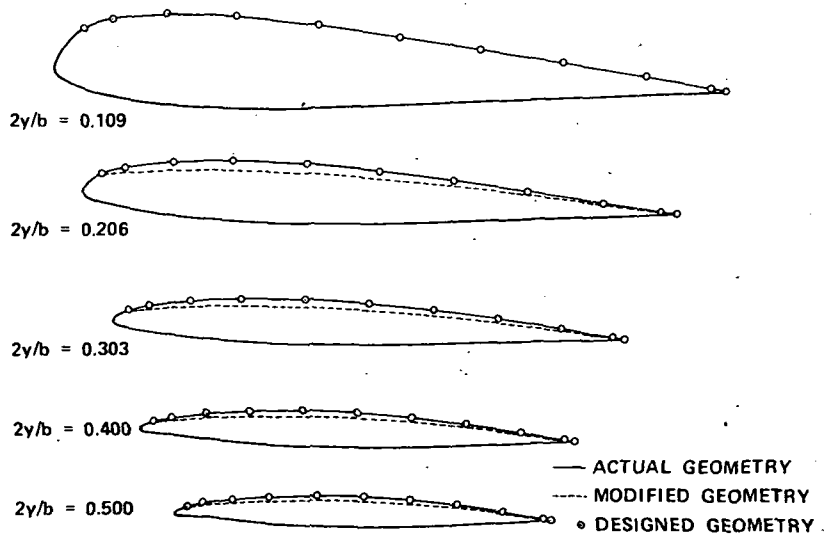
Figure 6.- Design of arbitrary airfoil.



(a) Paneling of design model.



(b) Wing-pressure profiles; analysis mode.



(c) Wing geometry.

Figure 7.- Wing design.

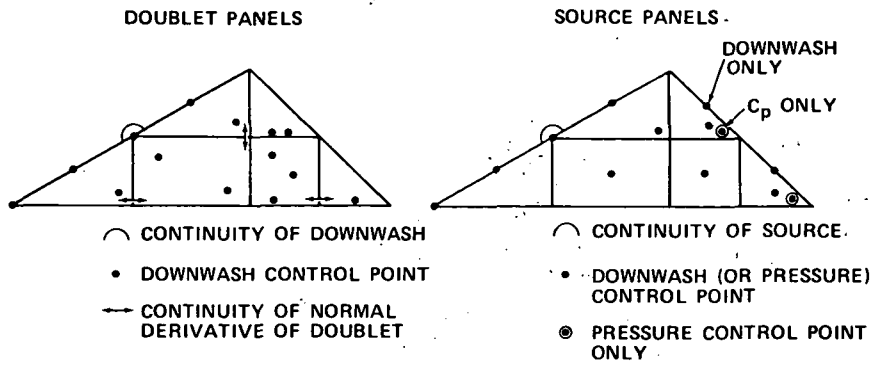


Figure 8.- Doublet and source panel and control-point location.

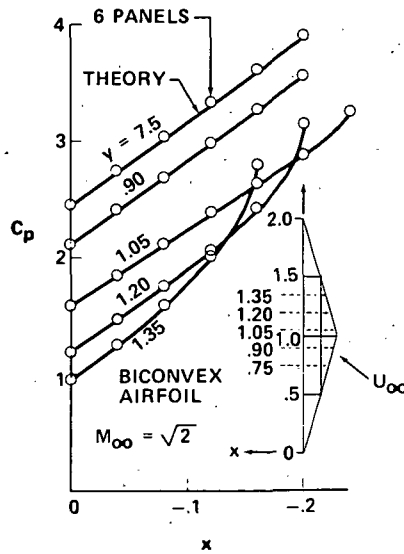


Figure 9.- Comparison of pressure coefficient C_p from the source panel method with linearized theory for a wing with a parabolic arc profile. Analysis-type boundary conditions.

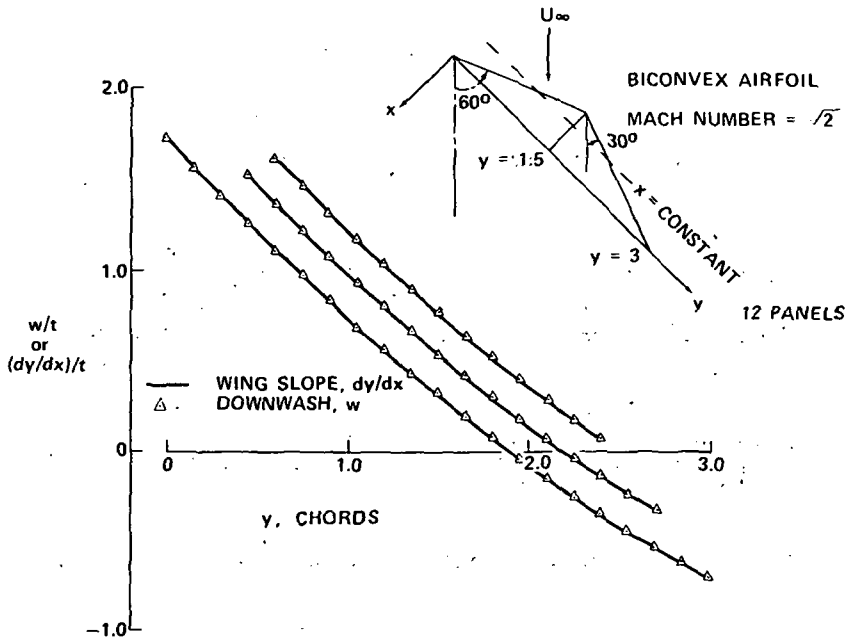


Figure 10.- Comparison of downwash from supersonic source design panel method with actual wing slope.

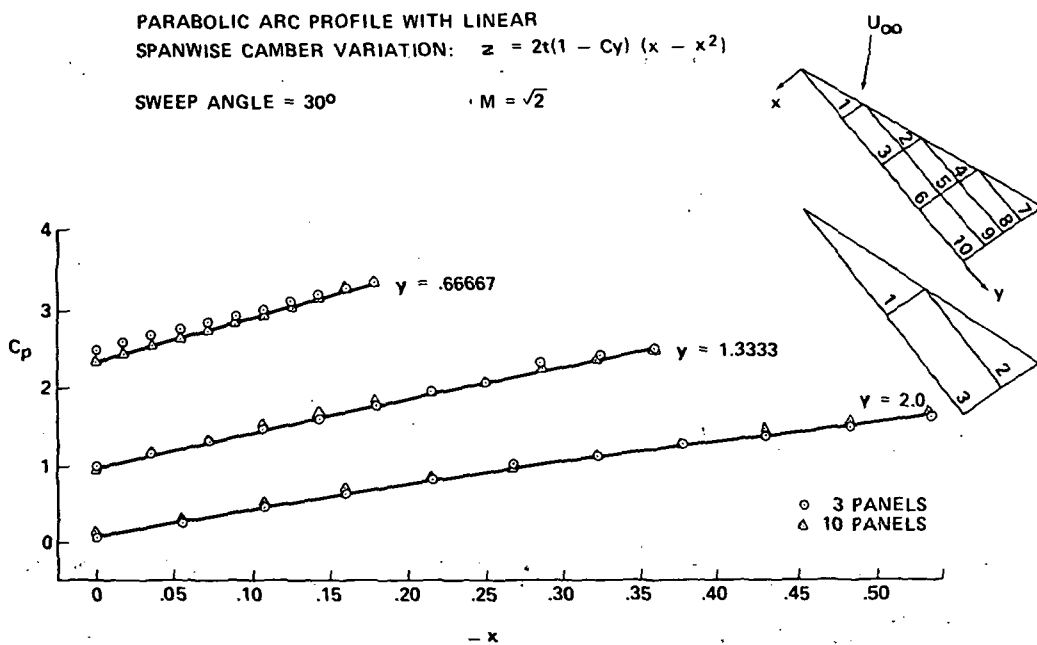


Figure 11.- Comparison of doublet panel method with exact linearized solution. Region behind supersonic leading edge.

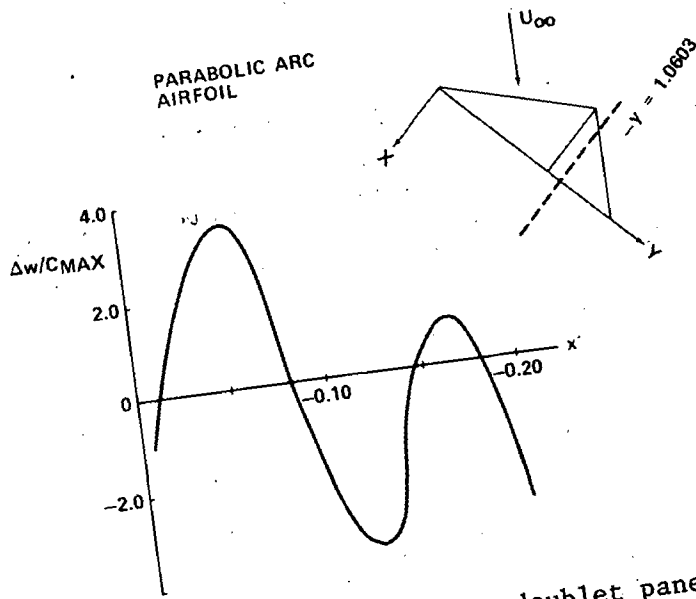
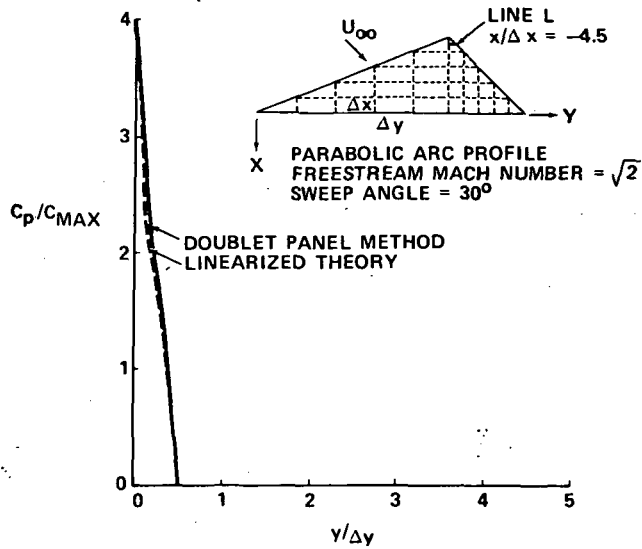
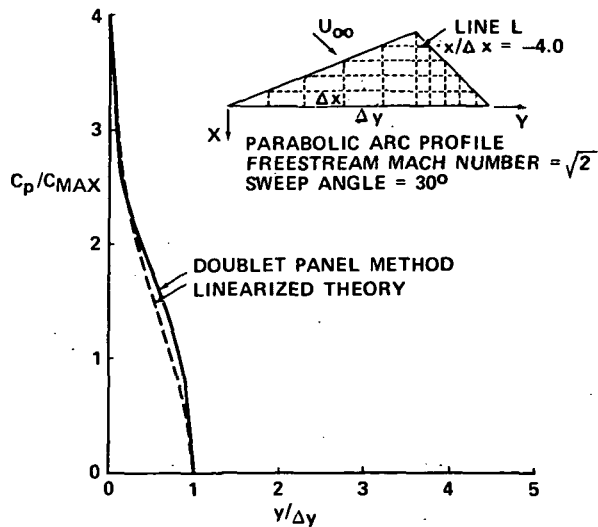


Figure 12.- Error in downwash from doublet panel method.



FLAT PLATE SOLUTION SUPERIMPOSED ON PANEL DOUBLET SOLUTION

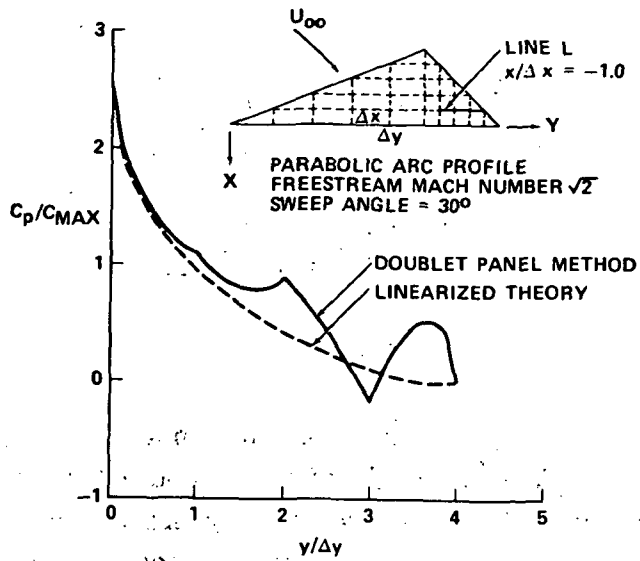
(a) $x/\Delta x = -4.5$.



FLAT PLATE SOLUTION SUPERIMPOSED ON PANEL DOUBLET SOLUTION

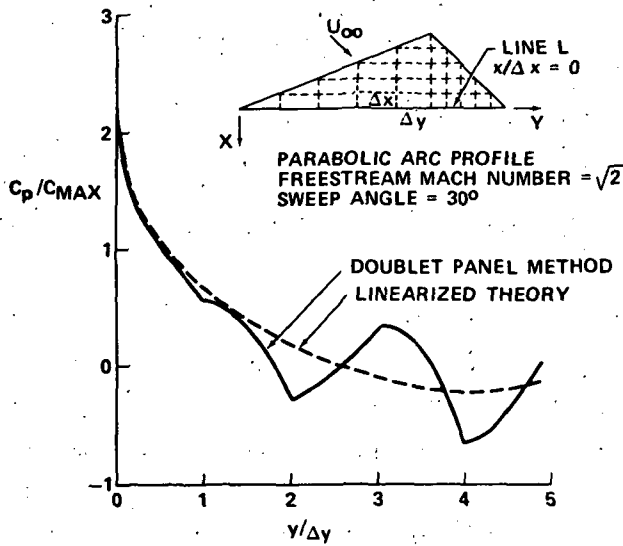
(b) $x/\Delta x = -4.0$.

Figure 13.- Pressure coefficient C_p normalized to maximum camber C_{MAX} versus Mach line coordinate y along line L shown in the figure. Limiting case of subsonic edge parallel to free stream.



FLAT PLATE SOLUTION SUPERIMPOSED ON PANEL DOUBLET SOLUTION

(c) $x/\Delta x = -1.0$.



FLAT PLATE SOLUTION SUPERIMPOSED ON PANEL DOUBLET SOLUTION

(d) $x/\Delta x = 0$.

Figure 13.- Concluded.

SOME RECENT APPLICATIONS OF THE SUCTION ANALOGY TO VORTEX-LIFT ESTIMATES

By John E. Lamar
NASA Langley Research Center

SUMMARY

This paper reviews a recent extension of the suction analogy for the estimation of vortex lift along the side edge of wings and develops the concept of an augmented vortex lift to account for the effect of the leading-edge vortex passing downstream over an aft part of the model. Applications of these extensions have resulted in an improved estimating capability for a wide range of isolated sharp-edge planforms and also for multiple lifting surfaces. Hence, the suction analogy concept can now have wider applicability at both subsonic and supersonic speeds, especially in the preliminary design cycle.

INTRODUCTION

In the design and analysis of high-speed aircraft, a detailed knowledge of the effects of flow separation is required, particularly with regard to critical wing loads and the stability and performance at various off-design conditions. Since attached-flow theories are inadequate for these conditions, the designer currently must rely on extensive and costly wind-tunnel tests which include detailed pressure distributions. In many cases, wind-tunnel tests occur too late in the cycle to impact the important aero/structural design trade-offs. One class of separation which is often encountered is leading- and side-edge separation and the resulting vortex-lift phenomena which are important with regard to the aero/structural trade-offs and also are being increasingly utilized to improve the maneuvering capability of fighters.

In reference 1, Polhamus introduced the concept of a suction analogy for estimation of the lift which arises from separated flow around sharp-edge delta wings reattaching on the upper surface (called vortex flows). The suction analogy states that the potential-flow leading-edge suction force, which no longer acts in the chord plane when leading-edge separation exists, is reoriented on the upper surface (rotated 90°) by the vortex flow action and thereby provides an additional normal force. Because of the change in direction of the suction force, the normal force is now the resultant aerodynamic force.

Figure 1 shows an example of a 75° swept sharp-edge delta wing at a low subsonic Mach number taken from reference 2. The plot of lift as a function of angle of attack

shows the large vortex lift which is well estimated by the suction analogy method. Also shown is the variation of vortex drag with lift and the data are again well estimated by the theory.

After the original application of the suction analogy to delta wings, it was applied to other pointed wings at subsonic speeds (refs. 3 and 4) and to delta wings at supersonic speeds (ref. 4).

This paper deals with recent applications of the suction analogy to more generalized configurations as shown in figure 2. As in the earlier application, the configurations are limited to planforms with sharp edges. At subsonic speeds, applying the analogy to the side edges of planforms leads to an estimate of the vortex lift associated with side-edge vortex flows. Analysis of this estimate has led to the concept of an augmented vortex lift. At supersonic speeds the effects of Mach number and high angle of attack are discussed for delta wings, evidence of vortex lift along the side edge of a rectangular wing is presented, and its magnitude determined. The vortex lift arising on multiple lifting surfaces, such as complete aircraft configurations, can also be treated by the suction analogy.

Subsonic solutions can be computed for potential-flow problems having matrix sizes less than 200×200 with the CDC digital computer in about three minutes and require a core of 53000g. Supersonic solutions obtained with the supersonic-linearized theory can be written in closed form.

SYMBOLS

A	aspect ratio
b	wing span
C_D	drag coefficient, $\frac{\text{Drag}}{q_\infty S_{\text{ref}}}$
$C_{D,0}$	experimental value of drag coefficient at $C_L = 0$
C_L	lift coefficient, $\frac{\text{Lift}}{q_\infty S_{\text{ref}}}$
ΔC_L	C_L increment associated with augmented vortex lift

- C_m pitching-moment coefficient about reference point which is located at $\frac{c_{ref}}{4}$
 unless otherwise stated, $\frac{\text{Pitching moment}}{q_\infty S_{ref} c_{ref}}$
- C_N normal-force coefficient, $\frac{\text{Normal force}}{q_\infty S_{ref}}$
- $\Delta C_{p,u}$ change in upper surface pressure coefficient from its value at $\alpha = 0^\circ$,
 $\frac{\text{Change in upper surface pressure}}{q_\infty}$
- C_S leading-edge suction-force coefficient, $K_{v,le} \sin^2 \alpha$
- c streamwise chord
- \bar{c} characteristic length used in determination of $\bar{K}_{v,se}$
- c_n section normal-force coefficient, $\frac{\text{Section normal force}}{q_\infty c}$
- c_s section suction-force coefficient, $\frac{\text{Section suction force}}{q_\infty c}$
- dF_S differential leading-edge suction force (fig. 5)
- $f_{s,se}$ distributed side-edge suction force
- $f'_{s,se} = \frac{2f_{s,se}(\Delta x')}{bq_\infty \alpha^2}$
- K_p potential-lift factor, $\frac{\partial (C_{N,p})}{\partial (\sin \alpha \cos \alpha)}$
- $K_{v,le}$ leading-edge-vortex-lift factor,
 $\frac{\partial \left(\frac{2 \text{ Leading-edge suction force from one edge}}{q_\infty S_{ref}} \right)}{\partial \sin^2 \alpha}$

$K_{v,se}$	side-edge-vortex-lift factor,	$\frac{\partial \left(\frac{2 \text{ Side-edge suction force from one edge}}{q_\infty S_{ref}} \right)}{\partial \sin^2 \alpha}$
$\bar{K}_{v,se}$	augmented-vortex-lift factor,	$\frac{K_{v,le}}{(b/2) \sec \Lambda} \bar{c}$
l	distance along leading edge from apex	
M	free-stream Mach number	
q_∞	free-stream dynamic pressure	
S	surface area	
U	free-stream velocity	
u	induced velocity in x-direction at point (x,y)	
v	induced velocity in y-direction at point (x,y)	
w_{net}	sum of induced downwash and $U\alpha$ at $\alpha = 1$ rad	
\bar{w}_{net}	average value of w_{net}	
x,y,z	distances from a coordinate origin located at leading-edge apex; x positive downstream, y positive toward right wing tip, z positive up	
x/c	fractional distance along streamwise chord	
Δx	distance along tip chord	
$\Delta x'$	$= \Delta x / c_t$	
α	angle of attack	
α_D	departure angle of attack	

Γ	equivalent circulation associated with leading-edge suction
$\bar{\Gamma}$	average value of Γ
γ	distributed bound vorticity at point (x,y)
δ	distributed trailing vorticity at point (x,y)
δ_t	tip rake angle, positive as trailing-edge tip moves inboard
ρ	density of fluid
Λ	leading-edge sweep angle, positive for sweepback
λ	taper ratio, $\frac{c_t}{c_r}$
μ	$= \sin^{-1}\left(\frac{1}{M}\right)$
ϕ	dihedral angle, positive for wing tip up

Subscripts:

av	average
c	centroid
i	particular item of location
le	leading edge
p	potential or attached flow
r	root
ref	reference; for S , true wing area; for c , mean geometric chord
se	side edge

t	tip
tot	total
vle	vortex effect at leading edge
vse	vortex effect at side edge
w	wing

SIDE-EDGE VORTEX LIFT

Concept

The suction analogy is not limited to vortex flows around the leading edge but can be applied wherever singularities in the potential-flow induced velocities produce an edge force. Figure 3 shows that this can occur along the side edges because of the singularities in v . Hence, with vortex flows associated with separation around the side edges, the forces no longer act in the wing plane but in the normal-force direction as in leading-edge separation.

A mathematical procedure for computing this side force has been developed for wings at subsonic speeds, initially, and is given in reference 5. The procedure employs the modified Multhopp method of reference 6 to provide the information needed to begin the side-force computation. In addition, three discrete-loading analyses employing the vortex-lattice method (refs. 7, 8, and 9) have been made and are discussed in reference 9. In reference 9, the vortex-lattice method is shown to yield results in close agreement with those of reference 5; hence, the reference 9 method is utilized in this report for some isolated planforms and all subsonic configurations for which the reference 5 method is not appropriate. Initially, the effect of the side-edge vortex lift is combined with the leading-edge and the potential-flow effects to yield estimates which are denoted on some figures as those of the present method. (Subsequently, the present method includes the augmented vortex lift as well.)

The following equations relate the potential- and vortex-lift factors to C_L , C_D , and C_m :

$$C_L = \overbrace{K_p \sin \alpha \cos^2 \alpha}^{C_{L,p}} + \overbrace{K_{v,le} \sin^2 \alpha \cos \alpha}^{C_{L,vle}} + \overbrace{K_{v,se} \sin^2 \alpha \cos \alpha}^{C_{L,vse}} \quad (1)$$

or

$$C_L = K_p \sin \alpha \cos^2 \alpha + K_{v,tot} \sin^2 \alpha \cos \alpha \quad (2)$$

$$C_D = C_{D,0} + C_L \tan \alpha = C_{D,0} + K_p \sin^2 \alpha \cos \alpha + K_{v,tot} \sin^3 \alpha \quad (3)$$

and

$$C_m = \overbrace{K_p \sin \alpha \cos \alpha \frac{\bar{x}_p}{c_{ref}}}^{C_{m,p}} + \overbrace{K_{v,le} \sin^2 \alpha \frac{\bar{x}_{le}}{c_{ref}}}^{C_{m,vle}} + \overbrace{K_{v,se} \sin^2 \alpha \frac{\bar{x}_{se}}{c_{ref}}}^{C_{m,vse}} \quad (4)$$

where the particular \bar{x} -terms equal $x_{ref} - x_{c,i}$ for i equal to p , le , and se . In this paper, x_{ref} is the quarter-chord location of the mean geometric chord.

Application

Figure 4 presents a comparison of experimental and theoretical subsonic aerodynamic characteristics of an $A = 1$ rectangular wing. Also shown are the potential- and vortex-lift factors and lift increments determined in reference 5. The figure shows that the present method estimates the C_L experimental data of reference 5 better than the other methods. (See ref. 5 for a discussion of the methods in refs. 10, 11, 12, and 13.) This figure also shows that the $C_{m,le}$ experimental data are better estimated by the present method up to $\alpha \approx 16^\circ$. For higher angles of attack, the data show a larger nose-down moment than the present estimate. This comparison indicates the magnitude of the error introduced by the present method in assuming that the potential and vortex lifts, in particular the leading-edge one, do not move with increasing α .

With the vortex lift from the side edge identified, its magnitude estimated, and good agreement with experimental data shown, the vortex lifts on more generalized planforms are now studied.

AUGMENTED VORTEX LIFT

Concept

The concept of augmented vortex lift arises from the well-established fact that for many delta wings the leading-edge vortex generated on the wing persists for a considerable distance downstream and therefore can act on other surfaces, such as the aft part of more generalized planforms or aircraft horizontal tails. This persistence is not accounted for in the suction analogy because the analogy deals only with the edge forces generated along a particular edge, such as leading-edge vortex lift resulting from the leading-edge suction force. Figure 5 shows examples of two systems employed that

account for vortex lift on delta and cropped-delta wings. They are (1) a theoretical one developed from a planar potential theory and utilizing the suction analogy and (2) a more realistic (actual) one that is due to action of the leading-edge shed vortex. The following important points are made from this figure: (1) the leading-edge suction distribution has a peak value somewhere along the leading edge away from the extremes and goes to zero at the tip because no edge forces are present beyond the point of maximum span; (2) for the cropped-delta wing, the aft part of the wing can generate additional (augmented) vortex lift because of the presence of the leading-edge vortex (as discussed in ref. 14); and (3) the side-edge suction distribution generally peaks near the trailing edge and is discussed subsequently.

Estimating Procedure

In order to estimate the augmented vortex lift, it is first necessary to quantify the circulation of the shed vortex along the wing leading edge. This can be done as indicated by the lower sketch on figure 5. The Kutta-Joukowski Law has been employed to relate the differential suction force along the leading edge to an unknown circulation $\Gamma(z)$. By a coordinate transformation, it can also be related to the leading-edge suction distribution along the span as

$$\frac{c_s c(y)}{\alpha^2} = -2 \sec \Lambda \frac{\Gamma_{w_{net,le}}(y)}{\alpha^2 U^2} \quad (5)$$

Figure 6 shows an idealized distribution of the product $\frac{-\Gamma_{w_{net,le}}}{\alpha^2 U^2}$ along with a fairly reasonable $\frac{-w_{net,le}}{U}$ (upwash) distribution for a cropped-delta wing. As a consequence, $\frac{\Gamma}{\alpha^2 U}$ can be estimated as shown. Because the actual circulation does not go to zero (hence the vortex persists downstream), the distribution of circulation cannot be used. Instead, an average value is employed. With an average value used for $\frac{\Gamma}{\alpha^2 U}$, it is consistent to utilize an average value for $\frac{-w_{net,le}}{U}$ as well. This result can be expressed in terms of the leading-edge-vortex-lift factor by

$$\int_0^{b/2} \frac{c_s c}{\alpha^2} dy = \frac{K_{v,le}}{2} S_{ref} = -2 \sec \Lambda \frac{\bar{\Gamma}_{w_{net,le}}}{\alpha^2 U^2} \frac{b}{2} \quad (6)$$

Hence,

$$\frac{\bar{\Gamma}}{\alpha^2 U} = \frac{-K_{v,le} S_{ref}}{2b \sec \Lambda \frac{\bar{w}_{net,le}}{U}} \quad (7)$$

Employing this result in the Kutta-Joukowski Law, this time along the side edge, permits the estimation of the augmented vortex lift. The details are

$$\frac{\text{Augmented vortex lift along one edge}}{\alpha^2} = \frac{\bar{\Gamma}}{\alpha^2} \tilde{c} \quad (8)$$

where the $\frac{-\bar{w}_{net,se}}{U}$ distribution and its average are again reasonably depicted at the bottom right of figure 6 and \tilde{c} is a characteristic streamwise length. By inspection of figure 6

$$\frac{\bar{w}_{net,se}}{U} \approx \frac{\bar{w}_{net,le}}{U} \quad (9)$$

Then defining the left side of equation (8) as $\frac{\bar{K}_{v,se}}{2} q_\infty S_{ref}$ leads to

$$\frac{\bar{K}_{v,se}}{2} q_\infty S_{ref} = q_\infty \frac{K_{v,le}}{b \sec \Lambda} S_{ref} \tilde{c} \quad (10)$$

or

$$\bar{K}_{v,se} = \left[\frac{K_{v,le}}{(b/2) \sec \Lambda} \right] \tilde{c} \quad (11)$$

The term in brackets results from the use of average values and amounts to assuming that the leading-edge-vortex-lift factor is developed at a constant rate along the leading-edge length $(b/2) \sec \Lambda$. For cropped-delta wings the value of \tilde{c} is taken to be the length of the tip chord.

Applications

Cropped-delta wings. - Figure 7 presents an application of the augmented vortex lift to a cropped-delta wing of $\Lambda = 45^\circ$ and $\lambda = 0.5$. The value of $\bar{K}_{v,se}$ is about two-thirds of the other vortex-lift factors, and its inclusion leads to improved agreement with both the C_L and the C_m experimental data. (For C_m estimates the augmented vortex lift is applied at the centroid of the side-edge suction distribution for cropped-delta wings and at the centroid of additional area behind or ahead of the delta part for pointed wings.)

At this taper ratio ($\lambda = 0.5$), C_L is reasonably well predicted over the range of α from 0° to 20° . Above $\alpha = 20^\circ$ the data fall below the theory curve. The angle of attack at which this occurs is called the departure angle α_D herein, and it is graphed as a function of aspect ratio for this wing and other cropped-delta wings in this same series which have a leading-edge sweep of 45° . The others have taper ratios of 0.4, 0.3, 0.2, 0.1, and 0. For comparison, the departure angles of sharp-edge delta wings are

also graphed (from ref. 2), and the addition of area behind the moderately swept delta ($\Lambda = 45^\circ$) increases the departure angle, just as increasing the sweep on a delta wing does. The explanation of the variation of α_D with A is hypothesized to be related to at least the leading-edge suction distribution and possibly to the side-edge suction distribution.

In order to determine the relationships, the cropped-delta leading-edge and side-edge suction distributions are presented in figures 8 and 9, respectively. For comparison, the leading-edge suction distributions for three delta wings are also presented in figure 8 (the upper two from ref. 15). For both sets the peak values of leading-edge suction distribution become larger and occur at a more outboard location with decreasing A . Hence, it can be stated that as the leading-edge suction distribution becomes more triangular, the angle of attack for departure increases.

Figure 9 shows that the side-edge suction distribution increases for increasing taper ratio and does not tend to zero at the trailing edge. The increase could be expressed in terms of an increase in circulation along the side edge by an analogous approach to that employed previously and would translate into a stronger "tip vortex." This increase could also be thought of as providing a favorable pressure gradient for the leading-edge vortex acting near the tip, so that a vortex flow would be produced there where an unorganized flow had existed previously. The reason that the side-edge suction does not go to zero at the trailing edge is that this suction force can be sustained along the edge of the trailing planar vortex sheet (ref. 16), unlike the spanwise extension of the leading-edge suction as discussed previously.

Generalized planforms. - Figures 10 and 11 present additional examples of the augmented-vortex-lift concept for wings with pointed and streamwise tips, respectively. (Some data of fig. 10 were taken from ref. 17.) The value of \tilde{c} used in the computation of $\bar{K}_{v,se}$ was determined empirically to be the streamwise distance from the trailing edge of the root chord to the leading edge of the wing tip. (Positive \tilde{c} values occur for wings such as the diamond type.) This definition of \tilde{c} enables one definition to be used for all wings, including the cropped ones. It should be noted that of the eight examples shown in these two figures, \tilde{c} is positive for all but two. The negative values can be thought of as due to the lack of complete flow reattachment on the more arrowlike wings.

From the examples presented, it can be seen that addition of the augmented vortex lift improves the agreement of the theory with the data at least slightly and more often significantly.

OTHER APPLICATIONS

Figure 12 shows two attempts to improve the vortex lift on pointed wings of low sweep by altering the planform along the leading edge. In each instance it was postulated

that by doing so the moderate-sweep leading-edge vortex system could be strengthened and thereby provide additional lift to higher values of α . The first attempt (top right) involved serrating the leading edges, but this resulted in two vortexes of opposite circulation being shed at each concave juncture. From the figure, it can be seen that this attempt was not successful.

The second attempt (bottom right) was to cause all of the shed vortexes along a leading edge to be shed in the same direction in order to eliminate the previous difficulty. However, comparison with the results for the basic delta wing (bottom left) shows that this attempt offered no significant improvement and hence can also be classified as unsuccessful.

Figure 13 presents the experimental and theoretical C_L values for a cropped-delta wing with varying tip rake angles δ_t . They are compared at two angles of attack and, in general, for each α the data fall between the two theory curves. The curve labeled "both side edges" is shown for reference and is simply the $\delta_t = 0$ result extended over the δ_t range. The other curve labeled "one side edge" is the asymmetrical wing solution¹ with only one side edge contributing to vortex lift. For each curve the contributions of potential lift and leading-edge, side-edge, and augmented vortex lift are summed. The conclusions from this figure are that: (1) the data are reasonably well estimated; and (2) rake angles $\delta_t \geq 13^\circ$ are necessary for the data to no longer exhibit an effective "side edge."

SUPERSONIC RESULTS

Delta Wings

The suction analogy has been applied to delta wings at supersonic speeds in reference 4; however, some more recent applications, such as the ones in reference 19, raise points which require attention. Figure 14 from reference 20 helps to illustrate the points. Like the $A = 1$ sharp-edge delta wing of reference 4, the $A = 1.1$ sharp-edge delta wing in this figure shows a similar reduction in the vortex lift available with increasing M . This is because the upwash field between the Mach cone and the wing leading edge becomes more restricted with the increase in M , thereby leading to a reduction in $K_{v,le}$. In addition, the angle of attack for departure decreases with increasing M because the upwash field is further reduced by the model being located offcenter with respect to the Mach cone axis. Therefore, the vortex lift realizable actually decreases with α . But in order to estimate the $K_{v,le}$ variation with α , better supersonic potential-flow solutions are needed.

¹These solutions were obtained by James M. Luckring of Langley Research Center with a recently developed asymmetric version of the computer program described in reference 18.

Rectangular Wing

Figure 15 presents evidence that side-edge vortex lift is present for rectangular wings at supersonic speeds. (The experimental data shown were taken from ref. 21.) At the left of the figure is the change in upper surface pressure with α for two locations, one outside and one inside the tip Mach cone. The values of $\Delta C_{p,u}$ outside the tip cone are well estimated by the potential theory of reference 22, whereas those inside and near the tip trailing edge are underestimated over a wide range of α . At subsonic speeds, this type of nonlinear $\Delta C_{p,u}$ growth with α for a sharp-edge wing would be attributed to vortex flow being present.

The middle graph shows a comparison similar to the left graph except that the difference in c_n at the outboard station is not as extreme as for $\Delta C_{p,u}$. This more linear behavior is attributed to (1) values of $\Delta C_{p,u}$ measured ahead of the illustrated location demonstrating a smaller amount of nonlinear variation with α and (2) the modifying effect of the lower surface pressure in the computation of c_n . The difference in c_n between the potential theory estimate and the data is, therefore, attributed to vortex lift which comes from the side edges located within the tip cones.

Hence, calculation of the attacked-flow side force and use of the suction analogy provide a means of estimating this vortex-lift effect. The linearized supersonic potential-flow solutions of reference 23 have been employed to develop the supersonic $K_{v,se}$ solutions presented in reference 14. These solutions are used herein. The graph at the right shows that: (1) vortex normal force is present in the data; and (2) the data are well estimated by the combination of potential and vortex normal force.

Variation of $K_{v,se}$

Figure 16 shows for two planforms the variation of $K_{v,se}$ with M obtained by using the method of reference 5 at $M \leq 1$ and the results of reference 14 at $M > 1$. Also, selected side-edge suction distributions for each planform are shown. The $K_{v,se}$ values increase with M in the subsonic regime and decrease in the supersonic. The beginning of the supersonic results are set by the Mach number for which the tip cones just intersect along the trailing edge. The short dashed lines used to connect the subsonic and supersonic results are assumed variations. The reasons for the behavior of $K_{v,se}$ with M are contained in the side-edge suction distributions and are now discussed.

For the rectangular wing, increasing the subsonic M is equivalent to decreasing A which in reference 5 was shown to lead to a rectangularization of the distribution and an increase in $K_{v,se}$. However, at supersonic M the side-edge suction distribution again goes to zero at the tip leading edge but now varies linearly over the side edge because of the conical flow nature of the solution. The falloff of $K_{v,se}$ with increasing

supersonic M is the result of two conflicting effects. The first is the reduction in size of the tip Mach cone and the magnitude of the upwash within it, and the second is the increase in sidewash due to the limits of the Mach forecone which eliminate the reducing effects of the other wing panel. The tip cone reduction appears to be the stronger effect.

For the cropped-delta wing, reference 14 illustrates the $K_{v,se}$ reduction which occurs with increasing subsonic M . In figure 16 the distributions are seen to peak at higher values with increasing M . At supersonic M and with a subsonic leading edge, there is an increase in the initial sidewash over the side edge due to the restrictive limits of the Mach forecone at the leading edge of the tip. This is due to the conical-flow assumption which results in the distribution being linear aft of this point. With increasing supersonic M the size of the tip Mach cone and the magnitude of the upwash within it also decrease, leading to a reduction in $K_{v,se}$.

Application

Figure 17 presents a comparison of the aerodynamic characteristics obtained on a cropped-delta wing-body model tested at $M = 1.2$ (ref. 24) with the results of the present method for the wing alone at the same Mach number. The comparison shows that inclusion of the leading-edge-, side-edge-, and augmented-vortex-lift effects leads to improved agreement. The pitching-moment contributions are obtained by having the vortex lifts act at their respective centroids, and by performing the analytic surface integration, both inside and outside of the tip cone, of the product of the potential-flow lifting pressure (given in ref. 23) and its chordwise position. (See ref. 25.) The potential theory drag curve contains $C_{D,o}$ and is presented for full leading-edge suction and with no separation around the side edges. The other theoretical drag curve also includes $C_{D,o}$.

MULTIPLE LIFTING SURFACES

Vortex-lift estimates have been made up to now for isolated wings, but in this section, multiple lifting surfaces are treated. Examples of these surfaces are wing-tail or wing-canard configurations; however, configurations such as a wing-body can also be considered multiple lifting surfaces when the body is taken to be a lifting one and is represented by a flat surface.

Figure 18 presents applications of the suction analogy to configurations. On the left are the lift results for a slender wing-body, and the data (taken from ref. 26) are well estimated by the combination of potential and vortex lifts. On the right of the figure are the wing lift results for a nonslender configuration. At the top the wing is in the presence of a forebody and at the bottom it is in the presence of a high canard ($z/c_{ref} = 0.185$). The top part shows a C_L variation typical of wings with moderate sweep because they

are known to have low angles of attack for departure and vortex breakdown (ref. 2). However, in the presence of the high canard, a favorable interference results, and even with the reduction in $C_{L,p}$ on the wing, due to canard downwash, the predicted amount of vortex lift is developed on the wing. The data (taken from ref. 27) are well predicted over the range of α and reach higher C_L values than those for the wing in the presence of the forebody.

Figure 19 presents the effect on the wing lift characteristics of changing the canard position. From the figure it can be seen that both the high canard with anhedral ($\phi = -18.6^\circ$) and the coplanar canard have a favorable interference effect on the wing. In neither case has the augmented vortex lift due to the leading-edge vortex of the canard been taken into account. This omission is proper for the canard in the anhedral position but questionable in the coplanar arrangement. This vortex lift was omitted because an appropriate \tilde{c} has yet to be determined.

CONCLUDING REMARKS

This paper has presented some recent extensions of the suction analogy for the estimation of vortex lift from the side edges and from the downstream effects of the leading-edge shed vortex. Applications of these extensions have resulted in an improved estimating capability for a wide range of isolated sharp-edge planforms and also for multiple lifting surfaces. Hence, the suction analogy concept can now have wider applicability at both subsonic and supersonic speeds, especially in the preliminary design cycle.

The following are areas in which additional research is needed:

- (1) An improved supersonic potential-flow program that properly accounts for the changing proximity of the model and its Mach cone with angle of attack
- (2) Development of a method for predicting the location and strength of the vortex flow originating on rounded-edge wings and the enlargements of the influenced region with angle of attack
- (3) Surface pressure distributions for wings which have vortex flows originating along the leading and side edges for use in critical design analyses

REFERENCES

1. Polhamus, Edward C.: A Concept of the Vortex Lift of Sharp-Edge Delta Wings Based on a Leading-Edge Suction Analogy. NASA TN D-3767, 1966.
2. Wentz, William H., Jr.; and Kohlman, David L.: Wind Tunnel Investigations of Vortex Breakdown on Slender Sharp-Edged Wings. NASA CR-98737, 1968.
3. Polhamus, Edward C.: Charts for Predicting the Subsonic Vortex-Lift Characteristics of Arrow, Delta, and Diamond Wings. NASA TN D-6243, 1971.
4. Polhamus, Edward C.: Predictions of Vortex-Lift Characteristics by a Leading-Edge Suction Analogy. *J. Aircraft*, vol. 8, no. 4, Apr. 1971, pp. 193-199.
5. Lamar, John E.: Extension of Leading-Edge-Suction Analogy to Wings With Separated Flow Around the Side Edges at Subsonic Speeds. NASA TR R-428, 1974.
6. Lamar, John E.: A Modified Multhopp Approach for Predicting Lifting Pressures and Camber Shape for Composite Planforms in Subsonic Flow. NASA TN D-4427, 1968.
7. Bradley, R. G.; Smith, C. W.; and Bhateley, I. C.: Vortex-Lift Prediction for Complex Wing Planforms. *J. Aircraft*, vol. 10, no. 6, June 1973, pp. 379-381.
8. Mendenhall, Michael R.; and Nielsen, Jack N.: Effect of Symmetrical Vortex Shedding on the Longitudinal Aerodynamic Characteristics of Wing-Body-Tail Combinations. NASA CR-2473, 1975.
9. Lamar, John E.; and Gloss, Blair B.: Subsonic Aerodynamic Characteristics on Interacting Lifting Surfaces With Separated Flow Around Sharp Edges Predicted by Vortex-Lattice Method. NASA TN D-7921, 1975.
10. Gersten, K.: Calculation of Non-Linear Aerodynamic Stability Derivative of Aeroplanes. AGARD Rep. 342, Apr. 1961.
11. Garner, H. C.; and Lehrian, Doris E.: Non-Linear Theory of Steady Forces on Wings With Leading-Edge Flow Separation. NPL Aero Rep. 1059, Brit. A.R.C., Feb. 15, 1963.
12. Belotserkovskii, S. M. (J. W. Palmer, transl.): Calculation of the Flow About Wings of Arbitrary Planform at a Wide Range of Angle of Attack. Libr. Transl. No. 1433, Brit. R.A.E., Feb. 1970.
13. Flax, A. H.; and Lawrence, H. R.: The Aerodynamics of Low-Aspect-Ratio Wings and Wing-Body Combination. Third Anglo-American Aeronautical Conference, Jean Bradbrooke and E. C. Pike, eds., Royal Aeronautical Soc., 1952, pp. 363-398.

14. Lamar, John E.: Prediction of Vortex Flow Characteristics of Wings at Subsonic and Supersonic Speeds. AIAA Paper No. 75-249, Jan. 1975.
15. Snyder, Melvin H., Jr.; and Lamar, John E.: Application of the Leading-Edge-Suction Analogy to Prediction of Longitudinal Load Distribution and Pitching Moments for Sharp-Edged Delta Wings. NASA TN D-6994, 1972.
16. Hancock, G. J.: Some Aspects of Subsonic Linearised Wing Theory, With Reference to Second Order Forces and Moments. Brit. A.R.C.34 689, Mar. 1973.
17. Davenport, Edwin E.; and Huffman, Jarrett K.: Experimental and Analytical Investigation of Subsonic Longitudinal and Lateral Aerodynamic Characteristics of Slender Sharp-Edge 74° Swept Wings. NASA TN D-6344, 1971.
18. Margason, Richard J.; and Lamar, John E.: Vortex-Lattice FORTRAN Program for Estimating Subsonic Aerodynamic Characteristics of Complex Planforms. NASA TN D-6142, 1971.
19. Fox, Charles H., Jr.; and Lamar, John E.: Theoretical and Experimental Longitudinal Aerodynamic Characteristics of an Aspect Ratio 0.25 Sharp-Edge Delta Wing at Subsonic, Supersonic, and Hypersonic Speeds. NASA TN D-7651, 1974.
20. Davenport, Edwin E.: Aerodynamic Characteristics of Three Slender Sharp-Edge 74° Swept Wings at Subsonic, Transonic, and Supersonic Mach Numbers. NASA TN D-7631, 1974.
21. Kaattari, George E.: Pressure Distributions on Triangular and Rectangular Wings to High Angles of Attack - Mach Numbers 1.45 and 1.97. NACA RM A54D19, 1954.
22. Woodward, Frank A.: Analysis and Design of Wing-Body Combinations at Subsonic and Supersonic Speeds. J. Aircraft, vol. 5, no. 6, Nov.-Dec. 1968, pp. 528-534.
23. Malvestuto, Frank S., Jr.; Margolis, Kenneth; and Ribner, Herbert S.: Theoretical Lift and Damping in Roll at Supersonic Speeds of Thin Sweptback Tapered Wings With Streamwise Tips, Subsonic Leading Edges, and Supersonic Trailing Edges. NACA Rep. 970, 1950. (Supersedes NACA TN 1860.)
24. Hightower, Ronald C.: Lift, Drag, and Pitching Moment of Low-Aspect-Ratio Wings at Subsonic and Supersonic Speeds - Comparison of Three Wings of Aspect Ratio 2 of Rectangular, Swept-Back, and Triangular Plan Form, Including Effects of Thickness Distribution. NACA RM A52L02, 1953.
25. Malvestuto, Frank S., Jr.; and Hoover, Dorothy M.: Lift and Pitching Derivatives of Thin Sweptback Tapered Wings With Streamwise Tips and Subsonic Leading Edges at Supersonic Speeds. NACA TN 2294, 1951.
26. Henderson, William P.: Studies of Various Factors Affecting Drag Due to Lift at Subsonic Speeds. NASA TN D-3584, 1966.

27. Gloss, Blair B.: The Effect of Canard Leading-Edge Sweep and Dihedral Angle on the Longitudinal and Lateral Aerodynamic Characteristics of a Close-Coupled Canard-Wing Configuration. NASA TN D-7814, 1974.

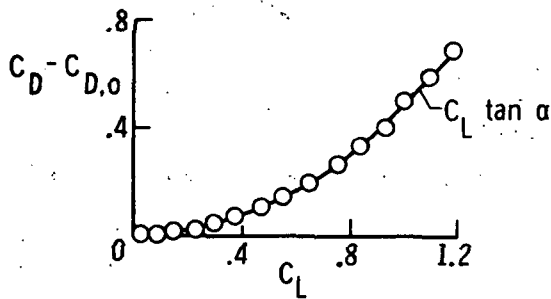
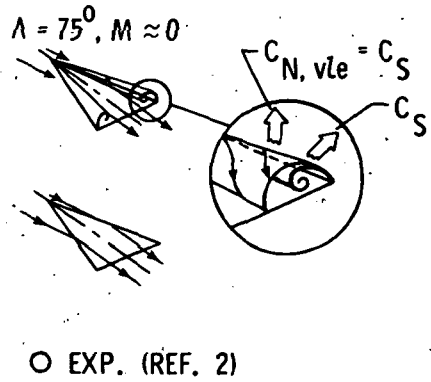
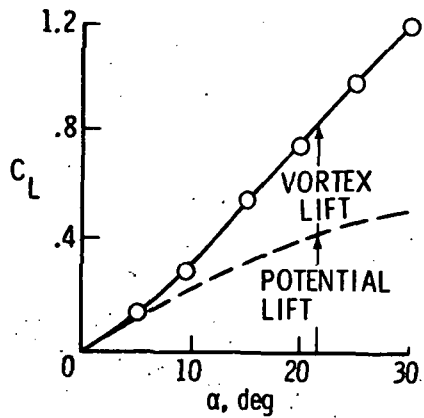


Figure 1.- Original application of suction analogy.

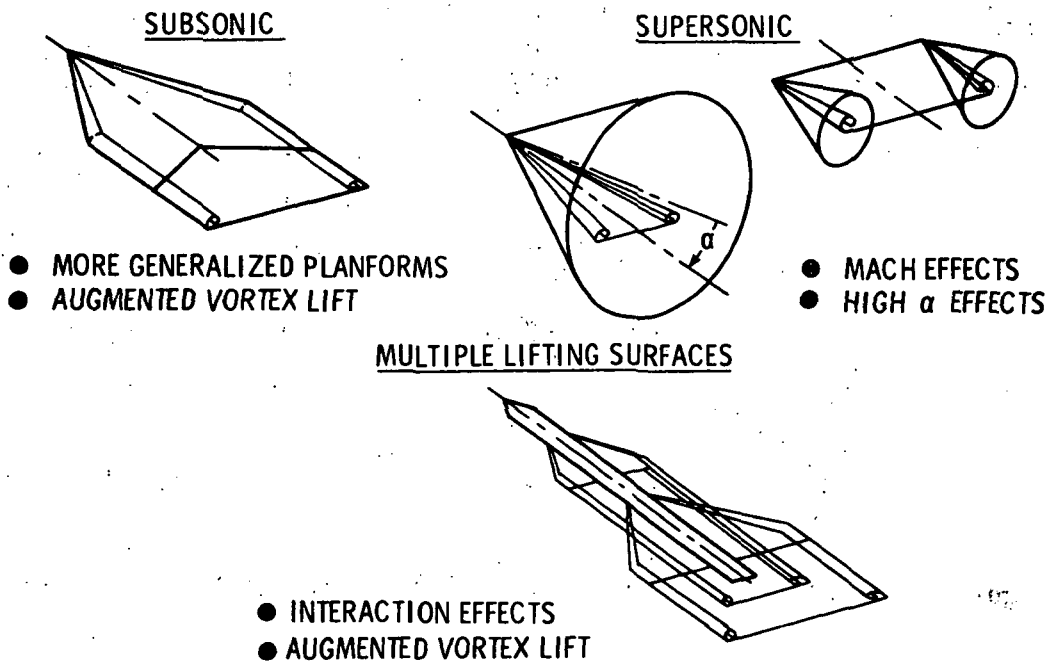


Figure 2.- Some recent applications of suction analogy to vortex-lift estimates.

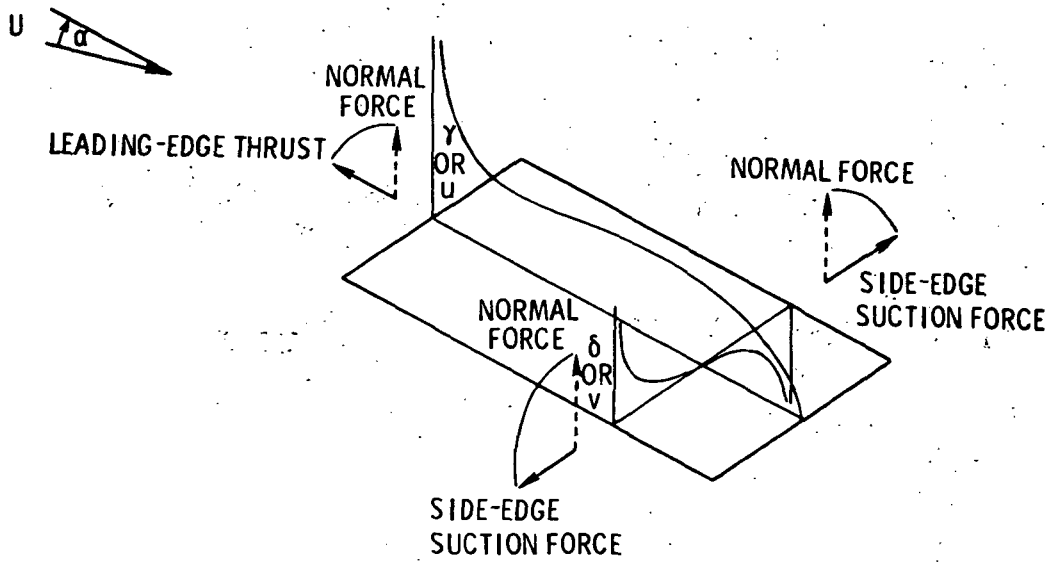


Figure 3.- Vortex-lift concept: Suction analogy applied to leading edge and side edge.

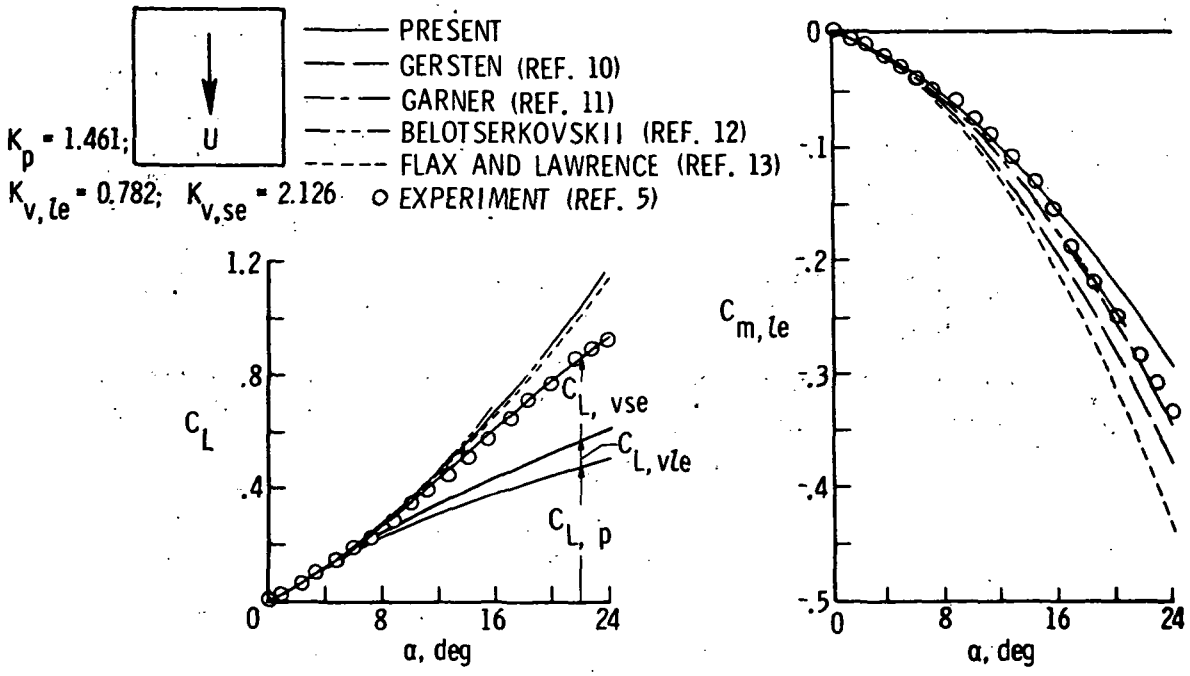
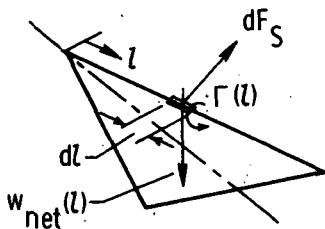
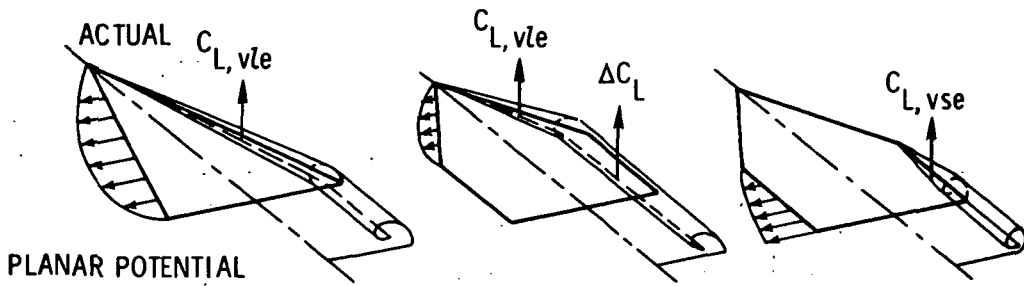


Figure 4.- Aerodynamic characteristics of rectangular wing. $A = 1$; $M \approx 0$.



KUTTA - JOUKOWSKI RELATIONSHIP

$$dF_S(l) = -\rho w_{net}(l) \Gamma(l) dl$$

LEADS TO

$$\bar{K}_{v,se} = \left(\frac{K_{v,le}}{\left(\frac{b}{2}\right) \sec \Lambda} \right) \tilde{c}$$

Figure 5. - Concept of augmented vortex lift.

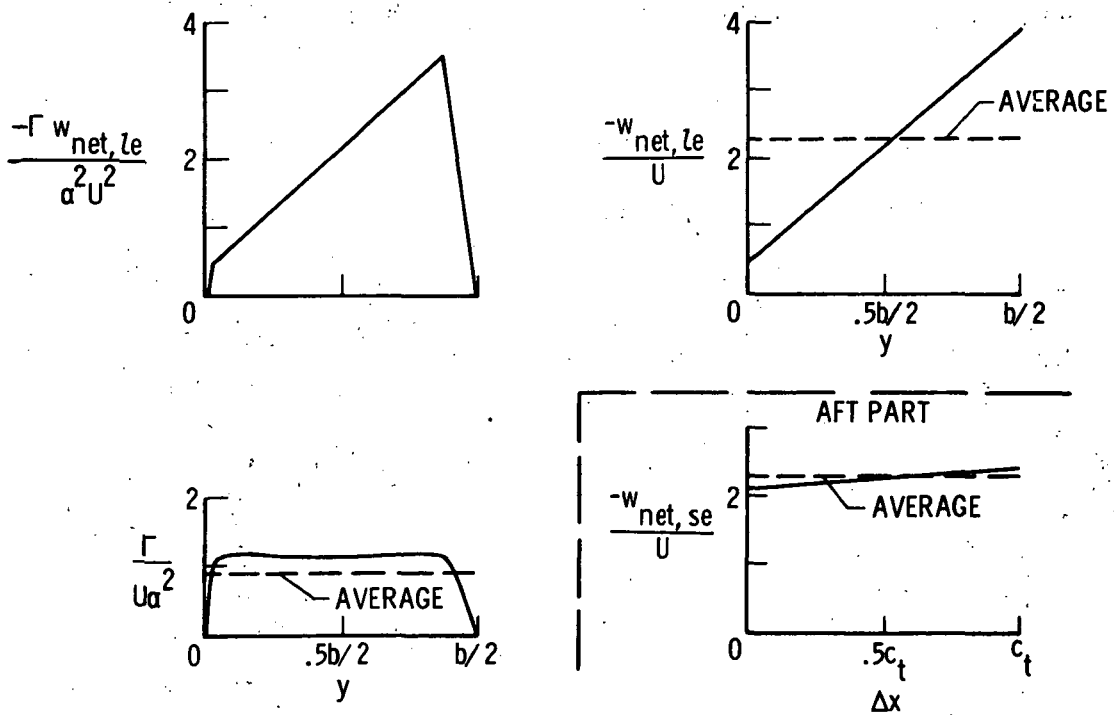


Figure 6. - Variables used in augmented-vortex-lift determination. Cropped-delta wings; delta part idealized.

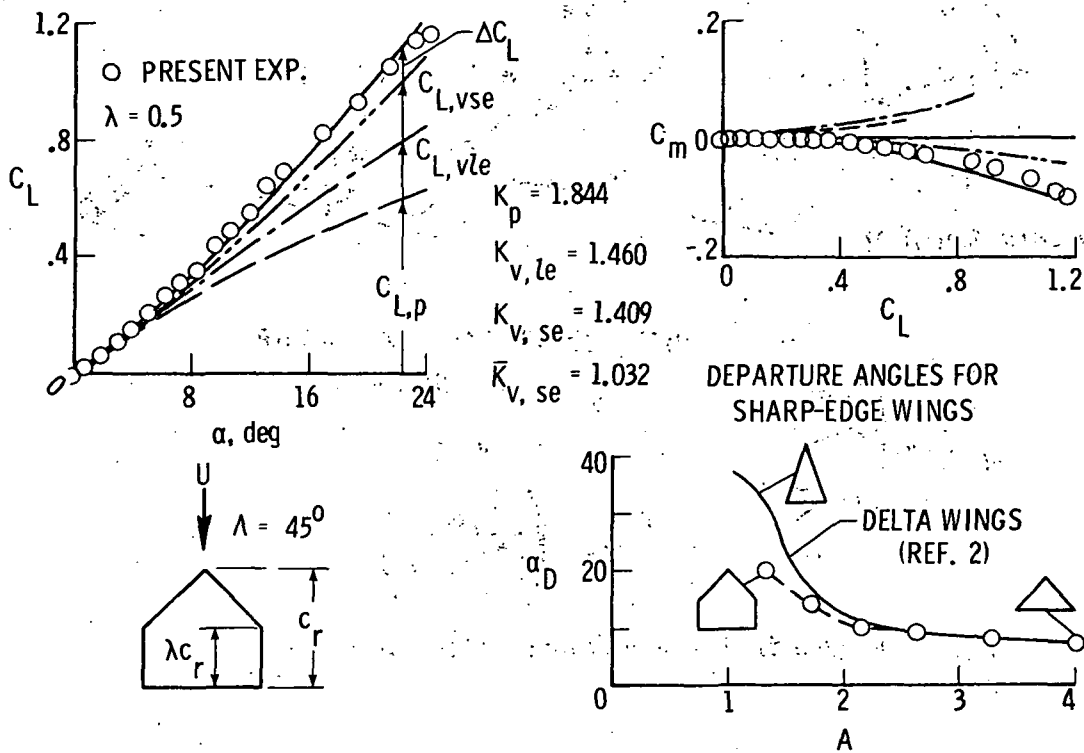


Figure 7.- Aerodynamic characteristics of cropped-delta wings. $M \approx 0$.

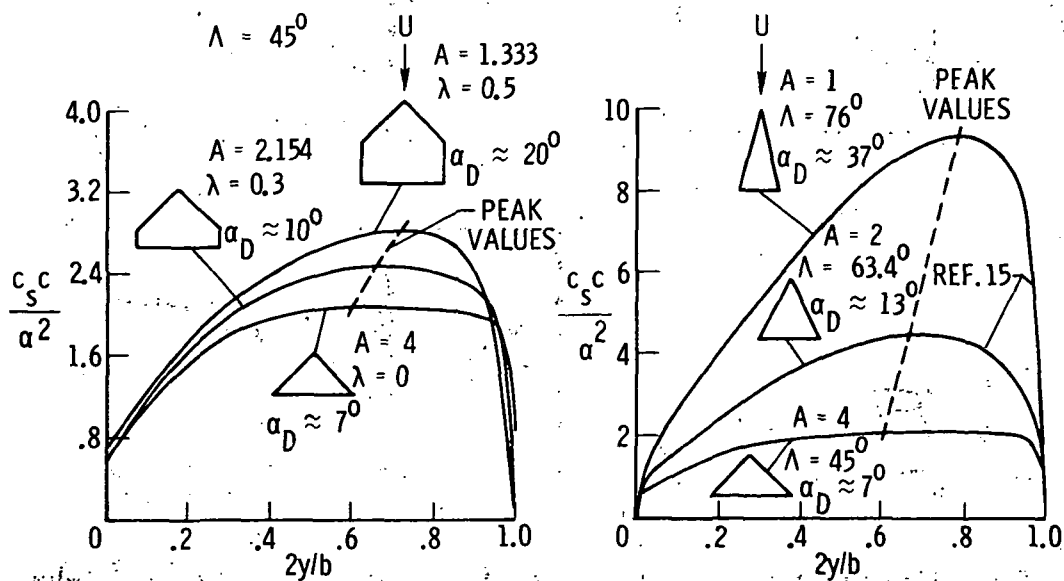


Figure 8.- Leading-edge suction distributions and departure angle of attack. $M \approx 0$.

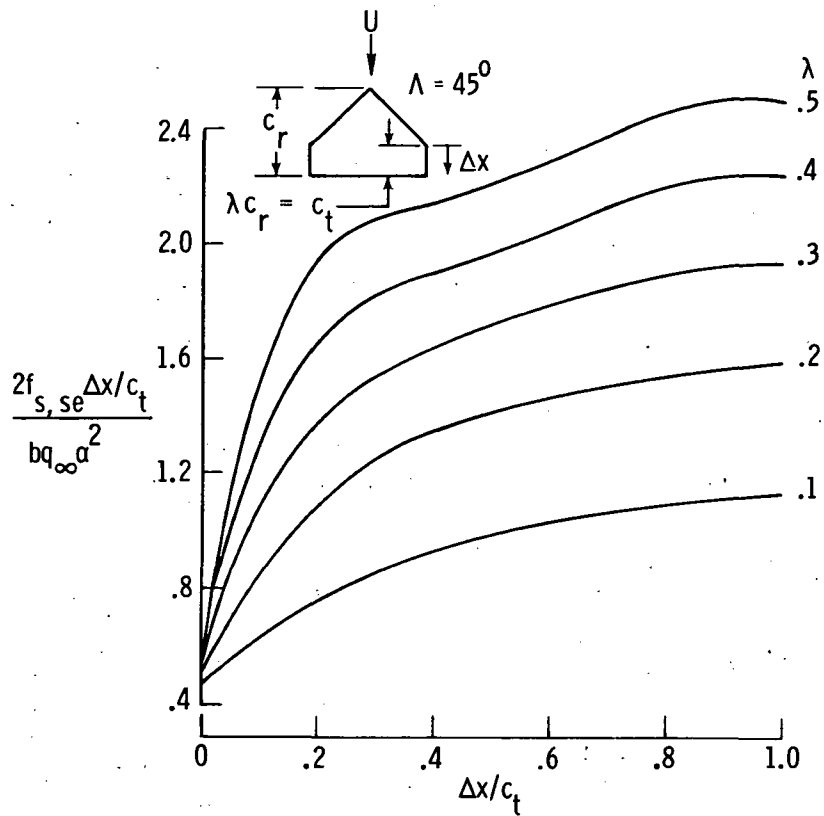


Figure 9. - Side-edge suction distribution for cropped-delta wings. $M \approx 0$.

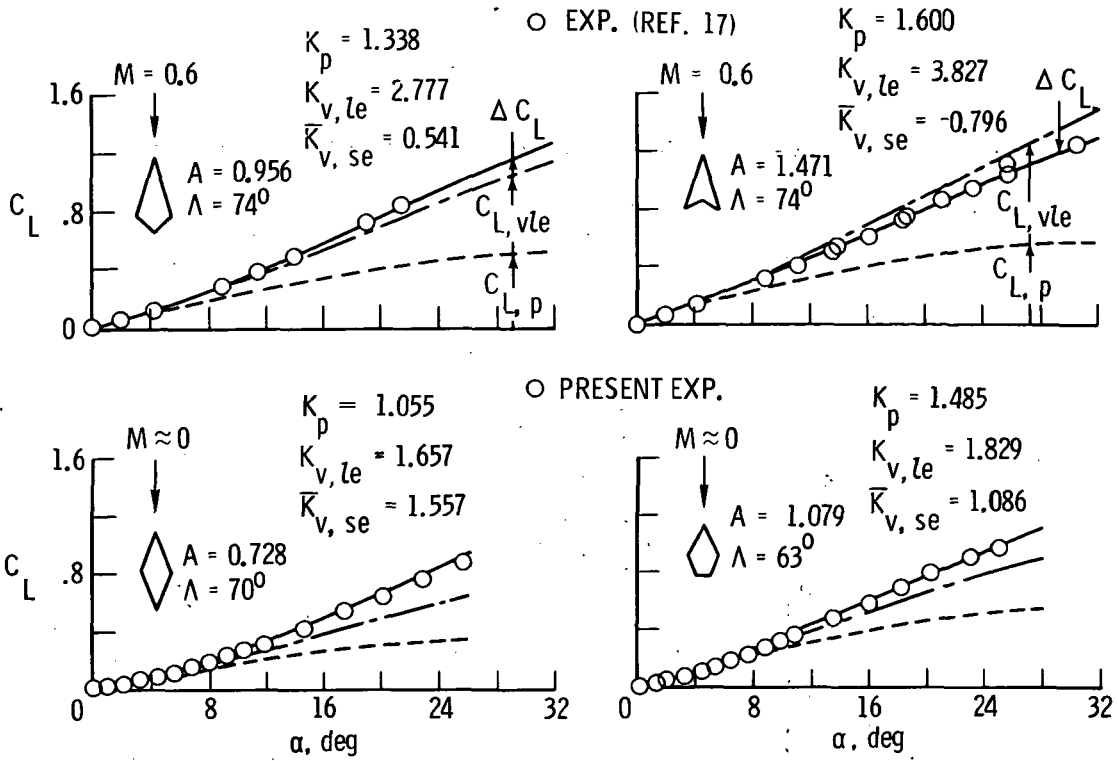


Figure 10.- Lift characteristics of pointed wings.

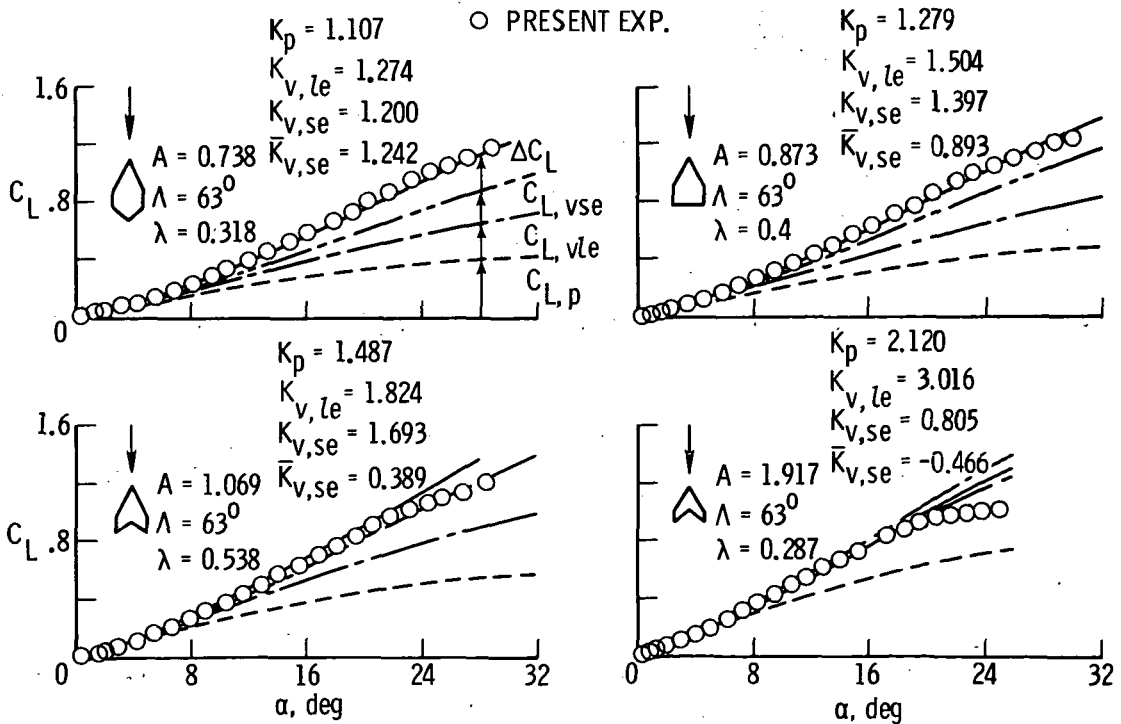


Figure 11.- Lift characteristics of wings with streamwise tips. $M \approx 0$.

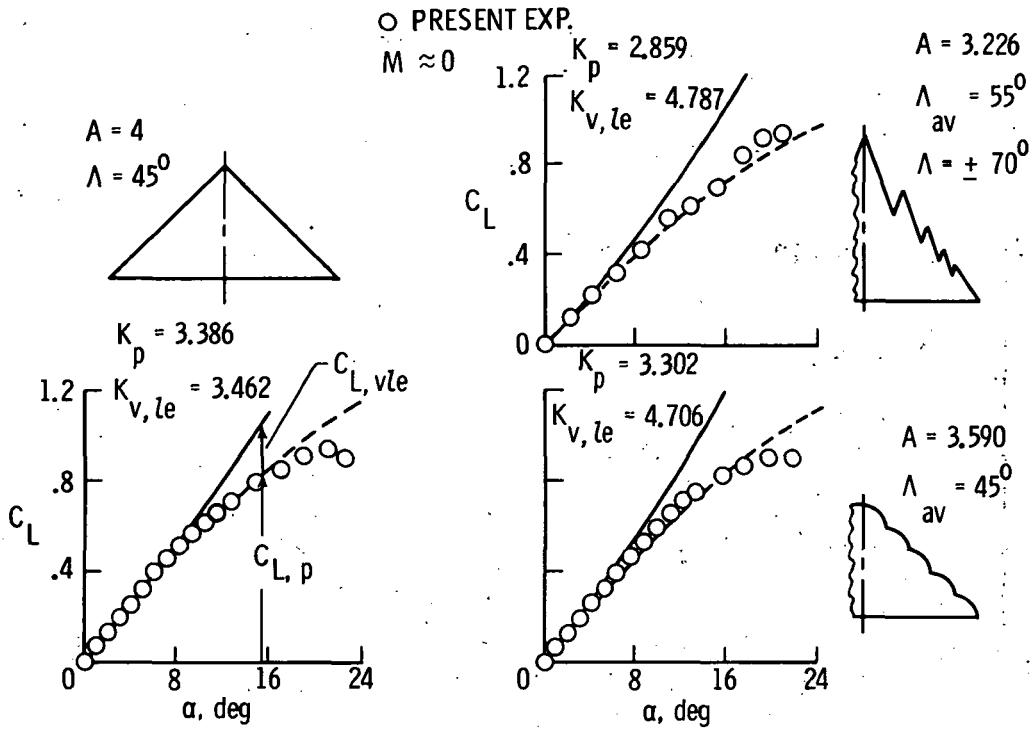


Figure 12. - Attempts to improve vortex lift on pointed wings of moderate sweep.

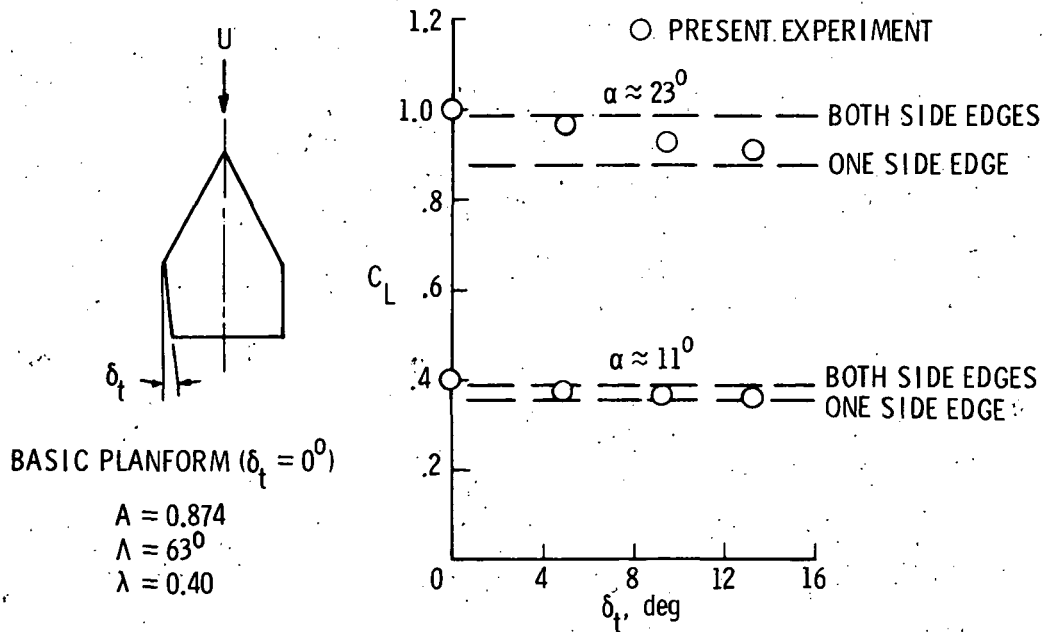


Figure 13. - Estimates of C_L for asymmetrical wings. $M \approx 0$.

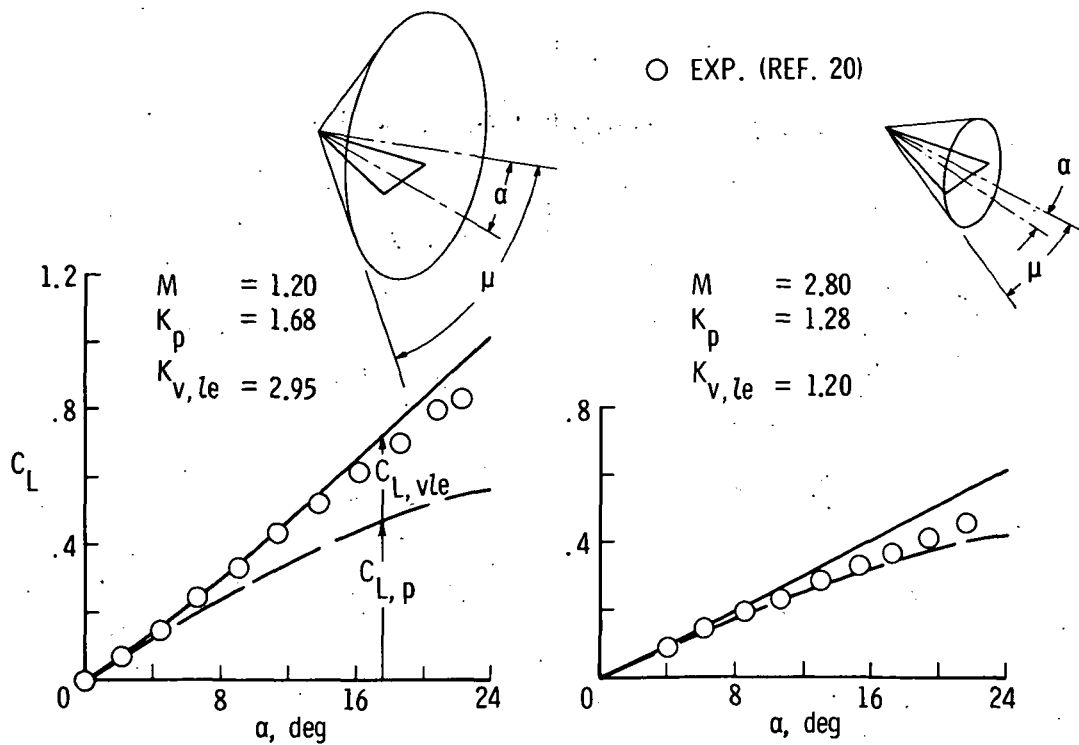


Figure 14.- Effect of supersonic Mach number on C_L for delta wing. $A = 1.1$.

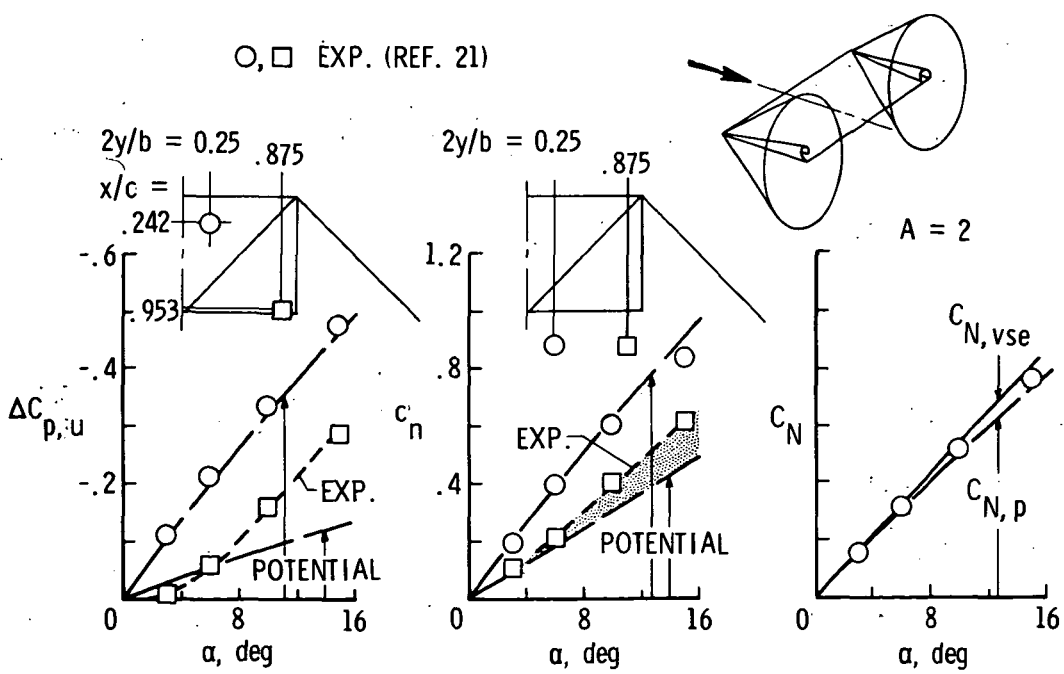


Figure 15.- Evidence of vortex lift within tip Mach cone. $M = 1.45$.

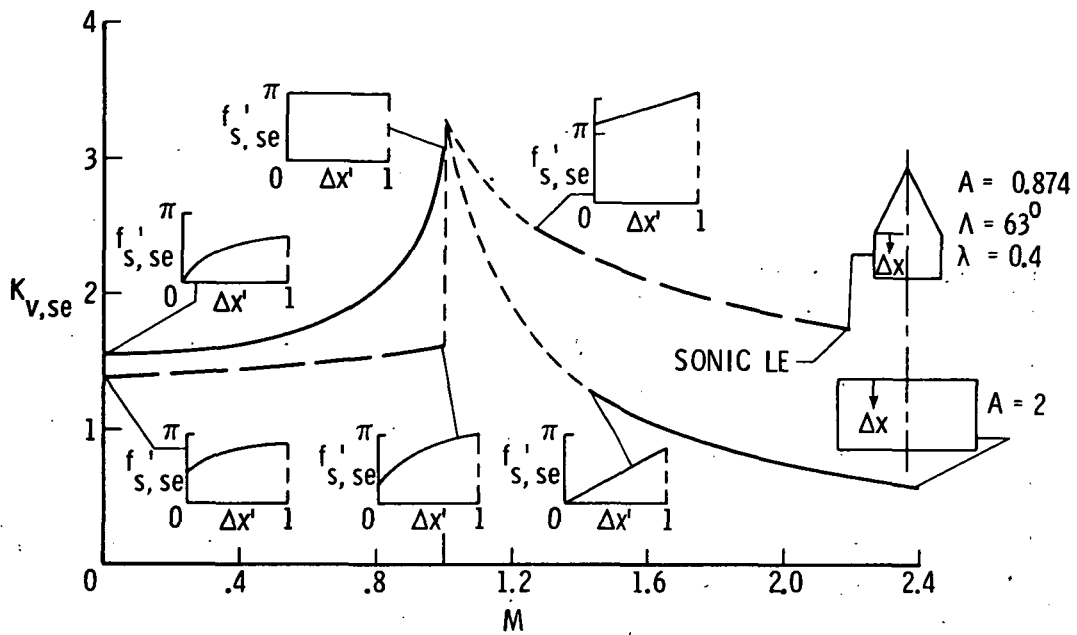


Figure 16.- Variation of $K_{V,se}$ with Mach number for two wings including selected side-edge suction distributions.

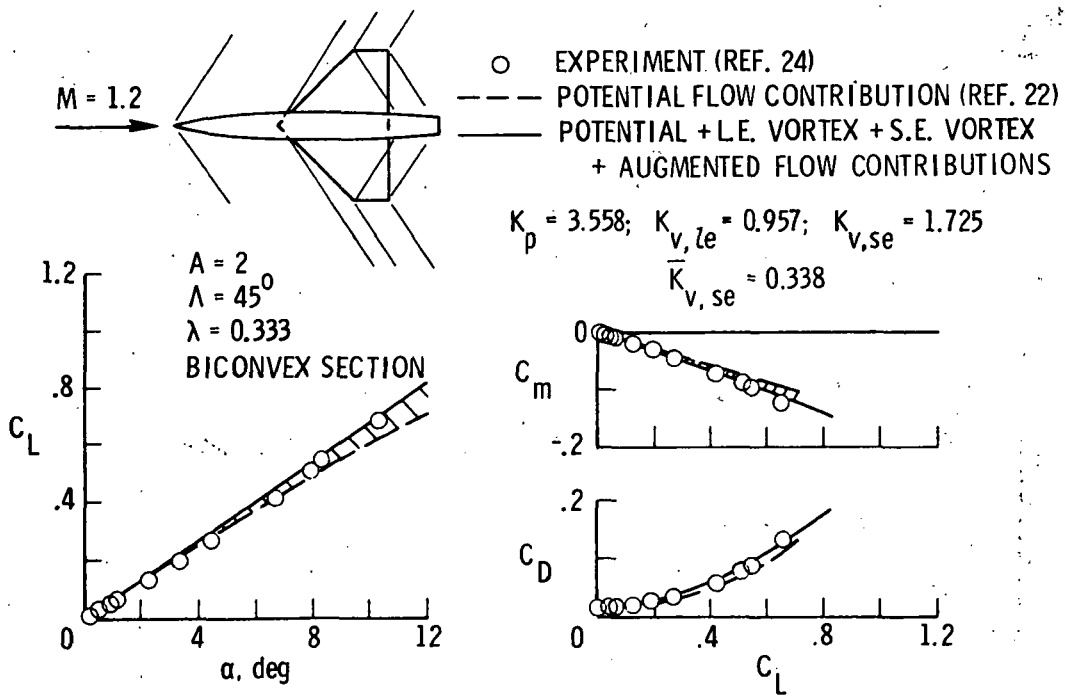


Figure 17.- Aerodynamic characteristics of a cropped-delta wing-body.

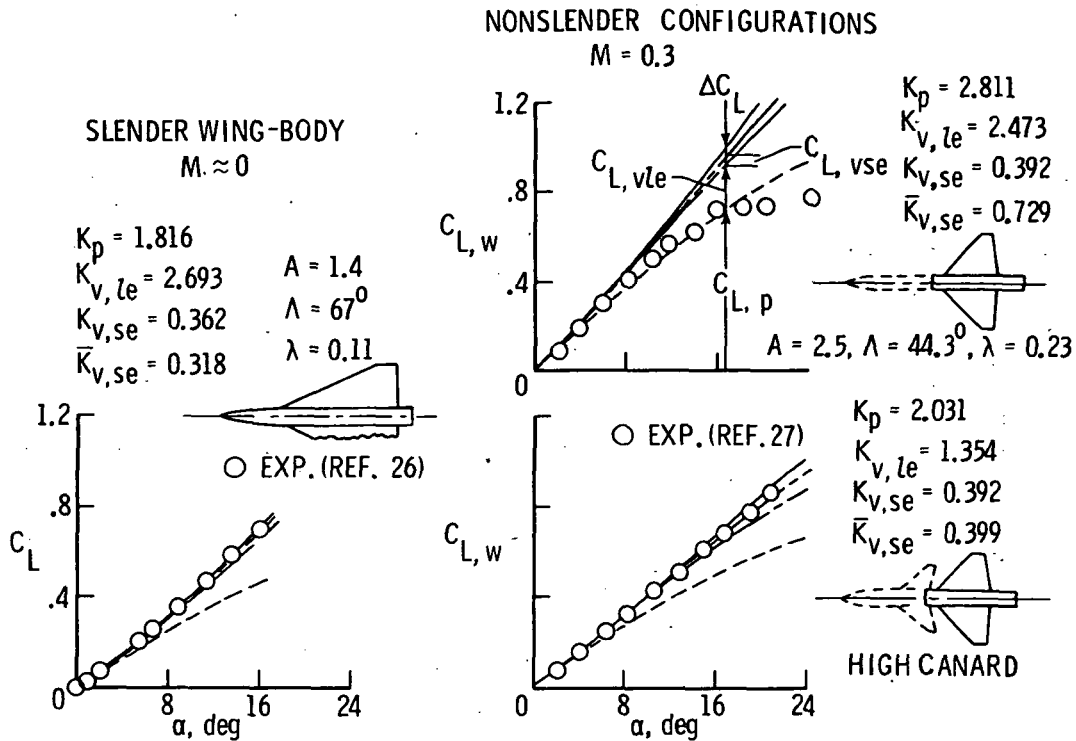


Figure 18. - Suction analogy applications to configurations.

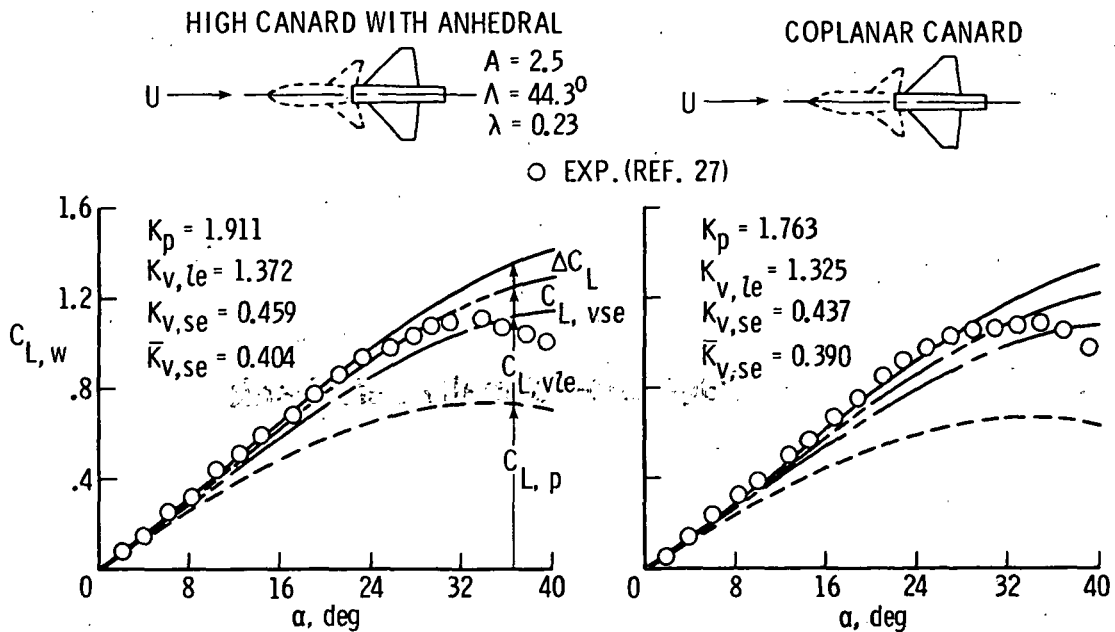


Figure 19. - Effect of canard position on wing lift characteristics for wing-canard configuration. $M = 0.3$.

Page Intentionally Left Blank

A THREE-DIMENSIONAL SOLUTION OF FLOWS OVER WINGS WITH LEADING EDGE VORTEX SEPARATION*

By James A. Weber, Guenter W. Brune, Forrester T. Johnson,
Paul Lu, and Paul E. Rubbert
The Boeing Company

SUMMARY

The application of a new, general, potential flow computational technique to the solution of the subsonic, three-dimensional flow over wings with leading edge vortex separation is presented. The present method is capable of predicting forces, moments, and detailed surface pressures on thin, sharp-edged wings of rather arbitrary planform. The wing geometry is arbitrary in the sense that leading and trailing edges may be curved or kinked and may have arbitrary camber and twist distributions. The method employs an inviscid flow model in which the wing, the rolled-up vortex sheets, and the wake are represented by piecewise continuous quadratic doublet sheet distributions. The Kutta condition is imposed and satisfied along all wing edges. Strengths of the doublet distributions as well as shape and position of the vortex spirals are computed in iterative fashion starting with an assumed initial sheet geometry. The method is verified by numerous computed results. The extension to supersonic flow and more general configuration types is suggested.

INTRODUCTION

The flow at the leading and tip edges of a swept wing with sharp edges separates at moderate to high angles of attack, the separation producing vortex sheets which roll up into strong vortices above the upper surface of the wing. The formation of these vortices is responsible for the well-known nonlinear aerodynamic characteristics exhibited over the angle-of-attack range (fig. 1).

The leading-edge-suction analogy described in references 1, 2, and 3 provides a method suitable for calculating the magnitude of the nonlinear vortex lift on a rather broad class of wing planforms. Polhamus (ref. 1) reasoned that the normal force needed for the flow around a leading edge to reattach to the wing is equivalent to the leading edge suction force necessary to force the flow to be attached to the leading edge in an unsepa-

*This work was supported by the NASA Langley Research Center under Contract NAS1-12185.

rated condition. The unseparated leading edge suction force is calculated, and is then rotated normal to the wing to obtain the lift contribution of the leading edge vortex. The total wing lift computed by this method agrees well with experimental data, but the leading-edge-suction analogy does not give flow-field details or detailed surface pressure distributions.

Several attempts had been made in the past toward the theoretical prediction of detailed pressure distributions and flow fields about swept wings with leading edge vortex separation. Most of these past methods are limited to slender configurations, a considerable simplification because the problem can be reduced to a solution of Laplace's equation in the cross flow plane, for which conformal mapping becomes a powerful tool. Smith (ref. 4) developed the best known method of this type by improving the work done earlier in collaboration with Mangler (ref. 5). Assuming conical flow, which is approximately valid near the apex of the wing, he was able to predict qualitatively the type of pressure distributions that had been observed experimentally. Those pressure distributions (fig. 2) exhibit a vortex-induced pressure peak at about 70 percent of the local semispan of the wing. Toward the trailing edge, Smith's method overpredicts the experimental load distribution by a considerable amount, the reason being that his conical theory does not satisfy the Kutta condition at the trailing edge. Figure 2 shows such a comparison of Smith's theory with experiments and also, for illustrative purposes, spanwise pressure distributions from linear lifting-surface theory (e.g., ref. 6) and from Jones' slender-wing theory (ref. 7) at two chordwise stations of a delta wing. This figure (supplied by Blair B. Gloss, of NASA Langley) shows clearly that none of these theories can even approximately predict aerodynamic load distributions of wings with leading edge vortex separation and demonstrates the need for an accurate prediction method for this type of flow phenomenon.

DESCRIPTION OF THE METHOD

Basic Concepts

Inviscid, irrotational, incompressible fluid flow is characterized by a perturbation velocity potential ϕ satisfying Laplace's equation

$$\phi_{xx} + \phi_{yy} + \phi_{zz} = 0 \quad (1)$$

Compressibility effects over a wide range of subsonic Mach numbers may be approximated by the Goethert rule, in which case a preliminary coordinate transformation again produces equation (1). Hence, for the purposes of this paper, only solutions to equation (1) are considered.

Green's theorem expresses ϕ , the solution to equation (1), in terms of its value and normal derivative on the fluid boundary S :

$$\phi(P) = \iint_S \frac{\partial \phi(Q)}{\partial n} \left(\frac{-1}{4\pi r} \right) dS + \iint_S \phi(Q) \frac{\partial}{\partial n} \left(\frac{1}{4\pi r} \right) dS \quad (2)$$

Here r is the distance from the field point P to a boundary surface point Q and $\partial/\partial n$ is the derivative in the direction of the surface normal \hat{n} pointing into the fluid. Equation (2) gives ϕ as a superposition of a source sheet $\sigma(Q)$ of strength $\partial\phi/\partial n$ and a doublet sheet $\mu(Q)$ of strength ϕ on the boundary of the fluid. The source and doublet are fundamental solutions of equation (1), their strengths being determined by an appropriate set of boundary conditions.

The boundary conditions may be of the Neumann type (specification of $\partial\phi/\partial n$), of the Dirichlet type (specification of ϕ), or of the mixed type. Neumann and Dirichlet boundary-value problems are referred to respectively as "analysis" and "design." In the present formulation all surfaces are considered as "thin," with continuity of $\partial\phi/\partial n$ across the surface, in which case the first term on the right-hand side of equation (2) becomes zero and the second term is replaced by an integral over a single side of the surface with $\phi(Q)$ replaced by $\Delta\phi(Q) = \mu(Q)$.

Numerical Procedures

A new computational scheme for the numerical solution of Laplace's equation for Neumann, Dirichlet, or mixed boundary-value problems was recently presented (ref. 8). A boundary-value problem is comprised computationally of an assemblage of boundary surfaces and their appropriate boundary conditions. A portion of the boundary surface is termed a "network." The boundary surface is discretized into logically independent networks, generally constructed by consideration of the specific characteristics of the physical problem to be solved. Each network consists of a boundary surface oriented arbitrarily in space, composed of source or doublet distributions and accompanied by a properly posed set of analysis (Neumann) or design (Dirichlet) boundary conditions. The computational scheme has been formulated as an aerodynamic influence coefficient method.

Essential features of the computational scheme are

- Geometry input for a network is a matrix of corner-point coordinates. Panel surface shape is obtained by fitting a paraboloid to corner points in an immediate neighborhood by the method of least squares.
- Discrete values of singularity strength are assigned to certain standard points on each network. A local distribution of surface singularity strength is

obtained by fitting a linear source or quadratic doublet form to these discrete values in an immediate neighborhood by the method of least squares.

- Certain standard points on each network are assigned as control points. These points include panel center points as well as edge abutment downwash points in the case of doublet networks. The latter serve to impose standard aerodynamic edge conditions automatically, for example, the Kutta condition, zero potential jump at thin edges, continuity of singularity strength across abutting networks, so as to produce logical independence for each network. In the case of the doublet design network, certain linear integral conditions are imposed to achieve closure. In all cases the number of boundary conditions on each network coincides with the number of assigned surface singularity parameters.
- Two expansions of the induced velocity kernel are employed. The near-field expansion is based upon the assumption of (relatively) small panel curvature; the far-field expansion is dependent upon a (relatively) large separation distance between the field point and panel. All resultant integrals are evaluated in closed form by means of recursion relations which contain the fundamental logarithm and arc tangent transcendental terms that appear in flat-panel, constant-strength techniques.

Theoretical Model

Experimental studies (e.g., refs. 9 and 10) of the principal vortex indicate that its shape and strength are relatively independent of Reynolds number. The relative lack of viscosity dependence suggests that the flow may be regarded as potential, with the free shear layer represented either as a vortex sheet, or equivalently, a doublet distribution, across which exists a discontinuity in tangential velocity.

The essential elements of the present inviscid and incompressible flow model are the wing, the trailing sheet (wake), the sheet emerging from the wing leading edge and tip (free sheet), and the rolled-up core or spiral region (fed sheet) fed by the leading-edge and tip vortex sheets (fig. 3).

The boundary conditions which are imposed on these elements are

- The flow must be everywhere parallel to the wing surface, that is, $\hat{n} \cdot \bar{V}^S = 0$, where the symbols \bar{V}^S and \hat{n} are the average velocity (i.e., the average of the velocities on opposing sides of the sheet) and normal vector on the sheet surface, respectively.
- The free sheet and wake cannot support a pressure differential ΔC_p and must be aligned with the local flow, that is, $\Delta C_p = 0$ and $\hat{n} \cdot \bar{V}^S = 0$.

- The fed sheet is an entirely kinematic extension of the free sheet, and no boundary conditions are applied to the fed sheet. This is a simplified model of the true physical vortex-core region which is viscosity dominated. The size of the fed sheet is taken from the conical-flow results of Smith (ref. 4).
- Kutta conditions are imposed along the leading, side, and trailing edges of the wing in the presence of free sheets emanating from these edges.

The geometric description is that of a general three-dimensional (not conical) configuration consisting of a thin wing, free sheet, wake, and fed sheet (fig. 3). The wing geometry is arbitrary in the sense that leading and trailing edges may be curved or kinked and the lifting surface may have arbitrary camber and twist. The configuration is subdivided into a network of quadrilateral panels whose corner points are defined by coordinates in transverse cutting planes. The trace of the kinematic fed sheet in a transverse cutting plane is either a circular arc extending over 180° or a single planar panel locally perpendicular to the free sheet.

Briefly, the main features of the numerical representation are the following. The wing and free sheet are represented by network distributions of doublets which vary as piecewise continuous quadratic functions in each of two coordinate directions over each panel of the network. The cumbersome shedding of wakes associated with vortex panels is thus avoided. An analysis type of network is employed on the wing (geometry of the wing is specified), and a design type network of doublets simulates the free sheet (unknown free-sheet geometry, zero pressure jump specified). Figures 4 and 5 display details of the two networks, showing the arrangements for the free doublet parameters from which the six coefficients of the quadratic panel distributions are determined by least-squares fits. All aerodynamic influence coefficients (AIC) are integrable in closed form, resulting in an efficient and reliable AIC computation. Details of the development of network formulation and AIC are reported in reference 8.

Network types used for the wake and fed sheet are specializations of the design type network.

Solution Procedure

The boundary-value problem of wings with leading edge vortex separation is non-linear because of the fact that the shape of the free vortex sheet (symbolized by \hat{n}) as well as its strength are unknown. The solution procedure must therefore be iterative. The basic approach driving the iteration involves a small perturbation from an initial guess which results in a linear formulation for the updated free-sheet position and strength.

The boundary-value problem can be written symbolically in terms of the following three equations:

$$E(\mu_e, \bar{\mu}, \hat{n}) = 0 \quad (3)$$

$$F(\mu_e, \bar{\mu}, \hat{n}) = 0 \quad (4)$$

$$G(\mu_e, \bar{\mu}, \hat{n}) = 0 \quad (5)$$

Here, those doublet strength parameters defined at certain edge points of networks are denoted by μ_e ; all remaining doublet parameters, by $\bar{\mu}$; and the panel normal vectors, by \hat{n} . The specific form of these equations is given by appendix A. The first equation expresses the stream surface boundary condition ($\hat{n} \cdot \bar{V}^S = 0$) at certain edge points of networks. Satisfaction of equation (3) is a necessary condition for the satisfaction of the Kutta condition postulated for wing leading and trailing edges. The second equation (4) symbolizes the boundary conditions $\Delta C_p = 0$ of the free sheet and wake and $\hat{n} \cdot \bar{V}^S = 0$ of the wing. The third equation (5) is the stream surface boundary condition of the free sheet and wake.

Small perturbations of these equations from an initial "starting solution" result in a set of linear equations governing perturbation variables $\Delta\mu_e$, $\Delta\bar{\mu}$, and $\Delta\hat{n}$. The specific form of the equations is given in appendix A. Symbolically,

$$\begin{bmatrix} \frac{\partial E}{\partial \mu_e} & \frac{\partial E}{\partial \bar{\mu}} & 0 \\ \frac{\partial F}{\partial \mu_e} & \frac{\partial F}{\partial \bar{\mu}} & \frac{\partial F}{\partial \hat{n}} \\ \frac{\partial G}{\partial \mu_e} & \frac{\partial G}{\partial \bar{\mu}} & \frac{\partial G}{\partial \hat{n}} \end{bmatrix} \begin{Bmatrix} \Delta\mu_e \\ \Delta\bar{\mu} \\ \Delta\hat{n} \end{Bmatrix} = \begin{Bmatrix} 0 \\ \Delta F \\ \Delta G \end{Bmatrix} \quad (6)$$

where ΔF and ΔG denote the error in satisfaction of boundary conditions arising at an intermediate, nonconverged point in the iteration cycle.

These equations are solved in each cycle of the iteration procedure to update doublet strength and configuration geometry. Numerical experimentation revealed that it is most advantageous to satisfy the first equation of (6) (i.e., the Kutta condition) exactly at every iteration step. It is assumed that the Kutta condition is not affected by the geometry update $\partial E / \partial \hat{n} = 0$. To avoid overshooting the correct solution, the step sizes are scaled. Specific details of the iteration scheme are given in appendix B.

VERIFICATION OF THE METHOD

A computer program has been developed which verifies the method. The program, which is presently restricted to 125 unknown parameters, is coded for the CDC 6600 computer, occupies 120 000 octal locations of central memory in an overlay structure, and uses 15 Input/Output units. (The program is also operational on the Langley CDC 6400 and 6600 computers.) Although quotation of execution time is qualitative at best because of the many influencing factors, solutions for delta wings have been executed in under 300 seconds of central processor time.

Numerous example cases have been executed to validate the method and its generality. Cases have been selected with a view to comparison with available theoretical and experimental data for a range of different geometric configurations including delta, gothic, and arrow wings.

The capability of the method to predict overall wing coefficients accurately is shown in figure 6 for a delta wing of aspect ratio 1 at low subsonic speed ($M_\infty = 0$). The right-hand side of the figure shows the well-known nonlinear variation of the normal-force coefficient C_N with angle of attack α . Several values of C_N were computed for angles of attack up to 20° and agree very well with experimental data of Peckham (ref. 10) and theoretical results from the leading-edge-suction analogy of Polhamus (ref. 2). To the left of the figure is shown C_N as a function of iteration number for two different angles of attack. The curves demonstrate the excellent convergence characteristics of the method. The corresponding load distribution at $\alpha = 20^\circ$ is plotted in figure 7 and compared with Peckham's experimental results. Although only 25 wing panels were used on one-half of the configuration, the completely three-dimensional non-conical load distribution was well predicted, including the location of the vortex-induced pressure peaks and the decrease of the load toward the trailing edge.

Figures 8 and 9 show detailed surface pressure distributions for another delta wing of aspect ratio 1.4559 at $\alpha = 14^\circ$ and $\alpha = 19.1^\circ$. Upper and lower surface pressures are very well predicted, as the comparison with experimental data (ref. 11) illustrates. The experimental results clearly show the effect of the secondary vortex separation which takes place on the upper surface just slightly outboard of the main vortex. The present method does not model secondary vortex separation and consequently produces a slightly different shape for the pressure peaks.

The method has application to more general configurations. For example, figure 10 shows the method applied to a gothic wing having a swept trailing edge and a curved leading edge. The right-hand side of the figure shows good agreement of the normal-force coefficient C_N with experiment at the relatively high angle of attack ($\alpha = 14.3^\circ$). The convergence characteristics shown on the left-hand side are excellent;

in this example the iteration scheme was modified such that the aerodynamic influence coefficients (whose computation consumes the largest fraction of computer run time) were updated only after the 5th and 10th iterations.

Figure 11 shows the predicted load distribution of an arrow wing. Experimental data are not available for comparison, but the plotted loads appear to be realistic and demonstrate that the method is capable of handling other than delta-wing planforms.

CONCLUSIONS

The work reported here demonstrates one of the applications of a new, general, subsonic potential flow computational technique recently developed (reported in AIAA Paper No. 75-50, 1975). With the use of this technique, a three-dimensional method for predicting the flow field about swept, sharp-edged wings characterized by the presence of vortex separation at the leading edge has been formulated and verified. The method has been highly successful in overcoming the most difficult aspects of the problem and provides a potential breakthrough to eventual development of this initial capability into a method suitable for supersonic flow and for complete configuration analysis in subsonic and supersonic flow. In addition, it has application to related problems involving free vortex sheets, which are encountered in the areas of powered lift, jet interactions, jet flaps, and so forth.

APPENDIX A

DERIVATION OF EQUATIONS

The set of boundary conditions defining the leading edge vortex problem were represented symbolically in equations (3), (4), and (5). The derivation of that set is outlined in this appendix.

First, consider several fundamental relationships which hold for a sheet across which a jump in tangential velocity exists (e.g., a doublet sheet). The average velocity for the sheet \bar{V}^S is given in terms of the upper-surface and lower-surface velocities \bar{V}_u and \bar{V}_l , respectively:

$$\bar{V}^S = \frac{1}{2}(\bar{V}_u + \bar{V}_l) \quad (A1)$$

The velocity difference across the sheet \bar{V}^D is given as

$$\bar{V}^D = \bar{V}_u - \bar{V}_l \quad (A2)$$

The pressure jump ΔC_p across the sheet is given as

$$\Delta C_p = \frac{2}{U_\infty^2} (\bar{V}^S \cdot \bar{V}^D) \quad (A3)$$

where \bar{U}_∞ is the free-stream velocity.

The jump of tangential velocity across the sheet is created by a doublet distribution μ defined by a set of free doublet parameters μ_p such that $\mu = \mu(\mu_p)$. The sheet velocities are directly related to μ and μ_p through the local point relationship for \bar{V}^D and the global matrix relationship for \bar{V}^S :

$$\bar{V}^D = \nabla \mu = \nabla \mu(\mu_p) \quad (A4)$$

$$\{\bar{V}^S\} = [A] \{\mu_p\} \quad (A5)$$

where $[A]$ is the matrix of aerodynamic influence coefficients relating \bar{V}^S to the doublet parameters μ_p .

The boundary conditions are

Wing:

$$\hat{n} \cdot \bar{V}^S = 0 \quad (A6)$$

Free sheet and wake:

$$\hat{n} \cdot \bar{V}^S = 0 \quad (A7)$$

$$\Delta C_p = 0 \tag{A8}$$

plus the Kutta condition, where \hat{n} is the normal vector.

Let the boundary conditions be represented symbolically in terms of the following independent variables: μ_e , doublet strength parameter on the edges of all networks at which the Kutta condition¹ is to be satisfied; $\bar{\mu}$, all remaining doublet strength parameters of all the networks; and \hat{n} , the normal vector representing a geometry parameter defining the spatial location of the networks (wing networks are spatially fixed). Equations (A6) to (A8) are grouped symbolically into the following set:

$$E(\mu_e, \bar{\mu}, \hat{n}) \equiv \hat{n} \cdot \bar{V}^S = 0 \tag{Kutta condition} \tag{A9}$$

$$F(\mu_e, \bar{\mu}, \hat{n}) \equiv \left. \begin{array}{l} \hat{n} \cdot \bar{V}^S = 0 \\ \Delta C_p = 0 \end{array} \right\} \begin{array}{l} \text{(Wing)} \\ \text{(Free sheets and wake)} \end{array} \tag{A10}$$

$$G(\mu_e, \bar{\mu}, \hat{n}) \equiv \hat{n} \cdot \bar{V}^S = 0 \tag{Free sheets and wake} \tag{A11}$$

To begin the iteration procedure, a linear perturbation of these nonlinear equations from an initial "starting solution" is performed. An example of the perturbation technique is illustrated by a linear perturbation of $E (= \hat{n} \cdot \bar{V}^S)$ from the "old" value to the "new":

$$E_{\text{new}} = E_{\text{old}} + \Delta E = \hat{n} \cdot \bar{V}^S + \Delta \hat{n} \cdot \bar{V}^S + \hat{n} \cdot \Delta \bar{V}^S + O(\Delta^2) \tag{A12}$$

or, rearranging and neglecting terms of order Δ^2 ,

$$E_{\text{new}} - E_{\text{old}} = E_{\text{new}} - \hat{n} \cdot \bar{V}^S = \Delta \hat{n} \cdot \bar{V}^S + \hat{n} \cdot \Delta \bar{V}^S = \Delta E \tag{A13}$$

where $\Delta \bar{V}^S$ is related to $\Delta \mu_e$, $\Delta \bar{\mu}$, and $\Delta \hat{n}$. A similar analysis of E , F , and G yields the symbolic matrix equation

$$\begin{bmatrix} \frac{\partial E}{\partial \mu_e} & \frac{\partial E}{\partial \bar{\mu}} & \frac{\partial E}{\partial \hat{n}} \\ \frac{\partial F}{\partial \mu_e} & \frac{\partial F}{\partial \bar{\mu}} & \frac{\partial F}{\partial \hat{n}} \\ \frac{\partial G}{\partial \mu_e} & \frac{\partial G}{\partial \bar{\mu}} & \frac{\partial G}{\partial \hat{n}} \end{bmatrix} \begin{Bmatrix} \Delta \mu_e \\ \Delta \bar{\mu} \\ \Delta \hat{n} \end{Bmatrix} = \begin{Bmatrix} \Delta E \\ \Delta F \\ \Delta G \end{Bmatrix} \tag{A14}$$

The iteration scheme (appendix B) is initiated by an initial geometry definition for the wing (fixed), free sheet and wake, and fed sheet. The boundary conditions will not, in

¹The Kutta condition is not treated as a separate boundary condition, since by the nature of the free-sheet boundary condition ($\Delta C_p = 0$) it will be satisfied when the solution is achieved. Instead, a smooth "off-flow" condition is imposed as a necessary condition (not sufficient) for the Kutta condition to be satisfied.

APPENDIX A

general, be satisfied. The perturbed equations (A14) define the linear, one-step values of the perturbed quantities necessary to reach the solution. In fact, however, when the geometry is updated and all quantities are recomputed, the boundary conditions will, once again, not be satisfied. Symbolically, the "old" values of E, F, and G will not be satisfied; it is required, however, that the "new" values will be satisfied such that $E_{\text{new}} = F_{\text{new}} = G_{\text{new}} = 0$. This establishes the iteration procedure.

It was found to be convenient to make the following approximations to equation (A14):

$\Delta E = 0$ insuring satisfaction of the Kutta condition for each iteration step

$\frac{\partial E}{\partial \hat{n}} = 0$ assuming the smooth "off-flow" condition is not affected by geometry update
($\Delta \hat{n} \neq 0$)

APPENDIX B

ITERATION SCHEME

Represent the quantities of equation (6) symbolically as $\Delta X = (\Delta\mu_e, \Delta\bar{\mu}, \Delta\hat{n})$, the coefficient matrix (Jacobian) as J , and the right-hand side as $-f$. Equation (6) becomes

$$J \Delta X = -f \quad (B1)$$

These equations are solved iteratively with a quasi-Newton scheme. Represent the i th iteration by superscript i . The scheme proceeds to find the corrections $\Delta X^{(i)}$ from the equation

$$J^{(i)} \Delta X^{(i)} = -f^{(i)} \quad (B2)$$

and forms the new approximate solution (next iterate).

$$X^{(i+1)} = X^{(i)} + \delta^{(i)} \Delta X^{(i)} \quad (B3)$$

where $J^{(i)} = J[X^{(i)}]$, $f^{(i)} = f[X^{(i)}]$, and $\delta^{(i)}$ is a scaling parameter to limit the step size of the correction vector. The Jacobian at $X^{(i+1)}$ is obtained by using the following update formula (ref. 12):

$$J^{(i+1)} = J^{(i)} + D^{(i)} \quad (B4)$$

where

$$D^{(i)} = \frac{[f^{(i+1)} - f^{(i)} - J^{(i)} \Delta X^{(i)}] \Delta X^{(i)T}}{\Delta X^{(i)T} \Delta X^{(i)}}$$

In this way, there is no need to reevaluate the partial derivatives comprising the elements of the Jacobian at every iteration.

Since the aerodynamic influence coefficients form an essential part of the method, included in the iterative scheme is a procedure for generating new aerodynamic influence coefficients only after every few iterations. This approach helps to reduce the overall computing costs.

The scaling parameter $\delta^{(i)}$ is introduced to alleviate the problem of overshoot in the classical Newton scheme. For each iteration cycle, the following criteria are used to determine $\delta^{(i)}$:

$$0 < \delta^{(i)} \leq 1 \quad \delta^{(i)} \|\Delta X^{(i)}\| \leq \gamma \|X^{(i)}\| \quad (B5)$$

APPENDIX B

where γ is a predetermined quantity to be set equal to a certain fraction of the length of the initial vector $X^{(0)}$ and the notation $\| \cdot \|$ is the Euclidean norm representing the length of a vector. In addition, a halving process of the scaling parameter $\delta^{(i)}$ is applied to ensure the inequality

$$\|f^{(i+1)}\| < \|f^{(i)}\| \quad (B6)$$

The quality of the solution is monitored by examination of the residuals defined by

$$R = \sum_k \left\{ \left[\Delta(\Delta C_{p_{\text{sheets}}}) \right]^2 + \left[\Delta(\hat{n} \cdot \vec{v}_{\text{wing}}^s) \right]^2 \right\} \quad (B7)$$

where k ranges over all appropriate boundary-condition points.

To initiate the solution process, only an initial geometry is required for the free sheet and fed sheet. This may be obtained from conical-flow results or, as experience allows, by assuming an initial geometry form.

REFERENCES

1. Polhamus, Edward C.: Predictions of Vortex-Lift Characteristics by a Leading-Edge-Suction Analogy. *J. Aircraft*, vol. 8, no. 4, Apr. 1971, pp. 193-199.
2. Polhamus, Edward C.: A Concept of the Vortex Lift of Sharp-Edge Delta Wings Based on a Leading-Edge-Suction Analogy. NASA TN D-3767, 1966.
3. Polhamus, Edward C.: Application of the Leading-Edge-Suction Analogy of Vortex Lift to the Drag Due to Lift of Sharp-Edge Delta Wings. NASA TN D-4739, 1968.
4. Smith, J. H. B.: Improved Calculations of Leading-Edge Separation from Slender Delta Wings. R.A.E. Tech. Rep. No. 66070, Mar. 1966.
5. Mangler, K. W.; and Smith, J. H. B.: A Theory of the Flow Past a Slender Delta Wing With Leading-Edge Separation. *Proc. Roy. Soc.*, May 1959.
6. Lamar, John E.: A Modified Multhopp Approach for Predicting Lifting Pressures and Camber Shape for Composite Planforms in Subsonic Flow. NASA TN D-4427, 1968.
7. Jones, Robert T.: Properties of Low-Aspect-Ratio Pointed Wings at Speeds Below and Above the Speed of Sound. NACA Rep. 835, 1946.
8. Johnson, F. T.; and Rubbert, P. E.: Advanced Panel-Type Influence Coefficient Methods Applied to Subsonic Flows. AIAA Paper No. 75-50, Jan. 20-22, 1975.
9. Maskell, E. C.: Some Recent Developments in the Study of Edge Vortices. *Proceedings of 3rd Congress of Int. Counc. Aero. Sci.*, 1962, pp. 737-749, Spartan Books, Inc., Washington 1964.
10. Peckham, D. H.: Low-Speed Wind-Tunnel Tests on a Series of Uncambered Slender Pointed Wings With Sharp Edges. R. & M. 3186, Brit. A.R.C., 1961.
11. Marsden, D. J., et al.: An Investigation Into the Flow Over Delta Wings at Low Speeds With Leading Edge Separation. Rep. No. 114, ARC 20409, Coll. Aeronaut., Cranfield (Engl.), Feb. 1958.
12. Broyden, C. G.: Quasi-Newton, or Modification Methods. *Numerical Solution of Nonlinear Algebraic System*, G. D. Bryne and C. A. Hall, eds., Academic Press, 1973.

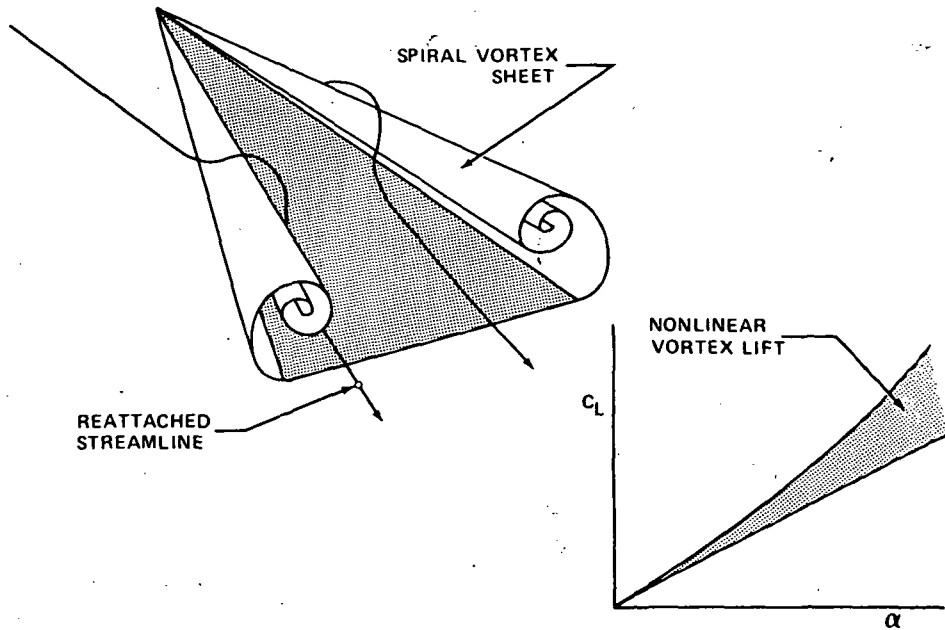


Figure 1.- Leading edge vortex flow.

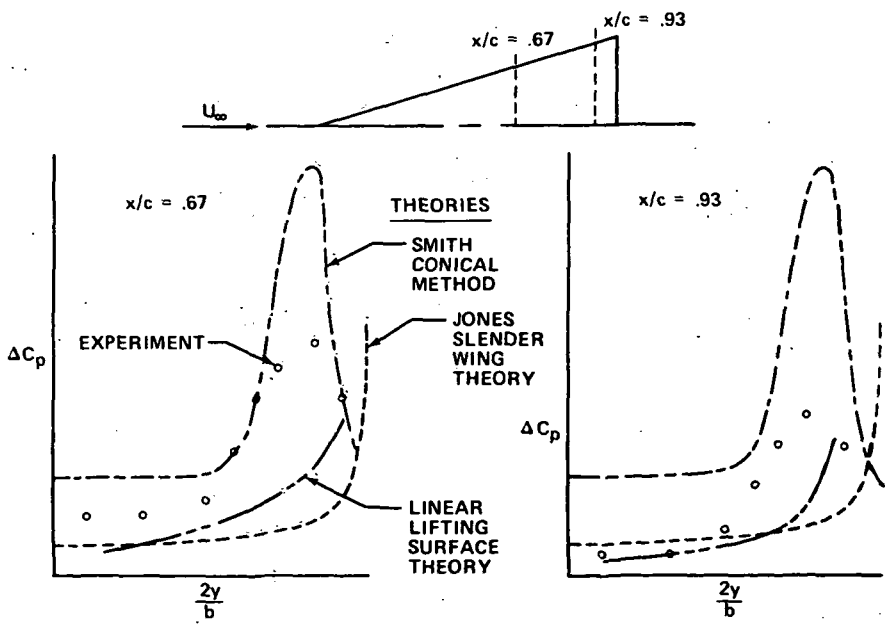


Figure 2.- Spanwise pressure distributions given by earlier theories.

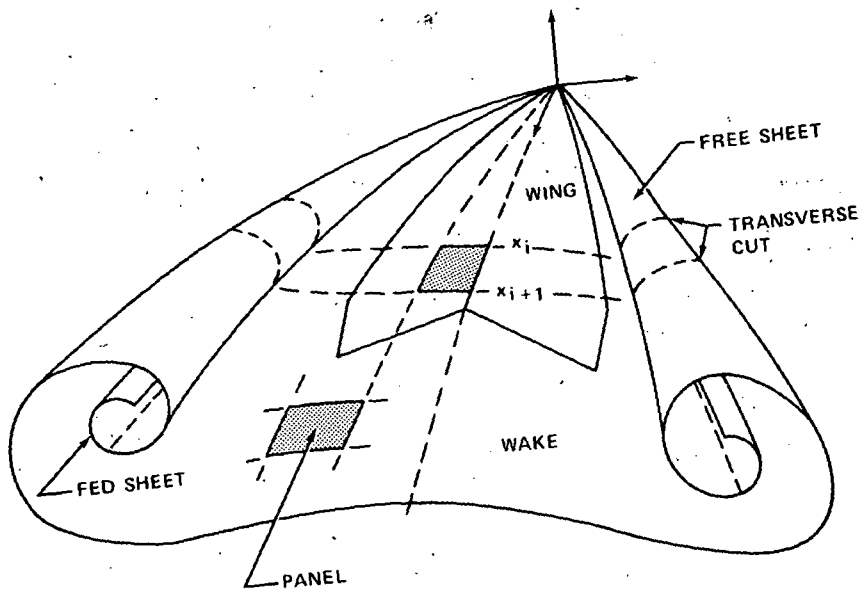


Figure 3.- Geometric description.

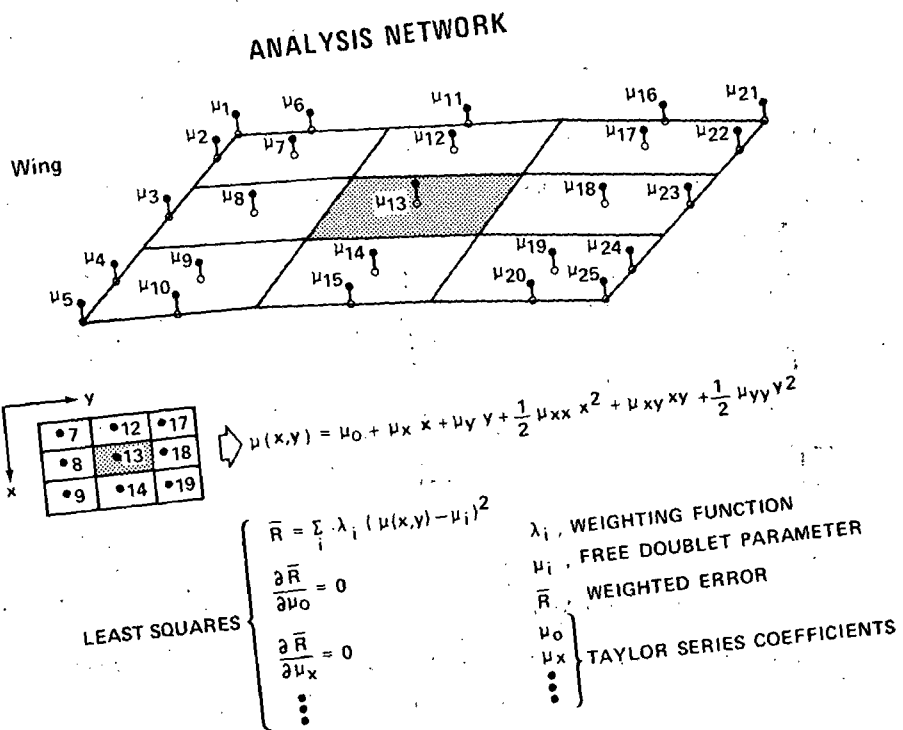


Figure 4.- Analysis network.

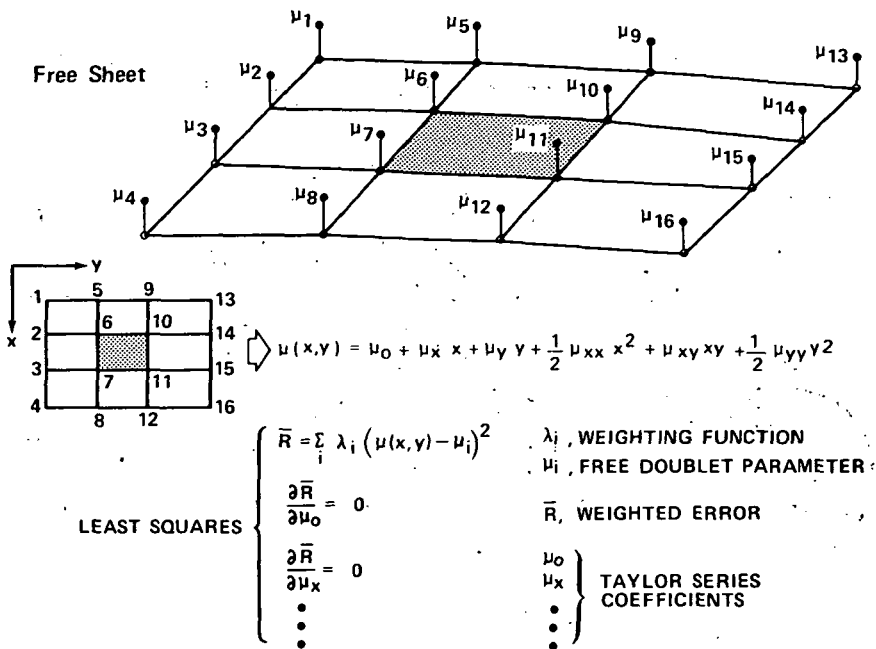


Figure 5.- Design network..

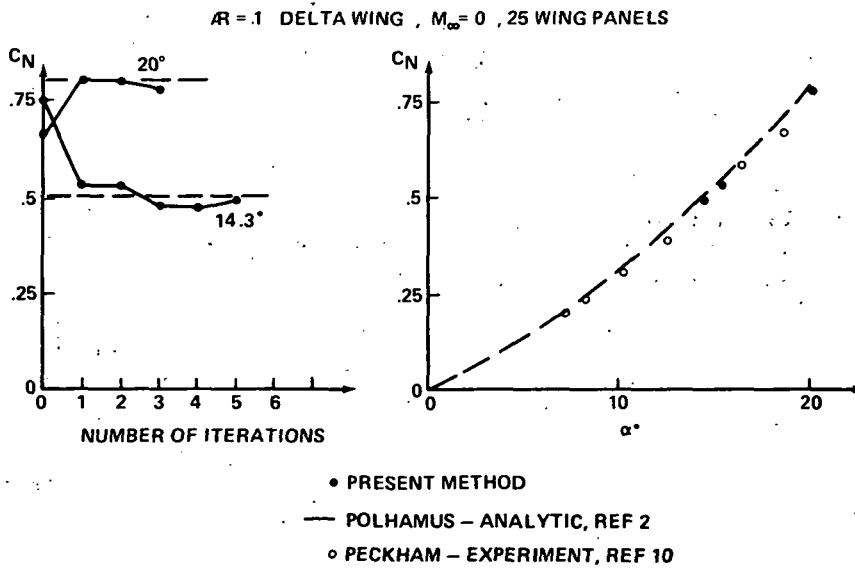


Figure 6.- Normal-force coefficient C_N .

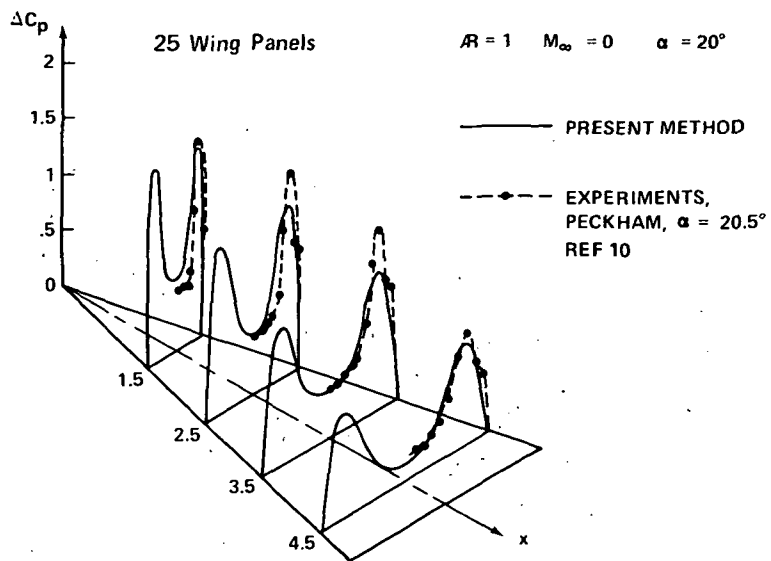


Figure 7.- Delta wing load distribution.

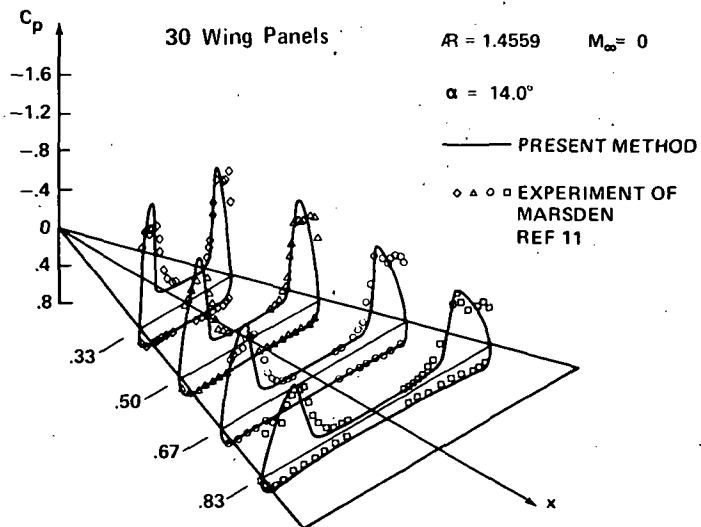


Figure 8.- Surface pressure distribution of delta wing. $\alpha = 14^\circ$.

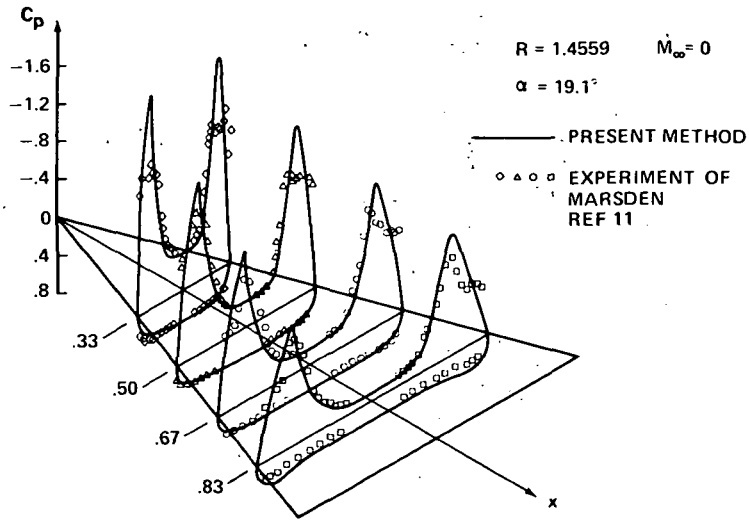


Figure 9.- Surface pressure distribution of delta wing. $\alpha = 19.1^\circ$.

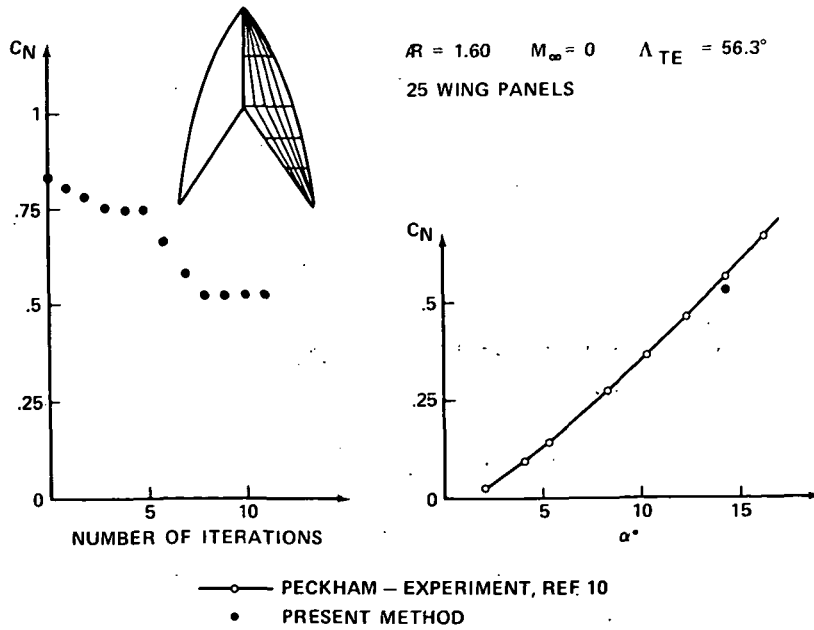


Figure 10.- Gothic wing.

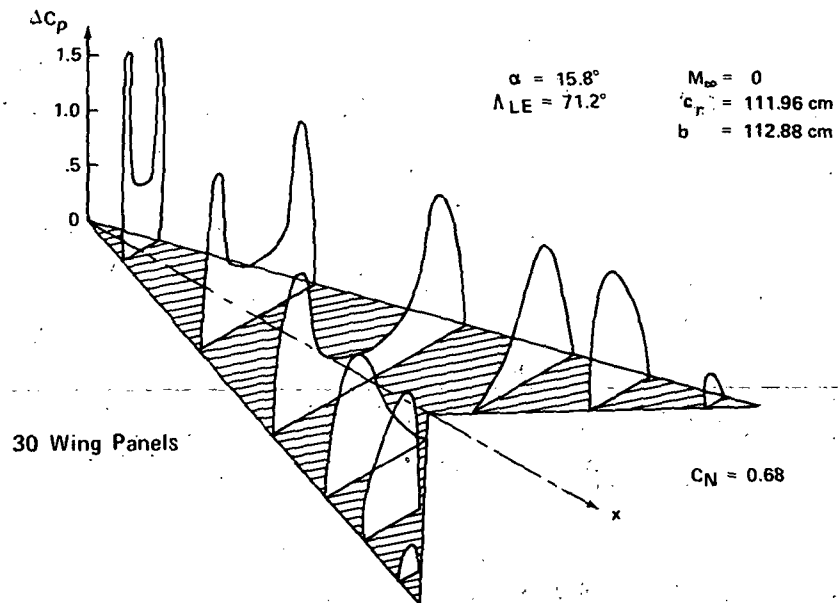


Figure 11.- Arrow wing load distribution.

ADVANCES IN SONIC BOOM THEORY*

By J.L. Lung, B. Tiegerman, N.J. Yu, and A.R. Seebass

Cornell University

INTRODUCTION

The theory required to predict the sonic boom of supersonic aircraft and the numerical codes that do so on a routine basis have been available for some time (references 1 and 2). This paper discusses recent advances in three aspects of sonic boom theory and briefly addresses the role of numerical calculations in each. We first discuss the maximum extent to which the sonic boom of supersonic aircraft can be reduced by careful aerodynamic design, and describe a computer program that determines the aircraft area development required to minimize various sonic boom signature parameters. We next describe a result that predicts the minimum sonic boom of hypersonic vehicles; this result is a consequence of a matching of numerical calculations with the results of weak nonlinear wave theory. Finally, we report on numerical results that advance our understanding of the behavior of sonic boom signals in the vicinity of a caustic surface. The numerical procedures developed for the latter problem have proved effective in calculating transonic flows with embedded shock waves.

COMPUTER PROGRAM FOR AERODYNAMIC MINIMIZATION

There are important trade-offs between the aerodynamic minimization of an aircraft's sonic boom and its performance. We ignore these trade-offs and ask: What is the maximum sonic boom reduction that can be achieved through careful aerodynamic design? Specifically, we have minimized each one of three signature parameters without any constraint imposed on the others or on the aircraft's performance. The aircraft is characterized by its weight, length and, in some cases, also by its volume and center of pressure. We use the supersonic area rule to pose the appropriate minimization problem in terms of the cross-sectional area development of the equivalent body of revolution for the vertical azimuthal plane.

Determining the shape of the body of revolution that minimizes a given signature parameter below an aircraft is equivalent to the specification of the Whitham F-function for that azimuthal plane. With a few well-known facts in hand, intuition may be used to guess the proper minimum. That this is indeed a local minimum can then be proved by considering infinitesimal variations of the F-function; the proof that it is a global minimum requires the use of control theory.

*Research was sponsored by NASA Langley Grant NGL-010-030-203.

We have considered minimization of the parameters shown in figure 1: 1) the impulse of the positive phase with a resulting shock pressure rise of P_J ; 2) the maximum overpressure in the signal P_{SO} ; 3) the minimum shock pressure rise, P_S , that can be achieved with the rest of the pressure increase occurring in a prescribed rise time, τ . The general procedures for this minimization have been outlined in reference 3; they lead to a system of four equations in the four unknowns. The evaluation of certain integrals with analytical formulas and the elimination of two unknowns result in two equations involving complicated combinations of transcendental functions; the unknowns are the length of the positive phase of the signal and the location of the rear shock wave.

A computer program has been developed (reference 4) that, with the input indicated in table 1, determines the appropriate area development needed to minimize the above signature parameters. The output provided, also delineated in table 1, is both numerical and graphical, and in the international system of units as well as in the more usual English units. The main parameters in the input are the Mach number, the aircraft's weight, length and altitude, the rise time prescribed for the pressure following the shock wave, and the ratio of the rear-to-front shock strength. For aircraft with "large" volumes, the volume and center of pressure also play a role. Known solutions to these equations are used to determine an initial guess for the unknowns. The solution is found by using Newton's method. Should the operator choose atypical initial conditions, then there is an option for the operator to choose his own initial guess.

There is nothing difficult about the numerical programming, and with an appropriate initial guess for the two unknowns, Newton's method quickly provides the solutions. One might say that this program requires an advanced programmable calculator rather than a computer. Typical computation times are about ten seconds per case on an IBM 370/168, corresponding to less than one minute on a 360/65.

For many practical designs with realistic volumes, the volume poses no constraint because volumes up to a certain limiting value can be obtained without penalty. Beyond that value, one must either compromise the minimum shape in order to accommodate the additional volume or have recourse to a Busemann biplane or ring wing.

The program we have developed treats only the case of an isothermal atmosphere. It is not difficult to generalize this program to standard atmospheric conditions. Darden, in reference 5, has carried through such a generalization to provide a simple means of correcting the results for an isothermal atmosphere so that they correspond to those for a standard atmosphere.

Sample results for the flight conditions typical of an SST are depicted in figures 2 and 3. Figure 3 shows the aircraft area development required to achieve the minimum overpressure signature shown in figure 3 with the constraint that the rear shock be no stronger than the front shock. The pressure rise through both the front and the rear shock are tabulated, as is the impulse of a positive phase of the signature. For this sample case, with equal

strength front and rear shocks, the impulse is about 30% larger than the minimum impulse that could be obtained for the same flight conditions; the shock strength has, however, been reduced 45%.

SONIC BOOM OF HYPERSONIC AIRCRAFT

While we can predict the sonic boom of slender aircraft at relatively high Mach numbers, at the present time it is not possible to predict a sonic boom of vehicles when the products of their slenderness ratios and Mach numbers are comparable to 1. This absence of a complete theory does not preclude the possibility of determining the minimum impulse that could be achieved by hypersonic vehicles. Furthermore, because of the strong non-linear effects near the body, it is logical to assume that the minimum impulse signature does not differ from that of minimum overpressure. In hypersonic flight the wave phenomenon associated with the drag of the vehicle undoubtedly sets a lower bound for its sonic boom.

We can invoke the hypersonic equivalence principle of Hayes to determine the flow near the body; the cylindrical analog of the inviscid Burgers' equation must describe the evolution of this flow field far from the body. In the region intermediate between these two regimes there is no simple theory, and one must meld the two flow regions with a numerical calculation of the flow field.

In the drag-dominated case, the flow field far from the vehicle will be that produced by the energy released by the vehicle per unit time, that is, the product of the vehicle's drag with its velocity. We make the assumption that this energy is released essentially instantaneously, that is that the vehicle is relatively short; then the flow in the near field can be interpreted to be that associated with a cylindrical blast wave through the equivalence principle. There is no reliable way of coupling the similarity solution to this problem, valid when the shock wave is strong, with the inviscid Burgers' description, valid when the shock wave is weak. A simple recasting of the results obtained by modifying the similarity solution to take into account the first term in ambient pressure so that it yields an inverse three-fourths power-decay asymptotically, provides a reasonable estimate of the overpressure, but does not provide information about the signature's impulse.

Atmospheric effects can be accounted for easily, provided the wave becomes relatively weak in some fraction of an atmospheric scale height. The conditions under which this assumption is a realistic one have been carefully delineated in reference 6.

In order to carry out this theory, then, one must have reliable numerical solutions for the cylindrical blast wave. We were concerned that the earlier numerical calculations for a cylindrical blast wave, carried to significant times by Plooster (reference 7), would not be reliable because he used a finite difference scheme which employed an artificial viscosity. While this

artificial viscosity should not affect the strength of the leading shock wave, we realized that it would prevent the steepening of the negative phase of the pressure signature into an N-wave; hence we undertook to recalculate the numerical solution for the cylindrical blast wave for even larger times without recourse to artificial viscosity. In carrying forth this numerical calculation, an implicit second-order scheme, modelled after that of Okhotsimskii (reference 8) was used. The numerical procedure we developed treats the front shock wave as a mathematical discontinuity and applies the Rankine-Hugoniot conditions across it. The position of this shock wave is determined by a shock-fitting procedure, which was not difficult to implement. While this procedure eliminates any artificial viscosity, it does mean that the leading truncation errors are dispersive and when steep gradients are encountered in the negative phase of the signal, these dispersive errors become so large that the calculation must be modified.

Near the origin of the blast wave the density of the gas is very low and its temperature very high, leading to an entropy core that is difficult to treat numerically. Consequently we treated the entropy core analytically and used this analytical behavior as inner boundary data for the numerical solution. Eventually the wave propagates far enough away from this region that it no longer needs to be considered. At that stage it is necessary to refine the computational grid in order to generate accurate numerical results. In the later stages of the calculations it is necessary to change the difference scheme to one that has a dissipative truncation error in order to damp the dispersive oscillations that originate in the steepening zone of the negative phase. The numerical results obtained extend essentially a decade further, in energy length scales, than those of Plooster. The results for the overpressure as a function of the energy length scale, defined here as $\bar{R} = (D/2\pi P_1)^{1/2}$, where D is the vehicle's drag and P_1 the ambient pressure, are shown in figures 4(a) and 4(b) (from reference 6). While there is little difference in the shock strength between these results and those of Plooster, there is a considerable difference in the signature shape, particularly that of the negative phase. The calculations are finally terminated by the growth of dispersive errors. Figure 5 shows the pressure profiles in terms of normalized distance to the shock wave for various distances. These numerical results provide the initial conditions for the inviscid cylindrical Burgers' equation. A careful monitoring of the numerical results that are appropriate for this matching show that even with this additional decade of calculation the matching can only be carried out to lowest order.

These results of this matching are in accord with those reported by Pan and Sotomayer (reference 9) for a homogeneous atmosphere, as later modified by them; they used Plooster's numerical results. When our results are modified to account for atmospheric effects, considering the atmosphere to be isothermal, the results for the overpressure and impulse shown in figure 6 are obtained; the formulas that give these curves may be found in references 3 and 6. These results, modified for flight path angle, are compared with measurements made on the Apollo 15 and 16 re-entries in figure 7 (references 10 and 11); the impulse is compared only in that case where it was clear there were no waves reflected from surrounding surfaces present in the signal. The agreement is surprisingly good and provides a proper vindication of the results.

The computations were carried out on an IBM 360/65 computer and involved four different stages of computation, beginning with a stage that took into account the entropy core and concluding with calculations with a truncation error that simulated viscosity. The total computation time for all four stages was about six hours.

BEHAVIOR AT A CAUSTIC

To determine the amplification of a sonic boom at a focus that results in a so-called superbomb requires the solution to a mixed nonlinear equation with discontinuous boundary data in the hyperbolic domain. We have developed a second-order numerical scheme that treats discontinuities as such by applying the appropriate jump conditions across them and, consequently, reduces the numerical dissipation and dispersion associated with large gradients. The results utilizing this shock-fitting algorithm are substantially superior to those computed by either a first-order or a second-order scheme. The results for this problem, which will be discussed shortly, illustrate three points: 1) computational difficulties and computational time can be reduced with shock-fitting; 2) for some problems shock-fitting is essential if physically meaningful results are to be obtained; 3) local analytical solutions may be required to achieve reliable results with reasonable computing times.

Consider a shock wave reflecting from a sound speed gradient as sketched in figure 8. This phenomenon, after an appropriate scaling (reference 12) is governed by

$$(y + \phi_x)_{xx} - \phi_{yy} = 0,$$

where ϕ may be thought of as a (perturbed) velocity potential, with boundary data prescribed in accordance with the nonlinear generalization on the properly posed problem for

$$y\phi_{xx} - \phi_{yy} = 0.$$

Numerical boundary data are supplied from the solution to the linear equation for an incoming signal of the form

$$-\phi_x \sim \begin{cases} y^{-1/4} [H(x + 2\sqrt{y^3}/3) - H(x + 2\sqrt{y^3}/3 + \delta)], & y + \phi_x > 0, \\ 0, & y + \phi_x < 0, \end{cases}$$

where H is the Heaviside unit function. Solutions to the linear problem are given by complicated combinations of hypergeometric functions; through care in choosing the expansion used to represent these functions the linear solution may be computed with any precision required (reference 12).

A first-order numerical solution to this nonlinear equation was first obtained by Seebass, Murman and Krupp (reference 13) using an implicit, backward difference approximation for x derivatives in the hyperbolic region. This scheme is unconditionally stable and the numerical calculations converge. However, the "solution" does not give a satisfactory representation of the discontinuities, nor can it determine the maximum value of the amplification of a sonic boom at a caustic for any realistic grid spacing. A second-order scheme that solves this equation has been developed, and while the discontinuities are still smeared out, they are considerably thinner than those obtained with a first-order scheme. The truncation errors, however, are dispersive, causing an unpleasant "wobble" on the downstream side of the compressions. These second-order results are used to provide the initial conditions for a second-order "shock-fitting" scheme that treats the discontinuities as such in order to satisfy the jump conditions to second order. The numerical scheme that we used is outlined in reference 14.

The computational region considered is indicated in figure 8, which also depicts a typical grid spacing. To understand the procedure, assume that the computation procedure has reached station "i", i.e., $x = x_1$. The upstream conditions are then all known, and the properties of the downstream shock point can be calculated by using the characteristic relations and the shock jump condition. At the point where the shock intersects vertical grid line $x = x_1$, the value of ϕ is calculated by direct integration of $d\phi$. Difference approximations to the x and y derivatives are then constructed by using the shock points instead of the regular grid points (see reference 14). Again, an implicit scheme is used when the equation is hyperbolic and a central-difference scheme when it is elliptic. During the computation the position of the shock is determined and the quantity $y + \phi_x$ is computed at each grid point so that the proper difference equations can be selected.

As the incident discontinuity approaches the line where $y + \phi_x = 0$ it grows in strength until the flow behind the incident wave becomes sonic. At that point we have assumed that a reflected wave is formed. The initial strength of the reflected wave is obtained by using backward differences to approximate properties behind the shock. The strength of the discontinuity increases rapidly and approaches its final value within 5 to 10 iterations. The reflected discontinuity is weak, but this is probably due to the procedure we invoked at the triple point.

Figures 9 and 10 show the results for typical second-order and shock-fitting calculations. They depict the variation of ϕ_x with x for various values of y . Note the marked difference between the results obtained with shock-fitting and those obtained by more standard procedures.

Our calculations show that the results are sensitive to the model picked for the behavior near the triple point. It is clear to us that the sensitivity of the results to this behavior is, indeed, critical. Various attempts to model the triple point numerically have been unsuccessful, and refining the grid in its neighborhood also leads to difficulties. Until we have an

analytical description of the local behavior at the triple point, it will probably be impossible to call our calculations a solution, although many computational fluid mechanicians would believe that it was one.

Both the first-order and the second-order schemes have approximately the same rate of convergence; the initial guess was the linear solution for both calculations. We could not use the linear solution as initial data with shock fitting, as it is too poor an initial guess. Our shock-fitting computation used the final results from the second-order scheme as initial data. It took only twenty computations to reduce the maximum "error" to one percent, a result that could not be achieved with any number of additional computations with the other two schemes. This fast rate of convergence with shock fitting derives from the accuracy of the second-order "solution" away from the discontinuities and the treatment of discontinuities as such.

The numerical scheme outlined here offers a reliable method of computing solutions to mixed nonlinear equations with discontinuities. Comparison of the graphical results from different schemes shows that the shock-fitting procedure provides quantitatively superior results for an equal investment in computational time, albeit at the expense of additional bookkeeping and more complicated programming. Typical computation times are about twenty minutes on an IBM 360/65. The results indicate the clear need to model one grid of the computation analytically.

Recent progress on the analytical solution for an entering-steepening simple wave indicates that we may soon have an analytical description of a simple transonic flow problem with an embedded discontinuity (K.Y. Fung, unpublished research). If we are successful in this pursuit, the results can be used to test the efficacy of various computational procedures. The problem posed by an entering-steepening wave removes the difficulty of having to treat the triple point analytically within the numerical calculations. However, it also seems desirable to obtain an analytical solution for an entering discontinuous signal so that this, too, can be used as a canonical test problem for transonic flow computations.

REFERENCES

1. Hayes, W.D.: Sonic Boom. Annual Review of Fluid Mechanics, Vol. 3, 1971, pp. 269-290.
2. Carlson, H.W. and Maglieri, D.J.: Review of Sonic-Boom Generation Theory and Prediction Methods. J. Acoust. Soc. Amer., Vol. 51, 1972, pp.675-685.
3. Seebass, A.R. and George, A.R.: Design and Operation of Aircraft to Minimize their Sonic Boom. J. Aircraft, Vol. 11, No. 9, 1974, pp. 509-517.
4. Lung, J.L.: A Computer Program for Sonic Boom Minimization. M.S. Thesis, Cornell University, January 1975.

5. Darden, C.M.: Comparison of Sonic Boom Minimization Results in Real and Isothermal Atmospheres. J. Aircraft (to be published).
6. Tiegerman, B.: Sonic Booms of Drag-Dominated Hypersonic Vehicles. Ph.D. Thesis, Cornell University, Sept. 1975.
7. Plooster, M.N.: Shock Waves from Line Sources. NCAR TN-37, Nov. 1968.
8. Okhotsimskii, D.Y. and Vlasova, Z.P.: The Behavior of a Shock Wave at Long Distances from the Point of Explosion". Zh. Vych. Mat. & Mat. Fiz., Vol. 2, 1962, pp. 107-124.
9. Pan, Y.S. and Sotomayer, W.A.: Sonic Boom of Hypersonic Vehicles. AIAA J., Vol. 10, No. 4, April 1972, pp. 550-551. See also Pan, Y.S. and Sotomayer, W.A.: Sonic Boom of Hypersonic Vehicles, AIAA J., Vol. 12, No. 3, 1974, p. 416.
10. Hilton, D.A., McKinney, R.L., and Henderson, H.R.: Sonic Boom Ground-Pressure Measurements from Apollo 15. NASA TN D-6950, 1972.
11. Holloway, P.F., et al.: Shuttle Sonic Boom-Technology and Predictions. AIAA Paper 73-1034, 1973.
12. Gill, P.M. and Seebass, A.R.: Nonlinear Acoustic Behavior at a Caustic: An Approximate Analytical Solution. Aeroacoustics: Turbo-machinery Noise; Sonic Boom; Fan Noise; Acoustic Instrumentation. H.T. Nagamatsu, ed., MIT Press, 1975, pp. 353-386.
13. Seebass, R., Murman, E., and Krupp, J.A.: Finite Difference Calculations of a Discontinuous Signal Near a Caustic. NASA SP-255, 1971, pp. 361-372.
14. Yu, N.J. and Seebass, R.: Computational Procedures for Mixed Equations with Shock Waves. Proceedings, International Conference On Computational Method in Nonlinear Mechanics, Austin, Texas, 1974, pp. 499-508.

TABLE 1. INPUT AND OUTPUT FOR SONIC BOOM MINIMIZATION PROGRAM

INPUT

M	MACH NUMBER
WT	WEIGHT OF AIRCRAFT IN LBS OR KGS
L	LENGTH OF AIRCRAFT IN FT OR M
H	ALTITUDE OF FLIGHT IN FT OR M
HS	ATMOSPHERIC SCALE HEIGHT IN FT OR M
T	RISE TIME IN SECS
R	RATIO OF REAR-TO-FRONT SHOCK STRENGTH
V	VOLUME OF AIRCRAFT IN FT ³ OR M ³
XCP	CENTER OF PRESSURE OF AIRCRAFT IN FT OR M
KR	GROUND REFLECTION FACTOR

OUTPUT

F(T)	WHITHAM F-FUNCTION (NORMALIZED)
A(X)	AREA DEVELOPMENT (NORMALIZED)
PSO	MINIMUM FRONT SHOCK OVERPRESSURE
PRO	MINIMUM REAR SHOCK OVERPRESSURE
ISO	IMPULSE CORRESPONDING TO MINIMUM OVERPRESSURE
PS	MINIMUM FRONT SHOCK PRESSURE RISE
IS	IMPULSE CORRESPONDING TO MINIMUM SHOCK PRESSURE RISE
PR	MINIMUM REAR SHOCK PRESSURE RISE
PMAX	MAXIMUM PRESSURE IN SIGNATURE
PMIN	MINIMUM PRESSURE IN SIGNATURE
PJF	FRONT SHOCK PRESSURE RISE FOR MINIMUM IMPULSE
IJ	MINIMUM IMPULSE
PJR	REAR SHOCK PRESSURE RISE FOR MINIMUM IMPULSE

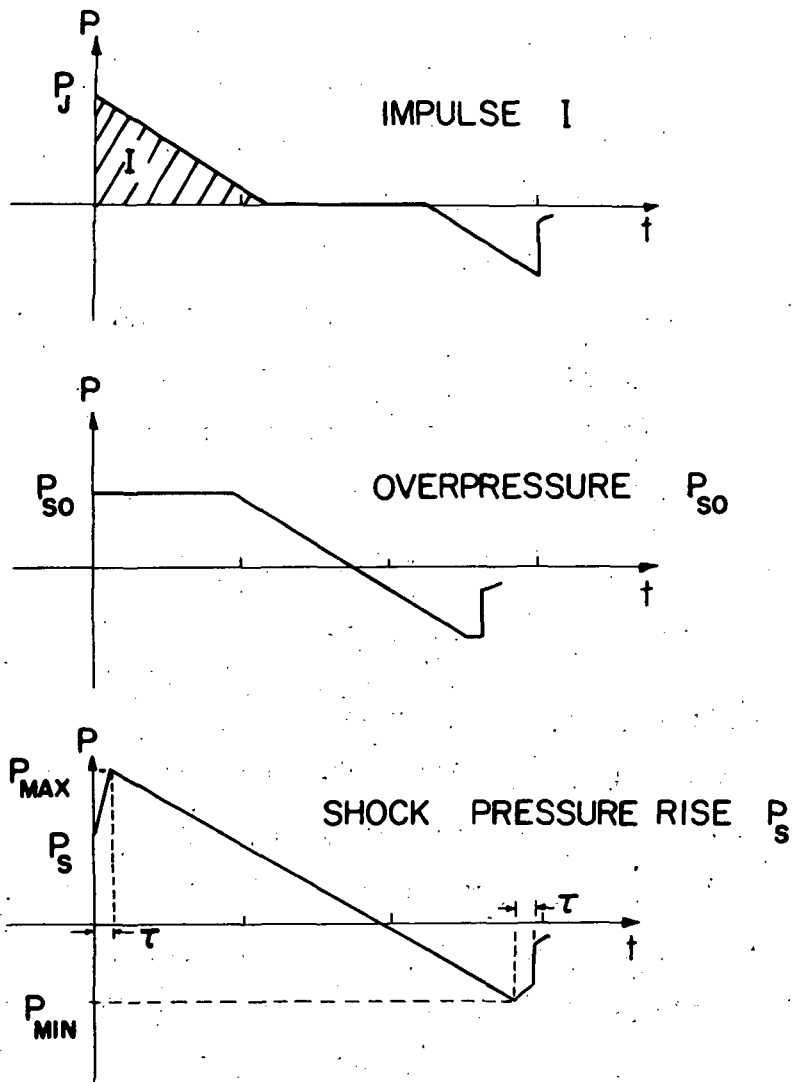


Figure 1.- Overpressure signatures considered. In the second and third, the rear shock strength is a specified fraction of the front shock strength.

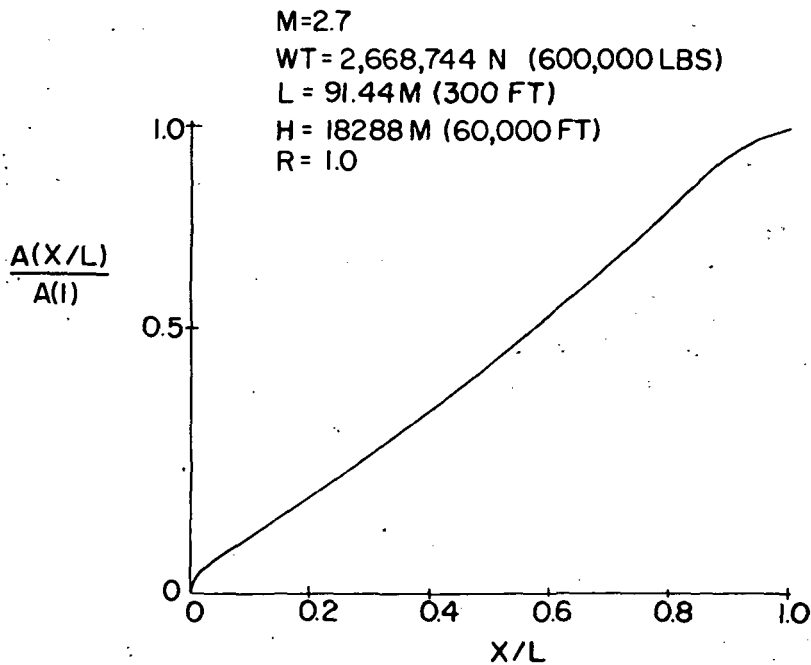


Figure 2.- Normalized area development required to minimize the shock pressure rise for typical SST flight conditions.

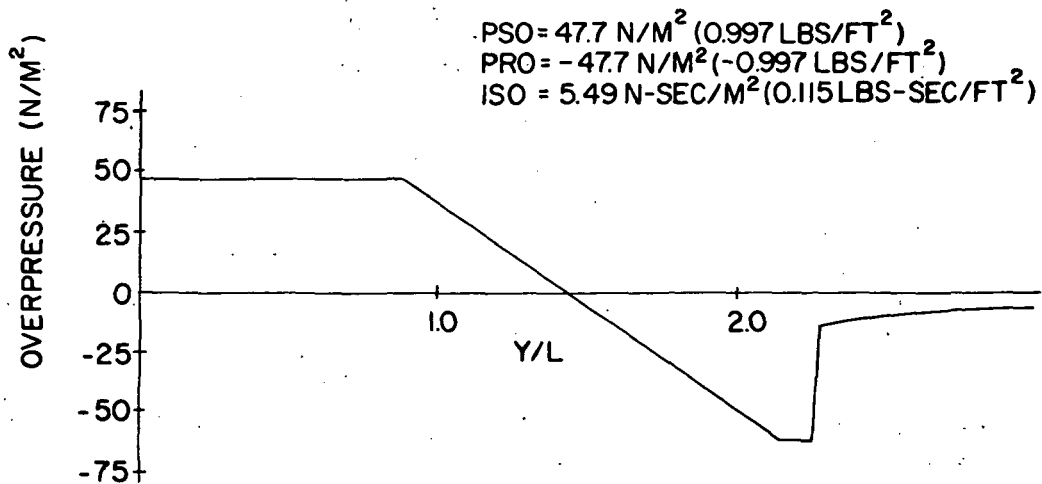


Figure 3.- Overpressure signature.

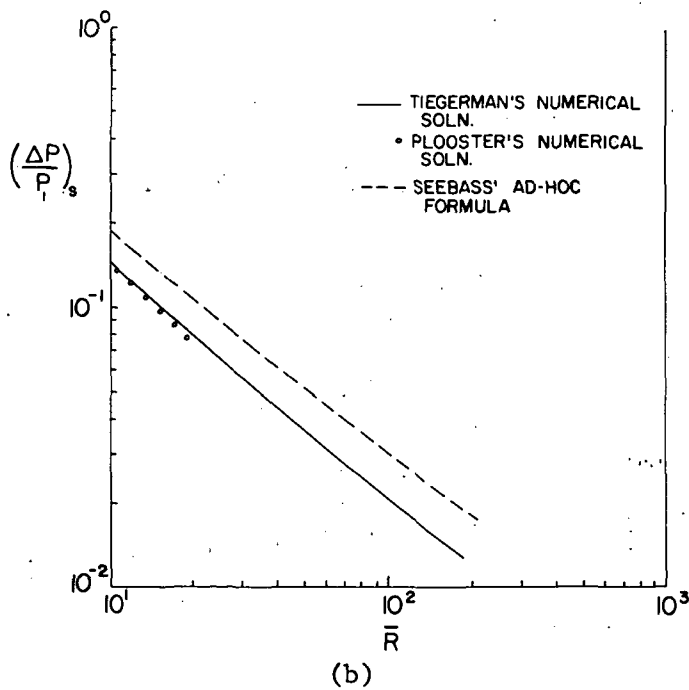
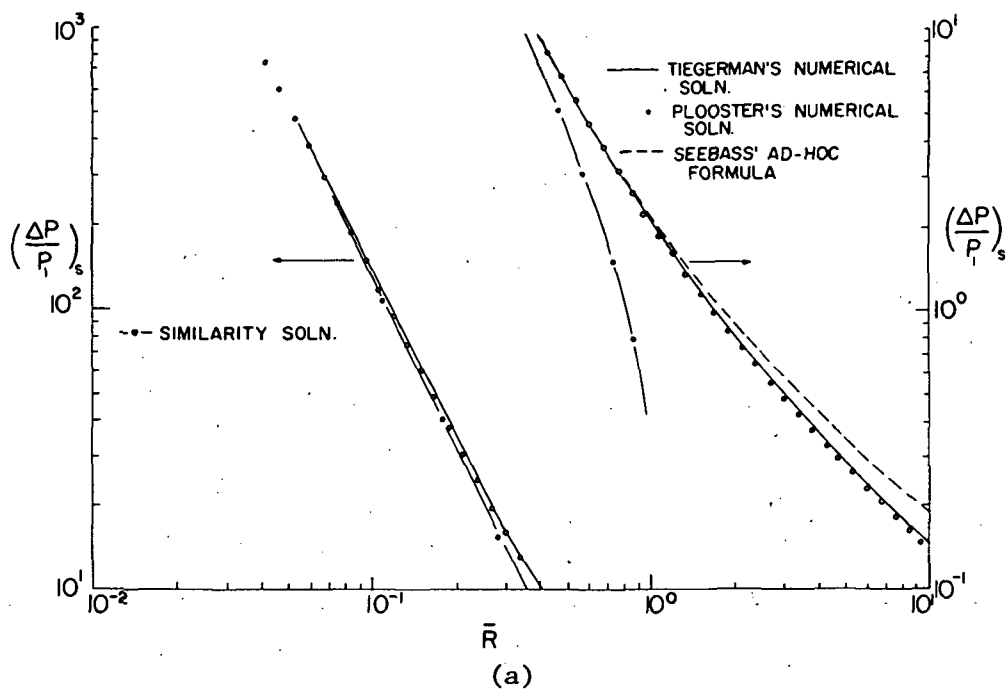


Figure 4.- Overpressure for a cylindrical blast wave as a function of \bar{R} .

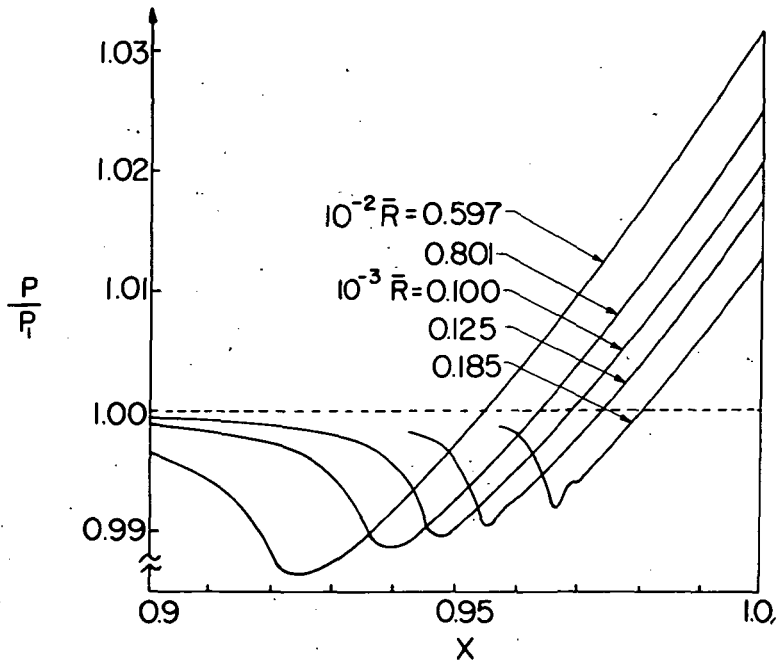


Figure 5.- Pressure signatures for various \bar{R} .

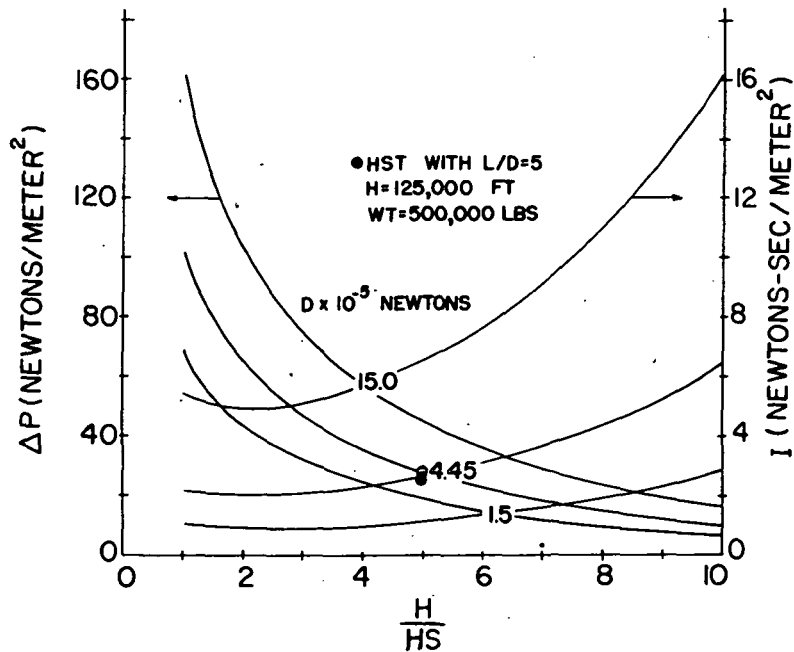


Figure 6.- Overpressure and impulse as a function of altitude, H , for hypersonic vehicles of given drag, D . Here L is the vehicle's lift and HS is the atmospheric scale height.

MISSION	SHIP	$(\Delta p)_{FSW}$ NEWTONS METER ²			Δt SEC			I_+ NEWTONS-SEC METER ²		
		MEAS.	CALC.	% ERROR	MEAS.	CALC.	% ERROR	MEAS.	CALC.	% ERROR
APOLLO 15	U.S.S. GENESEE	10.677	12.975	21.5	0.315	0.255	19.1		1.676	
APOLLO 15	U.S.S. KAWISHIWI	20.014	20.588	2.85	0.170	0.093	45.2		0.958	
APOLLO 16	U.S.S. PONCHA-TOULA	17.428	17.476	0.36	0.204	0.181	11.4	1.355	1.580	16.6

Figure 7.- Comparison of theoretical and measured overpressure and impulses for Apollo 15 and 16 re-entries.

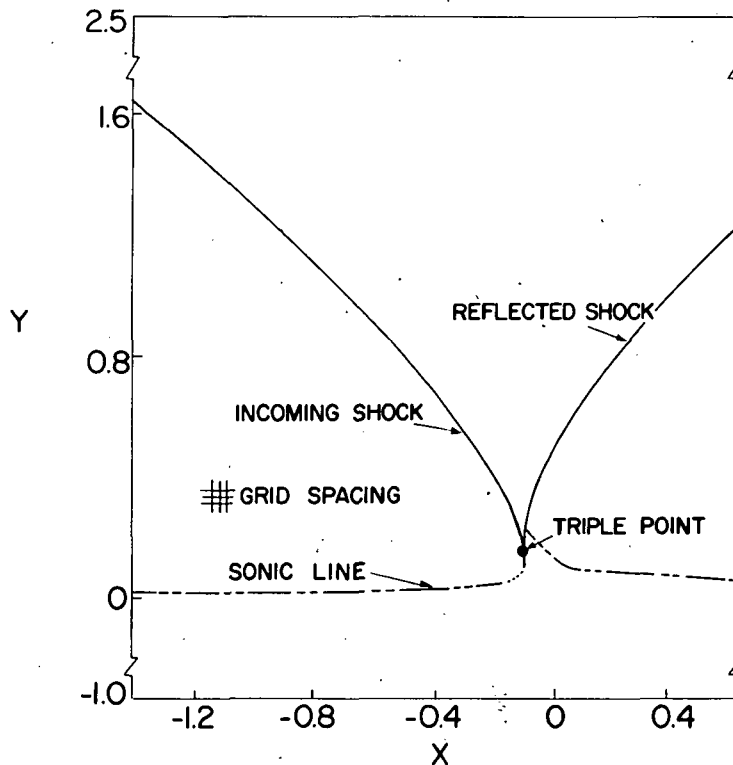


Figure 8.- Computational region, shock waves, and sonic line depicting the behavior at a caustic.

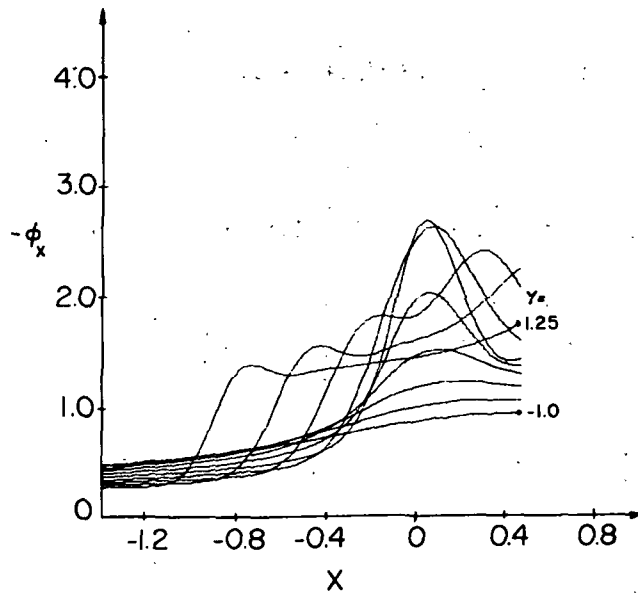


Figure 9.- Variation of ϕ_x with x at fixed y for a second-order calculation.

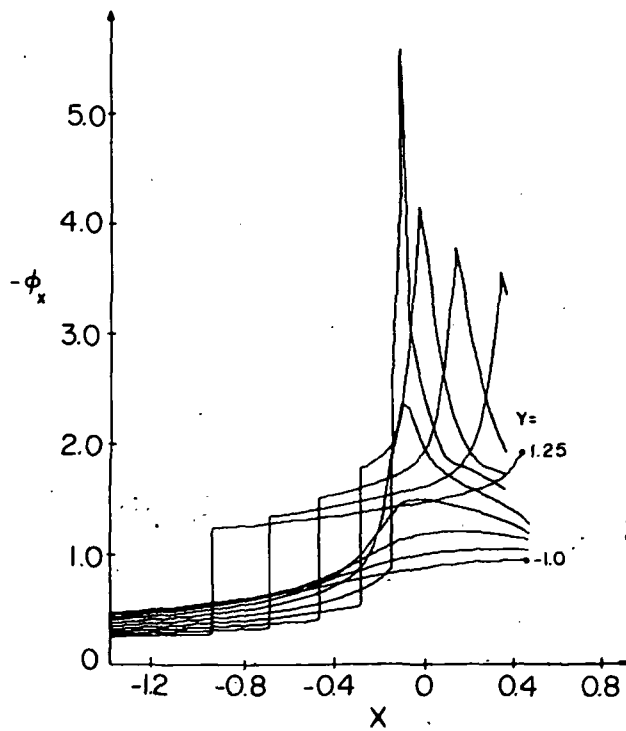


Figure 10.- Variation of ϕ_x with x at fixed y for a shock-fitting calculation.

Page intentionally left blank

AN INTEGRATED SYSTEM FOR THE AERODYNAMIC DESIGN AND ANALYSIS OF SUPERSONIC AIRCRAFT

By David S. Miller
NASA Langley Research Center

and

Wilbur D. Middleton
The Boeing Company

SUMMARY

An integrated system of computer programs for the aerodynamic design and analysis of complete supersonic aircraft has been developed as a result of research efforts conducted over a period of years at Langley Research Center and a recent Langley contract with the Boeing Company. The goals of the system have been to develop an easily used supersonic design and analysis capability with recognition of the need for constraints on linear theory to provide physical realism and with inclusion of interactive graphics capability for increased control over the design and analysis iteration cycles.

INTRODUCTION

An integrated system of computer programs for the aerodynamic design and analysis of complete supersonic configurations has been developed as a result of research efforts at Langley Research Center over a period of years and a recent Langley contract with the Boeing Company. The foundation for the integrated system consists of a series of individual computerized methods developed at Langley Research Center and at the Boeing Company for the design and analysis of supersonic aircraft. These individual computer programs are characterized by their reliability, as established in various configuration development and evaluation studies, and their input simplicity. The applicability and procedure for utilizing the individual programs have been thoroughly demonstrated and reported at various stages of their evolution. (See refs. 1 to 3.) The organization and assemblage of these individual computerized methods into an integrated system required considerable modification to some of the existing methods, development of several new methods, and creation of all necessary interface and interactive graphics routines. These requirements were accomplished under contract with the Boeing Company.

The goals of the integrated system have been to develop an easily used supersonic design and analysis capability with recognition of the need for modifications to linear theory methods to provide physical realism. The system operates from a single geometric configuration description and includes interactive graphics capability for increased control over the design and analysis iteration cycles.

In this paper a discussion is presented of the overall integrated system with emphasis on and detailed description of only the specific methods which offer new or improved design and analysis capability.

SYMBOLS

A_E	area of equivalent body
b	wing span
C_D	drag coefficient
ΔC_D	incremental drag coefficient due to lift
C_D/C_L^2	drag-due-to-lift factor
$C_{D,f}$	friction drag coefficient
C_L	lift coefficient
C_m	pitching-moment coefficient
$C_{m,o}$	pitching-moment coefficient at zero lift
C_p	pressure coefficient
ΔC_p	incremental pressure coefficient
M	Mach number
R	Reynolds number
X, Y, Z	Cartesian coordinates
α	angle of attack

DISCUSSION

Overall Integrated System

The integrated system is a single overlaid complex of computer programs consisting of nine basic program modules. A schematic diagram of the complete system along with sketches to illustrate some of the important features of each individual program module is shown in figure 1. The system has evolved from a complex of individual programs developed at Langley Research Center and at the Boeing Company over the past decade. Those program modules with the dotted pattern were incorporated into the system as originally formulated, those with hatching were modified considerably, and the remaining four modules were developed specifically for use as part of the system. As indicated in the figure, the system programs operate sequentially from a common geometric description of the configuration. The system is also integrated to allow for the necessary exchanges of information between programs and to operate with or without interactive graphics. The modular construction of the system permits the addition or replacement of program modules with a limited amount of effort.

Executive

The operational sequencing of the system is controlled by the executive program using special input "executive control" cards. Upon encountering one of these cards, the executive program relates the information to the geometry program which sets up the appropriate geometric description and then activates the computational module designated by the special input cards.

Geometry

The function of the geometry module is to read system geometry input, update it when called for, and arrange it in the required form for input to the other individual program modules of the system. The format of the system geometry is the same as that of the Langley Research Center plot program. (See ref. 4.)

The geometry module also serves as an intermediate step in the execution of any of the other basic modules. Acting in this capacity, the geometry program assembles both geometric information (stored in the geometry module) and nongeometric information (read into system following an executive control card) onto a single input file. The ability to use a common and easily generated geometric description in which the system performs any required manipulations internally is considered a major asset of the total integrated system.

Far-Field Wave Drag

The far-field wave drag program employs the supersonic area rule and slender body theory to calculate the zero-lift wave drag of complex configurations which may include fuselage, wing, nacelles, canards, and horizontal or vertical tails. The procedure employed and the assumptions, limitations, and accuracy involved are documented in reference 5. As indicated in the sketch of figure 1, the far-field wave drag program includes an optimization process. When given a set of constraint points on a cross-sectional area distribution, the program can generate an optimum area distribution which can be used to redesign the fuselage. Results obtained by using the optimization procedure (for examples, see ref. 2) may be used to update the fuselage definition in the geometry module. The ability to handle extremely complex configurations in a rather simple calculation procedure and the optimization capability make the far-field wave drag program module an indispensable part of the total system.

Near-Field Wave Drag

As shown in figure 1, the near-field wave drag program is a new addition to the system and computes the zero-lift wave drag by integrating surface pressure distributions over each of the configuration component surfaces. Not only does the near-field wave drag calculation complement that of the far-field method, but also the near-field method provides additional information pertaining to thickness surface pressure distributions.

For discussion purposes, the main features are presented in figure 2. Presently, the configuration components to be analyzed are limited to a fuselage that is nearly circular in cross section, a wing of arbitrary planform and thickness distribution, and up to three pairs of circular nacelles which can be located above or below the wing. Three basic calculations are performed to obtain the required pressure fields. The isolated wing surface pressures due to thickness are computed by use of a source lattice representation of the flow over a wing (ref. 6) and the isolated fuselage and nacelle surface pressures are obtained by application of Lighthill's slender body theory. (See ref. 7.) The pressure fields of the fuselage and nacelles are computed by using the Whitham theory (ref. 8) which is essentially a correction to the linear theory to allow for the non-linear propagation of pressure disturbances and provides for the possible formation of shocks.

The wave drag is obtained in the near field by superposition principles; that is, the wave drag of a particular component is due to its isolated drag plus interference drag contributions resulting from the pressure fields of all other components. For interference purposes the wing pressure field is calculated by zeroing the wing surface slopes in the region of the fuselage and the computed wing pressures are transferred from the wing

surface to the fuselage or nacelles along Mach lines. By summing the isolated and interference drags for each component, one can generate a wave drag build up component by component, as illustrated in figure 2, for first a wing, then a wing-body, and finally a wing-body-nacelle configuration. The near-field wave drag program also provides wing surface pressures due to thickness as data for use in other program modules where thickness and lifting pressures are combined into total pressure.

A typical example of an interference calculation is that of nacelle-on wing interference. As illustrated in figure 3, this example is particularly interesting because the application of superposition principles in this situation is not straightforward and the user has the option of selecting one of the two methods shown. In the first method a nacelle pressure field is assumed to propagate around the other nacelles unattenuated. The second method assumes that a pressure field will reflect from other nacelles in such a way that the reflected field will have no further influence on the wing surface and is thus terminated. Pressure fields for two pairs of nacelles have been computed using both methods and are presented in the figure at three wing span stations along with some experimental data for $M = 1.1$. The results indicate substantial differences between the two theoretical methods; however, the experimental data are too sparse to indicate clearly which method best represents the physical situation. It should be noted that the first nacelle-on wing interference option appears to have the same degree of transparency as employed in the far-field procedure.

If a nacelle is located next to the wing, the nacelle pressure field may reflect from the wing back onto itself or the other nacelles. This type of interference due to reflected pressure fields can become significant at the lower Mach numbers and is calculated directly in the near-field wave drag program. The far-field method does not account for any reflected pressure fields.

As previously stated, theoretical wave drag results may be obtained from either the near- or far-field wave drag programs. A comparison of results obtained by each of these methods can be made from the wave drag component build up presented in figure 4. For the near-field results, the first option for nacelle-on wing interference was used and interference contributions due to reflection were not included. At Mach numbers of 1.1 and 2.7, the wave drag was computed for an isolated wing, a wing-body, and a wing-body-nacelle configuration shown in the figure. In all cases but one, the near-field drag results were slightly higher than those of the far field. At most, the results differ by less than 10 percent and establish confidence in the near-field method of computing wave drag.

Drag-Due-to-Lift Analysis

The drag-due-to-lift analysis program module computes all the pressures and forces associated with the generation of lift. As indicated in figure 1, this program is based on previous Langley methods but has been modified considerably. The initial lift analysis method (ref. 9) was applicable to isolated cambered wings of arbitrary planform and was later adapted to include canards or horizontal tails (ref. 10).

Refinements and improvements which recently have been made to the basic calculation procedure are presented in reference 11. In these methods the effects of a fuselage could be included only by representing the fuselage as a planar extension of the wing, and the wing loading due to wing-nacelle interference was the result of a separate computation. (See ref. 12.) The details of the drag-due-to-lift analysis module, as modified for use in the integrated system, are presented in figure 5 along with a list of aircraft components amenable to analysis. The lifting pressure solution of a complete configuration may involve up to six principal calculation tasks as illustrated in figure 5. The fuselage is no longer represented as a planar extension of the wing, but it is represented as a circular cambered body of revolution. The isolated body upwash field is obtained in the wing, canard, and horizontal-tail regions by using a slender-body line source and doublet representation of the fuselage. For wing-body combinations in which the fuselage volume is not symmetrically distributed above and below the wing plane (that is, not a midwing arrangement), the asymmetric loading is calculated by the following approximate procedure. The fuselage volume is divided into above- and below-wing portions as determined by the wing-body intersection. The above-wing and below-wing volume contributions are combined with the actual fuselage forebody volume distribution to create effective above-wing and below-wing equivalent body representations. Whitham theory is then employed to calculate above- and below-wing pressures which are differenced to obtain the asymmetric wing loading. The wing loading due to the nacelle pressure field impinging on and reflecting from the wing camber surface is calculated by using the same application of Whitham theory as used for nacelle-on wing interference described in the near-field wave drag section of the paper. The wing and canard loadings are calculated in the presence of the body upwash by using a vortex lattice representation of the lifting surfaces (ref. 9) and the body loading is calculated by using slender-body theory in the presence of the wing and canard downwash fields. The horizontal-tail loading is calculated last for various specified angles of attack in the presence of the body, wing, and canard induced flow fields.

As illustrated in figure 5, basic solution results are applied to generate aerodynamic forces due to lift and to provide configuration-dependent wing loading definitions for the wing design and optimization program. The generation of lift, drag, and moment as a function of angle of attack is accomplished by superimposing two sets of basic solu-

tion results; one set is calculated for the configuration at input incidence and the other set gives the variation with angle of attack. The configuration-dependent wing loadings due to body upwash, asymmetric body volume distribution, and nacelles can be calculated for an uncambered wing at zero angle of attack and saved for future use in the wing design program.

Linear theory imposes no restrictions on the allowable wing pressure coefficients; consequently, it is possible to calculate pressure coefficients which are physically unattainable (less than vacuum). In order to restrict the linear theory to realistic solutions, a pressure-limiting option has been incorporated into the analysis program. This feature limits the wing surface pressure coefficients (thickness and lifting contributions) to a prescribed percent of vacuum. The procedure employed is an integral part of the pressure calculation method and the constraints are satisfied continuously rather than being imposed after the solution is completed. Calculated results obtained with and without pressure limiting for a cambered arrow wing at a Mach number of 2.05 are presented in figure 6 along with experimental force and pressure data from reference 13.

The dashed and solid lines represent calculated results obtained for surface pressures limited to 0.7 vacuum C_p and unlimited linear theory pressures, respectively. The force coefficient results indicate that pressure limiting provides considerably improved agreement between theory and experiment at angles of attack greater than 2° . Detailed chordwise lifting pressure distributions are also presented for angles of attack of 2° and 6° at extreme inboard and outboard span stations. As shown in figure 6 the pressure-limiting feature offers considerable improvements in detailed pressure distribution at large angles of attack for the outboard portion of the wing where the unlimited linear theory results are completely unrealistic.

Wing Design and Optimization

The wing design and optimization program solves the more direct problem of computing the wing camber surface which will support a given loading distribution as illustrated in figure 1. Moreover, it also includes an optimization procedure for determining the appropriate combination of linearly independent loading distributions which yield minimum zero suction drag due to lift subject to constraints on lift, pitching moment, and minimum wing upper surface pressure coefficient. Based on the ideas set forth by Grant (ref. 14), the initial wing design program (ref. 15) was developed to determine the optimum combination of three independent loading distributions and corresponding camber surface of an isolated wing of arbitrary planform at a specified lift coefficient. Subsequent modifications were made to the original version (ref. 16) to include a constraint on pitching moment and, consequently, the number of available independent loading distributions was increased to seven.

Considerable modifications and improvements have recently been made to the wing design procedure used in the integrated system. The more important solution features are listed in figure 7. Fourteen independent camber-induced loadings are available for optimization. Eleven of these loadings are analytic functions of planform position such as a constant loading, linearly varying chordwise and spanwise loadings, and so forth. The remaining three camber-induced loadings are directly proportional to the three configuration-dependent loadings.

In order to include the effects of fuselage and nacelles into the wing design procedure, three configuration-dependent loading distributions can be employed. These loadings are due to fuselage upwash, asymmetrical fuselage volume, and nacelle pressure field. The configuration-dependent loadings are generated in either the near-field wave drag or the drag-due-to-lift analysis programs and the loading distributions are made available to the wing design program. The design constraints include lift, pitching moment, and allowable upper surface pressure coefficient. Theoretical values of drag-due-to-lift factor (C_D/C_L^2) and corresponding values of $C_{m,o}$ are presented graphically in figure 7 for a supersonic cruise type configuration composed of a wing, body, and two pairs of nacelles. Solutions for a flat wing, uniformly loaded wing, and optimum 3 loading wing are shown to provide a comparison with the 17 loading solution. The solid line representing the 17 loading solution with no pressure limiting has a minimum value of C_D/C_L^2 at a value of $C_{m,o}$ of 0.014. The diamond symbols correspond to 17 loading solutions with the upper surface pressure C_p limited to values greater than 70 percent of vacuum C_p . The effect of pressure limiting is most pronounced at the large values of $C_{m,o}$ where the values of C_D/C_L^2 sharply break away from the unlimited solution curve.

The 17 loading solution, with or without pressure limiting, produces a considerable (25-percent) reduction in the theoretical drag-due-to-lift factor over the 3 loading solution, but these substantial gains must be viewed with caution. The 17 loading solution includes drag benefits from the fuselage upwash and nacelle pressure fields which are not recognized in the 3 loading solution. In addition, the 3 loading solution requires pressure distributions which have mild gradients, whereas the 17 loading solution requires a pressure distribution with gradients which are possibly prohibitive. It is anticipated that imposing pressure gradient constraints on the 17 loading solution, as is currently planned, will offer improvements over the 3 loading solution which will be significant but not as dramatic as those indicated in the figure.

Skin Friction and Plot Program

As indicated in figure 1 the skin friction and plot program were incorporated into the integrated system as originally formulated. The friction drag of a complete configuration is computed by strip integrating the various configuration components as illus-

trated in figure 1. The method assumes that smooth flat-plate, adiabatic-wall, and fully turbulent boundary-layer conditions exist on all components. The Karman-Schoenherr incompressible relationship between skin-friction coefficient and Reynolds number is employed and corrections for compressibility result from application of the Sommer and Short T-prime method (ref. 17). The total configuration friction drag is found by summing contributions of the individual components.

The plot program generates the necessary instructions for making drawings of the configuration description stored in the geometry program. Various view options are available and can be requested by program input cards. This program is most useful in checking and modifying configuration geometry. Documentation of the program is presented in reference 4.

Interactive Graphics

The system can be operated with or without the use of interactive graphics; however, this capability provides a considerable amount of on-line control of the system which has been found useful during design and analysis iteration cycles. Basically, the interactive capability consists of displaying and editing configuration geometry and some of the basic program calculation.

Figure 8 demonstrates how interactive graphics might be used during one design and analysis cycle. The user first views and, if necessary, corrects any errors in the input geometry. The far-field wave drag program is then executed and both the original and optimized area distributions may be displayed. If desired, the original fuselage description may be replaced by the optimized one in the basic geometry and modified. In order to prepare inputs for the wing design and optimization program, the near-field wave drag and the drag-due-to-lift analysis programs are executed next to generate wing-thickness pressures and configuration-dependent loadings, respectively. Only final results are presently displayed by the near-field wave drag program, but fuselage upwash and wing loadings due to the fuselage upwash can be displayed from the analysis program. When the necessary inputs have been set up, the wing design program is executed with the desired constraints. The results for a given wing design are then displayed in a plot of drag-due-to-lift factor as a function of $C_{m,0}$ as was shown in figure 7. The user has the option of saving a particular wing design or rejecting it and selecting another set of design constraints. Once a design has been selected, the wing geometry is updated. At this point the user can display and alter the new wing camber. As an example, shown in figure 8 is a display of the optimized wing trailing edge which may be edited to remove any unacceptable irregularities and then the camber line can be twisted to match the edited values. Satisfied with the modifications, one would proceed to analyze the new configuration. Shown are tabulated lift-drag polar results (C_L ,

C_D , and C_m) generated by the analysis program. To complete the analysis, wave drag and skin-friction drag results (not shown in fig. 8) would also be obtained.

To accomplish all these tasks on the CDC 6600 requires the user to spend approximately $1\frac{1}{2}$ hours at the scope and the total of 1100 seconds of CPU time. A breakdown of the approximate times required by each program module in a typical design and analysis project is given in the following table:

Program module	CPU time, sec
Geometry	14
Plot	7
Wing design	150
Drag-due-to-lift analysis (two executions)	250
Far-field wave drag	484
Near-field wave drag (two executions)	193
Skin friction	2
Total	1100

CONCLUDING REMARKS

An integrated system of computer programs with interactive graphics capability has been developed for the design and analysis of supersonic aircraft. The individual computer programs operate independently from a common geometry description and the operational sequencing is controlled by an executive program. Because of the modular and overlaid construction, additional computer programs can be interfaced with a limited amount of effort.

REFERENCES

1. Robins, A. Warner; Morris, Odell A.; and Harris, Roy V., Jr.: Recent Research Results in the Aerodynamics of Supersonic Vehicles. *J. Aircraft*, vol. 3, no. 6, Nov.-Dec. 1966, pp. 573-577.
2. Baals, Donald D.; Robins, A. Warner; and Harris, Roy V., Jr.: Aerodynamic Design Integration of Supersonic Aircraft. *J. Aircraft*, vol. 7, no. 5, Sept.-Oct. 1970, pp. 385-394.
3. Carlson, Harry W.; and Harris, Roy V., Jr.: A Unified System of Supersonic Aerodynamic Analysis. *Analytic Methods in Aircraft Aerodynamics*, NASA SP-228, 1970, pp. 639-658.
4. Craidon, Charlotte B.: Description of a Digital Computer Program for Airplane Configuration Plots. NASA TM X-2074, 1970.
5. Harris, Roy V., Jr.: An Analysis and Correlation of Aircraft Wave Drag. NASA TM X-947, 1964.
6. Ashley, Holt; and Landahl, Marten: *Aerodynamics of Wings and Bodies*. Addison-Wesley Publ. Co., Inc., c.1965.
7. Lighthill, M. J.: Supersonic Flow Past Slender Bodies of Revolution, the Slope of Whose Meridian Section Is Discontinuous. *Quarterly Jour. Mech. and Appl. Math.*, vol. I, pt. 1, Mar. 1948, pp. 90-102.
8. Whitham, G. B.: The Flow Pattern of a Supersonic Projectile. *Commun. Pure & Appl. Math.*, vol. V, no. 3, Aug. 1952, pp. 301-348.
9. Middleton, Wilbur D.; and Carlson, Harry W.: A Numerical Method for Calculating the Flat-Plate Pressure Distributions on Supersonic Wings of Arbitrary Planform. NASA TN D-2570, 1965.
10. Shrout, Barrett L.: Extension of a Numerical Solution for the Aerodynamic Characteristics of a Wing To Include a Canard or Horizontal Tail. Paper presented at AGARD Specialists Meeting on Aerodynamic Interference (Silver Spring, Md.), Sept. 1970.
11. Carlson, Harry W.; and Miller, David S.: Numerical Methods for the Design and Analysis of Wings at Supersonic Speeds. NASA TN D-7713, 1974.
12. Mack, Robert J.: A Numerical Method for Evaluation and Utilization of Supersonic Nacelle-Wing Interference. NASA TN D-5057, 1969.
13. Carlson, Harry W.: Aerodynamic Characteristics at Mach Number 2.05 of a Series of Highly Swept Arrow Wings Employing Various Degrees of Twist and Camber. NASA TM X-322, 1960.

14. Grant, Frederick C.: The Proper Combination of Lift Loadings for Least Drag on a Supersonic Wing. NACA Rep. 1275, 1956. (Supersedes NACA TN 3533.)
15. Carlson, Harry W.; and Middleton, Wilbur D.: A Numerical Method for the Design of Camber Surfaces of Supersonic Wings With Arbitrary Planforms. NASA TN D-2341, 1964.
16. Sorrells, Russell B.; and Miller, David S.: Numerical Method for Design of Minimum-Drag Supersonic Wing Camber With Constraints on Pitching Moment and Surface Deformation. NASA TN D-7097, 1972.
17. Sommer, Simon C.; and Short, Barbara J.: Free-Flight Measurements of Turbulent-Boundary-Layer Skin Friction in the Presence of Severe Aerodynamic Heating at Mach Numbers From 2.8 to 7.0. NACA TN 3391, 1955.

SUPERSONIC AERODYNAMIC DESIGN AND ANALYSIS SYSTEM

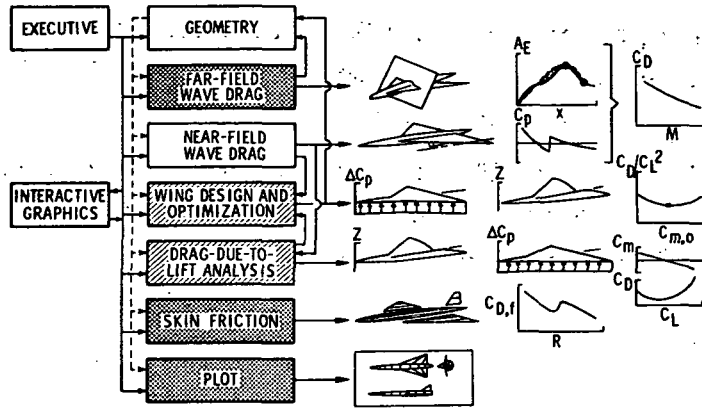


Figure 1

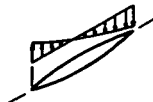
NEAR-FIELD WAVE DRAG

- AIRCRAFT COMPONENTS
FUSELAGE, WING AND NACELLES

- BASIC CALCULATIONS



WING THICKNESS
SURFACE PRESSURES



FUSELAGE AND NACELLE
SURFACE PRESSURES



FUSELAGE AND NACELLE
PRESSURE FIELDS

- APPLICATION OF BASIC SOLUTIONS



NEAR-FIELD
WAVE DRAG



WING DESIGN AND
ANALYSIS DATA

Figure 2

NACELLE-ON WING INTERFERENCE OPTIONS

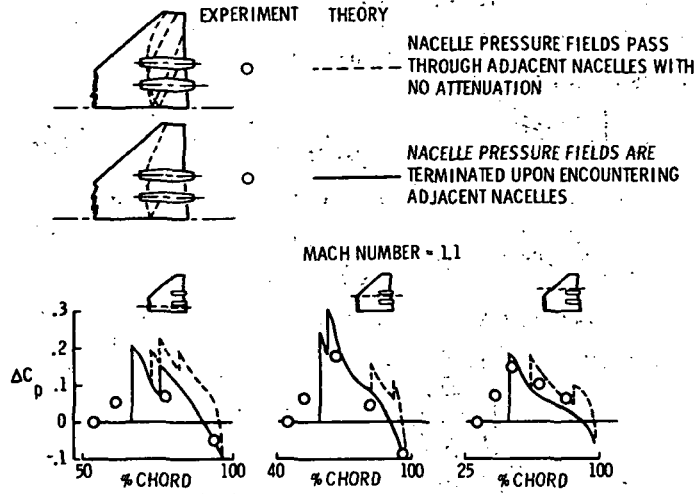


Figure 3

COMPARISON OF NEAR-FIELD AND FAR-FIELD WAVE DRAG

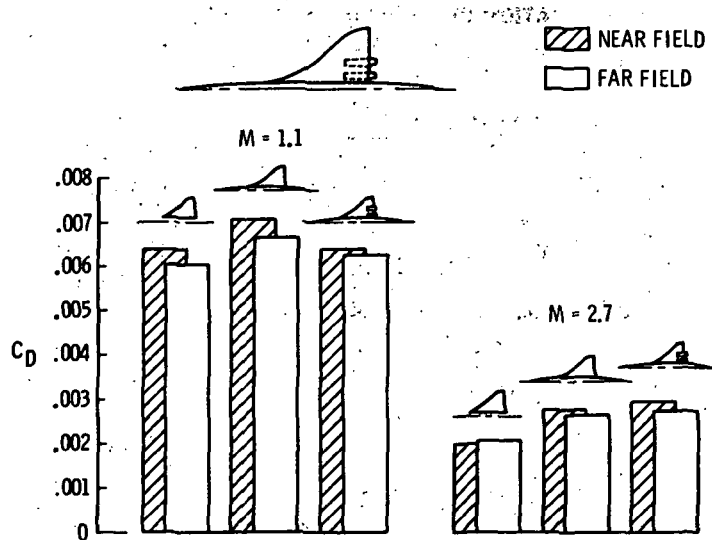
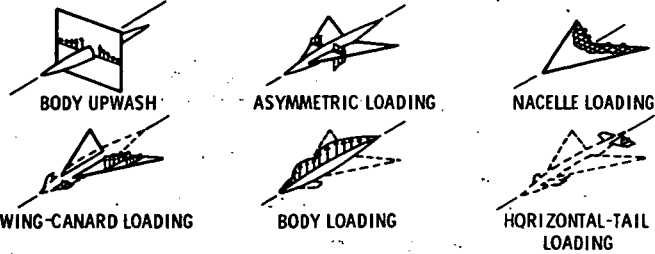


Figure 4

DRAG-DUE-TO-LIFT ANALYSIS

- AIRCRAFT COMPONENTS
FUSELAGE, WING, NACELLES, CANARD AND HORIZONTAL TAIL
- BASIC CALCULATIONS



- APPLICATION OF BASIC SOLUTIONS

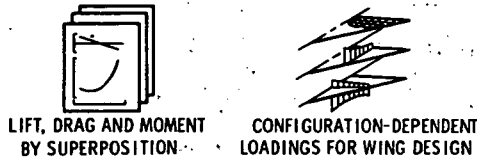


Figure 5

APPLICATION OF PRESSURE-LIMITING FEATURES

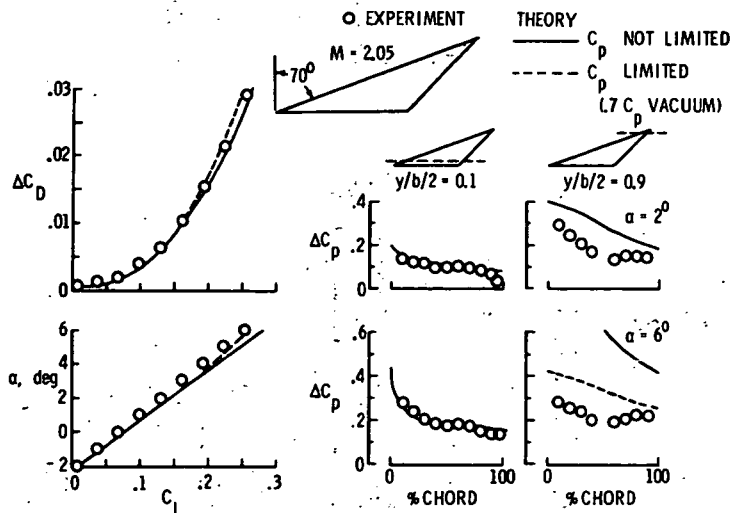


Figure 6

WING DESIGN AND OPTIMIZATION

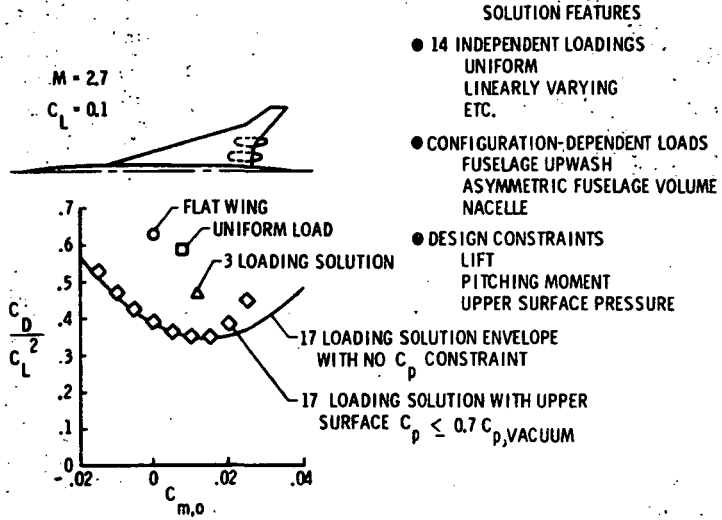


Figure 7

INTERACTIVE GRAPHICS

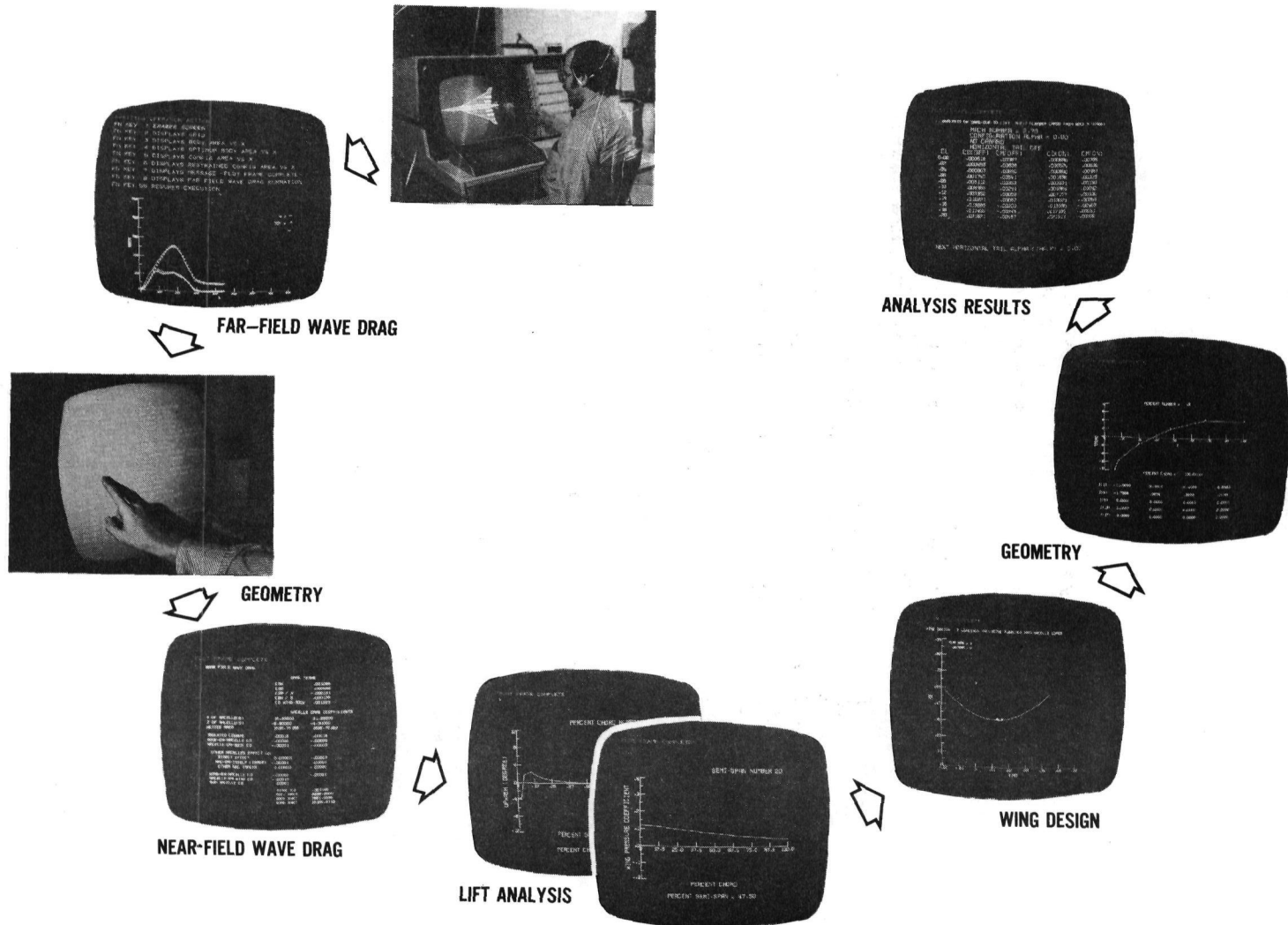


Figure 8

Page Intentionally Left Blank

INDICIAL COMPRESSIBLE POTENTIAL AERODYNAMICS AROUND COMPLEX AIRCRAFT CONFIGURATIONS*

By Luigi Morino and Lee-Tzong Chen
Boston University

SUMMARY

A general theory for indicial potential compressible aerodynamics around complex configurations is presented. The motion is assumed to consist of constant subsonic or supersonic speed for time $t \leq 0$ (steady state) and of small perturbations around the steady state for time $t > 0$. Using the finite-element method to discretize the space problem, one obtains a set of differential-delay equations in time relating the potential to its normal derivative on the surface of the body. The aerodynamic transfer function is then obtained by using standard methods of operational calculus. The theory is embedded in a computer code, SUSSA ACTS, which is briefly described. Numerical results are presented for steady and unsteady, subsonic and supersonic flows and indicate that the code is not only general, flexible, and simple to use but also accurate and fast.

INTRODUCTION

Presented herein is a general formulation of unsteady, subsonic and supersonic potential aerodynamics for an aircraft having arbitrary shape. The motion of the aircraft is assumed to consist of small perturbations (starting at time $t = 0$) with respect to the constant-speed motion (indicial potential aerodynamics). The objective of this formulation is to describe the time functional relationship between aerodynamic potential and its normal derivative (normal wash) in a form which can be used for computational analysis. The finite-element method is used for space discretization. Results obtained with the computer program SUSSA ACTS are also presented.

The analysis presented herein is based on a new integral formulation, presented in references 1 and 2, which includes completely arbitrary motion. However, the numerical implementation (refs. 3 and 4) was thus far limited to steady and oscillatory flows. On the other hand, in order to perform a linear-system analysis of the aircraft, it is convenient to use more general aerodynamic formulations, i.e., fully transient response for time-domain analysis and the aerodynamic transfer function (Laplace transform of the fully unsteady operator) for frequency-domain analysis. (See for instance, ref. 5.) Consistent

*This research is supported by NASA Langley Grant NGR 22-004-030.

with this type of analysis, the unsteady contribution is assumed to start at time $t = 0$, so that for time $t \leq 0$ the flow is in steady state. Furthermore, consistent with the linear flight dynamics analysis, the motion of the aircraft is assumed to consist of small (infinitesimal) perturbations around the steady-state motion.

Since the initial work by Wagner (ref. 6) on unsteady incompressible two-dimensional flow, several problems have been considered. While several methods are available for wings in subsonic and supersonic flow (see refs. 5 and 7), no tool has been available for subsonic and supersonic flows around arbitrary complex configurations for either time- or frequency-domain analysis. Such a tool is presented in reference 8, for both time and frequency domains. In this paper only the subsonic formulation is presented in detail; the supersonic formulation is only briefly outlined. For conciseness, material previously presented (in particular, the material of ref. 4) is not repeated herein. The computer program SUSSA ACTS, which is based upon this new formulation, is also briefly described. Numerical results obtained with this program are presented.

SYMBOLS

a_∞	speed of sound in undisturbed flow
AR	aspect ratio
$[\tilde{A}_{jh}]$	subsonic matrix transfer function, equation (27)
$[\tilde{A}'_{jh}]$	supersonic matrix transfer function, equation (39)
b	span
B	$= (M^2 - 1)^{1/2}$
B_h	defined by equation (18)
B'_h	defined by equation (35)
B_{jh}	defined by equation (21)
B'_{jh}	defined by equation (37)
c	chord

C_h	defined by equation (18)
C'_h	defined by equation (35)
C_{jh}	C_h for $P_* = P_j$
C'_{jh}	C'_h for $P_* = P_j$
C_l	lift distribution coefficient
$C_{l\alpha}$	lift distribution coefficient per unit α
C_L	lift coefficient
$C_{L\alpha}$	lift coefficient per unit α
C_M	moment coefficient around $x = x_M$
D_h	defined by equation (18)
D'_h	defined by equation (35)
D_{jh}	D_h for $P_* = P_j$
D'_{jh}	D'_h for $P_* = P_j$
$E(P)$	defined by equation (7)
F_n	defined by equation (18)
F_{jn}	F_n for $P_* = P_j$
G_n	defined by equation (18)
G_{jn}	G_n for $P_* = P_j$
$H(P)$	defined by equation (31)
J	number of nodes on body

k	reduced frequency, $\omega l/U_\infty$
l	reference length
$L_n(P)$	shape functions for $\Delta\Phi$
L_w	wake length
M	Mach number, U_∞/a_∞
\vec{N}	normal to Σ
N	number of nodes on wake
N_D	number of diaphragm elements
$N_h(P)$	shape functions for Ψ and Φ , equation (12)
N_w	number of wake elements in x-direction
N_x	number of elements in x-direction on half-wing
N_y	number of elements in y-direction on half-wing
P	point having coordinates (X,Y,Z)
P_*	control point (X_*, Y_*, Z_*)
R	defined by equation (4)
R'	defined by equation (30)
s	complex frequency (for Laplace transform)
S_{nh}	defined by equation (16)
t	time
T	nondimensional time, equation (2)

U_∞	velocity of undisturbed flow
x, y, z	space coordinates
x_m	pitch axis
x_M	moment axis
X, Y, Z	nondimensional space coordinates, equation (2)
α	angle of attack
β	$= (1 - M^2)^{1/2}$
δ_{jh}	Kronecker delta, 1 for $j = h$, 0 for $j \neq h$
$\Delta\Phi$	discontinuity of Φ across the wake
$\Delta\Phi_n$	nodal values of $\Delta\Phi$
Θ	time for a disturbance to propagate from P to P_* , equation (6)
Θ^+	defined by equation (33)
Θ^-	defined by equation (33)
Θ_h, Θ_n	Θ for $P = P_h$ or P_n
Θ_h^+	Θ^+ for $P = P_h$
Θ_h^-	Θ^- for $P = P_h$
Θ_{jh}, Θ_{jn}	Θ_h, Θ_n for $P_* = P_j$
Θ_{jh}^+	Θ_h^+ for $P_* = P_j$
Θ_{jh}^-	Θ_h^- for $P_* = P_j$
Π	convection time of wake vortices, equation (11)

Π_n	value of Π for $P = P_n$
Σ	surface surrounding body and wake in X, Y, Z space
Σ_B	surface of body
Σ_W	surface of wake
τ	thickness ratio
φ	velocity perturbation potential
ϕ	velocity potential, $U_\infty x + \phi$
Φ	nondimensional velocity perturbation potential, $\phi/U_\infty l$
Φ_j	nodal values of Φ
$\tilde{\Phi}_j$	Laplace transform of Φ_j
Ψ	normal wash in X, Y, Z space
Ψ'	conormal wash in X, Y, Z space
Ψ_j	nodal value of Ψ
$\tilde{\Psi}_j$	Laplace transform of Ψ_j
ω	frequency
Ω	nondimensional frequency, $\omega l/a_\infty \beta$ (subsonic), $\omega l/a_\infty B$ (supersonic)

Subscripts:

B	body
I	imaginary part of complex number
j, h, k	nodes on the body (range from 1 to J)

l	lower
m	nodes on trailing edge
n	nodes on wake (ranges from 1 to N)
R	real part of complex number
TE	trailing edge
u	upper
W	wake

Special notation:

$\tilde{(\)}$ Laplace transform of $(\)$

$\{ \}$ vector

$[\]$ matrix

$[\]^\ominus$ defined by equation (5)

$\text{ARG}(\)$ argument of $(\)$

SUBSONIC INDICIAL AERODYNAMICS

Integral-Differential-Delay Equation

Consider the subsonic flows first. Within the small-perturbation assumption, the motion of the surface of the aircraft with respect to a frame of reference traveling at uniform subsonic speed with respect to the undisturbed air can be assumed to be negligible except for the boundary conditions. (See ref. 1.) Thus the Green theorem for the equation of the aerodynamic potential is given by (refs. 1 and 2)

$$4\pi \mathbf{E}(\mathbf{P}_*) \Phi(\mathbf{P}_*, T) = - \oint_{\Sigma} [\Psi]^\ominus \frac{1}{R} d\Sigma + \oint_{\Sigma} [\Phi]^\ominus \frac{\partial}{\partial N} \left(\frac{1}{R} \right) d\Sigma - \oint_{\Sigma} [\dot{\Phi}]^\ominus \frac{1}{R} \frac{\partial R}{\partial N} d\Sigma \quad (1)$$

where

$$\left. \begin{aligned} \Phi &= \varphi / U_{\infty} \ell \\ X &= x / \beta \ell \quad Y = y / \ell \quad Z = z / \ell \\ T &= a_{\infty} \beta t / \ell \end{aligned} \right\} \quad (2)$$

Σ is a surface of the X, Y, Z space which surrounds (and is infinitesimally close to) the body and the wake, \vec{N} is the normal to the surface Σ , and

$$\Psi = \partial \Phi / \partial N \quad (3)$$

is the normal derivative of Φ on Σ (normal wash¹), which is prescribed by the boundary conditions (ref. 4). Furthermore,

$$R = \left[(X - X_*)^2 + (Y - Y_*)^2 + (Z - Z_*)^2 \right]^{1/2} \quad (4)$$

A dot over a symbol indicates differentiation with respect to T and

$$[\]^{\Theta} = [\] \Big|_{T-\Theta} \quad (5)$$

where

$$\Theta = M(X - X_*) + R \quad (6)$$

is the time necessary for a disturbance to propagate from P to P_* . In addition,

$$\left. \begin{aligned} E(P_*) &= 1 && \text{for } P_* \text{ outside } \Sigma \\ E(P_*) &= 1/2 && \text{for } P_* \text{ on } \Sigma \\ E(P_*) &= 0 && \text{for } P_* \text{ inside } \Sigma \end{aligned} \right\} \quad (7)$$

¹Note that the normal wash here indicates the component of the nondimensional velocity in the direction of the normal \vec{N} to the surface Σ of the X, Y, Z space (not in the direction of the normal to the surface of the physical x, y, z space).

In equation (1) the surface Σ is assumed to be fixed with respect to the frame of reference. However, the effect of the motion of the surface is retained in the boundary conditions (ref. 4).

Consistent with the hypothesis of small perturbations with respect to the constant-speed motion, is the assumption that the geometry of the wake is the one of the steady-state flow. If small-perturbation hypothesis can be used for steady flow as well, the wake may be assumed to consist of straight vortex lines emanating from the trailing edge. (See refs. 1 to 4.) It may be noted that since Σ is fixed, equation (1) represents a linear operator (integral equation on Σ , differential-delay equation in time). Hence the state-steady contribution can be subtracted from equation (1). Therefore, in the following development it is understood that Φ and Ψ are the unsteady parts of the potential and the normal wash, which (in line with the concepts of operational calculus) are assumed to be identically equal to zero for $T \leq 0$, i.e.,

$$\left. \begin{aligned} \Phi &\equiv 0 \\ \Psi &\equiv 0 \end{aligned} \right\} (T \leq 0) \quad (8)$$

In order to understand the nature of the aerodynamic operator, equation (1), it is convenient to isolate the contribution of the wake. This yields

$$\begin{aligned} 4\pi E(P_*) \Phi(P_*, T) = & - \iint_{\Sigma_B} [\Psi]^\ominus \frac{1}{R} d\Sigma_B + \iint_{\Sigma_B} \left\{ [\Phi]^\ominus \frac{\partial}{\partial N} \left(\frac{1}{R} \right) - [\dot{\Phi}]^\ominus \frac{1}{R} \frac{\partial R}{\partial N} \right\} d\Sigma_B \\ & + \iint_{\Sigma_W} \left\{ [\Delta\Phi]^\ominus \frac{\partial}{\partial N} \left(\frac{1}{R} \right) - [\Delta\dot{\Phi}]^\ominus \frac{1}{R} \frac{\partial R}{\partial N} \right\} d\Sigma_W \end{aligned} \quad (9)$$

where Σ_B is the (closed) surface of the body, Σ_W is the (open) surface of the wake, and $\Delta\Phi$ is the potential discontinuity across the wake, evaluated in the direction of the wake normal, i.e., $\Delta\Phi = \Phi_u - \Phi_l$ if the upper normal is used. For simplicity, the side corresponding to the wake normal will be called the upper side (even if this term is confusing in the case of vertical surfaces or for rolled-up wakes). It should be noted that the value of $\Delta\Phi$ is not an additional unknown, since (ref. 8)

$$\Delta\Phi(P, T) = \Delta\Phi(P_{TE}, T - \Pi) \quad (10)$$

where Π is the nondimensional time necessary for the vortex point to travel (within the steady flow) from the point P_{TE} (origin of the vortex line at the trailing edge) to the

point P. If small-perturbation hypothesis can be used for the steady-state flow, then Π can be approximated by (ref. 8)

$$\Pi = \frac{\beta^2(X - X_{TE})}{M} \quad (11)$$

Space Discretization

Equations (9) and (10) fully describe the problem of linearized unsteady subsonic potential aerodynamics around complex configurations. In order to solve this problem, it is necessary, in general, to obtain a numerical approximation for equation (9). This can be obtained by using the finite-element method.² Consider the integrals over Σ_B first. Using a typical finite-element representation, it is possible to write (ref. 9),

$$\left. \begin{aligned} \Psi(P, T - \Theta) &= \sum_{h=1}^J \Psi_h(T - \Theta_h) N_h(P) \\ \Phi(P, T - \Theta) &= \sum_{h=1}^J \Phi_h(T - \Theta_h) N_h(P) \end{aligned} \right\} \quad (12)$$

where J is the total number of nodes on the body and $\Psi_h(T - \Theta_h)$ and $\Phi_h(T - \Theta_h)$ are time-dependent values of Ψ and Φ at the node P_h at the time $T - \Theta_h$ (where Θ_h is the disturbance-propagation time from P_* to P_h); furthermore, the $N_h(P)$ are prescribed global shape functions, obtained by standard assembly of the element shape function. (See for instance, ref. 9.) For simplicity, the same shape functions are used for Φ and Ψ , although this is not essential to the method.

Next consider the integrals on the wake. In order to facilitate the use of equation (10), it is convenient to divide the wake into strips defined by (steady-state) vortex lines emanating from the nodes on the trailing edge. The strips are then divided into finite elements with nodes along the vortex lines. The potential discontinuity can then be expressed as

$$\Delta\Phi(P, T - \Theta) = \sum_{n=1}^N \Delta\Phi_n(T - \Theta_n) L_n(P) \quad (13)$$

²Whereas other interpolation methods can be used, the finite-element method appears to be the only method sufficiently general and flexible to be used in this formulation.

where N is the number of nodes on the wake, $\Delta\phi_n(T-\Theta_n)$ is the value of $\Delta\phi$ at the n th node $P_n^{(W)}$ on the wake at time $T - \Theta_n$ (where Θ_n is the propagation time from P_n to P_*), and $L_n(P)$ is the global shape function relative to the n th node of the wake. Note that according to equation (10)

$$\Delta\phi_n(T) = \Delta\phi_{m(n)}^{(TE)}(T - \Pi_n) \quad (14)$$

where $m(n)$ identifies the trailing-edge node which is on the same vortex line as the n th wake node $P_n^{(W)}$. Furthermore, Π_n is the time necessary for the vortex point to be convected from the trailing-edge node P_m to the wake node $P_n^{(W)}$. It may be worth noting that $\Delta\phi_m^{(TE)} = \phi_{h_u} - \phi_{h_l}$ where h_u and h_l identify the upper and lower trailing-edge nodes of the body corresponding to the m th node on the trailing edge. Therefore, it is possible to write

$$\Delta\phi_{m(n)}^{(TE)} = \sum_{h=1}^J S_{nh} \phi_h \quad (15)$$

where $S_{nh} = 1$ ($S_{nh} = -1$), if h identifies the upper (lower) node P_h on the body corresponding to the n th node $P_n^{(W)}$ on the wake (i.e., P_h coincides with the node $P_{m(n)}^{(TE)}$ on the trailing edge), and $S_{nh} = 0$ otherwise. Thus,

$$\left. \begin{aligned} S_{nh} = +1 & \quad \text{if } P_h \equiv P_{m(n)}^{(TE)} \text{ is on the upper side of } \Sigma_B \\ S_{nh} = -1 & \quad \text{if } P_h \equiv P_{m(n)}^{(TE)} \text{ is on the lower side of } \Sigma_B \\ S_{nh} = 0 & \quad \text{otherwise} \end{aligned} \right\} \quad (16)$$

Combining equations (9), (12), and (13) results in

$$\begin{aligned}
 2 E(P_*) \Phi(P_*, T) = & \sum_h B_h \Psi_h(T - \Theta_h) + \sum_h C_h \Phi_h(T - \Theta_h) + \sum_h D_h \dot{\Phi}_h(T - \Theta_h) \\
 & + \sum_n F_n \Delta \Phi_n(T - \Theta_n) + \sum_n G_n \Delta \dot{\Phi}_n(T - \Theta_n)
 \end{aligned} \tag{17}$$

where

$$\left. \begin{aligned}
 B_h &= \frac{-1}{2\pi} \oiint_{\Sigma_B} N_h(P) \frac{1}{R} d\Sigma_B \\
 C_h &= \frac{1}{2\pi} \oiint_{\Sigma_B} N_h(P) \frac{\partial}{\partial N} \left(\frac{1}{R} \right) d\Sigma_B \\
 D_h &= -\frac{1}{2\pi} \oiint_{\Sigma_B} N_h(P) \frac{1}{R} \frac{\partial R}{\partial N} d\Sigma_B \\
 F_n &= \frac{1}{2\pi} \iint_{\Sigma_W} L_n(P) \frac{\partial}{\partial N} \left(\frac{1}{R} \right) d\Sigma_W \\
 G_n &= -\frac{1}{2\pi} \iint_{\Sigma_W} L_n(P) \frac{1}{R} \frac{\partial R}{\partial N} d\Sigma_W
 \end{aligned} \right\} \tag{18}$$

and according to equations (15) and (16)

$$\Delta \Phi_n(T - \Theta_n) = \sum_n S_{nh} \Phi_h(T - \Theta_n - \Pi_n) \tag{19}$$

Next consider, in particular, that P_* coincides with the node P_j of the body. In this case $E(P_*) = 1/2$ and using equation (19), equation (17) reduces to

$$\begin{aligned}
 \Phi_j(T) = & \sum_h B_{jh} \Psi_h(T - \Theta_{jh}) + \sum_h C_{jh} \Phi_h(T - \Theta_{jh}) + \sum_h D_{jh} \dot{\Phi}_h(T - \Theta_{jh}) \\
 & + \sum_n \sum_h F_{jn} S_{nh} \Phi_h(T - \Theta_{jn} - \Pi_n) + \sum_n \sum_h G_{jn} S_{nh} \dot{\Phi}_h(T - \Theta_{jn} - \Pi_n)
 \end{aligned} \tag{20}$$

where

$$B_{jh} = B_h |_{P_* = P_j} \quad (21)$$

Similar definitions hold for C_{jh} , D_{jh} , F_{jn} , G_{jn} , Θ_{jn} , and Θ_{jh} .

Time-Frequency Transformation

Equation (20) indicates the nature of the aerodynamic operator relating potential and normal wash as obtained by using finite-element representation to discretize the spacial problem. The operator is a linear differential-delay operator to which the methods of operational calculus can be applied. However, before considering the Laplace transform of equation (20), it is convenient to make some remarks about the contribution of the wake. It may be noted that, according to equation (8), Φ is identically equal to zero for $T \leq 0$; therefore, according to equation (15)

$$\Delta \Phi_n \equiv 0 \quad (T \leq \Pi_n) \quad (22)$$

Hence, if the analysis is limited to $T \leq T_{\max}$, the contribution of the elements with $\Pi_n \geq T_{\max}$ is identically equal to zero. Therefore, the wake can be truncated to eliminate these elements. It may be noted that in any case these elements would contribute to the transfer function and thus to the transform of Φ but not to the final solution in the time domain for $T \leq T_{\max}$. The advantage is not only that less computational time is used (since less elements are employed) but also that the problem of convergence connected with the infinite wake (factors $e^{-s\Pi_n}$ with $s_R < 0$ and $\Pi_n \rightarrow \infty$) are bypassed.³

Next taking the Laplace transform of equation (20) yields

$$\left[\tilde{Y}_{jh} \right] \left\{ \tilde{\Phi}_h \right\} = \left[\tilde{Z}_{jh} \right] \left\{ \tilde{\Psi}_h \right\} \quad (23)$$

where $\tilde{\Phi}_h$ and $\tilde{\Psi}_h$ are the Laplace transforms of Φ_h and Ψ_h and

$$\tilde{Y}_{jh} = \delta_{jh} - (C_{jh} + sD_{jh})e^{-s\Theta_{jh}} - \sum_n (F_{jn} + sG_{jn})e^{-s(\Theta_{jn} + \Pi_n)} S_{nh} \quad (24)$$

and

$$\tilde{Z}_{jh} = B_{jh} e^{-s\Theta_{jh}} \quad (25)$$

³A more refined analysis implies the evaluation of the limit of the present analysis as the length of the wake goes to infinity.

Solving for $\{\tilde{\Phi}_h\}$ one obtains

$$\{\tilde{\Phi}_j\} = [\tilde{A}_{jh}]\{\tilde{\Psi}_h\} \quad (26)$$

where

$$[\tilde{A}_{jh}] = [\tilde{Y}_{kj}]^{-1} [\tilde{Z}_{kh}] \quad (27)$$

Equation (26) indicates that the matrix $[\tilde{A}_{jh}]$ is the desired subsonic matrix transfer function relating the transformed vector of the potential $\{\tilde{\Phi}_j\}$ to the transformed vector of the normal wash $\{\tilde{\Psi}_h\}$.

SUPERSONIC INDICIAL AERODYNAMICS

In this section the formulation for the supersonic case is briefly outlined. For conciseness, only supersonic trailing edges are considered so that the contribution of the wake can be ignored.⁴ Under small-perturbation assumption, the Green theorem for potential supersonic flow is given by

$$\begin{aligned} 4\pi E(P_*) \Phi(P_*, T) = & - \iint_{\Sigma_B} \left([\Psi']^{\Theta^+} + [\Psi']^{\Theta^-} \right) \frac{H(P)}{R'} d\Sigma \\ & + \iint_{\Sigma_B} \left([\Phi]^{\Theta^+} + [\Phi]^{\Theta^-} \right) \frac{\partial}{\partial N^c} \left[\frac{H(P)}{R'} \right] d\Sigma \\ & - \iint_{\Sigma_B} \left([\dot{\Phi}]^{\Theta^+} + [\dot{\Phi}]^{\Theta^-} \right) \frac{H(P)}{R'} \frac{\partial R'}{\partial N^c} d\Sigma \end{aligned} \quad (28)$$

where $\Psi' = \partial\Phi/\partial N^c$ ($\partial/\partial N^c$ is the conormal derivative (ref. 4)) is the conormal wash which is prescribed by the boundary conditions, and

$$X = \frac{x}{B\ell} \quad Y = \frac{y}{\ell} \quad Z = \frac{z}{\ell} \quad T = \frac{a_\infty Bt}{\ell} \quad (29)$$

with $B = \sqrt{M^2 - 1}$. Furthermore,

$$R' = \left[(X - X_*)^2 - (Y - Y_*)^2 - (Z - Z_*)^2 \right]^{1/2} \quad (30)$$

⁴If the trailing edge is not fully supersonic then the contribution of the wake can be treated similarly to the subsonic case with the only difference that the device of truncating the wake at finite distance is not necessary in the supersonic case, since only a finite portion of the wake can have an effect on the aircraft.

whereas

$$\left. \begin{aligned} H(P) = 1 \quad \text{for} \quad X_* - X > \left[(Y - Y_*)^2 + (Z - Z_*)^2 \right]^{1/2} \\ H(P) = 0 \quad \text{for} \quad X_* - X \leq \left[(Y - Y_*)^2 + (Z - Z_*)^2 \right]^{1/2} \end{aligned} \right\} \quad (31)$$

and

$$[]^{\Theta^\pm} = [] \Big|_{T-\Theta^\pm} \quad (32)$$

with

$$\Theta^\pm = M(X_* - X) \pm R' \quad (33)$$

Using equation (12) and following the same procedure used for the subsonic case, one obtains the supersonic indicial aerodynamic operator

$$\begin{aligned} 2 E(P_*) \Phi(P_*, T) = & \sum_h B'_h \left[\Psi'_h(T-\Theta_h^+) + \Psi'_h(T-\Theta_h^-) \right] \\ & + \sum_h C'_h \left[\Phi_h(T-\Theta_h^+) + \Phi_h(T-\Theta_h^-) \right] \\ & + \sum_h D'_h \left[\dot{\Phi}_h(T-\Theta_h^+) + \dot{\Phi}_h(T-\Theta_h^-) \right] \end{aligned} \quad (34)$$

where

$$\left. \begin{aligned} B'_h &= -\frac{1}{2\pi} \iint_{\Sigma_B} N_h(P) \frac{H(P)}{R'} d\Sigma_B \\ C'_h &= \frac{1}{2\pi} \iint_{\Sigma_B} N_h(P) \frac{\partial}{\partial N^c} \left[\frac{H(P)}{R'} \right] d\Sigma_B \\ D'_h &= -\frac{1}{2\pi} \iint_{\Sigma_B} N_h(P) \frac{H(P)}{R'} \frac{\partial R'}{\partial N^c} d\Sigma_B \end{aligned} \right\} \quad (35)$$

In particular, if P^* coincides with the node P_j , $E(P_*) = 1/2$, and equation (34) reduces to

$$\begin{aligned} \Phi_j(T) = & \sum_h B'_{jh} [\Psi'_h(T - \Theta_{jh}^+) + \Psi'_h(T - \Theta_{jh}^-)] + \sum_h C'_{jh} [\Phi_h(T - \Theta_{jh}^+) + \Phi_h(T - \Theta_{jh}^-)] \\ & + \sum_h D'_{jh} [\dot{\Phi}_h(T - \Theta_{jh}^+) + \dot{\Phi}_h(T - \Theta_{jh}^-)] \end{aligned} \quad (36)$$

where

$$B'_{jh} = B'_h \Big|_{P_* = P_j} \quad (37)$$

Similar definitions hold for C'_{jh} , D'_{jh} , Θ_{jh}^+ , and Θ_{jh}^- . Finally, taking the Laplace transform of equation (36) results in

$$\left\{ \tilde{\Phi}_j \right\} = \left[\tilde{A}'_{jh} \right] \left\{ \tilde{\Psi}'_h \right\} \quad (38)$$

where

$$\left[A'_{jh} \right] = \left[\delta_{kj} - (C'_{kj} + sD'_{kj}) \left(e^{-s\Theta_{kj}^+} + e^{-s\Theta_{kj}^-} \right) \right]^{-1} \left[B'_{kh} \left(e^{-s\Theta_{kh}^+} + e^{-s\Theta_{kh}^-} \right) \right] \quad (39)$$

Equation (38) indicates that the matrix $\left[\tilde{A}'_{jh} \right]$ is the desired supersonic matrix transfer function relating the transformed vector of the potential $\left\{ \tilde{\Phi}_j \right\}$ to the transformed vector of the conormal wash $\left\{ \tilde{\Psi}'_h \right\}$ for supersonic trailing-edge configurations. If the trailing edge is not fully supersonic, the formulation may be modified following the same ideas used for the subsonic case.

SUSSA ACTS

The formulation presented above is embedded in the computer code SUSSA ACTS (Steady and Unsteady, Subsonic and Supersonic Aerodynamics for Aerospace Complex

Transportation Systems) which uses zeroth-order shape functions. A few specific details of the SUSSA ACTS formulation are briefly illustrated here. The surface of the aircraft is divided into small elements, Σ_h . Consider the shape function $N_h(P)$ equal to one inside the element Σ_h and equal to zero outside the element Σ_h , i.e.,

$$\left. \begin{aligned} N_h(P) &= 1 && \text{if } P \text{ is inside } \Sigma_h \\ N_h(P) &= 0 && \text{otherwise} \end{aligned} \right\} \quad (40)$$

Equation (12) may thus be interpreted as saying that, within the element Σ_h the normal wash and the potential are approximated with the values Ψ_h and Φ_h at the centroid P_h of the element Σ_h . Similarly, the wake is divided into elements and the shape functions $L_h(P)$ (see eq. (13)) are defined in a similar way. It may be worth noting that the shape functions given by equation (40) may be called zeroth-order shape functions. Therefore, the formulation used in SUSSA ACTS is called zeroth-order finite-element formulation.

Next, note that using equation (40), equation (18) yields for instance

$$B_h = -\frac{1}{2\pi} \iint_{\Sigma_h} \frac{1}{R} d\Sigma_h \quad (41)$$

$$C_h = -\frac{1}{2\pi} \iint_{\Sigma_h} \frac{1}{R^2} \frac{\partial R}{\partial N} d\Sigma_h \quad (42)$$

The elements used in SUSSA ACTS are quadrilateral elements (in particular, triangular) which are approximated with a hyperboloidal element of the type (see ref. 4)

$$\bar{P} = \bar{p}_0 + \xi \bar{p}_1 + \eta \bar{p}_2 + \xi \eta \bar{p}_3 \quad (-1 \leq \xi < 1; \quad -1 \leq \eta \leq 1) \quad (43)$$

and the integrals which define B_h and C_h are evaluated analytically. The expressions for the analytical evaluation of the integrals are given in reference 4 and therefore are not repeated in this paper.

The version of SUSSA ACTS used for the results presented herein is a preliminary one in that (consistent with the oscillatory-flow formulation of SOSSA ACTS presented in ref. 4) the coefficients D_h are evaluated as

$$D_h = -\frac{1}{2\pi} \iint_{\Sigma_h} \frac{1}{R} \frac{\partial R}{\partial N} d\Sigma_h \approx -\frac{1}{2\pi} R_h \iint_{\Sigma_h} \frac{1}{R^2} \frac{\partial R}{\partial N} d\Sigma_h = R_h C_h \quad (44)$$

where R_h is the value of R at the centroid P_h of the element Σ_h . The evaluations of F_n and G_n are similar to the ones of C_h and D_h . The evaluation of the coefficients for supersonic flow is similar: the modifications are indicated in reference 4 and are not repeated herein.

The pressure coefficient is evaluated by finite difference, using the same method outlined in reference 4. The generalized forces are evaluated by integrating by parts the integrals which contain $\partial\phi/\partial x$. The integrals are then evaluated by using the mid-point rule with the same elements used for the evaluation of Φ . (See ref. 10.)

NUMERICAL RESULTS

Numerical results, obtained with the computer program SUSSA ACTS, for steady and oscillatory flows are presented in reference 10. These include the analysis of convergence, new results for supersonic delta wings, and the evaluation of generalized forces, which are presented in this paper along with some preliminary results for complex frequencies. Additional results are given in reference 10.

The analysis of convergence is presented in figures 1 to 6. For all the cases presented in these figures, previously obtained numerical results indicate good agreement with the experimental results of reference 11; such comparisons are presented in reference 4 and are not repeated herein. Steady-state flows are considered in figures 1 and 2 for subsonic ($M = 0.24$) and supersonic ($M = 1.3$) flow, respectively. Both figures show the distribution of the potential along the midsection of the wing ($y = 0$) for $\tau = 0.05$ and $\alpha = 0^\circ$ (thickness problem). The thickness problem was chosen because its convergence rate is lower than the one of the lifting problem (ref. 3). The number of elements of the diaphragm, for figure 2, is $N_D = 3N_x$. Next consider the oscillatory flows. Wings (with $\tau = 0.01$ and $\alpha = 0^\circ$) oscillating in bending mode, i.e.,

$$z = 0.18043|2y/b| + 1.70255|2y/b|^2 - 1.13688|2y/b|^3 + 0.25387|2y/b|^4 \quad (45)$$

are considered in figures 3, 4, and 5 for subsonic flow ($M = 0.24$) with $k = \omega c/2U_\infty = 0.47$. These figures show the values of \tilde{C}_l as a function of x/c at $2y/b = 0.1328$. In figures 3 and 4 the analysis of convergence with respect to the wake elements is presented. In both figures, $N_x = N_y = 7$. This is largely sufficient for convergence (fig. 5). In figure 3, the length of the wake is kept constant, $L_w/c = 4$, and the number of elements of

the wake in the flow direction is increased ($N_W = 5, 10, 20, 30, \text{ and } 40$). The number of elements of the wake in y-direction is the same as on the wing $N_y = 7$. The results indicate that $N_W = 40$ is largely sufficient for convergence. This corresponds to a wake element of length $\Delta x_W = 0.1c$, which is the value used in figure 4 where Δx_W is kept constant and the number of elements is increased ($N_W = 5, 10, 20, 30, \text{ and } 40$) so that the total wake length is increased ($L_W/c = 0.5, 1, 2, 3, 4$). The above results indicate that $N_W = 30$ with $L_W/c = 3.5$ are largely sufficient for convergence. These values are used in figure 5, where the analysis of convergence in terms of the number of elements on the wing ($N_x = N_y = 5, 6, 7$) is presented. Next consider the supersonic oscillatory flow. Convergence for a wing (with $\tau = 0.01$ and $\alpha = 0^\circ$) in bending mode, given by equation (45), is considered in figure 6 for supersonic flow ($M = 1.3$) with $k = \omega c / 2U_\infty = 0.10$. The figure shows the value of

$$\hat{\phi} = \tilde{\phi} e^{i\Omega M X} \quad (46)$$

as a function of x/c at $2y/b = 0.5$ for $N_x = N_y = 5, 6, 7$. The number of elements on the diaphragm is $N_D = 3N_x$. The analysis of convergence with respect to N_D is now under investigation and is not presented herein. All these results indicate that the rate of convergence is very high and that $N_x = N_y = 6$ (i.e., 144 elements over the whole wing) are sufficient for convergence, at least for the problems considered here.

Next, some new results obtained for supersonic delta wings are presented. Two possible types of element grids are depicted in figure 7. The one shown in figure 7(a) was used in reference 4. However, for supersonic delta wings, the flow is conical (ref. 12). Therefore, the element grid shown in figure 7(b) appears to be the more natural one. It may be worth noting that the use of this grid implies the use of a completely general quadrilateral element. This grid was used to obtain the results presented in figures 8 and 9 for subsonic and supersonic leading edges, i.e., for $B/\tan \Lambda = 0.833$ and 1.2, respectively, where Λ is the leading-edge angle. The results of figure 8 are obtained for $N_x = N_y = 7$, $\tau = 0$, and by using a diaphragm to separate the upper from the lower side. The number of elements on the diaphragm is $N_D = 7 \times 3$. The results of figure 9 were obtained for $N_x = 8$, $N_y = 12$, $\tau = 0$, and using only the upper side. For both figures, the results are compared with the exact analytical solution given, for instance, in reference 12. The comparison indicates that the results are in good agreement for the subsonic leading edge and in excellent agreement (with relative errors below 10^{-5} !) for the supersonic leading edge.

Next, consider the evaluation of the lift coefficient C_L and the moment coefficient C_M (with respect to the axis $x = x_M$). The results are presented in figures 10 to 16.

Figure 10 presents the lift coefficient per unit angle of attack $C_{L\alpha}$ as a function of the aspect ratio for a delta wing in steady subsonic flow, for $M = 0$. The results are obtained for $\tau = 0.001$ and $N_x = N_y = 7$ and are in good agreement with the lifting-surface results presented in reference 13. Lift and moment coefficients \tilde{C}_L and \tilde{C}_M as functions of the reduced frequency k , for $M = 0$, are presented in figures 11 and 12, respectively, for a delta wing with $AR = 4$ oscillating in pitch around the axis $x_m = x_M = c/2$. The pitch mode is $z = x - x_m$. The results are obtained for $\tau = 0.005$, $N_x = 10$, and $N_y = 6$. The number of elements of the wake in the direction of the flow is $N_W = 20$ and the wake length is $L_W = 2c$. Similarly, figures 13 and 14 give the values of \tilde{C}_L and \tilde{C}_M (with $x_M = c/4$) as a function of k for $M = 0$, for a rectangular wing with $AR = 2$ oscillating in plunge as $z = ce^{i\omega t}$. The results are obtained for $\tau = 0.001$, $N_x = 10$, $N_y = 6$, $N_W = 20$, and $L_W/c = 2$. The influence of the Mach number M is indicated in figures 14 and 15 where \tilde{C}_L and \tilde{C}_M are given as functions of M for $k = 1$ for a rectangular wing with $AR = 2$ oscillating in pitch as $z = (x - x_m)e^{i\omega t}$ around the axis $x = x_m = x_M = c/2$. The results are obtained with $\tau = 0.001$, $N_x = 10$, and $N_y = 6$. For subsonic flows $N_W = 20$ and $L_W/c = 2$, whereas for supersonic flows $N_D = 10 \times 3$. The results of figures 11 to 16 are in good agreement with the ones of reference 14.

Next some recent complex-frequency results are presented in figure 17 for subsonic flow. The problem is the same as the one of figure 5, i.e., a biconvex rectangular wing with $AR = 3$ oscillating in bending mode. (See eq. (45).) The results are obtained for $\tau = 0.01$, $\alpha = 0^\circ$, $M = 0.24$, $N_x = N_y = 7$, $N_W = 30$, and $L_W = 3.5c$. The values of the complex frequency $s = s_R + is_I$ are such that $s_R/s_I = -0.2, 0$, and 0.2 while $s_I = kM/\beta$ corresponds to $k = 0.47$. This yields $s = -0.023 + i0.115, i0.115$, and $0.023 + i0.115$.

Next preliminary supersonic complex-frequency results are presented in figure 18 for the same problem of figure 6, i.e., a biconvex rectangular wing with $AR = 3$ oscillating in bending mode. The values of \tilde{C}_l , presented as functions of x/c at $2y/b = 0.1328$, are shown in figure 18. The results are obtained for $\tau = 0.01$, $\alpha = 0^\circ$, $M = 1.3$, $N_x = N_y = 7$, and $N_D = 7 \times 3$. The values of s correspond to $s_R/s_I = -0.2, 0$, and 0.2 and $k = 0.1$, i.e., $s = -0.0314 + i0.157, i0.157$, and $0.0314 + i0.157$. Convergence analyses for complex-frequency results are now under investigation.

It may be worth mentioning the computer time used by the program SUSSA ACTS. This is given in table I for steady (real-variable coefficients) and unsteady (complex-variable coefficients) subsonic and supersonic flows in terms of the total number of elements on the wing $N_{ELEM} = 4N_xN_y$. All the results are obtained by taking advantage of the symmetry (or antisymmetry) in y - and z -directions. The wake for the subsonic flow

TABLE I.- COMPUTER TIME FOR SUSSA ACTS (ON IBM 370/145)

N_{ELEM}	Computer time, sec, for -			
	Subsonic flow		Supersonic flow	
	Steady	Unsteady	Steady	Unsteady
$4 \times 4 \times 4$	29	161	8	21
$4 \times 5 \times 5$	70	324	15	38
$4 \times 6 \times 6$	143	543	29	65
$4 \times 7 \times 7$	268	928	54	119

has $N_W = 1$ for steady and $N_W = 30$ for unsteady flows. The diaphragm for supersonic flow has $N_D = 9$. The computer times are expressed in seconds and were obtained on an IBM 370/145 computer of the Boston University Computing Center. It may be worth noting that the computer times for unsteady supersonic flows are remarkably low. Also, it should be noted that, once the results for one reduced frequency have been obtained, results for additional frequencies require minimal additional time (essentially the time for the matrix inversion).

Finally, it may be noted that for steady (real-variable coefficients) flows the memory requirement is approximately given by

$$N_{WORDS} = 9500 + 18N_{EQN} + N_{EQN}^2 \quad (47)$$

where N_{WORDS} is the number of words, whereas N_{EQN} is the number of equations. Similarly, for unsteady (complex-variable coefficients) flows the memory requirement is approximately given by

$$N_{WORDS} = 12\,500 + 22N_{EQN} + 2N_{EQN}^2 \quad (48)$$

In addition, the geometry preprocessor for wing-body configurations requires 4500 words.

COMMENTS

A general theory for indicial compressible potential aerodynamics has been presented. The motion is assumed to consist of small perturbations (starting at time $t = 0$) around a steady-state constant-velocity motion. In this case, the relationship between the

velocity potential and the normal wash is given by an integral operator in space and a differential-delay operator in time. Using the finite-element method to solve the spacial problem, one is left with a differential-delay system in time. This can be solved step by step in the time domain or by using the Laplace transform and thus obtaining the matrix transfer function for frequency-domain analysis.

The formulation presented in this paper represents a considerable improvement with respect to the state of the art since complex configurations could be analyzed only for steady and oscillatory flows (see for instance, refs. 3 and 4) while unsteady flows could be analyzed only for simple configurations such as zero-thickness wings. With this method, the analysis of unsteady flow around complex configurations is consistent with the control-theory analysis. Furthermore, note that the linear equations of flight dynamics imply the limitation of small perturbations around a steady-state motion, usually constant-speed horizontal flight. The indicial aerodynamics analysis presented herein does not require any additional limitation and therefore is the most general formulation within the framework of linear flight dynamics analysis.

In addition, it should be noted that the increase in generality of the formulation is obtained at no additional increase in computational complexity. For, if simple oscillatory problems are considered, the only advantage is to replace s with $i\Omega$ (refs. 3 and 4) with no particular computational saving.

Another advantage of the present approach is that the dependence of the matrix $\left[\tilde{A}_{jh} \right]$ upon the complex frequency s is given in a very simple explicit analytic form. This is a considerable computational advantage, since once the frequency-independent coefficients B_{jh} , C_{jh} , D_{jh} , F_{jn} , G_{jn} , S_{nh} , Θ_{jh} , and Θ_{jn} have been evaluated (and these are necessary even for the evaluation of the potential at one single reduced frequency), little additional time (essentially the time for the inversion of one matrix) is necessary to obtain the results at different values of s . Also advantage can be taken of the analytic dependence upon s to obtain approximate expressions for the matrix $\left[\tilde{A}_{jh} \right]$. For instance, at low frequencies, a Taylor's series expansion for equations (27) and (39) could be used.

It is essential to note the difference between this method and the classical approach for unsteady (oscillatory) aerodynamics. In the latter case the solution is assumed to be oscillatory (i.e., of the type $e^{i\Omega T}$) and then the problem is solved in space. Here the space-discretization precedes the time-frequency transformation. This inversion of the time and space solutions might appear to be irrelevant, but is not. For, in the classical formulation the convergence of the space solution is analyzed on the time-transformed

unknown which is highly oscillating in space. On the other hand, here the finite-element method is applied to the untransformed equation, where the unknown is smooth and therefore fewer elements are required for convergence. The transform applies to the discrete system and therefore high-frequency components do not involve a change in the number of elements. This question is analyzed in more detail in reference 8, where the Laplace transform is used first and then the transformed equation is solved by finite elements. This process yields

$$\left[\tilde{A}_{jh} \right] = \left[\delta_{kj} - \left(\tilde{C}_{kj} + s\tilde{D}_{kj} \right) - \sum_n \left(\tilde{F}_{kn} + s\tilde{G}_{kn} \right) \left(s_{nj} e^{-s\Pi_n} \right) \right]^{-1} \left[\tilde{B}_{kh} e^{-s\Theta_{kh}} \right] \quad (49)$$

where

$$\left. \begin{aligned} \tilde{B}_{jh} &= \left[-\frac{1}{2\pi} \oint_{\Sigma_B} N_h(P) e^{-s\Theta} \frac{1}{R} d\Sigma_B \right]_{P_*=P_j} \\ \tilde{C}_{jh} &= \left[\frac{1}{2\pi} \oint_{\Sigma_B} N_h(P) e^{-s\Theta} \frac{\partial}{\partial N} \left(\frac{1}{R} \right) d\Sigma_B \right]_{P_*=P_j} \\ \tilde{D}_{jh} &= \left[-\frac{1}{2\pi} \oint_{\Sigma_B} N_h(P) e^{-s\Theta} \frac{1}{R} \frac{\partial R}{\partial N} d\Sigma_B \right]_{P_*=P_j} \\ \tilde{F}_{jn} &= \left[\frac{1}{2\pi} \iint_{\Sigma_W} L_n(P) e^{-s\Theta} \frac{\partial}{\partial N} \left(\frac{1}{R} \right) d\Sigma_W \right]_{P_*=P_j} \\ \tilde{G}_{jn} &= \left[-\frac{1}{2\pi} \iint_{\Sigma_W} L_n(P) e^{-s\Theta} \frac{1}{R} \frac{\partial R}{\partial N} d\Sigma_W \right]_{P_*=P_j} \end{aligned} \right\} \quad (50)$$

Equation (49) should be compared to equation (27). Note that the integrals in equation (50) are not frequency independent and therefore a large number of elements are required for convergence. On the other hand, the integrals in equation (18) are frequency independent and the convergence may be evaluated on the time-domain solution.

Another advantage of the present approach is the already mentioned possibility of truncating the wake at finite distance if the analysis is limited to $T \leq T_{\max}$ (since $\Delta\Phi_n \equiv 0$ for $T < T_{\max} < \Pi_n$). This eliminates the problem of convergence as the length of the wake goes to infinity. Other questions which have not been discussed here are the Kutta condition and the role of the diaphragms in supersonic flow. These points are analyzed in references 3 and 4 for a zeroth-order finite-element solution (i.e., potential Φ and normal wash Ψ constant within each element). Further investigations for higher order solutions are now under way.

Furthermore, the computer program SUSSA ACTS is general since it applies to subsonic and supersonic, steady, oscillatory, and fully unsteady flows around arbitrarily complex aircraft configurations.⁵ Also, the use of the hyperboloidal elements makes the program extremely flexible: for instance, the finite-element grid for the aerodynamic analysis may coincide with the structural one. Furthermore, the program is simple to use, since the only input for subsonic flow is the geometry of the aircraft (in terms of the Cartesian components of the corners of the elements) and the location of the trailing edge (the straight-vortex-line wake is automatically generated). For supersonic flow, the program makes use of diaphragms. However, preliminary results presented in reference 10 indicate that for certain cases (such as a conical body) the use of the diaphragm is not necessary. Further analysis of this point is now underway. Finally, the program is accurate and fast. This is essentially due to the high rate of convergence of the method. It may be worth noting that no special technique (such as approximate evaluation of the integrals for distant elements) has been introduced yet in order to minimize the computer time. Some of these techniques are now under investigation.

FUTURE RESEARCH

It should be noted that although SUSSA ACTS is very general, additional work remains to be done. In addition to the previously mentioned current developments, items now under investigation include the evaluation of the pressure distribution by finite-element (instead of finite-difference) method, the evaluation of the generalized forces for arbitrary three-dimensional mode shapes (integrating directly on the pressure coefficient), the use of special-purpose elements (such as hinge elements for control surfaces), and the effect of the deformation of the wake. In addition, a new program which uses

⁵Results for wing-body configurations are presented in reference 4.

first-order shape functions for Φ and Ψ is now being developed. Good results have been obtained using simple rectangular elements. Also nonlinear effects (transonic flow) are now under investigation. Finally, applications to flutter and flight mechanics are now being considered.

CONCLUDING REMARKS

In conclusion, a new approach for small-perturbation indicial aerodynamics has been presented. Taking full advantage of the finite-element method and the operational calculus the problem is simplified considerably and the relationship between potential velocity and normal wash is reduced to a system of algebraic equations with simple explicit dependence of the coefficients upon the complex frequency s . The zeroth-order formulation is embedded in the computer program SUSSA ACTS which is general, flexible, simple to use, accurate, and fast. Numerical results are in good agreement with existing ones.

REFERENCES

1. Morino, L.: A General Theory of Unsteady Compressible Potential Aerodynamics. NASA CR-2464, 1974.
2. Morino, L.: Unsteady Compressible Potential Flow Around Lifting Bodies: General Theory. AIAA Paper No. 73-196, 1973.
3. Morino, L.; and Kuo, C. C.: Subsonic Potential Aerodynamics for Complex Configurations: A General Theory. AIAA J., vol. 12, no. 2, Feb. 1974, pp. 191-197.
4. Morino, L.; Chen, L. T.; and Suci, E. O.: Steady and Oscillatory Subsonic and Supersonic Aerodynamics Around Complex Configurations. AIAA J., vol. 13, no. 3, March 1975, pp. 368-374.
5. Lomax, H.: Indicial Aerodynamics. Aerodynamic Aspects. AGARD Manual on Aeroelasticity, Pt. II, Ch. 6, W. P. Jones, ed., North Atlantic Treaty Organization (Paris).
6. Wagner, H.: Uber die Entstehung des dynamischen Auftriebes von Tragflugeln. Z. Angew. Math. & Mech., Bd. 5, Heft 1, Feb. 1925, p. 17.
7. Garrick, I. E.: Nonsteady Wing Characteristics. Section F of Aerodynamic Components of Aircraft at High Speeds. Vol. VII of High Speed Aerodynamics and Jet Propulsion, eds. A. F. Donovan and H. R. Lawrence, Princeton Univ. Press, 1957.
8. Morino, L.: Subsonic and Supersonic Indicial Aerodynamics and Aerodynamic Transfer Function for Complex Configurations. Boston University, ENG-TN-74-01, September 1974.
9. Zienkiewicz, O. C.: The Finite Element Method in Engineering Sciences. McGraw-Hill Book Co., Inc., 1971.
10. Chen, L.-T.: Steady and Oscillatory, Subsonic and Supersonic, Aerodynamic Pressure and Generalized Forces for Complex Aircraft Configurations and Application to Flutter. M. S. Thesis, Boston Univ., 1975.
11. Lessing, H. C.; Troutman, J. C.; and Menees, G. P.: Experimental Determination of the Pressure Distribution on a Rectangular Wing Oscillating in the First Bending Mode for Mach Numbers from 0.24 to 1.30. NASA TN D-344, 1960.
12. Jones, R. T.; and Cohen, D.: High Speed Wing Theory. Princeton Aeronautical Paperback, no. 6, Princeton Univ. Press, Princeton, 1960.
13. Ashley, H.; and Landahl, M.: Aerodynamics of Wings and Bodies. Addison-Wesley Pub. Co., Inc., 1965.
14. Laschka, B.: Zur Theorie der harmonisch schwingenden tragenden Flache bei Unterschallstromung. Z. Flugwiss., Jahrg. 11, Heft 7, 1963, pp. 265-292.

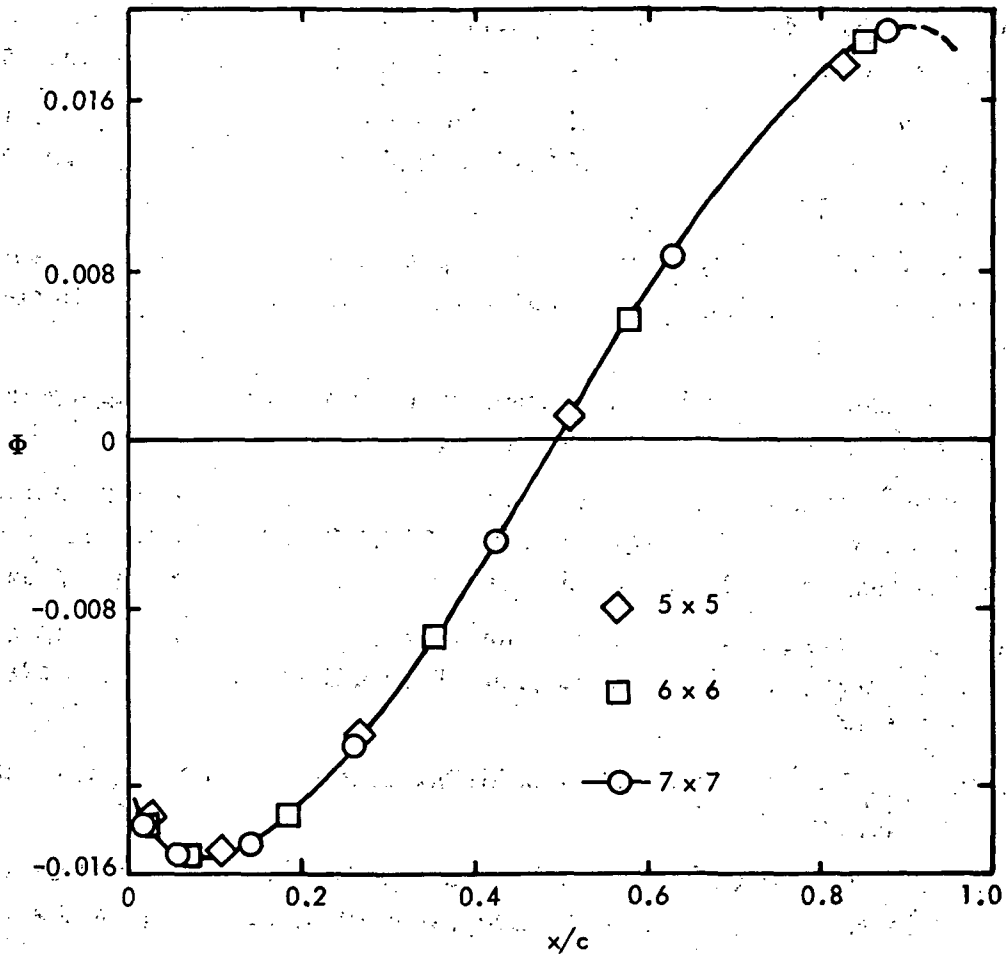


Figure 1.- Potential distribution as a function of x/c for $N_x = N_y = 5, 6,$ and 7 for rectangular wing with biconvex section in steady subsonic flow. $y = 0$; $AR = 3$; $\tau = 0.05$; $M = 0.24$; $\alpha = 0^\circ$.

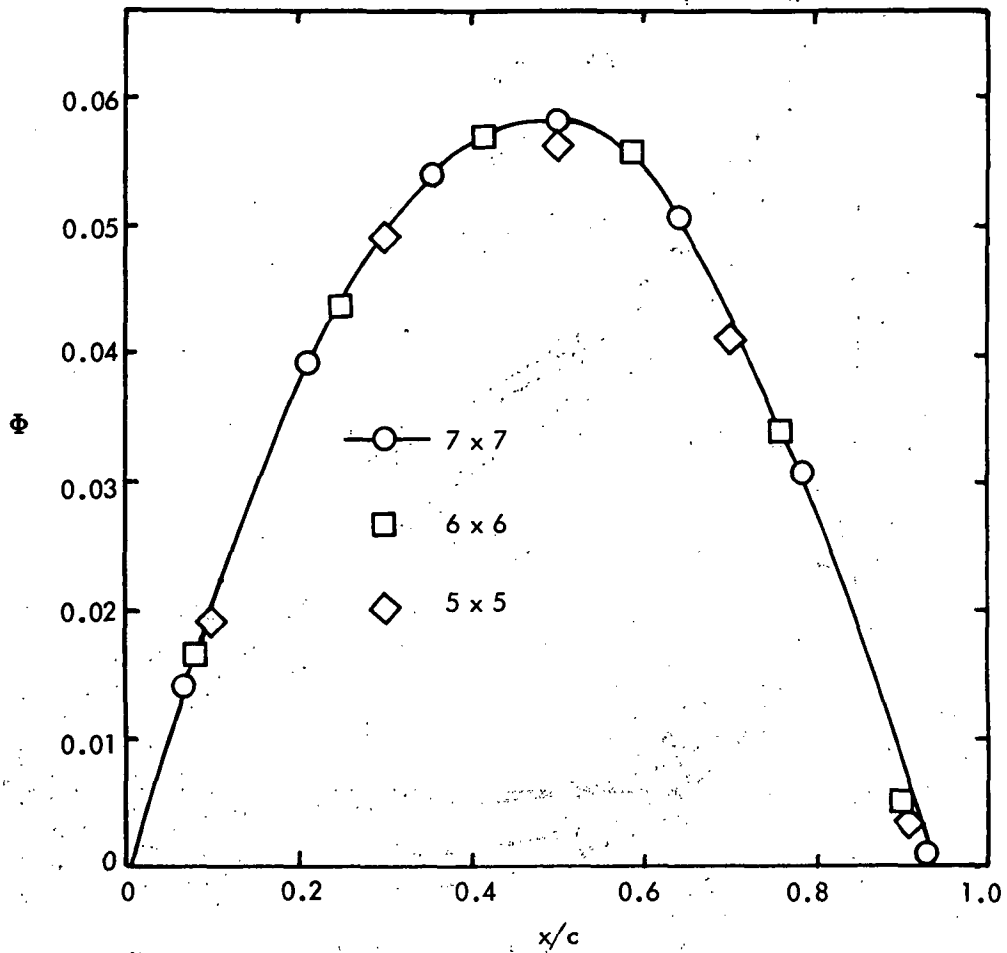


Figure 2.- Potential distribution as a function of x/c for $N_x = N_y = 5, 6,$ and 7 for rectangular wing with biconvex section in steady supersonic flow. $y = 0$; $AR = 3$; $\tau = 0.05$; $M = 1.3$; $\alpha = 0^\circ$; $N_D = 3N_x$.

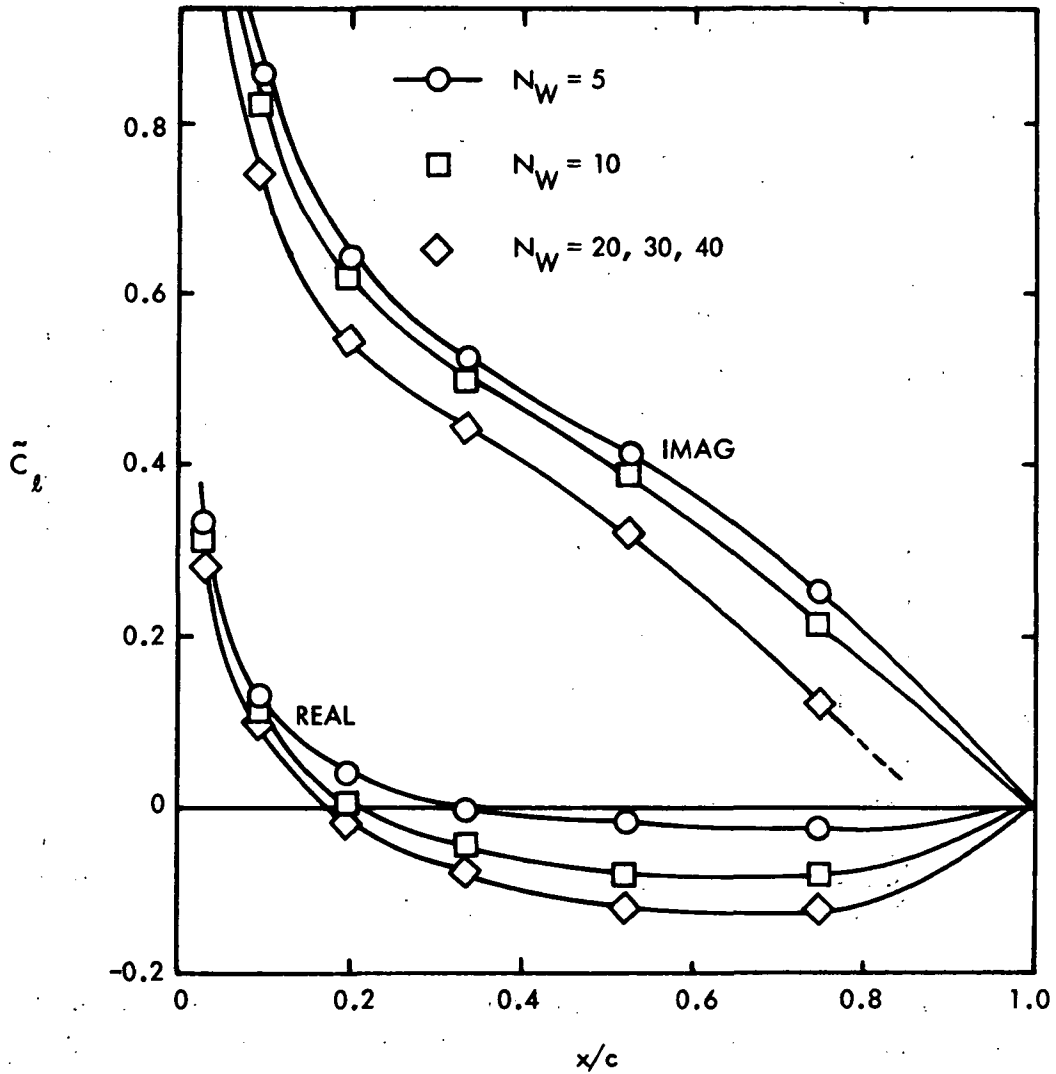


Figure 3.- Lift-distribution coefficient as a function of x/c for rectangular wing with biconvex section oscillating in bending mode in subsonic flow. $2y/b = 0.1328$; $AR = 3$; $\tau = 0.01$; $M = 0.24$; $\alpha = 0^\circ$; $k = 0.47$; $L_W = 4c$; $N_x = N_y = 7$.

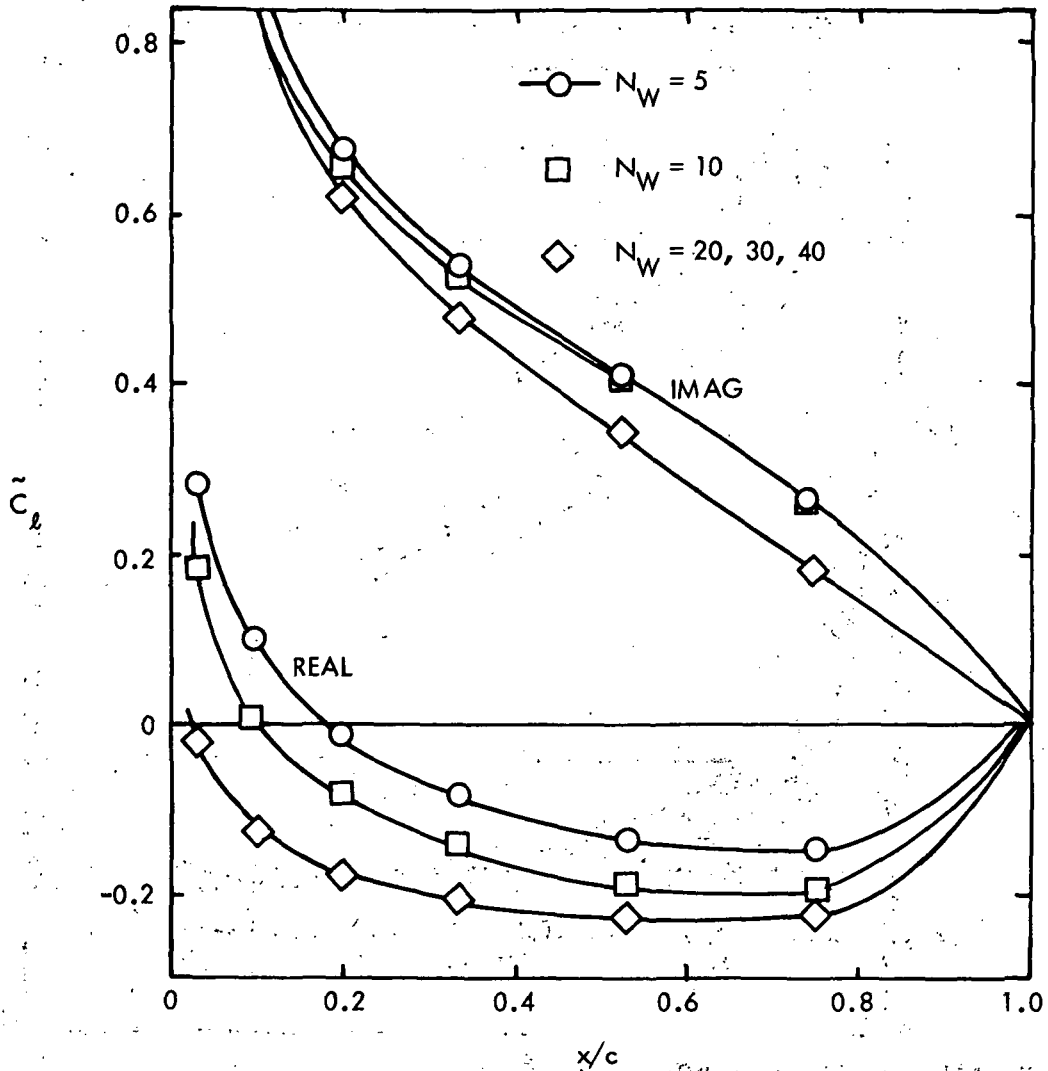


Figure 4.- Lift-distribution coefficient as a function of x/c for rectangular wing with biconvex section oscillating in bending mode in subsonic flow. $2y/b = 0.1328$; $AR = 3$; $\tau = 0.01$; $M = 0.24$; $\alpha = 0^\circ$; $k = 0.47$; $\Delta x_W = 0.1$; $N_x = N_y = 7$.

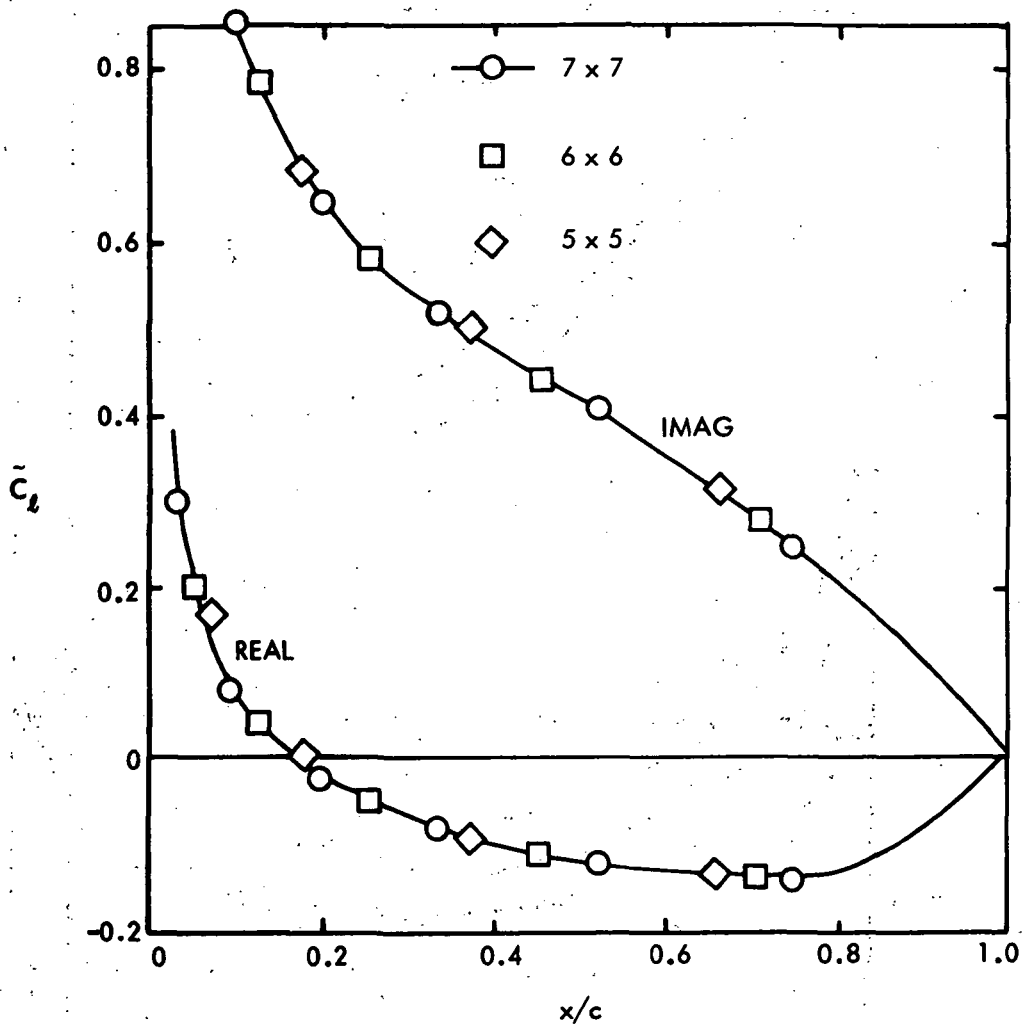


Figure 5.- Lift-distribution coefficient as a function of x/c for $N_x = N_y = 5, 6,$ and 7 for rectangular wing with biconvex section oscillating in bending mode in subsonic flow. $2y/b = 0.1328$; $AR = 3$; $\tau = 0.01$; $M = 0.24$; $\alpha = 0^\circ$; $k = 0.47$; $N_W = 30$; $L_W = 3.5c$.

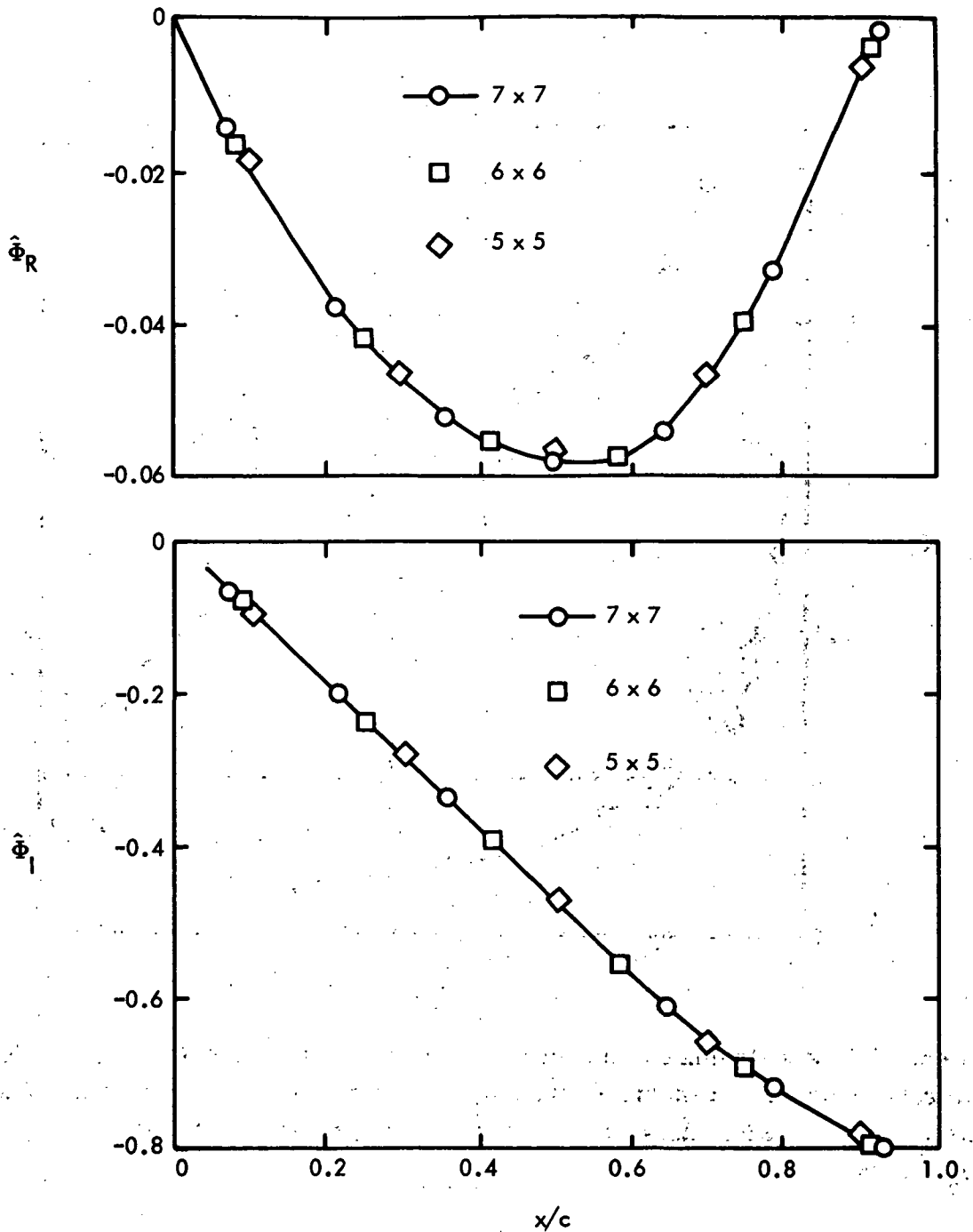
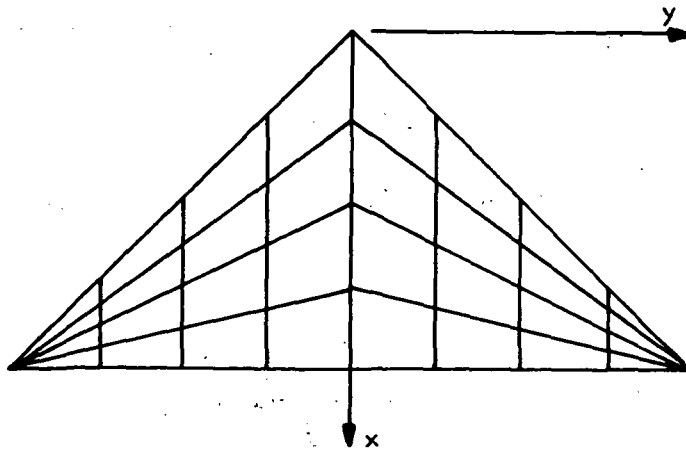
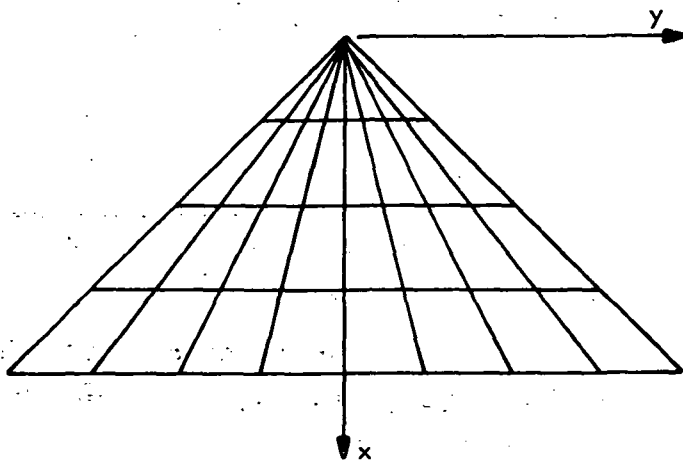


Figure 6.- Distribution of $\hat{\phi} = \tilde{\phi}e^{i\Omega MX}$ as a function of x/c for $N_x = N_y = 5, 6,$ and 7 for rectangular wing with biconvex section oscillating in bending mode in supersonic flow. $2y/b = 0.5$; $AR = 3$; $\tau = 0.01$; $M = 1.3$; $k = 0.1$; $\alpha = 0^\circ$; $N_D = 3N_x$.



(a) Used in reference 4.



(b) Used in this paper.

Figure 7.- Types of element grids for delta wings.

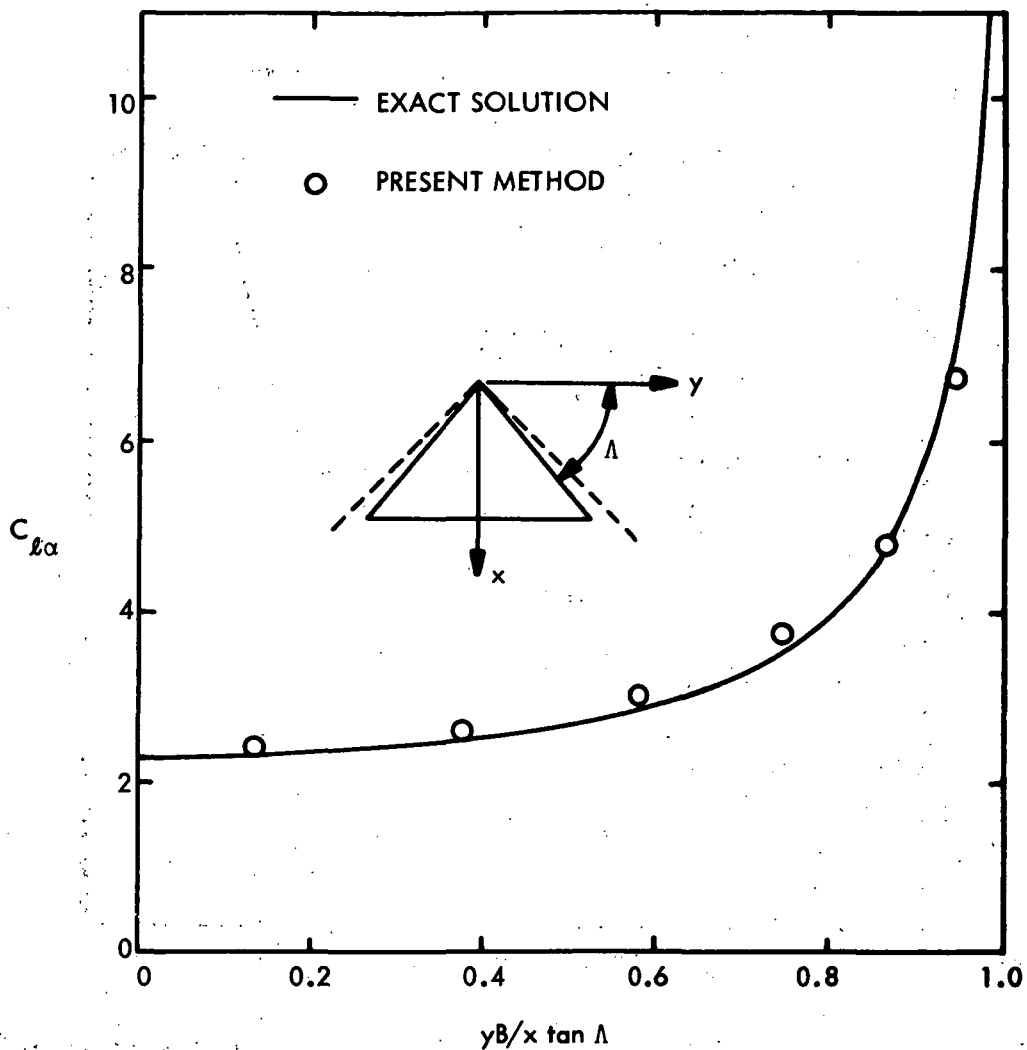


Figure 8.- Lift-distribution coefficient per unit α for delta wing with subsonic leading edge in steady supersonic flow... $B/\tan \Lambda = 0.833$; $\tau = 0$; $N_x = N_y = 7$. Comparison with exact conical-flow solution of reference 12.

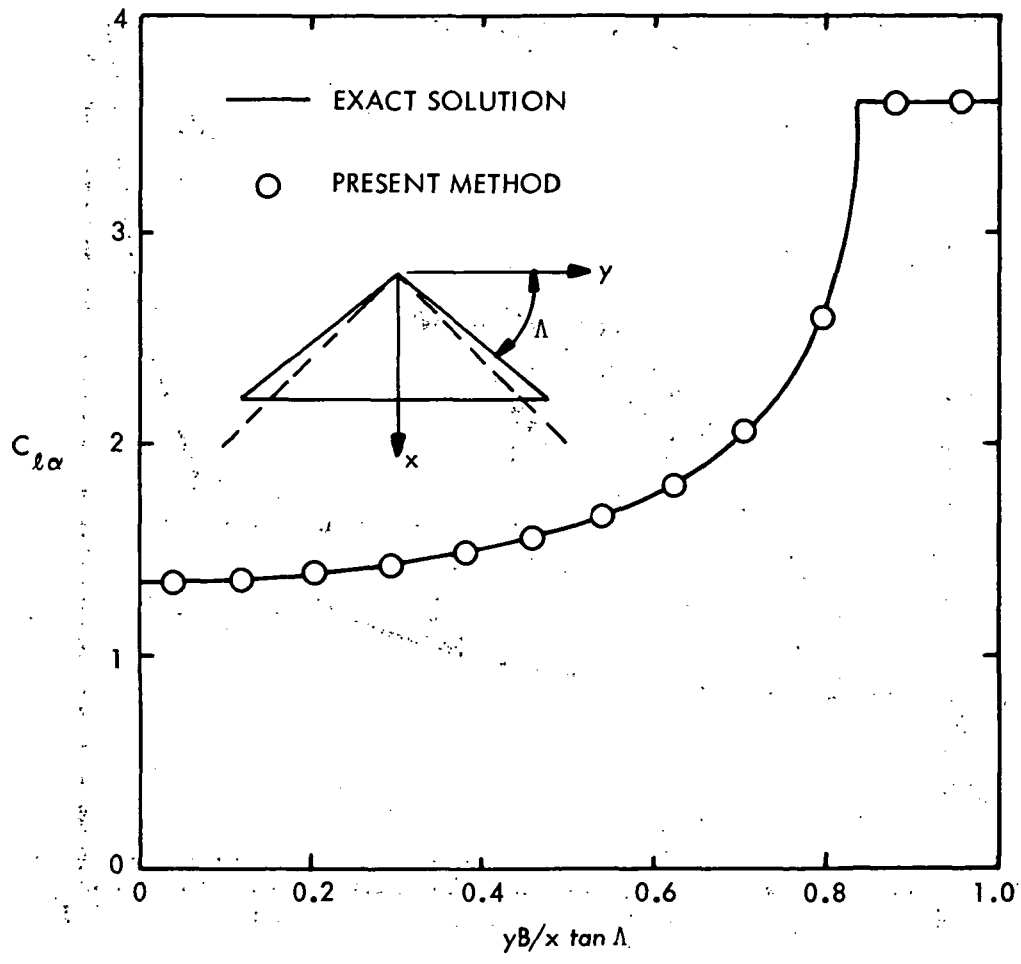


Figure 9.- Lift-distribution coefficient per unit α for delta wing with supersonic leading edge in steady supersonic flow. $B/\tan \Lambda = 1.2$; $\tau = 0$; $N_x = 8$; $N_y = 12$. Comparison with exact conical-flow solution of reference 12.

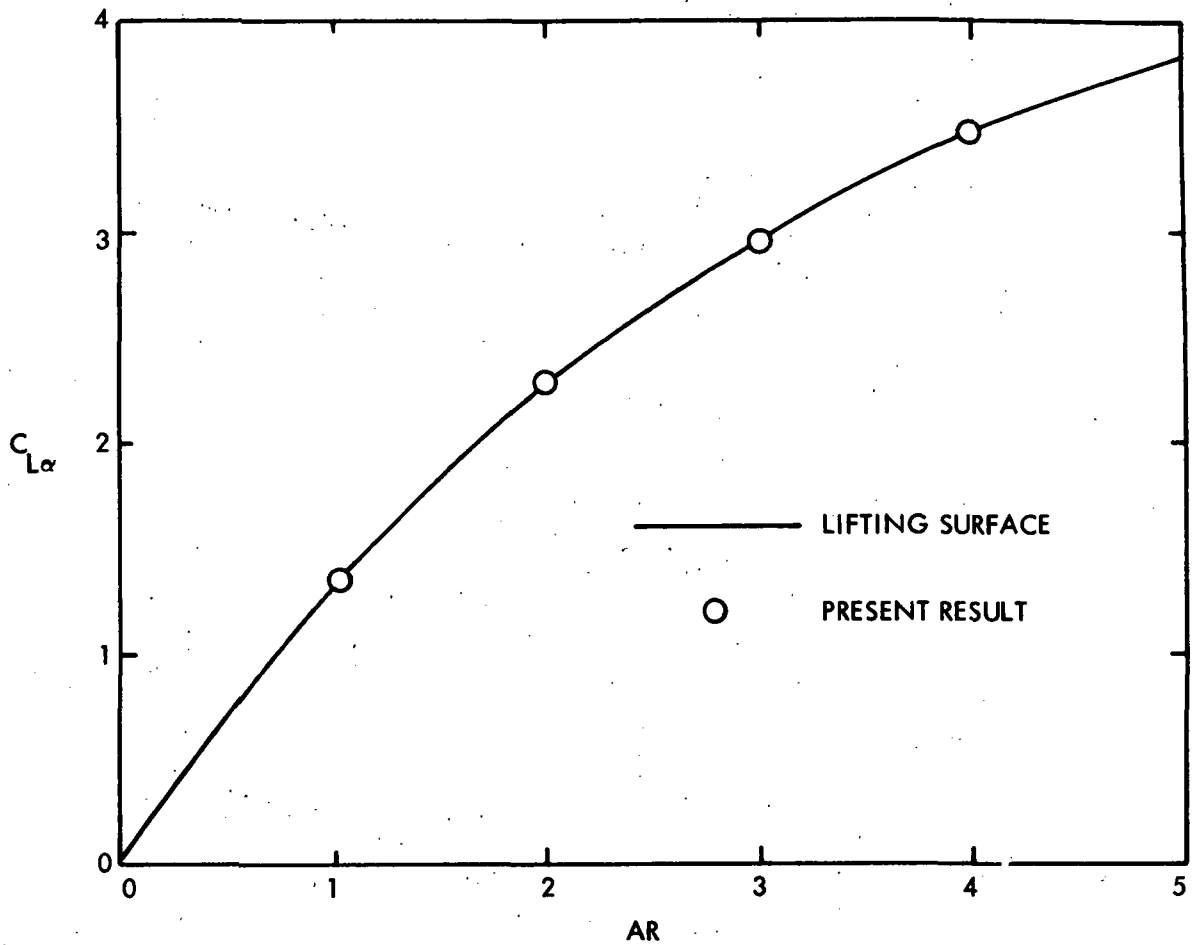


Figure 10.- Lift coefficient per unit α as a function of aspect ratio AR for delta wing in steady subsonic flow. $\tau = 0.001$; $M = 0$; $N_x = N_y = 7$. Comparison with lifting-surface theory of reference 13.

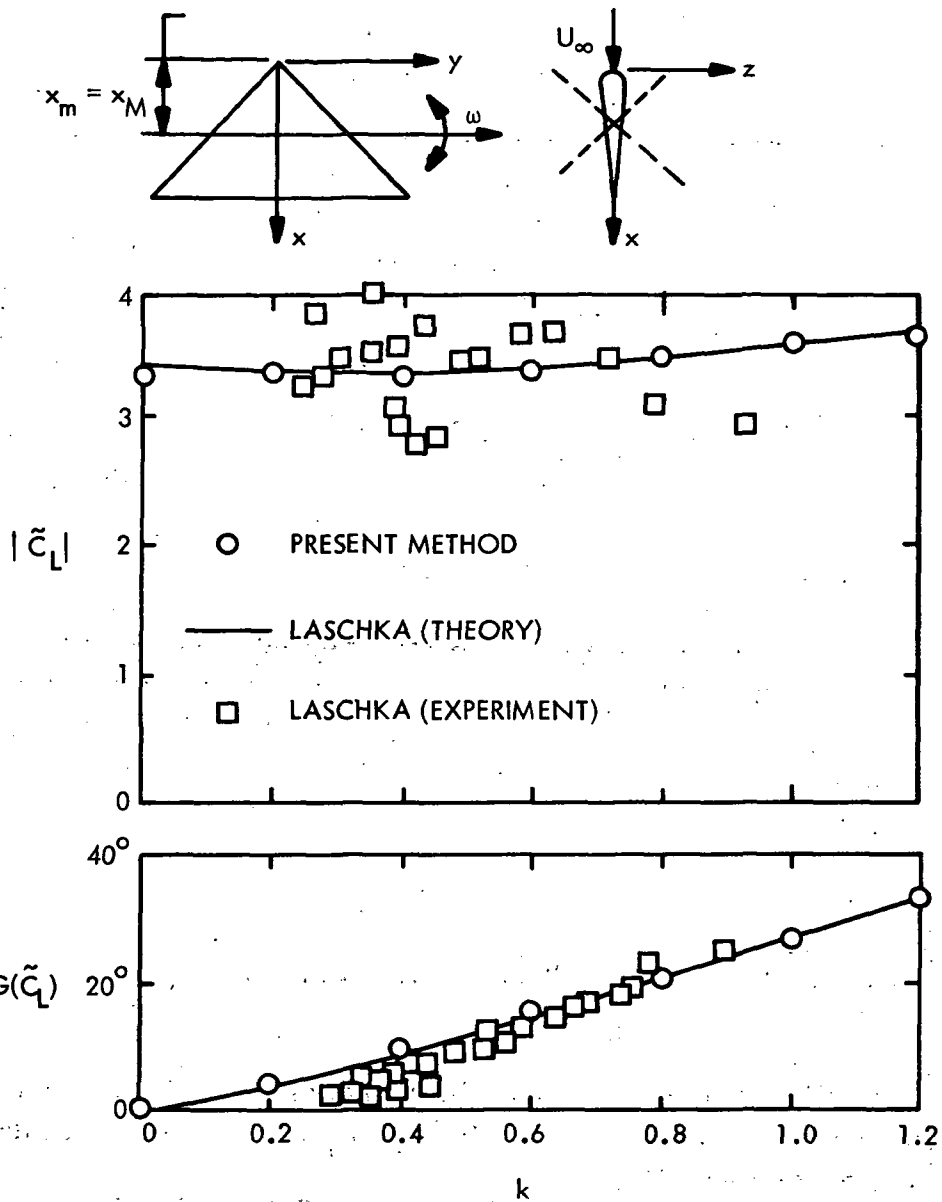


Figure 11.- Lift coefficient as a function of k for delta wing oscillating in pitch. $AR = 4$; $\tau = 0.005$; $M = 0$; $N_x = 10$; $N_y = 6$; $N_W = 20$; $L_W/c = 2$. Comparison with results of reference 14.

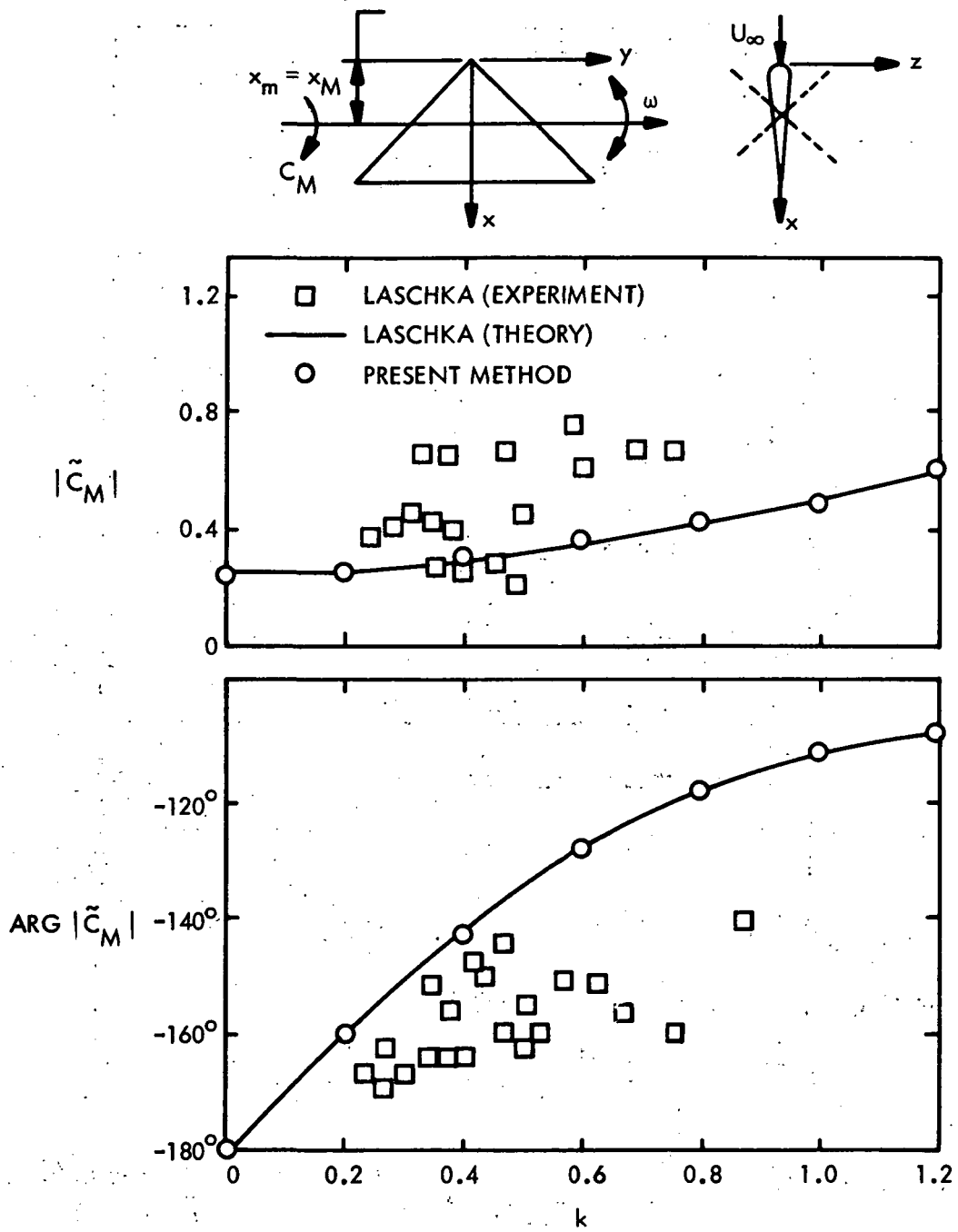


Figure 12.- Moment coefficient as a function of k for delta wing oscillating in pitch. $AR = 4$; $\tau = 0.005$; $M = 0$; $N_x = 10$; $N_y = 6$; $N_w = 20$; $L_w = 2c$. Comparison with results of reference 14.

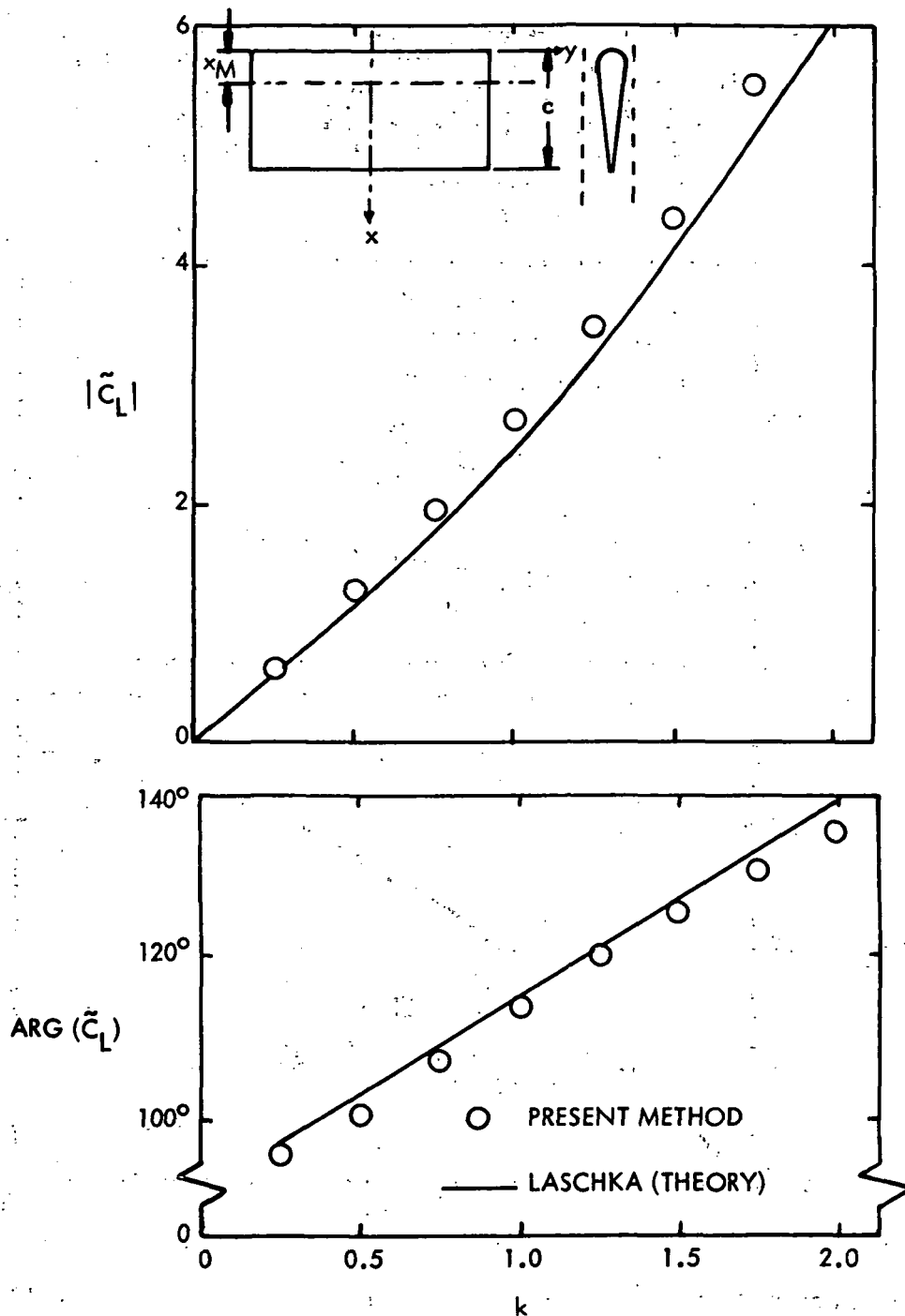


Figure 13.- Lift coefficient as a function of k for rectangular wing oscillating in plunge. $AR = 2$; $\tau = 0.001$; $M = 0$; $N_x = 10$; $N_y = 6$; $N_W = 20$; $L_W = 2c$. Comparison with results of reference 14.

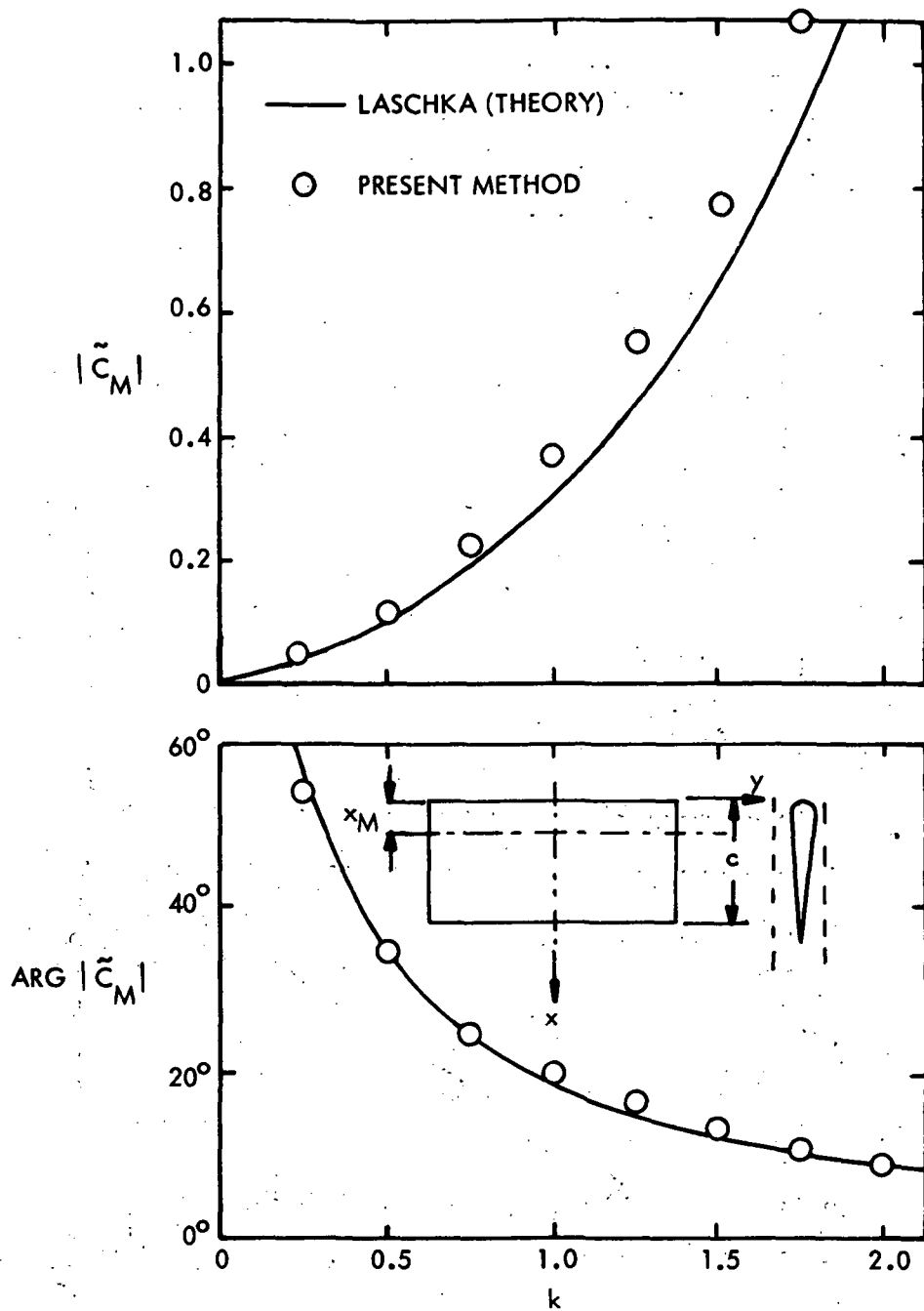


Figure 14.- Moment coefficient as a function of k for rectangular wing oscillating in plunge. $AR = 2$; $\tau = 0.001$; $M = 0$; $N_x = 10$; $N_y = 6$; $N_w = 20$; $L_w = 2c$. Comparison with results of reference 14.

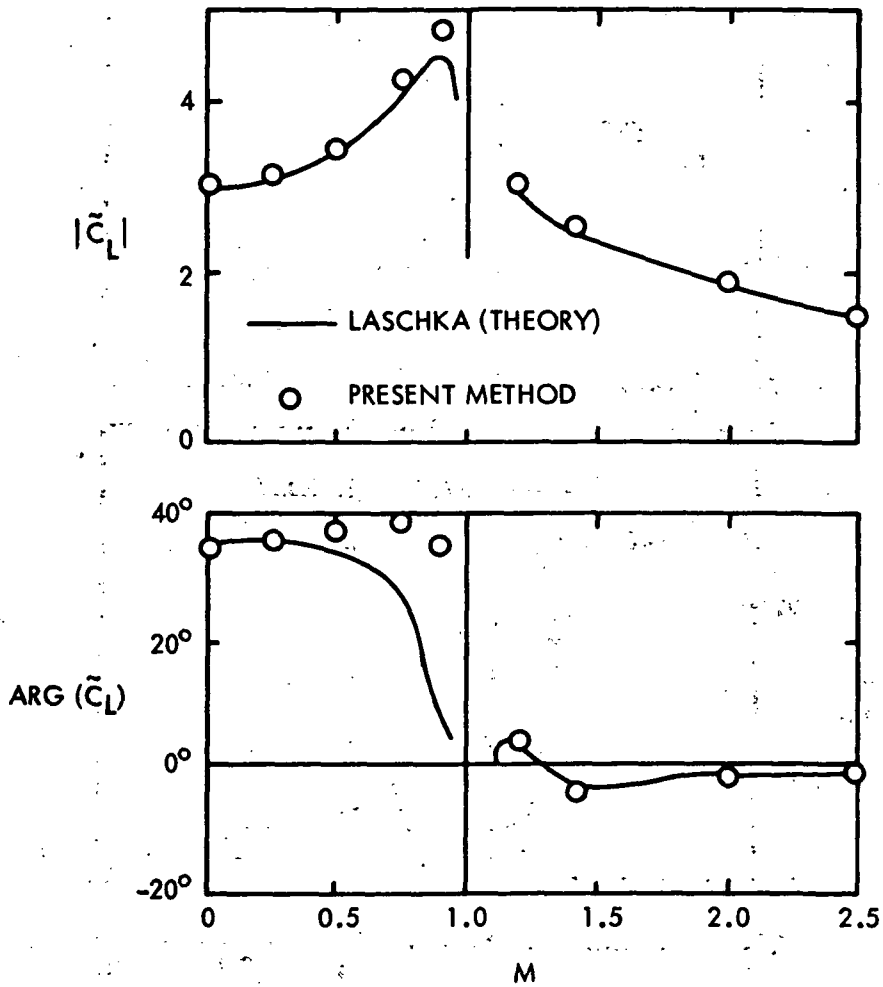
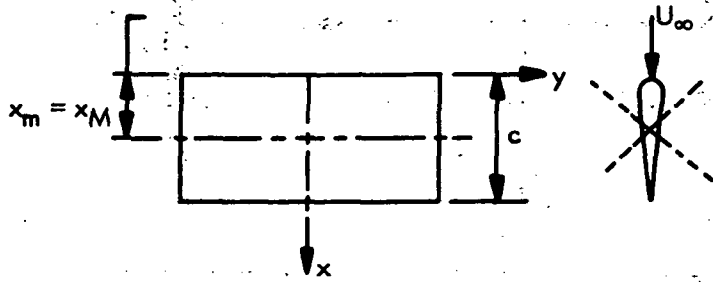


Figure 15.- Lift coefficient as a function of M for rectangular wing oscillating in pitch. $AR = 2$; $\tau = 0.001$; $k = 1$; $N_x = 10$; $N_y = 6$; $N_w = 20$; $L_w/c = 2$; $N_D = 30$. Comparison with results of reference 14.

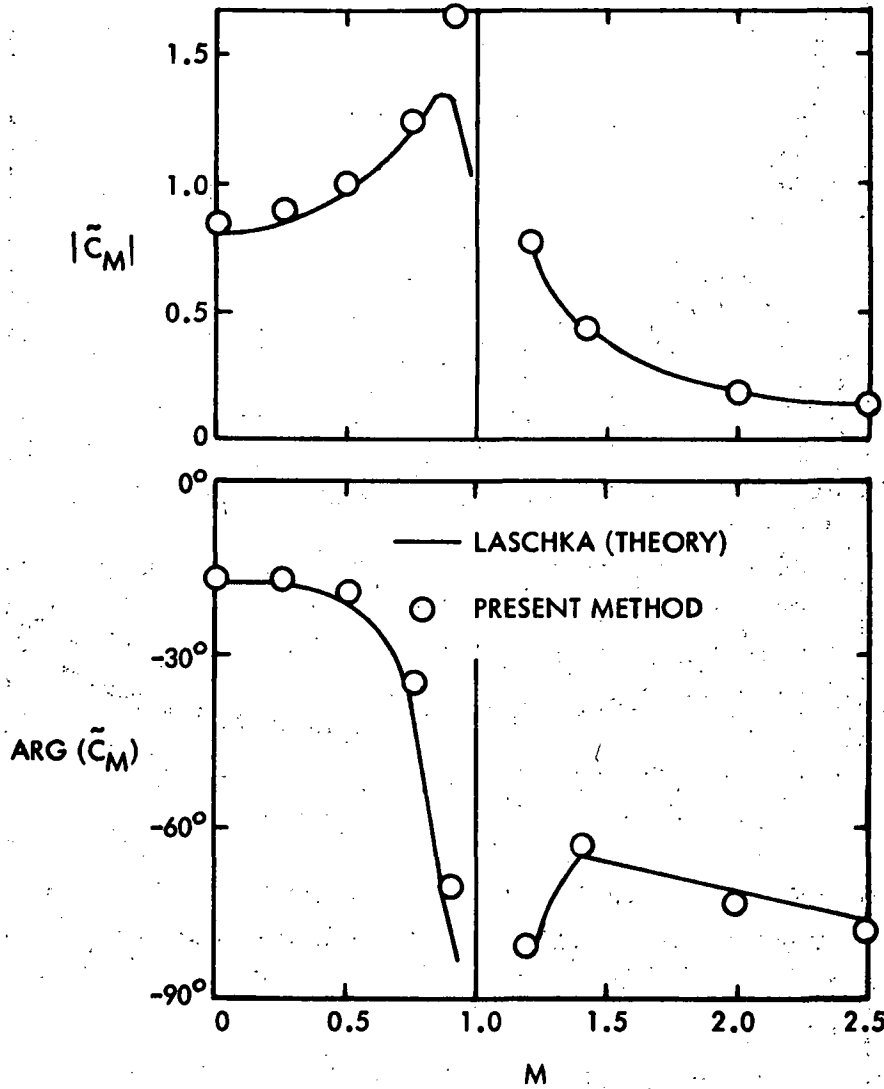
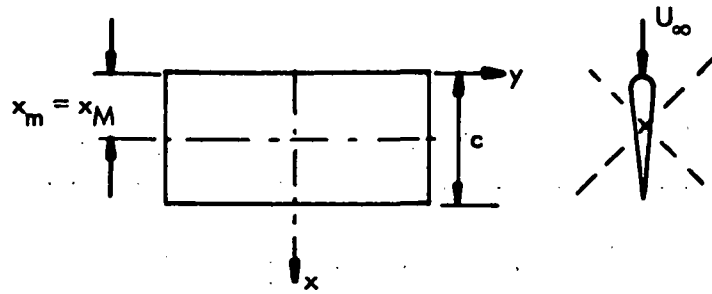


Figure 16.- Moment coefficient as a function of M for rectangular wing oscillating in pitch. $AR = 2$; $\tau = 0.001$; $k = 1$; $N_x = 10$; $N_y = 6$; $N_w = 20$; $L_w/c = 2$; $N_D = 30$. Comparison with results of reference 14.

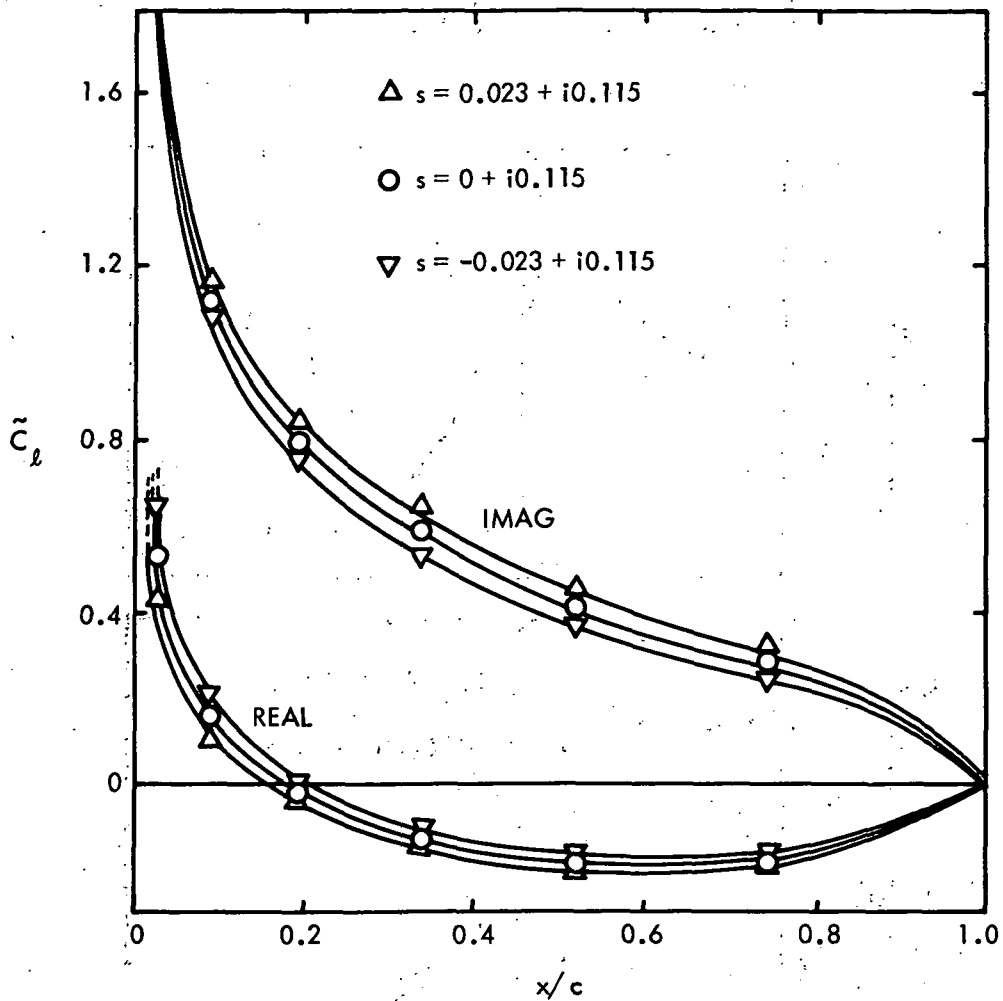


Figure 17.- Complex-frequency analysis of lift-distribution coefficient as a function of x/c for rectangular wing with biconvex section oscillating in bending mode in subsonic flow. $2y/b = 0.1328$; $AR = 3$; $\tau = 0.01$; $M = 0.24$; $\alpha = 0^\circ$; $N_x = N_y = 7$; $N_w = 30$; $L_w/c = 3.5$.

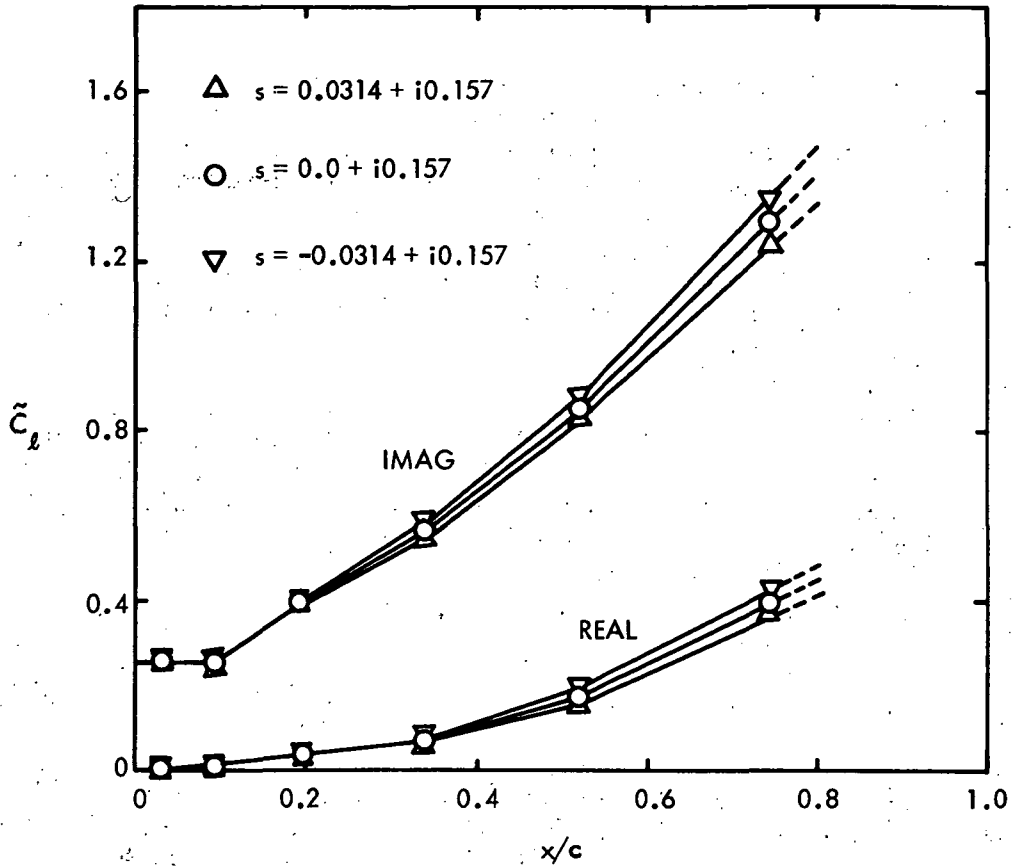


Figure 18.- Complex-frequency analysis of lift-distribution coefficient as a function of x/c for rectangular wing with biconvex section oscillating in bending mode in supersonic flow. $2y/b = 0.1328$; $AR = 3$; $\tau = 0.01$; $M = 1.3$; $\alpha = 0^\circ$; $N_x = N_y = 7$; $N_D = 21$.

THREE-DIMENSIONAL, SHOCK-ON-SHOCK INTERACTION PROBLEM*

By Paul Kutler
NASA Ames Research Center

and

Leonidas Sakell
Martin Marietta Aerospace, Orlando Division

SUMMARY

The unsteady, three-dimensional flow field resulting from the interaction of a plane shock with a cone-shaped vehicle traveling supersonically is determined using a second-order, shock-capturing, finite-difference approach. The time-dependent, inviscid gas dynamic equations are transformed to include the self-similar property of the flow, to align various coordinate surfaces with known shock waves, and to cluster points in the vicinity of the intersection of the transmitted incident shock and the surface of the vehicle. The governing partial differential equations in conservation-law form are then solved iteratively using MacCormack's algorithm.

The computer simulation of this problem, compared with its experimental counterpart, is relatively easy to model and results in a complete description of the flow field including the peak surface pressure. The numerical solution with its complicated wave structure compares favorably with available Schlieren photographs, and the predicted peak surface pressures obtained are shown to agree better with the experimental data than existing approximate theories.

INTRODUCTION

For over a decade, experimentalists and theoreticians have studied the flow field generated by the interaction of an incident shock wave (e.g., that generated by a nuclear explosion) with a vehicle traveling at supersonic speeds (see Fig. 1(a)). In the past, a great deal of attention focused on determining the strong-blast-induced transient pulse produced at the surface of the vehicle because of the belief that the forces generated might be structurally damaging. Recently, however, a new question has emerged concerning weak incident shocks ($p_3/p_1 < 2$); i.e., can such an encounter induce high-frequency disturbances capable of destroying the internal structure or appended equipment? The purpose of this paper is to compute the flow field generated by such an encounter and thus predict the resulting transient surface pressures required by the designer to determine the structural and vibrational responses of the vehicle.

*Presented as Paper 75-46 at the AIAA 13th Aerospace Sciences Meeting, Pasadena, Calif., January 20-22, 1975.

A typical flow field resulting from the interaction of a planar shock at Mach number M_i and inclination λ , and a pointed cone with half-angle σ at Mach number M_v and angle of attack α is shown in Fig. 1(b). It consists of a multitude of shock waves and slip surfaces which interact to yield a rather complicated three-dimensional, unsteady flow field. To the right of the incident shock, there exists a conical flow field generated by the vehicle in the free stream or preblast conditions, while to the left of the indicated sonic line there exists a second conical flow field generated by the body traveling in the postblast environment. Both conical flow solutions can be generated from existing three-dimensional, supersonic, steady flow computer codes. The region between these two flows which contains the intricate shock structure is the crux of the present problem and is determined here.

The region of the shock-on-shock flow field of most interest to the vehicle designer is where the transmitted incident shock strikes the body, for it is the circumferential variation of the flow variables behind this impingement line that can generate the undesirable forces. The transmitted shock at the body, depending on its inclination, can transit from a Mach reflection on the lower surface or leeward side to a regular reflection on the top surface or windward side, or result in a Mach reflection entirely around the body. Most of the interest and recent experimental testing centers around the incident shock, inclination angle that yields transition from regular to Mach reflection in the windward plane. This encounter angle is believed to result in the largest or "peak" surface pressure. Therefore, only values of the incident shock inclination near transition are considered here; thus such possibilities as the broadside encounter are ruled out.

In the past, there have been numerous theoretical attempts (refs. 1 to 9) to obtain solutions for the three-dimensional, shock-on-shock (TDSOS) problem, some of which have resulted in computer programs (refs. 6, 9 to 14). This paper does not try to summarize them by commenting on the relative merits or shortcomings of each, rather the reader is referred to papers by Aiello (ref. 15), and Kutler, Sakell, and Aiello (ref. 9) for brief summaries of some of the existing theories. In general, most of the early theories required assumptions regarding the position and structure of the existing shock waves for their model. Consequently, an incorrect assumption of the shock structure could invalidate the resulting theory. A big disadvantage of the approximate techniques that exist today for solving the TDSOS problem is that, in most of them, both the radial and circumferential gradients of the flow field are neglected. These gradients affect the position and inclination of the transmitted incident shock as it strikes the body and can therefore gravely affect shock transition and the predicted peak surface

pressure. Compared to available experimental data, all of the approximate theories grossly over-predict the value of the peak surface pressure. This over-prediction generated concern from the missile maker and led to a rather exhaustive and expensive experimental study.

There have been many experimental investigations (refs. 16 to 22) of the TDSOS problem in the past resulting in some very good Schlieren photographs of the interaction shock structure and surface pressure distributions. The most recent experimental testing (refs. 23 and 24) was performed at Holloman Air Force Base by using a rocket-propelled sled. The earlier studies involved relatively strong incident shocks while the latest tests dealt mainly with the weaker blast waves because of their greater probability of occurrence. The numerical results presented later are compared with both the earlier and most recent experimental data.

The approach used here to solve the TDSOS problem parallels that of the two-dimensional procedure (ref. 9) in which the shock-capturing technique (SCT) was employed. The self-similarity of the problem, which results from the absence of a characteristic length associated with the planar incident shock or the vehicle itself, is used to transform the three-dimensional unsteady problem to an equivalent steady flow problem. The resulting set of partial differential equations is of mixed elliptic-hyperbolic type, but is made totally hyperbolic by reintroducing the unsteady term. With correct application of the appropriate boundary conditions, the governing equations can be solved iteratively as a mixed initial boundary value problem using existing explicit, finite-difference algorithms.

The TDSOS procedure developed here properly accounts for both the radial and circumferential gradients generated by the conical flow solutions and results in a complete description of the entire flow field including the shock structure and surface pressure distribution. Unlike the experimental counterpart, a typical numerical solution is quite inexpensive and requires approximately 18 min of CDC 7600 computer time.

GOVERNING EQUATIONS

In extending the two-dimensional problem (ref. 9) to three dimensions, a cylindrical coordinate system (t, z, r, ϕ) is selected with the origin located at the vertex of the cone and ϕ measured from the lower plane of symmetry (see Fig. 2). The inclination λ of the incident shock is measured with respect to a plane perpendicular to the axis of the cone. In following the idea of aligning the coordinates with the position of

shock waves (refs. 25 and 9) to reduce the postcursor and precursor oscillations associated with the shock-capturing technique, an independent variable transformation is performed. The longitudinal coordinate z is transformed $\zeta = \zeta(t, z, r, \phi)$ so that the resulting constant ζ planes are parallel to and moving in the direction of the planar incident shock, while the radial coordinate r is transformed $\eta = \eta(t, z, r, \phi)$ to normalize the distance between the body and an outer boundary. The outer boundary is chosen so that in the two regions of known conical flow, namely, near the right- and left-hand end planes, it is a conical surface. Between these two regions, and in each meridional plane, the outer boundary is composed of a cubic polynomial that approximately parallels the peripheral shock. In addition to the shock-alignment transformations, the transformed longitudinal coordinate ζ is transformed $\mu = \mu(\zeta)$ to cluster points (ref. 26) near the impingement point on the body of the transmitted incident shock since the flow in this region is of paramount importance. Thus, including the self-similar property of the flow, the resulting independent variable transformation from (t, z, r, ϕ) to (τ, μ, η, ξ) space is

$$\left. \begin{aligned} \tau &= t \\ \mu &= \begin{cases} \zeta_{\max} \left\{ C + \frac{1}{\beta} \sinh^{-1} \left(\frac{\zeta}{\zeta_c} - 1 \right) \sinh \beta C \right\} & (\beta > 0) \\ \zeta & (\beta = 0) \end{cases} \\ \eta &= \frac{r - r_b(z)}{r_{ob}(t, z, \phi) - r_b(z)} \\ \xi &= \phi \end{aligned} \right\} \quad (1)$$

where

$$\zeta = [z - z_{p1}(t, r, \phi)]/t$$

$$C = \frac{1}{2\beta} \ln \left[\frac{1 + (e^\beta - 1) \zeta_c / \zeta_{\max}}{1 - (1 - e^{-\beta}) \zeta_c / \zeta_{\max}} \right]$$

$$z_{pl}(t, r, \phi) = \dot{z}_m t - r \cos \phi \tan \lambda$$

(equation of planes parallel to incident shock)

λ = incident shock inclination (see Fig. 2)

\dot{z}_m = velocity of left-hand boundary of computational volume = z_{min}/t (see Eq. (5))

ζ_c = value of ζ about which points are to be clustered

ζ_{max} = maximum value of ζ

β = clustering parameter; concentration of points increases with β

$r_b(z) = z \tan \sigma$ (equation of the body)

σ = cone half-angle

$r_{ob}(t, z, \phi)$ = equation of the outer boundary (discussed in the next section)

Applying this transformation to the three-dimensional, time-dependent Euler equations yields the following partial differential equation in conservation-law form:

$$U_\tau + E_\mu + F_\eta + G_\xi + H = 0 \quad (2)$$

where

$$U = U^*$$

$$E = \mu_\zeta (\zeta_t U^* + \zeta_z E^* + \zeta_r F^* + \zeta_\phi G^*)$$

$$F = \eta_t U^* + \eta_z E^* + \eta_r F^* + \eta_\phi G^*$$

$$G = G^*$$

$$H = H^* - U^* \left(\zeta_t \zeta + \mu_{\zeta_\mu} \zeta_t + \eta_{t\eta} \right) - E^* \left(\zeta_z \zeta + \mu_{\zeta_\mu} \zeta_z + \eta_{z\eta} \right) \\ - F^* \left(\zeta_r \zeta + \mu_{\zeta_\mu} \zeta_r + \eta_{r\eta} \right) - G^* \left(\zeta_\phi \zeta + \mu_{\zeta_\mu} \zeta_\phi + \eta_{\phi\eta} \right)$$

and

$$U^* = \begin{bmatrix} \rho \\ \rho u \\ \rho v \\ \rho w \\ e \end{bmatrix}, \quad E^* = \begin{bmatrix} \rho u \\ p + \rho u^2 \\ \rho uv \\ \rho uw \\ (e + p)u \end{bmatrix}, \quad F^* = \begin{bmatrix} \rho v \\ \rho uv \\ p + \rho v^2 \\ \rho vw \\ (e + p)v \end{bmatrix}$$

$$G^* = \frac{1}{r} \begin{bmatrix} \rho w \\ \rho uw \\ \rho vw \\ p + \rho w^2 \\ (e + p)w \end{bmatrix}, \quad H^* = \frac{1}{r} \begin{bmatrix} \rho v \\ \rho uv \\ \rho(v^2 - w^2) \\ 2\rho vw \\ (e + p)v \end{bmatrix}$$

$$\mu_\zeta = \begin{cases} \frac{\zeta_{\max} \sinh \beta C}{\zeta_c \beta \left\{ 1 + [(\zeta/\zeta_c - 1) \sinh \beta C]^2 \right\}^{1/2}} & (\beta > 0) \\ 1 & (\beta = 0) \end{cases}$$

$$\mu_{\zeta_\mu} = \begin{cases} \frac{-(\zeta/\zeta_c - 1) \sinh^2 \beta C}{\zeta_c \left\{ 1 + [(\zeta/\zeta_c - 1) \sinh \beta C]^2 \right\}} & (\beta > 0) \\ 0 & (\beta = 0) \end{cases}$$

$$\zeta_t = -(\dot{z}_m + \zeta)/t$$

$$\zeta_z = 1/t$$

$$\zeta_r = (\cos \phi \tan \lambda)/t$$

$$\zeta_{t\zeta} = 1/\tau$$

$$\zeta_{z\zeta} = 0$$

$$\zeta_{r\zeta} = 0$$

$$\begin{array}{ll}
\zeta_\phi = -r(\sin \phi \tan \lambda)/t & \zeta_{\phi\zeta} = \text{Num} \\
\eta_t = -\eta r_{ob_t} / (r_{ob} - r_b) & \eta_{t\eta} = \text{Num} \\
\eta_z = -r_{b_z} - \eta(r_{ob_z} - r_{b_z}) / (r_{ob} - r_b) & \eta_{z\eta} = \text{Num} \\
\eta_r = 1 / (r_{ob} - r_b) & \eta_{r\eta} = \text{Num} \\
\eta_\phi = -\eta r_{ob_\phi} / (r_{ob} - r_b) & \eta_{\phi\eta} = \text{Num}
\end{array}$$

Num implies that the partial derivative must be obtained numerically since the function $r_{ob}(t, z, \phi)$ is not known analytically. The calculation of the partial derivatives of r_{ob} are discussed in the next section.

In Eq. (2), p represents the pressure; ρ , the density; u , v , and w , the velocity components in the z , r , and ϕ directions; and e , the total energy per unit volume. The pressure, density, and velocity are related to the energy for an ideal gas by the following equation:

$$e = p/(\gamma - 1) + \rho(u^2 + v^2 + w^2)/2 \quad (3)$$

The transformed, time-dependent Euler equations are hyperbolic with respect to τ and can be solved in an iterative fashion (e.g., at $\tau = 1.0$) using an explicit, finite-difference scheme. Because of the self-similar transformation, the U_τ term in Eq. (2) approaches zero as the integration proceeds with respect to τ and results in a converged solution for large τ or after a large number of iterations at $\tau = 1.0$.

BOUNDARY AND INITIAL CONDITIONS

The transformation given by Eq. (1) results in the computational grid shown in Fig. 3. At the extremities of this computational volume, the correct boundary conditions must be applied. On the surface of the cone, the tangency condition is satisfied by using an Euler predictor/modified Euler corrector with one-sided differences in the η -direction and imposing the condition $v = u \tan \sigma$ after the corrector. Since the numerical technique is iterative with respect to the independent variable of integration, and we are only interested in the converged solution and not the transient, the body boundary condition is accurately simulated (refs. 9 and 27) by following this

procedure. At the 0° and 180° planes of symmetry, the "reflection principle" is applied using the conservative variables. Rather than use image planes to implement this boundary condition, the finite-difference scheme is modified (discussed briefly in the next section).

It is important to ensure that the permeable boundaries of the computational volume be hyperbolic (see ref. 25), i.e., the flow through these boundaries must be supersonic with respect to the self-similar coordinates. If this condition is satisfied, and the flow variables along such boundaries are known, then the associated grid points can be initialized using the known flow quantities and held fixed during the entire integration procedure. For the three-dimensional problem, this requires that z_{\min} (the distance along the z axis to the interaction of the left-hand boundary plane at $t = 1$) lie to the left of the sonic line, z_{\max} lie to the right of the incident shock, and the outer boundary encompass the peripheral shock structure (Fig. 3). The position of z_{\min} , z_{\max} , and the outer boundary depend on the conical flow at the end planes.

To determine the flow at the right- and left-hand boundaries (regions 2 and 4, respectively, in Fig. 2), an existing three-dimensional, supersonic flow field code (ref. 28) (TDSCT) was employed. Given the vehicle Mach number M_v , angle of attack α , cone half-angle σ , and ratio of specific heats γ , the TDSCT program, which treats the bow shock as a sharp discontinuity, is used to generate the conical flow field at the right-hand boundary. In addition, given the incident shock Mach number M_i and its inclination λ , the conditions behind the incident shock or the new free stream conditions M_3 and α_3 can easily be found using the normal shock relations:

$$\left. \begin{aligned}
 q_{i1} &= M_i a_1; \text{ velocity of incident shock with respect to still air} \\
 q_{i2} &= q_{i1} \left\{ 1 - [(\gamma - 1)M_i^2 + 2] / [(\gamma + 1)M_i^2] \right\}; \text{ velocity of air} \\
 &\quad \text{behind incident shock with respect to still air} \\
 p_3 &= p_1 [2\gamma M_i^2 - (\gamma - 1)] / (\gamma + 1) \\
 \rho_3 &= \rho_1 (\gamma + 1) M_i^2 [(\gamma - 1)M_i^2 + 2] \\
 a_3 &= \sqrt{\gamma p_3 / \rho_3}
 \end{aligned} \right\} \quad (4)$$

The velocity of the gas in region 3, which is a function of the velocity in region 1, is given in Table 1. The Mach number and flow direction are given by

$$M_3 = q_3 / a_3$$

and

$$\alpha_3 = \tan^{-1}(u_3/w_3)$$

These conditions are then used by the TDSCT code to generate the conical flow field at the left-hand boundary.

For the positive values of λ considered, z_{\min} (which must lie to the left of the sonic line) is determined by the flow at the body in the 180° plane, and its location can be found from

$$z_{\min} < (q_{4_b} - a_{4_b})(1 - \tan \sigma \tan \lambda) \cos \sigma \quad (5)$$

where q_{4_b} is the velocity and a_{4_b} is the speed of sound at the body in that plane. The location of z_{\max} depends on the position of the incident shock at time $t = 1$. The distance z_{is} (Fig. 3) is given by

$$z_{is} = q_{is} \cos \kappa / \cos \lambda \quad (6)$$

where q_{is} is given in Table 1 and $\kappa = \lambda + \tan^{-1}(u_{is}/w_{is})$. Since z_{is} is known, z_{\max} is selected to ensure that there is a sufficient number of longitudinal grid points to capture the Mach stem in the 0° plane.

The data describing the two conical flow solutions generated by the TDSCT program, in addition to the state variables, include the shock position r_s and the two shock slopes $\partial r_s / \partial z$ and $\partial r_s / \partial \phi$, which are used in defining the outer boundary. The position of the outer boundary near the end planes is chosen so that in both the meridional and longitudinal directions there is an equal number of grid points between the conical bow shocks and it, thus imposing a condition that $r_{ob\phi} / r_{ob} = r_{s\phi} / r_s$.

In the longitudinal direction near the end planes, the outer boundary is composed of conical rays from the vertex and cubic polynomials in between (Fig. 3). In the 0° plane, for example, the outer boundary is composed of a conical ray that extends from z_{\min} to z_{cbi} , followed by a cubic polynomial to z_{cbf} , and finally another conical ray to z_{\max} . At z_{cbi} and z_{cbf} , both r_{ob} and r_{ob_z} are continuous. Only the four constants z_{cbi} and z_{cbf} for the 0° plane and z_{cti} and z_{ctf} for the 180° plane need be specified. A simple linear interpolation between the bottom and top values is used for the analogous parameters in the remaining meridional planes. In some of the examples presented later, z_{ctf} and z_{cbi} were set equal to z_{is} based on the shock patterns of previously computed test cases.

Equation (2) requires that r_{ob_t} , r_{ob_z} , and r_{ob_ϕ} be known. For the conical portion of the outer boundary, these functions are easily determined from the known shape of the conical bow shocks ($r_{ob_t} = 0$). However, it is slightly more difficult to determine these functions for the nonconical portion.

In a given meridional plane, the cubic can be written as

$$f(\zeta) = a + b(\zeta - \zeta_1) + c(\zeta - \zeta_1)^2 + d(\zeta - \zeta_1)^3 \quad (7)$$

where

$$\zeta_1 = \text{value of } \zeta \text{ for } z_{ci}$$

$$\zeta_2 = \text{value of } \zeta \text{ for } z_{cf}$$

$$\left[\text{e.g., } z_{ci} = z_{cti} \frac{\phi}{\pi} + \left(1 - \frac{\phi}{\pi}\right) z_{cbi} \right]$$

and

$$a = r_{ob_1} / t$$

$$b = r_{ob_{z_1}} / (1 + r_{ob_{z_1}} \cos \phi \tan \lambda) = f_{\zeta_1}$$

$$x = \left[r_{ob_2} / t - r_{ob_1} / t - (\zeta_2 - \zeta_1) b \right] / (\zeta_2 - \zeta_1)^2$$

$$y = (f_{\zeta_2} - f_{\zeta_1}) / 2(\zeta_2 - \zeta_1)$$

$$d = 2(y - x) / (\zeta_2 - \zeta_1)$$

$$c = x - d(\zeta_2 - \zeta_1)$$

The quantities r_{ob_t} and r_{ob_z} are given by

$$r_{ob_t} = (f + t f_{\zeta} \zeta_t) / (1 - t f_{\zeta} \zeta_r) \quad (8)$$

and

$$r_{ob_z} = t f_{\zeta} \zeta_z / (1 - t f_{\zeta} \zeta_r) \quad (9)$$

where $f_{\zeta} = \partial f / \partial \zeta$ and ζ_t , ζ_z , and ζ_r are defined in Eq. (2).

Since the circumferential variation of the quantities a , b , c , and d in Eq. (7) is not known, r_{ob_ϕ} must be computed numerically. This is easily accomplished using the following expression and noting that r_{ob_ϕ} is zero at the planes of symmetry:

$$r_{ob_\phi} = r_{ob_\xi} - r_{ob_z} \frac{\partial z}{\partial \xi} \quad (10)$$

In Eq. (10), $r_{ob\xi}$ and $\partial z/\partial \xi$ are evaluated numerically using a second-order, central-difference formula.

With the computational volume established and the geometrical derivatives defined, the flow variables at the nodes can be initialized. Grid points that fall in region 1, i.e., between the original bow shock and the incident shock, are assigned values equal to the original free stream. For the cases considered here, p_1 and ρ_1 are set equal to 1.0, which implies that $q_1 = M_\infty \sqrt{\gamma}$. The individual velocity components for region 1 as a function of α and ϕ are given in Table 2. The conditions in region 3, i.e., behind the incident shock and above the new bow shock, are given by Eq. (4), while the velocity components of \vec{q}_3 are also presented in Table 2. Between z_{is} and z_{max} , and below the original bow shock, the right-side conical flow values (region 2) are assigned, while between z_{min} and z_{is} , and below the new bow shock, the left-side conical flow values (region 4) are assigned.

To initiate the calculation, the integration stepsize $\Delta\tau$ must be specified. Using a one-dimensional, amplification matrix, stability analysis (ref. 29) a governing stepsize for $\Delta\tau$ relative to the μ , η , and ξ directions can be found as follows:

$$\Delta\tau_\mu = \text{CN}\Delta\zeta/\mu \left| \zeta_t + u\zeta_z + v\zeta_r + \frac{w}{r}\zeta_\phi \right. \\ \left. \pm a \sqrt{\zeta_z^2 + \zeta_r^2 + (\zeta_\phi/r)^2} \right|_{\max} \quad (11a)$$

$$\Delta\tau_\eta = \text{CN}\Delta\eta \left| \eta_t + u\eta_z + v\eta_r + \frac{w}{r}\eta_\phi \right. \\ \left. \pm a \sqrt{\eta_z^2 + \eta_r^2 + (\eta_\phi/r)^2} \right|_{\max} \quad (11b)$$

$$\left. \pm a \sqrt{\eta_z^2 + \eta_r^2 + (\eta_\phi/r)^2} \right|_{\max} \quad (11c)$$

$$\Delta\tau_\xi = \text{CN}\Delta\xi / |w \pm a|_{\max}$$

where CN is the Courant number and is usually set equal to 1.0. For the calculation to be stable, the minimum of the stepsizes in Eqs. (11) is used:

$$\Delta\tau = \min(\Delta\tau_\mu, \Delta\tau_\eta, \Delta\tau_\xi) \quad (12)$$

During a typical calculation, $\Delta\tau$ is recomputed every 50 iterations, and it is generally Eq. (11b) evaluated at left-hand plane at the top ($\phi = 180^\circ$) of the outer boundary that governs the stepsize.

Equation (2) is solved iteratively at time $\tau = 1.0$ using the second-order, noncentered, finite-difference scheme devised by MacCormack (ref. 30). It has been demonstrated (refs. 9, 27, 31, and 32) that this scheme can accurately determine the correct strength and location of all discontinuities in the flow as well as the continuous regions. The version of MacCormack's scheme used here as applied to Eq. (2) is

$$\begin{aligned}
 U_{i,j,k}^{(1)} &= U_{i,j,k}^n - \frac{\Delta\tau}{\Delta\mu} (E_{i+1,j,k}^n - E_{i,j,k}^n) \\
 &\quad - \frac{\Delta\tau}{\Delta\eta} (F_{i,j+1,k}^n - F_{i,j,k}^n) \\
 &\quad - \frac{\Delta\tau}{\Delta\xi} (G_{i,j,k+1}^n - G_{i,j,k}^n) - \Delta\tau H_{i,j,k}^n
 \end{aligned} \tag{13a}$$

$$\begin{aligned}
 U_{i,j,k}^{n+1} &= \frac{1}{2} \left[U_{i,j,k}^n + U_{i,j,k}^{(1)} - \frac{\Delta\tau}{\Delta\mu} (E_{i,j,k}^{(1)} - E_{i-1,j,k}^{(1)}) \right. \\
 &\quad - \frac{\Delta\tau}{\Delta\eta} (F_{i,j,k}^{(1)} - F_{i,j-1,k}^{(1)}) - \frac{\Delta\tau}{\Delta\xi} (G_{i,j,k}^{(1)} - G_{i,j,k}^{(1)}) \\
 &\quad \left. - \Delta\tau H_{i,j,k}^{(1)} + D_{i,j,k}^n \right]
 \end{aligned} \tag{13b}$$

where

$$U_{i,j,k}^n = U(n\Delta\tau, i\Delta\mu, j\Delta\eta, k\Delta\xi)$$

$$E_{i,j,k}^n = E(U_{i,j,k}^n, n\Delta\tau, i\Delta\mu, j\Delta\eta, k\Delta\xi)$$

$$E_{i,j,k}^{(1)} = E \left[U_{i,j,k}^{(1)}, (n+1)\Delta\tau, i\Delta\mu, j\Delta\eta, k\Delta\xi \right], \text{ etc.}$$

The term $D_{i,j,k}^n$ is a fourth-order smoothing term in the μ and η directions (which does not affect the accuracy of the algorithm) and is given by

$$\begin{aligned}
D_{i,j,k}^n = & -d_{\mu} [U_{i+2,j,k}^n + U_{i-2,j,k}^n - 4(U_{i+1,j,k}^n + U_{i-1,j,k}^n) \\
& + 6U_{i,j,k}^n] - d_{\eta} [U_{i,j+2,k}^n + U_{i,j-2,k}^n - 4(U_{i,j+1,k}^n \\
& + U_{i,j-1,k}^n)] + 6U_{i,j,k}^n \quad (13c)
\end{aligned}$$

where d_{μ} and d_{η} are constants that control the degree of smoothing and are usually assigned values on the order of 0.01. The intervals $\Delta\mu$, $\Delta\eta$, and $\Delta\xi$ depend on the number of grid points selected in each direction, and the integration stepsize $\Delta\tau$ is defined in Eq. (12).

At the planes of symmetry, special differences for the G_{ξ} term of Eq. (2) are required to apply the reflection principle since an image plane is not used. The terms G_1, G_2, G_3 , and G_5 in Eq. (2) are odd functions with respect to the planes of symmetry while G_4 is an even function. In the predictor Eq. (13a) at $\phi = 180^\circ$ ($k = KM$ in Fig. 3), the forward difference of G_{ξ} , therefore, is replaced by

$$G_{\xi} = -\frac{\Delta\tau}{\Delta\xi} (G_{i,j,KM-1}^n + G_{i,j,KM}^n) \text{ for } G_1, G_2, G_3, \text{ and } G_5$$

and

$$G_{\xi} = \frac{\Delta\tau}{\Delta\xi} (G_{i,j,KM-1}^n - G_{i,j,KM}^n) \text{ for } G_4$$

In the corrector Eq. (13b) at $\phi = 0^\circ$ ($k = 1$), and the backward difference of G_{ξ} is replaced by

$$G_{\xi} = \frac{\Delta\tau}{\Delta\xi} (G_{i,j,2}^{(1)} + G_{i,j,1}^{(1)}) \text{ for } G_1, G_2, G_3, \text{ and } G_5$$

and

$$G_{\xi} = \frac{\Delta\tau}{\Delta\xi} (G_{i,j,1}^{(1)} - G_{i,j,2}^{(1)}) \text{ for } G_4$$

The geometric derivatives that are set equal to Num in Eq. (2) must be evaluated numerically for reasons explained earlier. To do this, the following second-order, finite-difference formula is used:

$$\frac{\partial A}{\partial x} = (\epsilon_1 A_{i+1} + \epsilon_2 A_i + \epsilon_3 A_{i-1}) / 2\Delta x \quad (14)$$

where

$$\epsilon_1 = -3, \epsilon_2 = 4, \epsilon_3 = -1; \text{ forward one-sided difference}$$

$$\epsilon_1 = 1, \epsilon_2 = 0, \epsilon_3 = -1; \text{ central difference}$$

$$\epsilon_1 = 3, \epsilon_2 = -4, \epsilon_3 = 1; \text{ backward one-sided difference}$$

NUMERICAL RESULTS

The experience gained in developing the two-dimensional shock-on-shock, flow field code (ref. 9) was invaluable and enabled a quick transition from an interactive graphics code to a completely automated program for the three-dimensional problem. During the course of the two-dimensional study, it was realized that the computing time for the TDSOS problem would be lengthy. The initial calculations bore this out. The computational grid for a typical TDSOS case consisted of 46 points in the longitudinal (μ) direction, 30 points in the radial (η) direction (8 of which were between the conical shocks and the outer boundary), and 10 points in the meridional (ξ) direction. A maximum of 500 iterations for the 13,800 points was required to obtain a converged solution. The computing was carried out on a CDC 7600 and required about 1 hr and 48 min of CPU time using the "initial coding."

The "initial coding" was a direct, logical extension of the FORTRAN programs that had been written for a serial machine (such as the IBM 360/67) to compute the two-dimensional problem. During the development of the TDSOS program, it was recognized that the CDC 7600 has hardware capabilities that can, if properly exercised by the software, take advantage of a high degree of both pipelining¹ and overlapping.¹ The critical part of the code, therefore, was rewritten, taking extensive advantage of this capability. Essentially, this revision consisted of two parts; first, a reorganization of the calculations so that vector operations could be identified, and, second, the introduction of a machine coded subroutine library (referred to as QUICK) that optimizes the computing of vector arithmetic. The result of the revised coding was to drastically reduce the computing time by a factor of 6 so that a typical TDSOS calculation now takes about 18 min. A report outlining the details of QUICK is in preparation.

The results generated by the TDSOS computer code yield data that describe the entire flow field. However, the distribution of the surface flow variables in the vicinity of the impinging shock (or where the peak pressure occurs) contain minor oscillations characteristic of the shock-capturing technique. Thus, to improve the prediction of the peak surface pressure from these data and at the same time check the TDSOS numerical results, a simple analytic procedure was developed to calculate the local flow at the transmitted shock impingement points. This supplemental calculation is performed in both the leeward plane ($\phi = 0^\circ$), where for the encounter angles considered, only Mach reflection can occur, and the windward plane, where either regular or Mach reflection of the transmitted incident shock can occur.

¹By pipelining, it is meant, for example, that an adding unit can be working on several add operations at the same time. By overlapping, it is meant that an adding unit, a multiplying unit, and an incrementing unit can all be operating independently and simultaneously.

The shock impingement points $(z/t)_i$, labeled R and M in Fig. 4 are determined from the numerical solution. The velocity of the impingement point with respect to the surface of the cone is then given by

$$q_i = (z/t)_i / \cos \sigma$$

Knowing this velocity, the right-side conical flow solution (region 2), and whether a Mach or regular reflection occurs (which can be determined for the most part from flow field contour plots), the post impingement flow can be determined.

For Mach reflection, the Rankine-Hugoniot relations for a normal shock are applied to easily obtain the postimpingement flow variables. For regular reflection, the inclination of the transmitted shock θ_a in Fig. 4 is required and can be measured from the computer-generated contour plots. In combination with the regular shock reflection relations, it is used to determine the flow behind and the inclination θ_b of the reflected transmitted shock. This simple analytic calculation can thus be used to define the peak pressure at the surface of the vehicle.

To verify the TDSOS numerical procedure, one of the head-on encounters experimentally tested by Merritt and Aronson (ref. 20) was modeled, namely, $M_v = 3.10$ and $M_i = 1.39$. The uniform preblast and postblast conditions required to generate the conical flow, end-plane solutions are given in Table 3. In Fig. 5, the numerical results in the form of a pressure contour plot are superimposed on a Schlieren photograph of the model during its flight. The agreement of the computed and observed shock structure is very good. An advantage of the numerical solution is that it can focus on the flow in a given meridional plane, whereas the experiment that includes both background and foreground flow cannot. Thus the structure of the experimental transmitted incident shock in Fig. 5 is lost, but can be observed from the numerical solution.

The surface pressure distribution for the numerical solution of this case and two others (see Table 3) for which experiments have been performed (ref. 22) is shown in Fig. 6. The numerical data points are plotted to indicate the degree of clustering used and the amplitude of the postcursor and precursor oscillations associated with the SCT. All three cases resulted in a Mach reflection of the transmitted incident shock, and the analytically determined postimpingement pressures or, in this case, peak pressures are shown and agree well with the numerical data.

A comparison of the peak surface pressures determined from the TDSOS code, experiment (ref. 22), and an approximate theory (ref. 20) is shown in Fig. 7. The approximate theory assumed that the axial location of the impingement point of the transmitted shock is the same as that of the intersection of the incident shock and original bow shock. This information is then used in conjunction with the normal shock relations to calculate the peak pressure. The agreement, as shown in Fig. 7, between this theory and the TDSOS results, is good mainly because the approximate theory's underlying assumption regarding the impingement point location is very good.

The latest experiment (see ref. 23) to be performed on this problem involved an 11.2° half-angle cone traveling at Mach 5 and was to have been struck by a Mach 1.23 ($p_3/p_1 = 1.6$) incident shock at encounter angles near the critical angle which results in transition from Mach to regular reflection of the transmitted shock. An effort was made to predict some of the flow fields prior to the actual experiment, and, toward this end, several numerical solutions were obtained. The specific encounter angles, including the post-blast, uniform flow conditions, are given in Table 3.

A sequence of density contour plots typical of the solutions obtained is shown in Fig. 8 for the $\lambda = 24^\circ$ encounter. The coalescence of constant density lines, indicative of a discontinuity, depicts a wave pattern in the $\phi = 0^\circ$ plane similar to that obtained for the internal corner flow problem (ref. 27), i.e., the existence of two triple points joined by a corner shock (also equivalent to the single tangent model of Smyrl (ref. 1)). Emanating from both triple points are slip surfaces, shown as a weak coalescence of lines, that eventually strike the body. The transmitted incident shock is curved (concave with respect to the vertex of the cone) due to the gradients in the radial direction and strikes the body perpendicularly. The flow in the region downstream of the transmitted shock is compressed and, therefore, the peak pressure in this plane does not occur directly behind the shock but farther downstream. In the $\phi = 80^\circ$ plane, the transmitted shock becomes convex, and compression waves begin to originate from the most curved region of the shock. With increasing ϕ , these compression waves coalesce and result in a " λ -shock" formation. As ϕ increases further, the small Mach stem of the λ -shock disappears and the transmitted incident shock, which is again concave, reflects regularly from the surface of the cone.

Pressure contours of the flow in the windward and leeward planes for the remaining encounter angles are shown in Fig. 9. For $\lambda = 0^\circ, 10^\circ,$ and 19° , Mach reflection of the transmitted shock in the windward plane occurs, while for $\lambda = 22^\circ, 24^\circ, 32^\circ,$ and 40° , regular reflection occurs. Using only the contour plots and for encounter angles near transition, it is difficult to determine whether Mach or regular reflection occurs. But in combination with the analytic technique described at the beginning of this section, the guesswork is minimized.

Plots of the surface pressure distribution in the 0° and 180° planes are shown in Fig. 10 for Mach reflection and Fig. 11 for regular reflection. The individual points are not plotted, but the degree of clustering (see Fig. 6) is the same for all cases ($\beta = 5$). The postimpingement pressures calculated from the analytic technique described earlier faired in nicely with the numerical data, and the peak pressures in the windward plane are summarized in Table 4. Note that the peak pressure in the leeward plane does not occur directly behind the impinging shock wave but is actually equal to the quasisteady conical value. For the Mach reflection cases, the pressure spike is much thinner than for the regular reflection cases (compare Figs. 10 and 11).

A comparison of the numerically predicted peak pressure as a function of the encounter angle λ with three approximate theories ((1) PRIMUS (ref. 8) - Picatinny Arsenal, (2) MDAC (ref. 6) - McDonnell Douglas Astronautics Co., and (3) MMC (see ref. 10) - Martin Marietta Corporation) and experimental data is shown in Fig. 12. All three theories overpredict the maximum peak surface pressure compared to the numerical results and the experimental data. The encounter angle for transition from Mach to regular reflection of the transmitted incident shock is different for each solution, and it is difficult to determine from the experimental data what should be the correct value of λ . Both the first and second series of Holloman sled test data are shown in this figure and appear to fall in the regular reflection regime (based on the numerical results). The three points plotted for each encounter angle of the 1974 data represent pressure data from probes at three different axial locations and are somewhat indicative of the experimental scatter.

The last sequence of sled tests at Holloman (December, 1974, January, 1975) were concerned with angle-of-attack effects. Prior to these tests numerical solutions for a Mach 5 cone with a half-angle of 11.2° and at -5° angle of attack were obtained for the three encounter angles of 18° , 22° , and 31° that were to be used in the experiment. The results of these calculations are shown in Figs. 13 and 14. Figure 13 shows the shock structure in the 0° and 180° planes for the three encounter angles. Mach reflection of the transmitted incident occurred for $\lambda = 18^\circ$ and 22° while regular reflection occurred for $\lambda = 31^\circ$. Fig. 14 shows a pressure and density contour plot of $\phi = 140^\circ$ for the $\lambda = 18^\circ$ encounter. A small Mach stem exists near the body, and a comparison of the two plots reveals a slip surface emanating from the triple point of the " λ - shock." The surface pressure distribution in the 0° and 180° planes for all three encounter angles is shown in Fig. 15. The effect of angle of attack is to yield a maximum peak pressure of more than twice that of the zero angle of attack case and also to increase the encounter angle for transition from Mach to regular reflection.

CONCLUDING REMARKS

The procedure developed to model the three-dimensional, unsteady, shock-on-shock problem accurately predicts the complicated interactive flow field, including the structure of the resulting shock pattern and the variation of the surface flow variables. The results obtained verify the early models for the shock structure suggested by Smyrl as did later experiments. Predicted values of the peak pressure in the windward plane for various encounter angles agree fairly well with existing experimental results and, in conjunction with the remaining flow field data, should provide the vehicle designer with an abundance of information. Finally, it is believed that, based on the results of these numerical solutions and the latest experimental data, the concern originally generated by the large peak pressures predicted by approximate techniques is somewhat unwarranted.

REFERENCES

1. Smyrl, J. L.: The Impact of a Shock-Wave on a Thin Two-Dimensional Aerofoil Moving at Supersonic Speed. *J. Fluid Mech.*, vol. 15, 1963, pp. 223-240.
2. Miles, J. W.: A Note on Shock-Shock Diffraction. *J. Fluid Mech.* vol. 22, 1965, pp. 95-102.
3. Blankenship, V. D.: Shock-Shock Interaction on a Slender Supersonic Cone. *J. Fluid Mech.*, vol. 22, 1965, pp. 599-615.
4. Inger, G. R.: Blast Wave Impingement on a Slender Wedge Moving at Hypersonic Speeds. *AIAA Journal*, vol. 4, no. 3, March 1966, pp. 428-435.
5. Inger, G. R.: Oblique Blast Impingement on Slender Hypersonic Bodies. *AIAA Journal*, vol. 4, no. 8, Aug. 1966, pp. 1475-1477.
6. Gardiner, C. P.: Shock-On-Shock Interaction. MDAC memorandum A3-830-BBB1-72-53, Aug. 1972.
7. Hayes, W.: Approximations for Shock-Shock Interactions at Near Normal Incidence. Aeronautical Research Associates of Princeton, Inc. Working Paper 72-18, Jan. 1973.
8. Hudgins, H. E.; and Friedman, E. M.: Shock-Shock Interaction Studies for Weak Incident Shocks. Picatinny Arsenal TR-4590, Dec. 1973.
9. Kutler, P.; Sakell, L.; and Aiello, G.: On the Shock-On-Shock Interaction Problem. *AIAA Paper* 74-524, June 1974.
10. Aiello, G. F.: A Pretest Analysis To Support Design of the Phase II Flight Test Program. Martin Marietta Aerospace, ANA 10721000-006, Mar. 1974.
11. Miller, W. D.; Schindell, L.; and Ruetenik, J. R.: Computer Program for the Calculation of the Interaction of a Blast Wave with a Non-uniform Shock Layer. Massachusetts Institute of Tech. Rep. ASRL-TR-121-2, Sep. 1964.
12. McNamara, W.: FLAME Computer Code for the Axisymmetric Interaction of a Blast Wave with a Shock Layer on a Blunt Body. *J. Spacecraft and Rockets*, vol. 4, no. 6, June 1967, pp. 790.
13. Hudgins, H. E.: SLAN, a Computer Program for Estimating Shock Interaction Loading. Feltman Research Labs, Picatinny Arsenal, TR-3676, April 1968.
14. Culotta, A.: Method of Characteristics Numerical Simulation of Unsteady Tunnel Flows with Reflections. Martin Marietta Aerospace, Orlando Division, OR 10,383, Jan. 1970.

15. Aiello, G. F.: The Broadside Encounter Between a Sharp Cone and a Planar Blast Wave. Martin Marietta Aerospace, Orlando Division, Document ANA 01900162-002, May 1973.
16. Brown, E. A.; and Mullaney, G. J.: Technique for Studying the Shock-On-Shock Problem. AIAA Journal, vol. 3, no. 11, Nov. 1965, pp. 2167-2168.
17. Brown, E. A.; and Mullaney, G. J.: Experiments on the Head-On Shock-Shock Interaction. AIAA Journal, vol. 3, no. 11, Nov. 1965, pp. 2168-2170.
18. Merritt, D. L.; and Aranson, P. M.: Wind Tunnel Simulation of Head-On Bow Wave - Blast Wave Interactions. NOLTR 67-123, Aug. 1967.
19. Baltakis, R. P.; Merritt, D. L.; and Aronson, P. M.: Two Techniques for Simulating the Interaction of a Supersonic Vehicle with a Blast Wave. NOLTR 67-154, Oct. 1967.
20. Merritt, D. L.; and Aronson, P. M.: Experimental Studies of Shock-Shock Interactions on a 9° Cone. NOLTR 67-182, Jan. 1968.
21. Merritt, D. L.; and Aronson, P. M.: Oblique Shock Interaction Experiments. NOLTR 69-108, May 1969.
22. Baltakis, F. P.: Shock Interaction Surface Pressures for Hemispherical and Conical Bodies. NOLTR 71-27, Feb. 1971.
23. Patrick, R. E.: Phase II Shock-on-Shock Experiment. Teledyne Brown Eng. Summary Rep., Dec. 1974.
24. Rutenik, J. R.; Cole, E. L.; and Jones, R. E.: Shock-On-Shock Pressure Measurements at Mach 5 from Rocket-Propelled Sled Tests, Phase I: Lateral Intercepts. KAMAN Avidyne Rep. KA TR-98, Aug. 1973.
25. Kutler, P.: Computation of Three-Dimensional, Inviscid Supersonic Flows. Computational Methods in Fluid Dynamics, Lecture Notes in Physics, AGARD, 1975. (To be published.)
26. Thomas, P. D.; Vinokur, Mr.; Bastianon, R.; and Conti, R. J.: Numerical Solution for the Three-Dimensional Inviscid Supersonic Flow of a Blunt Delta Body. AIAA Journal, vol. 10, no. 7, July 1972, pp. 887-894.
27. Kutler, P.: Supersonic Flow in the Corner Formed by Two Intersecting Wedges. AIAA Journal, vol. 12, no. 5, May 1974, pp. 577-578.
28. Kutler, P.; Reinhardt, W. A.; and Warming, R. F.: Multishocked, Three-Dimensional Supersonic Flowfields with Real Gas Effects. AIAA Journal, vol. 11, no. 5, May 1973, pp. 657-664.

29. Richtmyer, R. D.; and Morton, J. W.: Difference Methods for Initial-Value Problems. John Wiley & Sons, New York, 1967, pp. 302-303.
30. MacCormack, R. W.: The Effect of Viscosity in Hypervelocity Impact Cratering. AIAA Paper 69-354, 1969.
31. Kutler, P.; and Lomax, H.: Shock-Capturing, Finite-Difference Approach to Supersonic Flows. J. Spacecraft and Rockets, vol. 8, no. 12, Dec. 1971, pp. 1175-1182.
32. Kutler, P.; Warming, R. F.; and Lomax, H.: Computation of Space Shuttle Flowfields Using Noncentered Finite-Difference Schemes. AIAA Journal, vol. 11, no. 2, Feb. 1973, pp. 196-204.

Table 1 Cartesian velocity components (see Fig. 2) of regions 1 and 3, and the incident shock with respect to the cone ($\vec{q}_j = u_j \hat{i}_x + w_j \hat{i}_z$)

j	u_j	w_j
1	$q_1 \sin \alpha$	$q_1 \cos \alpha$
3	$q_1 \sin \alpha - q_{i_2} \sin \lambda$	$q_1 \cos \alpha + q_{i_2} \cos \lambda$
is	$q_1 \sin \alpha - q_{i_1} \sin \lambda$	$q_1 \cos \alpha + q_{i_1} \cos \lambda$

Table 2 Cylindrical velocity components of regions 1 and 3 with respect to the cone ($\vec{q}_j = u_j \hat{i}_z + v_j \hat{i}_r + w_j \hat{i}_\phi$)

j	u_j	v_j	w_j
1	$q_1 \cos \alpha$	$-q_1 \sin \alpha \cos \phi$	$q_1 \sin \alpha \sin \phi$
3	$q_3 \cos \alpha_3$	$-q_3 \sin \alpha_3 \cos \phi$	$q_3 \sin \alpha_3 \sin \phi$

Table 3 Uniform flow conditions in regions 1 and 3 for computational cases

$M_V = M_1$	α_1	σ	M_1	λ	M_3	α_3
3.10	0.0	9.0	1.39	0.0	3.27484	0.0
3.10	0.0	9.0	1.61	0.0	3.32252	0.0
3.12	0.0	9.0	2.07	0.0	3.36277	0.0
5.00	0.0	11.2	1.23	0.0	4.99344	0.0
				10.0	4.98882	-0.64850
				19.0	4.97685	-1.21885
				22.0	4.97125	-1.40404
				24.0	4.96709	-1.52577
				32.0	4.94703	-1.99609
				40.0	4.92180	-2.43389

Table 4 Peak surface pressure: $M_V = 5$, $\alpha = 0^\circ$, $\sigma = 11.2^\circ$ and $M_1 = 1.230563$; $\phi = 180^\circ$, $t = 1.0$

λ	p_p/p_1	$(z/t)_i$	θ_a	θ_b	M_b
Mach reflection:					
0.0	4.61	7.337	---	---	---
10.0	5.91	7.546	---	---	---
19.0	7.72	7.806	---	---	---
Regular reflection:					
22.0	6.85	7.913	45.3	54.3	0.99758
24.0	6.66	7.999	43.5	48.2	1.10434
32.0	6.57	8.398	36.5	34.8	1.45522
40.0	6.55	8.929	30.0	26.4	1.87248

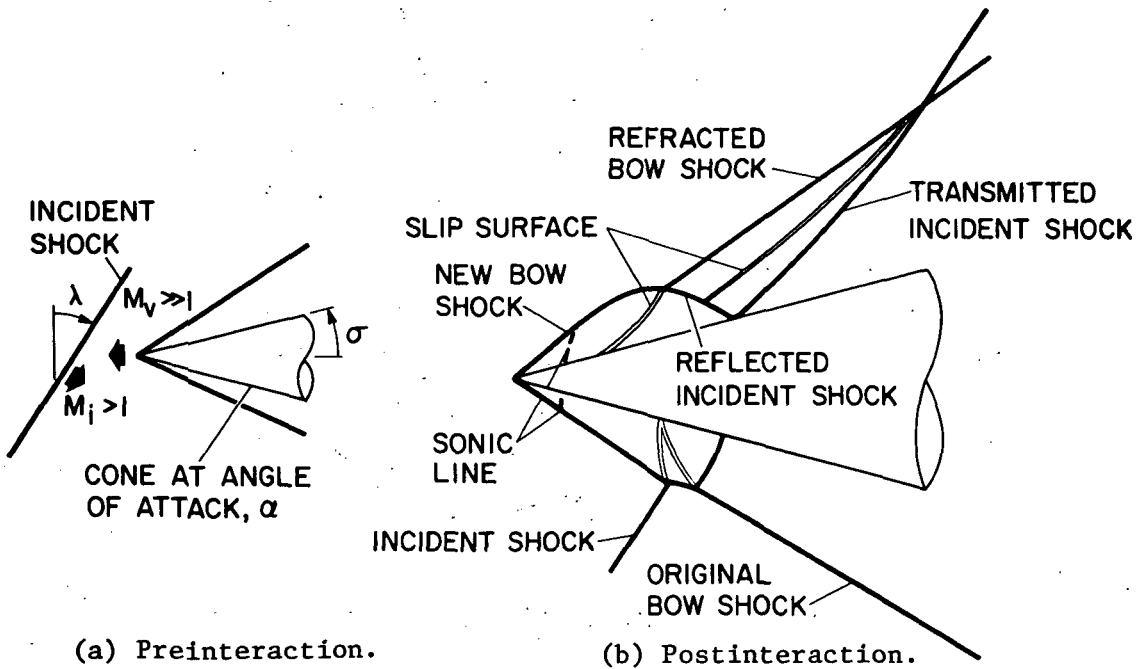


Figure 1.- Preinteraction and postinteraction wave patterns for the three-dimensional shock-on-shock problem.

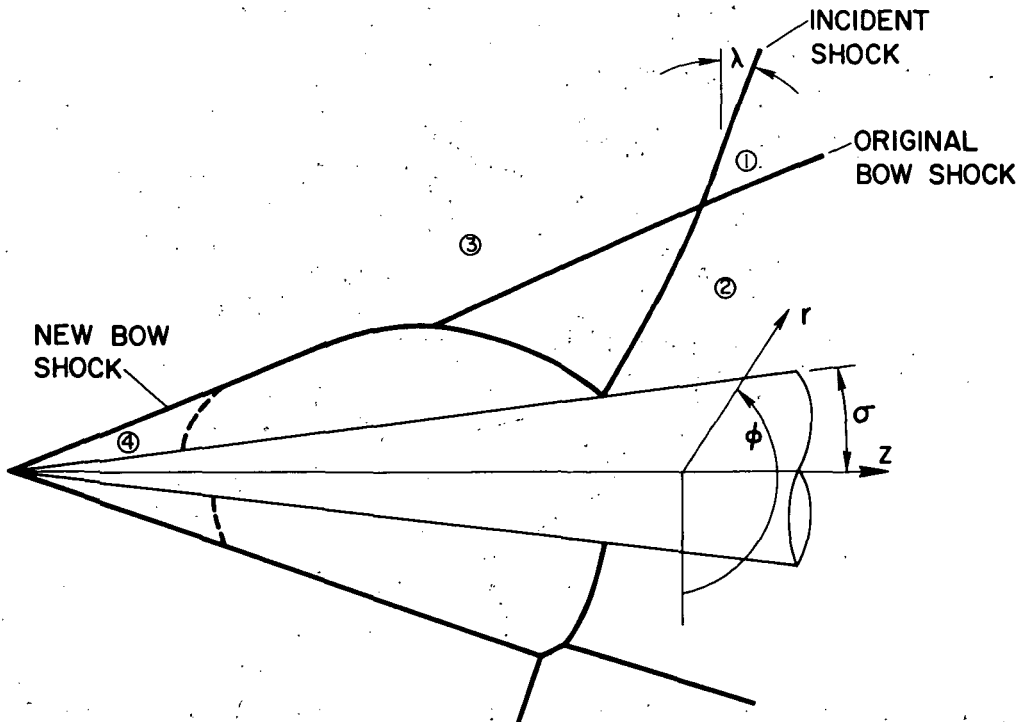


Figure 2.- Coordinate system.

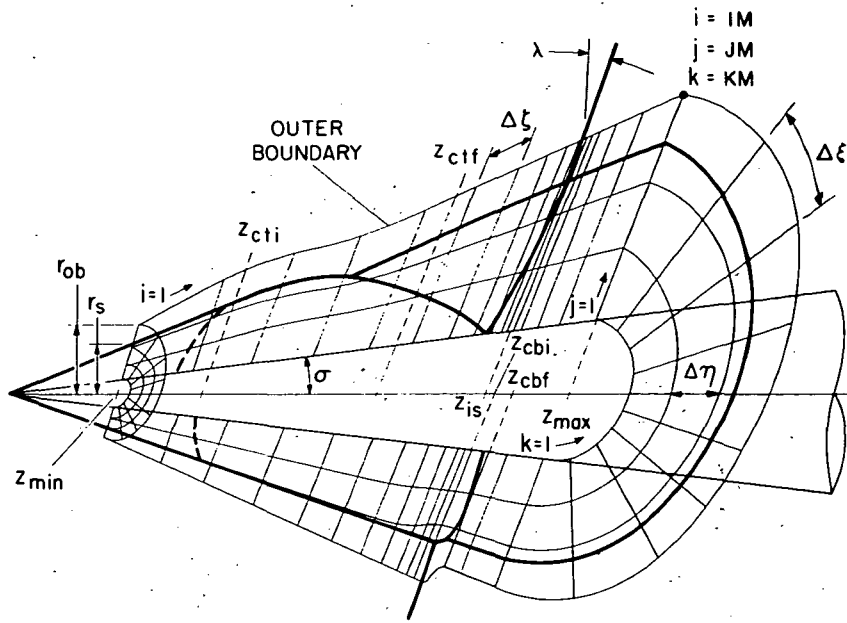


Figure 3.- Computational volume.

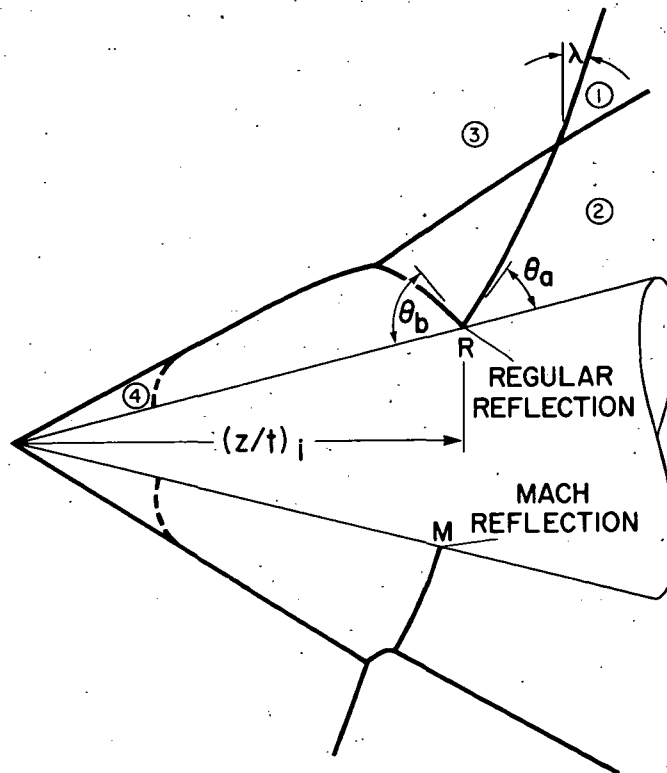


Figure 4.- Analytic calculation for regular or Mach reflection of transmitted incident shock at the body.

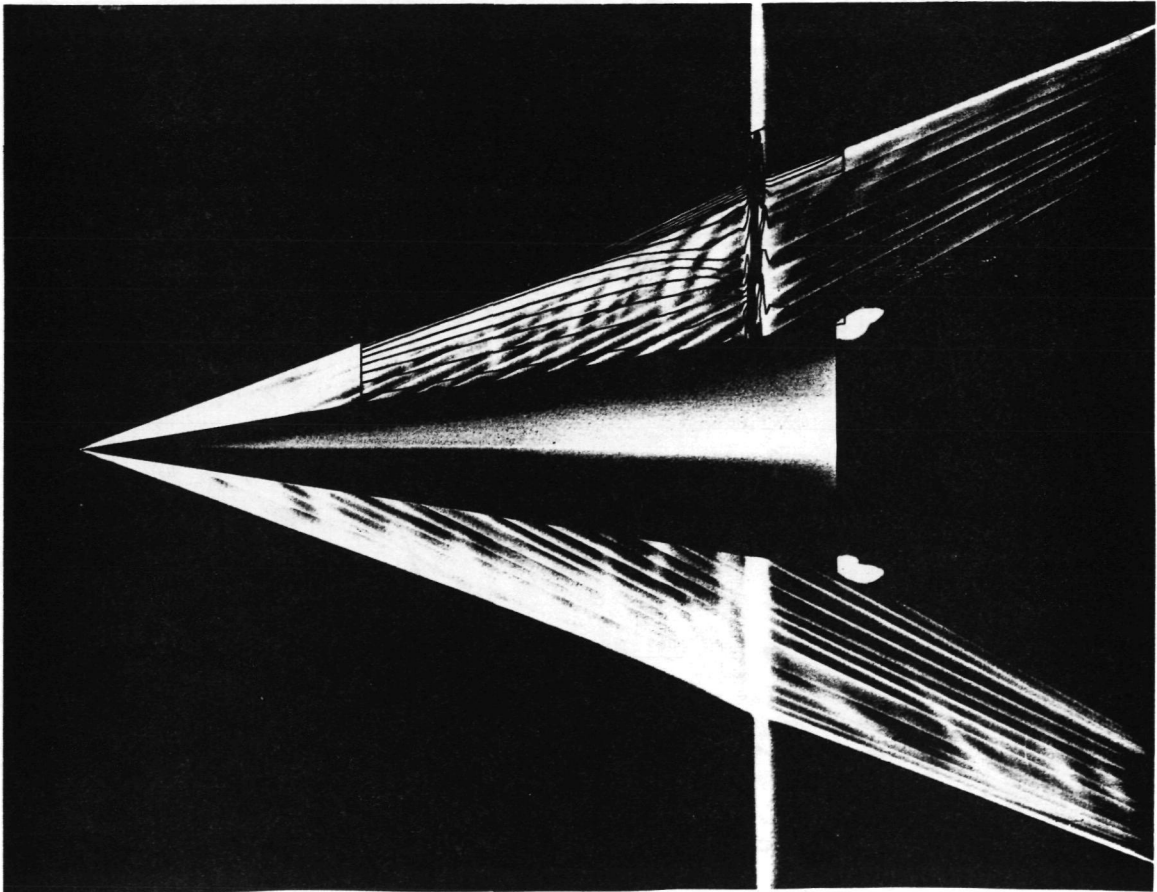


Figure 5.- Comparison of numerical solution with experiment for head-on encounter, $M_V = 3.1$, $\alpha = 0^\circ$, $\sigma = 9^\circ$, $M_i = 1.39$, $\lambda = 0^\circ$.

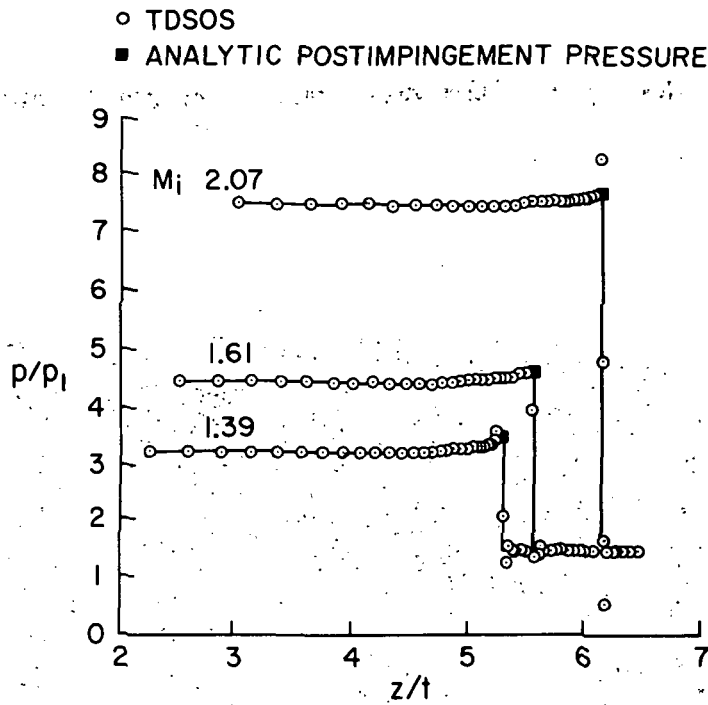


Figure 6.- Surface pressure distribution for head-on encounters;
 $M_v = 3.1$, $\alpha = 0^\circ$, $\sigma = 9^\circ$, $\lambda = 0^\circ$.

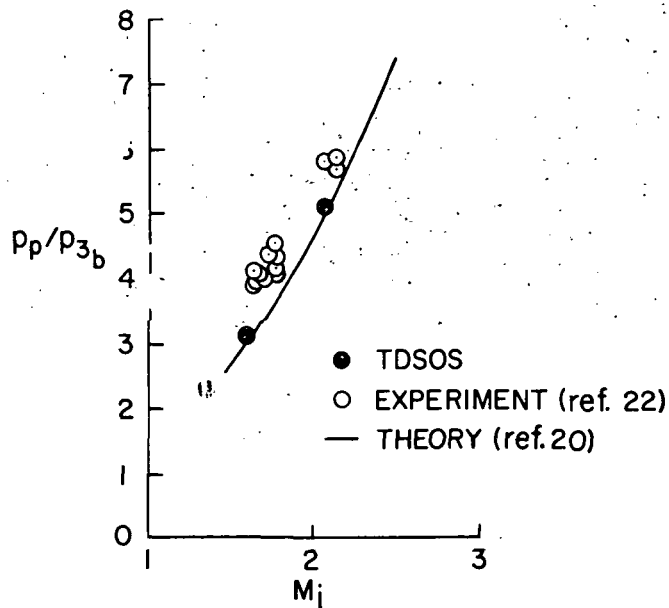


Figure 7.- Variation of peak surface pressure with incident shock Mach number for head-on encounters; $M_v = 3.1$, $\alpha = 0^\circ$, $\sigma = 9^\circ$, $\lambda = 0^\circ$.

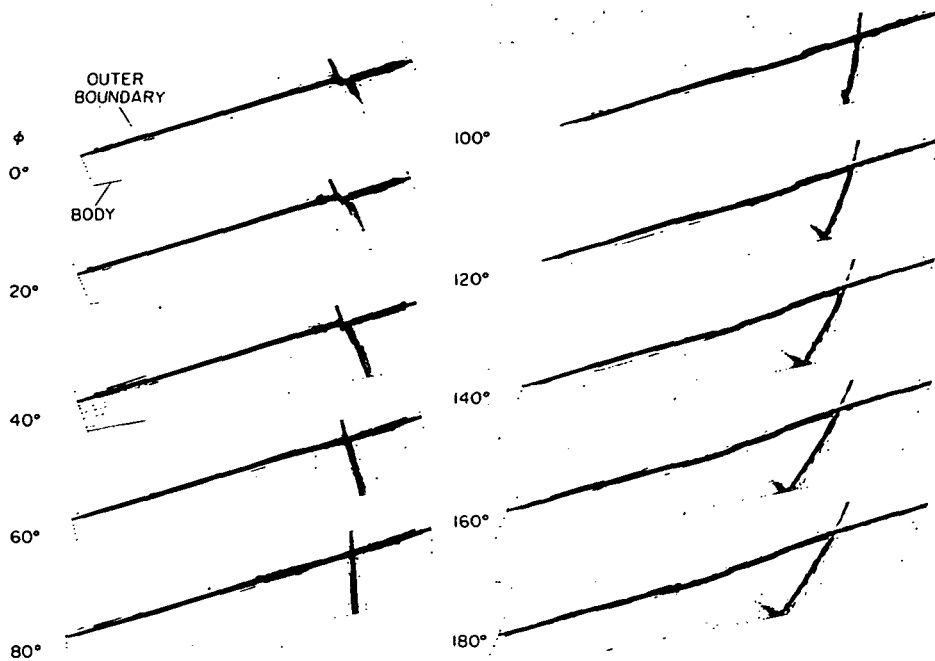


Figure 8.- Density contours in all meridional computational planes for an oblique encounter; $M_V = 5.0$, $\alpha = 0^\circ$, $\sigma = 11.2^\circ$, $M_i = 1.23$, $\lambda = 24^\circ$.

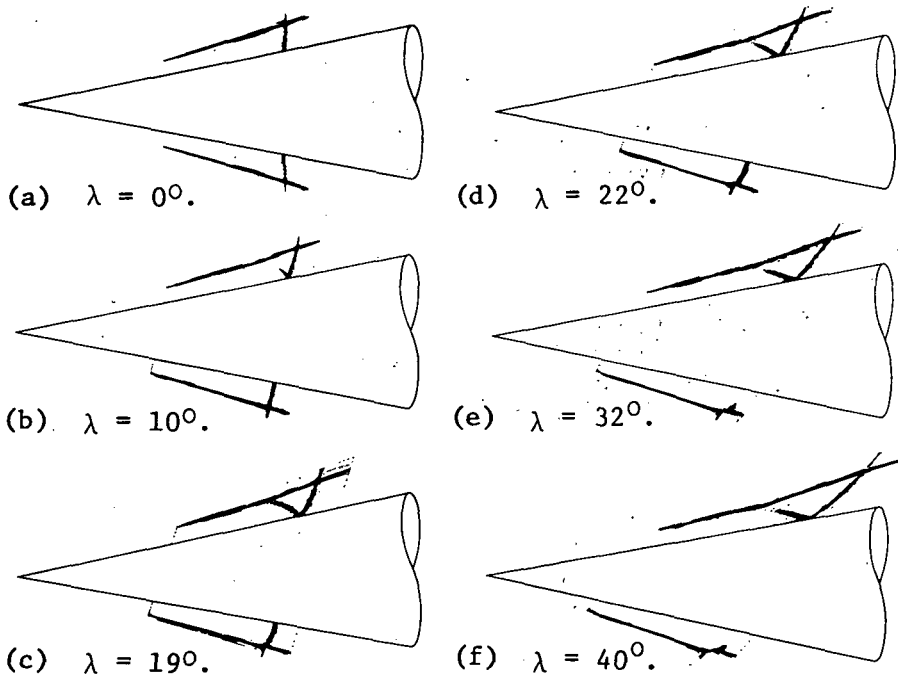


Figure 9.- Pressure contours of windward and leeward computational planes for oblique encounters; $M_V = 5.0$, $\alpha = 0^\circ$, $\sigma = 11.2^\circ$, $M_i = 1.23$.

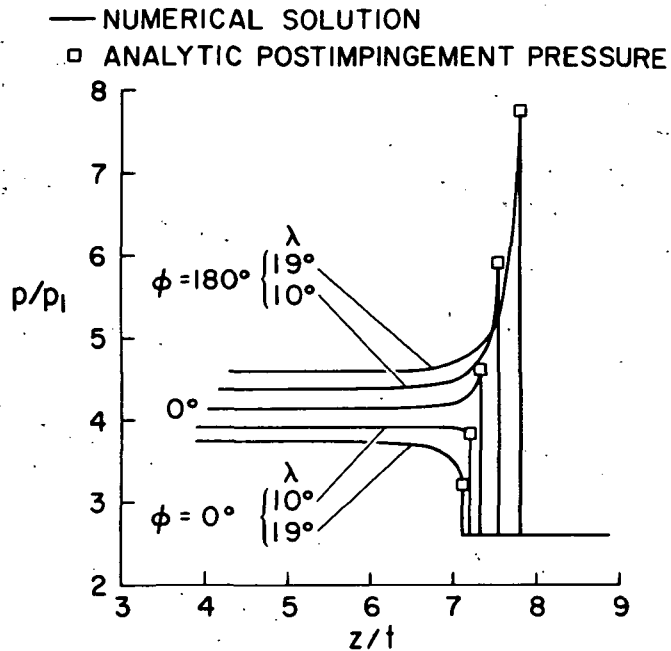


Figure 10.- Surface pressure distribution in leeward ($\phi = 0^\circ$) and windward ($\phi = 180^\circ$) planes (Mach reflection); $M_V = 5$, $\alpha = 0^\circ$, $\sigma = 11.2^\circ$, $M_i = 1.23056$ ($p_3/p_1 = 1.6$), $t = 1.0$.

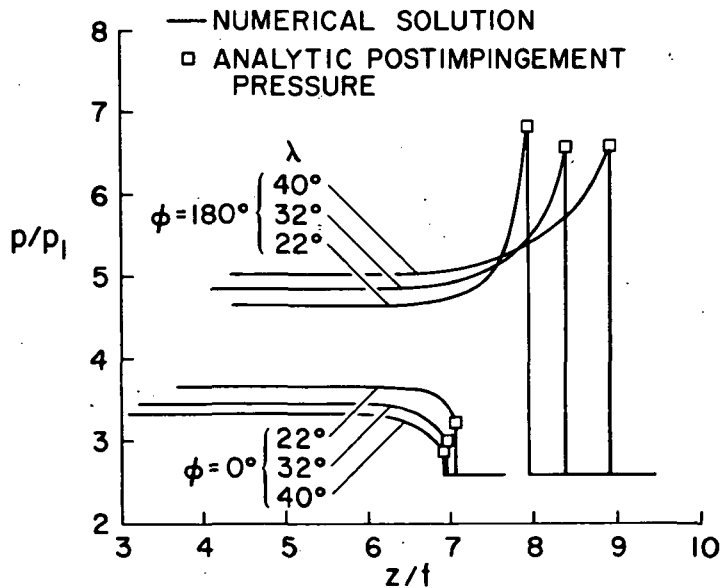


Figure 11.- Surface pressure distribution in leeward ($\phi = 0^\circ$) and windward ($\phi = 180^\circ$) planes (Regular reflection); $M_V = 5$, $\alpha = 0^\circ$, $\sigma = 11.2^\circ$, $M_i = 1.23056$ ($p_3/p_1 = 1.6$), $t = 1.0$.

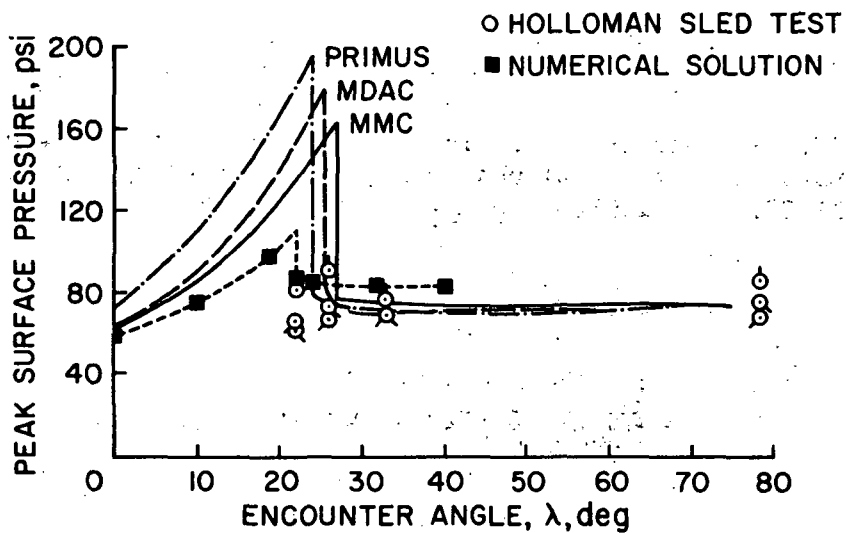


Figure 12.- Comparison of peak surface pressure vs encounter angle with experiment and an approximate theory; $M_v = 5$, $\alpha = 0^\circ$, $\sigma = 11.2^\circ$, $M_i = 1.23056$ ($p_3/p_1 = 1.6$), $t = 1.0$.

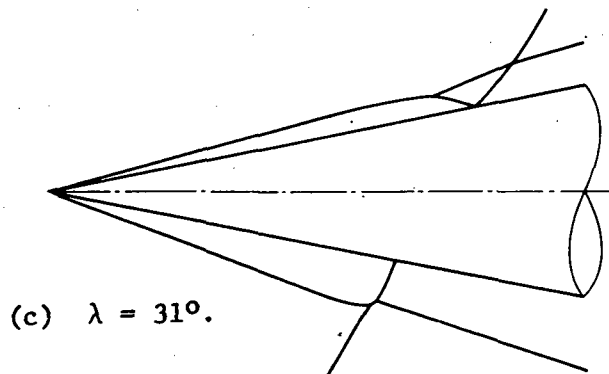
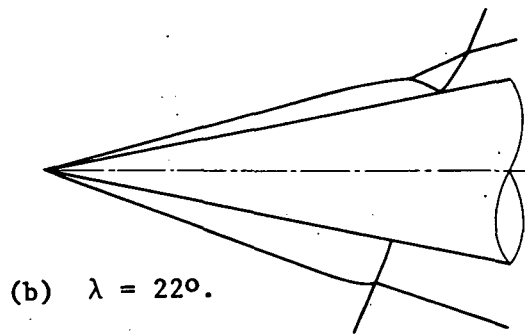
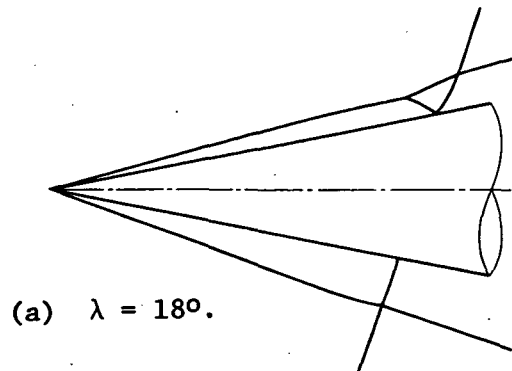


Figure 13.- Shock structure in windward and leeward planes;
 $M_V = 5$, $\sigma = 11.2^\circ$, $\alpha = -5^\circ$; $M_i = 1.54$.

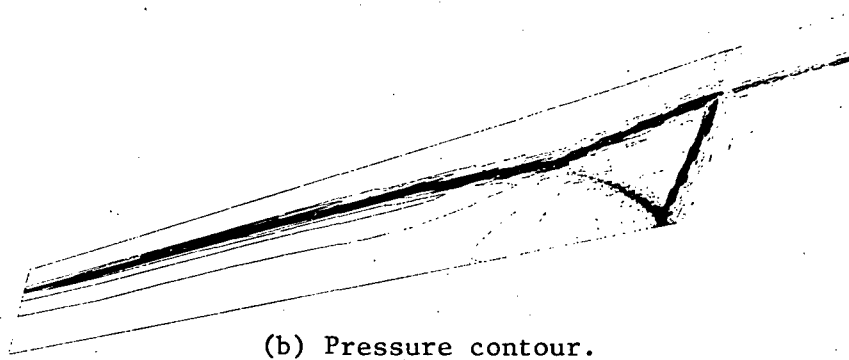
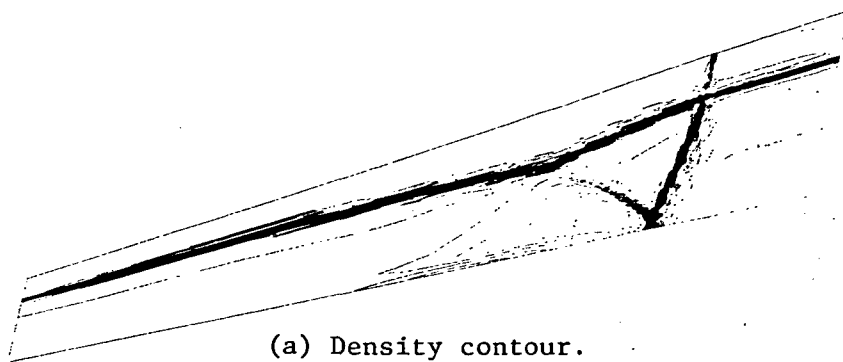


Figure 14.- Typical density and pressure contours of a meridional computational plane; $M_V = 5$, $\alpha = -5^\circ$, $\sigma = 11.2^\circ$, $M_i = 1.54$, $\lambda = 18^\circ$, $\phi = 140^\circ$.

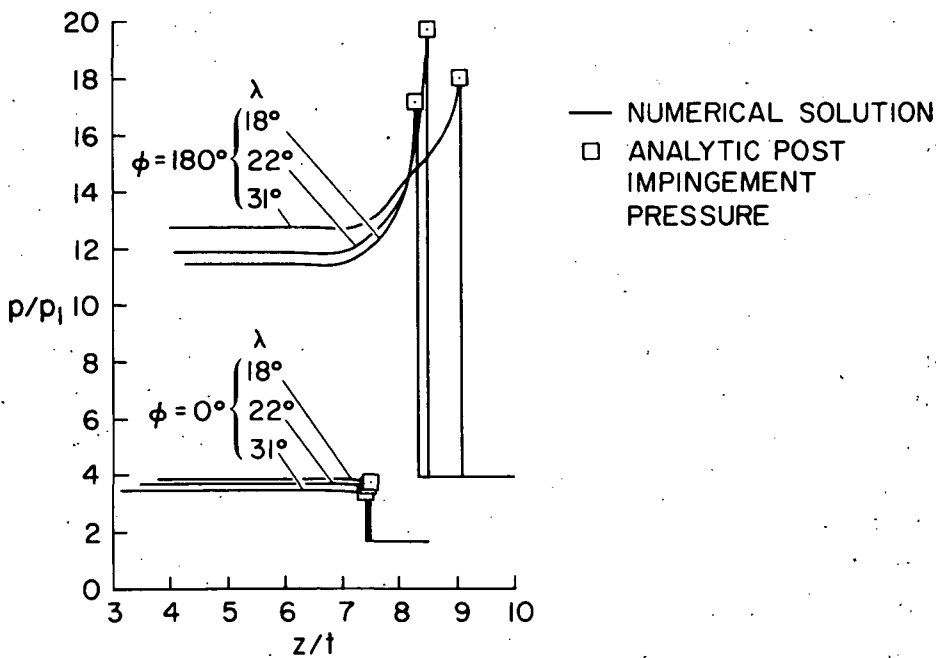


Figure 15.- Surface pressure distribution in leeward ($\phi = 0^\circ$) and windward ($\phi = 180^\circ$) planes; $M_V = 5$, $\alpha = -5^\circ$, $\sigma = 11.2^\circ$, $M_i = 1.54$ ($p_3/p_1 = 2.6$), $t = 1.0$.

COMPARISONS OF THEORETICAL AND EXPERIMENTAL
PRESSURE DISTRIBUTIONS ON AN ARROW-WING
CONFIGURATION AT TRANSONIC SPEEDS*

By Marjorie E. Manro, Edward N. Tinoco,
Boeing Commercial Airplane Company

Percy J. Bobbitt,
NASA Langley Research Center

and John T. Rogers
Boeing Commercial Airplane Company

SUMMARY

A wind-tunnel test of an arrow-wing—body configuration employing both a twisted and a flat wing, as well as a variety of leading- and trailing-edge flap deflections, has been conducted to provide an experimental data base for comparison with theoretical methods. The purpose of these comparisons was to delineate conditions under which the theoretical predictions are valid for aeroelastic calculations and to explore the use of empirical methods to correct the theoretical methods where theory is deficient. Test-theory comparisons of detailed pressure distributions are made using current state-of-the-art linear and separated flow computer programs. In addition, the results of attempting to make empirical corrections to the theoretical methods and of using two-dimensional separation criteria to predict flow separation are shown.

INTRODUCTION

For the design of large flexible aircraft, accurate analytical techniques are required for the prediction of aerodynamic load distributions including the effects of aeroelasticity. The problem of accurate load prediction becomes particularly acute when critical design conditions occur in the transonic speed regime. In this region, at typical design angles of attack and control deflections, the predictions are clouded by mixed flow, embedded shocks, separation, and vortex flow. The degree to which the intelligent application of the best state-of-the-art theoretical techniques or a combination of theory and experiment can account for these flow conditions is known in only a few circumstances. Clearly, if we

*Work supported by NASA Langley Contract NAS 1-12875 and by the Independent Research and Development Program of the Boeing Company.

are to continue to improve the accuracy of our predictive techniques as well as quantify their limitations, detailed comparisons of theoretical and experimental pressures on "typical" configurations of interest must be made on a continuing basis.

In the design process, pressure data obtained from wind-tunnel tests of a rigid model having a single wing shape (with twist and camber) are translated by means of an aeroelastic solution to the load distributions for the elastically deformed airplane. In this solution, equations that relate the changes in local pressure to changes in structural deformation are used. For typical high aspect ratio configurations at subsonic speeds, methods of incorporating experimental data in the elastic solution are well developed and have been substantiated by flight tests. However, for typical low aspect ratio (supersonic) configurations and/or transonic flight conditions where various nonlinear phenomena become important, no satisfactory methods of correcting the aeroelastic solutions with experimental data from rigid models have been developed. Until a validated analytical or empirical approach has been developed, the need for expensive and time-consuming wind-tunnel test programs simulating each flight design condition on the flexible airplane will remain.

The purpose of this paper is to report on the results of a comprehensive study carried out to define the ability of current state-of-the-art linear and separated flow techniques to predict detailed pressures over a highly swept arrow-wing configuration with flat and twisted wings. Comparisons will be shown of theoretical and experimental pressures for both the flat and twisted wings as well as for the incremental pressure changes due to twist. The latter is of interest since this calculation is similar to that required to correct basic rigid model wind-tunnel results for aeroelastic effects on the full-scale airplane. Results will also be shown in which empirical corrections were made to the elements of the aerodynamic influence matrix in an attempt to improve correlation with experimental data. Finally, results of attempts to determine if flow separation can be predicted by applying two-dimensional separation criteria will be shown.

SYMBOLS

b	wing span
c	chord length
\bar{c}	reference chord
C_L	lift coefficient
C_M	pitching-moment coefficient

C_N	normal-force coefficient
C_n	section normal-force coefficient
C_p	pressure coefficient
ΔC_p	net (lifting) pressure coefficient
$\Delta C_{p\alpha}$	$= \frac{\partial \Delta C_p}{\partial \alpha}$
M	Mach number
t	thickness
x,y,z	orthogonal coordinates
α	angle of attack
δ_F	flap deflection

THEORETICAL METHODS

The theoretical calculations performed for this study are based on inviscid theories for both attached and detached flows. The arrow-wing—body model analyzed features a highly swept thin wing and a body of high slenderness ratio (fig. 1). These characteristics lend themselves to minimizing the formation of strong shock waves and subsequent shock-induced separations. On the other hand, the highly swept thin wing also promotes early flow separation and subsequent vortex buildup along the wing leading edge. This separated flow rolls up and forms a spiral vortex which strongly influences the wing pressure distribution at angles of attack greater than about 4° .

For the configuration used in this study the attached flow theories can be expected to yield good agreement with experiment only at low angles of attack. The dominance of the leading-edge vortex flow suggests that detached flow theories may provide a more adequate representation. Although these theories are not as well developed in terms of the generalities of geometry they can handle, they will hopefully be able to more closely predict loading trends at the higher angles of attack. The effects of flap deflection on flow separation will be discussed in a later section of this paper.

Attached Flow Theories

Theoretical predictions of pressure distributions based on attached potential flow will utilize primarily the unified subsonic/supersonic panel technique of FLEXSTAB, which was developed by Boeing under NASA Ames sponsorship.¹ (See refs. 1 and 2.) The FLEXSTAB system of digital computer programs uses linear theories to evaluate static and dynamic stability, inertial and aerodynamic loading, and elastic deformations of aircraft configurations. The aerodynamic representation used in the FLEXSTAB system is based on the constant pressure panel method developed by Woodward (refs. 3 and 4) to solve the linearized potential flow equations for supersonic and subsonic speeds. The results may be used at transonic speeds, recognizing that the nonlinear terms of the transonic flow equations are neglected. The usual small perturbation assumptions are made. The severity of the above limitations is a function of the configuration and the flight conditions.

In the FLEXSTAB system the flow about a configuration is simulated by a three-dimensional array of singularities. Each singularity is a solution to the governing potential flow equation. The singularities are placed on a mean surface instead of the actual configuration surface. The boundary condition that the flow is tangent to the surface is satisfied at a discrete set of points on the mean surface. This results in a linear set of equations which may be solved to yield the singularity strengths necessary to satisfy the specified boundary conditions. From knowledge of these singularity strengths, the velocities, pressures, and aerodynamic loads on the configuration may be calculated.

The distribution of singularities employed in the analysis of this configuration is shown in figure 2. Line sources and doublets are distributed along the X-axis of the body to simulate its thickness and lifting effects. Source panels are placed in the plane of the wing to simulate its thickness. To account for the wing lifting effects and interference effects between the wing and body, constant pressure vortex panels are placed in the plane of the wing and on a shell around the body. This "interference" shell serves to cancel the normal velocity components on the body induced by the wing.

At subsonic Mach numbers, 50 line singularities, 168 interference panels, and 160 wing panels are used to represent the configuration. For the very low supersonic Mach numbers, the number of interference panels had to be greatly increased (to 330) in order to overcome instabilities associated with the solution. At higher supersonic Mach numbers the subsonic arrangement could again be used. For the wing, panel edges were chosen to coincide with flap hinge lines and the flap midspan break. The resulting panel arrangement has panels of nearly equal width and, in the chordwise direction, panel edges are at constant percent chord with closer spacing at the leading edge and the hinge lines.

¹The Ames program has been modified by Boeing to provide calculations of upper and lower surface pressures. This modification has not as yet been incorporated into the NASA version.

The same wing paneling arrangement was used at all Mach numbers. Because of the linearized boundary conditions employed by the method, flap deflections were treated as boundary condition changes and did not require any repaneling.

The second approach² to solve attached flow problems employs the general method of Rubbert and Saaris (refs. 5, 6, and 7) for the numerical solution of nonplanar, three-dimensional boundary-value problems. The method employs a panel solution to the exact incompressible potential flow equation (Laplace's equation) satisfying boundary conditions on the actual configuration surface. Compressibility effects are approximated by the Gothert rule. The method is incorporated into Boeing computer program TEA-230. The program is subject to the same limitations (inviscid, attached flow) as the linearized FLEXSTAB solution and it is further limited to the subsonic Mach numbers. However, it is not encumbered by the small perturbation approximation and is capable of treating problems of far more detail and generality than the linearized theories.

The paneling scheme used for the TEA-230 representation of the arrow-wing—body configuration without flap deflections is shown in figure 3. Eight hundred thirteen source panels were placed on the configuration surface, arranged to provide good over-all aerodynamic properties. Omitted from the figure are the internal and trailing linearly varying vortex panels, which were arranged in the manner discussed in reference 6. There was assumed to be no aft body vortex shedding or separation, so the circulation about the wing at the root carried through the fuselage with undiminished strength. A typical TEA-230 paneling scheme for the configuration with deflected flaps is shown in figure 4. The actual deflected geometry was paneled, with additional singularities being placed near the flap hinge line. Each flap deflection required different paneling. A total of 1106 singularities were used to analyze the flaps up configuration and 1150 singularities were required with the flaps deflected.

Detached Flow Theories

A promising new method still in the early stages of development was used to calculate the effects of the leading-edge spiral vortex. This three-dimensional vortex method of Weber, Brune, Johnson, Lu, and Rubbert (ref. 8) is capable of predicting forces, moments, and detailed surface pressures on thin, sharp-edged wings of rather arbitrary planform. The method can be applied to general three-dimensional (nonconical) wing configurations. The wing geometry is arbitrary in the sense that leading and trailing edges may be curved or kinked. The method employs an inviscid flow model in which the wing, the rolled-up vortex sheets, and the wake are represented by piecewise quadratic doublet distributions. The Kutta condition is imposed and satisfied along all wing edges.

²This work done by R. M. Thomas under sponsorship of the Independent Research and Development Program of the Boeing Commercial Airplane Company.

Strength of the singularity distribution as well as shape and position of the vortex spirals are computed in iterative fashion starting with an assumed initial sheet geometry.

The developmental computer program used for these calculations is still rather restricted in its capabilities. Some planform restrictions still exist and the wing thickness, camber, and twist effects cannot be analyzed yet. The simplified paneling scheme shown in figure 5 was the best available representation of this configuration. Thirty panels were used to describe the wing, 54 panels to describe the rolled-up vortex, and 14 panels to describe the wake.

The leading-edge suction analogy developed by E. C. Polhamus of NASA Langley Research Center (refs. 9 and 10) is an alternate way to obtain the vortex lift. This method is illustrated in figure 6. Lifting-surface theory treats the flow as remaining attached when passing around the leading edge. This results in a force at the leading edge acting in the plane of the wing (the leading-edge suction). In practice, as previously mentioned, the flow separates from the leading edge, vortices form above the wing, and reattachment occurs inboard of the leading edge. The Polhamus leading-edge suction analogy assumes that the force on the wing required to make the flow over the primary vortex attach to the upper surface of the wing is essentially the same as the leading-edge suction force required to maintain attached flow around the leading edge as predicted by potential flow theory. This force is the vortex lift produced on the wing. The total lift is calculated as the sum of potential lift plus the vortex lift. The actual calculation procedure consists of three parts:

Calculate the potential lift distribution by assuming attached flow and using lifting surface theory (FLEXSTAB in this case)

Calculate the leading-edge suction force from the potential flow lifting pressure distribution

Add the vortex lift obtained by rotating the leading-edge suction force normal to the plane of the wing

Since the solution is based on lifting surface theory, trailing edge and Mach number effects are automatically included. Comparisons made in references 9, 10, 11, 12, and 13 verify that this approach is able to predict lift and drag of wings with sharp leading edges at both supersonic and subsonic speeds. However, these results have not previously been verified for wing-body configurations nor does the method give any information regarding spanwise lift distribution.

Computing Resources

A summary of the computing statistics for the computer programs just described is given in table 1. The statistics are for analysis on the Boeing Computer Services

CDC 6600's operating under the KRONOS 2.0 system. The programs use an overlay structure to reduce the central memory size requirements and require several million words of peripheral disk storage. The central processor unit (CPU) times given are for the analysis of one geometry-flight condition. Both TEA-230 and FLEXSTAB have an analysis recycling capability which increases their efficiency in analyzing multiple conditions at a given Mach number. The 3-D Vortex Program is in an early developmental stage. No attempt has yet been made to optimize its algorithms to improve its computational efficiency. The leading-edge suction analogy calculations were made using small computer programs (requiring less than 10 CPU seconds) which used as input the results of the potential flow solution from the FLEXSTAB analysis.

MODEL DESCRIPTION AND EXPERIMENTAL RESULTS

The configuration selected to obtain experimental pressure data is a highly swept, thin wing on a slender body. The planform and basic geometry of the model are shown in figure 7. Two complete wings were constructed, one with no camber or twist, and one with no camber but a spanwise twist variation. (See fig. 8.) Both wings were designed with a full-span, 25 percent chord, trailing-edge flap with brackets to allow streamwise deflections of $\pm 4.1^\circ$, $\pm 8.3^\circ$, $\pm 17.7^\circ$, and $\pm 30.2^\circ$, as well as 0° . The flat wing was provided with a removable leading-edge segment (15 percent of streamwise chord). This leading edge was used in the undeflected position and also drooped 5.1° and 12.8° . An additional leading-edge segment for the flat wing was constructed with a sharp leading edge to examine the effects of leading-edge shape. Figure 9 shows the basic round leading edge and the sharp leading edge superimposed.

The 217 pressure orifices on the wing were equally divided into seven streamwise sections on the left wing. (See fig. 10.) The chordwise distribution is also shown. The body orifices were arranged in five streamwise rows of fifteen orifices each. An additional eight orifices in the area of the wing-body junction made a total of 83 orifices on the left side of the body. See figure 10 for orifice location.

The model was constructed of steel to minimize aeroelastic deflections. To ensure close control of the model contours, the GCS (geometry control system) computerized lofting program was used to provide data for machining the model components using numerically controlled operations.

This sting mounted model was tested in the Boeing Transonic Wind Tunnel in June 1974. This is a continuous flow, closed circuit, atmospheric facility with a 12.5-percent porosity test section measuring 8 by 12 by 14.5 feet. A photograph of the model installed in the test section is shown in figure 1. Seven Mach numbers were tested from 0.40 to 1.11, with angle of attack varying from -8° to $+16^\circ$. The major configurations tested are shown in table 2. The leading and trailing edges were split at 0.57 wing semispan and

some combinations of inboard or outboard leading-edge deflections with inboard or outboard trailing-edge deflections were also tested.

A comprehensive report of the experimental data will be reported as part of NASA contract NAS 1-12875. A sample of the experimental data characterizing the type of flow experienced on the model is shown in figures 11 to 14. A series of isobar plots for three angles of attack at Mach 0.40 are shown in each figure. This configuration develops a spiral vortex off the leading edge at relatively low angles of attack. Figure 11 shows upper surface isobars for the round leading-edge flat wing. Evidence of the vortex formation is first seen at an angle of attack of 4° and is clearly evident at 8° . The progression of this vortex with angle of attack is influenced by both leading-edge geometry and wing twist.

In figure 12, isobars are shown for the sharp leading-edge flat wing. The formation of the vortex is more evident at both 4° and 8° than was seen for the round leading edge. This phenomenon is less evident at the higher Mach numbers. Figure 13 illustrates the effects of twist on this wing. The formation of the vortex is delayed to an angle of attack of nearly 8° . Since the local angles of attack for the twisted wing are less than that of the flat wing, this behavior is expected. Figure 14 shows the lower surface isobar patterns which are typical of all three configurations at positive angles of attack.

TEST-THEORY COMPARISONS

The success of any theory must ultimately be measured by its ability to accurately predict experimental results. With this idea in mind, a series of comparisons of theoretical and experimental data has been made for the arrow-wing-body configuration just described. The theoretical results were derived from the analytical techniques previously discussed. Results of these comparisons will be presented first for the attached flow theories.

The configuration was analyzed over a Mach number range from 0.40 to 1.11 using the FLEXSTAB system and at Mach numbers of 0.40 and 0.85 with the TEA-230 program. Both the flat and twisted wing configurations were analyzed, including the effect of deflecting flaps. In order to get an idea of the gross aerodynamic properties, a comparison of experimental and theoretical normal-force slope and aerodynamic center over a range of Mach numbers is shown in figure 15. The results of the calculations show generally good agreement with experiment throughout the Mach number range. However, some discrepancies are apparent. More detailed comparisons of surface pressures on the wing and body are required to further evaluate the adequacy of these theoretical solutions.

A comparison of experimental and theoretical surface pressures on the flat-wing configuration is shown in figures 16, 17, and 18 for a series of Mach numbers. Data are

presented at a low angle of attack where the leading-edge vortex effects are minimal. Wing surface pressures at three wing stations for a Mach number of 0.40 are shown in figure 16. Generally good agreement with experimental results was obtained by the use of either theory.

The TEA-230 results show better agreement with the experimental data near the leading edge than the FLEXSTAB results which exhibit the typical linear theory leading-edge singularity. Figure 17 shows very similar comparisons for a Mach number of 0.85. The comparison of surface pressures at Mach 1.05 (fig. 18) between FLEXSTAB and experiment is not as good as at the subsonic Mach numbers. There is a definite shift of the surface pressure level between the theoretical and experimental distributions. However, the theoretical lifting (net) pressure distribution agrees well with the experimental distribution except at the leading edge. The discrepancy in the levels of the surface pressure distributions could be due to the inability of the linear theory to properly predict the symmetric or thickness part of the surface pressures at this transonic Mach number. It is this component of the theoretical solution which establishes the level of the surface pressures. It is also conceivable that this discrepancy could be due to wind-tunnel interference at this Mach number.

Comparisons at a higher angle of attack are shown in figures 19 and 20. Only the comparisons at Mach 0.85 and Mach 1.05 are shown since the Mach 0.40 results are essentially identical to those at Mach 0.85. The theoretical pressure distribution compares very well with the experimental data at the most inboard wing section ($2y/b = 0.09$). Proceeding outboard, the formation of the leading-edge vortex becomes quite evident. Neither the FLEXSTAB nor the TEA-230 results compare well with the experimental data at the midspan ($2y/b = 0.50$) and the outboard ($2y/b = 0.93$) stations. The presence of the leading-edge vortex has completely changed the nature of the flow over most of the wing. Neither attached potential flow theoretical method can predict the experimental results.

Spanwise load distribution comparisons are shown in figure 21. The theoretical methods tend to agree with the experimental results on the inboard 40 percent of the wing. Outboard of this section, the presence of the leading-edge vortex is quite evident with the peak in the loading occurring at 65 percent semispan. As the chordwise pressure distributions indicated, there is poor agreement between theoretical and experimental span loads in this region.

The effects of wing twist are shown in figure 22. The results shown are for Mach 0.85, other Mach numbers being similar. Surface pressures are compared at a moderate angle of attack. Both theories compare well with the experimental data, with differences between the two theories and experiment mainly limited to the wing leading edge. The wing twist suppresses the formation of the leading-edge vortex at this angle of attack allowing potential flow to exist over the wing. At higher angles of attack the vortex again

forms, resulting in test-theory comparisons similar to those on the flat wing shown in figures 19 and 20.

The effects of trailing-edge flap deflection are shown in figures 23 and 24. Surface pressure comparisons for the flat-wing configuration with a flap deflection of 8.3° are presented. Results are for zero angle of attack and Mach numbers of 0.40 and 1.05, Mach 0.85 being very similar to the 0.40 results. In figure 23, for Mach 0.40, the TEA-230 results agree well with the experimental data except on the flap at the inboard station ($2y/b = 0.09$). The FLEXSTAB results agree well ahead of the flap hinge line, but as is typical of linear theory overpredict the pressures on the flap. The experimental surface pressures indicate flow separation on the most inboard section of the flap. The TEA-230 results show a loss of lift in this section. Both phenomena appear to be due to the unporting (exposing to the free stream) of the inboard edge of the flap when the flaps are deflected down. This induces flow separation in the real flow and leads to a loss in lift in the TEA-230 potential flow solution. No such loss occurs in the FLEXSTAB solution since as the geometry is linearized there is no unporting of the flap inside edge.

Evident in the experimental data in figure 23 is the formation of a leading-edge vortex near the outboard wing station ($2y/b = 0.93$). Although the wing is at zero angle of attack, the circulation induced by the flap deflection is sufficient to cause separation on the outboard leading edge. Evidence of the vortex is also seen in figure 24 in the Mach 1.05 results, where the correlation is even worse than at the lower Mach numbers. Wing span loading is compared in figure 25. The TEA-230 results agree well with experiment at Mach 0.40, although the loss of lift in the TEA-230 solution on the inboard flap edge is evident. The FLEXSTAB results grossly overpredict the flap effectiveness.

Results for a greater flap deflection (17.7°) are shown in figures 26 and 27 for Mach numbers 0.85 and 1.05. The correlation of theory with experiment is poor. The flow separation along the entire flap and the strength and extent of the leading-edge vortex are greater.

The effects of leading-edge shape are shown in figure 28. Comparisons are shown between TEA-230 results and experimental data for both the sharp and round leading edges. FLEXSTAB results were not available for this comparison. At the low angle of attack shown ($\alpha = 2.1^\circ$), the theoretical results compare well with experiment in predicting the surface pressure distribution measured on the two leading edges. At the higher angle of attack ($\alpha = 7.9^\circ$), some vortex flow is starting to form at the wing station shown. It is evident at this station that the vortex is more pronounced for the sharp leading edge than the round. The effects of the leading-edge shape on the experimental pressures can be seen better in the isobar plots previously shown in figures 11 and 12.

The preceding comparisons have shown that the attached potential flow theories are only able to predict experimental pressures well for this configuration over a limited

range of angle of attack and flap-deflection conditions. The effects of Mach number do not appear to significantly alter the results on this configuration. The test-theory comparisons at Mach 1.05 were generally as good as those at the subsonic Mach numbers. There were no large differences between the TEA-230 and the FLEXSTAB results in comparison with experiment. TEA-230 with its on-the-surface paneling and boundary conditions did predict more closely the correct pressures near the wing leading edge and on the deflected flaps than did the linearized FLEXSTAB. For configuration development at subsonic speeds the TEA-230 method is preferred over the FLEXSTAB method because of its ability to better predict detailed surface pressures. At subcritical speeds on a configuration with a thicker wing or a wing in the presence of interference from underwing stores or nacelles, the TEA-230 surface pressure results would be significantly better than those of a linearized method.

For calculating load distributions, the FLEXSTAB method is generally as adequate as the TEA-230 method and is easier to implement. It is also applicable at supersonic speeds and includes the required aeroelastic solution.

Since it is evident that the flow on the model is dominated by a separated leading-edge vortex at all but a limited range of angles of attack and that the attached potential flow theories can not adequately predict the effects of the vortex, comparisons were made with two separated flow theories. Results of the 3-D vortex program of Weber, et al., are compared with experimental data in figures 29, 30, and 31 for nominal angles of attack of 8° , 12° , and 16° . Also shown in these figures are results from the attached flow FLEXSTAB program. Because of the sparsity of wing panels in the theoretical 3-D vortex solution compared to the number of pressure taps for the wind-tunnel model, the 3-D vortex results are indicated by symbols while the experimental data (which was interpolated to the same stations as the theoretical results) is designated by a solid line. The FLEXSTAB results are indicated by a dashed line.

The comparison between the experimental and the 3-D vortex results is surprisingly good for those stations ahead of the apex of the wing trailing edge, particularly considering the absence of the body in the theoretical model and the sparsity of the paneling definition. The attached flow results from the FLEXSTAB program show little resemblance to either the 3-D vortex program results or the experimental data. The 3-D vortex method predicts the approximate location and magnitude in the peak of the lifting pressure distribution, except at the two stations behind the trailing-edge apex. The cause of the discrepancies is unknown but could be caused in part by the crude geometric representation which neglects both the body and the streamwise wing tip. Also, compressibility is not accounted for in the present 3-D vortex computer program, while the experimental data are for Mach number 0.40. Nevertheless, the results are encouraging and correlation should improve as the method is further developed.

The leading-edge suction analogy of Polhamus was adapted for use with the FLEXSTAB program for calculation of lift, pitching moment, and longitudinal load distribution. The arrow-wing-body model was analyzed for four wing configurations; the flat wing, the twisted wing, and the flat wing with 5.1° and 12.8° leading-edge flap deflection. Results were available for this paper only for Mach 0.85. Detailed results of the complete study being done by R. M. Kulfan, Boeing Commercial Airplane Company, under contract NAS 1-12875 are unpublished at this time.

Comparisons of the predicted lift and pitching moment with experimental data are shown in figures 32 to 35 for the four wing configurations analyzed. Adding the vortex lift to the potential solution has the effect of overpredicting the experimental results. This could be due to the fact that the theory has been developed for sharp, flat wings while the experimental data are from a wing-body model whose wing has a finite leading-edge radius. The correlation with pitching moments could be improved by adding the viscous cross-flow forces on the forebody of the model which will make the pitching moment more positive without significantly affecting the lift.

Longitudinal load distributions for test and theory are compared in figures 36 to 39 for nominal angles of attack of 4° and 12° . Load distributions shown are for the wing only; the load distribution over the body is not included. At the low angles of attack, the contribution of the leading-edge suction to lift is negligible. At the higher angle of attack the addition of the vortex lift to the attached potential flow calculations improves the correlation between the predicted and measured results. Some major discrepancies still exist. The reasons for these are presently unknown.

While this method can be quite useful in calculating general aerodynamic stability characteristics, it lacks the capability to provide the detailed chordwise section loading required for design. The 3-D vortex method is capable of providing such pressure distributions but still needs much development.

EMPIRICAL CORRECTIONS

The comparisons of the preceding section show that there are many conditions where the available theories do not give adequate results for detail configuration design. In practice, theory is used mainly to increment wind-tunnel data from a rigid model to account for the elastic effects of the actual configuration airframe. The aeroelastic solution provides the means for translating the aerodynamic load distributions obtained from wind-tunnel tests on a single shape to that on the elastically deformed airplane. Equations that relate the changes in local aerodynamic pressure to changes in structural deformations are used. It is desirable to introduce aerodynamic corrections based on experimental data which would improve the accuracy of the theoretical estimate of elastic

increments. The range and scope of these corrections vary greatly in complexity and for low aspect ratio configurations are not well understood.

The simplest type of elastic correction is to scale experimental aerodynamic parameters by the ratio of theoretically calculated elastic to rigid values of the parameter in question. This scheme has limited value for structural design because it does not provide adequate load distribution detail. A very successful method which has been well developed for high aspect ratio surfaces at subsonic speeds has been to scale wing section characteristics along the span of the wing. Ideally, a method to correct low aspect ratio aerodynamics should influence both chordwise and spanwise loading.

Since low aspect ratio aerodynamic methods used for elastic predictions are based on some sort of aerodynamic influence coefficient (AIC) matrix, a method which modifies elements of the AIC matrix should prove useful. However, in such a matrix correction scheme there are always more unknown correction factors than equations available, requiring a number of assumptions to obtain a solution. Several schemes which have been used for matrix corrections are summarized in table 3.

The three schemes shown in table 3 which require knowledge of the variation of experimental lifting pressure with angle of attack have been attempted for this configuration. Figure 40 illustrates the typical variation of lifting pressure (lower surface pressure minus upper surface pressure) with angle of attack at two locations on the wing. Note that at the inboard location the lifting pressure ΔC_p varies quite linearly with angle of attack α . At the outboard location, the variation of ΔC_p with α is extremely nonlinear because of the inward movement of the core of the leading-edge vortex as angle of attack is increased. This nonlinearity makes correcting the matrix a very difficult task since the nature of an AIC matrix is to predict a linear variation of lifting pressure with incidence. The correction schemes considered only correct the slope of the $\Delta C_p - \alpha$ curve and the manner in which different elements of the matrix influence each other.

The experimental data were linearized around zero angle of attack. This procedure becomes somewhat arbitrary at the outboard sections because of the nonlinearity of the data. Data from the flat-wing configuration, without flap deflection, were used. Figure 41 illustrates the variation of the ratio of experimental to theoretical $\Delta C_{p\alpha}$ slopes on the flat-wing configuration. These ratios are shown as contours. Note that the experimental slopes are higher than the theoretical slopes near the leading edge (except for the first 2 percent chord) and much lower than the theoretical slopes near the trailing edge. Correction factors based on the row, column, and product correction schemes (see table 3) were calculated from these data. AIC matrices modified by these factors were used in the FLEXSTAB system in an attempt to improve the prediction of the effects of twist and flap deflection. One could consider these shapes as having been due to elastic changes.

A comparison of experimental data, theoretical results, and corrected theoretical results is shown in figure 42. Lifting pressure distribution on the flat-wing configuration at a small angle of attack is shown. On a rigid wing without camber, twist, or flap deflection, all three corrector schemes yield identical results. The uncorrected theory compares well with the experimental data except at the leading edge. The effect of empirical corrections applied to the AIC matrix has been to improve the theoretical correlation at the leading and trailing edges of the wing at this very small angle of attack. A similar comparison is shown for the twisted-wing configuration in figure 43. Here the corrector schemes do yield different, though similar, results. The differences between the corrector schemes are most evident at the wing leading edge. There is little difference between the row and product corrector schemes but the column corrector scheme tends to show some overshoot at the leading edge. This tendency would be aggravated on an elastic wing because of the resulting elastic deflections.

In the two preceding examples the basic theory was in good agreement with the experimental data. The application of either the row or product corrector scheme further improved the correlation with the experimental data. The next example (fig. 44) shows a comparison of lifting pressure distribution on the flat-wing configuration at an angle of attack of 8° . Unlike the favorable comparison shown in figure 42 for the same configuration at an angle of attack of 2° , very poor agreement between the theory and the experimental data is now seen. The corrector schemes offer no improvement since they are only capable of making linear corrections. The flow at this angle of attack is dominated by a detached leading-edge vortex which results in a very nonlinear variation of ΔC_p with α . The appropriate flow phenomena must be correctly modeled in the theoretical solution before empirical corrections can yield significant improvements.

Comparisons are shown for the flat wing with the trailing-edge deflected in figure 45 and the flat wing with leading-edge deflected in figure 46. The corrected matrix results improve upon the uncorrected theory but still leave some discrepancy. The area of greatest error in the theoretical results is at the flap hinge line. The logarithmic singularity which occurs in the theoretical solution is not a characteristic of the real flow solution. The present corrector methods do nothing to eliminate this singularity. For this configuration the corrector schemes appear to improve the prediction of flap loads and hinge moments.

From these results it is difficult to determine whether one method is superior to the others. It may in fact be impossible to choose between these or similar AIC correction schemes with rigid comparisons. All the methods correct the AIC matrix to give a required ΔC_{p_α} slope which may match experimental results only over a limited range. The methods differ mainly on how the corrections are distributed within the aerodynamic matrix. A flexible solution in which there is coupling between the loads and the resultant

elastic rotations would reveal greater differences between the methods but little experimental data exist for this type of comparison.

As previously stated, in practice theoretical results are used mainly to correct experimental data from a rigid wind-tunnel model for the effects of the elastic deformation of the flight airframe. Empirical corrections are introduced to improve the accuracy of these theoretical increments. An example of this procedure is shown in figure 47 for Mach 0.85 and an angle of attack of 8° . Here we have taken experimental data for the flat wing (rigid model) and have added to them a theoretically calculated increment due to the known twist of the model (supposed elastic deformation). The result is compared to the twisted-wing data at the same angle of attack (deformed airframe). As shown in figure 47 there are significant differences between the flat-wing data theoretically corrected for twist, and the twisted-wing results at the outboard stations. This is because the twist has changed the location and strength of the leading-edge vortex. The theoretical corrections are linear and work only on those cases where the actual flow changes are also linear. This example is indicative of the type of problems which must be overcome before a reliable prediction scheme for aerodynamic increments due to elasticity is available. Improper accounting for aeroelastic effects because of uncertainties in the theoretical methods may result in understrength or overweight designs. In addition, the correct prediction of loads and the resultant structural deformation are essential to the determination of aircraft stability and control characteristics. These results indicate that the use of empirical corrections in the aeroelastic solution to calculate flexible airplane loads is extremely risky, and much research is necessary to develop a practical method of using such corrections.

FLOW SEPARATION DUE TO CONTROL DEFLECTION

Another type of flow separation phenomenon in addition to the separated leading-edge vortex is that due to control surface deflection. The ability to be able to predict the onset of flow separation and hopefully the resultant pressure distribution is very important in estimation of control effectiveness and hinge moments. An attempt was made to determine if flow separation due to trailing-edge control deflection could be predicted by applying two-dimensional separation criteria to theoretical pressure distributions obtained from FLEXSTAB.

A computer program developed by Boeing (TEA-200) was used to predict separation. This program calculates boundary-layer growth by solving the boundary-layer equations using the Nash-Hicks momentum integral (ref. 14). Separation occurs at the point where the local skin friction becomes zero. This method is applicable to subsonic compressible flow without shock waves. For the Mach numbers covered by this test (M less than 1.15), the hinge line and trailing edge are always subsonic.

Several difficulties arise when one attempts to use surface pressures from FLEXSTAB in boundary-layer calculations. Pressure gradients are poorly defined by the limited number of points available, particularly near the hinge line. A closed form solution would have a singularity at the hinge line because of the discontinuity in camber-line slope which occurs at this point. In addition, the FLEXSTAB data exhibit small oscillations which appear to be inherent in the solution.

To avoid these problems, a curve was fitted to the points using a least squares technique. The singularity at the hinge line was smoothed out over a distance of 1 percent chord. This approximates the effect of a more realistic representation of the mean line which would be curved over a distance roughly equal to the local thickness (≈ 0.9 percent), rather than being discontinuous at the hinge line.

Figures 48 to 50 show comparisons of theoretical and measured surface pressure distributions at Mach 0.85 for three spanwise stations. Predicted separation points are also given. The pressure distributions vary little with Mach number, so that conclusions based on Mach 0.85 data should be valid throughout the range of Mach numbers tested. The investigation was carried out at zero incidence to minimize the effects of the vortex flow from the leading edge. As previously shown in figures 16 to 18, and again seen in these figures, good agreement between measured and predicted surface pressures occurs for the flat wing, $\delta_F = 0^\circ$.

Consider first the lower (compression) surface. Near the side of the body (fig. 48), separation is first predicted just ahead of the hinge line at $\delta_F = 17.7^\circ$. However, aft of the hinge line, significant differences between measured and predicted pressures occur even at $\delta_F = 4.1^\circ$. Surface pressure increases with control deflection, but at a rate much lower than predicted. The discrepancy between theory and experiment becomes greater at the outboard stations. Near the wing tip (fig. 50), experimental lower surface pressure is almost constant and independent of control deflection for deflection greater than $\delta_F = 4.1^\circ$. It is probable that the flow near the wing tip is dominated by a thick boundary layer, flowing spanwise from the wing root. Two-dimensional separation criteria therefore cannot be expected to provide any useful information.

On the upper surface, agreement is quite good for control deflections which do not produce regions of local supersonic flow ($C_p < -0.3$). At larger control deflections, the flow becomes locally supersonic and the high negative pressures predicted at the hinge line and wing leading edge do not occur. There is evidence of shock waves behind the hinge line. (See fig. 49, $\delta_F = 17.7^\circ$ and 30.2° , for example.) Two-dimensional criteria predict separation close to the trailing edge and only at the largest control deflection, when the theoretical predictions are already invalid because the local flow has become supersonic. No attempt was made to predict leading-edge separation because the linearized aerodynamic representation of FLEXSTAB is poor at the leading edge. However, the

experimental data (for example, fig. 50, $\delta_F = 17.7^\circ$ and 30.2°) suggest that at large flap deflections, the circulation induced by the flaps causes a vortex to form at the leading edge, even when the wing angle of attack is zero.

It is concluded that two-dimensional criteria are of no value when applied to highly swept wings such as the present model. This is true even at the wing root, where the flow is most nearly two-dimensional. Using the TEA-230 surface pressures for the boundary-layer analysis could have improved separation predictions somewhat, particularly on the lower surface. But without an adequate three-dimensional boundary-layer method available, it is doubtful that useful results could be achieved.

CONCLUDING REMARKS

It has been shown that the attached potential-flow methods can yield good agreement with experimental data for this type of configuration only over a limited range of conditions at low angles of attack. These analyses are generally adequate for the evaluation of a configuration at 1g (load factor one) conditions. At critical structural and control design conditions which usually involve large angles of attack and/or large control surface deflections, the attached flow theories are completely inadequate. Attempts to introduce empirical corrections to improve this situation have been unsatisfactory. Comparisons with detached flow theories have shown that these methods predict the general aerodynamic loading trends with angle of attack on this configuration, but are not capable of predicting the detailed pressure distributions required for general wing-body configurations.

Two-dimensional separation criteria have been shown to be of no value in predicting the onset of flow separation on highly swept wings, such as the present arrow-wing-body model. The development and implementation of a general three-dimensional boundary-layer method is needed. It is evident that the theoretical tools necessary to predict critical design conditions on low aspect ratio configurations which are dominated by nonlinear flow phenomena are lacking. Empirical methods to improve this capability are also lacking. Much research in developing the theoretical and empirical techniques is still necessary before confidence can be acquired in the prediction of aerodynamic loads on highly swept, low aspect ratio, flexible airplanes.

REFERENCES

1. Tinoco, E. N.; and Mercer, J. E.: FLEXSTAB - A Summary of the Functions and Capabilities of the NASA Flexible Airplane Analysis Computer System. Boeing Doc. D6-41098, Oct. 1974.
2. Dusto, A. R., et al.: A Method for Predicting the Stability Characteristics of an Elastic Airplane. Volume 1 - FLEXSTAB Theoretical Manual. NASA CR 114712, 1974.
3. Woodward, F. A.; Tinoco, E. N.; and Larsen, J. W.: Analysis and Design of Supersonic Wing-Body Combinations, Including Flow Properties in the Near Field. Part 1 - Theory and Application. NASA CR-73106, 1967.
4. Woodward, F. A.: Analysis and Design of Wing-Body Combinations at Subsonic and Supersonic Speeds. J. Aircraft, vol. 5, no. 6, Nov.-Dec. 1968, pp. 528-534.
5. Rubbert, P. E.; Saaris, G. R.; Scholey, M. B.; and Standen, N. M.: A General Method for Determining the Aerodynamic Characteristics of Fan-in-Wing Configurations. Boeing Doc. D6-15047-1, 1967.
6. Rubbert, P. E.; and Saaris, G. R.: A General Three-Dimensional Potential-Flow Method Applied to V/STOL Aerodynamics. SAE J., vol. 77, Sept. 1969. (Presented at SAE Air Transport Meeting, New York, April-May 1968.)
7. Rubbert, P. E.; and Saaris, G. R.: Review and Evaluation of a Three-Dimensional Lifting Potential Flow Analysis Method for Arbitrary Configurations. AIAA Paper 72-188, 1972.
8. Weber, James A.; Brune, Guenter W.; Johnson, Forrester T.; Lu, Paul; and Rubbert, Paul E.: A Three-Dimensional Solution of Flows Over Wings With Leading Edge Vortex Separation. Aerodynamic Analyses Requiring Advanced Computers, Part II, NASA SP-347, 1975, pp. 1013-1032.
9. Polhamus, E. C.: A Concept of the Vortex Lift of Sharp-Edge Delta Wings Based on a Leading-Edge-Suction Analogy. NASA TN D-3767, 1966.
10. Polhamus, E. C.: Predictions of Vortex-Lift Characteristics by a Leading-Edge Suction Analogy. J. Aircraft, vol. 8, no. 4, Apr. 1971, pp. 193-199.
11. Snyder, M. H., Jr.; and Lamar, J. E.: Application of the Leading-Edge-Suction Analogy to Prediction of Longitudinal Load Distribution and Pitching Moments for Sharp-Edged Delta Wings. NASA TN D-6994, 1972.
12. Naugia, R. K.; and Hancock, G. J.: Delta Wings With Longitudinal Camber at Low Speed. ARC CP 1129, 1970.

13. Lamar, John E.: Some Recent Applications of the Suction Analogy to Vortex-Lift Estimates. Aerodynamic Analyses Requiring Advanced Computers, Part II, NASA SP-347, 1975, pp. 985-1011.
14. Nash, J. F.; and Hicks, J. G.: An Integral Method Including the Effect of Upstream History on the Turbulent Shear Stress. Proceedings Computation of Turbulent Boundary Layers - 1968, AFOSR-IFP-Stanford Conference, Aug. 18-25, 1968.

TABLE 1.- COMPUTER RESOURCES REQUIRED FOR THEORETICAL ANALYSIS*

PROGRAM	NO. OF SINGULARITIES	CPU** TIME (SEC)	CENTRAL MEMORY (WORDS)	REMARKS
TEA-230	1150	3700	140K ₈	
FLEXSTAB	378 540	2900 4700	160K ₈ 160K ₈	SUBSONIC CASE LOW SUPERSONIC PANELING
3-D VORTEX	98 98	850 1300	120K ₈ 120K ₈	11 ITERATIONS 21 ITERATIONS
LEADING-EDGE SUCTION ANALOGY	COST DEPENDENT ON SOURCE OF POTENTIAL FLOW SOLUTION			

- * RESOURCES FOR BOEING COMPUTER SERVICES
CDC 6600 OPERATING ON KRONOS 2.0.
- ** TIMES BASED ON SOLUTION FOR ONE CONDITION, TEA-230 AND FLEXSTAB HAVE A RECYCLING CAPABILITY WHICH CAN GREATLY REDUCE THE COST OF ADDITIONAL CONDITIONS.

TABLE 2.- TEST CONFIGURATIONS

WING	TRAILING EDGE	LEADING EDGE DEFLECTION (DEGREES)	TRAILING EDGE DEFLECTION (DEGREES)
ROUND LEADING-EDGE FLAT WING	FLAT	0	0, ± 4.1, ± 8.3, ± 17.7, ± 30.2
		5.1, 12.8	0, ± 4.1, ± 8.3, ± 17.7
	TWISTED	0	0, ± 4.1, ± 8.3, ± 17.7
SHARP LEADING-EDGE FLAT WING	FLAT	0	0
ROUND LEADING-EDGE TWISTED WING	TWISTED	0	0, ± 4.1, ± 8.3, ± 17.7, +30.2

TABLE 3.- EXPERIMENTAL CORRECTIONS TO AERODYNAMIC
INFLUENCE COEFFICIENT (AIC) MATRIX

General problem	$\frac{dP_1}{d\alpha} = C_{11}A_{11} + C_{12}A_{12} + \dots + C_{1N}A_{1N}$ $\frac{dP_2}{d\alpha} = C_{21}A_{21} + C_{22}A_{22} + \dots + C_{2N}A_{2N}$ \vdots $\frac{dP_N}{d\alpha} = C_{N1}A_{N1} + C_{N2}A_{N2} + \dots + C_{NN}A_{NN}$	<ul style="list-style-type: none"> ● N equations available ● N² unknowns ● Assumptions are necessary to solve 	
Types of simplified methods	Equations	Assumptions	Type of solution
Scaling	$\frac{dP_1}{d\alpha} = C A_{11} + C A_{12} + \dots + C A_{1N}$ $\frac{dP_2}{d\alpha} = C A_{21} + C A_{22} + \dots + C A_{2N}$ \vdots $\frac{dP_N}{d\alpha} = C A_{N1} + C A_{N2} + \dots + C A_{NN}$	Distribution is correct, magnitude may be in error; equal correction at all panels	$C = \frac{C_{L\alpha} \text{ (experimental)}}{C_{L\alpha} \text{ (analytical)}}$
Row correction	$\frac{dP_1}{d\alpha} = C_1 A_{11} + C_1 A_{12} + \dots + C_1 A_{1N}$ $\frac{dP_2}{d\alpha} = C_2 A_{21} + C_2 A_{22} + \dots + C_2 A_{2N}$ \vdots $\frac{dP_N}{d\alpha} = C_N A_{N1} + C_N A_{N2} + \dots + C_N A_{NN}$	Equal corrections apply to loads induced on panel j by both local and remote points	<p>Separate linear equations</p> $\left\{ \frac{\Delta P}{\alpha} \right\} = [C] [A]$ $C_j = \left(\frac{dP_j}{d\alpha} \right) / \sum_{k=1}^N A_{jk}$
Column correction	$\frac{dP_1}{d\alpha} = C_1 A_{11} + C_2 A_{12} + \dots + C_N A_{1N}$ $\frac{dP_2}{d\alpha} = C_1 A_{21} + C_2 A_{22} + \dots + C_N A_{2N}$ \vdots $\frac{dP_N}{d\alpha} = C_1 A_{N1} + C_2 A_{N2} + \dots + C_N A_{NN}$	Equal corrections apply to loads induced by panel j on both local and remote points	<p>Simultaneous linear equations</p> $\left\{ \frac{\Delta P}{\alpha} \right\} = [A] [C]$ $\{C\} = [A]^{-1} \left\{ \frac{\Delta P}{\alpha} \right\}$
Product correction	$\frac{dP_1}{d\alpha} = C_1^2 A_{11} + C_1 C_2 A_{12} + \dots + C_1 C_N A_{1N}$ $\frac{dP_2}{d\alpha} = C_2 C_1 A_{21} + C_2^2 A_{22} + \dots + C_2 C_N A_{2N}$ \vdots $\frac{dP_N}{d\alpha} = C_N C_1 A_{N1} + C_N C_2 A_{N2} + \dots + C_N^2 A_{NN}$	Correction applied to both local and remote points proportional to product of local factors	<p>Simultaneous nonlinear equations</p> <p>Iterative solution</p>

A_{jk} = analytically derived coefficients of the AIC matrix, effect of panel k on panel j, L/q per radian

P = $\frac{L}{q}$ = experimental panel load coefficient, area

α = panel angle of attack, radians

C = correction factors

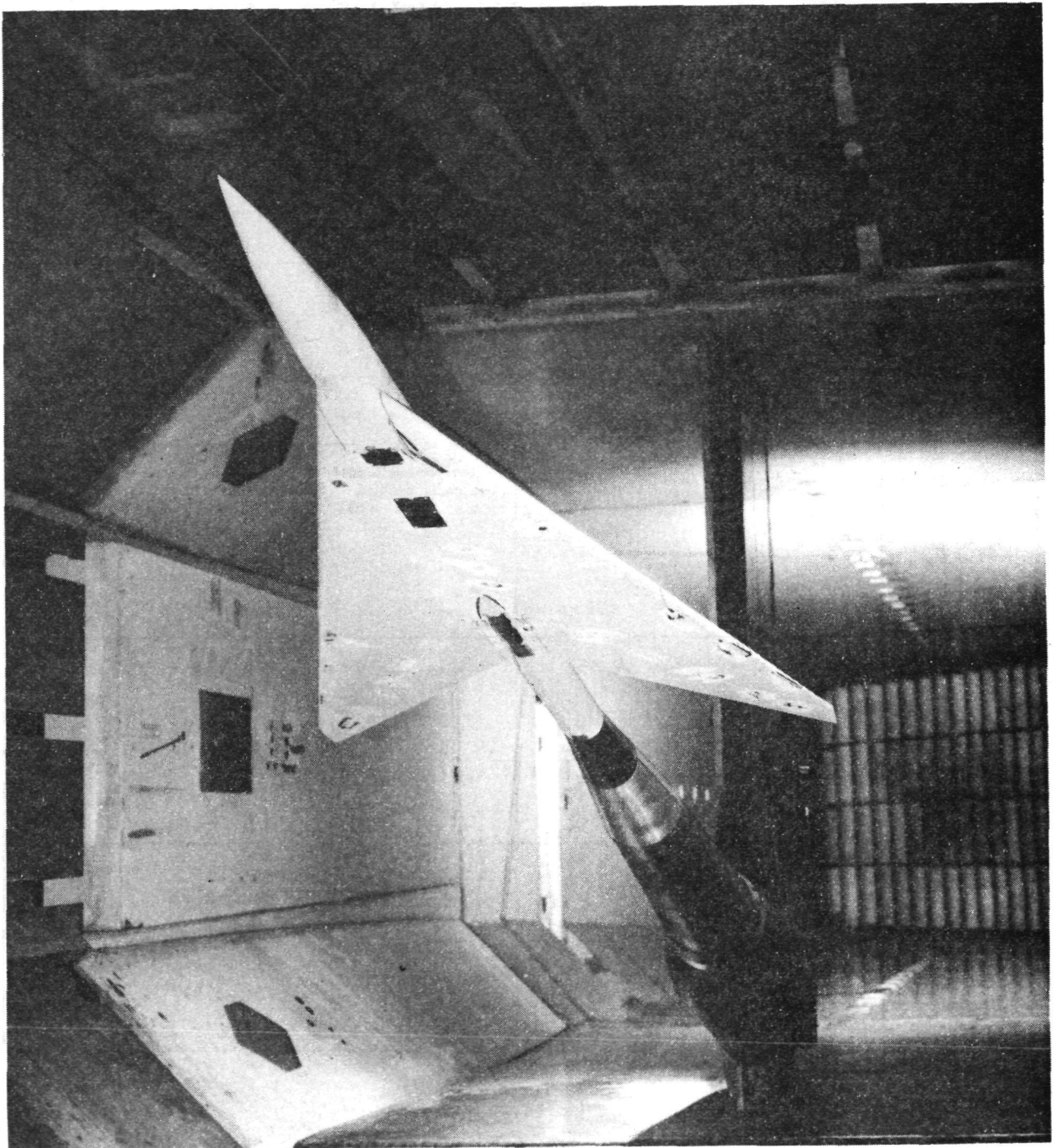


Figure 1.- Wind-tunnel pressure model for theory validation.

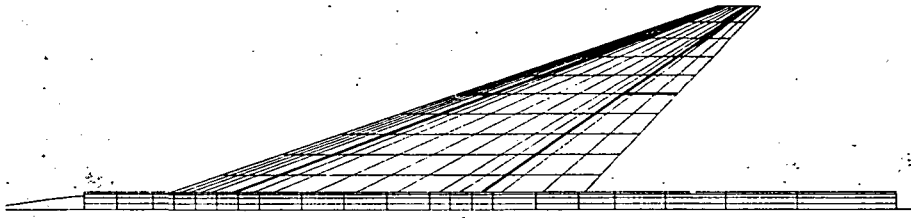


Figure 2.- FLEXSTAB paneling scheme.

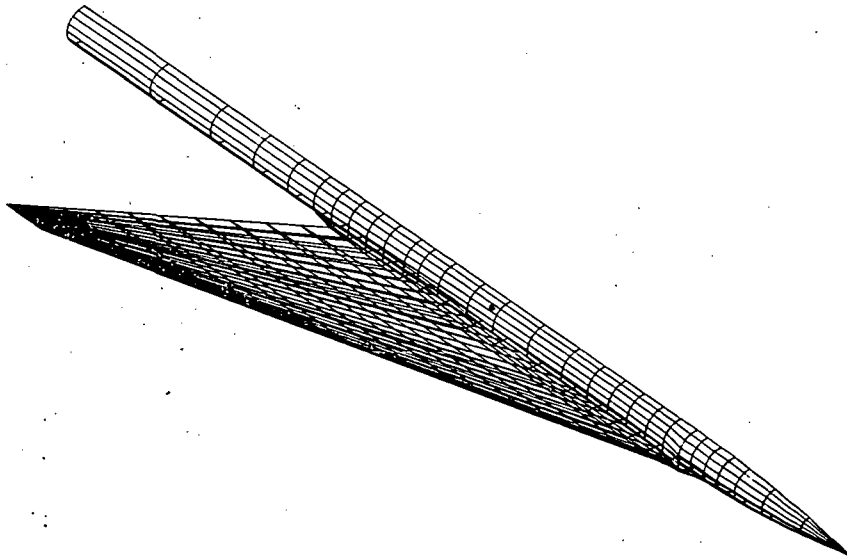


Figure 3.- TEA-230 paneling scheme. Flat wing.

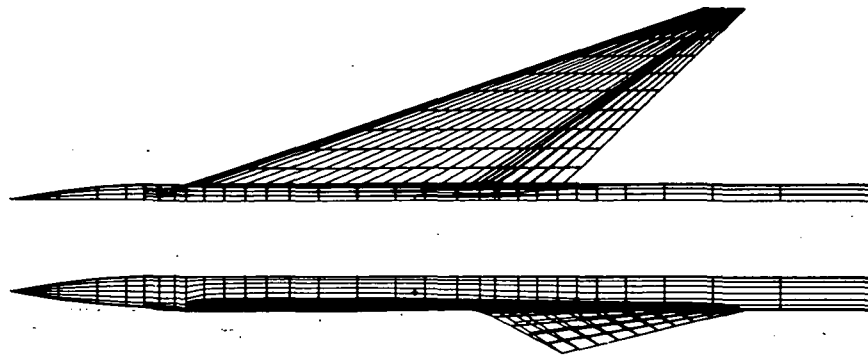


Figure 4.- TEA-230 paneling scheme. Trailing-edge flaps deflected.

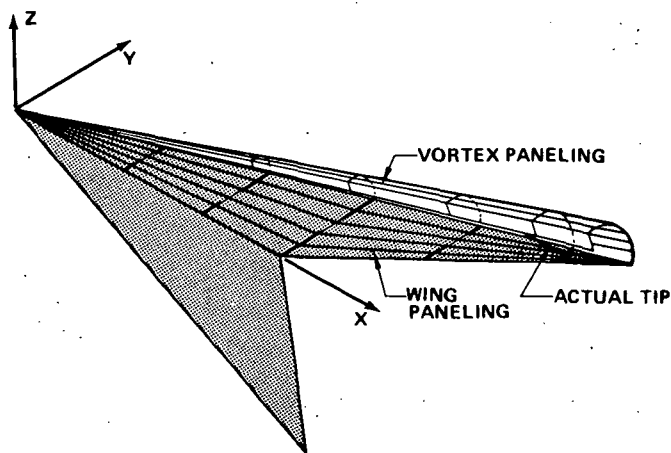


Figure 5.- 3-D vortex program paneling scheme.

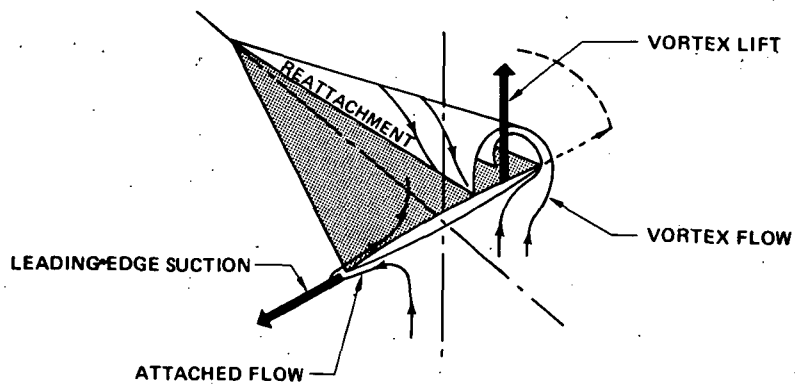


Figure 6.- Leading-edge suction analogy.

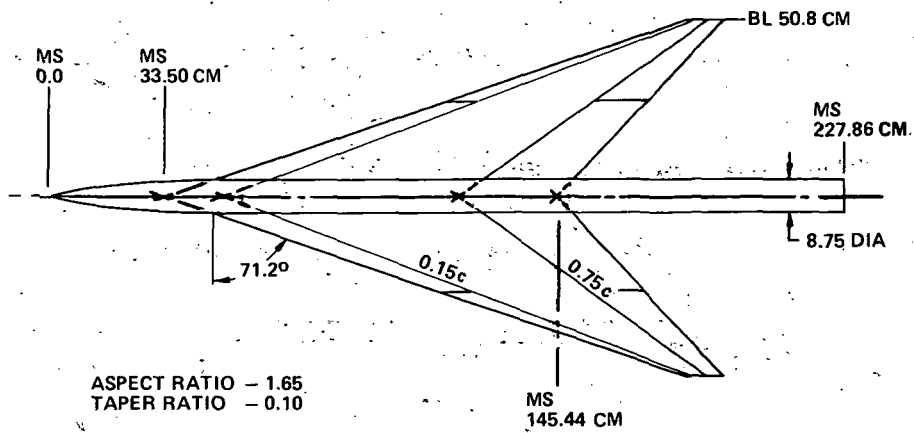


Figure 7.- Arrow-wing-body planform and basic geometry.

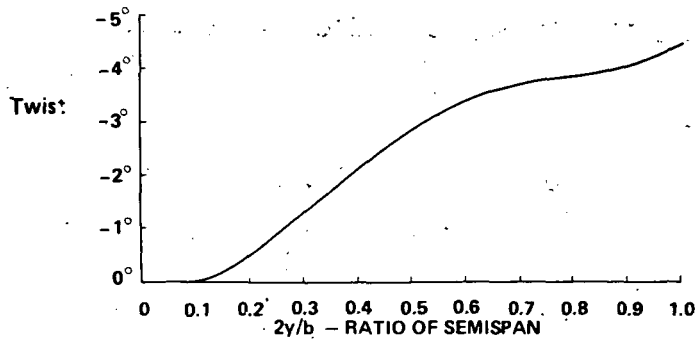


Figure 8.- Wing twist distribution. (Positive twist is leading edge up.)

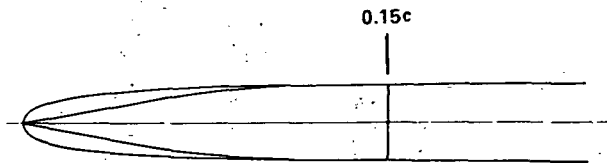


Figure 9.- Round and sharp leading edges.

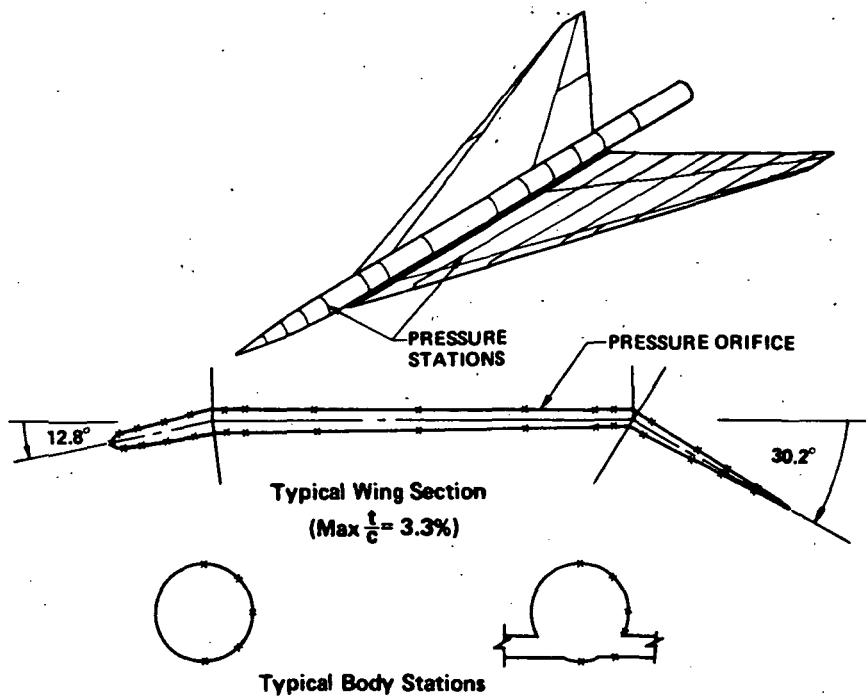


Figure 10.- Pressure orifice locations.

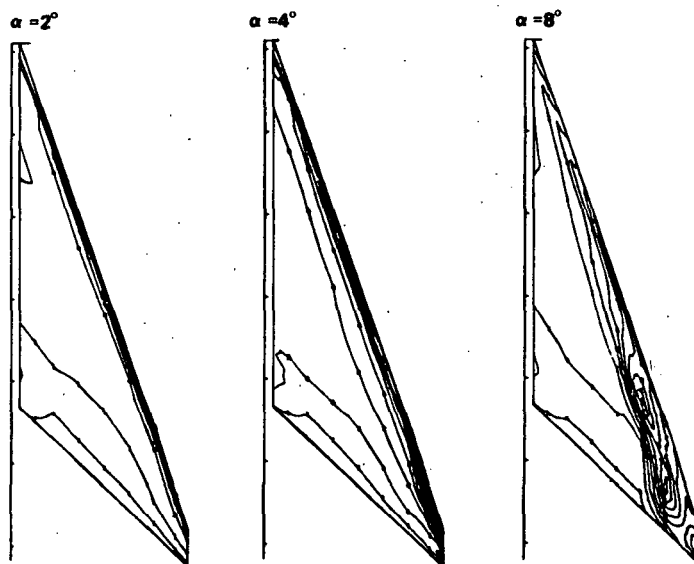


Figure 11.- Upper surface isobars. Flat wing;
round leading edge; $M = 0.40$.

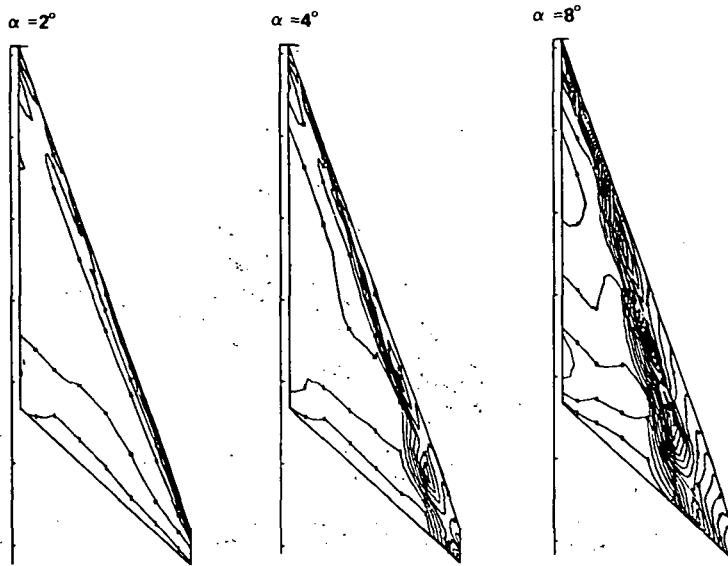


Figure 12.- Upper surface isobars. Flat wing;
sharp leading edge; $M = 0.40$.

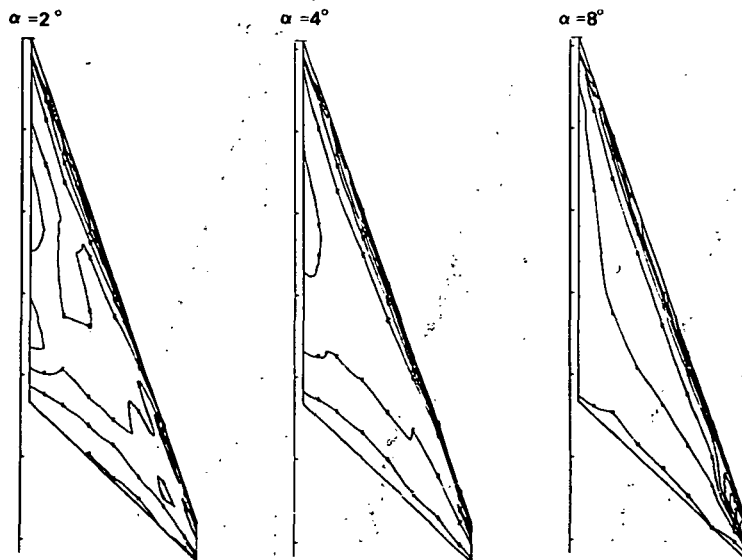


Figure 13.- Upper surface isobars. Twisted wing;
round leading edge; $M = 0.40$.

$\alpha = 2^\circ$

$\alpha = 4^\circ$

$\alpha = 8^\circ$

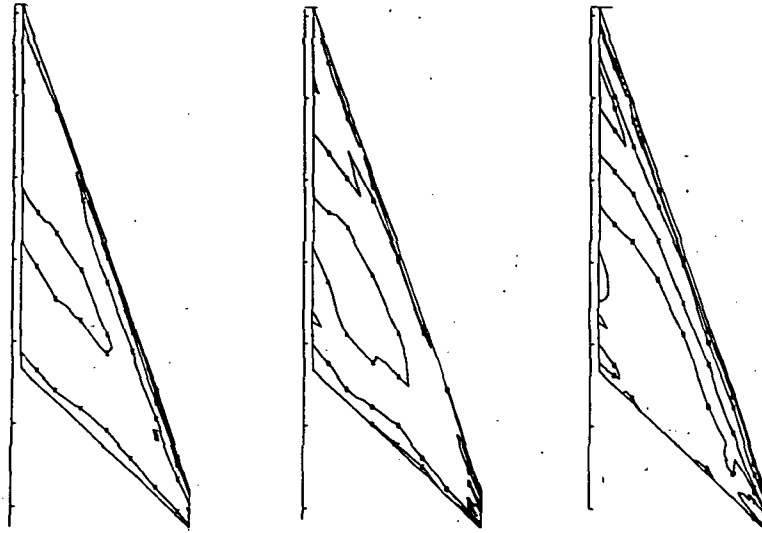


Figure 14.- Lower surface isobars. Typical; $M = 0.40$.

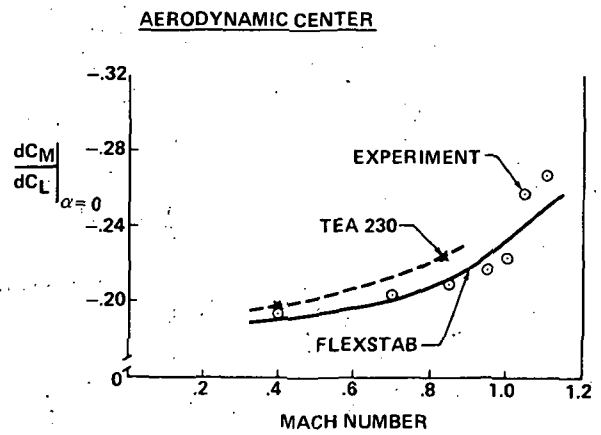
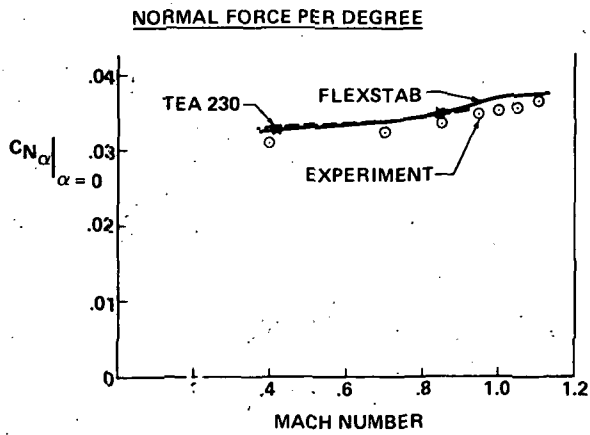


Figure 15.- Normal-force slope and aerodynamic center.

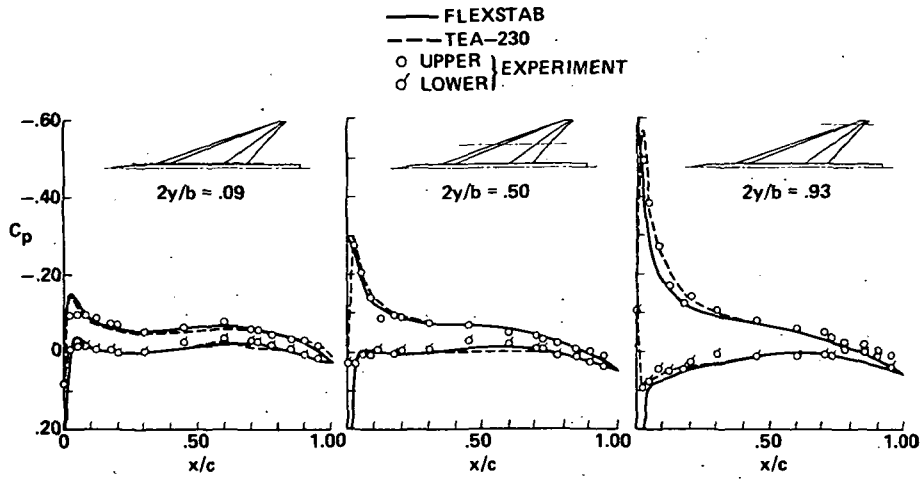


Figure 16.- Surface pressure distributions. Flat wing; $\alpha = 2^\circ$; $M = 0.40$.

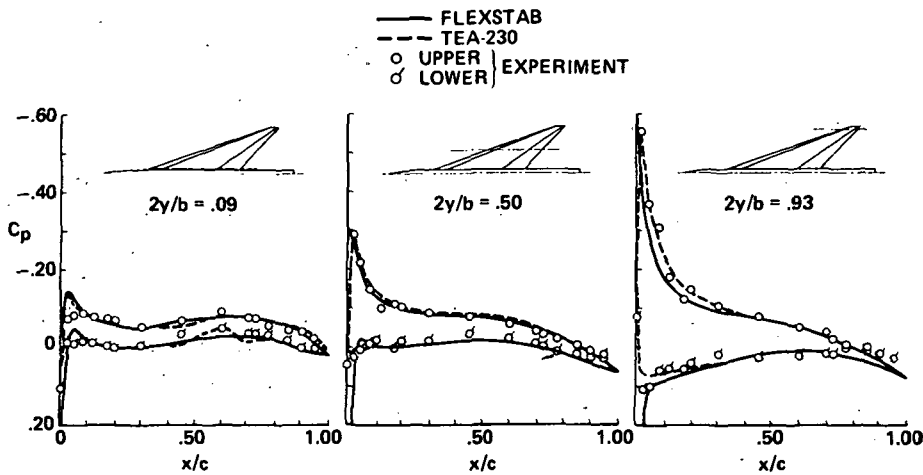


Figure 17.- Surface pressure distributions. Flat wing; $\alpha = 2^\circ$; $M = 0.85$.

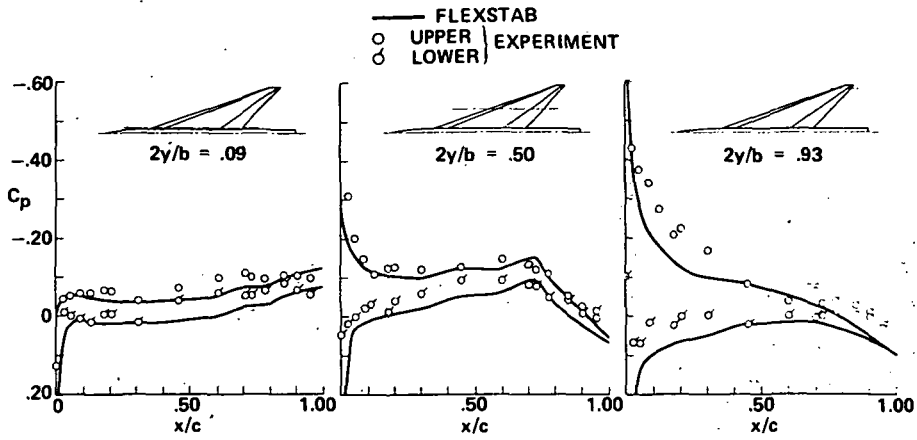


Figure 18.- Surface pressure distributions. Flat wing; $\alpha = 2^\circ$; $M = 1.05$.

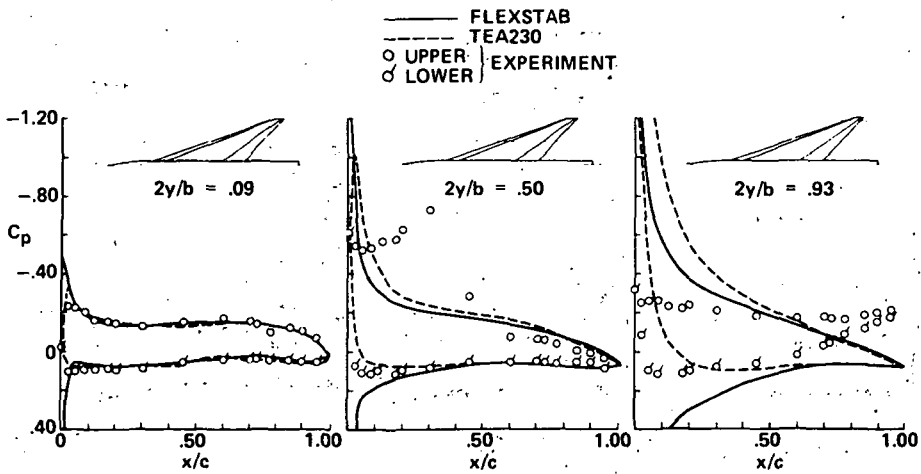


Figure 19.- Surface pressure distributions. Flat wing; $\alpha = 8^\circ$; $M = 0.85$.

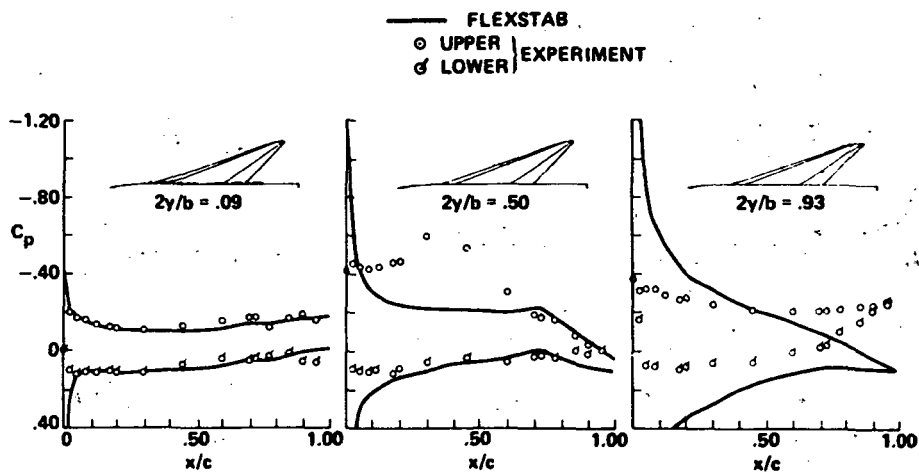


Figure 20.- Surface pressure distributions. Flat wing; $\alpha = 8^\circ$; $M = 1.05$.

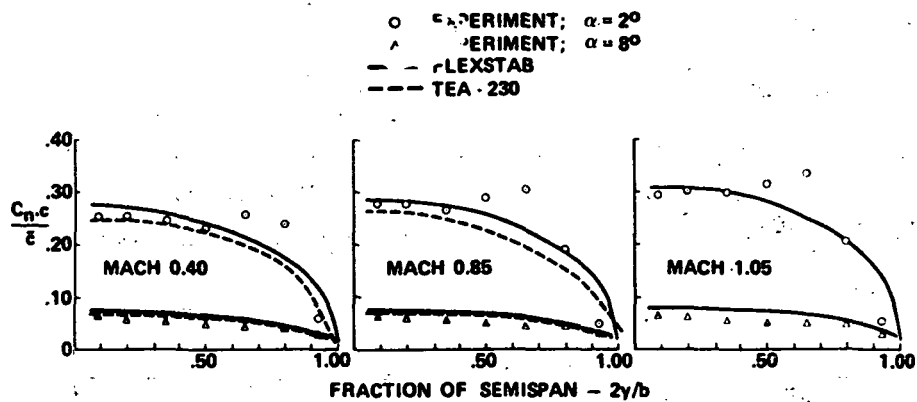


Figure 21.- Span load distributions. Flat wing; $M = 0.40, 0.85, \text{ and } 1.05$.

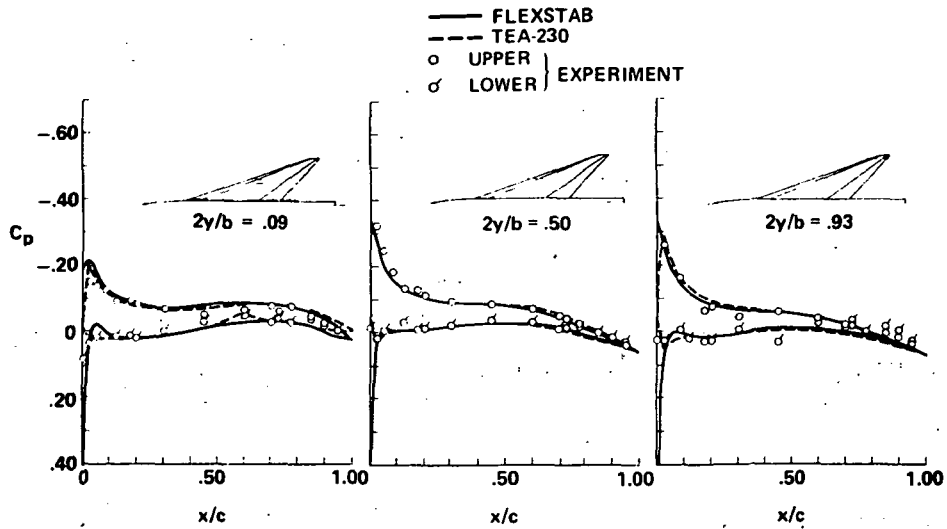


Figure 22.- Surface pressure distributions, Twisted wing; $\alpha = 4^\circ$; $M = 0.85$.

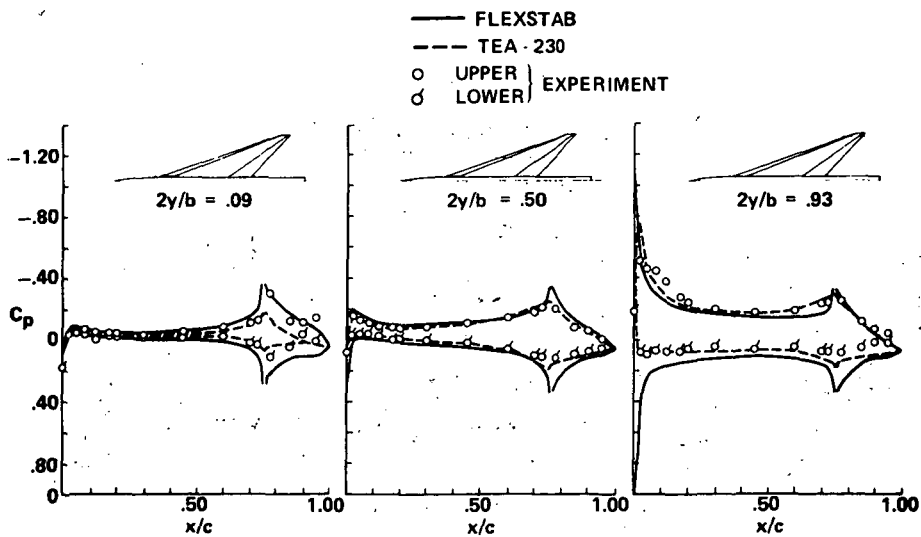


Figure 23.- Surface pressure distributions. Flat wing; trailing-edge $\delta_F = 8.3^\circ$; $\alpha = 0^\circ$; $M = 0.40$.

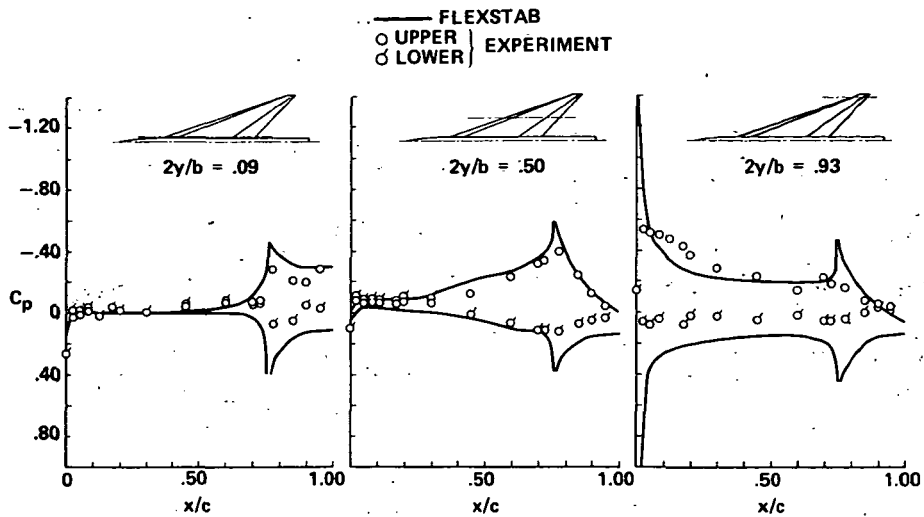


Figure 24.- Surface pressure distributions. Flat wing; trailing-edge $\delta_F = 8.3^\circ$; $\alpha = 0^\circ$; $M = 1.05$.

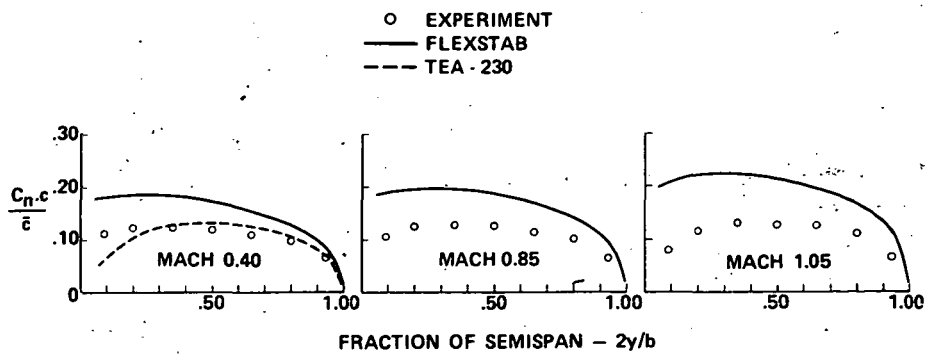


Figure 25.- Span load distributions. Flat wing; trailing-edge $\delta_F = 8.3^\circ$; $\alpha = 0^\circ$; $M = 0.40, 0.85, \text{ and } 1.05$.

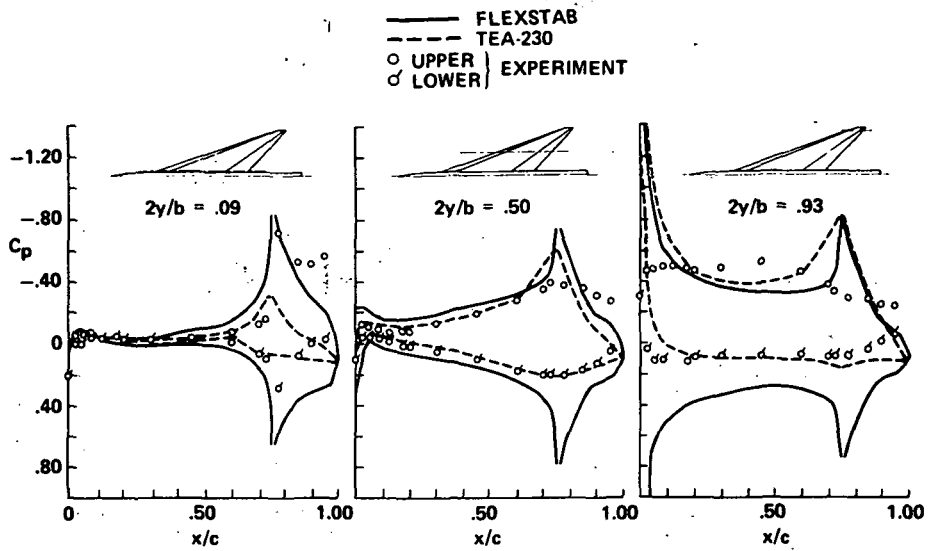


Figure 26.- Surface pressure distributions. Flat wing; trailing-edge $\delta_F = 17.7^\circ$; $\alpha = 0^\circ$; $M = 0.85$.

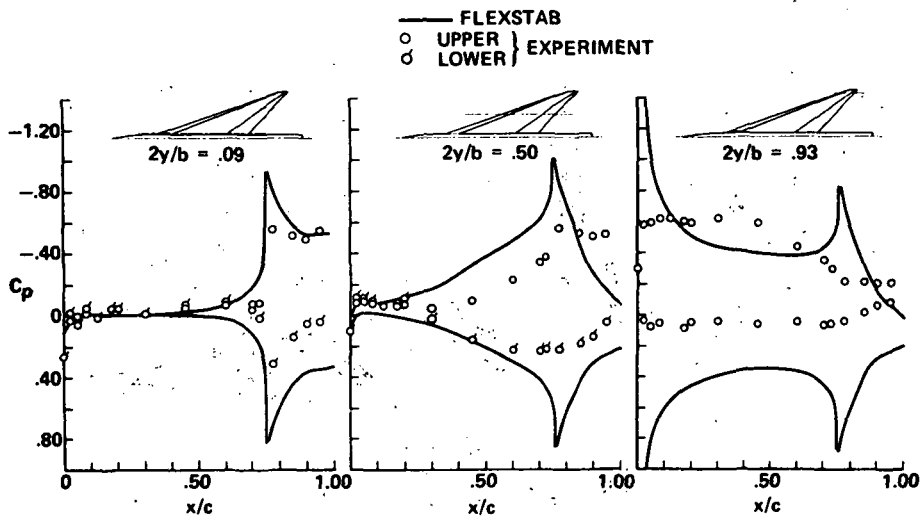


Figure 27.- Surface pressure distributions. Flat wing; trailing-edge $\delta_F = 17.7^\circ$; $\alpha = 0^\circ$; $M = 1.05$.

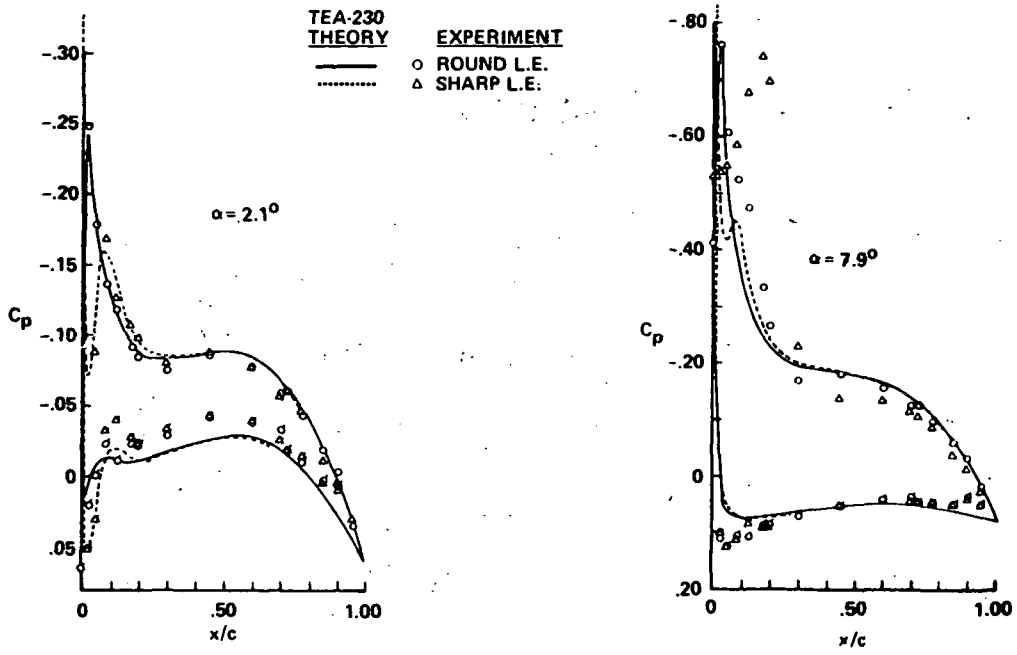


Figure 28.- Surface pressure distributions. Flat wing; sharp and round leading edges; $M = 0.85$; $2y/b = 0.35$.

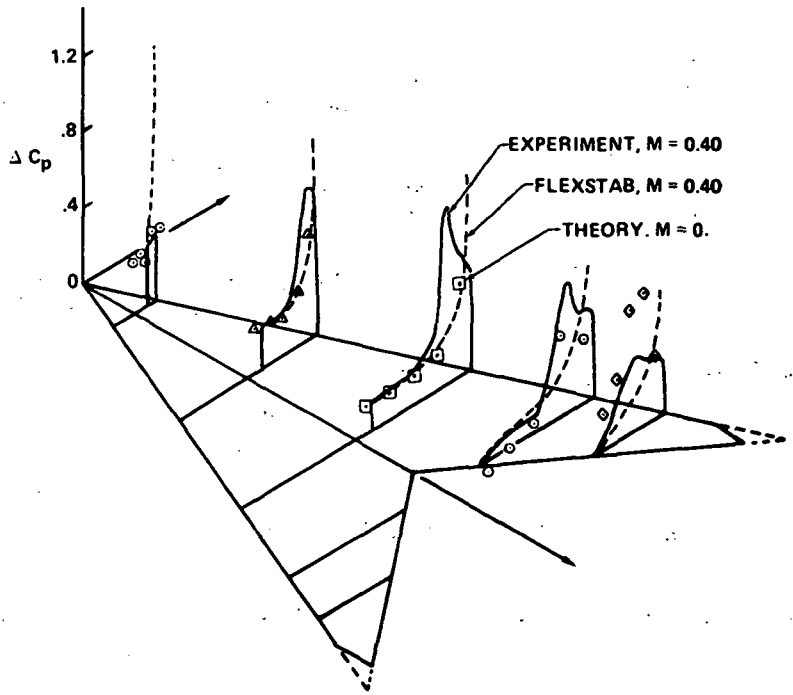


Figure 29.- Net pressure distributions. 3-D vortex program; $\alpha = 8.0^\circ$; $M = 0.40$.

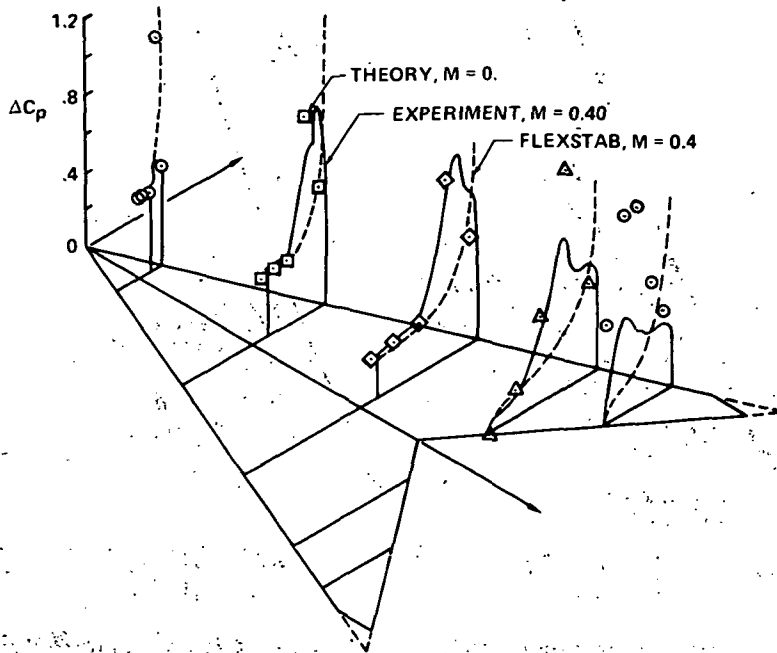


Figure 30.- Net pressure distributions. 3-D vortex program; $\alpha = 11.9^\circ$; $M = 0.40$.

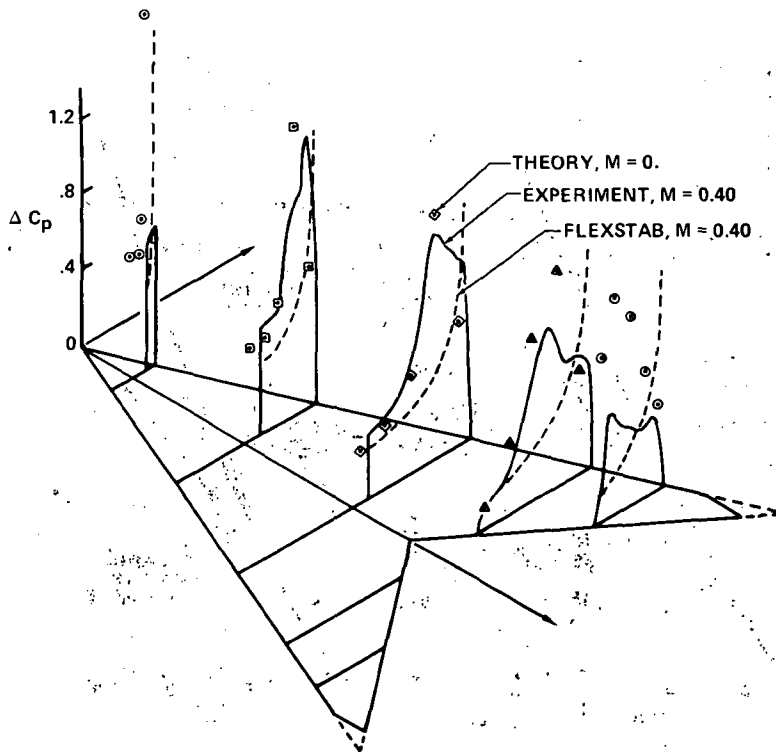


Figure 31.- Net pressure distributions. 3-D vortex program; $\alpha = 15.8^\circ$; $M = 0.40$.

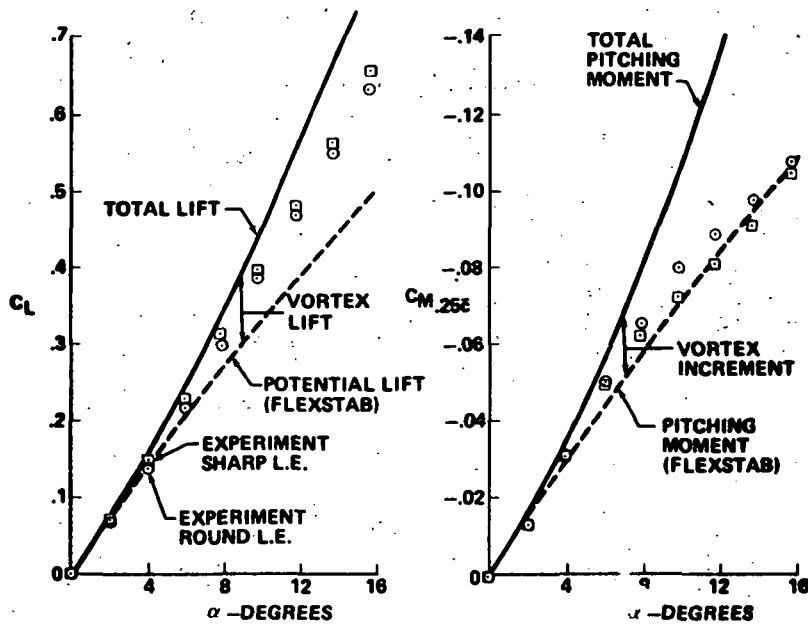


Figure 32.- Lift and pitching-moment coefficients. Leading-edge suction analogy; flat wing; $M = 0.85$.

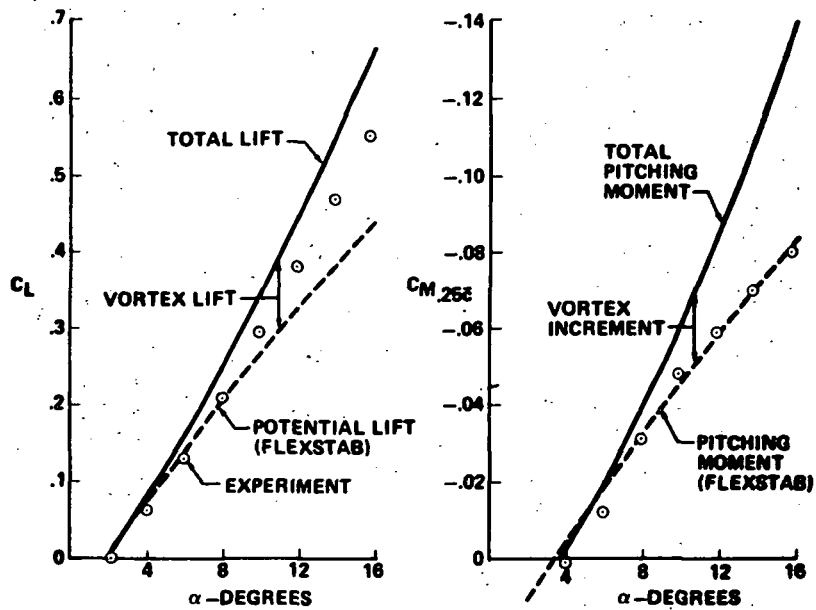


Figure 33.- Lift and pitching-moment coefficients. Leading-edge suction analogy; twisted wing; $M = 0.85$.

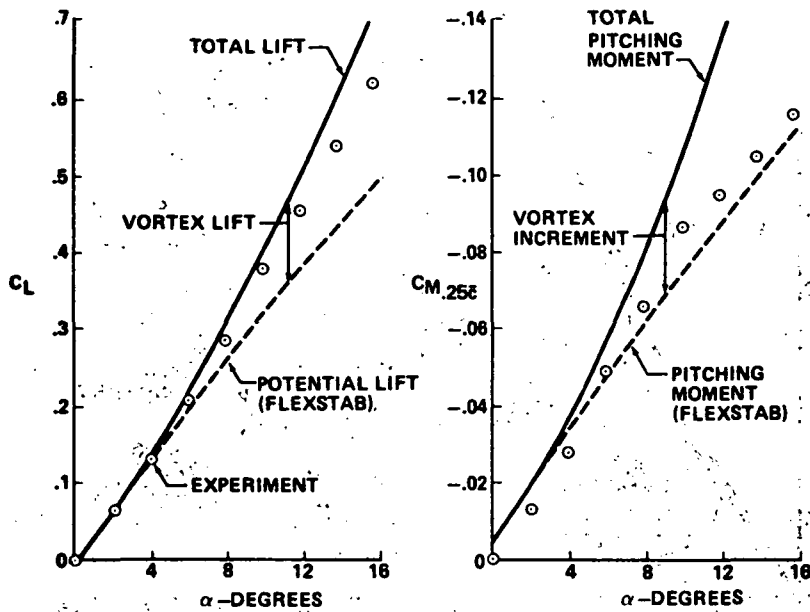


Figure 34.- Lift and pitching-moment coefficients. Leading-edge suction analogy; leading-edge $\delta_F = 5.1^\circ$; $M = 0.85$.

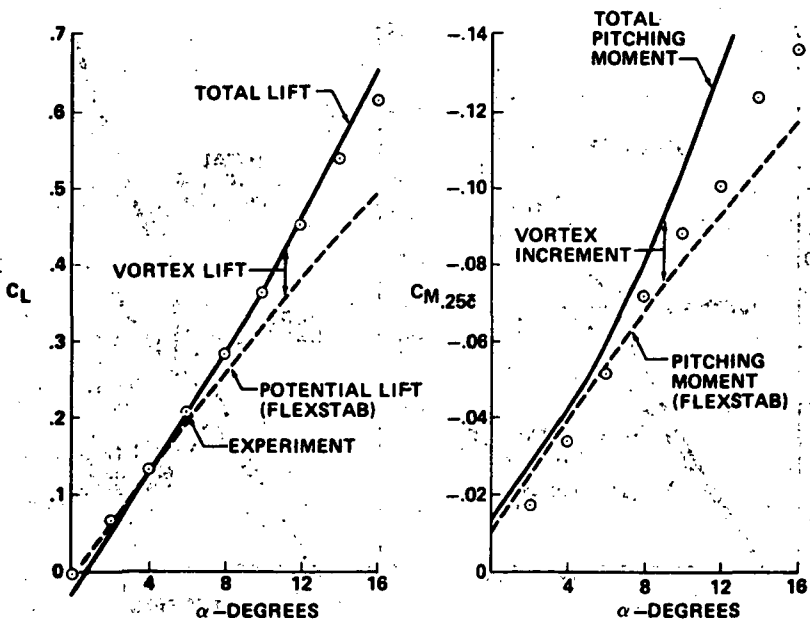


Figure 35.- Lift and pitching-moment coefficients. Leading-edge suction analogy; leading-edge $\delta_F = 12.8^\circ$; $M = 0.85$.

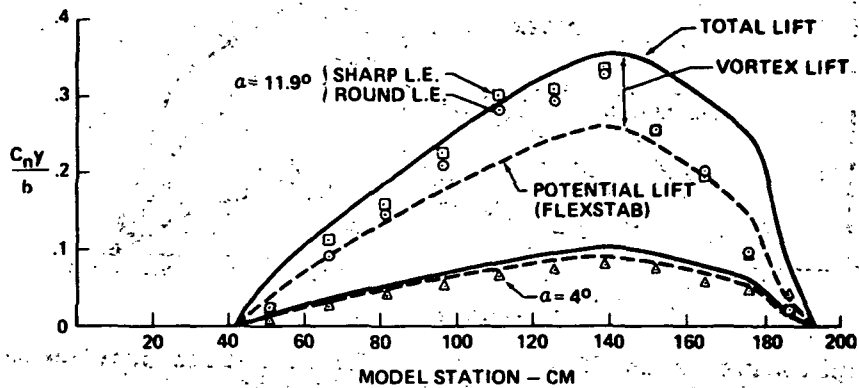


Figure 36.- Longitudinal load distribution. Leading-edge suction analogy; flat wing; $M = 0.85$.

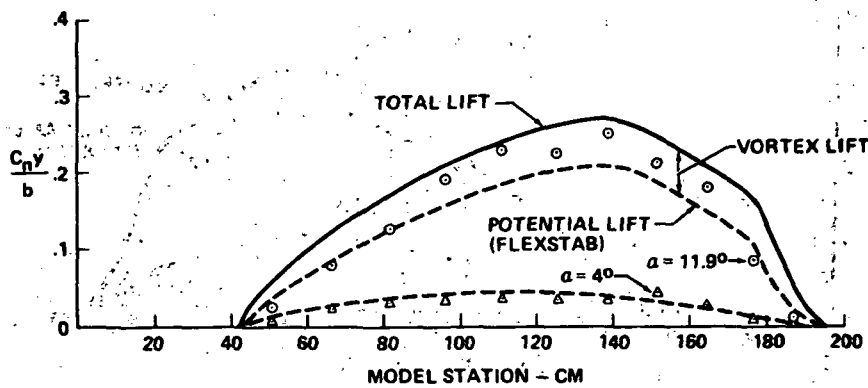


Figure 37.- Longitudinal load distribution. Leading-edge suction analogy; twisted wing; $M = 0.85$.

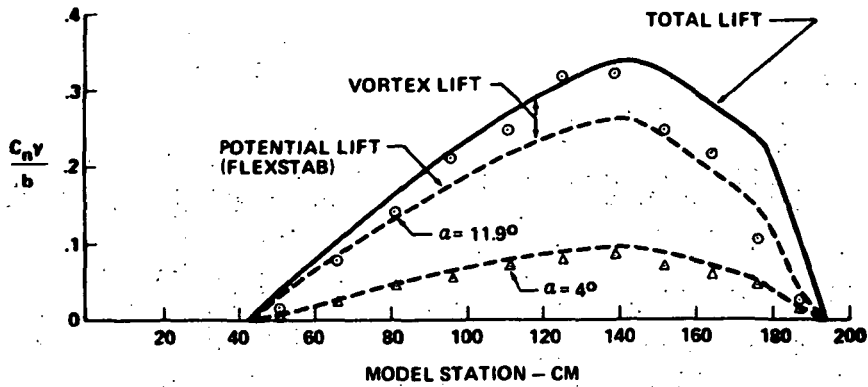


Figure 38.- Longitudinal load distribution. Leading-edge suction analogy; leading-edge $\delta_F = 5.1^\circ$; $M = 0.85$.

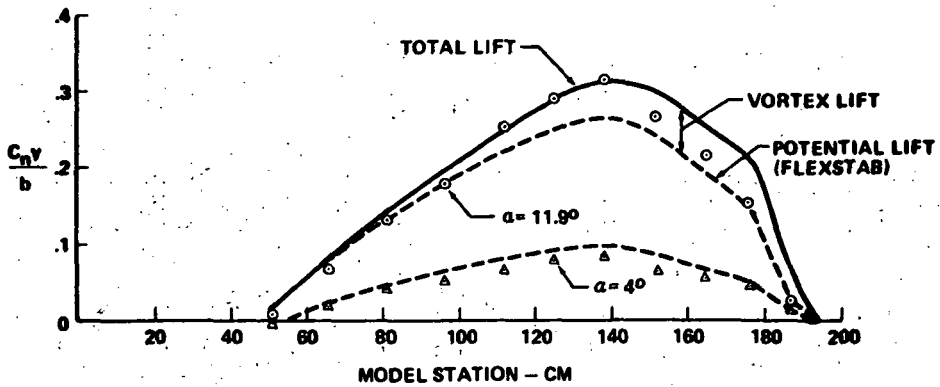


Figure 39.- Longitudinal load distribution. Leading-edge suction analogy; leading-edge $\delta_F = 12.8^\circ$; $M = 0.85$.

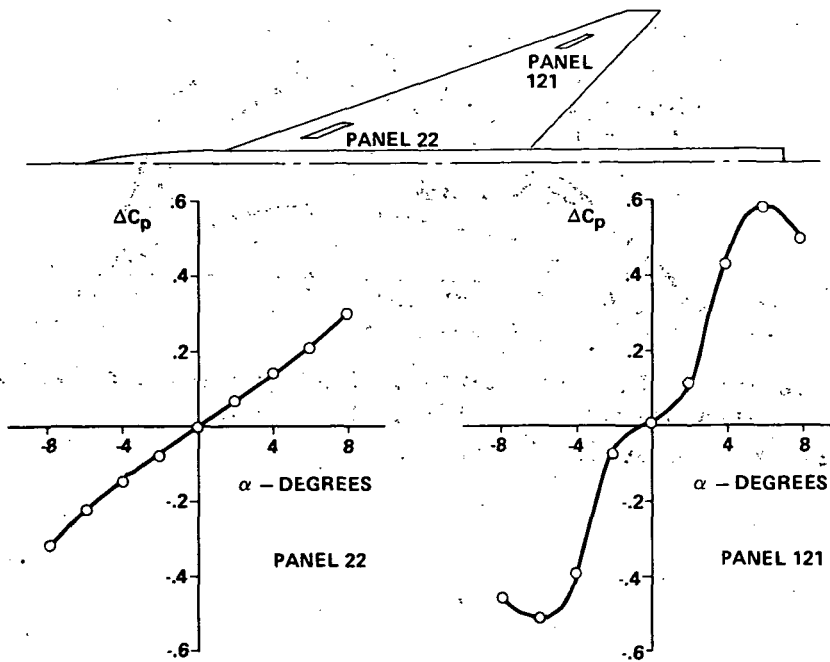


Figure 40.- Typical experimental net pressure variation with angle of attack.

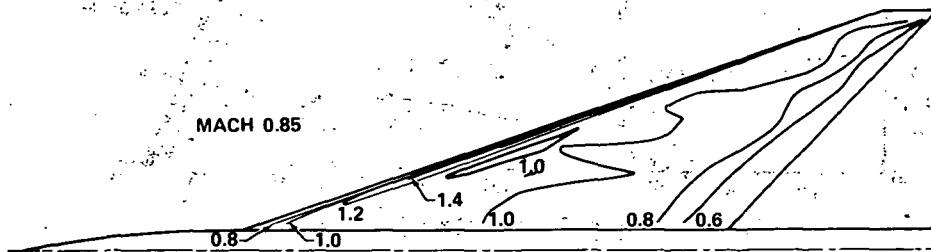


Figure 41.- Ratio of experimental to theoretical lifting pressure slopes,

$$\frac{\left(\Delta C_{p\alpha}\right)_{\text{experiment}}}{\left(\Delta C_{p\alpha}\right)_{\text{theory}}}$$

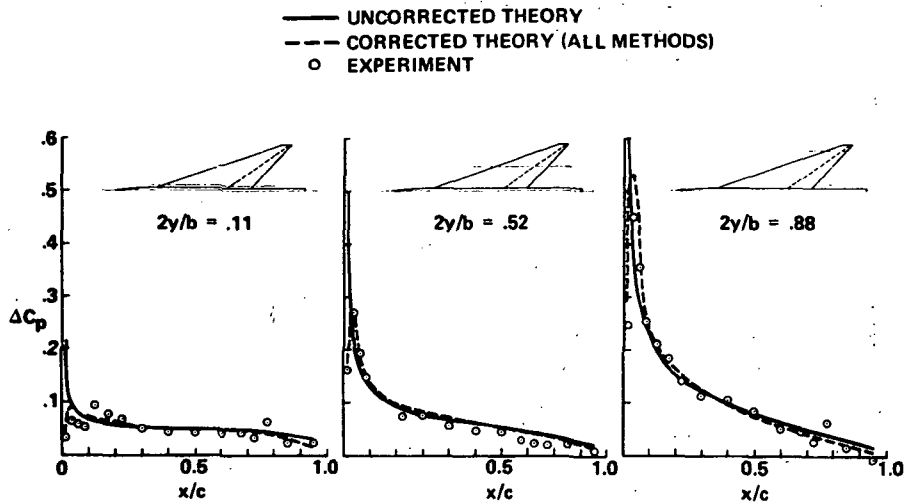


Figure 42.— Corrected theoretical results. Flat wing; $\alpha = 2^\circ$; $M = 0.85$.

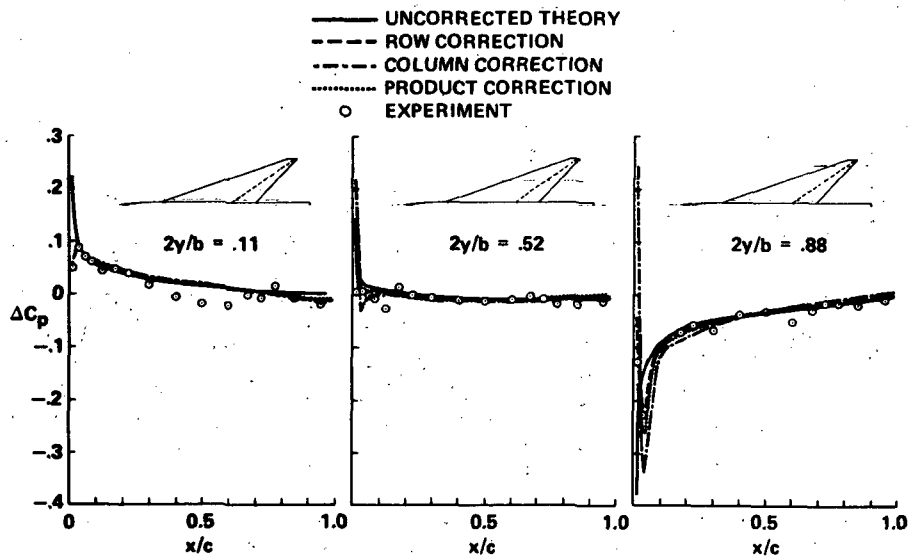


Figure 43.— Corrected theoretical results. Twisted wing; $\alpha = 2^\circ$; $M = 0.85$.

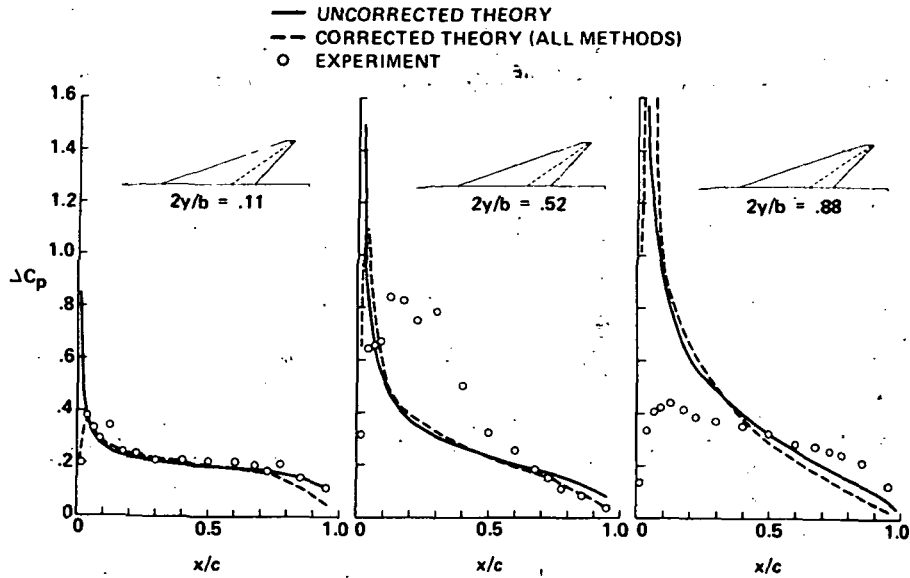


Figure 44.- Corrected theoretical results. Flat wing; $\alpha = 8^\circ$; $M = 0.85$.

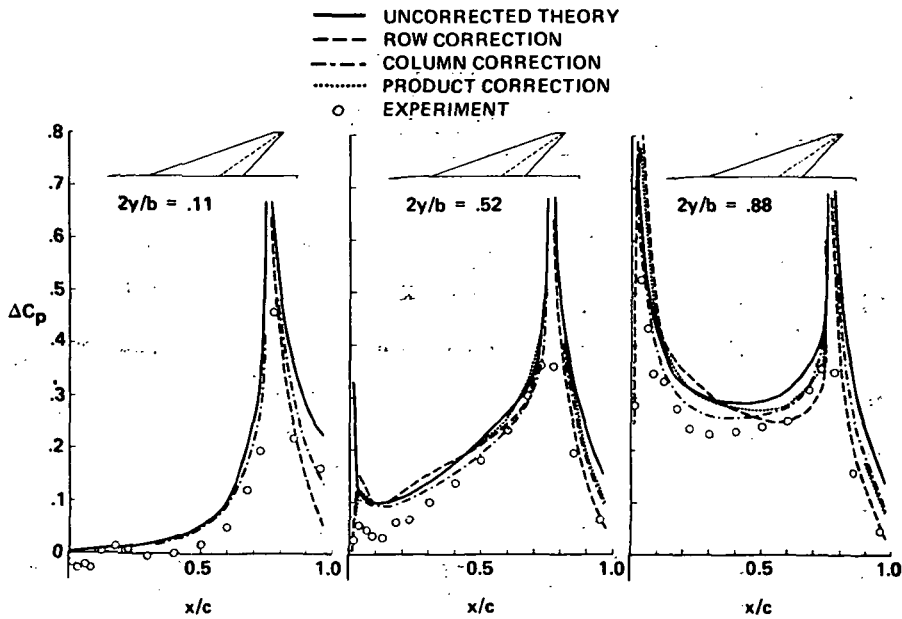


Figure 45.- Corrected theoretical results. Flat wing; trailing-edge $\delta_F = 8.3^\circ$; $\alpha = 0^\circ$; $M = 0.85$.

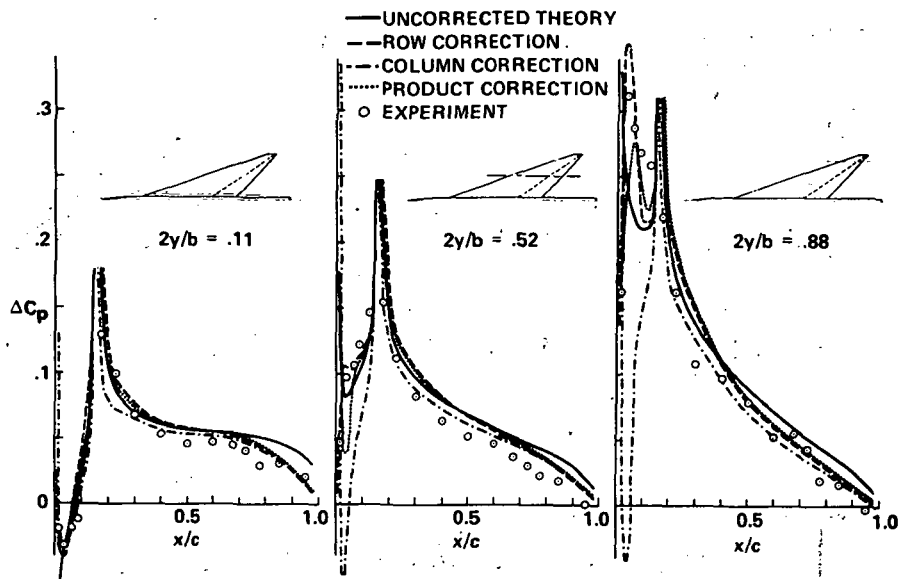


Figure 46.- Corrected theoretical results. Flat wing;
 leading-edge $\delta_F = 5.1^\circ$; $\alpha = 0^\circ$; $M = 0.85$.

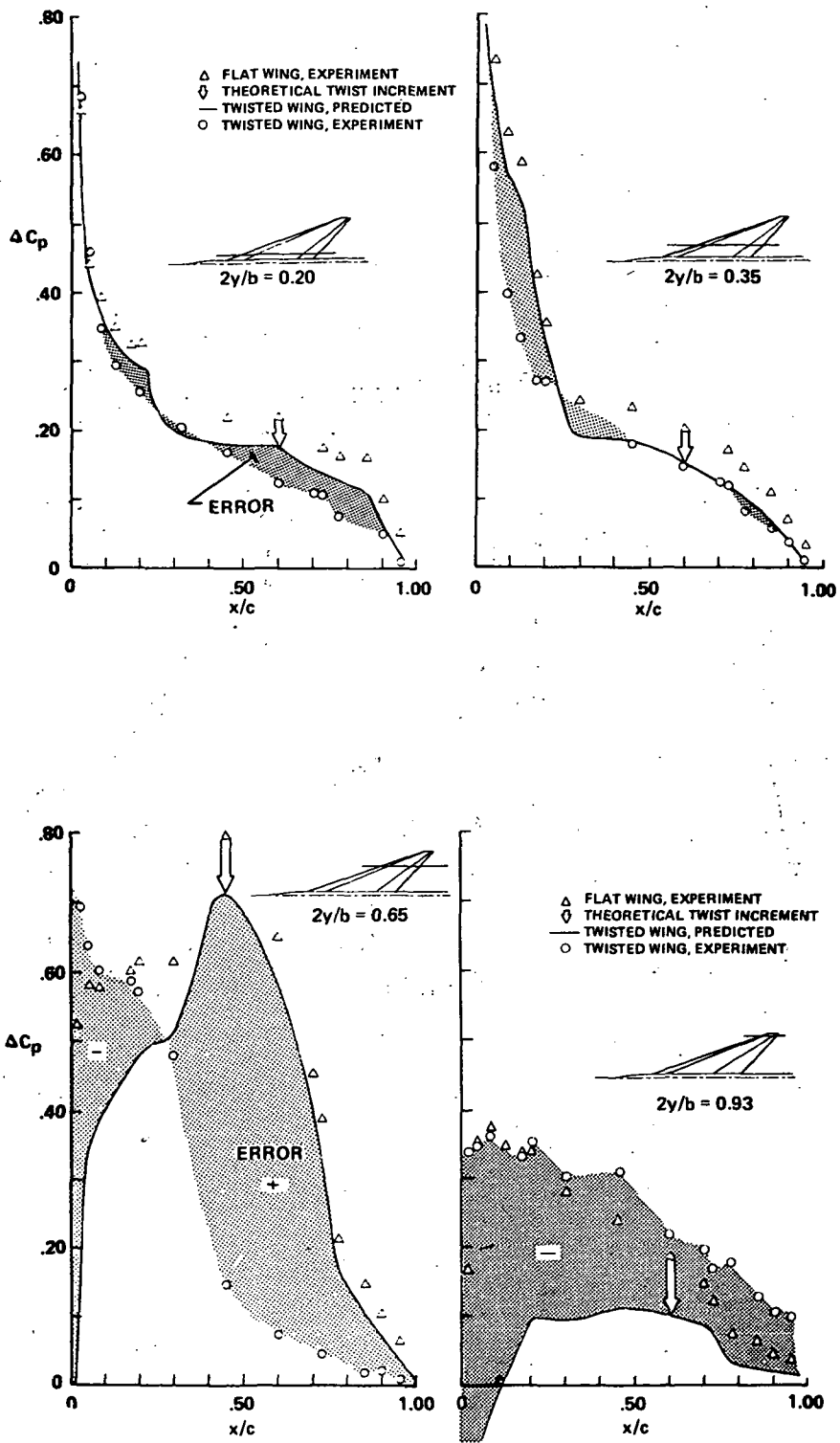


Figure 47.- Pseudo aeroelastic predictions. $\alpha = 8^\circ$; $M = 0.85$.

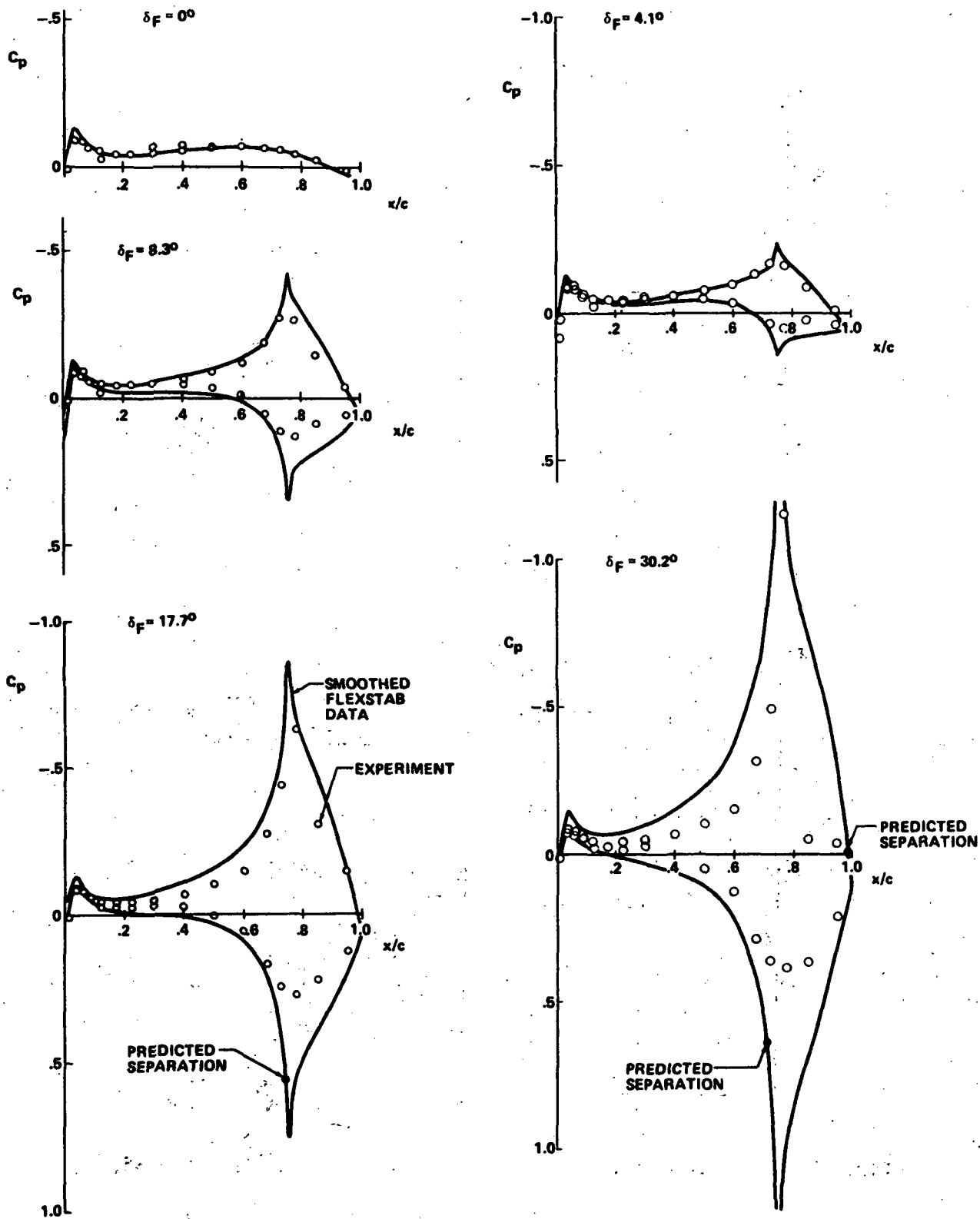


Figure 48.- Flow separation at trailing-edge flaps. Flat wing; $\alpha = 0^\circ$; $M = 0.85$; $2y/b = 0.22$.

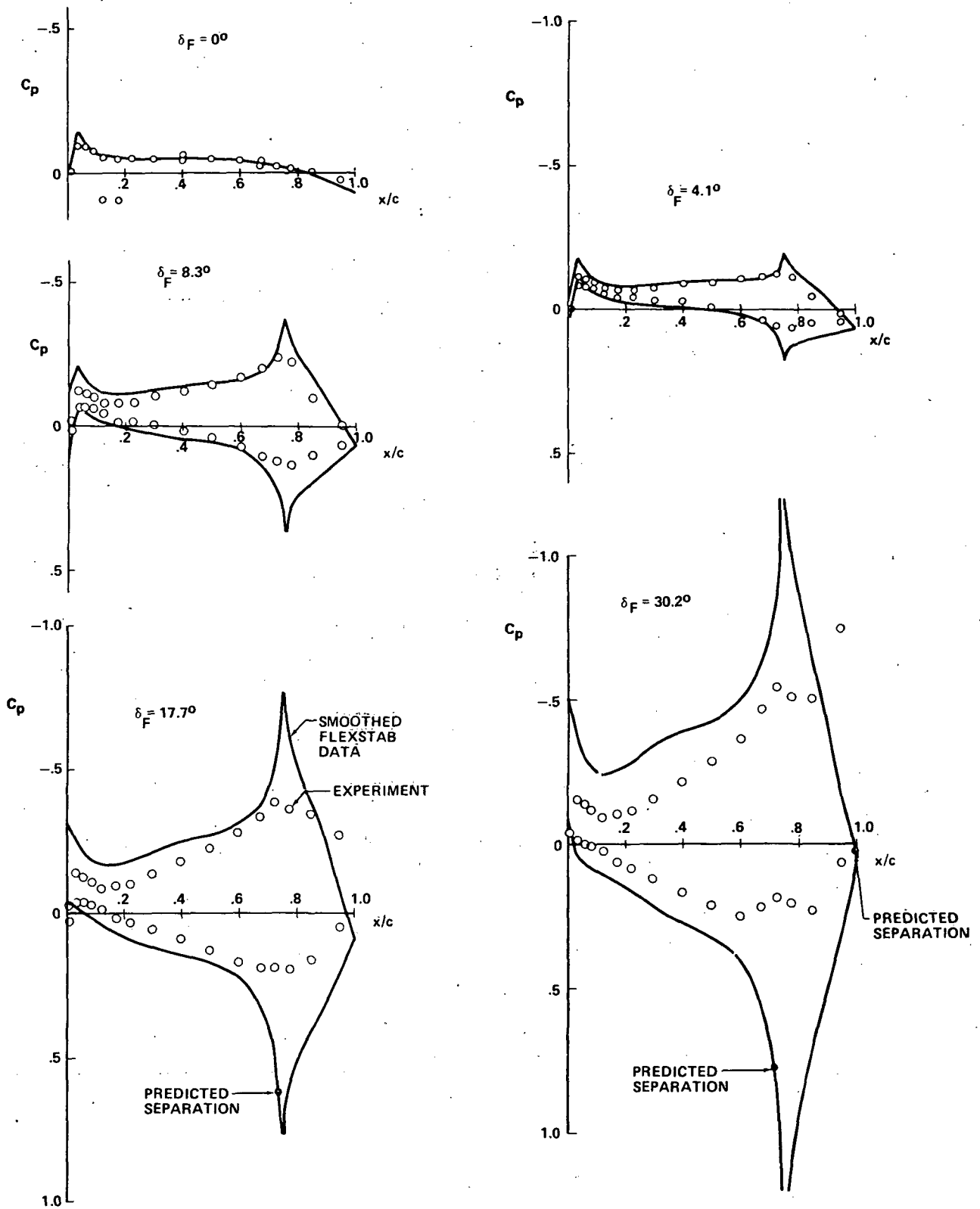


Figure 49.- Flow separation at trailing-edge flaps. Flat wing; $\alpha = 0^\circ$; $M = 0.85$; $2y/b = 0.52$.

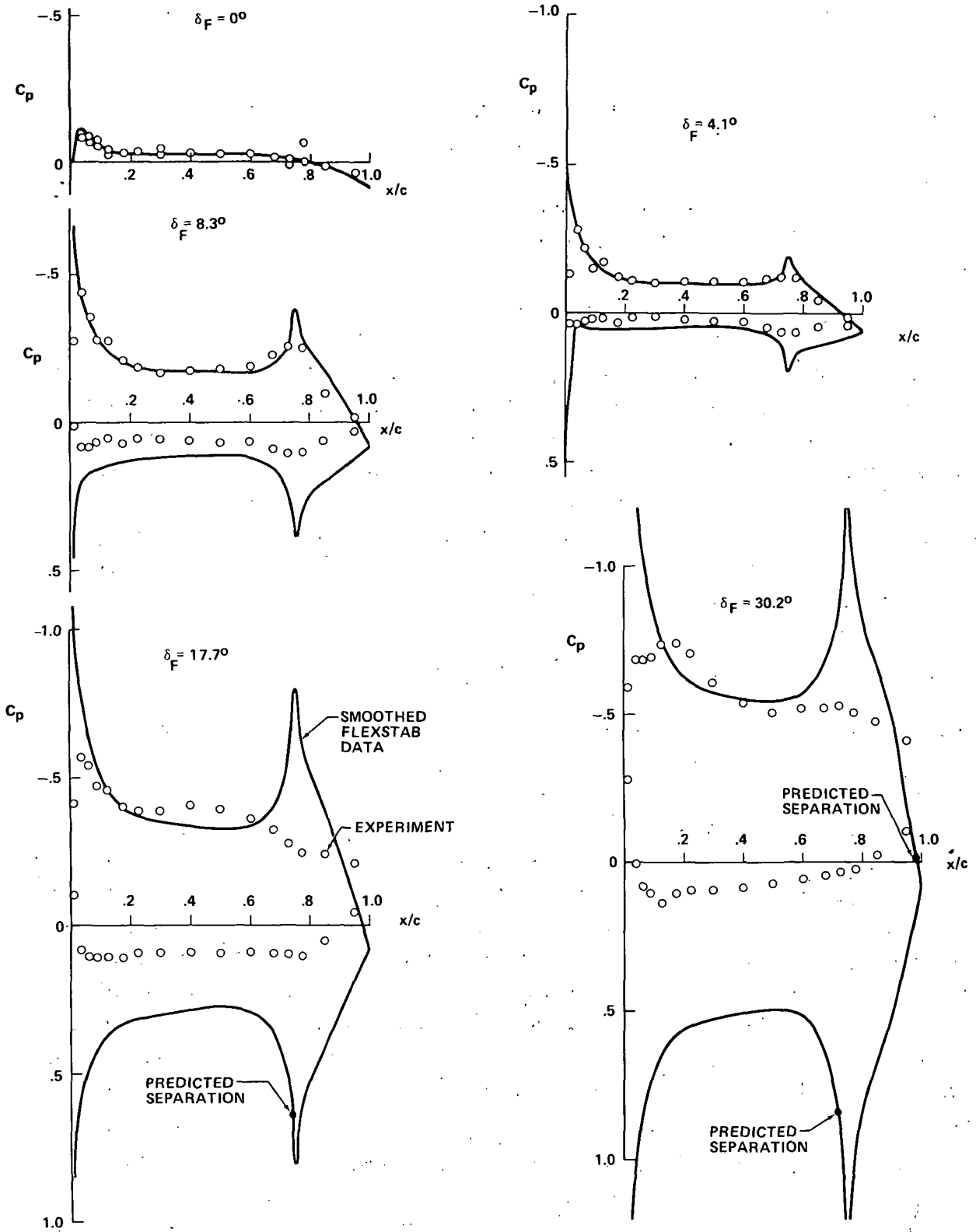


Figure 50.- Flow separation at trailing-edge flaps. Flat wing; $\alpha = 0^\circ$; $M = 0.85$; $2y/b = 0.88$.

NUMERICAL MODELING OF TUNNEL-WALL AND BODY-SHAPE EFFECTS ON TRANSONIC FLOW OVER FINITE LIFTING WINGS

By Perry A. Newman and E. B. Klunker
NASA Langley Research Center

SUMMARY

Preliminary computational results have been obtained for two problems relating to interference effects in transonic flow over finite lifting wings. The first is concerned with the numerical modeling of the flow about a three-dimensional wing configuration within a wind tunnel and the second is concerned with calculating favorable interference effects produced by the body of a wing-body configuration. For both problems, the calculations are based upon a small disturbance potential equation which is solved using a relaxation technique. A number of tunnel-wall boundary conditions are simulated and a comparison is made with experimental data.

INTRODUCTION

Numerical techniques for the computation of the inviscid potential flow about two-dimensional airfoils and bodies of revolution have attained a high state of development. For transonic flows, the relaxation algorithm has generally been used and the method has been adapted to both the full potential and small disturbance equation formulations. The success of these applications has led to the development of programs for more complex boundary-value problems such as flow about multiple airfoils, flow within bounded streams, and flow about some simple three-dimensional configurations. These latter developments have generally been based upon a small disturbance potential equation which both simplifies the calculations and minimizes the computer requirements. Three-dimensional results have been given for lifting wings (refs. 1 to 9) and also for wing-cylinder combinations (refs. 4, 8, and 10) which simulate some of the wing-body interference effects. In addition, some calculated results for the tunnel-wall problem have been given for two-dimensional (refs. 11 and 12) and axisymmetric (refs. 13 and 14) transonic flows.

The present paper presents some computational results for two transonic flow problems. The first is concerned with the numerical modeling of the flow about a three-dimensional wing configuration within a wind tunnel and the second is concerned with calculating favorable interference effects produced by the body of a wing-body configuration. For both problems, the calculations are based upon a small disturbance potential equation.

A number of tunnel-wall boundary conditions are simulated and some comparison is made with experimental data. Questions concerning the adequacy of the tunnel-wall modeling for ventilated walls are not addressed here – resolution of these questions requires more detailed experimental and numerical studies.

GENERAL METHOD

The basic Murman and Cole transonic relaxation technique (ref. 15) has been applied to successively more complex configurations and equations and a summary of its development is given in a recent review article (ref. 16). A variation of this technique is used herein to compute the flow about two three-dimensional configurations.

Governing Equations

The equation for the perturbation velocity potential ϕ used is

$$\left[\beta^2 - (\gamma + 1) M^2 \phi_x \left(1 + \frac{\phi_x}{2} \right) \right] \phi_{xx} + \phi_{yy} + \phi_{zz} = 0 \quad (1)$$

where M is the free-stream Mach number, $\beta^2 = 1 - M^2$, γ is the ratio of specific heats, and x, y, z are Cartesian coordinates. The term containing $\phi_x^2 \phi_{xx}$ has been retained (ref. 10) to better approximate the critical speed where the equation changes type from elliptic to hyperbolic.

The flow tangency condition on the wing is approximated by

$$\phi_z(x, y, 0) = f_x - \alpha \quad (2)$$

for x, y on the wing planform where $z = f(x, y)$ is the equation of the wing surface and α is the angle of attack.

The boundary condition on the trailing vortex sheet, assumed to lie in the $z = 0$ plane, is

$$\phi(x, y, 0^+) - \phi(x, y, 0^-) = \Gamma(y) \quad (3)$$

for x, y on the sheet. Note that the circulation $\Gamma(y)$ at each spanwise station y is determined as part of the solution by requiring the Kutta condition to be satisfied at the trailing edge of the wing section. If, however, the lift is specified, the distribution $\Gamma(y)$ may be obtained in some other way and the Kutta condition generally will not be satisfied if the angle of incidence α is also specified.

Far from the wing, the stream velocity is taken to be aligned with the tunnel or cylindrical-body axis; thus, the streamwise perturbation velocity ϕ_x vanishes as

$x \rightarrow \pm\infty$. At each of these limits, the differential equation (1) reduces to the two-dimensional Laplace equation. For a flow with lift, the jump condition, equation (3), must be enforced on the slit at the trailing vortex sheet.

Stability Considerations

Jameson (refs. 6 and 7) has shown that since line relaxation is not fully implicit in a three-dimensional problem, one must be careful in constructing the finite-difference operator which is used at supersonic points if it is to be iteratively stable. Note, however, that block relaxation of an entire plane normal to the flow direction would be. Jameson's analysis of equation (1) would indicate that (1) the relaxation factor at supersonic points should be exactly 1.0, and (2) some old values of ϕ should be used in the three-point backward difference for ϕ_{xx} (thus implicitly introducing some ϕ_{xt} where t is an artificial time). Both of these aspects have been included in the present algorithm. In fact, explicit addition of even more ϕ_{xt} at supersonic points has been found to stabilize some calculations. At computational grid points where the flow is subsonic, one generally tries to overrelax the solution. Since the coefficient of ϕ_{xx} in equation (1) vanishes as the local Mach number $\rightarrow 1$ whereas those of ϕ_{yy} and ϕ_{zz} do not, switching the value of the relaxation factor between subsonic and supersonic points which are adjacent to one another in either the y - or z -direction can produce a spurious ϕ correction. This phenomenon is observed when the sonic or shock surface is not normal to the flow direction. Therefore the relaxation factor is set equal to 1 for the contributions from ϕ_{yy} and ϕ_{zz} ; only the contribution from ϕ_{xx} is overrelaxed (or underrelaxed). Perturbations during a calculation caused by shock-wave movement, circulation adjustments, boundary updates, and so forth may trigger instabilities which can sometimes be damped by reducing the subsonic relaxation factor or increasing the explicit ϕ_{xt} at supersonic points (or both). The present algorithm monitors the maximum ϕ correction, and if it increases for too many cycles, the relaxation factor is automatically reduced or additional ϕ_{xt} is introduced at supersonic points.

TUNNEL-WALL PROBLEM

Several recent papers have included tunnel-wall boundary conditions in nonlinear transonic relaxation computations for two-dimensional (refs. 11 and 12) and axisymmetric problems (refs. 13 and 14). The present extension to a three-dimensional problem has incorporated some of the ideas expressed in these references. The problem considered is that of a rectangular planform wing with an arbitrary airfoil section mounted in a rectangular cross-section wind tunnel as depicted in figure 1.

Computational Considerations

Tunnel-wall boundary conditions.- The boundary condition used to model the tunnel walls is the integrated form of the generalized linear homogeneous condition as given in reference 17 with an inhomogeneous term added to account for integration constants and physical effects such as $C_p \neq 0$ in the plenum or contoured walls (unpublished notes of Richard W. Barnwell, Langley Research Center). This condition is

$$A\varphi_n + B\varphi_x + C\varphi + D = 0 \quad (4)$$

and the conventional linear wall conditions are obtained as

$$\left. \begin{array}{l} \text{Open jet: } A = C = D = 0, \quad B \neq 0 \\ \text{Straight solid: } B = C = D = 0, \quad A \neq 0 \\ \text{Contoured solid: } B = C = 0, \quad -D/A \text{ is wall slope} \\ \text{Porous: } C = D = 0, \quad B/A \text{ is porosity or restriction parameter} \\ \text{Slotted: } B = D = 0, \quad C/A \text{ is slot geometry parameter} \end{array} \right\} \quad (5)$$

Several points should be made concerning the tunnel-wall boundary condition. First, it is considered to be an average relationship between various local inviscid flow properties which applies near the wall rather than on it. Second, in an iterative finite-difference calculation there is a great deal of flexibility regarding the form of the boundary condition itself since (a) it need not even have a functional form (i.e., could be measured flow properties) much less be linear; (b) the parameters in it can vary with local tunnel geometry or local flow conditions; and (c) it is restricted, however, in that the relaxation calculation must be stable. Third, the porosity and slot geometry parameters must be determined experimentally. The consensus now seems to be that these parameters are dependent on local flow conditions near the tunnel wall which for transonic flows are influenced not only by the tunnel operating conditions but also by the test configuration.

Geometry and coordinates.- Calculations have been made on a nonuniform three-dimensional Cartesian grid. Figure 2 shows a plane section normal to the wing leading edge (i.e., containing the tunnel axis) and figure 3 shows a plane section normal to the free stream (i.e., the tunnel cross section). The rectangular wing dimensions and tunnel-wall locations indicated in these figures are those corresponding to the wall-interference model of reference 18 (subsequently called the AEDC model) in the AEDC Aerodynamic Wind Tunnel (4T). These were chosen for the present study since experimental data had been taken on the model in both the AEDC Tunnel 4T and the AEDC Propulsion Wind Tunnel (16T) specifically to investigate three-dimensional wall interference in a variable-

porosity transonic tunnel (ref. 18). The AEDC model has a rectangular wing with a chord of 22.8 centimeters (9 inches) and a span of 81.3 centimeters (32 inches); that is, aspect ratio $AR = 3.56$. The airfoil section is an NACA 63A006. The AEDC Tunnel 4T has a square cross section 122×122 centimeters (48×48 inches), and the ratio of total tunnel height to wing chord is $h/c = 5.3$ for this model.

The grid used for most of the calculations presented here was $48 \times 20 \times 26$ in the streamwise, spanwise, and wing normal directions, respectively. Upper and lower tunnel walls are located at grid planes 24 and 3 in the wing normal mesh while the root symmetry plane and tunnel side wall are at grid planes 2 and 15 in the spanwise mesh. It can be seen that there is a high concentration of grid lines near the wing plane and over the wing chord. In the streamwise direction, the grid extends from $x/c \approx -17$ upstream to $x/c \approx +7$ downstream of the wing. Boundary conditions appropriate to $|x| = \infty$ have been applied on these planes which are located at finite values of x .

The grid within the tunnel was not changed for the comparisons made in this paper; free-air results were obtained with additional points outside the boundaries. An analytic stretching was used in the wing normal direction so that $|z| \leq \infty$ was mapped into a finite domain. In the spanwise direction, the grid extended to $y/c \approx 4.1$ for the free-air results; the boundary condition appropriate to $y = \infty$ was applied on this plane.

Stability with tunnel-wall boundary condition. - The tunnel-wall boundary condition, equation (4), was imposed on the finite-difference calculation as follows:

(1) The open-jet condition, $\varphi_x = 0$, requires $\varphi = \text{Constant}$ on the boundary. This was implemented as the Dirichlet condition $\varphi = 0$ with equation (1) being satisfied at all interior points in the relaxation cycles.

(2) For all other conditions a false point behind the tunnel-wall boundary was introduced and the value of φ associated with it was determined by requiring the central difference expression for φ_n at the wall point to be given by equation (4). All the false points are updated (by point relaxation) each iteration cycle after line relaxation of equation (1) throughout the entire field (interior and wall-boundary points).

It was found that the stability of the iterative calculation was adversely affected by inclusion of the tunnel-wall boundary as in (2) in the preceding paragraph. The present results were obtained with the calculation stabilized by, first, underrelaxing the update of φ at false points behind the wall and, in some cases, the solution φ at all subsonic points and, second, holding $\varphi = 0$ at all false points for the first few iteration cycles (≈ 30) and slowly, over the next few cycles (30), introducing the value required by equation (4). It appears that the solution near or at the side wall is most sensitive; this may be due to having the column of updated points in the line-relaxation algorithm parallel to the side wall. Thus, at the side wall, every point in the column is in contact with a false point. In two-dimensional and axisymmetric problems the tunnel-wall boundary condition is in

contact with only the end points of the column, as is the case for the upper and lower wall conditions in the present calculation. There are a number of ways to introduce the wall condition, equation (4) (for example, refs. 11 to 14), which should be investigated since the present approach may not be the most efficient. This point is discussed in reference 19 where yet another means of incorporating equation (4) is given.

Results

Computational results for the wing of the AEDC model (ref. 18) are given for several of the conventional linear tunnel-wall boundary conditions. These are preliminary results from a new program and have been generated on a grid which is coarse by two-dimensional flow standards but typical of those for three-dimensional problems. They serve to indicate the feasibility of including tunnel-wall effects in three-dimensional transonic calculations and provide an initial estimate of the magnitude of the effects.

Porosity wall study. - The AEDC model is a full-span model with a rectangular planform wing centrally mounted on a sting body. (See ref. 18.) Experimental streamwise pressure distributions were measured on the upper and lower wing surfaces at the mid-semispan position and also on the windward and leeward sides of the sting body. In this section, computed streamwise pressure distributions for free-air, open-jet, solid-wall, and porous-wall boundary conditions are compared with one another at two different Mach numbers.

Figure 4 shows the chordwise wing-surface pressure distributions at the midsemi-span location for a free-stream Mach number of 0.88 and 3° incidence. This is a transonic flow and the sonic value of pressure coefficient C_p is indicated by the long tick mark on the ordinate. For this Mach number, the most noticeable effect, due to the tunnel walls, at the model location is a shift in the position of the shock wave on the wing upper surface. The key identifies the several results; in places where the differences are negligible, such as on the lower surface in this case, only a single curve is shown.

As indicated in equation (5) the ratio of coefficients B/A is a porosity parameter which is seen from equation (4) to be proportional to φ_n/φ_x . The symbol P is used for $|B/A|$. Porosity values P vary between 0 and ∞ with 0 corresponding to the solid wall and ∞ the open jet.

Streamwise tunnel-wall pressure distributions in the wing root plane on both the upper and lower walls are shown in figure 5 for the flow conditions of figure 4; however, the C_p scale in figure 5 is smaller by a factor of 8. The insert shows the location on the walls where the pressures are calculated. Those appropriate to the upper wall generally lie above the axis ($C_p = 0$), whereas those for the lower wall lie below the axis. The distributions are similar but the differences are felt to be significant and measurable. The open-jet condition is $C_p = 0$ on the boundary and is given by the C_p axis. The

solid wall results show the largest departures from $C_p = 0$. Two porous wall results are shown: One in which the porosity was the same constant value ($P = 0.65$) at all points on all walls and the other in which the porosity differed for local inflow to ($P_i = 0.65$) and outflow from ($P_o = 0.22$) the test section. (See ref. 12 for some discussion of this matter.) Where outflow occurs (i.e., below the wing where $C_p > 0$), a difference can be seen in the wall pressure levels for different P values. These three-dimensional results at the wing root plane exhibit the qualitative behavior of the two-dimensional experimental wall pressures (i.e., near the wall) presented in reference 15.

At a higher Mach number, the tunnel-wall effects are more pronounced. Figure 6 shows the chordwise wing pressure distributions at the midsemispan location for a free-stream Mach number of 0.93. Results for tunnel-wall boundary conditions similar to those of figure 4 are shown here; there are now noticeable differences in the location of the shock on the lower surface and the pressure levels on both surfaces. A larger spread in the location of the shock on the upper surface is also observed. In this case the flow fields are a good bit different. An indication can be seen in figure 7 which shows the pressure distribution on the upper and lower tunnel walls. The sonic value of C_p is denoted by the tick mark on the ordinate. For straight solid tunnel walls the supersonic bubble extends all the way to the upper wall and is terminated by a shock wave positioned on the wall above the trailing edge of the wing. A porous-wall computation is also shown in figure 7 and it is seen that the flow on the upper wall is everywhere subsonic. Thus the porosity has provided some relief so that the shock does not extend all the way from the model to the upper tunnel wall. More will be said about this case in the last section where results are also given for other tunnel boundary conditions.

Comparison with AEDC data. - The AEDC data shown in figures 8 and 9 and compared with the present calculations were taken as part of an experimental study but were not included in the final report (ref. 18); they were made available by T. W. Binion, Jr., in order to assess the transonic effects. Experimental data were taken in both the AEDC Tunnel 16T and AEDC Tunnel 4T. The Tunnel 16T data were assumed to be relatively interference free (at Mach numbers below 1) and free-air results are compared with them. The tunnel-wall boundary condition for the calculations corresponding to the Tunnel 4T data shown was taken as a porous wall with $P = 0.65$.

In comparing free-air results from the earlier versions of the present program with experimental data, it was found that two effects generally had to be accounted for. First, a small disturbance equation and linearized boundary conditions have been used without incorporating a transonic scaling of the variables. A number of such scalings have been proposed and used since there is not a unique one. Differences result from an empirical determination of arbitrary functions of the Mach number in order to more nearly approximate the critical speed and a shockless flow condition, or an experimental result (for

example, ref. 20). In the present work, a different approach is taken: simply adjust the input Mach number in the small disturbance solution until the resulting pressure distributions (shock locations) coincide with a full-equation solution result for a comparable wing configuration and flow condition. Second, viscous effects at the trailing edge modify the flow there so that imposing the Kutta condition in the calculation does not result in the experimentally measured lift. In two-dimensional flows, this viscous lift deficit can be approximated, in cases where there is not a large amount of separation, by imposing the experimental value of lift on the calculation. (See ref. 21.) For three-dimensional flows, one needs a spanwise distribution or values of lift at a number of sections in order to say that the lift has been matched. Since the experimental wing pressure data taken on the AEDC model were for only one station located at the midsemispan, the lift has been matched by renormalizing the spanwise circulation distribution (obtained by imposing the Kutta condition) so that the experimental section lift is matched at the midsemispan section.

Figure 8 shows comparisons of three different free-air results with AEDC experimental results from Tunnel 16T. The experimental conditions were $M = 0.896$ and $\alpha = 2.92^\circ$ with a tunnel-wall open ratio τ of 6 percent. Present calculations at these conditions with the Kutta condition imposed are seen to produce results where the lift is too large and, on the upper wing surface, the flow is not fully expanded and the shock wave is too far downstream. Matching the lift as indicated moves the shock closer to the experimental result. Adjustment of the Mach number so as to approximately align the computed and experimental shocks on the upper surface produces fairly good agreement. As stated before, this shift in Mach number is to compensate for the small disturbance equation and linearized boundary condition and should not be construed as an indication that the experimental Mach number is that uncertain. It should be noted that the shift in shock wave location due to these two effects is comparable with that due to the tunnel-wall effects as shown in figure 4 for the same flow conditions.

The Mach number shift determined for the free-air calculation is used in the tunnel-wall simulation. A comparison with the AEDC Tunnel 4T experimental results is shown in figure 9. The experimental conditions were $M = 0.900$ and $\alpha = 2.86^\circ$ with $\tau = 5\%$. The present calculations with porous walls ($P = 0.65$), lift matched, and Mach number shifted ($M = 0.88$) are shown as the solid curve. The agreement is similar to that shown for the free-air results in figure 8. Calculations with a more refined grid would likely improve the agreement near the shocks. At higher Mach numbers the tunnel-wall effects are more pronounced, but the experimental data appear to have much more separation around the wing trailing edge.

Other wall conditions. - In figures 6 and 7 it was seen that for straight solid tunnel walls the flow at $M = 0.93$ has a supersonic bubble terminated by a shock wave which extended from the wing surface to the upper tunnel wall. The supersonic flow and its

terminating shock did not extend to the tunnel wall for the porous-wall boundary condition result; this indicates that some relief was provided. The generalized wall boundary conditions given by equation (4) will approximate other wall conditions which should also provide relief for this case.

The integrated form of the linear slotted-wall boundary condition has been used in calculations where all walls are slotted as well as where only the upper and lower walls are slotted with the side wall solid. Results at the midsemispan section on the wing surface are shown in figures 10 and 11 for these two conditions. These results are compared with the results for free-air, solid-wall, and open-jet conditions; about all that can be said is that the trends are similar to those for the porous wall shown in figure 6. The slot geometry parameter S is the ratio $|C/A|$ of equations (4) and (5).

Contoured solid walls have also been proposed to reduce the tunnel-wall interference. The contouring was done only on the upper and lower tunnel walls; the side walls were left straight. The walls were contoured by calculating the normal disturbance velocity ϕ_z at the wall location from a free-air solution and using it as the wall slope $-D/A$ in the tunnel-wall boundary condition, equations (4) and (5). Sample results for this calculation are shown in figure 12 and compared with the free-air, straight solid-wall, and open-jet conditions. Again these wing pressure results are similar to those shown for porous and slotted walls.

Differences due to the various wall boundary conditions show up throughout the flow field. These are compared on the upper and lower tunnel walls in figure 13. The curves from figure 7 as well as the free-air result at the wall location are also included. Six curves identified in the key are shown for the upper wall and the sonic value of C_p is denoted by the long tick mark on the ordinate. It is seen that the choked condition above the wing which occurs for the straight solid tunnel-wall condition is relieved when linear porous, slotted, or contoured solid tunnel-wall conditions are included. These tunnel-wall results are all qualitatively like the free-air results at this Mach number; perhaps the slotted condition has more nearly the same shape. Only three curves are shown for the lower wall; these bracket the others. The shapes of the C_p distributions on the lower wall are very much alike; small differences are observed in the mean levels of C_p .

Tunnel side-wall pressure distributions in the wing plane are shown for the same six wall conditions in figure 14. For a rectangular planform wing, which spans two-thirds of the tunnel width, the supersonic bubble extends to the side wall in those cases where it is modeled as straight and solid. Again the ventilated side-wall conditions generate results qualitatively like the free-air results. No calculations have been made for a contoured side wall; however, it is not expected to cause difficulty.

BODY CONTOURING PROBLEM

Three-dimensional transonic flow calculations for wing cylinder combinations have been reported recently in references 4, 8, and 10. Results in reference 4 were for a non-lifting flow but included Mach 1 ruling of the cylindrical body whereas those presented in references 8 and 10 were for flows with lift about cylindrical bodies. The present work is an extension of the approach outlined in reference 10.

Computational Considerations

A schematic of the simple configuration considered is shown as figure 15. It is a rectangular planform wing centrally mounted on an infinite cylinder. To make a smoothly contoured body, with contouring proportional to a Mach 1 ruling in the region of the wing, it is necessary to extend the body contouring both upstream and downstream of the wing. For the present results, the contouring was done from 1/2 chord before the leading edge to 1/2 chord behind the trailing edge as follows:

- (1) The axisymmetric volume removal at the wing position is proportional to the chordwise change in wing volume.
- (2) At the leading and trailing edges the rate at which the body radius changes is required to be smooth and to produce a smooth volume change.
- (3) The rate of change in the body radius decays linearly to zero at 1/2 chord before the leading edge and behind the trailing edge.

Calculations have been made only for axisymmetric body contouring; however, the method is not restricted to that case.

A Joukowski transformation in planes normal to the cylinder axis

$$\sigma = \sigma_1 + \frac{R^2}{\sigma_1} \quad x = x_1 \quad \sigma_1 = y_1 + iz_1 \quad \sigma = y + iz \quad (6)$$

(where R is a constant) maps the circular cross section $y_R^2 + z_R^2 = R^2$ ($y = y_R$, $z = z_R$ denotes y, z on R) and the plane $z = 0$ for $|y| \geq R$ onto the plane $z_1 = 0$. If the body radius does not differ appreciably from R , then the boundary condition of zero normal velocity on both the wing and body can be enforced on the plane $z_1 = 0$. The computational coordinate mesh (x_1, y_1, z_1) is rectangular so that the wing-cylinder problem in this formulation is very much like the wing-alone problem. Figure 16 depicts a portion of the cross-flow plane computational grid (plotted on physical space) near the wing-cylinder configuration.

The flow tangency condition for a body of revolution is approximated by

$$\frac{y_R}{R} \varphi_y(x, y_R, z_R) + \frac{z_R}{R} \left[\alpha + \varphi_z(x, y_R, z_R) \right] = \frac{dr_o}{dx} \quad (7)$$

where R is the radius of the reference cylinder surface (the Joukowski constant), the subscripts R denote that the boundary condition is evaluated on the reference surface, and r_o is the local body radius. In terms of the computational x_1, y_1, z_1 coordinates, equation (7) is

$$\varphi_{z_1}(x_1, y_1, 0) = -\frac{\alpha}{2} + \frac{1}{2 \sin \theta} \left(\frac{dr_o}{dx_1} \right) \quad (8)$$

where $\sin \theta = \frac{y_R}{R}$. Additional terms involving $dr_o/d\theta$ must be included in equations (7) and (8) for bodies of noncircular cross section. The singularities at $y_R = 0$ ($\theta = 0$) in the transformation occur at the wing-cylinder junctions. The computational grid points straddle such a point in both the y_1 - and z_1 -directions so that the equations are not differentiated through this singularity.

Results

The calculations for a rectangular wing serve to demonstrate the feasibility of computing body contouring effects. The wing aspect ratio is 4, the airfoil section is parabolic with a thickness ratio of 0.05, and the cylinder radius is 1/2 chord. Sample wing pressure distributions at about the 70-percent semispan station for both upper and lower wing surfaces are shown in figure 17. The stream Mach number is 0.9 and the wing is at 1° incidence; this produces a supercritical flow. Results for the circular cylindrical body are shown by the open symbols. It can be seen that shock waves appear on both the upper and lower wing surfaces. When the cylindrical body is contoured by removing 2.25 times the wing volume, very subsonic like pressure distributions are obtained. These results are shown by the + and x symbols. There is a region of slightly supersonic flow but these results do not appear to contain a shock wave. The relatively large volume ratio, 2.25, is accounted for by the fact that the way in which the body contouring was done resulted in a large volume removal both upstream and downstream of the wing. Comparable results could likely be obtained with less volume removal by altering the contouring. Pressure distributions at two locations on the body are shown in figure 18 for the same case. The sketch shows the body locations above (upper) and below (lower) the wing plane where the streamwise distributions apply. For the cylindrical body results there is an expansion both above and below the wing around the wing position. The body contouring produces a compression which alleviates it, not only on the body but over the entire wing span. Recall that the wing results shown in figure 17 were at the 70-percent semispan location; at inboard locations the effect is even greater.

The effect of body contouring on pressure drag is shown in figure 19. Results are given for both lifting and nonlifting conditions. Pressure drags for the entire configurations are normalized in terms of that for the wing-cylinder at 1° incidence. They are shown as a function of volume removed normalized by the wing volume. It is seen that there is a drag reduction up to a point and then an increasing trend begins. Results shown in figures 17 and 18 were for the removed volume ratio equals 2.25 which is near the minimum in the drag curve. The nearly constant drag difference between the $\alpha = 0^\circ$ and $\alpha = 1^\circ$ cases is essentially that due to lift.

The spanwise distribution of pressure drag for the wing with cylindrical body (circles) is compared with that obtained for the contoured body (diamonds) in figure 20. The contoured body is that producing the minimum drag and the curves have been normalized so that the integrated drag is that given in figure 19. It is seen that the pressure drag reduction on the wing due to the absence of shocks is much greater than the increase on the body due to the contouring.

CONCLUDING REMARKS

The results presented herein suggest that similar computations for a wider class of configurations are feasible. These results were generated on a mesh of about 25,000 grid points. For a tunnel-wall case, about 160,000g storage and 1/2 hour CPU time was required on a Control Data 6600 computer system (with run compiler). The body contouring studies required about 150,000g storage and about 10 to 15 minutes CPU time per case. Thus, the entire computer resources have not yet been exhausted.

The results for tunnel-wall modeling demonstrate that various conventional tunnel-wall boundary conditions can be incorporated in numerical computations. Such modeling should be useful in assessing interference effects and as an aid in the design of wind tunnels. The computational method approximates the tunnel-wall boundary conditions only in an average sense. Both experimental results and numerical computations are required to determine a satisfactory method for approximating these complex boundaries.

The present results for simple configurations indicate that body contouring effects can be obtained numerically. The present technique is not limited to axisymmetric contouring such as demonstrated by these results. Thus, one should be able to examine some body interference effects in the preliminary design stage.

REFERENCES

1. Bailey, F. R.; and Steger, J. L.: Relaxation Techniques for Three-Dimensional Transonic Flow About Wings. *AIAA J.*, vol. 11, no. 3, Mar. 1973, pp. 318-325.
2. Newman, P. A.; and Klunker, E. B.: Computation of Transonic Flow About Finite Lifting Wings. *AIAA J.*, vol. 10, no. 7, July 1972, pp. 971-973.
3. Ballhaus, W. F.; and Bailey, F. R.: Numerical Calculation of Transonic Flow About Swept Wings. *AIAA Paper No. 72-677*, June 1972.
4. Bailey, Frank R.; and Ballhaus, William F.: Relaxation Methods for Transonic Flow About Wing-Cylinder Combinations and Lifting Swept Wings. *Proceedings of the Third International Conference on Numerical Methods in Fluid Mechanics, Volume II. Volume 19 of Lecture Notes in Physics*, Henri Cabannis and Roger Teman, eds., Springer-Verlag, 1973, pp. 2-9.
5. Lomax, Harvard; Bailey, Frank R.; and Ballhaus, William F.: On the Numerical Simulation of Three-Dimensional Transonic Flow With Application to the C-141 Wing. *NASA TN D-6933*, 1973.
6. Jameson, Antony: Numerical Calculation of the Three-Dimensional Transonic Flow Over a Yawed Wing. *Proceedings AIAA Computational Fluid Dynamics Conference*, July 1973, pp. 18-26.
7. Jameson, Antony: Iterative Solution of Transonic Flows Over Airfoils and Wings, Including Flows at Mach 1. *Commun. Pure & Appl. Math.*, vol. XXVII, no. 3, May 1974, pp. 283-309.
8. Schmidt, W.; Rohlf, S.; and Vanino, R.: Some Results Using Relaxation Methods for Two- and Three-Dimensional Transonic Flows. *Proceedings of the Fourth International Conference on Numerical Methods in Fluid Dynamics. Volume 35 of Lecture Notes in Physics*, Robert D. Richtmyer, ed., Springer-Verlag, 1975, pp. 364-372.
9. Hall, M. G.; and Firmin, M. C. P.: Recent Developments in Methods for Calculating Transonic Flows Over Wings. *ICAS Paper No. 74-18*, Aug. 1974.
10. Klunker, E. B.; and Newman, P. A.: Computation of Transonic Flow About Lifting Wing-Cylinder Combinations. *J. Aircraft*, vol. 11, no. 4, Apr. 1974, pp. 254-256.
11. Murman, Earll M.: Computation of Wall Effects in Ventilated Transonic Wind Tunnels. *AIAA Paper No. 72-1007*, Sept. 1972.
12. Kacprzynski, J. J.: Transonic Flow Field Past 2-D Airfoils Between Porous Wind Tunnel Walls With Nonlinear Characteristics. *AIAA Paper 75-81*, Jan. 1975.

13. Bailey, Frank R.: Numerical Calculation of Transonic Flow About Slender Bodies of Revolution. NASA TN D-6582, 1971.
14. Barnwell, R. W.: Transonic Flow About Lifting Wing-Body Combinations. AIAA Paper No. 74-185, Jan.-Feb. 1974.
15. Murman, Earll M.; and Cole, Julian D: Calculation of Plane Steady Transonic Flows. AIAA J., vol. 9, no. 1, Jan. 1971, pp. 114-121.
16. Bailey, F. R.: On the Computation of Two- and Three-Dimensional Steady Transonic Flows by Relaxation Methods. VKI Lecture Series 63 "Progress in Numerical Fluid Dynamics," Von Karman Institute for Fluid Dynamics (Rhode-St-Genese, Belgium), Feb. 11-15, 1974.
17. Keller, James D.: Numerical Calculation of Boundary-Induced Interference in Slotted or Perforated Wind Tunnels Including Viscous Effects in Slots. NASA TN D-6871, 1972.
18. Binion, T. W., Jr.: An Investigation of Three-Dimensional Wall Interference in a Variable Porosity Transonic Wind Tunnel. AEDC-TR-74-76, U.S. Air Force, Oct. 1974. (Available from DDC as AD 787 658.)
19. South, Jerry C., Jr.; and Keller, James D.: Axisymmetric Transonic Flow Including Wind-Tunnel Wall Effects. Aerodynamic Analyses Requiring Advanced Computers, Part II, NASA SP-347, 1975, pp. 1233-1267.
20. Krupp, James A.: The Numerical Calculation of Plane Steady Transonic Flows Past Thin Lifting Airfoils. D180-12958-1, Boeing Sci. Res. Lab., Boeing Co., June 1971.
21. Melnik, R. E.; and Ives, D. C.: On Viscous and Wind-Tunnel Wall Effects in Transonic Flows Over Airfoils. AIAA Paper No. 73-660, July 1973.

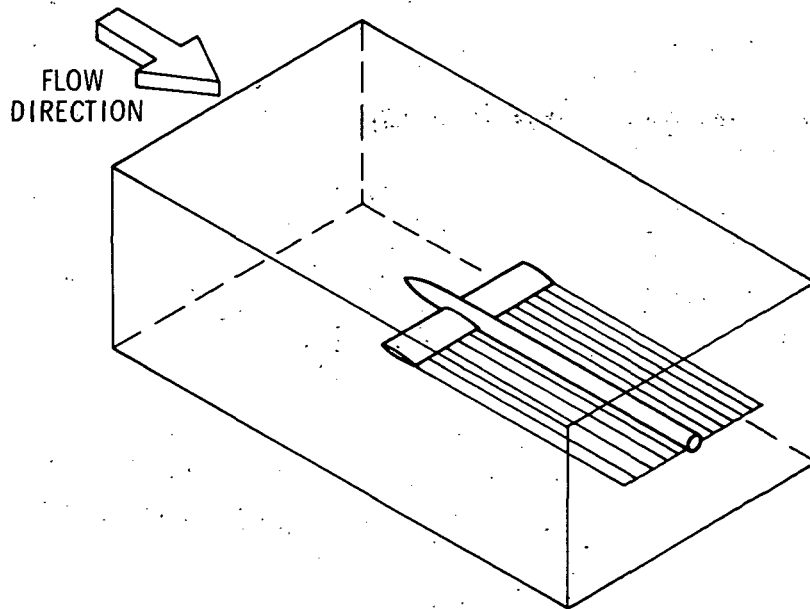


Figure 1.- Schematic of rectangular planform wing in rectangular-cross-section tunnel.

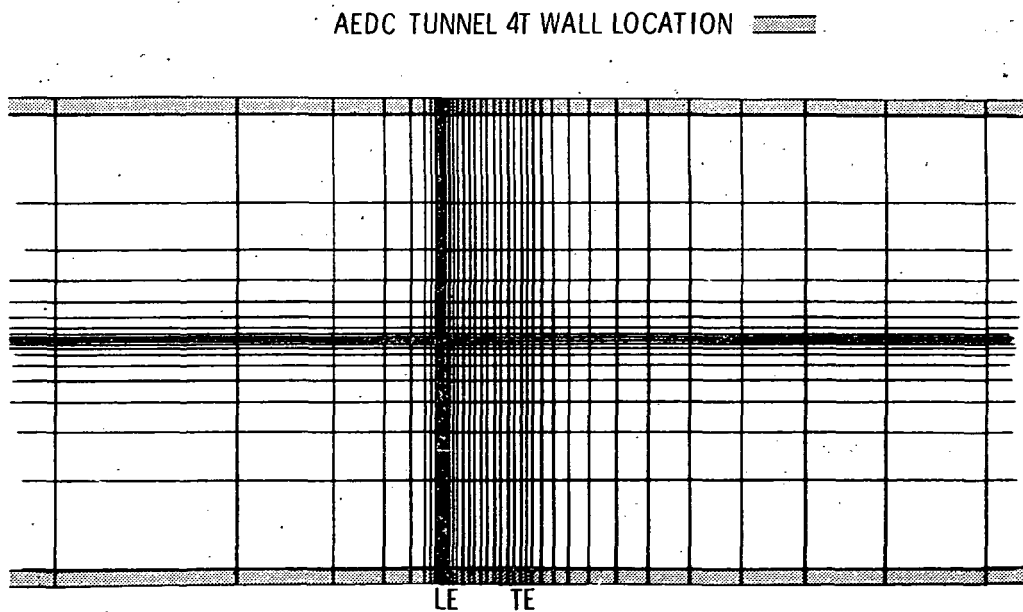


Figure 2.- Computational grid in plane normal to wing leading edge.

AEDC TUNNEL 4T WALL LOCATION

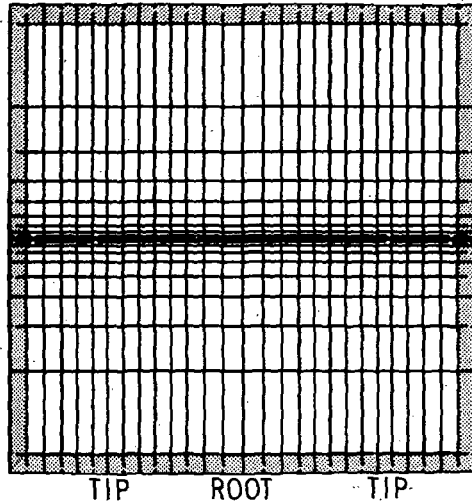


Figure 3.- Computational grid in plane normal to free stream.

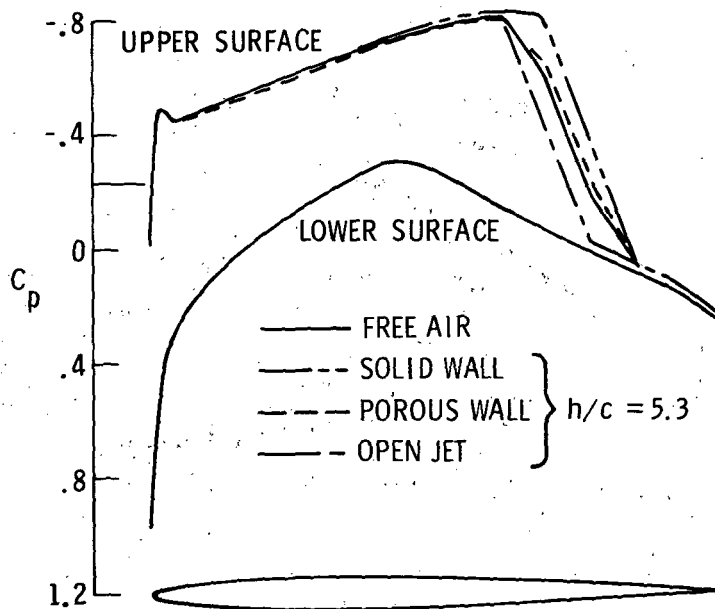


Figure 4.- Wing-surface pressure distributions at mid-semispan section. NACA 63A006 airfoil; $AR = 3.56$; $M = 0.88$; $\alpha = 3^\circ$; porous wall comparison.

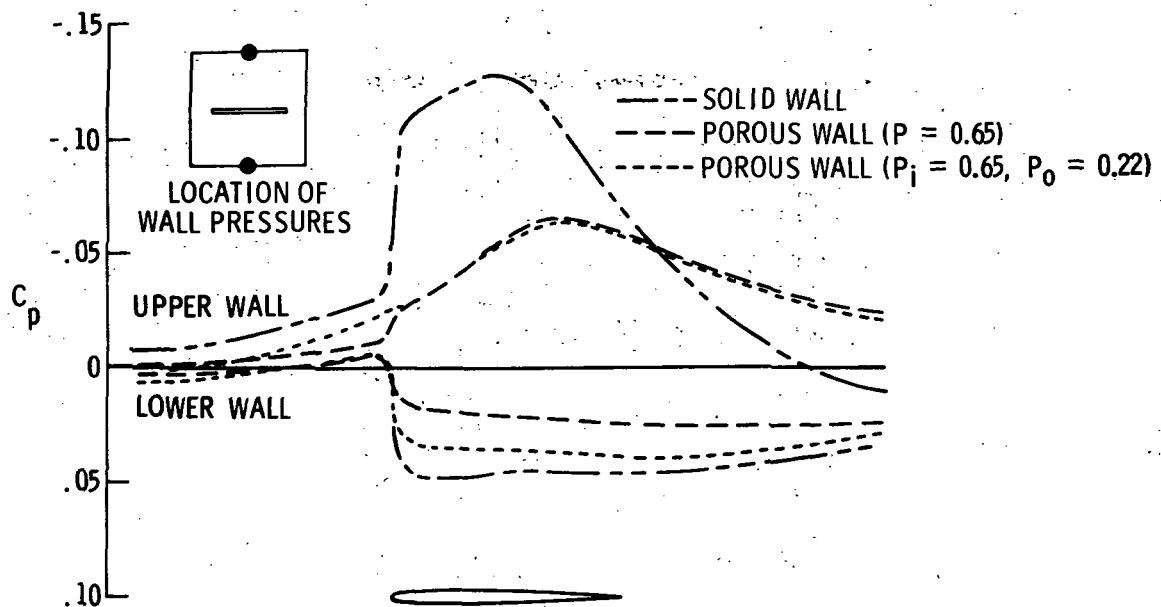


Figure 5.- Tunnel-wall pressure distributions in wing root plane. NACA 63A006 airfoil; $AR \approx 3.56$; $M = 0.88$; $\alpha = 3^\circ$; $h/c = 5.3$.

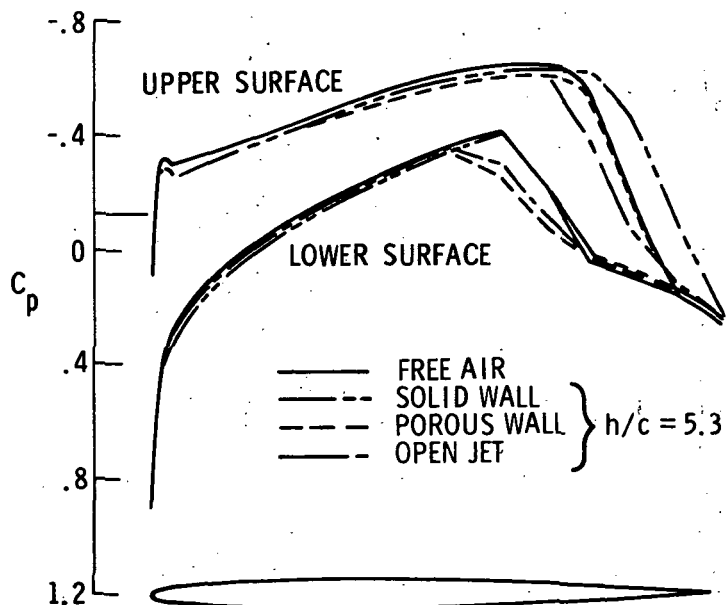


Figure 6.- Wing-surface pressure distributions at mid-semispan section. NACA 63A006 airfoil; $AR = 3.56$; $M = 0.93$; $\alpha = 2.76^\circ$; porous wall comparison.

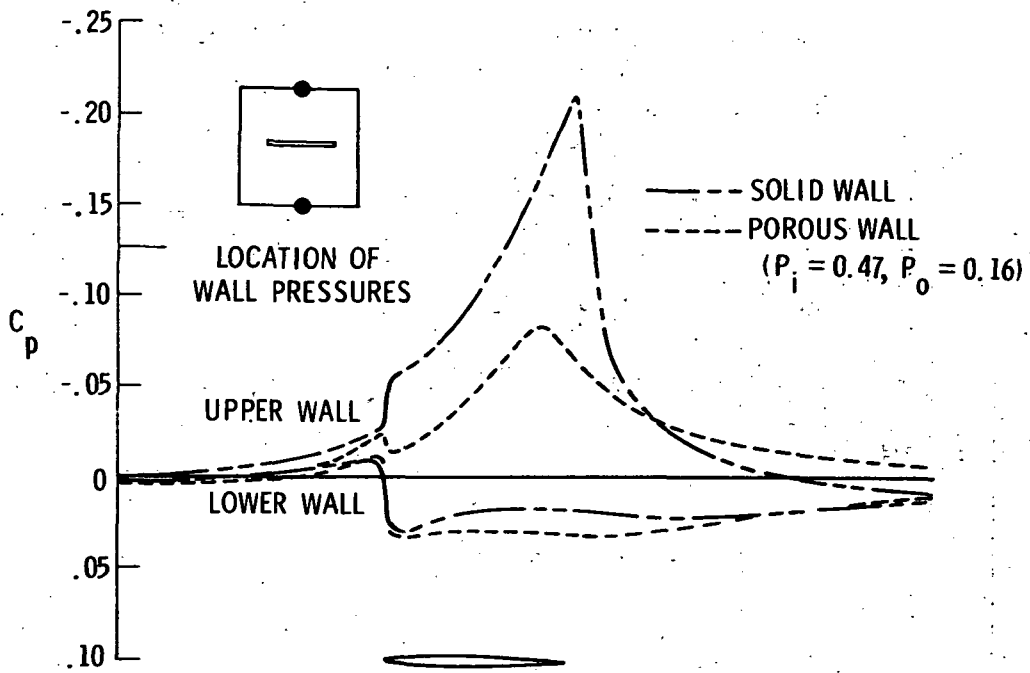


Figure 7.- Tunnel-wall pressure distributions in wing root plane. NACA 63A006 airfoil; $AR = 3.56$; $M = 0.93$; $\alpha = 2.76^\circ$; $h/c = 5.3$.

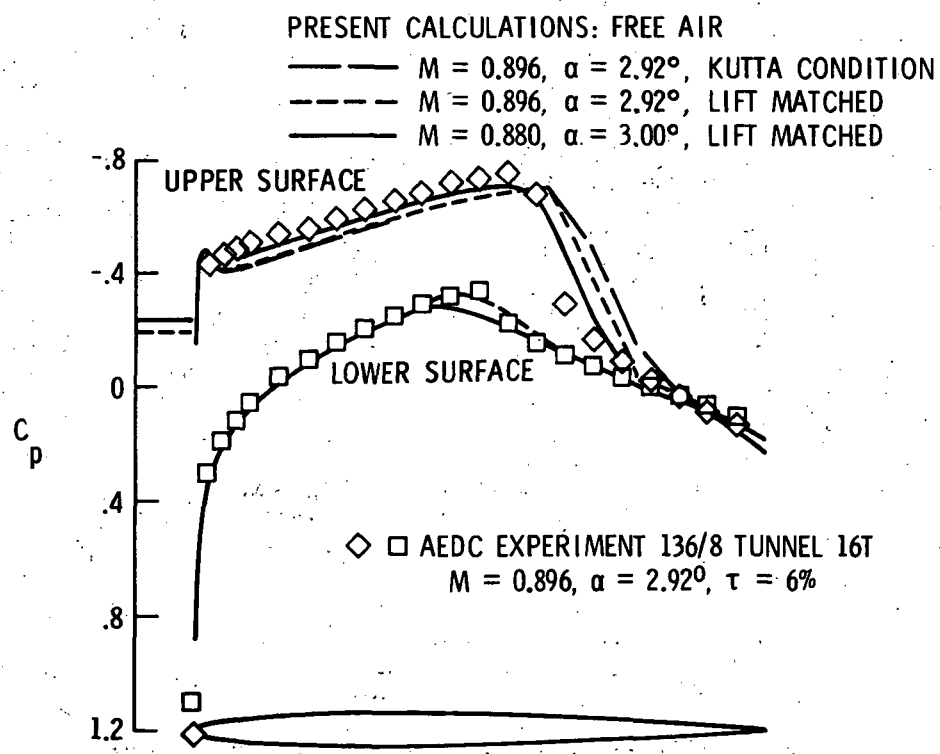


Figure 8.- Comparison of computed and experimental wing-surface pressure distributions at midsemispan section. NACA 63A006 airfoil; $AR = 3.56$.

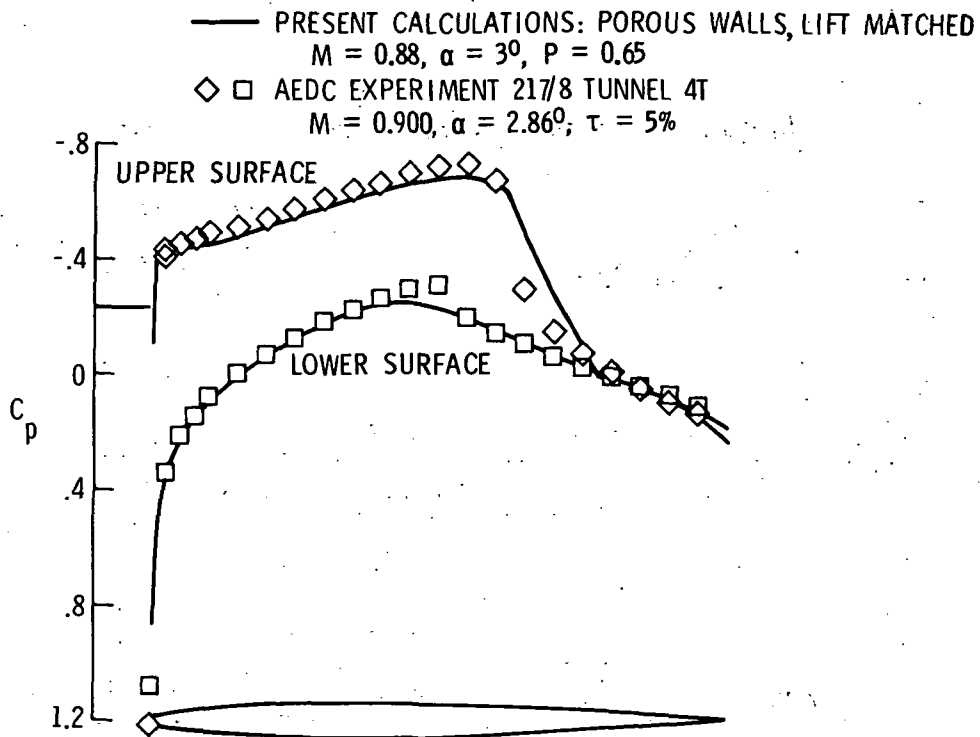


Figure 9.- Comparison of computed and experimental wing-surface pressure distributions at midsemispan section. NACA 63A006 airfoil; $AR = 3.56$; $h/c = 5.3$.

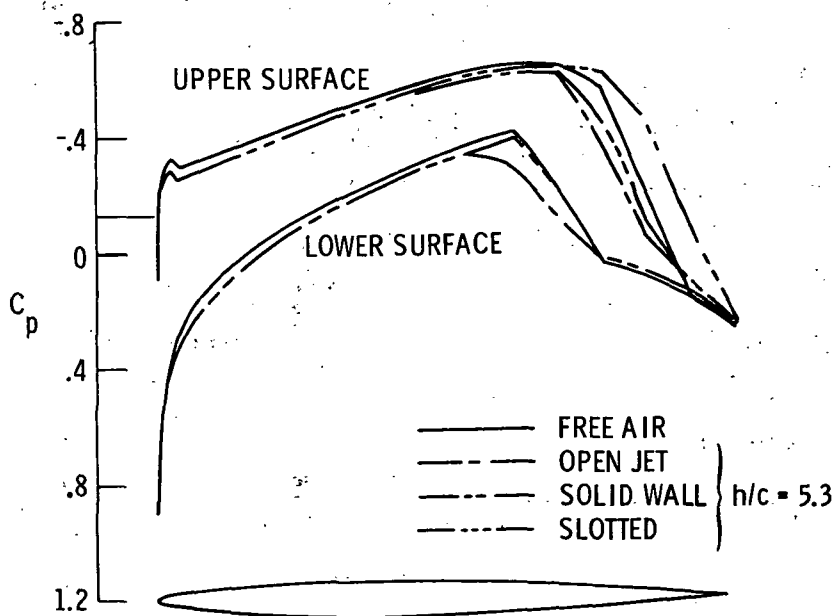


Figure 10.- Wing-surface pressure distributions at mid-semispan section. NACA 63A006 airfoil; $AR = 3.56$; $M = 0.93$; $\alpha = 2.76^\circ$; slotted wall comparison.

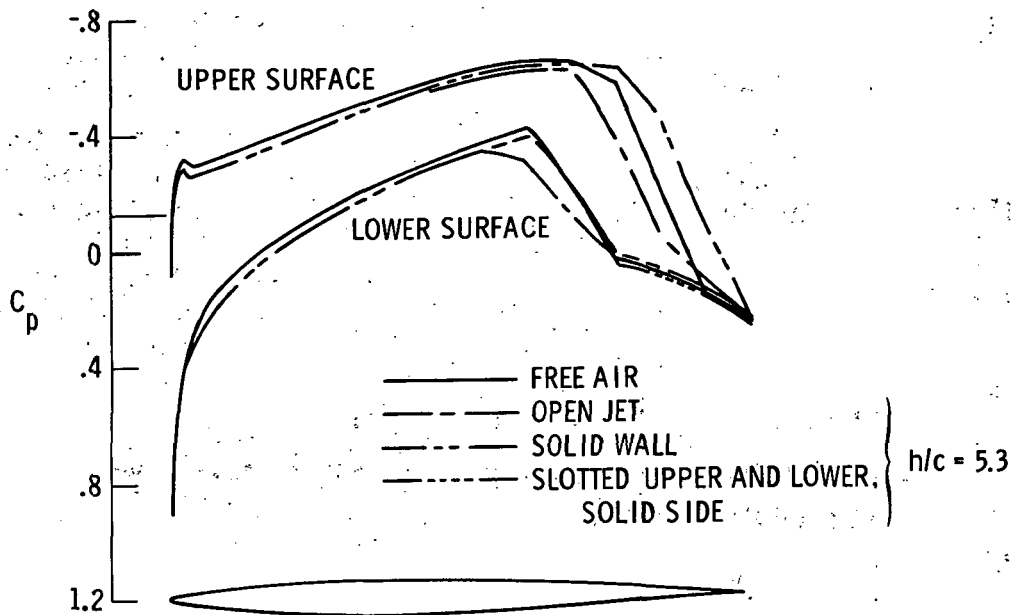


Figure 11. - Wing-surface pressure distributions at midsemispan section. NACA 63A006 airfoil; $AR = 3.35$; $M = 0.93$; $\alpha = 2.76^\circ$; slotted upper and lower wall comparison.

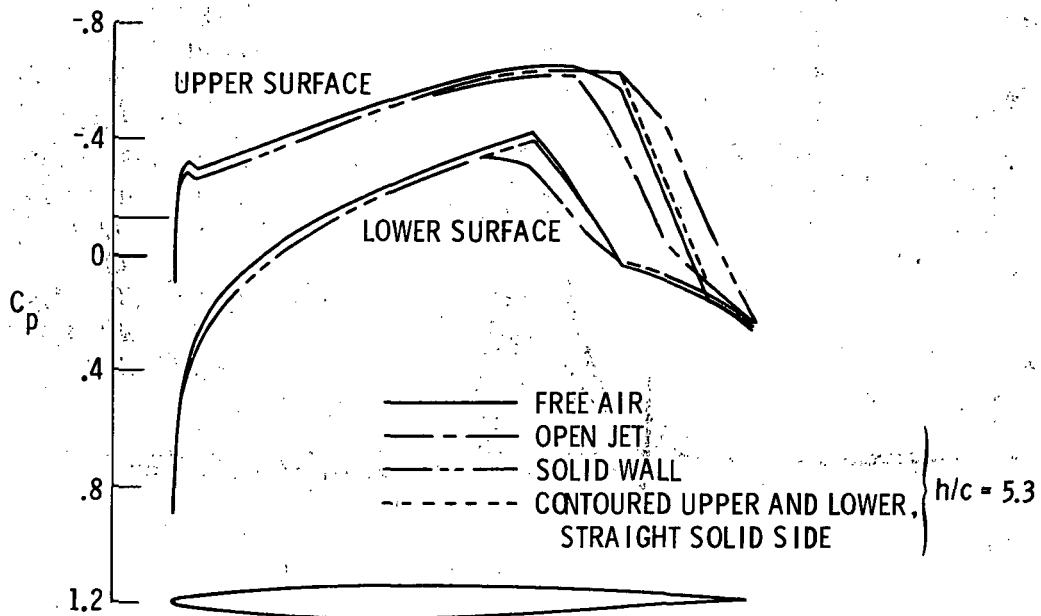


Figure 12. - Wing-surface pressure distributions at mid-semispan section. NACA 63A006 airfoil; $AR = 3.56$; $M = 0.93$; $\alpha = 2.76^\circ$; contoured wall comparison.

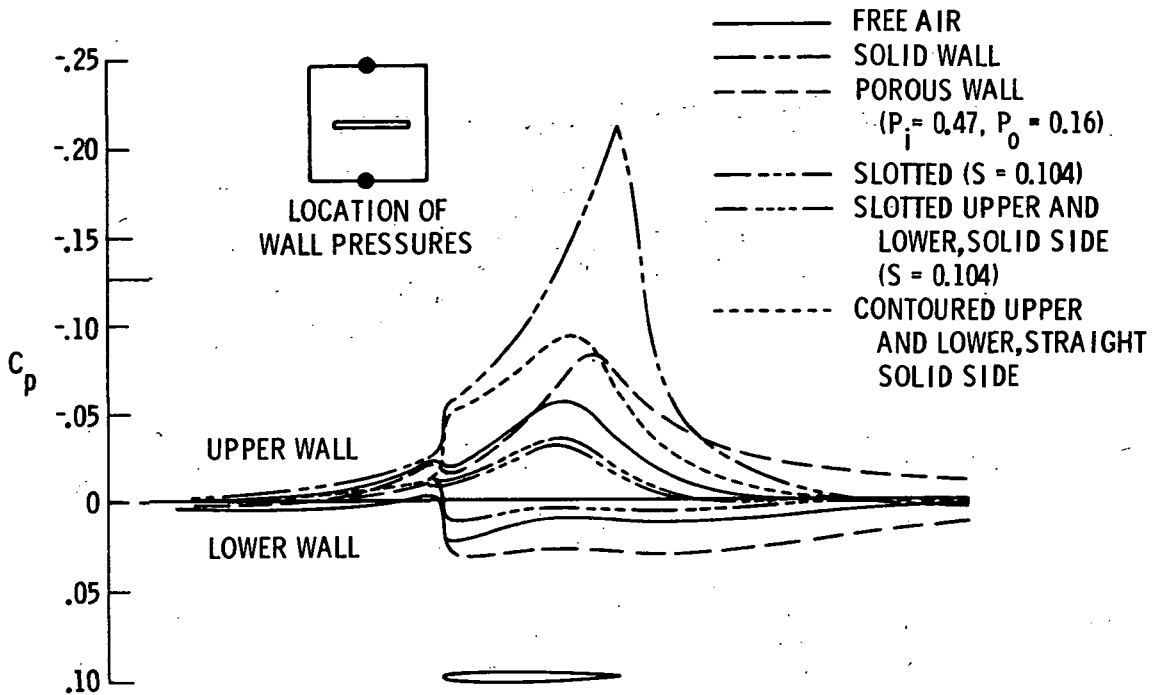


Figure 13.- Tunnel-wall pressure distributions in wing root plane. NACA 63A006 airfoil; $AR = 3.56$; $M = 0.93$; $\alpha = 2.76^\circ$; $h/c = 5.3$.

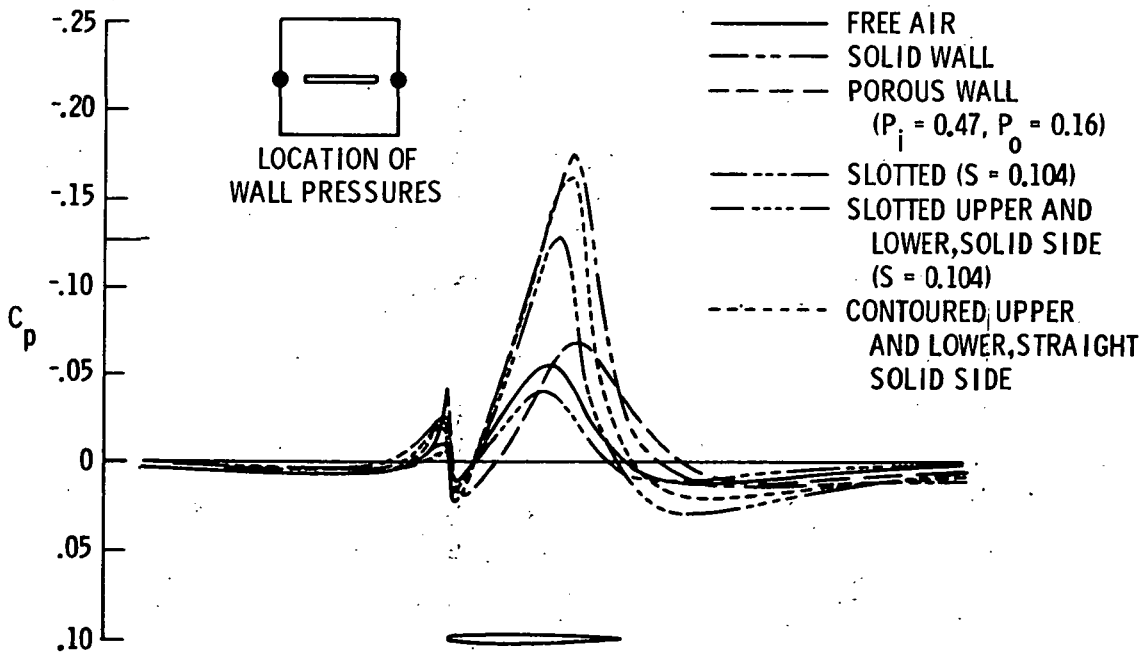


Figure 14.- Tunnel side-wall pressure distributions in wing plane. NACA 63A006 airfoil; $AR = 3.56$; $M = 0.93$; $\alpha = 2.76^\circ$; $h/c = 5.3$.

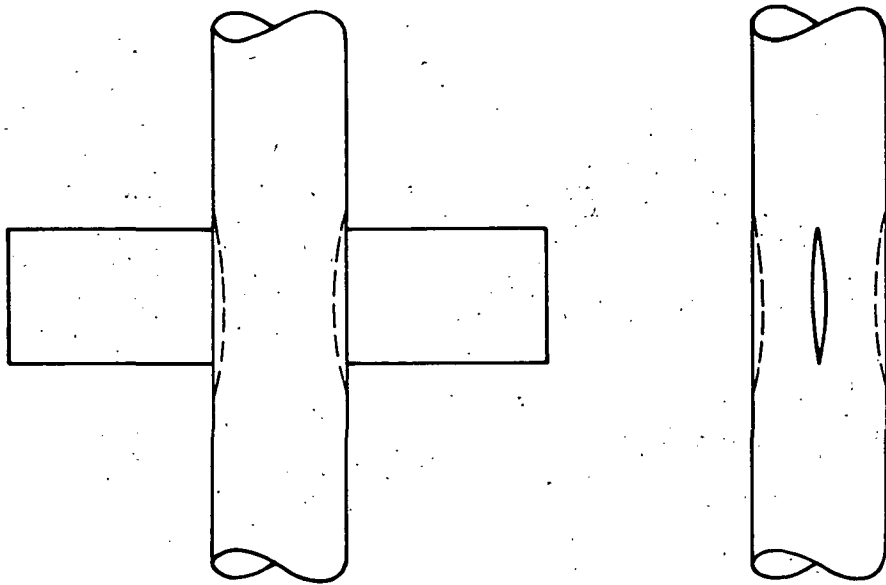


Figure 15.- Schematic of wing-body configuration with body contouring.

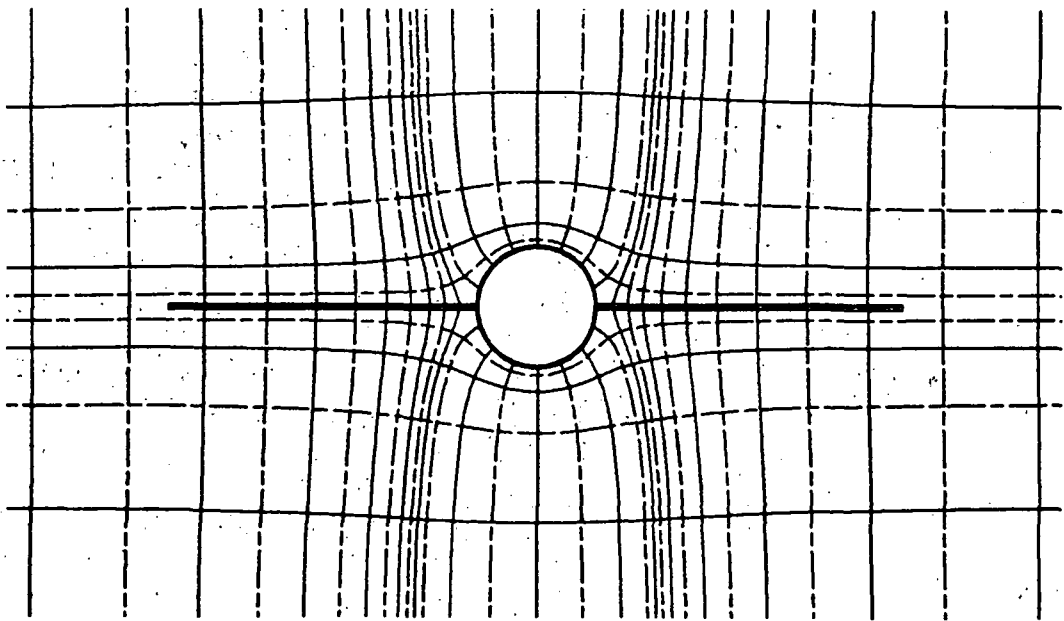


Figure 16.- Schematic of cross-flow plane computational grid.

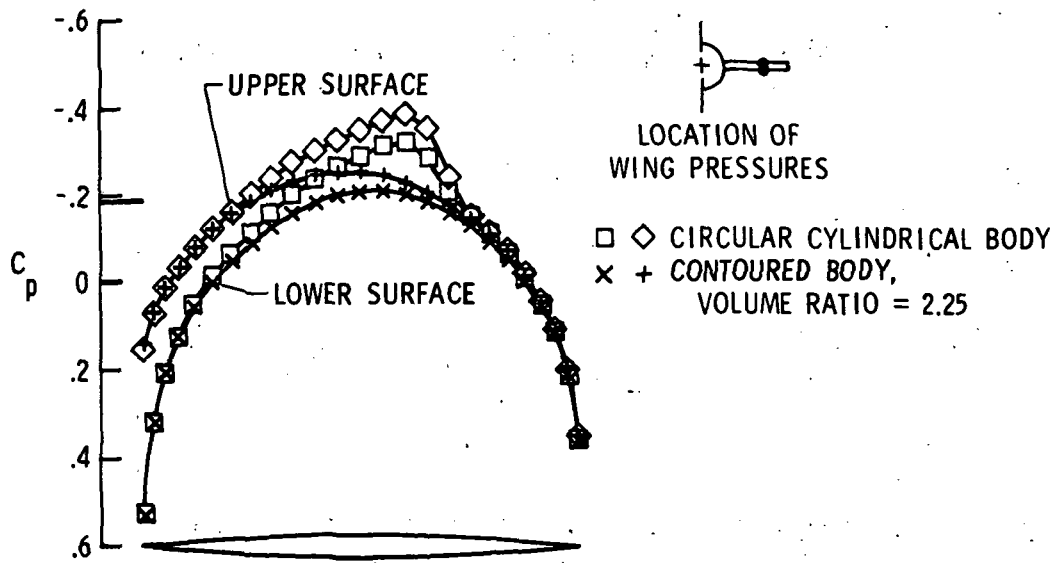


Figure 17.- Wing-surface pressure distributions. 5-percent-thick parabolic-arc airfoil; $AR = 4$; $M = 0.9$; $\alpha = 1^\circ$.

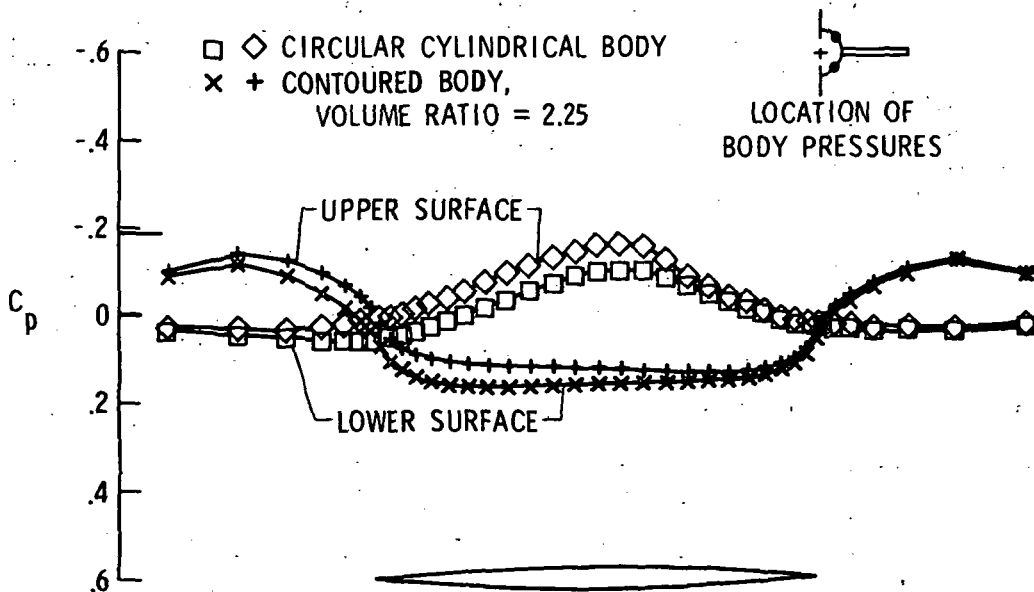


Figure 18.- Body-surface pressure distributions. 5-percent-thick parabolic-arc airfoil; $AR = 4$; $M = 0.9$; $\alpha = 1^\circ$.

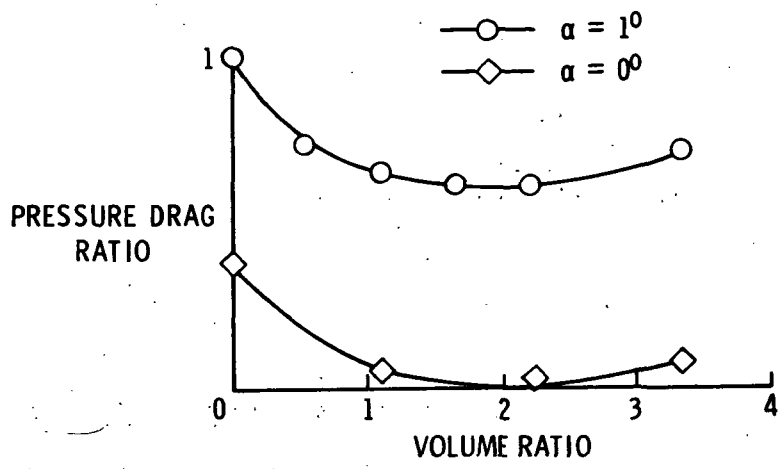


Figure 19.- Effect of body contouring on pressure drag. 5-percent-thick parabolic-arc airfoil; $AR = 4$; $M = 0.9$.

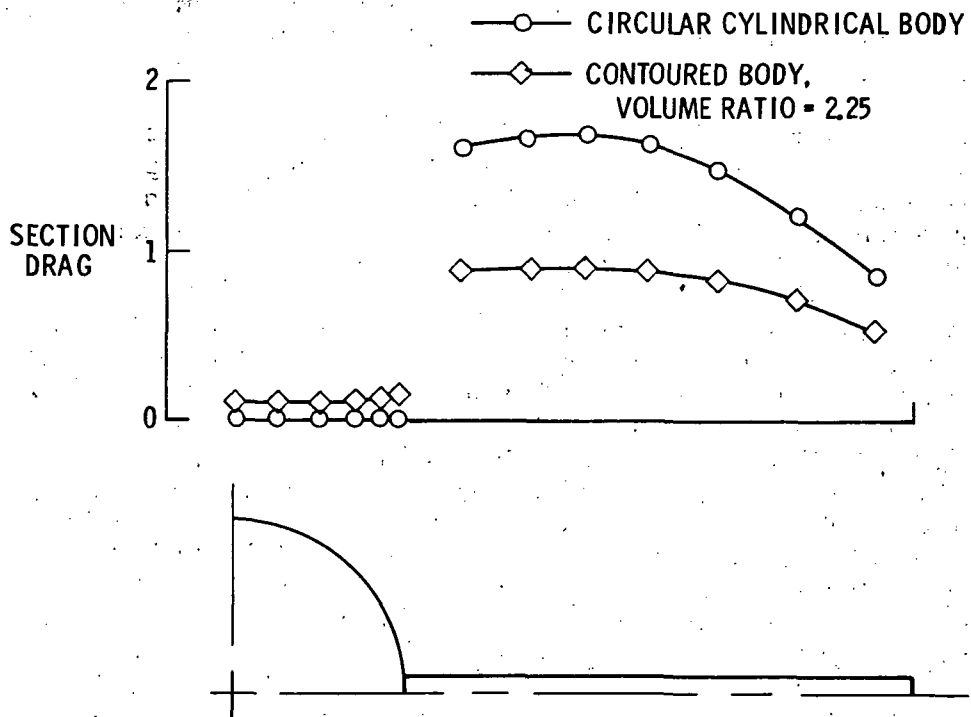


Figure 20.- Spanwise section drag distribution. 5-percent-thick parabolic-arc airfoil; $AR = 4$; $M = 0.9$; $\alpha = 1^\circ$.

COMPARISONS OF COMPUTED AND EXPERIMENTAL PRESSURES FOR TRANSONIC FLOWS

ABOUT ISOLATED WINGS AND WING-FUSELAGE CONFIGURATIONS

By F. R. Bailey

NASA Ames Research Center

and

W. F. Ballhaus

U.S. Army Air Mobility R&D Laboratory

42

INTRODUCTION

Most modern aircraft achieve optimum cruise performance and maneuverability when flying at high subsonic Mach numbers in the transonic regime. In this Mach number range, there exist in the flow field local regions of supersonic flow which are usually terminated by weak embedded shock waves. These mixed subsonic-supersonic flows are extremely sensitive to the shape of internal boundaries. For this reason aircraft performance depends strongly on aircraft configuration. The configuration design process requires parametric variation of the numerous geometrical variables that describe the shape of the aircraft, a procedure that is expensive to implement entirely by experiment. This fact has resulted in a significant effort to develop theoretical transonic flow analysis methods.

These theoretical techniques can be divided into two categories: (1) analytical methods and (2) numerical methods. The analytical approach is limited, in the general case, to linear theory, while most transonic flows of interest are governed by nonlinear equations of motion. The numerical approach, however, has no such limitation.

The present work describes a relaxation procedure for solving the transonic small disturbance equation for flows about wings and wing-fuselage combinations. The numerical method is based on the well-known relaxation method of Murman and Cole (ref. 1) and is a continuation of the work given by Ballhaus and Bailey (refs. 2 and 3; see also ref. 4). The small disturbance formulation is chosen because of the relatively simple manner in which the wing boundary condition is imposed. All the transonic relaxation methods for wings that have been developed to date (refs. 2 to 10) are based on the small disturbance approach, with the exception of Jameson's (ref. 11) method for yawed wings. In the present method, solutions are obtained over a sequence of successively refined computational grids with the final result obtained for a grid with about 10^5 points. The solution process requires about 5 to 15 min of run time on a Control Data Corporation (CDC) 7600 computer.

An early version of the isolated wing code was released to aircraft and research companies in 1974. Since that time, in a contracted effort with LTV Aerospace Corporation, the input, setup, and output have been streamlined

and adapted more toward the needs of the aircraft designer. The code has been documented and adapted for use on the CDC 6600 computer (ref. 12). The solution process has also been revised to decrease computer run time and to allow, as an option, either conservative or nonconservative differencing. The use of conservative differencing ensures that captured shock waves satisfy the shock conditions contained in the inviscid governing equation. Such is not the case for nonconservative differencing which, coincidentally, captures shock waves that agree better with experimentally measured shock waves which, of course, are affected by viscosity. (See ref. 13, fig. 6.) Computed surface pressures for both conservative and nonconservative differencing are compared with experimental pressures in the section on results.

Finally, the method has been extended for the treatment of wings mounted on finite length fuselages. Results, both conservative and nonconservative, are compared with experimental data for two such nonlifting configurations.

FINITE-DIFFERENCE APPROXIMATIONS

Governing Equation

The approximate equation and boundary conditions for transonic flow over slender body, thin wing configurations, such as shown in figure 1, are derived from transonic small disturbance theory under the assumptions of small flow deflections and a free-stream Mach number near unity. The governing equation is

$$\left[(1 - M_\infty^2) \phi_x - \frac{\gamma + 1}{2} M_\infty^n \phi_x^2 \right]_x + [\phi_y]_y + [\phi_z]_z = 0 \quad (1)$$

where ϕ is the disturbance velocity potential, M_∞ is the free-stream Mach number, and γ is the ratio of specific heats. The parameter n reflects the nonuniqueness of equation (1), and it can be adjusted to better approximate the exact sonic pressure coefficient. For example, see reference 14.

Murman (ref. 15) has shown that the shock jump relation implied by equation (1) is contained in the difference approximations if they are written in conservation form. That is, mass fluxes at cell boundaries interior to the computation mesh cancel identically. The present conservative finite difference equation is derived by applying the divergence theorem to the integral of equation (1) (the transonic approximation to mass conservation) over an elemental, rectangular, computation volume or cell as shown in figure 2. Define the mass flux as

$$\begin{aligned} \vec{F} &= f \vec{i}_x + g \vec{i}_y + h \vec{i}_z \\ &= \left[(1 - M_\infty^2) \phi_x - \frac{\gamma + 1}{2} M_\infty^n \phi_x^2 \right] \vec{i}_x + [\phi_y] \vec{i}_y + [\phi_z] \vec{i}_z \end{aligned} \quad (2)$$

Applying the divergence theorem to the volume integral and dividing by the cell volume results in the difference expression

$$\frac{f_{i+1/2,j,k} - f_{i-1/2,j,k}}{x_{i+1/2} - x_{i-1/2}} + \frac{g_{i,j+1/2,k} - g_{i,j-1/2,k}}{y_{j+1/2} - y_{j-1/2}} + \frac{h_{i,j,k+1/2} - h_{i,j,k-1/2}}{z_{k+1/2} - z_{k-1/2}} = 0 \quad (3)$$

for the point (x_i, y_j, z_k) . If the velocities are defined by

$$(\phi_x)_{i+1/2,j,k} = \frac{\phi_{i+1,j,k} - \phi_{i,j,k}}{x_{i+1} - x_i}$$

$$(\phi_y)_{i,j+1/2,k} = \frac{\phi_{i,j+1,k} - \phi_{i,j,k}}{y_{j+1} - y_j}, \text{ etc.}$$

the finite difference approximations to the fluxes are

$$\left. \begin{aligned} f_{i+1/2,j,k} &= (1 - \mu_{i,j,k}) \left[(1 - M_\infty^2) \phi_x - \frac{\gamma + 1}{2} M_\infty^n \phi_x^2 \right]_{i+1/2,j,k} \\ &\quad + \mu_{i,j,k} \left[(1 - M_\infty^2) \phi_x - \frac{\gamma + 1}{2} M_\infty^n \phi_x^2 \right]_{i-1/2,j,k} \\ f_{i-1/2,j,k} &= (1 - \mu_{i-1,j,k}) \left[(1 - M_\infty^2) \phi_x - \frac{\gamma + 1}{2} M_\infty^n \phi_x^2 \right]_{i-1/2,j,k} \\ &\quad + \mu_{i-1,j,k} \left[(1 - M_\infty^2) \phi_x - \frac{\gamma + 1}{2} M_\infty^n \phi_x^2 \right]_{i-3/2,j,k} \end{aligned} \right\} \quad (4)$$

$$g_{i,j+1/2,k} = [\phi_y]_{i,j+1/2,k}, \quad g_{i,j-1/2,k} = [\phi_y]_{i,j-1/2,k} \quad (5)$$

$$h_{i,j,k+1/2} = [\phi_z]_{i,j,k+1/2}, \quad h_{i,j,k-1/2} = [\phi_z]_{i,j,k-1/2} \quad (6)$$

which, when substituted into equation (3) and factored, give the final difference approximation

$$\begin{aligned}
& \left\{ (1 - \mu_{1,j,k}^{i-1})(1 - M^2)_{i,j,k} \left[(\phi_x)_{i+1/2,j,k} - (\phi_x)_{i-1/2,j,k} \right] \right. \\
& + \mu_{i-1,j,k} (1 - M^2)_{i-1,j,k} \left[(\phi_x)_{i-1/2,j,k} - (\phi_x)_{i-3/2,j,k} \right] \Bigg\} / (x_{i+1/2} - x_{i-1/2}) \\
& + \left[(\phi_y)_{i,j+1/2,k} - (\phi_y)_{i,j-1/2,k} \right] / (y_{j+1/2} - y_{j-1/2}) \\
& + \left[(\phi_z)_{i,j,k+1/2} - (\phi_z)_{i,j,k-1/2} \right] / (z_{k+1/2} - z_{k-1/2}) = 0 \quad (7)
\end{aligned}$$

where

$$(1 - M^2)_{i,j,k} = 1 - M_\infty^2 - (\gamma + 1) M_\infty^n \frac{1}{2} \left[(\phi_x)_{i+1/2,j,k} + (\phi_x)_{i-1/2,j,k} \right] \quad (8)$$

$$\mu_{i,j,k} = \begin{cases} 0 & \text{for } (1 - M^2)_{i,j,k} > 0 \\ 1 & \text{for } (1 - M^2)_{i,j,k} < 0 \end{cases} \quad (9)$$

The switching parameter $\mu_{i,j,k}$ gives the flux in the x-direction by a central difference operator in elliptic regions ($\mu_{i-1,j,k} = 0$, $\mu_{i,j,k} = 0$) and by a central operator shifted upstream one mesh point in hyperbolic regions ($\mu_{i-1,j,k} = 1$, $\mu_{i,j,k} = 1$) and thereby prevents upstream signal propagation. For evenly spaced meshes equation (7) is formally second order accurate in elliptic regions and first order in hyperbolic regions.

In addition to the elliptic and hyperbolic operators, equation (7) also contains the parabolic ($\mu_{i-1,j,k} = 0$, $\mu_{i,j,k} = 1$) and shock point ($\mu_{i-1,j,k} = 1$, $\mu_{i,j,k} = 0$) operators and, for evenly spaced meshes, is the three-dimensional equivalent of Murman's fully conservative relaxation (FCR) method (ref. 15). In the unequally spaced mesh case (both two and three dimensions), however, the first term of equation (7) differs by a factor of $\frac{x_i - x_{i-2}}{x_{i+1} - x_{i-1}}$ in hyperbolic regions because the mesh cells are centered about the point (i,j,k) in all flow regions. Consistency of the difference approximation is demonstrated for smoothly varying meshes by the expansion

$$\frac{x_i - x_{i-2}}{x_{i+1} - x_{i-1}} = 1 - \Delta\xi \frac{\xi''}{\xi'} + O(\Delta\xi^2) \quad (10)$$

where $\xi(x)$ is the inverse of the implied stretching function, that is, $\Delta\xi$ is uniform, and the primes denote derivatives.

A majority of 2-D transonic calculations and all reported 3-D calculations have been performed by use of nonconservative relaxation (NCR) methods. In the absence of viscosity corrections, the NCR solutions generally agree

better with experimental pressure measurements than the FCR results. This is because mass sources result from the failure of the NCR methods to cancel fluxes at shock points, where x-differences shift from upwind to centered (ref. 15). The source strengths do not vanish with vanishing mesh spacing, and they reduce the computed shock strengths to values nearly equal to those obtained experimentally, which are, of course, weakened by the interaction of the shock and boundary layer.

Two NCR methods are contained in equation (7). The first, that due to Murman and Cole (ref. 1), is obtained by setting

$$\mu_{i-1,j,k} = \mu_{i,j,k} \quad (11)$$

except at the expansion sonic line, and the second, that due to Garabedian and Korn (ref. 16), is obtained by setting

$$\left[(1 - M_\infty^2) \mu \right]_{i-1,j,k} = \left[(1 - M_\infty^2) \mu \right]_{i,j,k} \quad (12)$$

Wing Boundary Conditions

For a wing whose surface is given by $f(x,y,z) = 0$ and which is at angle of attack α , the linearized boundary condition is

$$f_x + (\phi_z + \alpha) f_z = 0 \quad (13)$$

This equation is applied on the wing mean plane midway between mesh planes by expressing the vertical derivative at the mesh plane adjacent to the upper surface as

$$\left(\phi_{zz} \right)_{i,j,k} = \frac{2}{z_{k+1} - z_{k-1}} \left\{ \frac{\phi_{i,j,k+1} - \phi_{i,j,k}}{z_{k+1} - z_k} + \left[\left(\frac{f_x}{f_z} \right)_u + \alpha \right] \right\} \quad (14a)$$

and the lower surface as

$$\left(\phi_{zz} \right)_{i,j,k} = \frac{-2}{z_{k+1} - z_{k-1}} \left\{ \frac{\phi_{i,j,k} - \phi_{i,j,k-1}}{z_k - z_{k-1}} + \left[\left(\frac{f_x}{f_z} \right)_l + \alpha \right] \right\} \quad (14b)$$

The Kutta condition requires that the pressure (ϕ_x) be continuous at the trailing edge. This fixes the section circulation Γ_j , which is equal to the difference in potential at the section trailing edge linearly extrapolated from points above and below. The potential jumps are convected downstream along straight lines to form the trailing-vortex sheet, across which both pressure and downwash (ϕ_z) are continuous. The potential jump through the sheet is taken into account in the ϕ_{zz} difference formula at the plane above by replacing $\phi_{i,j,k-1}$ with $\phi_{i,j,k-1} + \Gamma_j$ and at the plane below by replacing $\phi_{i,j,k+1}$ with $\phi_{i,j,k+1} - \Gamma_j$. Note that no points lie on the sheet, as in the original method (ref. 2). The present technique simplifies the coding with no significant loss in accuracy.

Fuselage Boundary Condition

In the present method the fuselage is treated in a rectangular mesh system. A similar two-dimensional procedure, which appears to be extendable to three dimensions, has been demonstrated for subsonic flow in reference 17. In the present method a simplified approach suggested by Allen Chen of the Boeing Co. is used in which the mesh is constructed so that points lie reasonably close to the fuselage surface, such as shown in figure 3. Points may lie either inside or outside the fuselage boundary. For a configuration described by $f(x,y,z) = 0$, the small-disturbance boundary condition becomes

$$f_x + \phi_y f_y + \phi_z f_z = 0 \quad (15)$$

By substituting three point-extrapolated differences at the boundary point i,j,k (for the upper surface, say) of the form

$$(\phi_y)_{i,j,k} = A_1 \phi_{i,j,k} + A_2 \phi_{i,j-1,k} + A_3 \phi_{i,j-2,k} \quad (16a)$$

and

$$(\phi_z)_{i,j,k} = B_1 \phi_{i,j,k} + B_2 \phi_{i,j,k-1} + B_3 \phi_{i,j,k-2} \quad (16b)$$

into equation (15), the expression for the boundary potential is found as

$$\phi_{i,j,k} = - \left[f_x + (A_2 \phi_{i,j-1,k} + A_3 \phi_{i,j-2,k}) f_y + (B_2 \phi_{i,j,k-1} + B_3 \phi_{i,j,k-2}) f_z \right] / (A_1 f_y + B_1 f_z) \quad (17)$$

Far Field

The condition applied at the outer boundary of the computational domain is given by the superposition of the asymptotic far-field solutions for wings derived by Klunker (ref. 18), and bodies of revolution derived by Krupp and Murman (ref. 19). At the downstream boundary, however, the lift contribution is obtained by the numerical solution to the cross-flow equation.

Nonrectangular Wing Transformation

The isolated wing code treats a swept and tapered wing by mapping the wing into a rectangle by the transformation

$$\left. \begin{aligned} \xi &= \frac{x - x_{LE}}{x_{TE} - x_{LE}} \\ \eta &= y \\ \zeta &= z \end{aligned} \right\} \quad (18)$$

where x_{LE} and x_{TE} are the x-coordinates of the leading and trailing edges. The divergence form of equation (1) becomes

$$\left[(1 - M_\infty^2) \epsilon_x \phi_\xi - \frac{\gamma + 1}{2} M_\infty^n \epsilon_x^2 \phi_\xi^2 + \frac{\epsilon_y}{\epsilon_x} (\epsilon_y \phi_\xi + \phi_\eta) \right]_\xi + \left[\frac{1}{\epsilon_x} (\epsilon_y \phi_\xi + \phi_\eta) \right]_\eta + \left[\frac{1}{\epsilon_x} \phi_\zeta \right]_\zeta \quad (19)$$

The conservative difference approximation of equation (19) is derived in the manner previously outlined and is given as

$$\begin{aligned} & \left\{ (1 - \mu_{i,j,k}) (1 - M^2)_{i,j,k} \left[(\epsilon_x \phi_\xi)_{i+1/2,j,k} - (\epsilon_x \phi_\xi)_{i-1/2,j,k} \right] \right. \\ & + \mu_{i-1,j,k} (1 - M^2)_{i-1,j,k} \left[(\epsilon_x \phi_\xi)_{i-1/2,j,k} - (\epsilon_x \phi_\xi)_{i-3/2,j,k} \right] \\ & + \left. \left[\frac{\epsilon_y}{\epsilon_x} (\epsilon_y \phi_\xi + \phi_\eta) \right]_{i+1/2,j,k} - \left[\frac{\epsilon_y}{\epsilon_x} (\epsilon_y \phi_\xi + \phi_\eta) \right]_{i-1/2,j,k} \right\} / (\epsilon_{i+1/2} - \epsilon_{i-1/2}) \\ & + \left\{ \left[\frac{1}{\epsilon_x} (\epsilon_y \phi_\xi + \phi_\eta) \right]_{i,j+1/2,k} - \left[\frac{1}{\epsilon_x} (\epsilon_y \phi_\xi + \phi_\eta) \right]_{i,j-1/2,k} \right\} / (\eta_{j+1/2} - \eta_{j-1/2}) \\ & + \left[\left(\frac{1}{\epsilon_x} \phi_\zeta \right)_{i,j,k+1/2} - \left(\frac{1}{\epsilon_x} \phi_\zeta \right)_{i,j,k-1/2} \right] / (\zeta_{k+1/2} - \zeta_{k-1/2}) = 0 \end{aligned} \quad (20)$$

where

$$(\phi_\xi)_{i+1/2,j,k} = \frac{\phi_{i+1,j,k} - \phi_{i,j,k}}{\epsilon_{i+1} - \epsilon_i}$$

$$(\phi_\eta)_{i+1/2,j,k} = \frac{1}{2} \left[\frac{\phi_{i+1,j+1,k} - \phi_{i+1,j-1,k}}{\eta_{j+1} - \eta_{j-1}} + \frac{\phi_{i,j+1,k} - \phi_{i,j-1,k}}{\eta_{j+1} - \eta_{j-1}} \right], \text{ etc.}$$

Note that equation (20) maintains the proper domain of dependence in hyperbolic regions by upwind differencing only the contribution from the x-direction (i.e., terms multiplied by $(1 - \mu_{i,j,k})$ and $\mu_{i-1,j,k}$) while the others remain centrally differenced.

In transformed coordinates the wing surface and vortex sheet conditions are unaltered. However, the boundary condition at the wing root becomes

$$\phi_y = \xi_y \phi_\xi + \phi_\eta = 0 \quad (21)$$

and is substituted into equation (20) at the root.

Relaxation Scheme

The solution of the difference equations is obtained by a vertical-column relaxation scheme. A number of variations of the method have been coded, and in what follows, we outline the scheme that we believe has the best stability properties.

Following Jameson (ref. 20), the iterations are viewed as steps in pseudo-time. The combination of new (ϕ^+) and old (ϕ) values in the difference operators is chosen so that the related time-dependent equation represents a properly posed problem whose steady-state solution approaches that of the steady equation. In addition, the linearized algorithm is required to satisfy the von Neumann stability criterion.

For ease of discussion, consider an evenly spaced rectangular mesh with $x_{i+1} = x_i + \Delta x$, etc. The relaxation equation for elliptic regions ($\mu_{i,j,k} = 0$ and $\mu_{i-1,j,k} = 0$) is written

$$\begin{aligned} (1 - M^2)_{i,j,k} \left[\phi_{i-1,j,k}^+ - \frac{2}{\omega} \phi_{i,j,k}^+ - 2 \left(1 - \frac{1}{\omega} \right) \phi_{i,j,k} + \phi_{i+1,j,k} \right] / (\Delta x)^2 \\ + \left[\phi_{i,j-1,k}^+ - 2\phi_{i,j,k}^+ + \phi_{i,j+1,k} \right] / (\Delta y)^2 \\ + \left[\phi_{i,j,k-1}^+ - 2\phi_{i,j,k}^+ + \phi_{i,j,k+1}^+ \right] / (\Delta z)^2 = 0 \quad (22) \end{aligned}$$

where ω is an overrelaxation parameter ($1 \leq \omega < 2$) and $M_{i,j,k}$ is evaluated from old values. Note that only the contribution from the x-direction is overrelaxed. This avoids an abrupt change in the diagonal term as the solution crosses the sonic surface suggested by J. C. South and P. A. Newman of the Langley Research Center.

In hyperbolic regions the relaxation equation is

$$\begin{aligned} (1 - M^2)_{i-1,j,k} (\phi_{i-2,j,k} - 2\phi_{i-1,j,k}^+ + 2\phi_{i,j,k}^+ - \phi_{i,j,k}) / (\Delta x)^2 \\ + (\phi_{i,j-1,k}^+ - \phi_{i,j,k}^+ - \phi_{i,j,k} + \phi_{i,j+1,k}) / (\Delta y)^2 \\ + (\phi_{i,j,k-1}^+ - 2\phi_{i,j,k}^+ + \phi_{i,j,k+1}^+) / (\Delta z)^2 = 0 \quad (23) \end{aligned}$$

It is of interest to look at the equivalent time-dependent equation

$$(M^2 - 1)\phi_{xx} - \phi_{yy} - \phi_{zz} + 2(M^2 - 1)\frac{\Delta t}{\Delta x}\phi_{xt} + \frac{\Delta t}{\Delta y}\phi_{yt} = 0 \quad (24)$$

inferred from equation (23). It can be shown that the condition

$$(M^2 - 1)\frac{\Delta t}{\Delta x} > \frac{(M^2 - 1)^{1/2}}{2}\frac{\Delta t}{\Delta y} \quad (25)$$

must hold for x to be the hyperbolic marching direction. To keep x the marching direction and to improve stability near sonic points, it may be necessary to add to equation (23) the quantity

$$\epsilon(M^2 - 1)^{1/2}\frac{\Delta t}{\Delta x}\phi_{xt} \quad (26)$$

where

$$\frac{\Delta t}{\Delta x}\phi_{xt} = (\phi_{i,j,k}^+ - \phi_{i,j,k} - \phi_{i-1,j,k}^+ + \phi_{i-1,j,k})/(\Delta x)^2$$

and ϵ is a chosen parameter.

RESULTS

In this section we discuss comparisons between present computed results, other theoretical solutions, and experimental data. Before beginning, however, we wish to point out the difficulties associated with comparing computed solutions with experiment. It is well known that viscous effects play a large role in determining surface pressure distributions in many transonic flows. This is particularly true in lifting cases (ref. 21) and when embedded shock waves occur. (See ref. 13, fig. 6.) Since the present method is entirely inviscid, considerable disagreement with data is encountered where viscous effects are significant. Furthermore, wind-tunnel results are often affected by interference from the tunnel walls. Although attempts are made to correct for interference effects, the corrected free-stream Mach number and angle of attack do not always closely correspond to free-air values. Also, as the free-stream Mach number approaches one, the wall effects on the sonic bubble and shock locations become even more significant and difficult to assess.

Violation of the small-disturbance assumption can also cause significant departures from the correct inviscid free-air solution. The assumption of small flow deflection is seriously violated near blunt leading edges and at high angles of attack. Thus, erroneous results can be obtained in the leading-edge region. Also, the small-disturbance theory predicts shock pressure jumps that become significantly stronger than the Rankine-Hugoniot value as the shock Mach number increases past about 1.3. Finally, the predictions for oblique shock waves also depart significantly from the exact values for shock wave angles in excess of about 20° (ref. 13).

We begin by considering comparisons for two isolated wings. The first, shown in figure 4, is for computed and experimental pressures furnished by M. G. Hall of the RAE on the RAE Wing C at $M = 0.95$ and $\alpha = 0^\circ$ which was tested in the RAE 8 ft x 6 ft transonic tunnel at $Re = 1.4 \times 10^6$. The computed results, which were obtained on a $51 \times 34 \times 48^c(x,y,z)$ grid, show generally good agreement with the experimental pressures, with some overexpansion near the leading edge at the root. The NCR and FCR solutions were virtually the same because of the absence of shock waves.

The second comparison, in figures 5 and 6, is for the ONERA M6 wing. The experimental data were obtained in the ONERA S2 transonic tunnel at $Re_c = 2.5 \times 10^6$ (ref. 22). Computations were performed on a sequence of three grids ($35 \times 20 \times 24$, $45 \times 23 \times 30$, $66 \times 37 \times 32$); using both the NCR and FCR methods, and required approximately 5 CPU minutes on the CDC 7600 computer utilizing the RUN 76 compiler. Figure 5 shows comparisons between the computed and measured pressures for $M = .84$ and $\alpha = 3^\circ$. The NCR results are very similar to those reported in reference 5. The FCR method predicts a slightly downstream shift in shock location, as expected from Murman's two-dimensional computations (ref. 15). Although the experimental pressures show evidence of both a forward and an aft shock wave, the calculations show clear evidence of only the aft shock. This is not surprising, because it has been shown in reference 13 that the small-disturbance equation (used here and in ref. 5) is a poor approximation to the full potential equation for shocks with sweep angles greater than about 20° . The experimental forward shock is swept at about 36° over most of its length. The agreement claimed in reference 5 between computed and experimental forward shock locations is not evident in the comparison of experimental and computed section pressures. It appears that the small-disturbance approach can, however, be modified to properly treat swept shock waves by retaining two additional terms in the governing equation. (See ref. 13.) Work in this area is currently being pursued.

Figure 6 shows pressure comparisons for $M = .92$ and $\alpha = 3^\circ$. Here the aft shock prediction from the FCR method is significantly downstream of that predicted by the NCR method. The NCR result, with the weaker shock, generally agrees better with the data but is still in serious disagreement. Neither method captures the forward shock, which is clearly evident in the experimental data at the three outboard span stations. The disagreement in upper surface, aft shock, and lower surface shock locations can probably be attributed primarily to the decrease in wing lift caused by trailing-edge viscous effects. This moves the upper shock upstream and the lower one downstream.

We now turn our attention to comparisons of computed and experimental pressures for a parabolic-arc body with sting, shown in figure 7, and wing-fuselage configurations, shown in figures 8 to 10. The present results are obtained by use of equation (17) as the body boundary condition. Figure 7 shows pressures at the body surface and in the flow field at two body diameters from the centerline for $M_\infty = .99$. Good agreement is shown between the present NCR calculation ($41 \times 40 \times 40$), an axisymmetric NCR calculation (ref. 23), and measured pressures (ref. 24). The x-mesh spacing used in the present calculation is 2.5 times coarser than that used in the axisymmetric

one, and accounts for the difference in shock resolution. The discrepancies in the pressures are primarily attributed to the mesh coarseness and the lack of boundary definition near the body nose. Figure 8 compares NCR, FCR, linear theory (ref. 25), and experimental pressures (ref. 25) for a Sears-Haack fuselage rectangular-wing combination at $M_\infty = .90$ and $\alpha = 0^\circ$. The data were obtained in the AEDC 16 ft wind tunnel at $Re_c = 3.0 \times 10^6$ (ref. 26). The present results were obtained on a $57 \times 35 \times 30$ grid. The pressure plots at the top of the body show that the present results overexpand near the nose compared with linear theory, as was noted in the previous example. As usual, the FCR-predicted shock location is aft of the NCR prediction, whereas linear theory shows no shock. Comparison with experiment is good although the sparseness of the data points precludes the accurate determination of the experimental shock location. A comparison is also shown at mid semispan. The interesting result here is that the experimental shock location is downstream of the computed locations. In figure 9 the mid-semispan solution is compared with an isolated wing calculation (ref. 25) from the Jameson 3-D program and data. The present results and those of Jameson compare favorably, particularly when the coarseness of the mesh used in the present calculation is considered. The disagreement between the computations and experiment does not appear to be caused by viscous effects, which generally move shocks upstream in such nonlifting cases. More likely the disagreement is caused by the test Mach number being slightly higher than .90.

Finally, figure 10 compares NCR calculated and experimental pressures for a swept wing-fuselage configuration at $M = .93$ and $\alpha = 0^\circ$. The computed results were obtained using a Cartesian grid ($81 \times 59 \times 27$) for the wing as well as the fuselage. The first x-mesh point at the wing leading edge was fixed at 2.5 percent chord with 23 mesh points along the root chord and 11 along the tip chord, distributed according to the methods used in references 3 and 5. The uncorrected experimental data were obtained in the Langley 8-ft tunnel (solid wall) at $Re_c = 2.0 \times 10^6$ (ref. 27). The agreement with experiment on the fuselage centerline and the two inboard panels is good. In the computed results, the wing root shock propagates laterally to $y/b = .60$, but the experimental shock dissipates before reaching this point. The source of the disagreement is not clear but perhaps is a viscous effect.

Clearly, the computed results lack sufficient leading-edge expansion at the outboard span stations $y/b = .80$ and $y/b = .95$, an effect that is caused by the coarse x mesh (about 12 points per chord) there. The Cartesian grid approach requires too many mesh points to obtain the required resolution near the leading edge. The calculation should be improved significantly by the use of the planform transformation, which was described previously in the treatment of isolated wings.

CONCLUDING REMARKS

A relaxation method has been developed which allows as an option either fully conservative (FCR) or nonconservative (NCR) differencing. The three-dimensional FCR and NCR solutions exhibit properties similar to those

reported by Murman for two-dimensional flow. That is, for weak shock waves there is little difference; as the shock strength increases, the FCR shock wave becomes stronger than the NCR shock wave and, consequently, is located further downstream. The NCR solutions correlate better with experimental pressures, but it is anticipated that the FCR method will prove superior when viscous effects are properly accounted for.

Clearly, the present solutions do not agree well with data in all cases, particularly when (1) there is extensive separation either at the shock or trailing edge, and when (2) there are highly swept shock waves embedded in the flow. The treatment of highly swept shocks should be improved by retaining two additional terms in the governing equation, as suggested in reference 13, or by solution of the full potential equations.

In flows about wing-fuselage configurations, the basic idea is to treat the fuselage with accuracy sufficient to obtain its effect on the wing without the use of complicated fuselage transformations. The present results are encouraging and felt to be quite good when the simple boundary approximations used are considered. The extension to lifting wing-fuselage configurations is straightforward and work in this area is being pursued.

REFERENCES

1. Murman, E. M., and Cole, J. D.: Calculation of Plane Steady Transonic AIAA Journal, vol. 9, no. 1, January 1971, pp. 114-121.
2. Ballhaus, W. F., and Bailey, F. R.: Numerical Calculation of Transonic Flow About Swept Wings. AIAA Paper 72-677, June 1972.
3. Bailey, F. R., and Ballhaus, W. F.: Relaxation Methods for Transonic Flow About Wing-Cylinder Combinations and Lifting Swept Wings. Lecture Notes in Physics, vol. 19, Springer-Verlag, 1972, pp. 2-9.
4. Bailey, F. R.: On the Computation of Two- and Three-Dimensional Steady Transonic Flows by Relaxation Methods. VKI Lecture Series "Progress in Numerical Fluid Dynamics," Von Karman Institute for Fluid Dynamics, Rhode-St-Genese, Belgium, February 11-15, 1974.
5. Schmidt, W., Rohlf, S., and Vanino, R.: Some Results Using Relaxation Methods and Finite Volume Techniques for Two- and Three-Dimensional Transonic Flows. Lecture Notes in Physics, vol. 35, Springer-Verlag, 1974, pp. 364-372.
6. Klunker, E. B., and Newman, P. A.: Computation of Transonic Flow About Lifting Wing-Cylinder Combinations. Jour. Aircraft, vol. 2, no. 4, April 1974, pp. 254-256.
7. Newman, P. A., and Klunker, E. B.: Computation of Transonic Flow About Finite Lifting Wings. AIAA Journal, vol. 10, no. 7, July 1972, pp. 971-973.

8. Bailey, F. R., and Steger, J. L.: Relaxation Techniques for Three Dimensional Transonic Flow About Wings. AIAA Paper 72-189, Jan. 1972.
9. Ballhaus, W. F., and Caradonna, F. X.: The Effect of Planform Shape on the Transonic Flow Past Rotor Tips. Aerodynamics of Rotary Wings, AGARD Conference Proceedings No. 111, Paper 17, Sept. 1972.
10. Isom, M. P., and Caradonna, F. X.: Subsonic and Transonic Potential Flow Over Helicopter Rotor Blades. AIAA Paper 72-39, Jan. 1972.
11. Jameson, A.: Numerical Calculation of the Three Dimensional Transonic Flow Over a Yawed Wing. Proceedings AIAA Computational Fluid Dynamics Conference, Palm Springs, CA, July 1973, pp. 18-26.
12. Lores, M. E., and Lemmerman, L. A.: A Numerical Method for Isolated Wing Transonic Flow Calculations. LTV Tech. Rept. no. 2-57110/4R-3190, Nov. 1974.
13. Lomax, H., Bailey, F. R., and Ballhaus, W. F.: On the Numerical Simulation of Three-Dimensional Transonic Flow With Application to the C-141 Wing. NASA TN D-6933, 1973.
14. Krupp, J. A.: The Numerical Calculation of Plane Steady Transonic Flows Past Thin Lifting Airfoils. Boeing Scientific Research Laboratories Report D180-12958-1, June 1971.
15. Murman, E. M.: Analysis of Embedded Shock Waves Calculated by Relaxation Methods. Proceedings of AIAA Computational Fluid Dynamics Conference, Palm Springs, CA, July 1973, pp. 27-40.
16. Garabedian, P. R., and Korn, D. G.: Analysis of Transonic Airfoils. Comm. Pure Appl. Math., vol. XXIV, 1971, pp. 841-851.
17. Parker, R., and Ma, C. Y.: Normal Gradient Boundary Condition in Finite Difference Calculations. Intl. Jour. Num. Meth. Eng., vol. 7, 1973, pp. 395-411.
18. Klunker, E. B.: Contributions to Methods for Calculating the Flow About Thin Lifting Wings at Transonic Speeds - Analytical Expression for the Far Field. NASA TN D-6530, 1971.
19. Krupp, J. A., and Murman, E. M.: The Numerical Calculation of Steady Transonic Flows Past Thin Lifting Airfoils and Slender Bodies. AIAA Paper 71-566, June 1971.
20. Jameson, Antony: Iterative Solution of Transonic Flows over Airfoils and Wings, Including Flows at Mach 1. Comm. Pure Appl. Math., vol. XXVII, 1974, pp. 283-309.

21. Melnik, R. E., and Ives, D. C.: On Viscous and Wind-Tunnel Wall Effects in Transonic Flows Over Airfoils. AIAA Paper 73-660, July 1973.
22. Monnerie, B., and Charpin, F.: Essais de Buffeting d'une Aile en Flèche en Transsonique. 10^e Colloque D'Aérodynamique Appliquée, Nov. 1973.
23. Bailey, F. R.: Numerical Calculation of Transonic Flow About Slender Bodies of Revolution. NASA TN D-6582, 1971.
24. Taylor, R. A., and McDevitt, J. B.: Pressure Distributions at Transonic Speeds for Parabolic-Arc Bodies of Revolution Having Fineness Ratios of 10, 12, and 14. NACA TN 4234, 1958.
25. Newman, P. A., and Allison, D. O.: Comparison of Interference-Free Numerical Results with Sample Experimental Data for the AEDC Wall-Interference Model at Transonic and Subsonic Flow Conditions. NASA TM X-71991, 1974.
26. Binion, T. W.: An Investigation of Three Dimensional Wall Interference in a Variable Porosity Transonic Wind Tunnel. AEDC-TR-74-76, 1973.
27. Loving, D. L., and Estabrooks, B. B.: Transonic-Wing Investigation in the Langley 8-Foot High-Speed Tunnel at High Subsonic Mach Numbers and at a Mach Number of 1.2. NACA RM L51F07, 1951.

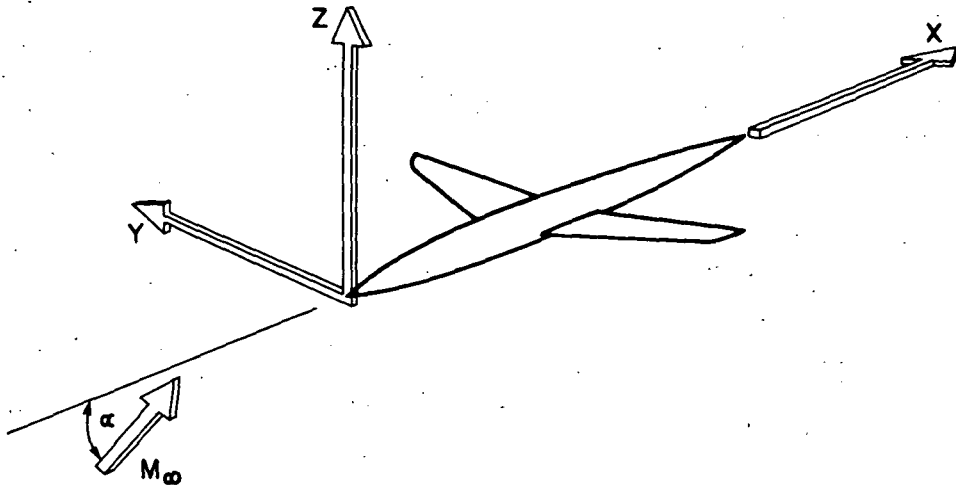


Figure 1.— Coordinate system.

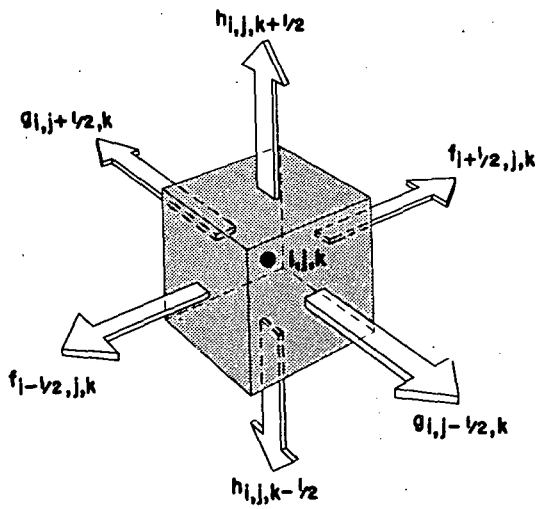


Figure 2.— Computational volume.

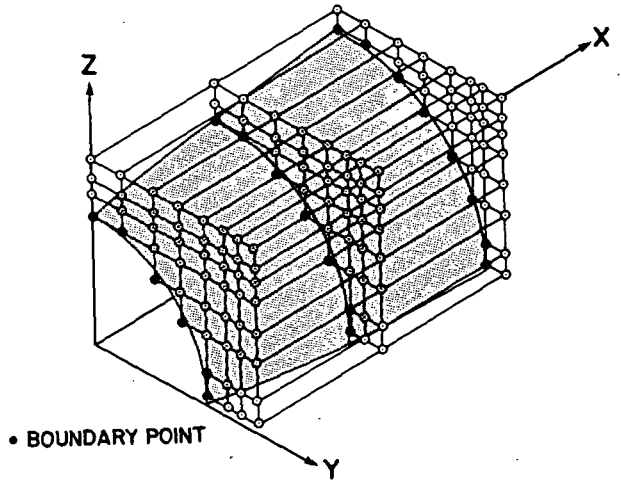


Figure 3.— Body boundary points.

$\Lambda_{c/2} = 44^\circ$

AR = 3.6

TR = .333

RAE 101 SECTION
5.4% STREAMWISE

EXPERIMENT, RAE, $Re_c = 1.4 \times 10^6$

RAE 8'x6' TUNNEL

COMPUTED (NCR, FCR)

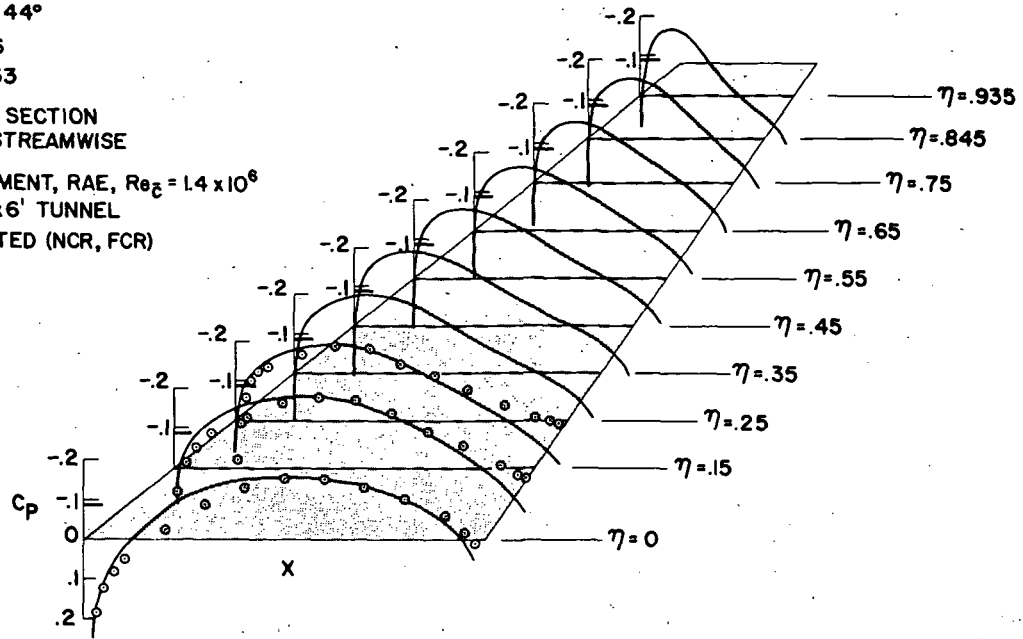


Figure 4.- Comparison of computed and experimental pressure coefficients C_p for the RAE wing C. $M_\infty = 0.95$; $\alpha = 0^\circ$; TR denotes taper ratio; and AR denotes aspect ratio.

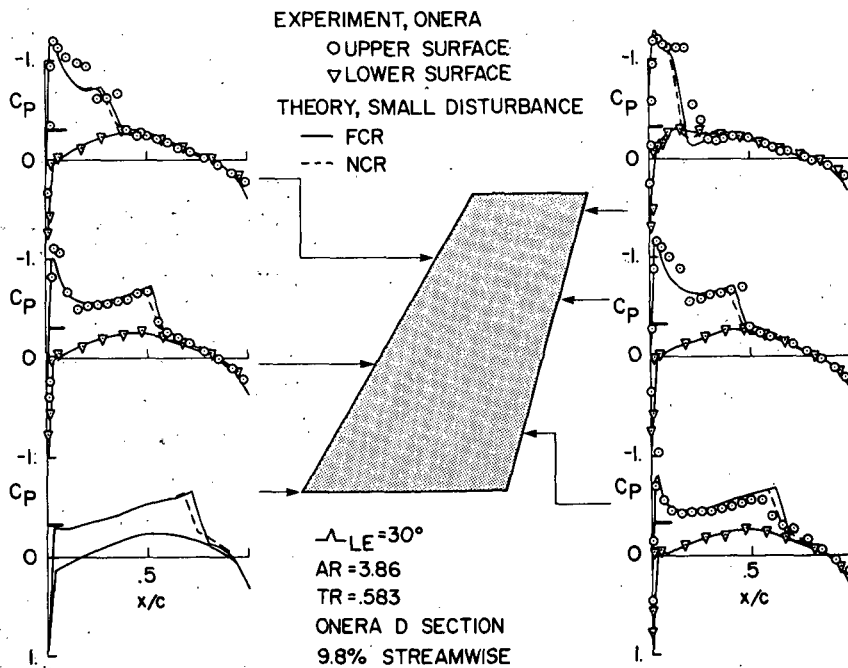


Figure 5.- Comparison of computed and experimental (ref. 22) pressure coefficients C_p for the ONERA M6 wing. $M_\infty = 0.84$; $\alpha = 3^\circ$.

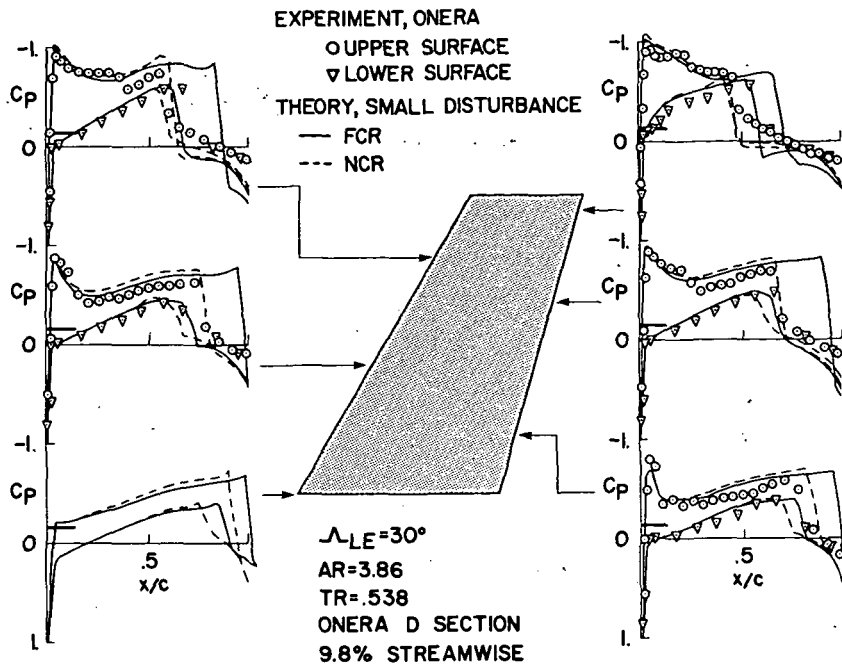


Figure 6.- Comparison of computed and experimental (ref. 22) pressure coefficients C_p for the ONERA M6 wing, $M_\infty = 0.92$; $\alpha = 3^\circ$.

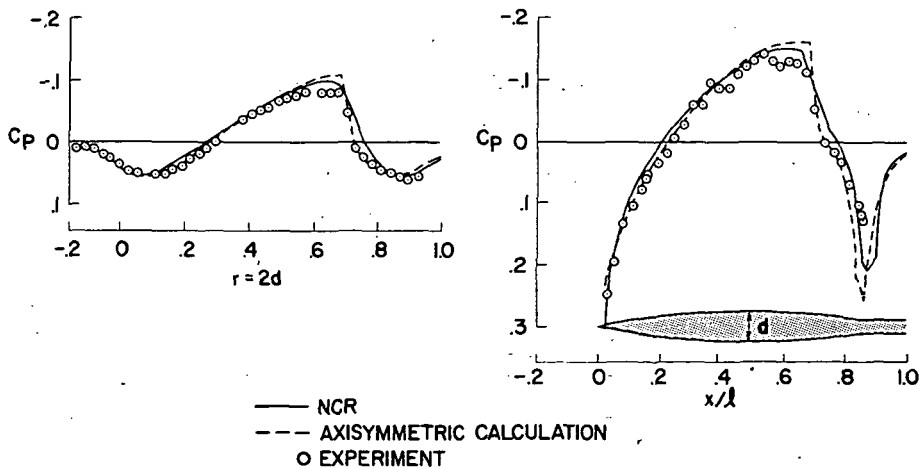


Figure 7.- Comparison with computed (ref. 23) and experimental (ref. 24) pressure coefficients C_p for a parabolic arc of revolution. Fineness ratio, 10; $M_\infty = 0.99$.

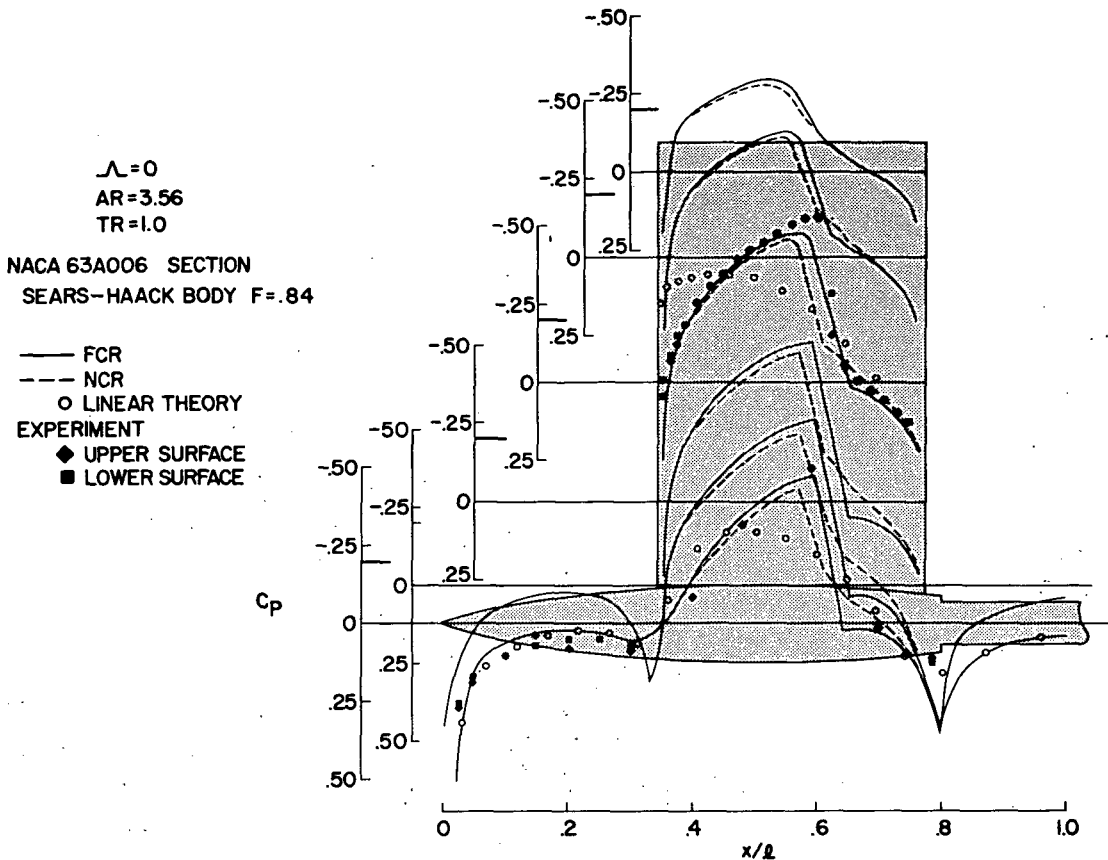


Figure 8.- Comparison with computed (ref. 25) and experimental (ref. 26) pressure coefficients C_p for a rectangular-wing-fuselage configuration. $M_\infty = 0.90$; $\alpha = 0^\circ$.

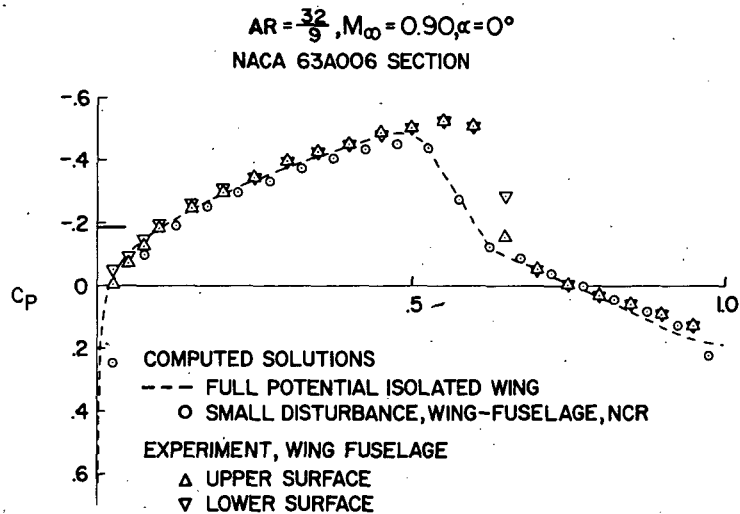


Figure 9.- Comparison of computed small disturbance and full potential (ref. 25) pressure coefficients C_p with experiment (ref. 26) at mid-semispan location.

F=12

$\Lambda_{c/4} = 45^\circ$

AR = 4

TR = .6

NACA 65A006 STREAMWISE

EXPERIMENT

LANGLEY 8 FT. WIND TUNNEL

$Re_x = 2.0 \times 10^6$

○ UPPER SURFACE TRANSITION NATURAL

◊ UPPER SURFACE TRANSITION FIXED

□ LOWER SURFACE TRANSITION NATURAL

◻ LOWER SURFACE TRANSITION FIXED

— NCR CALCULATION

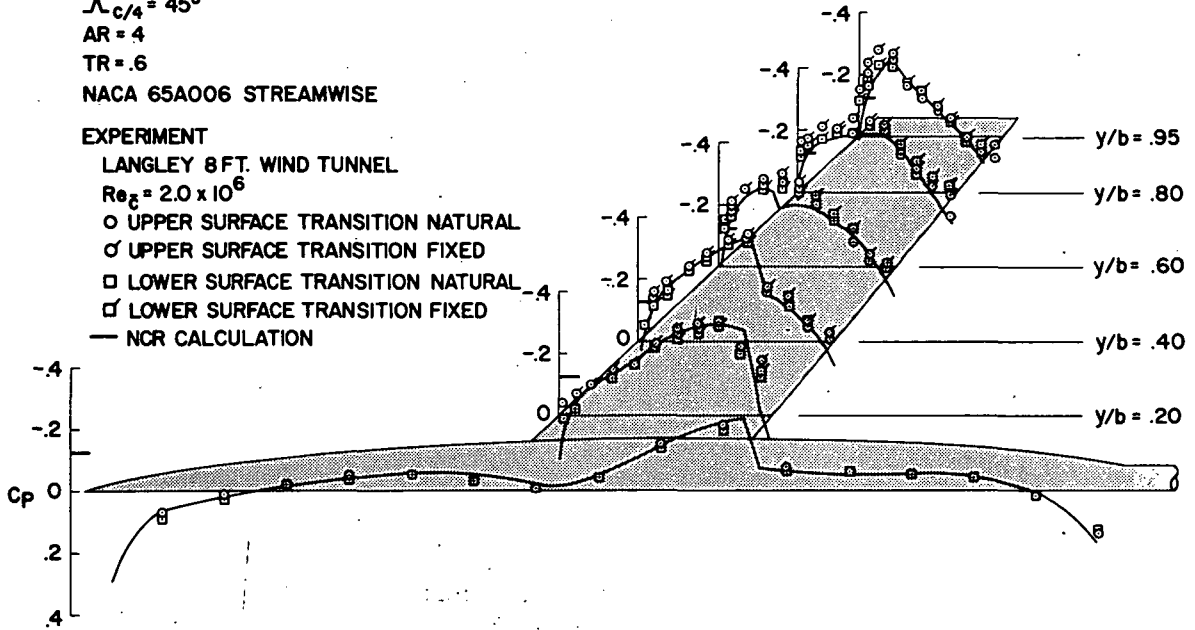


Figure 10.- Comparison of computed and experimental (ref. 27) pressure coefficients C_p for swept-wing-fuselage configuration. $M_\infty = 0.93$; $\alpha = 0^\circ$.

Page Intentionally Left Blank

AXISYMMETRIC TRANSONIC FLOW INCLUDING WIND-TUNNEL WALL EFFECTS

By Jerry C. South, Jr., and James D. Keller
NASA Langley Research Center

SUMMARY

A method is presented for obtaining numerical solutions to the problem of transonic flow past axisymmetric bodies in a wind tunnel. Parabolic coordinates are sheared and stretched so that the flow region between the body and the tunnel wall is mapped onto a rectangular computational plane. A finite-difference analog of the exact compressible potential equation is solved with a column iteration scheme which uses Jameson's rotated retarded differences in supersonic regions and central differences in subsonic regions. The flow tangency condition at the surface is enforced by a "dummy-point" method, and the wind-tunnel wall boundary condition is satisfied by a one-sided difference method. Solutions are obtained for a supercritical body of revolution and compared with previous calculations by RAXBOD, a program developed by South and Jameson for bodies in free air, and with experiments. The present results are not as accurate as the RAXBOD results for the same number of mesh points, and convergence is slow on the fine mesh. The method appears to work very well, however, for two-dimensional symmetric airfoils.

INTRODUCTION

Rapid progress has been made in the calculation of transonic flows through the use of iterative finite-difference schemes for the nonlinear potential equation. South and Jameson (ref. 1) have already developed a successful method for obtaining numerical solutions to axisymmetric transonic flow past blunt bodies of revolution in free air, using the full potential equation and exact boundary conditions. The method incorporates Jameson's "rotated" difference scheme (ref. 2) and is capable of treating both subsonic and supersonic free streams. The computer program that uses the method is called "RAXBOD," and is referred to by that name herein.

To support the effort at Langley Research Center in developing a new high Reynolds number transonic research tunnel, it was decided to extend the capability of RAXBOD to include wind-tunnel wall boundary conditions. The present paper reports progress in that direction. Described in the following sections are the coordinate systems that were considered, the boundary conditions, and finally some numerical results.

SYMBOLS

A,B,C,D	coefficients of the potential equation in computational coordinates
a	local speed of sound
a_1, a_2, a_3	coefficients of the general wind-tunnel wall boundary condition
c	a constant in the function $F(\xi)$
F	transformation function $X = F(\xi)$
G	transformation function $Y = G(\xi, \eta)$
H	defined by equation (15)
h	scale factor, $(\xi^2 + \eta^2)^{1/2}$
i	$= \sqrt{-1}$
l	slot parameter
M	Mach number
q	total velocity
R	residual
r	radial distance from axis
S	value of parabolic coordinate η on body (a function of ξ)
U,V	velocity components in direction of unsheared parabolic coordinates ξ and η , respectively
\tilde{U}	$= UG_\eta - VG_\xi$
\tilde{V}	$= UG_\xi + VG_\eta$

W_1, W_2, W_3 coefficients of transformed wall boundary condition

w part of function $G(\xi, \eta)$

X, Y computational coordinates

x, y Cartesian coordinates

$Y_1 = \eta - S(\xi)$

z auxiliary stretching function in $G(\xi, \eta)$

α exponent in equation (10)

γ ratio of specific heats

$\Delta X, \Delta Y$ mesh size in computational space

$\Delta \varphi$ change in φ for current iteration

$\zeta = \xi + i\eta$

ξ, η unsheared parabolic coordinates

φ disturbance velocity potential function

ω relaxation factor

Subscripts:

i, j mesh indices

JB value of j at body

JW value of j at wall

N derivative normal to local streamline direction

S derivative along local streamline direction

w at tunnel wall

∞ free stream

Variable subscripts such as x , y , ξ , η , X , Y , S , and N indicate partial derivatives; for example, $\varphi_{\xi\eta} = \frac{\partial^2 \varphi}{\partial \xi \partial \eta}$. Primes denote differentiation with respect to ξ whereas a superscript $+$ denotes a new value from the current iteration.

ANALYSIS

The coordinate system used in RAXBOD is a body-oriented one in the nose region, back to the first horizontal tangent; a "sheared" cylindrical system is used aft of that point. Hence, bodies with slope discontinuities in the forebody region are not correctly treated; gaps appear in the coordinate system, as shown in figure 1 where the RAXBOD coordinates are drawn for a Titan-Centaur-Viking launch shroud.

To improve this situation, it was decided to adapt sheared parabolic coordinates to the general axisymmetric problem. The parabolic coordinates have been used already by Jameson (ref. 3) for the wing problem, and they have the versatile capability of treating both blunt and pointed bodies. That is, for a blunt body, the singular point of the square-root transformation can be fixed inside the nose (about one-half of the nose radius for nearly parabolic noses is best), and for pointed bodies, the singular point is placed at the apex. The ξ, η parabolic coordinates are related to the x, y Cartesian coordinates as follows:

$$x - x_0 + iy = \frac{1}{2}(\xi + i\eta)^2 \quad (1)$$

where x_0 is the location of the singular point on the x -axis. A subsequent shearing to fit the body and a stretching to map the infinite region to a finite domain complete the transformation for free-air calculations. More details are given later. An example of the sheared parabolic coordinates for a pointed body is pictured in figure 2. Note that slope discontinuities do not leave gaps in the mesh.

Mapping the Wind-Tunnel Wall

It is desirable, although not necessary, to map boundary surfaces (including infinity, where appropriate) onto coordinate surfaces. When this is done, the differential equation becomes more complicated, but the application of the boundary conditions is considerably simplified. The basic idea in the present problem is to modify the sheared parabolic coordinates so that in a rectangular, computational X, Y plane, the wind-tunnel wall

coincides with $Y = 1$, the body with $Y = 0$, the stagnation streamline with $X = 0$, and downstream infinity with $X = 1$. A simple procedure exists which can incorporate the wind-tunnel wall into any of the mappings ordinarily used to map the infinite domain onto a finite rectangle for free-air calculations. This procedure specialized for the parabolic coordinates is as follows: First the relation between the computational coordinate Y , and the sheared parabolic coordinate, $Y_1 = \eta - S(\xi)$, is chosen, where $Y_1 = 0$ on the body surface. For example, one transformation that has been used is

$$Y_1 = z \tan \frac{\pi Y}{2} \quad (2)$$

where z is a parameter which controls the step size near the body, and can be made a function of ξ , so that the step size near the body can be better controlled as the distance from the nose increases. The inclusion of a variable parameter $z(\xi)$ is necessary for axisymmetric flows, since the parabolic coordinates tend to spread rapidly near the body tail, and the r^{-1} axisymmetric term in the differential equation is poorly approximated in the mesh cell nearest the surface unless the radial spreading is controlled. This feature was not evident in the two- and three-dimensional wing calculations by Jameson (ref. 3). An example of the type of function used for z is

$$z = a(1 + b\xi^2)^{-1/2}$$

where a and b are constants. This function is even in ξ at $\xi = 0$, behaves like ξ^{-1} for large ξ , and thus causes the lines $Y = \text{Constant}$ to approach horizontal lines of finite height as $\xi \rightarrow \infty$. The larger b is, the smaller the normal mesh near the body tail will be.

Second, to incorporate the wind-tunnel wall in the transformation, replace Y by wY in the relation between Y and Y_1 ; for example, equation (2) becomes

$$Y_1 = z \tan \frac{\pi wY}{2} \quad (3)$$

The equation for $w(\xi)$ is obtained by setting $Y = 1$ and $Y_1 = \eta_w - S$ and solving for w ; for example,

$$w = \frac{2}{\pi} \tan^{-1} \left(\frac{\eta_w - S}{z} \right) \quad (4)$$

where, for a straight wall at $y = y_w = \text{Constant}$, the parabolic coordinate η_w is obtained from equation (1) as

$$\eta_w = \frac{y_w}{\xi} \quad (5)$$

Note that the free-air mapping is recovered when $y_w \rightarrow \infty$, for then from equations (5) and (4), $w \rightarrow 1$ for all ξ ($0 \leq \xi < \infty$). Note also that the simple transformation equations (3) to (5) accomplish the desired goal; that is, the wind-tunnel wall coincides with $Y = 1$ and the body with $Y = 0$.

A picture of the mesh is shown in figure 3 for a wind-tunnel wall height of one body length and the tangent stretching that has served as an example. It can be seen that the $Y = \text{Constant}$ lines intersect the forward axis and the wall at angles which become progressively more acute upstream. To avoid possible instability along the forward axis, $X = 0$, some study was made to see what could be done to produce orthogonal intersections there.

At the axis $X = 0$, the slope of a line for $Y = \text{Constant}$ is given by

$$\frac{dy}{dx} = \frac{G_\eta}{G_\xi} \quad (6)$$

where, in general,

$$Y = G(\xi, \eta) \quad (7)$$

Hence, orthogonality at the axis requires

$$G_\xi = 0 \quad (X = 0) \quad (8)$$

If z is even near $X = 0$, then the requirement (eq. (8)) can be met if

$$w_\xi = 0 \quad (X = 0) \quad (9)$$

From equations (4) and (5) it can be seen that the tangent stretching, as presented, does not satisfy $w_\xi = 0$. One way to force $w_\xi = 0$ in the tangent stretching is to use a quadratic relation for the intermediate variable Y_1 ; that is, let $Y_1 = (\eta - S)^2$. This result is shown in figure 4, where the lines $Y = \text{Constant}$ are orthogonal to the axis, but now the step size next to the body is too large.

It happens that the family of algebraic stretch functions

$$\eta - S = \frac{z w Y}{(1 - w^2 Y^2)^\alpha} \quad (10)$$

satisfies the requirements very well. The relation between η and Y is linear near $Y = 0$, and for $0 < \alpha < 1$, $w_\xi = 0$ and hence orthogonality at the axis is obtained. In the present work, equation (10) is used with $\alpha = \frac{1}{2}$. Figure 5 illustrates this transformation.

There still remains the problem of nonorthogonal intersections at the wind-tunnel wall. Transformations certainly exist which have orthogonal intersections at both the axis and wall, but the ones considered do not seem to have a reasonable distribution of mesh points. One such transformation is pictured in figure 6; this mesh is clearly unsuitable for the present problem. At any rate, it was found that the nonorthogonal intersections at the wall caused no difficulty with the treatment of the boundary condition there, which is discussed later.

Equations

The partial differential equation for the disturbance velocity potential in parabolic coordinates can be written as follows:

$$(a^2 - U^2)\varphi_{\xi\xi} - 2UV\varphi_{\xi\eta} + (a^2 - V^2)\varphi_{\eta\eta} = H \quad (11)$$

where

$$U = h^{-1}(\varphi_{\xi} + \xi) \quad (12)$$

$$V = h^{-1}(\varphi_{\eta} - \eta) \quad (13)$$

$$h^2 = \xi^2 + \eta^2 \quad (14)$$

$$H = U^2 - V^2 - (U^2 + V^2)h^{-1}(\xi U + \eta V) - a^2h\left(\frac{U}{\xi} + \frac{V}{\eta}\right) \quad (15)$$

$$a^2 = a_0^2 - \frac{\gamma - 1}{2}(U^2 + V^2) \quad (16)$$

$$a_0^2 = 1 + \frac{2}{(\gamma - 1)M_{\infty}^2} \quad (17)$$

After transforming from the parabolic coordinates ξ and η to the computational coordinates X and Y , as discussed previously, where

$$\left. \begin{aligned} X &= F(\xi) \\ Y &= G(\xi, \eta) \end{aligned} \right\} \quad (18)$$

equation (11) becomes

$$A\varphi_{XX} + B\varphi_{XY} + C\varphi_{YY} = D \quad (19)$$

where the coefficients A, B, C, and D are complicated functions of ξ , η , φ_X , φ_Y , U, V, F_ξ , $F_{\xi\xi}$, G_ξ , G_η , $G_{\xi\xi}$, $G_{\xi\eta}$, and $G_{\eta\eta}$. Details are given in appendix A.

At mesh points where the flow is subsonic, central difference operators are used to approximate all the derivatives in equation (19); thus second-order truncation errors occur at such points. As in references 1 to 3, the "rotated" difference scheme is applied to the principal part (second derivatives) of equation (19) at locally supersonic points. That is, the equation is rearranged to identify the terms contributing to φ_{SS} and φ_{NN} , the derivatives along and normal to the local streamline, respectively. For convenience, this rearrangement is given in appendix B. The terms contributing to φ_{SS} are upwind-differenced, to first-order accuracy, and all the terms contributing to φ_{NN} are central-differenced, with second-order accuracy. As discussed in references 1 to 3, special care is required in choosing the mix between "old" and "new" values of φ_{ij} at the various mesh points in the computational molecule; otherwise instability can result on fine meshes. Appendix C describes the difference equations, the mix of old and new values of φ_{ij} , the solution algorithm, and the convergence criterion.

Boundary Conditions

In this section the boundary conditions and their numerical implementation are described.

Body surface.- At the body surface, the flow tangency condition must be imposed

$$V = S'U \quad (20)$$

where the prime indicates differentiation with respect to ξ . (Recall that $S(\xi)$ is the value of the parabolic η -coordinate along the body surface.) Substitution of equations (12) and (13) and the transformation equations given in appendix A into equation (20) gives

$$\varphi_Y = \frac{\eta + S'(F_\xi \varphi_X + \xi)}{[1 + (S')^2]G_\eta} \quad (21)$$

In deriving equation (21), the facts that $Y = 0$ on the surface and that F is a function of ξ alone have been used.

To impose the boundary condition (eq. (21)) on the numerical solution, a line of "dummy" points inside the body surface is generated in the computational plane, as illus-

trated at the top of figure 7. The value of $(\varphi_Y)_{JB}$ is obtained by evaluating the right-hand side of equation (21) by use of a central difference for φ_X with old values for φ_{ij} . The differential equation is solved at the surface point just as any other interior point on the column; after the column is updated, before proceeding to the next column, the dummy point φ_{JB+1} is updated as shown in figure 7 by using the new value for φ_{JB-1} just off the surface.

It should be noted here that in transonic flows with embedded shocks, better results are obtained when the differential equation is solved at the surface; the reason seems to be the singularity that occurs at the foot of the shock - a result of the interaction between the flow equations and the tangency condition at a curved surface, first discovered by Emmons (ref. 4). In earlier work by the authors, a second-order-accurate extrapolated boundary condition was used, similar to that used by Steger and Lomax (ref. 5); that is, the value of φ_{JB} at the surface was obtained by extrapolating the exterior flow field to satisfy the tangency condition only. The results of this approach were good in the absence of shock waves, but deteriorated rapidly as surface curvature and shock strength increased. For the extreme case of a transonic circular cylinder, the present dummy-point procedure gave much improved results near the shock and converged faster too.

Upstream and downstream infinity.- Upstream infinity corresponds to a single point in the computational plane: $X = 0$, $Y = 1$. At that point, $\varphi = 0$. Downstream infinity is located at the boundary $X = 1$ ($0 \leq Y \leq 1$) and there φ is set equal to 0 also, although it has not been analytically proved that this boundary condition is correct for all wind-tunnel wall boundary conditions. It is correct for free air, for the porous and slotted wall, and for the open jet; it is also used in the present work for the solid wall, even though Murman obtains a nonzero result for φ at downstream infinity for the solid-wall case in planar flow. (See ref. 6.) Nevertheless, imposing $\varphi = 0$ there produces correct numerical behavior of the derivatives, φ_X and φ_Y , and the flow returns smoothly to a uniform, parallel state which is the real requirement. Certainly, further study of this point is needed in the solid-wall case.

Wind-tunnel wall.- At the wind-tunnel wall, $Y = 1$, the open-jet, solid, porous, or ideal slotted-wall boundary conditions which are in current use can be represented by the equation

$$a_1\varphi + a_2\varphi_X + a_3\varphi_Y = 0 \quad (22)$$

where x and y are Cartesian coordinates. Transformation of equation (22) to the computational coordinates gives

$$\varphi_Y = W_1\varphi + W_2\varphi_X \quad (23)$$

where

$$W_1 = - \frac{a_1 h^2 \xi^3}{W_3} \quad (24)$$

$$W_2 = - \frac{(a_2 \xi^2 + a_3 y_w) \xi^2 F_\xi}{W_3} \quad (25)$$

$$W_3 = a_3 (\xi^4 + y_w^2) G_\eta \quad (26)$$

The dummy-point method cannot be used here, because the functions W_1 and W_2 become unbounded as $\xi \rightarrow 0$ (upstream infinity), and instability will result. The unboundedness of W_1 and W_2 is a direct result of the increasing nonorthogonality of the lines $X = \text{Constant}$ at the wall as $X = 0$ is approached. It is suggested that even in Cartesian coordinates, if the coefficients in the boundary condition were such that a_3 were smaller in magnitude than a_1 or a_2 , stability problems would occur. In the case of large porosity, for example, where $|a_2| > |a_3|$, the tangential derivative is dominant, and generating dummy points with a φ_y -extrapolation tends to become ill-conditioned.

Instead of the dummy-point method, φ was calculated at the wall by using one-sided derivatives for φ_X and φ_Y in equation (23) and solving for φ_{JW} , as shown in figure 7. By design, the coefficients of $\varphi_{i-1,JW}$ and $\varphi_{i,JW+1}$ are always less than unity for all known models of the wind-tunnel wall; this method is found to be stable in practice.

RESULTS AND DISCUSSION

The present method has been applied to a supercritical body of revolution which is designated D-1 in reference 7. Figure 8 shows the pressure distribution on this body at a Mach number of 0.991 for the free-air boundary condition (which was actually computed by setting the potential function to zero at a distance of about 50 body lengths above the body). Also shown in figure 8 are the results from the RAXBOD program for free air and the experimental results from the Langley 8-foot transonic pressure tunnel. It can be seen that the free-air results from the present program are not the same as the free-air results from the RAXBOD program in the region of the shock wave and the rear stagnation point. It is felt that these differences are caused by the fact that the truncation error in supersonic zones, formally of first order, is larger for the rotated difference scheme with the parabolic coordinates than the error of the rotated scheme with the RAXBOD coordinates. The RAXBOD coordinates are nearly cylindrical and well aligned with the flow in the large supersonic zone over the body, and they remain so to infinity. When the flow is aligned with the coordinates, the rotated scheme recovers the second-order-accurate,

central-difference approximation for ϕ_{YY} , although the retarded ϕ_{XX} -difference remains first order. For slender axisymmetric bodies near Mach 1, the supersonic zones extend to great lateral distances, where the coordinates are stretching out rapidly to infinity; it appears to be important to have a nearly second-order-accurate ϕ_{YY} -difference approximation in such cases. Unfortunately, the parabolic coordinates, and their modifications as used here, begin to incline upstream at distances very close to the body, and hence they are not well aligned with the flow in much of the supersonic zone where shock formation is occurring and where the mesh size is rapidly growing.

Further mesh refinement, at least in the Y-direction, would undoubtedly improve the present results, but it would be impractical to do so; the convergence rate is painfully slow on very fine meshes, as discussed in appendix C, and would require about 20 000 mesh points - a number which approaches some of the coarse-grid three-dimensional calculations. Figure 9(a) illustrates the convergence of the surface pressures with decreasing mesh size; results are shown for the three mesh refinements (25×23 , 49×45 , and 97×89 , the normal (ΔY) mesh being given second). The results in the nose region and in the subsonic portions of the flow are good, but the important region near the shock is still not accurate enough on the "fine" 97×89 mesh. RAXBOD, on the other hand, gives results very close to those shown here on its medium 49×49 mesh. Figure 9(b) shows the sonic lines obtained for each of the three meshes. The significant change in the extent and shape of the supersonic zone, as the mesh is refined, is evident. Also shown is the sonic line obtained by RAXBOD with 97×97 mesh. As in the case of the surface pressures, this RAXBOD result differs little from the RAXBOD results for the 49×49 mesh.

Despite the difficulty in obtaining accurate free-air results by use of the parabolic coordinates, it is still possible to compare the effects of different tunnel-wall boundary conditions. In fact, some of the problems with truncation error are likely to be alleviated somewhat for the tunnel case, since the grid is fairly compact in the supersonic zone between the body and the wall. It might be expected that the results for the body in the tunnel are more accurate, relatively, than the free-air calculations, if only for the reason that the normal grid does not stretch out rapidly.

Results for various wind-tunnel wall boundary conditions and a "fine" 97×89 mesh are shown in figures 10 to 12. In each of these figures, the wind-tunnel wall is located 1.78 body lengths away from the axis. This location for the wind-tunnel wall makes the cross-sectional area of the tunnel equivalent to that for the experimental data. The experiment, however, was performed in a tunnel with a square cross section which was slotted on the top and bottom walls and had solid side walls. Figure 10(a) shows the pressure-distribution results for the open-jet boundary condition ($\phi = 0$) applied at the wall location. It can be seen that the open-jet results show even less indication of a shock wave on the aft part of the body than in the free-air case. Figure 10(b) compares the open-jet and

free-air sonic lines. Figure 11(a) shows the pressure-distribution results for a solid-wall boundary condition ($\varphi_y = 0$). In this case the shock wave is located farther aft than the experimental shock. Figure 11(b) compares the solid-wall and free-air sonic lines. Figure 12(a) shows the pressure-distribution results for the ideal slotted-wall boundary condition ($\varphi + \ell\varphi_y = 0$) where the slot parameter ℓ has been computed by the method of Chen and Mears (ref. 8) by using a 3-percent open ratio, since the experiment was run in a tunnel with approximately 6-percent open ratio on the top and bottom walls, but with solid side walls. It can be seen that the shock location agrees well with the experiment. When the method of Davis and Moore (ref. 9) is used to compute the slot parameter ℓ for use in the ideal slotted wall boundary condition, ℓ is about 10 times smaller than the Chen and Mears value. The agreement is not as good; the theoretical results seem to correspond to a more "open" tunnel boundary condition.

Figure 13(a) shows the free-air pressure distribution results for a Mach number of 1.011, and figure 13(b) compares the sonic lines of the present method and RAXBOD. At this Mach number the present method and the RAXBOD program disagree even more than at the lower Mach number of figures 9 to 12 ($M_\infty = 0.991$). This result is in line with the contention that the more supersonic points there are in the disturbed part of the flow, the larger will be the truncation errors in the rotated difference scheme with the parabolic coordinates. The results are worst just in the neighborhood of the aft shock; they are so poor that it would be meaningless to attempt to show the effects of the various wall boundary conditions. For the sake of checking the stability of the numerical procedure for supersonic free streams, however, the case for the slotted wall with the Chen and Mears slot parameter was calculated. The calculation was stable and essentially duplicated the free-air results, for whatever they are worth.

The relatively poor accuracy of the present method (compared with RAXBOD for the same number of mesh points) created another problem, namely, slow convergence, as discussed in appendix C. It appears that to converge the solution of the difference equation within the accuracy of the truncation error, the present column-iterative method will be very expensive. For example, operating in a mesh-halving mode as described in reference 1, it has been found that converged solutions on each mesh were about 10 times as expensive as the previous coarser mesh. It is likely that a convergence-acceleration method, such as developed by Hafez and Cheng (ref. 10), or possibly a "direct-solver" approach, such as presented in this conference by Martin (ref. 11), may be far superior to the present column-iteration method, at least for the meshes with 5000 to 10 000 points.

Although the present program was written for axisymmetric flow, the axisymmetric term can be omitted to compute symmetric (nonlifting) two-dimensional (2-D) flow. This was done as a partial debug check to compare with Antony Jameson's unpublished, two-dimensional airfoil program which uses parabolic coordinates. The meshes of both

programs were duplicated very closely, and the results compared perfectly for both sub-critical and supercritical free-air cases; even the convergence histories were identical, the location and magnitude of the maximum residual agreeing at each iteration.

The results for two-dimensional supercritical flow, with characteristically smaller supersonic zones, are considered to be good. The present method seems to work well for the various wind-tunnel wall boundary conditions, as can be seen in figure 14, which shows an NACA 0012 airfoil at zero incidence at $M_\infty = 0.8$. The qualitative behavior of the solution is correct; that is, the shock position for the open-jet and solid-wall tunnel boundary conditions is, respectively, upstream and downstream from that of the free-air calculation. The slotted-wall simulations are also shown with the slot parameter ℓ given for a 6-percent open ratio by both the theories of references 8 and 9; the free-air results fall between the two slotted wall results.

The calculations were compared with several experimental results for the NACA 0012 and $M_\infty = 0.8$, with Reynolds numbers of about 3×10^6 to 4×10^6 . In all cases, the experimental shock location was closest to that for the open-jet calculation. Thus there is a disagreement between the experimental results and the computed inviscid results for the ideal slotted-wall boundary condition. To determine the effect of viscosity on the shock location, a transonic, viscous, analysis program (ref. 12) was used to calculate this case with a Reynolds number of 3.5×10^6 . It was found that the difference in shock location between the inviscid free-air case and the viscous case was about $2\frac{1}{2}$ percent chord, or about the same as the difference between the open-jet boundary condition and the slotted-wall boundary condition by using a 6-percent open ratio and the method of reference 9 to compute the slot parameter ℓ . It is felt that if the effects of viscosity were included in the present method, all the shock locations would be shifted forward and the calculation using the slotted-wall boundary condition would agree closely with the experiment. If the present method is extended to include lift and boundary-layer effects as in references 12 and 13, it should provide a powerful analysis tool for simulating a general two-dimensional airfoil in a wind tunnel. It appears that Kacprzyński (ref. 14) has developed a method for the conformal-mapping, "circle-plane" type of transonic airfoil analysis program whereby the wind-tunnel wall is included in the final transformation, as in the present paper. He gave no details of the numerical technique or the behavior of the coordinates in the physical plane, and he did not mention any numerical stability problems. He does, however, mention the added difficulty of including a boundary-layer interaction, because it is very costly to update the mapping function to account for the change in displacement thickness for each inviscid/viscous iteration cycle. Since the parabolic coordinates have a simple, closed-form relation with the Cartesian coordinates, it would seem that the present approach should be very efficient for the viscous/inviscid interaction problem.

CONCLUDING REMARKS

The use of parabolic coordinates with Jameson's rotated difference scheme for axisymmetric transonic flow does not produce results as accurate as those obtained by RAXBOD, which uses coordinates that are nearly cylindrical and aligned with the flow in most of the embedded supersonic zone above the body. The present method for mapping the body and the wind-tunnel wall to coordinate surfaces, coupled with a "dummy-point" method for enforcing flow tangency at the body and a one-sided difference method for the wind-tunnel wall boundary condition, is a good approach; it can be adapted to the RAXBOD type of coordinates.

The relatively poor accuracy of the present method creates a problem with slow convergence. It is likely that a convergence-acceleration method or possibly a direct-solver approach may be far superior to the present column-iteration method.

To end up on a pleasant note, the present method seems to work very well for two-dimensional symmetric flows, and it can be easily extended to lifting flows with viscous/inviscid boundary-layer interaction, since the relation between Cartesian and parabolic coordinates is so simple.

APPENDIX A

TRANSFORMATION OF THE POTENTIAL EQUATION

The potential equation in parabolic coordinates is transformed to the computational plane as follows, starting from equations (18):

$$\varphi_{\xi} = F_{\xi} \varphi_X + G_{\xi} \varphi_Y \quad (A1)$$

$$\varphi_{\eta} = G_{\eta} \varphi_Y \quad (A2)$$

$$\varphi_{\xi\xi} = F_{\xi}^2 \varphi_{XX} + 2F_{\xi} G_{\xi} \varphi_{XY} + G_{\xi}^2 \varphi_{YY} + F_{\xi\xi} \varphi_X + G_{\xi\xi} \varphi_Y \quad (A3)$$

$$\varphi_{\xi\eta} = F_{\xi} G_{\eta} \varphi_{XY} + G_{\xi} G_{\eta} \varphi_{YY} + G_{\xi\eta} \varphi_Y \quad (A4)$$

$$\varphi_{\eta\eta} = G_{\eta}^2 \varphi_{YY} + G_{\eta\eta} \varphi_Y \quad (A5)$$

Substitution of equations (A3) to (A5) into equation (11) gives equation (19), with

$$A = (a^2 - U^2) F_{\xi}^2 \quad (A6)$$

$$B = 2F_{\xi} \left[(a^2 - U^2) G_{\xi} - UVG_{\eta} \right] \quad (A7)$$

$$C = (a^2 - U^2) G_{\xi}^2 - 2UVG_{\xi} G_{\eta} + (a^2 - V^2) G_{\eta}^2 \quad (A8)$$

$$D = H - (a^2 - U^2) F_{\xi\xi} \varphi_X - \left[(a^2 - U^2) G_{\xi\xi} - 2UVG_{\xi\eta} + (a^2 - V^2) G_{\eta\eta} \right] \varphi_Y \quad (A9)$$

where H is given by equation (15).

The functions which are used for $F(\xi)$ consist of two cubics joined together from the nose to a location specified as an input parameter (usually the region of the body tail), followed by an algebraic stretching to downstream infinity like that in the "normal" direction; for example,

$$\xi = \xi_2 + \frac{cX}{\sqrt{1-X^2}} \quad (A10)$$

where ξ_2 is the value of the parabolic coordinate at the specified junction between the cubics and the square-root transformation, and c is a parameter needed to insure continuity of F_{ξ} . Note that $\xi \rightarrow \infty$ as $X \rightarrow 1$. It is straightforward to differentiate the function F to obtain F_{ξ} and $F_{\xi\xi}$. For example, by starting from equation (A10),

$$F_{\xi} = \frac{(1 - X^2)^{3/2}}{c} \quad (A11)$$

and

$$F_{\xi\xi} = -3XF_{\xi} \frac{(1 - X^2)^{1/2}}{c} \quad (A12)$$

in the region

$$X_2 \leq X \leq 1 \quad (A13)$$

where X_2 is the value of the computational coordinate at $\xi = \xi_2$. The expressions for F_{ξ} and $F_{\xi\xi}$ in the region $0 \leq X \leq X_2$ are similarly obtained by differentiating the cubic polynomials, and will not be written here.

The derivatives of $Y = G(\xi, \eta)$ are more complicated and are given as follows, starting from equation (10), for $\alpha = \frac{1}{2}$:

Let

$$T = \sqrt{1 - w^2 Y^2} \quad (A14)$$

Then

$$G_{\eta} = \frac{T^3}{zw} \quad (A15)$$

$$G_{\eta\eta} = -\frac{3TY}{z^2} \quad (A16)$$

Also, let

$$T_1 = \frac{w'}{w} \quad (A17)$$

$$T_2 = \frac{z'}{z} \quad (A18)$$

Then

$$G_{\xi} = -S'G_{\eta} - Y(T_1 + T_2 T^2) \quad (A19)$$

$$G_{\xi\eta} = -S'G_{\eta\eta} - [T_1 + T_2(1 - 3w^2 Y^2)]G_{\eta} \quad (A20)$$

APPENDIX A - Concluded

$$G_{\xi\xi} = -S''G_{\eta} - S'G_{\xi\eta} - \left[T_1 + T_2(1 - 3w^2Y^2) \right] G_{\xi} + \left(T_1^2 - \frac{w''}{w} \right) Y + T^2Y \left(T_2^2 - \frac{z''}{z} \right) + 2T_2ww'Y^3$$

(A21)

Recall that primes denote differentiation with respect to ξ .

APPENDIX B

CANONICAL FORM FOR EQUATION (19)

The first step in deriving the rotated difference scheme is to rearrange the principal part of equation (19) to simulate derivatives φ_{SS} and φ_{NN} , along and normal to the local flow direction. The appropriate grouping of terms is thus

$$q^2 \varphi_{SS} = (UF_\xi)^2 \varphi_{XX} + 2UF_\xi \tilde{V} \varphi_{XY} + \tilde{V}^2 \varphi_{YY} \quad (B1)$$

$$q^2 \varphi_{NN} = (VF_\xi)^2 \varphi_{XX} - 2\tilde{U}VF_\xi \varphi_{XY} + \tilde{U}^2 \varphi_{YY} \quad (B2)$$

where

$$\tilde{U} = UG_\eta - VG_\xi \quad (B3)$$

$$\tilde{V} = UG_\xi + VG_\eta \quad (B4)$$

$$q = \sqrt{U^2 + V^2} \quad (B5)$$

Then the canonical form for equation (19) can be written as

$$(a^2 - q^2) \varphi_{SS} + a^2 \varphi_{NN} = D \quad (B6)$$

where D is given by equation (A9). It is important to note that substitution of equations (B1) to (B5) into equation (B6) gives equation (19).

APPENDIX C

DIFFERENCE EQUATIONS AND ITERATION ALGORITHM

The potential equation (19) or (B6) is solved by a type-dependent, column-iteration, finite-difference scheme as in references 1 to 3. At each mesh point, the velocity components are calculated by using the equations

$$hU = F_{\xi} \phi_X + G_{\xi} \phi_Y + \xi \quad (C1)$$

$$hV = G_{\eta} \phi_Y - \eta \quad (C2)$$

where central differences are used for ϕ_X and ϕ_Y , with values of ϕ_{ij} from the previous iteration cycle. The speed of sound is then calculated from equation (16), and the appropriate difference equations are used, depending on whether the flow is locally subsonic or supersonic, as follows:

Subsonic Points

The difference equations at subsonic points are

$$\Delta X \phi_X = \phi_{i+1,j} - \phi_{i-1,j}^+ \quad (C3)$$

$$\Delta Y \phi_Y = \phi_{i,j-1} - \phi_{i,j+1} \quad (C4)$$

$$(\Delta X)^2 \phi_{XX} = \phi_{i+1,j} - \frac{2}{\omega} \left[\phi_{ij}^+ + (\omega - 1) \phi_{ij} \right] + \phi_{i-1,j}^+ \quad (C5)$$

$$\Delta X \Delta Y \phi_{XY} = \phi_{i+1,j-1} - \phi_{i-1,j-1}^+ + \phi_{i-1,j+1}^+ - \phi_{i+1,j+1} \quad (C6)$$

$$(\Delta Y)^2 \phi_{YY} = \phi_{i,j-1}^+ - 2\phi_{ij}^+ + \phi_{i,j+1}^+ \quad (C7)$$

In this appendix a "+" superscript denotes values of ϕ from the current iteration cycle whereas no superscript denotes values of ϕ from the previous cycle. The index i increases with increasing X , and the index j decreases with increasing Y . An over-relaxation factor ω has been introduced at the central point in equation (C5), but not in equation (C7). This procedure is another idea of Antony Jameson and is designed to promote a continuous iteration matrix across the sonic line.¹ If the three ϕ values in

¹This procedure was designed for the older, nonrotated difference scheme, but it works as well in the rotated scheme whenever $a^2 - U^2$ is small along the sonic line.

equation (C7) are also overrelaxed, the coefficients of the iteration matrix will indeed have a jump across the sonic line in most situations. It should be pointed out that a Garabedian-style estimate (ref. 15) has been made of the convergence rate of a similar procedure applied to a column-relaxation solution for Laplace's equation. The results indicate that in the limit of small mesh size, the convergence rate is unaffected by whether the three values of ϕ on the column are overrelaxed.

It should also be pointed out that the "new" value from the previous columns $\phi_{i-1,j}^+$ in the difference expression for ϕ_X is used. A linear stability analysis of the procedure applied to Laplace's equation on a variable mesh shows that the amplification factor can be greater than unity if an "old" value is used there, and the instability cannot be controlled by decreasing ω . This result is interesting in that stability is usually dominated by the highest order derivatives as the mesh size tends to zero; in the present case, the overrelaxation process causes the lowest order contributions of ϕ_{XX} and ϕ_X to be of the same order. Use of the new value $\phi_{i-1,j}^+$ in equation (C3) produces conditional stability; that is, the amplification factor will be less than unity for a sufficiently small positive ω .

Supersonic Points

At supersonic points, the difference equations and the mix of old and new values of ϕ are arranged according to the rules set down in reference 2. Both central and upwind differences are used, depending on whether they appear in ϕ_{NN} or ϕ_{SS} , as given in appendix B, as follows:

Derivatives in ϕ_{NN} . The derivatives appearing in the expression for ϕ_{NN} (eq. (B2)) are approximated by central differences. For ϕ_{XY} and ϕ_{YY} , equations (C6) and (C7) are used, but for ϕ_{XX}

$$(\Delta X)^2 \phi_{XX} = \phi_{i+1,j} - \phi_{ij}^+ - \phi_{ij} + \phi_{i-1,j}^+ \quad (C8)$$

is used.

Derivatives in ϕ_{SS} . The derivatives in the expression for ϕ_{SS} (eq. (B1)) are approximated by first-order-accurate upwind differences. The differencing is carried out in the quadrant containing the tail of the velocity vector as explained in references 1 and 2. The difference expressions are given as follows for the situation where the velocity component normal to a line $Y = \text{Constant}$, \tilde{v} , given in equation (B4), is negative:

$$(\Delta X)^2 \phi_{XX} = 2\phi_{ij}^+ - \phi_{ij} - 2\phi_{i-1,j}^+ + \phi_{i-2,j} \quad (C9)$$

APPENDIX C - Continued

$$\Delta X \Delta Y \varphi_{XY} = \varphi_{ij} - 2\varphi_{ij}^+ + \varphi_{i,j-1}^+ - \varphi_{i-1,j-1} + \varphi_{i-1,j}^+ \quad (C10)$$

$$(\Delta Y)^2 \varphi_{YY} = 2\varphi_{ij}^+ - \varphi_{ij} - 2\varphi_{i,j-1}^+ + \varphi_{i,j-2} \quad (C11)$$

When $\tilde{V} > 0$, the quadrant is switched, and appropriate changes are made in φ_{XY} and φ_{YY} . The quantities φ_X and φ_Y are evaluated as stated for equations (C1) and (C2).

Added damping.- At supersonic points, an added damping term may be needed as described in detail by Jameson in reference 2. For the coordinates, this term is proportional to

$$\begin{aligned} q\varphi_{ST} &= U\varphi_{\xi T} + V\varphi_{\eta T} \\ &= UF_{\xi}\varphi_{XT} + \tilde{V}\varphi_{YT} \end{aligned} \quad (C12)$$

where \tilde{V} and q are given by equations (B4) and (B5), and T represents the iteration number as a third space-like variable. The derivatives in equation (C12) are given in finite-difference form as

$$(\Delta X)^2 \varphi_{XT} = \left(\frac{\Delta X}{\Delta T} \right) (\varphi_{ij}^+ - \varphi_{ij} - \varphi_{i-1,j}^+ + \varphi_{i-1,j}) \quad (C13)$$

$$\Delta X \Delta Y \varphi_{YT} = \left(\frac{\Delta X}{\Delta T} \right) (\varphi_{i,j-1}^+ - \varphi_{i,j-1} - \varphi_{ij}^+ + \varphi_{ij}) \quad (C14)$$

Equation (C14) is given for the case $\tilde{V} < 0$. Note that the damping term φ_{ST} vanishes as the solution converges; that is,

$$\varphi_{ST} \rightarrow 0 \quad (\varphi_{ij}^+ - \varphi_{ij}) \quad (C15)$$

The unknown ratio $\Delta X/\Delta T$ is absorbed in a constant in the actual computer program.

Solution of the Difference Equations

The difference equations given in this appendix are written as a tridiagonal system on each column $i = \text{Constant}$; the unknowns are the corrections,

$$\Delta\varphi_{ij} = \varphi_{ij} - \varphi_{ij}^+ \quad (C16)$$

APPENDIX C - Continued

and the system on each column is in the form

$$a_{ij}\Delta\phi_{i,j-1} + b_{ij}\Delta\phi_{ij} + c_{ij}\Delta\phi_{i,j+1} = R_{ij} \quad (C17)$$

The a_{ij} , b_{ij} , and c_{ij} are the tridiagonal coefficients, and it is easy to construct them by collecting terms in the difference equations given here. By design, diagonal dominance exists, that is,

$$|b_{ij}| > |a_{ij}| + |c_{ij}| \quad (C18)$$

to guarantee stability of the solution of the equations on the column. The expression for R_{ij} is the "residual" (although it contains a mix of old and new values of ϕ_{ij}); its value at a local mesh point is close to the local error in satisfying the difference equations. The exact solution of the difference equations corresponds to

$$R_{ij} = 0 \quad (C19)$$

for all i and j .

The equations are solved by advancing from one column to the next, starting at the stagnation line and proceeding to the last column ahead of downstream infinity; thus one iteration cycle is completed. Iterations are continued until convergence is achieved, as described next.

Convergence

In practice, of course, only an approximate solution to the equations can be obtained, so the iteration is stopped when

$$\max_{ij} |R_{ij}| < \epsilon \quad (C20)$$

where ϵ is some preassigned convergence criterion. Now the difference equations have a formal truncation error at a local mesh point of order $(\Delta X)^2$ at subsonic points, and of order ΔX at supersonic points. Theoretically, ϵ should be small enough to insure that for a given mesh, the difference equations will be solved within the accuracy of the truncation error. This is a very stringent criterion; the implication is that, in the present case, ϵ should be something like

$$\epsilon = \text{Constant} \times (\Delta X)^{1+\sigma} \quad (C21)$$

APPENDIX C - Concluded

where σ is between 0 and 1, depending on how many supersonic points there are in the flow field. Many researchers have written their programs so that the difference equations have been multiplied through by $(\Delta X)^2$; then $\max_{ij} |\Delta \phi_{ij}|$ and $\max_{ij} |R_{ij}|$ are the same order of magnitude. In that case, the exponent in equation (C21) should be $3 + \sigma$; that is,

$$\max_{ij} |\Delta \phi_{ij}| < \text{Constant} \times (\Delta X)^{3+\sigma} \quad (\text{C22})$$

Some very crude estimates of the number of cycles to reach a given convergence criterion can be made, and they are very discouraging. For example, if equation (C22) must be satisfied, and if the asymptotic convergence rate estimated for successive overrelaxation for Laplace's equation (ref. 15) is assumed

$$\max_{ij} |\Delta \phi_{ij}| \approx 0(e^{-\lambda \Delta X n}) \quad (\text{C23})$$

where n is the number of iterations and λ is a constant, then the number of cycles to converge ($\bar{n}_{\Delta X}$) is proportional to

$$\frac{(3 + \sigma) \log_e (\Delta X)}{\Delta X} \quad (\text{C24})$$

Part of the present procedure is operation in a mesh-halving mode, as described in reference 1. By using the quantity (eq. (C24)), the ratio of the number of cycles to convergence between mesh halvings can be estimated as

$$\frac{\bar{n}_{\Delta X/2}}{\bar{n}_{\Delta X}} \approx 2 \frac{\log_e (\Delta X/2)}{\log_e (\Delta X)} \quad (\text{C25})$$

A typical sequence of three meshes would have $\Delta X = 0.04, 0.02,$ and $0.01,$ respectively; in this case, the ratio given by equation (C25) is about 2.4 between adjacent meshes. Since each mesh refinement has 4 times as many points as the previous mesh, calculation to convergence on the refined mesh may be 10 times as expensive as on the previous mesh. Of course, the whole idea of mesh halving is to try to reduce the estimate given by the expression (eq. (C24)) by providing better initial conditions for the new (finer) mesh. If the truncation error is large, however, it appears that the initial conditions provided by the coarser mesh are not close enough to the finer-mesh solution to be much help. In the present program, the expense factor of 10 for each mesh refinement is about right.

REFERENCES

1. South, Jerry C., Jr.; and Jameson, Antony: Relaxation Solutions for Inviscid Axisymmetric Transonic Flow Over Blunt or Pointed Bodies. AIAA Computational Fluid Dynamics Conference (Palm Springs, California), July 1973, pp. 8-17.
2. Jameson, Antony: Iterative Solution of Transonic Flows Over Airfoils and Wings; Including Flows at Mach 1. Commun. Pure & Appl. Math., vol. 27, no. 3, May 1974, pp. 283-309.
3. Jameson, Antony: Numerical Calculation of the Three Dimensional Transonic Flow Over a Yawed Wing. AIAA Computational Fluid Dynamics Conference (Palm Springs, California), July 1973, pp. 18-26.
4. Emmons, Howard W.: Flow of a Compressible Fluid Past a Symmetrical Airfoil in a Wind Tunnel and in Free Air. NACA TN 1746, 1948.
5. Steger, J. L.; and Lomax, H.: Transonic Flow About Two-Dimensional Airfoils by Relaxation Procedures. AIAA J., vol. 10, no. 1, Jan. 1972, pp. 49-54.
6. Murman, Earll M.: Computation of Wall Effects in Ventilated Transonic Wind Tunnels. AIAA Paper No. 72-1007, Sept. 1972.
7. Couch, Lana M.; and Brooks, Cuyler W., Jr.: Effect of Blockage Ratio on Drag and Pressure Distributions for Bodies of Revolution at Transonic Speeds. NASA TN D-7331, 1973.
8. Chen, C. F.; and Mears, J. W.: Experimental and Theoretical Study of Mean Boundary Conditions at Perforated and Longitudinally Slotted Wind Tunnel Walls. AEDC-TR-57-20, ASTIA Doc. No. AD-144320, U.S. Air Force, Dec. 1957.
9. Davis, Don D., Jr.; and Moore, Dewey: Analytical Study of Blockage- and Lift-Interference Corrections for Slotted Tunnels Obtained by the Substitution of an Equivalent Homogeneous Boundary for the Discrete Slots. NACA RM L53E07b, 1953.
10. Hafez, Mohamed M.; and Cheng, H. K.: Convergence Acceleration and Shock Fitting for Transonic Aerodynamics Computations. AIAA Paper No. 75-51, Jan. 1975.
11. Martin, E. Dale: Progress in Application of Direct Elliptic Solvers to Transonic Flow Computations. Aerodynamic Analyses Requiring Advanced Computers, Part II, NASA SP-347, pp. 839-870.
12. Bauer, Frances; Garabedian, Paul; Korn, David; and Jameson, Antony: Supercritical Wing Sections II. Lecture Notes in Economics and Mathematical Systems, M. Beckmann and H. P. Künzi, eds., Springer-Verlag, 1975.

13. Bavitz, Paul C.: An Analysis Method for Two-Dimensional Transonic Viscous Flow. NASA TN D-7718, 1975.
14. Kacprzyński, J. J.: Transonic Flow Field Past 2-D Airfoils Between Porous Wind Tunnel Walls With Nonlinear Characteristics. AIAA Paper No. 75-81, Jan. 1975.
15. Garabedian, P. R.: Estimation of the Relaxation Factor for Small Mesh Size. Math. Tables and Other Aids to Computation, vol. X, no. 56, Oct. 1956, pp. 183-185.

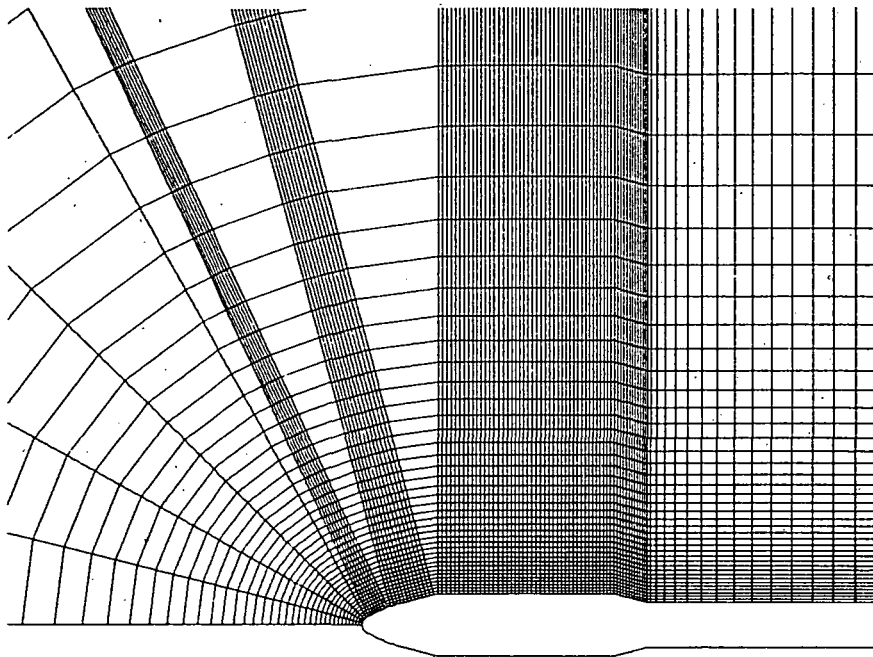


Figure 1.- Body normal coordinates for Titan-Centaur launch shroud.

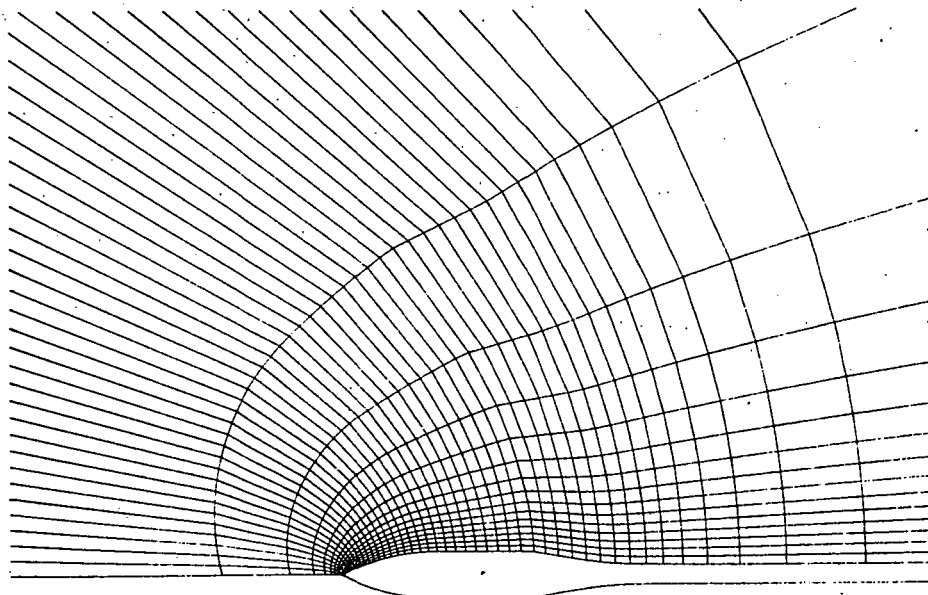


Figure 2.- Sheared parabolic coordinates for ogive/cylinder/boattail with simulated wake.

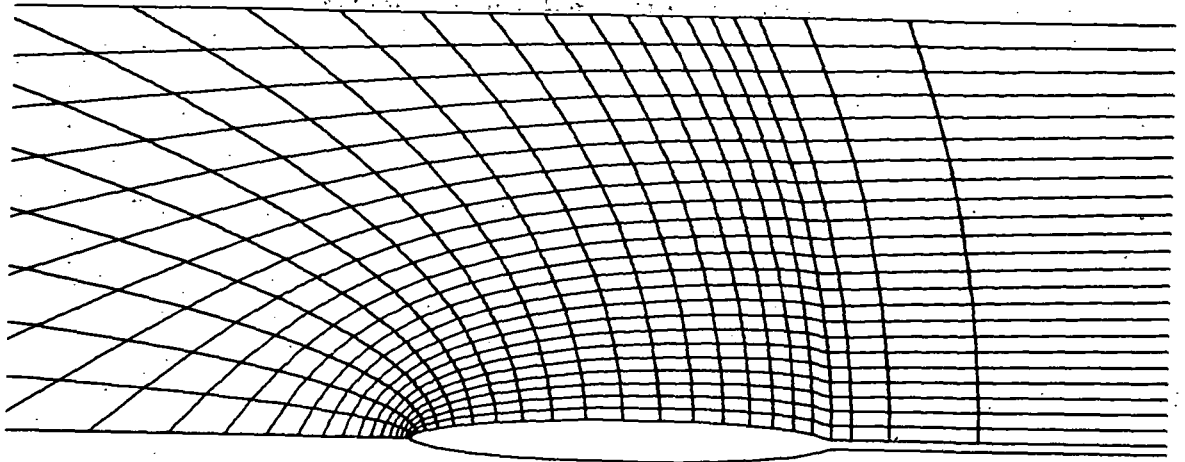


Figure 3.- Computational grid. $Y = \frac{\tan^{-1}(\eta - \eta_B)}{\tan^{-1}(\eta_W - \eta_B)}$.

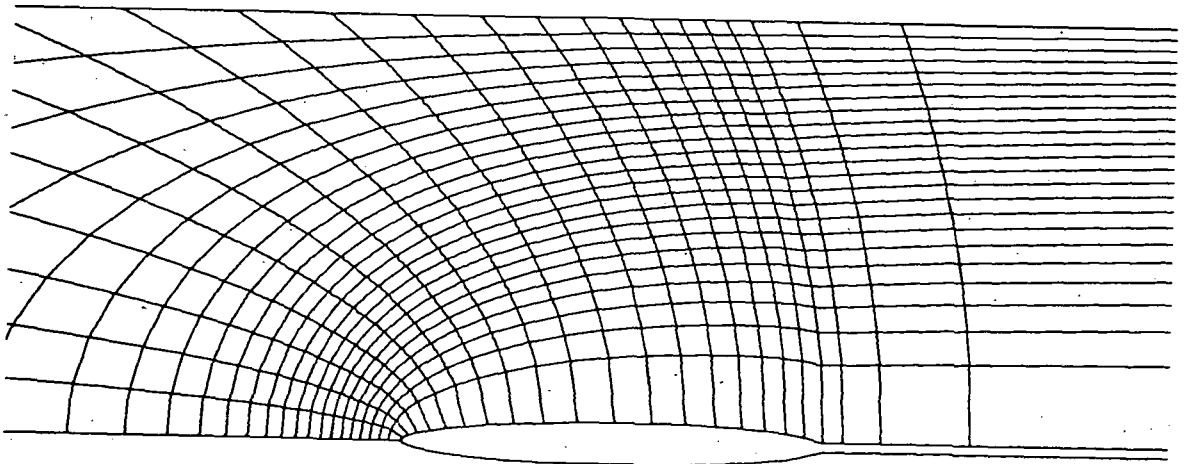


Figure 4.- Computational grid. $Y = \frac{\tan^{-1}(\eta - \eta_B)^2}{\tan^{-1}(\eta_W - \eta_B)^2}$.

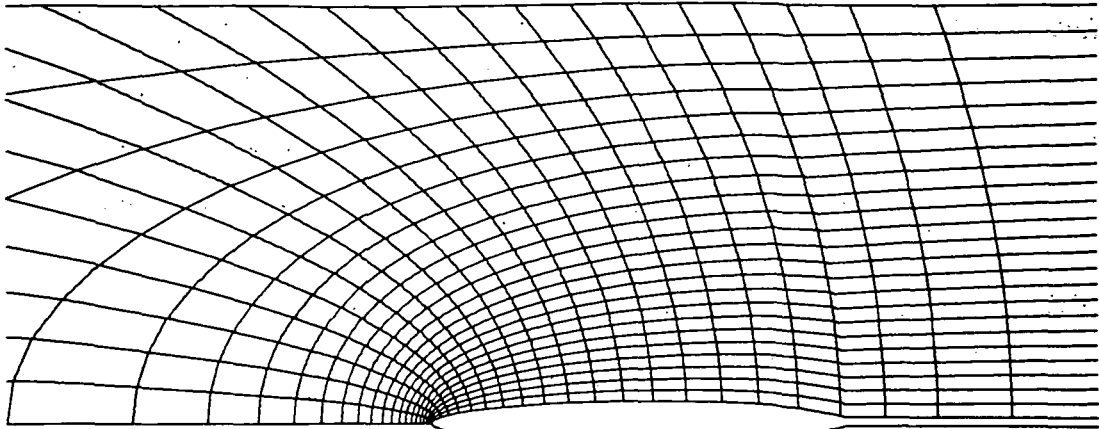


Figure 5.- Computational grid. $Y = \frac{\eta - \eta_B}{\eta_W - \eta_B} \left[\frac{1 + (\eta_W - \eta_B)^2}{1 + (\eta - \eta_B)^2} \right]^{1/2}$

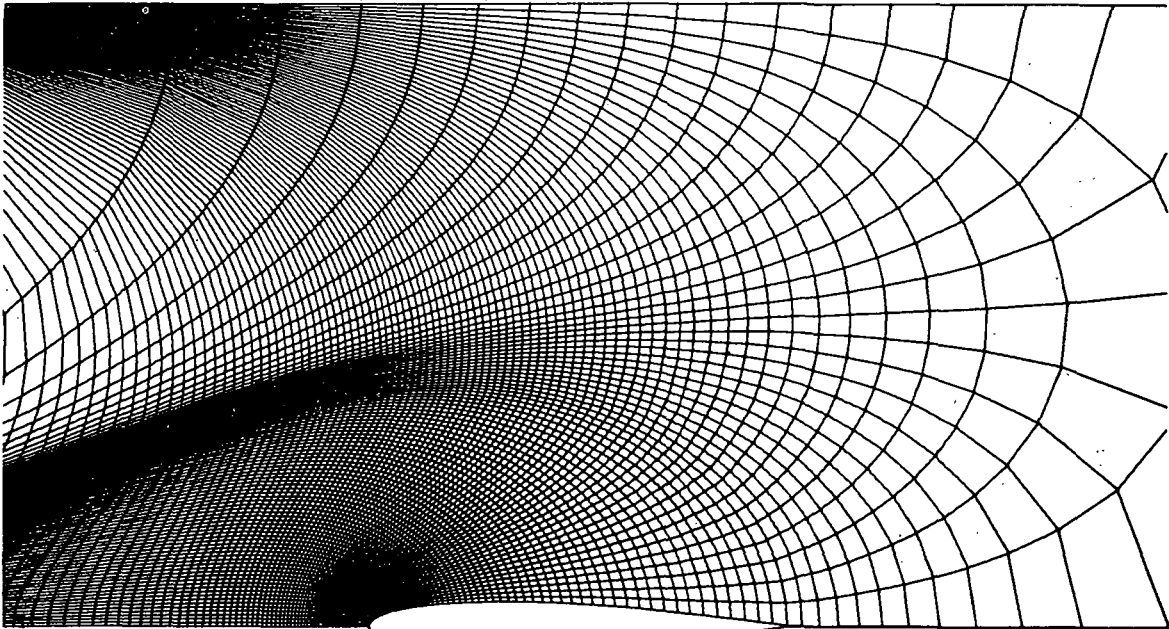
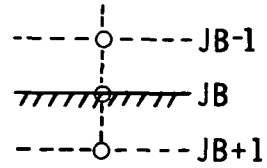


Figure 6.- Computational grid. $\zeta = \sqrt{1 - e^{-Z}}$

BODY SURFACE: $\varphi_n = 0 \Rightarrow \varphi_Y = B_1(X) + B_2(X) \cdot \varphi_X$

$$\varphi_{JB+1} = \varphi_{JB-1} - 2 \cdot \Delta Y \cdot (\varphi_Y)_{JB}$$



WIND-TUNNEL WALL:

$$a_1 \varphi + a_2 \varphi_x + a_3 \varphi_y = 0$$

$$\Rightarrow \varphi_Y = W_1(X) \varphi + W_2(X) \cdot \varphi_X$$

$$\Rightarrow \varphi_{i,JW} = \frac{W_2 \Delta Y \varphi_{i-1,JW} - \Delta X \varphi_{i,JW+1}}{W_2 \Delta Y - \Delta X + W_1 \Delta X \Delta Y}$$

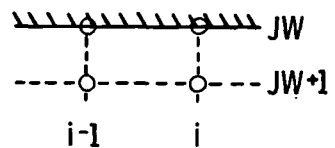


Figure 7.- Boundary conditions.

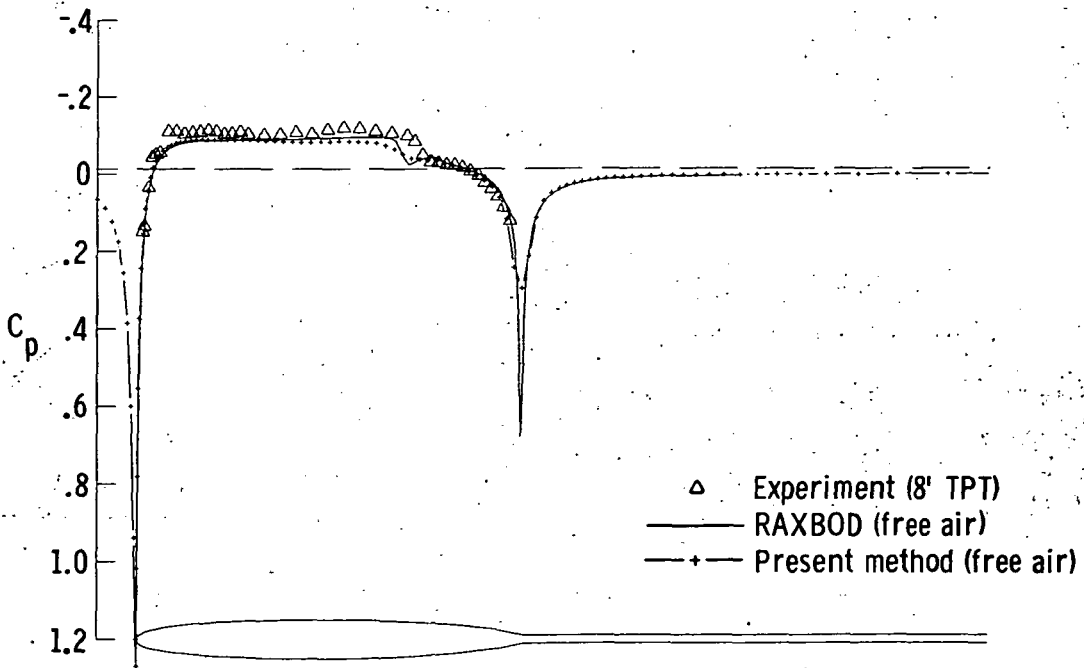
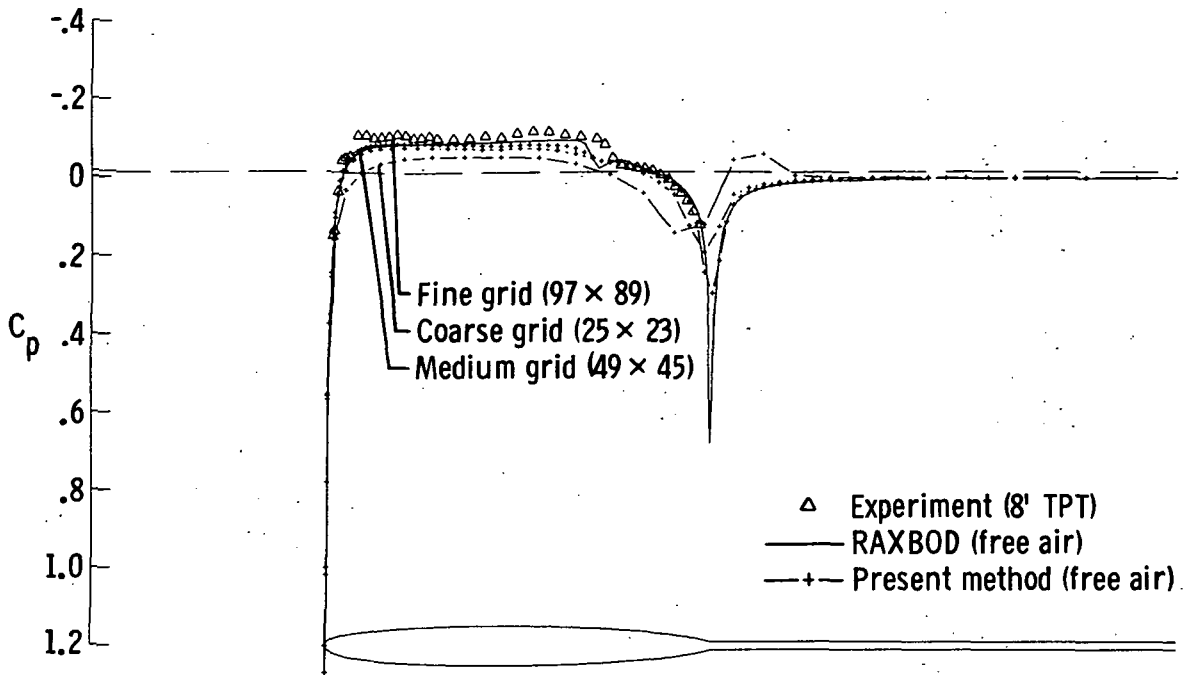
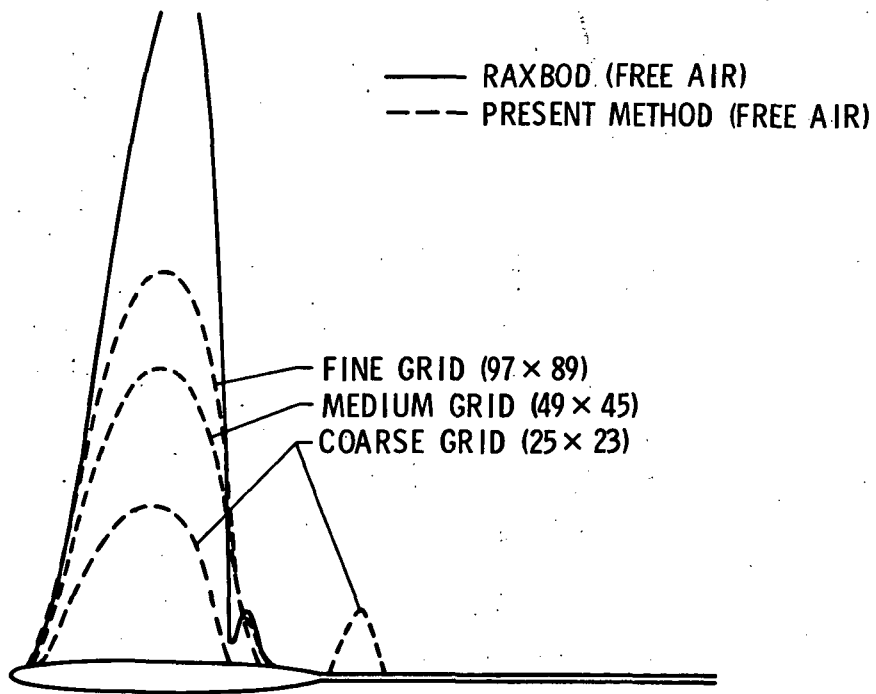


Figure 8.- Pressure distribution for SCBR at $M_\infty = 0.991$.

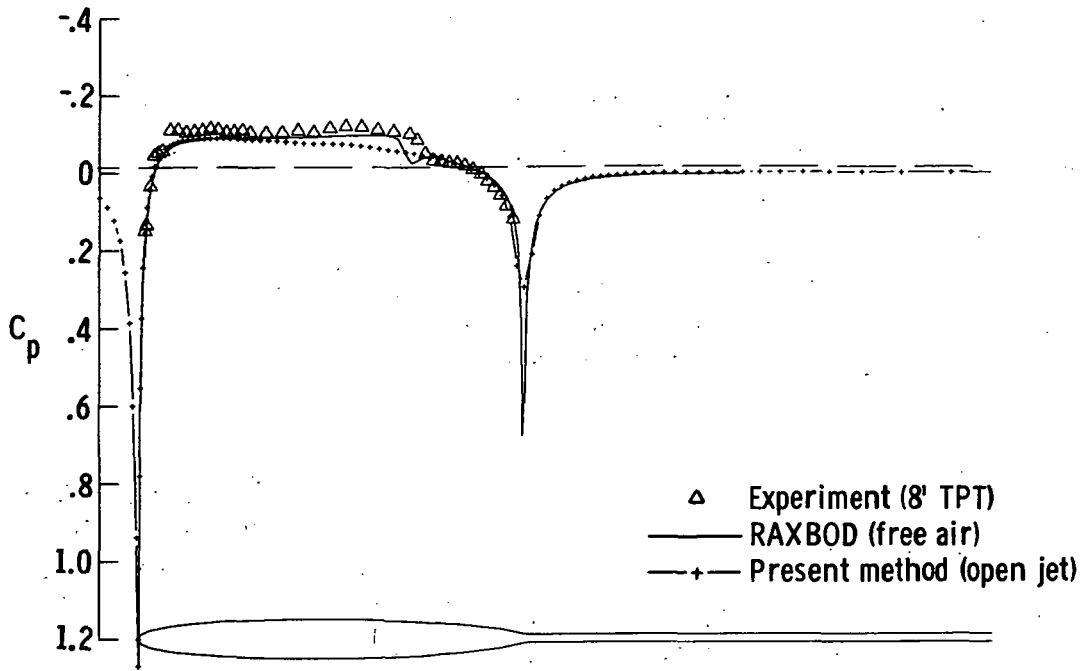


(a) Pressure distribution.

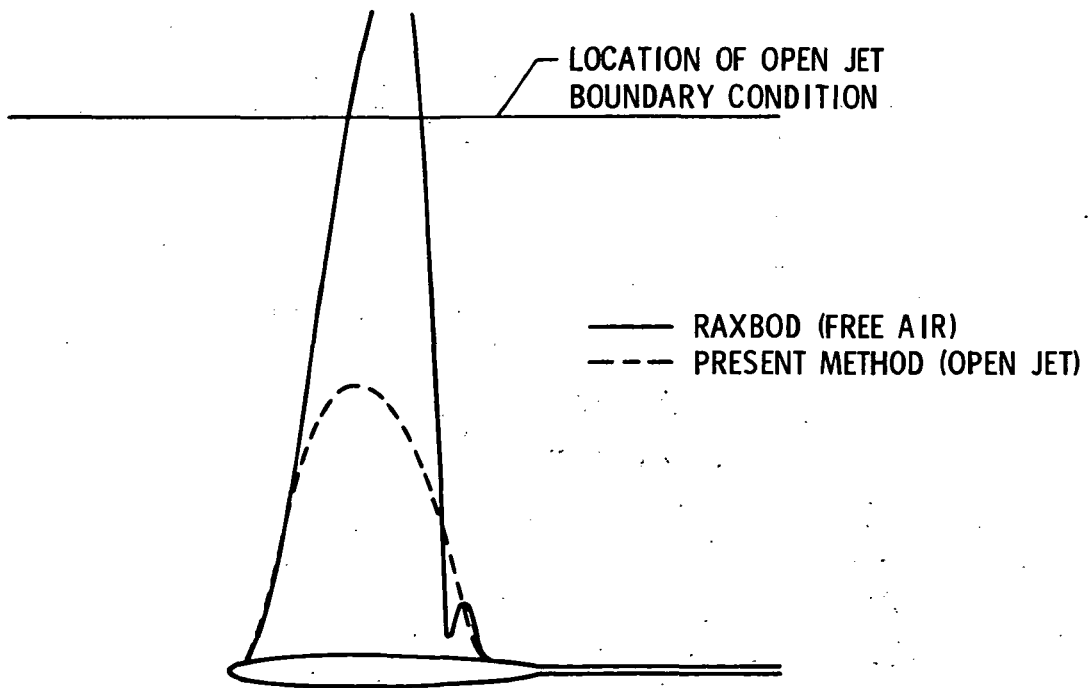


(b) Sonic line shape.

Figure 9.- SCBR at $M_{\infty} = 0.991$ with different grids and free air.

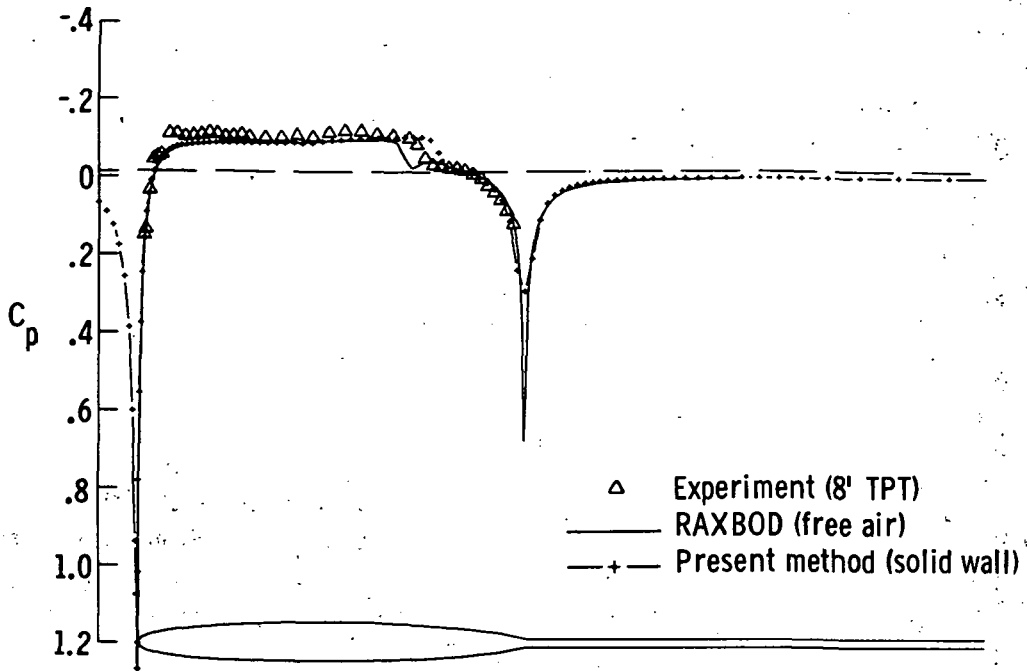


(a) Pressure distribution.

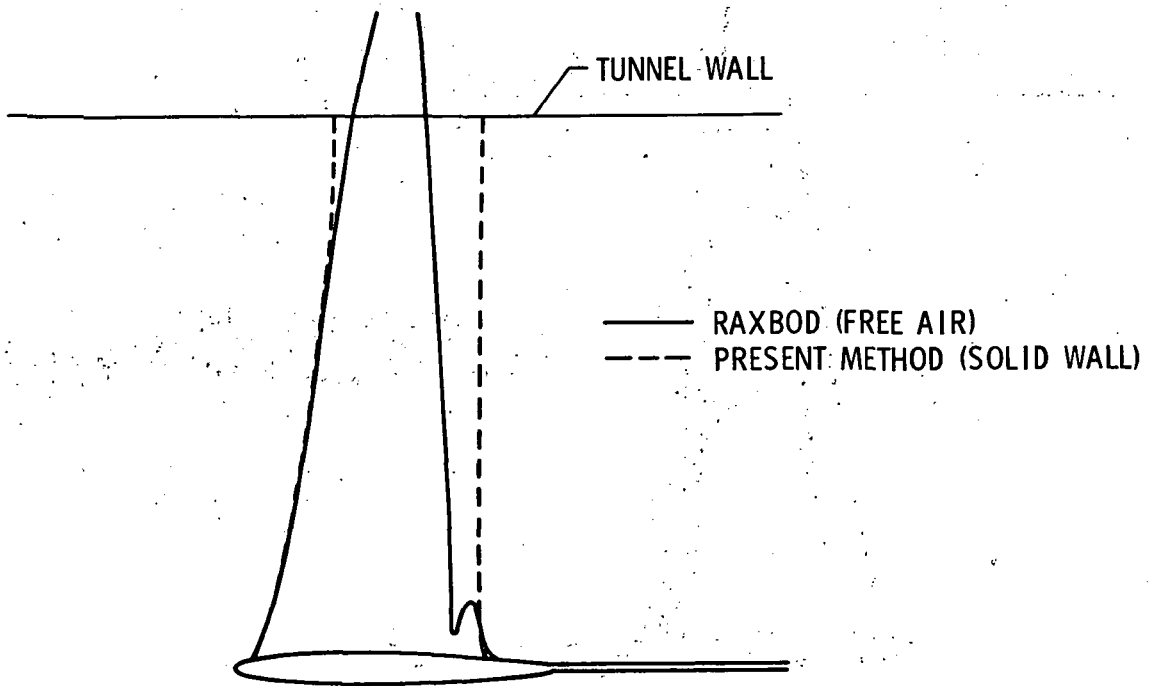


(b) Sonic line shape.

Figure 10.- SCBR at $M_\infty = 0.991$ using open-jet boundary condition for present method.

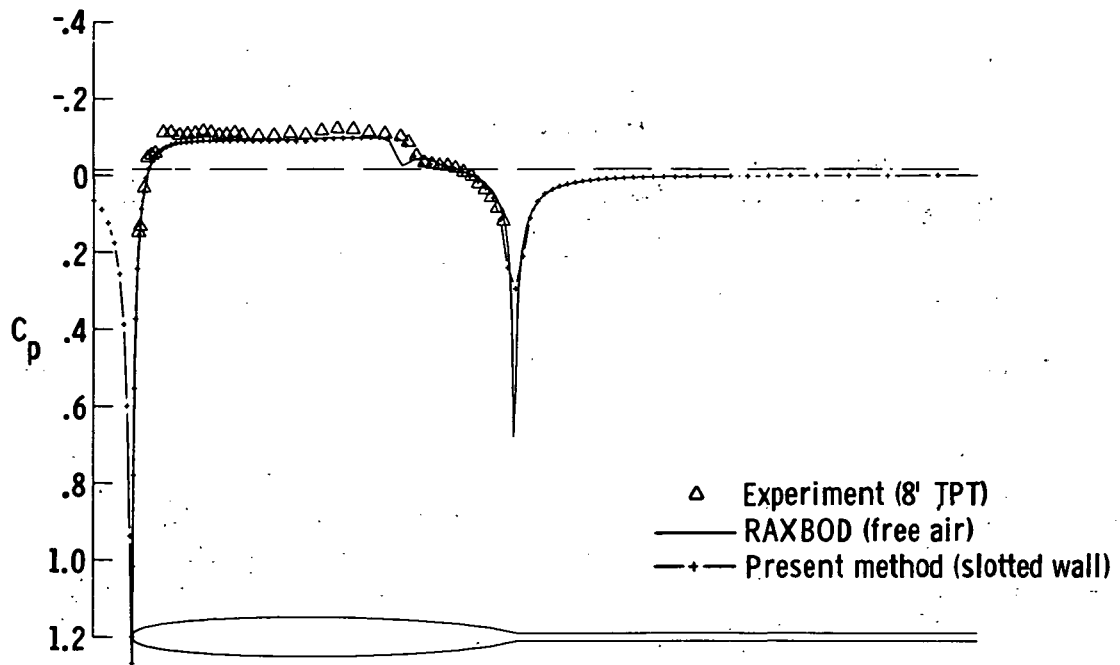


(a) Pressure distribution.

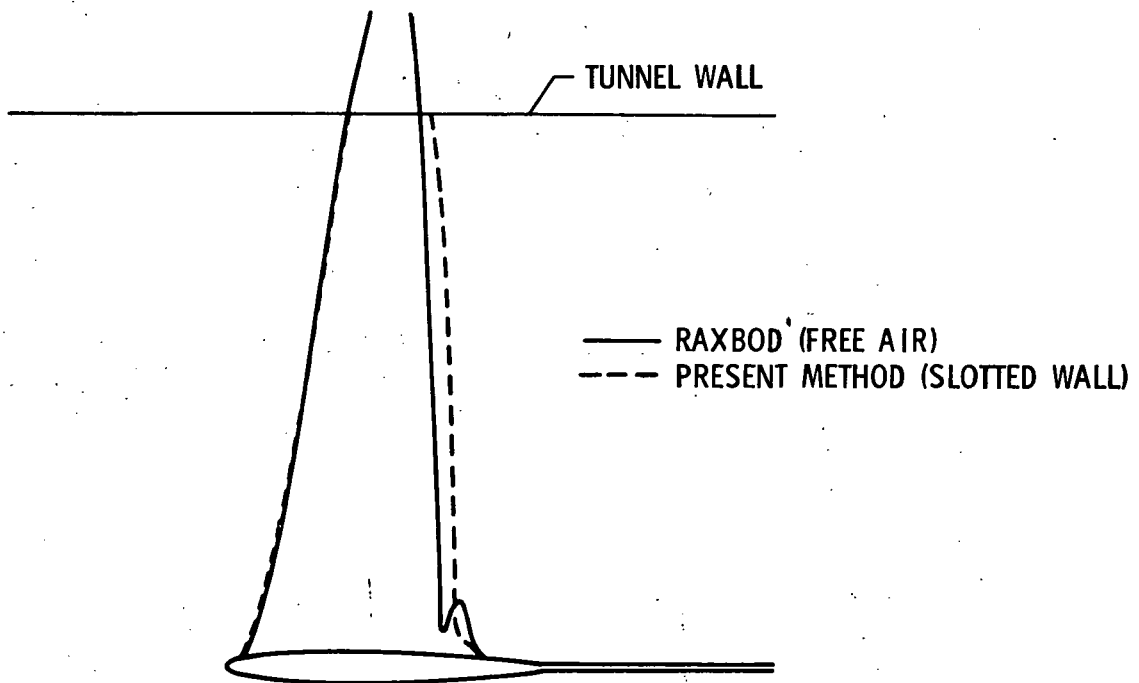


(b) Sonic line shape.

Figure 11. SCBR at $M_\infty = 0.991$ using solid-wall boundary conditions for present method.

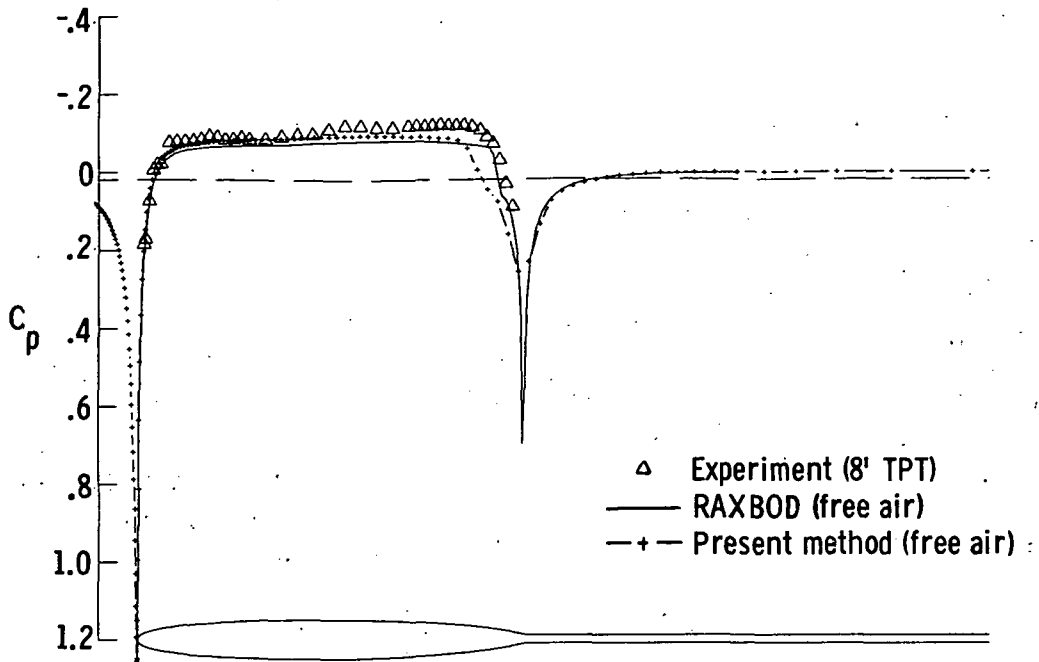


(a) Pressure distribution.

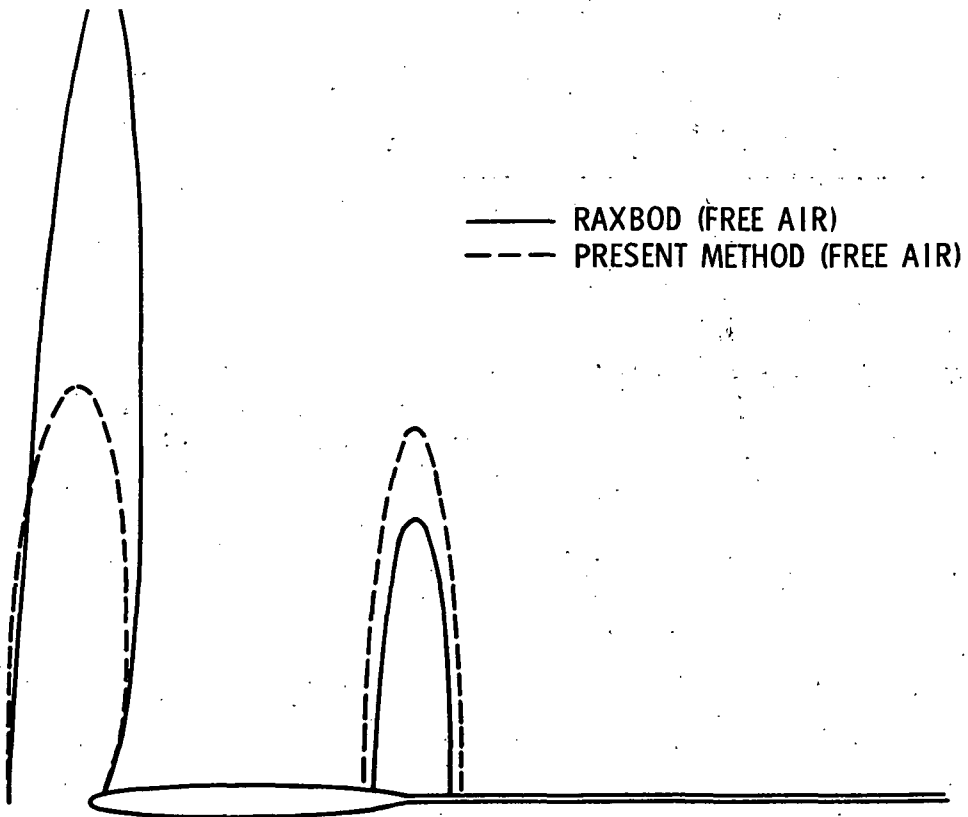


(b) Sonic line shape.

Figure 12.- SCBR at $M_\infty = 0.991$ using slotted-wall boundary conditions for present method.



(a) Pressure distribution.



(b) Sonic line shape.

Figure 13.- SCBR at $M_\infty = 1.011$.

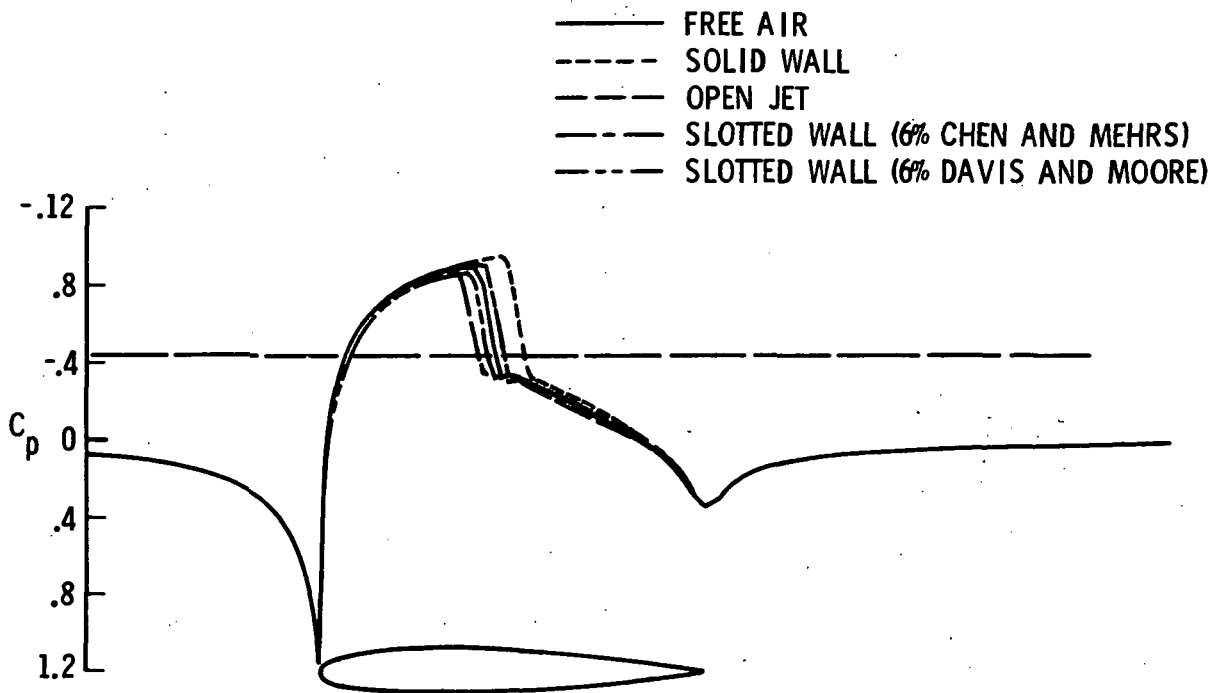


Figure 14. - Pressure distribution on NACA 0012 airfoil at $M_\infty = 0.8$.

Page Intentionally Left Blank

Page Intentionally Left Blank

COMPUTATIONAL TRANSONICS

By Paul R. Garabedian
New York University

SUMMARY

The purpose of this paper is to survey computational flow research supported by the National Aeronautics and Space Administration at the Energy Research & Development Administration Mathematics and Computing Laboratory of New York University on the analysis and design of supercritical wing sections. The computer programs to be described have important applications in the study of flight of modern aircraft at transonic speeds. Both two- and three-dimensional motions of a compressible fluid are considered, but the effect of changes in entropy across shock waves is neglected so that a velocity potential ϕ can be used. However, viscosity will be taken into account by introducing a semiempirical turbulent-boundary-layer correction. Good simulation of physically observed flows has been achieved, including an adequate prediction of the drag.

SYMBOLS

c	speed of sound
C_D	drag coefficient
C_L	lift coefficient
f	map function
g	arbitrary analytic function
H	shape factor
L	quasi-linear differential operator
M	local Mach number
p	pressure

q	speed
s	arc length
t	artificial time parameter
u, v	velocity components
x, y	coordinates in physical plane
x_1, x_2, x_3	coordinates at mesh points
y_1, y_2, y_3	
x_j	coordinates in plane or space
Δx_j	mesh size
α_j, β	relaxation coefficients
γ	ratio of specific heats
δ	displacement thickness
δ_{jk}	Kronecker delta
θ	momentum thickness
λ_+, λ_-	slopes of characteristics
ξ, η	complex characteristic coordinates
$\bar{\xi}, \bar{\eta}$	complex conjugates of ξ, η
ξ_0	point corresponding to trailing edge
τ	skin friction
ϕ	velocity potential

Subscripts:

j,k indices of coordinates

CalComp symbols:

C_p pressure coefficient

M*N dimensions of mesh

M local Mach number

NCY number of artificial time cycles

ALP angle of attack α

CL lift coefficient

CD drag coefficient

R Reynolds number

M1 inlet Mach number

M2 outlet Mach number

DEL TH turning angle

G/C gap-chord ratio

ANALYSIS

The partial differential equation for the velocity potential ϕ can be derived from a variational principle asserting that the integral over the flow field of the pressure p , considered to be a function of the speed $q = |\nabla\phi|$, is stationary in its dependence on ϕ . One application of the variational principle is to a nonlinear treatment of the vortex sheet trailing behind a wing in space of three dimensions. Another application is to the formulation of a finite-element method for wing-body combinations. Here it will suffice to state the equation for ϕ in the quasi-linear form

$$L[\phi] = \sum (c^2 \delta_{jk} - \phi_{x_j} \phi_{x_k}) \phi_{x_j x_k} = 0$$

where δ_{jk} is the Kronecker delta and c is the speed of sound, which is related to q by Bernoulli's law

$$\frac{q^2}{2} + \frac{c^2}{\gamma - 1} = \text{Constant}$$

The normal derivative of ϕ is set equal to zero at the boundary of the flow.

A finite-difference scheme for the transonic flow problem must include artificial viscosity terms to define the weak shock waves that occur. Moreover, the difference equations must be solved by a relaxation procedure that is best analyzed by thinking of ϕ as a function of an artificial time parameter t indicating the stage of the iteration. The process that has been programmed at New York University can be described in broad outline by writing down, rather than actual finite-difference equations, the time-dependent partial differential equation

$$L[\phi] = \sum \Delta x_j \min(1 - M^2, 0) \left| \phi_{x_j} \right| \phi_{x_k} \frac{\partial}{\partial x_j} \phi_{x_j x_k} + \sum \alpha_j \phi_{x_j t} + \beta \phi_t$$

for ϕ , where $M = q/c$ is the local Mach number. A second-order accurate central difference approximation of the quasi-linear differential operator L on the left is used. The first block of terms on the right, whose difference approximation has to be retarded appropriately in the direction of the flow, represents an anisotropic artificial viscosity proportional to the mesh sizes Δx_j . The second block of terms on the right controls the iterative scheme by means of coefficients α_j and β that are chosen to optimize the rate of convergence to a steady solution. The scheme as a whole has an invariance under transformation of the coordinates which enables one to implement it in curvilinear systems adapted to the geometry of specific models arising in practice. (See refs. 1 and 2.)

The finite-difference scheme determining ϕ that has been presented is similar to the method of Murman and Cole (ref. 3) for transonic flow computations. In particular, since the divergence form of the equation for ϕ is not used, the shock condition specifying conservation of mass becomes lost except to the extent that it is enforced by external boundary conditions. However, because of the central difference approximation of L , it is easy to arrive at the numerical equivalent of a conservation form of the equation. To that end one has only to bring the differential operator $\partial/\partial x_j$ appearing in the artificial viscosity out in front of the factors like $1 - M^2$ involving first derivatives of ϕ to obtain

$$L[\phi] = \sum \frac{\partial}{\partial x_j} \left[\Delta x_j \min(1 - M^2, 0) \left| \phi_{x_j} \right| \phi_{x_k} \phi_{x_j x_k} \right] + \sum \alpha_j \phi_{x_j t} + \beta \phi_t$$

This equation is found to give better resolution of the shock jump at the expense of larger truncation errors elsewhere in the flow field (ref. 4).

For the problem of boundary-layer—shock-wave interaction, it is more realistic to ignore the divergence form and return to the first version of the finite-difference scheme because, in practice, the speed behind a weak normal shock wave in a thick turbulent boundary layer tends to become barely subcritical, a property shared by the shocks calculated by using the first method. For the boundary-layer analysis, which has only been completed for two-dimensional flow around an airfoil, the displacement thickness $\delta = H\theta$ is computed by inserting semiempirical formulas of Nash and Macdonald (ref. 5) for the shape factor H and the skin friction τ into von Kármán's integral equation

$$\frac{d\theta}{dx} + (H - M^2 + 2)\frac{\theta}{q} \frac{dq}{dx} = \tau$$

for the momentum thickness θ . The flow calculation and the turbulent boundary-layer correction are iterated together in turn. The main difficulty lies in the numerical treatment of the Kutta condition at the trailing edge of the wing section, which involves too much intricate mathematical detail to discuss here (ref. 1).

It is possible to arrive at second-order accurate expressions for the artificial viscosity required in transonic flow computations (ref. 6). These ideas are of questionable value for use with the method of Murman and Cole because of nonuniqueness associated with the failure of the shock conditions. However, they have proved to be more successful for the conservation form of the equation for ϕ , where additional truncation error also makes them more of a necessity. Perhaps the most fruitful problem for higher-order accurate procedures, though, will be that of three-dimensional flow past an oblique wing on which the shocks tend to become smeared numerically when the speed behind them remains supersonic.

Computations from the code for analysis of the two-dimensional transonic flow past an airfoil with a turbulent-boundary-layer correction have been compared extensively with test data (ref. 1). The simulation of wind-tunnel pressure distributions is excellent for given free-stream Mach number and lift coefficient. Drag creep can be estimated adequately, although drag rise is predicted too early, with an increment in Mach number of the same order of magnitude as wall-effect corrections. As an example of the results obtained, figure 1 displays a comparison of the theoretical pressure distribution on Whitcomb's earliest supercritical wing section with recently declassified experimental data at an off-design condition with unusually large values of the lift and drag coefficients ($C_L = 1.3$ and $C_D = 0.06$). (See ref. 7.) The success of the calculation is striking.

Two-dimensional computation of transonic flow seems by now to have reached a level of advancement where it has become as useful a tool as wind-tunnel testing. It

would be desirable to achieve the same goal for three-dimensional flow past models of an airplane. Some of the mathematical techniques required for such an analysis have been indicated herein. So far in practice only the case of an isolated oblique wing has been treated numerically. The results compare favorably with experimental data collected by R. T. Jones in his research on an oblique-wing transonic transport (refs. 1 and 8).

DESIGN

Wind-tunnel tests have shown that it is feasible to design high-performance supercritical wing sections by solving mathematically the inverse problem of shaping an airfoil so that the transonic flow over it becomes shockless at specified conditions. The construction of shockless flows is most effectively carried out by means of a hodograph method based on complex characteristics (ref. 6). For practical applications it is essential to combine the method with a reliable turbulent-boundary-layer correction so as to completely suppress separation and any loss of lift associated with it.

The idea of the supercritical wing can be used to improve the performance of compressor blades. The computer program for calculating shockless flows by the method of complex characteristics has been extended to the model of a two-dimensional cascade of transonic airfoils (ref. 9). Preliminary estimates indicate that supercritical blades can achieve the same compression as standard subcritical blades for significantly greater gap-chord ratios. This means that the loss coefficient might be reduced by as much as 20 percent in the high compressor of a jet engine through the introduction of shockless transonic blades. There are plans for a test of this concept in the cascade wind tunnel of United Aircraft Corporation.

It is helpful to review the mathematical highlights of the design program in the context of both isolated airfoils and cascades. The partial differential equation for a velocity potential ϕ has characteristics which are solutions of the ordinary differential equation

$$(c^2 - u^2)dy^2 + 2uv \, dy \, dx + (c^2 - v^2)dx^2 = 0$$

where u and v are the velocity components. Consequently, the equations of motion reduce to the canonical system

$$y_\xi + \lambda_+ x_\xi = 0 = y_\eta + \lambda_- x_\eta$$

$$u_\xi - \lambda_- v_\xi = 0 = u_\eta - \lambda_+ v_\eta$$

in terms of characteristic coordinates ξ and η , where

$$\lambda_{\pm} = \frac{uv \pm ic^2 \sqrt{1 - M^2}}{c^2 - u^2}$$

Let the solution be continued analytically into the complex domain so that ξ and η become two independent complex variables. The equations for u and v can be integrated in the closed form

$$\int \sqrt{1 - M^2} \frac{dq}{q} - i\theta = \log f(\xi)$$

$$\int \sqrt{1 - M^2} \frac{dq}{q} + i\theta = \log \overline{f(\bar{\eta})}$$

where f is an arbitrary analytic function and $qe^{i\theta} = u + iv$.

To calculate x and y , appropriate paths of integration are laid down in the complex ξ -plane and η -plane. Then, for each pair of paths a stable finite-difference scheme of the form

$$y_3 + \lambda_+ x_3 = y_1 + \lambda_+ x_1$$

$$y_3 + \lambda_- x_3 = y_2 + \lambda_- x_2$$

is applied to solve a characteristic initial value problem with conjugate data

$$x(\xi, 0) = g(\xi) = \overline{x(0, \bar{\xi})}$$

This procedure transforms the arbitrary analytic function g of the complex variable ξ into a solution of the nonlinear equations of gas dynamics. The answer has the symmetry property

$$x(\xi, \eta) = \overline{x(\bar{\eta}, \bar{\xi})}$$

showing that the real physical plane corresponds to points with $\xi = \bar{\eta}$. The method also serves to generate the right singularities in the hodograph plane to associate with the flow at infinity for an isolated airfoil or a cascade (refs. 6 and 9).

There is only one independent analytic function in the representation of the general solution of the partial differential equation for the velocity potential ϕ . Hence, for any given flow, there exists a relationship between the functions f and g . However, the roles of the two functions are quite different in the numerical construction of shockless

airfoils. The function f may provide a conformal mapping of some canonical domain such as the unit circle $|\xi| < 1$ onto the usually unknown image of the flow in the modified hodograph plane. On the other hand, g can be viewed as serving to fulfill boundary conditions through the solution of an interpolation problem. It has been possible to generate a large collection of supercritical wing sections by using a quadratic polynomial for f that leads to a univalent correspondence between points in the physical plane and points in the ξ -plane (refs. 1 and 6). However, for airfoils with more camber, such as those in a cascade of compressor or turbine blades, additional branch points occur in the mapping to the hodograph plane and it becomes necessary to make more sophisticated choices of f (ref. 10). A compressor blade that turns the flow through an angle of 29° is displayed in figure 2 which was reproduced from reference 9. For this blade it was helpful to use for f a cubic that accounted for an auxiliary branch point appearing just inside the lower surface of the profile.

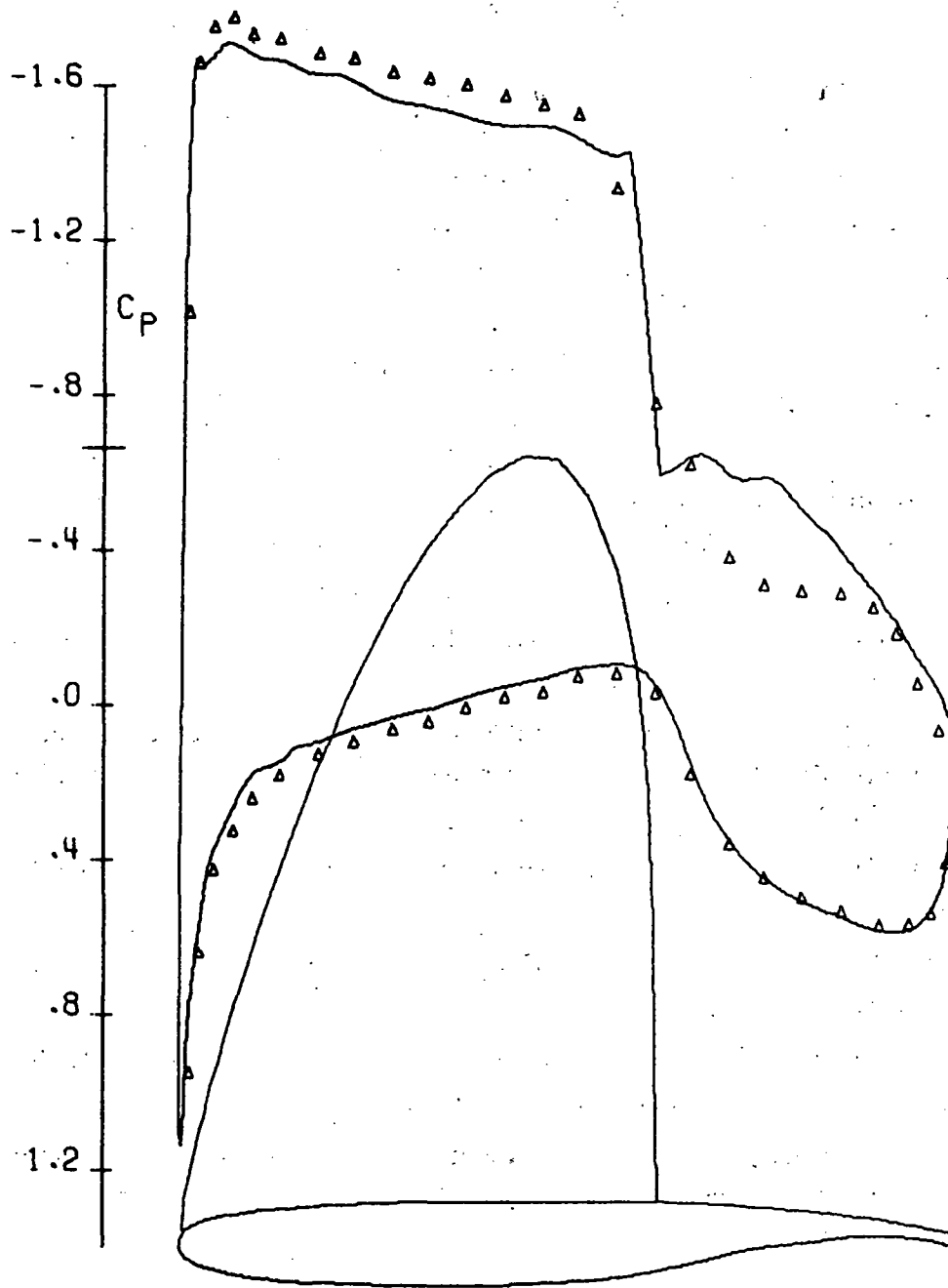
The design program is so efficient computationally that it has been tempting to resolve the conflicts between various physical requirements on a desired airfoil by trial and error. A more systematic approach is now under investigation in which the flow region will be mapped onto the unit circle in the ξ -plane, where the analytic functions $\log f$ and g will be represented by power series. Trigonometric interpolation at equally spaced nodes on the circle can be used to implement this idea numerically. In particular, the sonic locus $M = 1$, which is a singularity for the determination of g , can be circumvented by integrating in the complex domain over disjoint paths consisting of radial segments and circular arcs. The new approach has the advantage of eliminating the issue of choosing many inscrutable mathematical parameters in favor of deciding on a prescription for the speed q as a function of the arc length s along the profile being designed.

A problem where the specific analytic behavior of the functions f and g becomes important is the suppression of boundary-layer separation at the rear of the airfoil. For a supercritical wing section, the speed at the trailing edge must be rather large so as not to compare too unfavorably with speeds prevailing in the supersonic zone. One answer to the problem is to introduce heavy aft loading (ref. 7). To avoid separation, the adverse pressure gradient on the upper surface must remain bounded. On the other hand, an infinite positive gradient of the speed q is needed at the trailing edge of the lower surface to provide the desired aft loading. Therefore, in the hodograph plane the profile should become tangent to a level curve of q on the upper surface, but not on the lower surface, at the point ξ_0 corresponding to the trailing edge. One way to achieve such a profile is to include in the map function f a fractional power $(\xi - \xi_0)^\epsilon$ with $0 < \epsilon < 1$. Figure 2 shows the kind of pressure distribution that is under discussion. An airfoil incorporating some of these ideas has been tested by the Grumman Aerospace Corporation with considerable success.

There is under way a fairly extensive program of testing shockless airfoils designed by the method of complex characteristics. A new test is planned at the National Aeronautical Establishment in Ottawa, which has been the most prolific source of experimental data for comparison with the transonic flow computations described herein. In addition to the work by the United Aircraft Corporation and the Grumman Aerospace Corporation that has been mentioned, three-dimensional experiments will be conducted at the NASA Ames Research Center on a Boeing model of Jones's transonic transport furnished with an oblique supercritical wing designed at New York University. To justify the major mathematical effort that has been invested, it would be gratifying if one of the shockless airfoils were ultimately to find its way onto a prototype airplane to be flight tested.

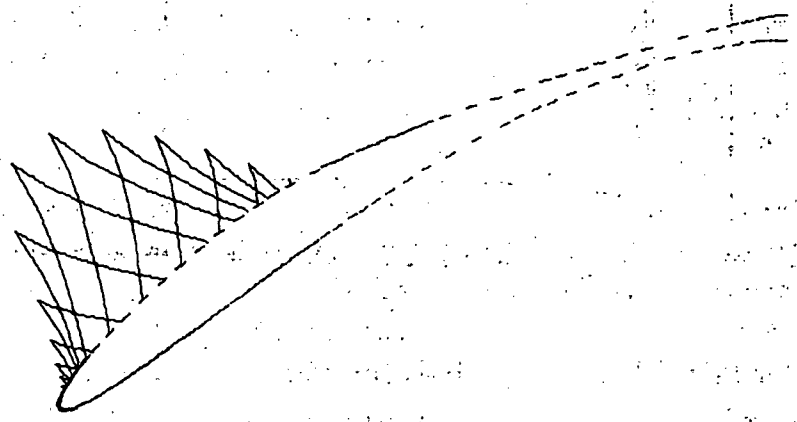
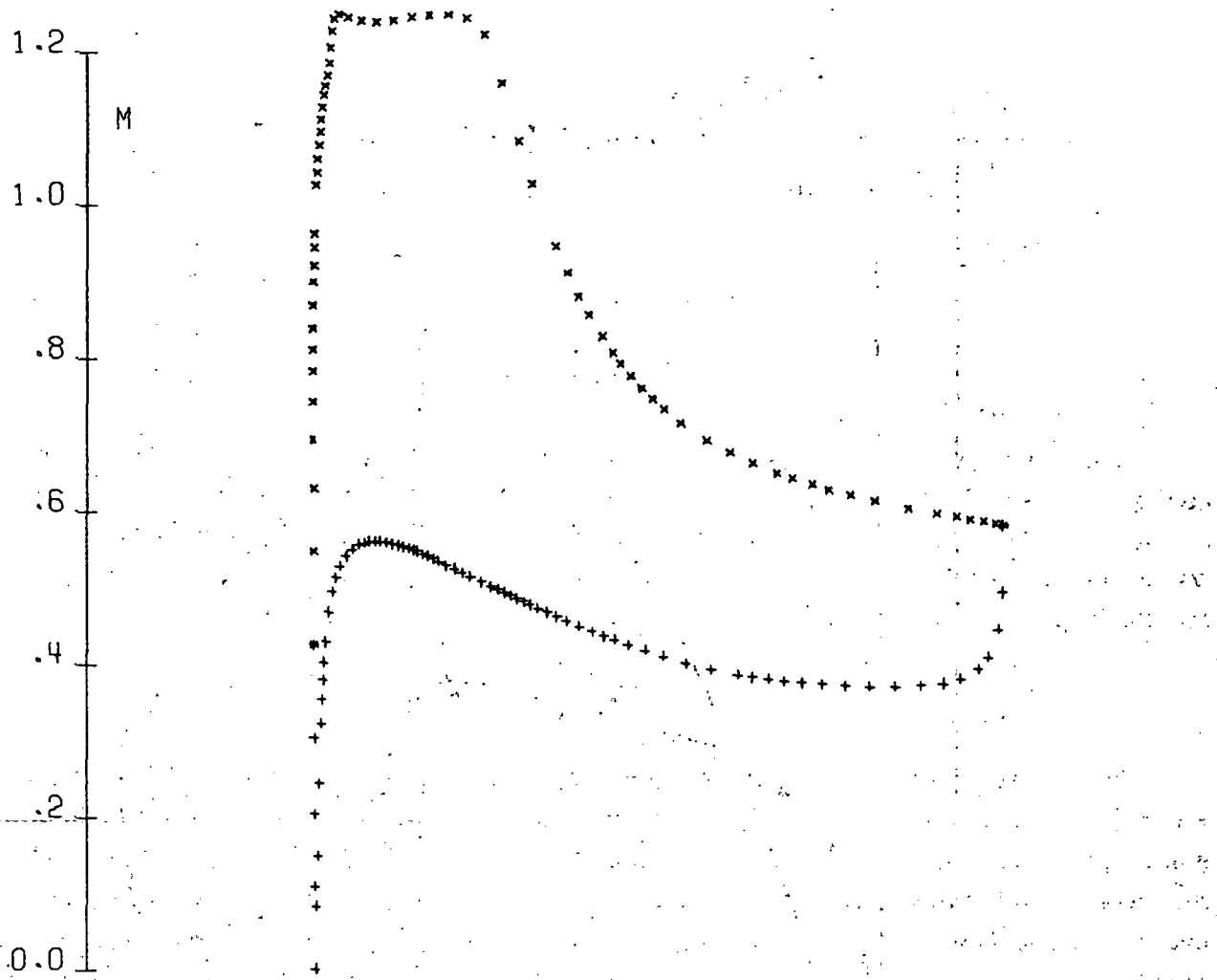
REFERENCES

1. Bauer, Frances; Garabedian, Paul; Korn, David; and Jameson, Antony: Supercritical Wing Sections II, A Handbook. Lecture Notes in Economics and Mathematical Systems, vol. 108, Springer-Verlag, c.1975.
2. Jameson, Antony: Iterative Solution of Transonic Flows Over Airfoils and Wings, Including Flows at Mach 1. Commun. Pure & Appl. Math., vol. 27, 1974, pp. 283-309.
3. Murman, E. M.; and Cole, J. D.: Calculation of Plane Steady Transonic Flows. AIAA J., vol. 9, 1971, pp. 114-121.
4. Jameson, Antony: Transonic Potential Flow Calculations Using Conservation Form. Paper to be presented at 2nd AIAA Computational Fluid Dynamics Conference (Hartford, Conn.), June 19-20, 1975.
5. Nash, J. F.; and Macdonald, A. G. J.: The Calculation of Momentum Thickness in a Turbulent Boundary Layer at Mach Numbers up to Unity. C.P. No. 963, British A.R.C., 1967.
6. Bauer, Frances; Garabedian, Paul R.; and Korn, David: A Theory of Supercritical Wing Sections, With Computer Programs and Examples. Lecture Notes in Economics and Mathematical Systems, vol. 66, Springer-Verlag, c.1972.
7. Whitcomb, R. T.: Review of NASA Supercritical Airfoils. ICAS Paper No. 74-10, Aug. 1974.
8. Jones, R. T.: New Design Goals and a New Shape for the SST. Astronaut. & Aeronaut., vol. 10, 1972, pp. 66-70.
9. Korn, David: Numerical Design of Transonic Cascades. R & D Rep. C00-3077-72, ERDA Mathematics and Computing Laboratory, New York University, Jan. 1975.
10. McIntyre, Eldon: Design of Transonic Cascades by Conformal Transformation of the Complex Characteristics. Ph. D. Thesis, New York University, 1975.



WHITCOMB WING	M*N=160*30	NCY= 400	R= 7 MILLION
— THEORY	M=.730	ALP= 3.44	CL=1.315
Δ EXPERIMENT	M=.730	ALP= 5.50	CL=1.315
			CD=.0630

Figure 1.- Analysis at an off-design condition.



M1 = .780 M2 = .480 DEL TH = 29:00 G/C = 1.07

Figure 2.- Design of a compressor blade.

APPROXIMATE METHOD FOR CALCULATING TRANSONIC FLOW ABOUT LIFTING WING-BODY COMBINATIONS

By Richard W. Barnwell
NASA Langley Research Center

SUMMARY

A fast approximate method is described for calculating transonic flow about lifting configurations with swept leading edges and aspect ratios of order 1 at angles of attack of the order of the equivalent-body thickness-length ratio. The method accounts for shock waves, leading-edge separation, and wind-tunnel wall effects and is applicable throughout the Mach number range from zero to low supersonic.

INTRODUCTION

The results of the analytical treatments of Barnwell (refs. 1 and 2) and Cheng and Hafez (ref. 3) are used to reduce the problem of transonic flow about lifting wing-body combinations with aspect ratios of order one at angles of attack of the order of the body thickness-length ratio to several simpler two-variable problems. As indicated in figure 1, this approach has been used successfully in previous studies of transonic flow past slender bodies at angles of attack of the order of the body thickness-length ratio (ref. 4) and wing-body combinations with aspect ratios of order one at angles of attack of the order of the wing thickness-chord ratio (refs. 5 and 6, for example). A more general requirement for the angle-of-attack range for the latter problem which accounts for flat-plate wings is that it be of the order of the square root of the equivalent-body thickness-length ratio.

The analysis given in references 1, 2, and 3, which was performed with the method of matched asymptotic expansions, can be used to reduce the problem of three-dimensional transonic flow past lifting wing-body combinations to two simpler problems. The first of these problems involves the determination of the basic lift solution by one of several approximate methods. This solution is of first order in $\sin \alpha$ where α is the angle of attack. The second problem is concerned with obtaining the solution to a coupled lift and thickness potential of second order in $\sin \alpha$ and the equivalent-body thickness-length ratio. The approximate governing equation for the second-order lift and thickness potential has derivatives with respect to only two independent variables and can be calcu-

lated numerically with the two-variable form of the method of relaxation developed by Murman and Cole (ref. 7).

SYMBOLS

B	constant in equation (26)
b	semispan
C_L	lift coefficient
C_p	pressure coefficient
C_p^*	sonic pressure coefficient
$f(x)$	lift distribution function for attached flow given by equations (8) and (13)
$f_v(x)$	lift distribution function due to leading-edge vortex given by equation (16)
l	characteristic length in x -direction, configuration length unless otherwise noted
M_∞	free-stream Mach number
P	coefficient for porous-wall boundary condition (see eq. (24))
R	distance defined by equation (10)
r	radial coordinate
$r_b(x)$	local body radius
S_{eff}	effective cross-sectional area of lifting configuration given by equation (26)
S_{ref}	reference area for lift coefficient
u, v, w	body-oriented perturbation velocity components in axial-, radial-, and cross-flow directions, respectively

x	coordinate in streamwise direction
y	coordinate in spanwise direction
$y_2(x)$	planform shape
z	coordinate in vertical direction
α	angle of attack
β	$= \sqrt{M_\infty^2 - 1}$
γ	ratio of specific heats
$\Delta\phi'_\alpha$	quantity defined by equation (25)
θ	body-oriented polar angle
ω	wind-oriented polar angle
κ	coefficient for slotted-wall boundary condition (see eq. (23))
Λ	function defined by equation (20)
λ	function defined by equation (21) or (22)
Φ_0	potential defined by equation (18)
ϕ_α	linear lift potential
φ	perturbation velocity potential
$\varphi_0, \varphi_1, \varphi_2$	coefficients of Fourier components of φ (see eq. (5))
∇_2^2	Laplace operator in cross-flow plane defined by equation (3)

Subscripts:

eb	equivalent body
ℓ	beneath wing
max	maximum value
te	trailing edge
u	above wing
v	vortex

Primes denote differentiation with respect to x . A bar over a symbol denotes transformation in cross-flow plane defined by equations (14). A tilde (\sim) over a symbol denotes transformation in cross-flow plane defined by equation (15).

DESCRIPTION OF METHOD

The coordinate systems which are used are depicted in figure 2. These coordinate systems are wind-oriented with the X-axis in the streamwise direction and the Z-axis in the vertical direction. The cylindrical polar system x, r, ω is used to compute the second-order coupled lift and thickness potential.

In the present method wing-body combinations are approximated with combinations composed of bodies of revolution with the equivalent-body area distribution and a flat-plate wing. Velocity components and lengths are made nondimensional with the magnitude of the free-stream velocity and the configuration length, respectively. The method is restricted to configurations with swept leading edges. The planform shape is specified with the function $y_2(x)$.

Let $\varphi(x, r, \omega)$ be the small-disturbance perturbation velocity potential and ϕ_α be the linear lift potential. It is shown in references 1 and 2 that for transonic flow φ and ϕ_α are governed by the equations

$$\left[1 - M_\infty^2 - (\gamma + 1)M_\infty^2 \frac{\partial \varphi}{\partial x} \right] \frac{\partial^2 \varphi}{\partial x^2} + \nabla_2^2 \varphi = 2M_\infty^2 \left(\frac{\partial \phi_\alpha}{\partial r} \frac{\partial^2 \phi_\alpha}{\partial x \partial r} + \frac{1}{r^2} \frac{\partial \phi_\alpha}{\partial \omega} \frac{\partial^2 \phi_\alpha}{\partial x \partial \omega} \right) \quad (1)$$

and

$$\nabla_2^2 \phi_\alpha = 0 \quad (2)$$

respectively, where M_∞ and γ are the free-stream Mach number and the ratio of specific heats, respectively, and where ∇_2^2 is the two-dimensional Laplace operator in the cross-flow plane which can be written in the forms

$$\nabla_2^2 = \frac{\partial^2}{\partial r^2} + \frac{1}{r} \frac{\partial}{\partial r} + \frac{1}{r^2} \frac{\partial^2}{\partial \omega^2} = \frac{\partial^2}{\partial y^2} + \frac{\partial^2}{\partial z^2} \quad (3)$$

Solutions to equation (2) are called slender-wing solutions and are applicable if the span-length ratio is small or, as in the present case, if M_∞ is near 1. More generally, the lift potential ϕ_α satisfies the equation

$$(1 - M_\infty^2) \frac{\partial^2 \phi_\alpha}{\partial x^2} + \nabla_2^2 \phi_\alpha = 0 \quad (4)$$

The present method consists of first determining the potential ϕ_α by analytical or numerical methods, and then using the known solution for ϕ_α and equation (1) to obtain an approximate, two-variable equation for φ which is solved numerically with the method of relaxation. The method can be applied in the Mach number range from zero to the supersonic value at which the wing leading edge becomes sonic.

In this paper both attached and separated leading-edge flows are considered. Three different methods for determining ϕ_α are employed depending on the Mach number. First consider the transonic regime where equation (2) applies and slender wing theory is applicable.

From equations (1) and (2) and the boundary condition for flow in free air, it can be shown with the method of matched asymptotic expansions (refs. 1, 2, and 3) that the solution for φ and ϕ_α for points near the configuration but beyond the wing tip where $r > y_2$ are of the form

$$\varphi(x, r, \omega) = \varphi_0(x, r) + \varphi_1(x, r) \sin \omega + \varphi_2(x, r) \cos 2\omega + \dots \quad (5)$$

and

$$\phi_\alpha(x, r, \omega) = \varphi_1(x, r) \sin \omega$$

where

$$\varphi_1(x, r) = \sin \alpha f(x) \frac{1}{r} \quad (6)$$

and

$$\varphi_2(x, r) = \sin^2 \alpha \left[\frac{\gamma + 1}{8} f'(x) f''(x) - \frac{1}{2} f(x) f'(x) \frac{1}{r^2} \right] \quad (7)$$

The primes in equation (7) denote differentiation with respect to x . The potential $\varphi_0(x, r)$ in equation (5) cannot be completely determined with the method of matched asymptotic expansions. It should be noted that the term $\varphi_2 \cos 2\omega$ in equation (5) results because of the presence of the nonlinear term $\frac{\partial \varphi}{\partial x} \frac{\partial^2 \varphi}{\partial x^2}$ in equation (1) and is significant only at transonic speeds.

For attached flow the function $f(x)$ in equations (6) and (7) is written as

$$f(x) = \frac{1}{2} \left\{ 1 + \left[\frac{r_b(x)}{y_2(x)} \right]^4 \right\} y_2^2(x) \quad (8)$$

where $r_b(x)$ is the body radius. This function gives the lift accumulated from the configuration nose to the axial station x .

It is shown in reference 2 that at large distances from the configuration, the potential φ_1 should be written as

$$\varphi_1(x, r) = \sin \alpha \left[\frac{x}{R} f(x) + \frac{1}{2} \left(1 - \frac{|x|}{R} \right) f(1) \right] \frac{1}{R} \quad (9)$$

where

$$R = \sqrt{x^2 + (1 - M_\infty^2) r^2} \quad (10)$$

$$f(x) = \begin{cases} f(1) & (x > 1) \\ 0 & (x < 0) \end{cases}$$

for $M_\infty < 1$ and as

$$\varphi_1(x, r) = \sin \alpha \frac{f(x - \beta r)}{(x - \beta r)^2} \left[x \sqrt{x^2 - \beta^2 r^2} + \beta^2 r^2 \log_e \left(\frac{\beta r}{x + \sqrt{x^2 - \beta^2 r^2}} \right) \right] \quad (11)$$

where

$$\beta = \sqrt{M_\infty^2 - 1}$$

on the interval $0 \leq x - \beta r \leq 1$ for $M_\infty > 1$. In this paper it is assumed that for $M_\infty < 1$, the function φ_2 varies as

$$\varphi_2(x, r) = \sin^2 \alpha \left[\frac{\gamma + 1}{8} \frac{x^2}{R^2} f'(x) f''(x) - \frac{1}{2} f(x) f'(x) \frac{1}{r^2} \right] \quad (12)$$

For $M_\infty > 1$, equation (7) is used in the region $r < \frac{x}{\beta}, x \leq 1$. Outside this region φ_2 is made to vanish.

For Mach numbers appreciably less than 1, solutions to equation (4) for ϕ_α are obtained with the approximate method of Lawrence and Flax (ref. 8) for wing-body configurations. This method, which is an extension of that of Lawrence (ref. 9) for wings alone, and which is applicable to configurations with straight trailing edges and aspect ratios of order one, obtains a solution directly for the lift distribution function $f(x)$. This solution satisfies the trailing-edge Kutta condition to lowest order whereas the slender-wing solution given by equation (8) does not. The terms in equations (6), (7), (9), (11), and (13) which depend on $f(x)$ and its derivatives are evaluated with this solution. It can be shown from the results of references 8 and 9 that the function $f(x)$ is obtained from the values of the potential ϕ_α on the upper and lower surfaces of the wing, which are designated as $\phi_{\alpha,u}$ and $\phi_{\alpha,l}$, respectively, by the equation

$$f(x) = \frac{1}{\pi} \int_{\bar{y}=0}^{\bar{y}=r_b^2(x)} [\phi_{\alpha,u}(x,\bar{y}) - \phi_{\alpha,l}(x,\bar{y})] d\bar{y} + r_b^2(x) \quad (13)$$

where the transformed coordinates \bar{y}, \bar{z} are related to the physical coordinates y and z by the equations

$$\left. \begin{aligned} \bar{y} &= y \left(1 - \frac{r_b^2}{y^2 + z^2} \right) \\ \bar{z} &= z \left(1 + \frac{r_b^2}{y^2 + z^2} \right) \end{aligned} \right\} \quad (14)$$

Approximate values for the potential ϕ_α on the configuration surface are obtained in this paper from equation (13) and the assumption that the spanwise variation of ϕ_α is proportional to that obtained from slender-wing theory.

For supersonic attached flow an approximate solution is obtained with the quasi-conical method of Carafoli (ref. 10) for flow past wings with subsonic leading edges. First the transformation given by equation (14) is applied. It should be noted that this transformation maps the body surface $r = r_b(x)$ to the vertical plane $\bar{y} = 0$ so that methods for flow past wings alone can be applied in the transformed space. Then the quasi-conical approximation for the potential ϕ_α in the transformed space is determined. The function $f(x)$ is then obtained by numerical integration of equation (13). It is assumed in the present paper that the wing leading edge is subsonic. It should be noted that the leading edge of a wing-body becomes supersonic at the wing-body junction at a much lower Mach number than simple sweep theory indicates because of the influence of the body.

Both Lawrence and Flax theory for subsonic flow and quasi-conical theory for supersonic flow reduce to slender-wing theory for $M_\infty = 1$. As a result, the linear lift approximation used in this paper varies uniformly throughout the transonic regime.

As mentioned previously, the present method can account for separation at the wing leading edge. As an example, the case of separated leading-edge flow over a delta wing is illustrated in figure 3. Several methods have been developed for calculating this type of flow, some of which are depicted in figure 3. In all these methods the linear lift potential ϕ_α is assumed to be composed of two components, one of which is the same as the attached-flow potentials previously discussed, and one which accounts for the flow due to the vortex. The Brown and Michael vortex-flow model (ref. 11) consists of a vortex core and vorticity feeding sheet located at each wing tip. The strength of the vortex core is adjusted so that the wing-tip singularity on the attached-flow solution is canceled. The Smith model (ref. 12) includes several sections of the vortex sheet as well as the vortex core and vorticity feeding sheet. For both these methods, it is assumed that the flow is governed by equation (2), the Laplace equation in the cross-flow plane, so that the solutions are of the slender-wing type. Although this type of solution describes the flow associated with the vortex fairly accurately, it does not provide a good estimate of the attached flow except for Mach numbers near 1.

In this paper the Brown and Michael method is modified for free-stream Mach numbers appreciably different from 1 so that, as indicated in figure 3, the vortex potential is governed by equation (2) and the attached-flow potential is governed by equation (4). It should be noted that this method has also been used by Sacks, Lundberg, and Hanson (ref. 13) for subsonic flow. In addition, these authors have combined a preliminary version of the Smith vortex-flow model, the model of Mangler and Smith (ref. 14), with the subsonic attached-flow theory of Lawrence. In the present paper, the modified Brown and Michael model, rather than the modified Smith model, is used because of its simplicity and speed of implementation.

In the process of determining the vortex-flow potential, the configuration cross section in each cross-flow plane is mapped to a vertical slit with equation (14) and the additional transformation

$$\left. \begin{aligned} \tilde{y} &= \frac{\sqrt{2}}{2} \left[\sqrt{(\bar{y}^2 - \bar{z}^2 - \bar{y}_2^2)^2 + 4\bar{y}^2\bar{z}^2} + (\bar{y}^2 - \bar{z}^2 - \bar{y}_2^2) \right]^{1/2} \\ \tilde{z} &= \frac{\sqrt{2}}{2} \left[\sqrt{(\bar{y}^2 - \bar{z}^2 - \bar{y}_2^2)^2 + 4\bar{y}^2\bar{z}^2} - (\bar{y}^2 - \bar{z}^2 - \bar{y}_2^2) \right]^{1/2} \end{aligned} \right\} \quad (15)$$

where

$$\bar{y}_2 = y_2 - \frac{r^2}{y_2}$$

If the location of the vortex core in the transform plane is designated as \bar{y}_v, \bar{z}_v , the contribution of the vortex flow to the linear lift distribution function is

$$f_v(x) = \bar{y}_v^2(x) + \bar{z}_v^2(x) \quad (16)$$

For separated leading-edge flow, $f_v(x)$ must be added to the function given in equation (8) or (13).

Once the linear lift potential ϕ_α has been obtained, the nonlinear potential ϕ can be calculated. In the present approximate method, it is assumed that the dependence of ϕ on ω at points beyond the wing tip where $r > y_2(x)$ is given by equation (5). When this equation is substituted into equation (1), the approximate two-variable equation

$$\left[1 - M_\infty^2 - (\gamma + 1)M_\infty^2 \frac{\partial \phi}{\partial x} \right] \frac{\partial^2 \phi}{\partial x^2} + \frac{\partial^2 \phi}{\partial r^2} + \frac{1}{r} \frac{\partial \phi}{\partial r} = \frac{1}{r^2} \left[\phi_1(x, r) \sin \omega + 4\phi_2(x, r) \cos 2\omega \right] + 2M_\infty^2 f(x) f'(x) \frac{1}{r^4} \quad (17)$$

is obtained. At points inside the wing tip where $r < y_2(x)$, it is assumed that the velocity potential ϕ can be approximated as

$$\phi(x, r, \omega) = \phi_\alpha(x, r, \omega) + \Phi_0(x, r) \quad (18)$$

where $\Phi_0(x, r)$ is assumed to be averaged over the region above the wing ($0 \leq \omega \leq \pi$) or beneath the wing ($0 \geq \omega \geq -\pi$) depending upon whether the sign of the computational ω -plane is positive or negative. If the computational ω -plane is the wing plane where $\omega = 0$, $\Phi_0(x, r)$ has two values, one above and one beneath the wing. The governing equation for $\Phi_0(x, r)$ is obtained from equations (1), (2) or (4), and (18), and an approximate form of the linear lift potential ϕ_α . This approximate form is simply the one-term expansion of ϕ_α about the configuration axis. The equation which governs $\Phi_0(x, r)$ is

$$\Lambda \frac{\partial^2 \Phi_0}{\partial x^2} + \frac{1}{r} \frac{\partial}{\partial r} \left(r \frac{\partial \Phi_0}{\partial r} \right) = \mp \sin \alpha \left[\lambda y_2' - 2M_\infty^2 \sin \alpha \left(\frac{1}{\pi} - \frac{r}{y_2} \right) \frac{r y_2'}{y_2^2} \right] \quad (19)$$

where

$$\Lambda = 1 - M_\infty^2 - (\gamma + 1)M_\infty^2 \left\{ \Phi_0' \pm \sin \alpha \left[y_2' + \frac{y_2}{y_2 \mp \bar{z}_v} \left(\frac{\bar{y}_v^2 + \bar{z}_v^2}{y_2} \right)' \right] \right\} \quad (20)$$

and where

$$\lambda = \Lambda \quad (21)$$

if ϕ_α is governed by equation (2) and

$$\lambda = \Lambda - (1 - M_\infty^2) \quad (22)$$

if ϕ_α is governed by equation (4). The upper and lower signs in equations (19) and (20) apply above and beneath the wing, respectively, and the prime denotes differentiation with respect to x .

The boundary condition at the configuration axis is

$$\text{Limit}_{r \rightarrow 0} \left(r \frac{\partial \Phi_0}{\partial r} \right) = r_b(x) r_b'(x)$$

As stated previously, the present method can account for the presence of solid, slotted, and porous tunnel walls. For slotted and porous walls the boundary conditions are

$$\frac{\partial \varphi}{\partial r} = -\frac{1}{\kappa} \varphi \quad (r = r_{\text{wall}}) \quad (23)$$

and

$$\frac{\partial \varphi}{\partial r} = -P \frac{\partial \varphi}{\partial x} \quad (r = r_{\text{wall}}) \quad (24)$$

respectively, where κ and P are constants which depend on the wall characteristics. (See ref. 15.) For solid walls the derivative $\partial \varphi / \partial r$ vanishes.

Equations (17) and (19) can be solved in a plane of constant ω with a two-variable successive line overrelaxation procedure. Separate solutions must be performed in each ω -plane where results are desired. The procedure which is used in this paper is similar to that used by Bailey (ref. 16) except that the shock difference operator developed by Murman (ref. 17) is included. This operator tends to predict the jump condition at strong shock waves more accurately than previous operators. A detailed description of the present relaxation procedure is given in reference 2.

For free-stream Mach numbers below 1, the trailing-edge Kutta condition must be satisfied at least approximately in order for the solutions to be physically realistic. For a configuration with a straight trailing edge located at $x = x_{te}$, this condition can be expressed as

$$\varphi(x_{te} + \Delta x, y, +0) - \varphi(x_{te} + \Delta x, y, -0) = \varphi(x_{te}, y, +0) - \varphi(x_{te}, y, -0)$$

where Δx is the mesh spacing for the x -coordinate and $z = \pm 0$ designates the upper and lower surfaces of the wing and trailing-vortex sheet. For shockless flow which is attached at the leading edge, this condition is enforced automatically if ϕ_α is obtained

from the theory of Lawrence and Flax. If ϕ_α is obtained from slender-wing theory, the condition is met for shockless attached leading-edge flow by requiring that the derivative y_2' approach zero at the trailing edge of the wing. It can be shown that if the flow at the leading edge is separated, the contribution of the leading-edge vortex system to the derivative ϕ_α' on the inboard portion of the wing is of the form

$$\Delta\phi_\alpha' = \pm \frac{\sin \alpha}{y_2 \mp \bar{z}_v} \left[(\bar{y}_v^2 + \bar{z}_v^2)' - (y_v^2 + z_v^2) \frac{y_2'}{y_2} \right] \quad (25)$$

Of course, equation (25) is not valid on the outboard portion of the wing near the vortex. If the computational plane is the wing plane where $\omega = 0$, partial account of the effect of shock waves and leading-edge separation on the Kutta condition is taken by imposing the condition

$$\Phi_{0,u}(x_{te} + \Delta x, r) - \Phi_{0,l}(x_{te} + \Delta x, r) = \Phi_{0,u}(x_{te}, r) - \Phi_{0,l}(x_{te}, r) - \left. \left\{ \frac{2 \Delta x \sin \alpha}{y_2^2 - \bar{z}_v^2} \left[y_2 (\bar{y}_v^2 + \bar{z}_v^2)' - (\bar{y}_v^2 + \bar{z}_v^2) y_2' \right] \right\} \right|_{x=x_{te}}$$

The subscripts u and l designate values on the upper and lower surfaces of the wing and vortex sheet. This additional adjustment for the Kutta condition is not made for computational planes other than the wing plane.

The pressure coefficients which are presented in this paper were calculated in terms of body-oriented coordinates. If the body-oriented velocity components in the axial-, radial-, and cross-flow directions are u , v , and w , respectively, the pressure coefficient is written to second order as

$$C_p = -2 \left[u + \sin \alpha (v \sin \theta + w \cos \theta) \right]^2 - v^2 - w^2$$

where θ is zero in the wing plane and positive above the wing. It is well known that the pressure coefficients obtained with slender-wing techniques for the upper and lower surfaces of the trailing vortex sheet do not agree if r_b' does not vanish aft of the trailing edge of the wing. However, the differences are small if $r_b/y_2 \ll 1$. In this paper these differences are shown when they occur.

NONLINEAR EFFECT OF LIFT

It is well known that the effect of thickness is to deflect streamlines outward from the configuration. It can be shown that for near-sonic flow, lift can also have this effect in addition to the usual downwash effect. The manner in which lift causes this outward deflection is shown in figure 4. The cross-sectional area of stream tubes is minimum

where the flow is sonic. The effect of lift is to increase the velocity in the stream tubes above the wing and decrease the velocity in the stream tubes beneath the wing. For configurations traveling at transonic speeds, both the increase and decrease are deviations from near-sonic flow. Thus the cross sections of practically all the stream tubes about the body increase so that the streamlines are deflected outward more than they would be by thickness effects alone. It should be noted that this phenomenon does not occur for completely subsonic or completely supersonic flow, where an increase in stream-tube size on one side of the wing is compensated by a decrease on the other.

From the analytical results of references 1 and 2, it can be shown that the effective cross-sectional area S_{eff} of a lifting wing-body combination with an aspect ratio of order one traveling at transonic speed is

$$S_{\text{eff}} = \pi \left[r_{\text{eb}}^2 + \frac{\gamma + 1}{2} B \left(\frac{S_{\text{ref}}}{4\pi} \frac{dC_L}{dx} \right)^2 + \frac{1}{2\pi} S_{\text{ref}} C_L \sin \alpha \right] \quad (26)$$

where r_{eb} is the radius of the equivalent body and S_{ref} is the reference area for the lift coefficient. The analysis indicates that the constant B is related to the maximum radius of the equivalent body $r_{\text{eb,max}}$, the semispan b , and the length scale in the x -direction l by the equation

$$B = \log_e \left(\frac{l^2}{b r_{\text{eb,max}}} \right) \quad (27)$$

No information about l can be obtained from the analysis other than the initial assumptions that it is of the same general order of magnitude as b and is much larger than $r_{\text{eb,max}}$. Although it was assumed in references 1 and 2 that l was the configuration length, it would probably be more realistic to assume that l is the length of the lifting region.

In view of the uncertainty in the identity of l , it may be preferable to obtain the constant B from experiment rather than from equation (27). This might be accomplished by placing the model in a solid-wall wind tunnel at the zero-lift condition and at a subsonic Mach number somewhat below that required to choke the tunnel. The lift on the model would then be increased until the tunnel becomes choked. The maximum effective cross-sectional area of the model $S_{\text{eff,max}}$ is simply the area required to choke the tunnel, which is known as a function of Mach number. The constant B could then be determined from equation (26) with the derivative dC_L/dx evaluated either experimentally or analytically.

RESULTS

The results of the present method for incompressible, attached flow past a wing-body combination are compared with those of a standard linear panel method (ref. 18) in figure 5. The linear lift potential is obtained from the theory of Lawrence and Flax. The configuration which is shown on the left side of the figure is composed of an ogive-cylinder-ogive body and a flat-plate wing with a leading-edge sweep of 45° . The length of each ogive is one-quarter of the body length. The results for the body pressure distribution in the wing plane, that is, the pressure distribution along the intersection of the body surface and the wing plane, are compared on the right. In the region of the wing, the results shown are those for the root-chord pressure distribution. It is seen that the results of the two methods are in fair agreement.

In figure 6 the results of the two methods are compared for supersonic attached flow. The linear lift potential is obtained from quasi-conical theory. The shock wave and sonic-line locations as predicted by the present method are shown on the left side of the figure. It is seen that there is a slightly detached bow shock, a tail shock which intersects the body just upstream of the rear apex, a weak shock in the vicinity of the wing, and small pockets of subsonic flow at the ends of the body. The results for the body pressure distribution in the wing plane are compared on the right side of the figure. It is seen that there is good agreement in the vicinity of the wing. There is some disagreement on the forebody where the flow is transonic and hence where linear methods tend to be inaccurate. The ability of the present method to calculate transonic flow over slender bodies has been demonstrated by Bailey (ref. 16) and Barnwell (ref. 2). The disagreement in the results for the afterbody is not fully understood. It has been observed that the results of the present method sometimes deteriorate in regions where the body curvature increases instantaneously. It should be noted that this configuration with discontinuous changes in body curvature was chosen because of the requirement for the linear method that the body radius must be constant in the region of the wing.

An example of the type of results which the present method can provide for transonic flow past wing-body combinations is given in figure 7. The free-stream Mach number is 0.98, and the angle of attack is 6° . Slender-wing theory is used to determine the linear lift potential. The configuration is composed of a parabolic-arc-of-revolution body with a fineness ratio of 10 and a flat-plate wing with a strake. The shock-wave and sonic-line locations in the wing plane are shown on the left side of the figure. Note that there are two pockets of supersonic flow. The first pocket is initiated by the expansion around the forebody and is terminated by a small shock near the beginning of the apparent bump due to lift. (See eq. (26).) The second pocket is initiated by the expansion around the apparent bump due to lift and is terminated with a shock near the trailing edge of the wing. The pressure distribution is shown at the right. It can be seen that there are

shocks both above and beneath the wing, and that the strength of the shock above the wing is much greater than that of the shock beneath the wing.

The results of the present method for the dependence of the lift coefficient C_L on the angle of attack α for separated flow past a delta wing are compared in figure 8 with experiment and the results of other methods. The comparisons for low-speed flow are presented on the left side of the figure. The experimental data are those of Peckham (ref. 19). It is seen that the results of both Brown and Michael (ref. 11) and Smith (ref. 12) overpredict the data, the latter being more accurate than the former, and that the results of the suction analogy of Polhamus (ref. 20) are essentially in agreement with the data. It is also seen that the results of the present method overpredict the data to about the same degree as those of Smith. The suction analogy was not employed in the present method because the spanwise effects of vorticity cannot be determined with it. Results for supersonic flow with $M_\infty = 1.96$ are shown on the right side of the figure. The experimental data are those of Hill (ref. 21). It is seen that the trends for supersonic flow are the same as those for low-speed flow. The suction-analogy results for supersonic flow were obtained from reference 22.

The effects of leading-edge separation on transonic flow past a lifting wing-body are shown in figure 9. In this figure the results for attached and separated flow past a wing-body combination with $M_\infty = 0.98$ and $\alpha = 6^\circ$ are compared. On the left side of the figure it can be seen that the only effect of leading-edge separation on the shock-wave and sonic-line locations in the wing plane is the slight backward shift of the rear shock toward the trailing edge of the wing. The body-surface pressure distributions in the wing plane are compared on the right side of the figure. It is seen that separation affects the pressure distribution considerably both above and beneath the wing.

The results for transonic flow past a lifting configuration in free air and in a slotted tunnel are compared in figure 10. The Mach number and angle of attack are $M_\infty = 0.98$ and $\alpha = 12^\circ$, respectively. The slotted-tunnel case is for a configuration with a span of 1.524 m (60 in.) in an axisymmetric model of the Ames 14-foot transonic wind tunnel. Since this is an almost square tunnel with evenly spaced slots on all four walls, it can be approximated reasonably well in this manner. The results show that the outer part of the supersonic region is truncated by the tunnel wall and that the effect of the wall is to shift the shock forward.

The effects of a solid tunnel wall on the shock-wave and sonic-line locations in the wing plane for slightly supersonic flow past a lifting wing-body combination are shown in figure 11. The Mach number and angle of attack are $M_\infty = 1.02$ and $\alpha = 10^\circ$, respectively. The results for free air are shown on the left, and those for flow in the tunnel are shown at the right. It is seen that the bow shock is reflected at the tunnel wall and that the reflected shock intersects the aft shock in such a manner that the subsonic pocket at

the rear of the configuration is enlarged considerably. The location of the reflected shock in the region of the intersection is not shown because of the difficulty in locating weak oblique shock waves.

CONCLUDING REMARKS

An approximate method for calculating transonic flow about wing-body combinations at angles of attack of the order of the body thickness ratio has been presented. The region of applicability of the method extends from the supersonic Mach number at which the leading edge is sonic to zero. The method accounts for shock waves, leading-edge separation, and wind-tunnel wall effects and is computationally efficient. None of the computations presented in this paper required more than 4 minutes of CPU time on the CDC 6600 computer.

REFERENCES

1. Barnwell, R. W.: Transonic Flow About Lifting Configurations. AIAA J., vol. 11, no. 5, May 1973, pp. 764-766.
2. Barnwell, R. W.: Transonic Flow About Lifting Wing-Body Combinations. AIAA Paper 74-185, Jan.-Feb. 1974.
3. Cheng, H. K.; and Hafez, M. M.: Equivalence Rule and Transonic Flow Theory Involving Lift. AIAA J., vol. 11, no. 8, Aug. 1973, pp. 1210-1212.
4. Messiter, Arthur, F., Jr.: Expansion Procedures and Similarity Laws for Transonic Flow. AFOSR-TN-57-626, DDC No. AD 136 613, U.S. Air Force, Sept. 1957.
5. Heaslet, Max A.; and Spreiter, John R.: Three-Dimensional Transonic Flow Theory Applied to Slender Wings and Bodies. NACA Rep. 1318, 1957. (Supersedes NACA TN 3717.)
6. Spreiter, John R.; and Stahara, Stephen S.: Aerodynamics of Slender Bodies and Wing-Body Combinations at $M_\infty = 1$. AIAA J., vol. 9, no. 9, Sept. 1971, pp. 1784-1791.
7. Murman, Earll M.; and Cole, Julian D.: Calculation of Plane Steady Transonic Flows. AIAA J., vol. 9, no. 1, Jan. 1971, pp. 114-121.
8. Lawrence, H. R.; and Flax, A. H.: Wing-Body Interference at Subsonic and Supersonic Speeds - Survey and New Developments. J. Aeronaut. Sci., vol. 21, no. 5, May 1954, pp. 289-324, 328.
9. Lawrence, H. R.: The Lift Distribution on Low Aspect Ratio Wings at Subsonic Speeds. J. Aeronaut. Sci., vol. 18, no. 10, Oct. 1951, pp. 683-695.
10. Carafoli, E.: Wing Theory in Supersonic Flow. Pergamon Press, Ltd., c.1969, pp. 525-539.
11. Brown, Clinton E.; and Michael, William H., Jr.: On Slender Delta Wings With Leading-Edge Separation. NACA TN 3430, 1955.
12. Smith, J. H. B.: Improved Calculations of Leading-Edge Separation From Slender Delta Wings. Tech. Rep. 66070, British R.A.E., Mar. 1966.
13. Sacks, Alvin H.; Lundberg, Raymond E.; and Hanson, Charles W.: A Theoretical Investigation of the Aerodynamics of Slender Wing-Body Combinations Exhibiting Leading-Edge Separation. NASA CR-719, 1967.
14. Mangler, K. W.; and Smith, J. H. B.: A Theory of the Flow Past a Slender Delta Wing With Leading Edge Separation. Proc. Roy. Soc. (London), ser. A, vol. 251, no. 1265, May 26, 1959, pp. 200-217.

15. Baldwin, Barrett S., Jr.; Turner, John B.; and Knechtel, Earl D.: Wall Interference in Wind Tunnels With Slotted and Porous Boundaries at Subsonic Speeds. NACA TN 3176, 1954.
16. Bailey, Frank R.: Numerical Calculation of Transonic Flow About Slender Bodies of Revolution. NASA TN D-6582, 1971.
17. Murman, Earll M.: Analysis of Embedded Shock Waves Calculated by Relaxation Methods. AIAA J., vol. 12, no. 5, May 1974, pp. 626-633.
18. Woodward, Frank A.: Analysis and Design of Wing-Body Combinations at Subsonic and Supersonic Speeds. J. Aircraft, vol. 5, no. 6, Nov.-Dec. 1968, pp. 528-534.
19. Peckham, D. H.: Low-Speed Wind-Tunnel Tests on a Series of Uncambered Slender Pointed Wings With Sharp Edges. R. & M. No. 3186, British A.R.C., 1961.
20. Polhamus, Edward C.: A Concept of the Vortex Lift of Sharp-Edge Delta Wings Based on a Leading-Edge-Suction Analogy. NASA TN D-3767, 1966.
21. Hill, William A., Jr.: Experimental Lift of Low-Aspect-Ratio Triangular Wings at Large Angles of Attack and Supersonic Speeds. NACA RM A57I17, 1957.
22. Polhamus, Edward C.: Predictions of Vortex-Lift Characteristics by a Leading-Edge Suction Analogy. J. Aircraft, vol. 8, no. 4, Apr. 1971, pp. 193-196.

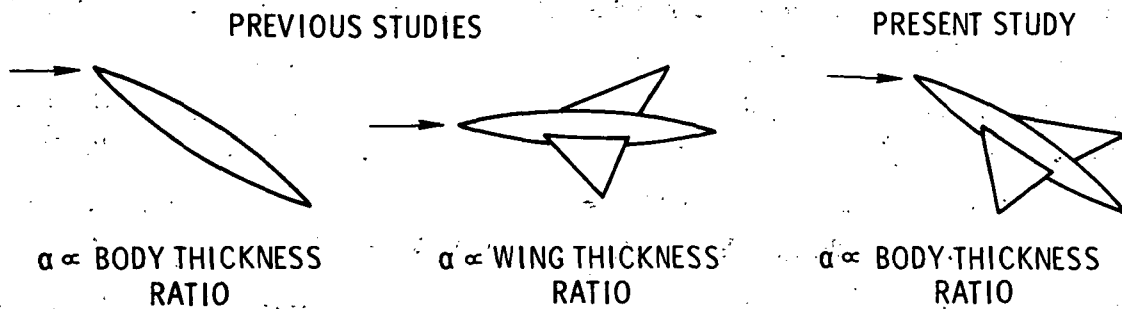


Figure 1.- Past and present applications of slender-wing and slender-body theory.

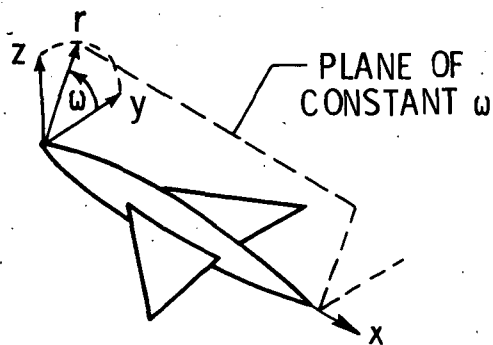
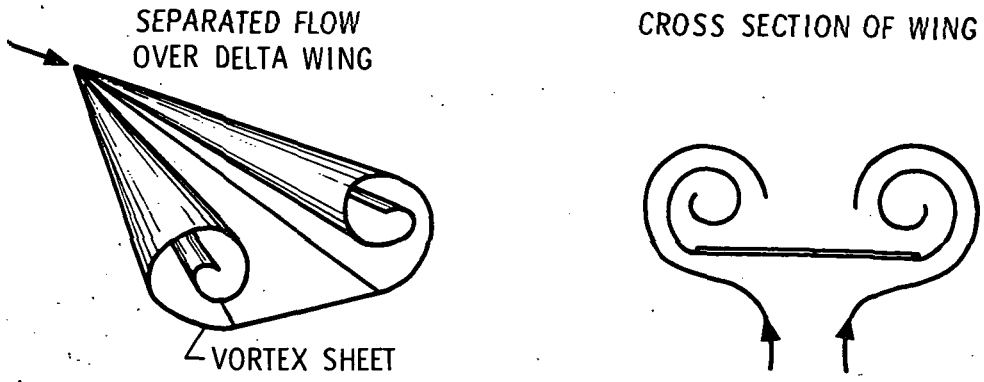


Figure 2.- Coordinate system.



APPROXIMATE MODELS




- BROWN AND MICHAEL:  + 2-D ATTACHED-FLOW SOLUTION
- SMITH:  + 2-D ATTACHED-FLOW SOLUTION
- PRESENT:  + 3-D ATTACHED-FLOW SOLUTION

Figure 3.- Models for leading-edge separation.

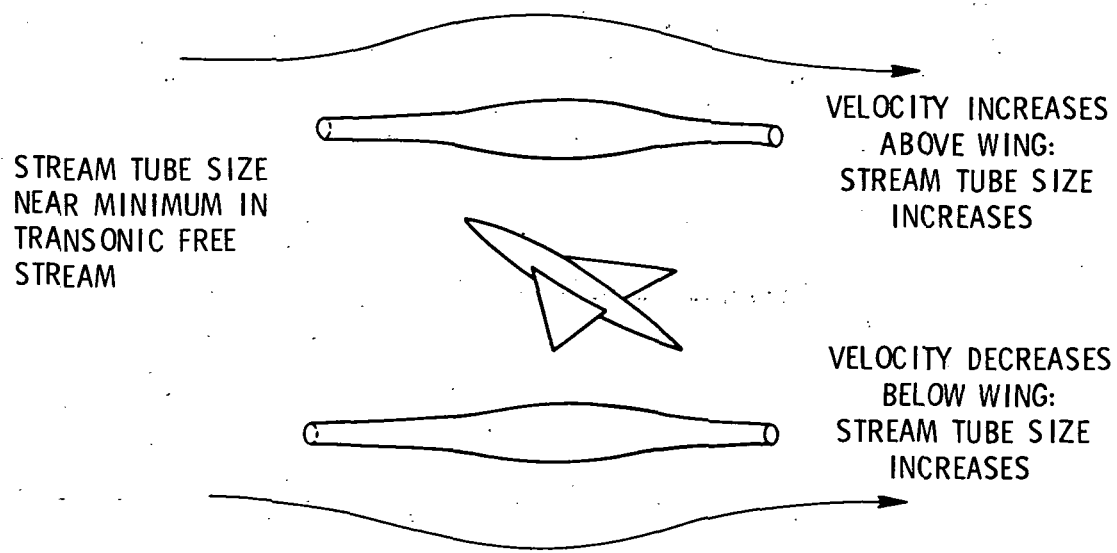


Figure 4.- Outward displacement of streamlines by both lift and thickness effects at transonic speeds.

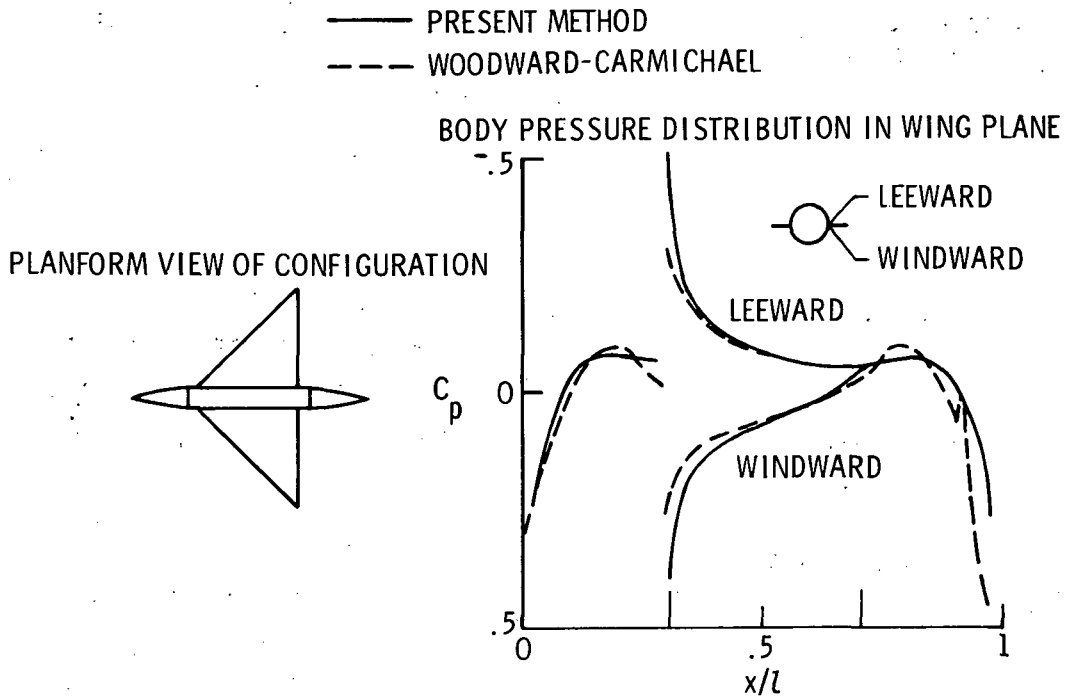


Figure 5.- Comparison of methods for subsonic flow. $M_\infty = 0$; $\alpha = 4^\circ$.

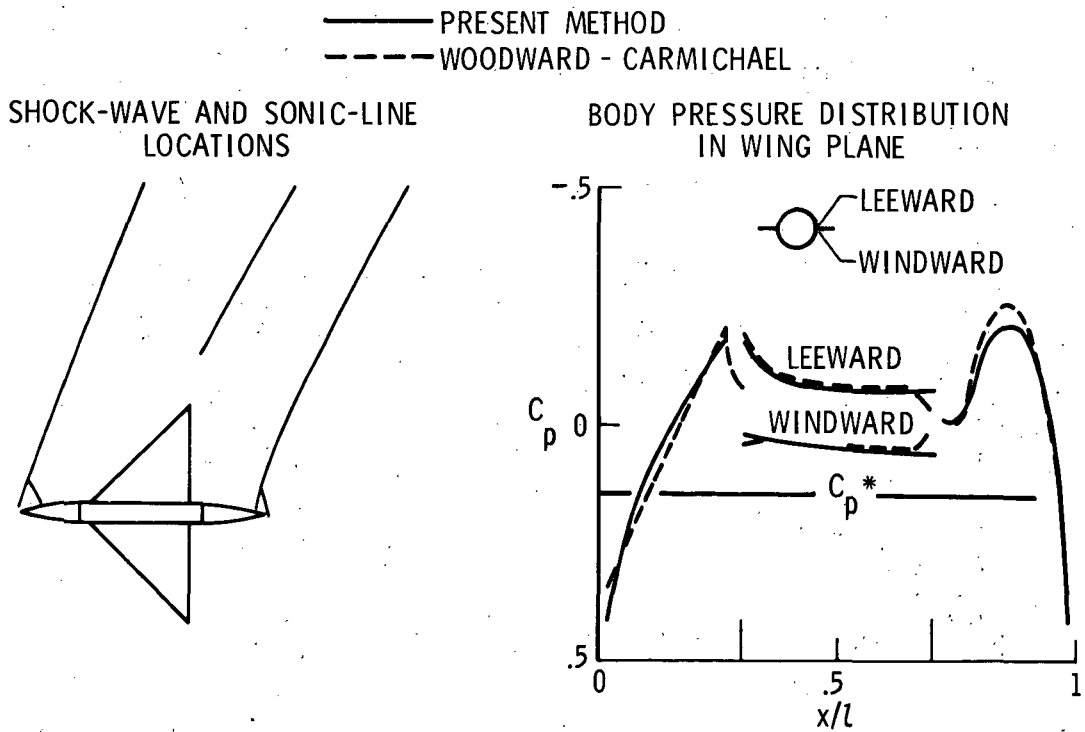
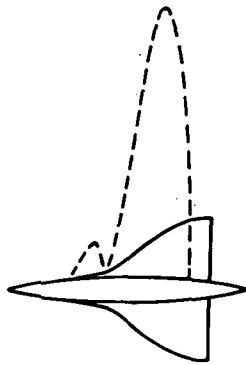


Figure 6.- Comparison of methods for supersonic flow. $M_\infty = 1.1$; $\alpha = 2^\circ$.

SHOCK-WAVE AND SONIC-LINE LOCATIONS



BODY PRESSURE DISTRIBUTION

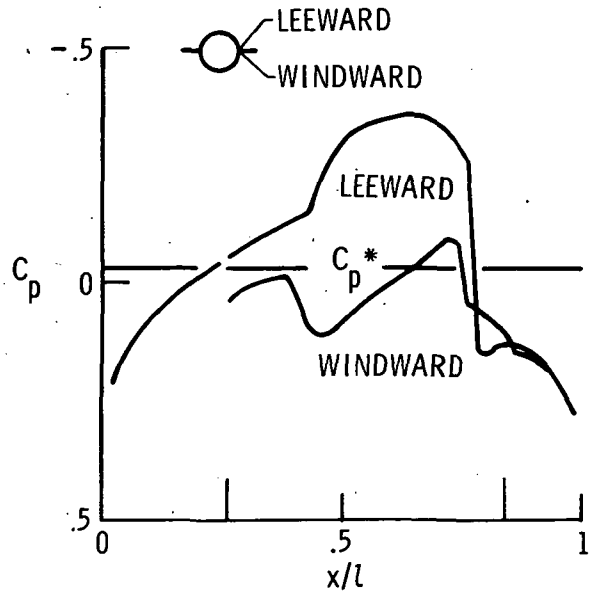


Figure 7.- Wing-plane results for transonic flow. $M_\infty = 0.98$; $\alpha = 6^\circ$.

- PRESENT METHOD
- - - BROWN AND MICHAEL
- SMITH
- - - SUCTION ANALOGY
- EXPERIMENT, PECKHAM
- EXPERIMENT, HILL

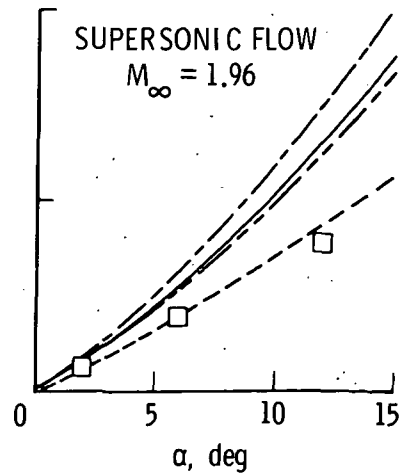
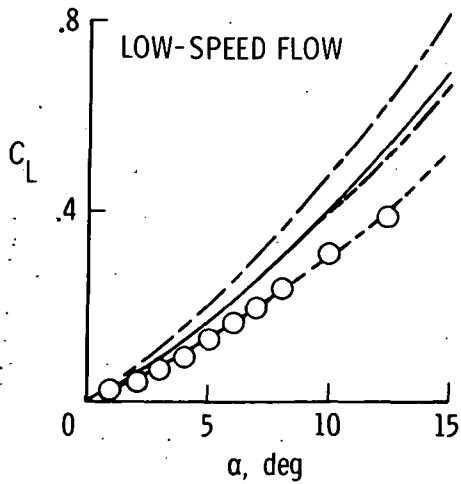


Figure 8.- Leading-edge separation for delta wing with aspect ratio of one.

SHOCK-WAVE AND SONIC-LINE LOCATIONS

BODY PRESSURE DISTRIBUTION IN WING PLANE

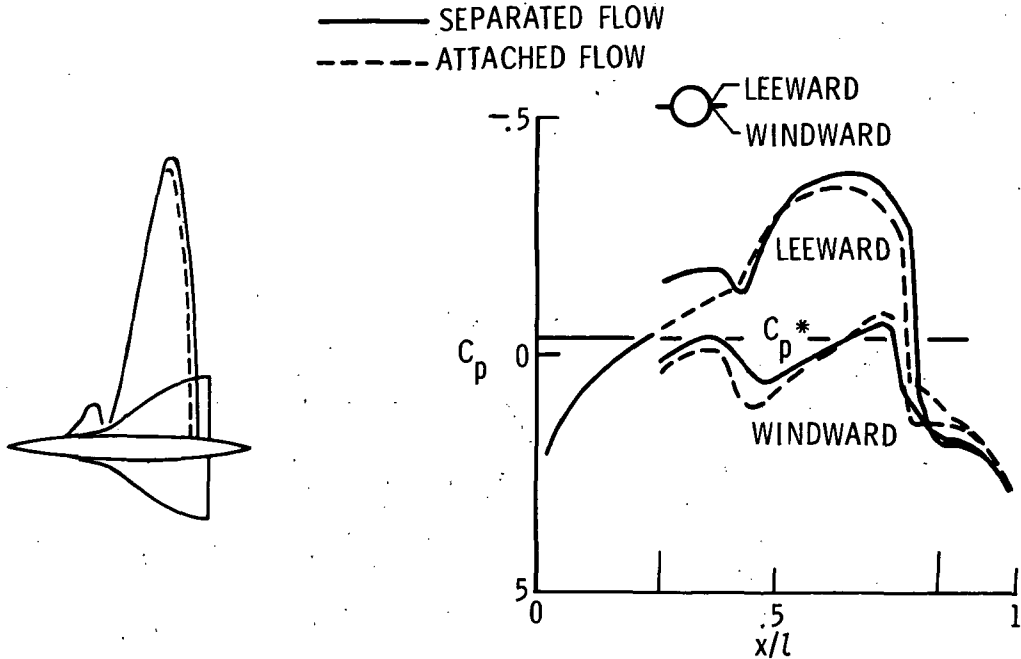


Figure 9.- Effect of leading-edge separation. $M_\infty = 0.98$; $\alpha = 6^\circ$.

SHOCK WAVE AND SONIC LINE

BODY PRESSURE DISTRIBUTION

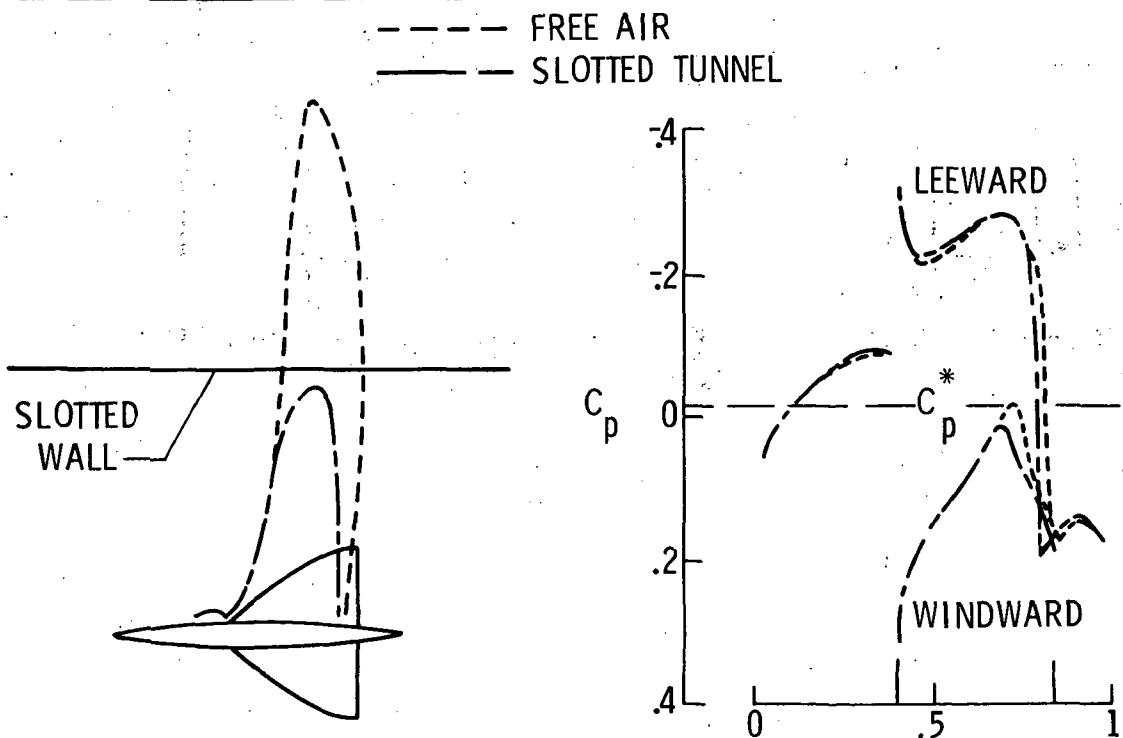


Figure 10.- Wing-plane results for free air and slotted tunnel. $M_\infty = 0.98$; $\alpha = 12^\circ$.

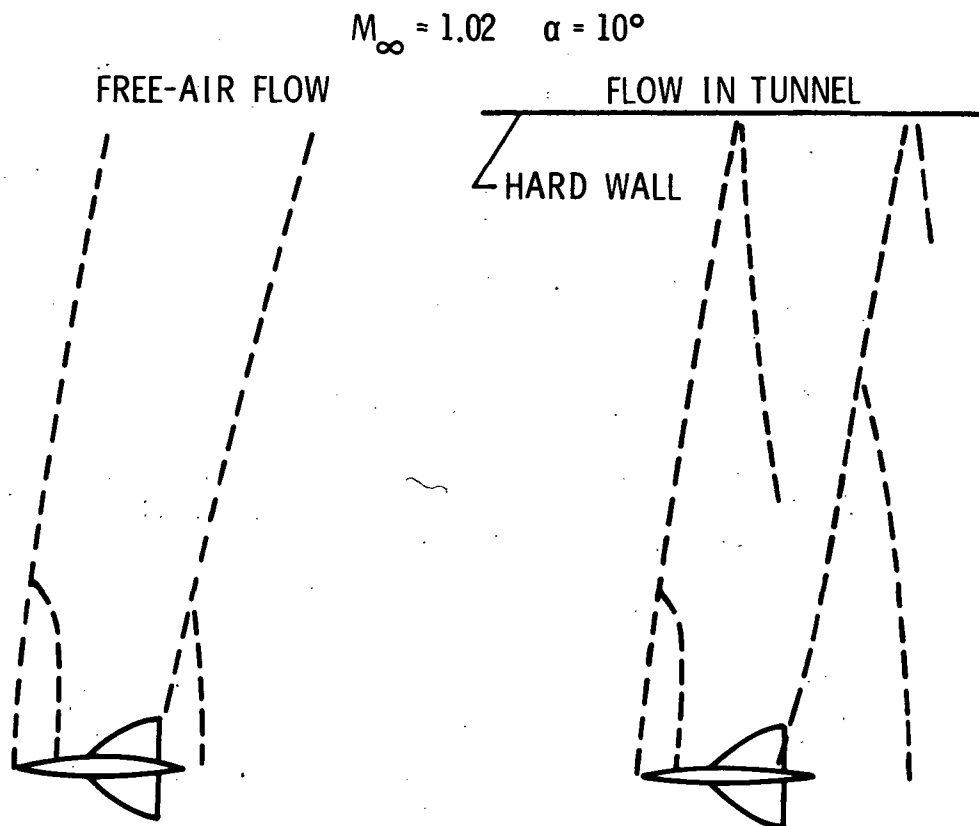


Figure 11.- Effect of tunnel wall on shock-wave and sonic-line locations.

$M_\infty = 1.02; \alpha = 10^\circ.$

Page intentionally left blank

RECENT ADVANCES AND CONCEPTS IN UNSTEADY AERODYNAMIC THEORY

By Samuel R. Bland
NASA Langley Research Center

SUMMARY

A survey of recent activity in unsteady aerodynamics is given with results taken from recent research sponsored by the Langley Research Center. The applicability of potential theory is illustrated for subsonic, transonic, and supersonic flows. The point of view is that of the aeroelastician, who is concerned chiefly with small amplitude harmonic motion. In the important area of transonic flow, the wide variety of current activities is described. The need for efficient approximate solutions, for high-quality benchmark solutions, and for reliable experimental data is pointed out.

INTRODUCTION

Historically, much of the interest in unsteady aerodynamic theory has been prompted by attempts to understand and predict flutter phenomena. Flutter is a self-excited aeroelastic instability in which aerodynamic, elastic, and inertia forces are coupled together (ref. 1, pp. 7-8). In flutter analysis, one is interested in the stability of infinitesimal oscillations of the structure. For this reason, the unsteady aerodynamicist is chiefly concerned with small amplitude harmonic motion. Since aircraft flutter problems generally are most severe at transonic speeds, the analyst must deal with this inherently difficult speed regime.

This paper provides a brief survey of recent research in unsteady aerodynamics. Although the results shown are taken from work performed for the Langley Research Center within the last 3 years, reference to other research is included. Since nearly all the work discussed depends on solution of the small disturbance potential equations, the paper first gives an outline of this theory. Results from linear lifting-surface theory for subsonic and supersonic flow are then presented. Currently, a variety of solutions to the unsteady transonic flow problem are under active development; this work is described in some detail. There is included in the paper some discussion of research which does not involve the potential flow formulation. The paper concludes with some comments on the current state of unsteady aerodynamic theory.

SYMBOLS

a_n	pressure series coefficients (eq. (26))
B	function describing body surface (eq. (3))
C_p	pressure coefficient
\hat{C}_p	steady flow part of C_p
\tilde{C}_p	unsteady flow part of C_p
\bar{C}_p	complex amplitude of \tilde{C}_p (eq. (19))
c	chord
f	steady flow part of h
g	unsteady flow part of h
\bar{g}	complex amplitude of g (eq. (18))
h	function describing body surface (eq. (6))
K	kernel function (eq. (25))
k	reduced frequency, $\omega l/U$
l	reference length
M	local Mach number
M_∞	free-stream Mach number
N	collocation order (eq. (26))
Δp	lifting pressure difference

q	dynamic pressure
s	semispan
t	time
U	free-stream velocity
w	vertical downwash velocity
x,y,z	Cartesian coordinates, x positive downstream
γ	ratio of specific heats
θ_n	pressure series functions (eq. (26))
ξ, η	dummy x,y variables (eqs. (25) and (26))
Φ	perturbation velocity potential
ϕ	steady flow part of Φ
$\tilde{\phi}$	unsteady flow part of Φ
$\bar{\phi}$	complex amplitude of $\tilde{\phi}$
ω	circular frequency of oscillation

Subscripts:

T	substantial time derivative, $U^{-1}(\)_t + (\)_x$
x,y,z,t	denotes differentiation

POTENTIAL THEORY

As is the case with steady flow, potential theory finds wide application in the analysis of unsteady flow. References 1 and 2 provide exhaustive treatments of the linearized theory of unsteady potential flow. Reference 3 presents the small perturbation equations for the nonlinear transonic flow. The results of such an analysis are briefly summarized below.

In terms of the potential for perturbations about a flow in the x-direction, the complete unsteady perturbation potential equation is

$$M_\infty^{-2} \nabla^2 \Phi - \Phi_{TT} = [(\gamma - 1) \nabla^2 \Phi + 2 \nabla \Phi \cdot \nabla] \Phi_T + \frac{1}{2} [(\gamma - 1) \nabla^2 \Phi + \nabla \Phi \cdot \nabla] (\nabla \Phi)^2 \quad (1)$$

where the substantial time derivative is indicated by

$$(\)_T = U^{-1} (\)_t + (\)_x \quad (2)$$

An alternate formulation employing local Mach number M rather than free-stream Mach number M_∞ is possible. The boundary condition for tangential flow on the surface of a body B is

$$B_T + \nabla \Phi \cdot \nabla B = 0 \quad (\text{on } B(x, y, z, t) = 0) \quad (3)$$

In addition, a suitable boundary condition on the wake and the requirement for outgoing waves at infinity are imposed. The expression for the pressure coefficient is

$$C_p = -\frac{2}{\gamma} M_\infty^{-2} \left(1 - \left\{ 1 - (\gamma - 1) M_\infty^2 \left[\Phi_T + \frac{1}{2} (\nabla \Phi)^2 \right] \right\}^{\gamma/(\gamma-1)} \right) \quad (4)$$

The small perturbation assumption may now be imposed to eliminate most of the nonlinear terms. Equation (1) becomes

$$\left[1 - M_\infty^2 - (\gamma + 1) M_\infty^2 \Phi_x - (\gamma - 1) \frac{M_\infty^2}{U} \Phi_t \right] \Phi_{xx} + \Phi_{yy} + \Phi_{zz} - 2 \frac{M_\infty^2}{U} \Phi_{xt} - \frac{M_\infty^2}{U^2} \Phi_{tt} = 0 \quad (5)$$

The nonlinear terms Φ_x and Φ_t are retained because for transonic flow they are of the same order as $1 - M_\infty^2$. The boundary condition on the body whose surface is specified by

$$z = h(x, y, z, t) \quad (6)$$

is

$$\Phi_z = h_x + U^{-1} h_t \quad (\text{on } z = 0) \quad (7)$$

and the pressure coefficient becomes

$$C_p = -2 \left(\Phi_x + U^{-1} \Phi_t \right) \quad (8)$$

The linear forms of these equations are consistent with the nonlinear equation (5).

In order to separate the unsteady from the steady flow effects the potential is written as the sum of steady and unsteady parts

$$\Phi(x, y, z, t) = \phi(x, y, z) + \tilde{\phi}(x, y, z, t) \quad (9)$$

The position of the body surface is represented in a similar fashion as

$$h(x,y,z,t) = f(x,y,z) + g(x,y,z,t) \quad (10)$$

The assumption is made that the unsteady terms $\tilde{\phi}$ and g are much smaller than the steady terms ϕ and f . The result of using equations (9) and (10) in equations (5) to (8) is a partial separation of the steady and unsteady flow effects. One obtains the usual small perturbation equation for the mean steady flow

$$\left[1 - M_\infty^2 - (\gamma + 1)M_\infty^2 \phi_x \right] \phi_{xx} + \phi_{yy} + \phi_{zz} = 0 \quad (11)$$

with boundary condition

$$\phi_z = f_x \quad (\text{on } z = 0) \quad (12)$$

and steady pressure coefficient

$$\hat{C}_p = -2\phi_x \quad (13)$$

The equations for the unsteady flow are

$$\begin{aligned} & \left[1 - M_\infty^2 - (\gamma + 1)M_\infty^2 \phi_x \right] \tilde{\phi}_{xx} + \tilde{\phi}_{yy} + \tilde{\phi}_{zz} - 2 \frac{M_\infty^2}{U} \tilde{\phi}_{xt} - \frac{M_\infty^2}{U^2} \tilde{\phi}_{tt} - (\gamma + 1)M_\infty^2 \phi_{xx} \tilde{\phi}_x \\ & - (\gamma - 1) \frac{M_\infty^2}{U} \phi_{xx} \tilde{\phi}_t = 0 \end{aligned} \quad (14)$$

with boundary condition

$$\tilde{\phi}_z = g_x + U^{-1}g_t \quad (\text{on } z = 0) \quad (15)$$

and unsteady pressure coefficient

$$\tilde{C}_p = -2(\tilde{\phi}_x + U^{-1}\tilde{\phi}_t) \quad (16)$$

The unsteady potential equation (14) is a linear equation for $\tilde{\phi}$. However, the equation has nonconstant coefficients which depend on the mean steady flow field ϕ . In particular, note that the type of equation (14) is the same as that of equation (11); that is, the unsteady flow problem is elliptic (subsonic) or hyperbolic (supersonic) at a point in accordance with the character of the mean steady flow at that point.

Since most applications of unsteady aerodynamics are concerned with harmonic motion, it is useful to eliminate the time variable in equations (14) to (16) by setting

$$\tilde{\phi}(x,y,z,t) = \bar{\phi}(x,y,z)e^{i\omega t} \quad (17)$$

$$g(x,y,z,t) = \bar{g}(x,y,z)e^{i\omega t} \quad (18)$$

$$\tilde{C}_p(x, y, z, t) = \bar{C}_p(x, y, z)e^{i\omega t} \quad (19)$$

Note that the amplitudes of the quantities on the right-hand side of these equations are complex. In terms of the reduced frequency $k = \omega l/U$ where l is a reference length, equations (14) to (16) become

$$\begin{aligned} & \left[1 - M_\infty^2 - (\gamma + 1)M_\infty^2 \phi_x \right] \bar{\phi}_{xx} + \bar{\phi}_{yy} + \bar{\phi}_{zz} - i2M_\infty^2 k \bar{\phi}_x + M_\infty^2 k^2 \bar{\phi} - (\gamma + 1)M_\infty^2 \phi_{xx} \bar{\phi}_x \\ & - i(\gamma - 1)M_\infty^2 k \phi_{xx} \bar{\phi} = 0 \end{aligned} \quad (20)$$

with boundary condition

$$\bar{\phi}_z = \bar{g}_x + ik\bar{g} \quad (\text{on } z = 0) \quad (21)$$

and unsteady pressure coefficient

$$\bar{C}_p = -2(\bar{\phi}_x + ik\bar{\phi}) \quad (22)$$

in which the reference length l was assumed to be equal to 1. It is important to note that the assumption of simple harmonic motion is useful only because the equations for $\bar{\phi}$ is linear.

Two further simplifications of equation (20) may be possible. If the free-stream Mach number is not close to 1, the product terms are small and may be neglected to obtain the usual constant coefficient equation for unsteady subsonic or supersonic flow

$$(1 - M_\infty^2) \bar{\phi}_{xx} + \bar{\phi}_{yy} + \bar{\phi}_{zz} - i2M_\infty^2 k \bar{\phi}_x + M_\infty^2 k^2 \bar{\phi} = 0 \quad (23)$$

Equation (23) implies that the local Mach number equals the free-stream Mach number. The second simplification of equation (20) is the linearized transonic flow equation (ref. 4)

$$\bar{\phi}_{yy} + \bar{\phi}_{zz} - i2M_\infty^2 k \bar{\phi}_x + M_\infty^2 k^2 \bar{\phi} = 0 \quad (24)$$

which may be used for relatively high reduced frequencies k , namely, for $k \gg |1 - M|$ where M is the local Mach number. Note that equation (24) is of parabolic type. Many solutions of equation (24) may be found in reference 4.

APPLICATIONS OF POTENTIAL THEORY

In this section of the paper, some recent results obtained through the use of potential theory are described. Separate subsections treat subsonic, supersonic, and transonic flow. Comparisons between theory and experiment are of two kinds. Where possible, measured and calculated pressures are shown. However, there is a dearth of recent experimental pressure data, especially at transonic speeds. The other kind of compari-

son involves flutter speeds. This comparison is less direct in that it involves factors in addition to the aerodynamics, namely, stiffness and mass characteristics of the surface.

Subsonic Lifting Surface Theory

In the case of subsonic flow, equation (23) may be solved by a superposition of elementary solutions, or by integral transform methods, to produce the downwash integral equation (ref. 5)

$$\frac{w(x,y)}{U} = \iint_S \frac{\Delta p(\xi,\eta)}{q} K(M_\infty, k, \xi-x, \eta-y) d\xi d\eta \quad (25)$$

which relates the known downwash velocity on the surface to the unknown lifting pressure distribution. The kernel function K is defined by a singular integral. The integration region S includes only the wing surface. The two solution methods in widespread use are described in the following subsections.

Doublet lattice method. - The doublet lattice method was first reported in reference 6. Subsequent refinements are given in references 7 and 8. In this procedure the lifting surfaces and bodies are covered with trapezoidal boxes as shown at the right in figure 1. Potential doublets are placed on the quarter-chord line of each box. The doublet strengths are determined by satisfying the known downwash condition at the box three-quarter-chord points. In addition, source singularities are placed along the center line of each body.

The results of a flutter calculation for the space shuttle vehicle are also shown in figure 1. These results are taken from reference 9. The experimental flutter speeds were obtained in the Langley 26-inch transonic tunnel for a series of nominally identical models. The agreement at $M_\infty = 0.65$ is good; the discrepancies at the higher speeds may be attributed to increasing wing-body interactions at transonic speeds. This particular result gives an indication of the kinds of complex configurations which may be treated with current subsonic theory.

Kernel function method. - The kernel function method (ref. 10) for the solution of the integral equation (25) proceeds as follows. The unknown pressure distribution is expanded in a series of known functions θ_n with unknown coefficients a_n such as

$$\frac{\Delta p(\xi,\eta)}{q} = \sum_{n=0}^N a_n \theta_n(\xi,\eta) \quad (26)$$

The functions θ_n are chosen to satisfy the known edge conditions on the lifting surface (e.g., the Kutta condition at the trailing edge).

Equation (26) is substituted into equation (25) and the integration performed for a set of N points (x_i, y_i) at which the downwash is known from the boundary condition. The resulting set of N simultaneous linear equations is then solved for the coefficients a_n .

Two recent applications of the subsonic kernel function method are shown in figures 2 and 3. The result in figure 2 gives the real part of the lifting pressure for a wing with an oscillating control surface, reported in reference 11. (Also, see ref. 12.) The method used treats the control surface edge singularities meticulously. The experimental data are from reference 13. The agreement is excellent except near the control edges - the analysis treats the edge gaps as sealed. Note also the singularity in the pressure at the leading edge which arises in the small disturbance linear theory.

A comparison of calculated and measured flutter speeds for a thin, sharp-edged wing with two simulated engine nacelles is shown in figure 3. The experimental data, taken from reference 14, were obtained in the Langley transonic dynamics tunnel. The dimension shown is for the "large" wing; the "small" wings were about half the size of the large wing. In an attempt to remove the scatter in the data caused by model differences, the data for the small wings have been adjusted so that the flutter speeds for all three wings agree at $M_\infty = 0.665$. The unpublished calculations were made by Robert M. Bennett of the Langley Research Center. These calculations used measured vibration data for the first nine elastic modes of the large wing. The collocation order was $N = 64$. The agreement between the measured and calculated results for this wing is excellent, even at $M_\infty = 0.907$. These subsonic theory calculations were made up to $M_\infty = 0.99$, well within the range where transonic flow effects are important. Such good agreement at transonic speeds would not normally be expected.

Supersonic Lifting Surface Theory

Although no results for supersonic flow are given herein, a brief outline of current methods is included in this section.

As in subsonic flow, equation (23) may be solved to yield an integral equation of the same form as equation (25). Recent work with this supersonic kernel function method of solution is reported in references 15 to 17.

For a planform with supersonic leading edge, a direct solution for the velocity potential as an integral transform of the downwash is possible. (See, e.g., ref. 18.) This technique is also applicable to a wing with subsonic leading edge by using Evvard's concept of adding a diaphragm of zero pressure difference to the wing. The Mach box methods of references 19 to 21 are implementations of this approach. The triangular element method of reference 22 is a recent development which avoids the Mach box problems of

fitting a swept wing with a grid of rectangular boxes and changing box shape with Mach number.

Recently, the method of reference 22 has been recast to use the integrated potential formulation of reference 23. This new implementation, which avoids the use of diaphragm regions, is reported in reference 24.

Transonic Theory

Currently, there is a great deal of research, using a wide variety of methods, being conducted on the unsteady transonic flow problem. The success occurring with steady flow solutions, the rapid increase in computer power, and the criticality of transonic aeroelastic problems have combined to encourage this development. In this section of the paper, many of these new developments are briefly described, and some results are given.

Local linearization method. - The local linearization method of Spreiter has been applied to the two-dimensional oscillating airfoil in reference 25. In this method, a form of equation (20) is solved as follows. First, the location of the sonic point is determined from the steady flow solution. Second, the nonconstant coefficients are replaced by different constants on the subsonic and supersonic portions of the surface. Third, the resulting simpler problem is solved for $\bar{\phi}(x,y)$ as a function of these constants. Fourth, $\bar{\phi}_{xx}(x,0)$ is evaluated on the airfoil surface. Fifth, the constants are replaced by the functions they represent. Finally, the equation is integrated twice numerically to obtain the potential on the surface.

Calculations for a 6-percent-thick parabolic arc airfoil oscillating in plunge for $M_\infty = 1.0$ are shown in figure 4. At the higher frequency, this nonlinear theory agrees quite well with the linear theory which assumes constant Mach 1 flow over the surface. At the lower frequency, the effect of thickness on the local Mach number produces significant differences between the linear and nonlinear results. This conclusion is consistent with the use of equation (24) at high frequencies.

A similar method to the one described in this section is reported in reference 26.

Layered medium analysis. - The layered medium theory (ref. 27) uses linear unsteady flow solutions separately for the subsonic and supersonic regions on an airfoil in supercritical flow. These solutions are coupled together by conditions on the sonic line and shock wave. The nonuniform flow within the supercritical region is approximated by dividing this region into several horizontal layers, within each of which the supersonic Mach number is constant. The vortex sheets separating these layers give rise to acoustic impedance changes which can result in pressure disturbances being reflected back onto the airfoil surface. No calculated results are available.

Finite-difference solution of parabolic equation. - The finite-difference analysis of references 28 and 29 is based upon the following approximation to equation (14):

$$\tilde{\phi}_{yy} + \tilde{\phi}_{zz} - 2 \frac{M_{\infty}^2}{U} \tilde{\phi}_{xt} - \frac{M_{\infty}^2}{U^2} \tilde{\phi}_{tt} - (\gamma + 1) M_{\infty}^2 \phi_{xx} \tilde{\phi}_x = 0 \quad (27)$$

Equation (27), which is of parabolic type, may be used when the local Mach number is close to 1. In reference 28, a three-dimensional difference method is used to solve this equation for the harmonic motion case. Coordinate transformations are used to develop a computationally efficient grid. The parabolic character of the equation allows a marching technique to be used in the downstream x-direction. The method does not account for shock waves on the surface and permits no upstream propagation of disturbances.

Coordinate transformation based on local Mach number. - In the method of reference 30, equation (14) is approximated by

$$\tilde{\phi}_{yy} + \tilde{\phi}_{zz} - 2 \frac{M^2}{U} \tilde{\phi}_{xt} - \frac{M^2}{U^2} \tilde{\phi}_{tt} = 0 \quad (28)$$

in which the nonconstant coefficients of equation (14) have been expressed in terms of local Mach number M . With the assumption of harmonic motion, this equation is also of parabolic type and is therefore subject to limitations similar to those of the preceding method. Given the local steady Mach number distribution $M(x,y)$ or pressure distribution $\hat{C}_p(x,y)$ the coordinate transformation

$$\tilde{y} = yM(x,y) \quad (29)$$

$$\tilde{z} = zM(x,y) \quad (30)$$

is used in equation (28) to obtain

$$\bar{\phi}_{\tilde{y}\tilde{y}} + \bar{\phi}_{\tilde{z}\tilde{z}} - i2k\bar{\phi}_x + k^2\bar{\phi} = 0 \quad (31)$$

which is the linearized transonic flow equation (24) for $M_{\infty} = 1$ in the transformed coordinates x, \tilde{y}, \tilde{z} . This transformation has the effect of distorting the original planform into a different planform in a uniform Mach 1 flow. Therefore, any method for solving the linearized transonic flow equation (24) may be used in this transformed space. The sonic-box method of reference 31 was used in references 30 and 32.

A flutter calculation (from ref. 32) using the method of local Mach number transformation is given in figure 5. The delta wing shown has an elliptical cross section in the spanwise direction. Flutter speed ratio is plotted as a function of wing thickness ratio. The detrimental effect of wing thickness on the flutter speed is due solely to the thickness effect in the aerodynamics.

Mixed flow analysis. - The method of references 33 to 35 may be used for multiple lifting surfaces in mixed subsonic-supersonic flow. The wing is divided into subsurfaces on which the flow is either subsonic or supersonic. Either subsonic or supersonic kernel function aerodynamics, as appropriate, is used on each subsurface. In addition, the local Mach number is used at each point. This method requires this mean (steady flow) local Mach number as input from another source. A recent refinement (ref. 35) is the inclusion of a doublet singularity to represent the unsteady flow shock condition.

Measured and calculated pressure distributions for an oscillating wing are shown in figure 6. The calculations are from reference 35; the measurements, from reference 36. The local Mach number distribution, shown for a section near midchord, was used as input; the supersonic kernel function was employed ahead of the shock and the subsonic kernel function aft of the shock. The uniform flow calculation was carried out with the subsonic kernel function at $M_\infty = 0.997$. The mixed flow calculation, which includes the shock condition, provides somewhat better agreement with experiment.

Finite-difference analysis. - The finite-difference solution for steady transonic flow (ref. 37) has been extended in references 3 and 38 to provide a solution of equation (20) for two-dimensional flow. A similar analysis is reported in reference 39.

The finite-difference solution uses a rectangular mesh of points as indicated in figure 7. The mean steady flow problem (eq. (11)) is solved first on the same mesh to provide the nonconstant coefficient data for the unsteady problem (eq. (20)). The mesh employs a nonuniform spacing which clusters grid points near the airfoil edges. The far-field boundary conditions are determined from an application of Green's theorem in a manner similar to that of reference 40. It was found that using a condition on the potential $\bar{\phi}$ on the upper and lower boundaries and a condition on the pressure $\bar{\phi}_x + ik\bar{\phi}$ on the up- and down-stream boundaries gave better results.

A result for an NACA 64A006 airfoil with an oscillating quarter-chord flap is shown in figure 8. The experimental pressure data are taken from reference 41. The calculation shown differs somewhat from the result for this case in figure 12 of reference 3. The calculation herein was made recently by the Boeing Company under NASA contract. At this supercritical $M_\infty = 0.85$, a shock wave is located near midchord. The second pressure peak is caused by the downwash discontinuity at the hingeline of the flap. In general, the agreement between theory and experiment is qualitatively good.

Reference 3 contains the analysis for the three-dimensional finite-difference solution for a swept, finite wing. A computer program for the wing case has been developed recently by the Boeing Company.

Finite-element analysis. - Finite-element methods are widely used in structural analysis, for which the governing equations are elliptic. Such methods offer promise for

solving aerodynamic problems with fewer elements than the number of points required in a finite-difference analysis. Recent applications of the method to the oscillating airfoil are reported in references 42 and 43.

Unified Methods

The implementations of potential theory described up to this point are each tailored to a specific Mach number range. There is a need for a unified approach to the subsonic, supersonic, and, if possible, transonic speed regimes. The introduction of aeroelastic calculations into NASTRAN (ref. 44) and other large computing programs and the trend towards automated design have emphasized this need. Currently, there is research underway in several aerospace companies to develop panel methods for supersonic flow which are compatible with the doublet lattice scheme for subsonic flow. Several of these efforts are reported in references 45 and 46. Within the present state of the art, the aeroelastic addition to NASTRAN has had to use different paneling methods for subsonic (doublet lattice) and supersonic (Mach box) flow.

The method of references 47 to 51, described in reference 52, is a notable success in providing a unified method. This analysis uses a Green's function procedure with a general quadrilateral paneling scheme on both lifting surfaces and bodies. Wing thickness is taken into account routinely. A time-dependent, as opposed to harmonic, formulation has also been developed.

NONPOTENTIAL FLOW

No attempt is made in this paper to give a complete survey of nonpotential flow analyses for the unsteady flow problem. However, several items are cited to give an indication of the possibilities.

Solutions of the inviscid, time-dependent Euler equations provide a needed check on the accuracy and limitations of potential theory, particularly at transonic speeds. Several groups are actively pursuing this approach using numerical integration in time of the finite-difference form of the Euler equations. References 53 and 54 represent one such approach. Another analysis of this type is reported in references 55 to 57. Results are given for pitch oscillations at several frequencies for an NACA 64A410 airfoil at $M_\infty = 0.72$.

The work of references 58 and 59 represents one attempt to include viscous effects in the analysis of the oscillating airfoil. A finite-element method is used to solve the Navier-Stokes equations for incompressible flow. Results are given for an oscillating NACA 0012 airfoil at a Reynolds number of 10^3 in reference 58.

CONCLUDING REMARKS

This paper has presented a survey of recent research in theoretical unsteady aerodynamics, primarily from the point of view of the aeroelastician concerned with fixed-wing aircraft. The problems of rotor aerodynamics, hypersonic flow, and vortex flows have not been addressed. Within this limited scope, several conclusions may be made as follows:

1. Potential theory can provide excellent results, at least for subsonic and supersonic flow.
2. Good results from potential theory depend on a careful implementation of the particular solution procedure employed.
3. The transonic problem is receiving the emphasis it warrants and progress is being made.
4. There is a strong need for benchmark solutions of the complete inviscid equations with which to assess the limitations of potential flow analyses, particularly in transonic flow.
5. The requirement in flutter analysis to perform many aerodynamic calculations leads to a need for approximate methods whose limitations are known.
6. Current interest in active control of aeroelastic response has pointed out a need for time-dependent, as opposed to frequency-dependent, aerodynamics and an increasing need to include separated flow effects.

An indication of the importance of careful implementation of a solution method may be seen from the following typical computing times and storage requirements to perform a subsonic calculation for one Mach number and frequency on the Control Data (CDC) 6600 computer system: (1) kernel function, 24 seconds, 16000g storage; (2) kernel function, 196 seconds, 65000g storage; (3) doublet lattice, 84 seconds, 70000g storage. Program (1) is highly optimized for a planar wing; program (2) includes sophisticated treatment of control surfaces; program (3) has the capability of treating nonplanar wing-body problems. By way of comparison, a finite-difference calculation of the potential flow for the two-dimensional oscillating airfoil requires several minutes. A benchmark solution of the time-dependent Euler equations for the airfoil can require as much as 7 hours on CDC 7600.

In addition to the need for benchmark analytical results, there is a need for accurate surface pressure measurements on both two- and three-dimensional configurations.

REFERENCES

1. Bisplinghoff, Raymond L.; Ashley, Holt; and Halfman, Robert L.: *Aeroelasticity*. Addison-Wesley Pub. Co., Inc., c.1955.
2. Miles, John W.: *The Potential Theory of Unsteady Supersonic Flow*. Cambridge Univ. Press, 1959.
3. Ehlers, F. Edward: *A Finite Difference Method for the Solution of the Transonic Flow Around Harmonically Oscillating Wings*. NASA CR-2257, 1974.
4. Landahl, Mårten T.: *Unsteady Transonic Flow*. Pergamon Press, Inc., 1961.
5. Watkins, Charles E.; Runyan, Harry L.; and Woolston, Donald S.: *On the Kernel Function of the Integral Equation Relating the Lift and Downwash Distributions of Oscillating Finite Wings in Subsonic Flow*. NACA Rep. 1234, 1955. (Supersedes NACA TN 3131.)
6. Albano, Edward; and Rodden, William P.: *A Doublet-Lattice Method for Calculating Lift Distributions on Oscillating Surfaces in Subsonic Flows*. AIAA J., vol. 7, no. 2, Feb. 1969, pp. 279-285; Errata, vol. 7, no. 11, Nov. 1969, p. 2192.
7. Rodden, W. P.; Giesing, J. P.; and Kalman, T. P.: *Refinement of the Nonplanar Aspects of the Subsonic Doublet-Lattice Lifting Surface Method*. J. Aircraft, vol. 9, no. 1, Jan. 1972, pp. 69-73.
8. Giesing, J. P.; Kálmán, T. P.; and Rodden, W. P.: *Subsonic Steady and Oscillatory Aerodynamics for Multiple Interfering Wings and Bodies*. J. Aircraft, vol. 9, no. 10, Oct. 1972, pp. 693-702.
9. Chipman, Richard R.; and Rauch, Frank J.: *Analytical and Experimental Study of the Effects of Wing-Body Aerodynamic Interaction on Space Shuttle Subsonic Flutter*. NASA CR-2488, 1975.
10. Watkins, Charles E.; Woolston, Donald S.; and Cunningham, Herbert J.: *A Systematic Kernel Function Procedure for Determining Aerodynamic Forces on Oscillating or Steady Finite Wings at Subsonic Speeds*. NASA TR R-48, 1959.
11. Rowe, W. S.; Redman, M. C.; Ehlers, F. E.; and Sebastian, J. D.: *Prediction of Unsteady Aerodynamic Loadings Caused by Leading Edge and Trailing Edge Control Surface Motions in Subsonic Compressible Flow - Analysis and Results*. NASA CR-2543, 1975.
12. Rowe, W. S.; Sebastian, J. D.; and Redman, M. C.: *Some Recent Developments in Predicting Unsteady Loadings Caused by Control Surface Motions*. AIAA Paper 75-101, Jan. 1975.

13. Försching, H.; Triebstein, H.; and Wagner, J.: Pressure Measurements on an Harmonically Oscillating Swept Wing With Two Control Surfaces in Incompressible Flow. Symposium on Unsteady Aerodynamics for Aeroelastic Analyses of Interfering Surfaces - Part II, AGARD CP-80-71, Apr. 1971.
14. Sandford, Maynard C.; Ruhlin, Charles L.; and Abel, Irving: Transonic Flutter Study of a 50.5° Cropped-Delta Wing With Two Rearward-Mounted Nacelles. NASA TN D-7544, 1974.
15. Cunningham, Herbert J.: Application of a Supersonic Kernel-Function Procedure to Flutter Analysis of Thin Lifting Surfaces. NASA TN D-6012, 1970.
16. Cunningham, Atlee M., Jr.: Oscillatory Supersonic Kernel Function Method for Isolated Wings. J. Aircraft, vol. 11, no. 10, Oct. 1974, pp. 609-615.
17. Cunningham, Atlee M., Jr.: Oscillatory Supersonic Kernel Function Method for Interfering Surfaces. J. Aircraft, vol. 11, no. 11, Nov. 1974, pp. 664-670.
18. Pines, Samuel; Dugundji, John; and Neuringer, Joseph: Aerodynamic Flutter Derivatives for a Flexible Wing With Supersonic and Subsonic Edges. J. Aeronaut. Sci., vol. 22, no. 10, Oct. 1955, pp. 693-700.
19. Andrew, Lowell V.: Unsteady Aerodynamics for Advanced Configurations. Part VI - A Supersonic Mach Box Method Applied to T-Tails, V-Tails, and Top-Mounted Vertical Tails. FDL-TDR-64-152, Pt. VI, U.S. Air Force, May 1971.
20. Donato, Vincent W.; and Huhn, Charles R., Jr.: Supersonic Unsteady Aerodynamics for Wings With Trailing Edge Control Surfaces and Folded Tips. AFFDL-TR-68-30, U.S. Air Force, Aug. 1968. (Available from DDC as AD 840 598.)
21. Li, Jack Morito; and Rowe, William S.: Unsteady Aerodynamics of Nonplanar Wings and Wing-Tail Configurations of Elastic Flight Vehicles in Supersonic Flight. J. Aircraft, vol. 10, no. 1, Jan. 1973, pp. 19-27.
22. Appa, Kari; and Smith, G. Charles C.: Finite Element Supersonic Aerodynamics for Oscillating Parallel Wings. J. Aircraft, vol. 11, no. 8, Aug. 1974, pp. 433-434.
23. Jones, W. P.: Supersonic Theory for Oscillating Wings of Any Plan Form. R. & M. 2655, British A.R.C., 1953.
24. Appa, Kari: Integrated Potential Formulation of Unsteady Supersonic Aerodynamics for Interacting Wings. NASA CR-132547, [1974].
25. Stahara, Stephen S.; and Spreiter, John R.: Development of a Nonlinear Unsteady Transonic Flow Theory. NASA CR-2258, 1973.
26. Isogai, K.: Unsteady Transonic Flow Over Oscillating Circular-Arc Airfoils. AIAA Paper No. 74-360, Apr. 1974.

27. Revell, James D.: Research on Unsteady Transonic Flow Theory. NASA CR-112114, 1973.
28. Kimble, K. R.; and Wu, J. M.: Numerical Solution for Unsteady Sonic Flow Over Thin Wings. NASA Grant NGR-43-001-102, Univ. of Tennessee Space Inst., Aug. 1974. (Available as NASA CR-141114.)
29. Kimble, K. R.; and Wu, J. M.: Numerical Calculation of Unsteady Forces Over Thin Pointed Wings in Sonic Flow. Abstracts of Papers for Symposium on Unsteady Aerodynamics (University of Arizona), U.S. Air Force Office Sci. Res., Mar. 1975, pp. 69-73.
30. Ruo, S. Y.; and Theisen, J. G.: Calculation of Unsteady Transonic Aerodynamics for Oscillating Wings With Thickness. NASA CR-2259, 1975.
31. Rodemich, E. R.; and Andrew, L. V.: Unsteady Aerodynamics for Advanced Configurations. Part II - A Transonic Box Method for Planar Lifting Surfaces. FDL-TDR-64-152, Pt. II, U.S. Air Force, May 1965.
32. Ruo, S. Y.; Yates, E. Carson, Jr.; and Theisen, J. G.: Calculation of Unsteady Transonic Aerodynamics for Oscillating Wings With Thickness. J. Aircraft, vol. 11, no. 10, Oct. 1974, pp. 601-608.
33. Cunningham, Atlee M., Jr.: The Application of General Aerodynamic Lifting Surface Elements to Problems in Unsteady Transonic Flow. NASA CR-112264, 1973.
34. Cunningham, Atlee M., Jr.: An Oscillatory Kernel Function Method for Lifting Surfaces in Mixed Transonic Flow. AIAA Paper No. 74-359, Apr. 1974.
35. Cunningham, Atlee M., Jr.: Further Developments in the Prediction of Oscillatory Aerodynamics in Mixed Transonic Flow. AIAA Paper No. 75-99, Jan. 1975.
36. Becker, J.: Vergleich gemessener und berechneter instationärer Druckverteilungen für den hohen Unterschall an einem elastischen gepfeilten Flügel. EWR-Bericht Nr. 403-69, Messerschmitt-Bolkow-Blohm, Sept. 1969.
37. Murman, Earll M.; and Cole, Julian D.: Calculation of Plane Steady Transonic Flows. AIAA J., vol. 9, no. 1, Jan. 1971, pp. 114-121.
38. Ehlers, F. Edward: A Finite Difference Method for the Solution of the Transonic Flow Around Harmonically Oscillating Wings. AIAA Paper No. 74-543, June 1974.
39. Traci, R. M.; Albano, E. D.; Farr, J. L., Jr.; and Cheng, H. K.: Small Disturbance Transonic Flows About Oscillating Airfoils. AFFDL-TR-74-37, U.S. Air Force, June 1974.

40. Klunker, E. B.: Contribution to Methods for Calculating the Flow About Thin Lifting Wings at Transonic Speeds – Analytic Expressions for the Far Field. NASA TN D-6530, 1971.
41. Tijdeman, H.; and Schippers, P.: Results of Pressure Measurements on an Airfoil With Oscillating Flap in Two-Dimensional High Subsonic and Transonic Flow (Zero Incidence and Zero Mean Flap Position). NLR TR 73078 U, Nat. Lucht-Ruimtevaartlab. (Amsterdam), July 13, 1973.
42. Chan, S. T. K.; and Brashears, M. R.: Finite Element Analysis of Transonic Flow. AFFDL-TR-74-11, U.S. Air Force, Mar. 1974.
43. Chan, S. T. K.; Brashears, M. R.; and Young, V. Y. C.: Finite Element Analysis of Transonic Flow by the Method of Weighted Residuals. AIAA Paper 75-79, Jan. 1975.
44. MacNeal-Schwendler Corp.: Aeroelastic Addition for NASTRAN (Subsonic Flutter). NASA CR-132334, 1973.
45. Brock, B. J.; and Griffin, J. A., Jr.: The Supersonic Doublet-Lattice Method – A Comparison of Two Approaches. AIAA Paper 75-760, May 1975.
46. Giesing, Joseph P.; and Kalman, Terez: Oscillatory Supersonic Lifting Surface Theory Using a Finite Element Doublet Representation. AIAA Paper 75-761, May 1975.
47. Morino, Luigi: Unsteady Compressible Potential Flow Around Lifting Bodies: General Theory. AIAA Paper No. 73-196, Jan. 1973.
48. Morino, Luigi; and Kuo, Ching-Chiang: Unsteady Subsonic Compressible Flow Around Finite Thickness Wings. AIAA Paper No. 73-313, Mar. 1973.
49. Chen, Lee-Tzong; Suciu, Emil O.; and Morino, Luigi: A Finite Element Method for Potential Aerodynamics Around Complex Configurations. AIAA Paper No. 74-107, Jan.-Feb. 1974.
50. Morino, Luigi; and Kuo, Ching-Chiang: Subsonic Potential Aerodynamics for Complex Configurations: A General Theory. AIAA J., vol. 12, no. 2, Feb. 1974, pp. 191-197.
51. Morino, Luigi: A General Theory of Unsteady Compressible Potential Aerodynamics. NASA CR-2464, 1974.
52. Morino, Luigi; and Chen, Lee-Tzong: Indicial Compressible Potential Aerodynamics Around Complex Aircraft Configurations. Aerodynamic Analyses Requiring Advanced Computers, Part II, NASA SP-347, 1975, pp. 1067-1110.
53. Beam, Richard M.; and Warming, R. F.: Numerical Calculations of Two-Dimensional, Unsteady Transonic Flows With Circulation. NASA TN D-7605, 1974.

54. Beam, Richard M.; and Ballhaus, William F.: Numerical Integration of the Small-Disturbance Potential and Euler Equations for Unsteady Transonic Flow. Aerodynamic Analyses Requiring Advanced Computers, Part II, NASA SP-347, 1975, pp. 789-809.
55. Magnus, R.; and Yoshihara, H.: Finite Difference Calculations of the NACA 64A-410 Airfoil Oscillating Sinusoidally in Pitch at $M_\infty = 0.72$. CASD-NSC-74-004 (Contract N00014-73-C-0294), Convair Div., General Dynamics, Aug. 1, 1974. (Available from DDC as AD 782 684.)
56. Magnus, R. J.; and Yoshihara, H.: Calculations of Transonic Flow Over an Oscillating Airfoil. AIAA Paper 75-98, Jan. 1975.
57. Ballhaus, W.; Magnus, R.; and Yoshihara, H.: Some Finite Difference Examples of Unsteady Planar Flows Over the NACA 64A-410 Airfoil at $M_\infty = 0.72$. Abstracts of Papers for Symposium on Unsteady Aerodynamics (University of Arizona), U.S. Air Force, Mar. 1975, pp. 92-93.
58. Bratanow, Theodore; Ecer, Akin; and Kobiske, Michael: Numerical Calculations of Velocity and Pressure Distribution Around Oscillating Airfoils. NASA CR-2368, 1974.
59. Bratanow, Theodore; and Ecer, Akin: Analysis of Three-Dimensional Unsteady Viscous Flow Around Oscillating Wings. AIAA J., vol. 12, no. 11, Nov. 1974, pp. 1577-1584.

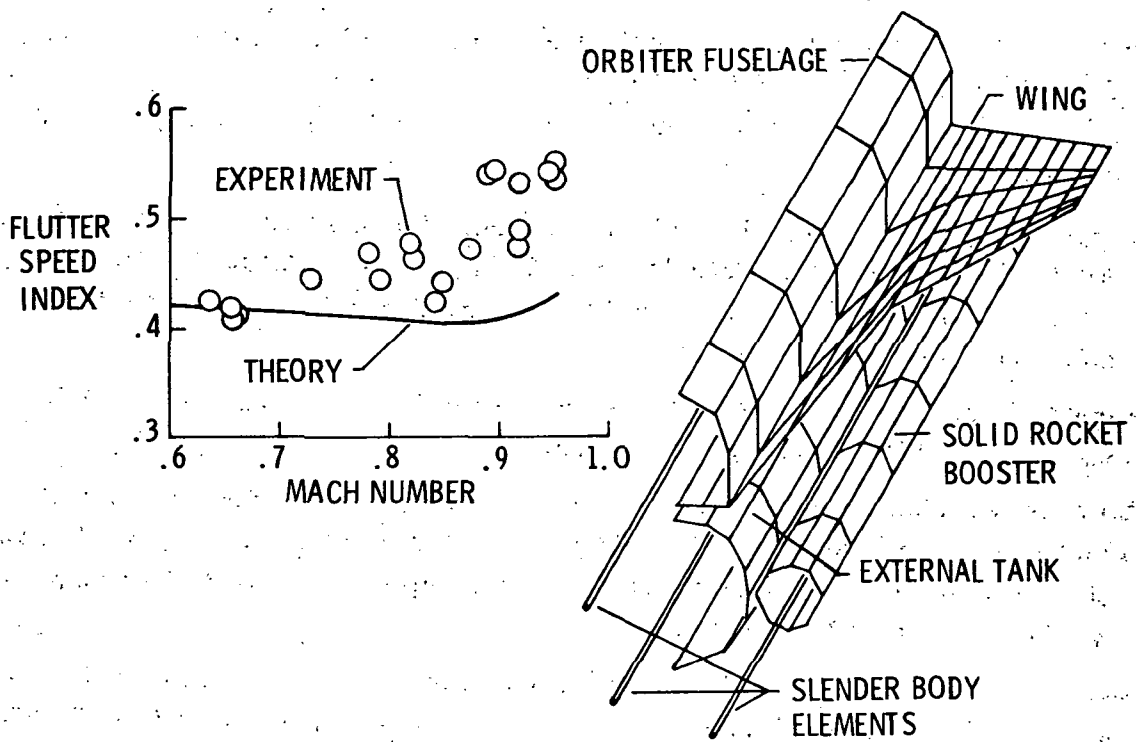


Figure 1.- Doublet lattice flutter analysis of space shuttle.

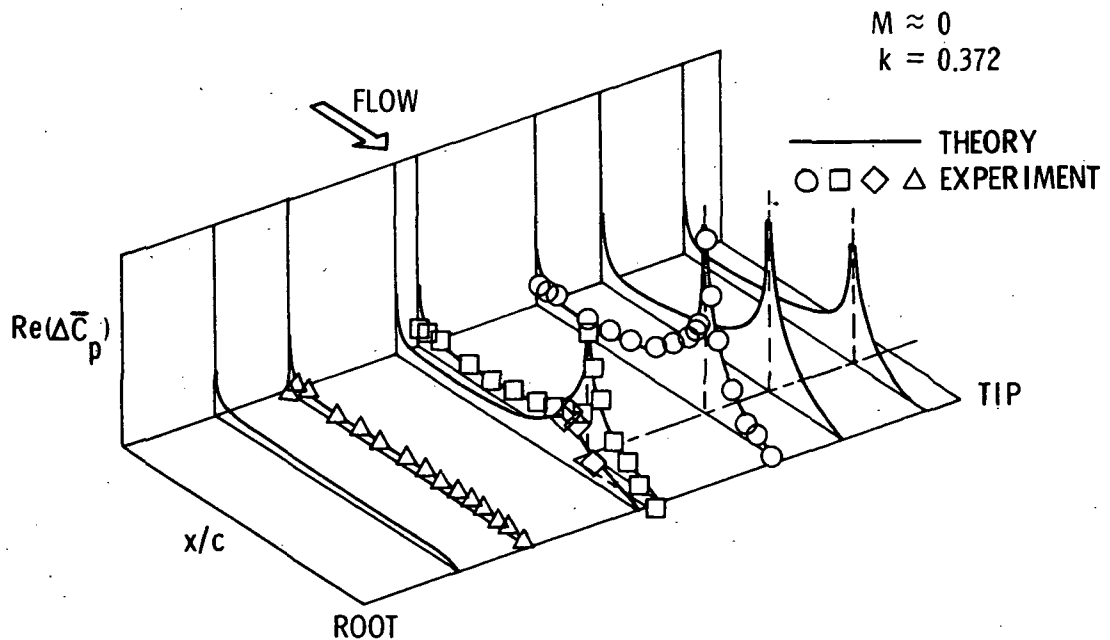


Figure 2.- Subsonic kernel function analysis of 25° swept, untapered wing with oscillating control surface.

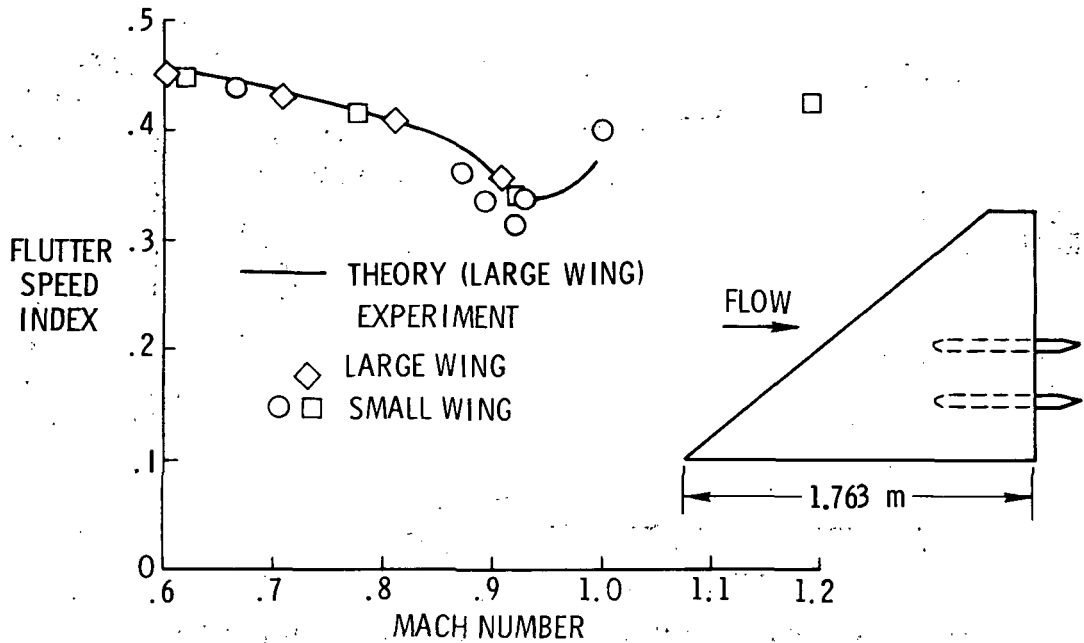


Figure 3. - Subsonic kernel function flutter analysis.

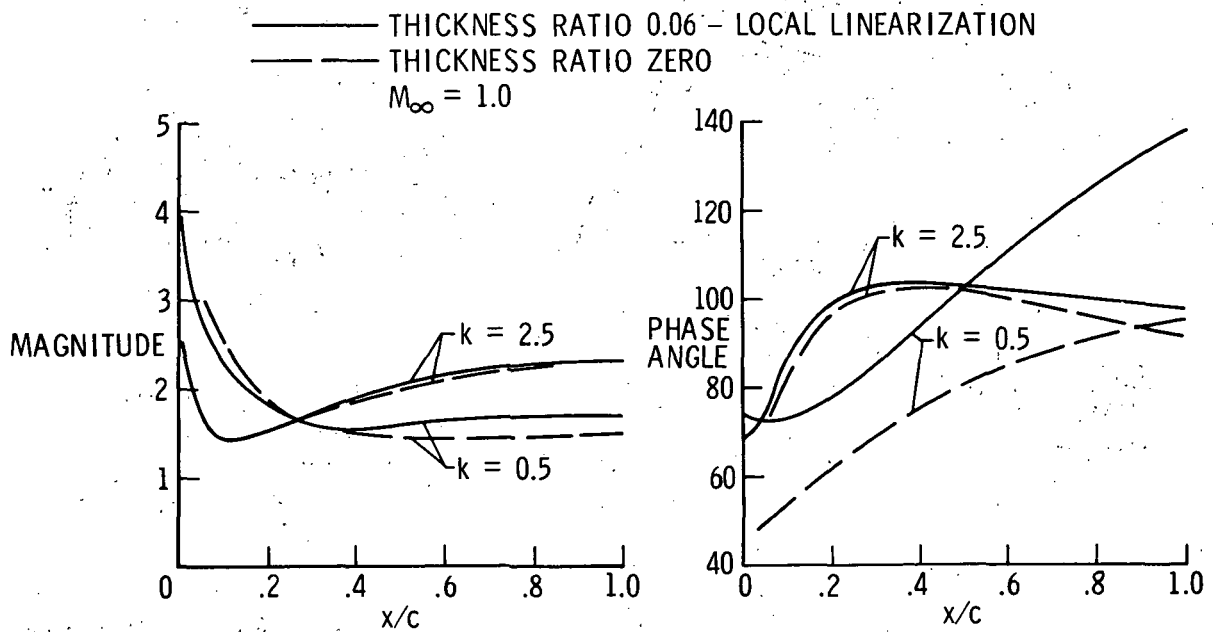


Figure 4. - Local linearization analysis for airfoil oscillating in plunge showing pressure distribution.

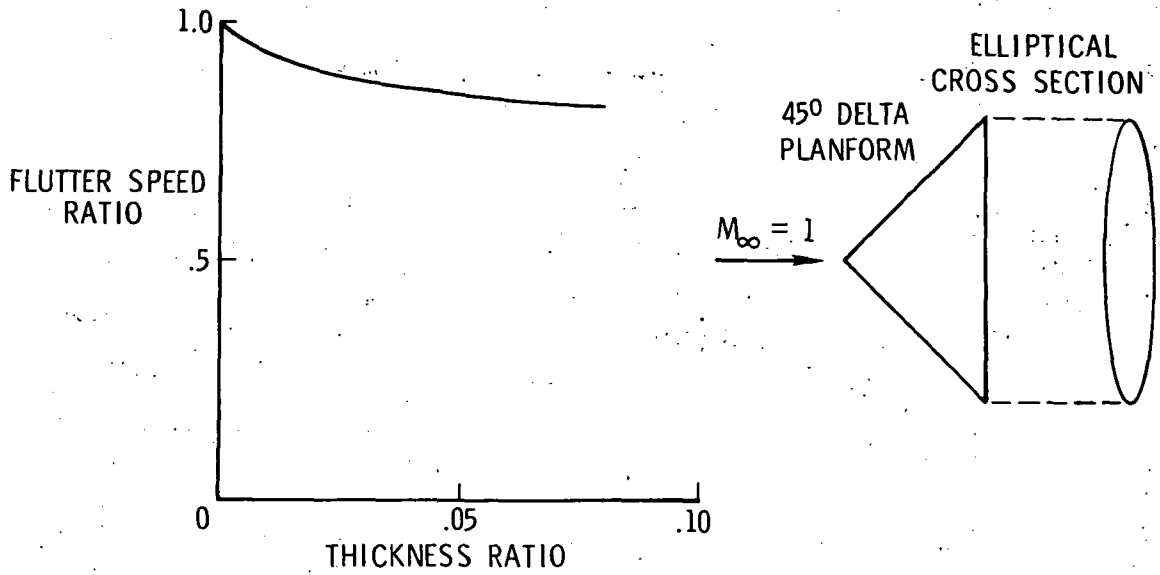


Figure 5.- Effect of thickness on flutter speed as calculated by the local Mach number transformation.

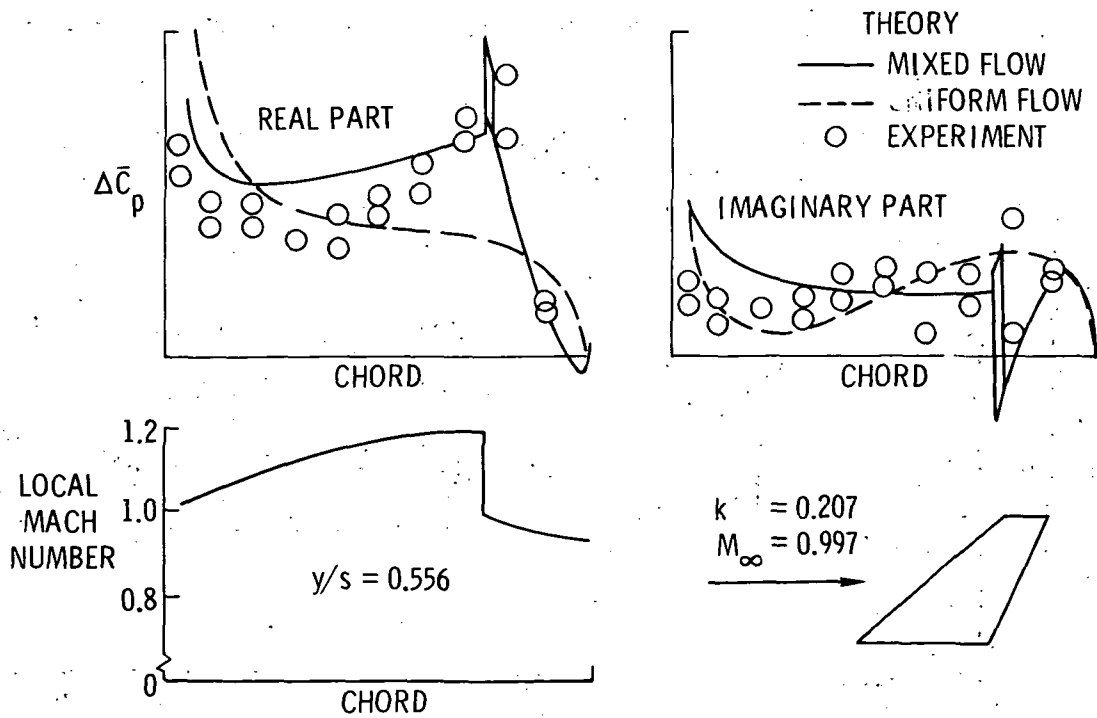


Figure 6.- Mixed subsonic-supersonic kernel function analysis for oscillating wing.

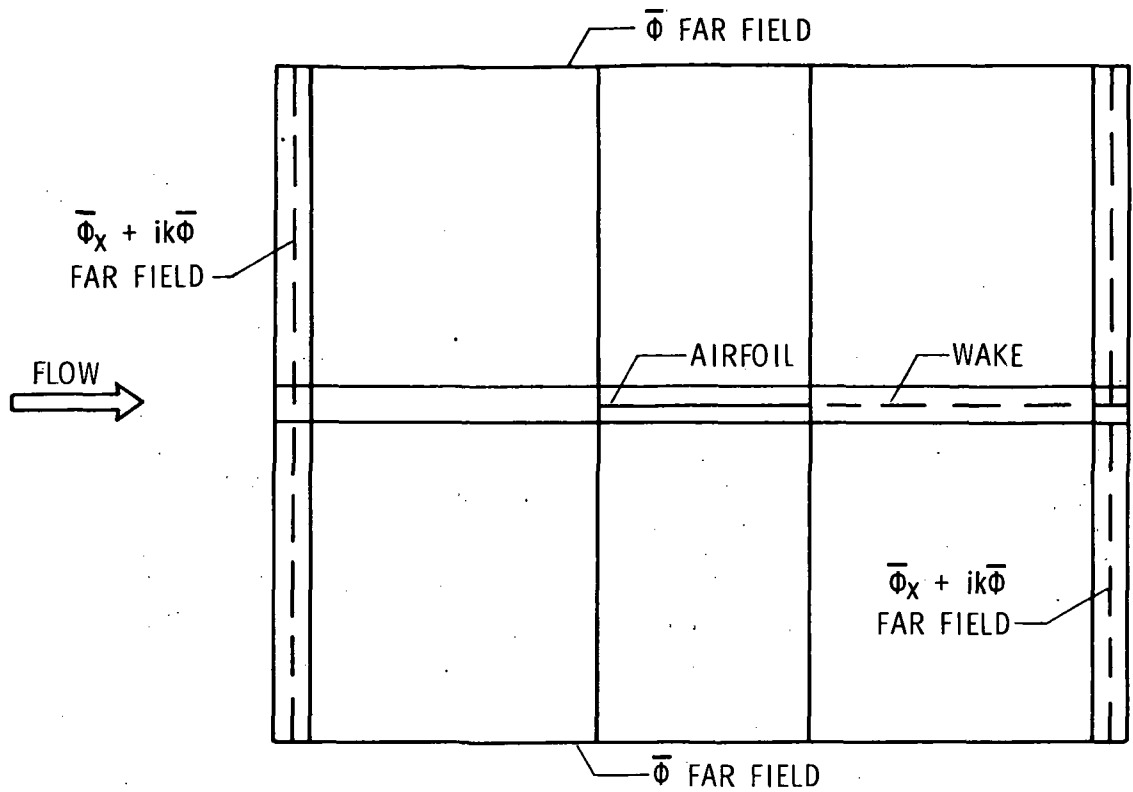


Figure 7. - Finite-difference mesh and boundary conditions for oscillating airfoil.

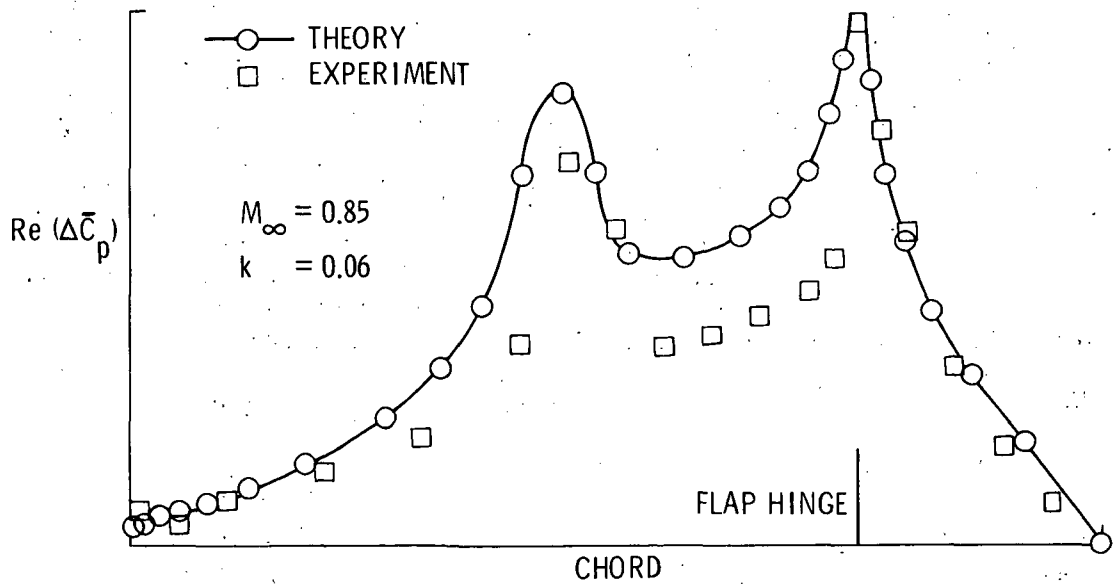


Figure 8. - Finite-difference analysis of NACA 64A006 airfoil with oscillating quarter-chord flap.

REACTING NONEQUILIBRIUM FLOW AROUND THE SPACE SHUTTLE

USING A TIME-SPLIT METHOD

By Arthur W. Rizzi and Harry E. Bailey

NASA Ames Research Center

INTRODUCTION

A detailed knowledge of the fluid and chemical phenomena that occur in air flowing around a vehicle traveling at a supersonic velocity and high altitude is of prime interest to the vehicle designer for the prediction of heat-transfer rates, boundary-layer effects, and aerodynamic loads acting on the aircraft. For moderate supersonic velocities and altitudes, the air flow remains in chemical equilibrium. The designer then need only be concerned with the fluid properties about the vehicle, and these can be determined by numerical simulation of the governing gasdynamic equations as well as wind-tunnel testing of appropriately scaled models. Several reliable numerical procedures for solving these equations have already been presented (refs. 1 to 3). For hypersonic velocities at high altitudes, however, in addition to a knowledge of the fluid particle path, its speed, and other flow properties, the designer must also reckon with the complex chemical processes that can occur among the constituents within the particle when thrown out of equilibrium by high temperature. If the time to return to equilibrium is comparable with the time it takes for the particle to pass through the field, the flow is then in a state of chemical nonequilibrium. When such nonequilibrium phenomena become important, the flow can no longer be scaled; thus, full-size testing which no present-day wind tunnel can handle is required. The designer must therefore turn to a theoretical description of these flow fields.

In the hypersonic flight regime, for example, a diatomic gas passing through a shock wave is compressed and most of the kinetic energy available in the free stream is converted to thermal energy sufficiently high to cause dissociation. Generally, the translational and rotational contributions to the internal energy of the gas return to equilibrium values in the time of a few molecular collisions whereas the vibrational and dissociative contributions adjust much more slowly. A detailed description of the nonequilibrium relaxation zone for a mixture of reacting diatomic gases (such as air) involves a complex system of coupled chemical reactions and fluid flow relations. The analysis of this problem in any detail, consequently, can only be carried out by solving numerically on a large computer the equations that govern the phenomena.

Several numerical methods (ref. 4) have been developed which calculate only the supersonic portion of the flow field about a vehicle. All these methods, however, require as input conditions the flow properties in the transonic region around the nose of the body. Such a requirement has generated renewed interest in reacting blunt-body methods, particularly ones that will handle complicated three-dimensional geometries at very high angles of

attack, which can occur, for example, on a space shuttle. It appears that existing blunt-body programs currently available (notably that of Li (ref. 5)) cannot without significant modification handle flows about three-dimensional bodies at large incidence angles. This paper presents an efficient numerical procedure for calculating the flow of an air mixture of chemically reacting nonequilibrium gases past a three-dimensional body by use of the time-splitting, finite-volume method introduced by MacCormack and Paullay (ref. 6) and extended by Rizzi and Inouye (ref. 3). Diffusion, heat conduction, and viscous effects are not considered in the analysis.

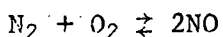
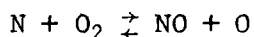
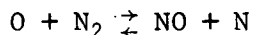
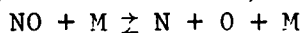
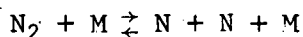
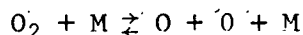
MATHEMATICAL FORMULATION

The formulation of flow problems including chemical reactions depends on general concepts from three areas essential to the study of reacting mixtures: chemical kinetics, thermodynamics, and gasdynamics. Useful ideas from each of these fields which are essential for the subject treated here are outlined briefly by generally following the presentation of Li (ref. 7) and Goulard (ref. 8) in their excellent review papers.

Chemical Kinetics

The description of high-temperature air flow past a vehicle involves not only the calculation of the bulk flow properties of every fluid element but also the chemical phenomena each of the individual gas species comprising the mixture are subjected to within the element. The problem is complex, and one must devise a molecular model sophisticated enough to represent the complicated forces at play between interacting atoms and molecules but simple enough to permit their numerical integration in the theory.

The chemical kinetics of air mainly involves the interplay of about 20 different chemical components entering into over 100 possible reactions. Fortunately, most of these reactions involve only chemical traces (refs. 9 and 10) and the list of components can be realistically reduced to 5 species - O_2 , N_2 , N , O , and NO - entering in 6 thermally significant reactions:



where M is any other molecule involved in the reaction and serves to absorb any excess energy in the collision process.

Fundamental Thermodynamic Equation

The thermodynamic state of a gaseous mixture of N component gases among which chemical reactions may occur is completely specified by $N+2$ independent variables. A study of thermodynamics (ref. 11) shows that other relations can be found that define a new set of variables, each as a function of the $N+2$ independent variables. A fundamental thermodynamic equation (ref. 11) is any equation relating these new variables to the $N+2$ independent ones. For instance, let p , ρ , and ϵ denote pressure, density, and specific internal energy of the mixture and let c_ℓ represent the mass fraction ρ_ℓ/ρ of the N species ($\ell = 1, \dots, N$); then the functional relation

$$p = p(\rho, \epsilon, c_\ell) \quad (1)$$

is a fundamental thermodynamic equation. The independent variables ρ , ϵ , and c_ℓ completely determine the thermodynamic state of the gaseous system. In a similar analysis, the functional form of the frozen isentropic speed of sound a can be derived as

$$a = (\partial p / \partial \rho)_{s, c_\ell} \quad (2)$$

where s is the specific entropy and the subscripts indicate which of the variables are held constant.

Continuum Equations for Reacting Gases

Kinetic theory provides a microscopic formulation of gasdynamics specified by molecular distribution functions for each species in the system. These equations can be interpreted as the microscopic equations of motion. We are, however, concerned with gas flows in which the characteristic length is much larger than the mean free path of the molecules. For such flows, a microscopically formulated problem must be coupled into an equivalent system of differential equations governing the macroscopic flow variables. The thermal properties of the mixture are then determined in principle for any given thermodynamic state (i.e., for given concentrations, energy, and density). In gasdynamics, the state of each fluid particle is in turn completely specified by the requirement that mass, momentum, and energy are conserved throughout the flow and along its time and space boundaries. The complete formulation of conservation for a reacting mixture of N reacting species is thus made of $N+6$ coupled nonlinear partial differential equations of continuum mechanics including mass conservation for the N species, momentum and energy conservation, and equation of state. The solution to these continuum equations of motion consists of $N+6$ variables and yields the composition, density, velocity, and thermal state of the system at every point of the flow.

The complete system of equations that describe the inviscid, adiabatic, and nondiffusive flow of a mixture of reacting gases in chemical nonequilibrium is well known (refs. 7 and 8). The macroscopic chemical kinetic equation for each of the N species is written

$$(\partial/\partial t)\rho c_\ell + \text{div } \rho c_\ell \vec{q} = \sigma_\ell \quad (\ell = 1, \dots, N) \quad (3a)$$

where \vec{q} represents the macroscopic velocity of the mixture, σ_ℓ denotes the chemical source function of species ℓ , that is, the mass rate of production of species ℓ per unit volume by chemical reactions. By definition, the relation $\sum_{\ell=1}^N c_\ell = 1$ holds. The continuity equation for the mixture is

$$\frac{\partial \rho}{\partial t} + \text{div } \rho \vec{q} = 0 \quad (3b)$$

and the momentum equation takes the form

$$\frac{\partial}{\partial t} \rho \vec{q} + \text{div}(\rho \vec{q} \vec{q} + p \vec{I}) = 0 \quad (3c)$$

where \vec{I} is the identity tensor. Finally, the energy equation may be written

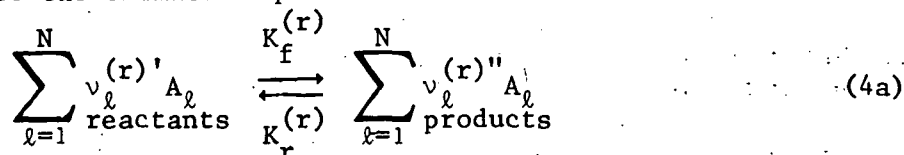
$$\frac{\partial e}{\partial t} + \text{div}[(e+p)\vec{q}] = 0 \quad (3d)$$

where the total energy per unit volume of the mixture is $e = \rho[\epsilon + (1/2)q^2]$. The system is completed by an equation of state (1) relating pressure to internal energy, density, and species concentration, the explicit form of which is presented later.

A suitable expression for σ_ℓ is obtained by use of concepts of chemical kinetics in the following section. At this point, note that the fluid and thermodynamic state of the gaseous system can be determined completely from the calculation of ρ , c_ℓ , \vec{q} , p , and ϵ satisfying the system of equations (3) under specific boundary and initial conditions for a given problem.

Specification of Chemical Source Function

Suppose that the mixture consists of N_a separate atomic species (A_1, A_2, \dots, A_{N_a}) plus N_m separate molecular species ($A_{N_a+1}, A_{N_a+2}, \dots, A_{N_a+N_m}$). The molecules are formed from combinations among the N_a different species of atoms. The total number of chemical species is $N = N_a + N_m$ capable of undergoing N elementary chemical reactions. For the r th chemical reaction, one may write the chemical equation



where $v_\ell^{(r)'}$ and $v_\ell^{(r)''}$ are stoichiometric coefficients of reactants and products giving the number of moles reacting, while $K_f^{(r)}$ and $K_r^{(r)}$ are the forward and reverse specific reaction rate constants for the r th reaction. The net rate of progress in the forward direction of the r th reaction is then expressed as

$$R(r) = K_f^{(r)} \prod_{\ell=1}^N [A_\ell]^{v_\ell^{(r)'}} - K_r^{(r)} \prod_{\ell=1}^N [A_\ell]^{v_\ell^{(r)''}} \quad (4b)$$

where $[A_\ell] = \rho c_\ell / M_\ell$ is the molar concentration of the ℓ species and M_ℓ is the molecular weight of A_ℓ . Since the r th reaction yields $v_\ell^{(r)''} - v_\ell^{(r)'}$ moles of A_ℓ , the corresponding mass rate production of A_ℓ is

$$\sigma_\ell^{(r)} = M_\ell [v_\ell^{(r)''} - v_\ell^{(r)'}] R(r) \quad (4c)$$

It follows that the net mass rate of production of A_ℓ in all N_m reactions is

$$\sigma_\ell = \sum_{r=1}^{N_m} \sigma_\ell^{(r)} \quad (4d)$$

Combining equations (4b) to (4d) yields

$$\sigma_\ell = \sum_{r=1}^{N_m} \frac{\rho M_\ell}{\tau(r)} [v_\ell^{(r)''} - v_\ell^{(r)'}] \left[K_f^{(r)} \prod_{\ell=1}^N c_\ell^{v_\ell^{(r)'}} - \prod_{\ell=1}^N c_\ell^{v_\ell^{(r)''}} \right] \quad (4e)$$

where

$$K(r) = \frac{K_f^{(r)}}{K_r^{(r)}} \prod_{\ell=1}^N \left(\frac{\rho}{M_\ell} \right)^{v_\ell^{(r)'}} e^{-v_\ell^{(r)''}} \quad (4f)$$

and

$$\tau(r) = \frac{\rho}{\left[K_r^{(r)} \prod_{\ell=1}^N \left(\frac{\rho}{M_\ell} \right)^{v_\ell^{(r)''}} \right]} \quad (4g)$$

The characteristic reaction time for the r th reaction $\tau(r)$ has the dimension of time.

If the r th reaction is at equilibrium, it follows from equation (4e) that

$$K_e^{(r)} = \prod_{\ell=1}^N (c_\ell) e^{v_\ell^{(r)'}} e^{-v_\ell^{(r)''}}$$

and from equation (4f) that

$$K_e^{(r)} = \frac{K_{f_e}^{(r)}}{K_{r_e}^{(r)}} \prod_{\ell=1}^N \left(\frac{\rho_e}{M_\ell} \right)^{\nu_\ell^{(r)} - \nu_\ell'^{(r)}}$$

and thus one obtains

$$K_{c_e}^{(r)} = \frac{K_{f_e}^{(r)}}{K_{r_e}^{(r)}} = \prod_{\ell=1}^N [A_{\ell_e}]^{\nu_\ell^{(r)} - \nu_\ell'^{(r)}} \quad (4h)$$

which is the condition of chemical equilibrium of the r th reaction and $K_{c_e}^{(r)}$ is the corresponding equilibrium constant. From statistical thermodynamic principles (ref. 12), $K_{c_e}^{(r)}$ can be expressed as a function of temperature.

Equation of State

For all calculations presented here, we have adopted the same gas model used by Davy and Reinhardt (ref. 4), namely, a mixture of pure air assumed to remain translationally and rotationally fully equilibrated while the vibrational mode is kept in a half excited state. The five component species are thermally perfect gases in thermal equilibrium.

In nonequilibrium flows, it is convenient to represent equilibrium quantities with subscript e and nonequilibrium ones with primes (ref. 13). For the gas model assumed here, the specific internal energy of the mixture is expressed as

$$\epsilon = \epsilon_e + \epsilon' \quad (5a)$$

where

$$\epsilon' = \sum_{\ell=1}^N c_\ell \epsilon_\ell^0 \quad (5b)$$

and ϵ_ℓ^0 represents the heat evolved in the formation of species ℓ per unit mass. These last two equations can be combined and solved for p to yield the explicit form of the equation of state (1):

$$p = (\gamma - 1) \rho \left(\epsilon - \sum_{\ell=1}^N c_\ell \epsilon_\ell^0 \right) \quad (5c)$$

where the ratio of specific heats γ is

$$\gamma = \frac{4(c_{O_2} + c_{N_2} + c_{NO}) + \frac{5}{2}(c_O + c_N)}{3(c_{O_2} + c_{N_2} + c_{NO}) + \frac{3}{2}(c_O + c_N)} \quad (5d)$$

Furthermore, an expression for temperature T can be derived as

$$T = \frac{P}{\rho R \sum_{\ell=1}^N (c_{\ell}/M_{\ell})} \quad (5e)$$

with R being the universal gas constant (ergs/mole-K).

NUMERICAL FORMULATION

Rizzi and Inouye (ref. 3) and MacCormack et al. (ref. 14) have presented a numerical procedure for blunt-body flow of a perfect gas based on transforming the differential governing equations to an integral formulation. The integral form is exactly equivalent to the differential representation but is shown by Rizzi et al. (ref. 15) to be more convenient computationally. Its principal advantage is, however, that arbitrarily shaped meshes may be used to fit irregular boundaries and to map asymmetric flow regions without the need for determining a suitable analytic coordinate transformation.

The governing differential equations (3) written in vector integral conservation-law form (see fig. 1) are

$$\frac{d}{dt} \iiint_{V(t)} U \, d\text{vol} + \oint_{S(t)} H \cdot \hat{n} \, ds = \Omega \quad (6)$$

where U is a column vector and H is a second-order flux tensor whose column elements are three-dimensional flux vectors defined as

$$U = \begin{bmatrix} \rho c_{\ell} \\ \rho \\ \rho u \\ \rho v \\ \rho w \\ e \end{bmatrix}, \quad H(U) = \begin{bmatrix} \rho c_{\ell} \vec{q} \\ \rho \vec{q} \\ \rho u \vec{q} + p \hat{i}_x \\ \rho v \vec{q} + p \hat{i}_y \\ \rho w \vec{q} + p \hat{i}_z \\ (e+p) \vec{q} \end{bmatrix}, \quad \Omega = \begin{bmatrix} \sigma_{\ell} \\ 0 \\ 0 \\ 0 \\ 0 \\ 0 \end{bmatrix}$$

for flow velocity \vec{q} , total energy e per unit volume, and momentum flux composed of components taken along the unit vector directions \hat{i}_x , \hat{i}_y , and \hat{i}_z of a rectangular Cartesian coordinate system x, y, z . The velocity referenced to this frame is $\vec{q} = u\hat{i}_x + v\hat{i}_y + w\hat{i}_z$. The unit vector \hat{n} is the direction of the outer normal to the surface and $H \cdot \hat{n}$ indicates the vector dot product of each column element of H with \hat{n} , the result of which is a column vector. This equation, integrated over the surface S enclosing the fluid volume V in a four-dimensional space consisting of three geometric dimensions and time t expresses the conservation of each species as well as total mass, momentum, and energy within that volume.

Difference Equations

Finite-difference approximations to the gasdynamic conservation laws are used to advance the flow in time from specified initial data. These finite-difference operators are constructed in this section to solve equation (6) for computational cells like the one depicted in figure 2. MacCormack and Paullay (ref. 6), MacCormack and Warming (ref. 16), and Rizzi and Inouye (ref. 3) have shown how these operators can be obtained by splitting a conventional finite-difference method. The resulting operators, essentially one-dimensional, are then arranged in sequences so that equation (6) is approximated to second-order accuracy.

Even though equation (6) is the unsteady equation for reacting flow and a mesh that moves in time with the motion of the bow shock is quite useful, our discussion of the splitting procedure will be clearer if we temporarily assume in this section that the mesh is fixed in time and that the species production term Ω is zero. If the solution is known at time t inside the topological hexahedron i, j, k depicted in figure 2 with volume $\text{vol}_{i, j, k}$ and bounded by the six sides $S_i, S_{i+1}, S_j, S_{j+1}, S_k, S_{k+1}$, then it can be determined at time $t + \Delta t$ from the following time-split difference equations:

$$\bar{U}_{i, j, k}^{n+1/3} = U_{i, j, k}^n - \frac{\Delta t}{\text{vol}_{i, j, k}} (H_{i, j, k}^n \cdot \vec{S}_{j+1} + H_{i, j-1, k}^n \cdot \vec{S}_j) \quad \left. \vphantom{\bar{U}_{i, j, k}^{n+1/3}} \right\} (7a)$$

$$U_{i, j, k}^{n+1/3} = \frac{1}{2} \left[U_{i, j, k}^n + \bar{U}_{i, j, k}^{n+1/3} - \frac{\Delta t}{\text{vol}_{i, j, k}} (\bar{H}_{i, j+1, k}^{n+1/3} \cdot \vec{S}_{j+1} + H_{i, j, k}^{n+1/3} \cdot \vec{S}_j) \right]$$

$$\bar{U}_{i, j, k}^{n+2/3} = U_{i, j, k}^{n+1/3} - \frac{\Delta t}{\text{vol}_{i, j, k}} (H_{i, j, k}^{n+1/3} \cdot \vec{S}_{i+1} + H_{i-1, j, k}^{n+1/3} \cdot \vec{S}_i) \quad \left. \vphantom{\bar{U}_{i, j, k}^{n+2/3}} \right\} (7b)$$

$$U_{i, j, k}^{n+2/3} = \frac{1}{2} \left[U_{i, j, k}^{n+1/3} + \bar{U}_{i, j, k}^{n+2/3} - \frac{\Delta t}{\text{vol}_{i, j, k}} (\bar{H}_{i+1, j, k}^{n+2/3} \cdot \vec{S}_{i+1} + \bar{H}_{i, j, k}^{n+2/3} \cdot \vec{S}_i) \right]$$

$$\bar{U}_{i, j, k}^{n+1} = U_{i, j, k}^{n+2/3} - \frac{\Delta t}{\text{vol}_{i, j, k}} (H_{i, j, k}^{n+2/3} \cdot \vec{S}_{k+1} + H_{i, j, k-1}^{n+2/3} \cdot \vec{S}_k) \quad \left. \vphantom{\bar{U}_{i, j, k}^{n+1}} \right\} (7c)$$

$$U_{i, j, k}^{n+1} = \frac{1}{2} \left[U_{i, j, k}^{n+2/3} + \bar{U}_{i, j, k}^{n+1} - \frac{\Delta t}{\text{vol}_{i, j, k}} (\bar{H}_{i, j, k+1}^{n+1} \cdot \vec{S}_{k+1} + \bar{H}_{i, j, k}^{n+1} \cdot \vec{S}_k) \right]$$

where subscripts $i, j,$ and k refer to the geometrical location of the cell and the superscripts refer to times $t = \sum_1^n \Delta t$ where Δt is the time step or increment that the solution is advanced during each cycle of the above three

equations. The mean values $U_{i,j,k}^n$ of the flow variables in the cell at time t are defined by

$$U_{i,j,k}^n = \frac{\iiint_{\text{vol}_{i,j,k}(t)} U \, d\text{vol}}{\iiint_{\text{vol}_{i,j,k}(t)} d\text{vol}} \quad (8)$$

where $\text{vol}_{i,j,k}(t)$ is the small but finite volume of the cell at that time step and, finally, $H_{i,j,k}^n = H(U_{i,j,k}^n)$. This set of equations can be written more conveniently in operator notation. Let $L_x(\Delta t)$ denote the operation performed by the set of equations (7a) in advancing the solution from $U_{i,j,k}^n$ to $U_{i,j,k}^{n+1/3}$, that is,

$$U_{i,j,k}^{n+1/3} = L_x(\Delta t)U_{i,j,k}^n$$

Let $L_y(\Delta t)$ and $L_z(\Delta t)$ be similarly defined by the next two sets.

The condition on Δt necessary for the stability of the above method is that the numerical domain of dependence must include all the physical one. Stability conditions can be determined analytically for each operator. For $L_x(\Delta t)$,

$$\Delta t_x \leq \min_{i,j,k} \left\{ \frac{\text{vol}_{i,j,k}}{(|\vec{q} \cdot \vec{S}_j| + aS_j)_{i,j,k}} \right\} \quad (9a)$$

For $L_y(\Delta t)$,

$$\Delta t_y \leq \min_{i,j,k} \left\{ \frac{\text{vol}_{i,j,k}}{(|\vec{q} \cdot \vec{S}_i| + aS_i)_{i,j,k}} \right\} \quad (9b)$$

and for $L_z(\Delta t)$,

$$\Delta t_z \leq \min_{i,j,k} \left\{ \frac{\text{vol}_{i,j,k}}{(|\vec{q} \cdot \vec{S}_k| + aS_k)_{i,j,k}} \right\} \quad (9c)$$

These requirements, again necessary for convergence, are the one-dimensional CFL conditions. Thus, the sequence of operators $L_z(\Delta t)L_y(\Delta t)L_x(\Delta t)$ representing equations (6) can advance the numerical solution from

$U_{i,j,k}^n$ to $U_{i,j,k}^{n+1}$ and is stable if

$$\Delta t \leq \min(\Delta t_x, \Delta t_y, \Delta t_z) \quad (9d)$$

Unfortunately, the sequence is only of first-order accuracy because of the noncommutativity of $L_x(\Delta t)$, $L_y(\Delta t)$, and $L_z(\Delta t)$. However, the component operators can be arranged in a symmetric sequence that can be shown to be second order accurate. For example, if the order of the three sets of equations (7) is reversed for each new n , the following symmetric sequence results:

$$L_x(\Delta t)L_y(\Delta t)L_z(\Delta t)L_z(\Delta t)L_y(\Delta t)L_x(\Delta t) \quad (10)$$

that can advance the solution from $U_{i,j,k}^n$ to $U_{i,j,k}^{n+2}$ with second-order accuracy.

This sequence approximates equation (6) if the production term Ω were identically zero. For nonequilibrium flow, however, this term must be introduced into the spatial operators (7), and equation (7a) would then have the form

$$\tilde{U}_{i,j,k}^{n+1/3} = U_{i,j,k}^n - \frac{\Delta\tau}{\text{vol}_{i,j,k}} \left(H_{i,j,k}^n \cdot \vec{S}_{j+1} + H_{i,j-1,k} \cdot \vec{S}_j - \Omega \right)$$

$$U_{i,j,k}^{n+1/3} = \frac{1}{2} \left[U_{i,j,k}^n + \tilde{U}_{i,j,k}^{n+1/3} - \frac{\Delta\tau}{\text{vol}_{i,j,k}} \left(\tilde{H}_{i,j+1,k}^{n+1/3} \cdot \vec{S}_{j+1} + \tilde{H}_{i,j,k}^{n+1/3} \cdot \vec{S}_j - \Omega \right) \right]$$

and the other two operators would remain unchanged.

Although the production term Ω is too complex for stability criteria on $\Delta\tau$ to be determined analytically, some empirical conditions derived from consideration of the chemical relaxation time have been proposed. Anderson (ref. 17) suggested $\Delta\tau \leq 0.1 \left| \partial\sigma_\ell / \partial c_\ell \right|$ for a binary reacting mixture whereas Li (ref. 5) found $\Delta\tau \leq 0.1 \min |U/\Omega|$ to be a satisfactory stability criterion. We have adopted a different empirical condition and simply set $\Delta\tau = 0.2\Delta t$; this has proven to be appropriate for the calculations presented here.

All these empirical stability criteria indicate that $\Delta\tau \ll \Delta t$, which means that the chemical reactions severely restrict the numerical step size and require prohibitively large computer times. Li circumvents this restriction by introducing two different time increments - one for the fluid dynamical processes and the other for the chemical reactions. While decreasing the computation time, this action seems theoretically unsound because now the macroscopic flow properties are inconsistent with the microscopic chemical ones; that is, the bulk flow is at a different time level than the chemical properties are.

A more logical way of proceeding is to split the production term from the spatial terms and apply the chemical kinetic operator $L_c(\Delta\tau)$:

$$\begin{aligned} \tilde{U}^{\mu+\delta} &= U^\mu + \frac{\Delta\tau}{\text{vol}_{i,j,k}} \Omega \\ U^{\mu+\delta} &= \frac{1}{2} \left[U^\mu + \tilde{U}^{\mu+\delta} + \frac{\Delta\tau}{\text{vol}_{i,j,k}} \tilde{\Omega} \right], \quad \delta = \Delta\tau/2\Delta t \end{aligned}$$

repeatedly for each cell i, j, k until the sum of successive time steps $\sum \Delta\tau$ equals the final time level t at which the bulk flow properties will be advanced by the end of the sequence. For example, if the flow operators (7) have a time step of Δt and the chemical kinetic one of $\Delta\tau$, then the sequence

$$U_{i,j,k}^{n+2} = L_x(\Delta t)L_y(\Delta t)L_z(\Delta t) \prod_{\beta=1}^{1/\delta} L_c(\Delta\tau)L_z(\Delta t)L_y(\Delta t)L_x(\Delta t)U_{i,j,k}^n \quad (11)$$

approximates the governing equation (6) to second-order accuracy. Splitting in this manner then requires only the chemical operator to proceed at the smaller time step while allowing the flow operators to continue at the faster rate and to remain idle until L_c "catches up" to the same time level. The advantage is a reduction in computer time while maintaining a consistent time level for both the fluid and chemical phenomena.

This feature of the splitting concept is illustrated with an explicit L_c operator, but the advantage remains essentially the same if L_c is implicit. Our experience with an implicit L_c is that the allowable $\Delta\tau$ is larger than the explicit one, but each cycle of it requires more computer time so that the net effect is about equal computation time required for either the implicit or explicit operator.

Computational Cell Network

To apply this finite-difference technique to blunt-body problems, the flow field is divided into small topological hexahedra by a construction based on the following use of a circular cone. A series of nested and arbitrarily positioned conical surfaces depicted in figure 3 and filling a given space is built up by varying each of the parameters governing the three aspects of general motion. Translation of the cone is accounted for by the location χ of its apex along the body axis, rotation by the angle ψ between its axis and the free stream, and, lastly, dilatation by its vertex angle ω . Each of these surfaces is then intersected by a plane rotated about the cone axis in specified angular increments. These intersections are straight lines or rays that delineate a system of contiguous pyramidal columns (fig. 4). All that is needed to specify the ray i, k are its two angles $\theta_{i,k}$ and $\phi_{i,k}$ made with the z and x axes and its intersection χ_i with the body axis. The columns, then, are partitioned into small hexahedra by a third sequence of surfaces that coincide with the body and bow shock and divide the distance ξ along each ray between the body and shock into J segments of any given interval. The partitioning is such that the innermost layer of cells lies on the body and the outermost in the shock layer is aligned with the shock surface. The cells compose a nonorthogonal mesh network floating in time and always exactly fills the time-dependent shock layer. The other boundaries are the pitch plane of symmetry and a downstream boundary immersed in supersonic flow. This mesh (fig. 4) is quite general and permits a very wide range of body shapes and computational spaces to be studied.

Moving Mesh

In the section on difference equations, we assumed that the mesh was stationary, but for blunt-body flows it is advantageous to adjust the mesh in time to the motion of the bow shock. For flows containing shock waves, various authors (refs. 3, 14, and 16) have shown that accurate calculations in the vicinity of the discontinuity can be obtained by keeping the mesh aligned with the shock. Otherwise, the numerical solution will be smeared across the shock, rather than having a sharp jump, and will contain oscillations.

Equation (6) and its corresponding difference equations (7) must now be modified to take into account the effect of the moving mesh because, if volume $V(t)$ now varies with time, the condition

$$\frac{d}{dt} \iiint_{V(t)} U \, d\text{vol} = \iiint_{V(t)} \frac{\partial}{\partial t} U \, d\text{vol}$$

incorporated in the difference equations (7) is no longer valid. The expression appropriate for a time-dependent region of space is the generalized form of Leibnitz's rule (ref. 18):

$$\frac{d}{dt} \iiint_{V(t)} U \, d\text{vol} = \iiint_{V(t)} \frac{\partial}{\partial t} U \, d\text{vol} + \oint_{S(t)} U \vec{\lambda} \cdot \hat{n} \, ds \quad (12)$$

where $S(t)$ is the time changing surface enclosing the region $V(t)$ and $\vec{\lambda}$ is the velocity of any element $\hat{n} \, ds$ of the surface $S(t)$.

For this case, the difference operators (7) can be thought of as adjusting the solution to the movement of the fluid through a fixed mesh. The difference operators now to be defined adjust the solution because of the movement of the mesh through the frozen fluid. Thus the dynamics of the flow problem are split into six operators: the dynamics of the three spatial coordinate mesh directions and the dynamics induced in each of these directions by the moving coordinate mesh.

For simplicity, consider the case where only one family of mesh surfaces moves with time, that is, $\vec{\lambda}$ is the velocity of one side of the hexahedron and its two adjoining sides are stationary (fig. 5). An explicit operator $L_{\text{mesh}}(\Delta t)$ that accounts for the effect of the moving mesh to second-order accuracy is

$$\left. \begin{aligned} \bar{U}_{i,j,k}^{n+1} &= U_{i,j,k}^n - \frac{\Delta t}{\text{vol}_{i,j,k}^n} \left(U_{i,j,k}^n \vec{\lambda}_j \cdot \vec{s}_{j+1} + U_{i,j-1,k}^n \vec{\lambda}_{j-1} \cdot \vec{s}_j \right) \\ U_{i,j,k}^{n+1} &= \frac{1}{2} \left[U_{i,j,k}^n + \bar{U}_{i,j,k}^{n+1} - \frac{\Delta t}{\text{vol}_{i,j,k}^n} \left(\bar{U}_{i,j+1,k}^{n+1} \vec{\lambda}_{j+1} \cdot \vec{s}_{j+1} + \bar{U}_{i,j,k}^{n+1} \vec{\lambda}_j \cdot \vec{s}_j \right) \right] \end{aligned} \right\} \quad (13)$$

which, in operator notation, is more conveniently expressed as

$$U_{i,j,k}^{n+1} = L_{\text{mesh}}(\Delta t)U_{i,j,k}^n \quad (14)$$

This operator is driven by the mesh velocity in steps of Δt . For the velocities of the interior mesh surfaces, a variety of appropriate values can be assigned whereas on the boundaries they are determined by the flow. At the body they must be zero everywhere and at the bow wave they must equal the local shock velocity. A scheme for calculating them at the bow wave is presented in the following paragraph. The operator $L_{\text{mesh}}(\Delta t)$, unlike L_x , L_y , and L_z , commutes with all operators and can be placed anywhere in an operator sequence for second-order accuracy. For stability, the condition on Δt_{mesh} is

$$\Delta t_{\text{mesh}} < \min_{i,j,k} \left\{ \frac{\text{vol}_{i,j,k}^n}{\vec{\lambda}_j \cdot \vec{S}_j} \right\} \quad (15)$$

which prohibits extreme movements of the mesh. This criterion will always be less restrictive than the conditions (9) provided that the mesh velocity $\vec{\lambda}$ is less than the signal propagation speed; that is, $\vec{\lambda} \cdot \vec{S}_j < |\vec{q} \cdot \vec{S}_j| + aS$.

The shock wave is treated as an interior feature of the flow field, and no special attention is given to it in the difference operators L_x , L_y , and L_z . On every iteration, the mesh is adjusted to maintain alinement with the shock because the conservation form of the difference operators will then implicitly satisfy the Rankine-Hugoniot shock-wave relations and accurately determine the solution in the vicinity of the shock (refs. 3 and 14).

To maintain alinement, the mesh surface coincident with the shock must move with the unsteady shock itself. The velocity of each cell segment of this mesh surface (fig. 6) is obtained by solving for the shock-wave velocity λ_s simultaneously from the jump relations for a moving discontinuity and one local characteristic relation, valid in the plane defined by the free-stream \vec{q}_∞ and the shock normal direction \hat{n}_s . The solution is carried out by iteration for λ_s , the pressure p_s at the shock, and the velocity $q_{\eta_s} = \vec{q}_s \cdot \hat{n}_s$ just behind and normal to the shock:

$$\left. \begin{aligned} p_s^{(0)} &= p_A \\ &\vdots \\ p_s^{(m)} &= \frac{1}{2} (p_s^{(m-1)} + p_{\text{char}}^{(m-1)}) \\ \lambda_s^{(m)} &= f(p_s^{(m)}, p_\infty) \\ q_{\eta_s}^{(m)} &= g(\lambda_s^{(m)}, q_{\eta_A}) \end{aligned} \right\} \text{Moving discontinuity relations}$$

$$p_{\text{char}}^{(m)} = p_A + \rho_A a_A (q_{\hat{n}_s}^{(m)} - q_{\hat{n}_A}) \quad \text{Characteristic relation}$$

$$p_s^{(m+1)} = \frac{1}{2} (p_s^{(m)} + p_{\text{char}}^{(m)})$$

The velocity component along the shock normal direction \hat{n}_s and located at point A is denoted by $q_{\hat{n}_A} = \vec{q}_A \cdot \hat{n}_s$. It and other values of the flow properties at point A can be obtained by interpolating data at mesh cells behind the shock, and those with subscript ∞ are obtained from the free-stream conditions. The shock-mesh surface is then moved by use of the shock-wave velocities calculated for each segment by the following procedure. The four rays comprising the four edges of each cell hexahedron that intersect the shock surface are fixed in time, and the new shock position on each ray is determined by integrating

$$d(\xi_{i,J+1,k} - \xi_{i,1,k})/dt = \langle W_{i,k} \rangle_{\text{av}} \quad (16)$$

where $\langle W_{i,k} \rangle_{\text{av}}$ is the simple average of the projections¹ onto the ray i,k of the velocities of the four shock segments adjacent to the ray. As time proceeds, the cells distend and distort within pyramidal columns bounded by the fixed rays.

Initial and Boundary Conditions

Because the governing equations are hyperbolic and the subsonic region is bounded by supersonic flow, the time-dependent method is well posed as an initial-boundary-value problem. To commence the calculation, a complete initial field must be specified at all points, but it can be quite approximate (ref. 3).

For the inviscid calculations presented here, three distinct types of boundaries are encountered at the edges of the overall mesh - entrance, exit, and streamline boundaries. Along the entrance boundary, the dependent variables U are held constant at their supersonic free-stream values, while at the exit they are calculated by use of one-sided differences. Across cell faces coincident with a streamline boundary, such as an impervious body, no transport

¹More explicitly, the projection is the shock velocity $W_{i,k}$ corresponding to λ_s but in the direction of the i,k ray so that $W_{i,k} = \lambda_s / \cos \beta$ where β is the angle between the normal \hat{n}_s and the i,k ray.

is allowed. The only variable actually needed at such a cell face is the pressure, which can be expressed in terms of the interior mesh values of pressure and the derivative of pressure normal to the face. This derivative $\frac{\partial p}{\partial \eta} \Big|_{\text{body}}$ is obtained from the momentum equation normal to a streamline:

$$\frac{\partial p}{\partial \eta} \Big|_{\text{body}} = \rho (u^2 F_{xx} + v^2 F_{yy} + w^2 F_{zz} + 2uv F_{xy} + 2uw F_{xz} + 2vw F_{yz}) (F_x^2 + F_y^2 + F_z^2)^{-1/2}$$

where the body is the surface $F(x,y,z) = 0$ and the subscripts indicate partial differentiation with respect to that variable.

RESULTS

To illustrate the capability of this method, results from the computation of reacting air flow about a general body traveling at 6.54 km/sec and 30° angle of attack are presented. The ambient free-stream pressure is $p_\infty = 106$ dynes/cm² while the temperature is $T_\infty = 236$ K. The body is a smooth three-dimensional configuration that closely resembles the proposed design plan for the nose of the space shuttle and is described by a series of third-degree polynomials in plan and profile views and ellipses in cross section. The mesh employed for the calculations consisted of 15 cells down the body in the latitudinal direction, 17 around the body in the meridional direction, and 9 across the shock layer. The computation time needed for this solution was over 1 hour on the CDC 7600 computer and required 300 time-step iterations.

The bow shock in the plane of symmetry displayed in figure 7 indicates the smooth nature of the shock surface. The solid dots denote the corners of each mesh cell and illustrate the asymmetry with respect to the stagnation region that the nonorthogonal mesh network is capable of handling. Such a capability is very useful at high angles of attack where one wants to exclude from the computations as much of the supersonic flow on the leeward side as possible while including, of course, all of the subsonic region on the windward side. Excluding as much supersonic flow as possible greatly reduces the number of time iterations required for the steady state. Figure 7 also presents the variation of density between the body and bow shock along the line ζ and characterizes the sharp compression at the shock and the smooth non-oscillatory variation behind it that the mesh-aligning procedure produces.

A plot of the shock-standoff distance z_s ($z = z_s$ at $x = 0$) is given in figure 8 as a function of the step number n and shows a monotonic approach to steady state after about 180 steps. Some unsteadiness may still appear to be present after 300 steps, but a check on the conservation of total enthalpy, an expression independent of the calculations and thus a valid indicator of overall error, shows that total enthalpy is constant to within less than 1 percent. Furthermore, flow properties on each successive step are now changing by an even lesser degree, and on this basis the solution of 300 steps is deemed to be at steady state for all practical purposes.

In figure 9 the variation of the species concentrations along the z axis between the body and shock is presented and indicates how the mixture of N_2 and O_2 for air immediately begins to dissociate on passing through the bow shock. This dissociation leads to the formation of atomic nitrogen N and oxygen O that increases to a maximum concentration at the body and a small amount of nitric oxide NO that is most abundant right behind the shock. All these results are consistent with the expected physical and chemical phenomena.

Figure 10 illustrates the variation of Mach number along the intersection of the body surface and the symmetry plane where the angle θ is measured from the z axis. On the leeward side, it increases monotonically from a small value near the axis to well over 1.6 at the downstream edge; on the windward side, it steadily increases with θ until about $\theta = 60^\circ$, at which point the flow undergoes a small recompression (see ref. 3) that lowers the Mach number for a small distance after which it then increases rapidly to above 2 at $\theta = 100^\circ$.

CONCLUDING REMARKS

The present numerical method accurately calculates three-dimensional reacting gas flow by use of a procedure that has been shown to be very efficient. The flow-field geometry and physics determine the computational mesh which is generally nonorthogonal, and the integral form of the difference procedure handles the required nonorthogonal mesh with less computation time than the equivalent differential form. The splitting techniques employed are beneficial because they allow larger time steps than nonsplit ones and, more importantly, split-difference operators can be arranged to form efficient sequences in which some operators appear less often than others. This is particularly useful for handling the chemical kinetic equations because of the large difference between fluid and chemical step size. In the difference operators presented, no special treatment is given to the shock wave unlike other difference schemes that accurately calculate shock waves in the interior of the mesh by testing for the shock's presence and treating it with special routines. The present shock-wave treatment by mesh alignment is done by an operator split from the flow operators and is applied only as often as required by the movement of the shock wave.

REFERENCES

1. Moretti, G. and Bleich, G.: Three-Dimensional Flow Around Blunt Bodies. AIAA J., vol. 5, no. 10, Oct. 1967, pp. 1557-1562.
2. Barnwell, R. W.: A Time-Dependent Method for Calculating Supersonic Angle-of-Attack Flow About Axisymmetric Blunt Bodies With Sharp Shoulders and Smooth Nonaxisymmetric Blunt Bodies. NASA TN D-6283, 1971.

3. Rizzi, A. W.; and Inouye, M.: Time-Split Finite-Volume Method for Three-Dimensional Blunt-Body Flow. AIAA J., vol. 11, no. 11, 1973, pp. 1478-1485.
4. Davy, W. C.; and Reinhardt, W. A.: Computation of Shuttle Nonequilibrium Flow Fields on a Parallel Processor. Aerodynamic Analyses Requiring Advanced Computers, Part II, NASA SP-347, 1975, pp. 1351-1376.
5. Li, C. P.: Time-Dependent Solutions of Nonequilibrium Airflow Past a Blunt Body. J. Spacecraft Rockets, vol. 9, no. 8, Aug. 1972, pp. 571-572.
6. MacCormack, R. W.; and Paullay, A. J.: Computational Efficiency Achieved by Time Splitting of Finite Difference Operators. AIAA Paper 72-154, 1972.
7. Li, T. Y.: Recent Advances in Nonequilibrium Dissociating Gasdynamics. ARS J., vol. 31, 1961, pp. 170-178.
8. Goulard, R.: High Temperature Aerodynamics. Appl. Mech. Rev., vol. 14, no. 4, Apr. 1961, pp. 257-261.
9. Wray, K.; Teare, J. D.; Kivel, B.; and Hammerding, P.: Relaxation Processes and Reaction Rates Behind Shock Fronts in Air and Component Gases. Eighth Symposium (International) on Combustion, Pasadena, Calif., 1960.
10. Wray, K. L.: Chemical Kinetics of High Temperature Air. Hypersonic Flow Research, F. R. Riddell, ed., vol. 7, Academic Press, New York, 1962.
11. Wilson, A. H.: Thermodynamics and Statistical Mechanics, Cambridge Univ. Press, ch. 3, London, 1957.
12. Fowler, R. H.; and Guggenheim, E. A.: Statistical Thermodynamics. Cambridge Univ. Press, London, 1956.
13. Denbigh, K. G.: The Thermodynamics of the Steady State. Methuen & Co., Ltd., London, 1951.
14. MacCormack, R. W.; Rizzi, A. W.; and Inouye, M.: Steady Supersonic Flow Fields With Embedded Subsonic Regions. Conference on Computational Problems and Methods in Aeronautical Fluid Dynamics, Univ. of Manchester, England, Sept. 24-26, 1974.
15. Rizzi, A. W.; Klazuis, A.; and MacCormack, R. W.: A Generalized Hyperbolic Marching Technique for Three-Dimensional Supersonic Flow With Shocks. Proceedings of Fourth International Conference on Numerical Methods in Fluid Mechanics, Volume 35 of Lecture Notes in Physics, Robert D. Richtmyer, ed., Springer-Verlag, 1975, pp. 341-346.

16. MacCormack, R. W.; and Warming, R. F.: Survey of Computational Methods for Three-Dimensional Supersonic Inviscid Flows With Shocks. Advances in Numerical Fluid Dynamics, AGARD Lecture Series 64, Brussels, Belgium, Feb. 1973.
17. Anderson, J. D.: A Time-Dependent Analysis for Vibrational and Chemical Nonequilibrium Nozzle Flows. AIAA J., vol. 8, no. 3, Mar. 1970, pp. 545-550.
18. Kaplan, W.: Advanced Calculus. Addison-Wesley, Reading, 1952, p. 300.

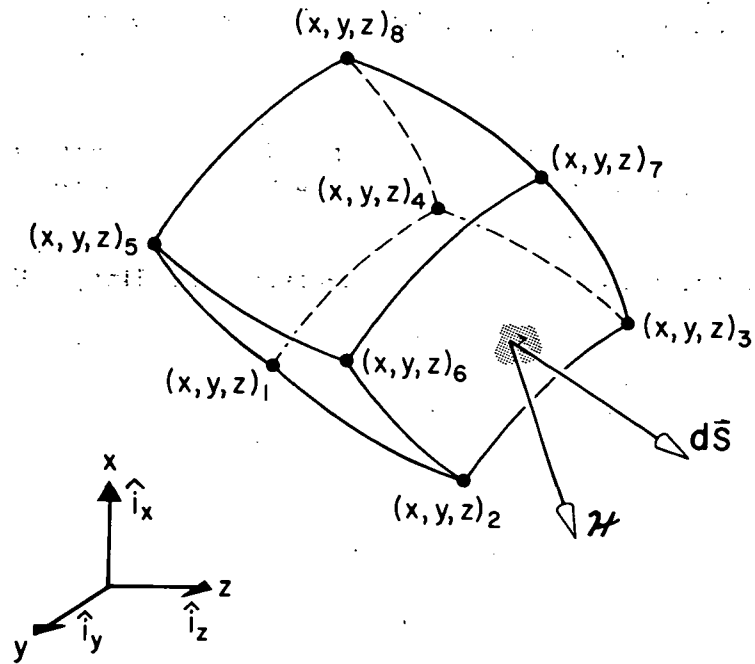


Figure 1.- A general six-sided finite volume of fluid.

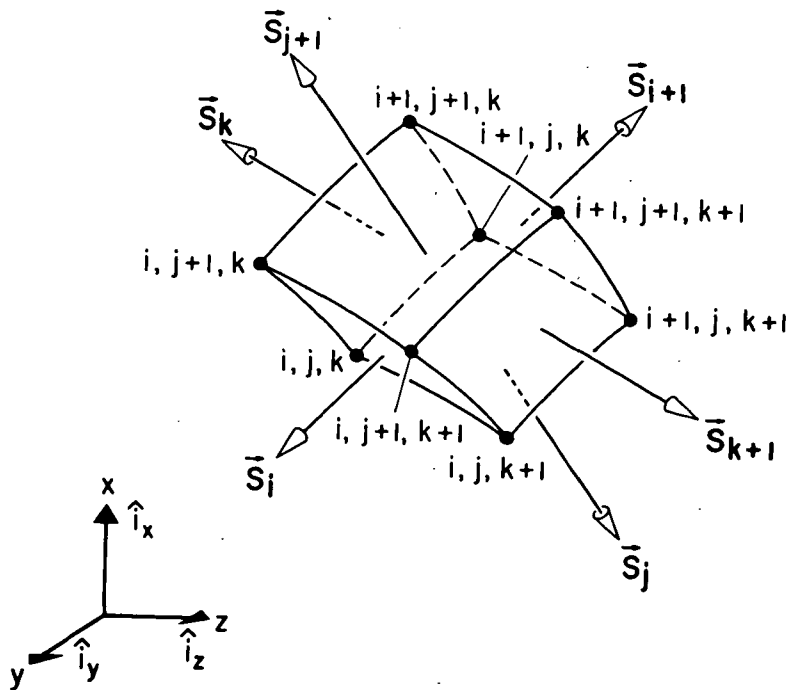


Figure 2.- A typical computational cell i, j, k .

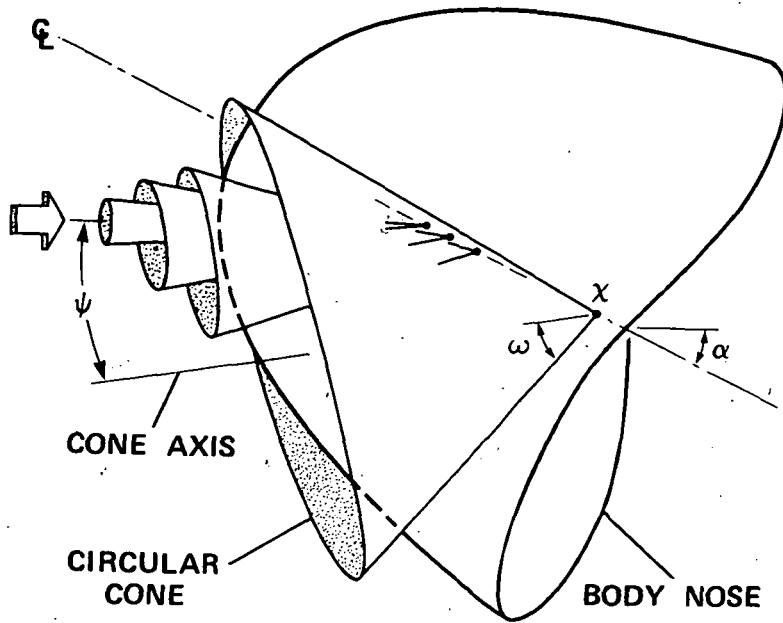


Figure 3.- Mesh geometry determined by series of nested cones.

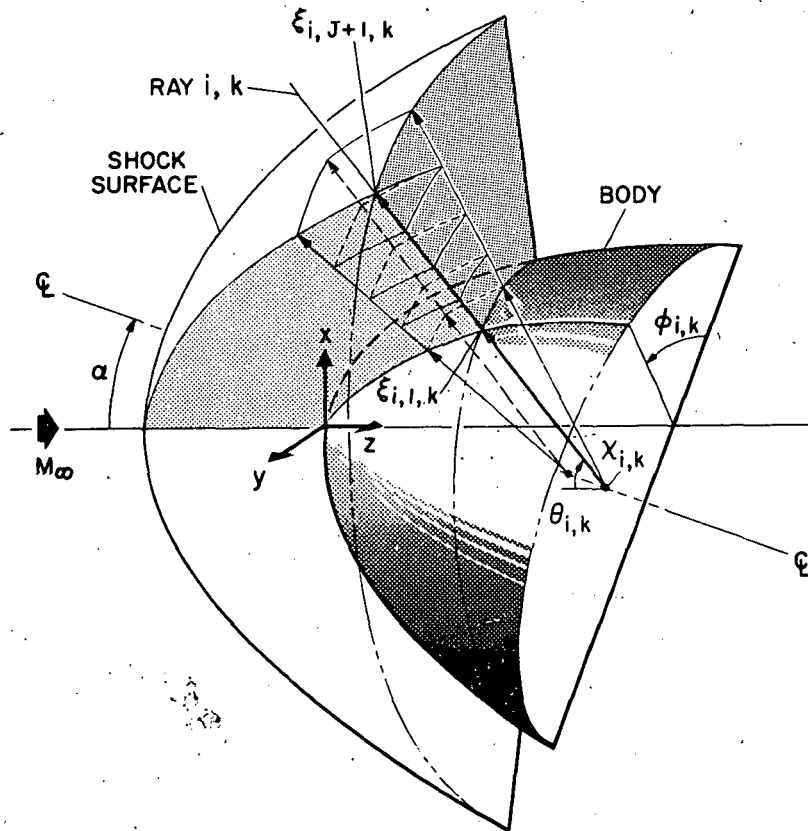


Figure 4.- Partitioning of the shock layer into finite volumes.

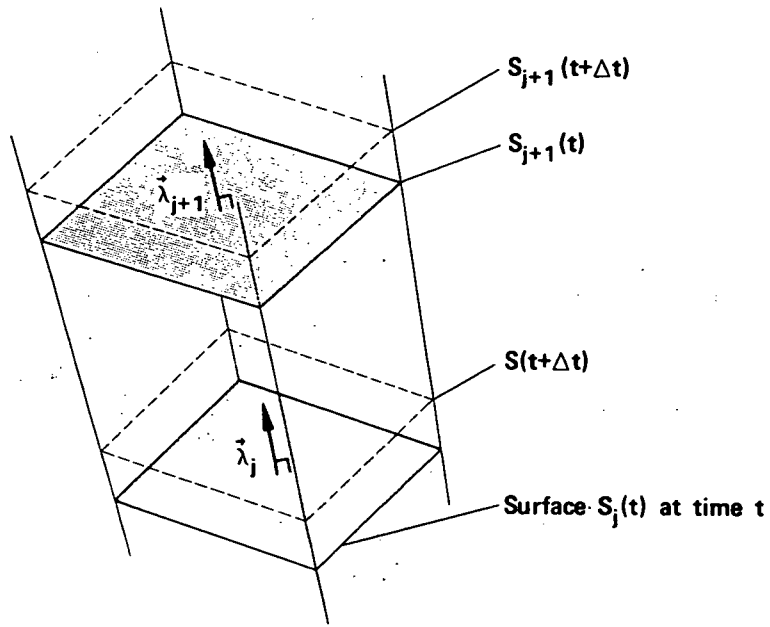


Figure 5.- Time-changing volume cell i, j, k .

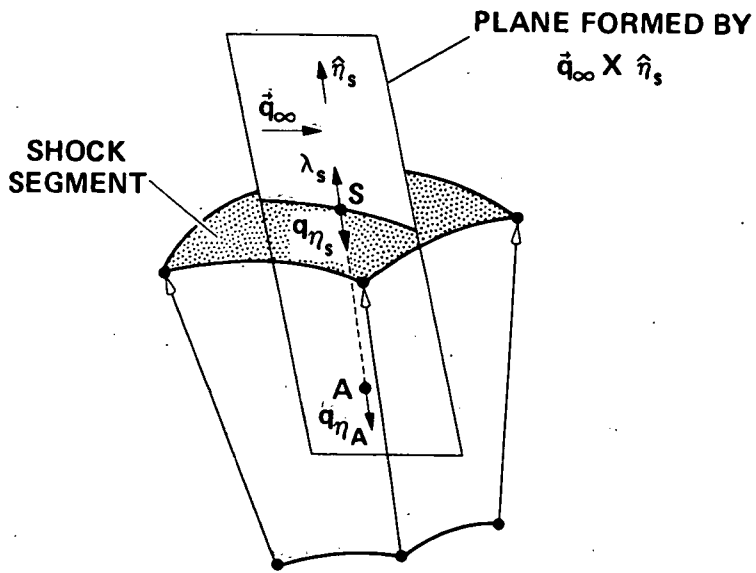


Figure 6.- Geometry for shock velocity evaluation.

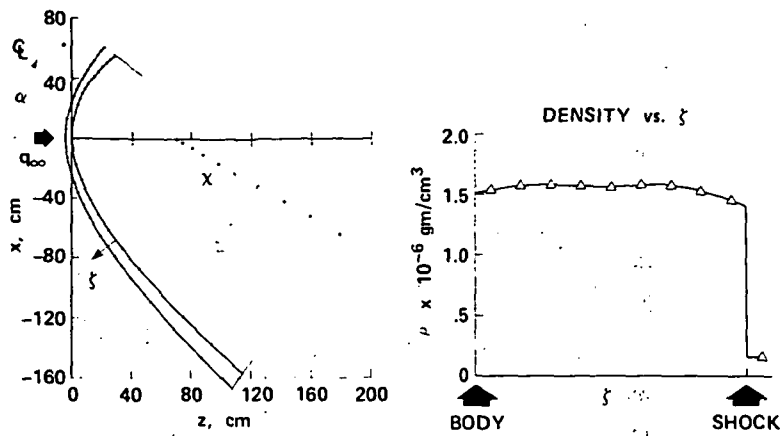


Figure 7.- Shock shape and density distribution in symmetry plane for reacting flow past three-dimensional body at velocity $q_\infty = 6.54$ km/sec, temperature $T_\infty = 236$ K, pressure $p_\infty = 106$ dynes/cm², and $\alpha = 30^\circ$ angle of attack. ζ is line between body and shock.

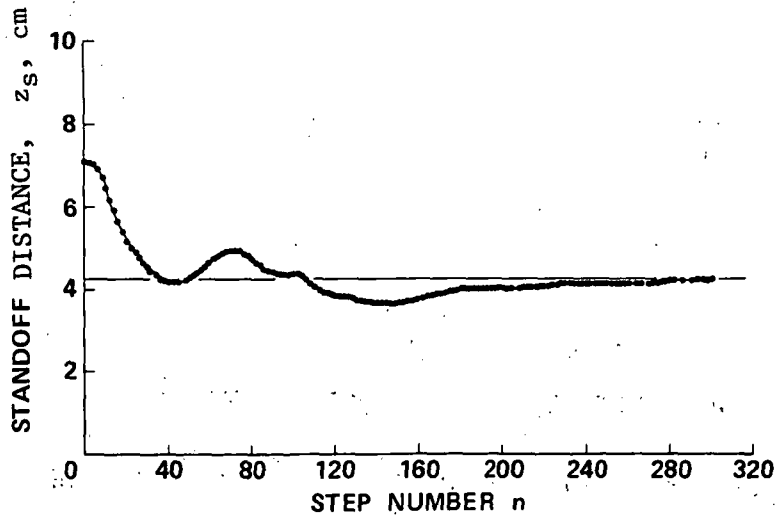


Figure 8.- Variaton of standoff distance z_s with iteration number for flow in figure 7.^s

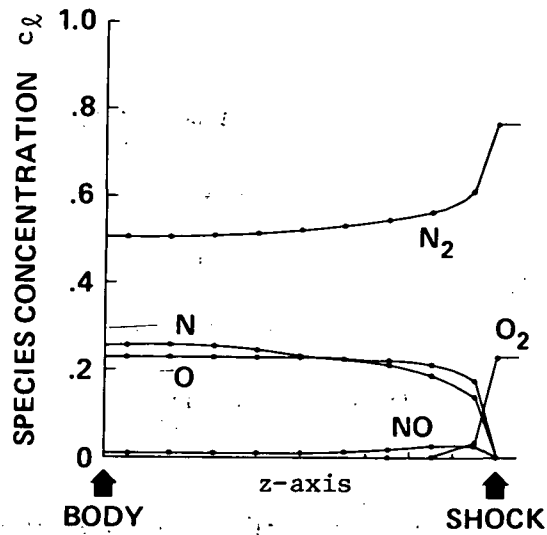


Figure 9.- Variation of the five species concentration in c_i along the z axis for flow in figure 7.

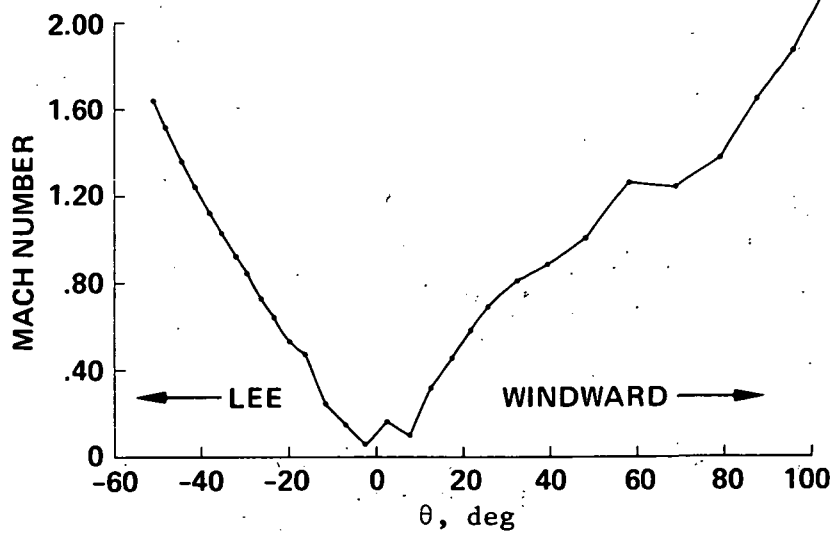


Figure 10.- Local computed Mach number on the body surface in the symmetry plane for flow in figure 7.

Page intentionally left blank

COMPUTATION OF SHUTTLE NONEQUILIBRIUM FLOW

FIELDS ON A PARALLEL PROCESSOR

By W. C. Davy and W. A. Reinhardt

NASA Ames Research Center

ABSTRACT

A finite difference computational procedure is described for calculating hypersonic, three-dimensional, chemically reacting, inviscid flow about Space Shuttle Orbiter wing-body configurations. The governing set of partial differential equations are integrated by combining explicit and implicit numerical methods. The outer shock wave is treated as a sharp boundary of the perturbed flow region and embedded surfaces of discontinuity are "captured." The methodology by which the procedure was adapted for the ILLIAC IV parallel processing computer and the CFD programming language are described. Convenient procedures leading to rapid program development are covered. Results are presented which are among the first to come from the ILLIAC IV.

INTRODUCTION

The advent of the new generation of very fast, special purpose, vector computers with large core storage (e.g., IBM 360/195, ILLIAC IV, CDC 7600, and CDC STAR) has made feasible the numerical simulation of complicated three-dimensional flow fields that can contain an intricate array of embedded discontinuities such as shock- or contact-surfaces. Also, these computers have necessitated the development of new programming languages to insure the generation of particularly efficient computer codes that take advantage of special hardware features such as "pipeline" or "parallelism" (CDC 7600, CDC STAR, and ILLIAC IV). This paper discusses the use of CFD language (ref. 1) programs in numerically simulating chemically-reacting, inviscid, hypersonic flow about Shuttle Orbiter design configurations. The results shown are among the first to come off the ILLIAC IV computer.

Several methods for numerically simulating a supersonic or hypersonic flow field for either perfect gas or equilibrium air are described in the literature (refs. 2, 3, 4). Some of these programs have been applied to various design versions of the Shuttle Orbiter with the goal of providing pressure and velocity data that might lead to design refinements. However, during the early portion of a typical entry trajectory for the Shuttle, where Mach numbers are greater than 20, it has been estimated (refs. 5, 6) that significant effects due to chemical reactions in the shock layer are to be expected. Among these are the changes in the temperature and species composition of the gas near the body, which are expected to have pronounced effects on energy and mass transport phenomena. The material surface activity in the environment of high

temperature and large nascent oxygen concentration necessitates a more complete understanding of chemical nonequilibrium flows. Rakich and Park (ref. 6) have described chemical nonequilibrium flow results obtained from a solution based on method-of-characteristics (MOC). The MOC approach, however, is not readily adaptable to complex shapes, such as bodies with wings. This paper introduces results for typical Shuttle entry conditions obtained from a shock-capturing (SC) method of solving the gas dynamic equations. Such methods have been researched for several years, in particular, by members of the staff at NASA Ames Research Center, where there exists a large reservoir of relevant knowledge and experience.

The basic method in many respects parallels that described in reference 2. The flow in the subsonic region about the blunt nose of a hypersonic spacecraft (or supersonic aircraft) is calculated by the methods described in references 7 and 8 which yield results on a plane normal to the body axis. With these results as initial data, this "computational" plane is then "marched" stepwise to the end of the body. The outer, or bow, shock wave, which separates the perturbed flow from the free stream, is treated as a sharp boundary. Embedded surfaces of discontinuity, whether shock waves or contact, are "captured" by the numerical method. Flow tangency on the body surface is satisfied by use of a scheme similar to that of Abbett (ref. 9), except that constant entropy, as a condition on the body stream-surface, is not explicitly imposed. Entropy production, caused by chemical relaxation, is allowed; isentropic flow in the body stream-surface is then a byproduct of such limiting phenomena as either "frozen" or equilibrium flow. The numerical algorithm by which the chemical relaxation effects are computed is briefly discussed in this paper.

The computation of chemically-reacting, three-dimensional flows, even with the simplest chemical models, seriously strains the capability of other than the new generation of vector computers. As mentioned earlier, these computers achieve their efficiency principally through special hardware features (parallelism or pipeline); but to take greatest advantage of their computational efficiency requires programming in a vector language. A particularly easily learned language, for programmers experienced with FORTRAN, is CFD (ref. 1). This language, developed within the Computational Fluid Dynamics Branch at NASA Ames Research Center, leads through the use of translators and compilers to very efficient code for both the ILLIAC IV parallel computer and the CDC 7600 pipeline computer. Also described in this paper is the modus operandi by which the same CFD Shuttle code is run on a variety of computers so that the best features of each computer can be effectively utilized.

BASIC EQUATIONS

The conservation of mass and momenta in a steady inviscid three-dimensional flow may be written in cylindrical coordinates as follows:

$$\frac{\partial \tilde{E}}{\partial z} + \frac{\partial \tilde{F}}{\partial r} + \frac{\partial \tilde{G}}{\partial \phi} + \tilde{H} = 0 \quad (1)$$

where \tilde{E} , \tilde{F} , \tilde{G} , and \tilde{H} are four component vectors defined by

$$\tilde{E} = \begin{bmatrix} \rho u \\ p + \rho u^2 \\ \rho uv \\ \rho uw \end{bmatrix} \quad \tilde{F} = \begin{bmatrix} \rho v \\ \rho vu \\ p + \rho v^2 \\ \rho vw \end{bmatrix}$$

$$\tilde{G} = \frac{1}{r} \begin{bmatrix} \rho w \\ \rho wu \\ \rho wv \\ p + \rho w^2 \end{bmatrix} \quad \tilde{H} = \frac{1}{r} \begin{bmatrix} \rho v \\ \rho vu \\ \rho(v^2 - w^2) \\ 2\rho vw \end{bmatrix}$$

In these equations p and ρ are conventional symbols for pressure and density, and u , v , and w are the three velocity components corresponding to the coordinate directions z , r , and ϕ , respectively. In addition to these four flow equations we have the species conservation given by¹

$$(\mathbf{V} \cdot \nabla)\gamma = R(T, \rho, \gamma_j) \quad (2)$$

where γ is the s -dimensioned vector,

$$\gamma = \begin{bmatrix} \gamma_1 \\ \gamma_2 \\ \cdot \\ \cdot \\ \cdot \\ \gamma_s \end{bmatrix}$$

¹The origin of these equations, as well as explicit representations for the production term R , can be traced in sources such as references 10 and 11.

and s denotes the number of species in the flowing mixture. The quantities γ_i are the species concentrations in units of moles per unit mass, and R denotes the species production term in $[\gamma_i]$ units per unit time. In cylindrical coordinates the convective or "material" operator is given by

$$\mathbf{V} \cdot \nabla = u \frac{\partial}{\partial z} + v \frac{\partial}{\partial r} + \frac{w}{r} \frac{\partial}{\partial \phi}$$

Equations (1) and (2) are $s+4$ partial differential equations that govern the behavior of the $s+5$ variables p , ρ , u , v , w , and γ_i . These equations are completed by introducing the integrated form of energy conservation to obtain the adiabatic flow, or caloric state, equation given by

$$\begin{aligned} H_t &= \text{constant} \\ &= h + V^2/2 \\ &= \frac{\gamma}{\gamma - 1} \frac{p}{\rho} + \frac{V^2}{2} + \sum_{j=1}^s \gamma_j h_j^0 \end{aligned} \quad (3)$$

where H_t is the total enthalpy, $h = \gamma p / \rho (\gamma - 1) + \sum \gamma_j h_j^0$ is the static enthalpy, V is the magnitude of the velocity vector, h_j^0 are the chemical heats of formation (see table 3), and γ (without subscript) is the specific heat ratio, defined as the ratio of the specific heat at constant pressure to the specific heat at constant volume (see appendix). More specifically, equation (3) follows by neglecting viscous and nonadiabatic energy dissipation effects and by assuming that the molecular vibrational energy can be approximated by the Lighthill model, where the vibrational states are assumed half-excited (ref. 6). The above set of equations is nearly complete except that the production terms, R in equation (2), contain rate constant parameters that depend on temperature. The system is completed by introducing the thermal equation of state, given by

$$T = p / \rho R_0 \sum_{i=1}^s \gamma_i \quad (4)$$

where R_0 is the universal gas constant ($R_0 = 8.31434 \times 10^7$ erg (g mole) $^{-1}$ K $^{-1}$). Atom conservation is satisfied by equations (2) and is not further introduced to reduce the rank of the system to be integrated. Two advantages follow from this procedure: the equations lend themselves more readily to vector-matrix formalism, and atom conservation can be used to estimate the extent of numerical integration errors.

Except for the addition of species conservation, equations (2), the above equations are analogous to those described in the paper by Kutler, Reinhardt, and Warming (ref. 2). In similar manner, the body geometry and the outer or peripheral shock surfaces, displayed in figure 1, can be represented by functions of the form

$$r_b = r_b(z, \phi) \quad (5a)$$

$$r_s = r_s(z, \phi; \gamma_\infty) \quad (5b)$$

where r_b is obtained by evaluating the equations defining the body surface described in reference 2, and r_s is determined during the course of the numerical computation by following a method parallel to that described in reference 2. Equation (5a) is independent of the state of the mixture; equation (5b) depends only on the specific heat ratio of the mixture at the peripheral shock, and since it is assumed that the species concentrations are "frozen" (constant) across the shock wave, the γ at the shock is that of the free stream. Using the procedure defined for obtaining equations (5), the radial coordinate is normalized to allow for a reclustering of mesh points in the meridional direction in similar manner to reference 2 (cf. fig. 2) by introducing the independent variable transformations given by

$$z = z$$

$$\xi(z, r, \phi) = (r - r_b) / (r_s - r_b) \quad (6)$$

$$\left. \begin{aligned} \eta(\phi) &= \pi \left\{ B + \sinh^{-1} \left[\left(\frac{\phi}{\phi_0} - 1 \right) \sinh(B) \right] \right\} / \beta \\ B(\beta, \phi_0) &= 0.5 \ln \left[\frac{1 + (e^\beta - 1)\phi_0/\pi}{1 + (e^{-\beta} - 1)\phi_0/\pi} \right] \end{aligned} \right\} (\beta > 0)$$

$$\eta(\phi) = \phi \quad (\beta = 0)$$

where β and ϕ_0 are arbitrary parameters that control the degree and location of clustering. No clustering occurs when β is zero. As β increases, the degree of clustering increases with the greatest density of points appearing about the ray defined by the angle ϕ_0 .

Application of the independent variable transformation relations, defined above, into equations (1) and (2) yields

$$\frac{\partial E}{\partial z} + \frac{\partial F}{\partial \xi} + \frac{\partial G}{\partial \eta} + H = 0 \quad (7a)$$

$$\frac{\partial Y}{\partial z} + a \frac{\partial Y}{\partial \xi} + b \frac{\partial Y}{\partial \eta} = R/u \quad (7b)$$

where

$$\begin{aligned}
 \mathbf{E} &= \tilde{\mathbf{E}} \\
 \mathbf{F} &= \xi_z \tilde{\mathbf{E}} + \xi_r \tilde{\mathbf{F}} + \xi_\phi \tilde{\mathbf{G}} \\
 \mathbf{G} &= \eta_\phi \tilde{\mathbf{G}} \\
 \mathbf{H} &= \tilde{\mathbf{H}} - (\xi_z)_\xi \tilde{\mathbf{E}} - (\xi_r)_\xi \tilde{\mathbf{F}} - [(\xi_\phi)_\xi + (\eta_\phi)_\eta] \tilde{\mathbf{G}}
 \end{aligned} \tag{8}$$

and

$$\begin{aligned}
 a &= \xi_z + \frac{v}{u} \xi_r + \frac{w}{ur} \xi_\phi \\
 b &= \frac{w}{ur} \eta_\phi
 \end{aligned}$$

The transform derivatives are given by

$$\begin{aligned}
 \xi_z &= - \frac{r_{bz} + \xi(r_{sz} - r_{bz})}{(r_s - r_b)} \\
 \xi_r &= \frac{1}{(r_s - r_b)} \\
 \xi_\phi &= - \frac{r_{b\phi} + \xi(r_{s\phi} - r_{b\phi})}{(r_s - r_b)} \\
 \eta_\phi &= \frac{(\pi/\phi_0) \sinh(B)/\beta}{\sqrt{[(\phi/\phi_0 - 1) \sinh(B)]^2 + 1}} \\
 (\xi_z)_\xi &= - \frac{r_{sz} - r_{bz}}{(r_s - r_b)} \\
 (\xi_r)_\xi &= 0 \\
 (\xi_\phi)_\xi &= - \frac{r_{s\phi} - r_{b\phi}}{r_s - r_b} \\
 (\eta_\phi)_\eta &= - \frac{\sinh(B)}{\phi_0} \frac{\sinh[\eta\beta/\pi - B]}{1 + \sinh^2[\eta\beta/\pi - B]}
 \end{aligned} \tag{9}$$

These relations follow conventional notation, where

$$r_{b_z} = \frac{\partial r_b}{\partial z}; \quad r_{s_z} = \frac{\partial r_s}{\partial z}$$

$$r_{b_\phi} = \frac{\partial r_b}{\partial \phi}; \quad r_{s_\phi} = \frac{\partial r_s}{\partial \phi}$$

The finite difference analogue of equations (7) is integrated with respect to the hyperbolic coordinate z to calculate values of the conservative vector \mathbf{E} . Within each integration step, however, values of the physical variables p , ρ , u , v , w , and γ_1 are also required. These are obtained by solving the set of equations represented by the vectors \mathbf{E} and γ . This "decoding" procedure parallels that described in reference 2. Let e_1 denote the components of the vector \mathbf{E} ; the velocity components v and w are easily found and are given by

$$v = e_3/e_1 \quad (10a)$$

$$w = e_4/e_1 \quad (10b)$$

By substituting these relations into that for total enthalpy, equation (3), and by using e_1 and e_2 to eliminate the variable dependence of p and ρ , we obtain

$$\sigma(u) = u^2/2 + h^+[p(u), \rho(u)] - \omega/2 = 0 \quad (11)$$

where

$$h^+(p, \rho) = \frac{\gamma}{\gamma - 1} \frac{p}{\rho}$$

$$p(u) = e_2 - e_1 u$$

$$\rho(u) = e_1/u$$

$$\omega = 2(H_t - \sum \gamma_1 h_1^0) - (e_3/e_1)^2 - (e_4/e_1)^2$$

Notice that the chemical enthalpy is not included in the special static enthalpy relation h^+ defined above. An advantage of assuming half-excited vibration (Lighthill model), where the vibrational energy is proportional to temperature, rather than adopting equilibrated internal molecular vibration, is that the decoding process is greatly simplified. We can decode explicitly to obtain

$$u = \frac{\gamma}{\gamma + 1} \frac{e_2}{e_1} + \left[\left(\frac{\gamma}{\gamma + 1} \frac{e_2}{e_1} \right)^2 - \left(\frac{\gamma - 1}{\gamma + 1} \right) \omega \right]^{1/2}$$

It can be shown that decoding also yields explicit relations in the more complex models where the vibrational energy is assumed in nonequilibrium (refs. 10, 11, 12), or when vibration-dissociation coupling is considered (refs. 13, 14), but not when equilibrium is considered (ref. 2). It is not expected that the inclusion of the more complex models would greatly alter the overall characteristics of the computed flows, but may only affect locally small regions of the flow. Their inclusion is certainly not warranted in context with the relatively simple chemical model that is considered in this paper, and discussed in the next section.

CHEMICAL MODEL

The set of chemical reactions considered are the three dissociation reactions and the two bimolecular exchange reactions involving five species given in table 1.

TABLE 1.- CHEMICAL MODEL

i	Chemical equation
1	$O_2 + M \rightleftharpoons 2O + M$
2	$N_2 + M \rightleftharpoons 2N + M$
3	$NO + M \rightleftharpoons N + O + M$
4	$O_2 + N \rightleftharpoons NO + O$
5	$N_2 + O \rightleftharpoons NO + N$

In reactions 1-3, the symbol M is the "third body" collision partner that can be any of the five species in the mixture.

Table 2 lists the rate and equilibrium constant data for the five reactions shown in table 1, as well as the collisional efficiencies which depend on the kind of "third body." The equilibrium constant is used to find the reverse rate constant from the expression $k_{r_i} = k_{f_i} / \kappa_i$, where k_{f_i} and k_{r_i} are the forward and reverse rate constants and κ_i is the equilibrium constant for the *i*th reaction. The dissociation rate constants in the table have units $\text{cm}^3 \text{mol}^{-1} \text{sec}^{-1}$, while the equilibrium constants have units mol cm^{-3} .

Table 3 provides heats-of-formation data in several basic units which are required in equation (3).

TABLE 2A.- FORWARD RATE EXPRESSIONS

$$k_{f_i} = \epsilon AT^B \exp(-C/T)$$

Reaction	A	B	C	E		Ref.
				Molecules M=O ₂ ,N ₂ ,NO	Atoms M=O,N	
1	2.75 E+19	-1.0	59 750	1	3	15
2	3.70 E+21	-1.6	113 200	1	3	16
3	2.30 E+17	-0.5	74 900	1	2	16
4	1.01 E+10	1.0	3 386	-	-	17
5	7.60 E+13	0.0	38 000	-	-	16

Note: ϵ is collisional efficiency factor.

TABLE 2B.- EQUILIBRIUM CONSTANTS^a

$K_i = \exp\left(\sum_{l=0}^3 B_{il} T^l - \theta_i/T\right) \quad i = 1, 2, 3$					
$K_4 = K_1/K_3$					
$K_5 = K_2/K_3$					
i	B _{il}				θ_i
1	2.6807	1.7379 E-4	-3.0429 E-8	1.2237 E-12	59,364
2	2.6408	1.2990 E-4	-1.7172 E-8	8.0627 E-13	113,260
3	1.2777	9.9571 E-5	-1.5647 E-8	7.0075 E-13	75,518

^aThese constants were obtained by least squares fitting of equilibrium constant data obtained from a computer program that evaluates partition functions based on spectroscopic data.

TABLE 3.- HEATS-OF-FORMATION SPECIFIED IN SEVERAL BASIC UNITS

Species	Heats-of-formation, h_i^0		
	Cal/Mol	Ergs/Mol	K
O ₂	0	0	0
N ₂	0	0	0
NO	2.1810×10 ⁴	9.1254×10 ¹¹	10 975
O	5.8990×10 ⁴	2.4681×10 ¹²	29 684
N	1.1250×10 ⁵	4.7070×10 ¹²	56 611

The chemical reaction system defined above is considered important in non-equilibrium studies involving spacecraft entry from near Earth orbits. With these reactions, the effects of chemical nonequilibrium on entry dynamics and on the thermal and chemical environment near the spacecraft's surface can be accurately calculated. Such results are in demand by vehicle designers to predict, in particular, surface heating rates and chemical corrosion effects on the surface materials of vehicles. The effect of gas ionization on these estimates is not expected to be significant, although data on the ion sheath occurring in the shock layer can be important in communication studies (e.g., the communication "blackout" problem). The algorithm discussed in this paper, as well as the computer code itself, readily permits for a generalization of the chemistry model; but these nonequilibrium flow simulations use about four times as much computer time as do perfect gas ("frozen" chemistry) calculations. Hence, complicating the chemical model is not desirable for preliminary investigations, while the computer program is in early stages of development.

FINITE DIFFERENCE EQUATIONS.

The fluid-flow equations, equations (7a), are approximated by use of MacCormack's second-order, predictor-corrector method.

The numerical algorithm can be written as

$$\begin{aligned} \overline{E}_{*,j}^{n+1} = & E_{*,j}^n - \frac{\Delta z^{n+1}}{\Delta \xi} \left(F_{*,j+1}^n - F_{*,j}^n \right) - \frac{\Delta z^{n+1}}{\Delta \eta} \left(G_{*,j}^n - G_{*,j-1}^n \right) - \Delta z^{n+1} H_{*,j}^n \\ & + \Delta E_{*,j}^n \Big|_m + \Delta E_{*,j}^n \Big|_r \end{aligned} \quad (12a)$$

$$\begin{aligned} E_{*,j}^{n+1} = & \frac{1}{2} \left[E_{*,j}^n + \overline{E}_{*,j}^{n+1} - \frac{\Delta z^{n+1}}{\Delta \xi} \left(\overline{F}_{*,j}^{n+1} - \overline{F}_{*,j-1}^{n+1} \right) - \frac{\Delta z^{n+1}}{\Delta \eta} \left(\overline{G}_{*,j}^{n+1} - \overline{G}_{*,j-1}^{n+1} \right) \right. \\ & \left. - \Delta z^{n+1} \overline{H}_{*,j}^{n+1} \right] + \Delta E_{*,j}^{n+1} \Big|_m + \Delta E_{*,j}^{n+1} \Big|_r \end{aligned} \quad (12b)$$

where

$$E_{*,j}^n = E(z^n, * \Delta \eta, j \Delta \xi)$$

$$F_{*,j}^n = F(E_{*,j}^n, z^n, * \Delta \eta, j \Delta \xi)$$

$$\overline{F}_{*,j}^{n+1} = F(\overline{E}_{*,j}^{n+1}, z^n + \Delta z^{n+1}, * \Delta \eta, j \Delta \xi)$$

etc.

$$z^n = \sum_{\ell=1}^n \Delta z^\ell$$

The argument $E_{*,j}$ in the latter two expressions implies the "decode" process of solving equation (11) to obtain the physical variables. The terms

$\Delta E_{*,j}^n|_{m,r}$ and $\Delta E_{*,j}^{n+1}|_{m,r}$ are fourth-order damping terms introduced to minimize nonlinear instabilities (ref. 18). The increments $\Delta\xi$ and $\Delta\eta$ are the mesh spacings in the radial and meridional directions, and Δz^n is the "marching step-size" between the $n-1$ and n th computational planes (see appendix). The damping terms, depending on whether damping is applied in the meridional and/or radial directions, are given by

$$\Delta E_{*,j}^L|_m = \frac{0.5(P_{*+l+1,j} - 2P_{*+l,j} + P_{*+l-1,j})(E_{*+1,j} - 2E_{*,j} + E_{*-1,j})}{(P_{*+l+1,j} + 2P_{*+l,j} + P_{*-l,j})} \quad (13a)$$

$$\Delta E_{*,j}^L|_r = \frac{0.5(P_{*,jj+1} - 2P_{*,jj} + P_{*,jj-1})(E_{*,j+1} - 2E_{*,j} + E_{*,j-1})}{(P_{*,jj+1} + 2P_{*,jj} + P_{*,jj-1})} \quad (13b)$$

where $L = n$ or $n+1$, $l = 0$ or 1 , and $jj = j$ or $j+1$, depending on whether the above formulas apply for the predictor step, equation (12a), or for the corrector step, equation (12b). The asterisk is introduced to reveal the "Processing Element" (PE) vector alignment on the ILLIAC IV. The above equations are somewhat similar to those given in reference 2, except for the addition of the damping terms and the parallel solution of the above equations. That is to say, they are solved simultaneously insofar as the Processing Elements (asterisk) are concerned. The subscripts $*+1$ and $*-1$ respectively label the variables as those to the right and left of the reference PE, labeled $*$, and the subscript j denotes the array location within the respective PE.

The above equations advance the solution everywhere within the region $2 \leq * \leq N_\eta$ and $2 \leq j \leq N_\xi - 1$ where N_η and N_ξ are the number of meridional and radial node points, respectively (cf. fig. 2).

On the boundaries, that is, on the body surface ($j = 1, 2 \leq * \leq N_\eta$) as well as on the shock-wave surface ($j = N_\xi, 2 \leq * \leq N_\eta$), different numerical algorithms are required. The state of the ILLIAC IV is also altered. This is accomplished by setting "MODE," which is nothing more than turning off the appropriate processing elements during the small amount of time that boundary points are computed. MODE setting permits considerable program flexibility on the parallel processing ILLIAC IV.

On the body surface, inviscid boundary conditions are applied where the flow is required to be tangent to the body surface. The flow at the shock-wave boundary is based on the Rankine-Hugoniot conditions. At the shock wave it is assumed that chemical relaxation cannot occur within the few mean-free-path lengths that define the viscous shock-wave thickness; hence, the species are set equal to their free-stream values. The flow across a shock-wave boundary, therefore, behaves as a perfect gas, and it follows that the procedure described in reference 2 for a perfect gas can also be extended to reacting

flow. The method is based on the scheme by Thomas et al., reference 19, which yields shock-wave slope from a set of predictor-corrector formulas derived from the Rankine-Hugoniot conditions. These formulas depend upon the downstream pressure, P_2 , being known, and this is found by integrating the fluid-flow and nonequilibrium equations, equations (7).

Application of flow tangency as a boundary condition on the body surface is complicated by the requirement that the flow within the body stream surface may not necessarily be isentropic because of entropy production resulting from chemical nonequilibrium. However, advantage can be taken of the fact that the nonequilibrium flow can be isentropically turned at a point. A procedure similar to that of Abbett (ref. 9) can be used. For three-dimensional flow the procedure parallels that described in the paper by Kutler, Reinhardt, and Warming (ref. 2), except that density is found by evaluating

$$\rho_2 = (p_1/p_2)^{1/\gamma} \rho_1$$

where the ratio p_1/p_2 is the ratio of pressures before (p_1) and after (p_2) a Prandtl-Meyer expansion or compression involving an angle $\pm\Delta\theta$, and γ is the isentropic exponent that is unchanged by these effects (see appendix). The quantity γ is a variable, however, that can be different at each point on the body surface from one plane to the next.

The species equations (7b) are solved by way of a modified form of the Crank-Nicolson differencing method. The derivation is not given here. Approximation of the species-continuity equations by a Crank-Nicolson method leads to the predictor-corrector form given by

$$\begin{aligned} \overline{\gamma_{*,j}^{n+1}} = & -\frac{\tilde{\Delta z}^{n+1}}{\Delta \xi} a_{*,j}^n \left(\gamma_{*,j+1}^n - \gamma_{*,j}^n \right) - \frac{\tilde{\Delta z}^{n+1}}{\Delta \eta} b_{*,j}^n \left(\gamma_{*,j+1}^n - \gamma_{*,j}^n \right) \\ & + \frac{\tilde{\Delta z}^{n+1}}{u_{*,j}^n} R_{*,j}^n + \gamma_{*,j}^n \end{aligned} \quad (14a)$$

$$\begin{aligned} \left(I - \frac{\tilde{\Delta z}^{n+1}}{2u_{*,j}^{n+1}} J_{*,j}^n \right) \left(\overline{\gamma_{*,j}^{n+1}} - \gamma_{*,j}^n \right) = & 0.5 \left[\overline{\gamma_{*,j}^{n+1}} - \gamma_{*,j}^n - a_{*,j}^{n+1} \frac{\tilde{\Delta z}^{n+1}}{\Delta \xi} \left(\overline{\gamma_{*,j}^{n+1}} - \overline{\gamma_{*,j-1}^{n+1}} \right) \right. \\ & \left. - b_{*,j}^{n+1} \frac{\tilde{\Delta z}^{n+1}}{\Delta \eta} \left(\overline{\gamma_{*,j}^{n+1}} - \overline{\gamma_{*,j-1}^{n+1}} \right) + \frac{\tilde{\Delta z}^{n+1}}{u_{*,j}^{n+1}} R_{*,j}^n \right] \end{aligned} \quad (14b)$$

Where $J_{*,j}^{\tilde{n}}$ is a Jacobian matrix, the elements of which are derivatives of the production terms with respect to the species variables, that is,

$$\left(J_{*,j}^{\tilde{n}} \right)_{k\ell} = \frac{\partial \left(R_{*,j}^{\tilde{n}} \right)_k}{\partial \gamma_\ell} \quad (15)$$

and I is the identity matrix. The notation has been defined earlier; the subscript and superscripts denote the same meaning as used for the flow equations. The tilde over the interval size, $\tilde{\Delta z}$, signifies that the chemical step-size can be different from that for the flow (described in the appendix). Depending on transients in the species variables, several steps governed by accuracy may be required to advance the species equations within the step size dictated by fluid-flow stability considerations (see the appendix).

CFD PROGRAMMING

General Features

The method described in the foregoing sections was coded in CFD language for the ILLIAC IV parallel processing computer. This language, described in reference 1, is a vector, FORTRAN-like language, which was developed within the Computational Fluid Dynamics (CFD) Branch at NASA Ames Research Center. Several worthwhile features characterize CFD. First, users familiar with FORTRAN find the transition to CFD easy. Second, once programs are coded in CFD, translators and compilers exist that generate FORTRAN code for serial computers or relocatable machine language code for the ILLIAC IV. Third, the architecture of the ILLIAC is not hidden from the programmer (cf. fig. 1, ref. 1) and this permits the programmer to produce efficient machine language code. Finally, since CFD is a vector language, translators can be designed to generate efficient code for vector computers such as the CDC 7600, and this effort is currently underway.

The CFD programmer who understands FORTRAN needs only a very basic understanding of the ILLIAC hardware (ref. 1), that is, the Control Unit (CU), the Processing Elements (PE's), and the Main Memory (MM) which is the disk area. The few non-FORTRAN CFD instructions are easily understood. The programmer can then concentrate on the logic of the numerical method without being encumbered with the language.

The CFDX translator, which generates the FORTRAN language code for serial computers, was designed to simulate accurately the parallelism. This translator can be exploited to great advantage. The ILLIAC program can be initially simulated on a serial machine. Thereby, considerable use can be made of the debugging aids already developed over the years that serial computers have been in use. The dynamic dumping and interactive graphic capabilities available at Ames Research Center have been utilized to great advantage. In fact,

with very few exceptions, it was possible to verify the entire program, consisting of some 30 subprograms, on the Ames IBM 360/67 system.

The vector features of CFD led to the development of a new translator, CFDX7600; that produces highly efficient FORTRAN code for the CDC 7600. This is accomplished by the translator insertion of "speedie" subprograms that take advantage of the "pipeline" capabilities of the CDC 7600 to process a selected set of arithmetic-vector operations. By hand coding "speedie" subroutines into the Shuttle program described here, it was possible to achieve a nearly threefold decrease in computer run time per integration step when compared to the standard FORTRAN compiled code.

This discussion has alluded to running on at least three separate types of computers, IBM 360/67, ILLIAC IV, and CDC 7600. In fact, this is the usual modus operandi. This multiple computer operation is illustrated in figure 3. Note that the complete cycle of program execution may be categorized in several phases, that is, language processing, program as well as initial data transmission, data generation, and data reduction. The translators and compilers have already been described. The value of the combined IBM 360/67-ILLIAC IV loop has been touched upon for program checkout. The pair of computers is connected within a network, known as the ARPA network, and data transmission is nearly automatic. The CDC 7600 used heretofore is located about 60 miles away in Berkeley and is connected via a Remote Job Entry (RJE) unit. Program and data transmission is by cards or tape. In the near future Ames will have installed a CDC 7600 which will not be within the network, but will be geographically more accessible. The dashed-line within the figure denotes that the CDC 7600 is not electrically connected within a loop.

As the performance of the ILLIAC IV improves, and the Ames CDC 7600 becomes available, the use of graphics, shown at the bottom of figure 3, will have even increasing value. The scheme outlined will permit rapid data processing to minimize the need for hard copy output. (In fact, the contours described later are reproduced Polaroid photos of an IBM 2250 CRT display.)

Special Features

The program described has been run on the ILLIAC-IV almost from the time when users were first allowed access to the machine. At that time it was difficult to identify faults originating in the hardware from those due to software. In the intervening time the performance of the machine and the accessing network has improved greatly. During this time, however, a troublesome problem from the users' point of view was occasional errors arising from intermittent failure of one or more of the 64 PE's. Such errors propagated to affect eventually the data in all the PE's. A strategy was developed to guard against such problems by internally checking the data after each integration step. Within the CFD program, the 64 PE's are divided into one, two, or three sectors. The three-sector division is illustrated in figure 4. By setting identical initial conditions in each of the sectors, and by appropriately setting MODE, briefly described earlier, so that the correct PE's are activated while boundary conditions are computed, it is possible to solve the same problem redundantly in each of the sectors. The results can be compared at the

end of each step to detect PE failure. In fact, it has been possible with this stratagem to identify particularly troublesome units. If data differ in only one of the three sectors, the data from this sector are replaced (identical failure in two sectors is highly improbable) and the integration is continued. If all three sectors differ, the data are recomputed from the previous step. If failures occur too often within a step, the program automatically exits. The two sector option allows for greater meridional resolution (32 meridional planes compared to 21), while still allowing for internal checking. The single sector option, which can include simultaneous computation in all PE's, allows for maximum radial resolution, and is also the option exercised in the CFD code when used on serial and "pipeline" computers where multiple sector operation has no advantage. The stratagem of using multiple sectors can be used to great advantage when parameter studies are desired, but with sacrifice in the degree of resolution (i.e., with less than 32 planes rather than possibly 64) for the meridional direction. For example, two separate trajectory points could, in principle, be simultaneously computed on the ILLIAC IV at a cost of about one-quarter of that required to obtain the 64-plane, maximum resolution. The program would require minor modification since its current design allows only for the simultaneous solution of redundant problems.

RESULTS AND CONCLUSIONS

A typical shuttle trajectory point has been studied to demonstrate the viability of method, CFD language, and parallel processing. The free-stream conditions, which correspond to a point on the Shuttle reentry trajectory at an altitude of about 65.5 km and a Mach number of 21.7, are as follows:

$$\begin{aligned} p_{\infty} \text{ (pressure)} &= 106.2 \text{ dynes/cm}^2 \\ \rho_{\infty} \text{ (density)} &= 1.566 \times 10^{-7} \text{ g/cm}^3 \\ V_{\infty} \text{ (velocity)} &= 6.544 \text{ km/sec} \\ \alpha \text{ (angle-of-attack)} &= 30^{\circ} \end{aligned}$$

The initial conditions (i.e., starting solution) were obtained by first solving the unsteady fluid-flow and species conservation equations (ref. 7) to obtain data on a conical data plane which encompasses the subsonic regime of the oncoming stream. This cone was then expanded to reach congruence with a plane normal to the axis by application of the method (see ref. 8). The data on this plane then served as initial conditions for the results described here. The body configuration is based on the Shuttle Orbiter 147 design and has the general attributes of the vehicle shown in figure 1. The planform, which includes the double delta wing, is accurately represented. It was considered worthwhile, at least during the early stages of program development, to sacrifice a degree of geometrical accuracy in describing the cross section to minimize difficulties caused by other problems. That is, among the many problems confronting the new procedure, it was desired to avoid possible flow overexpansion about regions of large curvature. The windward side is relatively accurately represented, while the lee-side profile roughly approximates "a separation bubble." The numerical algorithm is, however, not limited to such shapes.

The results of the calculation, which were obtained via the ARPA network from the ILLIAC IV parallel processing computer, are given in figures 5 to 8.

Figure 5 shows computed atomic oxygen and temperature radial profiles from both the windward and leeward symmetry planes. Also shown are comparisons with available results obtained by different computational methods. Results are plotted from method-of-characteristics (ref. 6) and from a finite-volume method (see ref. 8). Comparisons with flow quantities (not shown) were fairly precise (<1.0 percent), while greater deviations were observed for the concentration variables (<8 percent). Agreement is considered excellent. The chemical model was the same for all the methods compared.

The qualitative behavior of the profiles shown in figure 5 compare with similar data given in reference 6. The temperature decay from 7000 K to 5500 K on the windward plane is caused by chemical relaxation effects. In this region, almost 100 percent oxygen and 15 percent nitrogen (not shown) dissociation occurs. Effects resulting from the large angle of attack are observed by comparing windward and leeward symmetry plane data. The temperatures are generally higher on the windward side where the shock wave is very strong. The chemical relaxation zone also occurs closer to the peripheral shock wave. A temperature maximum appears on the lee side. This maximum, in effect, separates regions of the lee-side flow where different effects are important. The decreasing temperature observed in the direction of the body is caused by chemical relaxation (cf. atomic oxygen profile), while the decreasing temperature in the direction of the peripheral shock is a result of the "expansion fan" caused by the decreasing curvature away from the flow on the lee side.

Contour plots at two axial stations are shown in figures 6 to 8, inclusive. In all these figures the body and shock are described by the inner and outer curves, respectively, which are not necessarily contours. As mentioned earlier the concentrations are constant across the shock (i.e., "frozen"); hence, the species concentrations outside the first contour, for those presented here (O, N, NO), can be considered very small. In figures 6, atomic oxygen is shown. The qualitative behavior of atomic oxygen described in the preceding paragraph is also visible here. The relaxation zone, where the profiles lie close together, shifts from near the shock wave on the windward side to about midway between shock and body on the lee side. Figures 6a and 6b, when compared, show changing effects as the computational planes are marched down the body. The body shape changes to the extent that the windward surface flattens and the transition between bottom and side (chime line) becomes more distinct. Not displayed in these figures is the changing scale as the perturbed flow region expands (cf. fig. 1). The contours are obtained from a CRT device where, to maintain maximum display resolution, it was worthwhile to keep the size of the shock envelope constant.

In figures 7 and 8 contours are given for atomic nitrogen and nitric oxide. The underlying mechanisms that govern contour shapes are more complex for these species. In the case of oxygen, chemical dissociation (reaction 1 in table 1) principally governs the observed effects. For nitrogen and nitric oxide,

however, the bimolecular exchange reactions ($i = 4$ and 5 in table 1) are also very important and greatly complicate a description. The effect of cross-flow is also evidenced in these figures (cf. figs. 7a and 7b as well as 8a and 8b). The most noteworthy phenomenon is the NO overshoot shown in figures 8. Evidence of overshoots are the closed elliptical contours on the lee side of the bottom edge.

In conclusion, it has been found that the ILLIAC IV is not difficult to program using CFD. Furthermore, the ILLIAC IV can be effectively used to simulate the complicated, chemically-reacting, three-dimensional, flow problems. The use of CFD as a programming language has a number of distinct advantages of which the most prominent are its FORTRAN similarity and its relaxation of machine dependence.

The tools now developed as described in this paper will be used in subsequent investigations to study more complex and accurate body configurations and to study the effects of other chemical phenomena such as communications "blackout" during reentry.

APPENDIX

COMPUTATION OF THE STABILITY CONDITION FOR THE COMBINED SET OF
FLUID-FLOW AND SPECIES-CONSERVATION EQUATIONS

It is necessary to use as large a step size as possible commensurate with stability bounds to insure efficient use of the computer, which at the same time insures that the finite difference method is in some sense compatible with the method of characteristics (ref. 20). The stability bounds can be found by using amplification matrix theory (ref. 21) that requires evaluation of the eigenvalues of the coefficient matrices of the combined set of fluid-flow and species-conservation equations. The coefficient matrices are readily found from equations (1) and (2) in the nonconservative form

$$\left[\mathbf{I} \frac{\partial}{\partial z} + \mathbf{A}_r \frac{\partial}{\partial r} + \mathbf{A}_\phi \frac{\partial}{\partial \phi} \right] \begin{bmatrix} p \\ \rho \\ u \\ v \\ w \\ \gamma_1 \\ \gamma_2 \\ \cdot \\ \cdot \\ \gamma_s \end{bmatrix} + \mathbf{B} = 0$$

These matrices are denoted by \mathbf{A}_r and \mathbf{A}_ϕ corresponding, respectively, to the r and ϕ derivatives and \mathbf{B} is the matrix of inhomogenous terms. The \mathbf{A} matrices can be evaluated and their eigenvalues determined, although the algebra is tedious. The eigenvalues are given by

$$\sigma_{1,2}^r = \frac{M_u M_v \pm \beta_{uv}^2}{\beta_u^2}$$

$$\sigma_{3,4,5}^r = M_v / M_u$$

$$\sigma_{1,2}^\phi = \frac{M_u M_w \pm \beta_{uw}^2}{\beta_u^2}$$

$$\sigma_{3,4,5}^\phi = M_w / M_u$$

where the superscript denotes the respective matrix from which the eigenvalues are obtained, and

$$M_u, M_v, M_w = \frac{u}{a_f}, \frac{v}{a_f}, \frac{w}{ra_f}$$

$$\beta_u = \sqrt{M_u^2 - 1}$$

$$\beta_{uv} = \sqrt{M_u^2 + M_v^2 - 1}$$

$$\beta_{uw} = \sqrt{M_u^2 + M_w^2 - 1}$$

In the above equations the speed of sound is the "frozen" value given by

$$a_f^2 = \left(\frac{\partial p}{\partial \rho} \right)_{s, \gamma_i}$$

where the subscripts denote that the entropy and species concentrations are kept constant in the differentiation. Formally, the above relation is equivalent to

$$a_f^2 = \gamma p / \rho$$

where

$$\gamma = c_p / c_v$$

depends on the "frozen" representations for the specific heats at constant pressure and constant volume. These relations are given, respectively, by

$$c_p = \left(\frac{\partial h}{\partial T} \right)_{p, \gamma_i}$$

$$= \sum \gamma_i c_{p_i}$$

$$c_v = \left(\frac{\partial e}{\partial T} \right)_{v, \gamma_i}$$

$$= \sum \gamma_i c_{v_i}$$

where C_{p1} and C_{v1} are molar heat capacities. By comparison with the eigenvalues given in reference 22, it can be seen that the same result can be obtained by following the recipe implied in various references (such as refs. 10 and 11), where perfect gas fluid-flow quantities carry over to nonequilibrium flow by interchanging "frozen" flow representations with those for a perfect gas (e.g., γ , c_p , c_v).

The eigenvalues given by the above set of equations apply specifically to the cylindrical coordinate system governing equations (1) and (2). The coefficient matrix of the transformed equations, equations (7), can be found, and the corresponding eigenvalues are given by

$$\sigma_{1,2}^{\xi} = \xi_r + \frac{M_u \Lambda \pm \sqrt{\Lambda^2 + \beta_u^2 (1 + \xi_\phi^2 / r^2)}}{\beta_u^2}$$

$$\sigma_{3,4,5}^{\xi} = \xi_r + \Lambda / M_u$$

$$\sigma_{1,2}^{\eta} = \frac{[M_u M_w \pm \beta_{uw}] \eta_\phi}{\beta_u^2}$$

$$\sigma_{3,4,5}^{\eta} = \frac{M_w \eta_\phi}{M_u}$$

where

$$\Lambda = \xi_r M_v + \xi_\phi M_w$$

and the derivatives ξ_r , ξ_ϕ , and η_ϕ are given by equation (9). The following are now defined, $\sigma^{\xi} = \text{Max}(|\sigma_i^{\xi}|)$ and $\sigma^{\eta} = \text{Max}(|\sigma_i^{\eta}|)$; that is, these quantities are the largest of all those computed on a plane. It then follows that

$$\frac{(\Delta z)^{\xi}}{\Delta \xi} = f / \sigma^{\xi}$$

$$\frac{(\Delta z)^{\eta}}{\Delta \eta} = f / \sigma^{\eta}$$

where f is an arbitrary constant, which usually is set to 0.9. The intervals $\Delta \xi$ and $\Delta \eta$ depend on the radial mesh spacing. The actual value of the step size, Δz , used is the smaller of either $(\Delta z)^{\xi}$ or $(\Delta z)^{\eta}$.

REFERENCES

1. Stevens, K. G., Jr.: CFD - A FORTRAN-like Language for the ILLIAC IV. Paper presented at the NASA/ACM Conference: Programming Languages and Compilers for Parallel and Vector Machines, Goddard Institute for Space Studies (New York), Mar. 18-19, 1975.
2. Kutler, P., Reinhardt, W. A., and Warming, R. F.: Multishocked, Three-Dimensional Supersonic Flow Fields with Real Gas Effects. AIAA J., vol. 11, no. 5, May 1973, pp. 657-664.
3. Rakich, J. V.: Three-Dimensional Flow Calculations by the Method of Characteristics. AIAA J., vol. 5, no. 10, Oct. 1967, pp. 1906-1908.
4. Moretti, G., Grossman, B., and Marconi, F., Jr.: A Complete Numerical Technique for the Calculation of Three-Dimensional Inviscid Supersonic Flows. AIAA Paper 72-192, San Diego, CA, 1972.
5. Lordi, J. A., Vidal, R. J., and Johnson, C. B.: Chemical Nonequilibrium Effects on the Inviscid Flow in the Windward Plane of Symmetry of Two Simplified Shuttle Configurations. NASA TN D-7189, 1973.
6. Rakich, J. V., and Park, C.: Nonequilibrium Three-Dimensional Supersonic Flow Computations with Application to the Space Shuttle Orbiter Design. Symposium on Applications of Computers to Fluid Dynamic Analysis and Design, Polytech. Inst. of Brooklyn Graduate Center, Jan. 3-4, 1973.
7. Rizzi, Arthur W., and Bailey, Harry E.: Reacting Nonequilibrium Flow Around the Space Shuttle Using a Time-Split Method. Aerodynamic Analyses Requiring Advanced Computers, Part II, NASA SP-347, 1975, pp. 1327-1349.
8. Rizzi, A. W., and Bailey, H. E.: A Generalized Hyperbolic Marching Method for Chemically Reacting 3-D Supersonic Flow Using a Splitting Technique. Paper to be presented at 2nd AIAA Computational Fluid Dynamics Conference (Hartford, Conn.), June 19-20, 1975.
9. Abbett, M. J.: Boundary Condition Computational Procedures for Inviscid Supersonic Flow Fields. Proceedings, AIAA Computational Fluid Dynamics Conference, 1973.
10. Vincenti, W. G., and Kruger, C. H. Jr.: Introduction to Physical Gas Dynamics. John Wiley and Sons, Inc., 1965.
11. Clarke, J. F. and McChesney, M.: The Dynamics of Real Gases. Butterworths, 1964.

12. Landau, L., and Teller, E.: Zur Theorie Der Schalldispersion. Physikalische Zeitschrift der Sowjetunion, vol. 10, 1936, p. 34.
13. Marrone, P. V., and Treanor, C. E.: Chemical Relaxation with Preferential Dissociation from Excited Vibrational Levels. Phys. Fluids, vol. 6, 1963, p. 1215.
14. Reinhardt, W. A.: A Simplified Molecular Model for Studying Vibration-Dissociation Coupling in Fluid Flows. NASA TR R-324, 1969.
15. Johnson, H. S.: Gas Phase Reaction Kinetics of Neutral Oxygen Species. NSRDS - NBS 20, 1968.
16. Baulch, D. L., Drysdale, D. D., Horne, D. G., and Lloyd, A. C.: Evaluated Kinetic Data for High Temperature Reactions. Vol. 2, CRC Press (Butterworths), 1973.
17. Flower, W. L., Hanson, R. K., and Kruger, C. H.: Investigation of Nitric Oxide Decomposition in the Temperature Range 2500 - 4100° K. Paper presented at Meeting of the Western States Section of the Combustion Institute (Pullman, Wash.), May 6-7, 1974.
18. Baldwin, B. S., and MacCormack, R. W.: Numerical Solution of the Interaction of a Strong Shock Wave with a Hypersonic Turbulent Boundary Layer. AIAA Paper 74-558 (AIAA 7th Fluid and Plasma Dynamics Conference, Palo Alto, CA., June 17-19, 1974).
19. Thomas, P. D., Vinokur, M., Bastianon, R., and Conti, R. J.: Numerical Solution of the Three-Dimensional Inviscid Supersonic Flow. AIAA J., vol. 10, no. 7, July 1972, pp. 887-894.
20. Lomax, H., Kutler, P., and Fuller, F. B.: The Numerical Solution of Partial Differential Equations Governing Convection. AGARD-AG-146, 1970.
21. Warming, R. F., and Hyett, B. J.: The Modified Equation Approach to the Stability and Accuracy Analysis of Finite-Difference Methods. J. Comp. Phys., vol. 14, no. 2, Feb. 1974, pp. 159-179.
22. Kutler, P., Warming, R. F., and Lomax, H.: Computation of Space Shuttle Flowfields Using Noncentered Finite-Difference Schemes. AIAA J., vol. 11, no. 2, Feb. 1973, pp. 196-204.

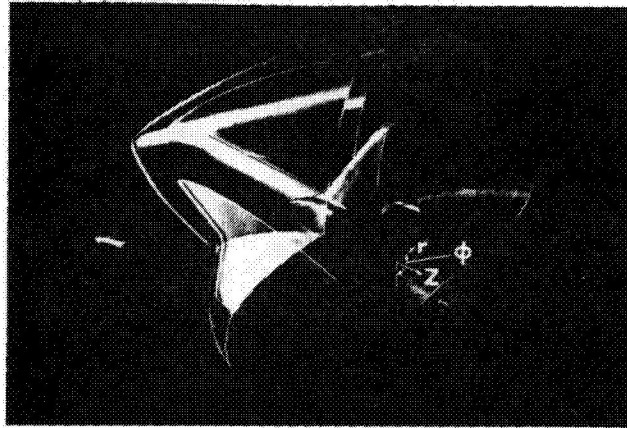


Figure 1.- Shuttle orbiter and shock structure.

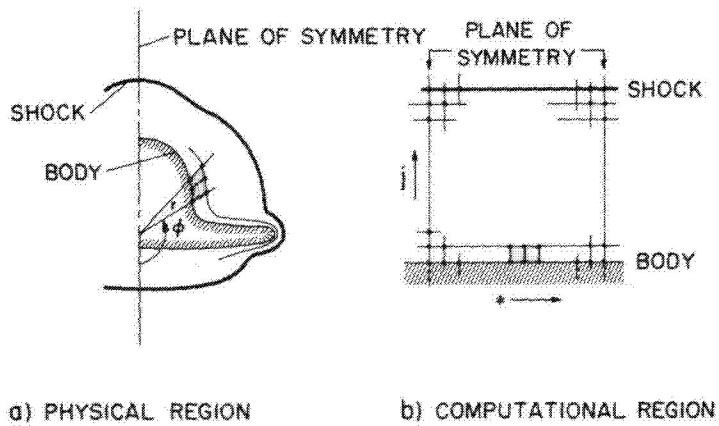


Figure 2.- Coordinate system and transformation procedure on axis normal plane.

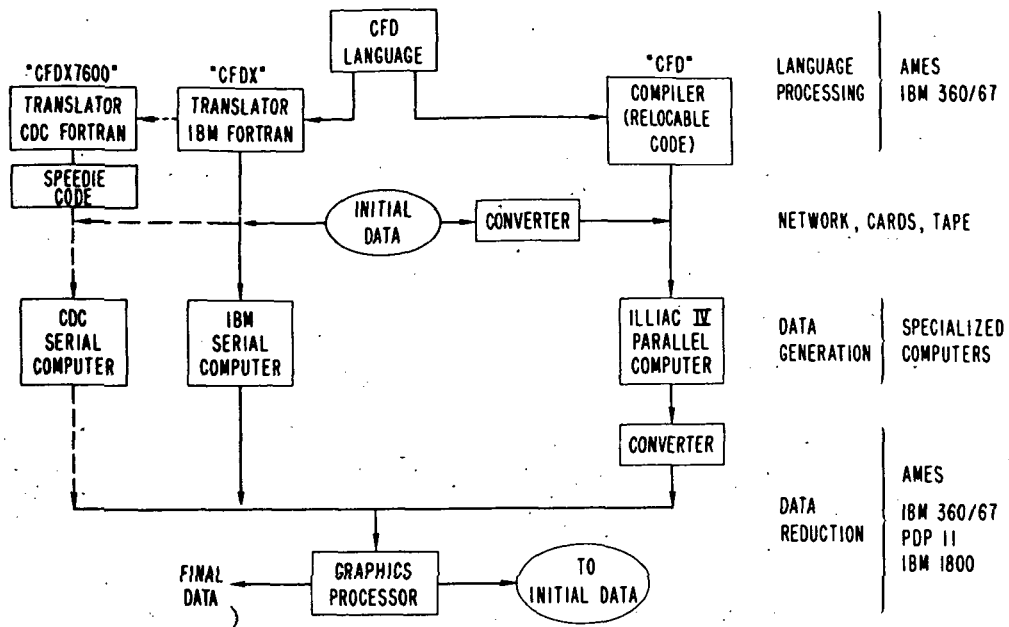


Figure 3.- Multiple computer operation.

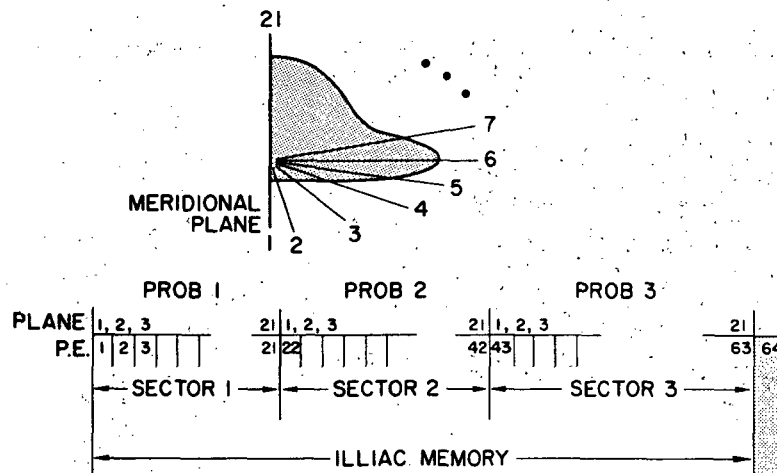
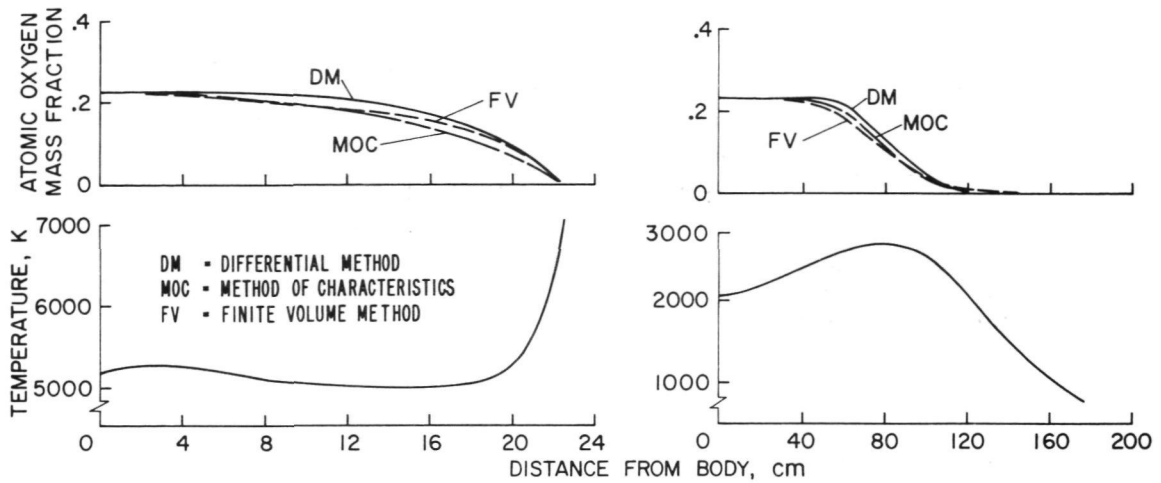


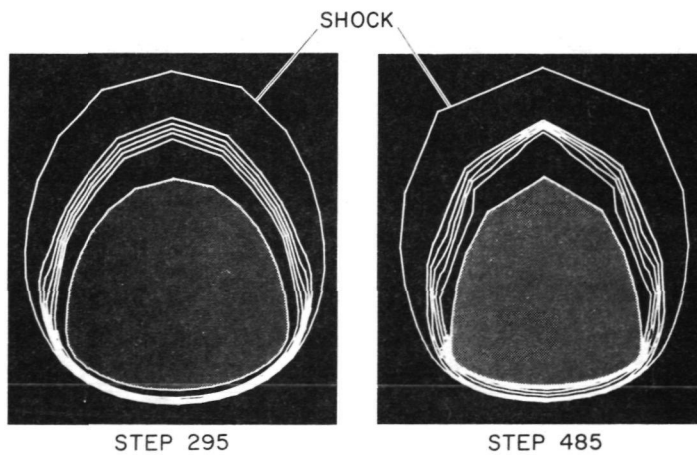
Figure 4.- ILLIAC IV processing element assignment.



(a) Windward.

(b) Leeward.

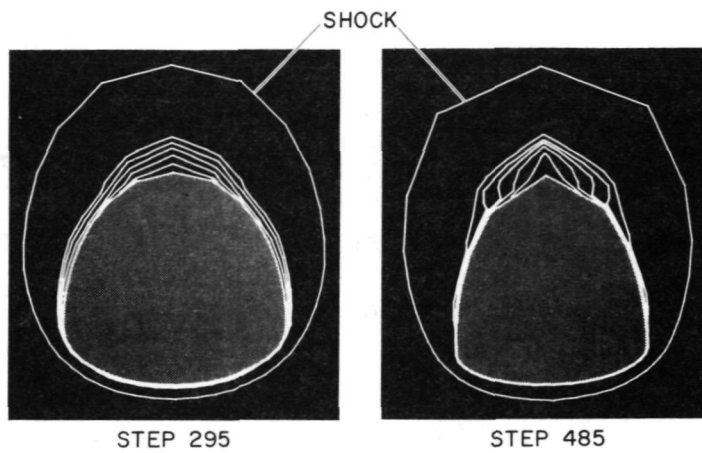
Figure 5.- Temperature and atomic oxygen comparisons on symmetry planes ($z = 3.5$ m).



(a) $z = 3.631$ m..

(b) $z = 7.643$ m.

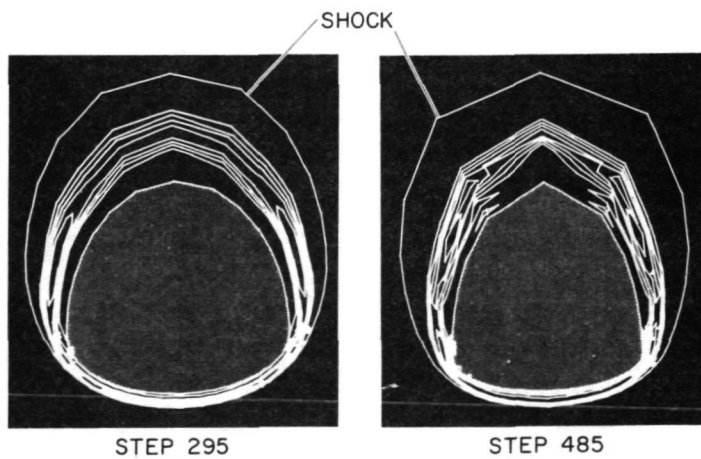
Figure 6.- Atomic oxygen contours.



(a) $z = 3.631$ m.

(b) $z = 7.643$ m.

Figure 7.- Atomic nitrogen contours.



(a) $z = 3.631$ m.

(b) $z = 7.643$ m.

Figure 8.- Nitric oxide contours.

FLOW FIELD AND HEATING ON THE
WINDWARD SIDE OF THE SPACE SHUTTLE ORBITER

By John V. Rakich and Eva B. Pegot

NASA Ames Research Center

SUMMARY

A numerical procedure for predicting the surface heating to the space shuttle orbiter is described and compared with wind-tunnel test data. The procedure, which is based on the axisymmetric analog, consists of calculating the surface streamline metric (or streamline divergence) using exact inviscid flow field solutions, and applying the metric with two-dimensional heating and boundary-layer analyses. This approach yields the dominant, or zero-order, three-dimensional heating rates to general body shapes, such as the shuttle orbiter. Two-dimensional boundary-layer methods, which include complex nonequilibrium chemical reactions, can thus be readily utilized to predict three-dimensional effects.

The numerical results are compared with experimental results for a 30° angle of attack and excellent agreement is obtained for the windward center-line heating rate and for one outboard station at 20 percent of the span. However, more comparisons are needed on the wing surface, especially in the region downstream of bow shock impingement, before the method can be fully justified.

INTRODUCTION

The space shuttle is expected to make its first orbital flight near the end of this decade, and it will encounter a heating environment that cannot be completely simulated by any current ground-based test facility. The environment will encompass laminar and turbulent flow regimes and a non-equilibrium dissociated-gas envelope which creates uncertainty about the surface heating and oxidation rates. Therefore it is imperative that advanced computational techniques and computers be applied to predicting the flight environment as completely as is technically possible. To this end, a

procedure is described for the prediction of the flight environment and surface heating of the shuttle.

Several computer codes have been developed at Ames Research Center and elsewhere for calculating the inviscid blunt nose and supersonic afterbody flows for the shuttle (refs. 1 to 6). Each of these programs requires large computer storage and execution time. Two or three separate codes may be required to calculate the complete subsonic-supersonic flow. Therefore it is usually necessary to store the inviscid solution for later coupling with a viscous boundary-layer code, which gives the surface heat-transfer rates and other surface conditions. To be precise, one should perform a three-dimensional boundary-layer calculation and determine the coupling of the viscous and inviscid flows (boundary-layer displacement effects). However, three-dimensional boundary-layer methods were not well developed at the time this study was started, and the consideration of boundary-layer displacement is, as yet, too involved in three-dimensional flows. Therefore, in the present work we have adopted the approach of DeJarnette and Hamilton (ref. 7), which employs a quasi-3-D boundary-layer calculation along the inviscid streamlines, that is, the axisymmetric analog (ref. 8). To apply the axisymmetric analog, a two-dimensional boundary-layer calculation is performed with the axisymmetric radius replaced by the actual metric (streamline divergence) of the three-dimensional inviscid surface streamlines. In contrast with previous work which employed Newtonian streamlines (ref. 7), the present method uses the exact inviscid streamlines. This method is applied to the shuttle body shape in the present paper, and the predicted heat-transfer rates are compared with experimental results.

STREAMLINE METRIC

In the present application of the axisymmetric analog, we make use of exact inviscid flow field solutions, which are stored on magnetic tape or disk and are available for computer processing. Since the inviscid solution is usually specified on a cylindrical coordinate system (x, r, ϕ) , it is necessary to set up the equations for the streamlines, and the streamline metric, in terms of these coordinates. This analysis was presented in reference 9, so only an outline is given here.

Let s, n, t be dimensional distances in orthogonal streamline coordinates, where s is along a streamline, n is normal and t tangent to the body surface (fig. 1). Let ξ, η, τ be generalized streamline coordinates, related to s, n, t by the following differential relations

$$ds = h_1 d\xi, \quad dn = h_2 d\eta, \quad dt = h_3 d\tau \quad (1)$$

The component h_3 is the "streamline metric" used in the axisymmetric analog. Since h_1 and h_2 are not needed, we will for brevity adopt the notation

$$h_3 = h \quad (2)$$

We consider the streamline locus to be given in terms of its circumferential position, ϕ , as a function of axial distance, x , and streamline parameter, τ . In general, one can write

$$\phi = \phi(x, \tau) \quad (3)$$

It is usually convenient to define $\tau = \phi_0$ at $x = x_0$ so that for a given ϕ_0 equation (3) defines a streamline path.

Now if we define

$$G = \left(\frac{\partial \phi}{\partial x} \right)_{\tau} \quad (4a)$$

and

$$F = \left(\frac{\partial \phi}{\partial \tau} \right)_{x} \quad (4b)$$

where the subscripts indicate the variable to be held constant, it is shown in reference 9 that

$$G(x, \phi) = \frac{w}{ru} \quad (5)$$

and

$$F(x, \phi) = \frac{hV}{ru} \left[1 + \left(\frac{\partial r}{\partial x} \right)^2 + \frac{1}{r^2} \left(\frac{\partial r}{\partial \phi} \right)^2 \right]^{-1/2} \quad (6)$$

Here, (u, v, w) are the velocity components along (x, r, ϕ) , and V is the velocity magnitude.

$$V = (u^2 + v^2 + w^2)^{1/2} \quad (7)$$

From equations (4a) and (5), one gets

$$\left(\frac{\partial \phi}{\partial x} \right)_{\tau} = \frac{w}{ru} \quad (8)$$

Also, it is shown in reference 9 that

$$\left(\frac{\partial F}{\partial x} \right)_{\phi} = F \left(\frac{\partial G}{\partial \phi} \right)_{x} - G \left(\frac{\partial F}{\partial \phi} \right)_{x} \quad (9)$$

Given the inviscid velocity field $\vec{V}(x, r, \phi)$, and the body shape $r(x, \phi)$, one can numerically integrate equations (8) and (9) by means of elementary numerical methods.

The initial conditions depend on the nature of the stagnation point flow field. For a spherical nose, the initial conditions at $x = x_0$ are

$$\phi = \phi_0 \quad \text{and} \quad h = r'_0 \quad (10)$$

where $r_0 = r_0(x_0, \phi_0)$ is any point on the sphere, and r'_0 is the radial distance to the point in a wind-axis coordinate system. Specifically, for $\phi = 0$:

$$r'_0 = r_0 \cos \alpha - (x_0 - R_N) \sin \alpha \quad (11)$$

where R_N is the spherical nose radius and α is the angle of attack.

Symmetry conditions at $\phi = 0, \pi$, for zero yaw, require that F be even and G an odd function of ϕ . (See eqs. (6) and (8).)

HEATING AND BOUNDARY-LAYER SOLUTION

Having determined the streamline metric, one can use it with the equations for axisymmetric two-dimensional flow to obtain heating rate predictions. This approach gives the dominant three-dimensional effects, and, accordingly, is called a quasi-three-dimensional method. The method is applied with both approximate solutions and detailed nonsimilar boundary-layer calculations.

Lees Heating Theory

In 1956, Lees (ref. 10) obtained an approximate expression for the heating rate of blunt bodies. This approximation, which is based on laminar boundary-layer similarity theory, simply requires an integration along a streamline to calculate the heating distribution. The equation given in reference 10 is

$$\frac{\dot{q}}{\dot{q}_0} = \frac{.5(p/p_0)(u_e/u_\infty)r R_N^{1/2}}{\left[\int_0^s (p/p_0)(u_e/V_\infty)r^2 ds \right]^{1/2} \left[1/u_\infty (du_e/d\theta)_0 \right]^{1/2}} \quad (12)$$

where \dot{q} is the heating rate, p is the pressure, u the velocity, the subscript 0 refers to the stagnation point and e to the boundary-layer edge. In the present application, r is replaced with the metric h , and the integration is performed along the three-dimensional inviscid streamlines.

We note that equation (12) applies to cold walls, that is, $T_{\text{wall}}/T_{\text{total}}$ small. Also, observe that equation (12) is independent of the Reynolds number, and that it can be evaluated in terms of the inviscid flow solution alone. This is due to the fact that the heating rate is expressed as a ratio; the stagnation heating does, of course, depend on Reynolds number. For like equations that can be used to treat turbulent flows, the reader should consult reference 7.

Boundary Layer Solution

For a detailed nonsimilar analysis, use is made of the integral matrix (BLIMP) code described in reference 11. This code has been recently modified to accept input data on magnetic tape, and this version is called AMBL. The AMBL version also includes finite-rate chemical reactions as described in reference 12. Thus, the quasi-three-dimensional approach allows the possibility of simulating the chemical reactions occurring at flight conditions. In contrast, complete three-dimensional boundary-layer solutions with nonequilibrium chemical reactions have not yet been obtained.

METDAT PROGRAM

A FORTRAN program has been written to (a) read the inviscid flow data from a magnetic storage device, (b) calculate the streamline metric and approximate heating, and (c) store data required by the boundary-layer program. (See fig. 2.) The subroutine that calculates the streamline metric is called METDAT. The main control program that takes care of data input/output is called CHAOS. A flow chart for CHAOS is provided in appendix A. Also included in the programs are subroutines for plotting the surface streamlines and other results generated. Some of these computer plots are shown in the next section for a typical case. Appendix B contains a description of the data cards and input data definitions which are needed to run the program.

RESULTS AND COMPARISON WITH EXPERIMENT

In order to verify the described methods, a test case has been run at wind-tunnel conditions of $M = 7.3$ and 30° angle of attack, for which data are available. Although the shape used for the calculations is called the shuttle orbiter 147 configuration, the experiment was performed with the 140B configuration. However, the windward surfaces of the two configurations are nearly identical and may be considered equivalent for present purposes. The wind-tunnel experiments were performed in the Ames 3.5-foot hypersonic wind tunnel by James W. Cummings of Rockwell International and William K. Lockman of Ames Research Center.

Numerical results for the inviscid surface streamlines are shown in figure 3, superimposed on the plan view of the shuttle orbiter configuration. These inviscid flow field results were obtained with a method-of-characteristics program (ref. 6) and did not include the outer wing part of the configuration. Accordingly, the streamlines are stopped roughly along the right running characteristic emanating from the wing root. It is known that a secondary shock is generated at the wing root, and special methods are needed to calculate that region of flow. The shock-capturing technique has been successfully applied to the wing but those results have not yet been employed in the present metric program. It is expected that this will be accomplished shortly.

Figures 4 and 5 show the surface pressure and streamline metric for the same streamlines as figure 3. The streamlines are numbered to identify the various curves. Note that there is a rapid drop in pressure as each streamline moves off the windward surface and around the chine, or maximum body span, while the metric tends to be a maximum on the chine. The metric, h , reaches values comparable in magnitude with the body length L in regions where the local radius, r , is only 15 percent of L .

The heating rate distribution, calculated with Lees' theory (eq. 12) is shown in figure 6 for each streamline as numbered. The heating rate peaks as the streamline passes the chine because the increase in the metric there overpowers the decrease in pressure.

In figure 7, the heating rate predictions are compared with the experiment for the windward center line and for two constant span locations, $y/y_{\max} = 0.2$ and 0.3 . The results from a detailed boundary-layer calculation are shown as a dashed line and there is very little difference from the Lees theory. The agreement of the approximate theory is attributed to the cold wall ($T_{\text{wall}}/T_{\text{total}} = .26$) and perfect gas conditions. For a hot wall, or for nonequilibrium flow conditions, it is expected that the boundary-layer solution would be required for an accurate prediction. The agreement between theory and experiment is excellent except on the centerline between $x/L = 0.1$ and 0.2 , and along $y/y_{\max} = 0.3$ beyond $x/L = 0.5$. The latter region is most probably influenced by the wing, which was neglected in the present calculations. The disagreement on $y/y_{\max} = 0$ may be a result of the quasi-3-D approximation. This conclusion is based on the work of Fanelop (ref. 13), who studied three-dimensional boundary layers by formal series expansions, with the axisymmetric analog as the zero order approximation. In applications to a blunt cone, he showed (fig. 9 of ref. 13) that the first-order three-dimensional effect is to reduce the heating rate in the region behind the blunt nose. Still, the difference in the present application is not large for the region shown in figure 7, and the quasi-3-D approach seems well justified. We note, however, that more comparison with experiments is needed in the outboard portion of the wing before use of the method can be fully justified. It is in this region that streamline curvature effects, neglected in the present approximation, may become

dominant. Also, the bow shock impinges on the wing shock, and causes large disturbances which may invalidate the present approximations.

CONCLUDING REMARKS

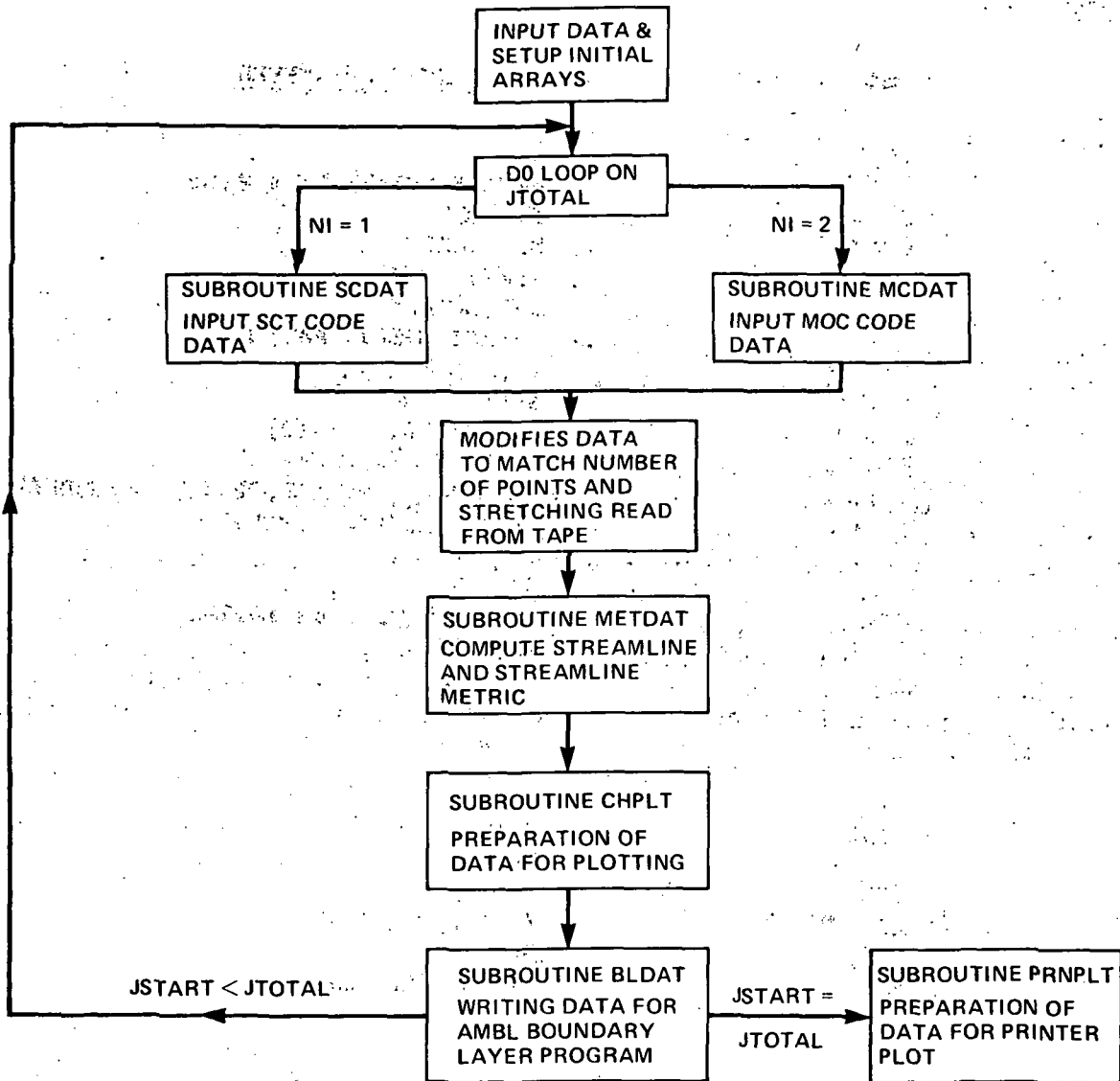
Even though three-dimensional inviscid flow computations for simple shapes have been available for nearly a decade, the combination of inviscid and viscous flow codes has progressed slowly. This may be due partially to the complexity of matching viscous and inviscid flows, and partially to the unavailability of three-dimensional flow computations. The present work seeks to eliminate these problems by extracting three-dimensional predictions from available two-dimensional boundary-layer codes. This permits one to include complex physical phenomena, such as nonequilibrium dissociation reactions, sooner than would be possible with fully three-dimensional methods. The reason for doing this is to predict the heating of the space shuttle for flight conditions, and to do so at an early enough date to affect the heat-shield design.

A comparison of the present techniques with wind-tunnel test data suggests that the method does an adequate job on, and just outboard of, the windward plane of symmetry. However, the flow field on the outboard part of the wing surface is more highly three-dimensional, and the present methods may not do as well there. Preliminary calculations for an earlier version of the shuttle indicate that the present technique might work well for the entire wing, except at the leading edge and in the regions of shock impingement. Additional work is needed, and is in progress, to establish the limitations of the method for predicting the heating to the complete windward surface of the shuttle.

APPENDIX A

FLOW CHART AND DESCRIPTION OF SUBROUTINES

PROGRAM CHAOS



APPENDIX B

CARD INPUT DATA DEFINITIONS

CARD INPUT DECK

<u>CARD</u>	<u>FORMAT</u>	<u>INPUT PARAMETER</u>
1	(I3)	JTOTAL
2	(3I3)	NMTAPE, NSTAPE, DIMENSION
3	(2I3)	NI, IOUT
4	(2I3)	NPHI, NREC
5	(2I3)	IN(5), IN(6)
6	(2I3)	JJR, NPSASF
7	(3I3)	NPRINT, NPLOTT, NPUNCH
8	(2F10.3)	PSCALE, PHIMAX
9	(2F10.3)	ALPHA, SCALE
10	(3F10.3)	FS(13), FS(3), FS(2)
11	(3F10.3)	FS(5), FS(6), FS(8)
12 ^a	(3F10.3)	(PHIAO(J), CDEL(J), CEX(J), J=1, NPHI)
13	(3I3)	NMTAPE, NSTAPE, DIMENSION
14	(2I3)	NI, IOUT
15	(2I3)	NPHI, NREC
13A ^b	(3I3)	NMTAPE, NSTAPE, DIMENSION
14A	(2I3)	NI, IOUT
15A	(2I3)	NPHI, NREC
13B	.	.
.	.	.
.	.	.
16	(A30)	HEAD1
17	(A30)	HEAD2
18	(I3)	NUM
19	(8(I3, 7X))	(J1(J), J=1, NUM)
20	(I3)	NO
21	(8F10.4)	(ZL(J), J=1, NO)

^a NPHI cards are read.

^b Cycle back to card 13 as many times as required for $\Sigma NREC = JTOTAL - 4$

DATA DEFINITIONS

<u>NAME</u>	<u>TYPICAL VALUE</u>	<u>DESCRIPTION</u>
ALPHA	30.	FS(1) Angle of attack (deg.)
CDEL	0.0	C1 = Boundary-layer thickness parameter for $\delta = C1*S**C2$
CEX	0.0	C2 = Boundary-layer thickness parameter for $\delta = C1*S**C2$
DIMENSION	17	Index giving array size for input data read in MCDAT
FS(2)	1716.	Gas constant
FS(3)	1.4	Gamma, specific heat ratio
FS(5)		PINF, free-stream pressure, psf
FS(6)		RHOINF, free-stream density, slug/ft ³
FS(8)		VINF, free-stream velocity, fps
FS(13)	1.4	Gamma-INF, free-stream specific heat ratio
HEAD1	'SHUTTLE 147'	Plot heading
HEAD2	'PERFECT GAS'	Plot heading
IN(5)	0	Gas type index, 0 for perfect, and -1 for equilibrium gas, and 1 for nonequilibrium
IN(6)	0	Gas file number for equilibrium gas, 2 for air
IOUT	2	Output control index for boundary layer data
J1(J)		Array of station numbers for heat transfer crossplots, $J_{\max} = 20$
JJR	0	Number of points above the body surface used for edge conditions

DATA DEFINITIONS (cont.)

<u>NAME</u>	<u>TYPICAL VALUE</u>	<u>DESCRIPTION</u>
JTOTAL	100	Total number of points to be calculated, four plus the number read from various tape files
NI		Index to control type of input data, 1 for SCDAT and 2 for MCDAT data
NMTAPE		Number assigned to the tape drive for input data from MCDAT
NO	7	Total number of interpolated stations at constant span locations, ZL
NPHI	19	Number of streamlines
NPLOT	0	Index to control type of data plotted, 0 = no plot, 1 = print plot only, 2 = print plot, calcomp, 3 = print plot, calcomp with dash lines, 4 = print plot, calcomp, data printout, 5 = contour plot
NPRINT	1	0 for debug print, 1 for standard, and 2 for special print in CHAOS
NPSASF	0	0 to fill Newtonian streamlines to stag point, and 1 to start directly from input data
NPUNCH	0	Index to control output for boundary layer program data, 0 = no output, 1 = write tape 10, 2 = write tape 10 and punch cards
NREC		Number of records of data to be read in for the present file on tape drive NMTAPE
NSTAPE		Number assigned to the tape drive for input from SCDAT
NUM	10	Number of values for J1

DATA DEFINITIONS (cont.)

<u>NAME</u>	<u>TYPICAL VALUE</u>	<u>DESCRIPTION</u>
PHIAO		Initial circumferential position of streamlines, deg. from <u>leeward</u>
PHIMAX	90.	Value of ϕ for terminating plots of streamlines
PSCALE		Used for scaling of length dimensions for plotting
SCALE		Used for scaling boundary-layer data; not used now
ZL		Location for interpolated data at constant span, number of values = NO

REFERENCES

1. Moretti, G., and Bleich, G.: Three Dimensional Flow Around Blunt Bodies. AIAA Journal, vol. 5, no. 9, 1967.
2. Li, C. P.: Time-Dependent Solutions of Nonequilibrium Dissociating Gases Past a Blunt Body. AIAA JSR, 9, 1972, pp. 571-572.
3. Rizzi, Arthur W., and Inouye, Mamoru: Time-Split Finite-Volume Method for Three-Dimensional Blunt-Body Flow. AIAA Journal, vol. 11, no. 11, Nov. 1973, pp. 1478-1485.
4. Rizzi, Arthur W., Klavins, Andrew, and MacCormack, Robert W.: A Generalized Hyperbolic Marching Technique for Three-Dimensional Supersonic Flow with Shocks. Presented at the Fourth International Conference on Numerical Methods in Fluid Dynamics, Boulder, Colorado, U.S.A., June 24-29, 1974.
5. Kutler, Paul; Lomax, Harvard; and Warming, R. F.: Computation of Space Shuttle Flow Fields Using Noncentered Finite-Difference Schemes. AIAA Paper No. 72-193, 10th Aerospace Sciences Meeting, Jan. 17-19, 1972.
6. Rakich, John V., and Kutler, Paul: Comparison of Characteristics and Shock Capturing Methods with Application to the Space Shuttle Vehicle. AIAA Paper No. 72-191, 10th Aerospace Sciences Meeting, Jan. 17-19, 1972.
7. DeJarnette, F. R., and Hamilton, H. H.: Inviscid Surface Streamlines and Heat Transfer on Shuttle-Type Configurations. AIAA JSR, vol. 10, no. 6, May 1973, pp. 314-321.
8. Cooke, J. C.: An Axially Symmetric Analogue for General Three-Dimensional Boundary Layers. British Aeronautical Research Council, R & M 3200, 1961.
9. Rakich, John V., and Mateer, George G.: Calculation of Metric Coefficients for Streamline Coordinates. AIAA Journal, vol. 10, no. 11, Nov. 1972, pp. 1538-1540.
10. Lees, Lester: Laminar Heat Transfer Over Blunt Nosed Bodies at Hypersonic Flight Speeds. American Rocket Society Journal, April 1956, pp. 259-269.
11. Bartlett, E. P., and Kendall, R. M.: Nonsimilar Solution of the Multi-component Laminar Boundary Layer by an Integral Matrix Method. AIAA J., vol. 6, no. 6, June 1968, pp. 1089-1097.

12. Tong., H., Buckingham, A. C., and Curry, D. M.: Computational Procedure for Evaluation of Space Shuttle TPS Requirements. AIAA Paper No. 74-518, 7th F & PD Conference, June 17-19, 1974.
13. Fannelop, Torstein K.: A Method of Solving the Three-Dimensional Laminar Boundary-Layer Equations with Application to a Lifting Re-Entry Body. AIAA J., vol. 6, no. 6, June 1968, pp. 1075-1084.

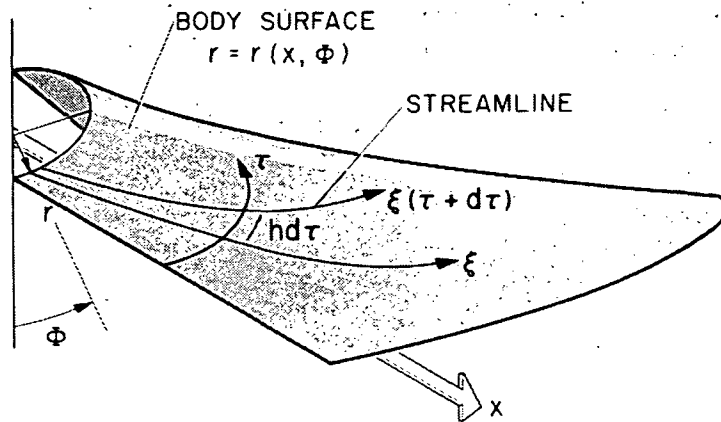


Figure 1.- Coordinates.

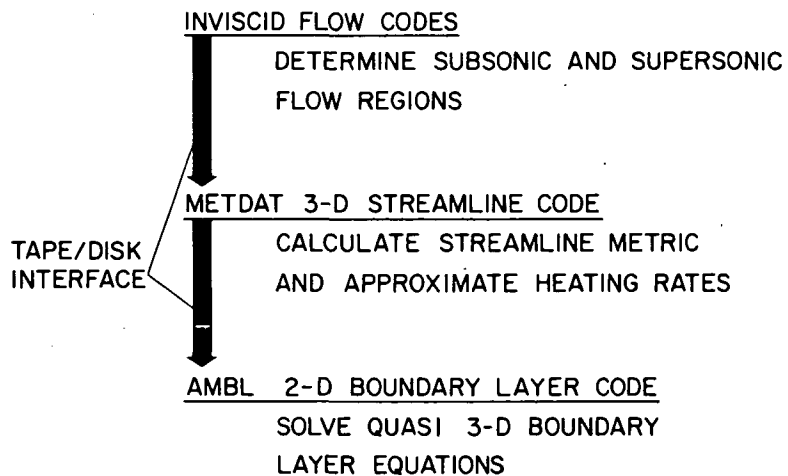


Figure 2.- Combined inviscid-viscous codes for flow field and heating analysis.

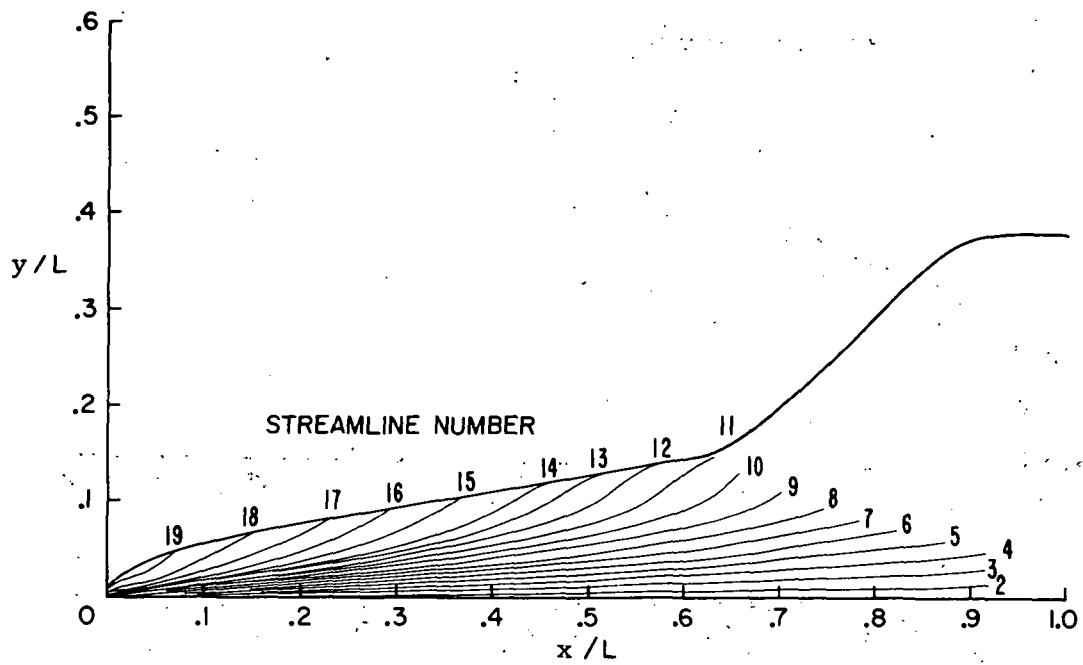


Figure 3.- Windward surface streamlines for shuttle 147 configuration;
 Alpha = 30°, Mach number = 7.3, perfect gas.

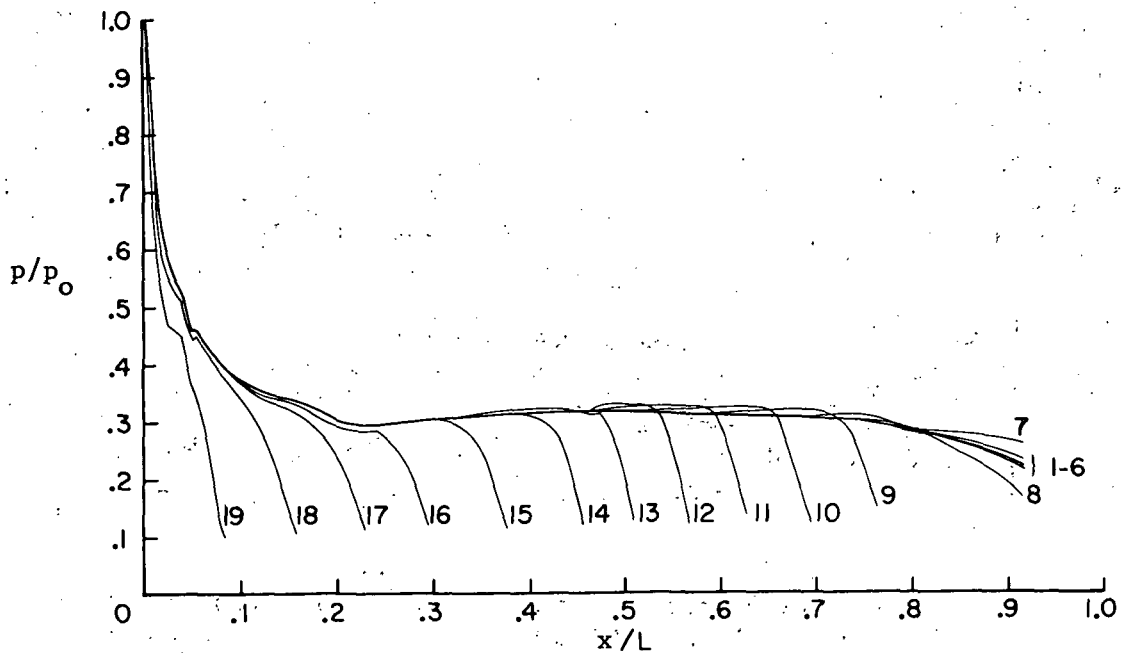


Figure 4.- Windward surface pressure for shuttle 147 configuration;
 Alpha = 30°, Mach number = 7.3, perfect gas.

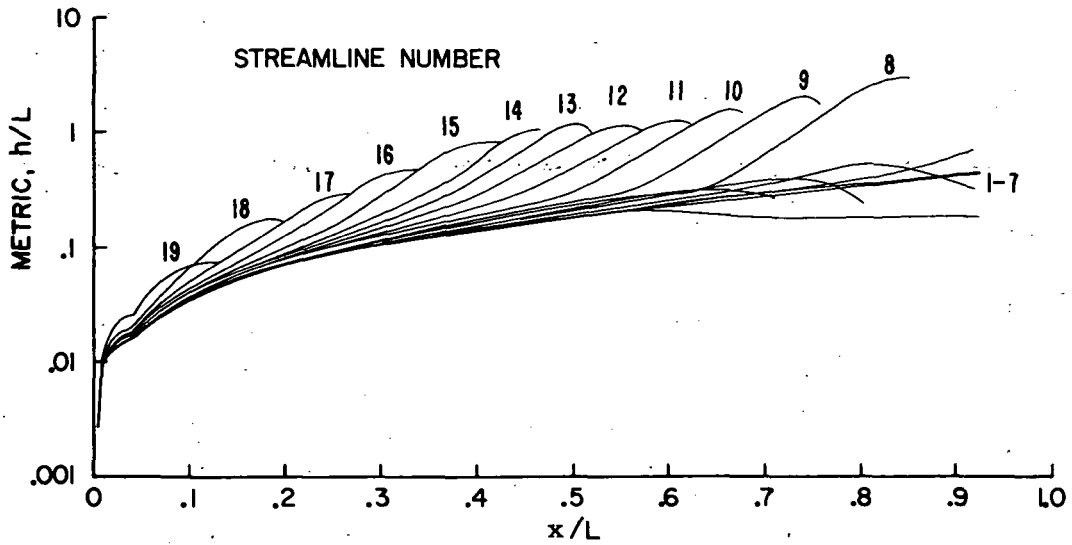


Figure 5.- Surface streamline metric for shuttle 147 configuration; Alpha = 30°, Mach number = 7.3, perfect gas.

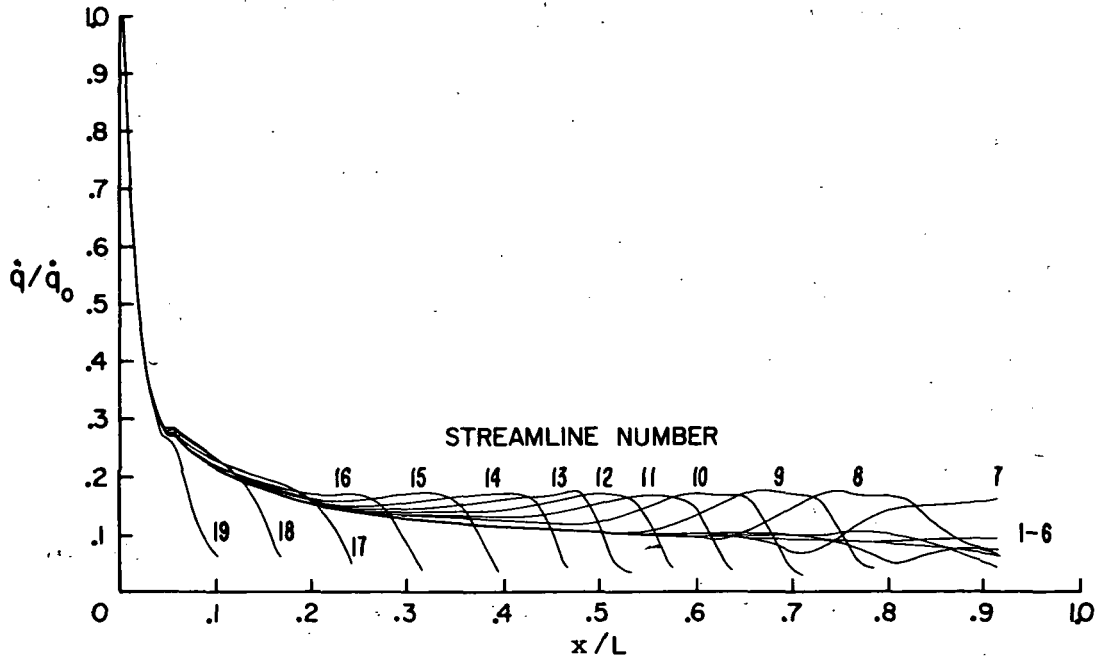


Figure 6.- Surface heating rate for shuttle 147 configuration; Alpha = 30°, Mach number = 7.3, perfect gas.

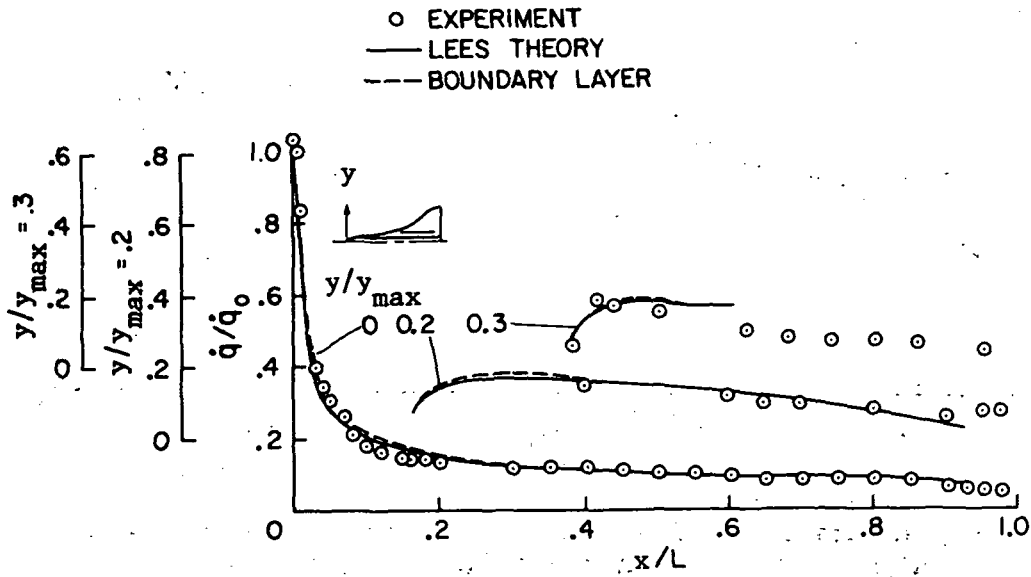


Figure 7.- Comparison of calculated and experimental surface heating rate for shuttle 147 configuration. $\alpha = 30^\circ$; Mach number = 7.3; perfect gas; $q_0 = 2.57 \text{ watts/cm}^2$; $T_w/T_t = 0.26$; $Re = 1.7 \times 10^6$.

SCALING OF ORBITER AEROTHERMODYNAMIC DATA
THROUGH NUMERICAL FLOW FIELD SIMULATIONS

By W. D. Goodrich,

NASA Lyndon B. Johnson Space Center

C. P. Li, C. K. Houston, R. M. Meyers, and L. Olmedo

Lockheed Electronics Company

SUMMARY

Aerothermodynamic data are presented for computer-aided numerical simulations of three-dimensional inviscid, Newtonian, and fully viscous flow fields around an analytical description of the Space Shuttle Orbiter geometry at 30 degrees angle-of-attack. These data were generated for both typical hypersonic wind tunnel conditions ($M_\infty = 8$, $Re_{\infty,L} = 10^6$, $T_0 = 725K$) and flight conditions associated with peak laminar heating encountered during Orbiter atmospheric entry (Altitude = 61 km, Velocity = 6.08 km/sec). Aerothermodynamic data obtained in hypersonic wind tunnels are used to verify the wind tunnel computations. Heat transfer scaling factors derived from these three-dimensional flow field computations are compared to scaling factors derived from two-dimensional-based flow field theories and scaling practices. Observations and conclusions are made regarding uncertainties in extrapolating heat transfer data from wind tunnel to flight conditions. Additional observations are made concerning "user-sensitivity" or "grid-induced" flow field uncertainties associated with using these computer codes.

INTRODUCTION

The Orbiter aerothermodynamic environment experienced during entry, particularly the surface heat transfer rates and distribution, strongly influence vehicle structural and thermal protection system (TPS) design. Specifically, heat transfer rates and integrated heat loads play a major role in TPS material selection, insulation thickness, and resultant system weight. Similarly, uncertainties in heating rates and loads lead to potential uncertainties in the TPS design, which often lead to a conservative

design. Conversely, reduced uncertainties can potentially lead to reduced conservatism and, in this case, could lead to reduced TPS insulation thickness and weight.

Currently, a well defined range of uncertainties associated with predicting the Orbiter flight heating environment does not exist, except for a few two-dimensional heating methodologies which have been calibrated with wind tunnel data and extrapolated to flight conditions. These two-dimensional methodologies have been "three-dimensionalized" for selected Orbiter body points with an empirically generated boundary layer length and divergence calibration factor. This factor, of course, guarantees agreement between wind tunnel heating data (within the uncertainty of the measurements) and two-dimensional-based heating methodologies for all calibrated body points at all calibrating wind tunnel conditions. However, no guarantees exist for flows outside of the calibration range (i.e., flight conditions).

The objective of the current study is to assess the applicability of these "three-dimensionalized" methodologies at flight conditions. More complete three-dimensional flow field simulation techniques will be used in making this assessment.

SYMBOLS

$(C_F)_x$	surface friction coefficient in axial direction
$(C_F)_\phi$	surface friction coefficient in circumferential direction
C_p	local pressure coefficient
$C_{p,o}$	stagnation point pressure coefficient
h	local heat transfer coefficient
h_{ref}	stagnation point heat transfer coefficient on a reference sphere (.304 meter radius)
\bar{h}	heat transfer sealing factor $\equiv (h/h_{ref})_{FLT} / (h/h_{ref})_{WT}$
L	Orbiter length (full scale length = 32.8 meters)
M_∞	free-stream Mach number
$Re_{\infty,L}$	free-stream Reynolds number based on Orbiter length
T_o	stagnation temperature
X, Y, Z	coordinate system defined in figure 1
α	Orbiter angle-of-attack

Subscripts:

FLT refers to flight conditions

WT refers to wind tunnel conditions

APPROACH

Scaling Philosophy - The basic hypothesis used in scaling heat transfer data from hypersonic wind tunnels to hypersonic flight conditions relies on the ability to predict, or model, local flow properties at both of these conditions. Obviously, if all local flow properties at flight conditions could be simultaneously simulated in a wind tunnel, scaling and flow field simulation technology would not be required. However, this is not the case for Orbiter entry conditions. Test facilities which are capable of providing enthalpies comparable to flight enthalpies are incapable of providing local Mach number and Reynolds number simulations, and vice versa.

A relatively simple scaling method which utilized the behavior of a predictable reference flow field (i.e., sphere) was developed for and applied to the Apollo Spacecraft in ref. 1. Basically, local flow conditions (and therefore heating) on the Apollo were assumed to vary like the flow (and heating rates) at the stagnation point of a sphere. Since the stagnation point heating on a sphere can be readily predicted at both wind tunnel and flight conditions by the method of ref. 2, Apollo flight heating rates could be predicted if the Apollo flow field behaved like that for a sphere. This behavior was verified in ref. 3 for the blunt face of the Apollo spacecraft within the accuracy of flight pressure and heat transfer measurements.

This basic procedure of normalizing local heating rates to the stagnation point heating rate on a reference sphere is currently being used to non-dimensionalize Shuttle Orbiter wind tunnel data. However, data have been presented in ref. 4 which show that the local windward surface flow on the Orbiter behaves more like a tangent cone than a sphere. Therefore, for scaling purposes, local heating rates are currently extrapolated to flight using simple two-dimensional flow field models (e.g., tangent cone, tangent wedge, cylinder, etc.) coupled to simple heat transfer prediction methods (e.g., Eckert reference enthalpy, etc.). However, these flow models have to be calibrated, or "three-dimensionalized", with wind tunnel data. In addition, calibration constants derived from this process are assumed to remain constant when these flow models are applied to flight conditions. Verification of this assumption requires either flight data or some form of reliable flight predictions.

Computational Methods - With the aid of three-dimensional flow field methods, an assessment of this assumption can be made without flight data

measurements. Basically, three-dimensional viscous flows at both wind tunnel and flight conditions can potentially be computed using the numerical flow simulation code described by Li in ref. 5. This code was developed to solve the Navier-Stokes equations by the time-dependent method. However, vast computer resources are required to apply this code to large three-dimensional flow fields. Therefore, for this study, this code was only used to simulate the viscous flow field around the relatively small nose-canopy region of the Orbiter (see figure 1).

For a relatively economical description of the complete Orbiter flow field, inviscid computations were employed, since spatial resolution requirements, and therefore computer size, were minimized. Local inviscid flow conditions can be used to establish surface streamlines and local edge conditions necessary for making boundary layer computations. In this study, the three-dimensional time-dependent inviscid version of the code described in ref. 5 was used to start the three-dimensional inviscid code of ref. 6. Data from these flow fields were used to calculate streamline and metric coefficient data by the method outlined in ref. 7. The two-dimensional boundary layer solution procedure described in ref. 8 was used to predict surface heating along streamlines through the use of the axisymmetric analogue developed in ref. 9.

The sensitivity of local heating rates to changes in local inviscid flow conditions was assessed with Newtonian flow theory. Using Newtonian theory to describe local pressures, streamline lengths, and metric coefficients, local boundary layer edge conditions were specified by two methods: (1) isentropic expansions using Newtonian pressures and normal shock entropy and (2) non-isentropic expansions using Newtonian pressures and local parallel shock entropies. These two limiting cases produced reasonable extremes in local boundary layer edge conditions. These conditions in turn were used to predict extremes in heat transfer rates for a given pressure level.

RESULTS OF WIND TUNNEL FLOW FIELD COMPUTATIONS

Using the previously described computational methods, flow field data were computed in the shock layer around an analytical description of the Orbiter geometry at 30 degrees angle-of-attack. The objectives of these wind tunnel computations were: (1) to establish that the three-dimensional codes could produce reasonably accurate flow field results by direct comparison to wind tunnel data and (2) to provide a computed flow field data base which could be used (along with flight computations) in forming three-dimensional heat transfer scaling factors, \bar{h} . These scaling factors, formed by non-dimensionalizing local heat transfer coefficient ratios obtained at flight conditions, $(h/h_{ref})_{FLT}$, to local heat transfer coefficients obtained at wind tunnel conditions, $(h/h_{ref})_{WT}$, provide the basic data necessary for assessing the scaling factors derived from two-dimensional flow methods.

Both two-dimensional and three-dimensional scaling factors were used to establish the computed data base necessary for predicting uncertainties in flight heating rates due to extrapolation methods.

Orbiter Geometry - The Orbiter geometry used for making these three-dimensional flow computations is shown in figure 1. Geometry data from the Rockwell 140-B Orbiter configuration were used to "guage" or calibrate the analytical description of Orbiter configuration. Details of data requirements and analytical curves used for this procedure are presented in ref. 6. Reasonably fine details of the basic geometric characteristics, suitable for making flow field computations, were maintained on both the windward and leeward surfaces.

Computed Shock Envelope - Figure 2 shows both the computed shock envelope and measured shock location for the Orbiter at 30 degrees angle-of-attack. Experimental shock locations were established from both schlieren photographs and pitot pressure data taken in AEDC-Tunnel B. Measured and computed shock locations and shape are in excellent agreement along the windward pitch plane and in very good agreement along the leeward pitch plane. These data were computed using the three-dimensional inviscid codes described previously.

Computed Surface Pressures - Surface pressures were computed over the entire Orbiter surface up to an axial station of $X/L = 0.8$. Both Newtonian flow theory and the inviscid flow codes were used for making these computations. Comparisons of these data with experimental data obtained in the NASA/ARC 3.5-foot wind tunnel are shown in figure 3.

Figure 3a depicts computed and measured pressure coefficients along the windward centerline as a function of axial station, X/L . Except in the vicinity of $X/L = 0.1$, where the measurements are consistently higher than the predictions, the data are comparable. Also, note that the measured data and three-dimensional computations are slightly, but consistently, higher than the Newtonian predictions.

Figure 3b presents a comparison of computed and measured pressure data along the leeward surface centerline from the nose to a point just downstream of the canopy. (Along the pitch plane, the canopy windshield starts at $X/L \approx 0.15$ and ends at $X/L \approx 0.18$.) The computed data obtained from the time-dependent Navier-Stokes equations were very erratic along the cowling but remained very stable along the canopy windshield. However, for clarity, only a smoothed version of these data are presented. This erratic behavior of the computed data can possibly be attributed to either numerical instabilities or perhaps an unstable flow process associated with incipient separation of at least one component of the flow. (Evidence of a partial flow separation will be shown later.) However, an indepth assessment of this phenomenon has not been made.

Pressure data along the cowling obtained using the inviscid codes are in very good agreement with the measured data. This is an indication that,

for these flow conditions, viscous forces play a minor role in establishing the pressures in this particular region of the flow field. In addition, the peak canopy pressure can be approximated at wind tunnel conditions with modified Newtonian theory by assuming that the canopy is exposed directly to the free-stream flow. This implies that the canopy is only marginally shrouded by the nose, even though geometric data indicate that it is totally shaded when the Orbiter is at 30 degrees angle-of-attack. The Newtonian peak pressure is also in good agreement with the peak pressure obtained from the inviscid computation.

Figure 3c depicts the circumferential distribution of both measured and predicted pressure data around the fuselage cross section at station $X/L = 0.1$. Measured data on the windward centerline are approximately 20 percent higher at this station than the data generated using either the inviscid flow or Newtonian computation. As the flow expands around the cross section, the measured data exhibit an overexpansion and drop to about 50 percent of the predicted levels and then return to the predicted levels. This departure from the predictions is not unexpected, since the predicted pressures were obtained from inviscid computations. Also, note that the side of the Orbiter at this station still "sees" the free-stream flow since the Newtonian values of $C_p/C_{p,0}$ are greater than zero.

Figure 3d, which shows pressure distributions for the Orbiter cross section located at $X/L = 0.4$, illustrates a similar trend between the measured and predicted data. Newtonian theory predicts these pressures about as well as the inviscid computations, even on the Orbiter leeward surface. This is, of course, fortuitous, since neither theory contains the physical considerations necessary to simulate fully separated flow fields.

Computed Heating Rates - Using the three-dimensional codes described previously, heat transfer coefficients were computed for most of the windward surface and for the leeward surface to $X/L = 0.2$. These predictions are compared to experimental data in figure 4. All local heat transfer coefficients have been normalized to the reference sphere stagnation point heat transfer coefficient, h_{ref} . Figure 4a presents these data for the windward surface centerline. The measured data and the inviscid/boundary-layer predictions are seen to be in excellent agreement. The detailed agreement of measurements and predictions can be seen at $X/L = 0.3$, where both sets of data increase in the axial direction at about the same rate. On the other hand, the data derived using Newtonian/boundary-layer flow field results do not reproduce the trend of the data at $X/L = 0.3$. This disparity possibly illustrates a global influence of the geometry on the flow field and heat transfer calculations. Consider that since Newtonian flows are sensitive only to local geometric shapes, Newtonian flow pressures and heating predictions should be proportional to local geometric changes. This was indeed the behavior of the Newtonian data. Contrary to this behavior, the three-dimensional shock layer computations apparently produced a local flow environment which was influenced by more than just the local surface shape. This disparity is illustrated in both the heat transfer and the pressure data.

Figure 4b presents heat transfer coefficient data computed using the time-dependent Navier-Stokes equations. As previously indicated, these computations produced erratic data on the leeward surface which had to be smoothed for clarity. In addition, the heat transfer data also had to be normalized to the inviscid/boundary-layer heating predictions on the windward centerline in order to predict reasonable magnitudes of heat transfer coefficients. Thus, with proper care, the Navier-Stokes data can be used to approximate both the magnitude and general distribution of the measured data.

The sensitivity of the data to local flow field changes is illustrated by the variation in measured heating with free-stream Mach number. These variations in flow conditions produce large changes in local heating, which tax both the measurement techniques and computational procedures. With the grid size shown in this figure, an amazing level of spatial resolution is maintained within the computed data. In addition, large variations in the predicted data were also noted when results from a computation made using one grid size were compared to the same computation made using a different grid size. This effect certainly needs more investigation before reliable three-dimensional Navier-Stokes computations can be made.

Figure 4c presents distributions of computed heat transfer coefficient data for the fuselage cross section at $X/L = 0.1$. The predictions basically agree with the measured data along the windward surface (note that in this figure, the Navier-Stokes results were normalized to the normal-shock-entropy Newtonian/boundary-layer predictions on the windward centerline). The Navier-Stokes predictions made using a relatively coarse finite-difference grid were confirmed by the measured data on the leeward side of the cross section. However, the peaks in the measured heat transfer data near the windward surface "chine-line" could not be accurately predicted. Additional computations using approximately six times more grid points (for a total of 21,000 grid points) produced better, but much more costly, data predictions.

The inviscid/boundary-layer computations also underpredicted the measured peaks in heating. Again, the sensitivity of heating to local flow conditions, as shown by the measured data, could be partly responsible for these differences. Apparently, accurate simulations of local flow conditions are very demanding in this region of the flow field. Despite a small transverse pressure gradient in the region of the peak heating, the measured heating increased by approximately 40 percent. A combination of longitudinal pressure gradients and boundary-layer spreading could be responsible for this peak. (Note that the current streamline spreading factors are derived from Newtonian and inviscid flows, which ignore viscous influences on boundary-layer spreading.) Obviously, additional study is required to properly evaluate this flow.

Similar heat transfer coefficient data are shown in figure 4d for $X/L = 0.4$. The Newtonian/boundary-layer predictions are shown to underpredict the measurements along the centerline and overpredict the data near the fuselage leading edge. These same observations were made concerning the

pressure data. The inviscid/boundary-layer predictions show much better agreement with the measured data on the fuselage centerline. Comparable predictions near the "chine-line" were not available in time for this study. The large difference between the predicted and measured data near the leading edge, or "chine-line", points to the existence of a rather complex flow behavior which certainly cannot be predicted with Newtonian theory alone. Again, additional simulations are required to help identify the nature of the flow near the "chine-line".

Separated Flow Results in Canopy Region - Figure 5 depicts predicted separated flow regions on an oil flow photograph taken in a Mach eight flow in Tunnel-B at AEDC. Areas of total flow separation are evident on either side of the pitch plane, starting well upstream of the canopy. Surface shear data obtained from the time-dependent Navier-Stokes computations accurately predict the line of separation (zero transverse shear) for the transverse component of the boundary-layer flow. This separation process produces a screw-vortex which is carried downstream by the longitudinal component of the flow field velocity. These computations also predict a line of separation for the axial component of flow which differs from the oil flow photograph primarily near the pitch plane. The flow field computations predict a very thin separation bubble ahead of the canopy which cannot be seen in the photograph. This flow phenomenon is qualitatively correct for flows with lower Reynolds numbers. Again, numerical finite difference grid size may be responsible for this behavior in the computer flow field. A systematic study using finer finite-difference grids which are spaced according to flow field gradients is required for better simulations of these flows. However, the qualitative nature of these flows can be described using current flow field simulation methods.

HEAT TRANSFER SCALING FACTORS

Three-dimensional heat transfer scaling factors, \bar{h} , which effectively illustrate changes experienced by normalized heat transfer coefficients, h/h_{ref} , upon extrapolation from wind tunnel to flight conditions, were generated for limited regions of the Orbiter surface. This process required that flow fields and heating rates be calculated around the Orbiter at both wind tunnel and flight conditions. For the purposes of this study, one wind tunnel ($M_\infty = 8$, $Re_{\infty, L} = 10^6$, $T_0 = 725K$) and one flight condition (Altitude = 61 km; Velocity = 6.08 km/sec) were selected to represent typical Orbiter test and flight conditions associated with laminar hypersonic flow fields.

In addition to the scaling factors for three-dimensional flows, two sets of two-dimensional scaling factors were developed along the windward surface centerline at the same free-stream conditions used for the three-dimensional flow fields. These factors were developed using data generated from the fully viscous shock layer (FVSL) computer code described in ref. 10 and the generally available tangent-cone/Eckert-reference-enthalpy method.

Studies conducted in ref. 11 indicated that scaling factors derived using tangent-wedge theory produced comparable results (within 5 percent at these flow conditions) with either totally equilibrium air or perfect gas thermodynamics. Computations made using the method of ref. 10 with both perfect gas and reacting air basically support this result. Therefore, scaling factors derived from the axisymmetric FVSL code using perfect gas relations will be presented as these data were readily available for this study. (These data were generated by Virginia Polytechnic Institute and State University as part of NASA/JSC Contract NAS 9-12630.) Since scaling factors using equilibrium air and tangent-cone/Eckert theory are relatively easy to compute, equilibrium air results are shown for this flow field model (unpublished data).

Figure 6a illustrates the range of scaling factors obtained using both two- and three-dimensional flow field methods for the Orbiter windward centerline. Generally, the following observations can be made: (1) for points downstream of the stagnation region, wind tunnel heating factor data, h/h_{ref} , must be increased when extrapolated to flight to properly account for changes in local flow field conditions, (2) Newtonian/boundary-layer flow fields, generated using both normal- and parallel-shock entropies, produce heat transfer scaling factors (and, consequently, heat transfer rates) which envelope the factors from all of the other methods that were considered in this study, (3) the maximum uncertainty in heating due to extrapolation using these methods is less than 60 percent, (4) data obtained using both the three-dimensional inviscid/boundary-layer method with equilibrium air and the axisymmetric FVSL method with perfect gas approach the equilibrium-air tangent-cone data at large values of X/L (i.e., $X/L > 0.5$), and (5) tangent-cone derived scaling factors provide a reasonable approximation (maximum differences of roughly 15 percent) of the three-dimensional inviscid/boundary-layer derived scaling factors. These results indicate that simple tangent-cone/Eckert theory, which has been "three-dimensionalized" with wind tunnel heating rate measurements, can be used to accurately predict the Orbiter centerline heating environment at flight conditions.

The picture is not quite as clear when the off-centerline heating environment is considered. Figure 6b shows distribution of scaling factors around the fuselage cross section at $X/L = 0.1$. These results indicate that the Orbiter "chine-line" heating rate predictions at flight conditions are extremely sensitive to the prediction method used. The two Newtonian/boundary-layer methods indicate that wind tunnel derived heating factors, h/h_{ref} , should be increased from 10 to 60 percent at flight conditions. However, the factors derived from simulations using the time-dependent solution to the Navier-Stokes equations tell a radically different story.

These results indicate that wind tunnel heating factors have to be increased from 100 to 200 percent when extrapolated to flight conditions. These are very preliminary results, however, and their accuracy must still be questioned. They are shown only as an indication of current efforts aimed at developing and applying fully viscous three-dimensional flow field methods. Therefore, conclusions concerning applications of these results to the design of the Orbiter will not be addressed.

OBSERVATIONS AND CONCLUSIONS

The paramount information gained from this study will be divided into two basic categories: (1) computed results applicable to Orbiter design and (2) qualitative observations concerned with the "user-sensitivity" associated with the numerical code used for this study.

Within the scope of this study, the following conclusions can be drawn with regard to predicting the Orbiter aerothermodynamic environment at flight conditions:

1. Two-dimensional tangent-cone flow field theory used in conjunction with the Eckert-reference-enthalpy heating correlation and "three dimensionalized" with wind tunnel heating measurements can be used to accurately predict the Orbiter windward centerline laminar heating environment.
2. Flight heating rates obtained using Newtonian flow fields with normal-shock and parallel-shock entropy predict, respectively, the lower and upper limits of flight heating rates along the Orbiter windward centerlines.
3. Either tangent-cone theory or the axisymmetric fully viscous shock layer theory can be used with perfect gas thermodynamics to predict the Orbiter windward centerline heating environment with reasonable accuracy.
4. The three-dimensional inviscid flow field codes coupled to boundary-layer codes as described herein provided the best overall description of the Orbiter windward centerline flow field and heating rates.

The following observations are made regarding the "user sensitivity" of the numerical codes employed in this study:

1. Results from three-dimensional inviscid computations proved to be sensitive to finite-difference grid spacing in such a way that as grid spacing decreased, probability of successful computations decreased.
2. Results from the three-dimensional time-dependent Navier-Stokes code are extremely sensitive to grid spacing; unfortunately, useful data relating restrictions on grid spacing to probability of successful computations were not developed during this study.

3. Multiple code interfaces required in using the inviscid/streamline/boundary-layer codes can be difficult for the novice.

These factors discourage the application of current three-dimensional codes as a general "design tool". However, the potential benefits of three-dimensional flow field simulations, coupled with a need for more exact design tools, suggests a need for automating more of the current functions performed by the user (namely, grid selection). These changes, coupled with the impending availability of the new fourth generation computers, would certainly promote more wide-spread application of these codes for design purposes.

REFERENCES

1. Bertin, John J.: "Wind-Tunnel Heating Rates for the Apollo Spacecraft" (U). NASA TM X-1033, January 1965.
2. Fay, J. A. and Riddell, F. R.: "Theory of Stagnation Point Heat Transfer in Dissociated Air". J. Aero/Space Sci., Volume 25, No. 2, February 1958, pp. 73-85, 121.
3. Lee, Dorothy B. and Goodrich, Winston D.: "The Aerothermodynamic Environment of the Apollo Command Module during Superorbital Entry". NASA TN D-6792, April 1972.
4. Martindale, W. R. and Carter, L. D.: "Flow-Field Measurements in the Windward Surface Shock Layer of Space Shuttle Orbiter Configurations at Mach Number 8". AEDC-TR-75-5, January 1975.
5. Li, C. P.: "A Numerical Study of Laminar Flow Separation on Blunt Flared Cones at Angle of Attack". AIAA paper No. 74-585, June 1974.
6. Kutler, P.; Reinhardt, W. A.; and Warning, R. F.: "Numerical Computations of Multishocked Three-Dimensional Supersonic Flow Fields with Real Gas Effects". AIAA paper No. 72-702, June 1972.
7. Rakich, John V. and Mateer, George G.: "Calculation of Metric Coefficients for Streamline Coordinates". AIAA J., Volume 10, No. 11, November 1972, pp. 1538-1540.
8. Tong, H.; Buckingham, A. C.; and Curry, D. M.: "Computational Procedure for Evaluation of Space Shuttle TPS Requirements". AIAA paper No. 74-518, June 1974.
9. DeJarnette, F. R. and Davis, R. M.: "A Simplified Method for Calculating Laminar Heat Transfer Over Bodies at Angle of Attack". NASA TN D-4720, 1968.

10. Miner, E. W. and Lewis, Clark H.: "Hypersonic Ionizing Air Viscous Shock-Layer Flows Over Nonanalytic Blunt Bodies". VPI-AERO-030, College of Engineering, Virginia Polytechnic Institute and State University, October 1974.
11. Bertin, John J.; Graumann, Bruce W.; and Goodrich, Winston D.: "High Velocity and Real-Gas Effects on Weak Two-Dimensional Shock-Interaction Patterns". J. Spacecraft and Rockets, Volume 12, No. 2, February 1975.

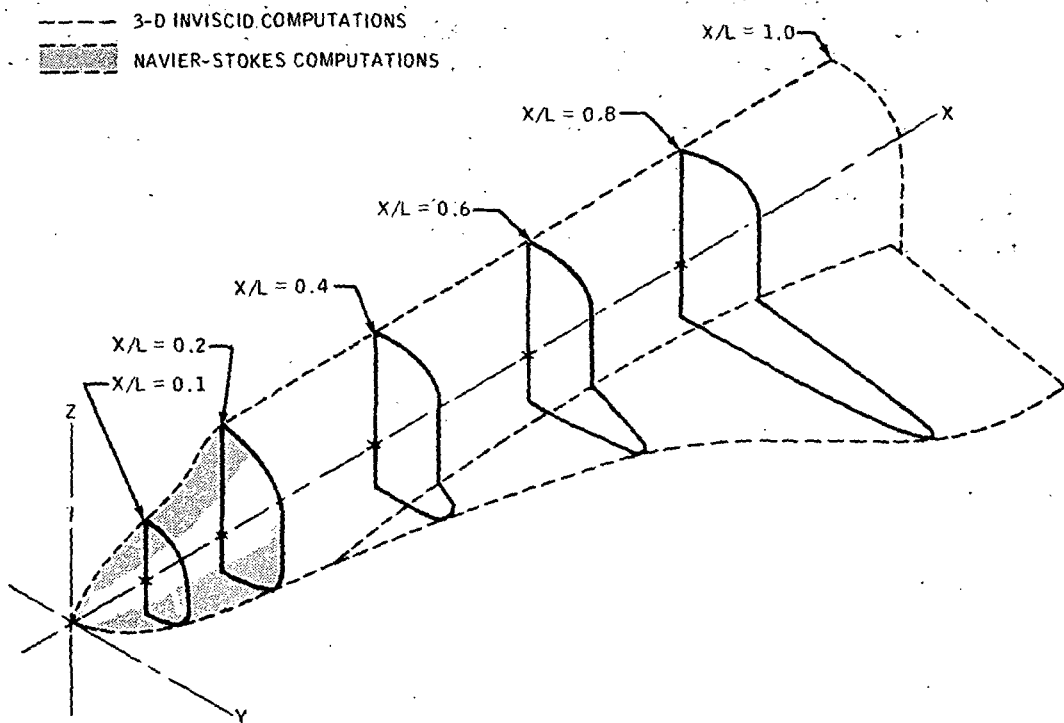


Figure 1.- Shuttle Orbiter configuration and regions of flow field computations.

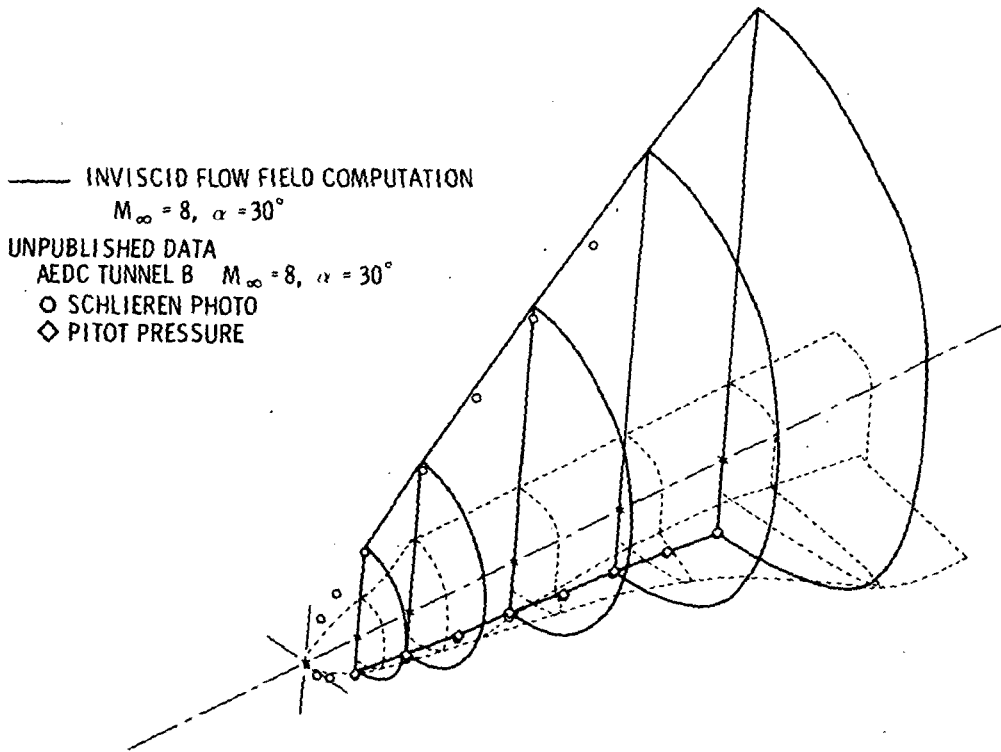
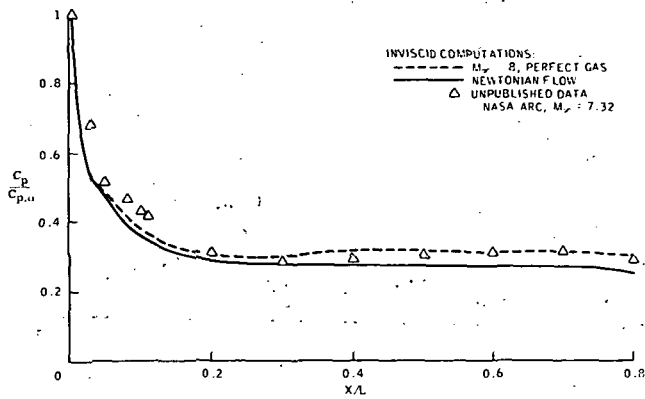
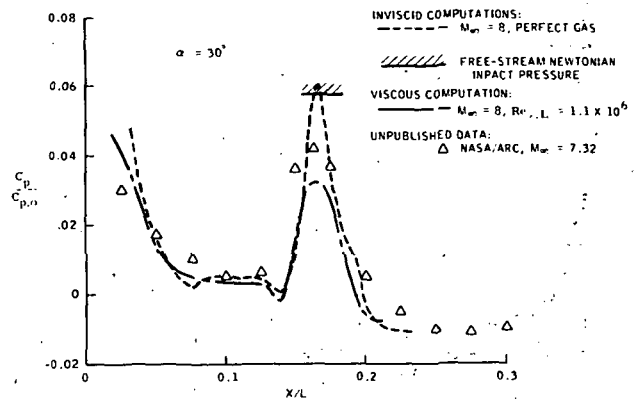


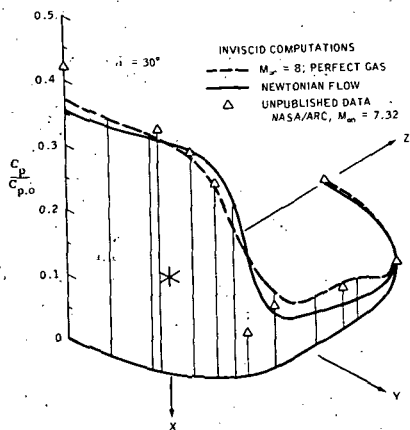
Figure 2.- Comparison of measured and computed shock envelope.



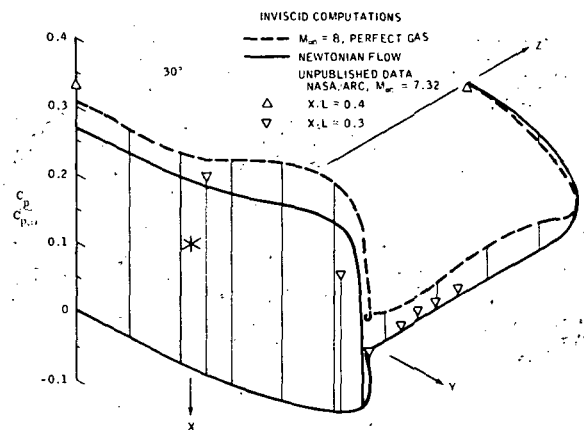
(a) Windward surface centerline.



(b) Leeward surface centerline.

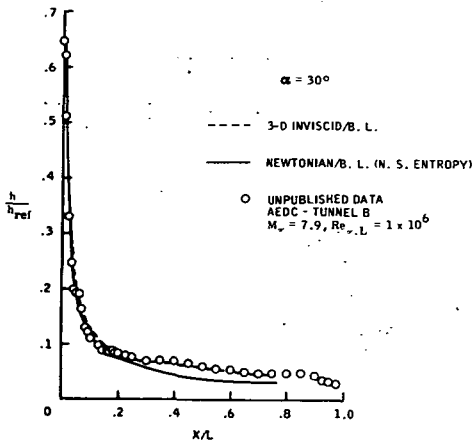


(c) Transverse section, $X/L = 0.1$.

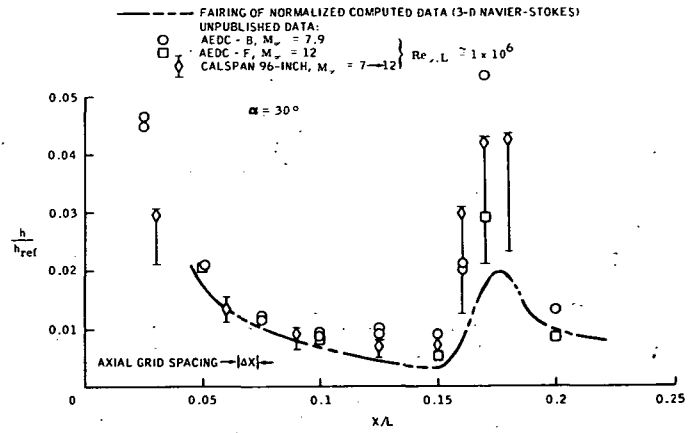


(d) Transverse section, $X/L = 0.4$.

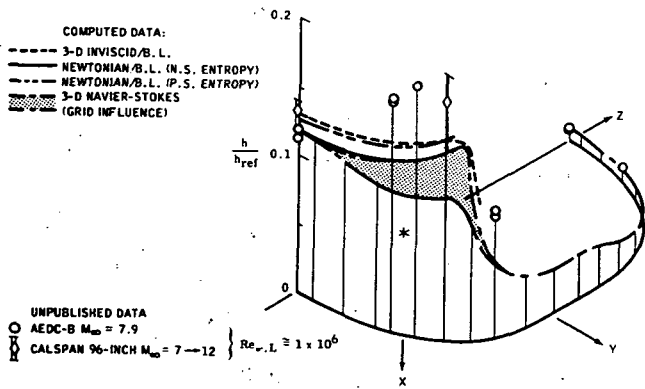
Figure 3.- Comparison of measured and computed pressure coefficients.



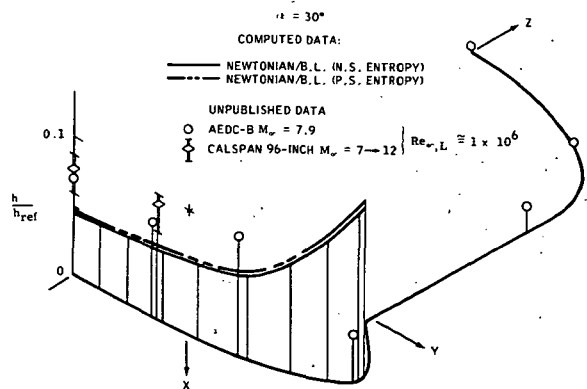
(a) Windward surface centerline.



(b) Leeward surface centerline.



(c) Transverse section, $X/L = 0.1$.



(d) Transverse section, $X/L = 0.4$.

Figure 4.- Comparison of measured and computed heat transfer coefficients.

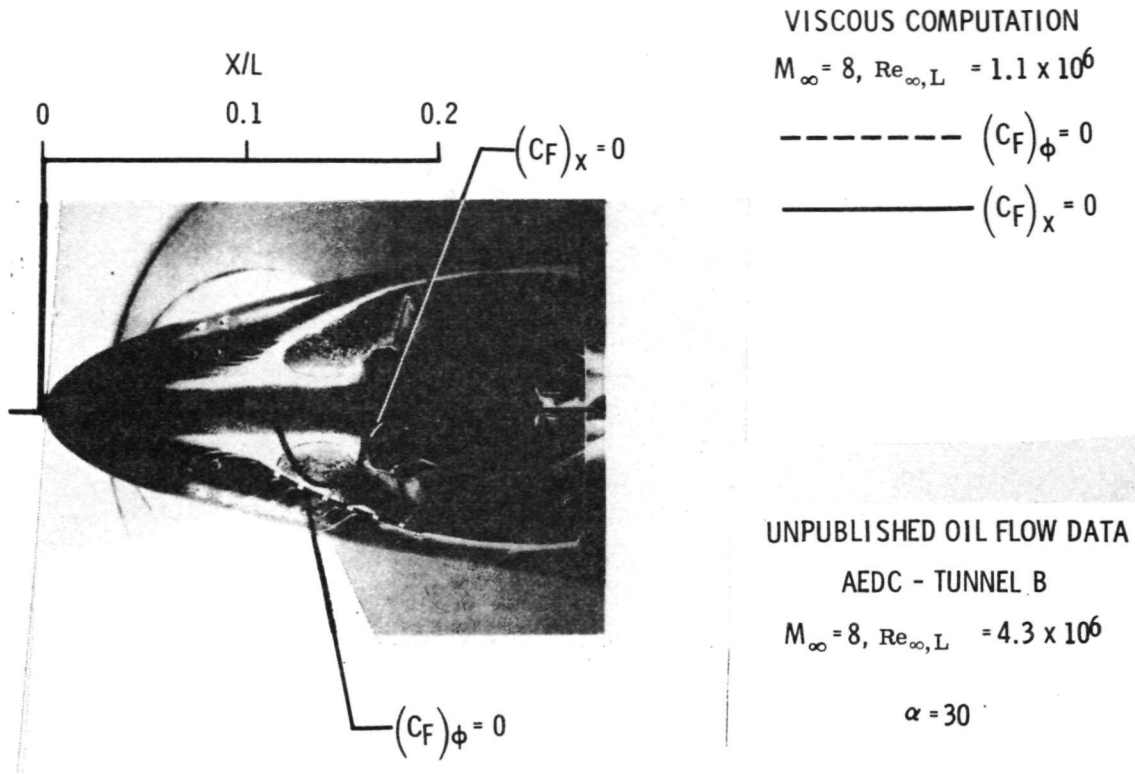
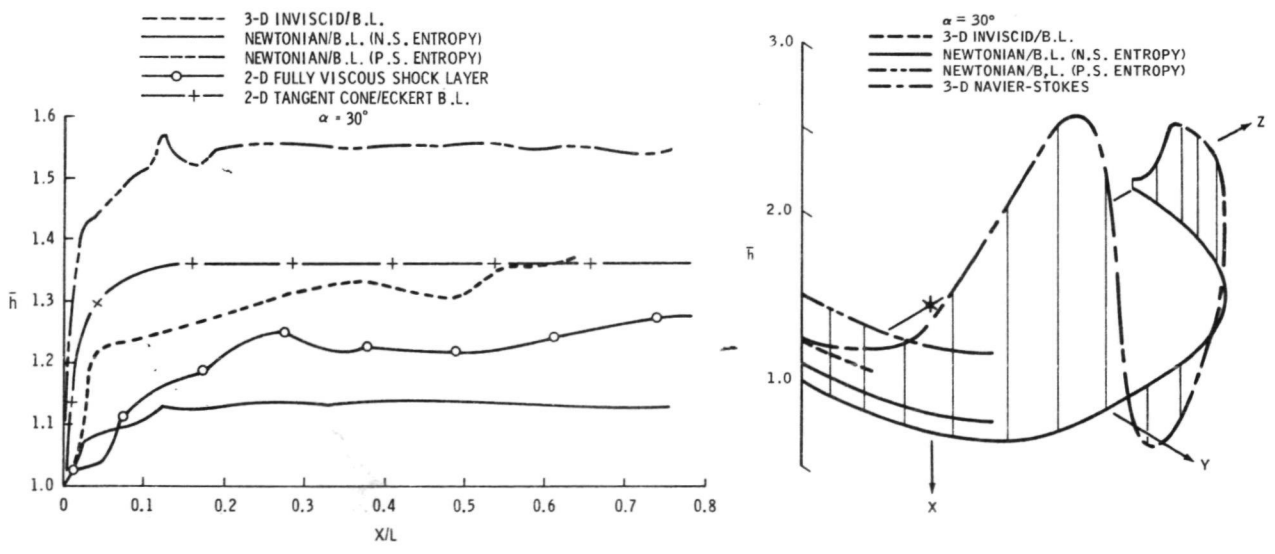


Figure 5.- Comparison of measured and computed separation lines.



(a) Windward surface centerline.

(b) Transverse section, $X/L = 0.1$.

Figure 6.- Magnitude of heat transfer scaling factors.

COMPUTATION OF HIGH-SPEED INVISCID FLOWS ABOUT REAL CONFIGURATIONS*

By Frank Marconi, Larry Yaeger,
Grumman Aerospace Corporation

and

H. Harris Hamilton
NASA Langley Research Center

SUMMARY

A numerical procedure for computing the three-dimensional inviscid flow about complex geometries is described. A second-order accurate finite-difference marching technique is used to integrate Euler's equations. Analytic conformal mappings are employed to develop a computational grid. All shocks in the flow field are treated explicitly as discontinuities satisfying the Rankine-Hugoniot jump conditions. Computational difficulties associated with blunt-nose entropy layers are avoided by explicitly following a stream surface located at the layer's outer edge and disallowing numerical derivatives of certain flow variables across this surface. Equilibrium air thermodynamics are included using curve fits of Mollier charts. A computer code which utilizes these computational procedures and a geometry package which simplifies the description of complex vehicles have been developed. This code has been used extensively to compute flow fields about a variety of complex vehicles and results are presented herein. Agreement with experimental data is shown to be good.

INTRODUCTION

Most of the flow-field data necessary in the development of high-speed vehicles have been obtained through wind-tunnel tests which are expensive, slow, and sometimes inadequate. The accurate and efficient calculation of the three-dimensional super/hypersonic flow about these vehicles would be very useful in supplementing these test programs. Techniques for calculating these flow fields are currently available, of course, but previous codes have not had so wide a range of applicability in terms of Mach number, angle of attack, and vehicle geometry as the technique described herein. Specific examples are small perturbation techniques (accurate for slender bodies at low

*This research was performed under Contract No. NAS 1-11525, NASA Langley Research Center.

supersonic Mach numbers) and Newtonian theory (reliable at large Mach numbers). In addition, some of these techniques cannot be used to obtain the details of the flow field throughout the shock layer.

The present technique has been used successfully to predict (ref. 1):

- (1) Inlet flow fields
- (2) Heat transfer rates (i.e., as input for a boundary calculation)
- (3) Aerodynamic load distributions, as well as total forces

In order to simplify the definition of three-dimensional geometries, a modeling package has been developed by Vachris and Yaeger (ref. 2). The numerical scheme used to compute the flow field has been inspired by Moretti (refs. 3 to 9) and follows a number of basic guidelines:

- (1) Conformal mappings are used to develop a computational grid.
- (2) A second-order accurate finite-difference marching technique (satisfying the CFL stability condition of ref. 10) is used to numerically integrate the governing partial differential equations.
- (3) All shock waves in the flow field are computed explicitly, and the Rankine-Hugoniot conditions are satisfied across them.
- (4) The intersection of two "same-family" shocks is computed explicitly.
- (5) The flow field at sharp-leading-edge wing tips is computed using a local two-dimensional wedge solution.
- (6) The body boundary condition is satisfied by recasting the equations of motion according to the concept of characteristics (ref. 11).
- (7) The edge of the entropy layer on blunt-nose vehicles is followed from its origin at the bow shock, and derivatives of certain flow variables are not allowed across it.
- (8) Real gas effects (equilibrium or frozen air) are included by using curve fits of Mollier charts.

The only limitation inherent in this formulation of the problem is that the velocity in the marching direction (fig. 1) must be supersonic at each point in the flow field. The flow over the nose of blunted bodies is computed using a time-dependent transonic computational procedure developed by Moretti and Bleich (ref. 12).

With the code developed using these procedures, the inviscid flow about a wide variety of vehicles (fig. 1) can be computed. Calculated results are presented which are indicative of the variety of complex flow fields for which this code may be used, and these results are compared with experimental data.

The authors wish to express their appreciation to M. D. Salas for his work and helpful discussions, particularly in the areas of conformal mapping and equilibrium air techniques.

SYMBOLS

$B(\theta, \beta)$	body definition in the mapped space ($r = B(\theta, \beta)$)
$c_\ell(\theta, \beta)$	radial boundary definition in mapped space
c_p	specific heat at constant pressure
c_v	specific heat at constant volume
C_L	lift coefficient
C_P	pressure coefficient
G	physical space (eq. (1) and fig. 5)
$h_i(r, \beta)$	circumferential boundary definition in the mapped space ($\theta = h_i(r, \beta)$)
IC	number of circumferential regions in cross section
$\hat{i}, \hat{j}, \hat{k}$	Cartesian unit vectors (fig. 4)
$\hat{I}, \hat{J}, \hat{K}$	unit vectors associated with intrinsic shock coordinate system
LC	total number of radial regions in cross section
M	Mach number; also mesh point counter in circumferential direction (fig. 9)
$MC(I)$	total number of mesh points in circumferential region I (fig. 9)
MM	mesh point counter in circumferential regions (fig. 9)
N	mesh point counter in radial direction (fig. 9)

NC(L)	total number of mesh points in radial region L (fig. 9)
NN	mesh point counter in radial regions (fig. 9)
p	dimensional pressure
P	$= \ln (p/p_{\infty})$
r, θ, β	mapped coordinates (fig. 6)
r', θ', z'	coordinates used in geometry interrogation (fig. 2(c))
R_N	nose radius
s	dimensional entropy; also surface distance (fig. 3)
S	nondimensional entropy, $(s - s_{\infty})/c_{v, \infty}$
T	temperature (eq. (6), ideal gas)
u, v, w	Cartesian velocity components (fig. 4)
W_1, W_2, W_3, W_4, W_5	intermediate mapped spaces (eq. (1) and fig. 5)
x, y, z	Cartesian coordinates (fig. 4)
X, Y, Z	computational space coordinates (fig. 8)
α	angle of attack
γ	ratio of specific heats (ideal gas), $c_{p, \infty}/c_{v, \infty}$
ζ	mapped space (eq. (1) and fig. 5)
Λ	wing sweep angle
ξ, η, ω	intrinsic coordinates used in shock computation (figs. 11, 14, and 15)
ρ	dimensional density

ϕ circumferential angle (fig. 27)

Superscripts:

$\hat{}$ unit vector

\sim predicted value; also intrinsic variable

Subscripts:

i counter for regions or boundaries in circumferential direction

l counter for regions or boundaries in radial direction

∞ free-stream conditions

Coordinate subscripts indicate differentiation with respect to the coordinate.

ANALYSIS OF METHOD

Geometry Description

"QUICK," a highly general and user-oriented three-dimensional geometry system, was developed in conjunction with the present flow-field effort by Vachris and Yaeger (ref. 2). This code allows a user to model a complex vehicle geometry in a quick, straightforward fashion.

QUICK consists of a group of initial defining and logical checkout routines, which sets up a mathematical model of the geometry from user input data, and a second group of interrogating routines, which examines the model and extracts the desired information. This interrogation section of QUICK, along with the mathematical model of the geometry, is incorporated directly into the present flow-field code (or any other code requiring a three-dimensional geometry description).

Basically, QUICK uses input data in the form of a logical word description of cross-sectional shapes (not actual sizes) and hangs these shapes on a frame created from sized numerical input of a few key control points described in segments over the length of the vehicle in a Cartesian coordinate (x,y,z) system; see figure 2. At no point in the procedure does a user have to generate any curve coefficients, and of course, continuities and/or discontinuities may be rigorously enforced.

The geometry model generated by QUICK from the user's input is interrogated in a cylindrical polar coordinate (r',θ',z') system (fig. 2(c)). Derivatives as well as coordinate positions are computed analytically; there are no splines or polynomial curve fits which can generate instabilities in a flow-field computation.

Computational Frame

The definition of a computational grid is a very important step when attempting to compute the flow about complex vehicle geometries. In the chosen coordinate system, the body and all shocks should be defined as single-valued functions. Grid points must be concentrated in regions where gradients are large or truncation error could destroy a calculation. Figure 3 shows the sharp peaks in pressure that occur near wing tips; if mesh points were not concentrated near the tip, these calculations could not be made. The transformations and their derivatives involved in defining a computational grid must be evaluated at each mesh point; therefore, it is important that these transformations be kept as simple as possible to avoid prohibitively large computational time.

Three coordinate systems or spaces are referred to in this paper: a physical space (x,y,z) , a mapped space (r,θ,β) , and a computational space (X,Y,Z) . The physical coordinate system is Cartesian and defines the three velocity components (u,v,w) used in the computation (fig. 4). The governing equations are written in the physical space, and then all derivatives are transformed into the computational space where the mesh points are at even intervals ΔX , ΔY , and ΔZ .

The computation proceeds by marching in the z -direction (fig. 4) so that data on a plane with $z = \text{Constant}$ are used to predict the flow field at $z + \Delta z$. Each $\beta = \text{Constant}$ plane in the mapped space is developed by conformally mapping the geometrical cross section in the physical plane ($z = \text{Constant}$) onto a "near" circle. The following series of mappings are used to develop each near circle:

$$\zeta = re^{i\theta} \quad (1a)$$

$$W_1 = \zeta - \frac{F}{\zeta} \quad (1b)$$

$$W_2 = W_1 + iE \quad (1c)$$

$$W_3 = W_2 + \frac{B}{W_2^2} \quad (1d)$$

$$W_4 = W_3 + iA \quad (1e)$$

$$W_5 = W_4 + \frac{D^2}{4W_4} \quad (1f)$$

$$G = W_5 + iC \quad (1g)$$

$$G = x + iy \quad (1h)$$

Figure 5 shows the transformation of the cross section from the physical plane (G) to the mapped plane (ζ). The coefficients A, B, C, D, E, and F are all functions of z and depend upon parameters of the cross section in the physical space (y_B , x_S , x_t , B_2 , and y_D ; fig. 5). These coefficients are analytic functions of the parameters and are evaluated simply and automatically from the geometry definition. The singularities of these mappings are placed inside the body so that they do not affect the flow-field computation. As a result of using these mappings, mesh points at even intervals of θ in the mapped plane are concentrated in regions of large curvature in the physical plane (fig. 6).

Equations (1) give $x = f(r, \theta, \zeta)$ and $y = f(r, \theta, \zeta)$; $z = \zeta$ completes the definition of the transformation. All the derivatives of this transformation are analytically obtainable, and the transformation is analytically invertible. This system of mappings has been applied to a wide variety of geometries with successful results. Considerable work is being done to develop mappings that can map totally arbitrary cross sections into circles or near circles (ref. 13). These transformations offer a greater flexibility than those used herein, but they also would require an increase in computational time.

The body is defined in the mapped space as $r = B(\theta, \zeta)$. Shocks imbedded in the flow are computed as internal boundaries in each cross section. The bow shock extends from the bottom symmetry plane to the top, but wing, tail, or canopy shocks do not. For the latter types of shocks the internal boundary must be completed using an "extension surface." In figure 7, a wing shock (solid line) is shown with an extension surface (dashed line) completing the internal boundary from the "end shock points" to the top and bottom symmetry planes. The Rankine-Hugoniot conditions are satisfied across the shock portion of these boundaries and flow-field information passes unaffected across the remainder. These surfaces are defined in the mapped space as $r = c_\ell(\theta, \zeta)$ with $\ell = 1$ corresponding to the body ($c_1(\theta, \zeta) = B(\theta, \zeta)$) and $\ell = LC + 1$ corresponding to the bow shock. A similar procedure is followed in the circumferential direction, for cross-flow shocks. These surfaces are defined in the mapped space using the relationship $\theta = h_i(r, \zeta)$. Now, $i = 1$ is the bottom symmetry plane ($h_1 = -\pi/2$), $i = IC + 1$ is the top symmetry plane ($h_{IC+1} = \pi/2$), and $1 < i < IC + 1$ are cross-flow shocks and surfaces. The computational space is defined by normalizing the radial and circumferential directions in the mapped space:

$$X = \frac{r - C_\ell}{C_{\ell+1} - C_\ell} \quad (2a)$$

$$Y = \frac{\theta - H_i}{H_{i+1} - H_i} \quad (2b)$$

$$Z = \beta \quad (2c)$$

where

$$C_\ell(Y, Z) = c_\ell[\theta(X, Y, Z), \beta(Z)] \Big|_{X=0} \quad (3)$$

and

$$H_i(X, Z) = h_i[r(X, Y, Z), \beta(Z)] \Big|_{Y=0} \quad (4)$$

Using this transformation each cross section is divided into IC \times LC regions, bounded by internal surfaces. Figure 8 shows a $z = \beta = Z = \text{Constant}$ plane in the physical, mapped, and computational spaces with a tail shock, wing shock, and two cross-flow shocks as internal boundaries. Figure 9 shows the region and mesh point notation used. Note that the internal boundaries have double mesh points on them (NN = NC(1), MM = MC(1)); flow variables satisfy the Rankine-Hugoniot jump conditions across the portions of these internal boundaries which are shocks.

To evaluate the derivatives of this final transformation is a straightforward process. One singularity of this transformation occurs when $C_\ell = C_{\ell+1}$ or $H_i = H_{i+1}$, that is, when shocks intersect. This problem is handled simply by an analytic shock intersection calculation. Another singularity occurs when a cross-flow shock and a wing-type shock become parallel. This difficulty has been overcome by using a cross-flow-type surface to adjust the mesh, but it seems that the only sure cure would be to allow shocks to "float" between mesh points (ref. 3).

Integration of Euler's Equations

In the physical space (x,y,z), Euler's equations are:

$$wP_z + \gamma w_z = -(uP_x + vP_y + \gamma u_x + \gamma v_y) \quad (5a)$$

$$wu_z = -(uu_x + vu_y + TP_x) \quad (5b)$$

$$wv_z = -(uv_x + vv_y + TP_y) \quad (5c)$$

$$TP_z + ww_z = -(uw_x + vw_y) \quad (5d)$$

$$wS_z = -(uS_x + vS_y) \quad (5e)$$

where all velocities are nondimensionalized with respect to $\sqrt{p_\infty/\rho_\infty}$, $P = \ln(p/p_\infty)$, and $S = \Delta s/c_{v,\infty}$ (entropy). For an ideal gas the equation of state is

$$\ln T = \frac{P(\gamma - 1)}{\gamma} + \frac{S}{\gamma} \quad (6)$$

where

$$\gamma = \frac{c_{p,\infty}}{c_{v,\infty}}$$

Now, transforming all derivatives to the computational space, equations (5) adopt the following general form:

$$f_Z = [A]f_X + [B]f_Y \quad (7)$$

where f is the vector (P, u, v, w, S) ; $[A]$ and $[B]$ are matrices depending on u, v, w, T , and the derivatives of the transformation; and f_X, f_Y , and f_Z are derivatives with respect to X, Y , and Z , respectively.

To integrate this set of equations, a modified form of the MacCormack (ref. 14) two-level finite-difference scheme is used. In the predictor step, the MacCormack scheme proceeds as follows:

$$\left. \begin{aligned} f_Z(Z_0) &= [A(Z_0)]f_X(Z_0) + [B(Z_0)]f_Y(Z_0) \\ \tilde{f} &= f(Z_0) + f_Z(Z_0) \Delta Z \end{aligned} \right\} \quad (8)$$

with the derivatives f_X and f_Y taken one-sided in increasing X and Y . At the body and on the low-pressure side of shocks, these derivatives are taken away from the boundary. Here \tilde{f} represents the predicted values of the dependent variables. After this step all the dependent variables are updated to their predicted values, the independent variables are updated to their values at $Z_0 + \Delta Z$, and all variables are set equal across the extensions of shocks, i.e., portions of internal boundaries that are not shock points ($\tilde{f}[N, MC(1)] = \tilde{f}[N, 1+MC(1)]$ and $\tilde{f}[NC(1), M] = \tilde{f}[1+NC(1), M]$, fig. 9). Then the corrector step proceeds as follows:

$$\left. \begin{aligned} \tilde{f}_Z &= [\tilde{A}]\tilde{f}_X + [\tilde{B}]\tilde{f}_Y \\ f(Z_0 + \Delta Z) &= \frac{\tilde{f} + f(Z_0) + \tilde{f}_Z \Delta Z}{2} \end{aligned} \right\} \quad (9)$$

The derivatives \tilde{f}_X and \tilde{f}_Y are taken one-sided in decreasing X and Y , and finally all variables are updated to their values at $Z_0 + \Delta Z$ (but now $f[N, 1+MC(1)] = f[N, MC(1)]$ and $f[NC(1)+1, M] = f[NC(1), M]$, fig. 9).

The step size ΔZ satisfies the CFL stability condition (ref. 10) using the characteristics in the Y, Z and X, Z planes.

Two modifications of the MacCormack scheme are used. The first is used only to handle blunt-nose entropy layer and is discussed subsequently. The second is used in all cases and is sometimes called windward differencing. In equations (5b), (5c), and (5e), the derivatives u_X , v_X , S_X , u_Y , v_Y , and S_Y are taken one-sided in the direction from which the velocity vector came (fig. 10) for both steps of the MacCormack scheme. If the flow-direction angles β_X or β_Y (fig. 10) are small then the direction of the derivative is changed between steps. Equations (5b), (5c), and (5e) express the variation of u , v , and S along streamlines, so windward differencing maintains the physical concept of domain of influence.

Through numerical experimentation, this integration scheme has been found to introduce a truncation error of the form

$$\frac{\partial^3 f}{\partial \chi^3} \Delta \chi^3$$

where χ is a length in the physical plane. In a region where $\partial^3 f / \partial \chi^3$ is large, the conformal mappings tend to assure that $\Delta \chi^3 \rightarrow 0$, while keeping the total number of mesh points to a minimum.

Shock Treatment

Most of the current three-dimensional inviscid supersonic flow calculations avoid computing shocks (or at least imbedded shocks) as discontinuities. Instead, the discontinuities caused by shock waves are spread out over a number of mesh intervals. Some difficulties associated with those techniques are pointed out by Moretti in references 3 and 7. The usual arguments cited against computing shocks explicitly are that such a method is too complex in three-dimensional calculations, has limited capability in handling shock intersections, and has difficulties predicting the formation of imbedded shocks (refs. 15 and 16). The following text outlines techniques which have been successfully applied for computing shocks off the body, detecting shocks imbedded in the flow field, computing shock intersections, and computing sharp leading-edge shocks attached to the body. Computed results for complex shock patterns and interactions are presented subsequently.

The low-pressure side of imbedded shocks are computed in the same way as interior points with the derivatives normal to the shocks taken one-sided into the low-pressure region.

To compute the high-pressure side of shocks, an intrinsic coordinate system (ξ, η, ω) with unit vectors \hat{I} , \hat{J} , and \hat{K} is used which is fixed to the shock point at $Z_0 + \Delta Z$. The unit vector \hat{I} is the normal to the shock, $\hat{K} = (\hat{I} \times \hat{k}) / |\hat{I} \times \hat{k}|$ (\hat{k} is the unit vector in the marching direction), and $\hat{J} = \hat{I} \times \hat{K}$. The system of equations to be solved includes

the Rankine-Hugoniot jump conditions and the compatibility relation on the characteristic reaching the shock in the ξ, ω plane (fig. 11). This calculation requires iteration which proceeds as follows for "wing-type" shocks: guess $c_{\ell, \beta}$ ($c_{\ell, \theta}$ is computed using finite differences and the shock location at $Z_0 + \Delta Z$); then compute the difference in pressure predicted by the jump condition and the compatibility condition. The procedure is continued until this difference vanishes. Cross-flow shocks are computed in a similar manner.

Shocks imbedded in the flow field are detected by monitoring the pressure distributions in the X-direction for wing-type shocks and in the Y-direction for cross-flow shocks. Here the fact that the body in the mapped space is a near circle is exploited. Wing-type shocks develop as compressions predominantly in the X (or radial) direction and cross-flow shocks develop as compressions in the Y (or θ) direction. This fact simplifies both the detection and the explicit computation of these imbedded shocks.

Figure 12 shows the pressure at the four mesh points adjacent to a maximum pressure gradient. In practice, a shock is inserted when a third-order curve fitted through these points predicts an infinite P_X (P_Y for cross-flow shock). Reference 7 demonstrates a number of techniques for detecting shocks including this one. The shock detection and insertion needs no user intervention (in the code that has been developed) except for the specification (as input) of two axial stations, between which the code tests for the formation of a shock. This was done primarily to minimize running times.

When the distance between two shocks becomes small compared with the total shock layer at some value of $Y = Y_0$ (fig. 13), the shocks are considered to have intersected. A two-dimensional same-family shock intersection calculation is performed in the plane containing the normal to the outside shock and the marching direction (fig. 14). The conditions behind the outside shock are set equal to those of the resulting shock and the contact surface is neglected (fig. 14).

Sharp leading-edge shocks are computed using the two-dimensional wedge calculation in the plane normal to the wing (or tail) leading edge. This calculation assumes the shock to be attached to the wing leading edge and uses a centered expansion fan if the velocity vector must be turned in an expanding direction to satisfy the body boundary condition at the leading edge. Figures 15(a) and 15(b) show the mesh point locations on a sharp leading-edge wing and figure 15(c) shows the local coordinate system used.

Body Point Calculation

The boundary condition at the vehicle surface is $\bar{U} = 0$, where \bar{U} is the velocity normal to the body. The entropy at the body is computed as it is at any other mesh point. At the body the coefficient of S_X vanishes, so that this derivative does not affect the calculation of entropy on the body.

To compute the body pressure, the continuity and three momentum equations are combined with the body boundary condition to write a compatibility equation along the characteristic (in the X,Z plane) reaching the wall from the flow field (ref. 11).

The cross-flow velocity is computed using the cross-flow momentum equation. The total velocity is computed using the integrated energy equation (total enthalpy equals constant). Finally the body boundary condition enables one to compute the three velocity components u , v , and w .

Blunt-Nose Entropy Layers

On blunt-nose bodies, as the computation proceeds downstream, the entropy gradient normal to the body becomes very large (near the surface). Streamlines that cross a weaker bow shock, and therefore have low entropies, approach the body which is wetted by the stagnation streamline, and therefore has a very large entropy. Figure 16 shows the entropy distributions plotted as a function of the normalized radial coordinates in the bottom symmetry plane of two different bodies (cone and shuttle orbiter). The three velocity components u , v , and w have similar distributions showing large gradients, whereas the pressure gradients remain small. This phenomenon can create numerical difficulties as the "edge" of this layer (defined by the *'ed points in fig. 16) approaches the body. A technique proposed by Moretti and Pandolfi (refs. 8 and 9) is used to handle this problem. In essence this technique disallows radial derivatives across the edge of the entropy layer for the flow variables (u , v , w , and S) which have large gradients across it.

The entropy minimum (or plateau depending on the body geometry) is detected as it is generated at the bow shock, in each circumferential plane, and followed from that point on. The locus of all these points (one in each $Y = \text{Constant}$ plane) forms a stream surface which, of course, always contains the same streamlines. In figure 17 this surface is shown (dashed lines) at several cross sections. This surface is not a coordinate line in the computational plane so that it "floats" between mesh points (fig. 18(a)). The dependent variables on this surface are computed in a manner similar to that used on the body. The pressure and the streamline slope in the X,Z plane are interpolated on this surface (from the adjacent mesh points), since their gradients across this surface are small. When a point on this surface is between two mesh points N and $N + 1$ (fig. 18(b)), instead of taking differences between N and $N + 1$, differences are taken between N and * or $N + 1$ and *. When the *'ed point becomes very close to the mesh point N (fig. 18(c)), the flow variables at N are set equal to those computed at the *'ed point.

When the distance between the body and this entropy layer surface becomes a small percentage of the total shock layer at some value of Y (figs. 17(c) and 17(d)), the values

of S , u , v , and w are changed from their previous body values to their values just outside the entropy layer. In some calculations the axial Mach number on the body may be approaching unity (because of the high body entropy), whereas the axial Mach number outside the entropy layer remains supersonic. In these cases the calculation could not be continued if the body entropy were not changed.

Real Gas Effects

Curve fits of Mollier charts (ref. 17) have been substituted for the ideal gas equation of state (eq. (6)) in the case of equilibrium air. The modifications to our computational procedures are minor but the running time for a typical case increases by 30 percent. Flow fields can also be computed which start near the vehicle nose in equilibrium but suddenly freeze (with an equivalent γ) at a given axial station.

RESULTS

During the course of this work the flow fields about a large number of geometries have been studied. This has been done (1) to be sure that the numerical techniques used worked for all these configurations, (2) to compare the results with existing data, and (3) to study flow-field phenomenon which can't be studied through other means. In this section some of the results of these calculations are discussed.

Figure 19 shows the surface streamlines and pressure distribution on an 80° slab delta wing at 30° angle of attack ($M_\infty = 9.6$). At this high angle of attack the cross-flow velocity expands around the wing tip and becomes supersonic on the lee side. This velocity component must vanish at the leeward symmetry plane and therefore a cross-flow shock (fig. 19(a)) is generated. The strength of this shock at the body is demonstrated by the streamline deflection across it. Figure 19(b) shows an axial and circumferential surface pressure distribution compared with experimental data (ref. 18). The jump in pressure (circumferential distribution) at about $\phi = 170^\circ$ is due to the cross-flow shock. The calculation of this flow from a starting plane ($Z/R_N \approx 0.8$) to the end ($Z/R_N = 15$) took about 15 minutes on the IBM 370/168 computer.

Figures 20, 21, 22, and 23 all describe the flow about an early version of a shuttle orbiter configuration flying at an angle of attack of 30° for $M_\infty = 26.1$. The calculation was performed for an ideal gas, $\gamma = 1.12$. Figure 20 shows the top and side views of the shocks and body; figure 21 shows the cross-sectional views. The shock pattern in this calculation is quite complex: a strake shock is generated at $Z \approx 380$ and intersects the bow shock at $Z \approx 440$, a cross-flow shock is generated starting at $Z \approx 550$, and a wing shock starts at $Z \approx 800$ and intersects the bow shock at $Z \approx 850$. Figure 22 shows the surface pressure variation with surface distance around the vehicle at several cross-sectional stations. Between $Z = 800$ and $Z = 850$ there is a large pressure raise

(fig. 22(b)) due to the beginning of the wing. The large peak in pressure at $Z = 850$ could not be computed without concentrating grid points in the wing tip region. Near $Z = 850$ the wing shock intersects the bow shock and causes an expansion fan which reduces the pressure (at the wing tip) further downstream. This phenomenon can be observed up to $Z = 1050$; whereas the peak pressure remains unchanged, the expansion moves toward the windward symmetry plane. The drop in the peak pressure between $Z = 1050$ and $Z = 1100$ is due to the wing tip turning parallel to the flow. Figure 23 shows the radial entropy distribution at three circumferential positions (X is the normalized radial coordinate). In these figures the thinning of the entropy layer is shown. This calculation (from $Z = 50$ to $Z = 1280$) took approximately 1.5 hours on the IBM 370/168 using a maximum of 20×30 grid points.

Figure 24 shows the surface pressure distribution in the windward symmetry plane on the forward portion of the 089-B shuttle orbiter. The calculations were performed using equilibrium air thermodynamics (at an altitude of 74 820 m (215 000 ft)) and ideal gases at $\gamma = 1.12$ and 1.4. In each case the Mach number was 26.1 and the angle of attack was 30° . The trends in the $\gamma = 1.12$ and real gas cases look very similar while in the $\gamma = 1.4$ calculation the recompression (after the nose expansion) seems weaker. In the real gas calculation the computer running time was increased by approximately 30 percent. Figure 25 shows the surface streamlines on the 089-B shuttle orbiter.

The windward symmetry plane surface pressure distributions on a modified version of the current 140-C space shuttle orbiter are shown in figure 26 for $M_\infty = 10.29$, $\gamma = 1.4$, and $\alpha = 20^\circ$ and 25° . The vehicle was modified for the computations by increasing the wing sweep from 45° to 55° (fig. 26) to avoid subsonic axial Mach numbers near the wing tip which would occur for this value of γ . This modification has little effect on the windward symmetry plane pressure distributions. The calculated results are compared with experimental data (unpublished) obtained at Ames Research Center. The agreement is very good except near the trailing edge. The underprediction near the trailing edge is due to a mismatch in lower surface slope (of approximately 5°) between the experimental and numerical geometry models.

The circumferential pressure distribution for this configuration at $Z/L = 0.3$ is compared with experimental data in figure 27, where L is the total length of the configuration. Again the agreement is very good. These calculations required approximately 1 hour of computing time on the CDC 6600 using a maximum of 15×32 grid points.

Another complex shock pattern is shown in figure 28. The vehicle is a fighter aircraft and the flight conditions are $M_\infty = 2.5$ and $\alpha = 6^\circ$. In this flow field there was a canopy shock, a wing shock, and an additional shock due to a recompression after the

canopy. Figure 28(c) shows a series of cross-sectional views in which the intersection of the canopy and bow shocks is evident. This calculation demonstrated that flow fields containing multiple imbedded shocks in a cross section can be computed treating all shocks explicitly.

Figure 29 compares the computed and experimental surface pressures on this vehicle ($M_\infty = 2.2$ and $\alpha = 5^\circ$ and 10°). The experiment was run by Grumman Aerospace Corp. at Ames Research Center and the data are unpublished. This calculation (from $Z = 0$ to $Z = 45$) took about 1 hour on the IBM 370/168 computer using a 24×29 grid in each cross section.

Figure 30 shows the inlet flow field for a supersonic fighter configuration. The axial station shown corresponds to the inlet forward lip station, so that this is the flow field ingested by the inlet. The maximum difference between calculation and experiment is less than 3 percent. The experimental data were obtained from reference 19 and the calculation took approximately 30 minutes on the IBM 370/165 with a 25×30 grid.

Figure 31 shows surface pressure distributions on the X-15 aircraft top and bottom symmetry planes. In figure 31(a) the flight Mach number is 6 and in figure 31(b) the Mach number is 4. The comparison with the experimental data is good. The deviation from the experimental results near the vehicle nose is due to the starting solution which was used (i.e., a conical flow solution was used to start the calculation).

Figure 32 shows a sample of the type of sharp-leading-edge wing configuration which can be computed. The figure shows the computed shock pattern with the bow shock intersecting the wing shock.

Shown in figure 33 is another complex shock pattern. The vehicle is a hypersonic research aircraft (HSRA) configuration and the flight conditions are $M_\infty = 6$, $\gamma = 1.2$, and $\alpha = 0^\circ$. As shown in the figure the canopy shock is generated ahead of $Z = 36$ and is intersecting the bow shock at $Z = 60$. A shock wave is generated by the vertical tail ahead of $Z = 50$. Figure 34 shows a lift curve for the HSRA vehicle. Both the experimental and Newtonian flow results were supplied by Lewis Clark of Langley Research Center. The figure shows that both the Newtonian calculation (with viscous effects included) and the present one compute lift accurately. The calculation of the HSRA flow field ($M_\infty = 6$ and $\alpha = 0^\circ$) took 1 hour on the IBM 370/168 computer using a 25×30 grid.

CONCLUDING REMARKS

The numerical techniques which have been presented here can be used to compute inviscid flow fields accurately and efficiently with reasonable running times on current day computers. The code which has been developed is a useful tool for studying three-dimensional flow field effects and can aid in the development of high-speed vehicles.

In order to gain flexibility in terms of even more complex geometries (such as configurations with tip fins, engine pods mounted on wings, etc.), a mapping must be developed which can transform these geometry cross sections into "near" circles efficiently. The computational techniques used can be modified to handle at least small pockets of subsonic axial Mach number. In order to compute flows with more complex shock patterns, imbedded shocks should be allowed to "float" between grid points to avoid difficulties sometimes encountered when using shocks as internal computational boundaries.

REFERENCES

1. Marconi, F.; and Salas, M.: Computation of Three Dimensional Flows About Aircraft Configurations. *J. Computers and Fluids*, vol. 1, p. 185, 1973.
2. Vachris, A.; and Yaeger, L.: QUICK-GEOMETRY User's Manual. Grumman Aerospace/Aerodynamic Section Technical Data Report No. 393-74-1, 1974.
3. Moretti, G.: Three Dimensional, Supersonic, Steady Flows With Any Number of Imbedded Shocks. AIAA Paper No. 74-10, 1974.
4. Moretti, G.; Grossman, B.; and Marconi, F.: A Complete Numerical Technique for the Calculation of Three Dimensional Inviscid Supersonic Flows. AIAA Paper No. 72-192, 1972.
5. Moretti, G.: The Choice of a Time Dependent Technique in Gas Dynamics. PIBAL Report No. 69-26, 1969.
6. Moretti, G.: Importance of Boundary Conditions in Numerical Treatment of Hyperbolic Equations. *Phys. Fluids*, Suppl. II, p. 12, 1969.
7. Moretti, G.: Thoughts and Afterthoughts About Shock Computations. PIBAL Report No. 72-37, 1972.
8. Moretti, G.; and Pandolfi, M.: Entropy Layers. *J. Computers and Fluids*, vol. 1, p. 19, 1973.
9. Moretti, G.; and Pandolfi, M.: Analysis of the Inviscid Flow About a Yawed Cone. Preliminary Studies. PIBAL Report No. 72-18, 1972.
10. Courant, R.; Friedrichs, K. O.; and Lewy, H.: Ueber die partiellen Differenzgleichungen der Mathematischen Physik. *Math. Ann.*, vol. 100, p. 32, 1928.
11. Kentzer, C.: Discretization of Boundary Conditions on Moving Discontinuities. Proceedings of the II Int. Conf. on Numerical Methods in Fluid Dynamics, September 1970.
12. Moretti, G.; and Bleich, G.: Three-Dimensional Flow Around Blunt Bodies. AIAA J., vol. 5, 1966.
13. Skulsky, R. S.: A Conformal Mapping Method to Predict Low-Speed Aerodynamic Characteristics of Arbitrary Slender Re-entry Shapes. *J. Spacecraft*, vol. 3, no. 2, 1966.
14. MacCormack, R. W.: The Effects of Viscosity in Hypervelocity Impact Cratering. AIAA Paper No. 69-354, 1969.

15. Walkden, F.; and Caine, P.: Application of a Pseudo-Viscous Method to the Calculation of the Steady Supersonic Flow Past a Waster Body. Int. J. Numeric, Math Engng., vol. 5, 1972.
16. Kutler, P.; Lomax, H.; and Warming, R. F.: Computation of Space Shuttle Flow Fields Using Noncentered Finite Difference Schemes. AIAA Paper No. 72-193, 1972.
17. Moretti, G.: Analytical Expressions for a Speedy Computation of Thermodynamical Properties of Air. General Applied Science Laboratory, TM-39, 1960.
18. Whitehead, A. H., Jr.; and Dunavant, J. C.: A Study of Pressure and Heat Transfer Over an 80° Sweep Slab Delta Wing in Hypersonic Flow. NASA TN D-2708, 1965.
19. Prokop C.: Investigation of the Effects of Airframe Design on Inlet Flow Fields. AFFDL-TR-72-11, vol. 1, 1972.

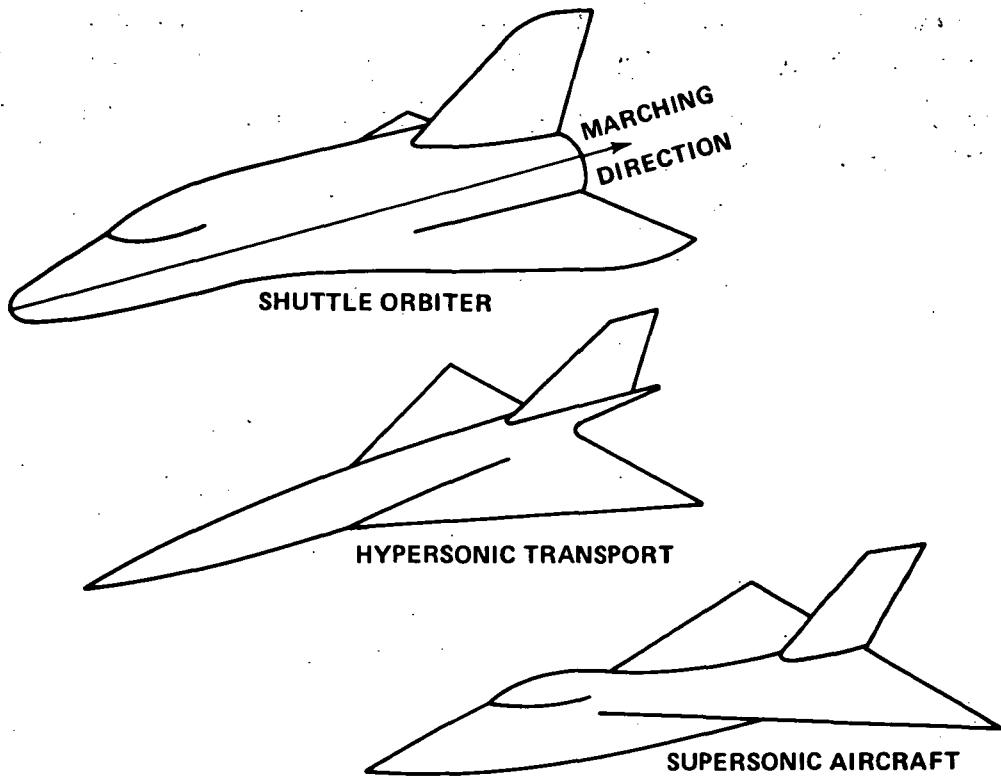
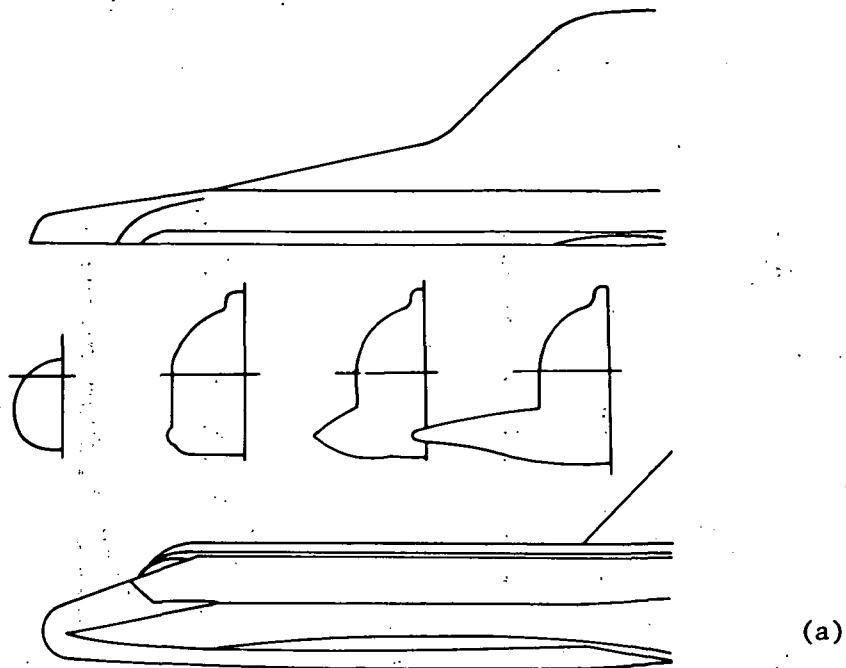


Figure 1.- Typical configurations.



+ TYPICAL QUICK
CONTROL POINTS

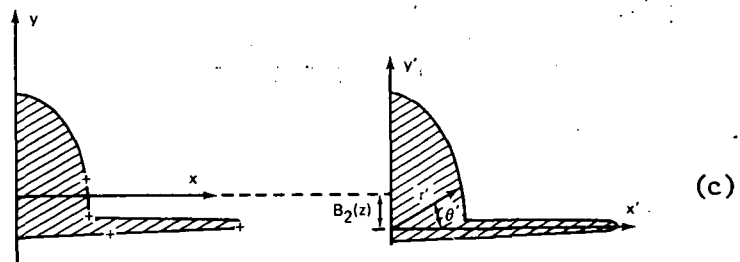
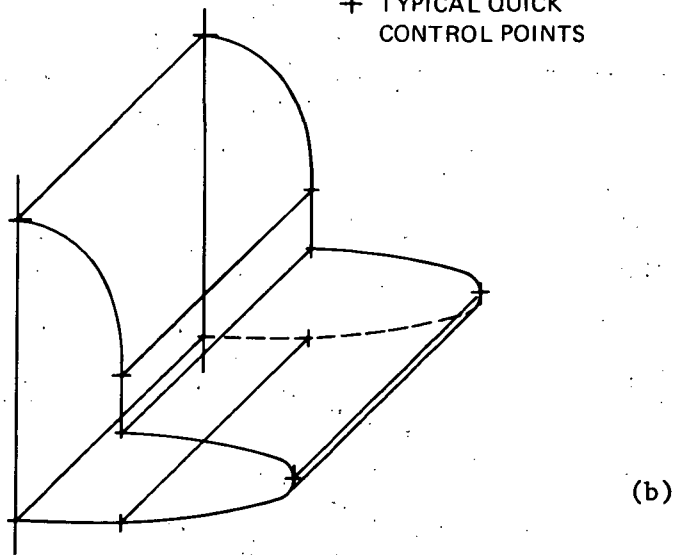


Figure 2.- QUICK geometry modeling procedure.

$$M_\infty = 10, \alpha = 15^\circ, \gamma = 1.4$$

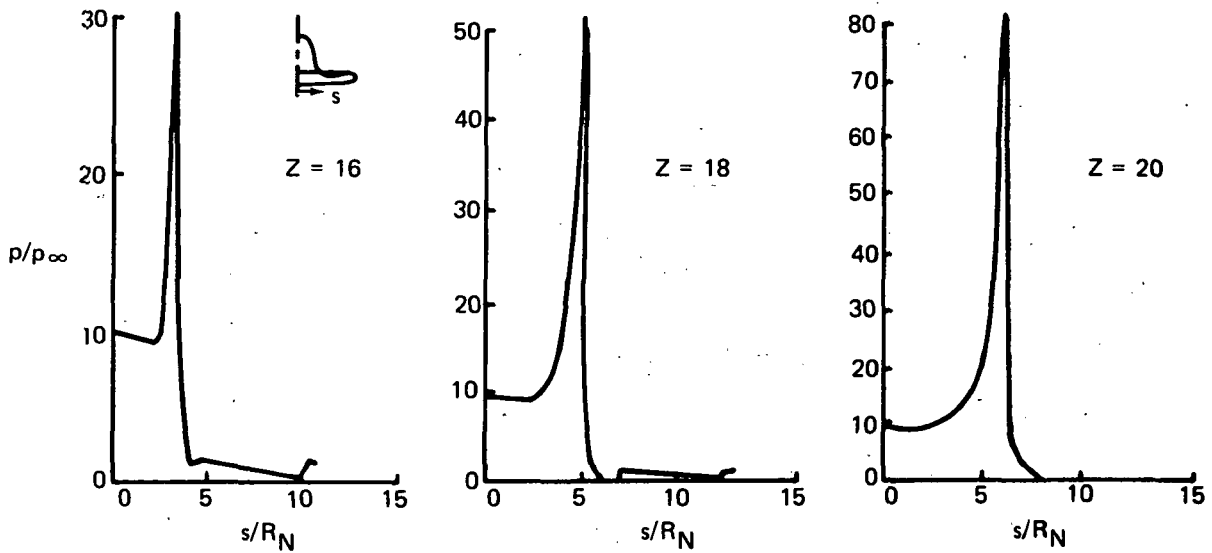
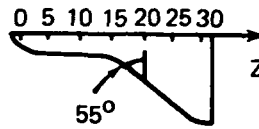


Figure 3.- Typical surface pressure distribution requiring mesh point concentration.

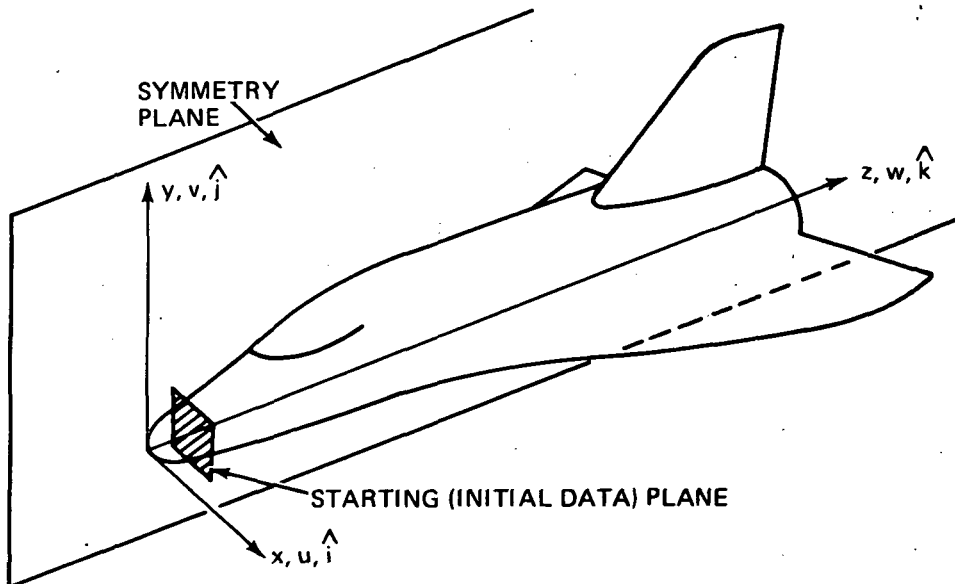


Figure 4.- Cartesian coordinate system.

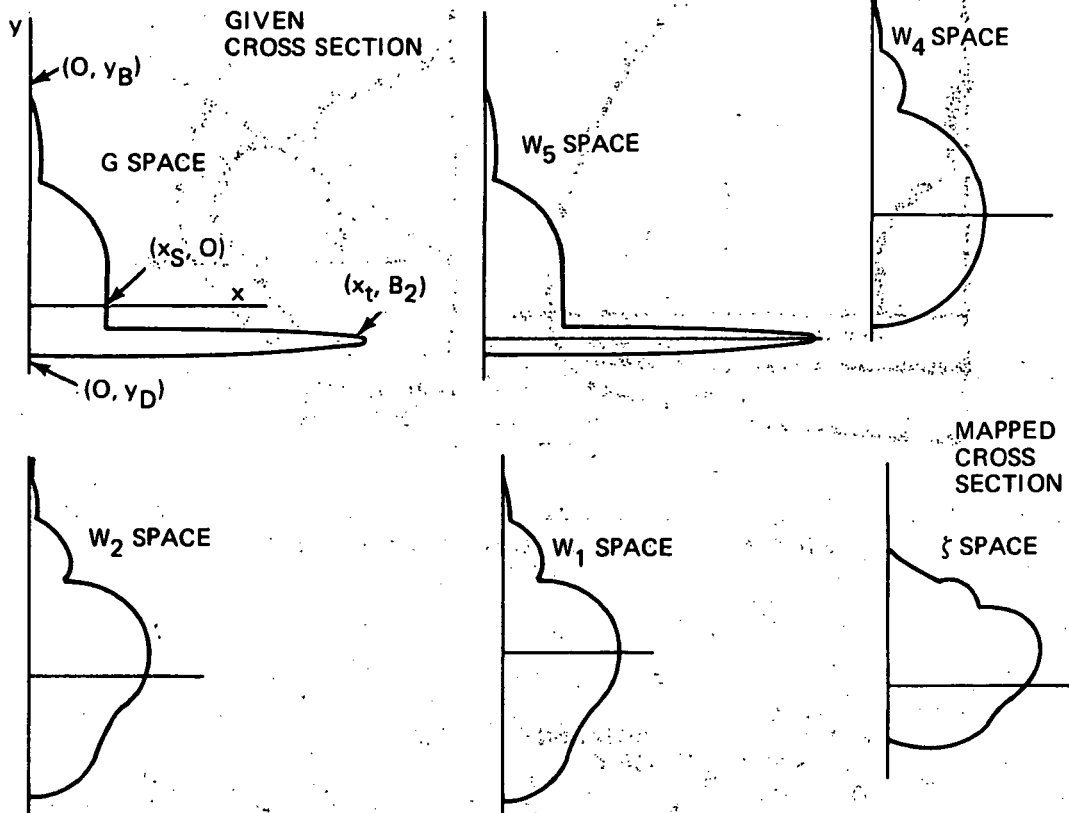


Figure 5.- Series of mappings.

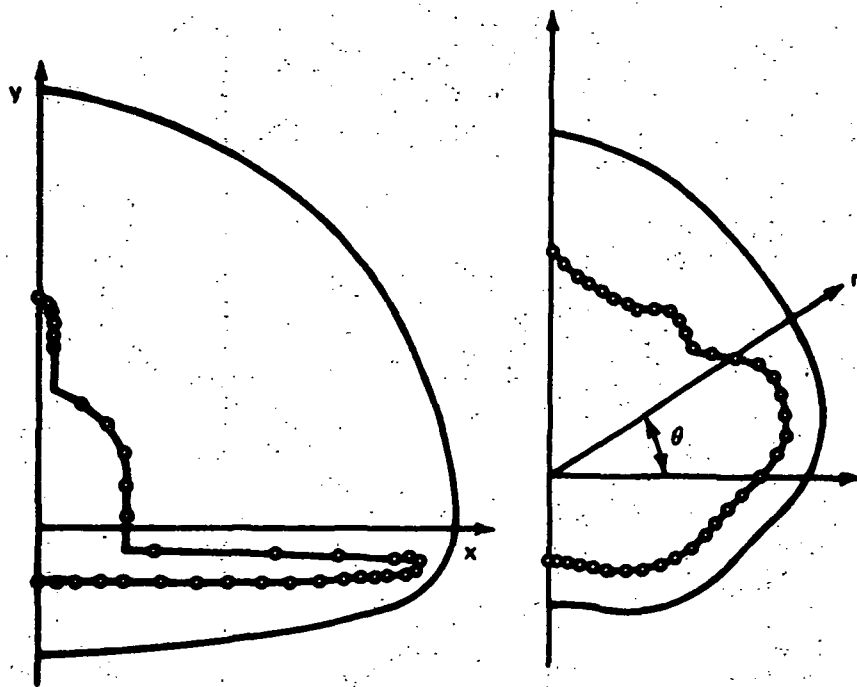


Figure 6.- Body mesh point distribution.

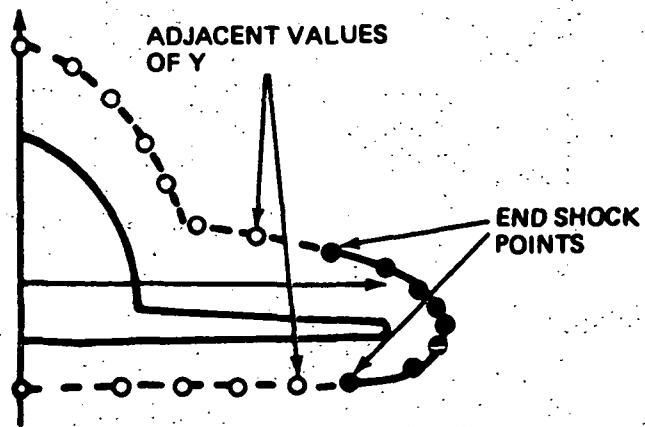


Figure 7.- Wing shock internal boundary.

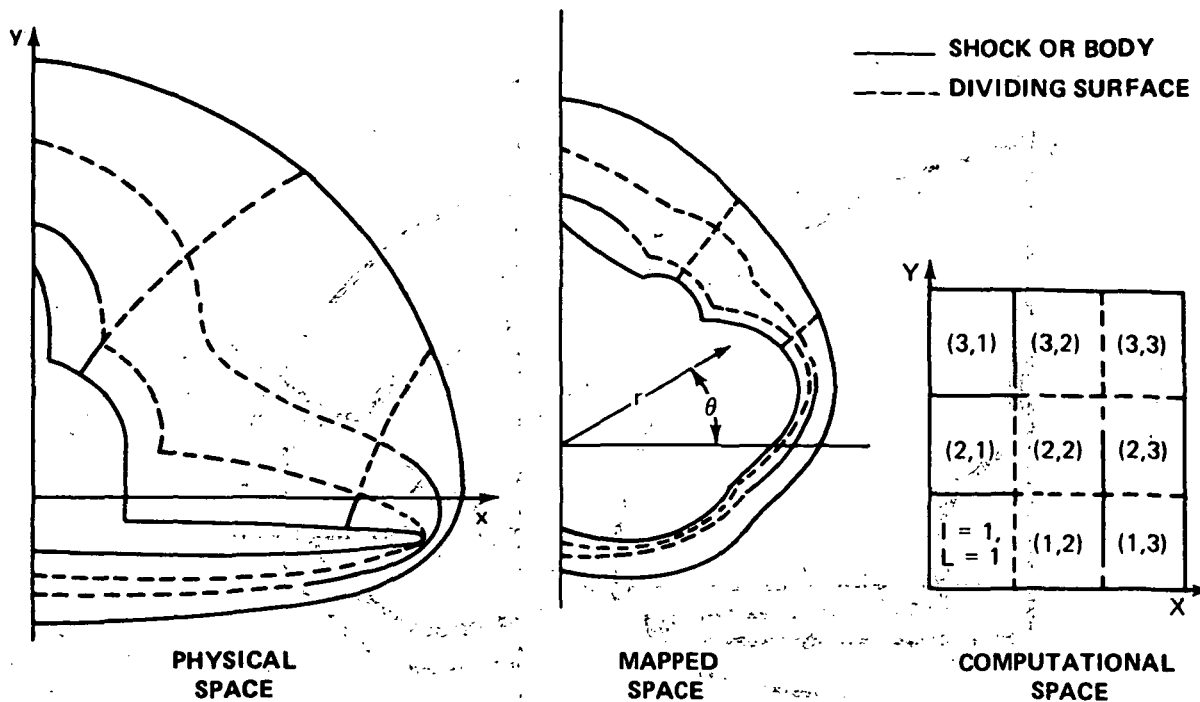


Figure 8.- $z = \text{Constant}$ plane in the physical, mapped, and computational spaces.

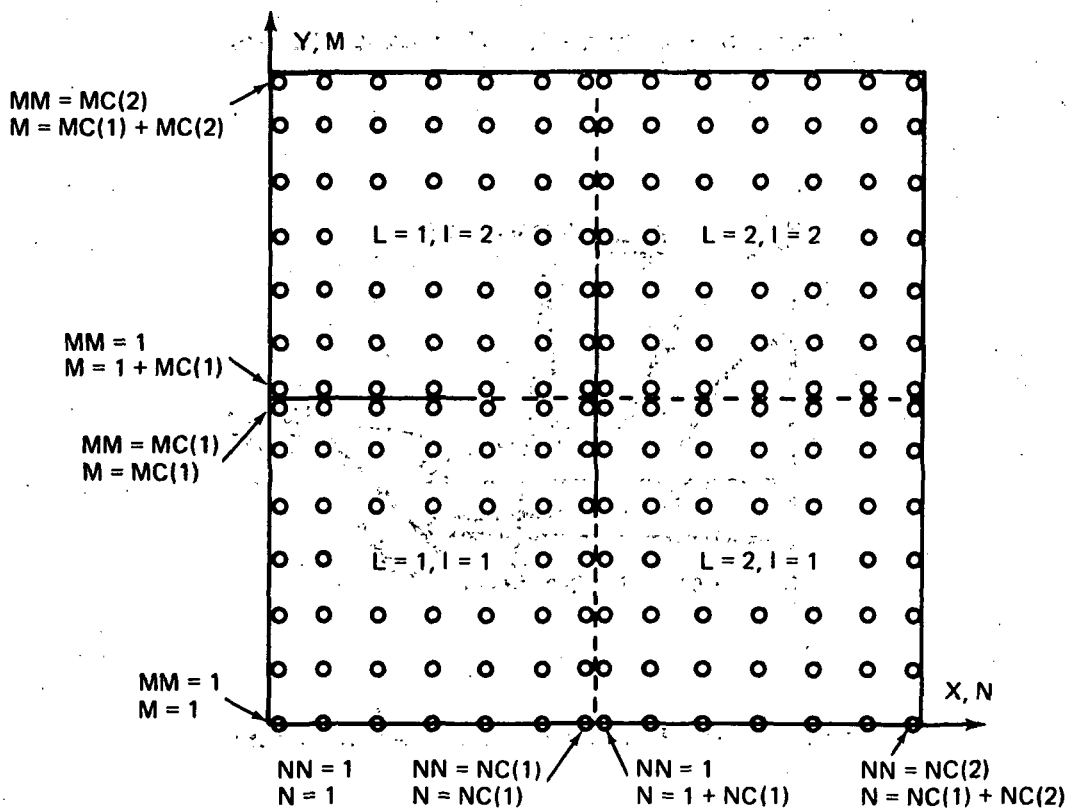


Figure 9.- Region and mesh point notation.

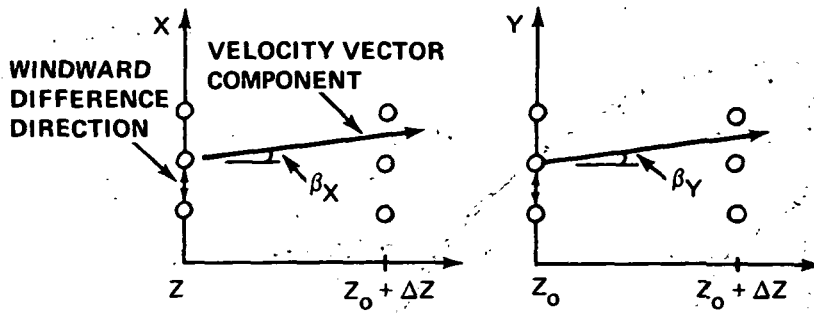


Figure 10.- Windward differencing.

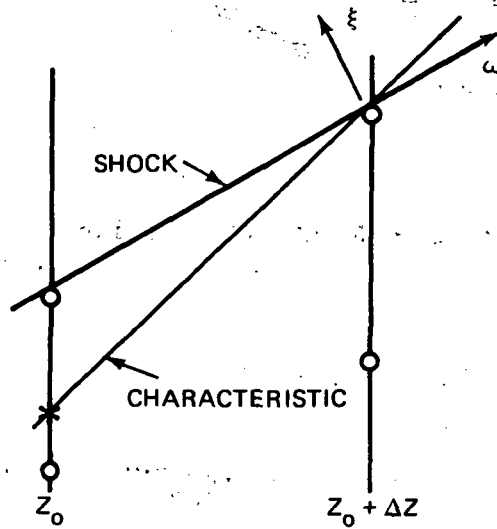


Figure 11.- Shock point calculation.

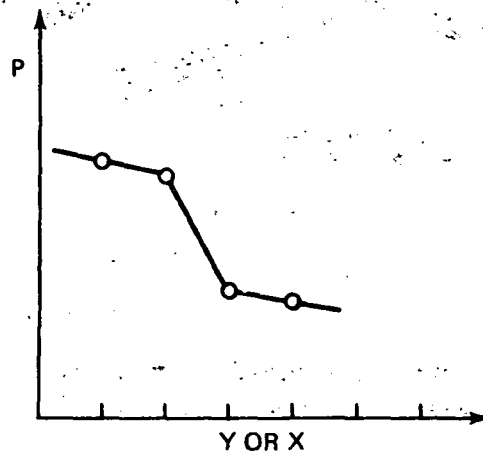


Figure 12.- Imbedded shock detection.

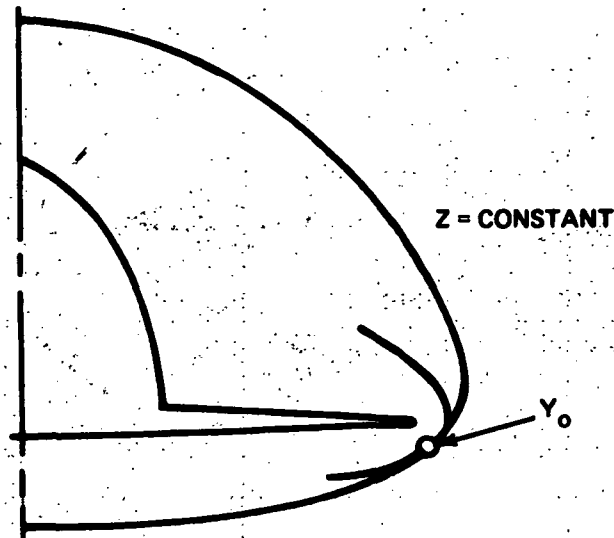


Figure 13.- Shock intersection.

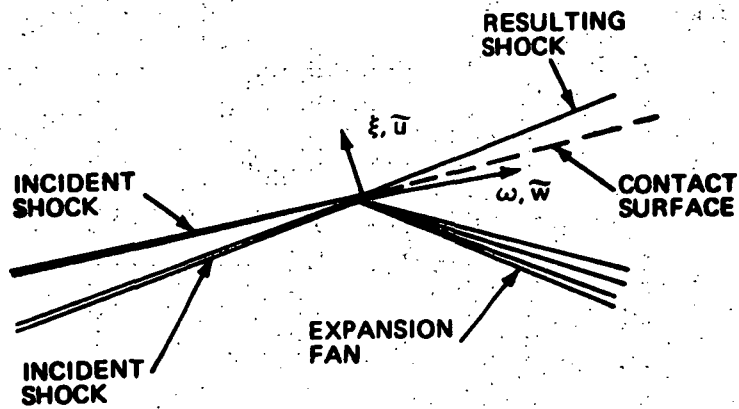


Figure 14.- Shock intersection in the ξ, ω plane.
 (~ denotes intrinsic variable.)

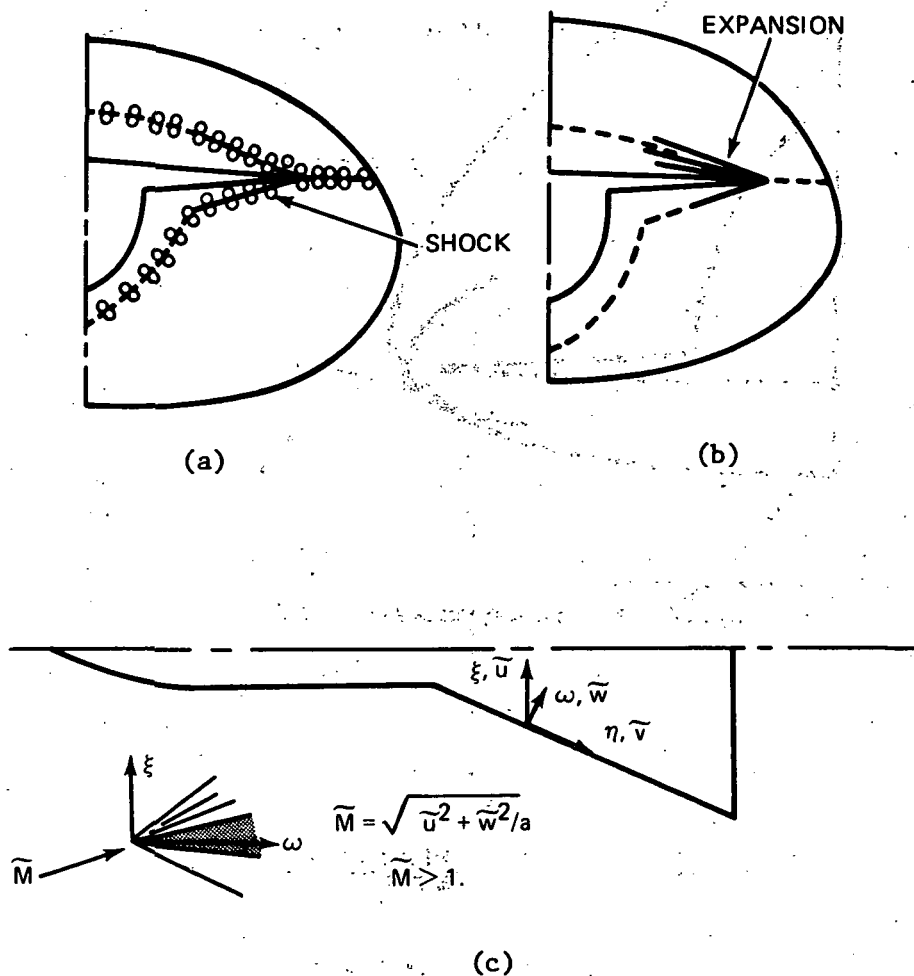


Figure 15.- Sharp-leading-edge wing calculation. (a is speed of sound and $\bar{\cdot}$ denotes intrinsic variable.)

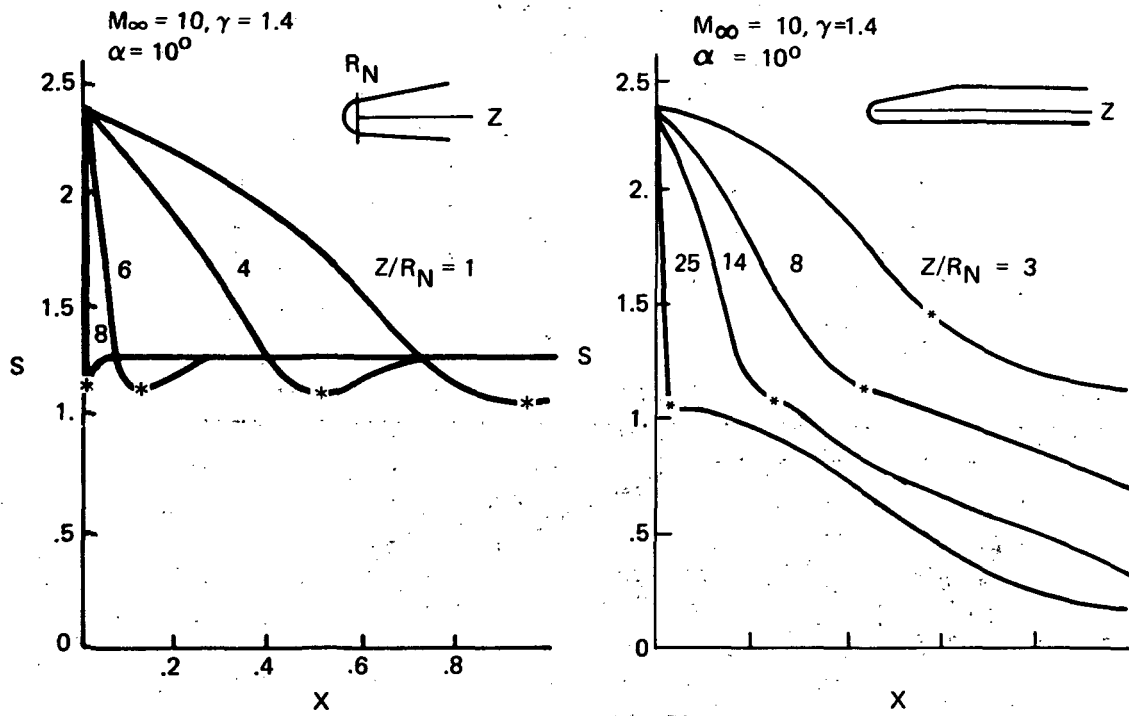


Figure 16.- Entropy distribution requiring special treatment.

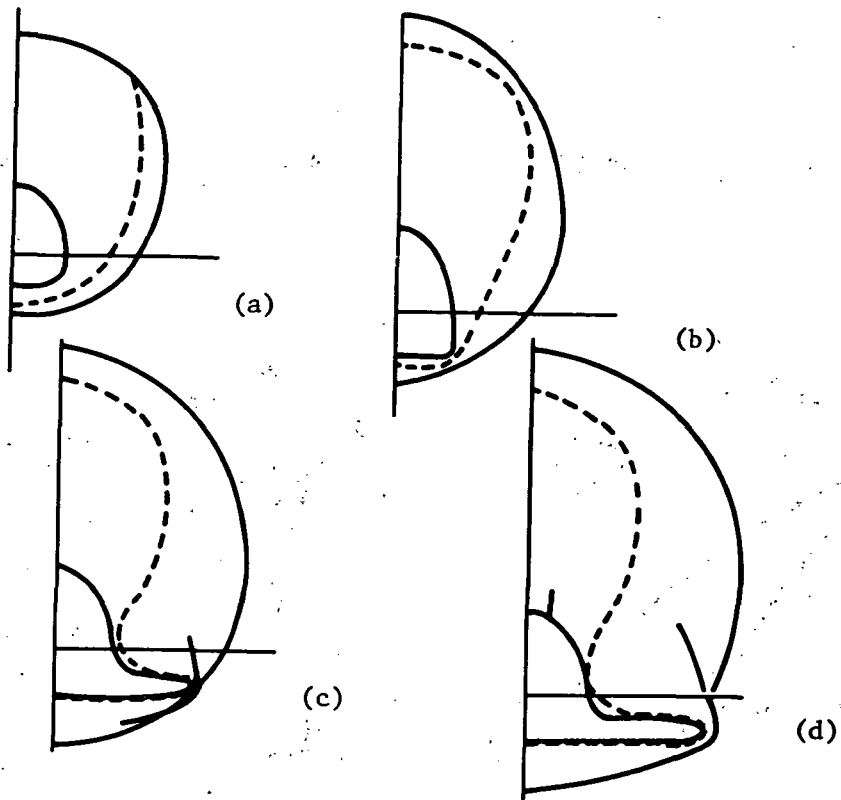


Figure 17.- Entropy layer surface in the physical plane.

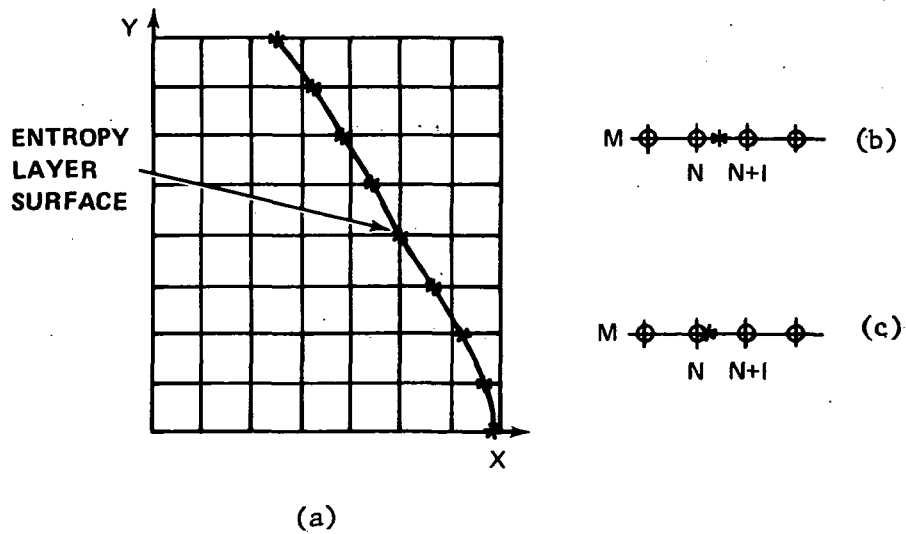


Figure 18.- Entropy layer surface in the computational plane.

80° SLAB DELTA WING AT $M_\infty = 9.6$, $\alpha = 30^\circ$ & $\gamma = 1.4$

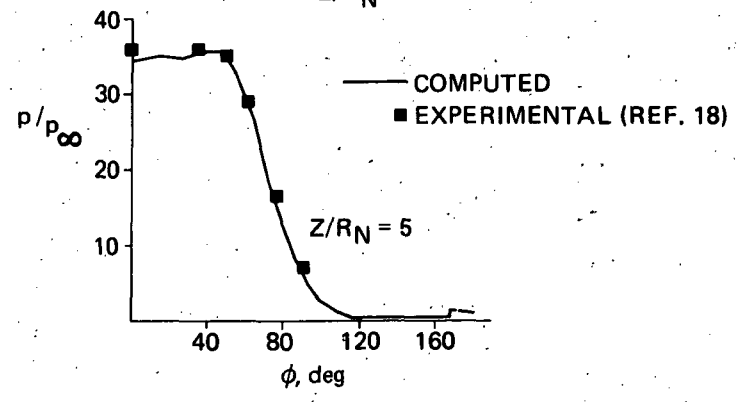
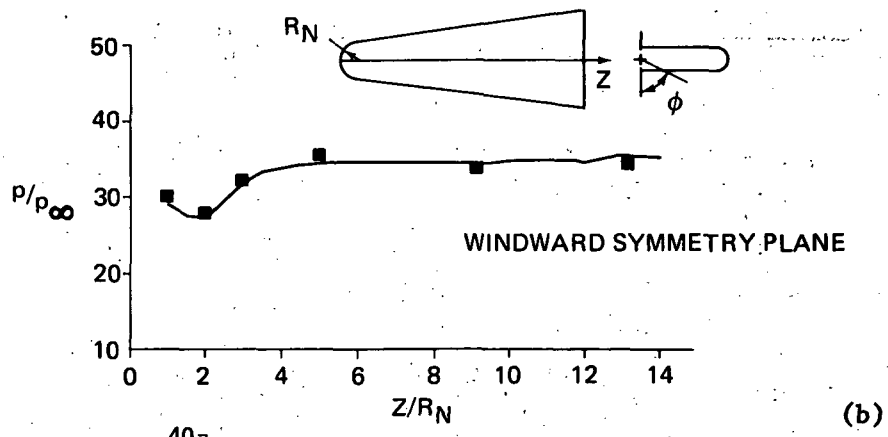
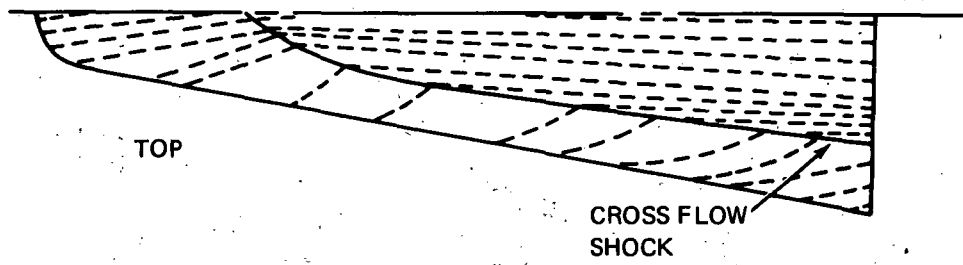
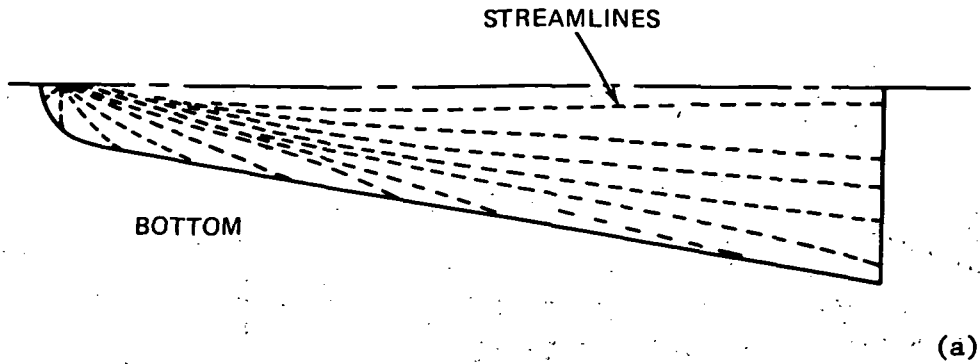


Figure 19.- Slab delta wing streamlines and surface pressure.

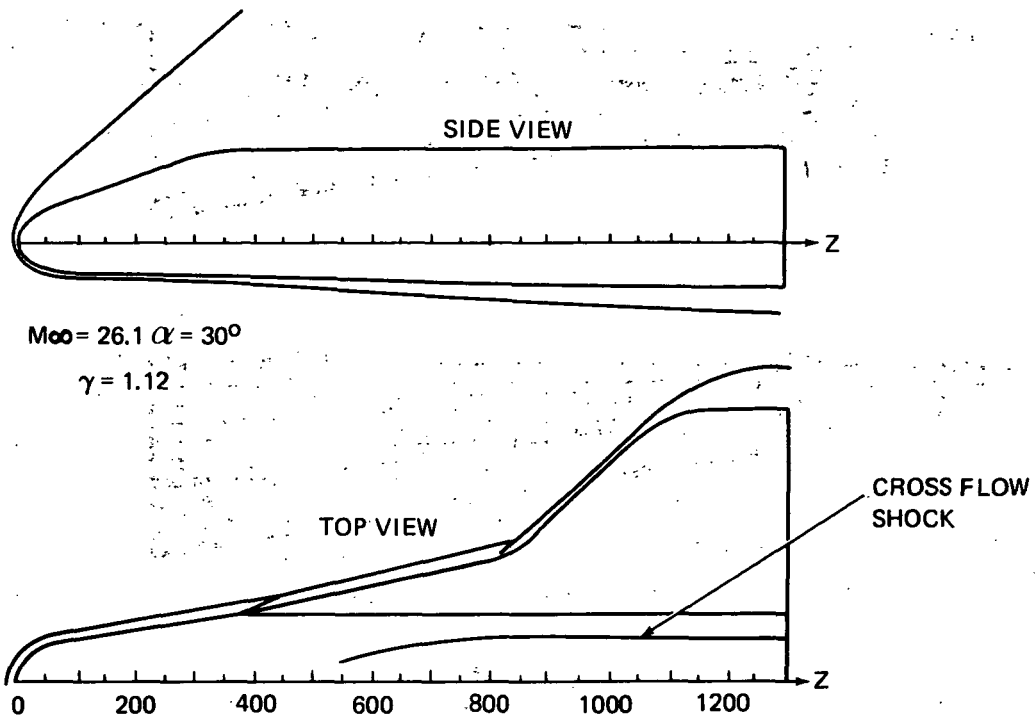


Figure 20.- 089-B shuttle orbiter shock patterns.

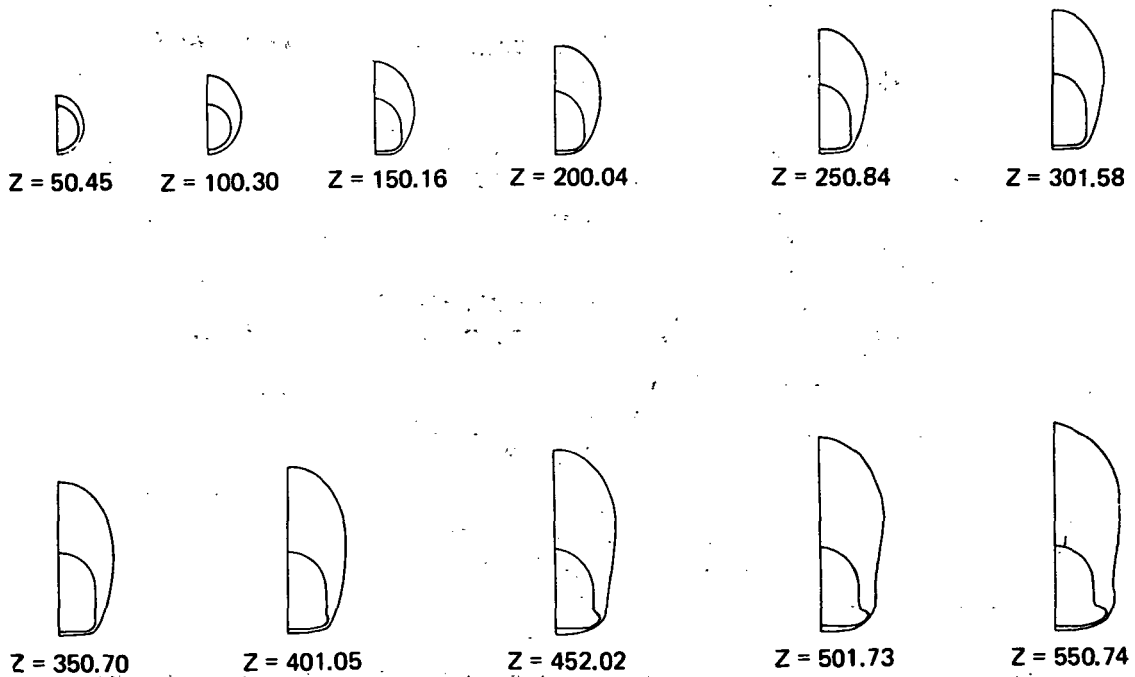


Figure 21.- 089-B orbiter cross-sectional shock patterns.

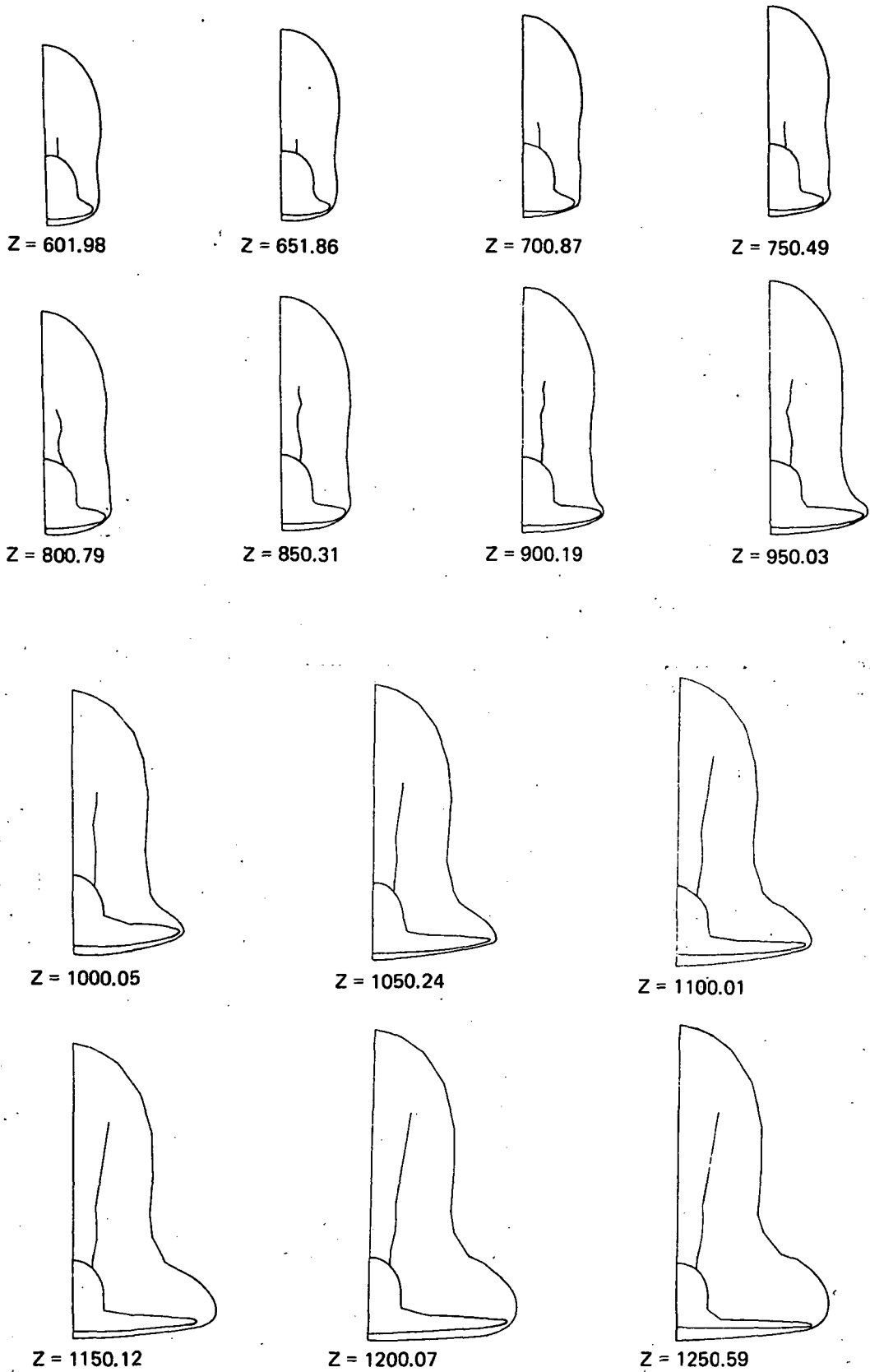


Figure 21.- Concluded.

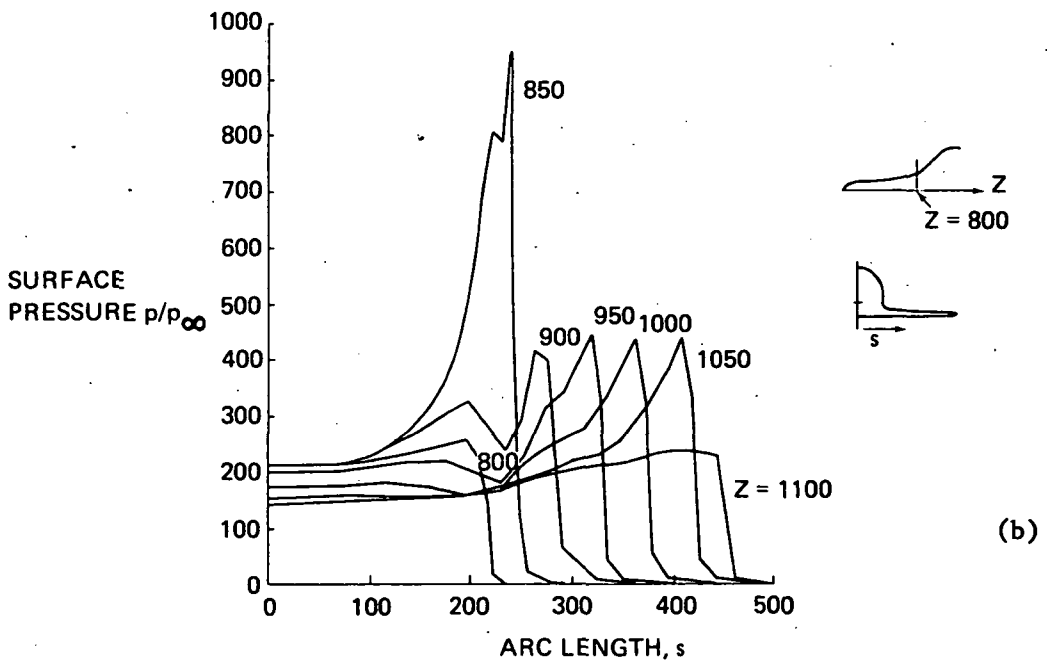
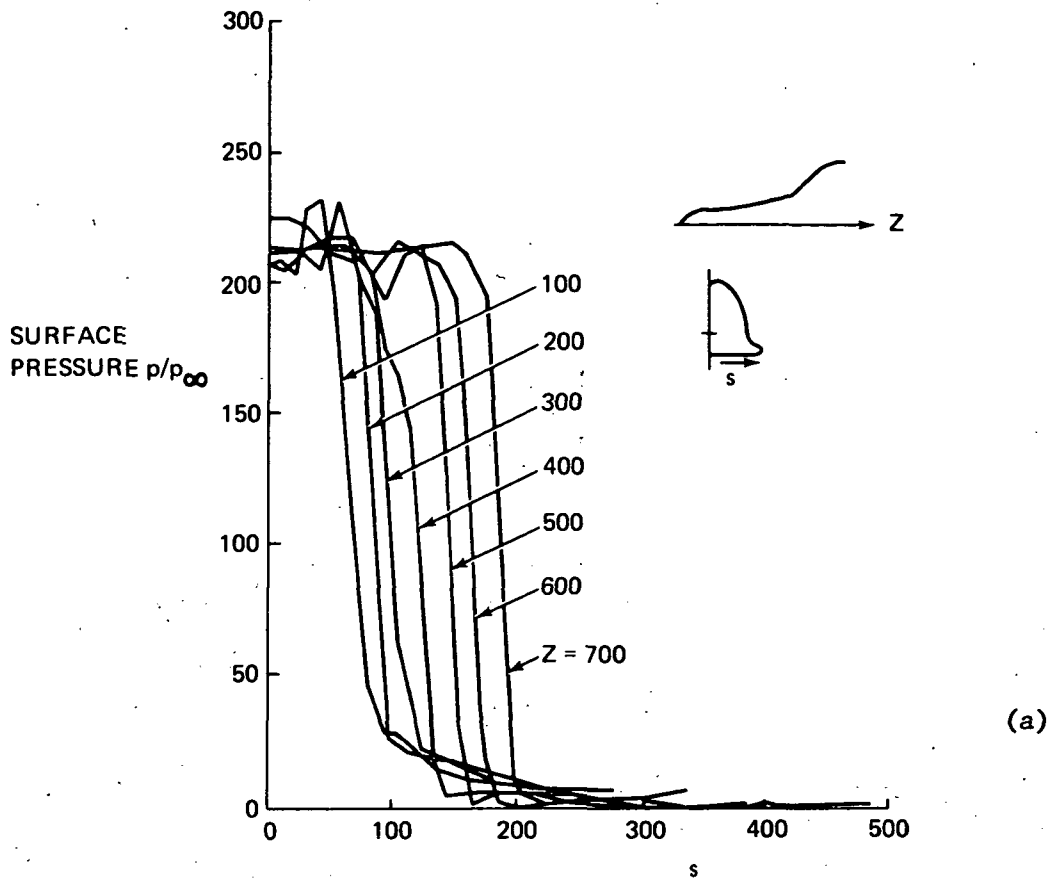


Figure 22.- 089-B orbiter surface pressure.

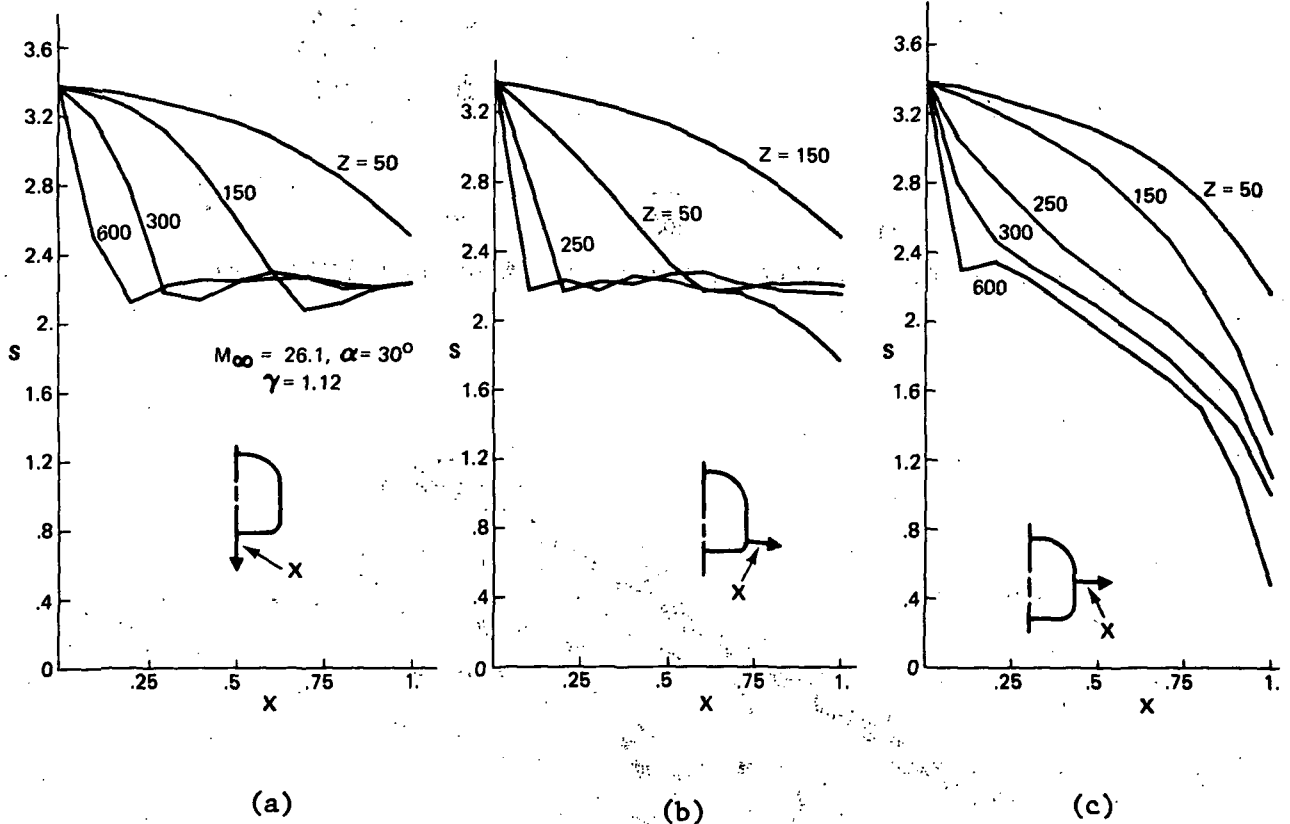


Figure 23.- 089-B orbiter entropy distribution.

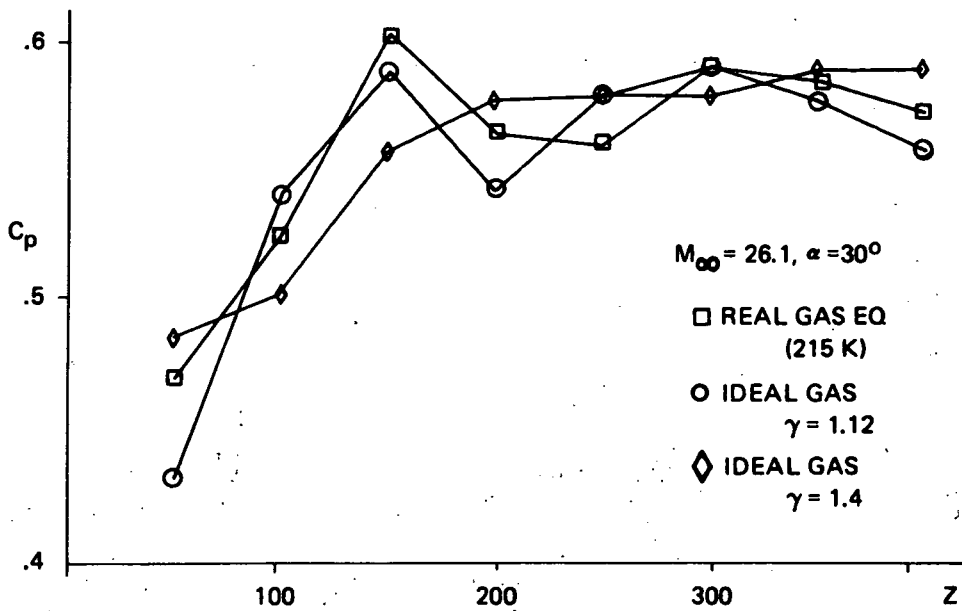


Figure 24.- 089-B orbiter windward plane surface pressure.

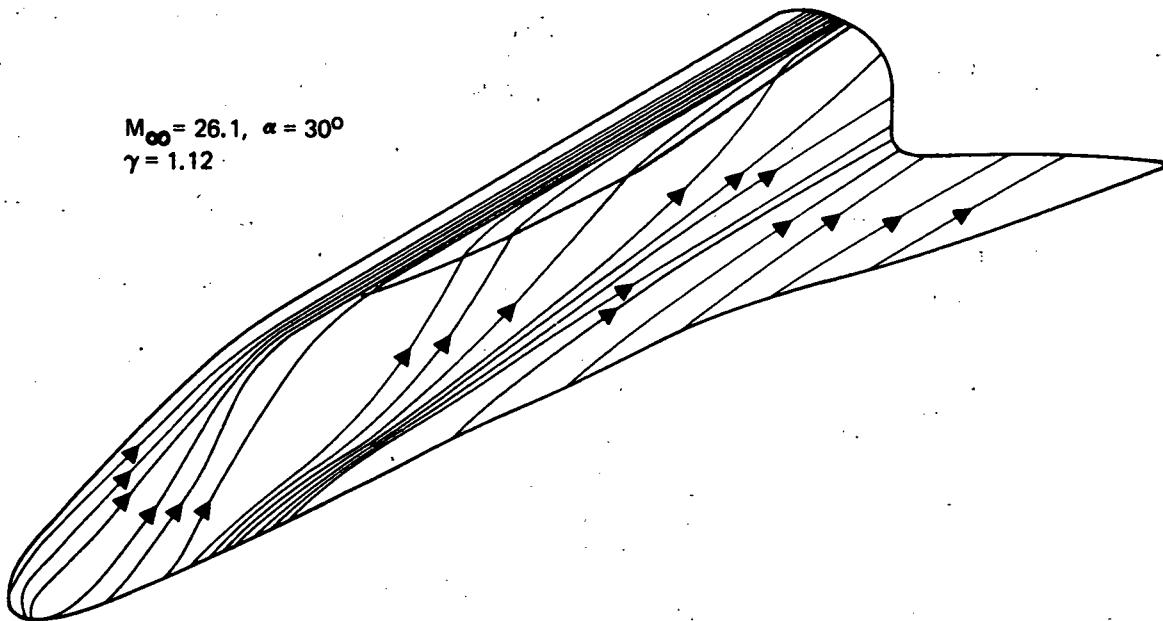


Figure 25.- 089-B orbiter surface streamlines.

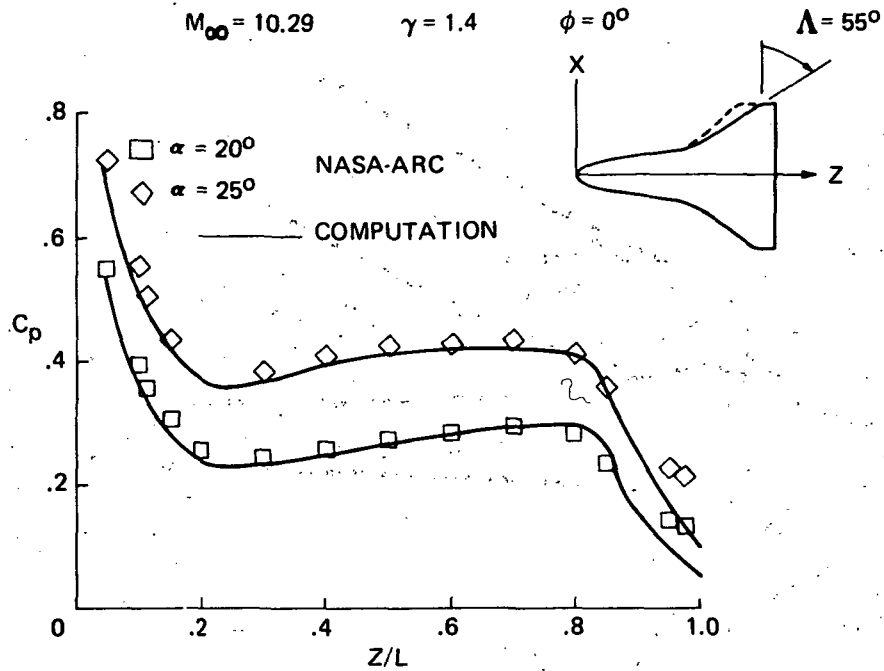


Figure 26.- Windward symmetry plane distribution, modified 140-C shuttle orbiter.

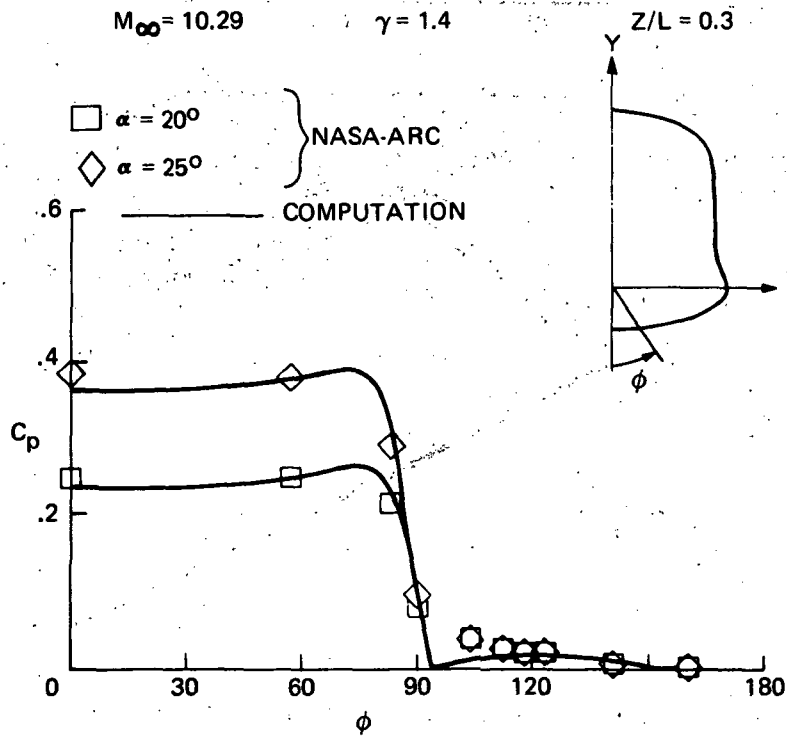


Figure 27.- Circumferential pressure distribution, modified 140-C shuttle orbiter.

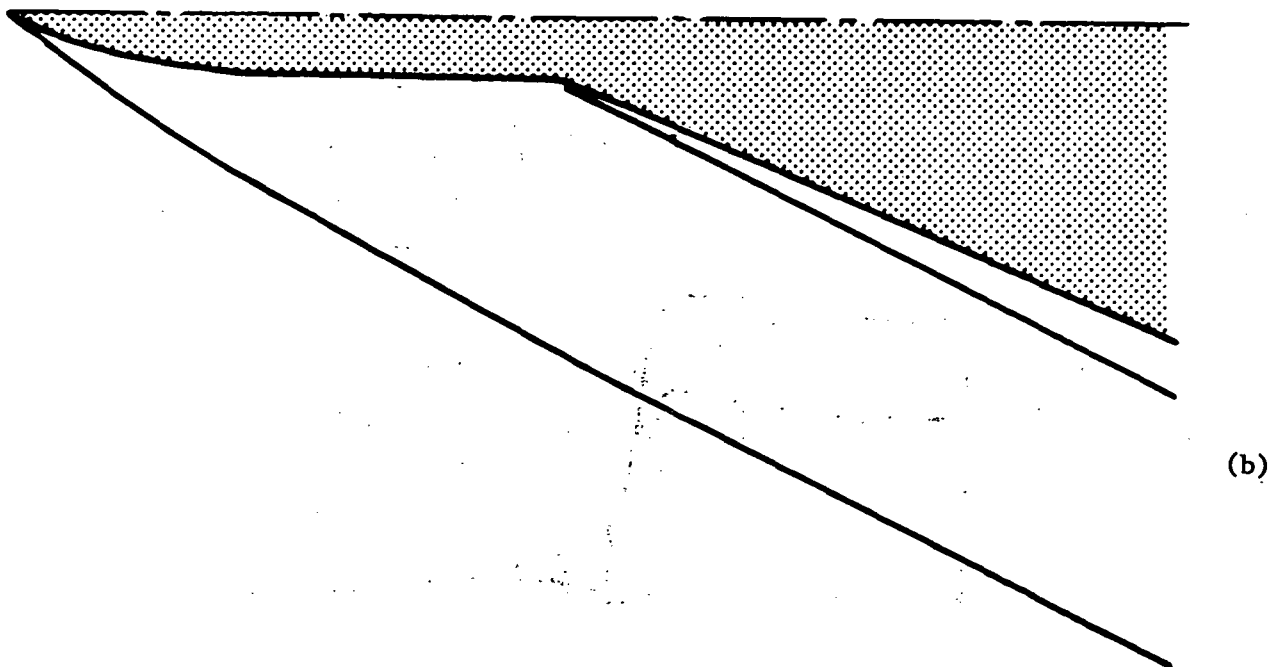
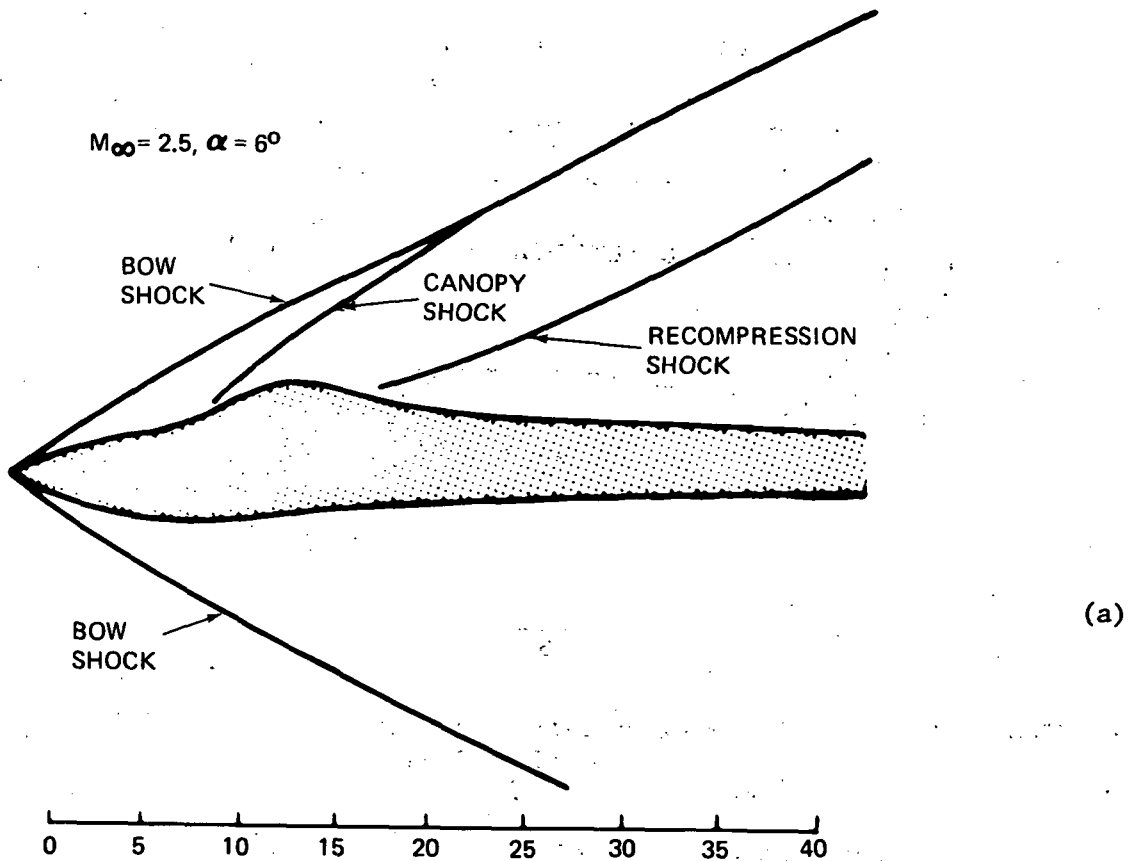
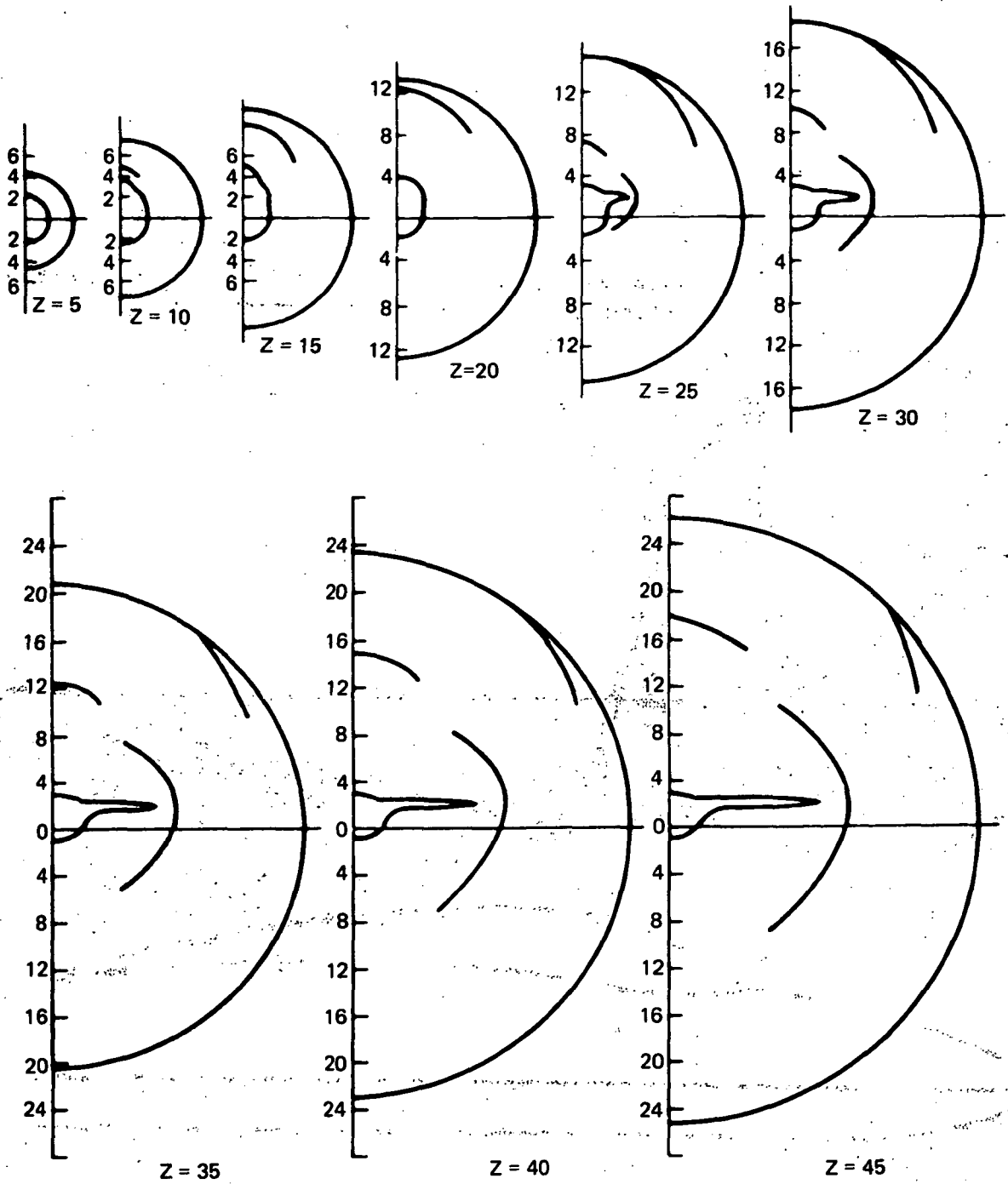


Figure 28.- Aircraft configuration shock pattern.



(c)

Figure 28.- Concluded.

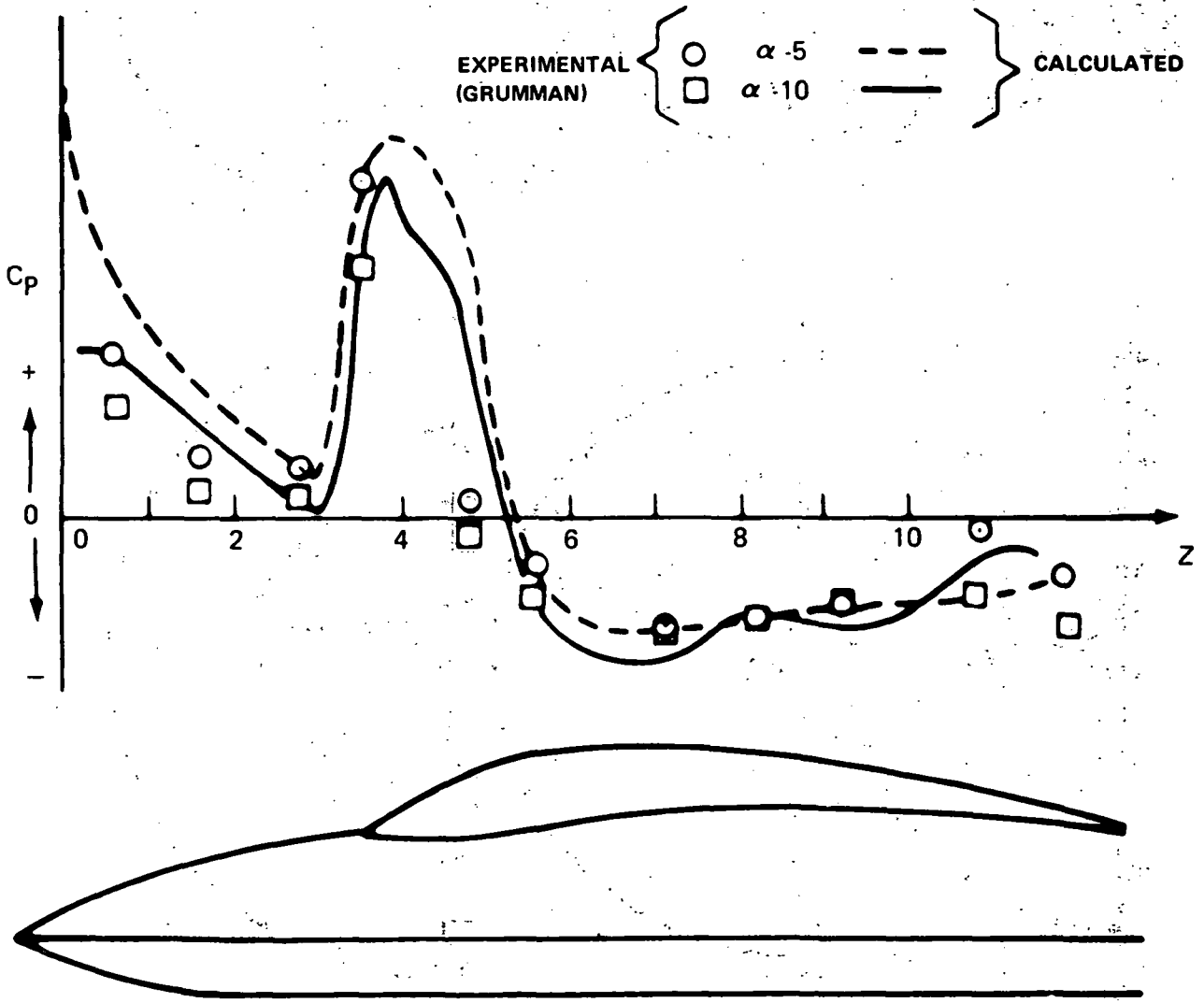


Figure 29.- Aircraft configuration, top symmetry plane surface pressure ($M_\infty = 2.2$).

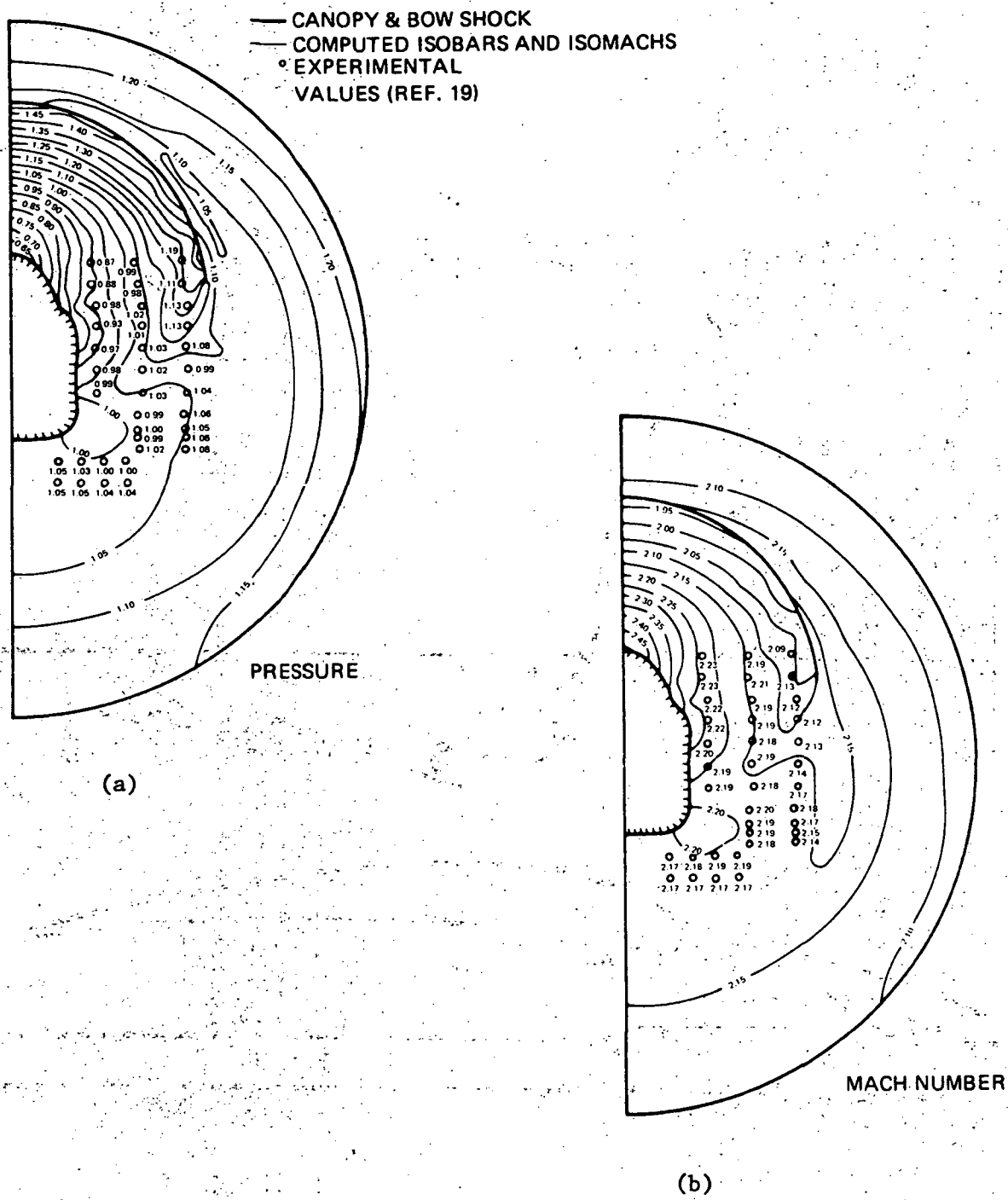


Figure 30.- Flow field at inlet forward lip ($M_{\infty} = 2.2$, $\alpha = 5^{\circ}$).

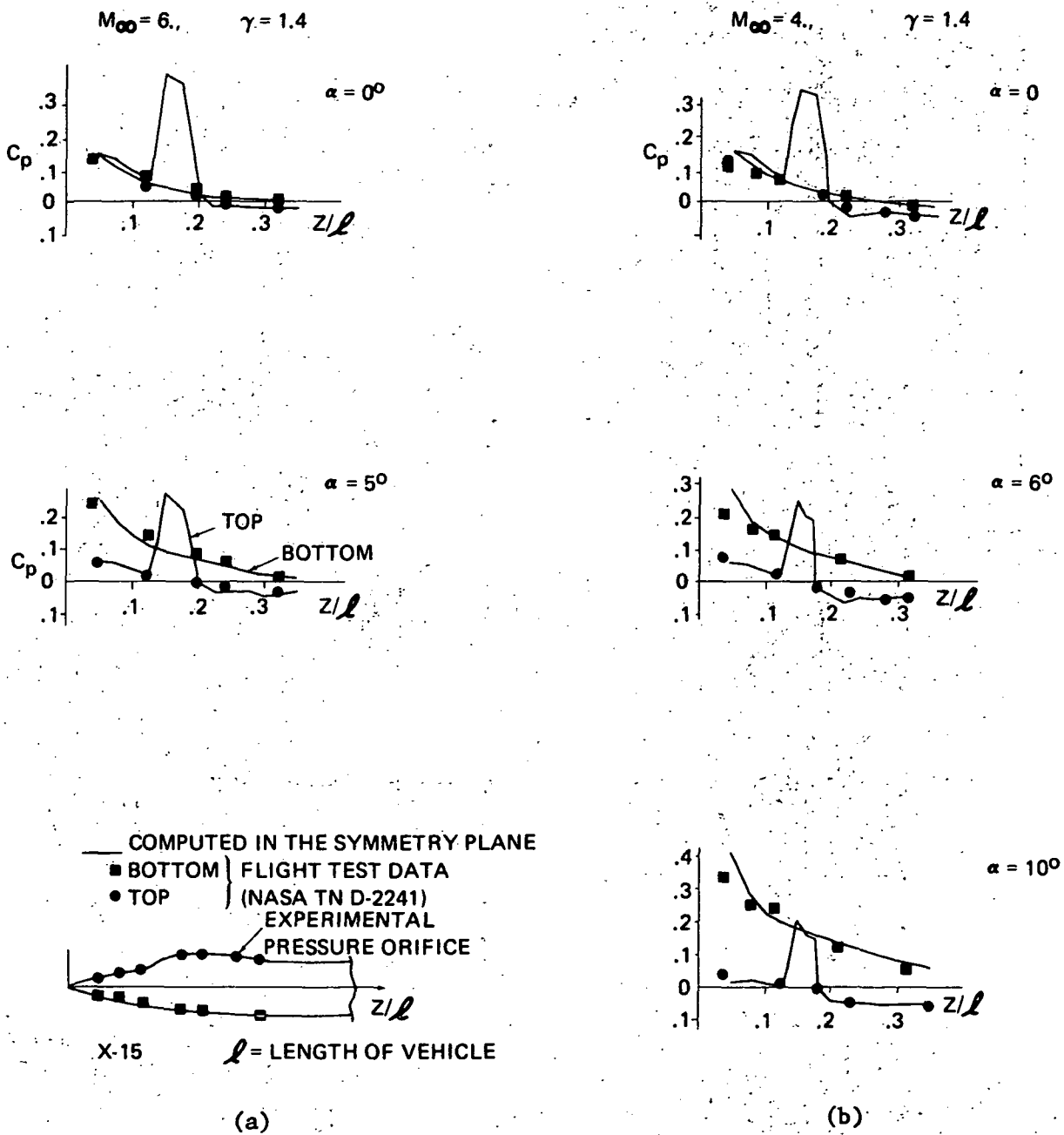


Figure 31.- X-15 surface pressures.

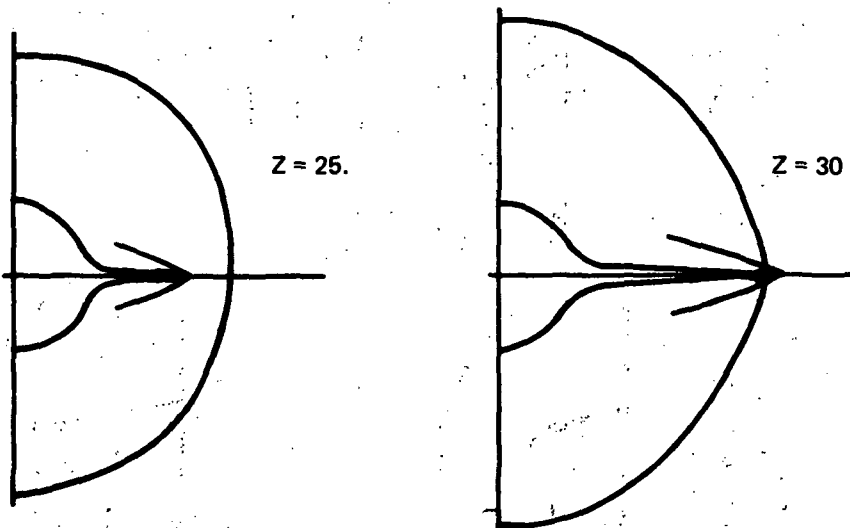
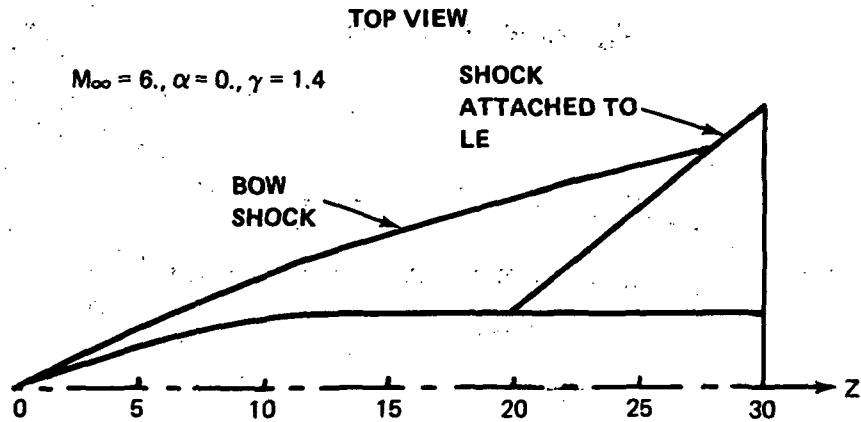


Figure 32.- Sharp-leading-edge wing configuration shock pattern.

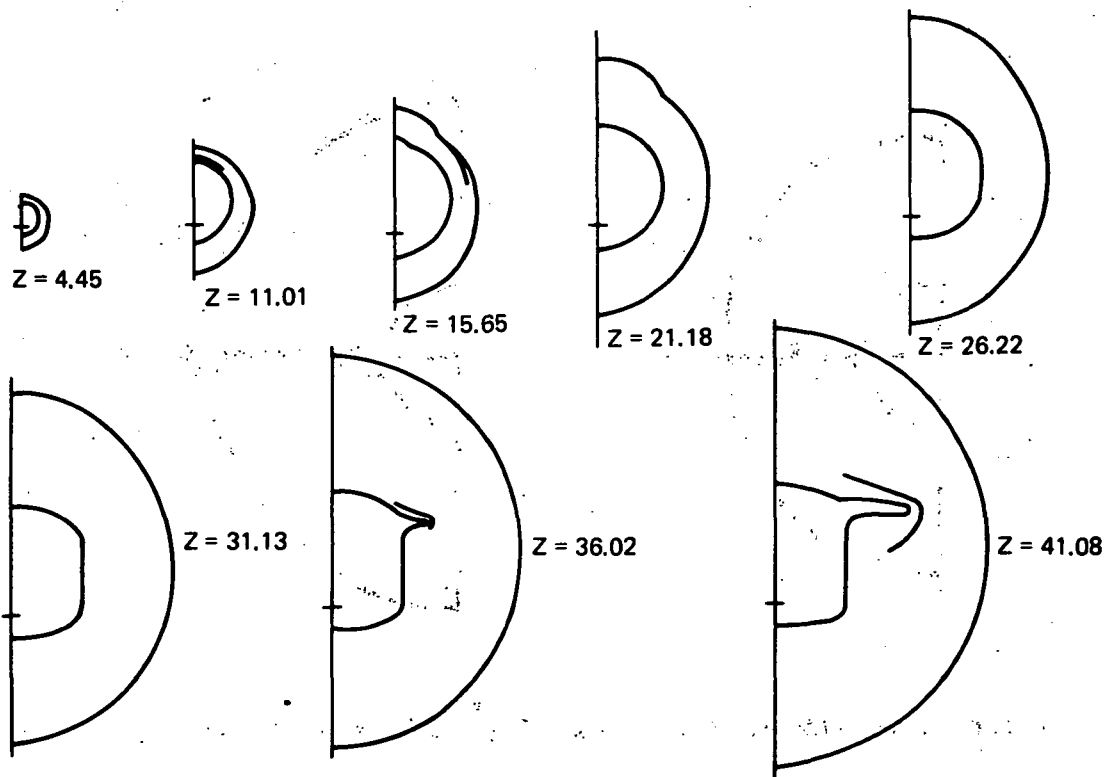
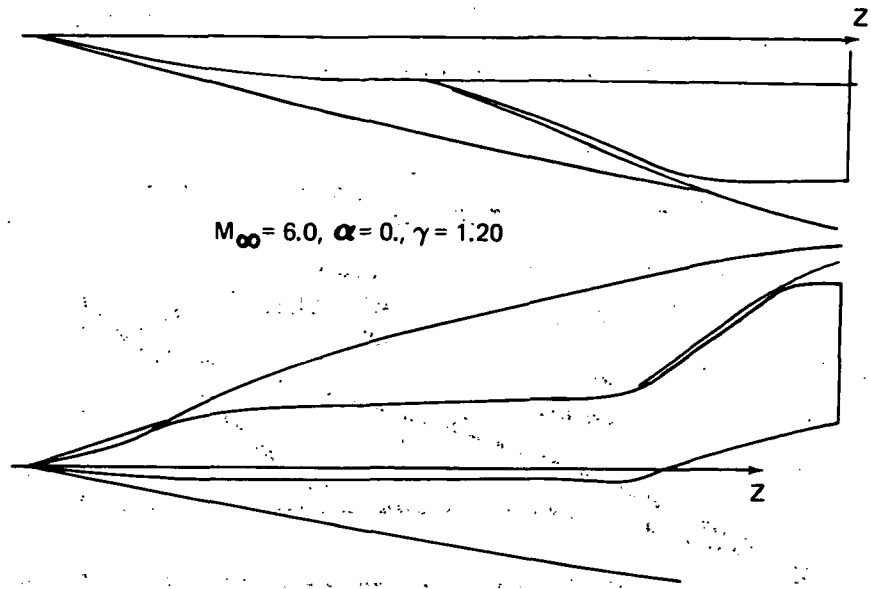


Figure 33.- Hypersonic transport shock patterns.

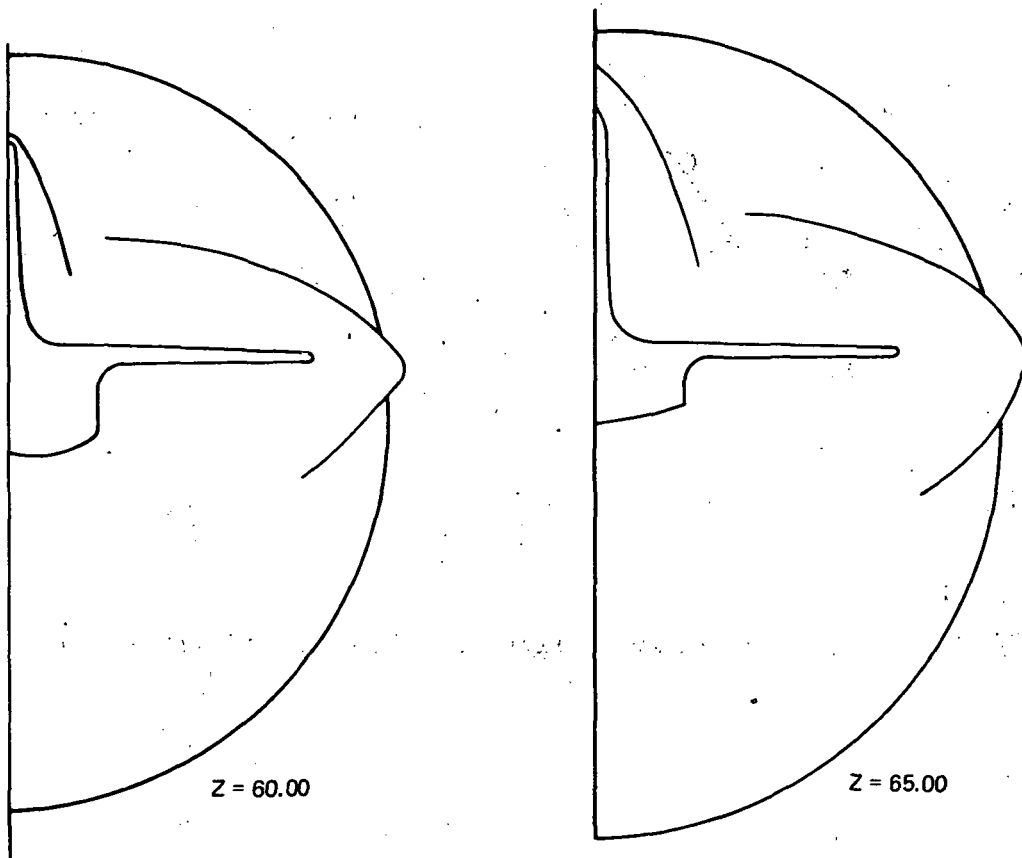
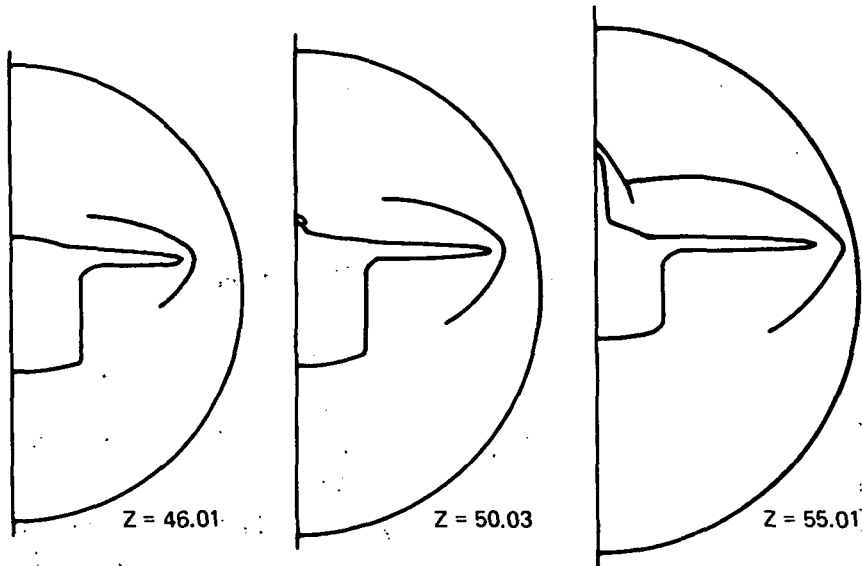


Figure 33.- Concluded.

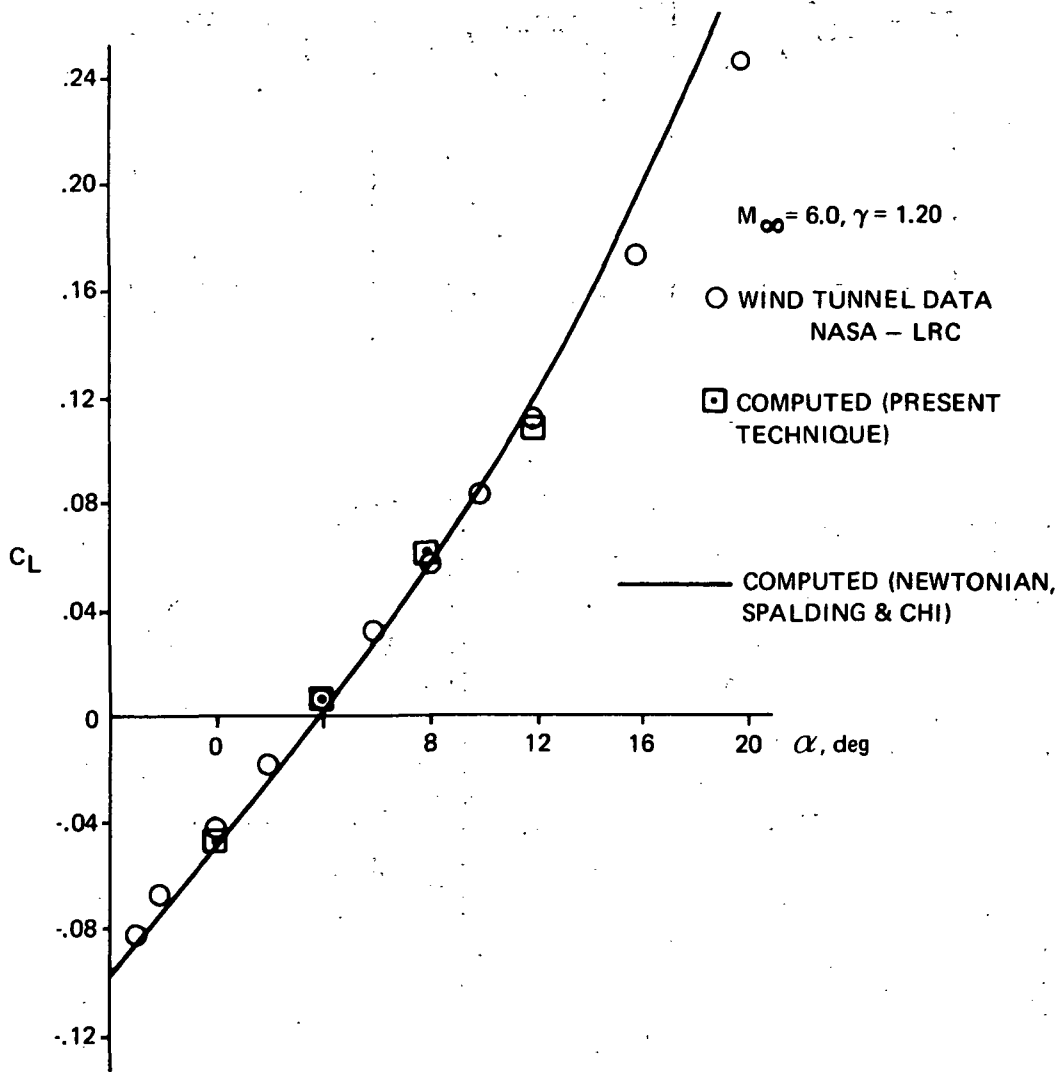


Figure 34.- Hypersonic transport lift as a function of angle of attack.

Page intentionally left blank

NUMERICAL COMPUTATION OF VISCOUS BLUNT BODY FLOWS WITH A PLANAR IMPINGING SHOCK*

By Terry L. Holst, John C. Tannehill,
Iowa State University

and

John V. Rakich
NASA Ames Research Center

SUMMARY

Two-dimensional and three-dimensional viscous blunt body flows with planar impinging shocks are computed using an explicit, time-dependent, finite-difference method to solve the complete set of Navier-Stokes equations. The bow shock is treated as a discontinuity, while all interior shock layer details, such as shear layers, shock waves, jets, and the wall boundary layer, are automatically captured in the solution. Numerical results are presented for cases in which planar shock waves of different strengths and orientations are allowed to impinge on the flow field surrounding an infinite cylinder with resultant two-dimensional and three-dimensional shock interference patterns. The numerical results are compared with experimental results.

INTRODUCTION

An extraneous shock wave impinging on a blunt body in a hypersonic flow has been observed to greatly increase both the heat-transfer rate and pressure near the impingement point (refs. 1 and 2). Flow fields of this type may occur on hypersonic vehicles such as the Space Shuttle.

The intense heating and high pressures occur over a small region where a disturbance, originating at the intersection of the impinging shock and bow shock, strikes the body. The disturbance may be a free shear layer, a supersonic jet, or a shock wave depending on the strength and location of the impinging shock and the shape of the body. Edney (ref. 1) has described six different types of shock interference patterns which can occur.

*Work sponsored by NASA Ames Grant NGR 16-002-038 and the Engineering Research Institute, Iowa State University.

In the present study, both two- and three-dimensional shock impingement flow fields have been numerically computed. In these computations, the impinging shock is planar and intersects the bow shock surrounding an infinite cylinder (fig. 1). In the two-dimensional case, the intersection line is parallel with the axis of the cylinder (z-axis) and, consequently, the flow in each z-plane is identical. This configuration can occur in hypersonic inlets. In the three-dimensional case, the intersection line is curved and is not parallel with the cylinder axis. This configuration can occur when the bow shock from the nose of a vehicle strikes the wing-leading-edge bow shock.

The numerical results of this study were computed by using a time-dependent, finite-difference method to solve the complete set of Navier-Stokes equations for a laminar, compressible flow. The time-dependent approach was chosen because a subsonic region exists in the two-dimensional case and may exist in the three-dimensional case. Since the governing time-dependent equations remain a hyperbolic-parabolic set for both subsonic and supersonic flows, all cases can be solved as an initial-value problem where the steady-state solution is approached asymptotically with time.

SYMBOLS

e	specific internal energy
E	total energy
k	coefficient of thermal conductivity
M	Mach number
p	pressure
Pr	Prandtl number
q	heat flux
q_r, q_θ, q_z	heat flux components
r, θ, z	cylindrical coordinates
r_b	body radius
r_s	shock radius

Re_D	Reynolds number based on cylinder diameter
t	time
T	temperature
u_r, u_θ, u_z	velocity components
β	stretching parameter
γ	ratio of specific heats
Λ	sweep angle
μ	coefficient of viscosity
ρ	density
τ_{ij}	shear stress tensor

Subscripts:

cyl	swept infinite cylinder value
stag	no impingement stagnation value
w	wall value
∞	free-stream condition

GOVERNING EQUATIONS

The equations governing the flow of a compressible, viscous fluid in the absence of body forces and electromagnetic effects can be written in the following weak conservation-law form using three-dimensional cylindrical coordinates:

$$\frac{\partial U}{\partial t} + \frac{\partial F}{\partial r} + \frac{\partial G}{\partial \theta} + \frac{\partial H}{\partial z} + D = 0 \quad (1)$$

where

$$U = r \begin{bmatrix} \rho \\ \rho u_r \\ \rho u_\theta \\ \rho u_z \\ E \end{bmatrix} \quad (2a)$$

$$F = r \begin{bmatrix} \rho u_r \\ \rho u_r^2 + p - \tau_{rr} \\ \rho u_r u_\theta - \tau_{r\theta} \\ \rho u_r u_z - \tau_{rz} \\ (p + E)u_r - \tau_{rr}u_r - \tau_{r\theta}u_\theta - \tau_{rz}u_z + q_r \end{bmatrix} \quad (2b)$$

$$G = \begin{bmatrix} \rho u_\theta \\ \rho u_r u_\theta - \tau_{r\theta} \\ \rho u_\theta^2 + p - \tau_{\theta\theta} \\ \rho u_\theta u_z - \tau_{\theta z} \\ (p + E)u_\theta - \tau_{r\theta}u_r - \tau_{\theta\theta}u_\theta - \tau_{\theta z}u_z + q_\theta \end{bmatrix} \quad (2c)$$

$$H = r \begin{bmatrix} \rho u_z \\ \rho u_r u_z - \tau_{rz} \\ \rho u_\theta u_z - \tau_{\theta z} \\ \rho u_z^2 + p - \tau_{zz} \\ (p + E)u_z - \tau_{rz}u_r - \tau_{\theta z}u_\theta - \tau_{zz}u_z + q_z \end{bmatrix} \quad (2d)$$

$$D = \begin{bmatrix} 0 \\ -(\rho u_\theta^2 + p - \tau_{\theta\theta}) \\ \rho u_\theta u_r - \tau_{r\theta} \\ 0 \\ 0 \end{bmatrix} \quad (2e)$$

$$E = \rho \left(e + \frac{u_r^2 + u_\theta^2 + u_z^2}{2} \right) \quad (2f)$$

The Navier-Stokes expressions for the components of the shear stress tensor and heat flux vector have been used in this study and are given by

$$\left. \begin{aligned} \tau_{rr} &= \mu e_{rr} - \frac{1}{3} \mu (e_{rr} + e_{\theta\theta} + e_{zz}) & \tau_{r\theta} &= \tau_{\theta r} = \mu e_{r\theta} \\ \tau_{\theta\theta} &= \mu e_{\theta\theta} - \frac{1}{3} \mu (e_{rr} + e_{\theta\theta} + e_{zz}) & \tau_{rz} &= \tau_{zr} = \mu e_{rz} \\ \tau_{zz} &= \mu e_{zz} - \frac{1}{3} \mu (e_{rr} + e_{\theta\theta} + e_{zz}) & \tau_{\theta z} &= \tau_{z\theta} = \mu e_{\theta z} \\ e_{rr} &= 2 \frac{\partial u_r}{\partial r} & e_{r\theta} &= \frac{1}{r} \frac{\partial u_r}{\partial \theta} + \frac{\partial u_\theta}{\partial r} - \frac{u_\theta}{r} \\ e_{\theta\theta} &= \frac{2}{r} \frac{\partial u_\theta}{\partial \theta} + 2 \frac{u_r}{r} & e_{\theta z} &= \frac{\partial u_\theta}{\partial z} + \frac{1}{r} \frac{\partial u_z}{\partial \theta} \\ e_{zz} &= 2 \frac{\partial u_z}{\partial z} & e_{rz} &= \frac{\partial u_z}{\partial r} + \frac{\partial u_r}{\partial z} \end{aligned} \right\} \quad (3a)$$

$$\left. \begin{aligned} q_r &= -k \frac{\partial T}{\partial r} \\ q_\theta &= -\frac{k}{r} \frac{\partial T}{\partial \theta} \\ q_z &= -k \frac{\partial T}{\partial z} \end{aligned} \right\} \quad (3b)$$

For the two-dimensional problem, the crossflow (z-component) terms are omitted.

To complete this set of equations the perfect gas equation of state is used. In addition, Sutherland's equation and a constant Prandtl number assumption are used to compute coefficients of viscosity μ and thermal conductivity k .

Equation (1) is transformed from the physical domain (r, θ, z, t) into the computational domain (x, y, z, t) by the following independent variable transformation:

$$\left. \begin{aligned} x &= f \left(\frac{r_s - r}{r_s - r_b} \right) \\ y &= \theta \\ z &= z \\ t &= t \end{aligned} \right\} \quad (4)$$

This transformation maps the z-plane between the bow shock and the blunt body into a rectangular region and stretches the radial distribution of grid points according to the function f. The function f chosen for all cases considered herein is given by (ref. 3)

$$f(a) = \frac{\ln\left(\frac{\beta + a}{\beta - a}\right)}{\ln\left(\frac{\beta + 1}{\beta - 1}\right)} \quad (5)$$

Equation (5) refines the grid near the body and thus permits better boundary-layer resolution. The parameter β controls the amount of refinement and has a practical range between 1 and 2 with the smaller values giving larger amounts of refinement.

NUMERICAL METHOD

Finite-Difference Scheme

Equation (1) is solved by MacCormack's explicit finite-difference method (ref. 4). This method is composed of a predictor-corrector sequence which is second-order accurate in both space and time. For this method to remain stable the allowable time step is limited by the CFL condition. To insure numerical stability in regions of large gradients, a fourth-order smoothing term (ref. 3) is applied in each spatial direction for both the predictor and corrector steps.

Boundary Conditions

Two-dimensional. - The wall boundary conditions are determined by specifying an isothermal wall, a zero normal pressure gradient, and the no-slip condition. The bow shock forms one boundary of the computational region and its location at each time step is determined by using a predictor-corrector method (ref. 3). Flow variables at the row of grid points just inside the bow shock are obtained by applying the exact shock jump relations (Rankine-Hugoniot equations). The impinging shock is introduced at the bow shock by discontinuously changing the free-stream conditions across the intersection point.

The tangential outflow boundaries, both top and bottom, are treated with second-order extrapolations. These boundary conditions are stable provided the outflow Mach number in the inviscid region of the shock layer is supersonic.

Three-dimensional. - The boundary conditions for the three-dimensional case are identical with those of the two-dimensional case with the following exceptions. The geometry in the three-dimensional case permits a plane of symmetry to be assumed along the stagnation line across which reflective boundary conditions are used. The flow con-

ditions at the inflow plane in the crossflow direction are held equal for all time to the conditions from a swept infinite cylinder solution calculated prior to the shock impingement solution. The flow conditions at the outflow boundary are determined by using a zeroth-order extrapolation in the crossflow direction.

RESULTS

Two-Dimensional Case

Two-dimensional shock impingement results were computed with the following free-stream conditions:

$$M_{\infty} = 4.6 \qquad p_{\infty} = 14.93 \text{ N/m}^2$$

$$\text{Re}_{D_{\infty}} = 10\,000 \qquad T_{\infty} = 167 \text{ K}$$

$$\text{Pr} = 0.72 \qquad \gamma = 1.4$$

The cylinder had a diameter of 0.3048 m and a constant wall temperature of 556 K. The free-stream Mach number and impinging shock angles were chosen to correspond with the three-dimensional tests of Edney (ref. 1) in which planar shocks were allowed to impinge upon a hemisphere.

The undisturbed blunt body flow field was computed first and the resulting solution was used as the initial condition for the shock impingement computations. Wall pressures and heat-transfer rates from this undisturbed case compared very well with independent results (ref. 3).

Two two-dimensional shock impingement cases are presented herein with identical intersection positions ($\theta = 90^\circ$) but with different impinging shock strengths. In the first case, the impinging shock made an angle of 16.1° with the free-stream velocity vector. The pressure ratio across this impinging shock was 1.73 with a flow deflection angle of 5° . The results of this computation are shown in figure 2 as a set of Mach number contours which were drawn by a computer plotter in Mach number increments of 0.05. A strong shear layer emanates from the intersection point and makes a tangential approach to the body surface. This shear layer causes moderate increases in heat transfer and wall pressure in the vicinity of the attachment point. The lower sonic line position remains essentially unchanged from the no-impingement case while the upper sonic line position is changed considerably. The new upper sonic line emanates from the intersection point and follows the shear layer to the body.

In the second case, the impinging shock made an angle of 20.9° with the free-stream velocity vector. The pressure ratio across this impinging shock was 2.98 with a flow deflection angle of 10° . The results of this computation are shown in figure 3 as a set of

Mach number contours drawn with the same Mach number increments as in figure 2. The bow shock distinctly shows a "double kink." A strong shear layer emanates from the intersection point (first kink) and strikes the body. An imbedded supersonic region exists between the shear layer and a shock emanating from the second kink in the bow shock. The stagnation point has been shifted approximately 45° around the cylinder by the impingement. At this new stagnation point occur the large increases in heat flux and wall pressure. The shock impingement also causes the bow shock standoff distance below the intersection point to increase dramatically.

Figure 4 is a schlieren photograph of the corresponding three-dimensional test of Edney. A qualitative comparison of the two-dimensional numerical results and three-dimensional experimental results shows the same general features: (1) "double-kinked" bow shock, (2) shear layer emanating from the first kink and striking the body, and (3) an imbedded shock emanating from the second kink in the bow shock. This good agreement gives credibility to the numerical computation.

Comparisons of the wall pressures and heat-transfer rates before and after shock impingement are shown in figures 5 and 6 for the 20.9° shock impingement case. Both curves represent numerical results as no experimental data were available for this set of conditions. The increases in wall pressure and heat transfer rate were both approximately 2.2 times greater than the no-impingement stagnation point values.

Three-Dimensional Case

The preliminary three-dimensional solution presented in this paper was computed with the following free-stream conditions:

$$\begin{array}{ll} M_\infty = 5.94 & p_\infty = 559.1 \text{ N/m}^2 \\ \text{Re}_{D_\infty} = 18\,000 & T_\infty = 59.6 \text{ K} \\ \text{Pr} = 0.72 & \gamma = 1.4 \\ \Lambda = 25.0^\circ & \end{array}$$

The cylinder was 0.025 m in diameter and had a constant wall temperature of 394 K. The free-stream conditions (except for Re_{D_∞}), impinging shock angle, and sweep angle were all chosen to agree with the experiment of Keyes and Hains (ref. 2). The free-stream viscosity was chosen to be an order of magnitude larger than in the experiment, thus making the Reynolds number 10 times smaller; this was done to physically thicken the boundary layer and make its resolution possible with fewer grid points.

At the start of the shock impingement computation, the flow variables in all z -planes were set equal to a previously computed swept infinite cylinder solution. Then, except for the flow variables at the inflow plane which were held fixed, the flow variables

in all other planes were allowed to change during the computation under the influence of the impinging shock.

A comparison of the stagnation plane shock shapes is shown in figure 7. The results of Keyes and Hains were obtained by allowing a planar impinging shock to strike the shock layer on a finite swept cylinder. The intersection point along the stagnation plane was only 3 cm downstream from one end of the cylinder. The shock standoff distance for the initial numerical z-plane is therefore considerably different from the corresponding value of the experimental results. When these curves are examined in light of this difference, the comparison seems quite good.

A comparison of the stagnation line wall pressures is shown in figure 8. The general trend of the comparison is reasonable. However, the peak value in the experimental curve, which is caused by a boundary-layer interaction with a transmitted shock, is not reproduced in the numerical results. A small peak does occur in the numerical results but differs slightly in position from the experimental peak.

A comparison of the stagnation line heat-transfer rates is presented in figure 9. A peak in the heating rate is measured for both the numerical and experimental results although the positions and heights of the peaks are not in good agreement. The coarse grid, numerical smoothing, and increased physical viscosity probably all contribute to the poor resolution of the transmitted shock and, therefore, to the poor agreement. Future investigations will either remove or improve these limitations.

For this preliminary three-dimensional solution, a coarse $21 \times 21 \times 41$ grid was used which requires 90 405 words of array storage. The total program storage (program and array storage) was 120 000 words. The execution time on a CDC 7600 computer was 47 min.

CONCLUDING REMARKS

Both two-dimensional and three-dimensional shock impingement flow fields have been computed by using a time-dependent finite-difference procedure to solve the complete set of Navier-Stokes equations. Good qualitative comparisons were obtained between the two-dimensional numerical results and corresponding three-dimensional experimental results. The three-dimensional numerical result was obtained with a coarse mesh, approximate inflow conditions, and a reduced Reynolds number, resulting in only a qualitative comparison with a corresponding three-dimensional experiment. Future computations will either remove or improve these limitations and approximations. Although the three-dimensional result is preliminary, it does demonstrate the feasibility of such a calculation with present day computers.

REFERENCES

1. Edney, B. E.: Anomalous Heat Transfer and Pressure Distributions on Blunt Bodies at Hypersonic Speeds in the Presence of an Impinging Shock. FFA Rep. 115, Aeronaut. Res. Inst. of Sweden, Feb. 1968.
2. Keyes, J. Wayne, and Hains, Frank D.: Analytical and Experimental Studies of Shock Interference Heating in Hypersonic Flows. NASA TN D-7139, 1973.
3. Tannehill, J. C.; Holst, T. L.; and Rakich, J. V.: Numerical Computation of Two-Dimensional Viscous Blunt Body Flows With an Impinging Shock. AIAA Paper No. 75-154, Jan. 1975.
4. MacCormack, R. W.: The Effect of Viscosity in Hypervelocity Impact Cratering. AIAA Paper No. 69-354, Apr. 1969.

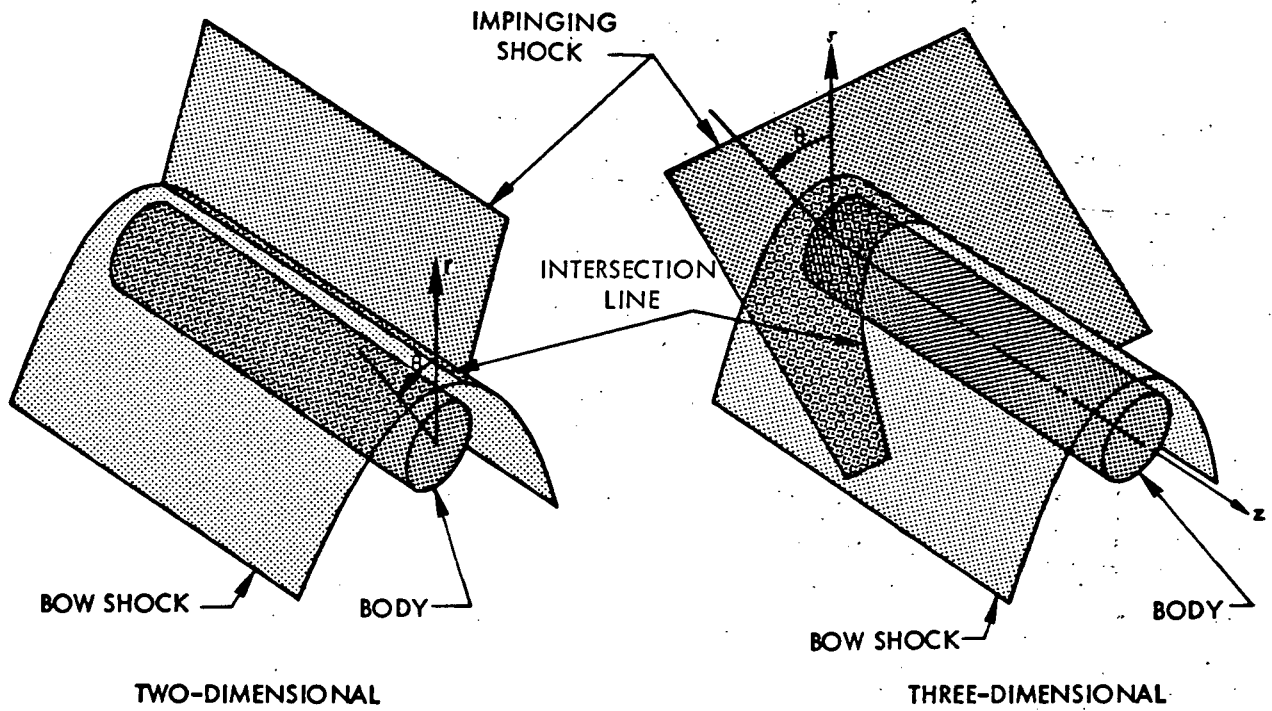


Figure 1.- Shock impingement geometries.

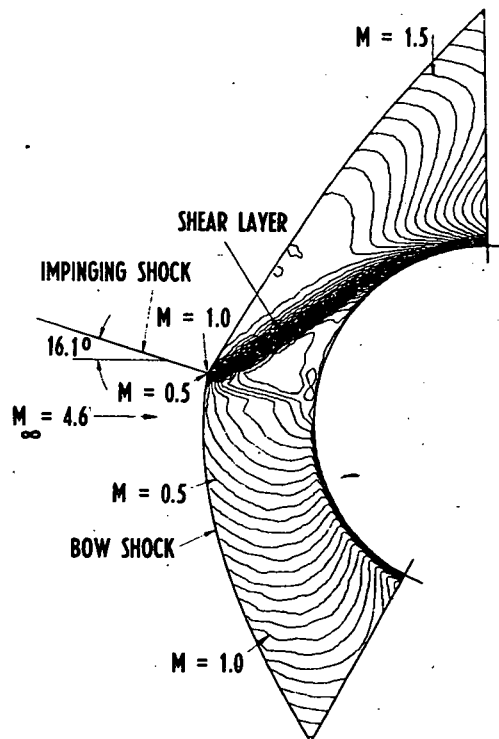


Figure 2.- Mach number contours for 16.1° shock impingement at $\theta = 90^\circ$.

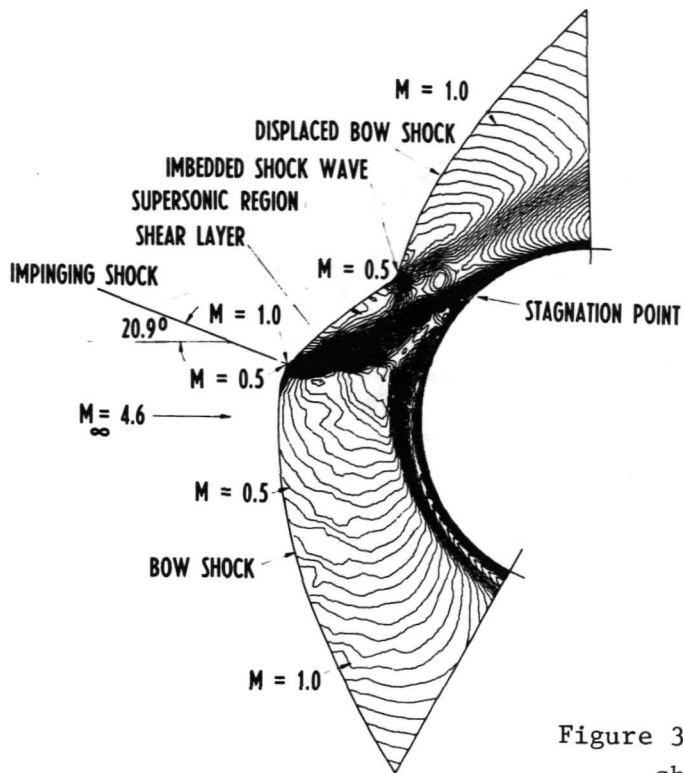


Figure 3.- Mach number contours for 20.9° shock impingement at $\theta = 90^\circ$.

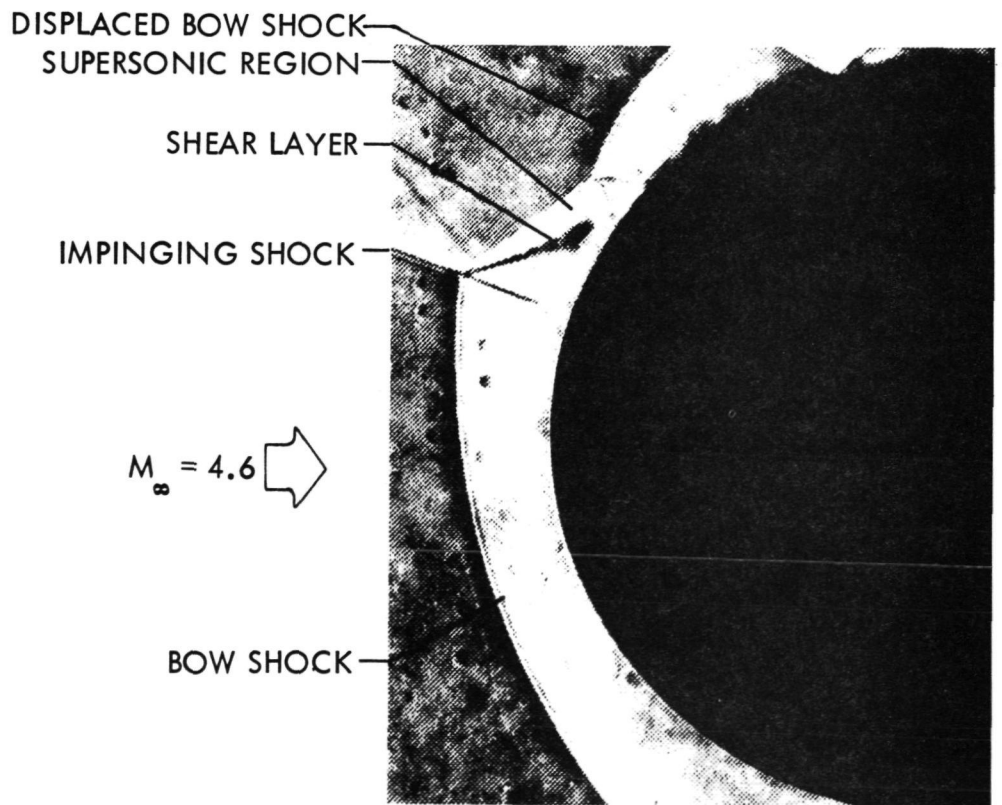


Figure 4.- Three-dimensional experimental result of Edney for 20.9° shock impingement.

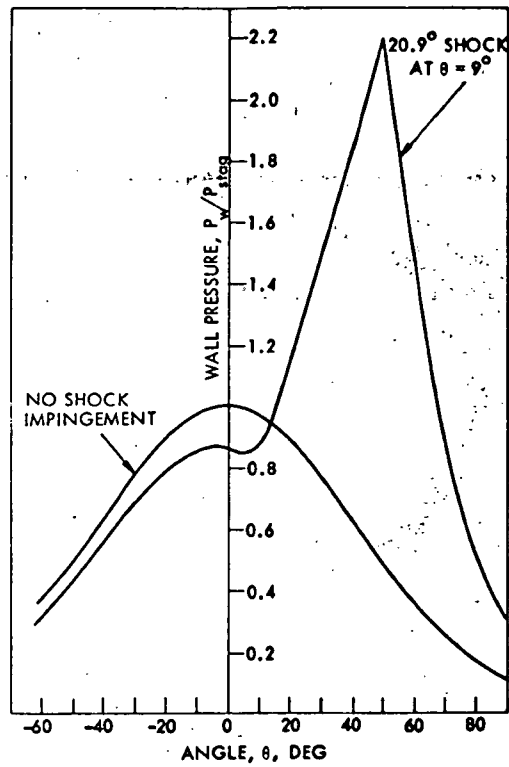


Figure 5.- Comparison of wall pressures.

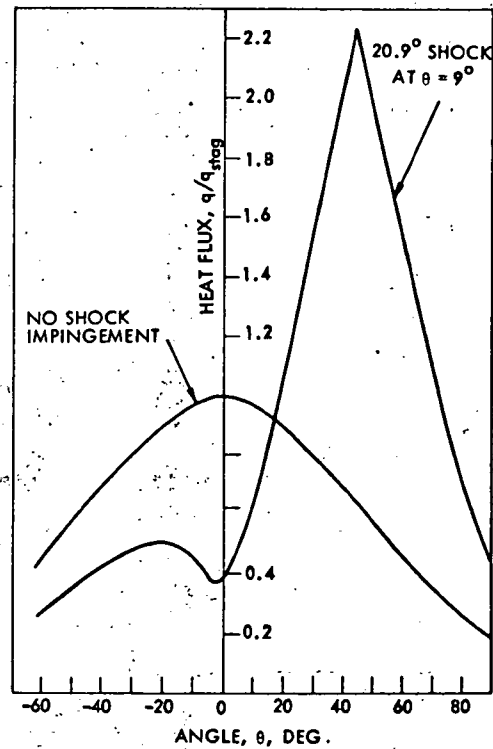


Figure 6.- Comparison of heat-transfer rates.

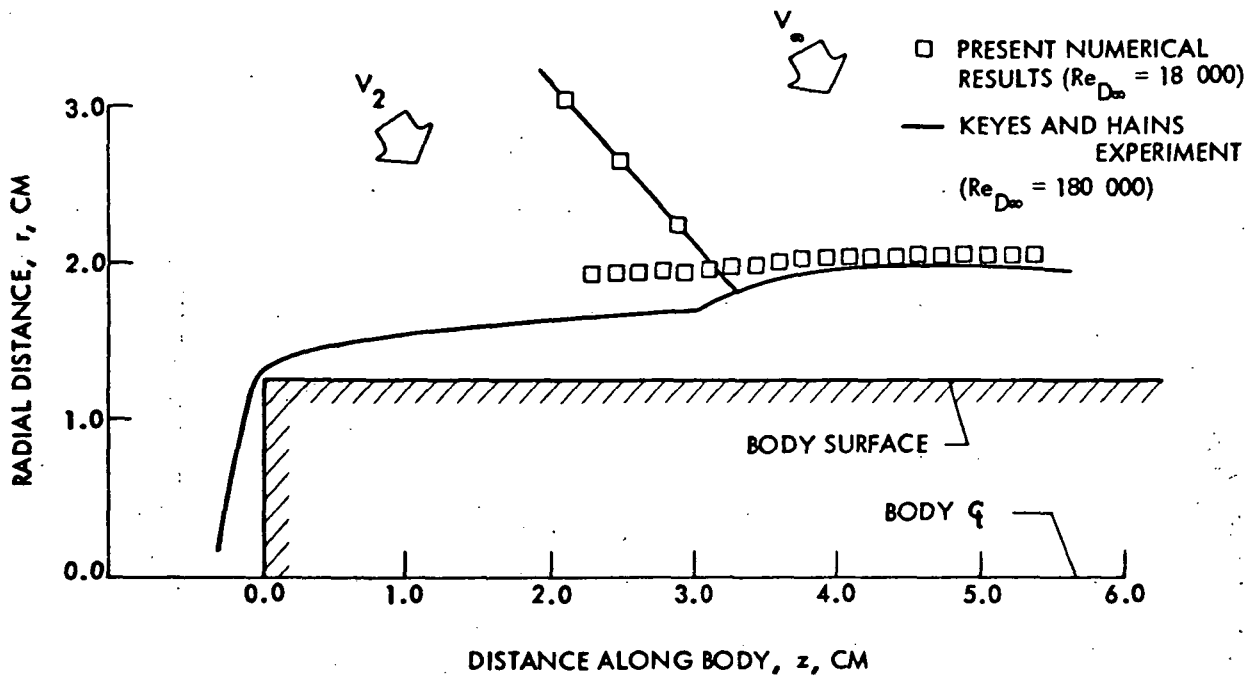


Figure 7.- Stagnation plane shock shapes.

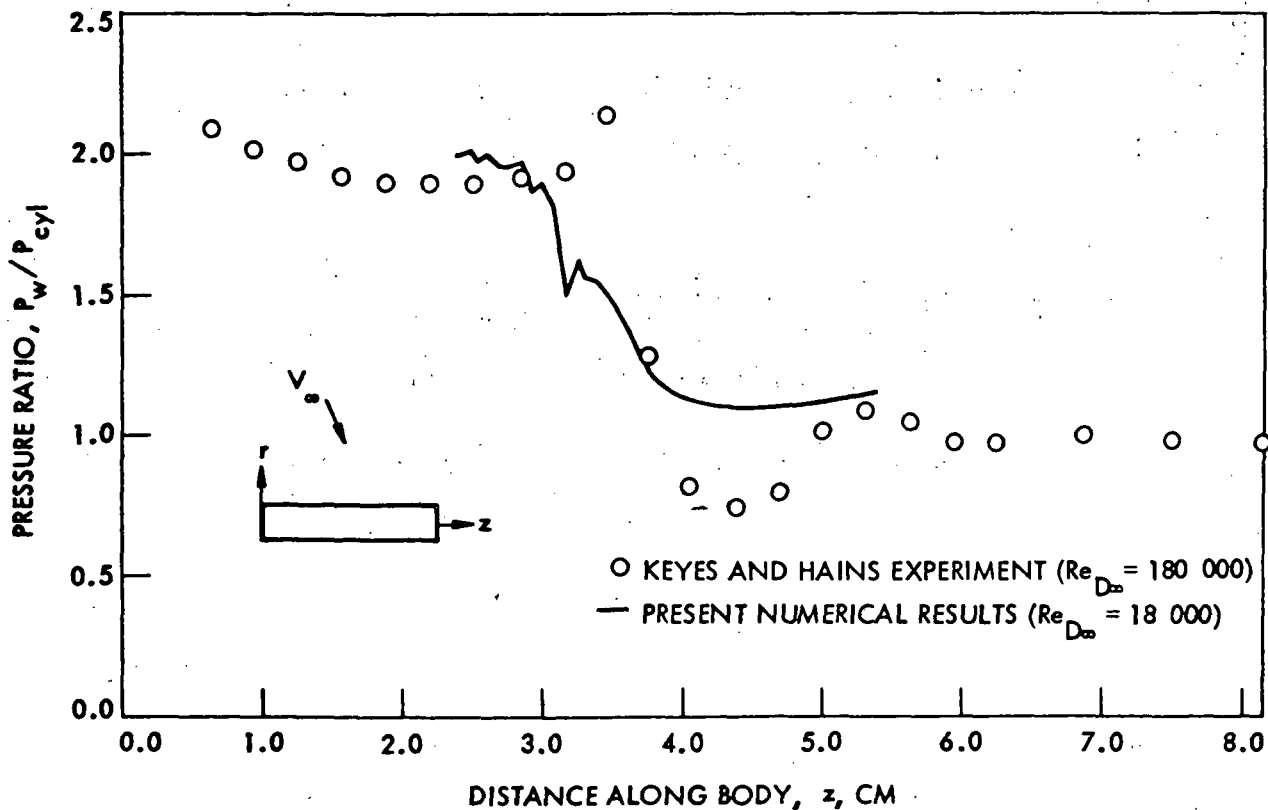


Figure 8.- Stagnation line wall pressures.

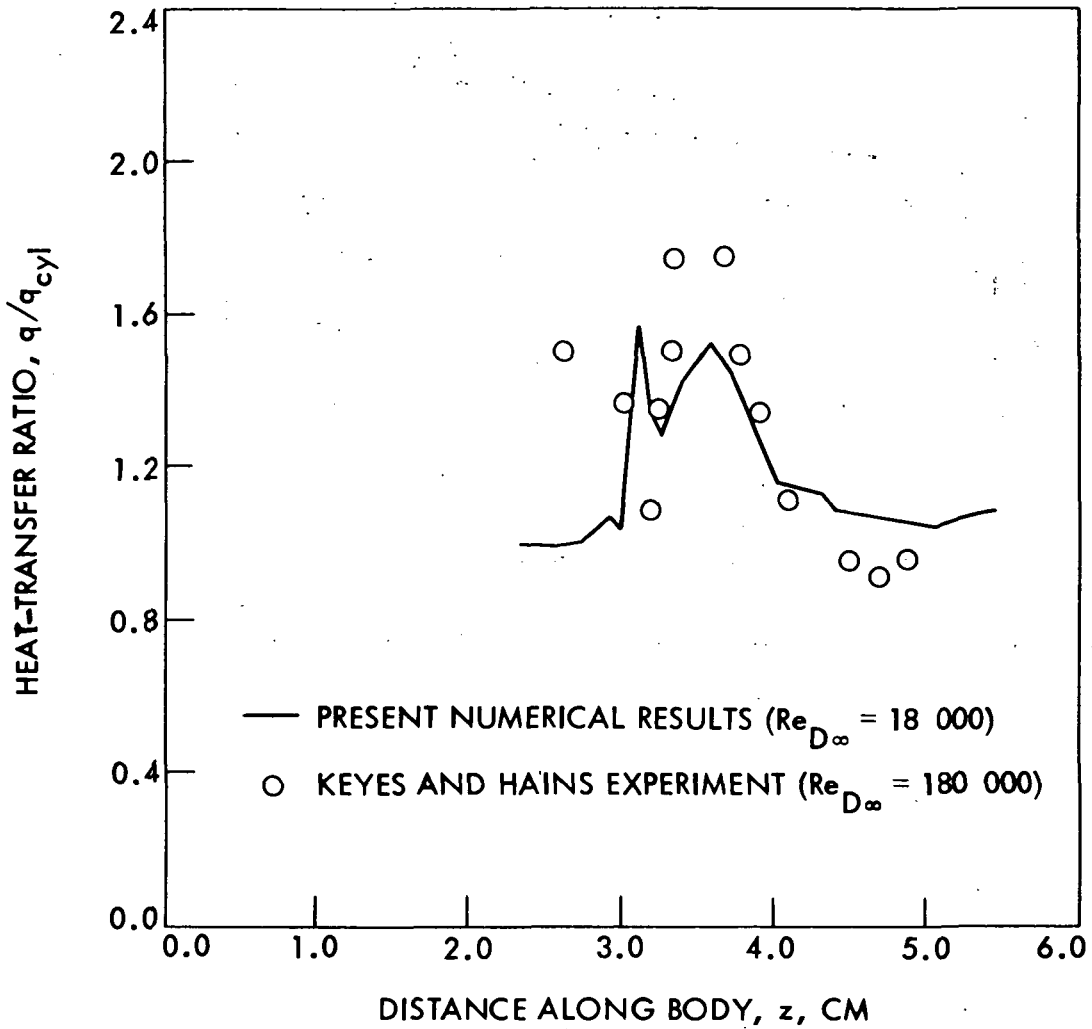


Figure 9.- Stagnation line heat-transfer rates.

NATIONAL AERONAUTICS AND SPACE ADMINISTRATION
WASHINGTON, D.C. 20546

OFFICIAL BUSINESS
PENALTY FOR PRIVATE USE \$300

SPECIAL FOURTH-CLASS MAIL

POSTAGE AND FEES PAID
NATIONAL AERONAUTICS AND
SPACE ADMINISTRATION



National Aeronautics and Space Administration

WASHINGTON, D. C. 20546

OFFICIAL BUSINESS
Penalty For Private Use, \$300.00

POSTAGE AND FEES PAID
NATIONAL AERONAUTICS AND
SPACE ADMINISTRATION
NASA-451



SPECIAL FOURTH CLASS MAIL
BOOK

795 001 C1 U A 750801 S00903DS
DEPT OF THE AIR FORCE
AF WEAPONS LABORATORY
ATTN: TECHNICAL LIBRARY (SUL)
KIRTLAND AFB NM 87117

Postage Not Returnable (Section 158
Postal Manual) Do Not Return

"The aeronautical and space activities of the United States shall be conducted so as to contribute . . . to the expansion of human knowledge of phenomena in the atmosphere and space. The Administration shall provide for the widest practicable and appropriate dissemination of information concerning its activities and the results thereof."

—NATIONAL AERONAUTICS AND SPACE ACT OF 1958

NASA SCIENTIFIC AND TECHNICAL PUBLICATIONS

TECHNICAL REPORTS: Scientific and technical information considered important, complete, and a lasting contribution to existing knowledge.

TECHNICAL NOTES: Information less broad in scope but nevertheless of importance as a contribution to existing knowledge.

TECHNICAL MEMORANDUMS: Information receiving limited distribution because of preliminary data, security classification, or other reasons. Also includes conference proceedings with either limited or unlimited distribution.

CONTRACTOR REPORTS: Scientific and technical information generated under a NASA contract or grant and considered an important contribution to existing knowledge.

TECHNICAL TRANSLATIONS: Information published in a foreign language considered to merit NASA distribution in English.

SPECIAL PUBLICATIONS: Information derived from or of value to NASA activities. Publications include final reports of major projects, monographs, data compilations, handbooks, sourcebooks, and special bibliographies.

TECHNOLOGY UTILIZATION PUBLICATIONS: Information on technology used by NASA that may be of particular interest in commercial and other non-aerospace applications. Publications include Tech Briefs, Technology Utilization Reports and Technology Surveys.

Details on the availability of these publications may be obtained from:

SCIENTIFIC AND TECHNICAL INFORMATION OFFICE

NATIONAL AERONAUTICS AND SPACE ADMINISTRATION
Washington, D.C. 20546